SELCUK UNIVERSITY
FACULTY OF TECHNOLOGY

ICENTE'21

INTERNATIONAL CONFERENCE ON ENGINEERING TECHNOLOGIES

November 18-20, 2021

Konya/TURKEY

PROCEEDINGS

Editor
Prof. Dr Sakir TASDEMIR

E-ISBN: 978-625-44427-7-3

International Conference on Engineering Technologies

5th International Conference, ICENTE
Konya, Turkey, November 18-20, 2021

Proceedings

Editor
Sakir TASDEMIR

International Conference on Engineering Technologies, **ICENTE'21**
Konya, Turkey, November 18-20, 2021

International Conference on Engineering Technologies

5th International Conference, ICENTE
Konya, Turkey, November 18-20, 2021

Proceedings

Editors
Sakir TASDEMIR

E-ISBN: 978-625-44427-7-3

November – 2021

PREFACE

International Conference on Engineering Technologies (ICENTE'21) was organized in Konya, Turkey on 18-20 November 2021.

The main objective of ICENTE'21 is to present the latest research and results of scientists related to Biomedical, Computer, Electrics & Electronics, Mechanical, Mechatronics, Metallurgy & Materials and Civil Engineering fields. This conference provides opportunities for the delegates from different areas in order to exchange new ideas and application experiences, to establish business or research relations and to find global partners face to face for future collaborations.

All paper submissions have been double blind and peer reviewed and evaluated based on originality, technical and/or research content/depth, correctness, relevance to conference, contributions, and readability. Selected papers presented in the conference that match with the topics of the journals will be published in the following journals:

- Artificial Intelligence Studies (AIS)
- Gazi Journal of Engineering Sciences (GJES)
- International Journal of Applied Mathematics, Electronics and Computers (IJAMEC)
- International Journal of Automotive Engineering and Technologies (IJAET)
- International Journal of Energy Applications and Technology (IJEAT)
- MANAS Journal of Engineering (MJEN)
- Open Journal of Nano (OJN)
- Selcuk University Journal of Engineering Sciences (SUJES)

At this conference, there are 267 paper submissions. Each paper proposal was evaluated by two reviewers. And finally, 206 papers were presented at the conference from 13 different countries (Albania, Cyprus, United Kingdom, Georgia, Morocco, Macedonia, Mauritania, Mexico, New Zealand, Pakistan, Poland, Tunisia, Turkey) with 134 local and foreign universities and organizations participating,

In particular, to Selcuk University Rector Prof. Dr. Metin AKSOY; we would like to thank the conference scientific committee, session chairs, invited speakers, referees, technical team, participants, and all our colleagues who have contributed. They have made a crucial contribution to the success of this conference. Our thanks also go to our colleagues in our conference office.

Prof. Dr. Sakir TASDEMIR
Editor

PROGRAMME COMMITTEES

HONORARY CHAIR :

Metin Aksoy, Rector of Selcuk University, Turkey

GENERAL CHAIRS :

Sakir Tasdemir, Selcuk University, Turkey

CO-CHAIRS :

Ilker Ali Ozkan, Selcuk University, Turkey
Ismail Saritas, Selcuk University, Turkey
Lilia Georgieva, Heriot Watt University, United Kingdom
Murat Koklu, Selcuk University, Turkey
Silyan Sibinov Arsov, Rousse University, Bulgaria

SECTION EDITORS :

Adem Golcuk, Fen Bilimleri, Turkey
Fatih Basciftci, Selcuk University, Turkey
Ismail Saritas, Selcuk University, Turkey
Mehmet Cunkas, Selcuk University, Turkey
Mustafa Acarer, Selcuk University, Turkey
Mustafa Altin, Konya Technical University, Turkey
Murat Ciniviz, Selcuk University, Turkey

INTERNATIONAL ADVISORY BOARD :

Abdulkadir Saday, Selcuk University, Turkey
Abdullah Erdal Tumer, Kirgizistan Turkiye Manas University, Kyrgyzstan
Ahmet Fenercioglu, Gaziosmanpasa University, Turkey
Ahmet Yonetken, Afyon Kocatepe University, Turkey
Ahmet Afsin Kulaksiz, Konya Technical University, Turkey
Alexander Sudnitson, Tallinn University of Technology, Estonia
Ali Yasar, Selcuk University, Turkey
Alina Ivan Dramogir, Gheorghe Asachitechnical University of Iasi, Romania
Almoataz Youssef Abdelaziz, Ain Shams University, Egypt
Amar Ramdane Cherif, University of Versailles, France
Anca Loana Andreescu, Academy of Economic Studies, Bulgaria
Anne Villems, University of Tartu, Estonia
Antonella Reitano, University of Calabria, Italy
Antonio Mendes, Universidade De Coimbra, Portugal
Arif Gok, Amasya Teknoloji Faculty, Turkey
Aristomenis Antoniadis, Technical University of Crete, Greece
Artan Luma, South East European University, MACEDONIA
Bahattin Karakaya, Istanbul University, Turkey
Biagio Lenzitti, University of Palermo, Italy
Binod Kumar, Jspm Jayawant Institute of Computer Applications Pune, India
Boris Akanaev, Kazak National University, Kazakhstan
Domenico Tegolo, Universita Degli Studi Di Palermo, Italy
Eisha Akanksha, Mvj College of Engineering, India
Elinda Kajo Mece, Polytechnic University of Tirana, Romania
Engin Ozdemir, Kocaeli University, Turkey
Erol Turkes, Kirklareli University, Turkey
Ertugrul Durak, Suleyman Demirel University, Turkey
Gabriel Luna Sandoval, Sonora State University, Mexico
Hamit Saruhan, Duzce University, Turkey
Hamza Bensouilah, Laboratoire de Mecanique et Structures, Algeria
Hasan Gokkaya, Karabuk University, Turkey
Howard Duncan, Dublin City University, Ireland

ORGANIZING COMMITTEE :

Adem Golcuk, Fen Bilimleri, Turkey
Ayhan Erol, Afyon Kocatepe University, Turkey
Angel Smrikarov, Rousse University, Bulgaria
Fatih Basciftci, Selcuk University, Turkey
Ismail Saritas, Selcuk University, Turkey
Lilia Georgieva, Heriot Watt University, United Kingdom
Mehmet Cunkas, Selcuk University, Turkey
Murat Ciniviz, Selcuk University, Turkey
Mustafa Acarer, Selcuk University, Turkey
Polyxeni Arapi, Technical University of Greece, Greece
Silyan Sibinov Arsov, Rousse University, Bulgaria

TECHNICAL COMMITTEE :

Esra Kaya, Selcuk University, Turkey
Burak Tezcan, Selcuk University, Turkey
Musa Doğan, Selcuk University, Turkey
Abdulkadir Saday, Selcuk University, Turkey

CONTENTS

Comparison of Bulk and Alternative Porous Fixation Plate used in Fracture Fixation in terms of Failure Probability

O. YAVUZ[1,*], I. KAYMAZ[2] , İ.H. KORKMAZ[3] ve F. MURAT[4]

[1] Erzurum Technical University,Erzurum/Turkey, osman.yavuz00@erzurum.edu.tr
[2] Erzurum Technical University,Erzurum/Turkey, irfan.kaymaz@erzurum.edu.tr
[3] Erzurum Technical University,Erzurum/Turkey, ismail.korkmaz@erzurum.edu.tr
[4] Erzurum Technical University,Erzurum/Turkey, fahri.murat@erzurum.edu.tr

***Abstract*- Conventional fixation plates that are permanently placed on the body may cause some adverse effects such as stress shielding and aseptic loosening due to their contact with the bone. As a result of the contact of the bulk fixation plates with the bone surface, blood flow is prevented and necrosis formation is observed on the contact surface. In recent years, porous implants have been used to minimize these mechanical and biological negative features brought about by conventional implants. In the deterministic approaches that are generally used for the design of porous implants, variations in material properties due to uncertainties in the design parameters, the loadings on the plate, and the additive manufacturing process parameters are not taken into account, thus the actual conditions that the plate will be exposed to are not modeled correctly. Therefore, in this study, both deterministic and probabilistic analyzes of a porous implant with a gyroid lattice structure placed on the humeral bone were performed. The results obtained were compared with the probability of failure of the conventional fixation plate. As a result of the study, it has been revealed that the uncertainties in the design parameters significantly affect the failure probability of the plate compared to the deterministic analysis, and probability-based analyzes play an important role for a reliable plate design.**

***Keywords*- Fixation Plate; Failure Probability; porous implants**

I. INTRODUCTION

The purpose of implant applications in bone fractures is to maintain the existing properties of the bone. Therefore, implants must show maximum compatibility both mechanically and biologically. With the development of additive manufacturing, periodic cellular lattice structures suitable for the morphological and mechanical properties of human bone have been produced.

Although porous implants meet the desired mechanical criteria, bone regeneration cannot be fully achieved. Triple periodic minimal surfaces (TPMS) are preferred in the production of porous biomaterials to promote bone regeneration [1], [2]. Gyroid structures, a type of TPMS, offer an alternative structure to increase the existing mechanical properties of orthopedic implants. The mechanical properties of gyroid structures similar to human cortical bone can be achieved by calibration of cell number and surface thickness [3].

There are many studies in the literature related to finite element analysis of porous implants [4]–[8]. However, the parameters and values used in these studies are deterministic. In deterministic analysis, safety factor is used to include only the given dimensions, material properties, uncertainties in the applied load and behavior of the element being analyzed. In order to make a safe design, the minimum strength value of the material under loading and the highest value of the load applied to the material are taken. But the worst-case scenario parameters lead to an excessive design. In probability-based analysis, unlike deterministic analysis, design parameters and other uncertainties are included in the analysis using statistical data. In this way, an excessive design is avoided [9].

There are many studies in the literature on deterministic analysis of porous implants or probability-based analysis of bulk implants [10]–[12]. However, there are few studies on probabilistic analysis of porous implants [13]. In this study, unlike other studies in the literature, probability-based finite element analysis of the fixation plate with gyroid lattice structure was performed.

II. PREPARATION OF THE BONE-IMPLANT MODEL

Computed Tomography images of the artificial humerus bone were modeled in MIMICS software as consisting of two layers, namely cortical and trabecular. The layered humerus bone model was transferred to SolidWorks program to simulate the transfers fracture determined within the scope of the study. To model the fracture without bone contact, the fracture gap was modeled as 10 mm. The mounting process was completed by placing the fixation plate on the anteromedial surface of the humerus bone.

In the studies, it was concluded that the appropriate pore size should be in the range of 100-700 μm in order for porous implants to be compatible with natural bone and to support new bone formation [14]. Accordingly, the ANSYS/SpaceClaim

module was used to model porous implants. In this module, the gyroid lattice structure is formed depending on the lattice length (L) and thickness (d). The cage length and thickness parameters were determined as 1.61 mm and 0.3 mm, respectively, to form a groid cage to support bone regrowth. The middle area is modeled as a gyroid cage, with an offset of 1 mm around the outer edges of the fixing plate and the screw holes (Figure 1). The pore size of the modeled gyroid lattice structure based on these parameters is 0.496 mm.

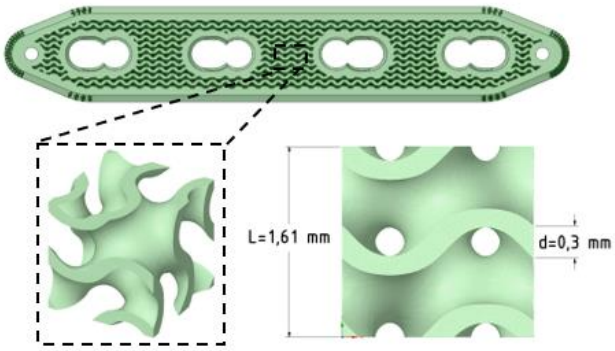

Figure 1: Design parameters of the gyroid fixation plate.

The bone-porous implant model was imported into ANSYS software in Parasolid (.x_t) format for finite element analysis. However, since the plate formed with the model gyroid mesh has too many curved surfaces, it requires too many mesh elements. The multibody part method used in the literature was used to reduce the solution time. Thanks to this method, the material properties of the part modeled as porous are assigned as having an equivalent material model to simplify the analysis, and thus to calculate the displacement, stress, etc. of the humerus-plate system.

III. Finite Element Analysis

For finite element analysis, the bone-implant assembly model was transferred to the structural analysis module of ANSYS software in Parasolid (.x_t) format. The material properties used in the finite element analysis are given in Table 1. The material properties of the composite humerus bone were obtained from the manufacturer [15], [16]. The material properties of the callus in the first week of surgery, were obtained from the literature [17]. The material properties of Ti6Al4V are defined for the 1 mm offset part surrounding the porous part and around the screw holes. [18]. In order to determine the material properties of the gyroid part, the compression tests were performed on cylinder (R=16.1, h=24.15) and cube (16.1x16.1x16.1) samples produced by joint production. Depending on the parameters determined as a result of the experiment, the elasticity modulus and poisson ratio of the gyroid lattice structure were calculated as 4519.917 MPa and 0.306267, respectively.

Table 1: Material properties determined for finite element analysis.

	Young's Modulus	Poisson 's Ratios
Cortical Bone	16000 MPa	0,30
Trabecular Bone	150 MPa	0,30
Bulk Plate	110 GPa	0,31
Bone Screws	110 GPa	0,31
Callus	20 MPa	0,30

The triangular element SOLID187 was chosen as the element type to mesh the bone-implant assembly model. Cortical and trabecular bones are meshed with 3 mm triangular elements. The callus, fixation plate and screws were meshed with 1 mm triangular elements. Depending on these mesh sizes, the skewness value of the bone implant mounting model was found to be 0.29434.

In the finite element analysis, the tensile-compression forces created by the muscles attached to the humerus bone were taken into account as the boundary condition. Bergmann et al. In his study, the resultant force $\left(F_x = -21{,}9\ N, F_y = 7{,}3\ N, F_z = 14{,}6\ N\right)$ occurring at the proximal end of the humerus bone that articulates with the glenohumeral joint during 15° abduction movement was taken as a basis [19]. The humerus bone is fixed at the distal end. Boundary conditions of the humerus bone are given in Figure 2.

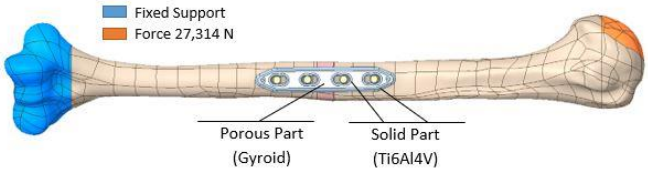

Figure 2: Boundary conditions of the bone-porous implant system.

IV. Probability Based Analysis

The ANSYS/Six Sigma Analysis module was used to calculate the failure probability of the bone-porous implant model. Random variables are parametrically defined in ANSYS to obtain new output values in response to the values of the design variable or the random variables in the inner loop. In the analysis, muscle strength (F_x, F_y, F_z components) that will affect the performance of the fixation plate and the tensile yield strength of the plate were considered as random variables. The mean and standard deviation values of random variables were determined with 10% variation in material property values and muscle strength values considered in deterministic stress analysis. Statistical magnitudes of random variables are given in Table 2.

Table 2: Material properties determined for finite element analysis.

Random Variable	Distribution Type	Mean	Standard Deviation
$F_x\ (N)$	Normal	21,9	2,19
$F_y\ (N)$	Normal	7,3	0,73
$F_z\ (N)$	Normal	14,6	1,46
Ti6Al4V E (MPa)	Normal	895	89,5
Gyroid E (MPa)	Normal	50	5

The probability distribution function type and standard

deviation of random variables are defined in the Design of Experiment cell. The parameters of the response surface method are entered in the response surface cell and statistical quantities showing the accuracy of the response surface function are calculated.

V. RESULTS

In this study, with the help of CT data of the composite humerus bone, a three-dimensional bone model in which the fixation plate will be placed was obtained. The mechanical behavior of bulk and porous fixation plates under anatomical boundary conditions was investigated. Since mean values are used in deterministic analysis, the results were obtained based on a single mean value. However, in probability-based analysis, statistical data was used instead of a single value. Probabilistic analysis of both bulk and porous fixation plates was performed. In this analysis, the material modulus of elasticity of the plate, the muscle forces and the modulus of elasticity of the gyroid lattice structure were defined as random variables.

A. *Deterministic Analysis Results*

The von Mises stress (MPa), strain (mm/mm) and displacement (mm) occurring in the porous plate as a result of the deterministic analysis are given below.

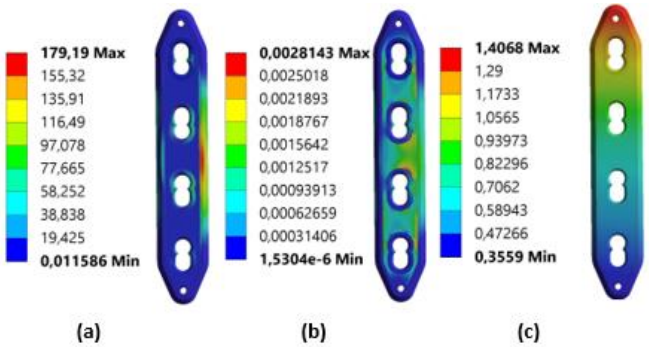

Figure 3: Distribution of von Mises stress (MPa) (a), strain (b) and displacement (c) on the fixation plate.

The new model obtained by the multibody part method represents the porous plate. Due to the pores created in the plate, there was a decrease in volume and density compared to the bulk plate. As a result, a new plate structure was formed, in which the strain shield effect would be less visible, thanks to the low modulus of elasticity of the gyroid porous structure.

When the stress distribution in the porous plate is examined, as expected, the maximum von Mises stress was observed in the middle part of the plate. As shown in Figure 3 (a), the von Mises distribution is not homogeneous. This is due to the difference in modulus of elasticity between the porous part (4,519 GPa) and the bulk part (110 GPa). However, as shown in Figure 3 (b), the stress distribution is homogeneous.

Since the humerus bone is taken into account in the first week of the surgery, the maximum stress value on the plate is low. Since the maximum stress value (179.19 MPa) is below the yield value (860-984 MPa) of the plate material, the fixation plate was evaluated as safe against permanent damage [20].

B. *Probability Based Analysis Results*

As mentioned in the previous chapters, an output value is obtained in response to an average input value in deterministic analyzes. However, in probability-based analysis, the input value is determined based on statistical values. Accordingly, the output data is also obtained as a statistical distribution. In this way, excessive designs made by determining a high factor of safety are avoided.

In this study, the von Mises stress value was obtained as the output parameter against the input parameters determined as muscle strength and material properties. The cumulative graphs and histogram graphs obtained as a result of the analysis performed in the ANSYS/Six Sigma Analysis module are given below. As shown in Figure 4, the probability of getting different values for the mean values used in the deterministic analysis is different from zero.

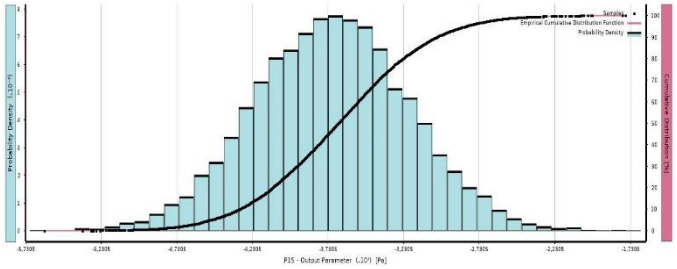

Figure 4: Cumulative distribution and histogram plot.

While calculating the probability of damage in ANSYS, firstly the performance function ($g(x) = \sigma_{max} - \sigma_{ys} \leq 0$) is defined in the Parameter Set cell as a new output parameter.

In probability design, performance functions are defined as limit state (= 0), damage state (0 ≥), and no damage state (≤ 0). In order to obtain the statistical values of the performance function in ANSYS, the probability of damage of the porous fixation plate was calculated by entering the zero value in the bottom line of the probability table obtained as a result of the six sigma analysis.

In this study, probabilistic analysis was performed to determine the effect of uncertainties on the tensile strength of the porous fixation plate. As a result of the analysis, it was observed that the variations of the material properties and force were effective on the stress occurring in the plate. As a result, it has been observed that the effect of probability-based analysis is highly effective in designing more reliable fixation plate design.

ACKNOWLEDGMENT

This study is supported by Scientific and Technological Research Council of Turkey (TUBITAK) under the Project

code 218M425. We would like to thank TÜBİTAK for their contributions.

REFERENCES

[1] M.-T. Hsieh, M. R. Begley, ve L. Valdevit, *Architected implant designs for long bones: Advantages of minimal surface-based topologies,* Materials & Design, 2021.

[2] C. Yan, L. Hao, A. Hussein, ve P. Young, *Ti–6Al–4V triply periodic minimal surface structures for bone implants fabricated via selective laser melting,* Journal of the Mechanical Behavior of Biomedical Materials,2015.

[3] E. Yang *vd.*, *Effect of geometry on the mechanical properties of Ti-6Al-4V Gyroid structures fabricated via SLM: A numerical study*, Materials & Design, 2019.

[4] H. E. Burton *vd.*, *The design of additively manufactured lattices to increase the functionality of medical implants*, Materials Science and Engineering: C,2018.

[5] B. Zhang *vd.*, *The biomimetic design and 3D printing of customized mechanical properties porous Ti6Al4V scaffold for load-bearing bone reconstruction*, Materials & Design, 2018.

[6] A. Rahimizadeh, Z. Nourmohammadi, S. Arabnejad, M. Tanzer, ve D. Pasini, *Porous architected biomaterial for a tibial-knee implant with minimum bone resorption and bone-implant interface micromotion,* Journal of the Mechanical Behavior of Biomedical Materials, 2017.

[7] A. Moussa, *Topology optimization of 3D-printed structurally porous cage for acetabular reinforcement in total hip arthroplasty,* Journal of the Mechanical Behavior of Biomedical Materials, 2020.

[8] H. Mehboob, F. Tarlochan, A. Mehboob, ve S.-H. Chang, *Finite element modelling and characterization of 3D cellular microstructures for the design of a cementless biomimetic porous hip stem,* Materials & Design, 2018.

[9] İ. Kaymaz ve R. Sadeler, *Mühendislik Tasarımında Olasılığa Dayalı Tasarım Yöntemlerinin Kullanımı*, Makine Tasarım ve İmalat Dergisi, 2002.

[10] C. Dopico-González, A. M. New, ve M. Browne, *Probabilistic finite element analysis of the uncemented hip replacement—effect of femur characteristics and implant design geometry*, Journal of Biomechanics, 2009.

[11] T. Guda, T. A. Ross, L. A. Lang, ve H. R. Millwater, *Probabilistic analysis of preload in the abutment screw of a dental implant complex,* The Journal of Prosthetic Dentistry, 2008.

[12] H. Wille, E. Rank, ve Z. Yosibash, *Prediction of the mechanical response of the femur with uncertain elastic properties*, Journal of Biomechanics,.2012.

[13] G. Wanki, S. Ekwaro-Osire, J. P. Dias, ve A. Cunha, *"Risk-Based Analysis of Femoral Stem Considering Uncertainty in its Design Parameters",* 2019 Design of Medical Devices Conference, Minneapolis, Minnesota, USA, Nis. 2019.

[14] L. Mullen, R. C. Stamp, W. K. Brooks, E. Jones, ve C. J. Sutcliffe, *Selective Laser Melting: A regular unit cell approach for the manufacture of porous, titanium, bone in-growth constructs, suitable for orthopedic applications,* J. Biomed. Mater. Res., 2009.

[15] Y.-K. Tu, *Finite Element Simulations of Bone Temperature Rise During Bone Drilling Based on a Bone Analog*, J. Med. Biol. Eng., 2013.

[16] R. Lamdan, M. Liebergall, A. Gefen, N. Symanovsky, ve E. Peleg, *Pediatric supracondylar humerus fractures: effect of bone–implant interface conditions on fracture stability,* J Child Orthop, 2013.

[17] H.-J. Kim, S.-H. Kim, ve S.-H. Chang, *Finite element analysis using interfragmentary strain theory for the fracture healing process to which composite bone plates are applied,* Composite Structures, 2011.

[18] Y.-K. Zhang, H.-W. Wei, K.-P. Lin, W.-C. Chen, C.-L. Tsai, ve K.-J. Lin, *Biomechanical effect of the configuration of screw hole style on locking plate fixation in proximal humerus fracture with a simulated gap: A finite element analysis,* Injury, 2016.

[19] G. Bergmann, F. Graichen, A. Bender, M. Kääb, A. Rohlmann, ve P. Westerhoff, *In vivo glenohumeral contact forces—Measurements in the first patient 7 months postoperatively,* Journal of Biomechanics, 2006.

[20] H. Galarraga, D. A. Lados, R. R. Dehoff, M. M. Kirka, ve P. Nandwana, *Effects of the microstructure and porosity on properties of Ti-6Al-4V ELI alloy fabricated by electron beam melting (EBM),* Additive Manufacturing, 2016.

EEG Based Automatic Sleep Staging via Simple 2D-Convolutional Neural Network

Ibrahim KAYA[1]

[1] Izmir Katip Celebi University, Izmir/Turkey, ibrahimkaya21@yahoo.com

Abstract **- Sleep disorders have high prevalence and cause various health problems. For the diagnostics of these disorders and assessment of the sleep quality, many physiological data are collected using polysomnogram (PSG) method. The most important PSG data is the EEG recorded from the brain during sleep. Analysis of hours of sleep EEG data by experts is an onerous task which requires high attention. Recently, many automatic sleep staging classifiers using EEG are developed in order to prevent human error, and to provide a quick objective analysis. They use machine learning techniques and predict the sleep stage of each EEG epoch. Compared to traditional machine learning, deep learning which requires no hand-crafted feature extraction was able to classify sleep stages better. 1D Convolutional Neural Networks (CNN) are the main methods used in automatic sleep staging recently. In this research a simple 2D-CNN based automatic sleep staging feasibility is investigated. It has been found that a 2D CNN can classify the sleep stages by accuracy of 92.55% and with a Cohen's kappa of 0.82.**

Keywords **- Automatic Sleep Staging, EEG, Deep Learning, Convolutional Neural Network (CNN).**

I. INTRODUCTION

SLEEP is a vital process for human health and function. Correct and early diagnosis of sleep problems is critical. Sleep staging is used to diagnose sleep disorders. It is done by collecting diagnostic data from subjects during sleep and evaluation by sleep experts. Overnight polysomnogram (PSG) is a gold standard method to investigate the quality of sleep and rate the sleep stages [1]. In PSG, many sensors are connected to the subject and various data such as EEG, EOG, EMG, ECG, respiratory efforts, airflows, and blood oxygenation are collected [2]. EEG is the most widely used reliable data related with the brain activity. Human sleep consists of repetitions of six different stages which are: wakefulness (W), and 4 Non Rapid Eye Movement (REM) stages (S1-S4), and REM sleep as described by Rechtschaffen and Kales (R&K) [3-4]. A night sleep usually involves 90 minutes cycles of N2 N3 REM and N1 [5]. This cycle repeats 4-5 times in one night sleep.

In the sleep staging various features such as K-complexes, spindles, alpha bursts, amplitudes, frequency content, EMG level, eye movements are used [6]. In a typical PSG, EEG data is segmented with 30s epochs and each epoch is classified as one of the 6 stages of sleep. However, the American Academy of Sleep Medicine (AASM) has another standard suggesting grouping sleep epochs into 5 distinct sleep stages [7]. Sleep staging used to be done by inspection of each epoch by a trained sleep expert, however since PSG data contains many hours of information it is very time consuming and prone to mistakes. Therefore, some sort of automatic sleep staging is required. While manual feature extraction based machine learning methods have reasonable performances in the automatic sleep staging by EEG, there exist some limitations such as prior knowledge and inability to generalizing to broader datasets and different subjects [8]. Thus, deep learning methods become a better alternative, since they do not require the hand crafted feature extraction and can be generalized to new different data easily.

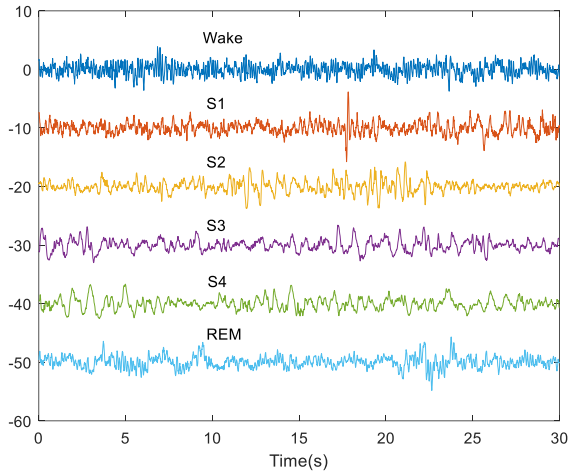

Figure 1: 6 Different sleep stages according to R&K.

Among the deep learning methods used in EEG research, Convolutional Neural Networks offer promising results. The most of the deep learning architectures for EEG signals consists of various CNN models [9]. CNN based architectures using multiple convolutional layers with maximum pooling layer designs dominate the field [9]. In CNN structures convolution layers and pooling layers extract features and the fully connected layer acts as a classifier. In these, the number of convolutional layers and type of the end classifiers constitute the critical design parameters. ReLU has been found to be the most widely used (70%) convolutional layer activation function [9]. Similarly, the trend in the classifier fully-connected layers is the use of a softmax activation function [9]. In terms of input design EEG based deep learning studies can be grouped into three; calculated features, images and single values as inputs [9]. It is possible to achieve higher accuracy using signal values as direct inputs instead of using images and calculated features as inputs. Bojarski, et al. found that neural networks with sufficiently large amounts of data can learn complex features easily without manually preparing the features [10]. Therefore smaller network designs are able to find solutions to

classification problem with the least number of computation. This allows researchers to feed raw EEG signal data as input to the CNN without preprocessing and obtain good performance [9-10]. CNN studies demonstrated higher accuracy using signal values as direct inputs rather than using images and calculated features as inputs [9]. Although there are many EEG based automatic sleep staging methods, most of the 2D CNN approaches involves spectrogram kind of 2D transformations of the EEG data [11].

In this 2D CNN approach, I introduced a direct time signal reshaped as the image matrix and feed to the 2D simple CNN architecture. CNN network is trained and tested on a subset of the large sleep-edf expanded dataset.

II. Materials and Method

The data is obtained from the sleep-edfx expanded database on physionet [12]. The dataset contains 197 whole-night PSG sleep recordings, however only the first 20 subject recordings are used, because there is a clear subject age difference between the first 20 subjects and the rest. The selected dataset consists of two PSG files for each of 20 subjects with ages ranging from 25 to 34. Each subject recordings took place during two consequtive day and night periods, except subject 13 who had only one night data. Also each PSG file is associated with a hypnogram file which basically labels the data epochs as Wake, REM, Stage 1, Stage 2,Stage 3, Stage 4, M (Movement time) and ? (not scored) according to R&K sleep staging method. In PSG data there are four electrode recordings from two EEG channels Fpz-Cz and Pz-Oz, one EOG and one EMG channels. In addition, there are Resporonasal, EMGSubmenta, Tempbody, and Eventmarker in the data. In this study, two channels of EEG data from Fpz-Cz and Pz-Oz electrodes are exploited. The sampling rate is 100Hz and one sleep EEG epoch contains 3000 time series data points corresponding to 30s. Epochs labelled as M and ? are excluded from the dataset. The sleep data stages are converted from 6 stage R&K standard to conventional AASM staging standard of 5 sleep stages by combining the stages 3 and stages 4 as N3. In AASM there are Wake ,three non-REM N1, N2, N3 stages and a REM stage. The distribution of sleep stages in the dataset is not even and this is a major problem with the proper training of the network.

A single dimensional time series EEG signal is converted into a 2D image to fit the input format and to train 2D CNN model as shown in Figure-2. EEG sleep epochs of 30s or 3000 data points from Fpz-Cz channel are reshaped into 50x60x1. Similarly another image color layer is created by subtracting the 30s, 3000 data points of Pz-Oz from the Fpz-Cz channel data and assigned as the second color of the 50x60x2 image.This subtraction which a basic spatial filtering, cancelled the common background activity between Fpz-Cz and Pz-Oz electrodes.

The hold out method is used to separate the test and train data. The first 14 subjects, Subjects S0 to S14 (excluding S13) are included in the training set and remaining 5 subjects (S15-S19) are grouped as the test dataset. Following the training, the model is tested with the data that has never been used in training.

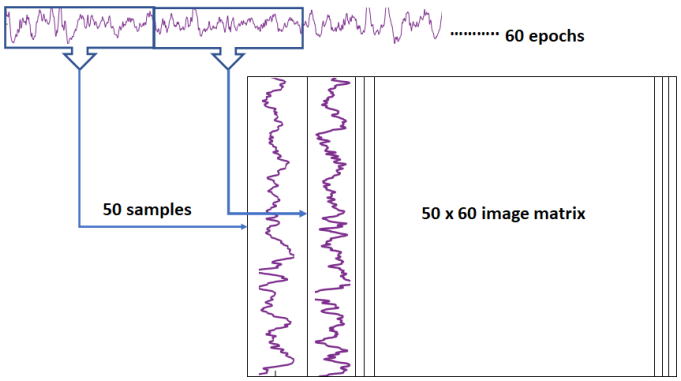

Figure 2: 2D image formation from time series EEG data

In CNN architecture, first a 2D convolution layer is used to extract the features. It applies sliding convolutional filters to 2D input. Batch normalization layer is used between convolutional layers and ReLU to speed up training of the convolutional neural network and reduce the sensitivity to network initialization. ReLU layer is used as the activation function between layers in order to account for nonlinearity of the network. It replaces all the negative pixel values with zeroes. A 2-D max pooling layer is inserted after ReLU layers to perform downsampling of the input. It divides the input into rectangular pooling regions then computes the maximum of each region. Therefore the number of parameters and computational load in the network is reduced and overfitting can be controlled. In the full connected layer, the input is multiplied by a weight matrix and then bias vector is added. Fully connected layer uses all of the features from the previous layers across the image to recognize the larger patterns. These layers are repeated a couple of times to increase the complexity of the model. Finally softmax layer together with a classification layer assigns the sleep stage with the highest probability as the output of the classifier. The overall diagram of the 2D CNN model is given in Figure-3. The number of convolutional level can be reduced further to minimize the complexity and the number of parameters. The filter sizes, paddings, strides can be optimized.

III. Results and Discussion

The results are evaluated by the accuracy, precision, recall, F1-score, and Cohen's Kappa (K) values computed for the test group, namely Subjects 15-19. The formulas for calculation of the above mentioned metrics are given in equations (1) (2) (3) (4) (5) in order [13].

$$Accuracy = \frac{TP + TN}{TP + TN + FP + FN} \quad (1)$$

$$Precision = \frac{TP}{TP + FP} \quad (2)$$

$$Recall = \frac{TP}{TP + FN} \quad (3)$$

$$F1 - score = \frac{2\ Precison\ Recall}{Precision + Recall} \quad (4)$$

$$K = \frac{\frac{\sum_{i=1}^{n} x_{ii}}{N} - \frac{\sum_{i=1}^{n} x_{ii} \left(\sum_{j=1}^{n} x_{ij} \sum_{j=1}^{n} x_{ji} \right)}{N^2}}{1 - \frac{\sum_{i=1}^{n} x_{ii} \left(\sum_{j=1}^{n} x_{ij} \sum_{j=1}^{n} x_{ji} \right)}{N^2}} \quad (5)$$

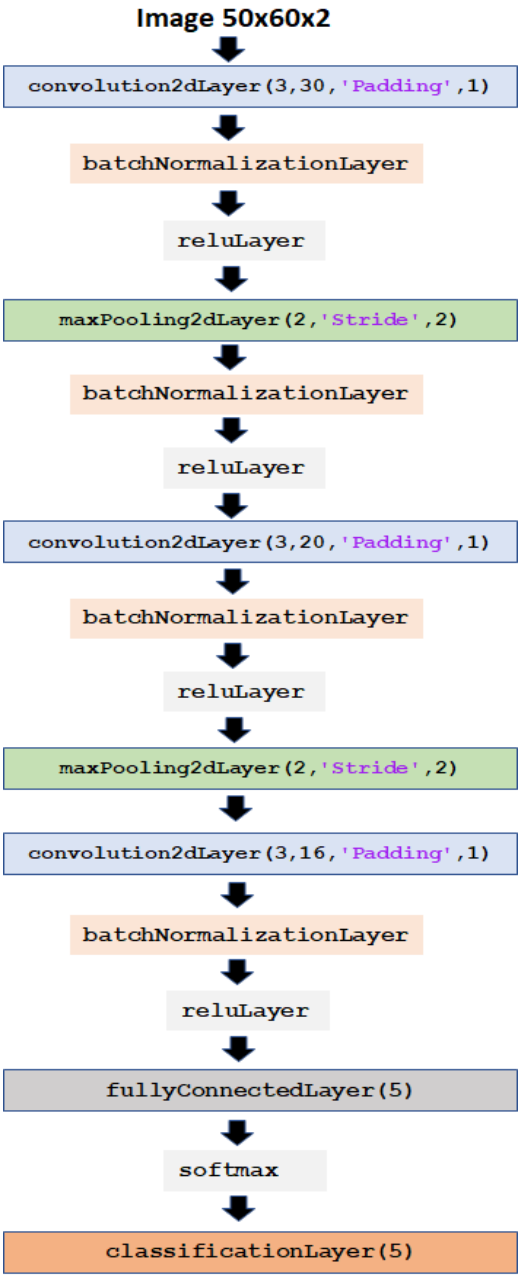

Figure 3: The 2D CNN model tested for sleep staging.

Table 1: The confusion chart for the test data is given.

		Predicted				
		Wake	**N1**	**N2**	**N3**	**REM**
True	**Wake**	17633	60	72	9	269
	N1	175	106	86	1	252
	N2	152	60	3832	262	353
	N3	3	3	183	1539	0
	REM	231	122	285	1	1595

In Table 1, each cell shows the number of epochs from the row label classified as column label. The low accuracy in the classification of N1 is observed in other studies as well [13].

Table 2: Classification performances for each sleep stage

Stage	**Prob.**	**Recall**	**Precision**	**F1-score**
Wake	0.66	0.98	0.97	0.97
N1	0.02	0.17	0.30	0.22
N2	0.17	0.82	0.86	0.84
N3	0.06	0.89	0.85	0.87
REM	0.08	0.71	0.65	0.68
Macro	1.00	0.72	0.73	0.72

Table 3: Accuracy and Cohen's kappa values for test subjects.

Subject	**Accuracy (%)**	**Cohen's Kappa (K)**
S15	94.63	0.89
S16	89.63	0.80
S17	86.14	0.74
S18	92.66	0.84
S19	89.59	0.82
Mean	90.55	0.82

Table 4:Results of the deep learning studies in this field.

Study	**Accuracy %**	**Macro F-1**	**Cohen's kappa**
Xu et al. [14]	85.53	81.18	0.80
Tsinalis et al. [15]	78.9	84	
Cai et al. [16]	87.21	-	0.80
Phan et al. [11]	81.9		0.75
Supratak et al. [17]	82	76.9	0.76
Fu et al. [18]	83.78	82.14	0.77
Mousavi et al. [19]	84.26	79.66	0.79
Khalili & Asl [20]	85.39	79.29	0.80
Salamatian & Khadem [21]	94.09	-	-
Zhou et al. [13]	86.1		0,81
This study	90.55	72.00	0.82

Deep learning method (1D CNN) presented in Yildirim et al. 2019 study achieved 90.98 % accuracy however they used EOG channel in addition to EEG [22].

Xu et al. found that sleep dataset annotation may be inaccurate due to high workload of the sleep experts [14]. Therefore this also deteriorates the automatic classification performance. Another point is the high misclassification of the N1 stage, this is attributed to the extremely small percentage of the N1 stage in the dataset and the similarity between N1 and REM stages [14].

Although Salamatian & Khadem developed a 1D CNN and obtained great accuracy, however the confusion matrix that is provided is from a very small data [21].

IV. Conclusion

This study demonstrates the efficient use of a simple 2D CNN in automatic sleep staging. It achieved performance comparable to the state of the art methods, however there are differences in the data and preprocessing steps. In future studies, first I am interested in optimizing the 2D image matrix generation Then I want to evaluate the efficacy of the method on the in bed data only, and broader sleep-edfx dataset or alternative datasets. I am also interested in incorporating multiple PSG data such as EOG EMG into the deep learning 2D CNN algorithm. Moreover, I want to tackle the problem of data imbalance which prevents the proper classification of N1 stage. Another direction could be comparison of the possible electrode channels and spatial filtering approaches before applying CNN architecture.

References

[1] W.H. Spriggs, Essentials of Polysomnography; Jones & Bartlett Learning: Burlington, MA, USA, 2014.

[2] H. Schulz, "Rethinking sleep analysis," Journal of Clinical Sleep Medicine. vol. 4 no. 2, pp. 99–103, 2008

[3] T. Hori, Y. Sugita, E. Koga, S. Shirakawa, K. Inoue, S. Uchida,; H. Kuwahara, M. Kousaka, T. Kobayashi, Y. Tsuji, et al. Proposed supplements and amendments to 'A Manual of Standardized Terminology, Techniques and Scoring System for Sleep Stages of Human Subjects', the Rechtscha_en & Kales (1968) standard. Psychiatry Clin. Neurosci., 55, 305–310. 2001.

[4] Carley, D.W.; Farabi, S.S. Physiology of sleep. Diabetes Spectr. 29, 5–9. 2016

[5] Özen G., Sultanov R., Özen Y., Güneş Z.Y. A Convolutional Neural Network Based on Raw Single Channel EEG for Automatic Sleep Staging. Sakarya University Journal of Computer and Information Sciences, 3(2), 149-158. 2020.

[6] Šušmákov K. "Human sleep and sleep EEG." Measurement science review 4.2 pp. 59-74, 2004.

[7] Berry, R.B., Brooks, R., Gamaldo, C.E., Harding, S.M., Marcus, C. and Vaughn, B.V., 2012. The AASM manual for the scoring of sleep and associated events. Rules, Terminology and Technical Specifications, Darien, Illinois, American Academy of Sleep Medicine, 176, p.2012.

[8] Mousavi, Z., T. Yousefi Rezaii, S. Sheykhivand, A. Farzamnia, and S. N. Razavi. "Deep convolutional neural network for classification of sleep stages from single-channel EEG signals." Journal of neuroscience methods 324 (2019): 108312.

[9] Craik A, He Y, Contreras-Vidal JL. Deep learning for electroencephalogram (EEG) classification tasks: a review. Journal of neural engineering. 2019 Apr 9;16(3):031001.

[10] Bojarski M, Del Testa D, Dworakowski D, Firner B, Flepp B, Goyal P, Jackel LD, Monfort M, Muller U, Zhang J, Zhang X. End to end learning for self-driving cars. arXiv preprint arXiv:1604.07316. 2016 Apr 25.

[11] Phan H, Andreotti F, Cooray N, Chén OY, De Vos M. Joint classification and prediction CNN framework for automatic sleep stage classification. IEEE Transactions on Biomedical Engineering. 2018 Oct 22;66(5):1285-96.

[12] Kemp, B.; Zwinderman, A.; Tuk, B.; Kamphuisen, H.; Oberye, J. Analysis of a sleep-dependent neuronal feedback loop: The slow-wave microcontinuity of the EEG. IEEE Trans. Biomed. Eng. 2000, 47, 1185–1194. [10]

[13] Zhou, D., Hu, G., Zhang, J., Wang, J., Yan, R., Li, F., ... & Cong, F. (2021). SingleChannelNet: A Model for Automatic Sleep Stage Classification with Raw Single-Channel EEG. bioRxiv, 2020-09.

[14] Xu K, Xia S, Li G. Automatic Classification of Sleep Stages Based on Raw Single-Channel EEG. InChinese Conference on Pattern Recognition and Computer Vision (PRCV) 2020 Oct 16 (pp. 356-368). Springer, Cham.

[15] Tsinalis O, Matthews PM, Guo Y, Zafeiriou S. Automatic sleep stage scoring with single-channel EEG using convolutional neural networks. arXiv preprint arXiv:1610.01683. 2016 Oct 5.

[16] Cai Q, Gao Z, An J, Gao S, Grebogi C. A graph-temporal fused dual-input convolutional neural network for detecting sleep stages from EEG signals. IEEE Transactions on Circuits and Systems II: Express Briefs. 2020 Aug 5;68(2):777-81.

[17] Supratak A, Dong H, Wu C, Guo Y. DeepSleepNet: A model for automatic sleep stage scoring based on raw single-channel EEG. IEEE Transactions on Neural Systems and Rehabilitation Engineering. 2017 Jun 28;25(11):1998-2008.

[18] Fu M, Wang Y, Chen Z, Li J, Xu F, Liu X, Hou F. Deep Learning in Automatic Sleep Staging With a Single Channel Electroencephalography. Frontiers in Physiology. 2021 Mar 3;12:179.

[19] Mousavi S, Afghah F, Acharya UR. SleepEEGNet: Automated sleep stage scoring with sequence to sequence deep learning approach. PloS one. 2019 May 7;14(5):e0216456.

[20] Khalili E, Asl BM. Automatic Sleep Stage Classification Using Temporal Convolutional Neural Network and New Data Augmentation Technique from Raw Single-Channel EEG. Computer Methods and Programs in Biomedicine. 2021 Jun 1;204:106063.

[21] Salamatian A, Khadem A. Automatic sleep stage classification using 1D convolutional neural network. Frontiers in Biomedical Technologies. 2020 Sep 30;7(3):142-50

[22] Yildirim O, Baloglu UB, Acharya UR. A deep learning model for automated sleep stages classification using PSG signals. International journal of environmental research and public health. 2019 Jan;16(4):599.

Evaluation of artificial heart pumps from an engineering perspective

Nazlıhan KILIÇASLAN[1], Kadir GÖK[1], Akil Birkan SELÇUK[1]
[1]Izmir Bakircay University, Izmir/Turkey, nazlihan.yildirim@bakircay.edu.tr
[1]Izmir Bakircay University, Izmir/Turkey, kadir.gok@bakircay.edu.tr
[1]Izmir Bakircay University, Izmir/Turkey, birkan.selcuk@bakircay.edu.tr

Abstract **- Today, circulatory system diseases are a very big problem. When circulatory system problems cause heart failure, the heart becomes unable to pump the blood needed by the body, and the cells begin to not receive enough nutrients and oxygen. In such cases, heart-supporting devices or total artificial hearts are used, depending on the functioning of the heart. Different types of designs of artificial heart pumps that perform this process are encountered. In some designs in practice, the structure of the blood may deteriorate because of some reactions in the blood in the hemodynamics that occurs with the mechanical effect while pumping the blood and at some points, the blood may enter turbulence and cause flow problems. In addition, undesirable turbulence can cause erosion corrosion in the blades of the artificial heart pump. We aim to design the most suitable pump in terms of both mechanical and biocompatibility. We will determine the conditions that we will consider while designing and create the model of the design. We will analyze the pump types that are used and can be used by using Computational Fluid Dynamics (CFD) and finite volumes/elements methods. In this way, we will be able to choose the most suitable pump type.**
When choosing a blood pump, in addition to its mechanical properties, considering the shear stresses caused by the blood flow and other forces that may act on the pump, the inlet-outlet pressures of the blood to the pump and the pressures it will exert on the vessel walls, the effect of the pump dynamics on the blood cells, whether it will cause any toxic effects (biocompatibility) are very important in terms of regular and stable operation of the pump and maintaining the health balance of the human body.

Keywords **– Artificial Heart Pump, Blood Circulation, CFD, Finite Elements, Finite Volume Method**

I. INTRODUCTION

When circulatory system problems cause heart failure, the amount of blood that needs to be pumped to the body cannot be pumped to the body, and this condition often causes death. Due to the difficulty of finding a suitable donor in organ transplants, it is necessary to wait for a long time and this situation is against the patient. Mechanical support should be provided to keep the patient alive during the waiting period for heart transplantation or to find a permanent solution that will not require heart transplantation. This mechanical support will perform the pumping action that the heart can no longer perform. In artificial heart pumps, pump types may vary depending on the type of flow or the purpose of the pump. The cavities in the heart where blood is collected to be sent to the body and lungs are called ventricles. Ventricular assist devices can be used when either the right or left ventricle is not working. Ventricular assist devices do not replace the whole heart. They only work in parallel with the left or right ventricle. Figure 1 demonstrated of the axial flow rotary blood pump by Chua and Su (1).

Because heart pumps partially or completely replace the heart, they remain in the body for a long time. In this case, it is important that the size of the device is as minimal as possible. In addition, long-term contact of the pump with body fluids and tissues requires high biocompatibility. Because if the pump causes any reaction in the body, it may result in damage such as thrombosis.

The biggest problem in the hemodynamics created by the pump is the shear stresses on the pump. High shear stresses cause deformations in blood cells, and as a result, hemolysis, which we call the destruction of erythrocytes, occurs. It is important to keep shear stresses on the pump to a minimum to prevent hemolysis. According to a study, the highest shear stress that blood cells can withstand is around 400 Pa (2). The duration of exposure to shear stresses is as important as the magnitude of the shear stresses that blood cells are exposed to. Long-term contacts will cause more damage (3).

Among the types of artificial heart pumps, axial pumps seem attractive due to their small size, but they have a high risk of deformation of blood cells due to their high rotational speed. However, centrifugal pumps have been shown to be safer and less damaging (4).

In their experiments and analyzes with water and water-glycerine solution, Çınar et al. obtained a pressure difference of 92 torr (8 torr less than the design pressure) at the design point in both CFD and experimental studies for water (5). They reached the design pressure of 100 torr at 10200 rpm. At the design point for water, the CFD and the test results matched exactly, but they saw that the difference between the CFD and the test results increased as they moved away from the design point. They found that the difference between CFD and experimental results for the water-glycerine solution was higher than for water.

Demir et al., investigated the effects of geometric design parameters of three wing heights and two curved tongue profiles on flow behavior and hydraulic performance. As a result, a steeper regime and a sharper curvature profile at the wing entrance gave better results. Finally, the Heart Turcica Centrifuge, which they produced with the best blade height and curved tongue profiles examined, successfully met the performance requirements of a blood pump. Geometries, streamline, and shear stress analyses of impellers were demonstrated by Demir et al (6).

Today, computer aided finite element analysis (FEA) and computational fluid dynamic (CFD) was used to solve processes such as metal turning, bone drilling, bone screwing, water jet process and erosion corrosion processes, fatigue behavior of implant materials, simulations of COVID-19 and other infections and optimal configuration of implant materials [7-20].

The finite element method (FEM) is a widely used method for numerically solving differential equations arising in engineering and mathematical modeling. Typical problem areas of interest include the traditional fields of structural analysis, heat transfer, fluid flow, mass transport, and electromagnetic potential [21]. CFD is a branch of fluid mechanics that uses numerical analysis and data structures to analyze and solve problems that involve fluid flows. Computers are used to perform the calculations required to simulate the free-stream flow of the fluid, and the interaction of the fluid (liquids and gases) with surfaces defined by boundary conditions. With high-speed supercomputers, better solutions can be achieved, and are often required to solve the largest and most complex problems [22].

Considering all these studies and conditions, we aim to design the most suitable pump in terms of both mechanical and biocompatibility. We will determine the conditions that we will consider while designing and create the model of the design. We will perform CFD analysis of our model under real boundary conditions with finite element/volume methods. With the results we have obtained with CFD, we will be able to analyze the flow conditions we aim for in our design and the deformations that may occur in the blood before production and reach the most efficient and innovative design.

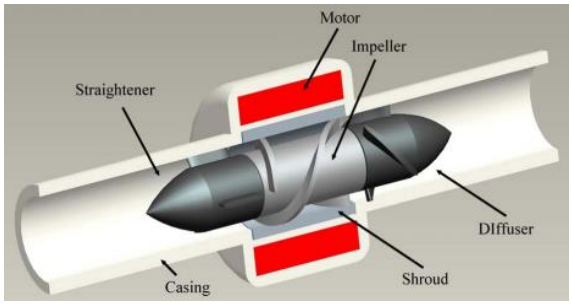

Figure 1. Demonstration of the axial flow rotary blood pump

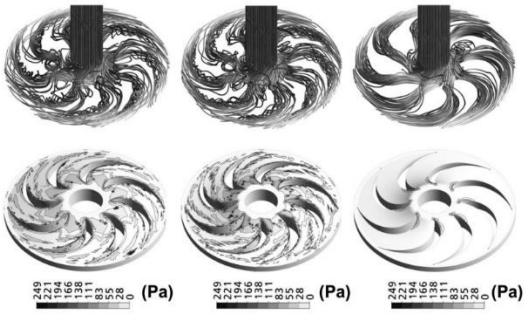

Figure 2. Geometries, streamline, and shear stress analyses of impellers

II. MATERIAL AND METHOD

While designing our artificial heart pump, we will use finite element/volume methods and CFD analyzes to see the forces acting on the blood and pump blades in the vessel and the pump, whether the blood cells will deform or not, and erosion and corrosion on the pump blades. Thus, because of CFD analysis, we will be able to calculate hydraulic properties such as shear stresses in the system, inlet-outlet pressures to the pump, flow lines, and flow rate.

After designing the pump in Solidworks, we will analyze the flow in the ANSYS program. In the ANSYS program, first of all, boundary conditions will be entered, and analysis will be made in line with these conditions. We will be able to change the design features such as the number of wings and wing angles to be used while analyzing. Performing analyzes in this way allows observing different results by changing the design features we make. Thus, we will be able to reach the most suitable design model.

Performing these analyzes before production provides the opportunity to detect both hydraulic properties and damages.

III. RESULTS AND DISCUSSION

After completing the results according to the boundary conditions and the selected models, flow velocities, pressure, turbulence kinetic energy, turbulence eddy dissipation, Eddy viscosity, inlet-outlet pressures to the pump, flow lines, and flow rate and wall shear stresses will be calculated in CFD platform.

We are planning to evaluate with relations and differences others of our artificial heat pump design.

IV. CONCLUSION

As a result of this study, an artificial heart pump with innovative and unique will be designed and prototyped. Designing a new pump has been important for a laminar flow in the vessel. Turbulent flow both damages blood cells and causes erosion corrosion of pump blades. It will be possible to change such undesirable situations after CFD analysis with finite element/volume methods and detecting them. These analyzes will be important to find the most appropriate values of design features such as the number of pump blades, the angle of the blades, flow rate, rpm and manometric head. Finding the most suitable features will ensure that the blood flow is free from turbulence and that the blood cells are dispersed harmlessly throughout the body.

Today, artificial heart pumps have become a hope for patients since most deaths are caused by heart diseases and patients wait for a long time in heart transplant lines. In addition, it is expected to contribute to the country's economy by producing the design. This study is of great importance to design and manufacture the artificial heart pump with the best design features.

REFERENCES

[1] L. P. Chua, B. Su, 2011, "Numerical Study on The Impeller of an Axial Flow Blood Pump", 2011 4th International Conference on Biomedical Engineering and Informatics (BMEI), 1153-1156.

[2] P. Lu, H. Lai ve J. Liu, 2001, A Reevaluation and Discussion on The Threshold Limit for Hemolysis in a Turbulent Shear Flow, Journal of Biomechanics, Vol. 34 (10), pp. 1361-136.

[3] J. H. Yen, S. F. Chen, M. K. Chern, P. C. Lu, 2014, "The Effect of Turbulent Viscous Shear Stress on Red Blood Cell Hemolysis, The Japanese Society for Artificial Organs, Vol. 17 (2), pp.178-185.

[4] J. Leme, C. da Silva, J. Fonseca, B. U. da Silva, B. Uebelhart, J. F. Biscegli, A. Andrade, 2013, "Centrifugal Blood Pump for Temporary Ventricular Assist Devices With Low Priming and Ceramic Bearings", Artificial Organs, Vol. 37 (11), pp. 942-945.

[5] H. Cinar, R. Yapici, 2017, "YENİ BİR YÜKSEK HIZLI KALP DESTEK POMPASININ SAYISAL VE DENEYSEL ANALİZİ", Selcuk University Journal of Engineering, Science and Technology, Vol. 6 (1), pp. 38-54.

[6] Demir, O., Biyikli, E., Lazoglu, I., Kucukaksu, S., 2011, "Design of a Centrifugal Blood Pump: Heart Turcica Centrifugal", Artificial Organs, Vol. 35 (7), pp. 720-725.

[7] A. Gok, K. Gok, M. B. Bilgin, 2015, Three-dimensional finite element model of the drilling process used for fixation of Salter–Harris type-3 fractures by using a K-wire. Mech Sci 6 (2):147-154.

[8] K. Gok, 2015, Development of three-dimensional finite element model to calculate the turning processing parameters in turning operations. Measurement 75:57-68.

[9] K. Gok, S. Inal, 2015, Biomechanical comparison using finite element analysis of different screw configurations in the fixation of femoral neck fractures. Mech Sci 6 (2):173-179.

[10] M. Erdem, K. Gok, B. Gokce, A. Gok, 2017, Numerical analysis of temperature, screwing moment and thrust force using finite element method in bone screwing process. Journal of Mechanics in Medicine and Biology 17 (01):1750016.

[11] K. Gok, S. Inal, A. Gok, A. M. Pinar, 2017, Biomechanical effects of three different configurations in Salter Harris type 3 distal femoral epiphyseal fractures. Journal of the Brazilian Society of Mechanical Sciences and Engineering 39 (4):1069-1077.

[12] S. Inal, K. Gok, A. Gok, A. O. Uzumcugil, S. N.Kuyubasi, 2018, Should we really compress the fracture line in the treatment of Salter–Harris type 4 distal femoral fractures? A biomechanical study. Journal of the Brazilian Society of Mechanical Sciences and Engineering 40 (11):528.

[13] K. Gok, S. Inal, L. Urtekin,A. Gok, 2019, Biomechanical performance using finite element analysis of different screw materials in the parallel screw fixation of Salter–Harris Type 4 fractures. Journal of the Brazilian Society of Mechanical Sciences and Engineering 41 (3):143.

[14] Y. Pirhan, K. Gok, A. Gok, 2020, Comparison of two different bowel anastomosis types using finite volume method. Computer Methods in Biomechanics and Biomedical Engineering 23 (8):323-331.

[15] E. Türkes, M. Erdem, K. Gok, A. Gok, 2020, Development of a new model for determine of cutting parameters in metal drilling processes. Journal of the Brazilian Society of Mechanical Sciences and Engineering 42 (4):169.

[16] H. D. Ada, M. Erdem, K. Gok, 2021, Computational Fluid Dynamics Simulation of Erosion-Corosion In Abrasive Water Jet Machining. Surface Review and Letters 28 (05):2150031.

[17] K. Gok, A. B. Selcuk, A. Gok, 2021, Computer-Aided Simulation Using Finite Element Analysis of Protect Against to Coronavirus (COVID-19) of Custom-Made New Mask Design. Transactions of the Indian Institute of Metals.

[18] K. Gok,Investigation Using Finite Element Analysis Of Effect On Crater Geometry Of Different Abrasive Types InAbrasive Water Jet Machining. Surface Review and Letters 0 (0):2150060.

[19] K. Gok, Investigation of the use of silicone pads to reduce the effects on the human face of classical face masks used to prevent from COVID-19 and other infections. Proceedings of the Institution of Mechanical Engineers, Part E: Journal of Process Mechanical Engineering 0 (0):09544089211019581.

[20] K. Gok, M. Erdem, Y. Kisioglu, A. Gok, M. Tumsek, 2021, Development of bone chip-vacuum system in orthopedic drilling process. Journal of the Brazilian Society of Mechanical Sciences and Engineering 43 (4):224.

[21] C. Olek Zienkiewicz, L. Robert Taylor, J. Z. Zhu, 2013, "The finite element method: Its basis and fundamentals", Butterworth-Heinemann. ISBN 978-0-08-095135-5.

[22]https://en.wikipedia.org/wiki/Computational_fluid_dynamics

The implemention of the new encryption matematical model for cryptosystems

Artan Luma*, Blerton Abazi*, Azir Aliu*, Halil Snopce* and Ylber Januzaj**
* South East European University / Faculty of Contemporary Sciences and Technologies, Tetovo, Republic of North Macedonia
a.luma@seeu.edu.mk, ba08539@seeu.edu.mk, azir.aliu@seeu.edu.mk, h.snopce@seeu.edu.mk
** University "Isa Boletini" Mitrovica / Faculty of Economics, Mitrovica, Kosovo
ylber.januzaj@umib.net

Abstract –

Data that is constantly on the move in today's digital communications can be "surveyed" easily and are typical cases where encryption can be applied. The development of computer systems in terms of interconnections in today's networks has increased the dependence of companies and individuals on the information that is stored or transmitted. At the same time, awareness has been raised about protecting data and communications against various intrusions, guaranteeing the authenticity of messages, and protecting systems against network attacks. In the following paper, we will present two operators as mathematical models, which can be used in many other ideas and approaches. We will see the power of these mathematical operators in creating a new cryptosystem for authentication for online users to make transactions through the use of a new cryptosystem.

Keywords - cyrptography; encryption; authentication; security;

I. INTRODUCTION

Encryption algorithms have found wide use in today's applications and services but it is always important to evaluate how secure a particular encryption scheme is. Some theoretically very secure cryptographic schemes can be very difficult to implement in practice.

Although today's cryptographic algorithms have many variations we can say that figures form the basis of the operation of an algorithm. Only the means of enforcing encryption and decryption and the application circumstances in which a cryptographic algorithm operates (internet, mobile phones, digital televisions or ATMs) have changed.

What distinguishes modern cryptography is the use of sophisticated mathematical equations or algorithms and keys for encrypting and decrypting data. Today's cryptographic algorithms are based on mathematically difficult problems - for example, factorization of prime numbers, discrete logarithms, and so on.

Among the most common uses of cryptography, we maintain the confidentiality and integrity of data as well as the authenticity and anonymity of our communications.

****Corresponding author: Ylber Januzaj**
E-mail: ylber.januzaj@umib.net

In recent years the demand for the application of cryptographic techniques has increased due to the interest in the industrial aspect (financial services that require secure electronic transactions and businesses that must keep significant secrets on personal computers), and in the individual aspect (secure wireless communications).

II. PERFORMANCE OF ALGORITHMS ON DIFFERENT PLATFORMS

There are many forms of implementation of cryptographic algorithms in software or hardware that have a certain efficiency and this has to do with the characteristics of an algorithm: architecture, scalability, security, etc. Extensive analytical work has also been performed on symmetric or asymmetric algorithms and their combined use according to different hardware platforms for different data. The results obtained by researchers Salama and Elminaam [1] identified a better performance of the Blowfish algorithm and superiority in throughput and power consumption on different platforms compared to AES. Meanwhile, according to Elkilani [2] after testing various encryption algorithms in relation to video streaming applications AES turned out to be the most efficient algorithm in terms of real-time video transmission security. According to the authors Ramesh and Umarani [3], after comparing different algorithms it was found that there was no significant difference in the performance of different schemes with symmetric key in the case of data transmission and encryption of image files, and the system of Windows 7 operation turned out to have better performance. According to Dixit [4], the Blowfish algorithm is suitable in applications where the key does not change often, such as a communication line or an automatic file encoder, and for small embedded systems such as mobile devices, smart cards, etc.

Encryption in AES is fast and flexible and can be done on different platforms especially on small devices, Naik [5]. An important estimate regarding key size is that the larger the key the more time and battery consumption we will have during the operation of an algorithm. Energy efficiency is another important issue nowadays in terms of schemes and protocols in information security. According to the results in Crypto ++ Benchmark [6], and the work of Nadeem [7] after implementing and testing different secret key algorithms in two different machines such as: P-II 266 MHz and P-4 2.4 GHz, the Blowfish algorithm turned out

to have quite good performance compared to the AES, DES and 3DES algorithms. Also AES had better performance than 3DES and DES and 3DES had a throughput value as much as 1/3 of DES. According to McKay [8], in the case of the AES algorithm increasing the key size led to a clear change in battery consumption and time. Switching from a 128-bit to 192-bit switch caused an increase in power and time consumption by about 8% and switching to a 256-bit switch increased by about 16% [8].

Even in the case of the RC6 algorithm increasing the key size (128-bit, 192-bit, and 256-bit) would lead to noticeable differences in terms of battery consumption and time. According to the results obtained by Rizvi [9], had a superiority of the Blowfish algorithm over AES and CAST, in text and image encryption, but the CAST algorithm performed faster in encrypting audio files. Algorithms usually performed faster on Windows XP than on Windows Vista and Windows 7. According to Çakiroglu [10] in his paper, the AES algorithm was better in terms of memory requirements and throughput value. A general idea about string digits and block digits is also given in the paper [11] where the authors after comparing algorithms using RC4 and Hill digit, concluded that the speed of encryption and decryption of string digits was higher compared to block digits because the technique of adding bits (bit padding) to block digits increased the consumption of time and power. Also according to [12] range digits were faster compared to block digits [12] and range digits met the requirements of high throughput multimedia applications, low H / W complexity depending on the technology.

A. Design features of cryptographic algorithms

There are always compromises regarding the features of cryptographic algorithms and their use in real world situations. A typical example is the number of rounds in each algorithm - a large number of rounds makes the algorithm slower but it is assumed to provide greater security [13]. Also, there is always compromise regarding the security and performance of similar algorithms - as in the case of symmetric key algorithms. According to Eli Biham [14], the performance of algorithms can be measured by the minimum number of safe rounds for each algorithm - which is the estimation of the number of rounds needed to perform and perform a gross key force search (hard to really ensure). There is a conclusion [15] according to which power consumption varies linearly with the number of rounds for some known cryptographic algorithms. However, in all cases, the performance and cost of implementation are really critical issues. An encryption algorithm would not be really usable if it were secure enough but slow in performance: because one of the common practices involves introducing encryption algorithms into other applications such as e-commerce, the banking sector, and online transaction processing applications. The integral inclusion of encryption algorithms in other applications also makes a hardware implementation impossible, and this becomes the main cause in degrading the performance of the system as a whole. A software implementation of a cryptographic scheme enables the benefits of flexibility, speed of implementation, and a lower cost over time. Hardware-level ciphers cannot be updated without the replacement of microcontrollers, which are costly and complicated. In the case of resizing the incoming package, Blowfish performed better than the other encryption algorithms followed by RC6, and in the case of resizing the key - increasing the key led to a fairly clear change in battery consumption. and time [7].

Technologies such as CPU and memory are growing and so are their power requirements, but battery technology is growing at a much lower rate, creating what is known as a "battery gap". For this reason, battery capacity plays a key role in the usability of various devices. The growing demand for wireless services has prompted technical research into finding ways to overcome these limitations. It is often difficult to make compromises between energy and security when we want to use a certain cryptographic algorithm [16]. Another essential feature about the security that blockchain can provide relates to the nature of replacement boxes. During the design process, it must be taken into account that the S boxes are nonlinear, which is realized thanks to the control of a series of formulations for nonlinearity.

III. PENTOR AND ULTRAPENTOR MATHEMATICAL MODEL

Mathematical operators: Pentori and UltraPentori

Next, present the two operators as a mathematical model, if many other ideas and approaches could be used. Demonstrate the mathematical power of the operator making a new cryptosystem to identify for Online users to make the transaction using for a new cryptosystem. [17]

A. Pentor

We will first define the first operator as a mathematical model, the Pentor of an integer n based on B and the rank m. For every natural integer n, there exists a Pentor for the given base B and rank m. To mathematically represent this operator, we will start from the congruence equation (1). Pentor of an integer n based on B and rank m, which must meet the condition $PMP(n, B^m) = 1$, where we will have:

$$B^m \cdot P(n) \equiv 1 \ (mod\ n) \quad ...(1)$$

where B is the base of the integer n, $P(n)$ is the Integer Pentor n, and m is the range Pentor of integer number n. From the congruence equation (1) we will move on to the equation of equation:

$$B^m \cdot P(n) = 1 + n \cdot k$$

$$P(n) = \frac{1+n \cdot k}{B^m} \quad ...(2)$$

where k is an integer and must satisfy the condition that the fraction is an integer. If we want to find the first-order integer Pentor n, then $m = 1$, but if we want to find the second-order integer Pentor n, then $m = 2$, and so on. [18]

B. *Ultra Pentor*

In the following, we will define the second operator as the Ultra Pentori mathematical model of an integer n based on B and the range m. For every natural integer n there exists an Ultra Pentor for the given base B and range m. To mathematically represent this operator, we will start from the congruence equation (3). Ultra Pentorin of an integer n based on B and rank m, which must meet the condition $PMP(n, B^m) = 1$, we will have:

$$B^m \equiv 1 \ (mod\ n) \quad ...(3)$$

where m is an integer. Next, from the congruence equation (3), we will move on to the equation of equation and operate with logarithmic operation from which we will find the Ultra Pentor of the integer n based on B and the rank m, and we will have:

$$B^m = 1 + n \cdot l \ / \log_B$$

$$\log_B B^m = \log_B(1 + n \cdot l)$$

$$m \cdot \log_B B = \log_B(1 + n \cdot l)$$

where $\log_B B = 1$, where it comes from:

$$m = \log_B(1 + n \cdot l)$$

where $m = UP(n)$, from which we obtain the Ultra Pentor of the integer n based on B and the rank m:

$$UP(n) = \log_B(1 + n \cdot l) \quad ...(4)$$

where l is an integer that satisfies the condition that $(1 + n \cdot l)$, can be written as B^a, where a is also an integer.

New cryptosystem for authentication of Online users who want to communicate with each other, based on these two operators as mathematical models, we will be able to create a new cryptosystem, which we can use to create a new cryptosystem for the authentication of online users in a system [19]. In the beginning, we will explain some basic concepts for creating this new cryptosystem.

Design of a new cryptosystem based on the operators Pentor and Ultra Pentor.

To communicate two people in a cryptosystem, $person\ A$ and $person\ B$, we will need to define public and private keys.

Now, we will start to define the public and private key of $person\ A$ as follows:

$$B^m \cdot P(n_1) \equiv 1 \ (mod\ n_1) \quad ...(5)$$

To divide convergence (5) with pentor $P(n_1)$, the following condition must be met:

$$PMP(P(n_1), n_1) = 1 \quad ...(6)$$

Once condition (6) is met, we can now divide congruence (5) by pentor $P(n_1)$, where we get:

$$B^m \equiv \frac{1}{P(n_1)} \ (mod\ n_1) \quad ...(7)$$

Congruence (7), we will pass in a draw, where we will get:

$$B^m \equiv \frac{1}{P(n_1)} \ (mod\ n_1) \quad ...(7)$$

Where B is the basis of the cryptosystem, and m is the rank of Pentor and Ultra Pentor in that cryptosystem, and n_1 is the secret value of $person\ A$. From n_1 is generated his Pentor and Ultra Pentor, and k is an integer that satisfies the condition that equality (8) be an integer.

It follows that the public key of $person\ A$ is $(P(n_1), B, m)$, while the private key $(n_1, k, UP(n_1))$.

We continue in the same way for $person\ B$. Now, we will start to define the public and private key of $person\ B$ as follows:

$$B^m \cdot P(n_2) \equiv 1 \ (mod\ n_2) \quad ...(9)$$

To divide by congruence (9) with Pentor $P(n_2)$, the following condition will need to be met:

$$PMP(P(n_2), n_2) = 1 \quad ...(10)$$

Once condition (10) is met, we can now divide the congruence (9) by the Pentor $P(n_2)$, where we get:

$$B^m \equiv \frac{1}{P(n_2)} \ (mod\ n_2) \quad ...(11)$$

Congruence (11), we will pass in a draw, where we will win:

$$B^m = \frac{1+n_2 \cdot l}{P(n_2)} \quad ...(12)$$

Where B is the base of the cryptosystem, and m is the rank of Pentor and Ultra Pentor in that cryptosystem, and n_2 is the secret value of $person\ B$. From n_2 is generated Pentor and its Ultra Pentor in that cryptosystem, and l is an integer that satisfies the condition that equation (12) be an integer.

It follows that the public key of $person\ B$ is $(P(n_2), B, m)$, while the private key is $(n_2, l, UP(n_2))$.

From equation (8) and (12), it is clear that we will be able to equalize these two equations, since on their left side is the same value B^m, from which we will get:

$$\frac{1+n_1 \cdot k}{P(n_1)} = \frac{1+n_2 \cdot l}{P(n_2)} \quad ...(13)$$

Now, from equation (13), we can find the ratio between $person\ A$ Pentor and $person\ B$, as follows:

$$1 + n_1 \cdot k = \frac{P(n_1)}{P(n_2)} \cdot (1 + n_2 \cdot l) \quad ...(14)$$

We pass equation (14) in congruence according to module n_2, where we will get:

$$1 + n_1 \cdot k = \frac{P(n_1)}{P(n_2)} \ (mod\ n_2) \quad ...(15)$$

Now, from equation (15), we can find the ratio between $person\ B$'s Pentor and $person\ A$, as follows:

$$1 + n_2 \cdot l = \frac{P(n_2)}{P(n_1)} \cdot (1 + n_1 \cdot k) \quad ...(16)$$

We pass equation (16) in congruence according to module n_1, where we will get:

$$1 + n_2 \cdot l = \frac{P(n_2)}{P(n_1)} \ (mod\ n_1) \quad ...(17)$$

Now, we will explain the operation of the new cryptosystem, using the public and private key for $person\ A$ and $person\ B$.

Suppose $person\ A$ wants to communicate with $person\ B$. Now, $person\ A$ sends $person\ B$ the public key $(P(n_1), B, m)$. $Person\ B$ accepts the public key of $person\ A$. $Person\ B$ will need to verify that he / she really communicates with $person\ A$.

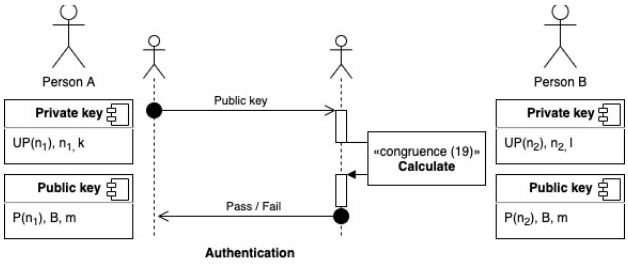

Figure 1 - Person B verifies (authenticates) person A for online communication

Congruence (5) will have to be passed in equality, as follows:

$$B^m \cdot P(n_1) = 1 + n_1 \cdot k \quad ...(18)$$

From equality (18) and congruence (15), it is clear that $1 + n_1 \cdot k$ have in common. Therefore, $1 + n_1 \cdot k$ could be replaced by $B^m \cdot P(n_1)$ from equation (18) to congruence (15), where we would gain:

$$B^m \cdot P(n_1) \equiv \frac{P(n_1)}{P(n_2)} (mod\ n_2) \quad ...(19)$$

Which means that if congruence (19) are valid, then $person\ B$ has verified the online communication with $person\ A$.

The same is true if $person\ B$ wants to communicate with $person\ A$.

Suppose $person\ B$ wants to communicate with $person\ A$. Now, $person\ B$ sends $person\ A$ the public key $(P(n_2), B, m)$. $Person\ A$ accepts the public key of $person\ B$. $Person\ A$ will need to verify that he / she actually communicates online with $person\ B$.

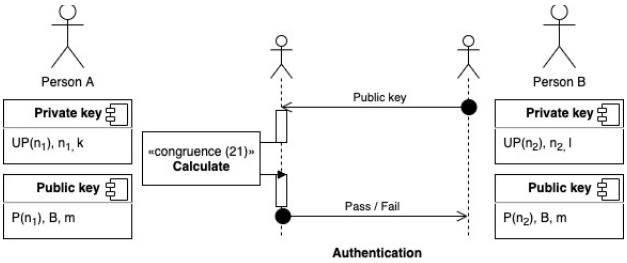

Figure 2 - Person A verifies person B for online communication

Congruence (9) will have to be passed in equality, as follows:

$$B^m \cdot P(n_2) = 1 + n_2 \cdot l \quad ...(20)$$

From equality (20) and congruence (17), it is clear that $1 + n_2 \cdot l$ have in common. Therefore, $1 + n_2 \cdot l$ could be replaced by $B^m \cdot P(n_2)$ from equation (20) to congruence (17), where we will obtain:

$$B^m \cdot P(n_2) \equiv \frac{P(n_2)}{P(n_1)} (mod\ n_1) \quad ...(21)$$

Which means that if the competition is valid (21), then $person\ A$ has verified the online communication with $person\ B$.

In the simple example, if $person\ A$ has as public key $(P(n_1), B, m) = (91, 10, 1)$ and as private key has $(UP(n_1), n_1, k) = (4, 101, 9)$, while $person\ B$ has as public key $(P(n_2), B, m) = (244, 10, 1)$ and as private key has $(UP(n_2), n_2, l) = (5, 271, 9)$. Then if $person\ A$ wants to communicate online with $person\ B$, he sends the public key (91,10,1) to $person\ B$. Now $person\ B$ has to do the authentication of $person\ A$, so he uses congruence (19) as in following:

$$B^m \cdot P(n_1) \equiv \frac{P(n_1)}{P(n_2)} (mod\ n_2)$$

$$10^1 \cdot 91 \equiv \frac{91}{244} (mod\ 271)$$

$$244 \cdot 10 \cdot 91 \equiv 91\ (mod\ 271) / \cdot 10 \quad \text{(where 10 is the multiple inverse)}$$

$$10 \cdot 244 \cdot 10 \cdot 91 \equiv 91 \cdot 10\ (mod\ 271)$$

$$910 \equiv 910\ (mod\ 271)$$

$$97 \equiv 97\ (mod\ 271)$$

From this we can conclude that congruence is valid, therefore $person\ B$ verifies (authenticates) $person\ A$ and gives him access to online communication.

Now, we do the same for $person\ B$, whereas public key it has $(P(n_2), B, m) = (244, 10, 1)$ and as private key it has $(UP(n_2), n_2, l) = (5, 271, 9)$, while $person\ A$ has as public key $(P(n_1), B, m) = (91, 10, 1)$ and has as private key $(UP(n_1), n_1, k) = (4, 101, 9)$. Then if $person\ B$ wants to communicate online with $person\ A$, he sends the public key (244,10,1) to $person\ A$. Now $person\ A$ has to do the authentication of $person\ B$, so he uses congruence (21) as in following:

$$B^m \cdot P(n_2) \equiv \frac{P(n_2)}{P(n_1)} (mod\ n_1)$$

$$10^1 \cdot 244 \equiv \frac{244}{91} (mod\ 101)$$

$91 \cdot 10 \cdot 244 \equiv 244\ (mod\ 101) / \cdot 10$ (where 10 is the multiple inverse)

$$10 \cdot 91 \cdot 10 \cdot 244 \equiv 244 \cdot 10\ (mod\ 101)$$

$$2440 \equiv 2440\ (mod\ 101)$$

$$16 \equiv 16\ (mod\ 101)$$

IV. CONCLUSION

From this we can conclude that congruence is valid, therefore $person\ A$ verifies (authenticates) $person\ B$ and gives him access to online communication.

This algorithm can be applied in many places for encryption and decryption of information, such as: for creating a certificate, for online logging in to an application that is important, for authorizing online purchases, can also be used for banking transactions or integrations in electronic card chips such as VISA, MASTER etc.

In this paper we introduced the new algorithm and the new cryptosystem, which is based on Pentors and Ultra Pentors, which can be used for Online authentication of users. From the numerical examples, it was seen that the cryptosystem works fully and can find implementation in various systems, where high security transactions are required.

Another important aspect is that authentication does not use a key for the authentication process itself, but it can be used additionally for line security, especially in cases where the user uses an insecure internet line.

The contribution of access is the use of small generator numbers, which we call Pentor and Ultra Pentor, which we use for data encryption and Online authentication for users.

REFERENCES

[1] D. S. Abd Elminaam, H. M. A. Kader, and M. M. Hadhoud, "Evaluating the performance of symmetric encryption algorithms," *Int. J. Netw. Secur.*, 2010.

[2] W. S. Elkilani and H. M. Abdul-Kader, "Performance of encryption techniques for real time video streaming," in *Innovation and Knowledge Management in Twin Track Economies Challenges and Solutions - Proceedings of the 11th International Business Information Management Association Conference, IBIMA 2009*, 2009.

[3] E. Thambiraja, R. G., and R. Umarani, "A Survey on Various Most Common Encryption Techniques," *Int. J. Adv. Res. Comput. Sci. Softw. Eng.*, 2012.

[4] D. Singh, P. Nand, R. Astya, and P. Dixit, "Improved DSA cryptographic protocol and its comparative study with RSA protocol," in *International Conference on Computing, Communication and Automation, ICCCA 2015*, 2015.

[5] Y. Rajput, D. Naik, and C. Mane, "An Improved Cryptographic Technique to Encrypt Text using Double Encryption," *Int. J. Comput. Appl.*, 2014.

[6] A. Al-Haj, G. Abandah, and N. Hussein, "Crypto-based algorithms for secured medical image transmission," *IET Inf. Secur.*, 2015.

[7] A. Nadeem and M. Y. Javed, "A performance comparison of data encryption algorithms," in *Proceedings of 1st International Conference on Information and Communication Technology, ICICT 2005*, 2005.

[8] S. Narayanan *et al.*, "A thermophysical battery for storage-based climate control," *Appl. Energy*, 2017.

[9] P. Nema and M. A. Rizvi, "Critical Analysis of Various Symmetric Key Cryptographic Algorithms," *Int. J. Recent Innov. Trends Comput. Commun.*, 2015.

[10] Z. Eksi and M. Cakiroglu, "Performance evaluation of the popular segmentation algorithms for bone fracture detection," *AWERProcedia Inf. Technol. Comput. Sci.*, 2012.

[11] S. Ahmad, D. M. R. beg, D. Q. Abbas, J. Ahmad, and S. M. Atif, "Comparative Study between Stream Cipher and Block Cipher using RC4 and Hill Cipher," *Int. J. Comput. Appl.*, 2010.

[12] S. O. Sharif and S. P. Mansoor, "Performance analysis of stream and block cipher algorithms," in *ICACTE 2010 - 2010 3rd International Conference on Advanced Computer Theory and Engineering, Proceedings*, 2010.

[13] B. Schneier and D. Whiting, "A Performance Comparison of the Five AES Finalists," *Proc 3rd Adv. Encryption Stand. AES Candidate Conf*, 2000.

[14] F. X. Standaert, G. Rouvroy, J. J. Quisquater, and J. D. Legat, "Efficient implementation of rijndael encryption in reconfigurable hardware: Improvements and design tradeoffs," *Lect. Notes Comput. Sci. (including Subser. Lect. Notes Artif. Intell. Lect. Notes Bioinformatics)*, 2003.

[15] R. Chandramouli, S. Bapatla, K. P. Subbalakshmi, and R. N. Uma, "Battery power-aware encryption," *ACM Transactions on Information and System Security*. 2006.

[16] E. Barka and M. Boulmalf, "On the impact of security on the performance of WLANs," *J. Commun.*, 2007.

[17] Auguste Kerckhoffs, "La Cryptographicee Militaire," *J. des Sci. Mil.*, 1883.

[18] W. Diffie, W. Diffie, and M. E. Hellman, "New Directions in Cryptography," *IEEE Trans. Inf. Theory*, 1976.

[19] A. J. Menezes, P. C. Van Oorschot, and S. A. Vanstone, *Handbook of applied cryptography*. 1996.

Cybersecurity challenges for organizations

Artan Luma*, Blerton Abazi*, Azir Aliu*, Halil Snopce* and Ylber Januzaj**
* South East European University / Faculty of Contemporary Sciences and Technologies, Tetovo, Republic of North Macedonia
a.luma@seeu.edu.mk, ba08539@seeu.edu.mk, azir.aliu@seeu.edu.mk, h.snopce@seeu.edu.mk
** University "Isa Boletini" Mitrovica / Faculty of Economics, Mitrovica, Kosovo
ylber.januzaj@umib.net

Abstract - **Internet security plays a vital role in an information technology ecosystem. Providing information has become so far the best challenge nowadays. When we think of cybersecurity, the first thing that comes in mind is cyber-crime, which is growing by the day. Governments and enterprises are taking many measures to prevent these cyber-crimes. In addition to various measures, internet security is still a big concern for many people . This paper focuses on explaining the challenges facing organizations in the event of a cyber-attack. Lately, we describe also the techniques, ethics and cyber defense including trends that change the credibility of the organizations online. The summary and discussion of the paper presented the results of the study which shows that the challenges of organizations nowadays in a cybernetic case are organized and need to sophisticate their walls to protect themselves with the security issues.**

Keywords **– cybersecurity, internet crime, ethics, social media, cloud security.**

I. INTRODUCTION

With the development of new technologies in many areas, threats have emerged regarding the security of information stored in many organizations. Internet security is the protection of systems in organizations, their data and networks in the Internet space. Internet security is a critical issue for many businesses. In a business or any organization, there are various threats associated with their systems, data and networks. Threats include cybercrime, cyber warfare and cyber terrorism. Internet security is being a major problem, in many countries around the globe and the research needs to be done on possible measures to alleviate the problem. Criminals in cyber-attacks use specific remote application that allows them to access other systems. Applications used by cyber attackers are referred to as malware (malicious software). Malicious software includes viruses, spyware and Trojans. Internet risk assessment is the step used by many organizations to discover how exposed systems are to cyber-attack.

****Corresponding author: Ylber Januzaj**
E-mail: ylber.januzaj@umib.net

The typical step of cyber security risk assessment is to identify the various assets of the organizations that may be affected, which include systems, databases, and other devices that contain essential data. After identifying potential hazards, the next step is to select control systems to prevent the attack.

When it comes to internet security, there are many solutions and issues that helps in making the internet safe. These basics include people management, processes and technology. Taking into account people management, personnel, skills and professional qualifications are required, as well as component resources. Process management includes IT auditing, systems management, governance frameworks, and best practices. The ultimate foundation is technology and includes competence and the support process.

Integrating the three primary approaches to cybersecurity is what makes an organization secure online. Technology is the key element in achieving the most effective security over the internet. Cyber security programs include the use of antivirus, anti-spyware and data encryption software. According to internet essentials, business organizations should not only recognize the cost of software to protect their database from malware, but also consider the cost of losing the most useful information.

II. LITERATURE REVIEW

A. Digital Business and Cybersecurity Threats

Nowadays, all organizations are digital by default. Not every organization delivers its products and services primarily through digital channels, but they all operate with the cultures, technology and processes of the internet age. Moreover, in the connected and convergent world provided by the Internet of Things (IoT), the digital landscape is vast, with any assets owned or used by the organization representing another node in the network.

No wonder the World Economic Forum [1] now rates a large-scale cyber security breach as one of the five most serious risks the world faces today. The threat rate is expanding dramatically: by 2021, the global cost of cyber security

breaches will reach $ 6 trillion by some estimates, double the total for 2015.

Cyber attackers can be either discriminatory or highly targeted, attacking large and small organizations in both the public and private sectors. They are well camouflaged: exposing attackers requires online security protection that identifies the threat, even when adopting the colors of its close environment. Organizations do not always manage this.

Last year, the WannaCry ransomware [2] attack in the UK affected a significant portion of the National Health Service (NHS); in France, a breach of Emmanuel Macron's presidential campaign [3] threatened to throw the election into chaos; in the U.S., Yahoo revealed that an uncompromising breach of 3 billion user accounts, while in India an attack paralyzed Mumbai's largest container port.

At the same time, it has never been more difficult for organizations to design the digital environment in which they operate, or their interact with. The technological infrastructure of any organization is both managed and complex, networks that include tools and technologies that can be in the premises or in the Cloud [4]. Moreover, it is becoming more difficult to define an "organization". This is due to the proliferation of devices belonging to employees, customers and suppliers (including laptops, tablets, mobile phones and more) with access to the organization's systems that disrupt the security perimeter [5]. Organizations need to think for themselves that they have long and attractive tentacles in all direction where connected devices add complexity. The IoT is not a collection of passive items; rather it is a network of interconnected and interconnected devices that interact actively and continuously. The convergence of these networks with those that were once separate and self-controlled and therefore more manageable systems represents a fundamental difference.

The shares could hardly have been higher. Organizations that fall prey to an online attack are at risk of significant reputational loss, as well as the direct costs of a breach, estimated to average $ 3.62 million by the Ponemon Institute [6]. There is also the possibility of damaging confrontations with authorities and regulators. The European Union General Data Protection Regulation (GDPR) [7], which entered into force in 2018, gives regulators powers over organizations fined up to 2% of their annual global turnover for breach-related failures, and 4% if an organization significantly mismanages responses.

Also, data privacy is not only vulnerable. The IoT exposes organizations' operating technologies to attackers, offering them an opportunity to shut down or destroy industrial control systems [8]. The threat could even be for life: imagine the attacker with the ability to turn off life support systems in hospitals or take control of cars tied to the road.

Rising threat levels call for a stronger response is important, and this year's GISS found that many organizations continue to increase their spending on cybersecurity [9]. Seventy percent say they want up to 25% more funding, and the rest want even more than that. However, only 12% expect to receive an increase of more than 25%.

For many organizations, the worst may have to happen for these calls to be met. Asked what kind of event would result in an increase in online security budgets, 76% of respondents from the survey said discovering a breach that caused damage would likely see larger resources allocated.

In contrast, 64% said an attack that did not appear to have caused any harm was unlikely to cause an increase in the organization's online security budget. This is higher than the figure reported last year, which is worrying given the reality that the damage was generally done by an attack is not even immediately clear. Violation can be a test attack that exposes the sensitivity or deviation created to distract attention from another more harmful threat; Otherwise, the attacker may simply be demanding their time before taking advantage of the offense. Organizations should assume that all attacks are harmful and conclude that where damage has not been identified [10], it only happens because it has not yet been detected.

After all, organizations that fail to devote the necessary resources to proper online security will find it very difficult to manage the risks they face. The survey suggested that organizations become increasingly aware of this: 56% of respondents say they have either made changes to their strategies and plans to address the risks posed by cyber threats, or that they will review the strategy in this context [11]. However, only 4% of organizations are convinced that they have fully considered the information security implications of their current strategy and have included all relevant risks and threats.

B. Understanding the threat landscape

The first step for organizations seeking to increase their online security capability is to develop a better understanding of the nature of the threat to them. It will not be possible to build greater internet security stability in the organization without first identifying the possible causes of the damage and how they may manifest. Awareness of the situation is essential what are the threats and what do they mean to you and your organization?

Moreover, the sphere of attacks and potential attackers is wide and is becoming more and more important to this day. Organizations may feel more confident about coping with the types of attacks that have become popular in recent years, but still do not have the ability to deal with more advanced, targeted attacks; they may not even be aware of the methods of attack that are emerging [12]. However, to be resilient to cybernetics, organizations need to increase their understanding rapidly

All organizations must assume that the worst can happen there is no excuse to assume otherwise. There have been many known attacks and all over the world that complacency is acceptable.

Taking as an example the Petya ransomware attack that organizations so badly affected worldwide in late June 2017, affecting tens of thousands of public and private sector enterprises. The vendor had previously released a snippet for the weakened exploited organizations that did not implement this update, perhaps because they did not understand the threat to them, they were left open to attack.

Rather, the Mirai [13] attack is more sophisticated and underscores the broader weaknesses that organizations need to understand and address. Such an attack on the DynS DNS provider last year brought most of the internet to a halt, disrupting organizations including Twitter and Spotify among others. In that attack, Mirai [13], [14] targeted unprotected webcams, but he also used CCTV camera networks, and could theoretically target any "intelligence" that is an Internet-connected device. In this case, the failure to understand or anticipate the left-wing threat of complacent organizations to ensure that factory-set passwords on all network-connected smart devices were up to date.

With so many different threats and abusers that can be anyone from a rogue employer to a terrorist group or state organizations of a nation they need to be vigilant across the board and be well acquainted with their threat landscape [15]. Moreover, as attackers have easy access to malware and sophisticated tools and can even hire cyber criminals [16].

III. CONCLUSIONS

Cyber-attack continues to deviate various paths with each passing year as well as information security. The latest and most disruptive technologies, along with new cyber tools and threats that come to light every day, are challenging not only how organizations secure their infrastructure, but also how they require new platforms and intelligence to do so. There is no perfect solution to cybercrime but we should try our best to minimize them in order to have a secure future in cyberspace [17][18].

Through the recommendations, these types of actions (both in the form of security, education and legislation) are suggested following the weak nature of global legal protection against cybercrime:

- Laws must be enforced on cybercrime. National governments are still the main authority that can regulate criminal behavior in most countries in the world. So, a conscious government effort to enact laws to tackle cybercrime would be quite necessary [19].
- Ensure that all applicable local legislation is complementary and in accordance with international laws, treaties and conventions;
- Establish progressive capacity building programs for national law enforcement agencies;
- There should be a symbiotic relationship between firms, government and civil society to strengthen the legal framework for cyber security. An act must be a crime in each jurisdiction before it can be prosecuted across a border. The nation should define cybercrime similarly, to enable them to enact legislation that would combat cybercrime domestically and internationally [20].

A. A. Safety recommendations

- Strengthening the trust framework, including information security and network security, authentication, privacy and consumer protection, is a prerequisite for developing the information society and building trust among ICT users.
- A global cybersecurity culture should be actively promoted, developed and implemented in collaboration with all stakeholders and international expert bodies.
- Housing and improving coordination in the implementation of information security measures at national and international level.
- Establish a framework for implementing information security in critical sectors of the economy, such as public services, telecommunications, transport, tourism, financial services, public sector, manufacturing and agriculture, and develop a framework for managing information security risks at the national level.
- Establish an institutional framework that will be responsible for monitoring the information security situation at the national level, disseminating advice on the latest information security alarms and managing information security risks at the national level, including reporting violations information security and incidents.
- Promoting secure e-commerce and e-government services.
- Protecting the privacy rights of individuals when using electronic communications and developing a national cybersecurity technology framework that specifies cyber security requirements controls and the initial basis for the individual network user.
- Firms must provide their information online. When organizations provide security for their networks, it becomes possible to enforce property rights laws and punish anyone who interferes with their property.

B. Recommendation for education

- Improving awareness and competence in information security and the exchange of best practices at the

national level through the development of an internet security culture at the national level.

- Formally coordinate and prioritize cybernetic research and security activities, deliver vulnerability advice and threat warnings in a timely manner.
- Implement an evaluation / certification program for the product and cyber security systems.
- Develop, promote and maintain a national security culture, standardize and coordinate online security awareness and education programs.

IV. REFERENCES

[1] W. E. Forum, "These are the top cybersecurity challenges of 2021," 2021. .

[2] G. Gluschke, *SECURITY POLICIES AND CRITICAL INFRASTRUCTURE PROTECTION*. .

[3] TheGuardian, "Emmanuel Macron's campaign hacked on eve of French election," p. https://www.theguardian.com/world/2017/may/06/emma.

[4] S. Subashini and V. Kavitha, "A survey on security issues in service delivery models of cloud computing," *Journal of Network and Computer Applications*. 2011.

[5] M. Stoll, "Innovations and Advances in Computing, Informatics, Systems Sciences, Networking and Engineering," vol. 313, pp. 9–17, 2015.

[6] P. Institute, "2018 Cost of Data Breach Study, Global Overview," 2018.

[7] F. Menges *et al.*, "Towards GDPR-compliant data processing in modern SIEM systems," *Comput. Secur.*, vol. 103, p. 102165, Apr. 2021.

[8] B. Abazi, "An approach to the impact of transformation from the traditional use of ICT to the Internet of Things: How smart solutions can transform SMEs," *IFAC-PapersOnLine*, vol. 49, no. 29, 2016.

[9] I. Lee, "Cybersecurity: Risk management framework and investment cost analysis," *Bus. Horiz.*, Feb. 2021.

[10] "Cybersecurity Is Critical for all Organizations – Large and Small | IFAC." [Online]. Available: https://www.ifac.org/knowledge-gateway/preparing-future-ready-professionals/discussion/cybersecurity-critical-all-organizations-large-and-small. [Accessed: 09-Jun-2021].

[11] H. J. Mattord, "Rethinking risk-based information security," 2008.

[12] P. Shamala, R. Ahmad, and M. Yusoff, "A conceptual framework of info structure for information security risk assessment (ISRA)," *J. Inf. Secur. Appl.*, vol. 18, no. 1, pp. 45–52, 2013.

[13] M. Antonakakis *et al.*, "Understanding the Mirai Botnet," *Proc. 26th USENIX Secur. Symp.*, pp. 1093–1110, 2017.

[14] "IoT Botnet Forensics: A Comprehensive Digital Forensic Case Study on Mirai Botnet Servers," *Forensic Sci. Int. Digit. Investig.*, vol. 32, p. 300926, Apr. 2020.

[15] R. Samani, B. Honan, and J. Reavis, "The Cloud Threat Landscape," in *CSA Guide to Cloud Computing*, Elsevier, 2015, pp. 35–61.

[16] W. Kim, O. R. Jeong, C. Kim, and J. So, "The dark side of the Internet: Attacks, costs and responses," in *Information Systems*, 2011, vol. 36, no. 3, pp. 675–705.

[17] B. Morin, Y. Thomas, and H. Debar, "Improving security management through passive network observation," in *Proceedings - First International Conference on Availability, Reliability and Security, ARES 2006*, 2006.

[18] M. I. Al-Ghamdi, "Effects of knowledge of cyber security on prevention of attacks," *Mater. Today Proc.*, Apr. 2021.

[19] ISO/IEC 27001:2013, "Information Technology — Security Techniques — Information Security Management Systems — Requirements," *Int. Organ. Stand.*, 2013.

[20] C. Donalds and K. M. Osei-Bryson, "Toward a cybercrime classification ontology: A knowledge-based approach," *Comput. Human Behav.*, vol. 92, pp. 403–418, Mar. 2019.

Life Expectancy Prediction After Heart Attack by Using Ensemble Learning Methods

G. EROL[1] and B. UZBAŞ[2]

[1] Konya Technical University, Konya/Turkey, gizemnurerol0@gmail.com
[2] Konya Technical University, Konya/Turkey, buzbas@ktun.edu.tr

Abstract **- Cardiovascular diseases (CVD) are one of the leading causes of death in the world. Deaths due to CVD diseases continue to increase every year. Heart attack is a condition in which blood flow to the heart muscle is interrupted, which occurs with cardiovascular diseases. This study aims to predict whether patients survive at least one year after a heart attack by using Echocardiography (ECHO) data. For this purpose, standardization and filling missing values with the Fully Conditional Specification (FCS) method was applied to the ECHO dataset which consists of the data of patients who had a heart attack. Then, classification was carried out with various machine learning algorithms. Classification performances were evaluated comparatively as ensemble learning-based classifier algorithms and popularly used classical classifier algorithms. As a result of the studies, the highest accuracy rate was obtained with Adaboost as 94.87%. It is concluded that the most effective model is produced by ensemble learning-based classifiers in the study of detection of whether patients survived at least one year after a heart attack.**

Keywords **- Machine Learning, ECHO, Standardization, Fully Conditional Specification, Ensemble Learning**

I. INTRODUCTION

CVD is commonly known as a group of diseases that include heart and blood vessel-related disorders [1]. Coronary artery disease, heart failure, cardiac dysrhythmia, and heart attack are among the main diseases included in this group. According to the data of the World Health Organization (WHO), 17 million people approximately die every year due to CVD while deaths due to CVD continue to increase every year. So, they are the number one cause of death worldwide as more people die yearly from it than any other disease [2,3].

Echocardiography (ECHO) is a diagnostic and research method that allows the examination of the internal structure and functions of the heart with the help of ultrasonic sound waves. ECHO is a very active method in CVD studies. Many studies have been realized using the data obtained from this method. To illustrate, through cardiac view classification studies using ECHO images [4, 5, 6], automatic classifications have been made, thereby reducing the expert burden, saving time, and rapidly getting a result. In addition, more reliable, successful, and cost-effective results have been obtained with studies on aortic dissection [7, 8], which is a serious and important condition, and important developments have been achieved in this field too. Lastly, Machine Learning (ML) algorithms have been increasingly utilized for CVD prediction as the predictive ability of this algorithms in cardiovascular diseases is promising [9]. In performed cardiovascular disease prediction studies [9, 10, 11, 12], by developing effective ML models, successful and sensitive systems have been generated to diagnose CVD such as coronary artery disease, heart failure, and cardiac arrhythmias. Jothikumar et al. [13] was done a C4.5 classification analysis with four different modes and the accuracies were measured. These measured accuracies show the possible survival rate of heart attack patients at different modes. Mode-4, the last of these developed modes, has performed the classification process with the C4.5 Algorithm by considering node splitting and tree pruning. As a result of the study, the performance of Mode-4 was found to be better than other mods, proving that attribute split criterion and tree pruning increase accuracy.

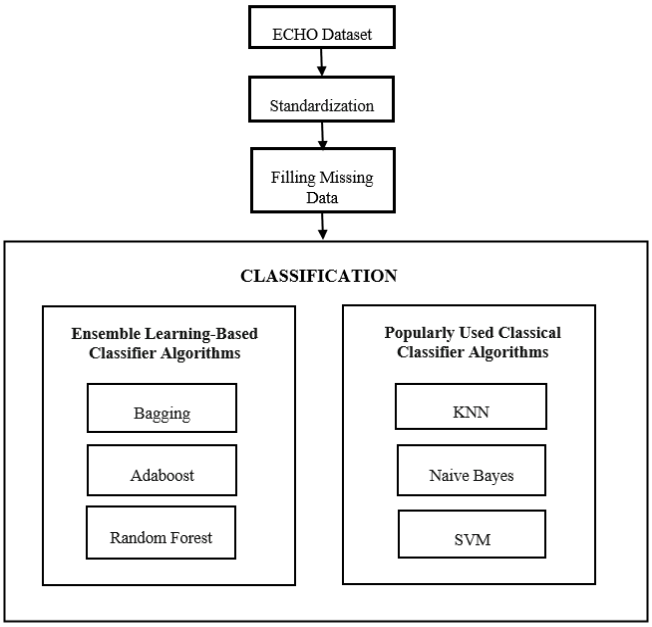

Figure 1: Study Flow Diagram

Heart attack, which is one of the CVD, is the blockage of the coronary veins that supply oxygen and nutrients to the heart or the interruption of blood flow to the heart muscle. This instantaneous situation may occur as a result of triggering many factors such as age, genetic factors, stressful life and it may occur lethal consequences. Besides, the life threat of patients who have had a heart attack at a certain point in their life threat continues even after the attack too. It was aimed to determine whether patients who had a heart attack have a life threat after the attack with the ECHO dataset from UCI source with 132 instances and 12 attributes in this study. In this paper, as a solution to the detection of after the attack life threat for patients who have had a heart attack, whether patients survive at least one year after a heart attack by using ECHO data was predicted. The process of the realized working model is presented in Figure 1.

As can be seen in Figure 1, firstly standardization was applied to the dataset consisting of the data of patients who had a heart attack. Later, the missingness of the dataset was filled by using the FCS method. Finally, classification processes were carried out with various machine learning algorithms. Classification performances were evaluated comparatively as ensemble learning-based classifier algorithms and popularly used classical classifier algorithms.

II. MATERIAL AND METHODS

The ECHO dataset used in this study was obtained from the UCI database. This dataset includes information of 132 patients who had a heart attack in the past and who are alive or who are not such as the age at which they had a heart attack, their survival time after a heart attack, and whether they are alive or not. In addition to these, it also includes the cardiological information of the patients and class information that shows whether patients survived at least 1 year after a heart attack.

A. Standardization

Each feature in datasets can have different values and different scales. Bringing the values to a certain range and fitting each value into this range facilitates the legibility of the data and its intro to the computer. For this reason, standardization processing was applied to the data in this study. Standardization is the rescaling of value distributions so that the mean of the observed values is 0 and the standard deviation is 1. Standardization is a common data preprocessing method as it calculates by assuming that the observations fit a Gaussian [14] distribution with an appropriate mean and standard deviation. Therefore, in this study, the standardization process was applied to the data with the *StandardScaler* method in the range of -1 to 1.

B. Filling Missing Values with FCS

Having missing value in data sets is one of the main problems frequently encountered in machine learning. Therefore, many methods have been developed to filling the missing value. The success of the method to filling the missing value is affected by many factors such as the characteristics of the data and the type of missing value [15]. For this reason, choosing the appropriate method to complete the missing data in the data sets is an important and necessary pre-process in machine learning studies.

Missing value filling methodology is realized in two basic ways, namely Single Imputation, and Multiple Imputation. In the Single imputation method, mean, median, or some other statistical operations are used to calculate missing values. The method, where statistical operations are performed in this way, creates uncertainty in determining the degree of influence of other data points that will affect that point while filling the missing value point. The multiple imputation method narrows this uncertainty about missing values by calculating several different options and several versions of the same dataset is created, which are then combined to obtain the best values [16]. FCS method, one of the multiple imputation methods, is a more flexible method than other multiple imputation methods [17]. FCS method is a rather useful method in terms of adapting univariate regression models appropriately [18] and missing values in this study were also filled with this method.

III. EXPERIMENTAL RESULTS AND DISCUSSION

It was aimed to determine whether patients who had a heart attack have a life threat after the attack with the ECHO dataset, in this paper. Firstly, standardization was applied to the dataset. Later, the missingness of the dataset was filled by FCS.

Dataset was separated randomly as 80% training set and 20% testing set. Classification processing was carried out using ensemble learning-based Bagging, Adaboost, and Random Forest algorithms and popularly used classical KNN, Naive Bayes, and SVM classifier algorithms. Classification performance was evaluated with the performance criteria of Classification Accuracy (CA), kappa coefficient, precision, sensitivity (recall), and Matthews correlation coefficient (MCC) [9, 19, 20]. In the classification, firstly the parameters that give the highest accuracy result were determined with the 10-fold CV technique using the training data set. Afterward, test processes were carried out. The obtained classification performance results were examined comparatively in the form of ensemble learning-based classification algorithms and popularly used classical classification algorithms. Test results obtained with Bagging, Adaboost, Random Forest classification algorithms, which are ensemble learning-based, are shown in Table 1. According to Table 1, when the highest CA with ensemble learning-based classifiers is considered; It is seen that 94.87% was obtained with the Adaboost classifier. For this classifier, the Precision and Recall criteria, which determine the precision and sensitivity of the system, were also found to be very successful at 95.2% and 94.9% respectively. MCC is a criterion used between observed and predicted binary classifications and is essentially a correlation coefficient value between -1 and +1. A coefficient of 1 indicates a perfect prediction, 0 indicates a mean random prediction, and -1 indicates an incorrect prediction. Contrary to CA, MCC provides a balanced measure that can be used even if classes are of very different sizes, taking into account positives and negatives [21]. Therefore, MCC is an important performance criterion in itself, and in this study, the best MCC value was reached as 94.9% with again Adaboost. When evaluated in

terms of the Kappa coefficient, the Adaboost classification algorithm has a very high success rate of 0.8434, with a notable difference when compared to other classifier algorithms.

Table 1: Test Results of Ensemble Learning-Based Classification Algorithms

CLASSIFIER	CA	Kappa	Precision	Recall	MCC
Bagging	87.17	0.5517	89.0	87.2	0.617
Adaboost	94.87	0.8434	95.2	94.9	0.854
Random Forest	92.30	0.7547	93.0	92.3	0.778

Table 2 shows test results obtained with KNN, Naive Bayes, and SVM, which are popularly used classical classification algorithms. When Table 2 is examined, it is seen that the highest accuracy rate is 92% obtained with the KNN classifier. As it is known, the KNN algorithm does not give effective results in multidimensional datasets [22], in addition, as the number of features in datasets increases, the success of classification with KNN decreases significantly [23]. Considering that 132 patients' ECHO data were used in this study, it can be said that successful results can be obtained with KNN in small-sized ECHO datasets with few features.

Table 2: Test Results of Popularly Used Classical Classification Algorithms

CLASSIFIER	CA	Kappa	Precision	Recall	MCC
KNN	92.0	0.7746	92.2	92.3	0.775
Naive Bayes	89.74	0.732	91.0	89.7	0.739
SVM	87.17	0.5912	86.8	87.2	0.610

When Table 1 and Table 2 are examined together, it is seen that the highest accuracy rate was obtained with Adaboost (94.87%), and then Random Forest, another ensemble learning-based classifier algorithm, achieved the second-highest accuracy rate with an accuracy of 92.30%. Besides, the accuracy of KNN (92%), which is one of the popularly used classical classification algorithms, was found to be higher than the other classical classification algorithms, Naive Bayes and SVM. However, as it is known, while the KNN algorithm generally cannot produce successful results in large data sets due to the increased feature size [24]. Considering that the ECHO data of 132 patients were used in this study, it is seen that the study was carried out with very little data. After obtaining a very successful result with such little data, it is not thought that the KNN algorithm will produce very successful results in more detailed studies to be made in the future by increasing the number of data. Considering the accuracy rate performances of Adaboost and Random Forest in this study, and examining the MCC values, which is another important performance criterion, it is seen that ensemble learning-based classifiers produce more consistent and precise results as well providing higher accuracy than classical classifiers.

IV. CONCLUSION

This study aims to develop an effective machine learning model that predicts whether patients survive at least one year after a heart attack by using ECHO data. Standardization and filling missing values with FCS were applied to the ECHO dataset. Then, classification processing was performed with various machine learning algorithms. The classification studies carried out were evaluated comparatively as ensemble learning-based classifier algorithms and popularly used classical classifier algorithms. As a result of the studies, the highest accuracy rate was obtained with Adaboost as 94.87%. It was concluded that the most effective model was produced by ensemble learning-based classifiers in the study of determining whether patients survive at least one year after a heart attack. And it is thought that more qualified studies can be done with an integrated system by including different heart data in the study.

REFERENCES

[1] World Health Organisation (WHO). Global atlas on cardiovascular disease prevention and control. 2011. whqlibdoc.who.int/publications/2011/9789241564373_eng.pdf.

[2] Department of Chronic Diseases and Health Promotion, World Health Organization. Preventing chronic diseases: a vital investment. Geneva: World Health Organization; 2005.

[3] Department of Chronic Diseases and Health Promotion, World Health Organization. Preventing chronic diseases: a vital investment. Geneva: World Health Organization; 2005.

[4] J. H. Park, S. K. Zhou, C. Simopoulos, J. Otsuki, and D. Comaniciu. Automatic Cardiac View Classification of Echocardiogram. *2007 IEEE 11th International Conference on Computer Vision*, 2007.

[5] S. V. Aschkenasy, C. Jansen, R. Osterwalder, A. Linka, M. Unser, S. Marsch, and P. Hunziker. Unsupervised image classification of medical ultrasound data by multiresolutionela stic registration. *Ultrasound in Medicine and Biology*, 32(7): 1047–1054, 2006.

[6] S. Zhou, J. Park, B. Georgescu, J. Simopoulos, J. Otsuki, and D. Comaniciu. Image-based multiclass boosting and echocardiographic view classification. In *CVPR*, pages 1559– 1565, 2006.

[7] R.Erbel, W.Daniel, C.Visser, R.Engberding, J.Roelandt, H.Rennollet and The European Cooperative Study Group For Echocardiography. In *The Lancet*, 333(8636): 457-461, 1989.

[8] Evangelista, F. Flachskampf, R. Erbel, F. Antonini-Canterin, C. Vlachopoulos, G. Rocchi, R. Sicari, P. Nihoyannopoulos, J. Zamorano, M. Pepi, O. Breithardt and E. Płońska-Gościniak. Echocardiography in aortic diseases: EAE recommendations for clinical practice. *European Journal of Echocardiography*, 11(8): 645-658, 2010.

[9] C. Krittanawong, H. U. H. Virk, S. Bangalore, Z. Wang, K. W. Johnson, R.l Pinotti, H. J. Zhang, S. Kaplin, B.Narasimhan, T. Kitai, U. Baber, J. L. Halperin and W. H. W. Tang. Machine learning prediction in cardiovascular diseases: a meta-analysis. *Scientific Reports*, 10(16057), 2020.

[10] S. F. Weng, J. Reps, J. Kai, J. M. Garibaldi and N.Qureshi. Can machine-learning improve cardiovascular risk prediction using routine clinical data ?. *PloS ONE*, 12(4), 2017.

[11] J.A. Quesada, A. Lopez-Pineda, V. F. Gil-Guillén, R. Durazo-Arvizu, D. Orozco-Beltrán, A. López-Domenech and C. Carratalá-Munuera. Machine learning to predict cardiovascular risk. *The International Journal of Clinical Practice*, 73(10), 2019.

[12] X. Su, Y. Xu, Z. Tan, X. Wang, P. Yang, Y.Su, Y. Jiang and S. Qin, L. Shang. Prediction for cardiovascular diseases based on laboratory data: An analysis of random forest model. *Journal of Clinical Laboratory Analysis*, 34(10), 2020.

[13] R. Jothikumar, S. Susi, N. Sivakumar and P. S. Ramesh. Predicting Life time of Heart Attack Patient using Improved C4.5 Classification Algorithm. *Research Journal of Pharmacy and Technology*, 11(5): 1951-1956, 2018.

[14] D. Karlis. An EM Type Algorithm for Maximum Likelihood Estimation of the Normal-Inverse Gaussian Distributions. *Statistics & Probability Letters*, vol.57 1(pg. 43-52), 2002.
[15] M. Albayrak, K. Turhan, & B. Kurt. Kümeleme ve Maksimum Olabilirlik Yaklaşımıyla Eksik Veri Tamamlama, *2017 Medical Technologies National Congress (TIPTEKNO)*, 242–245, 2017.
[16] S. Glen. Multiple Imputation for Missing Data: Definition, Overview Retrieved from 30. 01. 2017. https://www.statisticshowto.com/multiple-imputation
[17] S. van Buuren, H.C. Boshuizen and D.L. Knook. Multiple Imputation of Missing Blood Pressure Covariates in Survival Analysis. *Stat Med*, vol. 18 6(pg. 681-694), 1999.
[18] K.J. Lee, J.B. Carlin. Multiple Imputation for Missing Data: Fully Conditional Specification Versus Multivariate Normal Imputation. *American Journal of Epidemiology*, vol.171 5(pg. 624-632), 2010.
[19] N. Seliya, T. M. Khoshgoftaar and J. M. Hulse. A Study on the Relationships of Classifier Performance Metrics. *2009 21st IEEE International Conference on Tools with Artificial Intelligence*. 2009.
[20] A. Osareh, B. Shadgar. Machine learning techniques to diagnose breast cancer. *2010 5th International Symposium on Health Informatics and Bioinformatics*, May, 2010.
[21] F. Pedregosa, Varoquaux, Ga"el, A. Gramfort, V. , Michel, B. Thirion, O. Grisel, … others. Scikit-learn: Machine learning in Python. *Journal of Machine Learning Research*, *12*(Oct), 2825–2830, 2011.
[22] R.O. Duda, P.E. Hart and D.G. Stork. "Pattern Classification", John Wiley & Sons, New Jersey, 2000.
[23] A.E. Taşcı, A. Onan. K-En Yakın Komşu Algoritması Parametrelerinin Sınıflandırma Performansı Üzerine Etkisinin İncelenmesi. *Akademik Bilişim*, ss.1-8, 2016.
[24] H. Liu and S. Zhang. Noisy Data Elimination Using Mutual K-Nearest Neighbor for Classification Mining, *Journal of Systems and Software*, 85(5), 1067-1074, 2012.

Preventing Image Duplication Using Similarity Methods

H. TOPÇUOĞLU[1], B. MUTLU[2], C. SÖYLEMEZ[3],

[1]Enuygun.com, İstanbul/Turkey, hincal.topcuoglu@enuygun.com
[2]Enuygun.com, İstanbul/Turkey, behcet.mutlu@enuygun.com
[3] İzmir Bakırçay University, İzmir/Turkey, cevhernur.soylemez@bakircay.edu.tr

Abstract - **Enuygun.com works with different hotel providers to realize the sales of hotels. Different hotel names, meta-information and hotel images are retrieved for the same hotel from these providers using APIs and having different data for the same hotel causes a problem named "hotel duplication". In this study, it is aimed to find out whether the relevant images belong to the same hotel by evaluating the images from the providers. To make evaluations 100 images belonging to 36 hotels from different vendors were collected. Then a ground truth dataset to evaluate the performance of approaches was constructed and validated by 3 domain experts. Two different methods were experimentally tested. Color histograms were used to calculate the similarity of two images as the first method (Method1.HistogramBased). Although it is one of the important methods in the literature, false positive or false negative samples are frequently encountered because it makes a comparison-based on histogram distribution. In the second method (Method2.DeepLearningBased) VGG-19 architecture was used to expand dimensions of images in matrix form and then pre-processed its input and made predictions of images to get their feature-based representations. Histogram-based and deep learning-based methods were evaluated using the collected dataset. The accuracy (ACC) values of the methods are 57% and 87% respectively. When the literature is considered, it is seen that there are many different simple and complex methods to compare images. To the best of our knowledge, this study is one of the first studies that apply early pre-processing steps of a VGG-19 model to obtain dense matrices and calculate the similarity score using the correlation of these matrices in the hospitality domain.**

Keywords **– Image Similarity, Hotel Deduplication, Deep Learning, İmage Segmentation, Classification**

I. INTRODUCTION

The World Wide Web (WWW) has drastically increased the amount of electronically exchanged information. These developments bring new forms to the supply-demand model in the tourism industry.

Recently, travelers generally prefer booking via online travel agencies (OTAs) serving as a hotel reservation channel owing to provided price comparisons and the visualization of the holiday destination.

The content of the visuals is one of the most critical parameters while deciding holiday options. If the images do not reflect well the hotel experience, a traveler may be in doubt about booking. Therefore, the hotel images in OTAs must be classified with the most appropriate content to give reliable information to the travelers.

Enuygun.com provides an online platform that lets users search, list, and evaluate domestic and international flights, bus tickets, and tens of thousands of hotels within seconds. The company works with different hotel providers to realize the sales of hotels. From a technical perspective, each provider has its own integration service infrastructure, and the functions of the services are managed and deployed outside as APIs. Different hotel names, meta-information, and hotel images are retrieved for the same hotel from these providers using these APIs and having different data for the same hotel causes a problem named “hotel duplication”.

In this study, it is aimed to determine whether the relevant images belong to the same hotel by comparing the images from the providers. This experimental study is done using a color i) histogram-based approach (Method1), and ii) applying a deep learning-based approach (Method2). To evaluate the proposed methods a dataset containing 100 images that belong to 36 hotels is created and the results show that deep learning-based method is more accurate than traditional histogram-based approach.

The rest of the paper is organized as follows: In Section 2, the literature review is introduced. Section 3 presents the detailed materials and methods. In Section 4 presents and is discussed results for two different similarity approaches. At last, the conclusion and future works take part in Section 5.

II. LITERATURE REVIEW / RELATED WORKS

In literature, there are works related to calculating similarity between images using trained Convolutional Nets and fetching similar images from large databases using Siamese networks. Zagoruyko and Komodakis (2015) [1] trained a neural model to get a function between image patches. LeCun and Zbontar (2015) [2] trained a convolutional neural network model to predict how well two image patches match.

On the other hand, there are methods which use large image databases to find single image matches with other ones. Siamese networks is an example of this kind of matching,

splitting data into positive / negative and search. Lowe (2004) [3] developed a method that matches individual features to a database of features from known objects using nearest-neighbor algorithm. Wang et al. (2004) [4] used a different algorithm named getting hash codes for images and pairing them using similar hash codes for fast detection in web image search area. Karami et al. [5] compared different image matching algorithms such as SURF, SIFT, BRIEF and ORB with different scaled images with different distortions to get which algorithm reaches the best-more robust results against each other.

A study done by Appalaraju et al. [6] for a given reference image, fetching similar images with an algorithm named SimNet, a deep Siamese network trained on pairs of positive and negative images inspired by Curriculum learning. They showed that this multi-scaled network shows better results than traditional CNN's. Plummer et al. [7] introduced SANE (Salient Attributes for Network Explanation) to explain image similarities where model score measures the similarity between two inputs. Their work showed that SANE method can identify important image regions. Shimoda et al. [8] trained a CNN model for food application to get image similarities. They obtained that triplet network is the most powerful one between other CNN models. Stylianou et al. [9] made a work which highlights the key points of an image to get similarities. Their approach explicitly decomposes the entire similarity score between two images and assigns it to the relevant image regions. Zhang et al. [10] evaluated some measurement metrics and distance measures in the content-based image retrieval field. They showed that city block distance and chi square distance are more desirable distance measures than others. Wang et al. presented a multi-scale structural image similarity method. Silva et al. [11] presented a new similarity measurement metric using entropy notion besides to mean square error and peak signal to noise ratio.

Jia et al. [12] introduces color histogram-based representation of images which are used for object recognition. They compared six histogram-based image matching methods in their paper and also used them for classification. These methods were tested on vehicle number plate images for number plate classification. Experimental methods showed that the CRG method is the fastest while GWHI method is the most accurate. When both speed and matching performance are concerned, the CECH is the most promising.

III. Material and methods

In this section materials and methods related to the study such as the color comparison methods and the data used are described.

A. Dataset

In the study, 100 images belonging to 36 hotels from different vendors are collected. Then a ground truth dataset to evaluate the performance of approaches is constructed and validated by 3 domain experts. There can be pictures of a hotel in different categories such as indoor (room, bathroom pictures, etc.) and outdoor (such as remote view of the hotel, etc.). When comparing the hotels, only the pictures in the same categories were compared mutually.

B. Color Histogram-based Similarity

By far the most intuitive information that can be extracted from images for comparison is the color characteristics of an image. Color is one of the most prominent features of the image, and it is very easy to calculate. Additionally, color is of widespread interest to many researchers because it is not affected by the scaling, and translation of an image.

A number of algorithms have been developed since the late 1980s. The most common form of color retrieval involves specifying color values that can be searched for in a set of images. Computers represent all visible colors with a combination of a set of base color components Red, Green, and Blue (RGB).

A conventional approach comparing an image with another one is that of comparing their color histograms. The methodology relies on the fact that images are generally represented as a series of pixel values, each matching to the can be seen color. Color histograms are computed for each image so as for the purpose of identifying relative proportions of pixels within specific values. The color histogram represents the global color distribution of an image, and the intersection of histograms calculates the similarity of two probability distributions with possible values of intersection range between 0 and 1. In the image similarity concept, calculating color histograms of images and comparing them with some methods are widely used. The idea is that similar images probably contain a similar rate of specific colors.

Figure 1: A picture of a cat.

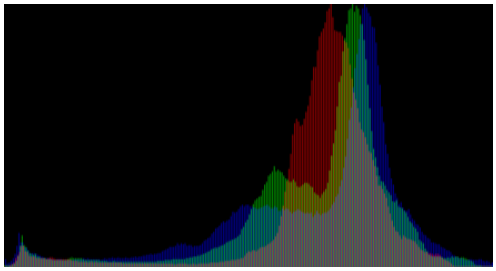

Figure 2: Color histogram of the in Figure 1 cat picture with the x-axis being RGB and y-axis being the frequency.

C. *Deep Learning-based Similarity*

With their high accuracy predictions in image detection and recognition tasks, Convolution Neural Networks (CNNs) are solid frameworks and most applied to analyze visual imagery. CNN in computer vision applications has demonstrated remarkable performance for content-based information retrieval models (CBIR). Recent studies have demonstrated that CNN can efficiently extract pattern features and classify images with high accuracy [13]. The availability of pre-trained networks makes it easier to apply CNNs to new tasks without incurring high computational costs or requiring a thorough understanding of how CNNs function. AlexNet, VGGNet, GoogleNets, and ResNet networks, are examples of well-known pre-trained networks that can be used as the foundation for new task applications.

The Visual Geometry Group Network (VGGNet) is a deep neural network with a multilayered operation. The VGGNet is based on the CNN model and is implemented in the ImageNet dataset. VGG-19 is a beneficial VGGNet version due to its simplicity as 3 × 3 convolutional layers are attached on the top to increase with depth level.

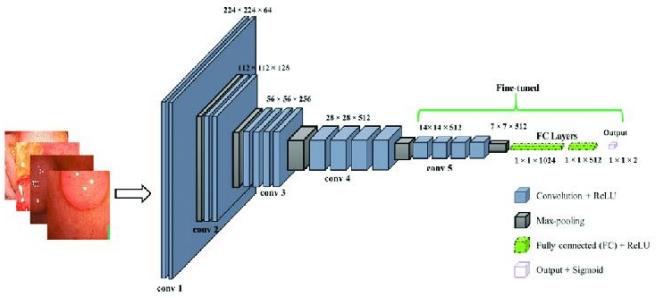

Figure 3: VGG-19 Architecture [15]

In this study, the methods used in the early steps of the VGG-19 pre-trained deep-learning model were used to calculate similarity scores between images.

The neural network steps that the VGG19 model uses while pre-processing the images are applied to the image data set. In other words, by employing the data pre-processing steps before running the model in our image data set, dense matrices are extracted and obtained from the images. Then, the similarity scores between the hotel images are calculated by considering the correlation of these matrixes formed for the two image pairs.

IV. Experimental Results

In the study, two different methods were experimentally evaluated. We utilized color histograms to calculate the similarity of two images in the first method (Method1.HistogramBased). Although it is one of the important and common methods in the literature, false positive or false negative samples are frequently encountered because it makes a comparison based on histogram distribution.

In the second method (Method2.DeepLearningBased) we used VGG-19 architecture to expand dimensions of images in matrix form and then pre-processed its input and made predictions of images to get their feature-based representations. After that we compared image matrixes with correlation coefficient to check how similar they are.

	True	**False**	**ACC**
Method1	63	47	0,57
Method2	87	13	0,87

Table 1. Experimental Results

Table 1 shows the results of experimental tuns in terms of accuracy metric values (ACC). The value of ACC is calculated as in Equation 1 using True Positive (TP), True Negative (TN), False Positive (FP), and False Negative (FN) baseline metrics.

$$ACC = \frac{TP + TN}{TP + TN + FP + FN} \quad (1)$$

The results indicate that deep learning-based and histogram-based methods have the ACC values 0,87 and 0,57 respectively. Although the histogram-based method is a very common approach in the literature, the state-of-the-art deep-learning-based method has achieved much better results.

V. Conclusion

Even though image comparison is a subject that has been studied for a long time, new researches have started to be done in the literature with the use of new start-of-the-art methods as deep learning. The aim of this study is to see if the relevant images from the different vendors belong to the same hotel. For testing purposes, a dataset including 100 photos from 36 hotels was constructed. As the result of the study, it was observed that the VGG19-based model gave better results than the histogram-based method and finally it can be concluded that that deep learning-based approaches like CNN can be more successful in image similarity.

VI. References

[1] S. Zagoruyko ve N. Komodakis, “Learning to Compare Image Patches via Convolutional Neural Networks,” *arXiv:1504.03641* , 2015.

[2] J. Zbontar ve Y. LeCun, “Computing the Stereo Matching Cost with a Convolutional Neural Network,” *IEEE Conference on Computer Vision and Pattern Recognition (CVPR),* 2015.

[3] G. D. LOWE, "Distinctive Image Features from Scale-Invariant Keypoints," *International Journal of Computer Vision*, pp. 91-110, 2004.

[4] Z. Wang, "Image Quality Assessment: From Error Visibility to Structural Similarity," *IEEE Transactions on Image Processing*, cilt 4, no. 13, pp. 600-612, 2004.

[5] E. Karami, S. Prasad ve M. Shehata, "Image Matching Using SIFT, SURF, BRIEF and ORB: Performance Comparison for Distorted Images," *arXiv:1710.02726*, 2017.

[6] S. Appalaraju ve V. Chaoji, "Image similarity using Deep CNN and Curriculum Learning," *arXiv:1709.08761*, 2017.

[7] A. B. Plummer, I. M. Vasileva, V. Petsiuk, K. Saenko ve D. Forsyth, "Why do These Match? Explaining the Behavior of Image Similarity Models," *ECCV 2020: Computer Vision*, pp. 652-669, 2020.

[8] W. Shimoda ve K. Yanai, "Learning Food Image Similarity for Food Image Retrieval," *2017 IEEE Third International Conference on Multimedia Big Data (BigMM)*, 2017.

[9] A. Stylianou, R. Souvenir ve R. Pless, "Visualizing Deep Similarity Networks," *arXiv:1901.00536* , 2019.

[10] D. Zhang ve G. Lu, "EVALUATION OF SIMILARITY MEASUREMENT FOR IMAGE RETRIEVAL," *International Conference on Neural Networks and Signal Processing*, 2003.

[11] K. Panetta, E. A. Silva ve S. S. Agaian, "Quantifying image similarity using measure of enhancement by entropy," *Proceedings Volume 6579, Mobile Multimedia/Image Processing for Military and Security Applications*, 2007.

[12] W. Jia, H. Zhang, X. He ve Q. Wu, "A Comparison on Histogram Based Image Matching Methods," *2006 IEEE International Conference on Video and Signal Based Surveillance*, 2006.

[13] M. Ramamurthy, Y.H. Robinson, S. Vimal, A. Suresh, Auto encoder based dimensionality reduction and [1]classification using convolutional neural networks for hyperspectral images, Microprocess. Microsyst. 79 (2020), 103280.

[14] J. Yue-Hei Ng, F. Yang, L.S. Davis, Exploiting local features from deep networks for image retrieval, in: Proceedings of the IEEE conference on computer vision and pattern recognition workshops, 2015, pp. 53–61.

[15] M. Billah, S. Waheed, M.M. Rahman, Hindawi International Journal of Biomedical Imaging Volume 2017, Article ID 9545920, 9 pages https://doi.org/10.1155/2017/9545920

Quantum Teleportation by Using Superdense Coding and Teleportation Algorithms in Qiskit and IBM Circuit Composer

Y. POYRAZ KOÇAK[1]

[1] Istanbul University-Cerrahpasa, Istanbul/Turkey, yasemin.poyraz@iuc.edu.tr

Abstract **- Quantum teleportation is a technique of sending a state vector from one place to another place. The distance between these two points can be even hundreds of thousands of light years. For quantum teleportation, there is no need for a channel between two points when sending the state vector from one place to another. Since classical information sharing is possible, it is also possible to send a state vector from one place to another place. Teleportation is the transfer of a quantum state from one place to another through classical channels. Superdense coding, a dual to teleportation, uses a single quantum bit to transmit two bits of classical information. Superdense coding, one of the quantum algorithms, uses a qubit to transfer 2 classical bits, while another algorithm so-called Teleportation performs 1 qubit transfer using 2 classical bits. In this article, teleportation and dense coding processes are carried out on both Qiskit and IBM quantum circuit composer, and the results obtained in Qiskit and real quantum computers are compared and presented in detail. The results revealed that whether faster-than-light signal transfer is possible using quantum mechanics depends on whether a copy of a quantum state is created or not.**

Keywords **– Teleportation, Superdense Coding, Quantum Computing, Qiskit, IBM Circuit Composer.**

I. INTRODUCTION

Quantum computing and quantum information use fundamental of quantum mechanical system to deliver a huge leap forward in computation and to solve certain problems. Today, IBM, Microsoft, Google, Rigetti and so many companies in China are trying to build quantum computers and reach perfectly working quantum computers. Thanks to the quantum computers developed by these companies, the certain algorithms have been developed so far. These algorithms are Berstain-Vazirani, Deutsch and Deutsch-Jozsa, Shor's algorithm, Grover's algorithm, Quantum Fourier Transformation (QFT), Quantum Phase Estimation. But today, it is not possible to do what classical computers can do, such as copying and transmitting information between two places with quantum computers. According to the rules of quantum mechanics, it is not possible to duplicate a state vector. There may be various physical reasons for this condition. Quantum mechanical states are very delicate, delicate states that can deteriorate at the slightest intervention. In this point, Quantum developers have sought to transfer quantum information from one location to another location without losing the information and preserving the information by using quantum two-state system and Superdense Coding, Teleportation algorithms have been emerged. While Superdense Coding uses a single qubit to send two classical bits of information, Quantum Teleportation uses two classical bits of information to send a single qubit [1,2].

Lots of application are realized by using quantum teleportation algorithms. To send more than one bit of information requires manipulation of more than one two-state particle. In [3], transition of one of three messages by manipulating only one of two entangled particles are demonstrated experimentally. [4] is present dense quantum coding for the quadrature amplitudes of the electromagnetic field. In [5] teleportation of continuous quantum variables is treated in complete analogy to the case of teleportation of qubits. In [6], unconditional teleportation of arbitrary quantum states between diamond spin qubits separated by 3 meters are demonstrated. In [7], a method is presented to create a variety of interesting gates by teleporting quantum bits through special entangled states. Quantum teleportation is a special case of the problem of reversing quantum operations. In [8], completely teleportation schemes of the type proposed by Bennett are characterized and simple necessary, sufficient conditions for an ideal quantum operation to be reversible by a unitary operation are derived. In [9], an experimental implementation of the full quantum teleportation operation over inter-atomic distances using liquid state nuclear magnetic resonance (NMR) is realized. This study deals with both Superdense Coding and Teleportation algorithms. The success rates of the algorithms are implemented both in the simulation environment using Qiskit and on real quantum devices, and detailed results are presented. I use IBM's 32 qubit real quantum device.

The rest of the paper is organized as follows: in Section 2, the Superdense Coding and Teleportation algorithms are explained; in Section 3, the experimental results are presented and comparisons are made and finally in Section 4, the conclusions are given.

II. QUANTUM TELEPORTATION

A. Superdense Coding Algorithm

Superdense coding is one of interesting and simple applications of quantum entanglement. In Superdense Coding, there are two people named Alice and Bob. Alice wants to send a two-bit string of classical information to Bob. There are

4 possible combinations of these two bits of information. These two bits of information have special messages. Alice wants to send any of these two bits of information but there is one rule. Alice is only allowed to send one qubit of information to Bob. But Alice wants to share two bits of information. This can happen if they have shared an entangled state among themselves before. This is called Superdense Coding protocol. Eve prepares an entangled state using two qubits. It passes the first qubit of a two-qubit system through the Hadamard gate, and a two-qubit system passes through the CNOT gates. Eve prepares an entangled state using two qubits. As seen quantum circuit design of Superdense Coding algorithm in the Fig. 1, There is two qubits in the system. One of them is belong to Alice and second is belong to Bob [1].

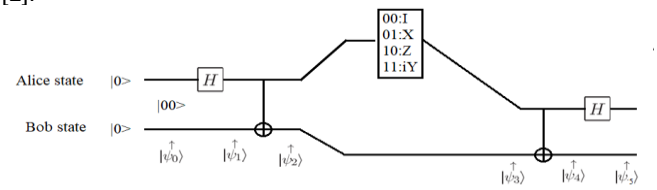

Figure 1: Quantum Circuit Design of Superdense Coding algorithm.

Suppose Alice and Bob initially share a pair of qubits in the entangled state as seen in (1):

$$|\Psi_0\rangle = |00\rangle \tag{1}$$

Alice sends the first qubit through a Hadamard gate, and obtaining (2):

$$|\psi_1\rangle = \frac{|00\rangle + |10\rangle}{\sqrt{2}} \tag{2}$$

Then a CNOT gate is applied to total state, and obtained state is (3):

$$|\psi_2\rangle = \frac{|00\rangle + |11\rangle}{\sqrt{2}} \tag{3}$$

If Alice wants to send 00 classic information, I operator is used and obtained state is $|\Psi_3\rangle$ as seen in (4):

$$|\psi_3\rangle = \frac{|00\rangle + |11\rangle}{\sqrt{2}} \tag{4}$$

When CNOT gate is applied, $|\Psi_4\rangle$ state is obtained as seen in (5):

$$|\psi_4\rangle = \frac{|00\rangle + |11\rangle}{\sqrt{2}} \xrightarrow{CNOT} \frac{|00\rangle + |10\rangle}{\sqrt{2}} \tag{5}$$

Finally Hadamard gate is applied $|\Psi_5\rangle$ state is obtained as seen in (6):

$$|\psi_5\rangle = \frac{|00\rangle + |10\rangle}{\sqrt{2}} \xrightarrow{H} \frac{\frac{|0\rangle + |1\rangle}{\sqrt{2}}|0\rangle + \frac{|0\rangle - |1\rangle}{\sqrt{2}}|0\rangle}{\sqrt{2}} \tag{6}$$

$$= \frac{1}{2}(|00\rangle + |10\rangle + |00\rangle - |10\rangle) = |00\rangle$$

When the obtained value is examined, it is seen that 00 information string is obtained with 100% probability.

If Alice wants to send 01 classic information, X operator is used and obtained state is $|\Psi_3\rangle$ as seen in (7):

$$|\psi_3\rangle = \frac{|00\rangle + |11\rangle}{\sqrt{2}} \xrightarrow{X} \frac{|10\rangle + |01\rangle}{\sqrt{2}} \tag{7}$$

When CNOT gate is applied, $|\Psi_4\rangle$ state is obtained as seen in (8):

$$|\psi_4\rangle = \frac{|10\rangle + |01\rangle}{\sqrt{2}} \xrightarrow{CNOT} \frac{|11\rangle + |01\rangle}{\sqrt{2}} \tag{8}$$

Finally Hadamard gate is applied $|\Psi_5\rangle$ state is obtained as seen in (9):

$$|\psi_5\rangle = \frac{|00\rangle + |10\rangle}{\sqrt{2}} \xrightarrow{H} \frac{\frac{|0\rangle - |1\rangle}{\sqrt{2}}|1\rangle + \frac{|0\rangle + |1\rangle}{\sqrt{2}}|1\rangle}{\sqrt{2}} \tag{9}$$

$$= \frac{1}{2}(|01\rangle - |11\rangle + |01\rangle + |11\rangle) = |01\rangle$$

When the obtained value is examined, it is seen that 01 information string is obtained with 100% probability.

If Alice wants to send 10 classic information, Z operator is used and obtained state is $|\Psi_3\rangle$ as seen in (10):

$$|\psi_3\rangle = \frac{|00\rangle + |11\rangle}{\sqrt{2}} \xrightarrow{Z} \frac{|00\rangle - |11\rangle}{\sqrt{2}} \tag{10}$$

When CNOT gate is applied, $|\Psi_4\rangle$ state is obtained as seen in (11):

$$|\psi_4\rangle = \frac{|00\rangle - |11\rangle}{\sqrt{2}} \xrightarrow{CNOT} \frac{|00\rangle + |10\rangle}{\sqrt{2}} \tag{11}$$

Finally Hadamard gate is applied $|\Psi_5\rangle$ state is obtained as seen in (12):

$$|\psi_5\rangle = \frac{|00\rangle + |10\rangle}{\sqrt{2}} \xrightarrow{H} \frac{\frac{|0\rangle + |1\rangle}{\sqrt{2}}|0\rangle + \frac{|0\rangle - |1\rangle}{\sqrt{2}}|0\rangle}{\sqrt{2}} \tag{12}$$

$$= \frac{1}{2}(|00\rangle + |10\rangle - |00\rangle + |10\rangle) = |10\rangle$$

When the obtained value is examined, it is seen that 10 information string is obtained with 100% probability.

If Alice wants to send 11 classic information, iY operator is used and obtained state is $|\Psi_3\rangle$ as seen in (13):

$$|\psi_3\rangle = \frac{|00\rangle + |11\rangle}{\sqrt{2}} \xrightarrow{iY} \frac{-|10\rangle + |01\rangle}{\sqrt{2}} \tag{13}$$

When CNOT gate is applied, $|\Psi_4\rangle$ state is obtained as seen in (14):

$$|\psi_4> = \frac{-|10>+|01>}{\sqrt{2}} \xrightarrow{CNOT} \frac{-|11>+|01>}{\sqrt{2}} \quad (14)$$

Finally Hadamard gate is applied $|\Psi_5>$ state is obtained as seen in (15):

$$|\psi_5> = \frac{-|11>+|01>}{\sqrt{2}} \xrightarrow{H} \frac{\frac{-|0>+|1>}{\sqrt{2}}|1> + \frac{|0>+|1>}{\sqrt{2}}|1>}{\sqrt{2}}$$
$$= \frac{1}{2}(-|01>+|11>+|01>+|11>) = |11> \quad (15)$$

When the obtained value is examined, it is seen that 11 information string is obtained with 100% probability.

B. Teleportation Algorithm

Quantum teleportation is a technique of sending a state vector from one place to another. The distance between these two points is measured in light years. But the interesting thing is this. When sending a quantum state from one place to another, there is no need for any quantum channel between two points. Once it is possible to share classical information, it is possible to send a situation from one place to another. Again, when Alice and Bob were together years ago, they shared an entangled state (one of the bell states) a qubit among themselves, Alice taking a qubit bob. They are moving away from each other. Let one stay in our world, and one go to another corner of the Milky Way galaxy. Years later, Alice wants to send a state vector to Bob. Alice and Bob cannot share any qubits between them, but they can share classical bits. In other words, it can communicate via a classical channel. This may seem impossible at first. The state vector of 1 qubit in Alice's hand is shown by (16) below [1].

$$|\Psi> = \alpha|0> + \beta|1> \quad (16)$$

α and β in equation 1 are complex numbers that can take all values. It will take endless time for Bob to consider all possible values and construct it. Secondly, Alice cannot know the coefficients α and β because when Alice wants to measure, her state vector will be distorted. Therefore, it is unlikely that Alice will send Bob the state vector. But it is possible to send this state with Teleportation algorithm. Figure 2 shows the circuit of Teleportation algorithm.

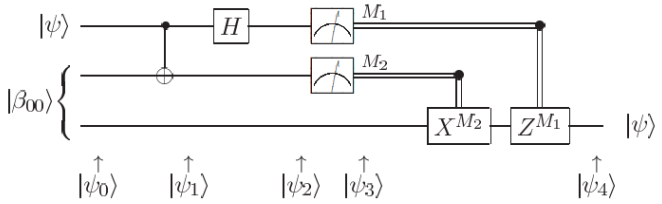

Figure 2: Quantum Circuit Design of Teleportation algorithm.

After the CNOT, Hadamart and Measurement operators, the indications with two lines indicate that the communication is via classical channels. Those indicated by a line are quantum channels. After a measurement has taken place, a classical number (0 or 1) is obtained if a measurement is made on a qubit or a state vector. And the state vector is destroyed. And a real number is obtained. If there will be a transmission, it will be through the classical channel [1].

Years ago, Alice and Bob shared one of the bell states among themselves. This is an entangled state, and this is one of the applications of quantum entanglement. The following (17) is an entangled state of 2. The first qubit is Alice, the second qubit is Bob's. But the distance between them is very far.

$$|B_{00}> = \frac{|00>+|11>}{\sqrt{2}} \quad (17)$$

It is an entangled state, so when one performs a measurement, the other is also affected. The situation $|\Psi>$ in Figure 2 is the one that Alice wants to send to Bob. $|B_{00}>$ is one of the bell states, that is, entangled states. Alice interacts the situation she wants to send to Bob with her share of the qubit. Therefore, Alice has two qubits and Bob has only one qubit. Alice performs the measurement after first passing her qubit through the CNOT and then through the Hadamart gate. In Figure 2, in the Quantum teleportation circuit, the general state that Alice wants to send to Bob before passing to the CNOT gate and one of the bell states they share among themselves is expressed as $|\Psi_1>$ in (18) below.

$$|\psi_1> = |\psi>|B_{00}> = (\alpha|0>+\beta|1>)\frac{|00>+|11>}{\sqrt{2}}$$
$$= \frac{1}{\sqrt{2}}[\alpha|000>+\alpha|011>+\beta|100>+\beta|111>] \quad (18)$$

The first two qubits in Equation 17 belong to Alice, and the last qubit to Bob. After the $|\Psi_1>$ state vector is passed through the CNOT gate, the $|\Psi_2>$ state vector specified by (19) is obtained. The CNOT gate acts only on the first two qubits.

$$|\psi_2> = \frac{1}{\sqrt{2}}[\alpha|000>+\alpha|011>+\beta|110>+\beta|101>] \quad (19)$$

Then, when the first qubit of the $|\Psi_2>$ state vector passes through the Hadamart gate, when we put the common qubits in common brackets, the state vector $|\Psi_3>$ specified by (20) is obtained.

$$|\psi_2> = \frac{1}{2}[|00>(\alpha|0>+\beta|1>)+|01>(\alpha|1>+\beta|0>)$$
$$+|10>(\alpha|0>-\beta|1>)+|11>(\alpha|1>-\beta|0>)] \quad (20)$$

If Alice obtains 00 after performing the measurement, Bob doesn't need to do anything like (21).

$$00: \text{Bob} => |\alpha|0> + \beta|1> = |\psi> \quad (21)$$

If Alice obtains 01 after performing the measurement, Bob should pass the state from X gate like (22).

$$01: \text{Bob} => \alpha|1>+\beta|0> \xrightarrow{X} \alpha|0>+\beta|1> = |\psi> \quad (22)$$

If Alice obtains 10 after performing the measurement, Bob should pass the state from Z gate like (23).

$$10: \text{Bob} \Rightarrow \ \alpha|0> - \beta|1> \xrightarrow{Z} \alpha|0> + \beta|1> = |\psi> \tag{23}$$

If Alice obtains 11 after performing the measurement, Bob should pass the state firstly from X gate then Z gate like (24).

$$11: \text{Bob} \Rightarrow \ \alpha|1> - \beta|0> \xrightarrow{X} \alpha|0> - \beta|1> \xrightarrow{Z} \alpha|0> + \beta|1> = |\psi> \tag{24}$$

III. EXPERIMENTAL RESULTS

In this section we implement Superdense Coding and Teleportation algorithms in Qiskit and IBM circuit composer and detailed results are presented respectively.

A. Implementation and Results of Superdense Coding algorithm in Qiskit and IBM Circuit Composer

The circuit designs of Superdense Coding algorithm realized by using IBM Quantum Circuit Composer are shown in Fig. 3,4, 5 and 6. In first place, Hadamard and CNOT gate are added. Then, depending on the 2-bit classical information to be sent, I, X, Z and iY quantum gates are added to the circuit, respectively. In the next step, CNOT and Hadamard gate are applied. Finally, since 2 bits of classical information will be sent, measurement processing has been performed for both qubits.

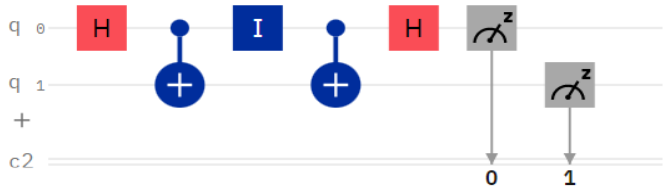

Figure 3: Circuit design of Superdense Coding for sending 00 classical information.

Figure 4: Circuit design of Superdense Coding for sending 01 classical information.

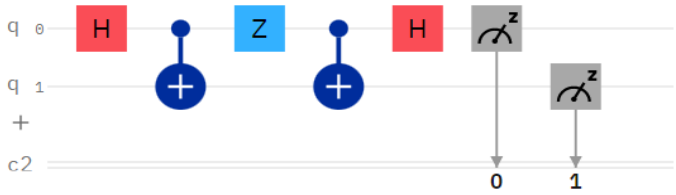

Figure 5: Circuit design of Superdense Coding for sending 10 classical information.

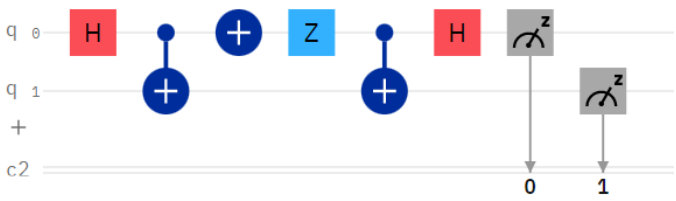

Figure 6: Circuit design of Superdense Coding for sending 11 classical information.

When the circuit of Superdense Coding algorithm is executed on IBM real quantum computer which have 32 qubit with 1024 shots, obtained results for each 2 bit-classical information are shown in Fig. 7 a, b, c and d as histogram. The results show that 2-bit classical information are transferred with %100 probability by using single qubit with Superdense Coding algorithm.

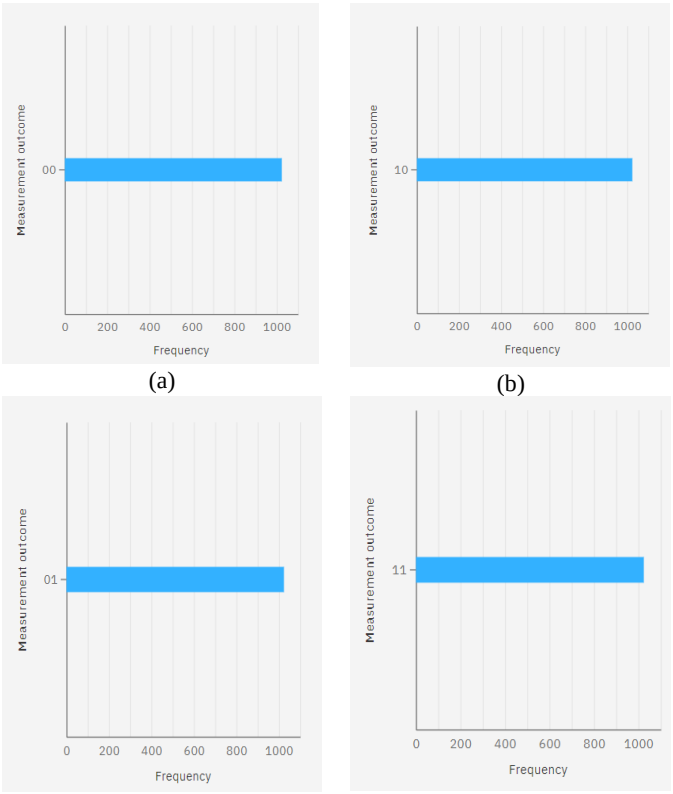

Figure 7: Results of the Superdense Coding algorithm as histogram in the real IBM Quantum Composer.

When Superdense Coding algorithm is executed on the simulation environment by using qiskit library, obtained results for each 2 bit-classical information are shown in Fig. 8 a, b, c and d as histogram. The results show that 2-bit classical information are transferred correctly by using single qubit with Superdense Coding algorithm.

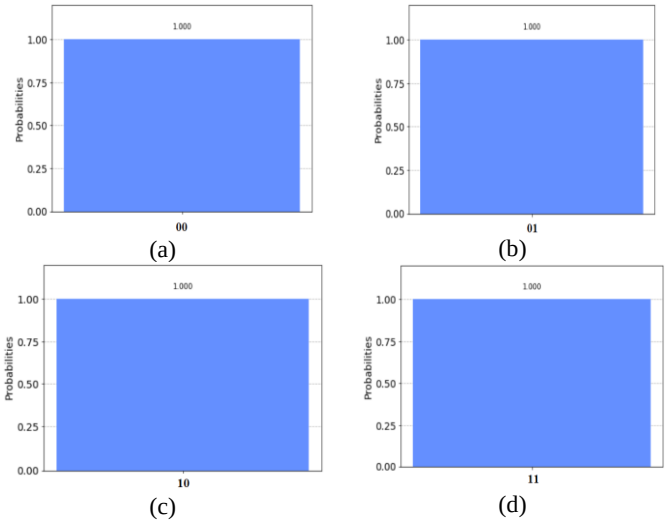

Figure 8: Results of the Superdense Coding algorithm as histogram on simulation environment by using qiskit.

B. Implementation and Results of Teleportation Algorithm in Qiskit and IBM Circuit Composer

The circuit design of Teleportation algorithm realized by using IBM Quantum Circuit Composer is shown in Fig. 9. In first place, Hadamard and CNOT gate are added. Then, since one qubit information will be sent, measurement processing has been performed. Finally, depending on the information obtained after performing the measurement, I, X, Z and iY quantum gates are applied on the classical channel.

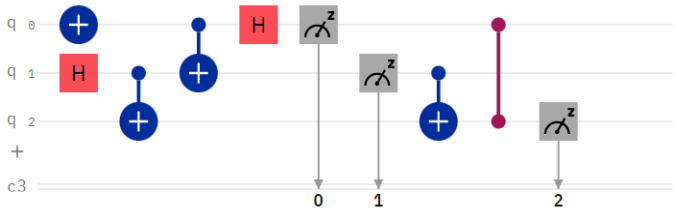

Figure 9: Circuit design of Teleportation algorithm.

When the circuit of Teleportation algorithm is executed on IBM real quantum computer which have 32 qubits with 1024 shots, obtained results for each probability are shown in Fig. 10 as histogram.

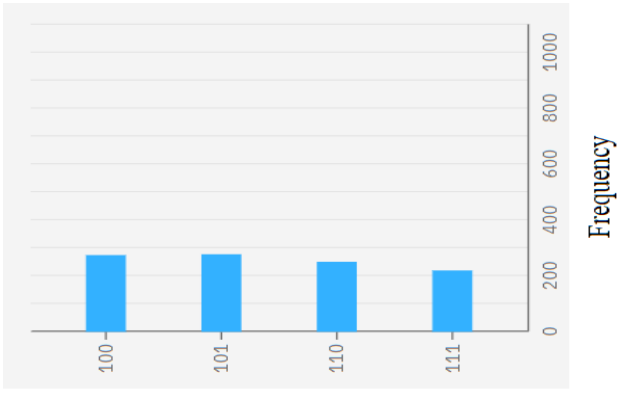

Figure 10: Results of the Teleportation algorithm as histogram in the real IBM Quantum Composer.

When Teleporation algorithm is executed on the simulation environment by using qiskit library, obtained results for each probability are shown in Fig. 11 as histogram.

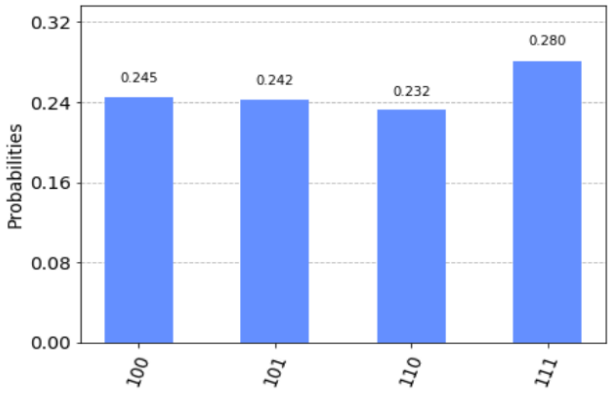

Figure 11: Results of Teleportation algorithm as histogram on simulation environment by using qiskit.

Thus, in the measurement phase of the quantum teleportation circuit, Alice reconstructs the qubit that Alice wants to show herself by using different logic gates depending on the information received with a classical channel (because these are two-bit classical information), after Alice measures both her own qubits. It is possible. This situation is called quantum teleportation, or sending a state vector from one place to another. For this to happen, Alice and Bob must share an entanglement state among themselves. If there is no entangled state, it is not possible to send any state from one place to another.

Today, it is not possible to reach a speed higher than the speed of light. Quantum teleportation algorithm does not violate this law. Because in order for Bob to receive the state vector, Alice needs to send two bits of classical information. This information must reach Bob first so that Bob can construct his state vector. And these two bits of classical information are limited to the speed of light.

Copying a state vector in a quantum mechanical system is not possible according to the Cloning no theorem. This law has not been violated either. Because Alice has measured her own qubits. One of these two qubits is his own and the other is an entangled state between them and Bob. When Alice made the measurement, she lost her state vector. Bob is reconstructing this state vector. Therefore, the state vector disappears in one place and reappears in another. Therefore, there is no irradiation. As a result, a state vector disappeared and reappeared [1].

IV. Conclusion

Quantum Teleportation and Superdense Coding algortihms are implemented using Qiskit and on real quantum devices for the purpose of putting forward results of running on simulation evrironment and real quantum devices. Our approach has proved that the results of the algorithms obtained on real quantum devices are very close to the results obtained in the simulation environment.

In the future, quantum teleportation is foreseen to be used not only in the field of transportation and communication, but

also in the medical and military fields. The era of "virtual medicine" will begin in medicine. The codes of each organ will be copied and stored, and in case of damage to the organ as a result of a possible disease or accident in the future, the organ will be restored and treated using these codes. These technologies, which are currently only being put forward as fiction and theory, are getting closer to the desired level day by day [10].

REFERENCES

[1] M. A. Nielsen, I. L. Chuang, Quantum Computation and Quantum Information, Cambridge University Press, New York, United States of America, 2000.

[2] E. Rieffel, W. Polak, An Introduction to Quantum Computing for Non-Physicists, *ACM Computing Surveys*, Vol. 32, No. 3, pp. 300–335, Sept. 2000.

[3] K. Mattle, H. Weinfurter, P. G. Kwiat, and A. Zeilinger. "Dense coding in experimental quantum communication", *Phys. Rev. Lett.*, vol. 76(25): pp. 4656–4659, 1996.

[4] S. L. Braunstein, H. J. Kimble, "Dense coding for continuous variables". Quantum Physics, October, 1999.

[5] S. L. Braunstein, H. J. Kimble, "Teleportation of continuous quantum variables", *Phys. Rev. Lett.*, pp. 80:869–72, 1998.

[6] W. Pfaff, B. Hensen, H. Bernien, S. B. van Dam, M. S. Blok, T. H. Taminiau, M. J. Tiggelman, R. N. Schouten, M. Markham, D.J. Twitchen, R. Hanson, "Unconditional quantum teleportation between distant solid-state qubits", Quantum Physics, Mesoscale and Nanoscale Physics, Science 345, 532-535, 2014. Doi: 10.1126/science.1253512

[7] D. Gottesman, I. L. Chuang, "Quantum teleportation is a universal computational primitive", *Nature*, vol. 402, pp. 390–392, 1999.

[8] M. A. Nielsen, C. M. Caves, "Reversible quantum operations and their application to teleportation", *Phys. Rev. A*, vol. 55(4) pp. 2547–2556, 1997.

[9] M. A. Nielsen, E. Knill, and R. Laflamme. Complete quantum teleportation using nuclear magnetic resonance. *Nature*, 396(6706):52–55, 1998.

[10] Richards-Sears-Wehr-Zemansky, Modern University Physics complete, Addison-Wisley Publishing Company, 1962.

Energy demand projection of Turkey based on Coot bird metaheuristic optimizer

İsmail KOÇ
Department of Software Engineering, Konya Technical University, Konya, Turkey, ismailkoc@ktun.edu.tr

Abstract **- The energy demand projection forms the basis of realistic energy planning. In this study, from 1979 to 2011, a 33-year data set including gross domestic product (GDP), population, import and export was used for energy demand forecasting in Turkey. Using this data set, two different energy estimation models, linear (COOT_L) and quadratic (COOT_Q), were developed with the Coot bird metaheuristic optimizer. These models were compared with different optimization algorithms in the literature. When the experimental results were examined, the COOT_L model produced a more successful result than the results of other algorithms. Furthermore, COOT_Q was seen to become more successful than PSO and ACO. In addition to these, the COOT_L and COOT_Q models forecasted the future energy demand between 2012 and 2030 in Turkey and their results were compared with those of DE methods. When the results were examined, while DE and COOT_L produced similar results in linear form, certain differences were observed among the results of COOT_Q and DE.**

Keywords **– Coot Bird Metaheuristic Optimizer, Swarm Intelligence, Forecasting, Energy Demand**

I. Introduction

Investigating energy consumption problems has become an important research area in recent years. The solution of energy problems is vital for the security and welfare of societies and states. Energy is one of the most economically important resources for industrial production [1]. Therefore, estimating energy consumption is an important step for accurate planning of industry and energy sectors in terms of future projection [2]. There are a variety of methods for electricity demand forecasting, including short-term and long-term [3].

The Turkish economy grew by 9.2% in 2010 and 8.8% in 2011, making it the 18th largest economy in the world and the 7th largest among European Union countries [4]. Developments in the economy have changed the travel habits of citizens who can buy personal vehicles and want to use their private vehicles rather than public transportation. Therefore, the developments in the economy directly affected an increase in the country's energy demand. According to the Turkish Statistical Institute (TSI), in terms of sustainable development indicators, the transportation sector has a 23% share in Turkey's energy consumption [5].

Classical regression analysis, a statistical method used in energy demand prediction (EDP) studies in the literature, is a simple and well-known method [6-9]. Recently, different artificial intelligence algorithms have been applied to EDP, which is an alternative to classical regression methods. As artificial intelligence techniques, there are many studies on EDP to predict future energy demand using some forecasting models. These are studies on artificial neural networks, meta-heuristic optimization algorithms [10].

Swarm intelligence optimization is a class of biologically inspired heuristic optimization algorithms that includes ant colony optimization (ACO), artificial bee colony (ABC), and particle swarm optimization (PSO) [11]. There are many different studies in the literature using ant colony optimization [12], genetic algorithm [13], artificial neural network [14], harmony search algorithm [15], artificial bee algorithm [16], differential evolution algorithm [17], grey wolf optimizer [18], gravitational search and invasive weed optimization algorithms [19] and particle swarm optimization [20] methods in order to estimate Turkey's demand for different energy types.

In this study, the COOT algorithm, which has been newly introduced to the literature, is used for the energy demand estimation of Turkey. For this, Turkey's export, import, GDP and population data between 1979 and 2011 were used as initial data set. With the help of these data, two different estimation models, linear (COOT_L) and quadratic (COOT_Q), were produced. The models obtained were compared with other models called DE, PSO and ACO in the literature. In addition, the training phase was carried out by using all the data for the future forecast, and the future energy demand forecast was generated with the help of artificial data produced with a determined scenario. The future energy demand prediction results between 2021 and 2030 produced by the proposed algorithm were compared with the results obtained by DE. It has been seen that the proposed algorithm produced better results than other algorithms especially for the linear model.

The rest of the paper is organized as follow. In the Section II, Coot bird metaheuristic optimizer is explained with the mechanism. Section III presents applying the proposed algorithm to the energy demand estimation problem. In addition, Section IV and V presents experimental results and conclusion.

II. Coot bird metaheuristic optimizer (COOT)

The Coot bird metaheuristic optimizer (COOT) algorithm has been developed by simulating different collective behaviors of coots, such as regular and irregular movements on the water surface [21]. By a few coots in front of the group, which is considered as the group leader, the whole group moves to the target (food).

Coots have the ability to transfer from the first stage to the second stage in two ways. The first is to speed up some adjacent coots and improve the positions of their leaders. The second approach is to accelerate high-potential coots and make them leaders rather than low-performing leaders. The time required to transition from one stage to the next depends on the density of the coot population [22]. Coots have four different mobility abilities that enable them to update their position on the water surface which are as follow:

1- Random movement
2- Chain movement
3- Updating the position according to the leaders
4- Leader movement

The pseudo-code of COOT is given in Fig. 1.

```
Initialize randomly coot population
Initialize the parameters of the algorithm
Select randomly leaders from the coots
Calculate fitness of both of leader and coots
Find the global optimum (gbest)

While Iter < max_Iteration

    For i= 1: number of coots
      Calculate parameter k (leader index)
      Update the position of coot_i
      Calculate the fitness of coot_i
       If the fitness of coot_i < fitness of leader_k
         Swap coot_i and leader_k
       End
    End

    For k= 1: number of leader
    Update the position of leader_k
    Calculate the fitness of leader_k
       If the fitness of leader_k < gbest
         Swap leader_k and global Optimum
       End
    End

Iter = Iter +1;
End
```

Fig. 1: Psode code of COOT algorithm

III. Applying the Proposed Algorithm to the Energy Demand Estimation Problem

In this study, two different models, linear and quadratic, were used for the energy demand forecasting of Turkey. While the linear model was trained with five independent parameters (Weights = W_1,..., W_5), the quadratic model was trained with fifteen independent parameters (W_1,..., W_{15}). The X_1, X_4 values given in Eq. 1 and 2 represent the four indicators that are observed to have the greatest impact on a country's energy demand and are the most frequently used in the literature for energy demand forecasting in Turkey. These indicators are respectively GDP, population, import and export data given in Table 1 [20, 23]. These parameters are given in Eq. 1 and 2, respectively. COOT algorithm is expected to calculate the weight values of using this input data. By using Eq. 3, it is aimed to minimize the difference between the known energy demand value and the calculated value.

Table 1. Turkey's energy demand, GDP, population, import, export data

Year	Energy Demand (TWh)	GDP ($ 10^9$)	Population ($ 10^6$)	Import ($ 10^9$)	Export ($ 10^9$)
1979	30.71	82	45.53	5.07	2.26
1980	31.97	68	44.44	7.91	2.91
1981	32.05	72	45.54	8.93	4.7
1982	34.39	64	46.69	8.84	5.75
1983	35.7	60	47.86	9.24	5.73
1984	37.43	59	49.07	10.76	7.13
1985	39.4	67	50.31	11.34	7.95
1986	42.47	75	51.43	11.1	7.46
1987	46.88	86	52.56	14.16	10.19
1988	47.91	90	53.72	14.34	11.66
1989	50.71	108	54.89	15.79	11.62
1990	52.98	151	56.1	22.3	12.96
1991	54.27	150	57.19	21.05	13.59
1992	56.68	158	58.25	22.87	14.72
1993	60.26	179	59.32	29.43	15.35
1994	59.12	132	60.42	23.27	18.11
1995	63.68	170	61.53	35.71	21.64
1996	69.86	184	62.67	43.63	23.22
1997	73.78	192	63.82	48.56	26.26
1998	74.71	207	65	45.92	26.97
1999	76.77	187	66.43	40.67	26.59
2000	80.5	200	67.42	54.5	27.78
2001	75.4	146	68.37	41.4	31.33
2002	78.33	181	69.3	51.55	36.06
2003	83.84	239	70.23	69.34	47.25
2004	87.82	299	71.15	97.54	63.17
2005	91.58	361	72.97	116.77	73.48
2006	99.59	483	72.97	139.58	85.54
2007	107.63	531	70.59	170.06	107.27
2008	106.27	648	71.13	201.96	132.03
2009	106.14	730	73.23	140.93	102.14
2010	109.27	615	74.47	185.54	113.88
2011	114.48	731	74.72	240.84	134.91

$$E_{\text{linear}} = w_1 + w_2X_1 + w_3X_2 + w_4X_3 + w_5X_4 \quad (1)$$

$$E_{quadratic} = w_1 + w_2X_1 + w_3X_2 + w_4X_3 + w_5X_4 + w_6X_1X_2 + w_7X_1X_3 + w_8X_1X_4 + w_9X_2X_3 + w_{10}X_2X_4 + w_{11}X_3X_4 + w_{12}X_1X_1 + w_{13}X_2X_2 + w_{14}X_3X_3 + w_{15}X_4X_4 \quad (2)$$

$$\min f_{ED}(x) = \sum_{i=1}^{N} (ED_i^{observed} - ED_i^{predicted})^2 \quad (3)$$

IV. EXPERIMENTAL RESULTS

In this paper, energy demand estimation in Turkey was realized with the help of two different models, linear and quadratic, using the COOT algorithm. Both models were trained under equal conditions. The data from 1979 to 2005 in Table 1 are used to perform energy demand estimation in the linear and quadratic models the best model results were reported. The population number was taken as 100 and maximum number of function evaluation (MaxFEs) was determined as 500,000. The results and the weight values obtained from the linear and quadratic models are respectively given in Table 2 and 3 in comparison with the DE [17], ACO [12] and PSO [20] in the literature.

Looking at the results given in Table 2, it is clear that the proposed method using the linear model is more successful with the value of 36.07 than the DE, PSO and ACO algorithms. In addition, the result of DE algorithm with the value of 41.71 is seen as the closest result to that of the COOT algorithm.

Table 2. Comparisons of coefficients and relative errors of linear model

Coefficients	COOT	DE	ACO	PSO
w1	-59.224	-55.899	-51.305	-55.902
w2	-0.006	0.004	0.012	0.002
w3	1.986	1.912	1.810	1.913
w4	0.402	0.374	0.352	0.343
w5	-0.512	-0.484	-0.444	-0.424
Error	**36.07**	**41.71**	**45.72**	**42.61**

When Table 3 is examined, according to the results obtained using the quadratic model, the COOT algorithm produced much better results than PSO and ACO. In addition, the proposed method with a value of 22.95 obtained results close to the DE algorithm. On the other hand, when the weight values (w1, .. , w15) are examined, it is seen that the COOT algorithm has very different weights compared to the other algorithms.

Table 3. Comparisons of coefficients and relative errors of quadratic model

Coefficients	COOT	DE	ACO	PSO
w1	-0.042	-97.146	-96.442	-96.441
w2	0.018	-0.483	-0.482	-0.482
w3	0.006	4.767	4.737	4.737
w4	0.078	1.099	1.094	1.094
w5	0.798	-2.921	-2.894	-2.935
w6	0.003	0.019	0.019	0.019
w7	0.007	0.023	0.023	0.023
w8	-0.004	-0.026	-0.026	-0.026
w9	-0.009	-0.063	-0.063	-0.063
w10	0.000	0.102	0.101	0.101
w11	0.033	0.092	0.092	0.092
w12	-0.001	-0.003	-0.003	-0.003
w13	0.012	-0.047	-0.047	-0.047
w14	-0.016	-0.039	-0.039	-0.039
w15	-0.031	-0.066	-0.065	-0.065
Error	**22.95**	**17.65**	**27.95**	**27.66**

Using all the data in Table 1 between the years 1979 and 2011, ten independent runs were carried out to predict future energy demand between 2012 and 2030 in Turkey, and the results of the best linear and quadratic models are given in Tables 4 and 5. According to the results in Table 4, DE and COOT algorithms reached exactly the same results in the linear model. However, according to the comparative results in Table 5, DE performed slightly better than COOT.

Table 4. Comparisons of coefficients and relative errors of quadratic model using all the data

	W1	W2	W3	W4	W5
DE - COOT	-50.13479	0.0239	1.7576	0.0999	-0.0363
DE – COOT Error	**152.6411**				

Table 5. Comparisons of coefficients and relative errors of quadratic model using all the data

	W1	W2	W3	W4	W5
DE	-40.3894	0.2724	0.9307	2.6684	-3.0019
COOT	-0.0120	0.0241	0.0182	1.3046	-0.0746
	W6	**W7**	**W8**	**W9**	**W10**
DE	-0.0052	-0.0045	0.0128	-0.0310	0.0386
COOT	0.0003	0.0015	0.0028	-0.0171	0.0024
	W11	**W12**	**W13**	**W14**	**W15**
DE	0.0835	-0.0004	0.0114	-0.0186	-0.1032
COOT	-0.0215	-0.0004	0.0126	0.0041	0.0075
DE (Error) =	**52.6208**				
COOT (Error) =	**77.9599**				

To predict the energy demand in Turkey for the years between 2012 and 2030, one scenario was formed and according to this scenario, new updated input data was created.

Scenario 1: It is assumed that the average growth rate of GDP is 4%, population growth rate is 0.5%, import growth rate is 2.5% and export growth rate is 3% during the period between 2012 and 2030.

Table 6 presents the comparative results of the algorithms for future projection of the energy demand of Turkey. According to the future estimation obtained by the linear model in Table 6, DE and COOT both produced the same results. As for Quadratic, while DE produced an increasing result over the years in the future energy demand forecast, COOT presented an increasing graph for energy demand until 2023 and decreasing after 2023. In addition, Fig. 2 presents future projections of total energy demand of the algorithms in terms of linear and quadratic models.

Table 6. Comparison of the algorithms for future projection of the energy demand in Turkey

	COOT		DE	
Year	**Linear**	**Quadratic**	**Linear**	**Quadratic**
2012	119.65	116.30	119.65	117.18
2013	121.50	117.44	121.50	119.94
2014	123.39	118.54	123.39	123.02
2015	125.33	119.61	125.33	126.46
2016	127.32	120.62	127.32	130.32
2017	129.35	121.57	129.35	134.63
2018	131.44	122.43	131.44	139.46
2019	133.57	123.20	133.57	144.85
2020	135.76	123.85	135.76	150.88
2021	138.00	124.36	138.00	157.62
2022	140.30	124.71	140.29	165.15
2023	142.65	124.86	142.65	173.55
2024	145.07	124.78	145.06	182.91
2025	147.55	124.44	147.54	193.35
2026	150.09	123.79	150.08	204.97
2027	152.70	122.79	152.69	217.90
2028	155.37	121.38	155.37	232.28
2029	158.12	119.51	158.12	248.25
2030	160.94	117.10	160.94	265.99

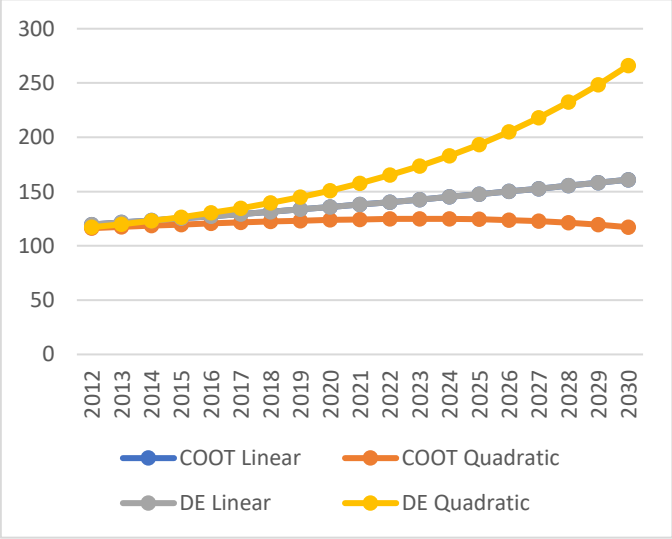

Fig 2: Future projections of total energy demand

V. Conclusion

In this study, the COOT algorithm was utilized for the energy demand forecast of Turkey. The algorithm has been tested with the help of both linear model and quadratic model. These models were trained with the data of Turkey between 1979 and 2011. The results obtained from the COOT algorithm were compared with the PSO, DE and ACO algorithms in the literature. In the linear model, the proposed algorithm produced the best result, while in the quadratic model, the DE produced the best result. In addition, for the future projection of Turkey, the COOT algorithm was compared with the DE. While COOT achieved the same results as DE in the linear model, DE and COOT algorithms produced different projection results in the quadratic model.

References

[1] I. Ghalehkhondabi, E. Ardjmand, G. R. Weckman, and W. A. Young, "An overview of energy demand forecasting methods published in 2005–2015," *Energy Systems*, vol. 8, no. 2, pp. 411-447, 2017.

[2] A. Kazemi and M. Hosseinzadeh, "A multi-level fuzzy linear regression model for forecasting industry energy demand of Iran," *Procedia-Social and Behavioral Sciences*, vol. 41, pp. 342-348, 2012.

[3] A. J. del Real, F. Dorado, and J. Durán, "Energy demand forecasting using deep learning: applications for the French grid," *Energies*, vol. 13, no. 9, p. 2242, 2020.

[4] M. Melikoglu, "Demand forecast for road transportation fuels including gasoline, diesel, LPG, bioethanol and biodiesel for Turkey between 2013 and 2023," *Renewable energy*, vol. 64, pp. 164-171, 2014.

[5] M. Sonmez, A. P. Akgüngör, and S. Bektaş, "Estimating transportation energy demand in Turkey using the artificial bee colony algorithm," *Energy*, vol. 122, pp. 301-310, 2017.

[6] M. Kankal, A. Akpınar, M. İ. Kömürcü, and T. Ş. Özşahin, "Modeling and forecasting of Turkey's energy consumption using socio-economic and demographic variables," *Applied Energy*, vol. 88, no. 5, pp. 1927-1939, 2011.

[7] F. B. Gorucu, "Evaluation and forecasting of gas consumption by statistical analysis," *Energy Sources*, vol. 26, no. 3, pp. 267-276, 2004.

[8] M. Tunc, Ü. Çamdali, and C. Parmaksizoğlu, "Comparison of Turkey's electrical energy consumption and production with some European countries and optimization of future electrical power supply investments in Turkey," *Energy Policy*, vol. 34, no. 1, pp. 50-59, 2006.

[9] N. Fumo and M. R. Biswas, "Regression analysis for prediction of residential energy consumption," *Renewable and sustainable energy reviews*, vol. 47, pp. 332-343, 2015.

[10] M. F. Tefek, H. Uğuz, and M. Güçyetmez, "A new hybrid gravitational search–teaching–learning-based optimization method for energy demand estimation of Turkey," *Neural Computing and Applications*, vol. 31, no. 7, pp. 2939-2954, 2019.

[11] S. Yu, K. Zhu, and X. Zhang, "Energy demand projection of China using a path-coefficient analysis and PSO–GA approach," *Energy Conversion and Management*, vol. 53, no. 1, pp. 142-153, 2012.

[12] M. D. Toksarı, "Ant colony optimization approach to estimate energy demand of Turkey," *Energy Policy*, vol. 35, no. 8, pp. 3984-3990, 2007.

[13] H. K. Ozturk, H. Ceylan, O. E. Canyurt, and A. Hepbasli, "Electricity estimation using genetic algorithm approach: a case study of Turkey," *Energy*, vol. 30, no. 7, pp. 1003-1012, 2005.

[14] A. Sözen, E. Arcaklioğlu, and M. Özkaymak, "Turkey's net energy consumption," *Applied Energy*, vol. 81, no. 2, pp. 209-221, 2005.

[15] H. Ceylan, H. Ceylan, S. Haldenbilen, and O. Baskan, "Transport energy modeling with meta-heuristic harmony search algorithm, an application to Turkey," *Energy policy*, vol. 36, no. 7, pp. 2527-2535, 2008.

[16] H. Uguz, H. Hakli, and Ö. K. Baykan, "A new algorithm based on artificial bee colony algorithm for energy demand forecasting in Turkey," in *2015 4th International Conference on Advanced Computer Science Applications and Technologies (ACSAT)*, 2015: IEEE, pp. 56-61.

[17] M. Beskirli, H. Hakli, and H. Kodaz, "The energy demand estimation for Turkey using differential evolution algorithm," *Sādhanā*, vol. 42, no. 10, pp. 1705-1715, 2017.

[18] I. Koc, H. Kivrak, and I. Babaoglu, "The estimation of the energy demand in turkey using grey wolf optimizer algorithm," *Annals of the Faculty of Engineering Hunedoara*, vol. 17, no. 1, pp. 113-117, 2019.

[19] I. Koc, R. Nureddin, and H. Kahramanlı, "Türkiye'de Enerji Talebini Tahmin Etmek İçin Doğrusal Form Kullanarak Gsa (Yerçekimi Arama Algoritması) Ve Iwo (Yabani Ot Optimizasyon Algoritması) Tekniklerinin Uygulanması," *Selçuk Üniversitesi Mühendislik, Bilim Ve Teknoloji Dergisi*, vol. 6, no. 4, pp. 529-543, 2018.

[20] A. Ünler, "Improvement of energy demand forecasts using swarm intelligence: The case of Turkey with projections to 2025," *Energy policy*, vol. 36, no. 6, pp. 1937-1944, 2008.

[21] I. Naruei and F. Keynia, "A New Optimization Method Based on Coot Bird Natural Life Model," *Expert Systems with Applications*, p. 115352, 2021.

[22] E. A. Gouda, M. F. Kotb, S. S. Ghoneim, M. M. Al-Harthi, and A. A. El-Fergany, "Performance Assessment of Solar Generating Units Based on Coot Bird Metaheuristic Optimizer," *IEEE Access*, vol. 9, pp. 111616-111632, 2021.

[23] M. S. Kıran, E. Özceylan, M. Gündüz, and T. Paksoy, "Swarm intelligence approaches to estimate electricity energy demand in Turkey," *Knowledge-Based Systems*, vol. 36, pp. 93-103, 2012.

Classification Of Electroluminescence Images Of Solar Cells Using Mobilenet

Y.KOÇ[1] and Y. ÜNAL[2]

[1] Amasya University, Amasya/Turkey, yucel-koc@hotmail.com
[2]Amasya University, Amasya/Turkey, yavuz.unal@amasya.edu.tr

Abstract **- Solar energy is an alternative energy source. Solar cells, forming the basis of a solar energy system, are made of crystalline silicon. Detection of many defects using traditional imaging systems is rather challenging. In this study, defect detection was conducted using electroluminescence (EL) images of solar panel cells by the deep learning method. Deep learning algorithm were used in image classification to achieve fast and excellent results. Images are divided into categories like good, broken, and inactive and trained with deep learning algorithm. Of the pre-trained networks, MobileNet was used and %75,58 classification accuracy was obtained.**

Keywords **- Deep Learning, MobileNet, Photovoltaic Module, Electroluminescence Image, Image Classification**

I. INTRODUCTION

Today, there is a great increase in energy usage due to the rise of living standards. Renewable energy sources will be able to play an important role in fulfilling these demands. One of the rapidly developing and promising applications of energy generation technology from these sources is solar panel systems [1, 2].

The photovoltaic (PV) systems are highly influenced by crystalline silicon solar cells and modules. For a dependable operation of PV systems, it is vital to make regular controls on PV modules in the field, to evaluate their operation in time, to solve problems in advance, and to detect problems that may occur during the operation [3, 4].

Electroluminescence (EL) imaging is a technique used for the visual audit of photovoltaic modules [5]. It allows capturing high-resolution images of photovoltaic modules' defect identification [6].

On the first image [7] the working logic of Electroluminescent imaging was shown. Using a special camera with an infrared filter, the image of the solar panel is taken in a dark environment and transferred to the digital environment.

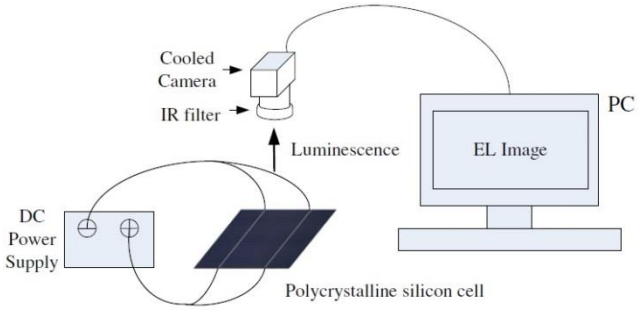

Figure 1: The structure of an electroluminescent system

On the 2nd image [8], there are good, broken, and inactive solar cells shown, obtained by an electroluminescence test. It is very difficult to detect the condition of solar cells without the help of external equipment.

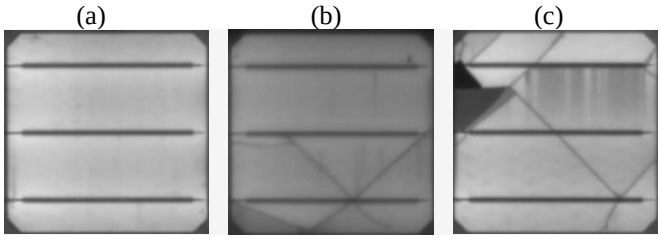

Figure 2: a) good solar cell b) Broken solar cell c) inactive solar cell

II. MATERIAL AND METHODS

A. Dataset

The dataset [8] consists of 525 samples of solid and faulty solar cells with 300x300 pixel, 8-bit grayscale with different degrees of defections of 18 different solar modules. Solar modules are monocrystalline. Images were categorized threefold as good, broken, and inactive.

Table 1: Features of images used in the dataset

Module Structure	Classification		
	Good	Broken	Inactive
Monocrystalline	346	121	58

B. Model Selection

In this study, mobilenet model used. This model is briefly summarized below.

1. MobileNet

MobileNet was first developed by Howard et al. in 2017 with the aim of effective performance on embedded systems and mobile devices. MobileNet is an aerodynamic-based architecture and a lightweight deep neural network using deep-separable convolution. It is designed to be used in many problems that can also be used in mobile devices such as object recognition, image classification [9].

The MobileNet model is based on a type of convolution called deep separable convolution, which can separate a standard convolution operation into point convolution operations using a deep convolution and a 1x1 filter. Deep convolution for MobileNet applies a single filter to each input channel. It then combines the outputs by applying a point convolution operation to a 1x1 convolution. A standard convolution both filters and combines the input at a time to produce an output. However, deeply separable convolution divides it into two layers, doing the filtering in separate layers and the merging in separate layers. This separation not only simplifies computation, but also greatly reduces the model size. Figure 3 shows a standard convolution, Figure 4 shows deep convolution, and Figure 5 represents a 1x1 point convolution operation [9].

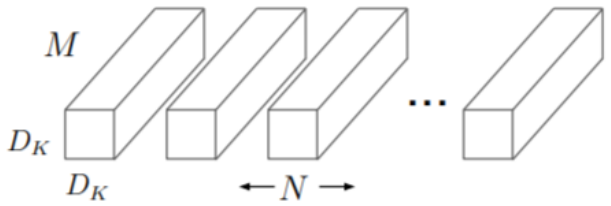

Figure 3: Standard Convolution Operation.

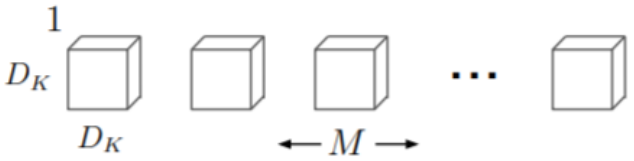

Figure 4: In-Depth Convolution Process.

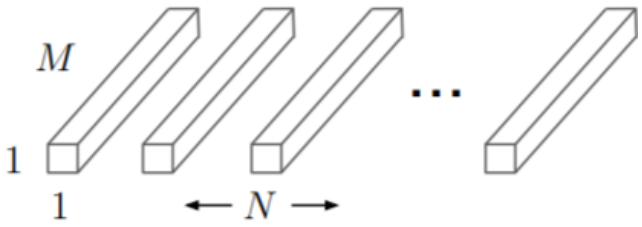

Figure 5: Point Convolution Process.

C. Evaluation Criteria

Recall is that shows how many of us predicted as Positively. Accuracy shows samples correctly classified. Precision shows how many of the predicted are true positives. The F1-score is the weighted average of recall (precision) and precision. F Score value shows us the harmonic mean of Precision and Recall values. The mathematical formula for these metrics is as follows:

$$Accuracy = \frac{TP+TN}{TP+TN+FP+FN} \quad (1)$$

$$\text{Precision} = \frac{\text{TP}}{\text{TP+FP}} \quad (2)$$

$$f1 - Score = \frac{2*\text{TP}}{2*TP+FP+FN} \quad (3)$$

$$\text{Recall} = \frac{\text{TP}}{\text{TP+FN}} \quad (4)$$

III. RESULTS AND DISCUSSION

In this study, image classification was performed on a virtual server with an Intel Xeon processor, 12 GB Ram, and 16 GB Nvidia Tesla T4 GPU via the Keras library in the lab environment. Networks to be used for Transfer Learning were selected between ImageNet trained networks. Deep learning models MobileNET were used. According to our results written in Table 2, MobileNET displayed the highest accuracy rate with 75.58%.

Table 2: Training accuracy of model.

Model	Accuracy	Val-accuracy	Train-loss	Val-loss
MobileNET	0.7708	0.7558	0.7749	0.8023

Table 3 contains the estimation report of the dataset divided into 3 classes as broken, inactive and good.

According to the values in Table 3, the classification of images in the broken and good category was lower than in the inactive category. This can be caused by the unequal number of images in the categories and the low number of images in the dataset for training.

Table 3: Classification Report.

	Precision	Recall	F1-Score
Crack	0.38	0.06	0.10
Inactive	0.84	0.92	0.88
Good	0.29	0.50	0.37

Figure 6 shows training and validation accuracy performance, figure 7 shows MobileNet training and validation loss values.

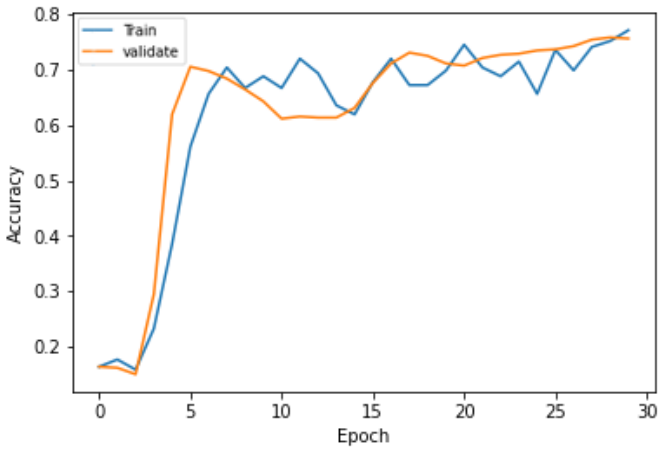

Figure 6: Training and Test accuracy values of MobileNet model.

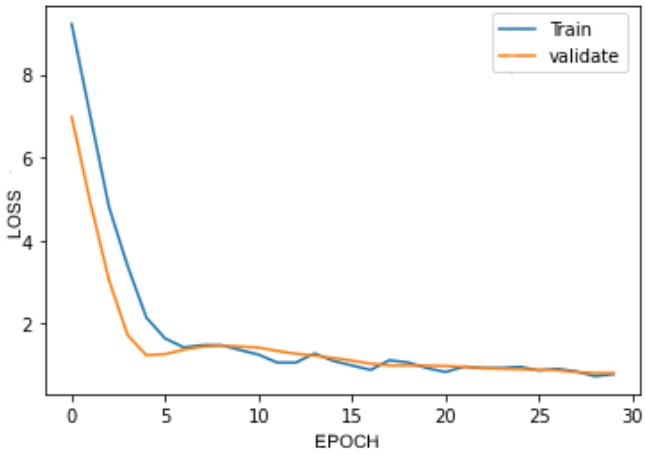

Figure 7: Training and Test Loss Values of MobileNet model.

IV. CONCLUSION

In this study, good, broken, and inactive electroluminescence images of solar panel cells were classified using deep learning. A public set of electroluminescence images was used for this purpose. 525 of the images in this dataset were used. CNN-based transfer learning algorithm MobileNet applied. Classification ratio, 75.58% accuracy was achieved with the MobileNet model.

The accuracy rate was low due to the small number of images in the dataset. In my future studies, I aim to increase the accuracy rate by increasing the number of images and deep learning models used for prediction.

REFERENCES

[1] Li, D. H. ve Lam, T.N. (2007) Determining the optimum tilt angle and orientation for solar energy collection based on measured solar radiance data, International Journal of Photoenergy, 1-9. doi:10.1155/2007/85402

[2] Taherbaneh, M., Rezaie, A.H., Ghafoorifard, H., Rahimi, K. ve Menhaj, M.B. (2010) Maximizing output power of a solar panel via combination of sun tracking and maximum power point tracking by fuzzy controllers, International Journal of Photoenergy, 1-13. doi:10.1155/2010/312580

[3] Köntges, M., Kurtz, S., Packard, C., et al., 2014. Review of failures of photovoltaicmodules. IEA-Photovoltaic Power Syst. Program.https://doi.org/978-3-906042-16-9.

[4] Bigaud, D., Laronde, R., Charki, A., 2010. Reliability of photovoltaic modules based onclimatic measurement data. Int. J. Metrol. Qual. Eng. 1 (1), 45–49.

[5] Köntges, M., Kurtz, S., Packard, C., et al., 2014. Review of failures of photovoltaic modules. IEA-Photovoltaic Power Syst. Program. https://doi.org/978-3-906042-16-9.

[6] K. Bothe, et al., 21st European Photovoltaic Energy Conference (2006) 597.

[7] Du-Ming Tsai , Shih-ChiehWu,Wei-ChenLi, 2011. Defect detection of solar cells in electroluminescence images using Fourier image reconstruction. Solar Energy Materials & Solar Cells 99 (2012) 250–262.

[8] Buerhop-Lutz, C.; Deitsch, S.; Maier, A.; Gallwitz, F.; Berger, S.; Doll, B.; Hauch, J.; Camus, C. & Brabec, C. J. A Benchmark for Visual Identification of Defective Solar Cells in Electroluminescence Imagery. European PV Solar Energy Conference and Exhibition (EU PVSEC), 2018.

[9] Howard, A., Zhu, M., Chen, B., Kalenichenko, D., Wang, W., Weyand, T., Andreetto, M., Adam, H. (2017). “MobileNets: Efficient Convolutional Neural Networks for Mobile Vision Applications”. ArXiv, abs/1704.04861.

Prediction Of Energy Generated From Solar Panels Using Machine Learning

H. A. KOÇ[1] and Y. ÜNAL[2]

[1] Amasya University, Amasya/Turkey, ayyildiz540@hotmail.com
[2]Amasya University, Amasya/Turkey, yavuz.unal@amasya.edu.tr

Abstract **- Increasing demand for energy has caused a search for dependable, cheap, and clean energy production methods. Photovoltaic systems (PV) have been a prevalent one among these energy resources in recent years. In the estimation of generated solar energy using machine learning methods, meteorological data like solar radiation, pressure, and temperature are influential elements. In this study, some of the machine learning algorithms and the electrical energy produced from solar panels were estimated. 17 features obtained from solar panels and meteorological data were reduced to 7 with the help of feature selection algorithms. These data, whose number of features were reduced, were analyzed with machine learning algorithms and R-Squared (R^2) values were determined by Random forest (RF) 0.9883, K-Nearest Neighbors (K-NN) 0.9263, Multilayer Perpection (MLP) 0.8845, Support Vector Regression (SVR) 0.8392, Bayesian Ridge (BR) 0.8305 and Adaboost regressor (AB) was found to be 0.8319. In the analyzes performed, improvements were obtained in Root Mean Square Error (RMSE), R-squared (R2) and Mean Sequared Error (MAE).**

Keywords **- Machine Learning, Solar Energy Prediction, Renewable Energy, Photovoltaic Module, Image Classification**

I. INTRODUCTION

The energy needs of countries constantly increase in line with their population growth. Concerns about the security of energy supply as a result of increased energy needs and intense debates regarding climate change resulted in a great rise in interest in renewable energy sources in Turkey, as like the rest of the World [1].

As an alternative to fossil fuels, one of the most popular renewable energy sources is solar power. Being clean, silent, economic, reliable, and non-depletable, solar power had become even more important in recent years [2, 3].

Energy market in Turkey is liberalized, allowing investors to install Solar Power Plants and operate. In order for a liberalized energy market to run in healthier conditions, it is necessary to maintain the supply-demand balance and to know the electrical energy that will be generated, a day in advance. In today's conditions, solar power plants that want to sell the energy they generate want to know how much energy they will generate in the next day. In this regard, informing the relevant organization about the amount of generation that will occur is very important for the sustainability of the energy market. Uncertainty about the amount of generation in power plants that generate electricity with renewable energy sources poses great risks [4].

II. MATERIAL AND METHODS

A. Dataset

Hourly energy production and panel temperature data of solar panels in Amasya University Ipekköy campus in 2016 were taken. The 17 features in the dataset were reduced to 7 by feature reduction in the weka program. Temperature, wind speed, solar radiation, humidity, Light Reflection, azimuth and energy data received from the Directorate General of Meteorology were provided on an hourly basis. There are a total of 2584 data and 7 attributes in our dataset.

Table 1: Dataset properties.

Qualifications	Properties			
	Average	Standard Deviation	Minimum	Maximum
Wind Speed m/s	1,28	1,16	0	9,71
Solar Radiation W/m^2	317,72	219,15	1	847,67
Temperature ^oC	22,40	8,69	-9,40	39,73
Humidity	52,92	19,66	10,08	100
Light Reflection	0,16	0,05	0,13	0,49
Azimuth	25,42	111,83	-180	180
Energy	71,79	53,15	1	180,10

B. Model Selection

In this study, Support Vector Regression (SVR), Random Forest (RF), Multilayer Perceptron (MLP), K-Nearest Neighbors (KNN), BayesianRidge (BR) and AdaBoost Regressor (AB) models used. These models is briefly summarized below.

1. Support Vector Regression

Support Vector Regression (SVR) is the learning algorithm used for learning, classification, grouping, density estimation, and finally, to produce regression rules using data. SVR may be used to solve binary class and multi-class classification problems. When classifying data, DVM finds the closest examples of classes and aims to maximize their perpendicular distance to separating hyperplane (which would be separating two classes). Separating hyperplane may have many alternatives without changing its success on the dataset.

Thanks to SVR, separating hyperplane is at the same and maximum distance from each class [5].

2. Random Forest

Random Forest classifier is a supervised learning algorithm. It can be used for both classification and regression. Additionally, it has a flexible and easy-to-use algorithm. Random forest creates decision trees on randomly selected data examples, predicts from each tree, and picks the best solution by voting [6].

3. Multilayer Perceptron

Multilayer Perceptron (MLP) is used today for the solution of many problems. It is the most widely used method, especially in classification processes. Multilayer Perceptrons use a learning method called Delta learning. The purpose of this rule is to minimize the error between the desired network output and the produced output [7].

4. K-Nearest Neighbors

The KNN method is one of the pattern recognition methods that classifies objects based on the closest learning examples in the attribute space [8]. In this method, for a new example that needs to be classified, the classification is made by looking at the proximity of each of the k's from the previously classified examples [9]. The new example is included in the class that is closest to it. During this process, the k-variable specifies the number of examples that are specific to the k number of class attributes that are closest to the example. Generally, euclidean distance is used in proximity calculation.

5. BayesianRidge

The Naive Bayesian classifier is represented in the most restrictive array of possible classification techniques [10]. Classes (groups) that need to be classified and which classes the example data belongs to are clear. It is proven to be very effective for text categorization [11]. As a Bayesian approximation, the vector x (x1....x2) defined in n-dimensional space looks for a class tag C that maximizes the last probability in the Ck (C1...Cn) data set with m classes.

6. AdaBoost Regressor

An ensemble of learners formed by combining single learners and their natural decisions is called collective learning. Generally, classification success in collective learning practices is higher than in single learning. AdaBoost is one the most widely used boosting algorithms and was first proposed by Freund and Schapire [12]. Because of its features like high prediction speed, low memory usage, and being more feasible, it is preferred over other collective methods.

C. Evaluation Criteria

The basic machine learning process is shown in Figure 1. Models are created with the aim of predicting the desired property in the most efficient, fastest way with the highest probability.

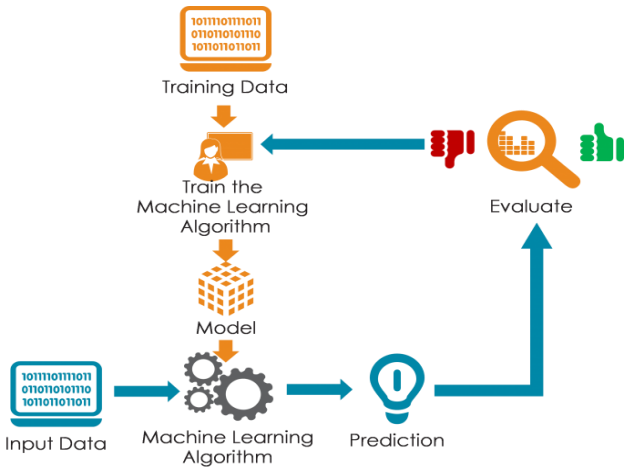

Figure 1. Basic Machine Learning Process

There are two important steps regarding prediction; the first is to prepare the data for prediction. The second is the comparison of prediction models. Criteria for comparing models are accuracy, speed, robustness, scalability, interpretability. Basic performance indicators used in performance assessments of artificial neural networks and machine learning methods include R^2, MSE, RMSE, and MAE [13].

In this study, the accuracy criteria given in the following are used. In these performance measurements, R^2 is the decision-making coefficient of the model's accuracy rate. Having a higher coefficient indicates a better prediction relation. On the other hand, since MSE, RMSE and MAE are measurements of error, low results indicate higher performance, inversely proportional to performance [14]. For instance, the RMSE value to be equal to zero indicates a good performance [15].

$$MSE = \frac{1}{n}\Sigma_{i=1}^{n} e_t^2 \quad (1)$$

$$RMSE = \sqrt{\frac{1}{n}\Sigma_{i=1}^{n} e_t^2} \quad (2)$$

$$MAE = \frac{1}{n}\Sigma_{i=1}^{n} |e_t| \quad (3)$$

III. RESULTS AND DISCUSSION

Calculations were performed on a virtual server with 2 Core Intel Xeon CPU, 12 GB ram, and 16 GB Nvidia Tesla T4 GPU allocated via Google Colab. In the study, the dataset was first passed through the pre-processing stage and the 15-minute measurement data was converted to hourly data format. Since the energy generation was to be predicted, non-productive hour data were deleted from the dataset. Then, the data for 2016 are trained with machine learning algorithms to create a model for potential solar energy prediction. Finally, the results obtained by data prediction using the created models were evaluated with the determinant coefficient (R^2), Root Mean Squared Error (RMSE) and Mean Absolute Error (MAE) metrics.

In the study, predictions were made using Adaboost Regressor, BayesianRidge, K-Nearest Neighbors, Random Forest, Support Vector Regression, and Artificial neural

network algorithms. R^2, RMSE, and MAE values obtained by using machine learning algorithms are presented in Table 2.

Table 2. Performance evaluation of Machine learning algorithms before feature reduction

	RMSE	R^2	MAE
SVR	24.728514	0.783590	19.869457
RF	6.122513	0.986734	3.730888
MLP	16.693160	0.901381	11.333827
KNN	15.247180	0.917726	9.758289
BR	20.710811	0.848199	15.956161
AB	20.639683	0.849239	17.548636

According to the results displayed in Table 2, the algorithms with the closest R^2 value to 1 were respectively Random Forest, K-Nearest Neighbors, and Multilayer Perpection algorithms. Algorithms with R^2 values close to 1 were found to be low in Mean Absolute Error – MAE values. Support vector regression, AdaBoost Regressor, and BayesianRidge algorithms have failed to make accurate predictions.

Table 3: Performance evaluation of Machine learning algorithms after feature reduction

	RMSE	R^2	MAE
SVR	21.538438	0.839274	14.497471
RF	5.810016	0.988304	3.159967
MLP	18.256077	0.884529	11.480621
KNN	14.575793	0.926392	8.246304
BR	22.113414	0.830579	17.009499
AB	22.021676	0.831981	18.793763

The performance of machine learning algorithms after feature reduction is given in table 3. According to the data in the table, R^2, RMSE and MAE values did not decrease in Bayesian Ridge and Adaboost algorithms. It was observed that the prediction rates increased in other algorithms.

IV. CONCLUSION

In this study, meteorological data of Amasya for 2016 was used to predict the solar energy power potential and tested with machine learning algorithms.

K-Nearest Neighbors, Random Forest, Support Vector Regression, Adaboost, BayesianRidge, and Multilayer Perpection algorithms were used as machine learning algorithms. The results show that the Random Forest algorithm has the lowest error rate with a value of 3.159967 MAE and that the energy generated from solar panels has been successfully predicted.

After feature reduction, it was seen that algorithms other than Adaboost and Bayesian Ridge gave higher prediction rate.

REFERENCES

[1] Yurdadoğ, V., & Tosunoğlu, Ş. (2017). Renewable energy support policies in Turkey. Eurasian academy of sciences eurasian business & economics journal, 9, 1-21.

[2] Koca, A, Oztop, H. F., Varol, Y, & Koca G. O. (2018). Estimation of solar radiation using artificial neural networks with different input parameters for Mediterranean region of Anatolia in Turkey. Expert Syst Appl 2011; 38(7), 8756–62.

[3] Parmaksiz, H., Karafil A., Özbay H., Kesler M. (2016). Farklı Eğim Açılarındaki Fotovoltaik Panellerin Elektriksel Ölçümlerinin Raspberry Pi ile İzlenmesi, Düzce Üniversitesi Bilim ve Teknoloji Dergisi, 4(2),pp. 711-718.

[4] Jamil, I., Zhao, J., Zhang, L., Rafique, S. F., & Jamil, R., (2019). Uncertainty Analysis of Energy Production for a 3× 50 MW AC Photovoltaic Project Based on Solar Resources. *International Journal of Photoenergy, 2019*.

[5] S. R. Gunn, "Support vector machines for classification and regression", Technical Report, Faculty of Engineering, Science and Mathematics, School of Electronics and computer Science, 1998.

[6] G. Louppe, "Understanding Random Forest", doktora tezi, University of Liege, 2015

[7] Ç. Çatal, L. Özyılmaz, Analysis of Multiple Myeloma Gene Expression Data by Multilayer Perceptron.

[8] Karakoyun, M. ve Hacıbeyoğlu, M.,"Biyomedikal Veri Kümeleri ile Makine Öğrenmesi SınıflandırmaAlgoritmalarının İstatistiksel Olarak Karşılaştırılması", Dokuz Eylül Üniversitesi Mühendislik Fakültesi Fen ve Mühendislik Dergisi, 2014.

[9] Liao, Y.ve Vemuri, V. R., "Use of k-nearest neighbor classifier for intrusion detection", Computers ve security, 21(5), 439-448, 2002.

[10] Mehran Sahami (1996), Learning Limited Dependence Bayesian Classifiers.

[11] Dai, Wenyuan, et al. "Transfering naive bayes classifiers for text classification." Proceedings of the national conference on artificial intelligence. London; AAAI Press; MIT Press;1999, 2007.

[12] Şimşek, H.; Demiral. Y., Aslan. Ö, Toğrul. B. Ü. Bir Üniversite Hastanesinde Koroner Kalp Hastalarına Uygulanan Tedavi Oranları, DEÜ Tıp Fakültesi Dergisi. 2012; 2, 111-117

[13] Karasu, S., Hacıoğlu, R. & Altan, A. (2018). Prediction of Bitcoin Prices with Machine Learning Methods using Time Series Data, 26th signal Processing and Communications Applications Conference.

[14] Wang, W. & Xu, Z. (2004). A Heuristic Training for Support Vector Regression, Neurocomputing, 61: 259-275.

[15] Çınaroğlu, S. (2017). Sağlık Harcamasının Tahmininde Makine Öğrenmesi Regresyon Yöntemlerinin Karşılaştırılması, Uludağ Üniversitesi Mühendislik Fakültesi Dergisi, 22(2): 179-200.

Security Issues in the RESTful API (Service) using OAuth 2.0 for Authentication and Authorization

ARBËR BESHIRI[1], ANASTAS MISHEV[2] and IVAN CHORBEV[3]

[1, 2, 3] "Ss. Cyril and Methodius" University, Skopje/North Macedonia, arber.beshiri@gmail.com, anastas.mishev@finki.ukim.mk, ivan.chorbev@finki.ukim.mk

***Abstract* – Security-related to the RESTful API (service) is discussed in this paper. Security implementation using OAuth is an essential part of strengthening security, which enables protecting the access to the service resources. The different authentication methods surveyed in this paper provide opportunities for authentication and authorization of resources and services by enabling their security at the same time. Web services are getting more and more advanced every day, so it is important to enable more sophisticated control of them and their resources to strengthen security. The interconnection between authentication and authorization has enabled proper control of services and resources either through rules applied by the organization, but also those set by the system administrators. OAuth presents an authorization framework and in combination with the appropriate authentication method provides security and efficiency in access control of the RESTful APIs (services). Except for discussing the benefits and flaws that can be identified in OAuth 2.0, in this paper, the OAuth implementation issues in web services and appropriate solutions for its proper use in favor of increasing the security level in modern web services are actualized. The purpose of this paper is to portray concrete cases of dismounting authentication and authorization issues, with particular emphasis on OAuth 2.0 security during its execution in the REST API services. The paper concludes by presenting the important recommendations for the RESTful APIs (services) protection from the different OAuth 2.0 attackers and the elimination of system flaws, thus contributing to increasing the level of overall security.**

***Keywords* - RESTful API (service), OAuth 2.0, security, authentication, authorization**

I. INTRODUCTION

NOWADAYS, the Internet is highly advanced, while for computer applications and resources there exist a need to exchange data without human intervention. Web services, commonly provided to share data between web servers and applications. The standardized service application interface methods are created to facilitate the development of applications and services by developers. One such method is Representation State Transfer (REST / RESTful) [1].

REST as an architectural style for web services represents a standardized method for accessing web services and their resources. In the REST architecture, the HTTP is used as a technology [2]. REST API via HTTP can access and transfer resources between services. This enables the reduction of server and client complexity and allows for easier service development. The REST architecture consists of six constraints that define the basis of the RESTful style: the uniform interface, stateless, cacheable, client-server, layered system and code on demand. Resources are an integral part of REST services, and unique URLs are used to identify them [3].

The REST architecture contains features like lightweight and scalability, which through HTTP enables the connection of clients and services and the information exchange between them. RESTful services can perform mostly with the following HTTP methods: GET, POST, PUT, PATCH and DELETE [4].

The REST APIs (services) are faced with different threats that they are mainly exposed. Security is essential to the RESTful service architecture, and it must be consistently applied to the controlled services and resources, which must be protected from threats or risks posed to them.

The service resources must be protected at each stage of their transfer, including:

- The access protection and control using authentication and authorization techniques.
- The protection against eavesdropping using HTTPS / SSL security mechanisms when transporting resources to the service.
- The resource protection even when delivered to the specific service, regardless the service requirements.

The purpose of this paper is to demonstrate how OAuth should be used to provide access permission, authorization and protection of the RESTful API (service) and its flaws. REST and OAuth interact with each other by enabling users to be more secure in the use of various service resources, while users can authorize applications on their behalf to access other service resources [5].

OAuth 2.0 as a security protocol was created in 2006 in order to enable the secure data access for applications (services) from other systems [6, 7]. OAuth 2.0 protocol provides the user authentication before authorizing the API (service) based on the user's approval. OAuth 2.0 uses a verification mechanism, where it identifies which service is authorized to access a part or all resources after the request is

approved by the resource owner [7].

OAuth also provides a consistent API for services and applications, where through REST enables access to resources once authorization is verified [6]. In sections 2 and 3 will be provided more details about the OAuth for authentication and authorization execution.

In Figure 1 is presented an example scenario for the application (service) authorization process, from the request submission to access the user resources (data) up to the access to the relevant resources. Initially, the user runs the application (service), which should necessarily use data (resources) of another application - this process is verified for permission. Once the relevant authorization has been granted, the client application submits a resource request to another application (service) based on the authorization token and the use of the request as a message directed towards the respective application (service).

The paper is organized as follows: in section 2, we have reviewed the literature related to the work, providing detailed information about the OAuth 2.0 protocol and its application in web services, various attacks, especially the CSRF attacks. Section 3 provides information about authentication and authorization methods in RESTful services and the application of token-based authentication in the respective services. Section 4 discusses in detail the application of OAuth 2.0 in RESTful services for authorization purposes. The authorization flows and their application to web services are presented through the scenarios in section 4. In section 5, we present an analysis of the OAuth 2.0 security and problems related to the security of web services. There are analyzed various threats, flaws and attacks that constantly threaten web services. Specifically, a case study about the CSRF attack is discussed and analyzed, while different scenarios are presented on how the RESTful services can be threatened by such attacks. Section 6 provides valuable recommendations for protecting and strengthening security against the CSRF attacks, and implementing and applying the OAuth 2.0 properly on the RESTful web services. In section 7, the conclusions about the paper are presented.

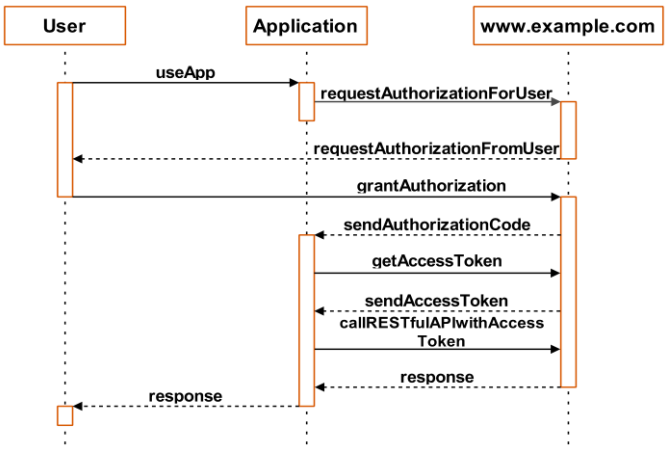

Figure 1: The application (service) authorization example

II. LITERATURE REVIEW

Our focus relates to research and analysis on the use of OAuth 2.0 for providing security in web services and relevant web standards within the security level. The work [8] highlights a number of different features of OAuth 2.0, taking into consideration the flaws that coming from the improper OAuth protocol implementation on the web, such as “the Cross-Site Request Forgery (CSRF) and open directories” [9] in the relay party and identity providers, as examples related to the relevant issue.

From in-depth research [8], the authors have identified various attacks that occurred as a result of improper implementation of OAuth 2.0 on Facebook, Twitter, etc. “The Alloy finite-state model checker” [8] is used as a model for identifying vulnerabilities in web services related to the OAuth 2.0 protocol. In the conducted research [8], the authorization code security was analyzed in terms of its composition by neglecting the HTTP status codes, cookies, and the composition of windows within the browser, which they are considered as the main features of the web.

Shernan et al. [9] have assessed the lack of protection against the CSRF in various OAuth implementations. Many of the research works listed here have resulted in the improvement of the OAuth security recommendations, which are specified in the IETF reports, RFC6749 [10] and RFC6819 [11].

Aspects of the design and specification of the OAuth protocol for security purposes have been the focus of previous research [10, 11]. For example, according to the research [12] was proven that the authorization code flow is secure based on cryptographic elements was assumed to be used the transport layer security as the security protocol. ProVerif was used as a software tool to detect security vulnerabilities such as “covert redirect and social CSRF attack” through web security mechanisms and a personalized attacker model [12].

The research studies reviewed here mainly focus on security-specific analysis, while our purpose is to uncover the OAuth 2.0 security issues related to web services, which may be caused by the flaws of its implementation in practice. The use of the CST technique [13] for protection of multiparty protocol transactions in the general aspect was then proposed.

There have been various evaluations of the OAuth protocol since its inception as the security mechanism. According to formal analysis, specific assumptions and protocol implementation, it has been proven that OAuth 2.0 enables the secure authentication. Also, according to these analyzes was shown that the approach of thinking that the implementation of OAuth is simple, and its improper implementation has led to the faulty implementation of the OAuth 2.0 protocol [9].

There are cases when supporting parties are usually improperly implemented, so they have practically failed to provide protection against common attacks such as “cross site scripting and click-jacking” [9] that have occurred in web services. Based on previous research, it has been found that OAuth 2.0 is susceptible to all attacks which affect all forms of

SSO, including phishing, eavesdropping or insecure communication channels [9].

Threats coming from various CSRF attacks can threaten the OAuth 2.0. Such threats, mainly affect the weaknesses found from improper implementation of implicit flow grant and authentication code flow [6].

In those two parts, the state parameter of OAuth 2.0 must necessarily be considered as the pseudorandom token recommended by the respective works [6, 7]. The state parameter was not required to be used as "the synchronizer token" [9] by the model created against threats. Other studies are mainly related to documenting CSRF threats in OAuth 2.0, especially on the server side [7, 8, 9].

III. Authentication and Authorization Methods in RESTful services

The need to upswing the security levels of web services is increasing more and more, because the web services are constantly evolving. They initially required modest protection, but with their rapid development even the protection (security) must be strengthened. On the Internet, data is constantly increasing and this has pushed the need to improve the data storage security, which is also reflected in the secure access. Such situations have increased the need for more sophisticated authentication and authorization mechanisms.

While a lot of data is available, not only secure authentication, but also the proper authorization control for relevant resources is needed. Authentication and authorization of access to resources and services are enabled through several methods, such as HTTP basic authentication [14, 15], HTTP digest authentication and token based authentication [14]. For reasons of relevance to the paper topic, only token-based authentication will be discussed below.

A. Token based authentication

Token based authentication (OAuth) is a more sophisticated authentication mechanism than previous mechanisms and uses a token instead of the credentials (ID and password) that are used by the aforementioned mechanisms. In Figure 2 is depicted how the token based authentication mechanism works and how the user is authenticated. The user makes a request for service on the resource server (RS), while the user's browser is redirected to the private key generator (PKG) through the RS. Initially, the user requests access to the authorization server (AS). Then, the user authentication is performed. The user makes a request to receive a token from the AS, and the token is received by the user. The RS then identifies the token received from the AS. Finally, the RS uses the token to verify the user's messages. Since a token is used during the communication between the user and the RS, the third party ensures that the user's ID and password are protected. The usage of token during the authentication process has pushed major companies that offering web services such as Twitter, Facebook, Google and Microsoft to implement the OAuth authentication method in their services [14].

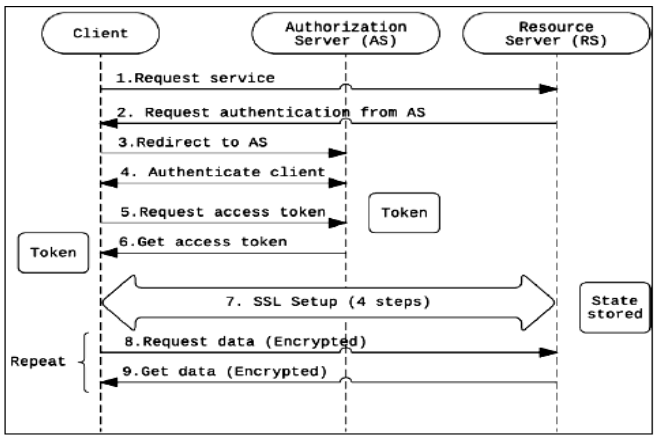

Figure 2: Token-based authentication scenario [14]

OAuth 2.0 as a protocol is created to enable applications / services to access data on other systems by taking into consideration authentication and authorization as key elements for accessing specific resources. It focuses on providing the authorization enforcement for web applications and services, desktop applications, mobile services, etc. [7].

Password is another grant mode function available in the OAuth 2.0. From this, we understand that applications can use credentials to authenticate the user to a system instead of using tokens and exchanging them with the corresponding system. This functionality is enabled concretely within an application (service). The Facebook Messenger application, for example, can use OAuth 2.0 to acquire the user login credentials from its native service [6].

IV. Authorization-Based on OAuth 2.0

OAuth 2.0 consists of four roles: client, resource owner, resource server and authorization server. It is presented as a framework that enables delegated access in an authorized manner. The resource owner represents an entity that has the authority for enabling access to a protected resource (for instance, an end-user) [16].

The server that hosts the resources secured by access tokens is known as a resource server. A client is introduced as an application that, with the permission of the resource owner, makes requests for the protected resource on its behalf. Authorization server is considered a server that releases tokens for the client access after successfully performing the resource owner authentication and securing authorization [16, 17].

OAuth specifies how an API client can get tokens that represent the permissions' collection of such API. Tokens are attached to the client invokes that address to the API by indicating its authorization in relation to the respective API.

In the OAuth are used two types of tokens: the authorization token and the access token. To obtain an access token, the client communicates with an authorization server (AS) by delivering a request that contains an access grant. In certain situations, the client can additionally submit its credentials to the AS in response to a request message [16].

OAuth's flows are the interactions between the various roles involved in seeking authorization. Flows are sometimes considered to be the kind of authorization that has been provided. Authorization code, implicit, resource owner password credentials and client credentials are the four flows available in OAuth 2.0 [6]. The flow is determined by the type of authorization grant and the kinds of grants supported by the API/service.

The flows are discussed and schematically depicted in the following this section:

- Authorization code flow is considered the most used flow, mainly with server-side services/applications.
- Implicit flow is utilized with mobile or web services/applications.
- Resource owner password credentials are the third type of flow that is mainly considered by trusted applications. The service can be the owner of a trusted application.
- Client credentials. The application APIs are used with this type of flow [8, 16].

A. *Authorization code flow*

It is considered the most used flow, and it is mainly involved in issues related to resource code on the server side. Here, the client confidentiality can also be maintained. Because redirection is used in this flow, the application/service must communicate to the user agent. In this type, the communication is performed between the client and authorization server, during which is generated the access token [6] (as described step by step in Figure 3).

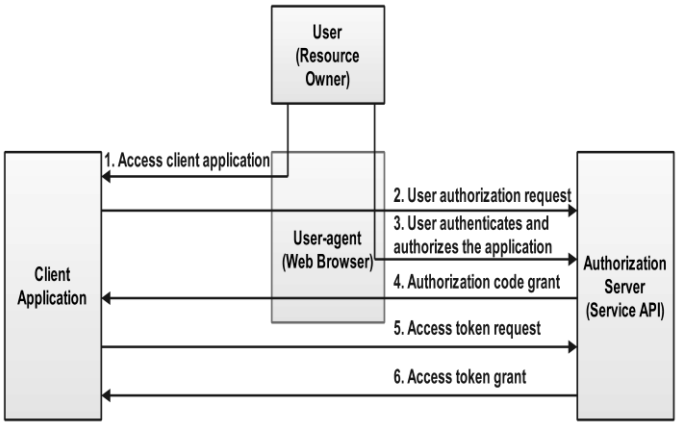

Figure 3: Authorization code flow scenario

In order to have more detailed information about the authorization code grant, a detailed scenario is shown in the Figure 4.

B. *Implicit authorization flow*

Implicit flow is the second type of OAuth 2.0 framework, in which the consumer accesses the authorization server to get the token for accessing. This flow is utilized in both mobile and web-based applications/services. The confidentiality of service is assured with this flow. The redirection is also used in the implicit flow. The token is handed to the user-agent, who then passes it to the application/service. The application is not directly authenticated in this flow. The action is redirected through the URI [12, 16]. The scenario about this flow is depicted step by step in Figure 5.

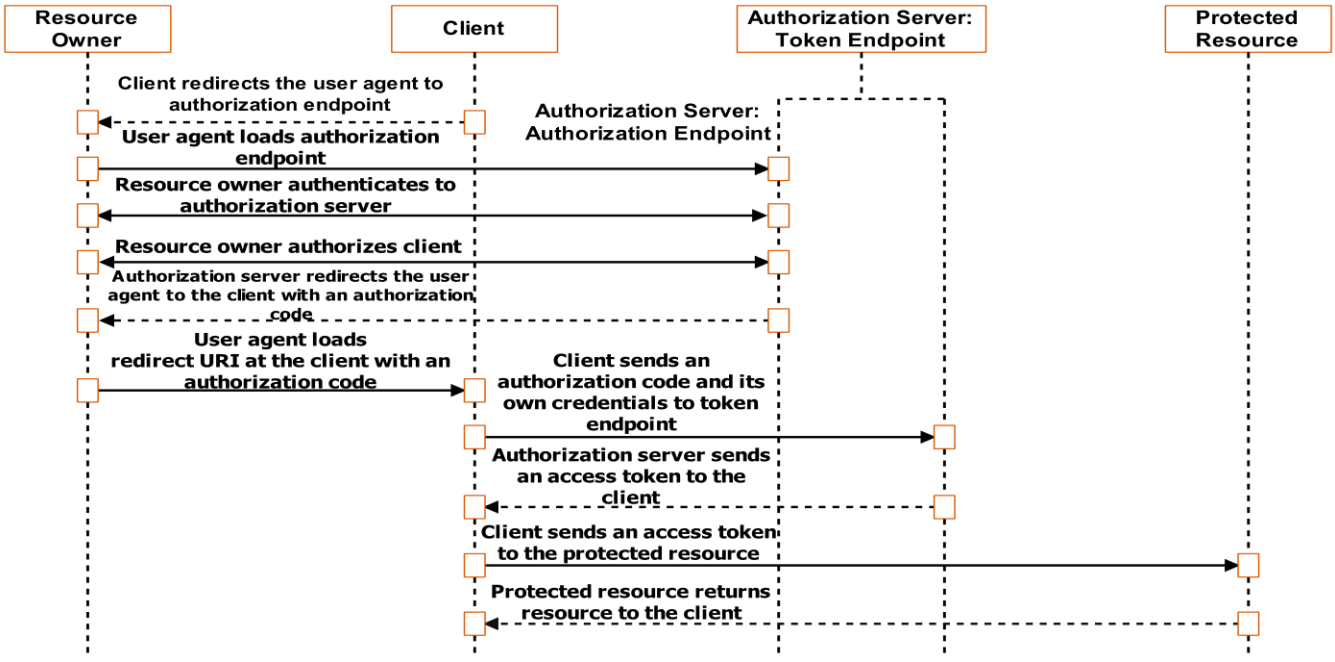

Figure 4: The detailed scenario of the authorization code grant

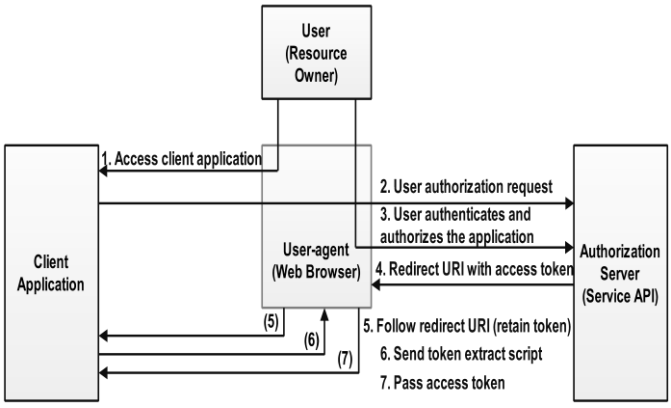

Figure 5: The implicit authorization flow step by step scenario

C. *Resource owner password credentials flow*

The third type is resource owner password credentials as shown in Figure 6. It is an authorization grant type in which the consumer provides the consumer ID and password for the application/service. Credentials are used by the application to obtain a service access token. Such a flow can be used whether no other flaws are enabled by the API service - in this case, the user must trust the respective application (service) [8, 16].

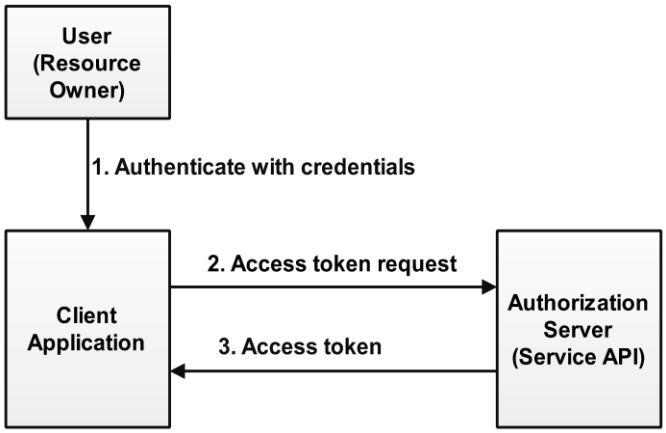

Figure 6: Resource owner password credentials flow

D. *Client credentials flow*

Client credentials flow (Figure 7) is the last type that supposes the authorization server need to have trust in the client application, so the authorization server authorizes all controls of the authorization to the client application. Then, the client application is allowed to access in its service [8, 16].

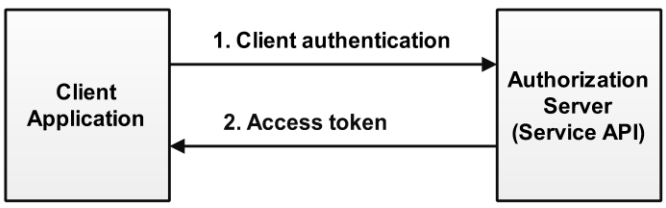

Figure 7: Client credentials flow

V. OAuth 2.0 Security - Authentication and Authorization problems

It should be taken into consideration that OAuth does not necessarily guarantee the data privacy. From this, we understand that this mechanism is not so convenient in providing privacy. OAuth's implementation errors have usually caused the security problems.

A. *Threats, flaws and attacks*

The majority of the attacks related to the client-side have aimed to steal the end-user's access token. The starting point of the attack mainly occurs when the attacker in one way controls the user's browser, or it has the ability to lure it by clicking on any URL, which in the background is a trap for the user itself. The phishing as the social engineering technique contributes to this approach.

This technique usually works when the attacker knows or in a way has information about the client ID and redirects the URI, and then the resource owner without being aware can be redirected to the attacker application by insidiously legitimizing the relevant application.

The threat on the client-side is the client impersonation by the attacker. It plays the role of imitator by hijacking the session or authorization code through retrieves of the service endpoint (using various weaknesses such as URL redirection, manipulating user activity by hiding hyperlinks under legitimate and clickable content, disclosing of the cross domain information and its use, etc.) and afterwards it ignores the original client request to avoid the authorization code from becoming stale [18].

The attacker, meanwhile, uses the victim's authorization code to initiate a session with the client. Normally, the applications and services strictly need to follow the requirements defined in RFC 6749, but this has not stopped to be appeared different weaknesses as the subject of vulnerability in terms of URL redirection, which it has made even the OAuth 2.0 tokens to be misused [18, 19].

B. *CSRF threat and attack - A case study*

The CSRF is considered one of the most dangerous attacks on the Internet and according to the OWASP Top Ten[1] is listed among the ten flaws and threats with the highest rate of risk and negative impact on the security of web applications. It is also accounted as an appropriate method used by attackers to threaten security on web services [19].

The CSRF is referred as a malicious application induces the user's browser to conduct an undesirable action in response to a website request in which the user is actually authenticated. We assume that the user is initially registered and then logged in to a website that provides the possibility to execute specific tasks and the attacker tricks the user's web browser by making requests to one of the user's tasks, specifically in the URL. In this case, the task is accounted to be performed by the user who is already logged in to the website [6, 19].

[1]https://www.owasp.org/index.php/Top_10_2013-A8-Cross Site_Request_Forgery_%28CSRF%29

Usually, the attacker in similar cases will integrate HTML or JavaScript code with malicious content in any email or website by using the request to execute the specific task through the URI, for which the user has no knowledge [6]. A detailed example of the CSRF attack scenario is shown step by step in Figure 8.

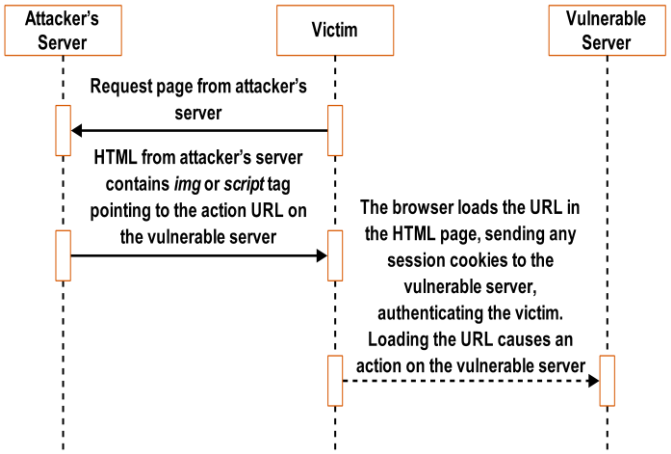

Figure 8: An example of the user attack using the CSRF attack

OAuth 2.0 has been compromised by CSRF attacks, especially on the issue of implementation, and this was discovered by Synack researchers[2]. OAuth's vulnerability has occurred exactly in Hotmail through the CSRF attack, where the attacker took control of the user's browser and acted on its behalf. It implemented in Hotmail could not validate tokens that were affected by CSRF on the server-side [6].

This has caused anyone to send requests by reading / writing in the Hotmail resources on behalf of the abused user (victim with the Hotmail account). A nonce token was sent by the client to the server-side, and it could not be validated by the server deleting all the nonce values. It was used to perform the intended action, so it was turned into a malicious worm through which the tokens of the Hotmail user (victim) were misused [6]. Such a scenario is shown in Figure 9.

A flaw that is encountered in the OAuth 2.0 implementation was mainly in the login process, which did not guarantee inherent security of the client application before allowing the client to request for the authorization token. Another problem presented in the implementation of the OAuth 2.0 was the attacker interference in privileges by influencing in actions outside the authorization token [20].

VI. Recommendations and Discussion

The solution for cases like phishing is considered the using of the protected URIs included in the whitelist and utilizing them as fields in the argument of the redirected URI. SSL/TLS cryptographic protocols must be strictly applied to web applications (services) because exchange the authorization tokens to prevent the client forgery.

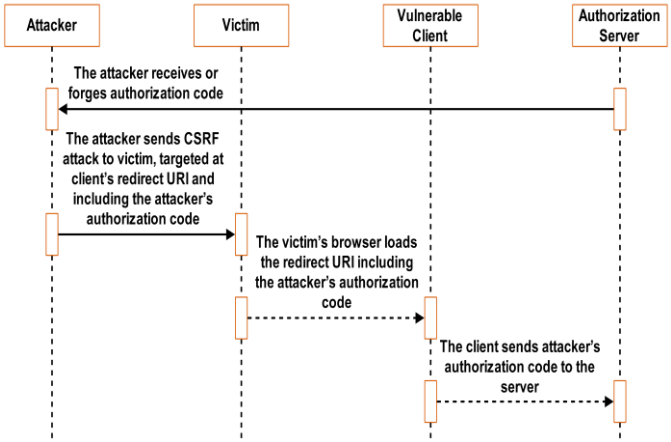

Figure 9: The scenario of OAuth attack via CSRF attack

Different strict measures should always be taken to protect the user from various attackers. It is much more important to take measures for CSRF tokens, which they have the role of cheating and attacking the user. Such tokens must necessarily be validated in order not to threaten web services and not to redirect requests to the fake clients, rendering them invalid and stop the eavesdropping on the real user for each targeted action.

To prevent the user from being deceived for actions that are not intended by it, the X-frame options[3] header should always be set to 'sameorigin'. A possibility for the secure implementation of OAuth 2.0 with a secret code of the client for the authorization purpose can be applied based on the framework shown in Figure 10.

Usually, the different implementations are performed according to various approaches, therefore the flaws of the authorization on the server-side cannot be said to be necessarily noticed. The solution in this case is to test each authorization element to identify these flaws. Also, the authorization tokens should be made with expiration period in order not to be misused by various attackers.

Or, if the authorization and access tokens are not set an expiration period, then they should be sent from the resource server with the web service secret code proof to the authorization server, notifying the user during the process, to avoid fraud by any attacker tends to exploit the system weaknesses and interfere on it.

This approach will secure the user because the access token will hold on the resource server and the attacker, even getting the token; it cannot know the secret code for using the service (application). The secret code of the application can be changed on the resource server and this renders impossible the attacker from misusing the resources of the user and the web application even if having the access token.

[2] https://www.synack.com/2015/10/08/how-i-hacked-hotmail/

[3] https://cheatsheetseries.owasp.org/cheatsheets/Clickjacking_Defense_Cheat_Sheet.html

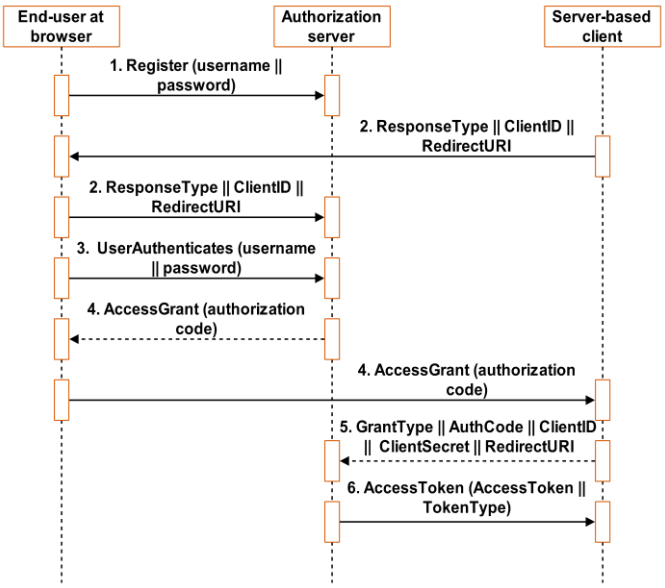

Figure 10: A possibility for the secure implementation of OAuth 2.0 with a secret code of the client for the authorization purpose

Implementing web services based on the style features of RESTful and OAuth 2.0 architecture enable secure access to service resources. Services designed and implemented by taking into consideration the secured access for the user have consideration explicitly for the resources and the user's access protection.

VII. Conclusion

The importance of web services in web applications is discussed in this paper, as well as the current authentication and authorization processes. In these processes, respectively in security, OAuth 2.0 is playing an essential role because it enables user authentication and authorization in the RESTful API (service). This has enabled access to applications and services without the need to insert credentials. However, this method also has its drawbacks, especially when the token is taken from the client or server. We have discussed and presented in detail a case study (CSRF attack) about that situation when the attacker takes the token and manipulates the system, thus impairing the OAuth effectiveness. In the most cases, it occurs as a result of insufficient knowledge in implementing OAuth in the RESTful service. The various attacks threatening the REST API (service) are elaborated for the client and server-side based on the different targets that have happened to the two interacting parties. Based on the research conducted, it is clearly specified that most attacks on services and applications have occurred as a result of improper implementation of the OAuth 2.0 authorization framework. The recommendations are presented in this work helps us to avoid attacks, threats and flaws during the OAuth 2.0 implementation in REST APIs (services).

References

[1] R. T. Fielding, “Architectural styles and the design of network-based software architectures”, Ph.D. dissertation, Univ. of California, Irvine, 2000.

[2] L. L. Iacono, H. V. Nguyen, and P. L. Gorski, “On the need for a general REST-security framework," *Future Internet*, MDI, vol. 11, no. 56, pp. 1-33, 2019.

[3] A. Beshiri, "Resource description language for distributed RESTful service permission management," *Technology, Education, Management and Informatics Journal*, vol. 5, no. 4, pp. 538-549, 2016.

[4] A. Beshiri, "Analyzing of REST services: integration services and authorization management," in *Sixth Int. Conf. for Information Systems and Technology Innovation: Inducing Modern Business Solutions*, pp. 1-8, 2015.

[5] C. Pautasso, "RESTful web services: principles, patterns and emerging technologies," in *Web Services Foundations*, New York, Springer, pp. 31-53, 2014.

[6] J. Richer and A. Sanso, *OAuth 2 in Action*. Shelter Island, New York: Manning Publications Co, 2017.

[7] E. Ferry, J. O. Raw, and K. Curran, “Security evaluation of the OAuth 2.0 framework,” *Information and Computer Security Journal*, vol. 23, no. 1, pp. 73-101, 2015.

[8] D. Fett, R. Küster , and Guido Schmitz. “A comprehensive formal security analysis of OAuth 2.0, ” *CCS '16: Proc. of the 2016 ACM SIGSAC Conf. on Computer and Communications Security*, pp. 1204-1215, October, 2016.

[9] E. Shernan, H. Carter, D. Tian, P. Traynor, and K. R. B. Butler. “More guidelines than rules: CSRF vulnerabilities from noncompliant OAuth 2.0 implementations,” in *DIMVA 2015*, LNCS, vol. 9148, pp. 239–260. Springer, 2015.

[10] D. Hardt (ed.). “RFC6749 – The OAuth 2.0 authorization framework”. *IETF*. October, 2012.

[11] T. Lodderstedt, J. Bradley, A. Labunets, and D. Fett, “OAuth 2.0 security best current practice,” *IETF*, draft-RFC, 2019.

[12] R. Yang, G. Li, Wing Cheong Lau, K. Zhang, and P. Hu., “Model-based security testing: an empirical study on OAuth 2.0 implementations,” in *ASIA CCS '16: Proc. of the Eleventh ACM on Asia Conf. on Computer and Communications Security*, pp. 651–662, May, 2016.

[13] E. Y. Chen, S. Chen, S. Qadeer, and R. Wang, “Securing multiparty online services via certification of symbolic transactions,” *IEEE Symposium on Security and Privacy*, pp. 833 – 849, 2015.

[14] A. Beshiri, “Authentication and authorization in service oriented cloud computing architecture,” in *Thirteenth ICT Innovation Conf.*, pp. 1-16, 2021.

[15] J. Reschke, “The 'basic' HTTP authentication scheme,” RFC 7617, *Internet Engineering Task Force (IETF)*, 2015.

[16] P. Siriwardena, *Advanced API Security - OAuth 2.0 and Beyond*. San Jose, CA, USA: Apress and Springer-Verlag, 2020.

[17] M. Argyriou, N. Dragoni and A. Spognardi, “Security flows in OAuth 2.0 framework: a case study,” in *Int. Conf. on Computer Safety, Reliability, and Security*, Springer, pp. 396-406, 2017.

[18] H. Wang, Y. Zhang, J. Li, H. Liu, W. Yang, B. Li, D. Gu, “Vulnerability assessment of OAuth implementations in android applications,” in *Thirty-first Annu. Computer Security Applications Conf. (ASAC 2015)*, ACM, pp. 61–70, 2015.

[19] W. Li, Ch. J. Mitchell, and Th. Chen, “Mitigating CSRF attacks on OAuth 2.0 systems,” *IEEE 1 Sixth Annu. Conf. on Privacy, Security and Trust (PST)*, IEEE, pp. 1-5, 2018.

[20] W. Li, Ch. J. Mitchell, Th. Chen, “OAuthGuard: protecting user security and privacy with OAuth 2.0 and OpenID Connect,” in *Fifth ACM Workshop on Security Standardization Research Workshop*, pp. 35-44, 2019.

Underwater fish recognition using deep learning

G. ALTAN[1]

[1] İskenderun Technical University, Hatay/Turkey, gokhan.altan@iste.edu.tr

***Abstract* – Image processing techniques enable generating robust representations. However, it is still method-dependent, and is computationally intensive due to high dimensionality in feature extraction. Generative models have been popular approaches in the last decades with the advantages of Deep Learning. The deep Belief Networks (DBN) classifier has a common use for various types of biomedical signal and images generates different presentations of the input data for each latent layer. Restricted Boltzmann machine algorithm supports the representations using energy and probability distributions of the input data and transfers the distributions to the joint layers. The DBN with detailed representational learning has more efficient and robust for underwater fish images on supervised learning-based classifiers.**

***Keywords* - Deep Learning, representational learning, Deep Belief networks, fish recognition.**

I. INTRODUCTION

HAND-CRAFTED features are efficient methods for image processing, recognition, and computer vision. But, the advancements in data size and image resolution lead to extracting hand-crafted features, including morphology, area, shape, and more. Addictively, they are not robust, method dependent, and are computationally intensive due to high dimensionality. Especially, big data on image datasets causes unpredictable long progress. It is a definite necessity to adjust the feature extraction algorithms to computer-assisted methods for image processing.

Representational Learning has become a popular approach in the last decades with the advantages of Deep Learning [1]. At this stage, a layer-by-layer transfer of dominant features is performed with representations obtained from various filters on images at a fixed size of an image instead of extracting individual hand-crafted features for each image [2]. The transfer learning at each layer creates a new representation of the transferred data from the previous layer and transfers the high-level features towards the output layer of the model. Some deep learning algorithms transfer the pre-trained weights, which are generated unsupervised ways considering the input and hidden layer structure, for the supervised classifiers to fast optimize by fine-tuning [2], [3]. In both representational learning approaches, the representations of the image at each layer given are generated using unsupervised models.

With the developments in GPU technology in recent years, the generation of these representations and transfer learning with multilayered models, the dominant generating features, and the gradual extraction of low-, mid-, and high-level features have become possible with Deep Learning algorithms. Deep Belief Networks (DBN) is one of the most common classifiers among these algorithms. DBN is a classifier that examines the weights of connections between each adjacent sequential layer during pre-training using Restricted Boltzmann Machines (RBM) [2]. Random weights are determined depending on the number of neurons between the layers with representations before the RBM. The initial determination of the random weights is performed by probabilistic and energy functions depending on the input structure and subsequent layer. The DBN was frequently utilized in image processing, including handwriting recognition [2], remote sensing by satellite images [4], 3D object recognition [5], medical image analysis [6], and more. In addition to the prosperity of the DBN model on the image processing, it was also used in the classification of time-series using the fiducial and non-fiducial features extracted using various signal analyzing methods as input to the DBN model. Altan et al. provided the classification of five arrhythmia types using statistical features of different modulation signals sifted by Hilbert-Huang transform to ECG signals [7]. Altan et al. also applied the Second-order difference plot to the ECG signals and quantified chaos distribution. Using quantization features with various shapes as input to the DBN model, they separated patients with coronary artery disease and healthy subjects with high classification performances [8]. Altan et al. applied the Hilbert-Huang transform to the EEG signals and extracted the statistical feature from the intrinsic mode functions. In their proposal, they fed the statistical feature dataset to the DBN model with two hidden layers. They reported that positive and negative brain activity trails could be determined successfully for stroke patients with the DBN classifier (Altan, Kutlu, & Allahverdi, 2016). Kutlu et al. used the morphological features extracted from fish images using 13 landmarks and succeeded in differentiating 3 types of species of the triglidae fish family. Literature shows that the DBN performed very successful classification performances in both hand-crafted features and direct image as inputs [10].

The aim of this study is to present the advantages and efficiency of the DBN classifier on the capabilities of generating representation on underwater fish images. This study evaluates underwater fish recognition performance by feeding the DBM model with directly fish images as input for two species. In order to implement a complete comparison, the classification parameters in previous work, such as model hidden layers, neuron numbers, and activation functions, were re-tried for representational learning. The analysis was performed by reducing the image dimensions as much as possible to cause the feature size to become closer.

II. Materials and Methods

A. Fish4Knowledge Database

Underwater fish images are selected from plectroglyphidodon dickii (PD) and chaetodon lunulatus (CL) species from the Fish4Knowledge dataset [11]. The images were taken using a similar composition near the fish and stable background for standardization [12]. PD is a kind of damselfish species that is commonly in sight of the Indian and Pacific Oceans. PD has a stocky body with 12 dorsal spines and one dorsal fin (see Fig.1.a). CL is a kind of oval butterflyfish that is colonized in sight of the Pacific Ocean. CL has a stock body with 13-14 dorsal spines and one dorsal fin (see Fig.1.b).

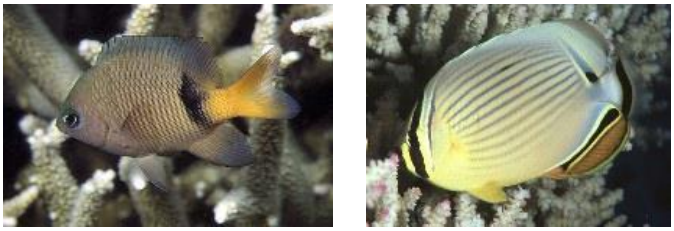

(a) (b)

Figure 1: High resolution samples for PD (a) and CL (b) [13].

The underwater fish images were analyzed with representational learning as input for DBN. Whereas the Fish4Knowledge database has a total number of 27370 fish images from 23 species, I only used two species due to the balanced number of samples. The deep learning-based underwater fish recognition was performed on 5214 images, including 2680 PD and 2534 CL.

B. Deep Belief Networks

The DBN is a specified model of Deep learning algorithms with fast training and representational learning advantages. While the first layers of the DBN model are used to learn low-level features, high-level features are obtained as the number of layers moves towards the top layer [14]. The DBN is a statistical and probabilistic model. It is performed by calculating the conditional probabilities of the other inputs in case the input state is binary. Unlike common deep learning algorithms, it can achieve very high training performance for a low number of datasets.

The DBN is a two-stage classifier that starts with an unsupervised stage to predefine the weights by generating different presentations using RBM and supervised model by unfolding the pre-trained weights into the neural network model for fine-tuning [2]. The RBM-based predefined weights are updated using greedily layer-wise training of the DBN model. Each RBM has a connection between adjacent layers as nth and $(n+1)^{th}$ layers. For instance, the first RBM consists of an input layer $h_0=v$ (for visible units) and first hidden layer h_1. The bias parameters are b_n and c_n for h_n and h_{n+1}:

$$E(h_n, h_{n+1}) = -h_{n+1} W h_n - b h_n - c h_{n+1} \quad (1)$$

$$P(h_n, h_{n+1}) = \frac{e^{-E(h_n, h_{n+1})}}{\sum e^{-E(h_n, h_{n+1})}} \quad (2)$$

$P(h_n, h_{n+1})$ is the joint distribution of the RBM, and $E(h_n, h_{n+1})$ is the energy function between nth and $(n+1)^{th}$ layers. The DBN model generates high-level features at the top levels of the DBN by generating RBM-based representations. The deepest presentation is able to generate using more hidden layers in the network [2].

Figure 1: Randomly selected underwater fish images for PD (left) and CL (right)

I. Experimental Results

The DBN enables generating various representations of the input data using different layer models. The number of the layers and neurons at each layer provides learning the descent features and transferring them to the next latent layer using the unsupervised methods. Using time-frequency features as the input of the DBN defines relational parameters in this way pre-training correlated weights.

Hand-crafted features were commonly utilized using descriptive 13 landmarks on fish images, including edges of fins, head and mouth points. The morphological features of fish images between the landmarks were calculated using a pixel-based radii distance algorithm depending on the

calibration coin metric [15]. Hereby, directly resized underwater fish images are given as input to the DBN classifier without using time-consuming preprocessing such as background subtraction and landmark pointing.

The fish images have varied in dimension due to the cropping options of the Fish4Knowledge. The fishes were located on different reef bases and background ocean spaces. Background subtraction is not performed to procure image diversity. Each fish image was resized to 64x64 pixels and was converted to a grayscale image. In this manner, standardized image size and channel for the representational learning have been handled as DBN model input.

The proposed fish recognition system was tested using a 5-fold cross-validation method. The DBN classifiers were modeled with one input layer, 2 hidden layers, and an output layer with three binary outputs. Each fish species was represented with a binary output neuron. Each input neuron belongs to one morphometric feature and one pixel for hand-crafted features and fish images. Greedy layer-wised pre-training was applied to pre-train the DBN. Each training had 500 epochs. The number of neurons at each hidden layer varied among 120~360, increasing by 10 neurons at each iteration. The learning rate for the supervised training was set as 0.01, the activation function of the output layer was the sigmoid output function. The activation function of hidden layers was set as a logarithmic sigmoid function. After training of the DBN was finalized to end, the remaining fold for the dataset was tested to calculate the classification performance. Statistical test metrics including overall accuracy, weighted sensitivity, and weighted specificity were calculated to evaluate the proposed models. The contingency table of the image fed DBN is seen in Table 1.

Table 1: Contingency table with underwater fish images on DBN.

	PD	CL	Total
PD	2603	41	3644
CL	77	2493	2570
Total	2680	2534	5214

When the underwater fish images were used as input of the DBN, the proposed model DBN achieved classification performance rates of 97.74%, 97.13%, 98.38%, and 98.45% for accuracy, sensitivity, specificity, and precision, respectively. The most successful classifier model is 350 neurons for the first hidden layer and 120 neurons for the second hidden layer. The proposed DBN model for underwater fish images has a sparse representation. It is more accurate for recognition of the experimented fish species. Deep representational learning has a classification accuracy dominance and less progression time on the fish images.

REFERENCES

[1] N. Le Roux and Y. Bengio, "Representational Power of Restricted Boltzmann Machines and Deep Belief Networks," *Neural Comput.*, vol. 20, no. 6, pp. 1631–1649, 2008, doi: 10.1162/neco.2008.04-07-510.

[2] G. E. Hinton, S. Osindero, and Y.-W. Teh, "A fast learning algorithm for deep belief nets.," *Neural Comput.*, vol. 18, no. 7, pp. 1527–54, 2006, doi: 10.1162/neco.2006.18.7.1527.

[3] G. E. Hinton and R. R. Salakhutdinov, "Reducing the dimensionality of data with neural networks," *Science (80-.).*, 2006, doi: 10.1126/science.1127647.

[4] S. Basu, S. Ganguly, S. Mukhopadhyay, R. DiBiano, M. Karki, and R. Nemani, "DeepSat - A learning framework for satellite imagery," 2015, doi: 10.1145/2820783.2820816.

[5] V. Nair and G. E. Hinton, "3D object recognition with Deep Belief Nets," 2009.

[6] A. Khatami, A. Khosravi, T. Nguyen, C. P. Lim, and S. Nahavandi, "Medical image analysis using wavelet transform and deep belief networks," *Expert Syst. Appl.*, 2017, doi: 10.1016/j.eswa.2017.05.073.

[7] G. Altan, Y. Kutlu, and N. Allahverdi, "A Multistage Deep Belief Networks Application on Arrhythmia Classification," *Int. J. Intell. Syst. Appl. Eng.*, vol. 4, no. Special Issue-1, pp. 222–228, Dec. 2016, doi: 10.18201/IJISAE.270367.

[8] G. Altan, N. Allahverdi, and Y. Kutlu, "Diagnosis of Coronary Artery Disease Using Deep Belief Networks," *Eur. J. Eng. Nat. Sci.*, vol. 2, no. 1, pp. 29–36, 2017, Accessed: Feb. 19, 2018. [Online]. Available: http://dergipark.gov.tr/ejens/issue/27741/293042.

[9] G. Altan, Y. Kutlu, and N. Allahverdi, "Deep Belief Networks Based Brain Activity Classification Using EEG from Slow Cortical Potentials in Stroke," *Int. J. Appl. Math. Electron. Comput.*, 2016, doi: 10.18100/ijamec.270307.

[10] Y. Kutlu, G. Altan, B. Iscimen, S. A. Dogdu, and C. Turan, "Recognition of Species of Triglidae Family using Deep Learning," *J. Black Sea / Mediterr. Environ.*, vol. 23, no. 1, pp. 56–65, 2017, [Online]. Available: http://www.blackmeditjournal.org/index.php/component/k2/item/574.

[11] B. J. Boom *et al.*, "Long-term underwater camera surveillance for monitoring and analysis of fish populations," *Work. Vis. Obs. Anal. Anim. Insect Behav. (VAIB), conjunction with ICPR 2012*, 2012.

[12] B. J. Boom, P. X. Huang, J. He, and R. B. Fisher, "Supporting ground-truth annotation of image datasets using clustering," 2012.

[13] FishBase, "2021," *Available at: http://www. fishbase. org (accessed on 13 August 2021)*, 2021. .

[14] G. Hinton, "Deep belief networks," *Scholarpedia*, 2009, doi: 10.4249/scholarpedia.5947.

[15] B. Iscimen, Y. Kutlu, A. N. Reyhaniye, and C. Turan, "Image analysis methods on fish recognition," in *2014 22nd Signal Processing and Communications Applications Conference (SIU)*, Apr. 2014, pp. 1411–1414, doi: 10.1109/SIU.2014.6830503.

Edge Detection of Aerial Images Using Artificial Bee Colony Algorithm

E. D. YELMENOĞLU [1] and N. AKHAN BAYKAN [2]

[1] Işık University, İstanbul /Turkey, deniz.yelmenoglu@isikun.edu.tr

[2] Konya Technical University, Konya/Turkey, nbaykan@ktun.edu.tr

***Abstract*— Edge detection techniques are the one of the best popular and significant implementation areas of the image processing. Moreover, image processing is very widely used in so many fields. Therefore, lots of methods are used in the development and the developed studies provide a variety of solutions to problems of computer vision systems. In many studies, metaheuristic algorithms have been used for obtaining better results. In this paper, aerial images are used for edge information extraction by using Artificial Bee Colony (ABC) Optimization Algorithm. Procedures were performed on gray scale aerial images which are taken from RADIUS/DARPA-IU Fort Hood database. Initially bee colony size was specified according to sizes of images. Then a threshold value was set for each image, which related with images' standard deviation of gray scale values. After the bees were distributed, fitness values and probability values were computed according to gray scale value. While appropriate pixels were specified, the other ones were being abandoned and labeled as banned pixels therefore bees never located on these pixels again. So the edges were found without the need to examine all pixels in the image. Our improved method's results are compared with other results found in the literature according to detection error and similarity calculations'. All the experimental results show that ABC can be used for obtaining edge information from images.**

***Keywords*— Image processing, Edge detection, Artificial Bee Colony Optimization, Aerial Images**

I. INTRODUCTION

Nowadays, image processing techniques are quite advanced with the development of technology. Image is a concept that may be encountered in each area. Camera Systems are used in wide area such as military technology, education and training techniques, space science and in many areas like these ones. This system used in many different areas is open to continuous improvement.

Computer vision systems are also changed by the views of the nature of the images obtained in the field. For example, gray scale images, thresholded images and so on. On each image dependent upon the nature of the operations performed can be varied. All of these operations encountered appears as "**image processing**" in the literature. Image processing is being used also in many areas such as the industry of military, oil exploration, medical technology, security, criminal laboratories, satellite imagery, remote sensing applications, farming (for example; determination of the quality of meat), robotics, radar, astronomy [1-7]. Edge detection is one of the most important and indispensable step in image processing. Therefore, edge detection algorithms can be used wherever image processing is used [8-14].

In this paper, an "**edge detection method**" which is one of basic step of these operations, is used. Edges are the borders that are generated by abrupt diversities in the pixels of between two different areas [8-9, 11, 14]. Edge detection is so important because of the characterize the boundaries. Detecting the edges of an image preserves the major structural properties of the image. The recognition of edges of views is so important for human visual system because of the strong association between edge information and object attributes. For this reason, in image processing, edge detection algorithms try to identify where the object is. Edge detection reduces the amount of data to process in the image while provides important information about the shapes of objects [12]. It must be effective and trustworthy because it is very important for determining how successful following operation steps will be [15].

The existing edge extraction methods which are still used today, most of the common point is that they are dependent on a mask. Without this mask information, edge detection process cannot be done. Derivative methods such as Laplacian, Canny, Roberts, Prewitt and Sobel are the common masks used for edge detection. Marr and Hildreth's method was developed by using edges of zero crossings with Gauss's Laplacian operator [9]. Haralick used the value of the gradient of the derivative to find a gradient of zero crossings in an image [8]. Canny's approach was based on the implementation of the Gaussian mask operator, which reduces the noise level on the image. This mask operator is produced by a sigma value. Then before the derivate process, a smoothing filter is applies on image. This method uses gradient value to find edge directions [16]. Roberts, Prewitt and Sobel methods are the some common techniques used in the image processing area. There is abundant literature [8-9, 11, 13, 16-18] on the subject of edge detection.

Optimization is to use available limited resources in the most optimal ways. Mathematically, it can be defined as maximizing or minimizing a function. It is a collection of processes comprising the best results. Optimization algorithms aim is to obtain the best results in the present circumstances. Because of the technology development and become more complex with each passing day, the problems raised by the optimization of the system also becomes more difficult to perform. For this reason, optimization algorithms must evolve with technology [19]. In the last years, new methods are developed by using modern global optimization algorithms such as the Genetic Algorithm (GA), Differential Evolution Algorithm (DE) and Simulated Annealing (SA). These kinds of algorithms are known as "**stochastic algorithms**". Yang describes the name of the all stochastic algorithms based on the randomization as "**metaheuristic**" [20].

The "**swarm**" definition is used for a group of animals. "Swarm intelligence", one of the metaheuristic approache's

term, is an expression for a group behavior of decentralized and self-organized swarms. Artificial Bee Colony (ABC) is a metaheuristic algorithm inspired by the behavior of foraging bees. It was developed in 2005 by Derviş Karaboğa and has been applied in many fields [21-28].

Our improved edge detection method is based on ABC optimization algorithm and detects edges without using any mask operator. By using ABC algorithm, the pixels which are parts of an edge can be detected. This paper is organized as follows. Section 2 concerns used dataset, basic ABC and modified ABC algorithm that will be used in this work. Section 3 includes experimental results are provided by comparing between our implementation and other methods' performance. Conclusions are given in Section 4.

II. Material and Methods

A. Dataset

In this study, 10 gray level images taken from the RADIUS/DARPA-IU Fort Hood aerial image dataset [29] were used for testing accuracy of the proposed algorithm. All of the images size ranges between 476x477 and 645x667 pixels. The ground truth images of the test images are also included in the dataset. Figure 1 shows the 10 aerial images and their ground truths (GT: Ground Truths) used in this study.

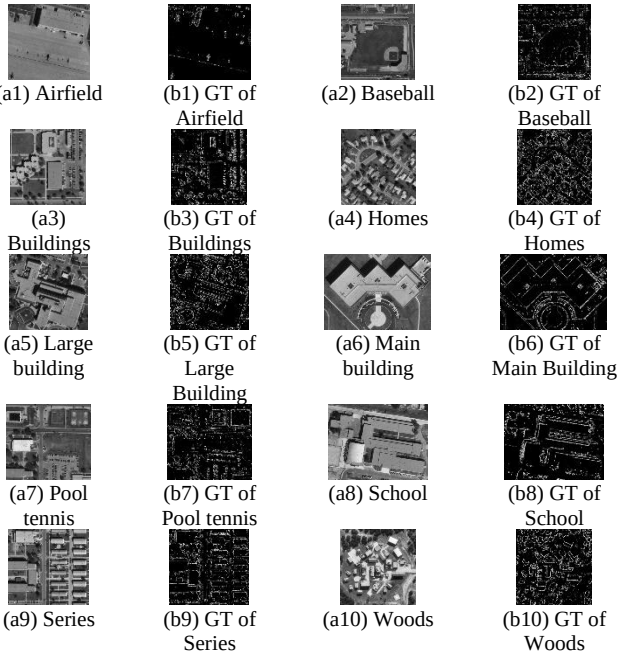

Figure 1: Images from RADIUS/DARPA-IU with their ground truths

B. Artificial Bee Colony (ABC) Optimization Algorithm

Inspection of the occurring intelligent behavior in nature has directed researchers to produce new optimization techniques. Therefore, many metaheuristic algorithms like ABC based on behavior of the swarms are developed.

In nature, honey bees live in colonies. These bees have some features such as foraging, dancing, task sharing, decision making, navigating, positioning, mating and pheromone spreading behaviors. That features can be used as models for intelligent systems. ABC is one of the popular swarm-based algorithms developed by Karaboğa and Baştürk [30-32]. There are a lot of studies with ABC algorithms [21-24, 31, 33].

ABC algorithm has three types of bees consists of employed bees, scout bees and onlooker bees. In the ABC algorithm, there is one worker bee for each food source and the number of employed bees is equal to the number of onlooker bees. The case of the scout bees depends on the conditions of the food sources.

A food source is found randomly by each employed bee in the search space. These locations are found by Eq. (1).

$$x_{i,j} = x_j^{min} + rand(0,1)(x_j^{max} - x_j^{min}) \quad (1)$$

x_i is a D -dimensional vector, $where\ i = 1,2,3,\dots,SN$ and $j = 1,2,3,\dots,D$ and x_j^{max}, x_j^{min} are the maximum and minimum limits $(SN = number\ of\ the\ food\ source)$.

All employed bees should complete their search steps, before they share their source information with the onlooker bees in the dancing area. Additionally this information includes and important data which is related the nectar amounts with onlookers.

Each onlooker bee first selects a food source based on the probability value of the food sources. Then, following the waggle dance, it creates a new candidate solution, a new food source, in the neighborhood of this food source.

Each employed and onlooker bee tries to improve the quality of their food sources by choosing their neighbor by Equation (2).

$$v_{i,j} = x_{i,j} + \varphi_{i,j}(x_{i,j} - x_{k,j}) \quad (2)$$

v_i is randomly selected from neighbors of x_i and it is called as candidate source. k is a random integer number between [1, SN] and it must be different from i. $\varphi_{i,j}$ is a real random number between [-1, 1] and j represents a random integer number between [1, D].

Works in the employed bees is done again by the greedy selection. If a resource's position cannot be improved after a certain number of cycles, that resource is banned. Meanwhile, the relevant worker bee becomes a scout bee. The banned and abandoned food source is replaced with a random food source [30-32].

The main steps are described below [28]:

1. Initial bee colony is X = $\{x_i|$ i = 1, 2,…, n}, where n signify the population size, $x_i$is the i'th bee in the bee colony.
2. Calculate the fitness f_i of each employed bee x_i, and save the maximum source quality as well as the corresponding food source according to the fitness function.
3. Find a new solution v_i in the neighborhood of the current solution. k is an integer near to i, k ≠i, and φ is a random number between [−1, 1].
4. Greedy criterion is used for update x_i. Compute the fitness of v_i. If v_i is superior to x_i, x_i is replaced with v_i; otherwise x_i is remained.
5. Get the likelihood value P_i by Eq. (3) and Eq. (4) according to the fitness f_i of x_i.

$$P_i = \frac{fit_i}{\sum_{i=1}^{n} fit_i} \quad (3)$$

$$fit_i = \begin{cases} \frac{1}{1+f_i}, & f_i \geq 0 \\ 1 + abs(f_i), & f_i < 0 \end{cases} \quad (4)$$

6. Depending on the probability P_i, onlookers choose food sources, search the neighborhood to generate candidate solutions, and calculate their fitness.
7. For updating the food sources, apply the greedy criteria.
8. Keep the best source data in memory.
9. Check the banned source situation. If located source is an abandoned source, replace it with a new random solution by using (1).
10. Repeat steps 3-9 until stopping criterion is satisfied.

The fitness function is so important factor in ABC algorithm. Also, control parameters of this algorithm, such as the value of limit criteria, the stopping condition and the number of employed bees or onlooker bees must be defined well. Because they affect the performance of convergence directly.

C. The proposed method

Our method uses ABC algorithm for edge detection in images. In general, edges of an image are found with masks, and the dependency on masks can be eliminated by this improved method.

The initial image is taken for the process of edge detection with ABC and this image represents the solution space. The initial values for control parameters are set. The limit is the limit value that requires the abandonment of a resource in the ABC algorithm if it cannot be developed.

The maximum number of cycles is the number of iteration. Colony size is the number of individuals in the population and is formulated by Eq. (5) because it should not be a constant value for each image. The colony size is equal to the square root of the product multiplied by the number of rows and columns of the image.

$$K = \sqrt{NxM} \quad (5)$$

K is the total number of sources and is calculated using thee values N and M. N and M are the row and column numbers of the image, respectively [35].

After determining the all parameters' values, the sources are located. First, the number of located sources is equal to half the total number of sources given in Eq. (6). At the same time, emloyee bees are randomly located on the image.

$$LocatedSourceNumber = \frac{K}{2} \quad (6)$$

The attributes of the located sources, such as coordinates, gray level values, failure counters, probability and fitness values are kept in the memory. The fitness value for the source pixel is the value of the gray level value getting from the fitness function. Searching and using resources is still allowed to continue.If directed source is permitted source, the source's neighbor data is held as the directed source. If there is no better source adjacent to the located source, failure counter is increased. Banned resource is the source whose failure counter becomes equal to limit. The probability value of all sources is calculated by the fitness values.

In this study, fitness function is calculated by on grayscale value of each pixel. First, fitness and then likelihood values are computed according to these values. Located source's probability and one of its neighbor's are selected randomly before the probability values are compared. Failure values of current resources are controlled whatif it is equal or not to limit value in each comparison steps . If a failure value is the same with limit value, the current source is banned and the number of scout individual count is increased. None of the bees position on these banned sources again. In this study, our limit criteria is set as 5.

There are three cases about the comparison steps:

1. If current source's probability value is worse than probability boundary value, current source's failure counter increased by 1.
2. If current source's probability value is better than probability boundary value, a random neighbor is selected from current source's neighborhood. If neighbor's value is worse than probability boundary value or current source's probability value, current source's failure counter increased by 1.
3. If current source's probability value is better than probability boundary value, a random neighbor is selected from current source's neighborhood. If neighbor's value is better than probability boundary value and current source's probability value, and neighbor becomes new (current) source and old source's failure counter value is set as 0.

Then, located sources are controlled for belonging to any edge line or not by the examining pixels in directional aspects (Figure 2).

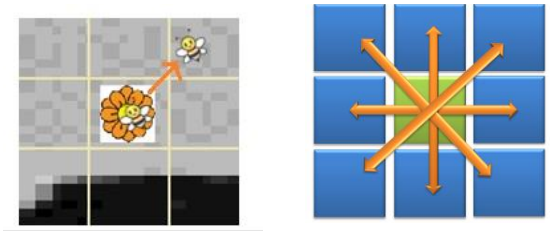

Figure 2: Examining the neighbor pixels

The threshold value for each image is specified by using the standard deviation of the image gray levels as given Eq. (7).

$$threshold\ value = \sqrt{\frac{1}{N}\sum_{i=1}^{N}(x_i - \bar{x})^2} \quad (7)$$

If the grayscale color difference is higher than the specified threshold value, this pixel can be belong to an edge line. If the current source is determined as an edge pixel and that pixel's value is set as 1 on the result image (Figure 3).

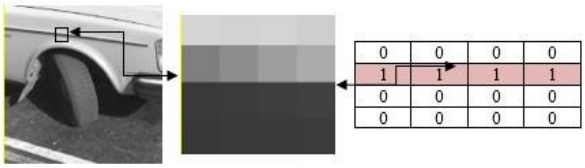

Figure 3: Labeling the edge boundary

III. Experimental Results

In [36], algorithm was tested for gray scale images and compared with the Canny, Sobel and Roberts edge detection methods using Hamming Distance (HD).

The sizes of populations was specified according to images' width and height values by using Eq.6 and the maximum number of iterations criteria was set as 50000. Some iteration numbers such as 1000, 2000, 5000 and 50000 were compared to find the optimum iteration number and the best edge result was achieved with 50000 iteration. The limit parameter was set as 5 because a pixel has maximum 8 neighbors. Threshold and boundary probability values were computed for all tested images. RADIUS/DARPA-IU Fort Hood gray level object images and their ABC method's results are given in Figure 4. ABC method can be used as an alternative method for edge detection according to obtained experimental results.

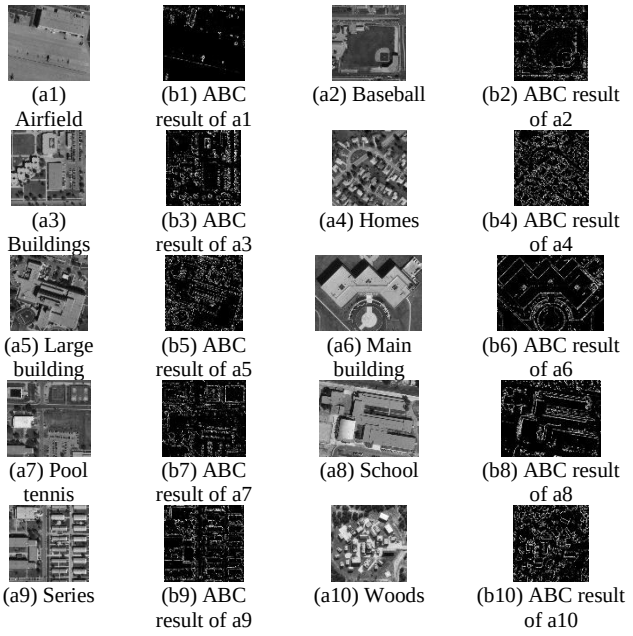

Figure 4: Edge detection results of ABC

Figure 5 shows operating times of test images which are given in Figure 4. Run time is increasing according to increasing the number of iteration.

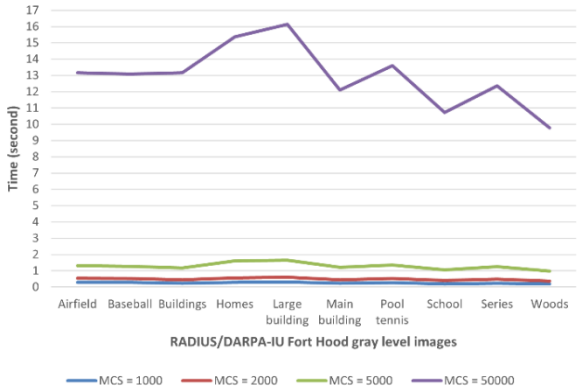

Figure 5: Operating times for RADIUS/DARPA-IU Fort Hood aerial images

Detection Error (DE) and Similarity (S) rates are used to compare results with the literature (Eq. 8-9). DE rate is computed according to result of values that are obtained from Specificity-Sensitivity analysis

$$DE = \sqrt{(1 - TP)^2 + (FP)^2} \quad (8)$$

$$S = \frac{1}{N}\sum_{i=1}^{N}\frac{1}{1 + d_i^2} \quad (9)$$

Table 1 shows Sensitivity-Specificity analysis values for edge detection. Eq. (8) gives Detection Error rates.

Table 1: Sensitivity-Specificity Analysis Values for Edge Detection

	Edge (+)	**Edge (-)**
Test (+)	True Positive (TP)	False Positive (FP)
Test (-)	False Negative (FN)	True Negative (TN)

Our results obtained from ABC which are applied on 10 aerial gray scale images are compared with the ground truth images. The HD, DE and S results of these comparisons are given in Table 2 [37].

ABC method's DE results and S results (in Table 2) of RADIUS/DARPA-IU Fort Hood aerial images were compared with previous experimental research in the literature [15].

DE rates comparison shows that 6 of our results are worst findings and the others are acceptable values. The reason for such high rates of the developed algorithm, which environmental factors' edge information is not mentioned in the ground truth images. Our method's sensitivity is high for environmental factor's edge information on test images.

S rates comparison shows that one of our rates is the best result which is obtained from Airfield test image, the other results are acceptable values.

Table 2: Comparisons of Edge Detection Algorithms on Aerial Images

		Airfield	Baseball	Buildings	Homes	Large building	Main building	Pool tennis	School	Series	Woods
Rothwell	***DE***	0.4707	0.5710	0.5506	0.5991	0.5292	0.5608	0.5273	0.5638	0.4321	0.5634
	S	0.7692	0.6815	0.6886	0.6332	0.6844	0.6967	0.6722	0.6495	0.7577	0.6581
Bergholm	***DE***	0.4643	0.5968	0.6047**	0.5703	0.5970**	0.5651	0.5639	0.5844	0.5297	0.5846
	S	0.7651	0.6359	0.5895**	0.5978**	0.5401**	0.6191	0.5923**	0.5846**	0.6084**	0.5912
Canny	***DE***	0.5057	0.5668	0.5593	0.5712	0.5328	0.6180	0.5086	0.5571	0.4143	0.5526
	S	0.7593	0.6961	0.6892	0.6851	0.6976	0.6612	0.7208	0.6743	0.7682	0.6849
Schunck	***DE***	0.5147	0.5689	0.5640	0.5743	0.5459	0.6130	0.5367	0.5647	0.4276	0.5695
	S	0.7382	0.6848	0.6804	0.6762	0.6730	0.6499	0.6596	0.6474	0.7656	0.6748
Lacroix	***DE***	0.5340	0.5865	0.5736	0.4851	0.5180	0.5193	0.5396	0.5701	0.4522	0.5274
	S	0.7162	0.6579	0.6570	0.7143	0.6823	0.6988	0.6527	0.6419	0.7259	0.6760
Deriche	***DE***	0.5276	0.5726	0.5500	0.6302	0.5194	0.6677**	0.4852	0.5928	0.5303	0.6856**
	S	0.7516	0.6934	0.6871	0.6169	0.7082	0.6088**	0.7100	0.6458	0.6810	0.5667**
ROC	***DE***	0.4634	0.5505	0.5425	0.5177	0.5084	0.5439	0.5029	0.5444	0.4139	0.5241
	S	0.7760	0.6995	0.6946	0.7064	0.7014	0.6998	0.7046	0.6669	0.7767	0.6922
Kappa (r = 0.7)	***DE***	**0.4126***	**0.5183***	**0.4885***	**0.4402***	**0.4440***	**0.4561***	**0.4343***	**0.5001***	**0.3619***	**0.4602***
	S	0.8492	**0.7249***	**0.7355***	**0.7599***	**0.7506***	**0.8357***	**0.7639***	**0.7835***	**0.8090***	**0.7448***
ABC	***DE***	0.86**	0.76**	0.59	0.64**	0.59	0.54	0.63**	0.66**	0.63**	0.68
	S	**0.85***	0.63**	0.69	0.68	0.73	0.73	0.66	0.74	0.70	0.64
	HD	0.0656	0.1406	0.1506	0.1988	0.1547	0.1086	0.1365	0.1335	0.1605	0.1561

**: Best for column **: Worst for column*

IV. Conclusion

In this work, the positioning of the ABC optimization algorithm's swarm individuals was carried out on a random pixel in the input image.

In the basic ABC, first resource is specified by the formula, but in the study 8 adjacent pixels of the first resource are defined as new resources. Gray scale values of an image are used as knowledge about the quality. The numbers of populations vary according to the image size so it makes the algorithm adaptive. For maximum number of cycles, different iteration numbers between 1000 and 50000 was used and the best of them selected. Also, the limit parameter is equal to 5 after the experiments. The threshold value is computed based on the standard deviation of each image by using a formula.

In the study, run times for each number of iterations were tested and these times showed us that if maximum iteration number was increased, run time became longer. But on the other hand, if maximum iteration number was increased, result image showed us more edge information for related image.

Most of the edge detection methods such as Sobel, Canny, etc. require a predefined mask. When masks are used, corner pixels of the image and pixels of the frame around the image are often either ignored or assumed to be zero. The edge extraction was done using the ABC without this kind of data loss and the dependency on the mask was removed. Therefore proposed method is faster than the others.

Also improved method's results are compared with Ground Truth (GT) images according to Detection Error (DE) and Similarity (S) calculations' results. The obtained results show that the proposed method can be used for edge detection implementation as an alternative method.

Our goal for the future is to include the surrounding pixels of the image in the identification of the edges to achieve better results. For this aim, we are working on the modified ABC algorithm.

Acknowledgment

This study is based on the Master Thesis of Elif Deniz Yigitbasi (Yelmenoglu) [37].

References

[1] Bovik A (2010) Handbook of Image and Video Processing. Academic Press.
[2] Gonzales RC, Woods RE (2007) Digital Image Processing. Pearson Press.
[3] Umbaugh SE (1999) Computer Vision and Image Processing: A Practical Approach Using CVIPtools. Prentice Press.
[4] Solomon C, Breckon T (2011) Fundamentals of Digital Image Processing: A Practical Approach with Examples in Matlab. Wiley Press.
[5] Joyce KE, Bellis SE, Samsonov SV et al (2009) A review of the status of satellite remote sensing and image processing techniques for mapping natural hazards and disasters. Progress in Physical Geography 33(2): 183-207 DOI: 10.1177/0309133309339563
[6] Huang J, Zhang S, Metaxas D (2011) Efficient MR image reconstruction for compressed MR imaging. Medical Image Analysis 15(5): 670-679 DOI:10.1016/j.media.2011.06.001
[7] Liming X, Yanchao Z (2010) Automated strawberry grading system based on image processing. Computers and Electronics in Agriculture 71(1): 32-39 DOI: 10.1016/j.compag.2009.09.013
[8] Haralick RM (1984) Digital step edges from zero crossing of second directional derivatives. IEEE Transactions on Pattern Analysis and Machine Intelligence 6(1): 58–68 DOI: 10.1109/TPAMI.1984.4767475
[9] Marr D, Hildreth E (1980) Theory of edge detection. Proc. R. Soc. Lond. *B* 207: 187–217
[10] Heath MD, Sarkar S, Sanocki T, Bowyer KW (1997) A Robust Visual Method for Assessing the Relative Performance of Edge-Detection Algorithms. IEEE Transactions on Pattern Analysis and Machine Intelligence 19 (12): 1338-1359 DOI: 10.1109/34.643893
[11] Argyle E, Rosenfeld A (1971) Techniques for edge detection. Proceedings of the IEEE 59 (2): 285-287 DOI: 10.1109/PROC.1971.8136
[12] Maini R (2011) Analysis and Development of Image Edge Detection Techniques. PhD Thesis, Punjabi University
[13] Abdou IE, Pratt WK (1979) Quantitative design and evaluation of enhancement/ thresholding edge detectors. Proceedings of the IEEE 67(5): 753-763
[14] Bhardwaj S, Mittal A (2012) A survey on Various Edge Detector Techniques. Procedia Technology 4: 220-226.
[15] Giannarou S, Stathaki T (2011) Optimal edge detection using multiple operators for image understanding. EURASIP Journal on Advances in Signal Processing 28 DOI: 10.1186/1687-6180-2011-28
[16] Canny J (1986) A computational approach to edge detection. IEEE Transactions on Pattern Analysis and Machine Intelligence PAMI-8(6): 679-698 DOI: 10.1109/TPAMI.1986.4767851
[17] Roberts LG (1969) Machine perception of three-dimensional solids. US Government Printing Office Press.
[18] Prewitt JM (1970) Object enhancement and extraction. Picture Processing and Psychopictorics: 75-149
[19] Rao SS (2009) Engineering Optimization: Theory and practice (Fourth edition). Wiley Press

[20] Yang XS (2010) Nature-Inspired Metaheuristic Algorithms: Second edition. Luniver Press.
[21] Akay B (2009) Performance Analysis of Artificial Bee Colony Algorithm on Numerical Optimization Problems, Phd Thesis, Erciyes University.
[22] Akay B, Karaboga D (2012) A modified Artificial Bee Colony algorithm for real-parameter optimization. Information Science 192: 120-142 DOI:10.1016/j.ins.2010.07.015
[23] Karaboga D, Gorkemli B, Ozturk C, Karaboga N (2014). A comprehensive survey: Artificial Bee Colony (ABC) algorithm and applications. Artificial Intelligence Review 42(1): 21-57 DOI: 10.1007/s10462-012-9328-0
[24] Pan Q, Tasgetiren MF, Suganthan P.N, Chua TJ (2011) A discrete artificial bee colony algorithm for the streaming flow shop scheduling problem. Information Science 181: 2455-2468 DOI:10.1016/j.ins.2009.12.025
[25] Szeto WY, Wu Y, Ho SC (2011) An artificial bee colony algorithm for the capacitated vehicle routing problem. European Journal of Operational Research 215: 126-135 DOI: 10.1016/j.ejor.2011.06.006
[26] Horng M (2011) Multilevel thresholding selection based on the artificial bee colony algorithm for image segmentation. Expert Systems with Applications 38: 13785-13791 DOI: 10.1016/j.eswa.2011.04.
[27] Das P, Sadhu AK, Vyas RR, Konar A, Bhattacharyya D (2015) Arduino based multi-robot stick carrying by artificial bee colony optimization algorithm, Proceedings of the 2015 Third International Conference on Computer, Communication, Control and Information Technology (C3IT) IEEE Conference
[28] Ma M, Liang J, Guo M, Fan Y, Yin Y (2011) SAR image segmentation based on Artificial Bee Colony algorithm. Applied Soft Computing 11: 5205–5214 DOI: 10.1016/j.asoc/2011.05.039
[29] RADIUS/DARPA-IU Fort Hood Aerial image dataset (http://marathon.csee.usf.edu/edge/edgecompare_main.html (accessed in 2014))
[30] Karaboga D (2005) An Idea Based on Bee Swarm for Numerical Optimization. Technical Report-TR06
[31] Karaboga D, Basturk B (2007) A powerful and efficient algorithm for numerical function optimization: Artificial Bee Colony (ABC) algorithm. Journal of Global Optimization 39(3): 459–471 DOI: 10.1007/s10898-007-9149-x
[32] Karaboga D, Basturk B (2008) On the performance of artificial bee colony (ABC) algorithm. Applied Soft Computing 8: 687–697 DOI: 10.1016/j.asoc.2007.05.007
[33] Karaboga D, Akay B (2009) A survey: algorithms simulating bee swarm intelligence. Artificial Intelligence Review 31: 61–85 DOI: 10.1007/s10462-009-9127-4
[34] Karaboğa D (2011) Yapay Zeka Optimizasyon Algoritmaları. Nobel Akademic Press.
[35] Nezamabadi-pour H, Saryazdi S, Rashedi E (2006) Edge detection using ant algorithms. Soft Computing 10(7): 623-628
[36] Yigitbasi ED, Baykan NA (2013) Edge detection using Artificial Bee Colony Algorithm (ABC). International Journal of Information and Electronics Engineering 3(6): 634-638 DOI: 10.7763/IJIEE.2013.V3.394
[37] Yigitbasi ED (2014) Yapay arı kolonisi optimizasyonu ile kenar bulma [Edge detection with artificial bee colony optimization] Master thesis, The Graduate School of Natural and Applied Science, Selcuk University, Konya, Turkey (in Turkish)

Comparison of Classification Algorithms for COVID19 Detection using Cough Acoustic Signals

Y.E. ERDOĞAN [1, 2] and A. NARİN [2]

[1] Electronic Automation Department, Eregli Iron and Steel Co., Zonguldak, Turkey, yeerdogan@erdemir.com.tr

[2] Electrical and Electronics Engineering Department, Zonguldak Bülent Ecevit University, 67100, Zonguldak, Turkey, alinarin45@gmail.com

***Abstract* - The epidemic disease, called the new coronavirus (COVID19), firstly occurred in Wuhan, China in December 2019. COVID19 was announced as an epidemic by World Health Organization soon after. Some of the symptoms of this disease are fever, cough, shortness of breath and difficulty in breathing. In more severe cases, death may occur as a result of infection. The most significant question in fighting the pandemic and controlling the epidemic is the early diagnosis of COVID19(+) patients and the follow-up of these patients. Therefore, various diagnostic mechanisms are used. Additionally to the RT-PCR test, medical imaging methods have been utilized, especially in the detection of COVID19(+) patients. In this study, an alternative approach was proposed by using cough data, which is one of the most prominent symptoms of COVID19(+) patients. The cough acoustic public dataset on the Virufy website was used. The entire data was normalized using z-normalization technique. The performance of the features obtained via the 5-layer empirical mode decomposition method and the performances of different classifiers has been compared. As the classifier algorithm, 5 different algorithms were used. The highest accuracy and F1-score performances were obtained by using Ensemble-Bagged-Trees algorithm as 90.6% and 90.5%, respectively. On the other hand, other classification algorithms used in the study are Support Vector Machines, Logistic Regression, Linear Discriminant Analysis and k-Nearest Neigbors, respectively. According to the results obtained, choosing the right classifier algorithm provides high results. Thus, it is clear that using cough acoustic data, those with COVID19(+) can be detected easily and effectively.**

***Keywords* - COVID19, Cough, Empirical Mode Decomposition, Prediction, Classification.**

I. INTRODUCTION

By October, 26 2021, there have been 243.572.402 confirmed cases of COVID19, including 4.948.434 deaths, reported to World Health Organization (WHO) and it is also disturbing life in most of the countries and territories all over the world [1]. This virus gives rise to serious respiratory infections with really high deadness and creates serious threats to people. Some symptoms of the COVID19 pandemic are serious fever, dry cough, and difficulty in breathing [2]. In addition to these signs, a range of tests have been done to find out COVID19(+) sicks. One of these tests is Reverse Transcription Polymerase Chain Reaction (RT-PCR) test known as the gold standard, and it is applied with advice of WHO [3]. But it is boring, costly and outcomes are achieved so late [4]. The other methods are medical imaging techniques which utilized to determine COVID19(+) sicks in addition to this test [5]. Researches based on cough acoustic signal analysis has lately taken its place in the literature.

Sharma et al. worked on a dataset which is named "Coswara" including signal data for cough, breath, and voice. They recommended a research with 28 spectral measurements and random forest classifiers. The general accuracy rate got was 67.7% [6]. In another research, Imran et al. purposed to detect Coronavirus sicks by seeking at these data with research they named AI4COVID19. They utilized mel-spectrogram images for convolutional neural network models. They engaged Mel Frequency Cepstral Coefficient (MFCC) and Principal Component Analysis (PCA) based on feature extraction and SVM classification algorithm for the traditional machine learning approach. As a conclusion, they had 95.6% accuracy and 95.6% F1-score [7]. Erdoğan and Narin utilized cough acoustic signals in their research. They utilized z-normalization as preprocessing method. In the research, they utilized intrinsic mode function (IMF) and discrete wavelet transform (DWT) based feature extraction via traditional machine learning approaches and they utilized SVM as a classification method. The overall accuracy for traditional machine learning approaches was 98.4% [8]. They also added deep features to this study. They used deep features on the ResNet50 deep learning model and obtained 97.8% overall accuracy.

In the studies mentioned above, researches using different voice data, especially cough data, were included. In this study, time domain and nonlinear features were obtained by using the 5-layer empirical mode decomposition (EMD) technique. The performances of five different classification algorithms were compared using the obtained features. The 5-layer EMD

method used in cough acoustic signals of COVID19(+) and COVID19 (-) persons is shown in Figure 1.

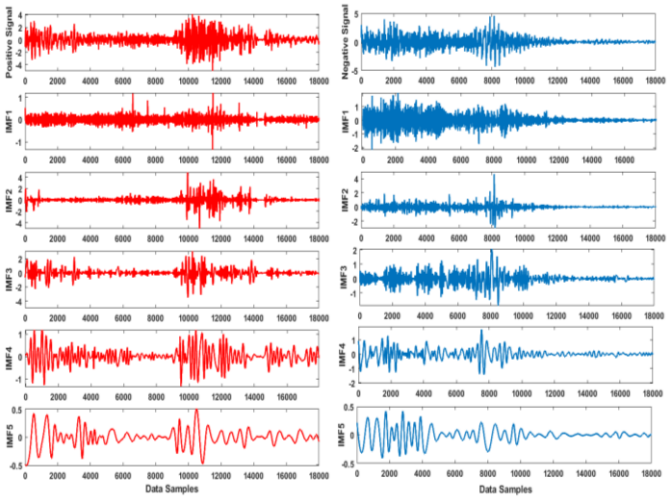

Figure 1: COVID19(+) and COVID19(-) cough acoustic data and 5-layer IMF signals.

II. METHODS

A. Dataset

Cough acoustic signal data for COVID19(+) and COVID19(-) were retrieved from the free accessible website virufy.org. The cough signals were supplied through a mobile app developed via Stanford University. The cough acoustic signals belong to a sum of 1187 people. Whole cough data were specified as negative and positive according to the outcomes achieved from the RT-PCR test. Thereupon, cough signal data of 595 COVID19(+) and 592 COVID19(-) people has been tagged. Whole cough signal data were done away with from the noise. Additionally, all signal data has been preprocessed using z-score normalization technique earlier the research done.

B. Z-Normalization

Z-score converts mean of variable to 0 and its standard deviation to 1. To do this, simply subtract the mean and divide by the standard deviation. The z-score normalization could be computed as [9]:

$$z = \frac{x - mean}{std} \quad (1)$$

Where x indicates any point in the dataset, *mean* indicates average of the dataset, and *std* indicates the standard deviation of the dataset.

C. Empirical Mode Decomposition

EMD is a suitable technique for analyzing stationary and non-linear series and oscillation signals at the local oscillation level are used. IMFs are decomposed into some oscillation structures in signals [10]. In the EMD algorithm, local peaks are first found in the input signal. By taking a 3rd degree curve at the local maximum point, an overwrap curve is created. By taking a 3rd degree curve at the local minimum point, a sub winding curve is created. The averages of the upper and lower winding curves are calculated. By subtracting these averages from the input signal, the low frequency component of the signal is eliminated. If the signal we get is IMF, the transaction is terminated. If the IMF is not, the processes are repeated for the new signal. To see if the signal is IMF, we look at the IMF conditions. In the first of the IMF conditions, the zero crossings of the signal are equal to or one more than the number of peaks. In the second condition, the winding curves determined by the local minimum and maximum are symmetrical.

D. Support Vector Machines

The support vector machine (SVM) is capable of separating data into two or more classes with linear separation mechanisms in two-dimensional space, planar in three-dimensional space, and hyperplane-shaped separation mechanisms in multidimensional space. The basic idea of the SVM is to construct an optimal separator hyperplane on linearly separable data. This idea was put forward by Vapnik in 1995 [11].

E. Logistic Regression

Logistic regression (LR) is a technique utilized to detect the reason and result relationship with the explanatory variables in cases where the response variable is observed in categorical, binary, triple and multiple classes. LR is a regression technique where the expected values of the response variable are obtained as probabilities according to the explanatory variables. In simple and multiple regression method, dependent variable should show normal distribution, independent variables should show normal distribution and error variance should show normal distribution with $\varepsilon \cong N(0, \sigma 2)$ parameter. Simple or multiple regression analyzes cannot be applied to data sets that do not contain these conditions. LR is a statistical process that provides the opportunity to classify according to probability rules by computing the estimated values of the dependent variable as probabilities.

F. Ensemble Bagged Trees

Ensemble learning is a classification method that uses some learner models together. Bagging is a method that randomly generates data sets and trains models in parallel. It combines models with voting. It is an example algorithm for the random forest (RF) bagging process. In RF, decision trees are randomly generated and trained in parallel. The results are combined with voting to form a forest.

G. K-Nearest Neighbors

The k-Nearest Neighbor (kNN) estimation method is a nonparametric classification and regression algorithm. Ease of application and having a simple mathematical basis have made the use of forecasting models widespread in many different

fields [12, 13]. It is based on the idea that the outcome of a case is the same as the outcome of its nearest neighbor cases. By means of the training set based on past observations, the dependent variables that are the result of each element (case) of the data set are determined. Forward estimates will be equal to the mean of the results of the current cases of the closest elements in the training dataset. Usually, the closest observations are defined as those with the smallest Euclidean distance to the data point under consideration. The Euclidean distance between the observations can be found depending on the linear distance x_i in the x-plane and the linear distance y_i in the y-plane in the example of the 2-dimensional solution set.

$$\text{Euclidean distance} = \sum_{i=1}^{k} (x_i - y_i)^2 \quad (2)$$

Model optimization is required to determine *k*, which represents the number of neighbors to consider. As the number of neighbors' k increases, although the calculation step increases, the vulnerability to noise in the training set will decrease and the fit to the test data will increase.

H. Linear Discriminant Analysis

Discriminant analysis is a multivariable statistical technique that allows an individual or an object to be assigned to one of a finite amount of known different populations according to its measured properties [14]. In discriminant analysis, the discrimination function is obtained according to some assumptions made on the masses. There are different discriminant functions depending on whether the variance-covariance matrices of the populations from which the samples are taken are equal or not. When the variance covariance matrices of the masses are equal, the linear discriminant function is obtained, while if they are different, the square discriminant function is obtained.

İ. Performance Metrics

In this study, the outcomes were evaluated utilizing five distinct performance measures [15, 16]. These:

$$Accuracy(Acc) = \frac{TP + TN}{TP + FN + FP + TN} \quad (3)$$

$$Recall(Rec) = \frac{TP}{TP + FN} \quad (4)$$

$$Specifity(Spe) = \frac{TN}{TN + FP} \quad (5)$$

$$Precision(Pre) = \frac{TP}{TP + FP} \quad (6)$$

$$F1 - score(F1) = \frac{2 * PRE * REC}{PRE + REC} \quad (7)$$

TP shows the people ,who are COVID19(+), number and identified as COVID19(+) by the classifier, FN is the number of people who are wrongly stated as COVID19(-), TN the people number, who are actually COVID19(-),and the classifier were stated them as COVID19(-), and FP shows the people number ,who are mistakenly identified as COVID19(+) [17].

III. EXPERIMENTAL RESULTS

In this research work, all the processes have been experimented via MATLAB 2021a software. Z-normalization technique was utilized as preprocessing method. Then, 45 IMF based measures were obtained. The comparison of the classification algorithms is shown in Table 1. As shown in the Table 1, the highest rate of accuracy was obtained as 90.56% using Ensemble Bagged Trees.

Table 1: Performance comparison of classification methods for all EMD based features.

Algorithm	Performances (%)				
	Acc	Rec	Spe	Pre	F1
Ensemble Bagged Trees	90.56	90.54	90.59	90.54	90.54
SVM Linear	89.64	88.34	90.92	90.64	89.48
Logistic Regression	89.39	88.18	90.59	90.31	89.23
Linear Discriminant Analysis	88.88	86.32	91.43	90.93	88.56
Medium kNN	87.95	88.68	87.23	87.35	88.01

IV. DISCUSSION

No doubt one of the most researched topics in the last few years is the coronavirus epidemic, which affected all over the world. The most vital point in overcoming this epidemic is the process of making the correct diagnosis. Therefore, there are many machine learning-based researches in the literature.

COVID19(+) detection on cough signal data, which suggests an extraordinary approach, has lately taken its place among the current alternative methods. Performance metrics comparisons of those classification methods among the studies conducted in this topic are given in Table 2. Traditional machine learning approaches and feature extraction processes were generally utilized in these studies. In some studies, in addition to traditional machine learning approaches, deep learning approaches was used to detect COVID19(+) people based on cough sounds. In this study, the performances of five different classification methods were analyzed over the features taken utilizing traditional machine learning approaches. With these five alternative approaches, which work with a very high success rate, a decision support mechanism was recommended to doctors for the detection of COVID19(+) people. The confusion matrices which belongs to classification algorithms are given in Figure 2. Highest accuracy rate belongs to bagged trees classification algorithm shown in Figure 2 (e).

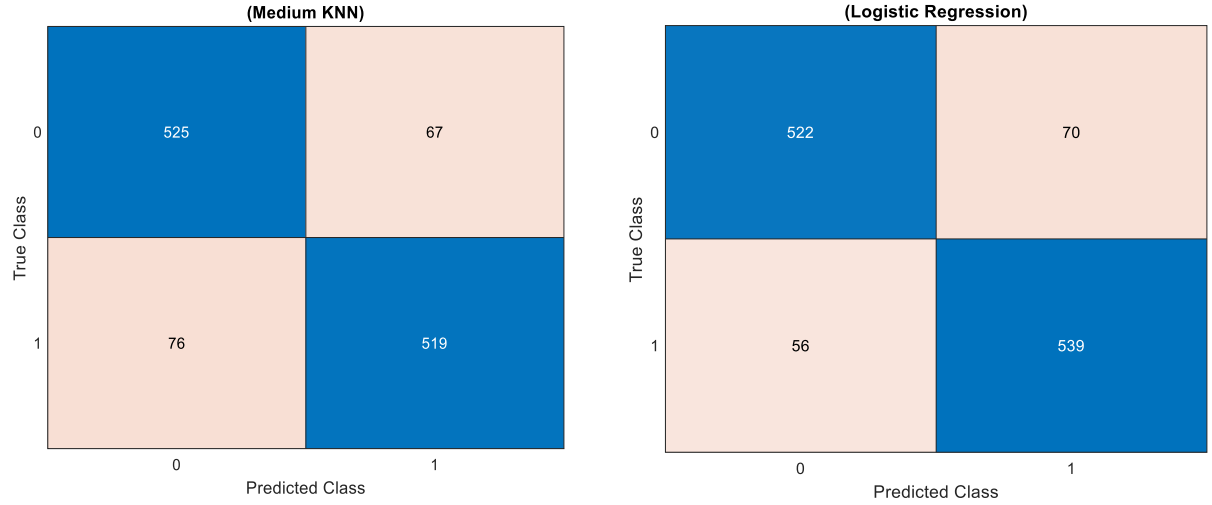

(a)

(b)

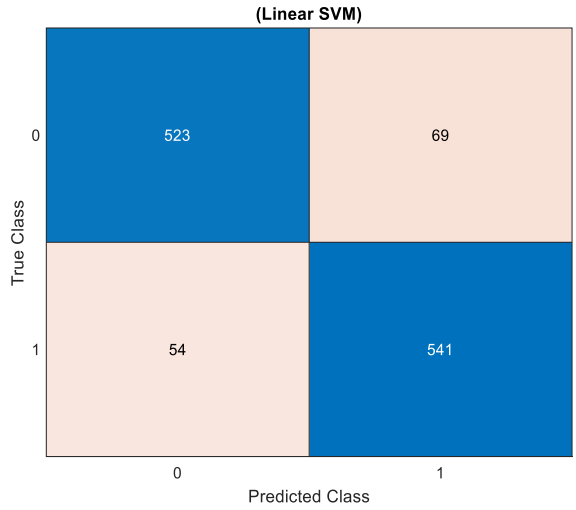

(c)

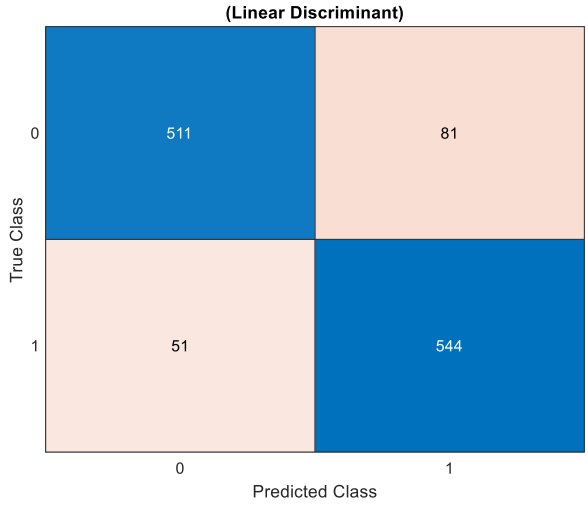

(d)

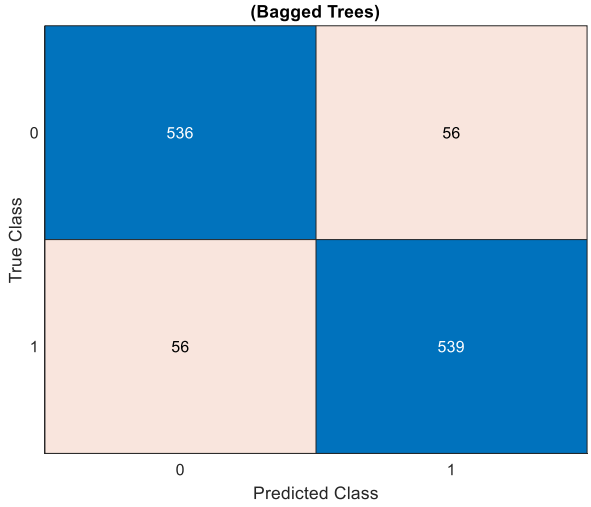

(e)

Figure 2: Confusion matrices belonging to the classification methods a) Medium kNN b) Logistic Regression c) Linear SVM d) Linear Discriminant e) Bagged Trees (0, COVID19(−), 1, COVID19(+)).

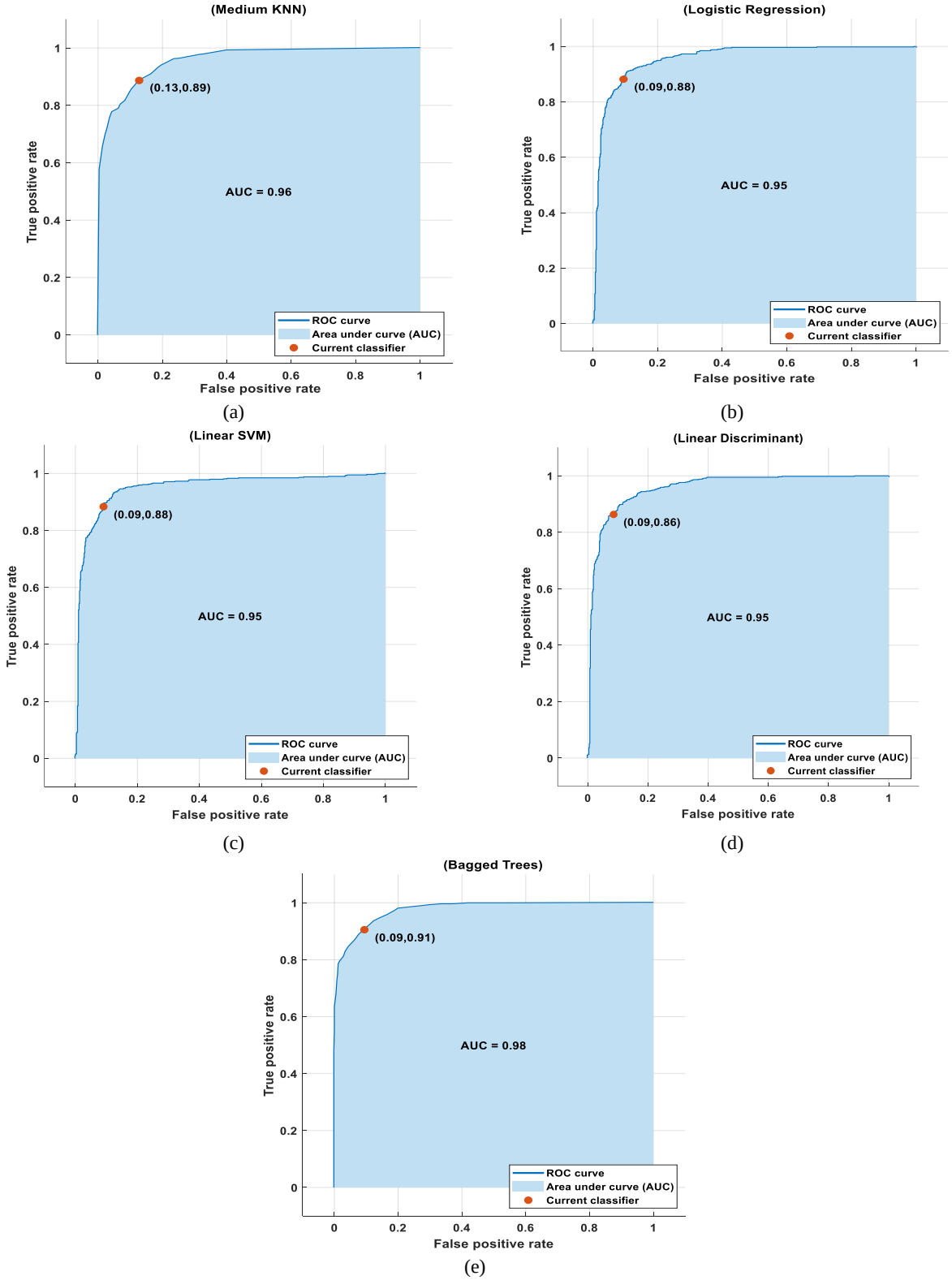

Figure 3: ROC curves belonging to the classification methods a) Medium kNN b) Logistic Regression c) Linear SVM d) Linear Discriminant e) Bagged Trees.

Table 2: COVID19 detection engaging cough acoustic signals in the literature. (Acc, accuracy, Spe, specificity, Rec, recall, F1, F1-score).

Authors	**Methods and Classifiers**	**Number of Data**	**Performance (%)**
Sharma et al. (2020) [6]	MFCCs, and other spectral measurements/random forest	941	Acc = 67.7
Imran et al. (2020) [7]	Mean Score + Mel-frequency cepstral coefficients and Principal component analysis / Support Vector Machines	543	Rec=96.0 Spe=95.2 Acc=95.6 F1=95.6
Erdogan and Narin (2021) [8]	Z-Score + Intrinsic Mode Functions and Discrete Wavelet Transform features + Support Vector Machines	1187	Rec=99.5 Spe=97.4 Acc=98.4 F1=98.6
Erdogan and Narin (2021) [8]	Z-Score + ResNet50 basis deep features + Support Vector Machines	1187	Rec=98.5 Spe=97.3 Acc=97.8 F1=98.0
This study	**EMD basis features + Z Score / Ensemble Bagged Trees**	**1187**	**Rec=90.5 Spe=90.6 Acc=90.6 F1=90.5**

As it can be seen from Figure 2(e), 56 people of those in the COVID19(+) class were detected incorrectly while 539 people were detected correctly. On the other hand 56 people of COVID19(−) class were detected incorrectly while 536 people of those were detected correctly. The receiver operating characteristic curve (ROC) is given in Figure 3. Area Under the ROC Curve (AUC) value is quite high as shown in Figure 3.

In addition to the detection of COVID19(+) with imaging methods, it is of great importance to detect these people with cough-based acoustic sound analysis. With this method, the detection of COVID19(+) can be easily achieved via a smartphone or computer application. With this application, the pandemic can be overcome more easily. From this point of view, it is of great importance that even a single person can be protected from the epidemic during the pandemic. We think that such systems showing high performance will be of importance during pandemic period. One of the most critical restrictions of this research is the restricted number of data. By enhancing the number of data near future, it is thought that the system will be successful on high data numbers. In future studies, it is planned to increase the number of nonlinear measurements.

REFERENCES

[1] World Health Organization. (2020) Coronavirus disease (COVID-19) outbreak situation. Accessed on: Oct 11, 2020. Available:https://www.who.int/emergencies/diseases/novel-coronavirus-2019.

[2] C. Menni, C.H. Sudre, C.J. Steves, S. Ourselin, T.D. "Spector Correspondence Quantifying additional will save lives," Lancet, 395 (2020), pp. e107-e108, 10.1016/S0140-6736(20)31281-210241

[3] J. Lim, J. Lee "Current laboratory diagnosis of coronavirus disease," Korean J Intern Med, 2019 (2020), pp. 741-748, 10.3904/kjim.2020.257

[4] A.A. Ardakani, A.R. Kanafi, U.R. Acharya, N. Khadem, A. Mohammadi "Application of deep learning technique to manage COVID-19 in routine clinical practice using CT images: results of 10 convolutional neural networks" Comput. Biol. Med., 121 (March) (2020), Article 103795, 10.1016/j.compbiomed.2020.103795

[5] C. He, D.-q. Wang, J.-l. Sun, W.-n. Gan, J.-y. Lu "The Role of Imaging Techniques in Management of COVID-19 in China: from Diagnosis to Monitoring and Follow-Up" (2020), pp. 1-10, 10.12659/MSM.924582

[6] N. Sharma, P. Krishnan, R. Kumar, S. Ramoji, S.R. Chetupalli, N. R, P.K. Ghosh, S. Ganapathy "Coswara – a database of breathing, cough, and voice sounds for COVID-19 diagnosis," Proceedings of the Annual Conference of the International Speech Communication Association, INTERSPEECH 2020-Octob (2020), pp. 4811-4815,10.21437/Interspeech.2020-2768 arXiv:2005.10548 http://arxiv.org/abs/2005.10548

[7] A. Imran, I. Posokhova, H.N. Qureshi, U. Masood, M.S. Riaz, K. Ali, C.N. John, M.I. Hussain, M. Nabeel "AI4COVID-19: AI enabled preliminary diagnosis for COVID-19 from cough samples via an app," Inform. Med. Unlocked, 20 (2020), p. 100378, 10.1016/j.imu.2020.100378 arXiv:2004.01275 http://arxiv.org/abs/2004.01275

[8] Y.E Erdoğan, A. Narin, "COVID19 detection with traditional and deep features on cough acoustic signals," Computers in Biology and Medicine, Volume 136, 2021,104765, ISSN 0010-4825, https://doi.org/10.1016/j.compbiomed.2021.104765.

[9] S Patro, and Kishore Kumar Sahu, "Normalization: A preprocessing stage," arXiv preprint ArXiv: 1503.06462, 2015/3/19,https://arxiv.org/abs/1503.06462

[10] A. J. McDonald, A. J. G. Baumgaertner, G. J. Fraser, S. E. George, and S. Marsh "Empirical Mode Decomposition of the atmospheric wave field," Ann. Geophys., 25, 375–384, https://doi.org/10.5194/angeo-25-375-2007, 2007.

[11] V. N. Vapnik, "An overview of statistical learning theory," in IEEE Transactions on Neural Networks, vol. 10, no. 5, pp. 988-999, Sept. 1999, doi: 10.1109/72.788640.

[12] A. Y. Kermani, F. Nasrollahi, M. Mahdavinejad "Investigation of the relationship between depth of overhang and amount of daylight indicators in office buildings of Kerman city." Environmental Health Engineering and Management Journal 2018; 5(3): 129–136. doi: 10.15171/EHEM.2018.18

[13] T. Ni, J. Lu, M. Zhu, L. Maddison, K. Boyd, L. Huskey, B. Ju, D. Hesselson, T. Zhong, P. Page-McCaw, D. Stainier, W. Chen "Conditional control of gene function by an invertible gene trap in zebrafish." Proceedings of the National Academy of Sciences of the United States of America. 109(38):15389-15394.

[14] C. Atakan, "Diskriminant Analizinde Gerçek Hata Oranına İlişkin Güven Aralığı için Bir Simülasyon Çalışması," Selçuk Üniversitesi Fen Fakültesi Fen Dergisi, c. 1, sayı. 22, ss. 89-96, Haz. 2003

[15] Y. E. Erdoğan and A. Narin, "Performance of Emprical Mode Decomposition in Automated Detection of Hypertension Using Electrocardiography," 2021 29th Signal Processing and Communications Applications Conference (SIU), 2021, pp. 1-4, doi: 10.1109/SIU53274.2021.9477887.

[16] A. Narin, M. Özer and Y. İşler, "Effect of linear and non-linear measurements of heart rate variability in prediction of PAF attack," 2017 25th Signal Processing and Communications Applications Conference (SIU), 2017, pp. 1-4, doi: 10.1109/SIU.2017.7960358.

[17] A. Narin, "Accurate detection of COVID19 using deep features based on X-Ray images and feature selection methods," Computers in Biology and Medicine,Volume 137,2021,104771,ISSN 0010-4825, https://doi.org/10.1016/j.compbiomed.2021.104771.

Analyzing the effects of random number generators on artificial gorilla troops optimizer in solving gear train design problem

A.C. CINAR[1]

[1] Selcuk University, Konya/Turkey, accinar@selcuk.edu.tr

Abstract **- Artificial gorilla troops optimizer (AGTO) is a recently developed metaheuristic optimizer for solving continuous unconstrained optimization problems. Random numbers are the backbone of metaheuristic optimization algorithms. Generally, most metaheuristic optimization algorithms are used uniformly distributed random numbers. The population is created with these uniformly distributed random numbers. Every random number is generated via random number generator algorithms. In this work, 6 different random number generator algorithms (Mersenne Twister, SIMD-oriented Fast Mersenne Twister, Combined multiple recursive, Multiplicative Lagged Fibonacci, Philox 4x32 generator with 10 rounds, and Threefry 4x64 generator with 20 rounds) are analyzed on AGTO. In the experiments, the gear train design problem was solved by variants of AGTO. Experimental results show that the default RNG of MATLAB produces the worst and slow random numbers. The Multiplicative Lagged Fibonacci RNG produces the best and fast random numbers for solving gear train design problems in AGTO.**

Keywords **- artificial gorilla troops optimizer, gear train design, random number generator, metaheuristic, uniformly distributed random number**

I. INTRODUCTION

Artificial gorilla troops optimizer (AGTO) is a recently developed metaheuristic optimizer for solving continuous unconstrained optimization problems by Abdollahzadeh et al. [1] in 2021. Random numbers are the backbone of metaheuristic optimization algorithms. Generally, most metaheuristic optimization algorithms such as artificial algae algorithm [2], galactic swarm optimization [3], whale optimization algorithm [4], spotted hyena optimizer [5], fruit fly optimization algorithm [6] are used random numbers for creating candidate solutions for solving optimization problems.

Every random number is generated via random number generator algorithms. The random number generators (RNGs) are divided into three groups: true RNGs (TRNGs), quasi RNGs (QRNGs), and pseudo RNGs (PRNGs). The random numbers have various distributions. Uniform distribution, normal distribution, and Cauchy distribution are well-known distributions.

In metaheuristic algorithms, the population is created with uniformly distributed random numbers. The binary mathematic-based RNGs can be more efficient than modulo mathematic-based ones.

In this work, 6 different binary mathematic-based RNGs (Mersenne Twister, SIMD-oriented Fast Mersenne Twister, Combined multiple recursive, Multiplicative Lagged Fibonacci, Philox 4x32 generator with 10 rounds, and Threefry 4x64 generator with 20 rounds) are analyzed on AGTO.

In literature, the gear train design problem is solved by metaheuristic algorithms such as tree-seed algorithm [7], flower pollination algorithm [8], genetic adaptive search [9], artificial bee colony algorithm [10], cuckoo search algorithm [11]. In the experiments, the gear train design problem was solved by variants of AGTO first time in the literature.

The experimental results showed that Multiplicative Lagged Fibonacci RNG produced more robust and fast solutions for optimizing the gear train design problem.

The remainder of the paper is arranged as follows: The original artificial gorilla troops optimizer algorithm is presented in a few words in Section 2, the features of the random number generator algorithms are given in Section 3, the presentation of the gear train design problem is in Section 4. The experimental setup and the results and discussion are presented in Section 5 and Section 6, respectively. Finally, the conclusion of this paper is given in Section 7.

II. ARTIFICIAL GORILLA TROOPS OPTIMIZER (AGTO)

Artificial gorilla troops optimizer (AGTO) is a metaheuristic optimization algorithm that mimics the lifecycle of the gorillas. Five distinct gorilla behaviors are mathematically formulated for solving optimization problems. These are battles for mature women, relocation to an unexplored area, relocation in the direction of an associated place, going after the Silverback (SB), and relocating to other gorillas. The only purpose of these analogies is mathematically formulated the exploration and exploitation phases in a metaheuristic optimization algorithm. The detailed pseudocode and mathematical formulations are given in Figure 1.

-Determine **N** as the number of population
-Determine **D** as the dimension of the problem
-Determine **ub** as the upper bound of the search space
-Determine **lb** as the lower bound of the search space
-Determine **iter** as the iteration counter and set as 1
-Determine **max_iter** as the number of maximum iterations
-Initialize the **SB** as the best solution
-Initialize the first random population of Gorilla (**X**)
-Calculate the fitness values of the population
-Determine the best solution as the **SB**
-Define the controlling parameters as **p**=0.03, **Beta**=3, **w**=0.8
-Copy the current iteration population (X) to next iteration population (GX)

```
WHILE iter < max_iter

a=(cos(2*rand)+1)*(1-iter/max_iter)
C=a*(2*rand-1)

-Start the exploration phase

FOR i=1:N
  IF rand<p
    GX(i,:) =(ub-lb)*rand+lb
  ELSE
    IF rand>=0.5
      Z = unifrnd(-a,a,1,D)
     H=Z.*X(i,:)
      GX(i,:)=(rand-a)*X(randi([1,N]),:)+C.*H
    ELSE
      GX(i,:)=X(i,:)-C.*(C*(X(i,:)-GX(randi([1,N]),:))+rand*(X(i,:)-
GX(randi([1,N]),:)))

    END IF
  END IF
END FOR

-Check the boundary of GX
-Calculate the fitness values of the population
-Replace the current gorillas with if new gorillas are better than them
-Determine the best solution as the SB
-Start the exploitation phase

FOR i=1:N
  IF a>=w
    g=2^C
    delta= (abs(mean(GX)).^g).^(1/g)
    GX(i,:)=C*delta.*(X(i,:)-SB)+X(i,:)
  ELSE
    IF rand>=0.5
    h=randn(1,D)
    ELSE
      h=randn(1,1)
    END IF
  r1=rand
  GX(i,:)= SB-(SB*(2*r1-1)-X(i,:)*(2*r1-1)).*(Beta*h)
  END IF
END FOR

Check the boundary of GX
Calculate the fitness values of the population
Replace the current gorillas with if new gorillas are better than them
Determine the best solution as the SB

END WHILE
```

Figure 1: The detailed pseudocode and mathematical formulations of AGTO

Readers can be found more explanations and all mathematical formulations in the paper of Abdollahzadeh et al. in 2021 [1].

III. RANDOM NUMBER GENERATOR ALGORITHMS

The names, MATLAB keywords, and abbreviations of RNGs used in this paper are given in Table 1.

Table 1: The names, keywords, and abbreviations of RNGs

The name of the RNG	Keyword	Abbrevation
Mersenne Twister	mt19937ar	RNG1
SIMD-oriented Fast Mersenne Twister	dsfmt19937	RNG2
Combined multiple recursive	mrg32k3a	RNG3
Multiplicative Lagged Fibonacci	mlfg6331_64	RNG4
Philox 4x32 generator with 10 rounds	philox4x32_10	RNG5
Threefry 4x64 generator with 20 rounds	threefry4x64_20	RNG6

The Mersenne Twister [12] is the default RNG of the MATLAB, and its MATLAB keyword is "mt19937ar". The potential random numbers are multiples of 2^{-53} in the interval (0, 1).

The SIMD-oriented Fast Mersenne Twister [13] is the faster version of the Mersenne Twister [12] and its MATLAB keyword is "dsfmt19937". The potential random numbers are multiples of 2^{-52} in the interval (0, 1).

The Combined multiple recursive [14] uses two 32 bit integers and its MATLAB keyword is "mrg32k3a". The potential random numbers are multiples of 2^{-53} in the interval (0, 1).

The Multiplicative Lagged Fibonacci [15] uses one 64 bit integer and its MATLAB keyword is "mlfg6331_64". The potential random numbers are multiples of 2^{-56} in the interval (0, 1).

The Philox 4x32 generator with 10 rounds [16] uses a Feistel network and integer multiplication and its MATLAB keyword is "philox4x32_10".

The Threefry 4x64 generator with 20 rounds [16] uses the Skein hash function [17] and its MATLAB keyword is "threefry4x64_20".

Sample random numbers between 0 and 1 of different RNGs are given in Table 2.

Table 2: Sample random numbers between 0 and 1 of different RNGs

	RN1	RN2	RN3	RN4	RN5
RNG1	0.8147	0.9058	0.1270	0.9134	0.6324
RNG2	0.0306	0.2131	0.2990	0.3811	0.8635
RNG3	0.7270	0.4522	0.9387	0.2360	0.0277
RNG4	0.6986	0.7413	0.4239	0.6914	0.7255
RNG5	0.3655	0.6975	0.1789	0.4549	0.4396
RNG6	0.3640	0.5421	0.6543	0.7436	0.0342

Time and mean comparisons of 1000000 random numbers of different RNGs are given in Table 3. The RNG2 is the fastest algorithm. The RNG4 is the most robust algorithm.

Table 3: Time and mean comparisons of 1000000 random numbers of different RNGs

	Time (seconds)	Mean
RNG1	0.0118	0.5003
RNG2	0.0031	0.4998
RNG3	0.0082	0.4998
RNG4	0.0314	0.5000
RNG5	0.0206	0.4996
RNG6	0.0078	0.5003

IV. GEAR TRAIN DESIGN PROBLEM

The gear train design problem is formulated by Sandgren [18] in 1990. It is an unconstrained mechanical optimization problem that has four integer variables. The scheme of the gear train is shown in Figure 2.

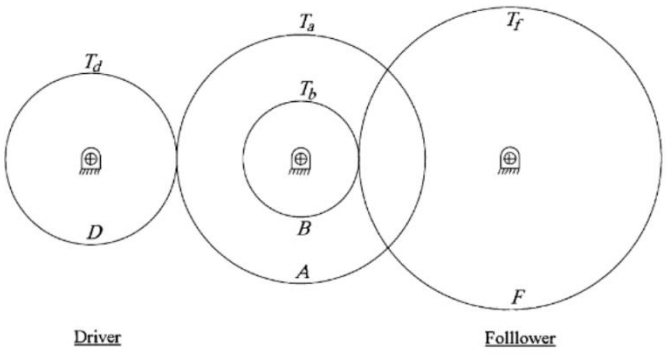

Figure 2: The gear train

The mathematical formula of the gear train design problem is given in Equation 1.

$$Minimize: f(T_d, T_b, T_a, T_f) = \frac{1}{6.931} - \frac{T_d T_b}{T_a T_f} \quad (1)$$

where T_d, T_b, T_a, T_f are all of integer values between 12 and 60. They all indicate the number of teeth of the gear. The main aim is to find the optimum values of these four integer values. The global optimum value of the objective function is 0.

V. EXPERIMENTAL SETUP

All experiments were conducted on a laptop that has an Intel(R) Core (TM) i3-10110U CPU @ 2.10GHz 2.59 GHz CPU and 8 GB of RAM. The software codes were written and executed in MATLAB (TM). The gear Train design problem is used as a benchmark function in the experiments. The number of gorillas in the population is set as 30. The maximum iteration number is set as 100. The maximum function evaluation number is set as 3000. All experiments are conducted with 30 independent runs with random seeds.

VI. RESULTS AND DISCUSSION

The experimental results of 30 independent runs are given in Table 4. RNG1 is the default RNG of MATLAB and it produces the worst solutions. The first RNG is RNG4, the second is RNG2, the third is RNG6, the fourth is RNG3, the fifth is RNG5 and the last is RNG1.

Table 4: The experimental results of 30 independent runs

Run	RNG1	RNG2	RNG3	RNG4	RNG5	RNG6
Run 1	5.25E-26	**0.00E+00**	7.70E-34	**0.00E+00**	5.76E-28	**0.00E+00**
Run 2	7.70E-34	**0.00E+00**	**0.00E+00**	**0.00E+00**	**0.00E+00**	**0.00E+00**
Run 3	2.96E-30	**0.00E+00**	**0.00E+00**	**0.00E+00**	**0.00E+00**	**0.00E+00**
Run 4	1.85E-30	**0.00E+00**	**0.00E+00**	**0.00E+00**	**0.00E+00**	**0.00E+00**
Run 5	2.08E-30	7.70E-34	**0.00E+00**	**0.00E+00**	**0.00E+00**	7.70E-34
Run 6	**0.00E+00**	**0.00E+00**	7.70E-34	**0.00E+00**	2.77E-32	7.70E-34
Run 7	5.83E-29	**0.00E+00**	**0.00E+00**	**0.00E+00**	**0.00E+00**	7.70E-34
Run 8	6.93E-33	7.70E-34	3.08E-33	**0.00E+00**	**0.00E+00**	**0.00E+00**
Run 9	**0.00E+00**	**0.00E+00**	**0.00E+00**	**0.00E+00**	**0.00E+00**	**0.00E+00**
Run 10	9.60E-29	**0.00E+00**	7.70E-34	**0.00E+00**	**0.00E+00**	**0.00E+00**
Run 11	**0.00E+00**	**0.00E+00**	**0.00E+00**	**0.00E+00**	7.70E-34	**0.00E+00**
Run 12	1.04E-27	**0.00E+00**	**0.00E+00**	**0.00E+00**	**0.00E+00**	**0.00E+00**
Run 13	7.70E-32	**0.00E+00**	**0.00E+00**	3.08E-33	**0.00E+00**	**0.00E+00**
Run 14	**0.00E+00**	**0.00E+00**	**0.00E+00**	**0.00E+00**	3.08E-33	**0.00E+00**
Run 15	3.73E-31	**0.00E+00**	**0.00E+00**	**0.00E+00**	3.08E-33	**0.00E+00**
Run 16	1.51E-31	**0.00E+00**	**0.00E+00**	**0.00E+00**	**0.00E+00**	**0.00E+00**
Run 17	2.70E-28	6.93E-33	7.70E-34	**0.00E+00**	2.77E-32	**0.00E+00**
Run 18	2.18E-27	7.70E-34	**0.00E+00**	**0.00E+00**	**0.00E+00**	**0.00E+00**
Run 19	6.93E-33	**0.00E+00**	**0.00E+00**	**0.00E+00**	3.08E-33	**0.00E+00**
Run 20	1.40E-28	**0.00E+00**	**0.00E+00**	7.70E-34	3.08E-33	**0.00E+00**
Run 21	**0.00E+00**	**0.00E+00**	**0.00E+00**	**0.00E+00**	6.93E-33	**0.00E+00**
Run 22	1.04E-29	**0.00E+00**	**0.00E+00**	**0.00E+00**	**0.00E+00**	**0.00E+00**
Run 23	1.05E-25	**0.00E+00**	**0.00E+00**	**0.00E+00**	1.73E-31	**0.00E+00**
Run 24	1.70E-27	**0.00E+00**	3.08E-33	**0.00E+00**	2.77E-32	**0.00E+00**
Run 25	7.70E-34	**0.00E+00**	**0.00E+00**	**0.00E+00**	1.11E-31	**0.00E+00**
Run 26	7.70E-34	**0.00E+00**	**0.00E+00**	**0.00E+00**	1.23E-32	1.29E-30
Run 27	**0.00E+00**	**0.00E+00**	**0.00E+00**	**0.00E+00**	3.77E-32	**0.00E+00**
Run 28	1.20E-29	**0.00E+00**	**0.00E+00**	6.93E-33	6.48E-31	3.08E-33
Run 29	**0.00E+00**	**0.00E+00**	**0.00E+00**	**0.00E+00**	7.70E-34	**0.00E+00**
Run 30	3.06E-30	**0.00E+00**	2.23E-31	**0.00E+00**	3.25E-30	**0.00E+00**
Hit	7	26	23	**27**	13	25

According to the experimental results, 27 of 30 runs, RNG4 produces the optimum solution for the gear train design problem. The time comparisons of the RNGs are given in Figure 3. The fastest RNG is RNG4 and the slowest RNG is RNG1. These time values are total time values of 30 different runs.

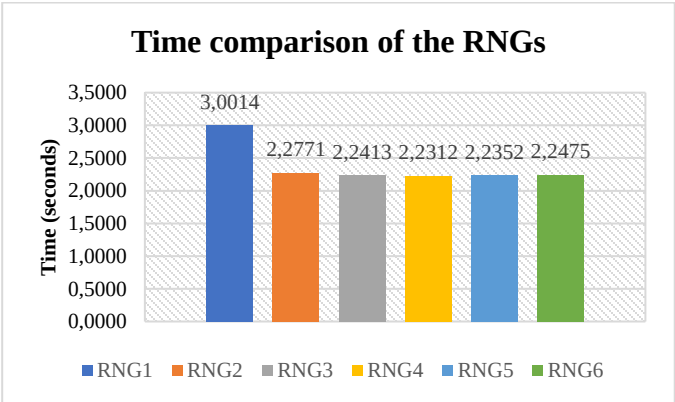

Figure 3: Time comparisons of the RNGs

The statistical results of the 30 independent runs are given in Table 5.

Table 5: The statistical results of the 30 independent runs

	Min	Max	Mean	Median	Std. Dev.
RNG1	0.00E+00	1.05E-25	5.44E-27	1.11E-30	2.11E-26
RNG2	0.00E+00	6.93E-33	3.08E-34	0.00E+00	1.27E-33
RNG3	0.00E+00	2.23E-31	7.73E-33	0.00E+00	4.06E-32
RNG4	0.00E+00	6.93E-33	3.60E-34	0.00E+00	1.37E-33
RNG5	0.00E+00	5.76E-28	1.94E-29	1.93E-33	1.05E-28
RNG6	0.00E+00	1.29E-30	4.33E-32	0.00E+00	2.36E-31

The RNG4 produces the best results in terms of mean, and according to the standard deviation values, RNG4 is the most robust RNG for solving gear train design problem with AGTO. The convergence graphs of the mean values of 30 independent runs are given in Figure 4.

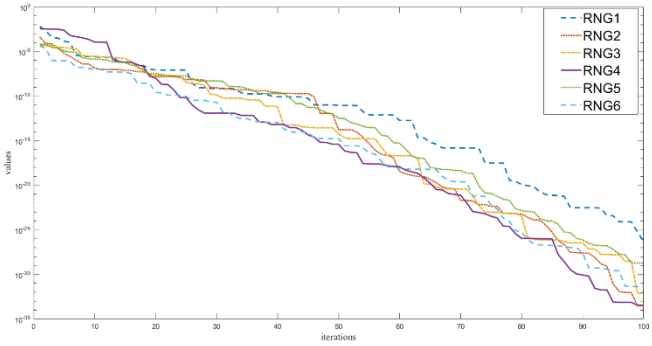

Figure 4: The convergence graphs of the mean values of 30 independent runs

According to Figure 4, RNG4 produces the best results and explore and exploits the search space step by step without not trapping in a local optimum.

VII. Conclusion

Random numbers are the backbone of metaheuristic optimization algorithms. Generally, most metaheuristic optimization algorithms are used uniformly distributed random numbers. The population is created with these uniformly distributed random numbers. Artificial gorilla troops optimizer (AGTO) is a recently developed metaheuristic optimization algorithm for solving unconstrained continuous optimization problems. The population of the gorilla is created in a predetermined search space with uniform random numbers. Every random number is generated via random number generator algorithms. In this work, six different random number generator algorithms (Mersenne Twister abbreviated as RNG1, SIMD-oriented Fast Mersenne Twister abbreviated as RNG2, Combined multiple recursive abbreviated as RNG3, Multiplicative Lagged Fibonacci abbreviated as RNG4, Philox 4x32 generator with 10 rounds abbreviated as RNG5, and Threefry 4x64 generator with 20 rounds abbreviated as RNG6) are analyzed on AGTO. In the experiments, a mechanical engineering design problem, the gear train design problem was solved by variants of AGTO. Experimental results show that the default RNG of MATLAB produces the worst and slow random numbers. The Multiplicative Lagged Fibonacci RNG produces the best and fast random numbers for solving gear train design problems in AGTO.

Acknowledgment

The author wish to thank Scientific Research Projects Coordinatorship at Selcuk University and The Scientific and Technological Research Council of Turkey for their institutional supports.

References

1. Abdollahzadeh, B., F. Soleimanian Gharehchopogh, and S. Mirjalili, *Artificial gorilla troops optimizer: A new nature-inspired metaheuristic algorithm for global optimization problems.* International Journal of Intelligent Systems, 2021. **36**(10): p. 5887-5958.
2. Turkoglu, B. and E. Kaya, *Training multi-layer perceptron with artificial algae algorithm.* Engineering Science and Technology, an International Journal, 2020. **23**(6): p. 1342-1350.
3. Kaya, E., S.A. Uymaz, and B. Kocer, *Boosting galactic swarm optimization with ABC.* International Journal of Machine Learning and Cybernetics, 2019. **10**(9): p. 2401-2419.
4. Kaya, E. and A. Babalik, *FUZZY ADAPTIVE WHALE OPTIMIZATION ALGORITHM FOR NUMERIC OPTIMIZATION.* Malaysian Journal of Computer Science, 2021. **34**(2): p. 184-198.
5. Şahman, M.A., *A discrete spotted hyena optimizer for solving distributed job shop scheduling problems.* Applied Soft Computing, 2021. **106**: p. 107349.
6. Babalık, A., et al., *An improvement in fruit fly optimization algorithm by using sign parameters.* Soft Computing, 2018. **22**(22): p. 7587-7603.
7. Sahman, M., et al. *Tree-seed algorithm in solving real-life optimization problems*. in *IOP conference series: materials science and engineering*. 2019. IOP Publishing.
8. Meng, O.K., et al. *Application of modified flower pollination algorithm on mechanical engineering design problem*. in *IOP conference series: materials science and engineering*. 2017. IOP Publishing.
9. Deb, K. and M. Goyal, *A combined genetic adaptive search (GeneAS) for engineering design.* Computer Science and informatics, 1996. **26**: p. 30-45.
10. Cui, L., et al., *A smart artificial bee colony algorithm with distance-fitness-based neighbor search and its application.* Future Generation Computer Systems, 2018. **89**: p. 478-493.
11. Gandomi, A.H., X.-S. Yang, and A.H. Alavi, *Cuckoo search algorithm: a metaheuristic approach to solve structural optimization problems.* Engineering with computers, 2013. **29**(1): p. 17-35.
12. Matsumoto, M. and T. Nishimura, *Mersenne twister: a 623-dimensionally equidistributed uniform pseudo-random number generator.* ACM Transactions on Modeling and Computer Simulation (TOMACS), 1998. **8**(1): p. 3-30.
13. Saito, M. and M. Matsumoto, *A PRNG specialized in double precision floating point numbers using an affine transition*, in *Monte Carlo and Quasi-Monte Carlo Methods 2008*. 2009, Springer. p. 589-602.
14. L'Ecuyer, P., *Good Parameter Sets for Combined Multiple Recursive Random Number Generators.* Operations Research, 1999. **47(1)**: p. 159-164.
15. Mascagni, M. and A. Srinivasan, *Parameterizing parallel multiplicative lagged-Fibonacci generators.* Parallel Computing, 2004. **30**(7): p. 899-916.
16. Salmon, J.K., et al. *Parallel random numbers: as easy as 1, 2, 3*. in *Proceedings of 2011 International Conference for High Performance Computing, Networking, Storage and Analysis*. 2011.
17. Ferguson, N., et al., *The Skein hash function family.* Submission to NIST (round 3), 2010. **7**(7.5): p. 3.
18. Sandgren, E., *Nonlinear integer and discrete programming in mechanical design optimization.* 1990.

Performance Comparison of Model Storage Formats for Deploying Data Mining Models

E. YILDIZ[1] and T.T. BİLGİN[1]

[1] CITS Bilisim Hizmetleri ve Yazılım San. Tic. A.Ş, Bursa/Turkey, eryildiz@cits.com.tr
[1]Bursa Technical University, Bursa/Turkey, turgay.bilgin@btu.edu.tr

Abstract **- Electronics and computer technology are rapidly changing. This trend has both changed the habits of the end-users and initiated a transformation in the industry. In addition, data collection, storage, and processing studies have gained importance with Industry 4.0 (I4.0). Nowadays, data has become an indispensable resource for information extraction. Recently, predictive models produced by machine learning and data mining have been frequently used in our daily life. The wide variety of environments in which these models can be developed is easy for developers while integrating models into existing systems is equally difficult and costly. In this study, two approaches are compared in terms of their performance in publishing model files serialized with predictive model markup language, which is accepted by frequently used software tools such as Knime, Weka, IBM SPSS Modeler. Python programming language and tools are used in interpreting predictive model markup language files and creating web services. The first approach was chosen to store predictive model markup language file contents in a database, and the second approach was to store these files in the file system, and these two methods were measured and reported on the parameters of response time, throughput (speed of processing requests) and latency in generating responses. As a result of the measurements made, it has been seen that the web service performance is higher when the model is kept as a file in the file system compared to the other method.**

Keywords **- Machine Learning, Data Mining, Web Service, PMML, Software Development**

I. INTRODUCTION

As a result of the advances in computer science, the internet, and electronic technologies, end users' access to computers has become very easy today, and the number of households with computers has experienced a continuous increase throughout the world [1]. In the early days when computers started to be used daily, users were in the position of consuming more data, but nowadays there are billions of smartphones, wearable devices, etc. thanks to this, they have become the data source. As a result, the volume of data produced worldwide doubles almost every two years [2].

From an industry perspective, digital transformation has increased the awareness of companies and led them to store and process the data they produce correctly. In addition, IoT devices that produce and process sensor-rich, dense data such as smart home systems, autonomous/connected vehicle systems also have a significant share in the data produced worldwide [3]. In today's world where data is produced so intensely, processing and evaluation of data have gained a lot of value. This situation has increased the importance of studies in the field of predictive analytics, which covers topics such as data modeling, data science, data mining, and machine learning [4]. Predictive analytics applications have a long history and are still widely used today. Based on market analysis data, it can be said that it still has a high potential [5].

The sectors in which predictive analytics applications are mainly used and sample applications in these sectors can be listed as follows:

- Suggesting products that are likely to be purchased by making use of past purchasing data in the retail sector [6].
- Performing disease diagnosis with higher accuracy with the help of models produced from historical data and cases in the health sector [7].
- To be able to suggest the optimum credit limit by estimating the risk score with the help of models produced by using banking data of customers in the finance sector [8].
- Estimation of traffic density based on historical vehicle traffic density data in smart city applications [9].

The number and variety of these examples are increasing day by day and applications are spreading faster among end-users. The need to make sense of raw data has led to the need for more professionals working in this field, and job opportunities in data mining and data science have diversified [10]. This situation has triggered the production of auxiliary tools in data mining and diversified in number and quality. There are many data mining tools available today. Knime, IBM SPSS Modeler, Weka are the best-known ones. Thanks to these tools, data mining studies can be designed, trained, and predicted in fast and simple interfaces. However, these tools do not offer a general solution for integrating the trained models into another platform.

Predictive Models are trained to benefit from a certain dataset and if it is seen that the model training is successful at the end of the study, it is integrated into the platform to be used. However, the ready-made tools mentioned in the previous paragraph have low integration capacities or are closed to integration. For example, when a data miner wants to integrate his heart attack prediction model into a mobile application, he has to re-code the entire training process as a Web API. Similar needs will increase with the spread of data mining applications.

In this study, it has been tried to easily publish the model that users train in any tool as a Web API, and two model storage approaches used in the development of this service are examined in terms of performance.

II. LITERATURE OVERVIEW

The fact that predictive analytical models can be easily integrated with other applications thanks to PMML (Predictive Model Markup Language), in other words, these models can be deployed, paved the way for studies in this field and led to an increase in the number of them. In one study, an early version of PMML language, which provides XML representation of predictive analytical models, is introduced with clear examples [11]. In another study describing developing and publishing analytical applications using PMML and UIMA, UIMA was used for structuring unstructured data, and PMML classifier, which is the representation of classification model, was used for classification of structured data [12]. In a study designed a scoring engine in which PMML models can be scored, PMML models are interpreted with python, and communication with other applications is provided with a library interface developed [13]. Incorporating important features in every major version update, PMML switched to version 4.0 in 2009. In the same year, studies were carried out on the innovations in this version and the current structure of PMML [14-15]. In a proposed study with the new features of PMML, predictive models can be estimated over the Internet with SOA (Service Oriented Architecture) Web service. The application is designed to run on cloud servers [16]. In a study in which PMML models are integrated into databases and data warehouses and scoring very high volumes of data with predictive analytical models, it is emphasized that the models can be easily and highly integrated into other platforms when serialized. Although the study was carried out on the EMC Greenplum data warehouse, it was emphasized that integration with other databases can be achieved with the Universal PMML (Zementis Universal PMML Plugin) plugin referred to in the study [17]. In a study aiming to increase the capabilities of rule engines, models serialized with PMML were included in the rules and estimated, and the rules were run as a result of these predictions. They proposed a system for extending the capability of rule engines by integrating predictive analytical models represented by PMML into rule engines [18]. PMML development is an ongoing standard, and many versions have emerged over the years. Applications supporting PMML could not immediately respond to this conversion, resulting in incompatibilities between supported versions. In a study conducted to prevent the problem experienced in this regard, an application has been proposed to convert PMML files produced in different versions to version 4.0. Thus, it is aimed to preserve the interoperability feature of PMML [19].

Looking at the studies carried out in the past, it is seen that PMML is mostly used to integrate predictive analytical models into existing systems. However, in most of the studies, this integration was carried out as an interpretation of PMML in existing development environments. There is only one study on the predicting of PMML models as a web service over the Web. Similarly, in this study, models will be deployed in a way that can be predicted over the Web. However, contrary to the work of Guazzelli et al. [16], the API developed was not designed with the SOA approach, but with the Restful API approach, which was measured to be more performance in comparisons [20-21]. In addition, in this study, a lightweight web framework was used to ensure that the application can run not only on cloud servers but also on local servers with more limited hardware. Since the studies differ in these aspects, it would not be correct to make a comparison on performance metrics.

III. MATERIAL AND METHODS

A. PMML

Predictive Model Markup Language is an open standard developed to enable portability, reusability, and cross-application shareability of data mining and machine learning models [16-22]. It was developed in 2008 by a vendor-led consortium called Data Mining Group (DMG), which develops independent, data mining standards [23]. While producing PMML, models are converted to XML codes by observing certain rules and a certain template. Thus, models can be moved between applications, eliminating time-consuming and costly steps such as retraining for each platform. With PMML, preprocessing and training processes can be done in an application, and then the serialized model can be moved to another application, and prediction process can be performed on this application. Thus, different data mining applications can be used together easily and their efficiency can be increased. The fact that the models are represented as PMML and can be integrated into different platforms without retraining has facilitated the integration of data mining models into different applications.

PMML has been in development since 2008. At the time of this study, the most current version is PMML 4.4.1. The range of data mining and machine learning algorithms that it can serialize has increased since the first release, and it supports 18 different types of algorithms in the current version [22]. The number of PMML compatible applications such as Knime, IBM SPSS, Weka is increasing day by day. At the time of this study, nearly 100 tools from about 50 different vendors were developed as PMML compatible [24].

A PMML file generally consists of the following elements:

- Header
- Data Dictionary
- Mining Schema / Model

Header section contains general information about the PMML document. The Data Dictionary section is the section that contains the definition of all the fields of the model. This section represents the model's inputs. The model section is the section where the trained data mining model is represented.

The PMML sample used in this study was obtained by training the Decision Tree model in Knime 4.2.2 using the Iris dataset and exporting it as PMML.

```
<?xml version="1.0" encoding="UTF-8"?>
<PMML version="4.2" xmlns="http://www.dmg.org/PMML-4_2">
  <Header copyright="eryildiz">
    <Application name="KNIME" version="4.2.2"/>
  </Header>
  <DataDictionary numberOfFields="5">
    <DataField name="SepalLengthCm" optype="continuous" dataType="double">
      <Interval closure="closedClosed" leftMargin="4.3" rightMargin="7.9"/>
    </DataField>
    ...
  </DataDictionary>
  <TreeModel modelName="DecisionTree" functionName="classification"
  splitCharacteristic="binarySplit" missingValueStrategy="lastPrediction"
  noTrueChildStrategy="returnNullPrediction">
    <MiningSchema>
    </MiningSchema>
    <Node id="0" score="Iris-setosa" recordCount="150.0">
    </Node>
  </TreeModel>
</PMML>
```

Figure 1: Sections of PMML

B. *Model Deployment with REST API*

In this study, a Web API has been developed to make PMML representations of the trained models predictable over the Web. The REST approach is preferred in the API, which is built on the Flask framework, which is frequently preferred in web applications developed with Python. While choosing the REST approach, the criteria with which endpoints the data mining models would need to be more integrated were considered. Considering that data mining models are used more and more in production areas, social media applications, web applications, IoT systems and the need in this area will continue, the web API to be developed will often need to be consumed from mobile devices and IoT devices working with limited hardware features. According to this need REST approach, which works better than SOAP on mobile devices and consumes fewer system resources, has been preferred [20-21].

RESTFul is a widely accepted architecture that communicates with HTTP developed by Fielding [25]. In REST architectures, resources are represented by a URI, and the CRUD operations that can be done with these resources are traced to the HTTP methods GET, PUT, POST, DELETE. REST makes it possible to create Web services with a simple and plain interface. Thus, it is preferred in scenarios where system resource is limited and performance and speed are important. In this study, REST was found to be more suitable for situations where models need to be predicted quickly.

C. *Software and Libraries*

a) Flask : Flask is a micro web framework developed with Python. Flask has a structure that can be expanded with extensions and plugins [26]. Started to be developed by Armin Ronacher in 2010, Flask has gained popularity day by day and has become the most popular web framework among Python developers, surpassing Django by 2020 [27]. The main reasons for preference in this study are its lightweight structure, rapid development, and performance. Applications developed with Flask are positioned behind a web server application via the WSGI (Web Server Gateway Interface) calling convention. As you can see in Figure 2, Gunicorn was preferred for the WSGI calling convention in this study.

b) PyPMML: PyPMML is a Python library where PMML files can be deserialized and predicted in Python applications.

c) PostgreSQL: PostgreSQL is an open-source Structured Query Language (SQL) powered relational database management system. In this study, the approach of reading PMML contents from the database (approach #2 in figure 2) is used to store XML codes.

d) Apache JMeter: Apache Jmeter is an advanced, open-source testing tool used to analyze the performance of web applications and perform load tests. Developed in Java, it has an advanced user interface and command-line interface [28].

D. *Implementation details*

The main purpose of the system, whose architectural drawing can be viewed in Figure 2, is to make a model predictable over the web. Users first upload the PMML file to the system with the terminals offered in the Restful API. The API gives users the endpoint information that they can use for prediction, and this endpoint is used for prediction.

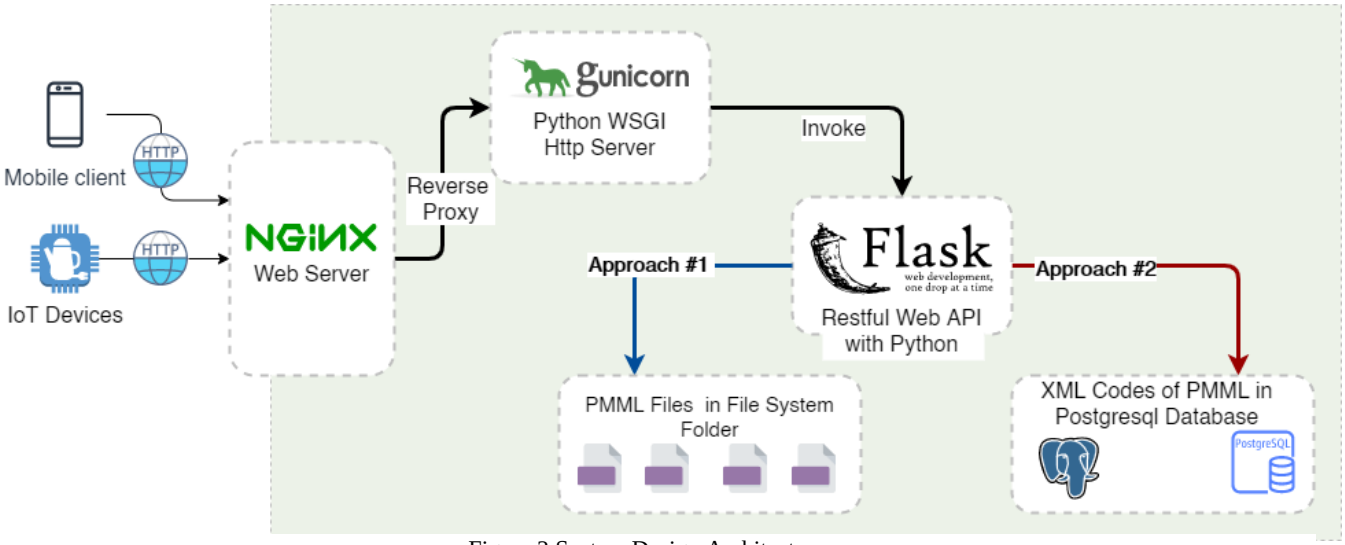

Figure 2 System Design Architecture

Nginx is preferred as a web server to meet user requests. Web applications developed with Python need an intermediate application that implements a WSGI calling convention to communicate with web servers such as Nginx. Gunicorn was used for this purpose. Two alternative approaches have been studied about how the files uploaded by the users will be kept in the system. In the first option (Figure 2, Approach #1), files with PMML extension are kept in the file system and read from there. In the second approach (Figure 2, Approach #2), XML codes, which are the contents of PMML files, are kept as records in the Postgresql database and accessed from there. In this study, tests of these two different approaches affecting performance were carried out.

E. Test Cases

For test studies, two separate restful endpoints are defined that implement two different approaches to the same application. Afterward, the application was published on a server in the configuration listed in Table 1.

Table 1 Test Server Specifications

Specification Type		**Specification**
Operating System		Ubuntu 20.04
Hard Disk Capacity		250 GB SSD
RAM		16 GB
Processors		4 Core Intel Xeon Gold 6238

The characteristics of the client computer running Apache Jmeter are given in Table 2.

Table 2 Test Client Specifications

Specification Type	**Specification**
Operating System	Windows 10 Pro
Hard Disk Capacity	500 GB SSD
RAM	24 GB
Processors	Intel Core i7-8564U

The tests were run with the Apache Jmeter CLI interface. As a result of these tests, *Elapsed Time*, *Throughput*, and *Latency* values were compared.

a) Elapsed Time: For elapsed time measurement, Jmeter's Elapsed Time measurement criterion was used. The Jmeter documentation describes Elapsed Time as "Jmeter measures the elapsed time from just before sending the request to just after the last response has been received" [28]

$$\Delta t = t_f - t_0$$

t_f is the time at the end of the request.
t_0 is the time at the beginning of the request.

b) Throughput: The Throughput value is a useful criterion to measure how many operations the application can respond to in a unit of time, and to get an idea of how it behaves under load. The study is based on Jmeter's throughput measurement. "Throughput is calculated as requests/unit of time. The time is calculated from the start of the first sample to the end of the last sample. This includes any intervals between samples, as it is supposed to represent the load on the server."[28]

$$\frac{NoR}{t_f - t_0}$$

NoR (Number of Requests) is the total count of samples of the test session.

c) Latency: "JMeter measures the latency from just before sending the request to just after the first response has been received. Thus the time includes all the processing needed to assemble the request as well as assembling the first part of the response, which in general will be longer than one byte" [28]

IV. RESULTS AND DISCUSSIONS

All tests were performed with random parameters prepared for the iris dataset as seen in Figure 3.

```
{
        "SepalLengthCm" : ${ __javaScript((Math.random() * (9) + 3).toFixed(2) * 1,)},
        "SepalWidthCm" : ${ __javaScript((Math.random() * (6) + 1).toFixed(2) * 1,)},
        "PetalLengthCm" : ${ __javaScript((Math.random() * (9) ).toFixed(2) * 1,)},
        "PetalWidthCm" : ${ __javaScript((Math.random() * (4)).toFixed(2) * 1,)}
}
```

Figure 3: Jmeter request payload with random values

Figure 4 shows the result of tests to find the elapsed time on requests. Elapsed time tests consist of 6 sessions with different request numbers. In the sessions, 20, 40, 80, 160, 320, and 640 requests were made within 1 second and tested for both approaches.

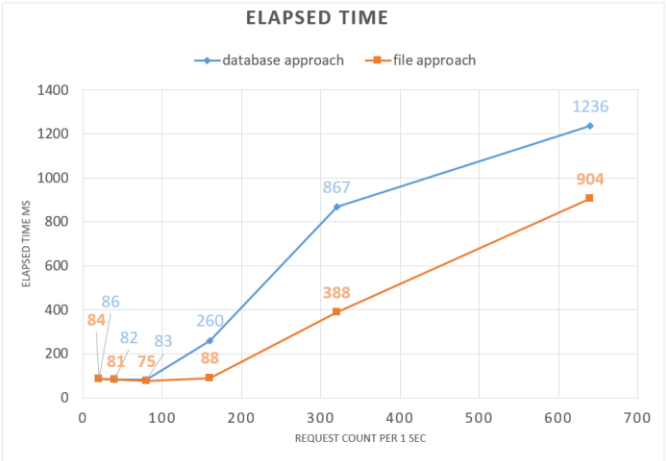

Figure 4: Elapsed Time Chart

For Throughput and Latency values, a session consisting of 2500 requests with 2 cycles of 3 seconds was planned and tests were carried out for both approaches. A total of 5000 requests were made within 6 seconds for each approach. Their results can also be seen in Figure 5.

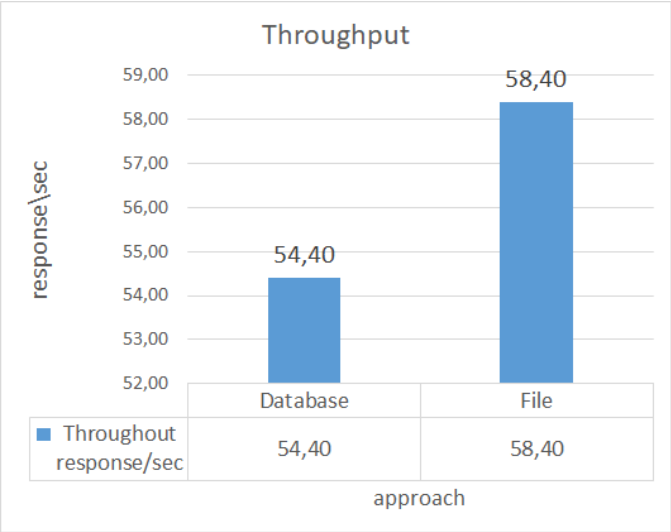

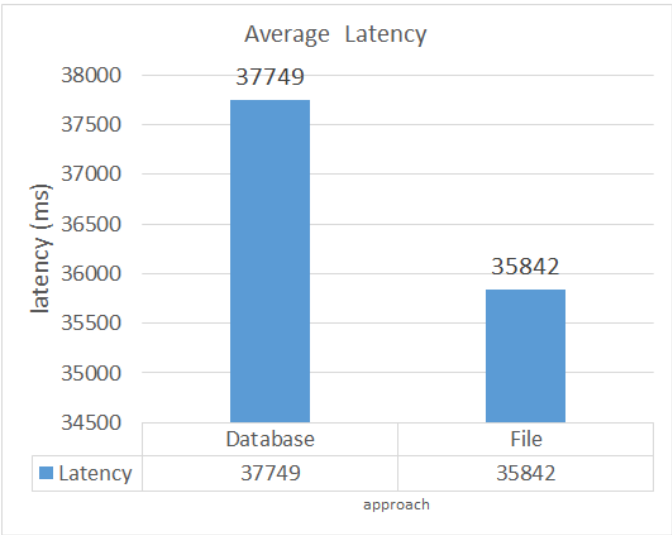

Figure 5 Throughput and Average Result Charts

According to the test results, it has been seen that the File System approach is more performant in the Elapsed Time criterion. In addition, when the Throughput and Latency Time results are examined, the File system approach showed higher performance. These results show that the approach of storing PMML files in the file system works more performance in applications that will be critical in terms of performance.

ACKNOWLEDGMENT

This study was funded by the Scientific and Technological Research Council of Turkey (TUBITAK) 2210-D National Scholarship Programme for MSc Students. This study is supported by Coşkunöz Holding.

REFERENCES

[1] T. Alsop, "Share of households with a computer at home worldwide from 2005 to 2019," 2021. https://www.statista.com/statistics/748551/worldwide-households-with-computer/.

[2] A. Holst, "Volume of data/information created, captured, copied, and consumed worldwide from 2010 to 2025," 2021. https://www.statista.com/statistics/871513/worldwide-data-created/.

[3] Fredrik Dahlqvist, "Growing opportunities in the Internet of Things | McKinsey," no. July, 2019.

[4] K. D. Foote, "A Brief History of Analytics - DATAVERSITY," *Dataversity.Net*, 2018. https://www.dataversity.net/brief-history-analytics/ (accessed Oct. 11, 2021).

[5] Grand View Research, "Predictive Analytics Market Size & Share | Industry Report, 2019-2025," 2019. https://www.grandviewresearch.com/industry-analysis/predictive-analytics-market (accessed Oct. 11, 2021).

[6] V. Kumar and M. L., "Predictive Analytics: A Review of Trends and Techniques," *Int. J. Comput. Appl.*, vol. 182, no. 1, pp. 31–37, 2018, doi: 10.5120/ijca2018917434.

[7] T. Hahn, A. A. Nierenberg, and S. Whitfield-Gabrieli, "Predictive analytics in mental health: Applications, guidelines, challenges and perspectives," *Mol. Psychiatry*, vol. 22, no. 1, pp. 37–43, 2017, doi: 10.1038/mp.2016.201.

[8] C. Gimeno-Gilles *et al.*, "ANOMALY DETECTION AND PREDICTIVE ANALYTICS FOR FINANCIAL RISK MANAGEMENT," *Euphytica*, vol. 18, no. 2, p. 22280, 2016.

[9] A. Mystakidis and C. Tjortjis, "Big Data Mining for Smart Cities: Predicting Traffic Congestion using Classification," *11th Int. Conf. Information, Intell. Syst. Appl. IISA 2020*, pp. 4–11, 2020, doi: 10.1109/IISA50023.2020.9284399.

[10] "The State of Data Engineering | Stitch Benchmark Report." https://www.stitchdata.com/resources/the-state-of-data-engineering/ (accessed Oct. 11, 2021).

[11] R. Grossman *et al.*, "Management and mining of multiple predictive models using the predictive modeling markup language," *Inf. Softw. Technol.*, vol. 41, no. 9, pp. 589–595, 2002, doi: 10.1016/S0950-5849(99)00022-1.

[12] D. Ferrucci, R. L. Grossman, and A. Levas, "PMML and UIMA based frameworks for deploying analytic applications and services," *4th Int. Work. Data Min. Stand. Serv. Platforms*, pp. 14–26, 2006, doi: 10.1145/1289612.1289614.

[13] J. Chaves, C. Curry, R. L. Grossman, D. Locke, and S. Vejcik, "Augustus: The design and architecture of a PMML-based scoring engine," *4th Int. Work. Data Min. Stand. Serv. Platforms*, pp. 38–46, 2006, doi: 10.1145/1289612.1289616.

[14] A. Guazzelli, M. Zeller, W. C. Lin, and G. Williams, "PMML: An open standard for sharing models," *R J.*, vol. 1, no. 1, pp. 60–65, 2009, doi: 10.32614/rj-2009-010.

[15] R. Pechter, "What's PMML and what's new in PMML 4.0?," *ACM SIGKDD Explor. Newsl.*, vol. 11, no. 1, pp. 19–25, 2009, doi: 10.1145/1656274.1656279.

[16] A. Guazzelli, K. Stathatos, and M. Zeller, "Efficient

deployment of predictive analytics through open standards and cloud computing," *ACM SIGKDD Explor. Newsl.*, vol. 11, no. 1, pp. 32–38, 2009, doi: 10.1145/1656274.1656281.

[17] K. K. Das, E. Fratkin, A. Gorajek, K. Stathatos, and M. Gajjar, "Massively parallel in-database predictions using PMML," *Proc. ACM SIGKDD Int. Conf. Knowl. Discov. Data Min.*, pp. 22–27, 2011, doi: 10.1145/2023598.2023601.

[18] D. Sottara, P. Mello, C. Sartori, and E. Fry, "Enhancing a production rule engine with predictive models using PMML," *Proc. ACM SIGKDD Int. Conf. Knowl. Discov. Data Min.*, pp. 39–47, 2011, doi: 10.1145/2023598.2023604.

[19] A. Guazzelli *et al.*, "The PMML Path towards True Interoperability in Data Mining," pp. 1–7, 2011.

[20] H. Hamad, M. Saad, and R. Abed, "Performance evaluation of restful web services for mobile devices," *Int. Arab J. e-Technology*, vol. 1, no. 3, pp. 72–78, 2010.

[21] S. Kumari and S. K. Rath, "Performance comparison of SOAP and REST based Web Services for Enterprise Application Integration," *2015 Int. Conf. Adv. Comput. Commun. Informatics, ICACCI 2015*, pp. 1656–1660, 2015, doi: 10.1109/ICACCI.2015.7275851.

[22] "PMML 4.4.1 - General Structure." http://dmg.org/pmml/v4-4-1/GeneralStructure.html (accessed Oct. 11, 2021).

[23] "Data Mining Group." http://dmg.org/ (accessed Oct. 11, 2021).

[24] "Data Mining Group - PMML Powered." http://dmg.org/pmml/products.html (accessed Oct. 11, 2021).

[25] R. T. Fielding, "Architectural Styles and the Design of Network-based Software Architectures," University of California, 2000.

[26] "Flask (web framework) - Wikipedia." https://en.wikipedia.org/wiki/Flask_(web_framework) (accessed Oct. 11, 2021).

[27] "Python Developers Survey 2020 Results | JetBrains: Developer Tools for Professionals and Teams." https://www.jetbrains.com/lp/python-developers-survey-2020/ (accessed Oct. 12, 2021).

[28] "Apache JMeter - User's Manual: Glossary." https://jmeter.apache.org/usermanual/glossary.html (accessed Oct. 11, 2021).

Hybrid Feature Selection Based on Whale Optimization Algorithm and Particle Swarm Optimization

M. S. UZER[1] and O. INAN[2]

[1] Electronics and Automation, Ilgın Vocational School, Selcuk University, Konya/Turkey, msuzer@selcuk.edu.tr
[2] Computer Engineering, Faculty of Technology, Selcuk University, Konya/Turkey, oinan@selcuk.edu.tr

Abstract **- Swarm-based optimization methods are frequently preferred in many areas such as feature selection. One of them, Whale Optimization Algorithm, has been very popular recently. In this study, a binary hybrid feature selection method named BWPFS, consisting of Whale optimization algorithm (WOA) and Particle Swarm Optimization (PSO), was developed. The purpose of this method is to select the most important features in the diagnosis of diseases. In this way, it is aimed to increase the diagnostic success by processing less data and to reduce the size of the dataset. After feature selection, Linear Discriminant Analysis (LDA) was used as a classifier. To measure the success of the proposed BWPFS method in medical data, Breastcancer, HeartEW and Lymphography datasets from the UCI database were used and compared with the literature. The mean classification success was 97% for Breastcancer, 87% for HeartEW, and 90% for Lymphography, respectively. According to the results, it seems that the proposed method provides for the diagnosis of medical data.**

Keywords **- WOA, Feature selection, PSO, Classification**

I. INTRODUCTION

Today, with the development of technologies in data collection systems, a large amount of data can be produced. Data are produced from many different fields, as well as in the medical field, thanks to the devices and methods developed. The processing of these medical data is of even greater importance for the diagnosis of diseases. Advanced computer systems and computer software are needed in order to process these data and obtain successful results as a result. In order to reduce the processing load of the computer systems used and to increase the success of computer software, it is necessary to pre-process the data. One of these data preprocessing steps is feature selection. This process is achieved by selecting features that are more meaningful from the data, that is, that contribute more to the classification. One of the filtering or wrapper methods can be used to achieve this. The wrapper method generally gives better results than filtering methods because it requires learning and evaluating the classifier for the selection of a subset of candidates [1]. In addition, since the number of data decreases after feature selection, the processing load of computer systems is reduced. Therefore, as less data is used, the time of classification is shortened.

WOA is an optimization algorithm that is inspired by nature [2, 3]. It uses meta-heuristic techniques as Simulated Annealing (SA), Particle Swarm Optimization (PSO), Tabu Search, Ant Colony Optimization (ACO), Genetic Algorithm (GA), Artificial Neural Networks (ANN) in the literature. Moreover, more recent or less studied meta-heuristics are Bee Colony Algorithm (BCA), Harmonic Search Algorithm and Kangaroo Algorithm [3, 4].

In this study, a more efficient feature selection method has been developed by using a hybrid of binary optimization method consisting of WOA and PSO. Three data sets were used for the evaluation of the proposed method. The WOA, PSO and LDA methods used are explained in Section 2, while the proposed method is explained in Section 3. The results obtained from the developed BWPFS method and the comparison of these results with literature studies are given in Section 4. The proposed method is evaluated in Section 5.

II. PRELIMINARIES

A. Whale Optimization Algorithm (WOA)

Metaheuristic optimization algorithms have a wide range of use in recent years, as they can produce solutions to problems in different fields. Whale optimization algorithm, one of them, was proposed by Mirjalili and Lewis in 2016. WOA is inspired by the techniques used by humpback whales for bubbling and squeezing the prey into a bubble spiral [2].

Humpback whales collect prey, which usually consists of small fish communities, thanks to air bubbles, then rise to the surface and narrow the circle of target fish by making the movement of narrowing the bubble circle. The representation of hunting whales is given in Figure 1 [2]. WOA consists of the following sections: encircling prey, bubble-net attacking method, and searching for prey.

1) Encircling prey

The location of prey is determined by humpback whales and so they wrap prey. The position of prey is the optimum solution in this algorithm. Other solutions are updated according to the best solution value determined to reach this optimum value. Eq. (1) and (2) are mathematically given this behavior.

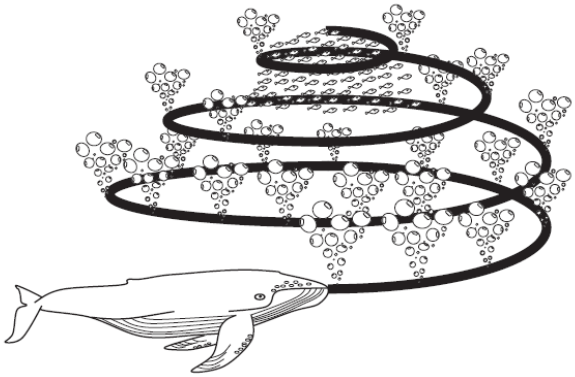

Figure 1: The representation of hunting whales [2]

$$\vec{D} = \left| \vec{C} . \vec{X}^*(t) - \vec{X}(t) \right| \quad (1)$$

$$\vec{X}(t+1) = \left| \vec{X}^*(t) - \vec{A} . \vec{D} \right| \quad (2)$$

where X refers to the position vector, X^* is the best solution position vector, t represents the current iteration.

$$\vec{A} = 2\vec{a} . \vec{r} - \vec{a} \quad (3)$$

$$\vec{C} = 2 . \vec{r} \quad (4)$$

The vectors A and C are coefficient vectors in Eqs. (3) and (4) are obtained using r that is a random vector between 0 and 1, and a that is linearly decreasing value a from 2 to 0. The a used in Eq. (3) is obtained by the following formula:

$$a = 2 - t \frac{2}{MaxIter} \quad (5)$$

In Eq. (5), the number of iterations is denoted as t, the maximum number of iterations is denoted as *MaxIter*. The path that has a spiral shape is calculated from the distance between the solution of X and X^* before the spiral equation between the current solution and the best leading solution is composed. While X is denoted solution, X^* is denoted leading solution.

2) Bubble-net attacking method

This method consists of decreasing encircling movement and spiral movement as seen in Figure 2. The decreasing encircling movement takes place by decreasing a in Eq.(3). The spiral movement occurs by Eq.(6).

$$\vec{X}(t+1) = D' . e^{bl} . \cos(2\pi l) + \vec{X}^*(t) \quad (6)$$

In Eq.(6), b denotes shape of the spiral, $\vec{D'}$ is the distance between a whale X and a prey, l is a random number between -1 and 1[5].

Whales randomly choose one of these two shaped paths and this situation is symbolized in Eq.(7).

$$\vec{X}(t+1) = \begin{cases} Use\ Eq.2 & if\ (p < 0.5) \\ Use\ Eq.6 & if\ (p \geq 0.5) \end{cases} \quad (7)$$

3) Search for prey

Normally, whale randomly search the prey. Thus, vector A is used, which generates random values. Mathematically, this mechanism is given in Eq. (8) and (9) [5].

$$\vec{D} = \left| \vec{C} . \vec{X}_{rand} - \vec{X} \right| \quad (8)$$

$$\vec{X}(t+1) = \vec{X}_{rand} - \vec{A} . \vec{D} \quad (9)$$

Eq.(1) is used in case of $|A| < 1$ and Eq.(9) is used in case of $|A| > 1$. In Figure 3, the pseudocode of the WOA algorithm is presented.

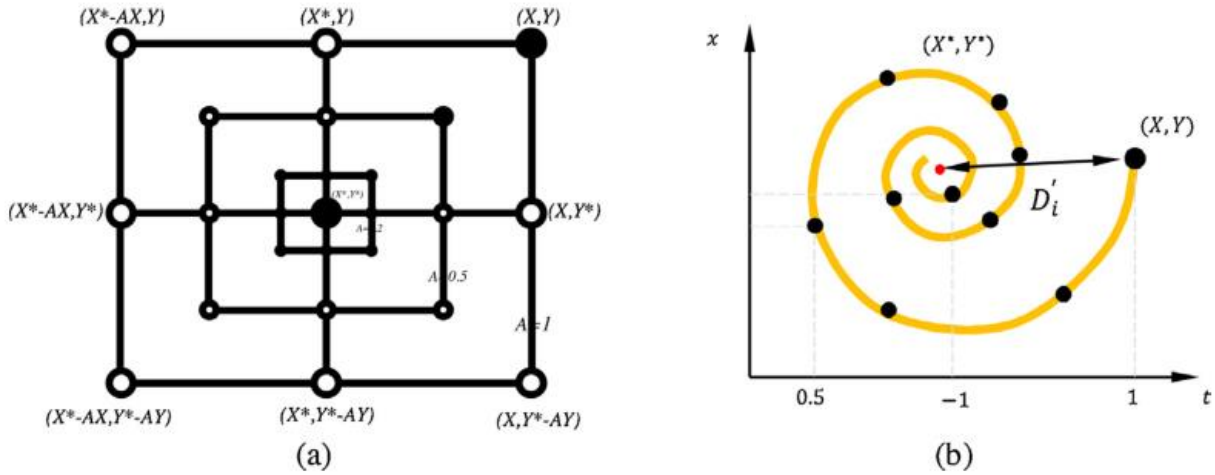

Figure 2: (a) Decreasing encircling movement (b) Spiral movement [5]

```
Generate Initial Population Xi (i = 1, 2,..., n)
Calculate the objective value of each solution
X*=the best solution
while (t < Max_Iteration)
        for each solution
                Update a, A, C, l, and p
                If1 (p<0.5)
                        if2 (|A| < 1)
                                Use Eq. (2) to update the position of the current solution
                        else if2 (|A| ≥1)
                                Select a random solution (x_rand)
                                Use Eq. (9)
                        end if2
                else if1 (p≥ 0.5)
                        Update the position of the current search by the Eq. (6)
                end if1
        end for
        Check if any solution goes beyond the search space and amend it
        Calculate the fitness of each solution If there is a better solution, update X*
        t=t+1
end while
return X*
```

Figure 3: Pseudocode of the WOA algorithm [2]

B. Particle Swarm Optimization (PSO)

PSO is an optimization algorithm inspired by the behavior of herd animals developed by Kennedy and Eberhart [6]. In PSO, each particle that consists of a velocity and position vector represents the possible solution. Each particle scans around the best solution in the search space and know the best position information of all parts. According to Eq.(10), velocity vector is updated. According to Eq.(11), position vector is updated [7]. Detailed description of the PSO method is given in [8].

$$v_i^{k+1} = v_i^k + c_1 r_1 (Pbest_i^k - x_i^k) + c_2 r_2 (gbest - x_i^k) \quad (10)$$

$$x_i^{k+1} = x_i^k + v_i^{k+1} \quad (11)$$

C. Linear Discriminant Analysis (LDA)

LDA is used for dimensionality reduction and data classification. LDA tries to find a linear combination of features that can separate the classes [9].

$$S_b = \frac{1}{N}\sum_{i=1}^{c} N_i (\overline{x_i} - \overline{x})(\overline{x_i} - \overline{x})^T$$
$$S_W = \frac{1}{N}\sum_{i=1}^{c}\sum_{s=1}^{N_i} (x_s^i - \overline{x_i})(x_s^i - \overline{x_i})^T \quad (12)$$

As given in Eq (12), S_b is the between-class scatter matrix and S_w is the within-class scatter matrix [10]. LDA tries to solve the following optimal problem [10].

$$\max_w \frac{tr(W^T S_b W)}{tr(W^T S_w W)} \quad (13)$$

where W is optimal projection transformation matrix. W is maximized the ratio of between-class scatter to within-class scatter in the projected space of $W \in R^{n\times d}$ ($d \le n$) [10].

In this study, LDA is used in two different places for two different purposes. First, it is applied to the objective function of the optimization algorithm used in feature selection. Secondly, it was also used to measure the classification accuracies of the selected features.

III. The Proposed Method (BWPFS)

A binary hybrid method consisting of WOA and PSO is proposed to select more relevant features that will contribute more to the accuracy of the classification. This developed feature selection method is named BWPFS.

X_{t+1} has taken as x_1 in Eq. (9) for the feature selection. It can be converted to Eq. (14) so that the position update works in binary space [7, 11].

$$x_d^{t+1} = \begin{cases} 1 & if\ sigmoid(x_1) \ge rand \\ 0 & otherwise \end{cases} \quad (14)$$

In Eq. (14), x_d^{t+1}, the position of iteration t in dimension d, is updated as 0 or 1, *rand* is a randomly chosen number between 0 and 1. In Eq. (15), *sigmoid(a)* is given [11]:

$$sigmoid(a) = \frac{1}{1+e^{-10(x-0.5)}} \quad (15)$$

According to Eq. (16), the position and velocity are regenerated [12].

$$v_i^{k+1} = w * (v_i^k + c\, r(x_1 - x_i^k)) \quad (16)$$

Note that in Eq. (16) the best solution x_1 are updated according to Eq. (17).

$$x_i^{k+1} = x_d^{t+1} + v_i^{k+1} \quad (17)$$

In Eq. (17), x_d^{t+1} and v_i^{k+1} are formulated in Eq. (14) and Eq. (16), respectively.

The fitness function of the binary optimization algorithm used for the proposed BWPFS is given in equation Eq. (18).

$$fitness = \alpha \rho_R(D) + \beta \frac{|S|}{|T|} \quad (18)$$

where $\rho_R(D)$ is the error rate of the LDA classifier, $|T|$ is the number of all features in the dataset, $|S|$ is the number of selected features. While α is a parameter with a value between 0 and 1, β is a parameter that is equal to $(1 - \alpha)$ [7, 11]. β is taken as 0.01 in our application. The number of search agents is10 and the maximum number of iterations is 100 in the proposed method. The flowchart of the proposed BWPFS is given in Figure 4.

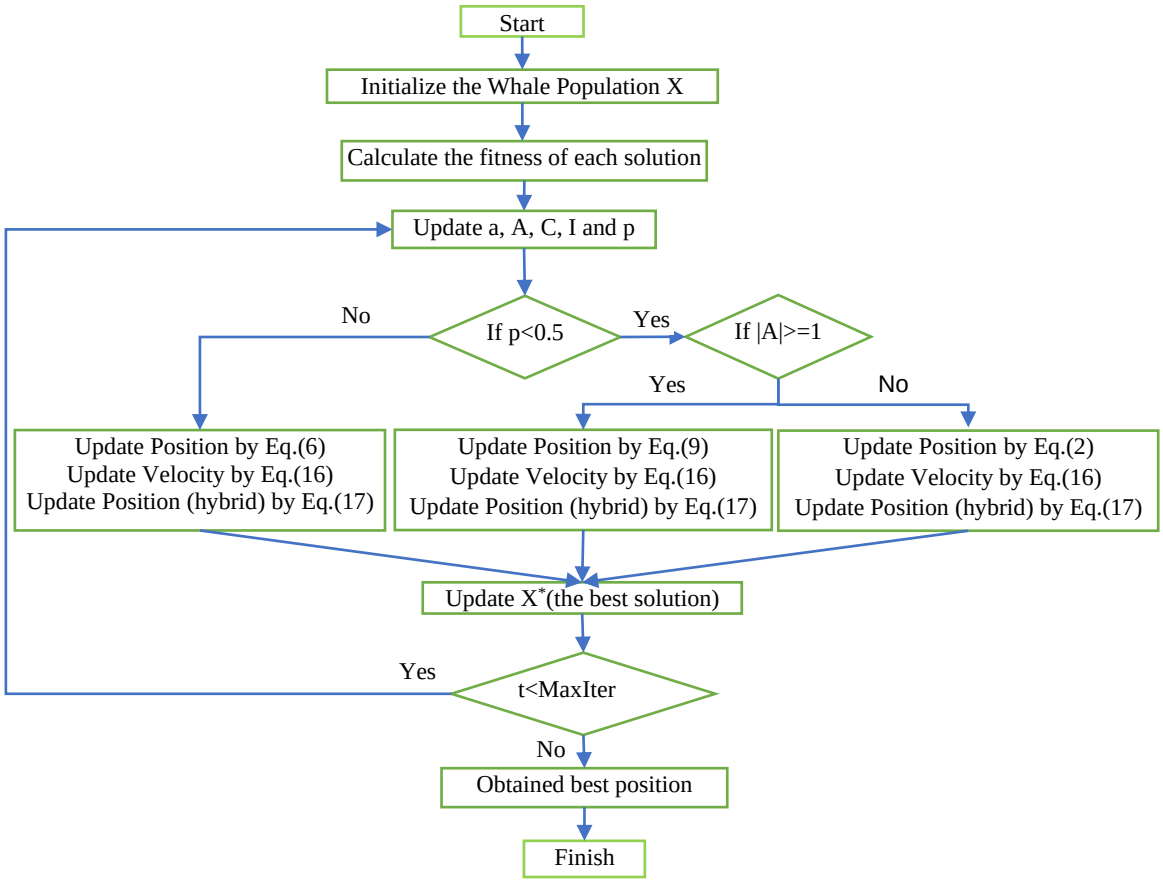

Figure 4: Flowchart of the proposed BWPFS

In the BWPFS method, important features were determined by using three medical datasets. The dataset consisting of these features was given to the LDA classifier to provide a more accurate diagnosis of diseases. In order to compare with similar studies with swarm optimization algorithms in the literature, the rate of training and testing was set to 50%.

IV. The Proposed Method Results and Discussion

The characteristics of the Breastcancer, HeartEW and Lymphography datasets used in the BWPFS method are shown in Table 1. The average results obtained by running the proposed BWPFS method and classification together 10 times were compared with the literature.

Comparison of average classification accuracies is shown in Table 2. It has been seen that the proposed BWPFS gives the same or higher results with the literature studies in terms of classification accuracy. Average fitness function comparisons are given in Table 3. Comparison of the average numbers of selected features is given in Table 4. All operations were carried out by the computer with Intel Core i5 10300H@2.50 GHz processor, 8 GB memory, 64 bit operating system.

Table 1. Properties of the data sets used for the BWPFS method

Dataset	# Features	# İnstances
Breastcancer	9	699
HeartEW	13	270
Lymphography	18	148

Table 2. The comparison of the classification accuracies between the proposed BWPFS and literature studies

Dataset	PSO [13]	ALO [13]	GA [13]	WOASAT-2 [13]	BWPFS
Breastcancer	0.95	0.96	0.96	0.97	**0.97**
HeartEW	0.78	0.83	0.82	0.85	**0.87**
Lymphography	0.69	0.79	0.71	0.89	**0.90**

Table 3. Mean fitness function comparisons between the proposed BWPFS and literature studies.

Dataset	PSO [13]	ALO [13]	GA [13]	WOASAT-2 [13]	BWPFS
Breastcancer	0.03	0.02	0.03	0.04	0.03
HeartEW	0.15	0.12	0.14	0.16	0.13
Lymphography	0.19	0.14	0.17	0.11	0.11

Table 4. The comparison of average numbers of selected feature between the proposed BWPFS and literature studies

Dataset	PSO [13]	ALO [13]	GA [13]	WOASAT-2 [13]	BWPFS
Breastcancer	5.72	6.28	5.09	4.2	5.2
HeartEW	7.94	10.31	9.49	5.4	5.8
Lymphography	8.98	11.05	11.05	7.2	9.5

V. CONCLUSION

In this study, a more efficient binary hybrid feature selection method called BWPFS was created by using WOA and PSO, which are very popular optimization methods. The proposed method was tested on 3 medical datasets from UCI. With the proposed feature selection, unnecessary or useless features have been discarded and thus the number of features in the data set has been reduced to approximately half. The features selected by the proposed method increased the classification success. Processing less data by selecting the features naturally shortened the classification time. Selected features are classified by LDA. The classification system consisting of the proposed feature selection was run 10 times. For the proposed feature selection, the average number of features, average fitness function and average classification success values were calculated. In this system, which we tested using medical datasets, the mean classification success was 97% for Breastcancer, 87% for HeartEW, and 90% for Lymphography, respectively. The obtained results were compared with the literature and the results appeared to be promising.

ACKNOWLEDGMENT

The authors are grateful to Selcuk University Scientific Research Projects Coordinatorship for support of the manuscript.

REFERENCES

[1] R. Kohavi, and G. H. John, “Wrappers for feature subset selection,” *Artificial Intelligence,* vol. 97, no. 1-2, pp. 273-324, Dec, 1997.

[2] S. Mirjalili, and A. Lewis, “The Whale Optimization Algorithm,” *Advances in Engineering Software,* vol. 95, pp. 51-67, May, 2016.

[3] A. Karadeniz, and Y. Çelik, “Whale Optimization Algorithm for Numerical Constrained Optimization,” *Academic Platform Journal of Engineering and Science,* vol. 8, no. 3, pp. 547-554.

[4] M. C. Akkoyunlu, and O. Engin, “Kesikli Harmoni Arama Algoritması İle Optimizasyon Problemlerinin Çözümü: Literatür Araştırması,” *Selçuk Üniversitesi Mühendislik, Bilim ve Teknoloji Dergisi,* vol. 26, no. 4, pp. 140-148, 2011.

[5] M. Mafarja, and S. Mirjalili, “Whale optimization approaches for wrapper feature selection,” *Applied Soft Computing,* vol. 62, pp. 441-453, Jan, 2018.

[6] J. Kennedy, and R. Eberhart, "Particle swarm optimization." pp. 1942-1948.

[7] Q. Al-Tashi, S. J. A. Kadir, H. M. Rais, S. Mirjalili, and H. Alhussian, “Binary Optimization Using Hybrid Grey Wolf Optimization for Feature Selection,” *Ieee Access,* vol. 7, pp. 39496-39508, 2019.

[8] F. Marini, and B. Walczak, “Particle swarm optimization (PSO). A tutorial,” *Chemometrics and Intelligent Laboratory Systems,* vol. 149, pp. 153-165, Dec 15, 2015.

[9] K. Al-Dulaimi, V. Chandran, K. Nguyen, J. Banks, and I. Tomeo-Reyes, “Benchmarking HEp-2 specimen cells classification using linear discriminant analysis on higher order spectra features of cell shape,” *Pattern Recognition Letters,* vol. 125, pp. 534-541, Jul 1, 2019.

[10] C. N. Li, Y. H. Shao, Z. Wang, N. Y. Deng, and Z. M. Yang, “Robust Bhattacharyya bound linear discriminant analysis through an adaptive algorithm,” *Knowledge-Based Systems,* vol. 183, Nov 1, 2019.

[11] E. Emary, H. M. Zawba, and A. E. Hassanien, “Binary grey wolf optimization approaches for feature selection,” *Neurocomputing,* vol. 172, pp. 371-381, Jan 8, 2016.

[12] N. Singh, and S. Singh, “Hybrid algorithm of particle swarm optimization and grey wolf optimizer for improving convergence performance,” *Journal of Applied Mathematics,* vol. 2017, 2017.

[13] M. M. Mafarja, and S. Mirjalili, “Hybrid Whale Optimization Algorithm with simulated annealing for feature selection,” *Neurocomputing,* vol. 260, pp. 302-312, Oct 18, 2017.

A Review on Predicting Evolution of Communities

A. KARATAŞ[1] and S. ŞAHİN[1]

[1] İzmir Institute of Technology, İzmir/Turkey, arzum.karatas@iyte.edu.tr
[1] İzmir Institute of Technology, İzmir/Turkey, serapsahin@iyte.edu.tr

***Abstract* – In recent years, research on dynamic networks has increased as the availability of data has grown tremendously. Understanding the dynamic behavior of networks can be studied at the mezzo-scale (e.g., at the community level), as communities are the most informative structure in nonrandom networks and also evolve over time. Tracking the evolution of communities can provide evolution patterns to predict their future development. For example, a community may either grow into a larger community, remain stable, shrink into a smaller community, split into several smaller communities, or merge with another community. Predicting these evolutions is one of the most difficult problems in social networks. Better predictions of community evolution can provide useful information for decision support systems, especially for group-level tasks. So far, this problem has been studied by some researchers. However, there is a lack of a survey/review of existing work. This has prompted us to conduct this study. In this paper, we first categorize the existing works according to their methodological principles. Then, we focus on the works that use machine learning classifiers for prediction in this decade as they are in majority. We then highlight open problems for future research. In this way, this paper provides an up-to-date overview and a quick start for researchers and developers in the field of community evolution prediction.**

***Keywords* – Community, Evolving Communities, Predicting Evolution of Communities.**

I. INTRODUCTION

With the advances in computerization and technology in dynamic networks such as social networks, mobile networks, collaborative networks, etc., huge amounts of data have been created. Thus, the availability of data has increased tremendously, consequently the research on dynamic networks has also increased. Understanding the dynamic behavior of networks can be elaborated at the community (mezzo-scale) level, as communities are the most meaningful structure in nonrandom networks.

A community is a subgroup of at least three members that are more closely connected than the rest of the network. Communities in a dynamic network evolve over time. Therefore, the community may go through some evolutionary events. For example, a community may be stable, become larger or smaller in terms of the size of its members, split into several communities, or merge into a new community. Tracking the evolution of communities means observing the evolutionary behavior of communities over a period of time. Predicting community evolution is the task of predicting the most likely evolutionary event for communities based on their history of tracked communities. Tracking and predicting these evolutionary events can provide valuable information for decision support systems, especially for group-level tasks. For example, tracking and predicting the evolution of groups of criminals can be very useful in criminology.

In the literature, many researchers have addressed the prediction of community evolution. Unfortunately, there is no work that classifies these works. However, such a classification would both organize the diversity of existing work and promote development in the field. This motivated us to write this paper.

The main contributions of this paper are (i) a categorization of existing community evolution prediction methods according to their techniques, (ii) an overview of supervised learning based methods due to the majority in this field, (iii) highlighting the open research areas for future researchers.

The rest of this paper is organized as follows. Section II introduces the basic concepts of community evolution analysis and the problem of community evolution prediction. Our proposed classification of existing methods for predicting community evolution is presented in Section III. Then, a recent overview of supervised learning based methods is presented in Section IV. Then, open problems for supervised learning based methods are presented in Section V to motivate potential researchers. Finally, the paper concludes with a brief discussion of current research directions in Section VI.

II. PRELIMINARIES

A. Basic Concepts

Nonrandom networks contain an inherent community structure. The widely accepted definition of a community is that a subgroup within the network is strongly connected to each other and has a loose connection to the rest of the network. Communities in the network may be overlapping (multiple communities may have members in common) or disjoint (communities have no members in common). Detecting the hidden communities in the network is called community discovery. In the literature, there are many methods for detecting disjoint or overlapping communities, such as Louvain [1], Leiden [2], and CPM [3].

When networks are dynamic, communities exhibit evolutionary behavior over time. The possible evolutionary events for an existing community are "grow", "shrink", "continue", "merge", "split", and "dissolve". That is, a

community becomes larger/smaller/stable in terms of its membership, it may merge into a new community, split into smaller communities, or disappear. Observing the evolutionary behavior of communities in a given time interval is called tracking the evolution of communities. First, a dynamic network is represented as a series of snapshots. Then, a two-step methodology (e.g., (i) independent detection of communities in each snapshot and (ii) matching of detected communities) is usually applied for tracking. Some communities appear in each snapshot (e.g., consecutive evolution), while others do not (e.g., nonconsecutive evolution). Figure 1 illustrates the types of community evolution, with communities represented by circles. In the figure, the community in the blue circles evolves consecutively, while the community in the purple circles evolve nonconsecutively.

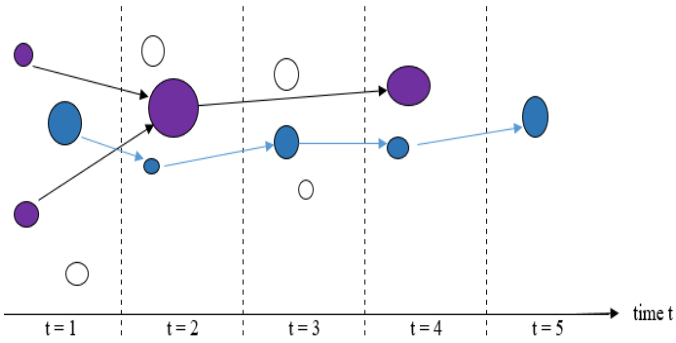

Figure 1: Illustration of evolution types of communities

B. *Problem Definition*

Let $G_t = (V_t, E_t)$ be a static graph representing a snapshot of a static network at time t, where V_t represents the vertices of the network and E_t represents the set of edges, and let D be a dynamic network represented by a time-ordered sequence of static networks such as $D = \{G_1, G_2, \cdots, G_t\}$ where t is the total number of static networks.

We define a partition $\{C_t^1, C_t^2, \cdots, C_t^k\}$ representing the discovered communities on each G_t, where a community is a subset of densely connected members instead of the rest of the G_t using an existing community detection method.

For each community C, a sequence of communities reflecting evolution over time is discovered at each time step using an existing method for tracking community evolution. This task requires that the communities in ascending time steps be matched to represent the evolution of the communities. Therefore, matching communities must be similar in terms of their nodes. Jaccard similarity (the ratio of the number of common members to the number of total members of two compared communities) is most commonly used to determine their similarity.

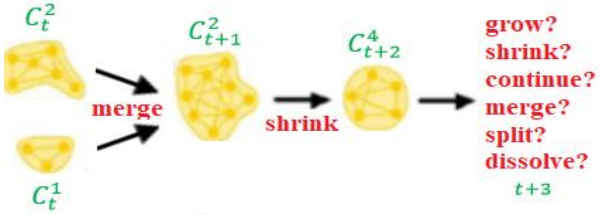

Figure 2: Predicting evolution of communities

Figure 2 illustrates the process of predicting community evolution. In the figure, C^1 and C^2 merge at time step *t* to C^2 at time step *t+1*, and C^2 has lost some of its members at time step *t+1* and shrinks consecutively at time step *t+2*. The prediction process takes this sequence and generates the most likely outcome as an evolution event (e.g., shrink, grow, merge, split, continue or dissolve).

The problem is informally defined as predicting future evolution events for matching communities based on their alignments over time.

III. CLASSIFICATION OF THE EXISTING PREDICTION METHODS FOR COMMUNITY EVOLUTION

There is no classification of predictive methods for community evolution in the literature. However, such a classification is helpful and organizes the variety of existing methods in this field. Thus, such a classification helps the developments in this field. Therefore, we propose a classification of existing prediction methods for community evolution according to the techniques used. There are three main classes, which are schematically shown in Figure 3:

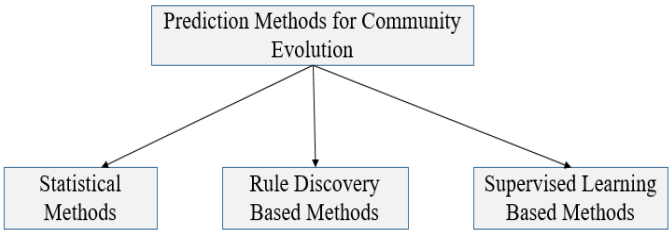

Figure 3: Classification chart of the existing prediction methods for community evolution

- Statistical Methods
- Rule Discovery Based Methods
- Supervised Learning Methods

Statistical methods provide a formal approach to modeling and predicting the evolution events of communities based on their history (e.g., aligned/matching communities) [4]. Rule discovery based methods first look for patterns in the time series representation of communities, then create rules for evolutionary events based on these patterns, and then make predictions based on these rules [5]. Supervised learning based methods first determine features to represent communities and then train supervised classifiers based on these features and the evolutionary history of the communities.

IV. SUPERVISED LEARNING BASED PREDICTION METHODS

The most common strategy for predicting community evolution is to use supervised classifiers. Methods using this strategy follow a two-step methodology: (i) analyzing the

evolution of communities and (ii) applying supervised classifiers based on selected features of communities for predetermined evolution events. Work in the literature over the last decade (between 2011 and 2021) is reviewed. Related work is summarized below.

In their work, Brodka et al [6] present and evaluate a supervised learning method for predicting the evolution of communities with respect to six events of community evolution such as growing, shrinking, continuing, merging, splitting and dissolving. They use the Group Evolution Detection method (GED) [7] to detect events between successive time steps and construct event sequences to describe the evolution of a given community. Each event sequence consists of the member sizes and events of all three previous communities. These sequences serve as input to the classifiers such as Naïve Bayes, Decision Tree, Random Forest and others provided by the data mining software WEKA [8] to predict the next event for a given community.

İlhan and Öğüdücü [9] propose a new approach to predict the next event of a community using a time series ARIMA model. In their study, community events are predicted by predicting community characteristics. The feature values are used to classify the possible events. The authors [10] propose a framework for detection of most prominent subset of community features to predict evolution of communities. They assert that their framework requires extraction of minimal number of community features.

Takaffoli et al. [11] use a two-step technique to predict the near future of a community through supervised learning. In this technique, they first decide whether the community survives, and then make the prediction whether the community survives. They diversify the type of features by using not only structural features of the community, but also features of influential members, temporal changes in features, contextual attributes, and features of past events. They consider only evolutionary sequences that have only two lengths.

Saganowski et al. [12] present two methods for predicting the following evolution event of a community. The first method uses the Stable Group Changes Identification (SGCI) method [13] and the other uses the GED method [7]. They use the CPM method [3] for community detection. The authors use evolution chain lengths, group features (e.g., size, density, leadership, etc.), node features (e.g., total degree, in-degree, etc.), and group aggregation (e.g., sum, average, minimum, and maximum). They then perform feature selection using ordinary (J48 and Random Forest) and ensemble classifiers (AdaBoost and Bagging). They conclude that longer group history leads to better prediction and the most recent group history has the largest impact on the next community change.

Diakidis et al. [14] address the problem of predictability of community evolution as a task of supervised learning. However, they predict four events of community evolution, namely continuation, shrinking, growth and dissolution. They use both sequential (e.g., Conditional Random Fields with Linear Chain and with Skip Chain) and ordinary classifiers (e.g., Naïve Bayes, Bayes Net, Logistic Regression, SVM, etc.) for the prediction task and compare the performance of the classifiers. These classifiers were trained on structural (e.g., size, density, etc.), content (topic diversity with TF-IDF), and contextual features (e.g., number of hashtags, size of tweets, and number of tweets with promotional URLs, etc.), as well as the previous state of a community as features for Twitter. They conclude that the sequential features are better than the ordinary ones because they also capture the past information first.

Pavlopoulou et al [15] present a framework for predicting community evolution. They study how past evolutions of a community affect the prediction of four evolution events such as growth, continuation, shrink, and dissolution. They use some structural (e.g. density, cohesion, diameter, etc.) and temporal features (e.g. lifespan, aging, join nodes ratio and left nodes ratio, etc.) to predict through supervised learning. They also specify the number of ancestors to be used for computing the temporal features, e.g., two or four ancestors according to their dataset from Mathematics Stack Exchange. They used the GED method [4] to track the evolution of the community, and Support Vector Machine (SVM) with RBF kernel (an exponential kernel) as a classifier for predicting the next evolution event. However, they did not consider merge and split events.

Dakiche et al [16] proposed a method for predicting the evolution of communities by capturing the interdependence of the rates of change of characteristics describing a community over time instead of the actual values. They considered only the rates of change in the structural and characteristic traits of influential members of a community. They examined the length of evolution sequences and concluded that the length of the sequences directly affects the amount and quality of information obtained. However, the quality of information may decrease with long sequences.

Dakiche et al. [17] propose a new framework for studying the distribution of activities over time to enable proper partitioning of the network. They claim that a properly partitioned network enables more accurate prediction of community events. After applying their novel network partitioning method, they proceed with a simple prediction method. That is, they apply the method GED [7] to detect group evolutions. Then they proceed to the prediction part. For this task, they specify characteristics. In their study, structural (e.g., density, cohesion, size ratio, etc.) and influential member characteristics (e.g., average leadership degree, average leadership closeness, and average leadership eigenvector) are used. Later, well-known supervised learning classifiers such as J48, Random Forest, Bagging and SVM were used.

Table 1 summarizes related work, with some important criteria listed in the first column. For tracking, they mainly use GED [7], SCGI [13] and some special methods developed by them. In the *Prediction Manner* row, the studies make predictions for consecutively or nonconsecutively evolving networks or both, where *CE* is for consecutively evolving communities and *NE* is for nonconsecutively evolving communities. Only the ML model of Takaffoli et al. [11] can predict the next stage of a community either at the next time step or at later time steps. While the method of Brodka et al. [6], Saganowski et al. [12], the method of İlhan and Ögüdücü [9], and the two methods of Dakiche et al. [16, 17] makes

prediction for all possible events of community evolution, others cannot characterize all events for prediction. For software attributes, Weka [8] is used for developing, training and testing ML models, CFinder is used for applying CPM and MODEC for community tracking, and CRFSuite is used for sequential classifiers such as Conditional Random Fields (CRF) [18].

Table 1: Related works using supervised learning in last decade

	Related Work							
Attributes	Brodka et al. [6]	İlhan& Öğüdücü [9]	Takaffoli et al. [11]	Saganowski et al. [12]	Diakidis et al. [14]	Pavlopoulou et al. [15]	Dakiche et al. [16]	Dakiche et al. [17]
Year	2012	2013	2014	2015	2015	2017	2019	2021
Tracking Method	GED [7]	A specific method	MODEC [19]	SCGI [13]	GED[7]	GED[7]	GED[7]	GED[7]
Prediction Manner	CE	CE	CE &NE	CE	CE	CE	CE	CE
Unpredicted events	None	None	Continue	None	Merge Split	Merge Split	None	None
Software	CFinder[1] Weka[2]	Weka	MODEC [19] Weka	CFinder Weka	CFinder Weka CRFsuite [3]	Weka	CFinder Weka	Weka

V. OPEN PROBLEMS FOR SUPERVISED LEARNING BASED PREDICTION METHODS

Predicting the evolution of communities is a challenging subject. In this section, we only address the research opportunities that arise from prediction methods that use supervised classifiers, as these are the most commonly used in this area.

Public datasets containing the ground truth evolution events for predicting community evolution are not available. The works in Table 1 use the results of tracking methods as ground truth. However, there is no tracking method that works with 100% accuracy for datasets. Therefore, we need datasets that tell the truth as a benchmark.

In addition, it is necessary to develop a *methodology* for creating the ground truth dataset for a given dataset.

Machine learning is a very powerful tool when the data set is large. As we have more and more data to analyze, we should take advantage of it. That is, there is a need to find evolutionary patterns of communities in the *data without labeling them*.

With the emergence and proliferation of the mobile web and consequently mobile networks, we propose a model/method for predicting the evolution of communities in dynamic *mobile networks*. This will provide the ability to analyze these datasets in a limited-memory environment, which will contribute to the areas of mobile networks, tracking, and community evolution prediction.

VI. CONCLUDING DISCUSSION

Communities are the most meaningful structure in real networks. Knowing their evolution and making predictions about their future provides very useful information for decision support systems in many domains. Therefore, many researchers are concerned with these issues.

Table 2 summarizes our proposed classes, some related works, their limitations and possible research areas. Since existing statistical methods for predicting community evolution only consider topological features, possible future solutions should diversify the types of features, such as temporal features, content-based features, and the features of influential members, rather than only structural features. In addition, solutions must also cover the prediction of dissolution events.

As it is seen from the table, existing rule discovery based methods discover prediction patterns/rules in time series. However, unsupervised learning based methods are better at discovering patterns/rules in data, even if they are not time series. Therefore, unsupervised machine learning methods can be used to develop possible solutions for features. Since existing methods only consider structural features, the solutions can also consider content-based features.

As mentioned in Section V, supervised learning methods require public benchmark datasets that contain evolution events with evolving communities, or a tool to generate these benchmark datasets. Therefore, such datasets or tools can be developed. Since supervised learning methods require labeled data to be trained, potential feature solutions can also be developed with unsupervised learning. In addition, mobile networks are an active research area, and developing a

[1] http://www.cfinder.org/
[2] https://www.cs.waikato.ac.nz/ml/weka/
[3] http://www.chokkan.org/software/crfsuite/

model/method that works with dynamic mobile networks can be considered as a research direction.

Since there is no taxonomy of existing methods for predicting community evolution, we propose a classification in this paper. Since most of the works belong to supervised learning based methods, we focus on them by reviewing related works and giving an outlook on open research problems. Finally, we give a discussion. Thus, this paper provides an up-to-date overview and a quick start for researchers and developers in the field of community evolution prediction.

Table 2: Summary of prediction method classes and research directions

Prediction Class	Some Example works	Limitations	Research Directions
Statistical Methods	Tajeuna et al. [4]	• Disregard dissolution of communities • Regard only topological features	• Diversifying feature types such as influential members, temporal changes in features, contextual attributes etc. • Analysis of dissolution event
Rule Discovery Based Methods	Koloniari et al. [5]	• Discovery of rules on time series • Regard only topological features	• Developing unsupervised machine learning classifiers to uncover prediction patterns/rules • Regarding content based features
Supervised Learning Based Methods	Brodka et al. [6] İlhan&Öğüdücü [9] Takaffoli et al. [11] Saganowski et al. [12] Diakidis et al. [14] Pavlopoulou et al. [15] Dakiche et al. [16] Dakiche et al. [17]	• No available public benchmark datasets • No method to generate benchmark datasets • Need to labeled data • Mobile network datasets are not considered.	• Developing benchmark datasets • Developing a methodology for generating the benchmark datasets • Developing unsupervised machine learning classifiers • Developing a model/method working on dynamic mobile networks.

REFERENCES

[1] V. D. Blondel, J. –L. Guillaume, R. Lambiotte, and E. Lefebvre, "Fast unfolding of communities in large networks", *J. Stat. Mech. Theory Exp.*, vol. 2008, Oct. 2008. Art. no. 10008. DOI: 10.1088/1742-5468/2008/10/P10008

[2] V. A. Traag, L. Waltman, and N. J. Van Eck, "From Louvain to Leiden: guaranteeing well-connected communities," *Sci. Rep.*, vol. 9, Mar. 2019. Art. no. 5233. DOI: 10.1038/s41598-019-41695-z

[3] G. Palla, A. L. Barabási, and T. Vicsek, "Quantifying social group evolution," *Nature*, vol. *446, no.* 7136, pp. 664-667, Apr. 2007. DOI: 10.1038/nature05670.

[4] E. G. Tajeuna, M. Bouguessa, M., and S. Wang, "Modeling and predicting community structure changes in time-evolving social networks," *IEEE Trans. Knowl. Data Enq*, vol.31, no. 6, pp. 1166-1180, June 2019. DOI: 10.1109/TKDE.2018.2851586.

[5] G. Koloniari, G. Evangelidis, N. Sachpenderis, and I. Milonas, "A Framework for Predicting Community Behavior in Evolving Social Networks," in Proc. ACM the 9th Balkan Conf. Inform., Sofia, Bulgaria 2019, pp. 1-4. DOI: 10.1145/3351556.3351583

[6] P. Bródka, P. Kazienko, and B. Bartosz, "Predicting group evolution in the social network," in Proc. Int. Conf. Soc. Inf., Lausanne, Switzerland, 2012, pp. 54-67. DOI: 10.1007/978-3-642-35386-4_5

[7] P. Bródka, S. Saganowski, and P. Kazienko, "GED: the method for group evolution discovery in social networks." Soc. Netw. Anal. Min., vol. 3, no. 1, pp. 1-14, Mar. 2013. DOI: 10.1007/s13278-012-0058-8

[8] E. Frank, M. A. Hall, and I. H. Witten, "The WEKA Workbench". Online Appendix for "Data Mining: Practical Machine Learning Tools and Techniques", Morgan Kaufmann, Fourth Edition, 2016.

[9] N. Ilhan, and Ş. G. Öğüdücü, "Community event prediction in dynamic social networks," in 12th Int. Conf. Mach. Learn. Appl., Miami, USA, 2013, pp. 191–196. DOI:10.1109/ICMLA.2013.40

[10] N. İlhan, Ş. G. Öğüdücü, "Feature identification for predicting community evolution in dynamic social networks," *Eng. Appl. Artif. Intell.*, vol. 55, pp. 202-218, Oct. 2016. DOI: 10.1016/j.engappai.2016.06.003.

[11] M. Takaffoli, R. Rabbany, and O. R. Zaïane, "Community evolution prediction in dynamic social networks," in 2014 IEEE/ACM Int. Conf. Adv. Soc. Netw. Anal. Min., Beijing, China, 2014, pp. 9-16. DOI:10.1109/ASONAM.2014.6921553

[12] S. Saganowski, B. Gliwa, P. Bródka, A. Zygmunt, P. Kazienko, and J. Koźlak, "Predicting community evolution in social networks," *Entropy*, vol. 17, no. 5, pp. 3053-3096, May 2015. DOI: 10.3390/e17053053

[13] B. Gliwa, S. Saganowski, A. Zygmunt, P. Bródka, K. Przemyslaw, and J. Kozak, "Identification of group changes in blogosphere," in 2012 IEEE/ACM Int. Conf. Adv. Soc. Netw. Anal. Min., Istanbul, Turkey, 2021, pp. 1201-126. DOI: 10.1109/ASONAM.2012.207

[14] G. Diakidis, D. Karna, D. Fasarakis-Hilliard, D. Vogiatzis, and G. Paliouras, "Predicting the evolution of communities in social networks," in the 5th Int. Conf. Web Intell., Min. Semant., Larnaca, Cyprus, 2015, pp. 1-6. DOI: 10.1145/2797115.2797119

[15] M. E. G. Pavlopoulou, G. Tzortzis, D. Vogiatzis, and G. Paliouras, "Predicting the evolution of communities in social networks using structural and temporal features," in the 12th Int. Workshop Semant. Soc. Media Adapt. Pers., Bratislava, Slovakia, 2017, pp. 40-45. DOI: 10.1109/SMAP.2017.8022665

[16] N. Dakiche, F. T. Benbouzid-Si, Y. Slimani, and K. Benatchba, "Community evolution prediction in dynamic social networks using community features' change rates," in the 34th ACM/SIGAPP Symp. Appl. Comput., Limassol, Cyprus, 2019, pp. 2078–2085. DOI: 10.1145/3297280.3297484

[17] N. Dakiche, F. T. Benbouzid-Si, K. Benatchba, and Y. Slimani, "Tailored network splitting for community evolution prediction in dynamic social networks," *New Gener. Comput.*, vol. 39, pp. 303–340, April 2021. DOI: 10.1007/s00354-021-00122-6

[18] J. Lafferty, A. McCallum, and F. C. Pereira, "Conditional random fields: Probabilistic models for segmenting and labelling sequence data," in Proc. Int. Conf. Mach. Learn., Massachusetts, USA, 2001, pp. 282-289.

[19] M. Takaffoli, F. Sangi, J. Fagnan, and O. R. Zaïane, "MODEC — Modeling and Detecting Evolutions of Communities," in 5th Int. AAAI Conf. Web Soc. Media, Catalonia, Spain, 2011, pp. 626-629.

Medical Image Steganalysis using Deep Convolutional Neural Network

Rukiye KARAKIS[1]

[1] Sivas Cumhuriyet University, Department of Software Engineering, 58140, Sivas/Turkey,
rkarakis@cumhuriyet.edu.tr

Abstract **- Image steganography ensures that secret data is hidden in a cover image and aims to transmit the resulting stego image through a communication channel without being noticed by a third party. On the other hand, image steganalysis detects the hidden data in the stego images. Traditional steganalysis techniques focus on obtaining hidden data. However, the presence of secret data must be revealed before obtaining it. Machine Learning (ML) classifiers are used for this purpose with promising high-performance values. ML techniques other than deep learning (DL) require complex and costly feature analysis performed in spatial or transform space. In recent years, DL models have been used to detect the presence of secret messages in the BOSSBase dataset, but there is no study for medical image steganalysis. Therefore, this study aimed to perform medical image steganalysis using a DL model that performs feature analysis on its convolutional layers. An original medical image dataset containing brain MR images was obtained from epileptic patients and healthy volunteers. Two deep convolutional neural networks (CNN) were used. One of them was trained without transfer learning while the feature layers and weights of DenseNet, ResNet, Inception, and Efficient models were transferred to the other one. The training data was obtained by hiding the secret data to the brain images, with different capacity ratios between 0.1 and 1.0 bit per pixel (bpp) using the WOW technique. The results can be summarized in two aspects. First, as expected, the higher the capacity ratio was, the higher classification performance it was obtained. Second, using transfer learning increased the classification performance of the DL model.**

Keywords **- Medical Image Steganalysis, Deep Learning, Convolutional Neural Network, Transfer Learning.**

I. INTRODUCTION

Image steganography deals with embedding secret data in a cover image without being noticed by a third party. It consists of two stages: data hiding and data extraction. In data hiding, a stego key and embedding algorithm are used to hide the data into cover image, resulting in a stego image. In the data extraction, the hidden data is obtained from the stego image using the same stego key and algorithm as before. Image steganalysis, on the other hand, detects hidden data in stego images. There are two types of image steganalysis attacks: passive and active [1-2]. Active attacks reveal the embedding scheme, whereas passive attacks determine if there is a message in the image [2-3].

The image steganalysis, which is concerned with determining if an image is a stego or cover, is essentially a binary classification problem. Consequently, Machine Learning (ML) approaches such as the Support Vector Machine (SVM) and the ensemble classifier are employed to tackle the problem. These classifiers include two stages: feature extraction and classification. In feature extraction, several analyses such as Subtractive Pixel Adjacency Matrix (SPAM), Spatial-Domain Rich Models (SRM), and maxSRM, are used to derive the features, which are high-dimensional and are obtained by complex analysis [2, 4]. Selecting the most accurate features to classify a problem is a significant challenge in ML. For this reason, in recent years, Deep Learning (DL) models that perform feature analysis within their building blocks have been applied to overcome these feature extraction challenges.

In 2014, Tan et al. [5] proposed the first DL model. To detect the HUGO embedding method with 0.4 bit per pixel (bpp) payload, a Convolutional Neural Network (CNN) with 9 layers was trained and tested on BOSSBase. The performance results were lower than those achieved with SRM, but were comparable to those obtained with SPAM. Qian et al. [6-7] proposed CNN models for the HUGO, Wavelet Obtained Weights (WOW), and S-UNIWARD methods, which were trained on the BOSSBase and ImageNet datasets for steganalysis of diverse message payloads. First, images were subjected to high pass filtering (HPF) with a 5x5 kernel to strengthen the stego-noise signal while separating it from the image content. In the convolution layers, a Gaussian activation function was used instead of a Rectified Linear Unit (ReLU). Compared to SPAM, the detection error values were higher, and they were extremely near SRM. In another study [7], the same architecture was used in pre-trained models. For instance, the weights from the architecture trained for 0.6 bpp payload were transferred to all models trained for the payload ranging 0.5 to 0.1 bpp. These two studies [6-7] have shown that image preprocessing and transfer learning improved the performance of deep learning models.

Xu et al. [8] performed a CNN model with the five-block. First, they applied HPF to the images. In the first block, they used an ABS layer that takes the absolute values of the features calculated after the first convolution layer, batch normalization (BN) and TanH activation function. In the deep convolution layers, it was applied with 1x1 filter kernels on feature maps. The performance values calculated for the HILL and S-UNIWARD techniques competed with the results of SRM classifier. Ye et al. [9] developed a CNN model to detect WOW, S-UNIWARD, and HILL algorithms. Instead of a single HPF, the first layer of the CNN had a high-pass filter set that

calculated residual maps in the SRM classifier [4]. Furthermore, the truncated linear unit (TLU) activation function was used after the first convolution layer. The CNN model's detection error was relatively high in comparison to the SRM classifier. These studies [8-9] have shown that performing particular operations on the first blocks of CNN improves the detection of the stego signal in the deep layers. Thus, it was possible to develop deeper architectures in subsequent studies by utilizing big datasets.

For both the clairvoyant and cover-source mismatch scenarios, Pibre et al. [10] analyzed the BOSSBase and LIRMMBase datasets, which were augmented by cropping in the proposed DL architecture. During the preprocessing step, they employed HPF. They used RELU and did not use pooling layers in the feature layers. It was assumed that the down-sampling process in the pooling layer causes denoising in the feature maps [11]. According to the results, the classification accuracy of the DL model increased by 8%. The absence of the pooling layer, on the other hand, has increased the number of trainable parameters in the deep network.

One of the main problems in deep architectural design is that when the network learns new information, it abruptly forgets previously learned information. The concept of residual learning was introduced to deal with this issue. Residual learning has also been successful results in distinguishing low stego signal from image content in image steganalysis. After applying HPF to images, Wu et al. [12] used non-bottleneck and bottleneck building blocks to provide learning and increase dimension. Similarly, You et al. [13] presented the RestegNet architecture, which contained residual connection-based sharpening and smoothing blocks. Boroumand et al. [14] proposed the SRNet residual learning model. In the early layers of the SRNet, they did not use pooling to segment the noise; however, residual connections and pooling were used in the following deeper layers. Ozcan et al. [15] detected HUGO and WOW methods with various payloads using pre-trained ResNet50 models. Butora et al. [16] employed pre-trained models for spatial and JPEG image steganalysis as well. The results revealed that residual connections and transfer learning achieved higher performance values in image steganalysis than conventional learning [12-16].

Medical image steganography aims to protect patient personal information and health records by hiding them into medical images. As a result, many steganography security schemes have been proposed in the spatial or transform domain [17-20]. On the other hand, there are few studies in the literature that used SVM and CNN classifiers for medical image steganalysis [21-22]. By using the Least Significant Bit (LSB) technique on Brain Magnetic Resonance Imaging (MRI) images, data were sequentially embedded at different bpp payloads. In the studies, the payload information was ignored, and the cover and all stego images were analyzed together. This situation has resulted in a data imbalance problem between cover and stego classes. For this reason, 30 different data augmentation techniques were applied only to cover images. This may have caused that the architectures learning about the change in image contents caused by data augmentation, rather than detecting noise. Furthermore, it is easy to estimate the statistical distribution of the sequential LSB approach without using DL or ML classifiers.

The aims of this study are to (1) provide a dataset for medical image steganalysis, (2) classify cover/stego images using pre-trained DL models, and (3) contribute to the development of robust methodologies for medical image steganography. In the study, a real dataset consisting of brain MRI images was gathered. For the cover-source mismatch scenario, messages in the range of 1.0 and 0.1 bpp payload were embedded on cover medical images using the WOW embedding technique. In the deep CNN architecture, the low stego signal was amplified by first applying HPF to the images. Then, the feature layers of the CNN were transferred from the DenseNet, ResNet, Inception, and Efficient architectures [23-24]. Performance metrics such as Area Under Curve (AUC), specificity, precision, recall, accuracy, F1-score were used to evaluate which model performed better in medical image steganalysis.

II. Material And Method

In this study, two datasets previously used for medical image steganography were combined for medical image steganalysis. The first dataset includes brain MRI images of 15 epilepsy patients and 15 healthy individuals who applied to Gazi University Faculty of Medicine, Department of Neurology [18]. The second dataset includes MRI images of 30 patients with focal epilepsy collected from the Department of Neurology and Radiology, Sivas Cumhuriyet University [19]. In the study, axial, coronal, and sagittal slices from T1, T2 and FLAIR weighted MRI images were selected for the analyses. The dataset containing 5961 images was separated into 90% and 10% training and validation sets, respectively. In the study, a figshare brain dataset including 3064 T1-weighted brain MR images was used as a test set [25]. Images with ".dcm" extension in different sizes were resized to 224x224 using MATLAB's imresize function.

WOW technique (http://dde.binghamton.edu/download/) was used to prepare stego images since it causes low distortion on the cover image, and its statistical distribution is difficult to obtain by steganalysis [26]. A total of 10 different stego image datasets were created by hiding data in the range of 1.0 and 0.1 bpp on the cover images. Data hiding processes were carried out using MATLAB software. Figure 1 shows the difference images obtained between cover and stego MRI images. As the amount of payload is reduced, the distortion caused by the stego signal in the images reduces.

In the study, the pre-trained CNN models given in Figure 2 include three stages: image preprocessing, feature extraction, and classification. HPF filtering was applied to the images in the image processing stage to amplify the low stego signal. The 5x5 filter kernel used in the study is given in Eq.1. [6-7, 27].

$$K = \frac{1}{12}\begin{pmatrix} -1 & 2 & -2 & 2 & -1 \\ 2 & -6 & 8 & -6 & 2 \\ -2 & 8 & -12 & 8 & -2 \\ 2 & -6 & 8 & -6 & 2 \\ -1 & 2 & -2 & 2 & -1 \end{pmatrix} \quad (1)$$

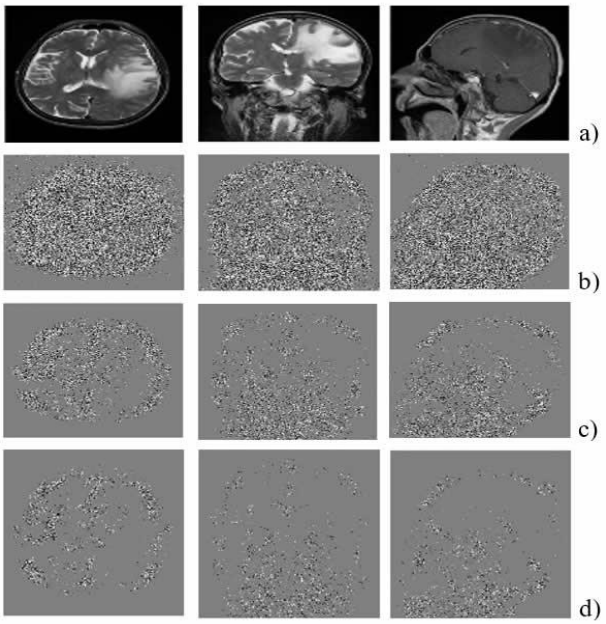

Figure 1: Cover and Difference Images, a) cover images, b) difference images with 1.0 bpp payload, c) difference images with 0.4 bpp payload, d) difference images with 0.2 bpp payload

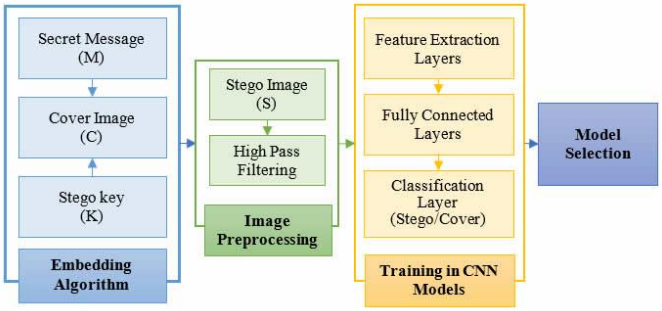

Figure 2: Proposed medical image steganalysis model.

In the study, the feature layers of the CNN architecture were transferred from the DenseNet, ResNet, InceptionV3, and EfficientB0 networks used in transfer learning. All models were trained without weight transfer or pre-trained on 10 datasets for the WOW technique.

A. Convolutional Neural Network (CNN)

CNN automatically and adaptively learns the characteristics of the input data presented to the network using backpropagation learning. CNN is composed of multiple building blocks such as convolution layers, pooling layers, and fully connected layers. Convolution and pooling layers are utilized to extract features maps. In the convolution layers, filter sets with different kernel sizes (2x2, 3x3, 5x5, etc.) are convolved with the image. The feature maps obtained by convolutions are passed activation functions such as sigmoid, tanh, ReLU, or LeakyReLU to make them non-linear [28-30].

In the pooling layer, feature maps are down-sampled using average or maximum pooling to reduce their dimension and the number of trainable parameters in the network. Following the last convolution or pooling layer of CNN, the feature maps are flattened and transferred to a fully connected layer (FCL) via weights. In each neuron in the FCLs, the outputs of the neurons of previous layers are multiplied by the weights and summed to obtain input information. This information is passed through an activation function such as ReLU to calculate the output of the neuron. In the classification layer, the multiple classification probabilities of the outputs are calculated using the softmax activation function [28-30]. The classification layer in medical image steganalysis has two output neurons to represent cover and stego.

To generalize a problem, CNN uses the objective/loss function ($\mathcal{L}$) defined in Eq. 2. The primary purpose of CNN is to update the weight and bias values, which are the network's trainable parameters. For this reason, the error between the actual output (y) and the predicted output (o) is iteratively minimized using an optimization technique.

$$\mathcal{L} = \frac{1}{N}\sum_{n=1}^{N} l(\theta; y^{(n)}, o^{(n)}) \quad (2)$$

The CNN is trained using an optimization method such as SGD, ADAM, RMSprop, which minimizes the penalty function. The performance of the deep network is measured by test data it has never seen before.

Transfer learning (TL) overcomes the big data problem required for DL through pre-trained networks. According to the literature, there are two transfer learning strategies. The first is to utilize a pre-trained network as a feature extractor; the second is to fine-tune a pre-trained network using different data. Studies show that these two strategies significantly improve the accuracy of classification problems [23-24].

In this study, medical image steganalysis was performed using ResNet, DenseNet, InceptionV3, EfficientB0 architectures, which achieved successful accuracy results in the ImageNet competition. Each model was trained separately using 10 stego datasets with cover images. Two methods were used to train these models. First, the feature layers of the CNN architecture were transferred from the feature layers of the four models. Then, two FCLs with 128 neurons and an output layer with two neurons were added to the architecture.

Two experiments were implemented to train and test pre-trained models. In the first experiment, the architectures of TL models (ResNet, DenseNet, Efficient, and Inception) were transferred to our models for detecting WOW and payload, and were fine-tuned. In the second experiment, both the architecture of pre-trained models and the weights of the architectures trained with 10 datasets starting from 1.0 to 0.1 were transferred to each other. A base model was trained using an initial dataset. The data with a payload of 1.0 bpp was concealed on medical images using the sequential LSB approach, resulting in the creation of an initial dataset. The weights of the models trained on this dataset were applied to the 4 models for WOW with 1.0 bpp steganalysis. This procedure (1.0bpp→0.9bpp→0.8bpp→0.7bpp→0.6bpp→0.5bpp→0.4bpp→0.3bpp→0.2bpp→0.1bpp) was performed consecutively until the last dataset.

III. Obtained Results

Optimization of the trainable parameters of the CNN was

performed using the Stochastic Gradient Descent (SGD) optimization technique. Learning rate, momentum, and decay values were selected as 0.0001, 0.9, and 0.02, respectively. Dropout and L2 regularization were used to prevent overfitting problem. In addition, the weights of the model with the highest validation accuracy were recorded using the validation dataset, and the tests were also performed on the CNN model with these weights. The training epoch and batch size values are 20 and 32, respectively. Training in each CNN was repeated by 5 fold cross-validation.

The performance values obtained by the fine-tuned models are given in Table 1. While all models can detect WOW with high data payloads, their performance has decreased in detecting the low data payloads. DenseNet was more successful than other networks in 0.4 and 0.2 payload detection, but the EfficientB0 network achieved lower performance values compared to other networks.

Table 1: The performance metrics of fine-tuned models

Performance Metrics	0.4 Payload				0.2 Payload			
	M1[a]	M2[b]	M3[c]	M4[d]	M1[a]	M2[b]	M3[c]	M4[d]
AUC	**0.992**	0.989	0.963	0.982	**0.876**	0.631	0.727	0.691
Specificity	**0.992**	0.989	0.963	0.982	**0.876**	0.631	0.727	0.691
Accuracy	**0.992**	0.989	0.963	0.982	**0.876**	0.631	0.727	0.691
Precision	**0.992**	0.989	0.963	0.983	**0.876**	0.636	0.731	0.709
Recall	**0.992**	0.989	0.963	0.982	**0.876**	0.631	0.727	0.691
F1-Score	**0.992**	0.989	0.963	0.982	**0.876**	0.625	0.726	0.671

[a] M1: DenseNet, [b] M2: ResNet, [c] M3:InceptionV3, [d] M4:EfficientB0

Fig. 3 shows the accuracy values of fine-tuned models in the detection of WOW and payload size. The classification accuracy values of all models were very close to each other. However, the performances of the DenseNet in detecting WOW with payloads ranging from 0.5 to 0.2 bpp were relatively higher than other models.

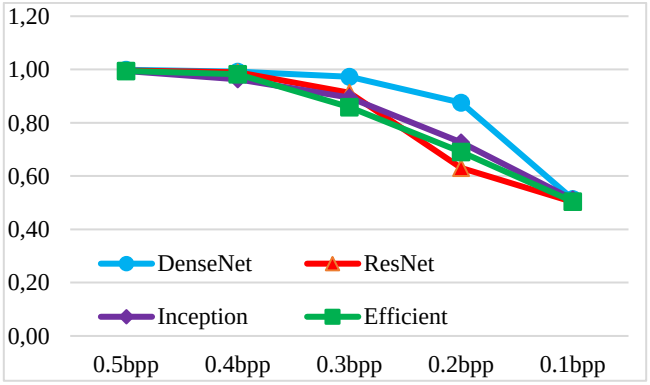

Figure 3: Accuracy values of fine-tuned models

In the study, all experiments were repeated by 5-fold cross-validation. While performing cross-validation training on the fine-tuned models without weight transfer, it was observed that they became more unstable as the payload size decreased. The primary reason for this is the big data requirement of the deep network to generalize a problem. For this reason, in the second experiment, the weights were transferred between models to deal with this problem. In Table 2, the performance values calculated for 0.4 and 0.2 bpp of pre-trained models were given. In this case, all models achieved successful results for 0.4 bpp. The performance results of the models were similar each other for 0.2 bpp. However, Inception's performance was relatively better than the other models.

Table 2: The performance metrics of pre-trained models

Performance Metrics	0.4 Payload				0.2 Payload			
	M1[a]	M2[b]	M3[c]	M4[d]	M1[a]	M2[b]	**M3[c]**	M4[d]
AUC	0.998	0.997	**0.999**	0.998	0.931	0.933	**0.951**	0.935
Specificity	0.998	0.997	**0.999**	0.997	0.931	0.933	**0.951**	0.935
Accuracy	0.998	0.997	**0.999**	0.997	0.931	0.933	**0.951**	0.935
Precision	0.998	0.997	**0.999**	0.997	0.931	0.933	**0.952**	0.937
Recall	0.998	0.997	**0.999**	0.997	0.931	0.933	**0.951**	0.935
F1-Score	0.998	0.997	**0.999**	0.997	0.931	0.933	**0.951**	0.935

[a] M1: DenseNet, [b] M2: ResNet, [c] M3:InceptionV3, [d] M4:EfficientB0

As illustrated in Fig. 4, the accuracy values of the pre-trained models for detecting payloads are extremely close to each other. In addition, they obtained stable results compared to fine-tuned models. The main difference between the two experiments was to detect 0.2 and 0.1 bpp. Especially for 0.1 bpp, the accuracy values of fine-tuned models were between 0.503 and 0.514, while the accuracy values of the pre-trained models were found between 0.738 and 0.752.

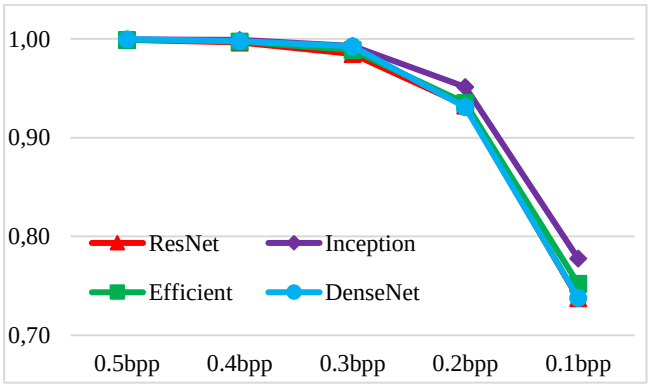

Figure 4: Accuracy values of pre-trained models

A. Literature Comparison

There are two studies on medical image steganalysis in the literature. In these studies, the LSB technique was used to embed data in the range of 0.1 to 1.0 bpp in brain MRI images. Ozcan et al. [21] first obtained the DCT-based features of the medical images and classified them using SVM. In the other study [22], CNN was used to avoid hand-crafted feature analysis.

Basically, LSB with different payload sizes was analyzed in both studies. However, the distribution of the stego-noise caused by the sequential LSB technique can be determined using statistical analysis. In addition, cover and stego images with different payload sizes were classified together. As a result, there were data imbalance problem between the cover-stego classes in the datasets. In order to overcome this problem,

many data augmentation techniques have been applied. Although high accuracy values were obtained in the studies, the data augmentation process may have caused the classifiers to classify based on image contents rather than detecting stego-noise. For this reason, in this study, both the sequential LSB technique was avoided and the WOW technique was evaluated separately for each data payload size. The study results have indicated that deep pre-trained models can be used for medical image steganalysis.

IV. CONCLUSION

In recent years, DL models have been successfully used in image steganalysis to determine if an image is a cover or a stego. In this study, the question whether medical image steganalysis is possible. Basically, the aims of the study are to contribute to the development of medical image steganography techniques and to perform a medical steganalysis method in case medical images are used in cyber-attacks. For this reason, a data set containing original brain MRI images was prepared in the study. The developed pre-trained DL models were tested using another brain dataset. For the first time in image steganalysis, apart from DenseNet and ResNet, the analyzes were performed with Inception and Efficient models. Deep CNN models achieved the high classification accuracy values in the cover-source mismatch scenario. Although the datasets used in literature have not used medical images, this study achieved promising results for using DenseNet and Inception architectures in steganalysis.

ACKNOWLEDGMENT

I would like to thank Dr. Kali Gurkahraman from the University of Sivas Cumhuriyet for helpful discussions on the use of DL.

REFERENCES

[1] K. Karampidis, E. Kavallieratou, G. Papadourakis, "A Review of Image Steganalysis Techniques for Digital Forensics", *Journal of Information Security and Applications*, vol. 40, pp. 217-235, 2018.

[2] A. Selvaraj, A. Ezhilarasan, S. L. J. Wellington, A. R. Sam, "Digital image steganalysis: A survey on paradigm shift from machine learning to deep learning based techniques", *IET Image Processing*, vol. 15, pp. 504-522, 2021.

[3] R. Karakis, K. Gurkahraman, "Steganalysis with Deep Learning on Medical Images", Journal of Information Technologies, vol. 14, no. 2, pp. 151-159, 2021.

[4] J. Fridrich and J. Kodovsky, "Rich models for steganalysis of digital images," *IEEE Transactions on Information Forensics and Security*, vol. 7, no. 3, pp. 868-882, 2012.

[5] S. Tan, B. Li, "Stacked convolutional auto-encoders for steganalysis of digital images," *in Conf. Rec. 2011 Signal and Information Processing Association Annual Summit and Conference (APSIPA)*, pp. 1-4.

[6] Y. Qian, J. Dong, W. Wang, T. Tan, "Deep learning for steganalysis via convolutional neural networks," *in Conf. Rec. 2015 Proc. SPIE 9409, Media Watermarking, Security, and Forensics 2015*, 94090J.

[7] Y. Qian, J. Dong, W. Wang, T. Tan, "Learning and transferring representations for image steganalysis using convolutional neural network," *in Conf. Rec. 2016 IEEE International Conference on Image Processing (ICIP)*, pp. 2752-2756.

[8] G. Xu, H. Wu, Y. Shi, "Structural Design of Convolutional Neural Networks for Steganalysis," *IEEE Signal Processing Letters*, vol. 23, no. 5, pp. 708-712, 2016.

[9] J. Ye, J. Ni, Y. Yi, "Deep Learning Hierarchical Representations for Image Steganalysis," *IEEE Transactions on Information Forensics and Security*, vol. 12, no. 11, pp. 2545-2557, 2017.

[10] L.Pibre, J. Pasquet, J. D. Ienco, D., M. Chaumont, "Deep learning is a good steganalysis tool when embedding key is reused for different images, even if there is a cover sourcemismatch," *in Conf. Rec. 2016 Proceedings of the IST International Symposium on Electronic Imaging*, pp. 14-18.

[11] J.F. Couchot, R. Couturier, C. Guyeux, M. Salomon, "Steganalysis via a convolutional neural network using large convolution filters for embedding process with same stego key," arXiv:1605.07946v3, 2016.

[12] S. Wu, S. Zhong, Y. Liu, "Deep residual learning for image steganalysis," *Multimed Tools Appl*., vol. 77, pp. 10437-10453, 2018.

[13] W. You, X. Zhao, S. Ma, Y. Liu, "RestegNet: a residual steganalytic network," *Multimed Tools Appl*., vol. 78, pp. 22711-22725, 2019.

[14] M. Boroumand, M. Chen, J. Fridrich, "Deep Residual Network for Steganalysis of Digital Images," *IEEE Transactions on Information Forensics and Security*, vol. 14, no. 5, pp. 1181-1193, 2019.

[15] S. Ozcan, A.F. Mustacoglu, "Transfer learning effects on image steganalysis with pre-trained deep residual neural network model," *in Conf. Rec. 2018 IEEE International Conference on Big Data (Big Data)*, pp. 2280-2287.

[16] J. Butora, Y. Yousfi, J. Fridrich, "How to Pretrain for Steganalysis," *in Conf. Rec. 2021 IH&MMSec '21: Proceedings of the 2021 ACM Workshop on Information Hiding and Multimedia Security*, pp. 143-148.

[17] R. Karakis, I. Guler, *Chapter 22: Steganography and Medical Data Security*, Cryptographic and Information Security Approaches for Images and Videos, Editor Ramakrishnan, S., CRC Press, 627-660, ISBN: 9781138563841, 2019.

[18] R. Karakis, I. Guler, I. Capraz, E. Bilir, "A novel fuzzy logic based image steganography method to ensure medical data security," *Computers in Biology and Medicine*, vol. 67, pp. 172-183, 2015.

[19] R. Karakis, K. Gurkahraman, B. Cigdem , I. Oztoprak, A.S. Topaktas, "Evaluation of Segmented Brain Regions for Medical Image Steganography," *Journal of the Faculty of Engineering and Architecture of Gazi University*, vol. 36, no. 4, pp. 2301-2314, 2021.

[20] R. Karakis, K. Gurkahraman, "Edge-based watermarking in regions of none interest for the security of medical images," *Adiyaman Universitesi Muhendislik Bilimleri Dergisi*, vol. 8, no. 14, pp. 154-168, 2021.

[21] F.B. Maroof Ozcan, R. Karakis, I. Guler, "Steganalysis on Medical Images with Support Vector Machine," in Conf. Rec. 2020 28th Signal Processing and Communications Applications Conference (SIU), pp.1-4.

[22] R. Karakis, K. Gurkahraman, "Steganalysis with Deep Learning on Medical Images," *Journal of Information Technologies*, vol. 14, no. 2, pp. 151-159, 2021.

[23] K. Gurkahraman, R. Karakis, "Brain Tumors Classification with Deep Learning using Data Augmentation," *Journal of the Faculty of Engineering and Architecture of Gazi University*, vol. 36, no. 2, pp. 997-1011, 2021.

[24] S. Savaş, "Detecting the Stages of Alzheimer's Disease with Pre-trained Deep Learning Architectures," *Arab J. Sci. Eng.*, 2021, https://doi.org/10.1007/s13369-021-06131-3.

[25] Internet: Figshare brain tumor dataset. Available: https://doi.org/10.6084/m9.figshare.1512427.v5.

[26] Holub, V., Fridrich, J., "Designing steganographic distortion using directional filters", in the IEEE International Workshop on Information Forensics and Security, pp. 234–239, 2012.

[27] T. Reinel, R. Raúl, I. Gustavo, "Deep Learning Applied to Steganalysis of Digital Images: A Systematic Review", *IEEE Access*, vol. 7, pp. 68970-68990, 2019.

[28] I. Goodfellow, Y. Bengio, A. Courville, *Deep learning (Adaptive computation and machine learning)*, The MIT Press, Cambridge, Massachusetts, 2016.

[29] A. Krizhevsky, I. Sutskever, I., G. Hinton, "ImageNet classification with deep convolutional neural networks", *in Conf. Rec. 2012 NIPS'12 Proceedings of the 25th International Conference on Neural Information Processing Systems*, vol. 1, pp. 1097-1105.

[30] R. Yamashita, M. Nishio, R.K.G. Do, K. Togashi, "Convolutional neural networks: an overview and application in radiology", *Insights Imaging*, vol. 9, pp. 611-629, 2018.

The algorithm for new secret sharing scheme – I

Bukurie Ibrahimi, Zamir Dika[1], Artan Luma[1]

[1] Faculty of Contemporary Sciences and Technologies, South East European University Tetovo, Macedonia

bukurieshabani@hotmail.com, z.dika@seeu.edu.mk, a.luma@seeu.edu.mk

Abstract - Visual Cryptography is a cryptographic technique whose goal is to hide a secret within images. These images are encrypted into *n* parts known as shares and decrypted without computer calculations. In this work, we briefly describe a new proposed (*n*,*n*) Secret Sharing Scheme for grayscale/color images. We will use the algorithm of Cheng et al. and we will modify it such that new obtained secret sharing scheme becomes more efficient and more secure. The scheme uses XOR operation sharing images, algebraic function for creating a secret image for authentication, while the size of the original image and shadows are the same. In the paper, we will also use the Cantor function, which makes possible the generation of respective codes for each participant.

Keywords*: Visual Cryptography, Secret Image Sharing, XOR operation, Cantor function*

1. Introduction

The fast development of technology has made possible to transmit and store easily a large number of digital data. However, the transmission of data over the internet or their storage in computers can be easily intercepted by "attackers", if such data are not secure enough. Therefore, information security, especially in the world of Big Data and new Cloud “paradigm”, represents a very emergent issue.

One of the proposed schemes for information security is Visual Cryptography. It was firstly presented by Naor, Shamir [1]. Visual Cryptography (VC) is a new type of cryptography that hides a secret within images. These images are encrypted into *n* shares and decrypted without computer calculations.

Some of the practical applications could be in medical images where the patient information is sensitive and needs to be protected during storage and transmission, especially in the cloud [15,19]; the internet voting system [16,17]; biometry privacy [20,21], etc. References [13], [14] provide additional useful information about the most recent important trends in Visual Cryptography.

In the following, we will describe some of the trends and directions of scientific research in the field of Visual Cryptography. Visual Cryptography schemes mainly concerned with black and white images. It was Verheul and Van Tilborg [2], who for the first time propose Visual Secret Sharing Scheme for color images, which presently is known as color scheme of k out of n. Because Visual Cryptography in color images allows the use of natural color images to store information, it has become a very important field of study.

More advanced schemes based on Visual Cryptography are presented in [4, 5, 6]. In those schemes colored image is hidden in many meaningful covered images. Chang [4] in 2000 has introduced a new secret colored sharing scheme in which the ordinary collection of sub-pixels and rows are modified [5]. This new technique does not require the collection of transparent and as such is suitable for real-time applications, however, this scheme, to restore the image without losses, requires the use and storage of a Color Index Table (CIT). The disadvantages of this method are: it requires large space for storage of information, a long time during searching in the CIT as well as a loss of image

resolution in the case of an increase of colors in the image secret.

Chang and Yu [6] presented an advanced scheme to hide color images into numerous images that do not require CIT. This technique achieves a restoring of the secret image without loss; however, created divisions (covered images) contain redundant noise. They use meaningful shares to hide the secret image, and each pixel is transformed into 9 subpixels. The scheme needs only the XOR operation. The advantage of this scheme is that it can share complex images.

Youmaran, Adler and Miri [3] proposed an improved algorithm based on Chang and Yu's scheme in order to enhance the quality of covered images. Through this method, one achieves the restoring of data without loss and also there is noise reduction in images without changing at all the complexity of the calculations.

The purpose of the research [18] by Askari and Heyse is EVC (Extended Visual Cryptography) security scheme, which requires no more pixels during sharing and recovering images than the secret original image, and it still retains the image of good quality during the process. They used two methods, one for processing the secret image, and the other one for balancing the image after processing the secret image. This proposed scheme realizes high-security scheme based on EVC [19].

In [7] Wang, are proposed two methods without pixel expansion: probabilistic $(2,n)$ scheme for binary images, and deterministic (n,n) scheme for grayscale and color images. Both of these methods are based on Boolean operations and both provide high security.

The deterministic (n,n) algorithm of Wang et al. [7] is an algorithm that uses a random grid to generate share images. It requires no codebook. It's based on Xor operation and the size of secret images is the same as share images.

Wu and Chen [23] were the first who have encrypted two secret images into two meaningful images, say A and B, where the first image was obtained as a result of merging A and B, and the other one as a result of first the opposite clockwise rotation of A for 90° and then merging it with the image B. Extensions and modifications to the above method are given in papers [24-26].

Chen and Wu [27] have proposed an effective method for a multi-secret sharing scheme based on Boolean operators. The advantage of this scheme stands in the fact that the scheme is expanded to encode n images comparing to one image as it was previously.

Latter, Reddy and Prasad [28] proposed a new scheme based on [27]. It uses meaningful shares for multiple secret sharing and also for covering images. It also uses Boolean operations and lossless recovers multiple secrets.

Independently from the security issues in VC, many researchers have experimented with the idea of cheating the system. The methods for cheating the basic schemes on VC and EVC as well as their techniques have been presented in [13].

Yang and Laih [29] have proposed a method for cheating prevention. In this method, one requires a Trusted Authority (online) to verify the sharing of participants.

Another method for cheating prevention is described by Horg [30]. In this case, the cheater needs to have exact information about the distribution of black and white subpixels of sharings of "honest" participants.

Hu and Tzeng [31] proposed improvements in the method of Yang and Laih from [29]. According to them, the scheme for cheating prevention needs no support from direct Trusted Authority. Instead, it is needed the verification of images for each participant to be different and to be known only for participants.

Recently, there were research studies linking VC and graph theory. In [33] it is considered a new visual cryptography scheme that allows for sharing of multiple secret images on graphs. More precisely, given an arbitrary graph (V,E) where every node and every edge are assigned an arbitrary image. Images on the vertices are "public" and images on the edges are "secret".

The remainder of this paper is organized as follows: in Section 2 we briefly review related work and 2.1 explain the proposed scheme. Section 3 describes our structure-aware VC algorithm in detail. Section 4 presents results and compares them to those obtained by previous methods. The conclusions are drawn in Section 5.

2. Proposed scheme

In this paper, we propose an algorithm (n,n) -Visual Secret Sharing (VSS) as a result of modification of the algorithm of Chang and Yu [6].

We will obtain a new scheme, through which we aim to increase the level of security. Firstly, we use the Cantor function together with a random image to create a secret image. Then through the algorithm in [6], we will create share images in the form of a tree, as explained in the scheme in figure 1. We consider dividing the image into sub-image shares in order to enlarge the cases of combinations between sharing images and to make it very hard to be decrypted. Thus, through this approach, we aim to improve the level of security.

2.1. The Algorithm

This scheme is divided into three phases. In the first stage, we are dealing with the creation of a pin code for each participant. We will accomplish this by using the generalized Cantor function. In this way, we will get an additional security element. In the second phase, the encryption of the secret image will be carried out, i.e. the image will be camouflaged for each participant. We will do this by sharing the secret image in n - meaningless shared images. Our approach will be based on the algorithms presented in [6]. And naturally, in the third stage, we have the process of decryption, first of the pin code and then of the secret image. In the first case we use the modular arithmetic and in the second the Boolean algebra of the XOR operator.

2.1.1. Generation of value B

1) Suppose that there are n - participants and the secret dealer gives each of them an m -digit number. The algorithm generates a natural number b , that meets the following conditions:

i. $b = b_1 b_2 ... b_{m \cdot n}$ is of length $m \cdot n$ (i.e it contains $m \cdot n$ digits).

ii. Each b_i satisfy the relation $b_{m \cdot i+1} < b_{m \cdot (i+1)+1}$, for $i = 0,1,...,n-2$.

Note. 'The first digit ' (as well as other digits) not necessarily should be digits (from 0 to 9). The first digit, for example, can be 491 ($b_1 = 491$), the second digit can be 27 ($b_2 = 27$), the third digit can be 1001 ($b_3 = 1001$),and so on. In such cases, to avoid confusion, values b_i ($i = 1,2,...,n$) are separated by a comma. In the above example $b_1 b_2 b_3$ which corresponds to the sequence 491271001, will be written as 491,27,1001.

2) After obtaining the number b satisfying above conditions, the dealer gives to each n -participants m -digit number

$$b_{m \cdot i+1} b_{m \cdot i+2} ... b_{m \cdot i+m}, i = 0,1,2,...,n-1,$$

and then the value of b will be erased.

3) Next we use generalized Cantor function [32], by combining values of each participant x_i , $i = 1,2,...,n$ to obtain a unique natural number B given by

$$B = \langle x_1,...,x_n \rangle = \sum_{h=1}^{n} \left\{ \frac{1}{h!} \prod_{j=0}^{h-1} \left[\left(\sum_{i=1}^{h} x_i \right) + j \right] \right\}, \forall (x_1,...,x_n) \in \mathbb{N}^n \quad (1)$$

.

2.1.2 Proces of encrypting the image

1) We first take an image I (face, fingerprints, retina, etc.,), to which we associate a matrix of order $m \times n$.

2) Each pixel a_{ij} of the above image is associated with a new number B obtained by the function given in (1). As a result, we obtain a new pixel s_{ij} of the secret image. The secret image is given through the following function (and should be done for each RGB pixel alone):

$$s_{ij} = (a_{ij} + B + a_{ij} \cdot B) \bmod 257 \quad (2)$$

where $i \in \{1,2,...,m\}$, $j \in \{1,2,...,n\}$.

From this relation are determined and saved (for each a_{ij}) values of $\bar{k}_{ij}$ given by

$$\bar{k}_{ij} = \frac{a_{ij} + B + a_{ij} \cdot B - s_{ij}}{257}.$$

Secret image S, based on the given algorithm in [6] is divided into n sharing images $G_1, G_2, ..., G_n$, of the same dimension as the secret image S. By applying again the above-mentioned algorithm from [6], each sharing image $G_i, i \in \{1,2,...,n-1\}$ gets divided into two other sharing sub-images which we denote by $G_{i,i-1}, G_{i,i}$, while image G_n maps into itself. Again, all sharing sub-images have the same dimension as a secret image S.

Using the approach given in [7], from matrices that represent sharing sub-images $G_{i,i-1}, G_{i,i}$ are formed matrices $S_j, j \in \{1,2,...,n\}$ that are obtained as follows:

When $k = 2$, i.e when we have two shares, one gets

$$S_1 = G_{10}$$

$$S_2 = G_{11} \oplus G_2$$

In the case of three shares, so when $k = 3$ we have

$$S_1 = G_{10}$$

$$S_2 = G_{11} \oplus G_{21}$$

$$S_3 = G_{22} \oplus G_3$$

In general for $k = n$ one has

$$S_k = \begin{cases} G_{10,} & for \quad k = 1 \\ G_{k-1,k-1} \oplus G_{k,k-1}, & for \quad k = 2,3,...,n-1 \\ G_{k-1,k-1} \oplus G_k, & for \quad k = n \end{cases}$$

.

It is easy to see that

$$S = \bigoplus_{i=1}^{n} S_i = S_1 \oplus S_2 \oplus ... \oplus S_n.$$

More specifically, for the encryption process, we will use the first Chang et al. algorithm. This algorithm will be used to create share images $G_{10}, G_{11}, ..., G_n$ from the original secret image S. These images will be covered and denoted by $S_1, S_2, ..., S_n$. Then these covered images will be used to share the secret image. In the following it is given the schematic description:

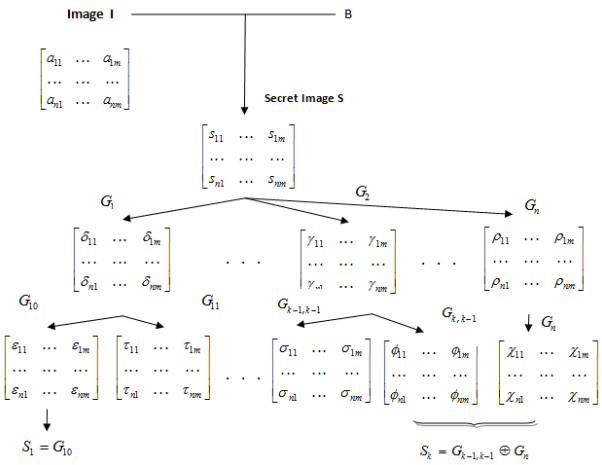

Figure 1

2.1.3. Decryption process

During the decryption process, in the first stage is done the verification of $m \cdot n$ digits pin-code. Each of n participants put its pin-code with $m \cdot n$ digits, in any order. According to the description, sorting algorithm based on increasing order of first digits, through (1), verifies the pin-code.

Verification for a_{ij} is done based on the following formula:

$$a_{ij} = \left(\bar{k}_{ij} \cdot 257 + S - B\right) \cdot (1+B)^{-1} \mod 257 \qquad (3)$$

where $(1+B)^{-1}$ is the inverse element of $(1+B) \bmod 257$.

For retrieving the secret image S we should collect all the n sharing images with XOR operator to revile the secret image. Any $n-1$ or fewer shares cannot retrieve any information about the secret. Therefore, the reconstructed secret image is:

$$S = S_1 \oplus S_2 \oplus S_3 \oplus ... \oplus S_n.$$

Verification for a_{ij} is done from the following formula:

$$a_{ij} = \left(\bar{k}_{ij} \cdot 257 + s_{ij} - B\right) \cdot (1+B)^{-1},$$

where $(1+B)^{-1}$ is inverse element of $(1+B)$ modulo 257.

2.2. Performance comparisons

In Table 1 we compare our proposed scheme with the scheme of Chang [6]. The reason for implementing the Chang and Yu [6] scheme is that it can share complex images, while its disadvantages are such as pixel expansion. Also, insecurity will be eliminated in our scheme.

Table 1. Comparisons of schemes

Features	**Chang and Yu scheme [6]**	**The proposed scheme**
Pixel expansion	Yes	No
Sharing capacity	1/*n*	1/*n*
Image format	Binary gray-level-color	Binary gray-level-color
Type of algorithm	(*n*, *n*)	(*n*, *n*)
Security enhancement	NO	Yes
Sharing shapes	Rectangular	Rectangular

3. Discussion

From the described process we understand that in our proposed scheme we involve two levels of security and in both of them, the encryption process is 'easy' while decryption is very difficult. In the first level, one easily generates numbers b_i and B, while conversely to obtain B one needs all values x_i (to obtain Cantor function one needs to know all the values of participants x_i). It is important to mention that this process is used only once in the beginning of the encryption and thus does not take too many resources. Similarly, in the second level, it is easy to determine shares S_i from the secret image S, while for generating secret image S one needs all shares S_i (in order to reconstruct the secret image). Therefore the reconstruction of the secret image is very hard to be decrypted since it is obtained as a combination of all values x_i, coefficients k_{ij} and shares S_i.

As explained previously, our algorithm modifies the algorithm from [6]. Now, we get to the main point on why we decided to modify this algorithm.

From the literature we reviewed, we found that the algorithm given in [6] is very appropriate for dividing the image into sub-images and since we did not use the same approach of pixel expansion, we have chosen the modified formulas of [7] to cover those sub-images. It is worth mentioning that dividing the image into sub-images that we carried in section 2, increases a number of combinations when one considers attacking the system, by making the scheme very secure.

4. Conclusions

From the extended literature review, one can understand that we have to do with a new, interesting, and important field of study. Visual Cryptography appeared as a result of daily necessities to hide information and then recovering them in the cases when it is not possible or necessary to carry out computer calculations.

We also understand that in the field of Visual Cryptography, one can orient in different directions of research such as the creation of new models, improving existing models, cheating prevention in Visual Cryptography, etc.

Regarding the focused review of the literature, we identified the most appropriate present methods, where we considered found two important algorithms that were modified to developing our scheme. We achieved to built and prove the correctness of our algorithm in this regard. In later stages, we expect to program and test this algorithm to show also practical whether it presents an advantage compared to other contemporary algorithms in Visual Cryptography.

References

[1] M. Naor and A. Shamir, *Visual Cryptography*, Advances in Cryptology-EUROCRYPT'94, LNCS 950, Springer-Verlag, pages 1-12, 1994.

[2] E. R. Verheul and H. C. A. Van Tilborg, *Constructions and properties of k out of n visual secretsharing schemes*, Designs, Codes and Cryptography, Vol. 11, No. 2 (1997) pp. 179–196.

[3] R. Youmaran, A. Adler and A. Miri, *An improved visual cryptography scheme for secret hiding*, School of Information Technology and Engineering (SITE), University of Ottawa, Ontario, Canada

[4] C. Chang, C. Tsai, and T. Chen, *A new scheme for sharing secret color images in computer network*, In the Proceedings of International Conference on Parallel and Distributed Systems, pages 21–27, July 2000.

[5] C. Yang and C. Laih., *New colored visual secret sharingschemes*, Designs, Codes and Cryptography,20:325–335,2000.

[6] C. C. Chang and Yu. T. X., *Sharing a Secret Gray Image in Multiple Images*, In the Proceedings of International Symposium on Cyber Worlds: Theories and Practice, Tokyo, Japan, Nov. 2002, pp.230-237.

[7] D. S. Wang, L. Zhang, N. Ma, and X. Li. *Two secret sharing schemes based on Boolean operations*, Pattern Recognition 2007.

[8] C. C. Thien and J. C. Lin, *An image-sharing method with user-friendly shadow images*, IEEE Trans. Circuits Syst. Video Technol. 13 (12) (2003)1161–1169.

[9] R. Z. Wang and C. H. Su, *Secret image sharing with smaller shadow images*, Pattern Recognition Lett. 27 (6) (2006) 551–555.

[10] Y. S. Wu, C. C. Thien and J. C. Lin, *Sharing and hiding secret images with size constraint*, Pattern Recognition 37 (7) (2004) 1377–1385.

[11] C. C. Chang and I.C. Lin, *A new (t, n) threshold image hiding scheme for sharing a secret color image*, in: Proceedings of the ICCT2003, vol. 1, Beijing, China, 2003, pp. 196–202.

[12] V. Goebel, Th. Plagemann, *Research / Scientific Methods in Computer Science*, Department of Informatics, University of Oslo.

[13] J. Weir and W. Yan, *Visual Cryptography and Its Applications*, Jonathan Weir and WeiQi Yan &Ventus Publishing ApS, 2012.

[14] S. Cimato and Ch. Yang, *Visual Cryptography and Secret Image Sharing*, August 2011, CRC Press.

[15] K. Pachiappan, S. Annaji and N. Jayakumar, *Security in Medical Images using enhanced Visual Secret Sharing Scheme*, ISSN 2319-8885, Vol.03,Issue.09, May-2014, Pages:1642-1645, International Journal of Scientific Engineering and Technology Research.

[16] A. Bhise, N. Borate, A. Garje and Y. Karkal, *Security Internet Voting System*, The international Journal of Engineering and Science, Volume 4, pp.71-75, 2015

[17] A.B Rajendra and H. S. Sheshadri, *Visual Cryptography in Internet Voting System*, Innovative Computing Technology (INTECH), pp. 60 - 64, 2013.

[18] N. Askari, H. M. Heys and C.R. Moloney, *An extended visual cryptography scheme without pixel expansion for Halftone images*, 2013.

[19] M. Ulutas, G. Ulutas and V. Nabiyev, *Medical image security and EPR hiding using Shamir's secret sharing scheme*, The Journal of Systems and Software, 2011@Elsevier.

[20] A. S. Akotkar and Ch. Choudhary, *Security of Face Authentication using Visual Cryptography*,

[21] A. Ross and A. Othman, *Visual Cryptography for Biometric Privacy*, IEEE Transactions on Information Forensics and Security (Volume:6 , Issue: 1), May 2011.

[22] G. Ateniese, C. Blundo, A. De Santis and D. R. Stinson,*Extended Capabilities for VisualCryptography*, TheoreticalComputer Science, vol. 250, pp. 143-161, 2001.

[23] C. C. Wu and L. H. Chen, *A study on visual cryptography*, Mater Thesis, Institute of Computer and Information Science, National Chiao Tung University, Taiwan, 1998.

[24] R. Z. Wang and C. H. Su, *Secret image sharing with smaller shadow images*, Pattern Recognition Lett. 27 (6) (2006) 551–555.

[25] Y. S. Wu, C. C. Thien and J. C. Lin, *Sharing and hiding secret images with size constraint*, Pattern Recognition 37 (7) (2004) 1377–1385.

[26] C. C. Chang and I. C. Lin, *A new (t, n) threshold image hiding scheme for sharing a secret color image*, in: Proceedings of the ICCT2003, vol. 1,Beijing, China, 2003, pp. 196–202.

[27] Tzung-Her Chen and Chang-Sian Wu, *Efficient multi-secret image sharing based on Boolean operations*, Elsevier@2011.

[28] L. S. Reddy and M. V. N. K. Prasad, *Extended Visual Cryptography Scheme for Multi-secret Sharing*, Springer@2016, Volume 44 of the series Smart Innovation, Systems and Technologies, pp 249-257

[29] C.-N. Yang and C.-S. Laih, *Some new types of visual secret sharing schemes*, In Proc. Nat. Computer Symp., 1999, vol. 3, pp. 260–268.

[30] G. B. Horng, T.-G. Chen and D.-S. Tsai, *Cheating in visual cryptography*, Designs, Codes, Cryptog., vol. 38, no. 2, pp. 219–236, 2006.

[31] Chih-Ming Hu and Wen-GueyTzeng, *Cheating Prevention in Visual Cryptography*, IEE Transactions on Image Processing, vol. 16, no. 1, January 2007.

[32] M. Lisi, *Some remarks on the Cantor pairing function*, Le Matematiche, Vol. LXII (2007) - Fasc. I, pp. 55-65

[33] S. Lu, D. Manchala, and R. Ostrovsky, *Visual cryptography on graphs*, J Comb Optim 21, 47–66 (2011). https://doi.org/10.1007/s10878-009-9241-x

Comparative Analysis of Genetic Crossover Operators for the P-Median Facility Location Problem

Nazife Nur ERDOĞMUŞ[1], Bilal ERVURAL[2] and Hüseyin HAKLI[3]

[1] HAVELSAN Inc., Naval Combat Management Technologies Center, Istanbul/Turkiye, nerdogmus@havelsan.com.tr
[2] Necmettin Erbakan University, Konya/Turkey, bervural@erbakan.edu.tr
[3] Necmettin Erbakan University, Konya/Turkey, hhakli@erbakan.edu.tr

Abstract **- The p-median problem is a well-known combinatorial optimization problem with various formulations and many real-life applications. In this study, performance of genetic algorithm (GA) with different crossover operators is studied. Well-known test problems in the literature are used to test the performance of crossover operators. The comparative experimental results show that the two-point crossover operator and the operator that randomly uses the one-point and two-point crossover operators can effectively solve problems represented by direct value coding, such as the p-median facility location problem.**

Keywords **- Genetic algorithm, p-median, facility location, crossover**

I. INTRODUCTION

Facility location decisions play a critical role in designing supply chain networks. The main purpose of the location selection problem is to determine the location of one or more new facilities from a series of discrete or continuous locations. The location problem finds applications in many different areas, such as the location of hubs [1], warehouses [2], computer and communication networks [3], [4], emergency services [5], [6]. The p-median problem is one of the most common facility location problems. The p-median problem aims to meet demands by locating p facilities among a certain number of demand points while minimizing the total weighted distance between them and the facilities.

Kariv and Hakimi [7] showed that the p-median problem is an NP-hard combinatorial optimization problem in a general graph. Since exact methods require high computational effort, various heuristic methods have been used to solve large-sized problems with reasonable computation times. The most commonly proposed heuristic algorithms for the p-median problem include genetic algorithm [3], [8], [9] and tabu search algorithm [10]–[12]. In contrast, in recent years, the stochastic Lagrange search method [13], random search algorithm [14], [15], variable neighbour search algorithm [16] are other heuristic algorithms used in the literature.

Genetic algorithm (GA), a subdivision of evolutionary algorithms, look for solutions to constrained or unconstrained optimization problems with the help of operators such as selection, crossover and mutation. The performance of a GA depends on the strategies and operators used as well as the parameters. The use of the crossover and mutation operator suitable for the problem has a significant effect on the performance of the algorithm [17]. Various crossover operators have been compared for some problems in the literature. Adeli and Cheng [18] compared one-point, two-point, and uniform operators for continuous optimization problems and reported that the best results were obtained with the two-point crossover operator. De Jong and Spears [19] analyzed various crossover operators in terms of the number of crossover points and determined that the quality of the solution improves as the number of crossover points increases. Erbatur and Hasançebi [20] proposed combining two crossover operators in their study about the effects of crossover operators on the behavior of GA. Similarly, Kaya [21] introduced two new crossover operators that use the most common operators in the literature sequential and mixed and investigated the effect of new operators on the behavior of GA.

In this study, the effect of six different crossover operators on the behavior of GA was investigated using a p-median facility location problem. The performance of the crossover operators is analyzed by an experimental study on test problems with different sizes.

In section 2, we provide an overview of the p-median problem. In section 3, we present the characteristics of GA in general terms and describe the proposed GA. Experimental results are discussed in Section 4 followed by the conclusion in Section 5.

II. PROBLEM FORMULATION

The p-median problem is an optimization problem aiming to locate p facilities on the network to minimize the total weighted distance between the demand points and the facilities. It is assumed that each demand will be met from the nearest facility. The p-median problem can be represented by different mathematical models. We can formulate the p-median problem as the integer programming model. Let us define a set of decision variables: (i) $y_j = 1$, if a facility is opened and 0, otherwise; (ii) $x_{ij} = 1$, if customer i is served from a facility located in j and 0, otherwise. The parameter of

d_{ij} indicates the shortest distance from node *i* to node *j*. The formulation of the p-median problem in which demand points and facility sites are restricted to sets *N* and *M*, respectively, is as follows:

$$Min \sum_i \sum_j d_{ij} x_{ij} \quad (1)$$

$$\sum_j y_j = p, \quad (2)$$

$$\sum_j x_{ij} = 1, \quad \forall\, i \in N, \quad (3)$$

$$x_{ij} \leq y_j, \quad \forall\, i \in N, \forall\, j \in M, \quad (4)$$

$$x_{ij},\ y_j \in \{0,1\} \quad \forall\, i \in N, \forall\, j \in M. \quad (5)$$

Equation (1) is the objective function to minimize the total distance. The total number of open facilities is set to p by Equation (2). Equation (3) states that the demand of each customer must be met. Equation (4) guarantees that the demand of each node is allocated only to an opened facility.

III. Genetic Algorithm

The genetic algorithm is an optimization method that works in a similar way to the evolutionary process observed in nature. It seeks the global best solution according to the principle of survival of the fittest among individuals produced by changes in gene structure in a complex, multidimensional search space. To solve any real-life problem with GA, first a set is created to represent a solution in the solution space and a fitness function is defined that measures the quality of the solution. Then three basic operators are used to obtain the better solutions; selection, crossover and mutation. The selection (reproduction) operator is the process of selecting chromosomes to move from the current population to the next population. While the crossover operator obtains new solutions by exchanging information between different chromosomes, the mutation operator obtains new points in the solution space by providing random variation in some existing chromosomes. The general structure of GA is given in Fig. 1.

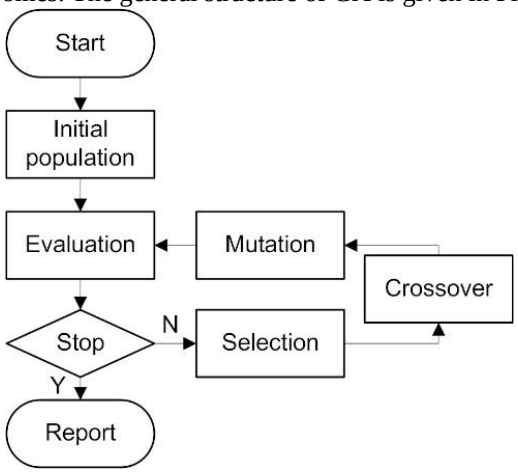

Figure 1: Structure of genetic algorithm

A. Crossover Operators

The role of crossover operators in genetic algorithm is to inherit some traits from generally two parents to create new individuals. Some important points should be considered in the design or use of a crossover operator [22]:

- Inheritance: The main characteristic of the crossover operator is heritability. The crossover operator must inherit genetic material from both parents. An operator is a pure crossover operator (strong heritability) if two identical individuals produce the same offsprings.
- Validity: The crossover operator should produce valid solutions. This is not always possible for constrained optimization problems.

The crossover ratio ($\rho_c \in [0,1]$) represents the ratio of parents to be crossed over. This ratio is determined by other parameters such as population size, selection procedure, mutation operator and is usually in the range of [0.45-0.90].

For linear representations, one-point crossover, the generalized form of one-point crossover, n-point crossover, and uniform are well-known crossover operators. In the case of non-linear representation, the crossover must be reconsidered. One of the most common problems is that the solution space is a permutation of numbers. The use of permutation-based coding is more suitable in many combinatorial optimization problems such as traveling salesman problem, scheduling problem. Partially mapped crossover (PMX), order-based crossover (OX), circular crossover (CX) are the most well-known permutation-based crossover operators.

B. Proposed Algorithm

The proposed algorithm for the p-median facility location problem is presented in this section.

1) Encoding

Since the traditional binary representation is not adequately suited for the p-median problem [2], [3], a direct encoding method is selected where the location facilities are represented as chromosomes. The chromosome length is determined as the total number of facilities to be opened (p). The value of each gene in the chromosome corresponds to the indices of the selected facilities.

$$S = \{s_1, s_2, \dots, s_p\}$$

where s_i indicates the facility point i, $s_i \in L$, and $L = \{l_1, l_2, \dots, l_N\}$. For example, a feasible solution for a 5-median problem is represented as S = (2, 7, 55, 34, 42). These values correspond to the demand points where the facilities will be located.

2) Fitness function and selection mechanism

In order to solve the p-median facility location problem using a GA, the fitness of a chromosome is calculated by the objective function given in Eq. (1). Accordingly, the best-fit individual in a population will be the one that provides the best objective function value among all the individuals in the population.

The roulette strategy is adopted for choosing parents from the population as the selection strategy.

3) Crossover

Crossover operation is performed by selecting one or more random points on the chromosome where the parents' parts exchange happens. The crossover operator plays a significant role in GA.

Direct encoding is more efficient for the p-median facility location problem [2]–[4]. There are different types of crossover often used for direct encoding: one-point crossover, two-point crossover, and uniform crossover. In addition to these operators, the segregation crossover and their different combinations are used in this study.

a) Uniform crossover

In a uniform crossover, a random array should be generated in the binary string. The chromosome length of this array is equal to chromosome lengths in the population. Using this array, each element of the new individual is selected randomly from either parent. This approach is represented in Fig. 2.

P_1	2	7	55	34	42
P_2	85	74	11	32	4
Binary string	0	1	0	0	1
O_1	2	*74*	55	34	*4*
O_2	85	*7*	11	32	*42*

Figure 1: Uniform crossover sample

b) One-point crossover

In this operator, the combination point is arbitrarily selected between 1 and $I - 1$, where I is the length of the chromosome. Two new individuals are obtained by swapping parts; then, the cut-off point is matched in two individuals. An example of this operator is presented in Fig. 3.

P_1	2	7	55	34	42
P_2	85	74	11	32	4
O_1	2	7	11	32	4
O_2	85	74	55	34	42

Figure 2: One-point crossover sample

c) Two-point crossover operator

This operator is similar to one-point, but instead of one, two arbitrary cut-off points are selected between 1 and $I - 1$. New individuals are obtained by replacing parts between the cut-off points of the parent chromosomes (Fig. 4).

P_1	2	7	55	34	42
P_2	85	74	11	32	4
O_1	2	7	11	32	42
O_2	85	74	55	34	4

Figure 3: Two-point crossover sample.

d) Segregation crossover operator

In the segregation operator, two different points on the chromosome are selected for each individual. The length between the selected points must be equal. Then, the parts between the points are replaced, and new individuals are obtained as Fig. 5.

P_1	2	7	55	34	42
P_2	85	74	11	32	4
O_1	11	32	55	34	42
O_2	85	74	2	7	4

Figure 4: Segregation crossover sample

e) Mixed crossover strategy

A mixed crossover approach is proposed by mixing the four different crossover operators. In this approach, new individuals are obtained by randomly selecting one of the uniform, one-point, two-point and segregation operators in each iteration.

f) Mixed one or two-point crossover

In this approach, one of the one-point or two-point crossover techniques is used randomly in each iteration.

4) Mutation

The mutation operation is applied by randomly changing one or several bits of individuals with a certain probability (p_m). It helps avoid stuck local search in the searching space and increases the probability of finding the global optimum.

IV. Experimental Study

In order to test the performance of the algorithm and to compare the efficiency of the crossover operators, 40 test problems are used from the OR Library [26]. Optimal solutions to these problems are known, and problem sizes range from n = 100 to 900 p = 5 to 200 [25].

Table 1 shows the optimal results of the test problems, the total number of nodes (n) and the number of facilities to be opened (p). In this study, the experiments presented below were carried out to evaluate the effect of different crossover operators on the performance of direct coding based GA. For each problem, the proposed GA was run 30 times. The population size was determined as 100, the crossover rate was 90%, and the mutation rate was 10%.

A. Statistical Analysis

In this section, six different crossover operators are compared using test problems from the OR Library. An experimental study has been carried out using 40 test problems with nine different problem sizes and p values ranging from 5 to 200. The best deviation and average deviation values obtained from 30 independent runs with each crossover operator are presented in Table 1.

As shown in Table 1, the mixed one or two-point crossover operator and the two-point crossover operator achieved a better mean deviation than the other operators in twenty-two test problems. The two-point crossover operator has achieved the second best result in nine test problems and the mixed one or two-point crossover operator in six test problems. Both

crossover operators did not rank last in any test problem. Although the results presented in Table 1 allow us to have a general idea, it is necessary to prove whether these results were statistically significant or not. Therefore, first, the parametric test assumptions (conformity to normal distribution and homogeneity of variance) were tested. Non-parametric tests are used since the results do not show normal distribution. For this, nonparametric statistical tests Friedman test and post hoc Wilcoxon test have been performed to uncover significant differences among crossover operators further. The Friedman test is used to see significant statistical differences between operators. Then, Wilcoxon test is used to determine a significant and clear ranking among the operators.

Table 1: Performance results of compared operators

Problem	(n, p)	Best deviation						Average deviation and ranks					
		Uniform	One-point	Two-point	Segregation	Mixed	Mixed 1or2	Uniform	One-point	Two-point	Segregation	Mixed	Mixed 1or2
pmed1	(100, 5)	0.000	0.000	0.000	0.000	0.000	0.000	0.000 (1)	0.000 (1)	0.000 (1)	0.000 (1)	0.000 (1)	0.000 (1)
pmed2	(100, 10)	0.000	0.002	0.003	0.003	0.002	0.001	0.021 (5)	0.012 (1)	0.013 (2)	0.013 (2)	0.021 (5)	0.015 (4)
pmed3	(100, 10)	0.002	0.000	0.000	0.003	0.001	0.000	0.020 (6)	0.016 (4)	0.012 (1)	0.018 (5)	0.014 (3)	0.012 (1)
pmed4	(100, 20)	0.029	0.025	0.020	0.027	0.024	0.019	0.062 (5)	0.056 (4)	0.047 (2)	0.062 (5)	0.051 (3)	0.046 (1)
pmed5	(100, 33)	0.058	0.070	0.079	0.068	0.066	0.059	0.128 (6)	0.108 (1)	0.111 (3)	0.113 (4)	0.113 (4)	0.110 (2)
pmed6	(200, 5)	0.000	0.000	0.000	0.000	0.000	0.000	0.002 (3)	0.001 (2)	0.000 (1)	0.002 (3)	0.002 (3)	0.002 (3)
pmed7	(200, 10)	0.004	0.006	0.004	0.008	0.006	0.004	0.026 (6)	0.020 (2)	0.023 (5)	0.022 (3)	0.022 (3)	0.019 (1)
pmed8	(200, 20)	0.060	0.036	0.041	0.048	0.023	0.049	0.090 (6)	0.072 (1)	0.074 (3)	0.075 (4)	0.072 (1)	0.080(5)
pmed9	(200, 40)	0.125	0.106	0.103	0.120	0.110	0.094	0.158 (6)	0.137 (1)	0.137 (1)	0.144 (5)	0.142 (4)	0.137 (1)
pmed10	(200, 67)	0.209	0.217	0.202	0.206	0.225	0.193	0.288 (6)	0.260 (2)	0.262 (3)	0.265 (4)	0.269 (5)	0.253 (1)
pmed11	(300, 5)	0.000	0.000	0.000	0.000	0.000	0.000	0.003 (3)	0.002 (2)	0.001 (1)	0.003 (3)	0.003 (3)	0.003 (3)
pmed12	(300, 10)	0.017	0.008	0.005	0.014	0.012	0.008	0.035 (6)	0.026 (2)	0.025 (1)	0.029 (5)	0.028 (4)	0.026 (2)
pmed13	(300, 30)	0.078	0.062	0.068	0.061	0.073	0.074	0.112 (6)	0.098 (4)	0.097 (2)	0.095 (1)	0.099 (5)	0.097 (2)
pmed14	(300, 60)	0.154	0.156	0.150	0.147	0.160	0.158	0.204 (6)	0.192 (3)	0.187 (1)	0.192 (3)	0.196 (5)	0.187 (1)
pmed15	(300, 100)	0.293	0.253	0.255	0.283	0.246	0.267	0.326 (6)	0.309 (3)	0.306 (2)	0.311 (5)	0.309 (3)	0.299 (1)
pmed16	(400, 5)	0.000	0.000	0.000	0.000	0.000	0.000	0.002 (1)	0.002 (1)	0.002 (1)	0.004 (6)	0.002 (1)	0.002 (1)
pmed17	(400, 10)	0.016	0.009	0.014	0.004	0.014	0.009	0.038 (6)	0.035 (4)	0.029 (2)	0.036 (5)	0.033 (3)	0.028 (1)
pmed18	(400, 40)	0.108	0.090	0.080	0.090	0.089	0.098	0.130 (6)	0.113 (2)	0.109 (1)	0.113 (2)	0.114 (5)	0.113 (2)
pmed19	(400, 80)	0.208	0.202	0.189	0.198	0.192	0.177	0.241 (6)	0.225 (2)	0.226 (3)	0.226 (3)	0.227 (5)	0.224 (1)
pmed20	(400, 133)	0.342	0.339	0.342	0.337	0.335	0.334	0.405 (6)	0.377 (3)	0.373 (1)	0.380 (4)	0.382 (5)	0.373 (1)
pmed21	(500, 5)	0.000	0.000	0.000	0.000	0.000	0.000	0.008 (3)	0.008 (3)	0.006 (1)	0.011 (5)	0.011 (5)	0.006 (1)
pmed22	(500, 10)	0.017	0.014	0.016	0.015	0.019	0.010	0.041 (6)	0.032 (1)	0.035 (5)	0.032 (1)	0.033 (3)	0.033 (3)
pmed23	(500, 50)	0.128	0.119	0.122	0.118	0.122	0.105	0.160 (6)	0.144 (2)	0.146 (3)	0.147 (4)	0.150 (5)	0.140 (1)
pmed24	(500, 100)	0.225	0.207	0.220	0.229	0.214	0.218	0.262 (6)	0.247 (2)	0.245 (1)	0.253 (5)	0.249 (3)	0.251 (4)
pmed25	(500, 167)	0.373	0.355	0.340	0.368	0.369	0.371	0.417 (6)	0.397 (2)	0.393 (1)	0.403 (4)	0.407 (5)	0.397 (2)
pmed26	(600, 5)	0.000	0.000	0.000	0.000	0.000	0.000	0.006 (3)	0.005 (2)	0.004 (1)	0.009 (6)	0.008 (5)	0.007 (4)
pmed27	(600, 10)	0.019	0.017	0.015	0.016	0.016	0.011	0.034 (6)	0.029 (1)	0.029 (1)	0.029 (1)	0.029 (1)	0.029 (1)
pmed28	(600, 60)	0.151	0.141	0.136	0.139	0.137	0.131	0.175 (6)	0.161 (3)	0.156 (1)	0.164 (5)	0.163 (4)	0.156 (1)
pmed29	(600, 120)	0.246	0.236	0.238	0.240	0.247	0.241	0.280 (6)	0.264 (1)	0.266 (4)	0.265 (3)	0.270 (5)	0.264 (1)
pmed30	(600, 200)	0.384	0.346	0.369	0.363	0.371	0.379	0.416 (6)	0.404 (4)	0.394 (1)	0.397 (2)	0.404 (4)	0.402 (3)
pmed31	(700, 5)	0.000	0.000	0.000	0.000	0.000	0.000	0.005 (1)	0.006 (3)	0.005 (1)	0.010 (6)	0.007 (4)	0.007 (4)
pmed32	(700, 10)	0.017	0.016	0.019	0.009	0.015	0.019	0.043 (6)	0.039 (4)	0.033 (1)	0.035 (2)	0.041 (5)	0.036 (3)
pmed33	(700, 70)	0.160	0.152	0.152	0.170	0.163	0.164	0.196 (6)	0.187 (3)	0.182 (2)	0.187 (3)	0.187 (3)	0.180 (1)
pmed34	(700, 140)	0.290	0.274	0.277	0.272	0.287	0.276	0.314 (6)	0.300 (3)	0.298 (2)	0.301 (4)	0.304 (5)	0.297 (1)
pmed35	(800, 5)	0.000	0.000	0.000	0.000	0.000	0.000	0.009 (1)	0.010 (3)	0.009 (1)	0.012 (5)	0.014 (6)	0.011 (4)
pmed36	(800, 10)	0.023	0.019	0.019	0.013	0.018	0.013	0.043 (6)	0.033 (3)	0.032 (2)	0.037 (4)	0.038 (5)	0.031 (1)
pmed37	(800, 80)	0.177	0.176	0.171	0.144	0.167	0.168	0.206 (6)	0.194 (3)	0.191 (1)	0.194 (3)	0.196 (5)	0.192 (2)
pmed38	(900, 5)	0.000	0.000	0.001	0.000	0.005	0.000	0.007 (1)	0.009 (4)	0.008 (3)	0.010 (5)	0.011 (6)	0.007 (1)
pmed39	(900, 10)	0.016	0.010	0.021	0.018	0.017	0.025	0.044 (6)	0.036 (3)	0.034 (1)	0.034 (1)	0.037 (5)	0.036 (3)
pmed40	(900, 90)	0.190	0.181	0.173	0.171	0.182	0.168	0.221 (6)	0.205 (5)	0.198 (2)	0.202 (3)	0.204 (4)	0.196 (1)

Figure 6 shows the average ranking values obtained using the Friedman method. To check whether there is a difference between the means of all operators, the Friedman test is applied using the mean deviation values presented in Table 1 (considering a level of significance as $\alpha = 0.05$). As a result of the test, Friedman's statistic is higher than the critical value, so the hypothesis of equivalence of results is rejected. Afterwards, the post-hoc Wilcoxon test was performed to define the superiority relations between crossover operators.

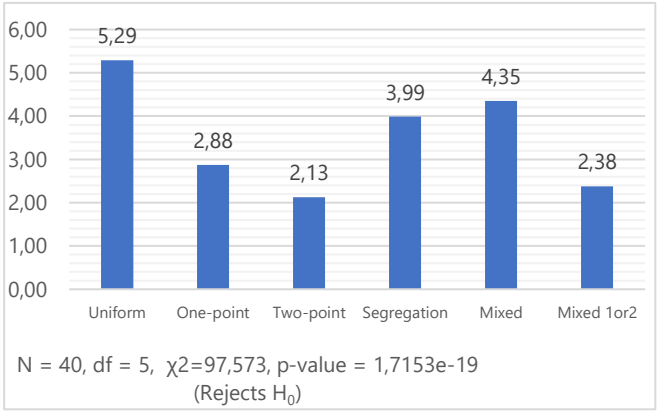

Figure 5: Accuracy Friedman rankings

As a result of the Wilcoxon test, all hypotheses have been rejected except for two operator pairs (Mixed one or two-point with two-point and segregation with mixed). Accordingly, no significant difference has been found between Mixed one or two-point and two-point crossover operators. Similarly, no significant difference has been observed between the segregation and mixed crossover operators. The ranking of the operators according to their solution quality was obtained as follows:

Two-point ~ Mixed One or Two point ≻ One-point ≻ Segregation ~ Mixed ≻ Uniform.

Box plots were constructed for the four selected test problems to display the differences between the crossover operators statistically more clearly. In Fig. 7, the results obtained in all 30 independent runs are summarized in the box plot.

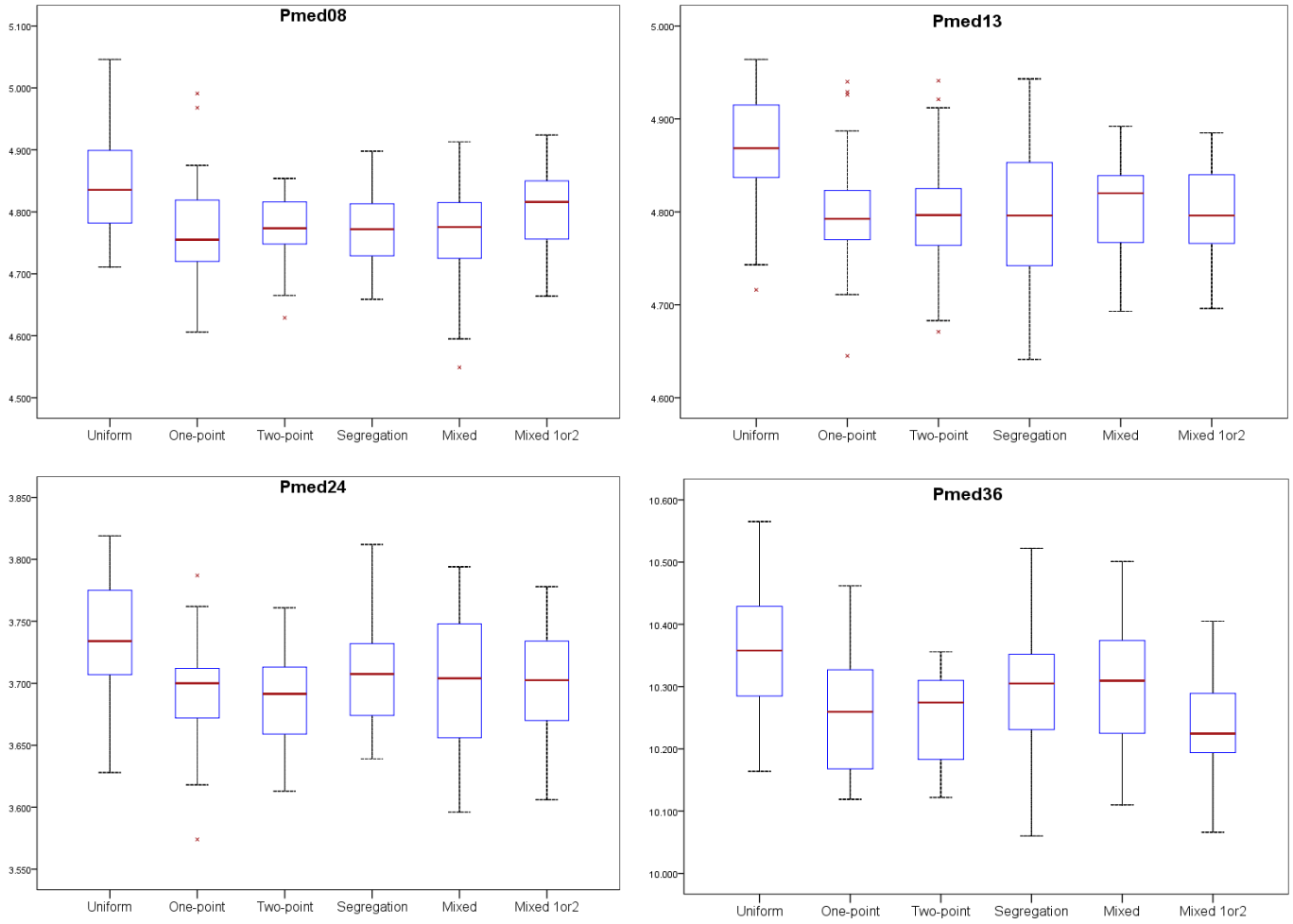

Figure 7: Box-plot charts for some benchmark problems.

V. Conclusion

The selection of the appropriate crossover operator in the genetic algorithm directly affects the algorithm's ability to search for the best solution. In this study, the effect of four available crossover operators and two mixed crossover operators on the performance of the GA developed for the p-median facility location problem has been compared. To compare the effectiveness of crossover operators, 40 test problems with known optimal solutions from the OR Library have been used. Our results in the comparative study provided that two-point crossover and mixed one or two-point crossover operators are more effective than the other operators.

References

[1] Ç. Özgün-Kibiroğlu, M. N. Serarslan, and Y. İ. Topcu, 'Particle Swarm Optimization for Uncapacitated Multiple Allocation Hub Location Problem under Congestion', Expert Syst. Appl., vol. 119, pp. 1–19, Apr. 2019.

[2] E. Aghezzaf, 'Capacity planning and warehouse location in supply chains with uncertain demands', J. Oper. Res. Soc., vol. 56, no. 4, pp. 453–462, Oct. 2005.

[3] S. Salcedo-Sanz et al., 'Optimal switch location in mobile communication networks using hybrid genetic algorithms', Appl. Soft Comput. J., vol. 8, no. 4, pp. 1486–1497, Sep. 2008.

[4] D. Pamučar, L. Vasin, P. Atanasković, and M. Miličić, 'Planning the City Logistics Terminal Location by Applying the Green p -Median Model and Type-2 Neurofuzzy Network', Comput. Intell. Neurosci., vol. 2016, 2016.

[5] F. Silva and D. Serra, 'Locating emergency services with different priorities: the priority queuing covering location problem', J. Oper. Res. Soc., vol. 59, no. 9, pp. 1229–1238, Sep. 2008.
[6] M. K. Oksuz and S. I. Satoglu, 'A two-stage stochastic model for location planning of temporary medical centers for disaster response', Int. J. Disaster Risk Reduct., vol. 44, p. 101426, Apr. 2020.
[7] O. Kariv and S. L. Hakimi, 'An Algorithmic Approach to Network Location Problems. II: The p -Medians', SIAM J. Appl. Math., vol. 37, no. 3, pp. 539–560, Dec. 1979.
[8] Z. Drezner, J. Brimberg, N. Mladenović, and S. Salhi, 'New heuristic algorithms for solving the planar p-median problem', Comput. Oper. Res., vol. 62, pp. 296–304, Jul. 2015.
[9] O. Alp, E. Erkut, and Z. Drezner, 'An Efficient Genetic Algorithm for the p-Median Problem', in Annals of Operations Research, 2003, vol. 122, no. 1–4, pp. 21–42.
[10] E. Rolland, D. A. Schilling, and J. R. Current, 'An efficient tabu search procedure for the p-Median Problem', Eur. J. Oper. Res., vol. 96, no. 2, pp. 329–342, Jan. 1997.
[11] G. Erdoğan, N. Stylianou, and C. Vasilakis, 'An open source decision support system for facility location analysis', Decis. Support Syst., vol. 125, p. 113116, Oct. 2019.
[12] M. B. Bernábe-Loranca, R. González-Velázquez, E. Granillo-Martinez, M. Romero-Montoya, and R. A. Barrera-Cámara, 'P-median problem: A real case application', in Advances in Intelligent Systems and Computing, 2021, vol. 1181 AISC, pp. 182–192.
[13] J. Q. Hale, E. Zhou, and J. Peng, 'A Lagrangian search method for the P-median problem', J. Glob. Optim., vol. 69, no. 1, pp. 137–156, Sep. 2017.
[14] J. M. Colmenar, P. Greistorfer, R. Martí, and A. Duarte, 'Advanced Greedy Randomized Adaptive Search Procedure for the Obnoxious p-Median problem', Eur. J. Oper. Res., vol. 252, no. 2, pp. 432–442, Jul. 2016.
[15] A. Antamoshkin and L. Kazakovtsev, 'Random Search Algorithm for the p-Median Problem', Informatica, no. 37, pp. 267–278, 2013.
[16] A. Herrán, J. M. Colmenar, and A. Duarte, 'A Variable Neighborhood Search approach for the Hamiltonian p-median problem', Appl. Soft Comput. J., vol. 80, pp. 603–616, Jul. 2019.
[17] S. Picek, M. Golub, and D. Jakobovic, 'Evaluation of crossover operator performance in genetic algorithms with binary representation', in Lecture Notes in Computer Science (including subseries Lecture Notes in Artificial Intelligence and Lecture Notes in Bioinformatics), 2011, vol. 6840 LNBI, pp. 223–230.
[18] H. Adeli and N. Cheng, 'Concurrent Genetic Algorithms for Optimization of Large Structures', J. Aerosp. Eng., vol. 7, no. 3, pp. 276–296, Jul. 1994.
[19] K. A. De Jong and W. M. Spears, 'An analysis of the interacting roles of population size and crossover in genetic algorithms', in Lecture Notes in Computer Science (including subseries Lecture Notes in Artificial Intelligence and Lecture Notes in Bioinformatics), 1991, vol. 496 LNCS, pp. 38–47.
[20] O. Hasançebi and F. Erbatur, 'Evaluation of crossover techniques in genetic algorithm based optimum structural design', Comput. Struct., vol. 78, no. 1, pp. 435–448, Nov. 2000.
[21] M. Kaya, 'The effects of two new crossover operators on genetic algorithm performance', Appl. Soft Comput. J., vol. 11, no. 1, pp. 881–890, Jan. 2011.
[22] E.-G. Talbi, M. Basseur, A. J. Nebro, and E. Alba, 'Multi-objective optimization using metaheuristics: non-standard algorithms', Int. Trans. Oper. Res., vol. 19, no. 1–2, pp. 283–305, Jan. 2012.
[23] S. S. Chaudhry, S. He, and P. E. Chaudhry, 'Solving a class of facility location problems using genetic algorithms', Expert Syst., vol. 20, no. 2, pp. 86–91, May 2003.
[24] B. Bozkaya, J. Z. Zhang, and E. Erkut., 'A Genetic Algorithm for the p-Median Problem', in Facility Location: Applications and Theory., Z. Drezner and H. Hamacher, Eds. Springer Berlin Heidelberg, 2002.
[25] J. E. Beasley, 'A note on solving large p-median problems', Eur. J. Oper. Res., vol. 21, no. 2, pp. 270–273, Aug. 1985.
[26] 'p-median - uncapacitated test problems'. [Online]. Available: http://people.brunel.ac.uk/~mastjjb/jeb/orlib/pmedinfo.html. [Accessed: 13-Oct-2021].

A Deep Learning-based Approach for Effective Diagnosis of Coronavirus Disease Using Clinical Data

Ahmet KARA[1]

[1] Hitit University, Çorum/Turkey, ahmetkara@hitit.edu.tr

***Abstract* –With the first case seen in December 2019, the novel coronavirus disease (COVID-19) has rapidly affected millions of people all over the world. Due to the high fatality risk, this outbreak has generated a global crisis shaking all the areas of human life. Hence, it is exceptionally significant to perform a reliable and effective diagnostic system in terms of achieving timely and accurate patient care and combating the outbreak spread. This study aims to achieve a promising solution by proposing a data-driven approach based on deep learning for the diagnosis of COVID-19 disease. In the proposed approach, convolutional neural network (CNN), gated recurrent unit (GRU), and fully-connected layers are utilized to provide an artificial intelligence-based diagnostic model. Besides, a dropout technique is employed to avoid overfitting, which is a potential issue. The performance of the proposed model is performed on a dataset including 18 different laboratory findings in blood samples of 600 patients (520 negative findings and 80 positive findings). As a result of the experiments carried out, it is seen that the proposed approach can provide remarkable results compared with state-of-the-art methods.**

***Keywords* - Deep learning, Covid-19 disease, Diagnosis, Convolutional neural network (CNN), Gated recurrent unit (GRU)**

I. INTRODUCTION

IN December 2019, the novel coronavirus disease, referred to as COVID-19, has emerged in Wuhan, China, and has affected all over the world. Since this issue has become a major public health problem, it was reported by the World Health Organization (WHO) that the COVID-19 disease is a global pandemic [1]. As of October 2021, the total number of infected people around the world has been declared as approximately 235 million, of which about 4.8 million resulted in death. In severe cases, this infection can cause pneumonia, extreme acute respiratory issues, multiple organ failure, and death in more critical patients [2]. Furthermore, the COVID-19 pandemic has impacted the people in all geographic regions in different ways regarding health, education, and economic reasons [3]. Therefore, most researchers and scientists seek promising solutions for precise early diagnosis and timely treatment of this disease.

To combat the COVID-19 pandemic and prevent the spread of the virus, one of the most influential and significant steps is to precisely identify and treat infected patients. Recently, as the golden standard to detect the disease, a real-time reverse transcription-polymerase chain reaction (RT-PCR) test is considered by medical experts [4]. However, the method provides an approximately 60-70% true-positive rate. This means that it gives an accurate result in about 60 out of 100 infected COVID-19 patients. Besides, it can complicate the diagnosis of the disease due to the drawback such as time-consuming, low sensitivity, complex manual operations, and costly [5]. Therefore, the diagnosis of this disease should be supported by various methods consisting of radiological and clinical findings.

Nowadays, artificial intelligence-based approaches that automate the detection of various diseases have been proposed by many researchers due to their high effectiveness and reliability. Especially, deep learning-based systems provide more effective results in diagnosing many diseases using clinical and radiological data. Furthermore, these methods have been extensively used in different fields because of their automatic feature extraction ability from raw data rather than manually capturing features [6]. The convolutional neural network (CNN), gated recurrent unit (GRU), long short-term memory (LSTM), and deep belief network (DBN) are the most preferred deep learning techniques to accomplish complex and nonlinear problems [7]. For these reasons, many researchers believe that deep learning-based approaches may be an effective and reliable solution for the diagnosis of the COVID-19 disease.

With the rapid spread of the COVID-19 disease and its negative impact on people, there has been an important rise in researches on the diagnosis of the COVID-19 from medical outcomes of infected patients. It has been observed that these studies are mostly approaches based on deep learning. For instance, Song et al. [8] introduced a deep learning-based method, which is called Deep Pneumonia, to provide a more accurate COVID-19 diagnosis using radiologic images. In another study [9], the authors proposed a novel approach that combines transfer learning and DensNet-121network so as to achieve more accurate results in the identification of the COVID-19. Göreke et al. [10] developed a new integrated approach based on deep learning and an artificial bee colony (ABC) algorithm for the COVID-19 detection using the blood findings, and the accuracy of their approach was obtained as 94.95 %. With the aim of identifying the COVID-19 with the laboratory outcomes, Alakus and Turkoglu [11] compared the

classification performances of different deep learning approaches. Wu et al. [12] presented the ULNet method to diagnose the COVID-19 patients from chest X-ray images. Shankar et al. [13] designed an intelligent COVID-19 diagnosis system that integrates the recurrent neural networks and a barnacle mating optimization algorithm.

This study proposes an automatic COVID-19 detection model based on deep learning to more accurately identify the disease using routine clinical data. The proposed deep learning-based approach is constructed by the convolutional neural network (CNN), gated recurrent unit (GRU), and the fully-connected layers. Moreover, the experimental results of the proposed model are compared to the state-of-the-art techniques.

The organization of the remaining study is as follows: Section 2 introduces the proposed deep learning-based approach and the clinical dataset. Experimental outcomes are given in section 3. Finally, this study is concluded in section 4.

II. Material And Methods

In this section, the dataset used in this research is first briefly described, and then the methodology of the proposed approach for the COVID-19 classification based on the clinical findings is introduced in detail.

A. Dataset

The dataset used in this study, which is publicly available on Kaggle, was collected at the Albert Einstein Israelita Hospital in Sao Paulo, Brazil [14]. This clinical data obtained from different 5644 patients have 108 features consisting of clinical blood findings and 559 patients infected with COVID-19. To improve the accuracy of the diagnosis, the data preprocessing processes consisting of removing noise data and selecting appropriate features were performed. Therefore, 18 features from this data set have been identified to play a significant role in detecting COVID-19 disease [11], [15]. In addition, only 600 patients' data are available for these selected features, of which 520 patients are COVID-19 positive, and 80 patients are negative.

B. Proposed Method

In this research, to detect COVID-19 disease using laboratory findings, an integrated approach based on deep learning that consists of CNN, GRU, and fully-connected layers is used to extract superior features from the data.

CNN, which is a special kind of multilayer perceptron, has been preferred in many applications such as image classification, signal processing, and object detection. The primary aim behind a CNN is to extract local features by reducing dimensions from the raw input data. A typical CNN structure includes the convolutional layers, the pooling layers, and the fully connected layers. The convolution layer comprises some kernels to learn high-level features from the input data [12]. The output of this operation can be given as:

$$v_i^l = \gamma(\sum w_i^{l-1} * x^{l-1} + b_i^l) \quad (1)$$

Where v_i^l represents the generated feature maps, w_i^{l-1} denotes the kernel weight vectors, x^{l-1} is the input features, b_i^l is the bias vectors. γ and $*$ the activation function and the convolutional operator, respectively.

As another significant deep learning method used in the proposed approach, GRU is an extended version of RNN units in accomplishing the vanishing and exploding gradient issue. GRU has been extensively applied in various real-world applications to capture long-term patterns from the input data. Besides, it is combined with two gates that allow the current input to connect with the previous inputs. These gates are the reset gate and the update gate [16]. The last component in the proposed approach is the fully-connected layers that integrate the more characteristic patterns obtained from CNN and GRU networks. In classification applications, this component is utilized to provide more categorical outputs to fulfill the classification task [12].

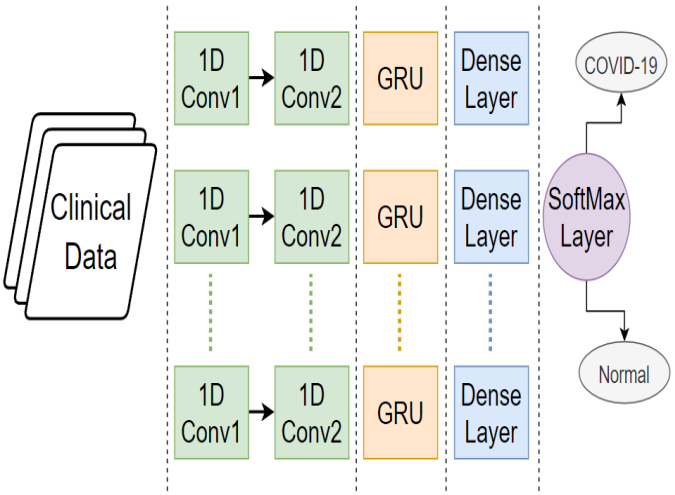

Figure 1: The architecture of the proposed approach.

Figure 1 illustrates the architecture of the proposed hybrid approach for COVID-19 diagnosis. This approach aims to provide a more accurate and effective diagnosis of COVID-19 disease from input data acquired by clinical findings. Firstly, three 1D CNN with different kernel size is applied to effectively capture feature maps from the raw clinical findings. The second one is the GRU, and it is leveraged to learn the long-term dependencies from the features extracted by CNN. Then, two fully-connected layers are employed to complete the classification task. Moreover, the dropout technique is applied to overcome the overfitting problem in the training stage. After extracting the superior features, the SoftMax function in the last layer is implemented to classify cases as COVID-19 positive or normal. As formulated below.

$$\delta_q = \frac{exp(z_q)}{\sum_{k=1}^{K} exp(z_k)} \quad (q = 1, 2, \dots, K) \quad (2)$$

Where K represents the number of categories and z_q is the input vector to the $SoftMax$ function.

III. Experimental Setting And Results

This section addresses the experimental setting, the benchmark methods, and the results of the proposed approach for the COVID-19 diagnosis.

A. Experimental Setting

The deep learning method proposed in the research comprises two convolution layers with kernel sizes of 5 and 3, a GRU layer with 16 units, and two fully connected layers with 64 and 2 hidden units to accurately detect COVID-19 disease. To avoid the overfitting issue in this network, a dropout layer with a rate of 0.25 is used between different layers. In the proposed approach, binary cross-entropy is applied as the loss function during the training stage. Also, the Adam function with a learning rate of 0.001 is employed to optimize the loss function. Finally, the number of epochs and batch size are 150 and 16, respectively.

In order to validate the results of the proposed approach, it is preferred the machine learning-based support vector machine (SVM), the fully-connected network with two dense layers (DNN), and the RNN-based network with two layers. The dataset used for COVID-19 diagnosis is divided into two groups: a training set and a testing set, which is applied to the train-test split approach with a 70:30 ratio.

The performance indices consisting of accuracy, precision, recall, and F1-score are utilized to evaluate the classification efficiency of the proposed approach. The calculations of these indices are defined as follow:

$$Accuracy = (TP + TN)/(TP + TN + FP + FN) \quad (3)$$

$$Recall = TP/(TP + FN) \quad (4)$$

$$Precision = TP/(TP + FP) \quad (5)$$

$$F1\_score = 2 * TP/(2 * TP + FP + FN) \quad (6)$$

Where TP, TN, FP, and FN denote true positive, true negative, false positive, and false negative, respectively.

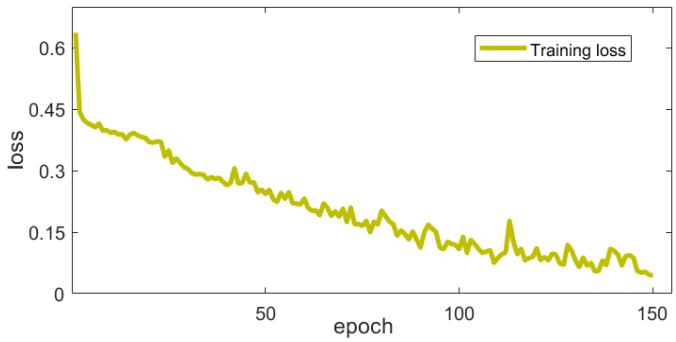

Figure 2: Training loss curve.

B. Results

This part addresses the experimental results of the proposed approach to diagnose the COVID-19 disease correctly. The performance of the proposed method is compared with different benchmark models such as SVM, DNN, and RNN. First, Figure 2 depicts the loss curve of the proposed approach during the training stage with the number of epochs. In the end epoch, it can be observed that the training loss is reduced to 0.1. It can be said that it appears to be steady in the last periods. This means that the proposed model has converged effectively.

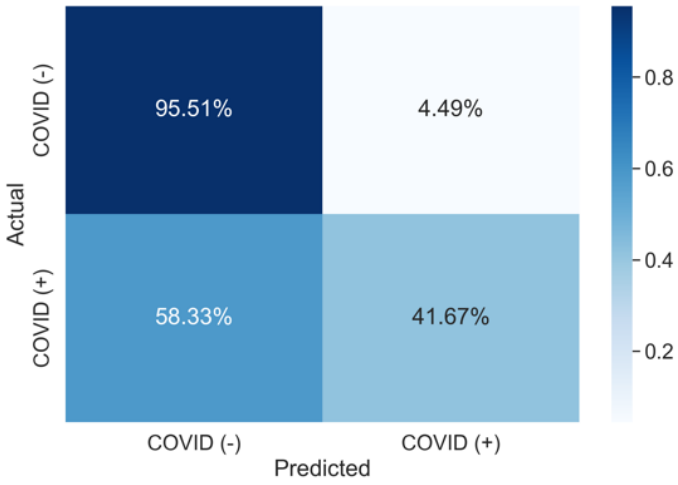

(a) Proposed model

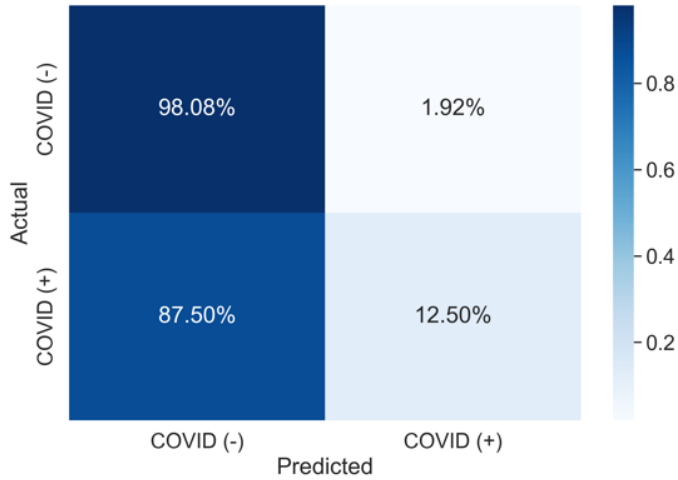

(b) DNN model

Figure 3: Confusion matrix results of our method and DNN

To assess the classification accuracy of the proposed approach, confusion matrices determined according to the classification results are demonstrated in Figure 3. In the negative cases, the proposed approach has a 95.51% success rate, misclassifying 4.49%. Considering the figure, the proposed method and DNN have exhibited superior results in the COVID-19 negative cases. Besides, in the COVID-19 positive cases, the proposed model provides a better classification compared to DNN. On the other hand, the proposed method achieves a 41.67% success rate in the COVID-19 positive cases.

In addition, accuracy, F1-score, recall, and precision for the proposed model and the benchmark methods are depicted in Table 1. As clearly observed from the table, the proposed approach outperforms the benchmark methods and an existing

study in terms of accuracy, F1-score, recall, and precision. It achieved 88.33% accuracy, 87.47% F1-score, 87.07% precision, and 88.33% recall. Besides, the second-best results are obtained by RNN with 87.78% accuracy, 86.36% F1-score, 85.93% precision, and %87.78 recall. Considering all these consequences, the presented approach can be revealed promising outcomes to diagnose the COVID-19 disease effectively.

Table 1: Comparison of the performance metrics of each method.

	Accuracy	F1-score	Precision	Recall
SVM	0.8667	0.8048	0.7511	0.8667
DNN	0.8667	0.8303	0.8287	0.8667
RNN	0.8778	0.8636	0.8593	0.8778
Batista et al. [17]	0.8420	0.7800	0.7800	0.8000
Proposed	**0.8833**	**0.8747**	**0.8707**	**0.8833**

IV. Conclusion

This study has introduced a deep learning-based hybrid approach that aims to diagnose the COVID-19 disease using clinical blood findings. The developed approach comprises the integration of two convolution layers, a GRU layer and the fully connected layers for learning the superior features from raw clinical data. To evaluate the performance of the proposed approach, comparisons with the benchmark models, including DNN, RNN, and SVM, have been carried out. Experimental consequences on a real-world clinical blood findings dataset indicate that the developed approach can achieve competitive performance in detecting the COVID-19 patients, compared with the benchmark methods and an existing study.

References

[1] K. Hu et al., "Deep supervised learning using self-adaptive auxiliary loss for COVID-19 diagnosis from imbalanced CT images," *Neurocomputing*, vol. 458, pp. 232–245, Oct. 2021.

[2] S. Prasanth, U. Singh, A. Kumar, V. A. Tikkiwal, and P. H. J. Chong, "Forecasting spread of COVID-19 using google trends: A hybrid GWO-deep learning approach," *Chaos, Solitons & Fractals*, vol. 142, p. 110336, Jan. 2021.

[3] Z. Li et al., "A deep-learning-based framework for severity assessment of COVID-19 with CT images," *Expert Syst. Appl.*, vol. 185, p. 115616, Dec. 2021.

[4] L. Wynants et al., "Prediction models for diagnosis and prognosis of covid-19: systematic review and critical appraisal," BMJ, p. m1328, Apr. 2020.

[5] A. Saygılı, "A new approach for computer-aided detection of coronavirus (COVID-19) from CT and X-ray images using machine learning methods," Appl. Soft Comput., vol. 105, p. 107323, Jul. 2021.

[6] D. M. Ibrahim, N. M. Elshennawy, and A. M. Sarhan, "Deep-chest: multi-classification deep learning model for diagnosing COVID-19, pneumonia, and lung cancer chest diseases," Comput. Biol. Med., vol. 132, p. 104348, May 2021.

[7] K. N. Qureshi, A. Alhudhaif, M. Ali, M. A. Qureshi, and G. Jeon, "Self-assessment and deep learning-based coronavirus detection and medical diagnosis systems for healthcare," Multimed. Syst., Sep. 2021.

[8] Y. Song et al., "Deep learning Enables Accurate Diagnosis of Novel Coronavirus (COVID-19) with CT images," IEEE/ACM Trans. Comput. Biol. Bioinforma., pp. 1–1, 2021.

[9] C. Li, Y. Yang, H. Liang, and B. Wu, "Transfer learning for establishment of recognition of COVID-19 on CT imaging using small-sized training datasets," Knowledge-Based Syst., vol. 218, p. 106849, Apr. 2021.

[10] V. Göreke, V. Sarı, and S. Kockanat, "A novel classifier architecture based on deep neural network for COVID-19 detection using laboratory findings," Appl. Soft Comput., vol. 106, p. 107329, Jul. 2021.

[11] T. B. Alakus and I. Turkoglu, "Comparison of deep learning approaches to predict COVID-19 infection," Chaos, Solitons & Fractals, vol. 140, p. 110120, Nov. 2020.

[12] T. Wu, C. Tang, M. Xu, N. Hong, and Z. Lei, "ULNet for the detection of coronavirus (COVID-19) from chest X-ray images," Comput. Biol. Med., vol. 137, p. 104834, Oct. 2021.

[13] K. Shankar et al., "An optimal cascaded recurrent neural network for intelligent COVID-19 detection using Chest X-ray images," Appl. Soft Comput., vol. 113, p. 107878, Dec. 2021.

[14] "Diagnosis of COVID-19 and its clinical spectrum," Kaggle, 2020. https://www.kaggle.com/einsteindata4u/covid19 (accessed Sep. 20, 2021).

[15] M. AlJame, I. Ahmad, A. Imtiaz, and A. Mohammed, "Ensemble learning model for diagnosing COVID-19 from routine blood tests," Informatics Med. Unlocked, vol. 21, p. 100449, 2020, doi: 10.1016/j.imu.2020.100449.

[16] Ren L, Cheng X, Wang X, et al., "Multi-scale Dense Gate Recurrent Unit Networks for bearing remaining useful life prediction," Futur Gener Comput Syst vol. 94, p. 601–609, 2019.

[17] A. F. de M. Batista, J. L. Miraglia, T. H. R. Donato, and A. D. P. Chiavegatto Filho, "COVID-19 diagnosis prediction in emergency care patients: A machine learning approach," medRxiv, 2020.

Forecasting Traffic Density Based on a Hybrid Artificial Neural Network Model

Z.I.ERZURUM CICEK[1] and Z. KAMISLI OZTURK[2]

[1] Eskisehir Technical University, Eskisehir/Turkey, zierzurum@eskisehir.edu.tr
[2]Eskisehir Technical University, Eskisehir/Turkey, zkozturk@eskisehir.edu.tr

Abstract **- Traffic density, the number of vehicles per unit length of the road, is one of the basic properties of a traffic stream. One way to detect traffic congestion before it happens is to predict near future traffic density. Traffic density data is a time series by nature, and as it is known, various statistical methods or machine learning methods can be used in the forecasting of time series. In this study, for traffic density forecasting, a forecasting model is generated based on a hybrid artificial neural network approach, which was proposed in one of our previous studies. In this approach, the parameters of the artificial neural network are optimized using a biased random key genetic algorithm. To test the proposed forecasting model, the hourly traffic density data of Istanbul is used. In addition, the proposed approach is compared with the forecasting models based on the most used machine learning models.**

Keywords **- Forecasting, artificial neural networks, metaheuristics, genetic algorithms, support vector regression.**

I. INTRODUCTION

TRAFFIC is a dynamic network in which everyone living in society is constantly involved. This network is not fluid throughout the day. Traffic jams are events that are frequently encountered during the day and cause loss of time. For this reason, researchers are studying forecasting various traffic characteristics to detect traffic congestion in existing traffic networks.

There are three characteristics of traffic: flow, density and speed. Traffic flow and density are concepts that can be confused with each other due to daily use. While traffic flow is defined as the number of vehicles passing from a specific point in a given time period, traffic density is defined as the number of vehicles covering a unit-length highway at a time. Traffic speed is the speed of movement of a vehicle.

In this study, traffic density occurred in Istanbul, Turkey is tried to be forecasted using a hybrid Artificial Neural Network model that was proposed in a previous study. The performance of the proposed model is compared with Artificial Neural Networks (ANN) and Support Vector Regression (SVR) models. The remaining of the study is organized as follows. In Section 2, the studies about traffic density forecasting will be given. The methodology of ANN and SVR are explained and the proposed hybrid model is described in Section 3. The computational results and conclusions are given in Sections 4 Experimental study, 5 Conclusions respectively.

II. LITERATURE REVIEW

In recent years, researchers have been presenting forecasting studies on traffic speed, flow, density, state, etc. Since the traffic characteristic discussed in this study is traffic density, forecasting studies presented in recent years on this subject have been examined.

Nam et al. [1] proposed a long short-term memory neural network for traffic density data, which were obtained from Connected and Autonomous Probes. Ketabi et al. [2] compared multiple variants of recurrent neural network models and seasonal models based on 40 day-long traffic density data from 58 cameras in London. Tas and Sezen [3] presented a multivariate ANN model for traffic density forecasting using variables such as day, working hours, general weather conditions, temperature, wind speed, humidity levels, etc. for Istanbul, Turkey. Kriegel et al. [4] propose a novel statistical approach to forecast the density on any edge in such a network at a future point of time.

As can be seen from the studies in the literature, different types of ANN models are used in traffic density forecasting. In this study, a previously proposed metaheuristic-based ANN model is used in traffic density forecasting.

III. BACKGROUND

In this section, ANN and SVR, which are the methods used in traffic density forecasting, will be briefly explained and the artificial neural network model based on the biased random key genetic algorithm that we have proposed in our previous study will be described.

A. Artificial Neural Networks

Inspired by biological systems, particularly by research into the human brain, ANNs are able to learn from and generalize from experience [5]. An example of an ANN model with an input layer, a hidden layer and an output layer is given in Figure 1.

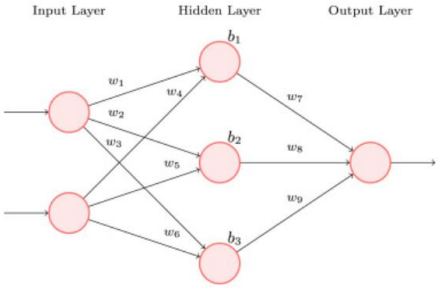

Figure 1: A basic ANN model.

The output value of an ANN is obtained by forward computation. This process provides the output by transmitting the information received from the input layer through the weight values *w* and differentiable transfer functions between the layers. The error calculated as the deviation of the obtained output value from the true value is propagated back to the network and thus the weights are updated. This process, which is carried out to train the ANN, is called backpropagation.
The backpropagation algorithm is one of the most used algorithms for the ANN training process, which means finding the most appropriate weight values. The algorithm searches for the minimum of the error function in the weight space using the gradient descent method. The value of weights that minimizes the error function is the output of this learning problem.

B. *Support Vector Regression*

Support Vector Regression (SVR) is an extension of Support Vector Machines (SVM), one of the machine learning algorithms for classification. After being developed by Vapnik for classification, SVM was extended for regression modeling by Schlköpf et al. [7]. In the expression $(x_1,y_1),...,(x_t,y_t)$ with a specific training set, y_i is the target value of x_i. SVR trains a regression model that will be used to predict future target data. The SVR function is formulated as in Equation (1).

$$f(x) = w^T \varphi(x) + b \tag{1}$$

Where *x* is a nonlinear mapping from the input space to the feature space. *w* is the vector of the weighting coefficients and b is the deviation constant. The values of *w* and *b* are obtained by minimizing the mathematical model of SVR given in Equations (2), (3), and (4):

$$minimize\ \frac{1}{2}\|w\|^2 \tag{2}$$
$$y_i - (\langle w, \varphi(x_i) + b\rangle) \leq \varepsilon \tag{3}$$
$$(\langle w, \varphi(x_i) + b\rangle) - y_i \geq \varepsilon \tag{4}$$

Outlier points are not removed from the dataset to make the method stronger. To deal with this problem, outlier points are penalized with idle variables ξ,ξ* as given in Equations (5), (6) and (7).

$$minimize\ \frac{1}{2}\|w\|^2 + C\sum_{i=1}^{l}(\xi_i + \xi_i^*) \tag{5}$$
$$y_i - (\langle w, \varphi(x_i) + b\rangle) \leq \varepsilon + \xi_i \tag{6}$$
$$(\langle w, \varphi(x_i) + b\rangle) - y_i \geq \varepsilon + \xi_i^* \tag{7}$$
$$\xi_i; \xi_i^* \geq 0 \tag{8}$$

Where the cost constant C > 0 determines the tradeoff between model complexity and training error.

$$f(x) = \sum_{i=1}^{l}(\alpha_i + \alpha_i^*)\, K(x_i, x) + b \tag{9}$$

Equation (9) is the solution of the dual of the problem. (α_i, α_i^*) non-class Lagrangian multipliers and $K(xi,x)$ is the kernel function that expresses the inner product. Linear, polynomial, Gaussian functions and Radial Basis Function (RBF) are among the frequently used kernel functions.

C. *Biased Random Key Genetic Algorithm Based Artificial Neural Networks*

Biased Random Key Genetic Algorithm Based Artificial Neural Network (BRKGA-NN) algorithm was proposed in one of our proposed study [6]. The biased random key genetic algorithm basically tries to optimize the number of hidden neurons, bias values of hidden neurons and the connection weights between nodes. Thus, the number of hidden neurons and their threshold values in the hidden layer, which can be determined by trial-and-error during the artificial neural network design and training phase, are determined by the algorithm automatically. In addition, the training phase is completed with BRKGA-NN instead of backpropagation algorithm.

It is shown by using different time-series datasets and real-life datasets that BRKGA-NN algorithm mostly makes more successful forecasts than ANN with backpropagation, Genetic algorithm-based ANN, Support Vector Regression, and ARIMA as a statistical forecasting method.
The basic working principle of BRKGA–NN algorithm is given in Figure 2.

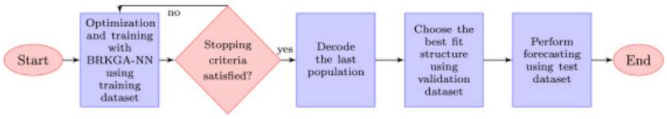

Figure 2: The basic working principle of BRKGA–NN algorithm.

More detailed information about the BRKGA-NN algorithm can be obtained from the aforementioned study.

IV. COMPUTATIONAL EXPERIMENTS

A. *Data*

As we mentioned before, traffic density refers to the number of vehicles on a part of the road that covers a certain length at a certain and fixed time scale. Traffic density is collected by sensors, cameras, etc. on the roads. Traffic density, like traffic flow, is a one-day cycle. During this cycle, traffic density peaks at "peak times". These peaks often come with traffic jams. It has a seasonal characteristic with this cycle of traffic density that renews itself every day.

In this study, traffic density datasets are extracted from Istanbul hourly traffic density data in the Istanbul Metropolitan Municipality (IBB) Open Data Platform [8]. The data source includes traffic density data from January 2020 to May 2021. In this data source, when Istanbul is divided into equal parts geographically, the number of individual vehicles in the parts, the average speed, maximum speed, and minimum speed of these vehicles are included.
In this study, 4 traffic density datasets were created using the mentioned data source. By choosing different locations and date ranges, datasets of different sizes were created. The dataset is a time series containing only variable density data. Table 1 summarizes the properties of the generated datasets.

Table 1: Datasets.

Dataset	Size	Information
sxk3pz	1422	Traffic density of 'sxk3pz' location (January, February, 2020)
sxk9bk	735	Traffic density of 'sxk9bk' location (January, 2020)
sx7fw9	1714	Traffic density of 'sx7fw9' location (October, November, December, 2020)
sxkbbe	2843	Traffic density of 'sxkbbe' location (June, July, September, October, 2020)

The generated datasets are visualized in Figure 3.

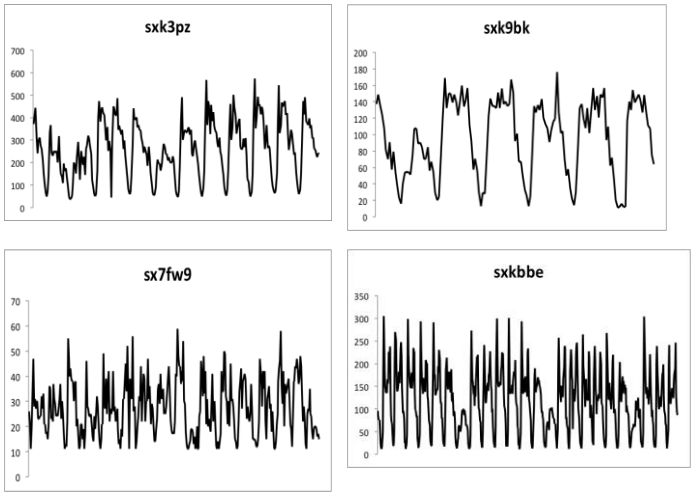

Figure 3: The datasets.

B. Computational Results

The parameters of the BRKGA-NN algorithm were determined by the grid search technique applied for a part of the parameter range suggested by Gonçalves and Resende [9] and the parameter combination that gave the best forecasting values was selected among the parameter values given. The parameters of ANN model was adjusted by using the parameters obtained after the BRKGA-NN was run. Grid search technique was applied to determine the SVR parameters. The methods used in the study were coded using the Python 3 programming language.

The datasets are divided into three parts as training, validation and testing. 70% of each dataset is allocated to training dataset, 10% is validation and 20% is testing. Before forecasting, min-max normalization was applied to the considered datasets.

As error metrics, Mean Absolute Error (MAE), Mean Square Error (MSE) and Mean Absolute Percentage Error (MAPE), which are used in time series forecasting generally, were used. These metrics are calculated as given in Equations (10), (11) and (12) respectively.

$$MAE = \frac{1}{n}\sum_{t=1}^{n} e_t \quad (10)$$

$$MSE = \frac{1}{n}\sum_{t=1}^{n} {e_t}^2 \quad (11)$$

$$MAPE = \frac{1}{n}\sum_{t=1}^{n} \left|\frac{e_t}{y_t}\right| \quad (12)$$

where e_t refers to error between actual and forecasted values and y_t denotes the actual value of observation *t.*

The obtained results for time series datasets are given in Table 2.

Table 2: The performance values of each forecasting method.

Dataset	Method	MAE	MSE	MAPE
sxk3pz	ANN	53.641	**5023.438**	29.724
	BRKGA-NN	**53.363**	5050.767	**28.056**
	SVR	54.383	5241.296	29.300
sxk9bk	ANN	19.665	591.266	35.269
	BRKGA-NN	**18.454**	**559.579**	**30.199**
	SVR	18.931	575.100	30.975
sx7fw9	ANN	6.816	77.747	26.817
	BRKGA-NN	6.586	**70.248**	27.300
	SVR	**6.539**	70.451	**26.600**
sxkbbe	ANN	29.678	1693.133	42.205
	BRKGA-NN	**29.075**	1678.444	**37.270**
	SVR	29.756	**1671.771**	43.160

As can be seen from Table 2, BRKGA-NN algorithm provides mostly better-forecast values for considered dataset than ANN. Also, the test results showed that the performance of BRKGA-NN is comparable to SVR. The actual and forecasted values using BRKGA-NN for each dataset are visualized in Figure 4. As can be seen from the figure, BRKGA-NN succeed in capturing the pattern of the data with the proposed algorithm. However, it is also seen that sometimes BRKGA-NN cannot reach the maximum and minimum points completely. Error-values are also mostly due to these deficiencies.

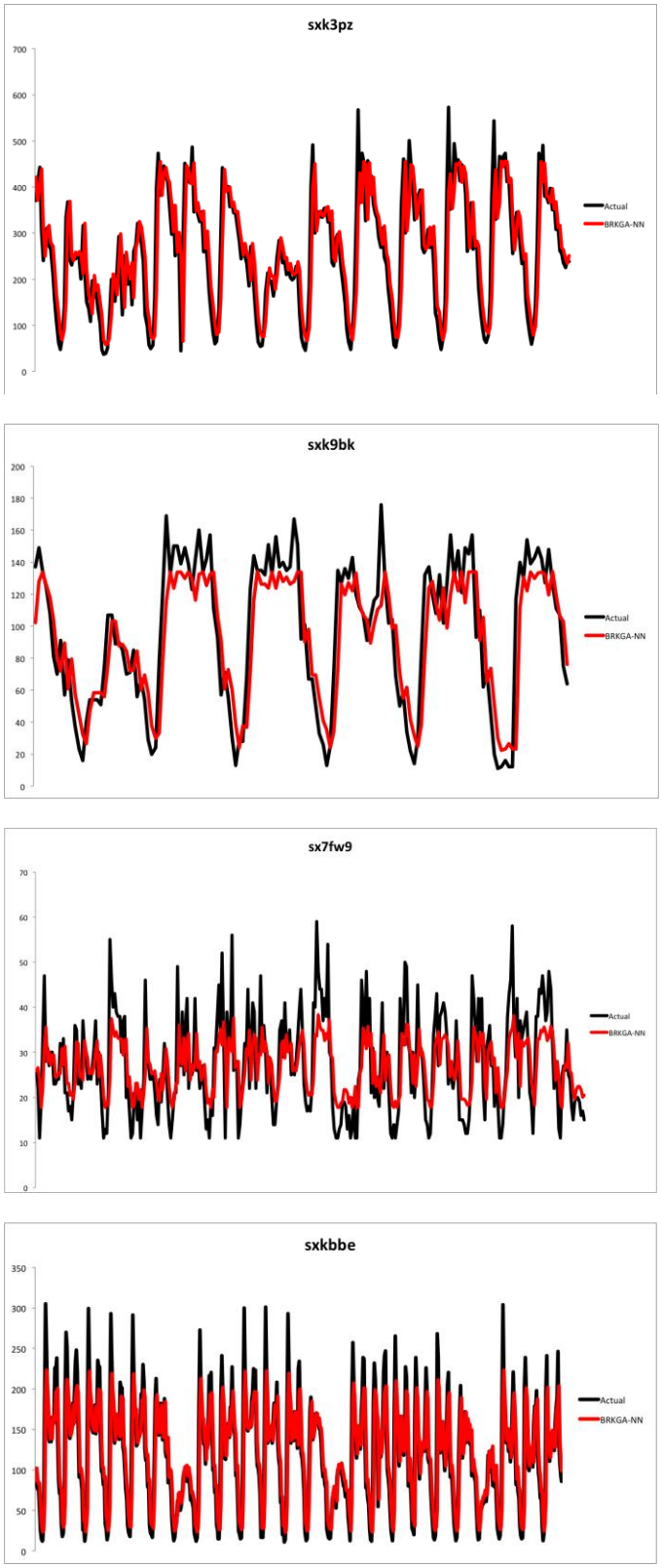

Figure 4: The actual values and forecasts using BRKGA-NN

V. Conclusion

In this study, a previously proposed metaheuristic-based ANN model for traffic flow forecasting is used for traffic density forecasting. The proposed model performance has been tested using Istanbul hourly traffic density data. Also, the model performance is compared with classical back propagation ANN and SVR. The test results showed that the proposed metaheuristic-based ANN model was mostly more successful than the classical ANN. It has shown once again that it is more advantageous to use the BRKGA-NN method, in which the optimal parameters of ANN are determined by the algorithm itself. In addition, the BRKGA-NN algorithm has been found to be competitive with the SVR, which is quite successful in forecasting performance.

As future studies, various improvements are planned to accelerate the proposed BRKGA-NN method and to reduce the forecasting errors.

Acknowledgment

This study is supported by Eskisehir Technical University Scientific Research Projects Committee (1709F506).

References

VI.

[1] Daisik Nam, Riju Lavanya, R. Jayakrishnan , Inchul Yang, and Woo Hoon Jeon, "A Deep Learning Approach for Estimating Traffic Density Using Data Obtained from Connected and Autonomous Probes ," *Sensors*, vol. 20, no. 4824, 2020.

[2] Roozbeh Ketabi, Mimonah Al Qathrady, Babak Alipour, and Ahmed Helmy, "Vehicular Traffic Density Forecasting through the Eyes of Traffic Cameras; a Spatio-Temporal Machine Learning Study ," in *DIVANet '19*, Miami, USA, 2019, pp. 81-88.

[3] Nurullah Tas and Bulent Sezen, "Yapay Sinir Ağları ile Trafik Yoğunluğu Tahmini*," *Afyon Kocatepe University Journal of Social Sciences*, vol. 22, no. 4, pp. 1020-1034, 2020.

[4] Hans Peter Kriegel, Matthias Renz, Matthias Schubert, and Andreas Zuefle, "Statistical Density Prediction in Traffic Networks ," in *8th SIAM Conf. on Data Mining* , Atlanta, USA, 2008.

[5] G. Zhang, B. E. Patuwo, and M. Y. Hu, "Forecasting with artificial neural networks: The state of the art ," *Int. J. Forecast.*, vol. 14, no. 1, pp. 35-62, 1998.

[6] Zeynep Idil Erzurum Cicek and Zehra Kamisli Ozturk, "Optimizing the artificial neural network parameters using a biased random key genetic algorithm for time series forecasting," *Applied Soft Computing*, vol. 102, no. 107091, 2021.

[7] Schölkopf, B., Platt, J. C., Shawe-Taylor, J., ve Smola, A. J. (2001). Estimating the support of a high-dimensional distribution. *Neural Computation*, 13, 1443-1471.

[8] IBB Open Data Portal: Hourly Traffic Density Data Set, https://data.ibb.gov.tr/en/dataset/hourly-traffic-density-data-set, accessed: 01.10.2021

[9] J.F. Gonçalves and M.G. Resende, "Biased random-key genetic algorithms for combinatorial optimization. *Journal of Heuristics*, 17, 487-525.

A Hybrid Phishing Detection Model Based on Transformer CharacterBERT from URLs

Muhammad Sanwal [1] and Alper Ozcan [1]

[1] Akdeniz University, Antalya/Turkey, 202151075006@ogr.akdeniz.edu.tr
[1] Akdeniz University, Antalya/Turkey, alperozcan@akdeniz.edu.tr

***Abstract* – The security concerns in the cybersecurity area are increasing and, the fundamental purpose of such crimes is to obtain the benefits by achieving confidential data. Phishing is one of the easiest ways to accomplish the private information of the target users. Such attacks exist triggered by multiple methods such as emails, messages, phone calls, etc. Therefore, many machine learning techniques have been proposed to detect phishing URLs before affecting the target users. Lately, the popularity of deep learning techniques has also gained attention in the cybersecurity area. This paper proposes a hybrid deep learning model for the classification task between legitimate and phishing URLs. The proposed model consists of CharacterBERT and DNN based techniques. The CharacterBERT is a modification of the baseline BERT model that learns features from the characters of the given URL instead of complete words. Moreover, deep neural networks are applied to train the model. The PhishTank dataset is used for evaluation purposes, and the obtained results indicate that the proposed model outperforms the previous baseline models in the literature.**

***Keywords* – Phishing, Machine Learning, Deep Learning, Deep Neural Networks, CharacterBERT**

I. INTRODUCTION

We live in an era in which everyone is surrounded by technology. The rapid pace of development in technology has created many opportunities in the field of information technology. However, it is not distinct that everyone that interacts with technology will use it positively. The advancement in information technology has generated potential risks to the secrecy of the people where hackers can access the private information by different techniques. Phishing is one of those techniques used by hackers to access potential target information such as username, password, and other information by using several means of communication such as email or messaging. This specific technique encourages the potential target to open the malicious link or download malicious applications on the device. It is a general approach in which malware communications are sent to hundreds of potential targets, and out of all targets, a specific set of users become a victim [1, 2]. Generally, the number of victims is small, but their information is precious. There are different variants of phishing, such as spear-phishing, in which malware is sent to specific individuals or companies. Another type is clone phishing, in which an email is sent with slightly changed original email content that looks legitimate to the potential targets [3]. Moreover, whaling is another type in which communications are made with high-profile targets, and it seems like it is originated from legal departments. Attackers also use search engine optimization techniques in which phishing pages are ranked higher than legitimate web pages.

Generally, the phishing targets are banking services, emails portals, and social media platforms. In the banking service, the typical user provides their debit/credit card credentials, and through phishing, the information can be retrieved by the hackers. People post a large amount of content on social media platforms, and that information is generally more valuable. The attacker can easily fetch detailed knowledge of the target user by using the techniques mentioned above [4].

Phishing is also a common security concern in the health department. The health department contains the information of patients, doctors, and hackers who are keen to access such data, and this information can be used for different kinds of frauds. The IBM report generated in 2018 states that Health Care Industry is more affected by the data breach. Approximately 15 million patients' data was breached in a single year, and phishing was one of them [5]. Another report generated by the US Federal Bureau of Internet Crime in 2019 indicates that a financial loss of $3.5 billion was estimated by such crimes [6].

The number of malicious web pages is minimal compared to web browsers' total number of web pages. However, these numbers are increasing rapidly, and researchers are providing multiple

techniques to detect phishing URLs. Recently, many machine learning and deep learning techniques have been proposed for such tasks. Moreover, in recent times semi-supervised machine learning has also been used for the generation of text embeddings. Such practices are based on natural language processing methods such as BERT based on the transformers and offer significant improvements over the previous methods [7]. In this paper, we proposed a CharacterBERT-DNN based model to detect phishing URLs. Our model comprises of two steps 1) It generates word-level contextual representations by using a features-based mechanism on character embedding 2) it benefits from the hybrid model that is based on DNN and Transformers called CharacterBERT. It is the modified version of the general BERT model.

Furthermore, this paper is organized in the following structure. The Literature review is presented in Section 2, and detailed information of previously proposed important models is provided in Section 3. Moreover, the proposed work is discussed in Section 4. Section 5 describes the datasets and the experiments for this study, and finally, Section 6 describes the future work and conclusion.

II. LITERATURE REVIEW

The popularity of machine learning gained the attention of researchers in the field of cybersecurity. Many machines learning conventional models have been proposed for phishing detection. The machine learning models commonly used in phishing detection are Support Vector Machines, Decision Trees, Random Forest, Bayesian Additive Regression, etc. Generally, the prepared datasets are used in machine learning methods, and these algorithms are beneficial to detect phishing attacks [8]. Sahingoz et al. proposed multiple machine learning algorithms to recognize phishing URLs. Throughout the different sets of experiments, this study achieved high accuracy from Random Forest with Natural Language Processing [9].

Deep learning is evolving rapidly, and deep learning models such as Recurrent Neural Networks, Deep Neural Networks, Convolution Neural Networks, and multi-layer feed-forward networks are commonly used in the literature to detect phishing attacks. The benefit of deep learning models over traditional machine learning models is that such models extract features directly from the given data.

For example, le et al. [10] proposed a deep learning model based on CNN on words and characters of the URLs. This model outperformed the previous models, but there is a possibility of failure if the phishing URL is short. Yi et al. proposed a deep learning framework to extract the original features of the URL, and later they applied Deep Belief Networks to achieve better accuracy [11]. Another study [12] used a self-structuring neural network model for the detection of phishing URLs. In this study, a total of 600 legitimate and 800 phishing websites have been used to build the model. The results of this study indicate that it achieves better results than many studies in this area.

The other commonly used strategy to detect phishing URLs is heuristic feature-based models. This technique predicts the malware URLs by using features in the URL itself or the page content. This model generally classifies the page as malicious or benign. But these types of models tend to perform worse if there are no heuristic features in the websites. Finally, visual Similarity-based models are another detection technique that is used to detect clone websites. Generally, malicious websites are the clone of legitimate websites. The user believes that they are using the legitimate website because it uses the same HTML tags and CSS that generate the overall format of the website. So, such methods compare the features of legitimate and malicious websites and make a verdict on either the website is malicious or legitimate [13].

Pranav et al. proposed a transformers-based model URLTran in which comprehensive analyses are made on the phishing URLs [14]. This study compared standard language masked models and pre-trained domain-specific tasks with fined tuned models such as BERT and RoBERTa. This model improved the performance significantly to detect the false-positive phishing URLs. Moreover, this model was fined adjusted with the adversarial samples to maintain the low false-positive ratio FPRs under controlled scenarios.

Katherine et al. proposed a phishing detection model specifically from website URLs in which the URLs were opened in the mobile devices. They applied ANN as a baseline performance model to HTML and URL-based website features, and this model achieved more than 96% accuracy compared to other states of the art studies in the literature. Further, the deep ANN model was tested only on the URL. The model performed poorly, achieving an accuracy of 86%, indicating that only URL features are not enough to detect phishing websites. Inspired by language transformer, this study applied two states of the art transformers, BERT and ELECTRA, to see phishing websites as the transformers are good at

achieving better contextual information from the text used in the URLs. However, they tested standard and custom vocabularies and found that pre-trained models with fine-tuning achieve better performance for mobile devices than other models [15].

Zhiqiang et al. [16] proposed a dynamic convolutional neural network to extract the malicious features efficiently. A new folding layer is added in the original network that replaces the pooling layer of the web with the kmax-pooling layer. Moreover, this study proposed a new embedding method for word embeddings that are based on character embedding. The character embedding has leverage over the word embedding to learn better vector representation of a URL. The experiments indicate that word embeddings based on character embeddings achieve higher accuracy of 96%.

III. METHODOLOGY

In this section, we will discuss some state-of-the-art studies that are present in the literature. The primary purpose of this section is to provide some details of well-known methods in the Natural Language Processing domain.

A. Phishing URL

A phishing URL contains hurtful words and characters that target legitimate websites to obtain confidential data. In the literature, multiple techniques are mentioned in the literature review section. But in the below part of this section, we try to summarize some of the popular methods extensively used in the literature to provide you with a basic understanding of these models.

B. Transformers

Recently, transformers have been popular and efficient in Natural Language Processing tasks, usually for time series data analysis. Transformers work in a bidirectional manner, and these are popular attention models for language modelling. As transformers work on the encoder-decoder mechanism in which text as an input is provided to the encoder and decoder outputs the possible prediction. A typical transformer model consists of six components: Embeddings, Positional Encoding, Multi-Headed Attention Layers, Feed-Forward Layers, Residual Connections, and Masks. The details of these components can be read from this article [19].

C. LSTM

It is a recurrent neural network architecture that also deals with time-series data. The architecture of LSTM consists of multiple cells that are recursive. This ability allows it to remember and store the information from the previous intervals. The LSTM cell states can be modified by the forget gate and input modulation gate. The unnecessary data can be overlooked from the forget gate, and new information is added. The activation functions play an essential role for each gate. Afterward, the decision is made by the model to classify the input into its respective category. Moreover, LSTM has shown promising results in the field of cyber security, such as phishing detection. One of the applications of LSTM combined with deep neural networks is described in [20], where the model distinguishes between malicious or legitimate URLs.

D. BERT

In the case of BERT, only an encoder is required as it reads the entire sentence at once. This model tries to learn the context of the word by its surroundings. Technically, it is trained on the Masked Language Model (MLM) with Next Sentence Prediction (NSP). The training of MLMs is done by masking out the tokens in the given sentence randomly, and then these masked out tokens are replaced by unique tokens called MASK. Afterward, the model tries to predict the context of these unique masked tokens given in a sequence. Then, NSP models distinguish between input sentences, either those are continuous segments or not. In BERT, the input sequence is tokenized, flows through the encoders, and outputs the hidden state. These hidden states are the representation of word embeddings [10].

E. Convolutional Neural Networks

CNN's have shown promising results in image processing, especially in the image classification tasks. It is the most popular deep learning architecture in the literature. The key to its popularity is it automatically detects the features from the input without supervision. It is composed of convolutional layers that are the building block of its architecture. Generally, the input is provided to the network, which is processed through several convolutional and pooling layers and fully connected layers. The output is the predicted class of the given input. The power of CNNs is recognized in cyber security, and many methods such as [10] use CNNs to classify the URLs into malicious or legitimate. For example, in the study of phishing URLs, the word or characters of the URL are fed.

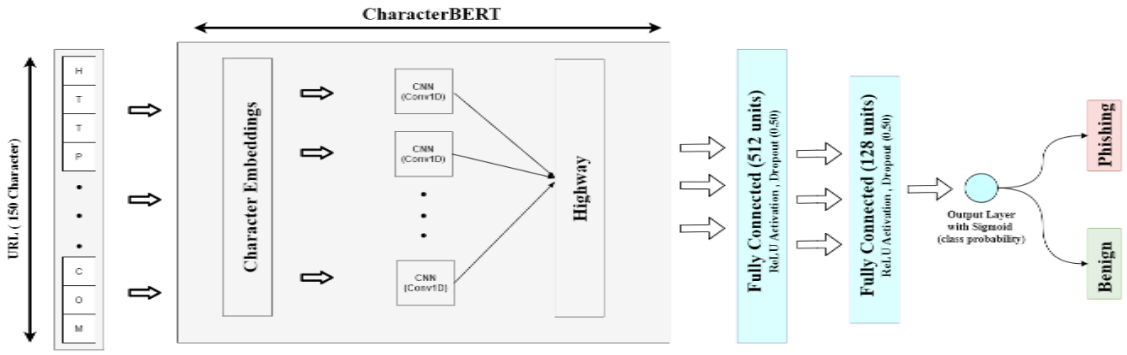

Figure 01: Overview of CharacterBERT model

IV. PROPOSED WORK

In this study, we propose a hybrid model that is the combination of pre-trained transformers and DNN. Precisely for this study, the CharacterBERT transformer is used. This model captures the valuable information and sequential patterns from the URLs of the websites, while most of the other methods require the target websites' content. It uses the sequential string pattern from the URL and classifies them to detect malware or not. The main property of the CharacterBERT model is it learns the representations directly from the URL text and classifies it as legitimate or malicious URLs.

Moreover, it learns non-linear URL embeddings as it is a deep learning framework. In our experiments, this model produced better results than the other baseline models. The below figure illustrates the architecture of the proposed model.

The proposed hybrid model has three layers: 1) CharacterBERT layer, 2) fully connected layers 3) output layer.

A. CharacterBERT layer

It is a new variant of the original BERT model that uses each character to represent the entire word using the Character-CNN module. In contrast, the original model utilizes the whole word for representation in the network. It uses the tokenization technique to represent a single character of the word that is used in [17]. CharacterBERT extracts the features automatically and learns the semantics and patterns from the given URL. Also, we need to define the length of the character in the URL that is being processed in which the longer URLs need trimming, and shorter ones need padding. The padding in the shorter URLs is done by inserting empty characters. The embedding matrix is created with the length of the input sequence of characters. Each character is mapped to its corresponding vector irrespective of the previous or subsequent vectors in the series.

Moreover, the learn embeddings of each character are fed sequentially to the 1-d CNN with filters. Thus, the character embeddings produced earlier are spanned entirely through the CNN filter. Afterward, the max-pooling is done between the character sequence and output layer to create a single representation. Furthermore, the representation from the CNN layers passes through highway layers for non-linearities with residual connections for final embeddings as presented in [17].

B. Fully Connected Layer

To produce a final output, two fully connected layers are defined to receive the input of the CharacterBERT model. Each of these layers is followed by the ReLU activation functions and dropout modules.

C. Output Layer

The last layer only uses the sigmoid function to classify the URLs as either legitimate or malicious.

For novelty, CharacterBERT and DNN algorithms are integrated for phishing detection.

V. EXPERIMENTS AND RESULTS

To compare the proposed work with state-of-the-art studies, we used a PhishTank [18] dataset. This dataset consists of two classes of the URLs legitimate and phishing URLs. As the PhishTank does not

provide free access to the dataset, the Yandex search API is used to find the phishing URLs from the web engines. For this task-specific query, words were constructed by this study [18], and URLs with a very low possibility of phishing were obtained. As the phishing URLs have a concise life, such web pages were among the low-ranked web pages. However, for the testing purpose, the dataset contains 73,575 URLs, of which 36,400 are legitimate, and 37,175 are phishing URLs. To evaluate the performance of the proposed method, we calculated the accuracy, F1-measure value, and AUC as performance metrics. The following formula gives the accuracy:

$$\text{Accuracy} = (TP + TN) / (TP + FP + TN + FN) \quad (1)$$

The F1-measure is the harmonic mean of the precision and recall values. The following formula calculates it.

$$F1 = 2 * \text{Precision} * \text{Recall} / (\text{Precision} + \text{Recall}) \quad (2)$$

For the experiment of the proposed model, the Google Collab environment is used, and the PyTorch library is preferred for the CharacterBERT and DNN models. We experimented with the datasets on different hyperparameters to obtain the best possible results, and the best values were selected. Moreover, ReLU is used as an activation function and sigmoid as a non-linear function for the output layer. Finally, the dropout rate of 0.5 is selected for all layers, and each fold, 40 epochs are used with a batch size of 128.

The achieved results are illustrated in the following table:

TABLE 1: Comparison of different performance metrics for CharacterBERT-DNN and the two baseline models.

Model	Accuracy (%)	F1-Score (%)	AUC (%)
CNN	95.23	95.12	95.49
LSTM	97.24	97.65	97.30
ELECTRA	91.13	91.40	91.82
BERT	97.10	97.38	97.52
CharacterBERT-DNN	98.41	98.23	98.38

As the results in the above table indicate that CharacterBERT-DNN outperformed both baseline models in this area.

VI. CONCLUSION

In this paper, we proposed a CharacterBERT-DNN based model that classifies the legitimate URLs from Phishing. Most of the existing approaches used word-based embedding techniques that are generally based on the original BERT model. However, as the URL size is small compared to the content of the website, so it is difficult to detect the phishing URLs from the legitimate ones. URL contains different characters that may not create valuable embeddings and contextual meaning for the regular model. The proposed model overcomes this deficiency and uses Character-based embeddings to obtain the maximum possible features from the URL and learns it to classify the phishing URLs. The results from the experiments indicate that our approach is better than the baseline models present in the literature. In the future, we plan to apply ELECTRA based on pre-training text encoders that work as a discriminator rather than the generator in the field of natural language processing.

REFERENCES

[1] CSO Types of phishing attacks and how to identify them. Available: https://www.csoonline.com/article/3234716/phishing/types-of-phishing-attacks-and-how-to-identify-them.html [Accessed 16 Feb 2018].

[2] Priestman, Ward et al. "Phishing in healthcare organisations: threats, mitigation and approaches." BMJ health & care informatics vol. 26,1 (2019): e100031. doi:10.1136/bmjhci-2019-100031.

[3] Abdelhamid M. The role of health concerns in phishing susceptibility: survey design study. J Med Internet Res. 2020;22:e18394.

[4] Maneriker, Pranav & Stokes, Jack & Lazo, Edir & Carutasu, Diana & Tajaddodianfar, Farid & Gururajan, Arun. (2021). URLTran: Improving Phishing URL Detection Using Transformers.

[5] IBM Security. Cost of a Data Breach Report. Traverse City, MI: Ponemon Institute LLC; 2019.
URL: https://www.ibm.com/downloads/cas/ZBZLY7KL [accessed 2020-04-13].

[6] Davis J. Health IT Security. Danvers, MA: intelligent Healthcare Media; 2019. The ten most significant healthcare data breaches of 2019
URL: https://healthitsecurity.com/news/the-10-biggest-healthcare-data-breaches-of-2019-so-far [accessed 2020-04-13].

[7] Ashish Vaswani, Noam Shazier, Niki Parmar, Jakob Uszkoreit, Llion Jones, Aidan N Gomez, Łukasz Kaiser, and Illia Polosukhin. 2017. Attention is all you need. In Advances in neural information processing systems. 5998–6008.

[8] Zhang, Y., Hong, J. I. and Cranor, L. F. (2007). Cantina: A content-based approach to detecting phishing websites. 16th Int. World Wide Web Conf. WWW2007, (pp. 639–648). DOI: 10.1145/1242572.1242659.

[9] Sahingoz, O. K., Buber, E., Demir, O. and Diri, B. (2019). Machine learning-based phishing detection from URLs. Expert System Applications. (117), (pp. 345–357). DOI: 10.1016/j.eswa.2018.09.029.

[10] Le, H., Pham, Q., Sahoo, D. and Hoi, S. C. H. (2018). URLNet: Learning a URL representation with deep learning for malicious URL detection. arXiv, no. i.

[11] Yi, P., Guan, Y., Zou, F., Yao, ., Wang, W. and Zhu, T. (2018). Web phishing detection using a deep learning framework. Wireless Communication Mobile Computing. DOI: 10.1155/2018/4678746.

[12] Mohammad, R. M., Thabtah, F. and McCluskey, L. (2014). Predicting phishing websites based on self-structuring neural networks. Neural Computing Application. (25)(2), (pp. 443–458). DOI: 10.1007/s00521-013-1490-z.

[13] Khan, M. F. (2021). Detection of Phishing Websites Using Deep Learning Techniques. Turkish Journal of Computer and Mathematics Education (TURCOMAT), 12(10), 3880-3892.
[14] Maneriker, P., Stokes, J. W., Lazo, E. G., Carutasu, D., Tajaddodianfar, F., & Gururajan, A. (2021). URLTran: Improving Phishing URL Detection Using Transformers. arXiv preprint arXiv:2106.05256.
[15] Haynes, K., Shirazi, H., & Ray, I. (2021). Lightweight URL-based phishing detection using natural language processing transformers for mobile devices. Procedia Computer Science, 191, 127-134.
[16] Wang, Z., Li, S., Wang, B., Ren, X., & Yang, T. (2020, September). A malicious URL detection model based on a convolutional neural network. In International Symposium on Security and Privacy in Social Networks and Big Data (pp. 34-40). Springer, Singapore.
[17] El Boukkouri Hicham, Ferret Olivier, Lavergne Thomas, Noji Hiroshi, Zweigenbaum Pierre, and Tsujii Junichi. 2020.
[18] Sahingoz, O. K., Buber, E., Demir, Ö., & Diri, B., (2019). Machine learning-based phishing detection from URLs. EXPERT SYSTEMS WITH APPLICATIONS, vol.117, 345-357.
[19] Sabty, C., Islam, M., & Abdennadher, S. (2020). Contextual Embeddings for Arabic-English Code-Switched Data. WANLP.
[20] Ozcan, A., Catal, C., Donmez, E. et al. A hybrid DNN–LSTM model for detecting phishing URLs. Neural Comput & Applic (2021). https://doi.org/10.1007/s00521-021-06401-z.

Melanoma Detection with EfficientNet

E. DUMAN[1] and Z. TOLAN[2]

[1] Firat University, Elazig/Turkey, erkanduman@firat.edu.tr
[2]Firat University, Elazig/Turkey, ztolan@hotmail.com

Abstract **- In this study, the performance levels of solution candidates from the EfficientNet family, which is today's most up-to-date and leading CNN architecture, in detecting Melanoma skin cancer were analyzed. Starting with B0, the basic model of the EfficientNet family, the CNN model was effectively scaled up to reach B7 to achieve higher accuracy values. When scaling up a model from the EfficientNet family, fewer parameter increments than expected are the most fundamental gains. EfficientNet models were trained using color lesion images provided by the International Association for Skin Imaging (ISIC). The ISIC archive is the world's largest repository of pathologically verified images from skin cancer patients. For the validation of CNN models, 5-fold cross validation was preferred. In addition, the optimum values of hyper-parameters were tried to be caught for performance improvement of CNN models. During the training phase, f1-score was chosen as the performance measurement metric and ROC curves were drawn for the test data and AUC values were revealed.**

Keywords **- EfficientNET Models, Dermoscopic Images, Skin Diseases Diagnosis, Melanoma Detection**

I. INTRODUCTION

During the pandemic process, the importance of early detection of disease diagnosis and treatment methods has become more evident. Computer-aided systems used to categorize color lesion images, which are the subject of this study, are ideal examples for remote diagnosis [1, 5].

In this study, it is aimed to measure the success of EfficientNet architectures, one of the newest deep learning models, to detect melanoma disease from skin lesion images. Scientifically, melanomas are less common than other skin cancers. However, approximately 75% of skin cancer-related deaths are due to melanomas. Cancer cells exhibit a very fast growing and systemically spreading behavior. As with all types of cancer, early diagnosis is of great importance for the treatment of skin cancer. Therefore, early recognition and correct evaluation of the signs of cancer on the skin is extremely important. The success achieved in deep learning-based classification of colored lesion images has surpassed even dermatologists.[8] Therefore, when a color change on the skin or a change on the body mole is noticed, it should be followed in terms of color and shape, and the bumps in skin color or pink tones should be taken into account. Dermatologists often recommend regular skin examination to identify and rule out Melanoma in its early stages. Dermatoscopy is a widely used diagnostic technique to identify benign and malignant skin cancers [6, 7].

Convolution Neural Network (CNN) based image processing applications come to the fore in the early diagnosis of skin cancers, which is the most common type of cancer. As in all areas of deep learning, popular and ambitious new architectures are emerging every day in image processing convolution models [14]. Even the oldest of the models for which performance comparisons were made in this study was not more than 5 years old [2, 3, 4]. CNN-based intelligent image processing applications are the solutions needed not only in desktop or hosting systems, but also in hardware with limited resources such as smartphones that we can carry in our pocket. The number of parameters that can run on these limited resources is low, in other words, the need for lighter architectures has created the MobileNet family [12, 17].

The basic principle of the work is we estimate a binary target for each image. Our EfficientNET model should estimate the probability that the lesion in the image is malignant, between 0.0 and 1.0. The train.csv file is used in the training data. A value of 0 means benign and a value of 1 means malignant. We use test.csv file for test data. Dermatoscopy is a widely used diagnostic technique to identify benign and malignant skin cancers. It is used to automatically diagnose skin diseases compared to examination with the naked eye. There are various hardware devices used to take dermatoscopic images. Dermatoscopy, which can also be defined as a method of examining the skin with a microscope, is a computer-assisted analysis of skin images. With this method, a map of moles on the body is created and the localization of each point is determined. Then, dermatoscopic images are taken and recorded for each mole. Thus, it is possible to compare the new image to be obtained in the next control with the previous state by the specialist physician.

Although a solution from the NASNet family costs a lot of money, the basic idea, namely trying to optimize the architecture of the model according to the dataset, has led to a very important development [11] Named as EfficientNet, this new family, unlike NASNet, has chosen to scale the architecture with only one coefficient instead of optimizing the architecture in a costly manner. E.g; When the current value of the scale is doubled, the depth in the architecture, the width and resolution of the intermediate outputs at the layer outputs are also doubled. This new strategy, which can also be called composite scaling, is very simple and straightforward, but gives very effective results. In our study, our main aim is to determine which is more successful in detecting benign or malignant Melanoma using EfficientNet architectures. In this study,The largest international dataset consisting of digital images needed by researchers who want to use artificial intelligence techniques in the diagnosis of skin diseases is offered as open source by the ISIC (International Skin

Imaging Collaboration) community. For our lesion classification application, we used the HAM10000(Human Against Machine with 10.000 training images) dataset in the ISIC-Archive, which consists of colored skin images taken from dermoscopy devices [9, 10].

II. HAM10000 DATASET

In this study, the HAM10000 (Human Against Machine with 10.000 training images) data set consisting of 10,015 colored lesion pictures presented to the participants to train their models in the international competition organized by ISIC in 2018 was used as a benchmark [11]. The "ISIC Archive" is the largest global storage area where volume images are made publicly available in digital image format. This dataset includes pre-processed dermoscopic images that can be used for early diagnosis of seven different skin diseases, along with Melanoma, the most widely known skin cancer.

These digital pictures taken from more than 10,000 patients in different countries using various devices and methods were used as a training data set at the international "Medical Image Computing and Computer Assisted Intervention - MICCAI 2018" conference held in Spain in 2018. In this contest, the models developed by the researchers reached the success point of nearly 90% correct disease diagnosis [9]. In ISIC competitions, the test data set is presented to the contestants with the real disease labels hidden in order to isolate the test data from the training data. For this purpose, in the HAM10000 data set, besides 10,015 tagged training samples, 1,512 unlabeled volume images were published. Because the real world labels of the test data are not known and are not included in the training data; Overfitting of the classifiers developed by the competitors is prevented. Participants have been participating in the award-winning contest organized by ISIC since 2016, with short papers describing their algorithms and their performance on the test data of the method they developed. In addition, in order for new researchers to test their performance, the website of the ISIC community has an online performance evaluation system for data sets separated by years (challenge.isic-archive.com). In this way, the success of each new algorithm developed, as in our study, on test data can be calculated instantly online.

Table 1:The descriptions and image counts of the all diseases in the HAM10000 dataset.

Name	Description	count
Melanoma	It is a type of skin cancer that occurs with the uncontrolled division and proliferation of skin cells called melanocytes.	1.113
Nevus	benign states of melanocytes.	6.705
Basal cell carcinoma	A type of cancer in basal cells that dies old cells in the skin and produces new ones instead.	514
Actinic keratosis	Prolonged sun exposure has a very low risk of developing cancer.	327
Benign keratosis	It is known as benign keratosis. They are generally seen in the elderly and are harmless skin growths.	1.099
Dermatofibroma	It is a benign skin disease in terms of proliferation. They are hard, high-looking, fiber-like lesions that occur in different sizes.	115
Vascular lesion	Due to vascular problems, the superficial capillaries in the skin are enlarged or more frequent than normal.	142

In the Ham10000 dataset, images are labeled according to criteria such as id, age, gender, benign or malignant under the title of train.csv and test.csv files according to their attributes. These data are stored in jpeg file types in TFrecord files. All images from a patient are fully contained in a single Tensorflow record as a three-layer TFRecord file. All TFRecords have equal data class ratio (ie each TFRecord now contains 1.8% malignant images).[18]

	image_name	patient_id	sex	age_approx	anatom_site_general_challenge	diagnosis	benign_malignant	target
0	ISIC_2637011	IP_7279968	male	45.0	head/neck	unknown	benign	0
1	ISIC_0015719	IP_3075186	female	45.0	upper extremity	unknown	benign	0
2	ISIC_0052212	IP_2842074	female	50.0	lower extremity	nevus	benign	0
3	ISIC_0068279	IP_6890425	female	45.0	head/neck	unknown	benign	0
4	ISIC_0074268	IP_8723313	female	55.0	upper extremity	unknown	benign	0

Figure 1: Train.csv and Test.csv files outputs

At this stage of the study, graphs according to characteristics such as gender, belign or malignant are shown in figure 2, figure 3 and figure 4.

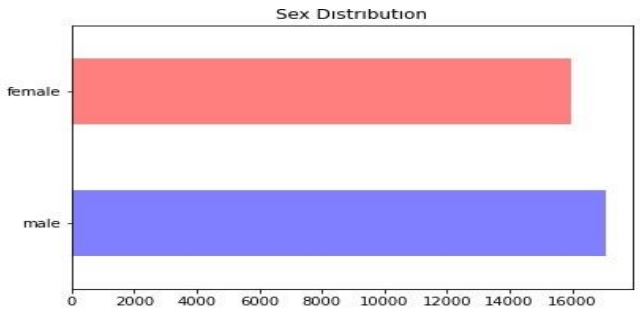

Figure 2: Data distribution by gender

It is noteworthy that there are significantly more benign images in the training dataset compared to malignant images. This will be important when dividing the training and validation set and for layering during cross validation. Another advantage is that it will be useful to prevent loss so that benign images are less weighty. As can be seen in Figure 3, there is a numerical difference between the appearance of benign and malignant melanoma. This facilitates the detection of malignant melanoma.

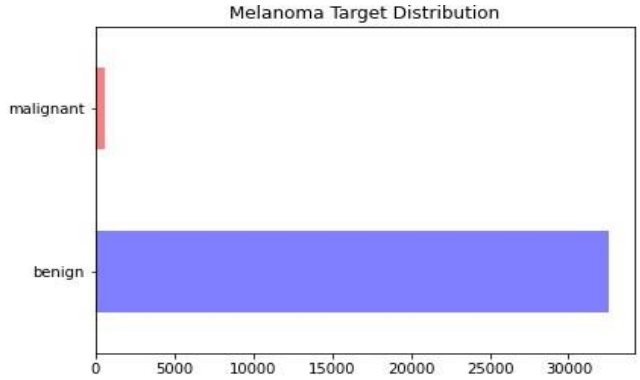

Figure 3: Data distribution of benign and malignant melanoma

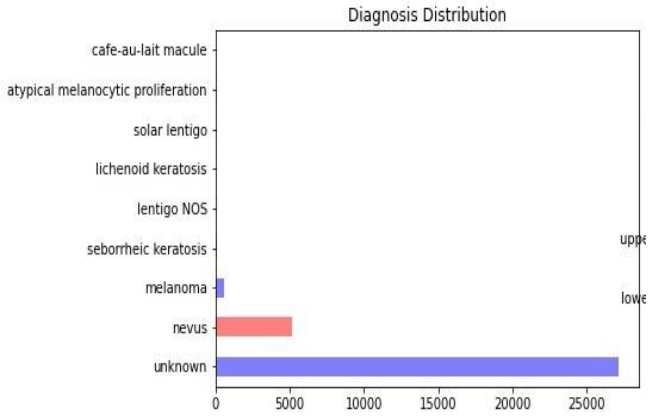

Figure 4: Data distribution by Diagnosis

III. DETECTION MELANOMA WITH EFFICIENTNET

After the data set and csv files were uploaded to the system and the training and validation sets were introduced to the system, it started with establishing an artificial intelligence processor TPU (Tensor Processing Unit) in order to provide a faster and more efficient training. This technology offered by Google is used to train artificial intelligence applications.

TPUs only support Tensorflow. They are models with intensive matrix calculations. They are structures that work with very large models on very large effective sets.

A. Setting Hyperparameters

It is noteworthy that there are significantly more benign images in the training dataset compared to malignant images. This will be important when dividing the training and validation set and for layering during cross validation. The features of malanoma are indicated in Fig.5. Another advantage is that it will be useful to prevent loss so that benign images are less weighty. Having more than one value for some hyperparameters is for training and experimenting with different models during each kfold. Also, in the training phase of the final dataset, all kfolds must be the same for all hyperparameters [18].

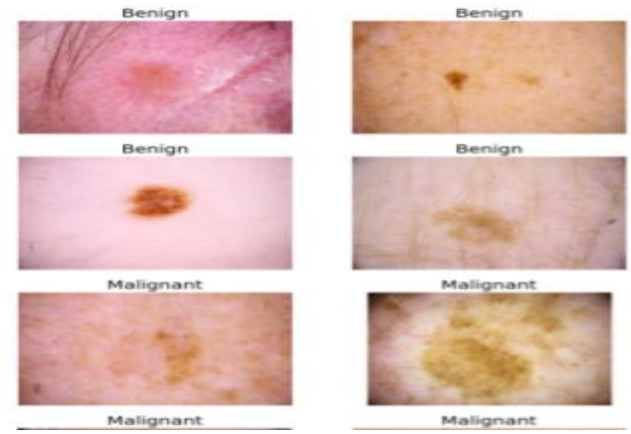

Figure 5: Melanoma Samples

B. Learning Rate Train Schedule

This is a non-formal training program for transfer learning. The learning rate starts near zero, then increases to a maximum, then decreases over time. If this is the case consider changing the program's learning rates. With larger data sizes, the learning rate increases more. It has been determined that the maximum learning rate increases in direct proportion to the data size.

The learning rate program we use get_lr_callback provides learning rate detection by creating a loop. sets the learning rate from an initial learning rate to a maximum learning rate and then from that maximum learning rate to a minimum learning rate that is much lower than the initial learning rate. In Figure 6, this policy is first written as Super Convergence and is explained as Very Fast Training of Neural Networks Using Large Learning Rates [18].

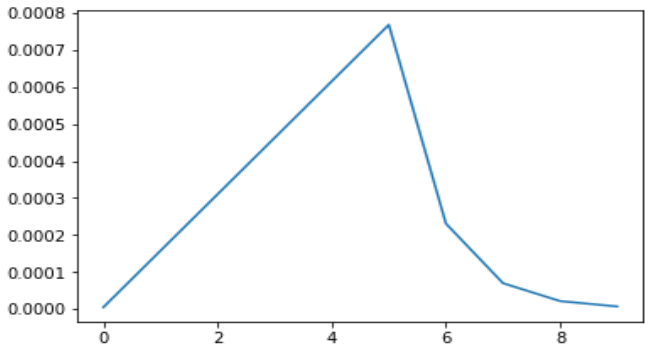

Figure 6: Learning Rate Schedule

C. Image Loading Functions

At this stage of the work, some functions were first created to load the TFRecords we used to generate the images, target and image names. Image loading functions were performed in 4 stages. These stages are;

- **Decode Image**

In this phase, the necessary coding is done to transform the images into a tensor, normalize them and reshape them into the correct shape for the TPU.

- **Read_tfrecord**

At this stage, where we read and process TFRecord, we return the image tensor and create the label value and image name according to the input arguments.

- **Load Dataset**

After reading data from TFRecords, we can choose whether to shuffle the data with this command. We will do this for the train dataset, but not for the validation and test dataset. The current process is run only for the training dataset.

- **Count Data Items**

It is the step of the command we use to count the number of images in a file.

- **Data_augment**

In order to enlarge the data on the data set, augmentation was performed and the data was increased.

- **plot_transform**

It is the command phase that draws some examples of augmented images. In addition to these operations, geometric enlargement operations were also performed. The rotation can be done in tf.image, but only with 90 degree factors, so we performed it manually instead. Data duplication operations were performed with several geometric amplification operations.

IV. Train and Evaluate Model

In training convolutional neural networks, scaling is often done to increase the accuracy of the model, but also helps to increase the efficiency of a model. So the faster it trains, the greater the efficiency. A CNN has three scaling dimensions: depth, width, and resolution. Depth refers to how deep the meshes are, which is equal to the number of layers in it. Width refers to how wide the mesh is. For example, a width measure is the number of channels in the Conv layer, while Resolution is just the image resolution passed to a CNN [15, 16].

While depth scaling can allow a network to learn more complex and richer features, techniques such as hopping connections are used in network structures. The payoff is usually low as the depth becomes too large due to disappearing gradients. Width scaling, on the other hand, allows models to be small. Larger meshes tend to capture finer grained features. Because they are smaller, they train faster. However, performance again drops with wider width. Resolution scaling is pretty intuitive. It is always better to use larger resolutions but the relationship is not linear. Therefore, increasing any size of the mesh (width, depth or resolution) improves accuracy, but for larger models the accuracy gain decreases.EfficientNet is an architecture created with the idea of using Compound Scaling.

This uses a composite coefficient ϕ to evenly scale mesh width, depth, and resolution. ϕ is a coefficient determined by the manufacturers of EfficientNets B1-B7. In Figure 7, the Efficient architecture is explained with all it details [13].

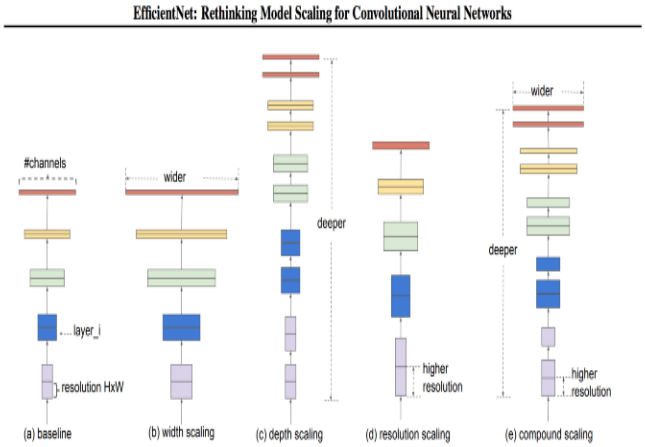

Figure 7: EfficientNet Model Architecture

The EfficientNet group consists of 8 models from B0 to B7. The larger the number, the higher the number of parameters calculated and the accuracy. Then "what is effective?" one asks! However, it was seen that the success increased as the models became more complex in the ImageNet dataset after 2012, but most of them are not effective in terms of processing load. In recent years, more efficient approaches have been tried to be adopted with smaller models. So much so, that while trying to shrink the model, scaling not only in one of the depth, width and resolution, but also in all three, provides much more effective results. Performance comparisons of EfficentNET B0-B7 and other architectures on ImageNET in terms of calculated parameters and accuracy are shown in Figure 8 [13].

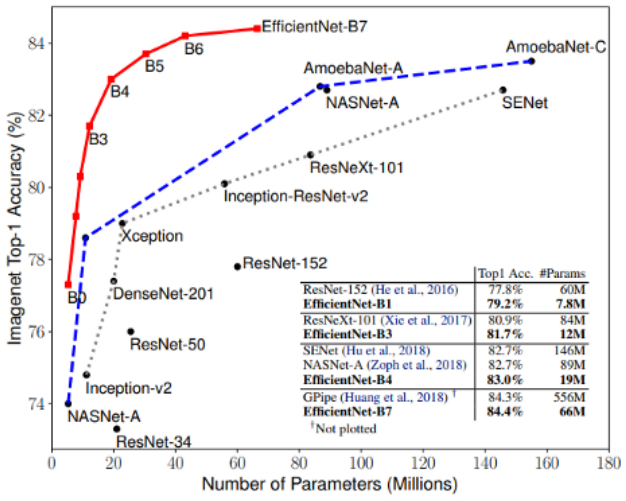

Figure 8: Parameter and ImageNet accuracy comparison

Depthwise Convolution + Pointwise Convolution: Splits the original convolution into two phases to significantly reduce the computational cost with minimal loss of accuracy.

Inverted Res: The original ResNet blocks consist of a layer that compresses the channels (seqeeze) and then a layer that expands the channels. Thus, it connects skip connections and rich channel layers. But in MBConv, the blocks consist of a

layer that first expands the channels and then compresses them, so layers with fewer channels are connected by skipping.

Linear bottleneck: It uses linear activation in the last layer in each block to avoid loss of information from ReLU.

The main building block for EfficientNet is the inverted bottleneck MBConv, originally known as MobileNetV2. In Figure 9 by using shortcuts between bottlenecks connecting far fewer channels compared to expansion layers, it is combined with deeply separable convolution that reduces computation by almost k^2 compared to traditional layers. It specifies the height and width of the 2-dimensional convolution window, where k denotes the kernel size.

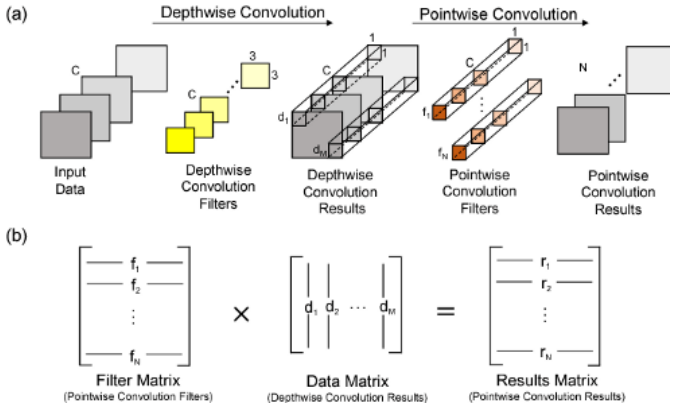

Figure 9: Basic representation of Depth and Point wise Convolutions

A. *Test Time Augmentation*

Similar to the data augmentation done on the training set, we performed Test Time Augmentation (TTA). The purpose of this process is to make random changes to the test images. Instead of using the trained model to make an estimate on the noise-free and original test images, we magnify the images several times, make an estimate on each, and average each corresponding image. This is the final estimate we get for that image. The advantage of working TTA is that we average the errors just as we average our estimates. We can apply Test Time Augmentation to the validation dataset to get more efficiency from the validation set.

B. *K-Fold Cross Validation*

It is common to evaluate the performance of a machine learning algorithm on a dataset using a resampling technique such as K-fold cross validation.

In K-Folds Cross Validation, we divide our data into k different subsets. We use k-1 subsets to train our data and leave the final subset as test data. The mean error value resulting from k experiments indicates the validity of our model. The k-fold cross validation procedure involves dividing a training dataset into k groups and then using each of the k sample groups in a validation set while the remaining samples are used as a training set. . This means that k different models are trained and evaluated [16]. The performance of the model is estimated using the predictions of the models made at all k-folds. The K value is usually chosen as 3 or 5. This value can be selected as 10 or 15, but this will cause a very expensive calculation and time loss.

C. *EfficienNET Performance*

Finally, we used the best model of each floor to get the best prediction in the Test set during the training and evaluation phase of the model. Estimates were then averaged across the number of floors. In Figure.10 Shows K-Fold Cross Validation Results for two steps.

At the end of the process, we found that the Validation and Training AUC were quite close to each other, but we found that the curves diverged in some parts. This indicates that the loss is increasing and the learning is slowing down.[18]

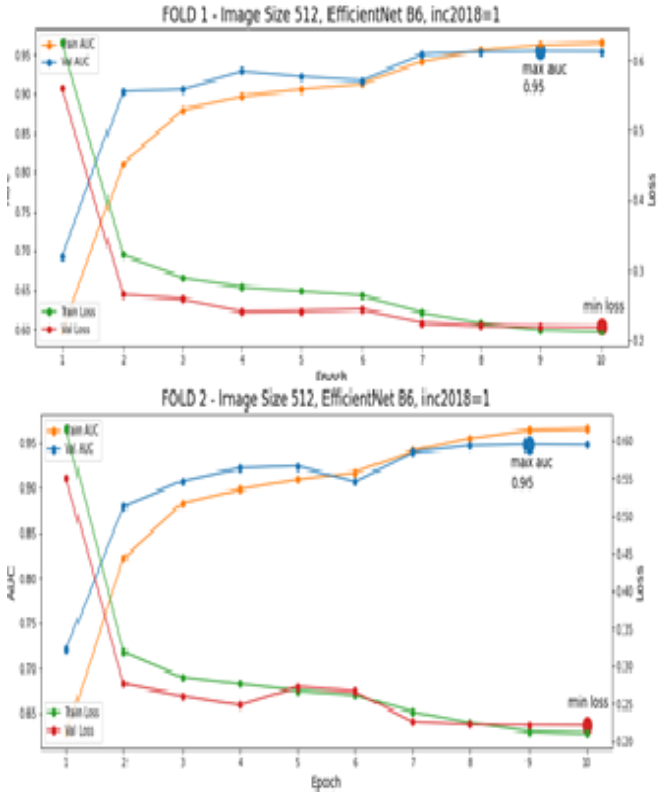

Figure.10: K-Fold Cross Validation Results for two steps

D. *ROC and Precision-Recall Curves*

If the number of benign images greatly exceeds the number of malignant images in the absence of even distribution between classes, AUROC may give an overly optimistic view of the performance of the model. This situation is better in terms of graphics.

In Figure 11 , that is a large improvement in the number of false positives results in only a small change in the false positive rate when using ROC. Sensitivity, on the other hand, captures the impact of large numbers of negative samples on model performance by comparing false positives with true positives rather than true negatives. The AP value on the axis is the AUPRC value

Accuracy is not a good measure of evaluation when there is big data class imbalance. If we have 100 samples: 99 melanomas and 1 normal, then a model that predicts

everything as melanoma will have 99% accuracy. In that case, it's better to look at precision, harmonic mean, F1 score.

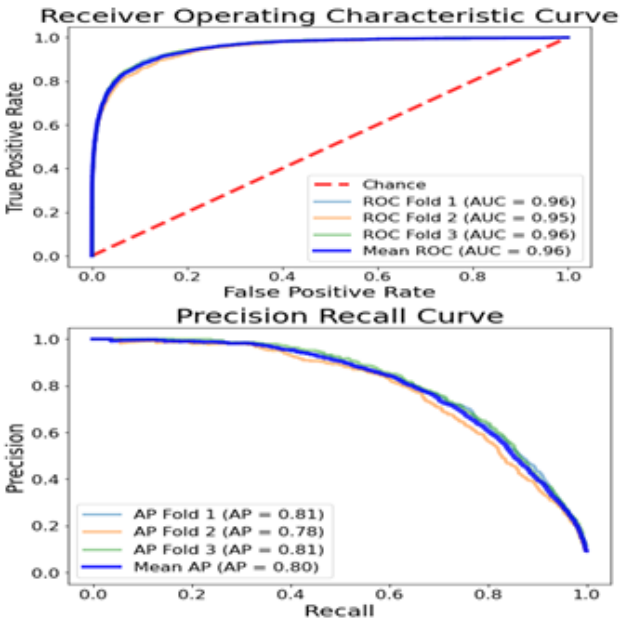

Figure 11: ROC and PR Curve

V. CONCLUSION

In conclusion, our model performs quite well according to AUROC data, but considering the AUPRC curve it is clear that it still needs further development and improvements. In the diagnosis of melanoma (to classify the lesions as malignant or benign), we need to have a high recall/sensitivity as we want to accurately identify all true malignant cases. For our model, our sensitivity will suffer greatly if we set a low threshold to get a high recall, meaning that many people will get a false melanoma diagnosis during analyzing (high false positives).

The imbalanced distribution in the selected dataset is the main reason for the complexity in our application in this study. In order to overcome this problem, we must collect more data for the minor classes or increase the existing one by various augmentation methods. However, this is not possible for health data, which is very difficult to collect and share. In reality, malignant cases will also be less common than benign cases. Synthetics images creation has to be tried and we will test this option in future study.

APPENDIX

Supplementary data to this article can be found online at https://challenge.isic-archive.com/data.

ACKNOWLEDGMENT

The authors declare that they have no known competing financial interests or personal relationships that could have appeared to influence the work reported in this paper.

REFERENCES

[1] Rezvantalab, A., Safigholi, H., & Karimijeshni, S. (2018, 10). Dermatologist Level Dermoscopy Skin Cancer Classification Using Different Deep Learning Convolutional Neural Networks Algorithms.

[2] Majtner, T., Yildirim-Yayilgan, S., & Hardeberg, J. Y. (2018, 10). Optimised deep learning features for improved melanoma detection. Multimedia Tools and Applications, 78, 11883–11903. doi:10.1007/s11042-018-6734-6

[3] Okuboyejo, D. A., & Olugbara, O. O. (2018, 4). A Review of Prevalent Methods for Automatic Skin Lesion Diagnosis. The Open Dermatology Journal, 12, 14–53. doi:10.2174/1874372201812010l4.

[4] Mishra, N. K., & Celebi, M. E. (2016, 1). An Overview of Melanoma Detection in Dermoscopy Images Using Image Processing and Machine Learning.

[5] Esteva, A., Kuprel, B., Novoa, R. A., Ko, J., Swetter, S. M., Blau, H. M., & Thrun, S. (2017, 1). Dermatologist-level classification of skin cancer with deep neural networks. Nature, 542, 115–118. doi:10.1038/nature21056

[6] Salido, J. A., & Jr., C. R. (2018, 2). Using Deep Learning for Melanoma Detection in Dermoscopy Images. International Journal of Machine Learning and Computing, 8, 61–68. doi:10.18178/ijmlc.2018.8.1.664 (ISIC).

[7] Sandler, M., Howard, A., Zhu, M., Zhmoginov, A., & Chen, L.-C. (2018, 1). MobileNetV2: Inverted Residuals and Linear Bottlenecks. The IEEE Conference on Computer Vision and Pattern Recognition (CVPR), 2018, pp. 4510-4520.

[8] He, K., Zhang, X., Ren, S., & Sun, J. (2015, 12). Deep Residual Learning for Image Recognition.

[9] Do, T. T., Hoang, T., Pomponiu, V., Zhou, Y., Chen, Z., Cheung, N. M., . . . Tan, S. H. (2017, 11).Accessible Melanoma Detection using Smartphones and Mobile Image Analysis.

[10] Vasconcelos, C. N., & Vasconcelos, B. N. (2017, 2). Convolutional Neural Network Committees for Melanoma Classification with Classical And Expert Knowledge Based Image Transforms Data Augmentation.

[11] Tschandl, P., Rosendahl, C., & Kittler, H. (2018, 3). The HAM10000 dataset, a large collection of multi-source dermatoscopic images of common pigmented skin lesions. Sci. Data 5, 180161 (2018). doi:10.1038/sdata.2018.161.

[12] Huang, G., Liu, Z., van der Maaten, L., & Weinberger, K. Q. (2016, 8). Densely Connected Convolutional Networks.

[13] Mingxing Tan, Quoc V. Le. Machine Learning (cs.LG); Computer Vision and Pattern Recognition. https://arxiv.org/abs/1905.11946

[14] Kassani, S. H., & Kassani, P. H. (2019, 6). A comparative study of deep learning architectures on melanoma detection. Tissue and Cell, 58, 76–83. doi:10.1016/j.tice.2019.04.009

[15] Li, Y., & Shen, L. (2018, 2). Skin Lesion Analysis towards Melanoma Detection Using Deep Learning Network. Sensors, 18, 556. doi:10.3390/s18020556

[16] Majtner, T., Yildirim-Yayilgan, S., & Hardeberg, J. Y. (2018, 10). Optimised deep learning features for improved melanoma detection. Multimedia Tools and Applications, 78, 11883–11903. doi:10.1007/s11042-018-6734-6

[17] Sandler, M., Howard, A., Zhu, M., Zhmoginov, A., & Chen, L.-C. (2018, 1). MobileNetV2: Inverted Residuals and Linear Bottlenecks. The IEEE Conference on Computer Vision and Pattern Recognition (CVPR), 2018, pp. 4510-4520

[18] Https://www.kaggle.com/teyang/melanoma-detection-using-effnet-and-meta-data/data

Performance Analysis of Image Processing Techniques for Memory Usage and CPU Execution Time

F.KILIÇKAYA[1] and S.OKDEM[2]

[1] Erciyes University, Graduate School of Natural and Applied Sciences, Computer Engineering Department, Kayseri/Turkey, 4010930039@erciyes.edu.tr

[2] Erciyes University, Engineering Faculty, Computer Engineering Department, Kayseri/Turkey, okdem@erciyes.edu.tr

***Abstract* – In recent years, many applications that use algorithms like artificial neural networks, deep learning, and fuzzy logic have been developed in order to improve tasks such as image classification, object perception, image enhancement, and image processing. These applications are technology products of image enhancement that are utilized in the military, industry, robotic, advertising, astronomy, medicine, geography, traffic, and many areas of daily life. Today, having every process done by autonomous systems instead of human beings has increased the significance of image processing. Processing a large number of images in one computer varies by processor and memory type. The image processing of a slower processor may last longer than a faster one does. The study consists of two phases. In the first phase, image data has been processed by an ideal technique. In the second phase, the performances of image process, on CPU and processor with respect to their calculation speed have been compared.**

***Keywords* – Image Processing, Image Processing Algorithms, Performance Analysis**

I. INTRODUCTION

In parallel with the rapid developments in the IT world, digital images show a great improvement and with the increasing usage of them, the importance of databases that contain images is increasing [1]. In the processing of digital images, many algorithms that are desired to be developed require very fast systems. Within the content of this paper, studies on the examination of performance analysis of image processing algorithms on the computer with different features have been carried out. The goal is to maximize the efficiency of CPU and memory usage of processing sources. The most important point that affects the speed of your computer is the data transfer rate between CPU and RAM. Thus, the relationship between CPU and RAM is very important for computers. A computer's CPU address and data ends are connected with the address and data ends of RAM. Likely, the control ends of CPU and RAM are also interconnected. CPU has a maximum physical RAM capacity. This physical capacity is directly related to the number of address ends of the CPU. Generally, 2,80 and 8080 processors have 16 address ends. The processor that has such a feature can use 64 kilobytes (KB) of memory [2].

The intention in all of these areas is to obtain high-quality images by keeping the occupied areas of memory low. For that purpose, image improvement and repair can be performed on images that require quality enhancements. It will be observed that required memory capacities and CPU execution times of image processing technique.

II. METHOD AND MATERIAL

In this section, a brief information about linear and non-linear filters to be used in image processing is given.

A. Non-Linear Filters

1. Mean (Average- Box Blur) Filter

Mean filter is a simple and easy-to-implement method of smoothing images. Generally, it is used to reduce noise in images [3]. While the image is softened, the noise becomes less apparent. It provides the sharp edges to disappear and the picture to alter.

2. Median Filter

It is used to remove noise and reduce salt & pepper noise. The difference from the mean filter is that, it does not generate unrealistic pixel values, so it preserves sharp edges better [4].

3. Max Filter

The highest greyscale value is assigned in the mask, so in the resulting image, the luminous area is cleared [5].

4. Bilateral Filter

It is non-linear for noise, an edge-preserving, and a smoothing filter in terms of noise-reduction. In Bilateral filtered images, while smile scales disappear, large scales and sharp edges are preserved. If a bilateral applied image is subtracted from a real image, a detailed image is obtained [6].

5. Guided Filter

It works as an operator that protects edges and provides smoothing. The difference from the bilateral filter is that it supplies better results near different edges [7].

6. Gaussian Filter

Gaussian smoothing operator is a 2D convolution operator used to "blur" images and remove details and noises [4].

7. Anisotropic Diffusion Filter

It applies an inhomogeneous process that reduces spreading in parts more likely to edge. Edge detection is proven to perform better than a linear Canny edge detector even without applying non-maximum compression and hysteresis threshold [8].

B. Linear Filters

1. Sobel Edge Detection Algorithms

The Sobel operator is used to get vertical, horizontal, and diagonal edges. It reveals sharp edges [8].

2. Prewitt Edge Detection Algorithms

Prewitt filter is used to extract data and filter and detect edges. Sobel operator gives better results in determining edges on pictures [8].

3. Robert Cross Edge Detection Algorithms

It reveals sharp edges by measuring 2D transitions on images [8].

4. **Compass Edge Detection Algorithms**

Like Sobel, Prewitt, and Robert Cross edge detection algorithms, Compass algorithms is an alternative filter to detect sharp edges on an image that uses color transition difference on both sides of an edge [8].

5. Canny Edge Detection Algorithms

The canny operator first softens images with a Gaussian filter. That's why small noises cause some problems with images. Then, it calculates the gradient. It records edges without changing its direction for every pixel. At the same time, it preserves the natural states of images [8].

6. Laplacian Edge Detection Algorithms

It is a linear filter based on quadratic logic used to define the limits of images and clarify them [9].

7. **Laplacian Of Gaussian (LoG)**

The LoG is a smoothing filter as the Gaussian algorithm that detects edges and ovals in images and is used before applying the Laplace algorithm to images [9].

III. Experiments

Linear and nonlinear filter images are introduced in image processing techniques in this section and the data obtained as a result of the application are given as a table.

A. Data Processing with methods

The images of the results obtained using the MATLAB program are given in figure-1.

In figure 1-a, 0.1 rated salt & pepper image is added to the image

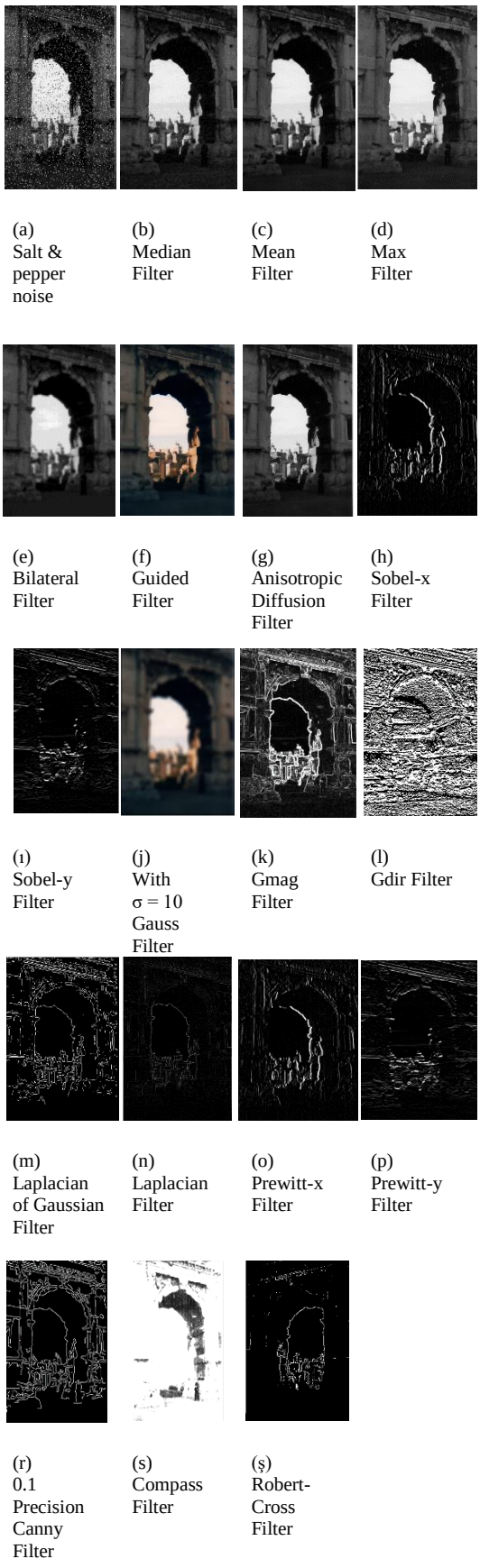

Figure -1. Images of linear and non-linear filters after filtering with 3x3 mask

B. Performance of the processed data on CPU and processor based on computational rates

Performances of linear and non-linear filters for process times are given in the table below.

Processor type and data memory capacity	*Mean*	*Median*	*Max*	*Bilateral*	*Guided*	*Anisotropic Diffusion*	*Gaussian*
I7 processors, 16 GB	1.8s	2s	1.9s	17.3s	2.1s	1.7s	1s
I5 processors, 4 GB	2.6s	6.9s	13.6s	58.7s	3.3s	3.5s	2.1s
I3 processors, 2 GB	3.4s	10.4s	12.7s	33.8s	2.6s	3s	3.3s

Table-1. Performances of Non-Linear Filters

Processor type and data memory capacity	Sobel	Prewitt	Robert Cross	Compass	Canny	Laplacian	LoG
I7 processors, 16 GB	1s	1.5s	0.5s	0.6s	0.5s	1.2s	1.3s
I5 processors, 4 GB	1.2s	3.4s	3.3s	2.1s	2.1s	3.4s	4.1s
I3 processors, 2 GB	1.6s	4.9s	4.6s	3s	1s	2.8s	4s

Table-2. Performances of Linear Filters

Memory usage performances of linear and non-linear filters are given below in megabytes (MB) as a table.

Processor type and data memory capacity	*Mean*	*Median*	*Max*	*Bilateral*	*Guided*	*Anisotropic Diffusion*	*Gaussian*
I7 processors, 16 GB	2431 MB	2549 MB	2563 MB	2538 MB	2561 MB	2581 MB	2573 MB
I5 processors, 4 GB	7503 MB	7318 MB	7331 MB	7308 MB	7329 MB	7347 MB	7340 MB
I3 processors, 2 GB	1415 MB	1484 MB	1492 MB	1477 MB	1491 MB	1502 MB	1498 MB

Table-3. Memory usage performances of Non-Linear Filters

Processor type and data memory capacity	Sobel	Prewitt	Robert Cross	Compass	Canny	Laplacian	LoG
I7 processors, 16 GB	2667 MB	2988 MB	2548 MB	3154 MB	2660 MB	2737 MB	2701 MB
I5 processors, 4 GB	7426 MB	7718 MB	7317 MB	7869 MB	7421 MB	7489 MB	7457 MB
I3 processors, 2 GB	1552 MB	1739 MB	1483 MB	1836 MB	1548 MB	1593 MB	1572 MB

Table-4. Memory usage performances of Linear Filters

IV. RESULTS

Nowadays, image processing is used in many areas of daily life. Data processing applications work on the dynamic nature of images, workload, the memory usage of CPU, and processing time of applied data. In this study, performance results are obtained in terms of memory usage, execution time, and image quality. The results of each technique are compared, then they are shown in figures.

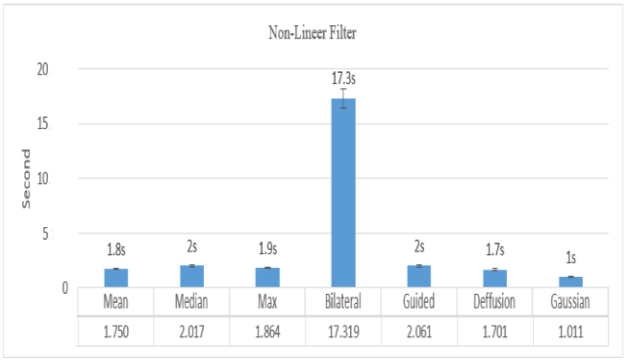

Figure-2. Processing time of image processing technology

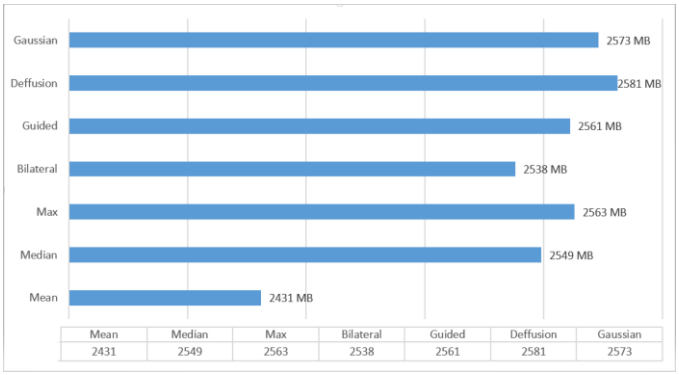

Figure-3. Memory Usage of image processing technology

Median and Mean filters are non-linear filters used to remove noises and smooth images. The median filter does not give unwanted smoothing and transitions. It does not disappear edges and brings values from existing pixels. It does not produce, like a mean filter, a pixel value getting a

value that is not in that neighborhood. For that, it gives better results in removing noises. The disadvantage compared to the Mean filter is to work slower in time.

Like the Mean filter, the Gaussian filter is a low-pass non-linear filter that softens images, removes noises, and blurs images. The Gaussian filter gives better results in image blurring and sharpening and gives a shorter processing time. Also, the Gaussian filter supplies a more realistic image in images originating from the limited depth of areas.

Guided and Bilateral filters are non-linear filters that protect edges of images and supply smoothing. Compared to the results, the Guided operator gives better results for both processing time and image quality.

Anisotropic Diffusion and Canny filters are operators used for image edge detection and sharpening. The canny filter gives better results.

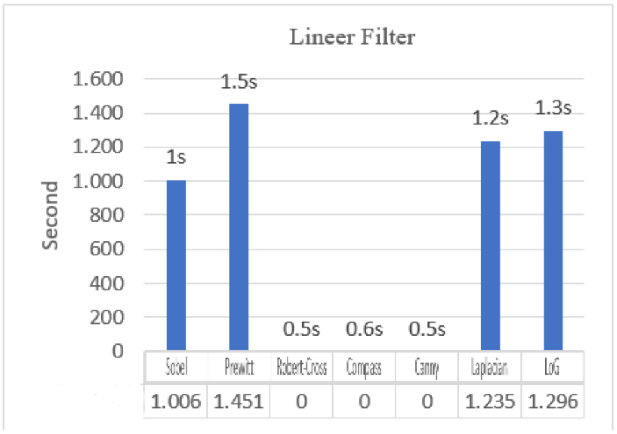

Figure-4. Processing time of image processing technology

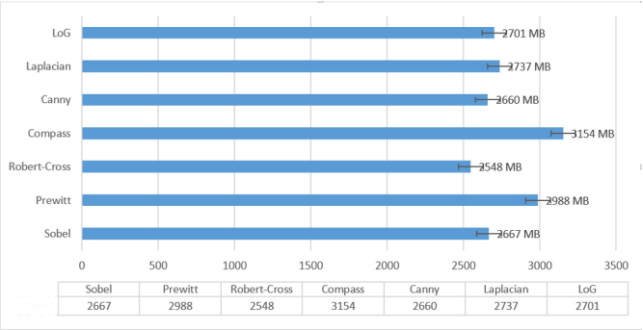

Figure-5. Memory Usage of image processing technology

In this study, among edge detection algorithms, Sobel, Prewitt, Robert-Cross, and Compass operators are listed. It is used to get vertical, horizontal, and diagonal edges in an image and reveals sharp edges. Although the processing time is shorter, it has been observed that the Robert-Cross technique can not find edges in blurred images. Sobel and Prewitt's filters are used for data extraction and edge detection. Sobel filter gives better results than the others in terms of determining edges on pictures. Compass algorithm is an alternative linear filter that uses the color transition difference on both sides of an edge on images.

V. REFERENCES

[1] M. Karakoç, "Görüntü işleme, teknolojiler ve uygulamaları", Akademik Bilişim, Uşak Üniversitesi, Uşak, 2012.

[2] S. Matuska, R. Hudec and M. Benco, "The comparison of CPU time consumption for image processing algorithm in Matlab and OpenCV," 2012 ELEKTRO, Rajecke Teplice, Slovakia, pp. 75-78, 2012. doi: 10.1109/ELEKTRO.2012.6225575.

[3] I. Cayiroglu, *Bulanıklaştırma (Yumuşatma) Algoritmaları* (ders notları) Karabük Üniversitesi, Mühedendislik Fakültesi. Karabük, 2011.

[4] R.C. Gonzalez, R.C, Woods, *Digital Image Processing*. Prentice Hall, pp. 53-136, New Jersey, 1992.

[5] N. Ken-Ichi, M. Kobayashi, and A. Ichikawa. "Small target detection from image sequences using recursive max filter." Signal and Data Processing of Small Targets. Vol. 2561. International Society for Optics and Photonics, 1995.

[6] F. Kutan, Ö. Aynur, "Evaluation of Performance of Noise Filtering Applications on Medical Images", European Journal of Science and Technology Special Issue, pp. 265-271, 2020.

[7] A. Levin, L. Dani, and W. Yair, "A closed-form solution to natural image matting." IEEE transactions on pattern analysis and machine intelligence, pp. 228-242.2007.

[8] W. Joachim, *Anisotropic diffusion in image processing* Vol 1 Stuttgart: Teubner, 1998.

[9] G.M. Perihanoğlu, "Dijital Görüntü İşleme Teknikleri Kullanarak Görüntülerden Detay Çıkarımı", Yüksek Lisans Tezi, İstanbul Üniversitesi, İstanbul, 2015.

Selçuk University Weather Tracking System and Selçuk Meteorology Website

F. BASCIFTCI[1], E. AGBAHCA[1], K. UYAR[1], Z. YILMAZ ACAR[1], B. TEZCAN[1]

[1] Selçuk University, Konya/Turkey, basciftci@selcuk.edu.tr
[1] Selçuk University, Konya/Turkey, agbahca@selcuk.edu.tr
[1] Selçuk University, Konya/Turkey, kubrauyar@selcuk.edu.tr
[1] Selçuk University, Konya/Turkey, zuleyhayilmaz@selcuk.edu.tr
[1] Selçuk University, Konya/Turkey, btezcan@selcuk.edu.tr

Abstract **- In this paper, a system for reading meteorological data like temperature, humidity, air pressure, wind speed, wind direction, and rainfall at regular intervals, deployed in Selçuk University Alaeddin Keykubat Campus. The system also provides real-time images and video time-lapses of the campus sky. These data are made available to university people via a website. The website provides a clear experience for the users, also explaining the icons and terms used on the website. Users can access the system archive in graphical ways.**

Keywords **- Weather Tracking, Sensor Data, Meteorology**

I. INTRODUCTION

Meteorology is the study of changes and developments in weather events in relation to their causes. Meteorological systems provide information to forecast the effects of these events on daily life. Weather changes on daily basis have a great impact on mood [1] and human activities like agriculture, tourism, or entertainment [2]. Changes in weather events became more unpredictable after the twentieth century due to high population growth, global warming, etc. Modern weather stations include many sensors for reading temperature, humidity, air pressure, wind speed, wind direction, and rainfall. Ground-based meteorological data are considered the golden standard in the field [3].

In this study, meteorological data is collected using sensors at one-minute intervals and presented to the user with ten minutes update cycles.

Although there is no universally accepted definition, heat waves are unusually hot-dry or hot-humid weather events that have subtle onset, are intermittent, last 2-3 days, and have visible effects on humans and the environment [4]. Therefore question of which temperatures cause heatwaves depends on the region's climate: the same meteorological situation may cause heatwaves in one region and not in another region [4]. In the last decade, the frequency, intensity, and duration of weather events raised significantly. Heatwaves are extreme weather events that affect society, ecology, and the economy [5]. The frequency of heatwaves has increased in much of Asia, Australia, and Europe [6]. Data collected in this study can be used to detect climate conditions that cause heatwaves in Konya which is an agriculturally important place in Turkey.

DURSUN [7] studied machine learning performance on the classification of meteorological data. Temperature, humidity, air pressure, and dew point of Elazığ province were gathered and classification performance of some fuzzy logic and neural networks were compared. He also forecasted weather conditions using meteorological data of Elazığ province. Ünal Çalargün [8] analyzed real meteorological data for Turkey recorded between 1970 and 2007. It is aimed to find fuzzy relationship rules from spatial and temporal data. Smith and Lakshmanan [9] created a system reporting important weather changes. Williams and Cornford [10] argued that meteorological data such as real-time temperature and rain rate can be accessed free over the internet, but they should be made more understandable for users. They also developed forecast methods using interpolation. TURAL and SAMET [11] studied collecting, analyzing, and mapping real-time meteorological data. The system enables access to real-time meteorological data and analysis over the web. It gathers real-time data from meteorological stations and after some preprocessing creates instances in a geographical database. Developed system published as a web service and users can access from a desktop, mobile or web apps. Altan [12] studied wavelet transform to diagnose and fix errors in agricultural meteorological data. He compared wavelet transform results with a regression model created using meteorological data from nearby stations. Gökrem and Durgun [13] developed a dynamic graphical system for collecting and analyzing data. Users can access the data in real-time. Arroyo and Herrero [14] analyzed different clustering methods using Spain Meteorological Agency's data from 4 different stations between 2004-2010. Chu and Zheng [15] studied on an image collection of rich weather events and graphical dynamics. Also, using geography-labeled image collection, they detected some correlations between weather properties and metadata and statistical results associating human behavior and weather conditions were given.

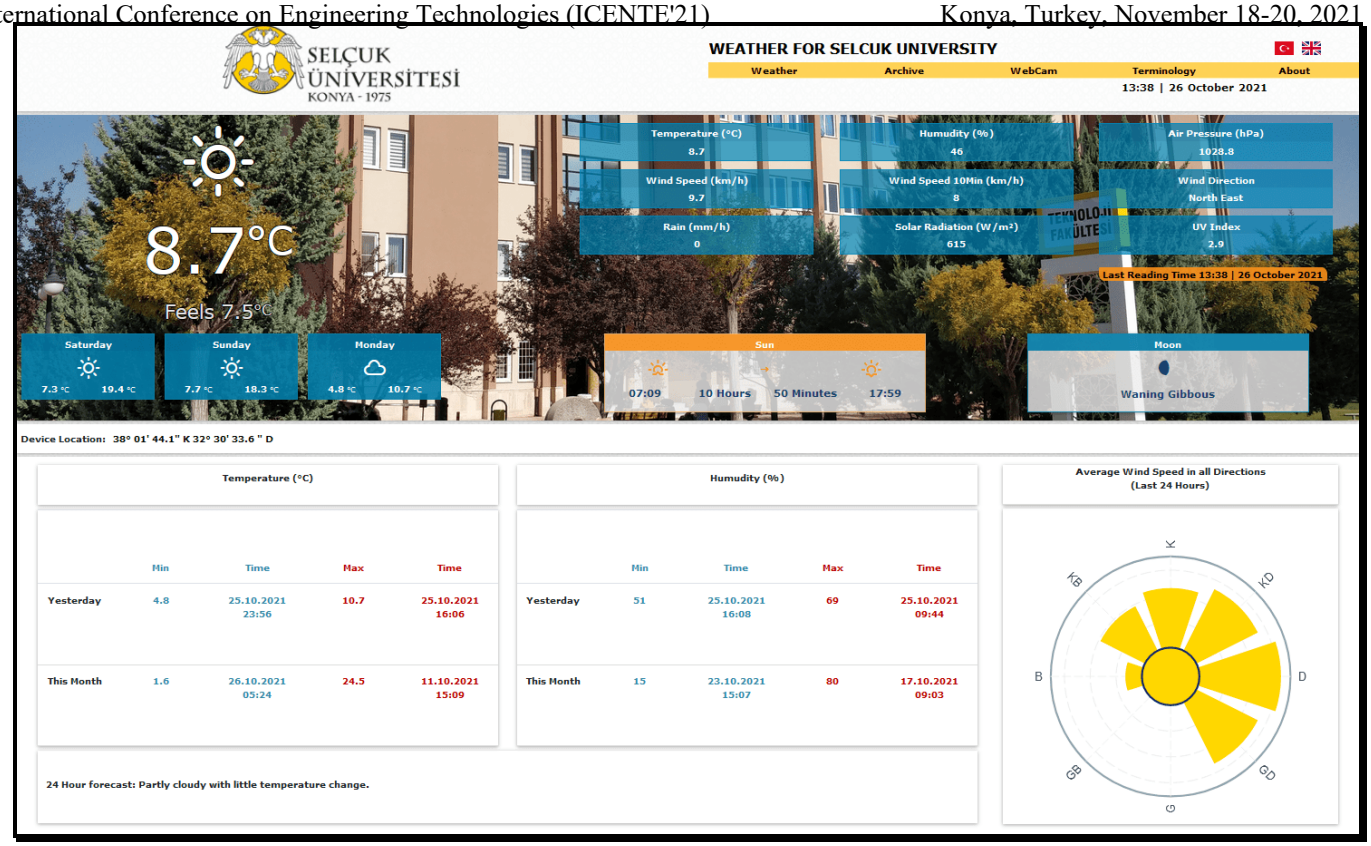

Figure 1: Homepage - Weather Interface

Figure 2: Placement of the meteorological station

II. MATERIAL AND METHODS

In this study, meteorological data of a weather station (Figure 2) is presented to users around Selçuk University Campus on a user-friendly website (Figure 1). It also shares images of the campus sky and a forecast for the next 24 hours (Table 1).

Table 1: Sample Forecast Messages

Forecast Message
Mostly clear
Increasing clouds. Precipitation is possible within 12 to 24 hours. Windy
Partly cloudy with little temperature change
Mostly cloudy and cooler
Mostly cloudy and cooler. Windy with a possible wind shift to the NW
Clearing and cooler. Precipitation ending within 6 hours

A. Materials

Materials used in the collection and presentation of weather data are explained below.

Wind Speed/Direction Sensor: The wind direction sensor has a sensitivity range of (0°-360°), resolution (1°) and maximum error margin of (+3°). Wind speed sensor has sensitivity of (1-80 m/s), resolution of (0,1 m/s).

Rain Rate Sensor: This sensor can measure both rain rate and rainfall intensity. It has a sensitivity of (0-6550 mm) and a resolution of (0,2 mm).

Temperature/Humidity Sensor: Due to high sensitivity and long lifetime, a capacitive sensor has been chosen. Temperature-wise, it has a sensitivity in the range of (-40°, +65°) and an error margin of (±0,3°C). Humidity-wise, it has a sensitivity in the range of (%1 - %100) and a maximum +%2 error margin.

Atmospheric Pressure Sensor: The pressure sensor has a sensitivity in the range of (540mb - 1100mb) and an error margin of ±1 mb.

Solar Radiation Sensor: Solar radiation is the calculated heat of light. This sensor has a sensitivity of (0 W/m^2 - 1800 W/m^2) and an error margin of maximum ±%5.

Ultraviolet (UV) Sensor: This sensor has a sensitivity of %5 and (0 MED) - (199 MEDs) range. UV index has %5

sensitivity and (0)-(16) range.

Wireless Data Transmitter: Communication with the weather station is being done via wireless data transmitter. It generates its energy via a solar panel.

Wireless Receiver Module: It can collect, display and transfer data coming from the transmitter. Live data transfer can be done to a computer via a wired connection.

IP Camera: IP cameras are suitable for outdoor conditions and are used for collecting images of the campus sky.

Server and Power Source: All processing and saving jobs of the meteorological data are being done on this system. The server is supported by an uninterruptible power supply.

Web Elements: Mainly, the website's back-end programming has been done using ExpressJS [16], and front-end programming using React [17]. React is a fast, scalable, and simple web framework. React component logic provides an easy and fast structure to present frequently changing data to users. React solves the expensive DOM manipulation problem using virtual DOM. All operations related to DOM are first done on virtual DOM and react detects the differences on this virtual DOM. This way, only the different parts are manipulated on actual DOM, and DOM manipulations are minimalized.

B. Interfaces

The system includes five interfaces which are developed to be user-friendly and functional. These are Weather, Archive, Camera Images, Terminology, and About.

1) Weather

The weather interface is also the homepage of the website (Figure 1). Weather station data presented on this screen is updated every minute. The weather interface consists of five parts. The top left of the screen includes the current temperature and feels like temperature with big font and appropriate icon. Also, recorded minimums and maximums for the last three days are given. The top right gives the current values for the temperature, humidity, air pressure, wind speed, wind direction, rain rate, solar radiation, and UV. Sunrise, sunset times, and moon cycles are given below this part. The below part includes yesterday and this month's values for temperature and humidity which are most relevant for the people. Also, approximate wind direction for each direction throughout 24h is given as a chart.

2) Archive

The archive interface provides daily, monthly, and yearly data as graphics (Figure 4). The archive includes data starting from 01.01.2020. Advanced filtering can be done for 24 hours, 1 month, or 1-year basis for temperature, humidity, air pressure, wind speed, rain rate, and solar radiation. Also provides quick filtering for the last 24 hours, the last month or the last year.

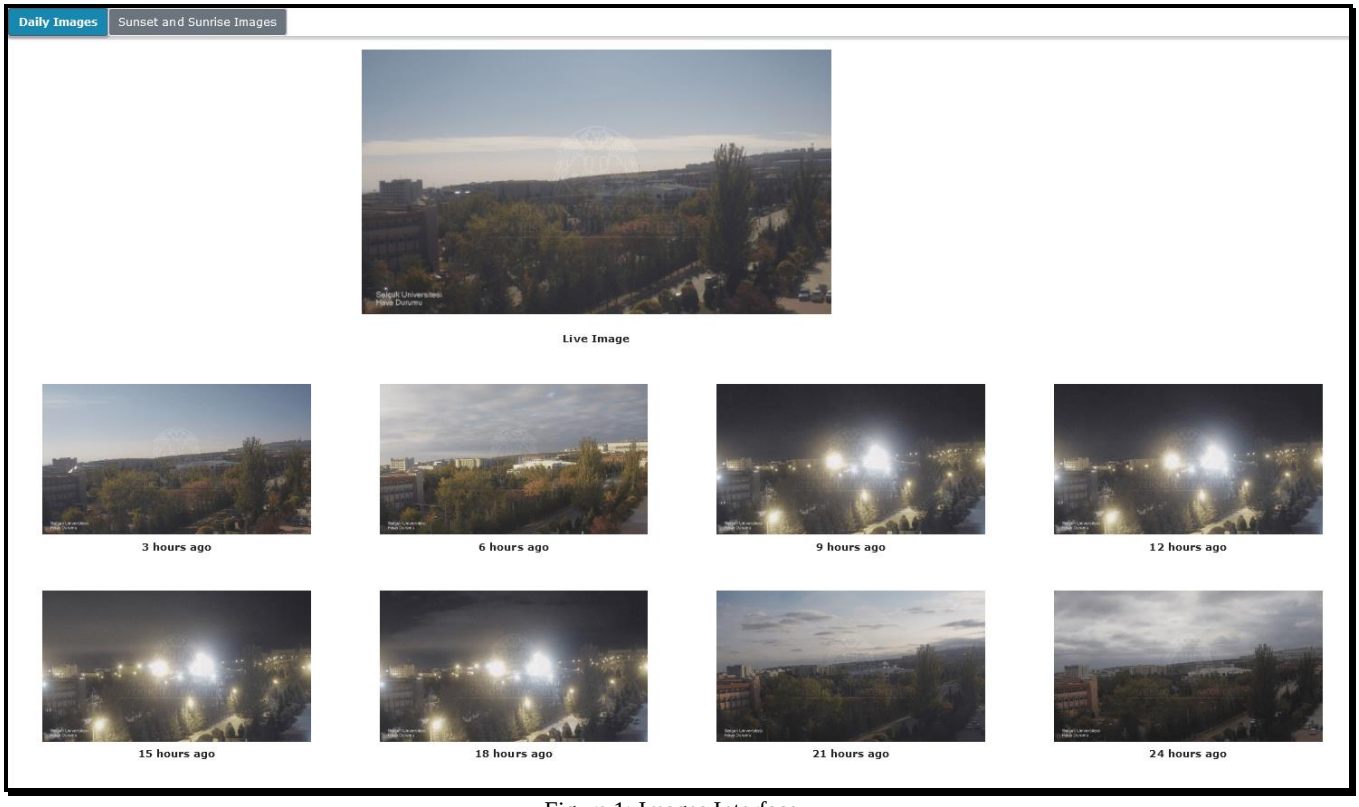

Figure 1: Images Interface

Figure 4: Archive Interface

3) *Images*

Images interface provides images of the campus sky for the last 24h with three-hour intervals (Figure 3). Also, daily sunrise and sunset time-lapses are available.

4) *Terminology*

The terminology interface provides the user with the necessary knowledge of the meteorological concepts used on the website (Figure 5).

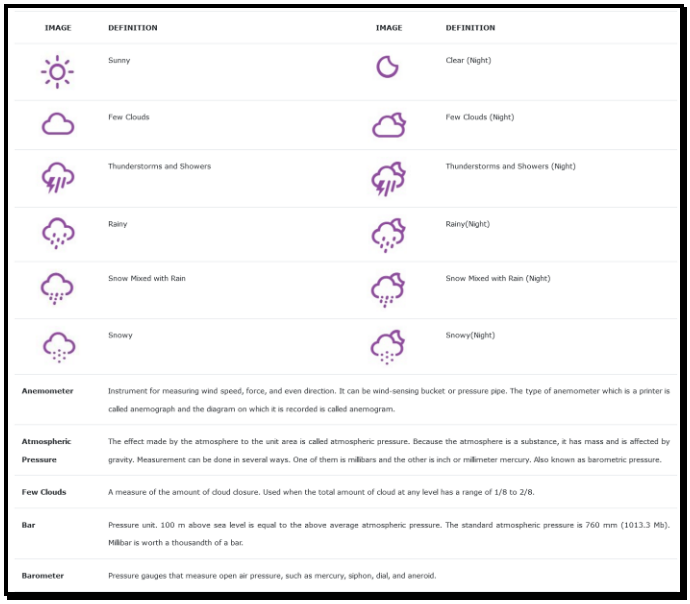

Figure 5: Terminology Interface Sample

5) *About*

About interface provides information about the website, developers, and mobile versions of the website.

III. CONCLUSIONS

In this paper, we have developed a system to collect meteorological data of Selçuk University Alaeddin Keykubat Campus. The main meteorological data system collects are temperature, humidity, air pressure, rain rate, wind speed, wind direction, solar radiation, and UV. The collected data is shared with people living around the campus via a website. This website is designed to provide people with necessary information about the weather around them. Users can better understand the weather situation with live images and time-lapses from the sky around the meteorological system. These data will also be provided via mobile applications both for Android and IOS. After a few years, collected data may be used in climate change studies.

ACKNOWLEDGMENTS

This study is supported by Selçuk University Administration of Scientific Research Projects. Project No: 18301006

REFERENCES

[1] Denissen, J.J.A., et al., *The effects of weather on daily mood: A multilevel approach.* Emotion, 2008. **8**(5): p. 662-667.
[2] Trenberth, K.E., et al., *Effects of changing climate on weather and human activities*. 2000, University Science Books Sausalito, CA.
[3] Colston, J.M., et al., *Evaluating meteorological data from weather stations, and from satellites and global models for a multi-site epidemiological study.* Environmental research, 2018. **165**: p. 91-109.
[4] McGregor, G.R., et al., *Heatwaves and health: guidance on warning-system development*. 2015: WMOP.
[5] Keggenhoff, I., M. Elizbarashvili, and L. King, *Heat wave events over Georgia since 1961: climatology, changes and severity.* Climate, 2015. **3**(2): p. 308-328.
[6] Pachauri, R.K., et al., *Climate change 2014: synthesis report. Contribution of Working Groups I, II and III to the fifth assessment report of the Intergovernmental Panel on Climate Change*. 2014: Ipcc.
[7] DURSUN, Ö.O., *Meteorolojik verilerin akıllı yöntemlerle sınıflandırılması/The classification of the meteorological data using the intelligent methods.* 2005.
[8] Ünal Çalargün, S., *Fuzzy association rule mining from spatio-temporal data: an analysis of meteorological data in turkey*. 2008, Middle East Technical University.
[9] Smith, T.M. and V. Lakshmanan, *Real-time, rapidly updating severe weather products for virtual globes.* Computers & Geosciences, 2011. **37**(1): p. 3-12.
[10] Williams, M., et al., *Automatic processing, quality assurance and serving of real-time weather data.* Computers & Geosciences, 2011. **37**(3): p. 353-362.
[11] TURAL, S.Y. and R.T.D. SAMET, *Gerçek zamanlı meteoroloji verilerinin toplanması, analizi ve haritalanması.* 2011, Ankara Üniversitesi Fen Bilimleri Enstitüsü Bilgisayar Mühendisliği Anabilim ….
[12] Altan, N.T., *Dalgacık Dönüşümü Kullanılarak Zirai-meteorolojik Verilerin Hata Teşhis Ve Tamiri*. 2012, Bilişim Enstitüsü.
[13] Gökrem, L., M. Durgun, and Y. Durgun, *İnternet Tabanlı Meteorolojik Ölçüm Cihazının Geliştirilmesi ve Performansının Belirlenmesi.*
[14] Arroyo, Á., et al., *Analysis of meteorological conditions in Spain by means of clustering techniques.* Journal of Applied Logic, 2017. **24**: p. 76-89.
[15] Chu, W.-T., X.-Y. Zheng, and D.-S. Ding, *Camera as weather sensor: Estimating weather information from single images.* Journal of Visual Communication and Image Representation, 2017. **46**: p. 233-249.
[16] *ExpressJS*. 2021; Available from: https://expressjs.com/.
[17] *React JS*. 2021; Available from: https://reactjs.org/.

The Mobile Application of Selçuk University Weather Tracking System

F. BASCIFTCI[1], E. AGBAHCA[1], K. UYAR[1], Z. YILMAZ ACAR[1], B. TEZCAN[1], M. S. RENKYORGANCI[1], B. C. YUVA[1]

[1] Selçuk University, Konya/Turkey, agbahca@selcuk.edu.tr
[1] Selçuk University, Konya/Turkey, kubrauyar@selcuk.edu.tr
[1] Selçuk University, Konya/Turkey, zuleyhayilmaz@selcuk.edu.tr
[1] Selçuk University, Konya/Turkey, btezcan@selcuk.edu.tr
[1] Selçuk University, Konya/Turkey, basciftci@selcuk.edu.tr
[1] Selçuk University, Konya/Turkey, samirenkyorganc@gmail.com
[1] Selçuk University, Konya/Turkey, canyuva06@gmail.com

***Abstract* - In this paper, a mobile application was developed by using the meteorological data measured by the weather tracking system established in Selçuk University Alaeddin Keykubat Campus. With the application, the users can access daily and historical weather information of Selçuk University, information about the moon and sun. The application has been designed and made available for users on every mobile platform. With the Selçuk University weather tracking system, high accuracy measurements are obtained within the campus. Based on the data received in the weather tracking system, the users are provided with a simple interface, ease of use, and the opportunity to quickly access the desired information. A mobile application with a clear, user-friendly interface has been developed in order to easily deliver the collected data to the end-users.**

***Keywords* – Mobile application, Weather tracking system, Selçuk University, Hybrid mobile development.**

I. INTRODUCTION

Since the first release of smartphones, mobile application usage has grown significantly and some of the applications became ubiquitous in our daily life. The number of available applications in the Google Play store has reached 2.8 million as of 2021 [1]. The popularity of weather applications has increased each year [2] and the Google Play store has 8985 weather applications with an average rating of 4.07 as of 2021 [3].

Real-time weather data is required in various fields such as plant water requirements estimation [4], energy and mass balance measurements over glaciers [5], or for discovering wind energy-potential areas in Oman [6]. Accessing weather data provided from weather stations should be made available through mobile applications. Because especially for students, convenience is the dominant factor when choosing a source of information [7].

In this study, a mobile application for a weather tracking system is developed which is also supported by a website. According to [8], weather apps use three kinds of main screen presentation styles: Essential/Nowcast, Table Shaped, and Map-centered. Our app follows the Essential style because providing essential information without exhausting the user is provided convenience. Also, people tend to stay away from complex menus or secrets when using weather apps [9].

The next section explains the materials and the workings of the mobile app.

II. MATERIAL AND METHOD

A. Material

Selçuk meteorology mobile application uses the data of Selçuk University Weather Tracking System and Selçuk Meteorology Web Site project titled numbered 18301006, which is supported by Selçuk University Scientific Research Projects. With the Selçuk University Weather Tracking System, meteorological information received at regular intervals through sensors is stored. Selçuk University Alaeddin Keykubat campus weather data has been provided by this study to access the end-users with a user-friendly mobile application. The meteorological data used are listed in Table 1.

Table 1: Meteorological data used in the developed mobile application.

Meteorological Data Units	Units
Instant Temperature	°Celsius
Sensed Temperature	°Celsius
Pressure	hectopascal
Wind direction	-
Wind Intensity	kilometer/hour
Moisture	%

In addition to Table 1, the lowest and highest temperature information for the past 3 days, sunrise and sunset times, the phase of the moon daily, and the weather forecast for the next 24 hours are also used.

Along with meteorological data, short sunrise and sunset accelerated videos obtained from the camera images taken from the Selçuk University Weather Monitoring System within the campus are also included in the mobile application.

B. Method

There are many platforms for developing mobile applications. For these platforms to be used in the project, it is considered that they are compatible with Android or iOS operating systems. Android Studio is used to develop Android applications, and XCode programs are used to develop iOS applications. Developing mobile applications for both Android and iOS can be provided on many platforms today. These platforms are in two forms as native and hybrid mobile application platforms.

1) Native mobile application

Native applications are developed directly for a mobile operating system and that can provide direct access to software and hardware facilities. They are disadvantaged in terms of time and efficiency [10, 11].

2) Hybrid mobile application

Hybrid applications can adapt to all platforms. While the design is usually created for a single operating system in native applications, it is a highly preferred application type in hybrid applications due to its ability to adapt to both Android and iOS operating systems [11]. The hybrid mobile application process is shown in Figure 1.

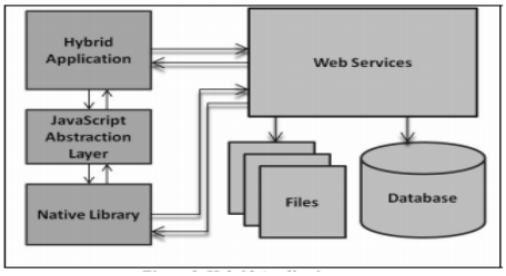

Figure 1: Hybrid mobile application process [11]

Some hybrid application platforms are listed as React Native, Flutter, and Ionic Framework. Considering the features of the project, the plugins to be used and the usefulness of the environment, we chose Ionic Framework as the most appropriate choice compared to other alternatives.

Ionic framework is a kind of open-source framework that uses HTML5, CSS, and Javascript. While the framework offers a typescript option with AngularJS, it can be built on both Android and iOS with Cordova Plugins [12]. The architecture is shown in Figure 2.

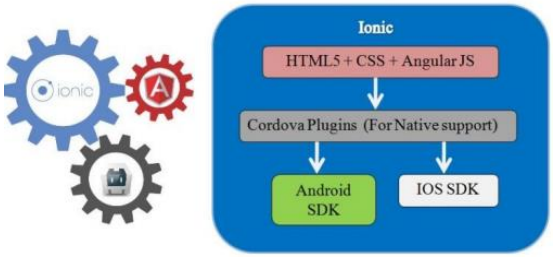

Figure 2: Ionic framework architecture [12]

III. The Developed Mobile Application

While developing the Selçuk University meteorology mobile application, the stages of establishing the preferred environments, making the configuration settings, realizing the graphical designs, and creating the algorithms were carried out.

A. The splash screen and mobile application icon

When the application is opened, a picture is shown to the user during the installation of the components. The content of the picture is an advertisement of the application, in short, with the logo, application name, and background design. The designed splash screen is illustrated in Figure 3(a).

The application icon is the image of the application that appears in the phone menu. With a simple and striking design, a design that can appeal to every user has been made. The application icon is illustrated in Figure 3(b).

(a) The splash screen

(b) The mobile application icon

Figure 3: The screen and icon images of the mobile application

B. The home page of the mobile application

The home page is designed as five panels: the top panel, the historical temperature information panel, the panel with the solar information, the panel with the moon phases, and the forecast panel.

Since the top panel of the home page is the first part that catches the eye of the user, the design in this section is designed remarkably and understandably. It is the screen where the user receives instant information such as air temperature, pressure, wind strength and direction, humidity. It is also the part where the user will interact the most. The panel is intended to have animations shaped by the weather. Depending on the weather conditions, graphical designs that inform the user better, such as snowy, rainy, foggy, and sunny, are dynamically programmed on the panel. Weather conditions are symbolized by an icon so that the user can learn the weather more simply and clearly. Depending on the time, the current day or night situation is also visualized with a background image.

The historical temperature information panel is aimed to display the current weather conditions on a panel at certain time intervals during the day. The user can learn the weather conditions a few hours ago from this panel. In addition, the

lowest and highest temperature of the air for the past three days can be accessed on this panel. When the user touches on any line on this panel, he can get detailed information about the humidity and wind for that day.

The sunrise and sunset times of the day are displayed on the panel with the sun information. In addition, the current position of the sun is calculated mathematically. Mathematical calculations have been added for a more precise and realistic sun movement near sunrise and sunset times. Visually, a more effective interface has been prepared for the user.

On the other hand, the panel with the moon information is designed as a panel that shows the phase of the moon for the day. The data sent under the name of the day, month, year parameters are found with an algorithm in which phase the moon is. This data is displayed to the user in the form of icons.

Finally, a section has been added in the forecast panel that allows users to be informed about the forecasts of the 24-hour weather conditions on the home page. The home page image of the application is shown in Figure 4.

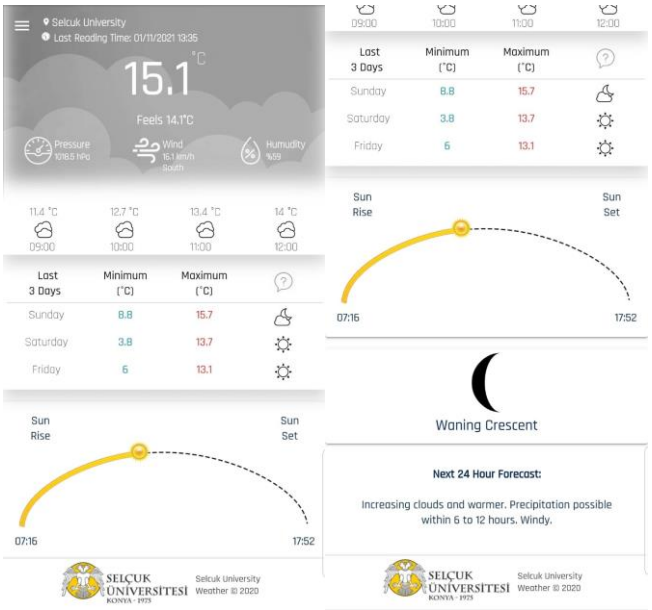

Figure 4: The home page screen

C. *The side menu*

It is the panel that comes in front of the user as a result of swiping from the icon in the upper left on the main page or by swiping from left to right with his finger. From here, the user can access different pages with one touch.

This menu contains symbols and icons, warnings, images, about, settings, sharing options, and language options. The image of the application side menu is given in Figure 5.

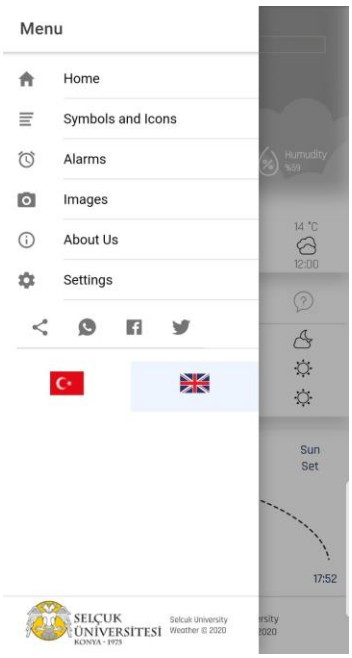

Figure 5: The side menu panel

The symbols and icons option is aimed to convey to the user what the symbols and icons in the application mean on this page. Symbols and icons in the application are in Figure 6.

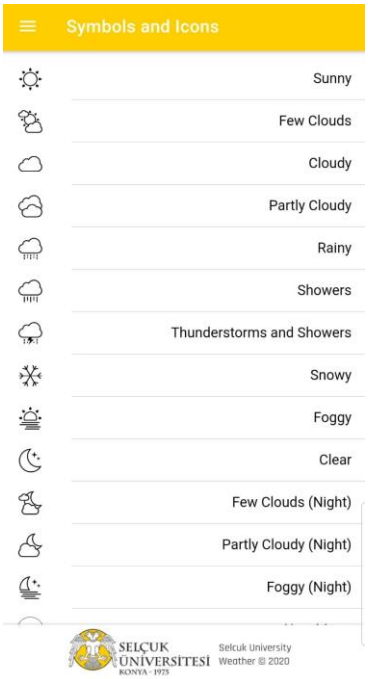

Figure 6: The symbols and symbols pages

On the settings page, there is a section that allows the user to turn the application notifications on or off and to select the update frequency of the data on the main page in minutes. Application notifications are sent to the user's phone morning and evening at 07:15 and 20:15. If the weather conditions of the day are unusual, a warning message is sent to the user. This notification is listed in the alerts option in the side menu. When extraordinary weather conditions occur, there are some

criteria determined to be included in both notification and warnings on the page. These are listed below.

- High temperature,
- The possibility of icing,
- Strong wind,
- The dominant wind from the southeastern direction,
- Dangerous ultraviolet levels,
- Heavy rain

Certain mathematical calculations are made for the above-mentioned criteria. According to these, the system sends a warning message when a result matching these criteria is found. Thus, information is transferred to the user both in the form of a notification and in the form of a table. In addition, if there is an ongoing criterion, it is shown on the table with the phrase "Continuing". If it does not continue, the last seen date and time information are presented within 24 hours.

With the camera in the Selçuk University weather tracking system, the images are obtained from the campus at certain intervals. An accelerated short video was obtained by combining images at a certain interval from these images at sunrise and sunset times. These short videos are integrated into the developed mobile application. Thus, the sunset and sunrise short videos of the campus area lasting six seconds can be accessed via the mobile application. The images page is illustrated in Figure 7.

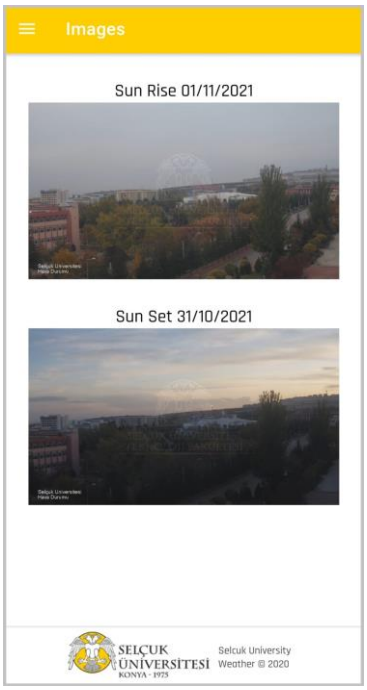

Figure 7: The images page

The about page, information about the Selçuk University weather tracking system project, to which the data used by the mobile application belongs, and the information of the developers are given.

Finally, there is a section on the side menu where users can switch different language options with one click. Users can choose the language they want in this section and use it in their preferred language without closing the application or restarting it.

IV. Conclusion

In this paper, we developed a mobile application to access the meteorological information of Selçuk University Alaeddin Keykubat Campus. The meteorological information in the mobile application is the data obtained by the Selçuk University weather tracking system. The mobile application was developed by a hybrid application method with an Ionic framework and designed as a user-friendly interface. With the developed mobile application, the users can access instant weather information, historical weather information, and moon and sun information of Selçuk University Alaeddin Keykubat Campus. In addition, an alarm system that warns the users of extreme weather conditions has been integrated into the application. The proposed mobile application appeals to both campus staff and students as well as residents of the neighborhood.

Acknowledgment

This study is supported by Selçuk University Administration of Scientific Research Projects with project number 18301006.

References

[1] *Number of available applications in the Google Play Store from December 2009 to July 2021* 2021; Available from: https://www.statista.com/statistics/266210/number-of-available-applications-in-the-google-play-store/.

[2] Li, T., et al., *"What Apps Did You Use?": Understanding the Long-term Evolution of Mobile App Usage*, in *Proceedings of The Web Conference 2020*. 2020, Association for Computing Machinery: Taipei, Taiwan. p. 66–76.

[3] *Most popular Google Play categories* 2021; Available from: https://www.appbrain.com/stats/android-market-app-categories.

[4] Kuśmierek-Tomaszewska, R., J. Żarski, and S. Dudek, *Meteorological automated weather station data application for plant water requirements estimation.* Computers and Electronics in Agriculture, 2012. **88**: p. 44-51.

[5] Abbate, S., et al., *Deploying a communicating automatic weather station on an Alpine Glacier.* Procedia computer science, 2013. **19**: p. 1190-1195.

[6] Sultan, A.-Y., et al., *Assessment of wind energy potential locations in Oman using data from existing weather stations.* Renewable and Sustainable Energy Reviews, 2010. **14**(5): p. 1428-1436.

[7] Bomhold, C.R., *Educational use of smart phone technology: A survey of mobile phone application use by undergraduate university students.* Program, 2013.

[8] Zabini, F., *Mobile weather apps or the illusion of certainty.* Meteorological Applications, 2016. **23**(4): p. 663-670.

[9] Popelka, S., A. Vondrakova, and P. Hujnakova, *Eye-tracking evaluation of weather web maps.* ISPRS International Journal of Geo-Information, 2019. **8**(6): p. 256.

[10] Wasserman, A.I. *Software engineering issues for mobile application development*. in *Proceedings of the FSE/SDP workshop on Future of software engineering research*. 2010.

[11] Khandeparkar, A., R. Gupta, and B. Sindhya, *An introduction to hybrid platform mobile application development.* International Journal of Computer Applications, 2015. **118**(15).

[12] Waranashiwar, J. and M. Ukey, *Ionic Framework with Angular for Hybrid App Development.* International Journal of New Technology and Research, 2018. **4**(5): p. 263068.

A deep learning topology to diagnose of assistance request based Lip-reading

U. SORUC[1], H. ERKAYMAZ[2] and O. ERKAYMAZ [3]

[1]Baykar Defense Company – Computer Engineer, Istanbul/Turkey, ugurcan.soruc@gmail.com
[2]National Defense Uni., Turkish Naval Academy, Elc. Elect. Eng., Istanbul/Turkey, herkaymaz@dho.edu.tr
[3]National Defense Uni., Turkish Naval Academy, Computer Eng., Istanbul/Turkey, oerkaymaz@dho.edu.tr

***Abstract* –Lip-reading is an important research subject for autonomous help systems in Human-Computer Interaction recently. Therefore many different decision models are recommended in literature and they have been continued to be developed. In this context, we propose a 2D-CNN model to classify of words with transfer learning technique. To train of the model MIRACL-VC1, Avletters2 and HLipWords-V1 datasets are used in training process. Moreover, we compare networks obtained from different network parameters and criteria. The results show that the proposed CNN topology has performed better for MIRACL-VC1 (84.2%), HLipWords-V1 (98.9%) and Avletters2 dataset (62%), respectively.**

***Keywords* - Deep Learning, Lip-reading, Convolution Neural Network (CNN), Help Detection, Real-Time Object Recognition and Detection**

I. INTRODUCTION

Visual information such as lip movements, facial expression, tongue and tooth movements helps us to understand a personal speech without audio data. It has a variety of practical applications such as lip-reading, silent film transcription, aids for the hearing impaired, speech recognition in noisy environments, and medical support. For such reasons, lip-reading has been a research topic that has been emphasized in recent years [1] and has gained more importance with the emergence of deep learning.

Feature extraction is difficult because of differences in appearance and speech production diversity among individuals. In addition to these, different lighting conditions of the environment where the image was taken, and different face positions make this process extra difficult. At this stage, there are 4 main approaches for extracting visual speech information from image sequences. These are as follows [2]:

- Image Based
- Visual Motion Based
- Geometric Feature Based
- Model Based

In the image-based approach, gray-level images or feature vectors created by some image transformations are used [3, 4]. In the visual motion-based approach, visual motion is assumed to contain speech data [5]. In the geometric feature-based approach, features such as mouth opening, and width are used [6]. In the model-based approach, a model of lip contours is created with speech articulators [7]. Among these 4 main approaches, we focus on the image-based approach because of its lower cost of feature extraction, high performance in many different models and applicability [2,8].

Lip-reading can be considered as a classification problem in letter and word-based approaches. Hidden Markov model, support vector machines, k-nearest neighbor are the most frequently used basic classification algorithms [9]. In recent years, with the increase in the success rates of deep learning methods, it has started to be applied frequently in classification problems. Deep learning models can be designed in many ways, and hybrid approaches are introduced by combining multiple deep learning architectures [10-12]. Firstly, 3D convolutional neural network (CNN) models are used then LSTM and GRU are started to be used together in time series problems [13-15]. The output formats produced by the developed models can be at the level of alphabet, word, expression, and sentence.

In this study, we aimed to exhibit a lip-reading topology using a 2D-CNN with different topological conditions to diagnose of human request. The topology performance is tested with three different lip-reading dataset which is dataset commonly used in literature. In addition, we discuss the real-time use of lip-reading architecture and its applicability in the field of security.

II. DATASETS

Within the scope of the project, 3 datasets were used. Two of the datasets are publicly available MIRACL-VC1 and AVLetters2. The last used dataset is the HLipWords-V1 dataset created within the scope of the project.

MIRACL-VC1 is a lip-reading dataset containing both depth and color images. Fifteen speakers (five men and ten women) say 10 words and phrases 10 times in front of a body-level Microsoft Kinect sensor. Each instance of the dataset consists of a synchronized array of color and depth images (640x480). The dataset contains a total of 3000 examples of 1500 words and 1500 expressions.

Avletters2 is a dataset of color video images. Six speakers say all the letters from A to Z with 7 times in the dataset. Each sample consists of 1 second recording, 25 frame rate videos at 1920x1080 dimensions.

HLipWords-V1 is a dataset that has been started to be created within the scope of the project for help request detection. A speaker says the words “help” and “good” 50 times at different angles. Each word spoken by the speaker consists of 22 lip images in gray level 250x148 dimensions. The dataset contains a total of 100 samples.

III. DATA PRE-PROCESSING

We apply preprocessing methods on three datasets to increase performance of the topology in this section.

MIRACL-VC1: The words and expressions spoken by each speaker are included in the form of images with color and depth in the dataset. As a first step, the lip portions of the color images were cropped, and the gray level images were converted to 150x150 images. In the next step, the pictures were combined by filling the missing frames on the same column with a length of 22 frames through the y-axis and the images are obtained with 3300x150 dimensions.

Avletters2: Each letter is represented as color video images. The images were converted to framed images with a size of 150x150 in gray level by cropped lip sections in 22 images. They were combined on the y-axis as 22 frames and represented in 3300x150 dimensions

HLipWords-V1: The words spoken by the speaker are included in the dataset in the form of pictures with the lip part cropped. The images are scaled to 150x150 and combined on the y-axis on the same column with 22 frames in length. Output dimensions are 3300 x 150.

IV. MODEL

A. 2D-CNN Network

CNN is an advanced deep learning topology. It can take 3D images and descript different objects of images. Important of this topology is that it has lower feature extraction processes than the other classification models [16-17]. The basic architecture of CNN consist of three types layers (Convolutional, Pooling and Fully-Connected layer (FC)).

Convolutional Layer: This layer extracts the important features from the input images by using different small size kernel matrixes (convolved). that are individually convolved.

Pooling Layer: The layer reduces the spatial dimensions of the extracted Features (convolved) and controls overfitting of convolution process [18].

Fully connected layer: The neurons of the previous layer similar to feed forward neural networks are connected to each neuron in this layer. It has flattened outputs of the pooling or convolutional layers.

We designed a 2D-CNN topology to detect help request words. The topology includes four 2D convolitional layers, four 2D Max-pooling layers and two FC layers as shown in Figure 1.

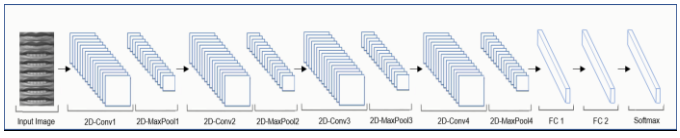

Figure 1: 2D-CNN Networks Architecture

The model topology takes the input images which is moved thorough the height and width dimensions.

B. Model Building Process

The model was firstly trained using the MIRACL-VC1 dataset with 1200 samples and 10 different classes. It was tested with test dataset with 300 samples. The trained model was used to predict letters in the Avletters2 dataset with the transfer learning method. During the training process, all parameters were set as trainable and randomly selected 599 samples in the Avletters2 dataset were used for training and 179 samples for testing. The last FC layer of the model was removed and the Softmax layer with 26 classes was added. After the model was trained with Avletters2 dataset, the trained model was used to detect help request in HLipWords-V1 dataset with transfer learning. Therefore the model was trained with HLipWords-V1 dataset by setting all parameters as trainable. In this process, sigmoid layer was added instead of the Softmax layer, arranged according to the number of classes. 80 samples of the dataset were used for training and 20 samples for testing. In addition, tests using k-fold cross validation were performed to measure the accuracy of loss functions, batch sizes and distribution of the dataset using the MIRACL-VC1 dataset.

V. RESULTS

In this section, performance analysis of the designed CNN topology was carried out for different conditions. The analyses were performed with Tensorflow library and Python programming language. Firstly, the overall model performance and the effect of optimizing algorithms on the performance for MIRACL-VC1 are observed with testing on designed 2D-CNN network. The results obtained for different optimizer algorithms are given in Table 1.

Table 1: Model Optimizer Test Results

Dataset	Optimizer	Accuracy
MIRACL-VC1	Adadelta	0.190
	Adagrad	0.220
	Adam	0.550
	Adamax	0.485
	Ftrl	0.100
	Nadam	0.645
	RMSprop	0.600

As seen in Table 1, the models based on Nadam, RMSprop and Adam optimizers show the highest performance, respectively. In addition, we test the models with different loss functions and obtained results are given in Table 2.

Table 2: Model Loss Function Test Results

Dataset	Optimizer	Loss Function	Accuracy
MIRACL-VC1	Adam	SCC	0.770
	Adam	CC	0.766
	Nadam	SCC	0.826
	Nadam	CC	0.846
	RMSprop	SCC	0.823
	RMSprop	CC	0.830

It is seen that the Nadam optimizer and the Categorical Crossentropy loss function have the highest accuracy values (Table 2). When the results in Tables 1 and 2 were examined, the results indicate that the model based on Nadam optimizer

and Categorical Crossentropy(CC) as the loss function achieved best performance.

Secondly, we modified the model with Nadam optimizer and CC loss function parameters and analyzed performance of the model for different batch sizes. The observed results are shown in Table 3.

Table 3: Model Batch Size Test Results

Dataset	Optimizer	Loss Function	Batch Size	Accuracy
MIRACL-VC1	**Nadam**	**CC**	2	0.780
			5	0.803
			10	0.826
			16	0.806
			20	0.813
			32	0.846
			64	0.843

As seen in Table 3, the highest accuracy value is obtained when the batch size is selected as 32 so optimum batch size is defined with this test. Thirdly, we researched the overfitting problem on the model and training process is realized with the K-fold Cross Validation method. During process, our 2D-CNN model by selecting K value of 5 is tested with MIRACL-VC1 dataset. Observed results are shown in Table 4.

Table 4: K-Fold Cross Validation Test Results

Dataset	K-Fold	Accuracy
MIRACL-VC1	1	0.813
	2	0.850
	3	0.810
	4	0.823
	5	0.815

The designed model has been tested with different performance experiments by using MIRACL-VC1 dataset and the optimal CNN topology is obtained. Finally, we research performance of optimal CNN topology with three different dataset and we show overall performance of the designed model (Table 5).

Table 5: Different Datasets Test Results

Dataset	Output	Accuracy
MIRACL-VC1	Word	0.842
Avletters2	Alphabet	0.620
HLipWords-V1	Word	0.989

As seen in Table 5, while the designed model achieved success performance for word based datasets with 0.989 and 0.842 accuracy to detect of real-time help request, it shows acceptable performance for alphabet based dataset with 0.62 accuracy.

VI. CONCLUSION

Lip-reading process may be used for different help recognition applications such as deaf people actions, criminal attempts and hostage rescue, etc. In this paper, we propose a 2D CNN model to recognize of help words with lip-reading. The model has been trained with three dataset for selecting different initial topologic parameters and transfer learning method. The proposed model demonstrated that the call for help can be successfully detected by the lip-reading process. Our results also show that a real-time recognition framework based on the proposed topology can be created to automatically detect of the human request. As a future work, we plan to create a concatenated Deep neural network framework for real time lip-reading.

REFERENCES

[1] Z. Zhou, G. Zhao, X. Hong, and M. Pietik¨ainen, "A review of recent advances in visual speech decoding", *Image and vision computing*, vol. 32, no. 9, pp. 590–605, 2014.

[2] S. Dupont and J. Luettin, "Audio-visual speech modeling for continuous speech recognition", *IEEE Trans. Multimedia*, vol. 2, pp. 141–151, Sept. 2000.

[3] B. P. Yuhas, M. H. Goldstein, T. J. Sejnowski, and R. E. Jenkins, "Neural network models of sensory integration for improved vowel recognition", *Proc. IEEE*, vol. 78, pp. 1658–1668, Oct. 1990.

[4] G. Potamianos, H. P. Graf, and E. Cosatto, "An image transform approach for HMM based automatic lipreading*" in Proc. IEEE Int. Conf. Image Processing*, 1998, pp. 173–177.

[5] K. Mase and A. Pentland, "Automatic lipreading by optical flow analysis", *Syst. Comput. Jpn.*, vol. 22, no. 6, 1991.

[6] E. D. Petajan, "Automatic lipreading to enhance speech recognition," *in Proc. IEEE Conf. Computer Vision and Pattern Recognition*, 1985, pp. 40–47.

[7] T. Coianiz, L. Torresani, and B. Capril, *2D deformable models for visual speech analysis*. in Speechreading by Humans and Machines: Models, Systems and Applications, D. G. Stork and M. E. Hennecke, Eds. Berlin, Germany: Springer-Verlag, 1996, vol. 150 of NATO ASI Series, Series F: Computer and Systems Sciences, pp. 391–398.

[8] I. Matthews, T. Cootes, J. Bangham, S. Cox and R. Harvey. (2002) Extraction of Visual Features for Lipreading, *IEEE Transactions on Pattern Analysis and Machine Intelligence*. *24 (2)*. pp. 779--789.

[9] A. Basturk and T. Ozcan. (April 2019). Lip Reading Using Convolutional Neural Networks with and without Pre-Trained Models. *Balkan Journal Of Electrical & Computer Engineering*. 7(2) . pp. 195-201

[10] C. Bi, D. Zhang, L. Yang and P. Chen, "An Lipreading Modle with DenseNet and E3D-LSTM", in *Conf Rec 6th International Conference on Systems and Informatics (ICSAI 2019)*, pp 511-515, DOI: 10.1109/ICSAI48974.2019.9010432.

[11] H. Akbari, H. Arora, L. Cao, and N. Mesgarani, ''Lip2Audspec: Speech reconstruction from silent lip movements video'', in Proc. *IEEE Int. Conf. Acoust., Speech Signal Process.* (ICASSP), Calgary, AB, Canada, Apr. 2018, pp. 2516–2520.

[12] A. Thanda, D. K. Margam, P. A K, R. Aralikatti, S. Roy, S. M. Venkaresan and T. Sharma, "*LipReading with 3D-2D-CNN BLSTM-HMM and word-CTC models*" arXiv preprint arXiv:1906.12170, 2019.

[13] K. Xu, D. Li, N. Cassimatis, and X. Wang, "*LCANet: End-to-end lipreading with cascaded attention-CTC",* in Proc. *13th IEEE Int. Conf. Autom. Face Gesture Recognit. (FG)*, May 2018, pp. 548–555.

[14] M. Bansode, P. Limaye, R. Mestri and S. Khuteta, "Analysis of Feature Extraction and Classification Models for Lip-Reading", *Proceedings of the Third International Conference on Trends in Electronics and Informatics (ICOEI)* ,pp. 911-915, IEEE 2019.

[15] Y. M. Assael, B. Shillingford, S. Whiteson, and N. De Freitas, "*Lipnet: End-to-end sentence-level lipreading*," arXiv preprint arXiv:1611.01599, 2016.

[16] Bayoudh, K., Hamdaoui, F. & Mtibaa, A. (2021). Transfer learning based hybrid 2D-3D CNN for traffic sign recognition and semantic road detection applied in advanced driver assistance systems. *Appl. Intell.* 51. pp. 124–142.

[17] Fu, Y., Zhang, Y., Gao, Y., Gao, H., Mao, T., Zhou, H., Li, D., (2017). Machining vibration states monitoring based on image representation

using convolutional neural networks. *Eng. Appl. Artif. Intell*. 65. pp. 240–251.

[18] Liang, P., Deng, C., Wu, J., Yang, Z., Zhu, J., Zhang, Z., (2019). Compound fault diagnosis of gearboxes via multi-label convolutional neural network and wavelet transform. *Comput. Ind*. 113. pp.103132.

Energy management intelligent Street Lighting System in Ahar City with the internet of things - A Case Study

H.MORADI[1] and I. KIYAK[1]

[1] Marmara University, Istanbul/Turkey, hesammoradi@marun.edu.tr
[1]Marmara University, Istanbul/Turkey, imkiyak@marmara.edu.tr

Abstract **- In an advanced world where every city strives for progress and intelligence, using the existing infrastructure in cities and upgrading them is the most cost effective way to develop them and make them intelligent. One of the features of the smart city is the use of new urban lighting and illuminants such as smart street lighting. There are more than 300 million streetlights in the world, but most have not yet been upgraded to LED lights, even though they offer clear technological and economic benefits. Traditional light bulbs are gradually being replaced by more efficient and controllable LED light bulbs. The design proposed in this article for smarter lighting of downtown arcades includes various components such as intelligent LED control loops, gateways, sensors, and a centralized management operating system. In this paper, the lighting of a two-lane expressway is designed and modeled, then the energy consumption of both traditional lighting and intelligent lighting with motion sensor is studied. A case study in this regard is one of the highways of Ahar city.**

Keywords **- smart city, smart street lighting, energy efficiency, Illumination**

I. INTRODUCTION

At the moment, more than 50% of the world's population lives in cities [1] [2] [3]. The rapid emergence of the concept smart Cities as a prospective vision of today's cities promises to remarkably change our lives and provide stories, modern services. These services, and the basic advanced information and Communication Technologies that support them, will also help solve a diversity of contemporary problems that current solutions and technologies struggle to address [4]. Recently, the use of light emitting diodes (LED) in street lighting has increased dramatically. The LED -based street lighting technology has significant advantages in both energy efficiency and optical luminescence compared to traditional street lighting technologies such as high-pressure sodium (HPS) and low-pressure sodium (LPS) lamps [5]. To increase productivity and meet existing standards, the street lighting system should have control features to ensure road safety and maintain energy consumption at an optimal level by intermittently adjusting the lighting level. This paper points out the need to pay attention to the control and monitoring of street lighting systems, and presents the structure and architecture of intelligent street lighting systems and their economic calculations. In this article, we study turning lights on and off with motion sensors. First, we examine the amount of energy used for traditional street lighting, and then we examine how much energy we save when the smart lighting system is used instead of the current system. Previous work, including replacing traditional lights with patterns. Advanced [6-8], are useful but insufficient. In addition, reference [9] used dimming mode to centrally control the lighting level of the passages or the use of the system. Multi-level lighting with two different ballasts for each lamp is a design done in reference [10]. A similar article analyzed a street lighting system in a smart city where energy consumption was calculated for only two months in a row. However, in this article, we study the amount of energy consumption for street lighting in different three months of the year. Another article uses motion detection sensors to detect the movement of objects on the road and provide a solution to control light intensity.

II. METHODOLOGY OF SMART STREET LIGHTS SYSTEMS

The ingredients of the AHAR City lighting system are listed below :

A. Intelligent LED control loops

In fact, this controller receives signals from the sensors and sends the necessary commands to the lights for intelligent control.

B. Gateways

The gateway is one layer above the controllers. The connection between the Gateway and the controller can be in the form of RF(WiFi, Zigbee,...) or through power cables and in the form of PLC (Power Line Carrier). This layer refers to the data management software that exchanges information with the gateway through the server. The communication between the software and the gateway can be over 5G/4G /3G / LTE and Ethernet or over the Internet and TCP / IP protocol. It is connected to the nodes via the ZigBee wireless protocol (IEEE 802.15.4) [11].

C. Sensors

In order to have an intelligent performance of the system, it is necessary to have appropriate measurement equipment capable of detecting the phenomena that occur and

transmitting them to the programmable decision system. To this end, motion detectors have been placed at a suitable height from lighting bases, both to be able to detect the movement of vehicles, and this height has been placed to be as far away from public access as possible to avoid possible sabotage. These sensors must be able to cover the acceptable radius and also have the appropriate energy consumption.

D. Central management operating system

This system has created a unique and versatile intelligent street lighting control system with centralized management system software. This is a great solution for managing large outdoor lighting networks to control and monitor street lighting infrastructure while saving energy and reducing maintenance costs. The centralized lighting management system is just the first step in the process of developing a more sophisticated smart city operating system [12]. Figure 1 shows the ingredients of an intelligent street light.

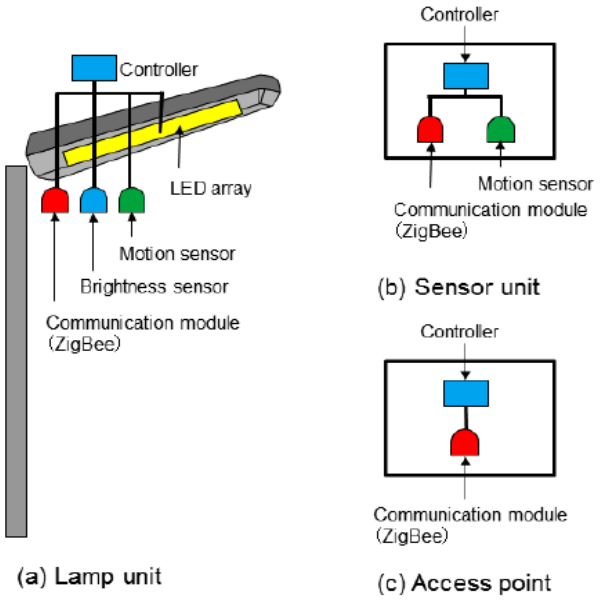

Figure 1: The ingredients of the intelligent street light[13]

III. PROJECT PROPOSAL

The model that we want to present in this project is the installation of an intelligent lighting system with a traditional lighting system in the city of Ahar.

A. Project location

In this study, the roadway is considered as a highway with two lanes in opposite directions, and each lane may include multiple lanes (Figure 2). The lights are installed in the middle of the highway so that each light pole consists of two lights, each of which can illuminate its respective lane independently of the other. The length of this highway is about 4.46 km, which extends from Islamic azad university ahar to Basij Square. The locations of the selected road are shown in Figure 3.

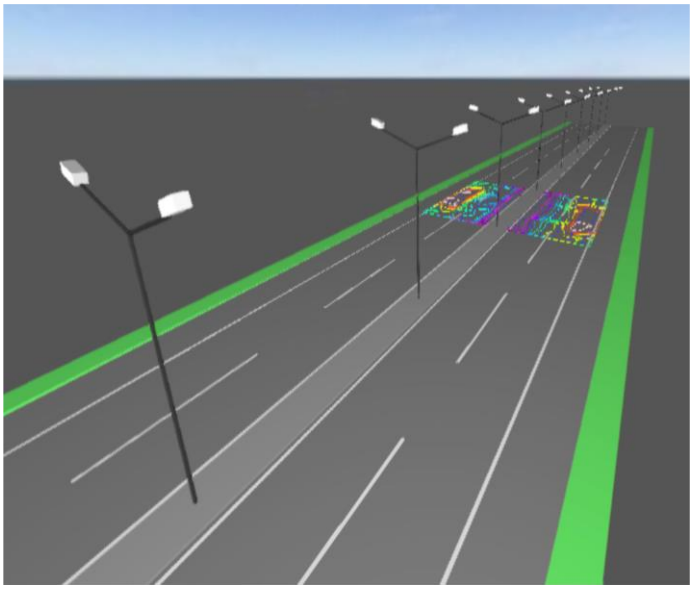

Figure 2: Hypothetical highway and street lights

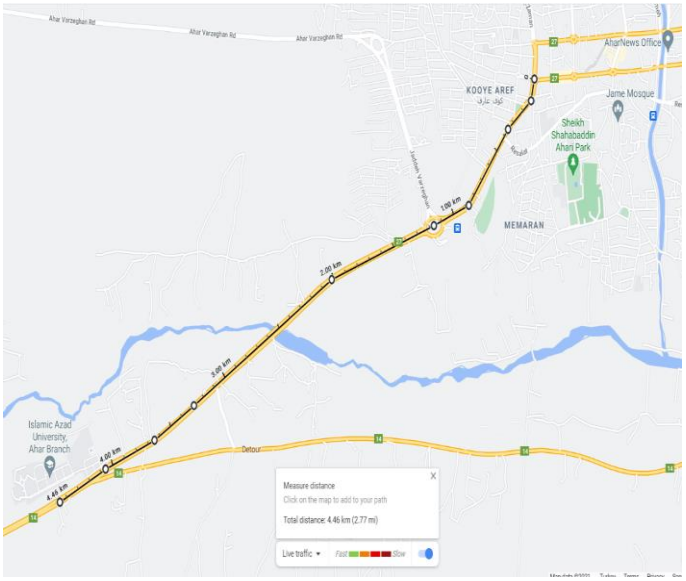

Figure 3: Location of the distance in Ahar

B. Elements

The following are the elements are using:

1) Intelligent LED light: In this project we use Philips LED streetlights with IP65 which are 120W LED with 120 LM /W.
2) Road Light Controller: In this IoT street lighting control system, the street lights are automatically ON and OFF switched. The street lights can work automatically by detecting the movement of objects on the road. IR sensor is used to detect the object. This system has some features like Automatically turn on/off with any device within the IoT street light control system, Street lights can work with different time frame based on actual needs and Automatically predict and diagnose the fault of street light without personal on site. IoT based street light monitoring system can include WIFI, charging station and video

surveillance [14].

3) Wireless Gateway: Wireless networks are capable of receiving and retransmitting data from gateways, ZigBee / WLAN based communication protocol is used to communicate between neighboring wireless networks, create a wireless network mesh network with other communication gateways, set up a larger network using Wi-Fi and GPS to transmit data from a base station to the cloud accessible through a central control and monitoring system. The proposed system uses ZigBee network to communicate with the street lights, gate nodes and management software for real time monitoring and control. Light sensors are used to adjust the brightness of the street lights.

4) Control Center Software: The main function of the control center is to collect and analyze information, make a decision to unload or turn on/off, send commands to controllers, and store information. The control center consists of hardware, software and a network coordinator. The coordinator collects all the information sent from the network to the computer. This information includes details about the status of each controller (central controller and local controllers). The user interface that controls such a lighting system is an integrated software platform that is responsible for remote control and monitoring of lighting systems. Through the graphical interface, the user can switch off the automatic control and take command himself. It is also possible to graphically display the position of the lamp and the area where the system is installed, and information related to the position of the lamp and its power consumption is displayed.

Figure 4 shows the flow chart for an intelligent street lighting system. Motion detection sensors are installed in all the streetlights. They communicate with the wireless interface using the ZigBee protocol. wireless routers are connected to web servers in the data center that send data over telegraph cables (Table 2).

For simulation this project we used this elements and formula include:

$i = \text{its from 1 to 24 related to days of months}$

$j = \text{its from 1 to 120}$

$$\text{Power}(1,i) = \text{Power}(1,i) + 25/12;$$

$$\text{Power}(1,i) = \text{Power}(1,i) + 5/6;$$

$$\text{Power\_new}(1,n) = \text{Power\_new}(1,n) + \text{sum}(\text{Power});$$

$$\text{Power}(1,i) = (\text{Power}(1,i) + 250) * 31;$$

$$\text{Power\_new1} = \text{sum}(\text{Power\_ new});$$

$$\text{power\_old} = 250 * 10 * 30$$

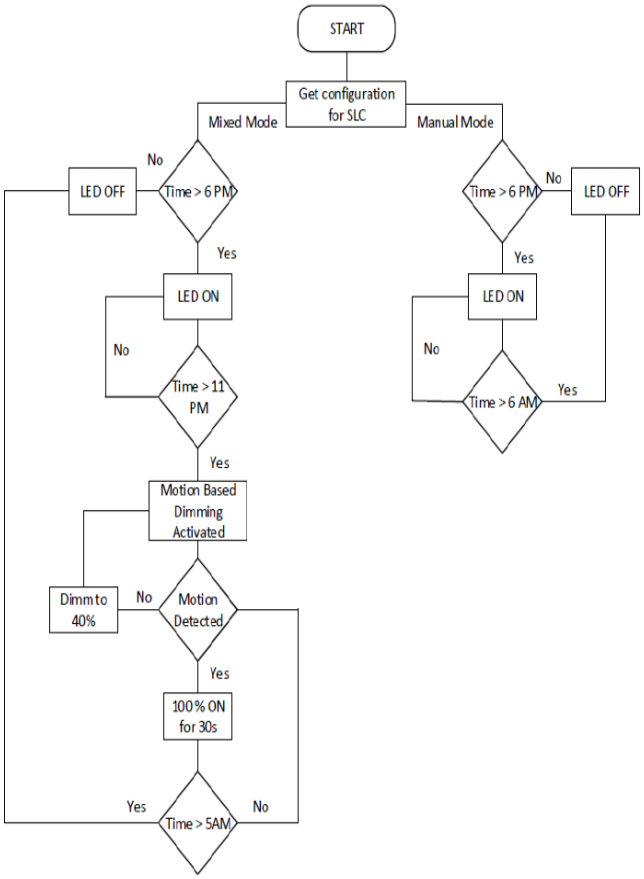

Figure 4: Flow chart of smart street lights in Ahar

The sensors used in this project detect motion and adjust dimming, which is controlled manually via central management software. The controller has two modes: schedule-based dimming and motion sensor-based dimming. In the first mode, the motion sensor plays no role and the light turns on and off based on time. The Lux rotary switch is used to detect sunrise and sunset. In the second mode, the sensors play an important role and control the switching on and off, as you can see in Tables 1 and 2. Due to traffic in the evening until midnight, the lights are always at 100% and then the brightness of the lights works with the sensor. If see any objects, the lights will turn on at 100% brightness for 30 seconds, otherwise the brightness of the lights is 40%.

Table 1: Mode of schedule based dimming

Set Configuration		Get Configuration	
Analog input scaling high value	N/A	Analog input scaling high value	N/A
Analog input scaling low value	N/A	Analog input scaling low value	N/A
Luminary control value	N/A	Luminary control value	N/A
Luminary control tolerance	N/A	Luminary control tolerance	N/A
Dimming type	Schedule based dimming	Dimming type	Schedule based dimming
Motion pulse rate	N/A	Motion pulse rate	N/A
Motion dimming percentage	N/A	Motion dimming percentage	N/A
Motion dimming time (Seconds)	N/A	Motion dimming time (Seconds)	N/A
Dimming delay time (Minutes)	0	Dimming delay time (Minutes)	0
Gradual dimming type (Seconds)	0	Gradual dimming type (Seconds)	0
Normal dimming percentage	N/A	Normal dimming percentage	N/A
Motion detect timeout (Seconds)	N/A	Motion detect timeout (Seconds)	N/A
Motion broadcast timeout (Seconds)	N/A	Motion broadcast timeout (Seconds)	N/A
Motion sensor type	N/A	Motion sensor type	N/A
Daylight harvesting start offest (Minutes)	N/A	Daylight harvesting start offest (Minutes)	N/A
Daylight harvesting stop offest (Minutes)	N/A	Daylight harvesting stop offest (Minutes)	N/A

Table 2: Mode of motion sensor based dimming

Set Configuration		Get Configuration	
Analog input scaling high value	N/A	Analog input scaling high value	N/A
Analog input scaling low value	N/A	Analog input scaling low value	N/A
Luminary control value	N/A	Luminary control value	N/A
Luminary control tolerance	N/A	Luminary control tolerance	N/A
Dimming type	Motion sensor based dimming	Dimming type	Motion sensor based dimming
Motion pulse rate	1	Motion pulse rate	1
Motion dimming percentage	0	Motion dimming percentage	0
Motion dimming time (Seconds)	30	Motion dimming time (Seconds)	30
Dimming delay time (Minutes)	0	Dimming delay time (Minutes)	0
Gradual dimming type (Seconds)	0	Gradual dimming type (Seconds)	0
Normal dimming percentage	40	Normal dimming percentage	40
Motion detect timeout (Seconds)	20	Motion detect timeout (Seconds)	20
Motion broadcast timeout (Seconds)	20	Motion broadcast timeout (Seconds)	20
Motion sensor type	High	Motion sensor type	High
Daylight harvesting start offest (Minutes)	N/A	Daylight harvesting start offest (Minutes)	N/A
Daylight harvesting stop offest (Minutes)	N/A	Daylight harvesting stop offest (Minutes)	N/A

C. Power consumption with normal lighting

We obtained this information online from the website [15]. Is from three different months Contains 1 Feb 2020 - 28 Mar 2022, where the middle duration of night is about 13 hours, 1 Aug 2020 - 31 Aug 2020 where the middle duration of night is about 10 hours and 1 Oct 2020 - 31 Oct 2020 where the middle duration of night is about 13 hours, at term of ordinary labor, Ordinary street lights had on and off times. Total time to stay on the moon for Feb is 28*13 = 364 hours, for Aug is 31*10= 310 hours and for Oct is 31*12= 372 hours. Ahar city have 350 H.P.S.V. /Metal halide 250 Watt street lights.

$$\begin{aligned} Feb &= [(Qty * UnitPower * Consumption * 28)]/1000 \\ Aug &= [(Qty * UnitPower * Consumption * 31)]/1000 \\ Oct &= [(Qty * UnitPower * Consumption * 31)]/1000 \end{aligned} \quad (1)$$

There are also 69 LED lamps installing on the smart tape that using 120 watts energy. According to these conditions, we calculate power consumption excluding the "SMART" functions for the months of February, August and October, which are listed in Table 3. The following formula is used to calculate the amount of energy consumption.

Table 3: Power consumption

Type	***Qty.***	***Unit Power (W)***	***Feb (KWh)***	***Aug (KWh)***	***Oct (KWh)***
H.P.S.V.	350	250	31850	27125	32550
LED	69	120	3013	2566	3080
		Total	34863	29691	35630

D. Power consumption

By placing 350 ordinary light bulbs with smart lights, this tape had lights that operated in two different modes.

1) Hand worked State : In this state, the lights are turned on and off by setting a specific time. The rules are given to the data controller and transmitted to the road light controller. This is provides signals to turn the lights on and off at 18:00 to 07:00 for February, 20:00 to 06:00 for August and 18:00 to 06:00 for October.
2) Mixed State: In this state, the lights are set to maximum in the early hours of the night from 6:00 to 23:00. Thereafter, the lights are dimmed until the motion detection sensors are activated. These sensors are sensitive to turning the lights on and off from 23:00 to 6:00.

IV. CONCLUSION

Alongside the growing importance of energy conservation due to limited energy resources and increased environmental impact due to the use of current systems with high energy consumption, the need to improve road and night safety and to respond appropriately to changes in the environment. doubles the need to use systems for monitoring and control of street lighting. Since this system can be implemented on any

suburban route with two bypass lanes and with a lighting system in the middle of the route, a 4.46 km hypothetical route was used as an example for the calculations in this article. The distance between the two lighting bases is 50 meters.

Table 4: Amount of energy savings in month

	February	***Augost***	***October***
Smart Light System (kWh)	22750	19375	25188
Current Light System (kWh)	34863	29691	35630
Savings (kWh)	12113	10316	10442
Savings (%)	65.2	65.2	70.6

Table 4 shows the power consumption of the traditional lighting system in terms of SSL. It was found that a huge amount of energy is saved by replacing the H.P.S.V./metal halide with LED lights and controls. By implementing this system, the system can save more than 65% energy compared to the traditional mode when it is in smart mode (Figure 5). Using modern solutions to light cities can be a valuable way to make cities as smart as possible. This has many benefits, the most important of which are a significant reduction in energy costs, increased safety of public spaces, an improved traffic situation through better visibility of potential hazards for drivers, and a minimization of cu pollutant emissions into the air by reducing energy consumption in cities.

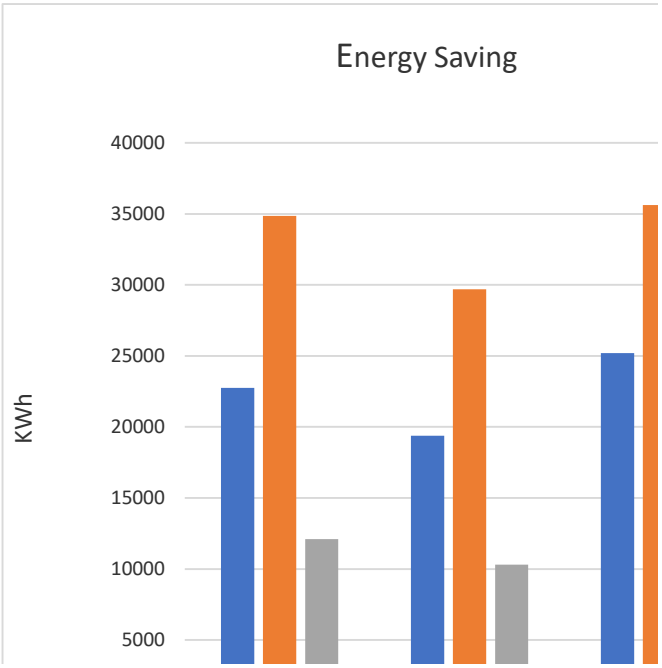

Figure 5: Flow chart of smart street lights in Ahar

REFERENCES

[1] "World's Population Increasingly Urban With More Than Half Living in Urban Areas", New York, NY, USA, Dec. 2014.

[2] United Nations, "World Urbanization," https://www.un.org/development/desa/publications/- revision-of-world-urbanization-prospects.html,2018..

[3] H. Ritchie, "How is an urban area defined?," https://ourworldindata.org/how-urban-is-the-world, 2018.

[4] D. Payne. "Poor ambulance response causes 700 deaths annually in Ireland". British Medical Journal, Nov. 11, 2000, 321(7270): 1176.

[5] *A. Kimber, J. Roberts, J. Logan, and M. Lambert, LED Street Lighting : A Handbook for Small Communities. Ankeny, IA, USA: Iowa Association of Municipal Utilities, 20012.*

[6] F. J. Nogueira, L. A. Vitoi, L. H. Gouveia, C. G. Casagrande, D. P. Pinto and H. A. C. Braga, "Street lighting LED luminaires replacing high pressure sodium lamps: Study of case," in 11th IEEE/IAS International Conference on Industry Applications, Juiz de Fora, 2014.

[7] R. M. Ramli and Y. Z. Arief, "Application of LED Technology into Public Road Lighting in Malaysia for Replacing The High Pressure Sodium Vapour Lighting," in International Conference on Sustainable Energy Engineering and Application (ICSEEA), Gombak, Selangor, Malaysia, 2015.

[8] Abolfazl Bagheri and Hossein Shirdel "Study of energy consumption optimization in one of the cities of Golestan province by replacing the first conference" LED street lights with a normal source of energy management and optimization, Aliabad Katoul, 2015.

[9] A. Burgio and D. Menniti, "A novel technique for energy savings by dimming high pressure sodium lamps," Electric Power Systems Research, vol. 96, pp. 16-22, 2013.

[10] Ardeshir Bahirai; Afshin Maarefpour and Iraj Hassanzadeh "Intelligence and remote control of street lighting in order to improve energy consumption management" Iranian Conference on Lighting and Lighting, Shiraz, 2013.

[11] P.C., Vena, P., Tharakan, H., Haridas, K., Ramya, R., Joju, T.S.,Jyothis, "Smart street light system based on image processing,"in IEEE International Conference on Circuit, Power and Computing Technologies (ICCPCT), 2016.

[12] Thomas Novak, Klaus Pollhammer, Heimo Zeilinger, Samer Schaat,"Intelligent streetlight management in a smart city" Proceedings of the 2014 IEEE Emerging Technology and Factory Automation (ETFA),978-1-4799-4845-1

[13] Y. Yang, S. Lee, G. Chen, C. Yang, Y. Huang and T. Hou, "An Implementation of High Efficient Smart Street Light Management System for Smart City," in IEEE Access, vol. 8, pp. 38568-38585,2020.

[14] Yusaku Fujii, Noriaki Yoshiura, Akihiro Takita and Naoya Ohta, "Smart street light system with energy saving function based on the sensor network," Conference'04, Month 1-2, 2004, City, State, Country.

[15] Available [Online] : https://www.cimconlighting.com/products-islc-3100-7p

Arduino Based System Design for Measuring Heart Rate and Body Temperature

A.M.A. SHAKARJI[1] and A.GOLCUK[2]

[1] Institute of Sciences, Selcuk University, Konya/Turkey
[2] Biomedical Engineering Department, Selcuk University, Turkey
Corresponding Author: Adem Golcuk, adem.golcuk@selcuk.edu.tr

Abstract **-** In this study, a multi-sensor and low-cost biosensor system has been developed using the Arduino microcontroller board. With the established system, it is aimed to digitally measure the heart rate and body temperature of people. In this way, vital body values of people with health problems will be monitored regularly and sudden changes in values will be determined. In the development of the system; Arduino uno electronic control card, heart rate sensor and temperature sensor are used together. With these tools, a software that is sensitive to detecting heart rate and changes in body temperature has been developed and a general working diagram has been created. The system created has a structure open to future additions and improvements. It has been determined that the data obtained with the help of the sensors on the system can be transferred to the computer environment via wifi and followed on the internet. More sensors can be placed in the biosensor tracking system in accordance with the intended use. As a result of the tests, it was seen that the system successfully transmitted the information received from the sensors visually to the user within the desired time period and warned with an audible warning at the critical values determined. It is considered that the developed biosensor system can be used to access information consisting of heart rate and body temperature, which are vital for humans, remotely and instantaneously, and will contribute to the field of medicine in this context.

Keywords **- Arduino, Sensor, Biosensor, Heart Rate, Body Temperature.**

I. INTRODUCTION

In recent years, rapid developments in computer and electronic technologies are widely used in the field of health, as in all areas of life. Robotic systems are rapidly replacing humans, especially in performing repetitive tasks [1,2]. The fact that the work to be done in this context is different requires the realization of systems that can fulfill different tasks. Electronic systems designed for such tasks generally consist of three parts. These; The hardware part where the electronic cards are located, the sensor and sensor peripherals that provide data acquisition, and the software part that enables the data processing and decision making [3,4,5].

Arduino based electronic control cards are widely used microcontrollers in this direction. These electronic cards offer researchers a flexible, easy-to-use and complete hardware and software environment with different features. Arduino based systems are developed using the Arduino language based on C/C ++ programming. In addition, Arduino's integrated development environment (IDE) for Windows, OS X and Linux systems is also available [6].

In this study, it is aimed to develop a multi-sensor and low-cost biosensor system using the arduino microcontroller card. Digital measurement of heart rate and body temperature of people was investigated with the established system. In this way, it is ensured that vital body values of people with health problems can be followed regularly and sudden changes in values are determined. It is considered that the developed arduino based biosensor system can be used to access information consisting of heart rate and body temperature, which are vital for humans, remotely and instantaneously, and will contribute to the field of medicine in this context.

II. MATERIAL AND METHODS

Materials

Arduino Uno Control Card: Arduino Uno is an Arduino board containing an ATmega328 microcontroller. It can be said that Arduino is the most widely used board. Arduino Uno contains all the necessary components to support a microcontroller. It is possible to power the Arduino Uno by connecting it to a computer with a USB cable, with an adapter or with a battery. It requires DC 7 ~ 12V as the operating voltage.

I^2C Serial Interface and LCD Module: The LCD I^2C module is a module that works with the I^2C serial communication protocol. It is used to visually transmit the outputs of the Arduino system to the users. The 16x2 character LCD screen normally operates according to the 4/8 bit parallel data communication system.

Warning System (Buzzer): The buzzer card is used to transmit audible warnings to the user. The module works between 3.3V-5V. It is connected to the digital output of the microcontrollers and generates a warning tone at the specified tone.

Heart Rate Pulse Sensor: Arduino pulse sensor is used to determine the heart rate. The sensor is designed for scientific research. The pulse sensor can be attached to the finger or the earlobe. There is an optical amplifier and noise suppressor electronic circuit on the pulse sensor. The sensor outputs analog signals. The module is basically based on the principle of whether the oxygen flow in the blood transmits IR (infrared) signal.

Temperature and Humidity Sensor: Since DHT22 pulse sensor ise widely preferred in Arduino systems with its ready to use library this sensor was used in this project.

L293 Motor Driver: L293 ICs are quad, half-H drivers. The L293 is designed to provide bidirectional driver currents of up to 1 A at voltages of 4.5 V to 36 V.

Method

The study is an experimental system study. In the development of the system; Arduino uno electronic control card, heart rate sensor and temperature sensor are used together. With these tools, a software that is sensitive to detecting heart rate and changes in body temperature has been developed and a general working diagram has been created. The system created has a structure open to future additions and improvements. It has been determined that the data obtained with the help of sensors on the system can be transferred to the computer environment via wifi and can be followed on the internet. More sensors can be placed in the biosensor tracking system in accordance with the intended use.

The development phase of the system consists of two parts: hardware and software. In the realization of electronic design; A general diagram was created using the Arduino Uno control card, heart rate sensor and temperature sensor. The software part developed within the system undertakes two different tasks. The first is the determination of the heart rhythm (pulse) and the calculation of the heart rate (BPM), the second is the measurement of the body temperature with the help of a sensor. The calculated heart rate and body temperature values are then visually presented to the user with the help of the LCD screen. The software also analyzes whether the data obtained is at vital or critical levels and this situation is announced to the user with audible alerts. The flow diagram that includes the operation of the system is shown in Figure 2.

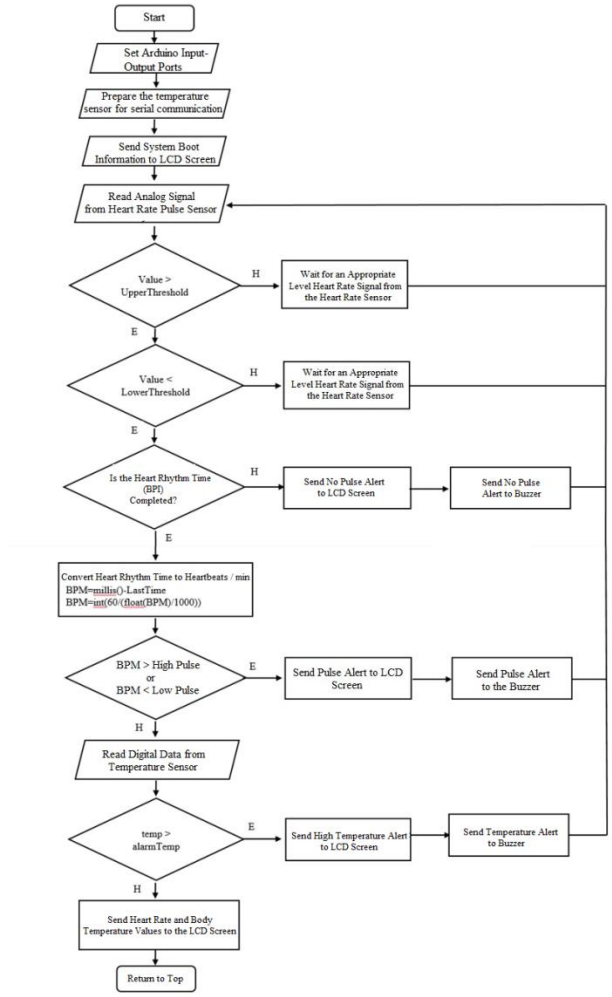

Figure 1: Flow diagram of the software developed for the biosensor system

III. RESULTS

The software developed for the Arduino biosensor system has several functions. With the software, the input / output port properties of the Arduino electronic control card are set first. Then, I2C serial communication information is loaded with the temperature sensor and finally, the system opening screen is prepared by loading Turkish characters on the LCD screen.

In the general cycle part of the software, firstly the analogue signals coming from the heart rate (pulse) sensor are analyzed and the heart rhythm is tried to be determined. When the pulse level is determined in milliseconds, the heart rate (Heart Beat/Pulse Rate, BPM) is calculated. The following conversion formula is used to determine the heart rate from the heart rate.

BPM = millis () - LastTime

BPM = int (60 / (float (BPM) / 1000))

In the temperature measurement part of the biosensor software, digital data communication is made with the temperature sensor. Digital heat values from the heat sensor are automatically converted in the Arduino library. The heat data of the system is obtained as ºC.

The heart rate and temperature values determined lastly with the biosensor software are sent to the LCD screen to be visually transmitted to the user. In this way, whether the heart rate and temperature values obtained through the sensors are within the specified threshold values are communicated to the user visually through the LCD screen and audibly with the buzzer. If there is any abnormal value, the user is warned.

First of all, the general hardware design of the developed biosensor system has been completed. Then, the electronic part was formed by placing microcontrollers and sensors. Finally, the programming of the Arduino system has been made and tested to perform the intended functions. The simplified general diagram of the designed biosensor system is shown in Figure 2. As seen in Figure 2, the information obtained from the heart rate (pulse) sensor and temperature sensors is sent to the arduino uno module. These measurements can be monitored instantly as analogue and digital. Whether the data obtained through the sensors are within the specified threshold values is communicated to the user visually through the LCD screen and audibly through the buzzer.

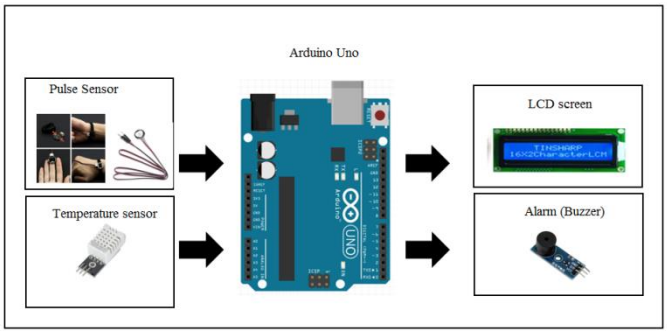

Figure 2: General diagram of Arduino based biosensor system

Arduino Uno control card, heart rate measurement sensor (pulse sensor) and DHT22 temperature and humidity sensor are used in the electronic design of the system. Only the temperature feature of the DHT22 temperature and humidity sensor in the system was used. The electronic design of the biosensor system is shown in Figure 3.

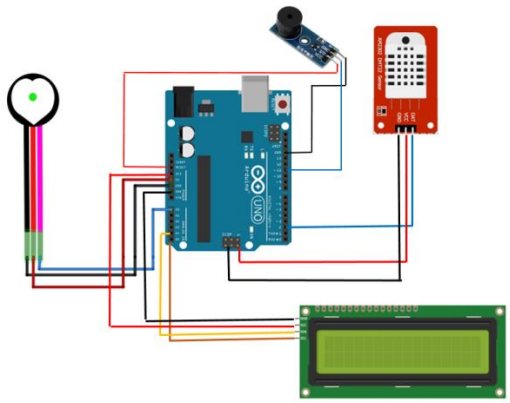

Figure 3: Electronic design of the biosensor system

Two important sensor modules are used in the Arduino based biosensor system. Heart rate beat (pulse) sensor works according to the principle of reflection of the level of oxygen in the blood from the IR (infrared) signal depending on the heartbeat. The purpose here is to determine the heart rhythm for each beat and to calculate the time between two rhythms in milliseconds. With the heart rate sensor (Pulse sensor) working analogically, the heartbeat is determined as BPM (Heart Beat/Pulse Rate) per minute. The other sensor module of the system is the heat sensor (DHT22). The digitally operating temperature sensor performs very accurate measurement. Body temperature is determined in °C. Both data are then successfully transmitted to the user via the LCD screen. The display of the biosensor system's heart rate and body temperature value to the user is shown in Figure 4.

The heart rate graph obtained with the pulse sensor is shown in Figure 4.

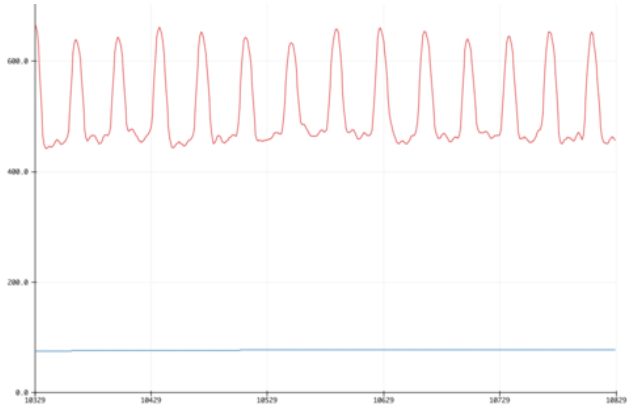

Figure 4: Heart rate sensor graphic

The heart rate and temperature values determined lastly with the biosensor software are sent to the LCD screen to be visually transmitted to the user. In this way, whether the heart rate and temperature values obtained through the sensors are within the specified threshold values are communicated to the user visually through the LCD screen and audibly with the buzzer. If there is any abnormal value, the user is warned (Figure 5).

Figure 5: The display of body temperature and heart rate with biosensor system

The PC application first reads 600 consecutive samples sent by the Arduino Uno board. The sampling rate is 5 ms. Therefore, it takes 3 seconds to read 6000 samples. After the DC component (minimum 600 samples) is subtracted from the samples, the range of samples is calculated. If the range is below 50, the received waveform is rather weak. This can happen when no signal is received with the fingertip. Since two consecutive samples are 5 ms apart, the time difference

between any two peaks can be easily calculated from their indices. Two heart rates are calculated from three consecutive wave peaks, and their average value is displayed as the instantaneous heart rate.

When the temperature value exceeds 27°C, and when the pulse sensor cannot detect a heartbeat the buzzer gives an alarm. In the project we designed, the Pulse sensor sends analogue data to the system, while the DHT22 sensor sends digital data. Thanks to the USB port on the Arduino Uno microcontroller, the system can be connected to the computer and the data can be transferred to the computer environment. Thus, data on daily temperature and heartbeat rhythm can be easily accessed at any time. This is extremely important in terms of instant monitoring of the health status of the person.

IV. CONLUSIONS

Biomedical engineering is an engineering field that combines the design and problem-solving skills of engineering with biological sciences and medicine in order to improve the health care and quality of life of patients. Therefore, its importance is increasing day by day. The monitoring of body temperature and heart rate, which are among the important indicators in the diagnosis of diseases and in the follow-up of patients, is of vital importance in this context. Thanks to this system we have designed, heart rate and body temperature can be measured with fingertips.

In this study, a multi-sensor and low-cost biosensor system has been developed using the Arduino microcontroller board. With the established system, the heart rate and body temperature of people were measured digitally. In this way, it is possible to regularly monitor the vital body values of people with health problems and to detect any sudden changes that may occur in values.

In this project we have designed, heart rate is measured by pulse sensor and body temperature is measured by temperature sensor. The measured values are displayed on the LCD screen via the Arduino Uno control card. If the heart rate and body temperature value are abnormally high, the alarm (buzzer) is activated and gives a warning.

The arduino-based biosensor system, which has been developed, can monitor the heart rate and body temperature information, which is vital for humans, remotely and instantaneously. As a result of the applications and tests, it has been observed that the system works quickly and successfully.

In addition, the developed system includes an infrastructure ready for future additions and improvements. For example, it has been determined that the data obtained with the help of the sensors on the system can be transferred to the computer environment via wifi or bluetooth or can be monitored on the internet environment. It is thought that more sensors or sensors with different features can be added to the biosensor tracking system in accordance with the intended use.

As a result, it is evaluated that the developed biosensor system will contribute to the field of medicine and health with its features, it can be used in the follow-up of people working for military purposes or in dangerous work environments by mounting on wearable clothes.

REFERENCES

[1] W.M. Kadir, R.E. Samin, & B.S. Ibrahim “Internet controlled robotic arm.”, *Proc Eng*, 2012;41, 1065–1071.

[2] W.A. Mohammad, and K.D. Choton. wireless heartbeat and Temperature Monitoring System for Remote Patients. *(Proceedings of the International Conference on Mechanical Engineering and Renewable Energy 2013)*

[3] D. Özdemir, & C.Köse. “Gezgin robotların çiftliklerde ürün yeri belirleme ve taşıma işlemlerinde kullanımı”, *EÜFBED - Fen Bilimleri Enstitüsü Dergisi*, 2008;1(1), 49-60.

[4] S.T. Salomi, S. Amar, S. Anurag and B. Visal. *Sensing Heart Beat and Body Temperature Digitally Using Arduino* (International conference on Signal Processing, Communication, Power and Embedded System (SCOPES 2016)). 1721-1724

[5] C. Neramitr, T.Thadsanee and C. Yuwathida. Heart rate measurement and electrical pulse sign analysis for subjects span of 20-80 years. *Journal of Electrical Systems and Information Technology.*2018;112-120

[6] J.Sarik, & I.Kymissis. “Lab kits using the Arduino prototyping platform”, in IEEE Frontiers in Education Conference, Washington, 1-5, October 27 – 30, 2010

Applying PART, JRIP and OneR Algorithms on Diabetes, Breast Cancer and Iris Dataset for Comparative Analysis

Çağrı Dükünlü[1] and Mehmet Uğraş Cuma[2]

Koluman Otomotiv Endüstri A.Ş. R&D Center Mersin/Turkey

[1] Cukurova University, Adana/Turkey, cagridknl@gmail.com
[2]Cukurova University, Adana/Turkey, mcuma@cu.edu.tr

Abstract – Classification is the operation of predicting class of the given data by preparing a model that makes use of data whose categories already predicted. Data mining techniques are regularly used to form a classifier that predicts belonging class of a new data among the previous given classes. This paper intends to provide comparative analysis of the rule based classifiers used in data mining applications. Analyzing the performance of rule based classifiers namely PART, JRIP, OneR.

The goal of this paper is to specify the best technique from classification rules techniques under the chosen datasets and also provide a comparison result each classifier. The rule based classifiers applied to diabetes, breast cancer and iris datasets due to the purpose of determining better technique for classification. Comparison results are made with accuracy, precision, sensitivity and confusion matrixes.

Keywords **-** Data Mining, Rule Based Algorithms, PART, JRIP, OneR.

I. INTRODUCTION

Data mining is mostly known as KDD or "Knowledge Discovery in databases" and is used to turn raw data into useful information by companies [1]. The data of the world is getting bigger every day and it is getting difficult to handle the complexity of data every minute. With new collected data and different types of classification methods, mankind is getting advantage of important areas like health care, technology.

Thousands of data sets are processed every day in these fields [2]. To get healthy and organized data or to train a model, it becomes serious and Data Mining comes into play in this step. With the help of data mining techniques, the collected data can be used and organized to generate the knowledge about the data. Data mining also has tools to find out unknown patterns and validate the patterns with relationships from big data.

Some of the well-known tools of Data Mining are "Knime, Weka, Orange, R, Matlab". Every day the capacity of the tools are increased and the datasets are growing with time. With more and more data and improved models, humanity and research will be able to solve bigger and bigger problems with time and take advantage of technology with Data Mining. Due to the efficiency and models variety; Weka tool is used for model training. Weka is an open source software and implementing it to data is easy [3]. These two factors show its maintainable and easy of use to any company who wants to train their models.

Three different classification techniques are chosen for the processing the different datasets to determine in which rule based algorithm has least loss and higher accuracy. From classification techniques JRIP(RIPPER), OneR (OneRule) and PART (Projective Adaptive Resonance Theory) are selected based on literature researches.

Researchers of the study [4] has found various crime patterns. Study has obtained JRip, OneR, Decision Table methods accuracy are compared for crime patterns. JRip was most accurate classifier of all, even though it takes the maximum time to build the model which it is 21.2 sec.

In [5], the study has taken two different algorithms to compare accuracy in datasets. JRip and Hoeffding trees accuracies were similar to each other's but as for the outcomes, JRip model not only gives a prediction, but also provides insight of the problem.

In [6], researchers are studied role of PB2 in influencing influenza A virus virulence in mice. OneR, JRip and PART methods used. Accuracies ranged from 65.0% to 84.4%. PART models were better than random forest models and moreover PART models were better than other rule based learning approaches for estimating contribution to virulence.

[7] is considering performance comparison of rule based classifier: JRip and Decision Table using WEKA (Waikato Environment for Knowledge Analysis) data mining tool on car reviews. As a conclusion JRip is excellent, efficient and accurate model rather than Decision Table for test mode training set.

II. CLASSIFICATION TECHNIQUES

Classification techniques are important in knowledge mining. Characterization is an information mining strategy that assigns things in a collection to a particular class. Classification models predict categorical class labels; and prediction models predict continuous valued functions [8]. The reason for classification is to accurately capture the target class for each case in the information.

Three classification procedures are taken as benchmarking calculations that are read for the taken wellbeing data set of Hypothyroid. The calculations of the three mentioned procedures are described below, these are the algorithms PART, JRIP, ONER algorithms.

2.1 PART: PART (Rule-based-Classification algorithm) is a different and overcome rule. The computation creates sets of rules, called "decision lists", which are ordered arrays of rules. Another information is contrasted with each standard in the rundown thusly, and the thing is appointed the class of the main coordinator with a rule [9,10].

2.2 JRIP: JRip (Rule-based-Classification algorithm) is one of the basic and most popular algorithms. Classes are examined in growing

size, and using incrementally reduced error initial set of rules for the class is generated. JRip proceeds finds a set of rules that cover all members of a class with treating all examples of a particular decision in the training data as that class. After it proceeds to the next class and does the same, repeating this until all classes have been covered [11,12].

2.3. ONER: OneR (Rule-based-Classification algorithm), another way of saying "One Rule", is a basic computation that creates a one-level choice tree. OneR can regularly derive simple but accurate ordering rules from a bundle of events. OneR is likewise able to deal with missing qualities and numerical features, showing adaptability despite straightforwardness. The OneR computation creates a guideline for each quality in the preparation information and then at that point chooses the standard with the base mistake rate as its [13,14].

III. DATABASE STRUCTURES

The JRIP, OneR and PART classification algorithms are applied on the databases given below following structures.

Databases:	breast_cancer	
Instances:	286	
Attributes:	10	
Sum of Weights	286	
Sr.No	Attributes	Type
1	age	Nominal
2	menopause	Nominal
3	tumor-size	Nominal
4	inv-nodes	Nominal
5	node-caps	Nominal
6	deg-malig	Nominal
7	breast	Nominal
8	breast-quad	Nominal
9	irradiat	Nominal
10	Class	Nominal
Test mode	3-fold cross-validation	

Table 1: Breast cancer dataset.

Databases:	diabetes	
Instances:	768	
Attributes:	9	
Sum of Weights	768	
Sr.No	Attributes	Type
1	preg	Nominal
2	plas	Nominal
3	pres	Nominal
4	skin	Nominal
5	insu	Nominal
6	mass	Nominal
7	pedi	Nominal
8	age	Nominal
9	class	Nominal
Test mode	3-fold cross-validation	

Table 2: Diabetes cancer dataset.

Databases:	iris	
Instances:	150	
Attributes:	5	
Sum of Weights	150	
Sr.No	Attributes	Type
1	sepal_length	Nominal
2	sepal_width	Nominal
3	petal_length	Nominal
4	petal_width	Nominal
5	class	Nominal
Test mode	3-fold cross-validation	

Table 3: Iris dataset.

IV. PARAMETERS FOR MEASURING PERFORMANCE OF CLASSIFICATION TECHNIQUES

$$Accuracy = \frac{True\ Positive + True\ Negative}{Total}$$

$$Precision = \frac{True\ Positive}{True\ Positive + False\ Positive}$$

$$Recall = \frac{True\ Positive}{True\ Positive + False\ Negative}$$

$$F1\ Score = 2 * \frac{Precision * Recall}{Precision + Recall}$$

V. RESULTS

Testing results are evaluated from the iris dataset, diabetes dataset and breast cancer dataset. Data mining tool Weka Explorer is used for testing and taking results.

Various rule-based algorithms used with three different sample datasets to determine the best classifier rule. Comparing the various algorithm techniques can be made to find out the better mining classification algorithm.

	breast cancer	**diabetes**	**iris**
Accuracy	66.4	72.5	94.6
Precision	0,653	0,730	0,948
Recall	0,664	0,725	0,947
F-Measure	0,658	0,727	0,947
ROC Area	0,599	0,781	0,953

Table 4: PART Rule

	breast cancer	diabetes	iris
Accuracy	67.1	70.9	94.0
Precision	0,645	0,697	0,940
Recall	0,671	0,710	0,940
F-Measure	0,654	0,695	0,940
ROC Area	0,566	0,646	0,955

Table 5: OneR Rule

	breast cancer	diabetes	iris
Accuracy	70.9	74.8	95.3
Precision	0,688	0,741	0,954
Recall	0,710	0,749	0,953
F-Measure	0,693	0,740	0,953
ROC Area	0,598	0,717	0,966

Table 6: JRIP Rule

	breast cancer	diabetes	iris
JRIP	70,9	74,8	95,3
OneR	67,1	70,9	94
PART	66,4	72,5	94,6

Table 7: Rule Algorithm Comparison

Visualization graph of distributions and algorithm accuracy, precision, recall, f-measure, roc area given with tables and in Fig1 and Fig 2. It gives insight about algorithm prediction is well or not. The below graphs shows the superiority of algorithms to each other.

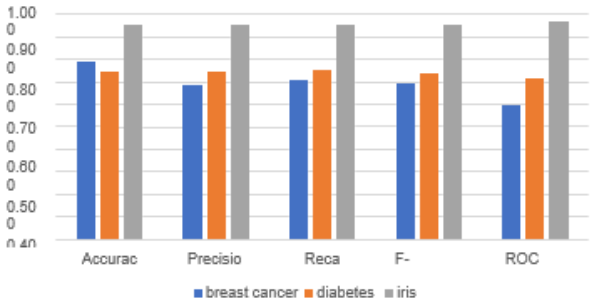

Fig 1: Dataset Result Comparison

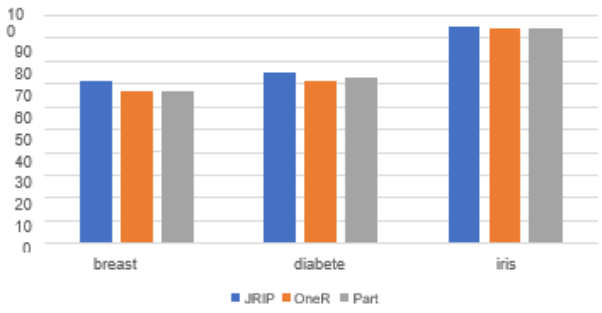

Fig 2: Algorithm Accuracy Comparison

VI. Conclusion

As a result of taken datasets from iris, diabetes and breast cancer, the parameters values for classification techniques JRIP, OneR, PART rule can be compared. The resultants table reveals that the best results for the specified rules are seem to be JRIP. In this rule based classifier training cross validation (n=3) is used. The results in the table also show accuracy, precision, recall, f-measure, roc-area value are also seeming to be better at JRip algorithm rather than the others.

For an another vision, excluding JRIP algorithm; for low instanced datasets PART algorithm accuracy is more preferable over OneR algorithm. We may conclude sensitivity is a key for deciding the better algorithm due to having more data in dataset is more accurate for determining the true algorithm. Thus OneR algorithm can be more useful with more instanced datasets.

VII. References

[1] A. Twın ,"Data Mining, How Data Mining Works", Investopedia, September 17 2021.
[2] V.Parsania, N.Bhalodiya and N Jani Applying naïve bayes , bayesnet , part , hrip , andoner algoritms on hypothyroid database for comparative analysis.(2014)
[3] Mark Hall, Eibe Frank, Geoffrey Holmes, Bernhard Pfahringer, Peter Reutemann,and Ian H. Witten (2009). The WEKA Data Mining Software: An Update. SIGKDD Explorations Volume 11, Issue 1.
[4] A Comparative Study of Classification Algorithm using Data Mining: Crime and Accidents in Denver City the USA. Authors: Amit Gupta,Ali Syed, Azeem Mohammad, Malka N.Halgamuge. IJACSA) Vol. 7, No. 7,(2016)
[5] AlMuhaideb S, Alswailem O, Alsubaie N, Ferwna I, Alnajem A. Prediction of hospital no-show appointments through artificial intelligence algorithms. Ann Saudi Med 2019; 39(6): 373-381 DOI: 10.5144/0256-4947.2019.373
[6] Ivan, F.X., Kwoh, C.K. Rule-based meta-analysis reveals the major role of PB2 in influencing influenza A virus virulence in mice. *BMC Genomics* 20, 973 (2019). https://doi.org/10.1186/s12864-019-6295-8
[7] Dr. S. R. Kalmegh and Mr. S. A. Ghogare, "PERFORMANCE COMPARISON OF RULE BASED CLASSIFIER: JRIP AND DECISIONTABLE USING WEKA DATA MINING TOOL ON CAR REVIEWS", *IEJRD - International Multidisciplinary Journal*, vol. 4, no. 5, p. 5, May 2019.
[8] Tutorials Point , Data Mining: Classification & Prediction. Retrieved from https://www.tutorialspoint.com/data_mining/dm_classification_prediction.htm
[9] Aubaid, Asmaa M., and Alok Mishra. 2020 "A Rule-Based Approach to Embedding Techniques for Text Document Classification" Applied Sciences 10, no. 11: 4009.(2020) https://doi.org/10.3390/app10114009
[10] "PART Algorithm" Retrieved from : https://weka.sourceforge.io/doc.dev/weka/classifiers/rules/PART.html, (2013)
[11] Anil RAJPUT, Ramesh Prasad Aharwal, Meghna Dubey,S.P. Saxena(2011) "J48 and JRIP Rules for E-Governance Data" IJCSS-448
[12] "JRIP Algorithm" Retrieved from: https://weka.sourceforge.io/doc.dev/weka/classifiers/rules/JRip.html, (2013)
[13] Gaya Buddhinath and Damien Derry,"A Simple Enhancement to One Rule Classification" Department of Computer Science & Software Engineering University of Melbourne,Australia,(2006)
[14] "OneR Algorithm" Retrieved from http://www.saedsayad.com/zeror.htm, (2013)
[15] Breast Cancer Wisconsin(Diagnostic) Data Set,UCI Machine Learning Repository,Creator:Dr. William H.Wolberg,University of Wisconsin Hospitals,Madison,Wisconsin,USA (1994)
[16] Diabetes Data Set,UCI Machine Learning Repository,Source:Micheal Kahn,MD,PhD,Washington University,St.Louis,MO,AIM(1994)
[17] Iris Data Set,UCI Machine Learning Repository,Creator:R.A. Fisher (1936)
[18] A probabilistic Interpretation of Precision,Recall and F-Score,with Implication for Evaluation. Authors:Cyril Goutte,Eric Gaussier

(LNCS,volüme 3408).ECIR 2005:Advances in Information Retrieval pp 345-359

[19] Towards Data Science (2018) Accuracy , Precision , Recall ,F1. Retrieved from https://towardsdatascience.com/accuracy-precision-recall-or-f1-331fb37c5cb9

Artificial Intelligence Based Concrete Compressive Strength Detection

Tahir KARAÇETE[1], Muhammed Kürşad UÇAR[2]
[1]Gaziantep University, Faculty of Engineering, Civil Engineering, Gaziantep, Turkey
tahirkaracete@gmail.com, https://orcid.org/0000-0002-8760-1073
[2]Sakarya University, Faculty of Engineering, Electrical and Electronics Engineering, Sakarya, Turkey
mucar@sakarya.edu.tr, https://orcid.org/0000-0002-0636-8645

***Abstract*—Concrete, in which additives can be added according to the desired properties, is a composite construction material obtained by combining the aggregate with water and cement. Concrete, which can be used to construct many structures such as dams, buildings, roads, bridges, tunnels is one of the most used construction materials due to its high compressive strength, easy workability, durable structure, and being more economical than other construction materials. In order to determine the compressive strength of concrete, samples are taken from fresh concrete and waited until the concrete hardens. When the concrete reaches a certain age, its strength is determined with the help of a hydraulic press. This process is called the concrete compressive strength test. This test creates a cost due to the use of materials and takes a certain amount of time depending on the age of the concrete. For this reason, new high technologies are needed to replace concrete compressive strength tests. This study aims to develop an artificial intelligence-based system that can be used instead of a concrete compressive strength test without performing a compressive strength test. The results of 1030 different concrete compressive strength tests were used in the study. Data were obtained from the UCI Machine Learning Repository (archive.ics.uci.edu). In the data set, there are eight properties based on the number of materials used in the production of concrete and the age of concrete. Decision tree methods were preferred as machine learning algorithms in the study because they have many advantages, such as high performance and easy implementation in embedded systems. When the performance of the Model 1 and Model 2 is examined, the Root Mean Square Deviation (RMSE) value varies between 6.78-9.74. In addition to this success, the system's response to each new data occurs within seconds. It is considered that the proposed system can be used to help engineers determine the compressive strength of concrete in concrete plants due to its high accuracy and fast operation.**

***Keywords*—Concrete, Concrete Compressive Strength, Artificial Intelligence, Regression**

I. INTRODUCTION

Concrete, in which additives can be added according to the desired properties, is a composite construction material obtained by combining the aggregate with water and cement. This material, which can be used in constructing many structures such as dams, buildings, roads, bridges, tunnels, is one of the most used construction materials today due to its high compressive strength, easy workability, durable structure and being more economical than other construction materials [1].

Concrete compressive strength can be named as the highest pressure that concrete can withstand under axial load [2]. In order to determine the compressive strength of the concrete, samples are taken from the fresh concrete and waited until the concrete hardened. When the concrete reaches a certain age, its compressive strength is determined with the help of a hydraulic press. This process is called the concrete compressive strength test. Concrete compressive strength test creates a cost due to the use of materials and takes a certain amount of time depending on the age of the concrete.

There are various studies in the literature to determine the compressive strength of concrete. In these studies, concrete compressive strength estimation is made using image processing techniques, ultrasonic sound wave propagation velocity, and fuzzy logic [3], [4], [5]. The general deficiency of the studies is that they are not in a structure that can be applied easily and quickly by the engineer in the field.

This study aims to develop an artificial intelligence-based system that can be used instead of performing a concrete compressive strength test. The dataset containing the concrete compressive strength test results was obtained from the UCI Machine Learning Repository (archive.ics.uci.edu). Initially, there were eight parameters, including the amount of 7 materials used in concrete production and the concrete age but these parameters were reduced with the feature selection algorithm.

In this study, an artificial intelligence-based system has been developed that makes concrete compressive strength estimation different from the studies in the literature. The benefits of the system are: (1) It predicts the compressive strength of concrete. (2) With the feature selection algorithm, the materials with a high effect on the concrete compressive strength were determined. (3) It can predict the compressive strength of concrete that has not yet been produced. (4) It predicts concrete compressive strength with high accuracy.

II. MATERIAL AND METHOD

This study was carried out according to the flow diagram steps in Figure 1. While initially eight property data were used, the properties that are effective in concrete compressive strength were selected from eight properties with the help of the property selection algorithm. Rule-based models were created with the help of decision trees to estimate concrete compressive strength over these selected features.

A. Data Collection

The data set used in the study was obtained from the UCI Machine Learning Repository (archive.ics.uci.edu) [6]. The

Figure 1: Flow Diagram

dataset contains the results of 1030 different concrete compressive strength tests. In addition, there are eight properties based on the number of materials used in the production of concrete and the age of concrete. The data distribution of the features found in the data set is shown in Table I.

Table I: Data Distribution

No	Feature Name	Mean	Std	Min	Max
1	Cement	281.20	104.51	102.00	540.00
2	Blast Furnace Slag	73.90	86.28	0.00	359.40
3	Fly Ash	54.20	64.00	0.00	200.10
4	Water	181.60	21.36	121.80	247.00
5	Superplasticizer	6.20	5.97	0.00	32.20
6	Coarse Aggregate	972.90	77.75	801.00	1145.00
7	Fine Aggregate	773.60	80.18	594.00	992.60
8	Age	46.00	63.17	1.00	365.00

Std Standard Deviation, Min Minimum, Max Maximum

B. Feature Selection

Feature selection is the process of selecting the subset in the dataset that best describes the dataset. Spearman Correlation coefficient, a feature selection algorithm, was used to select the most important and effective ones for concrete compressive strength in the data set (Table II) [7], [8].

Table II: Distribution of Selected Features

No	Feature Name	Correlation Number (R)
8	Age	0.60
1	Cement	0.48
5	Superplasticizer	0.35
4	Water	0.31
6	Coarse Aggregate	0.18
7	Fine Aggregate	0.18
2	Blast Furnace Slag	0.16
3	Fly Ash	0.08

C. Decision Trees

Decision tree methods have been preferred as machine learning algorithms because they have many advantages such as easy implementation in embedded systems, having high performance [9]. The use of decision trees in this study is to extract algorithms that can be integrated into embedded systems. In this way, artificial intelligence-based embedded system design will be created.

D. Performance Evaluation Criteria

In order to evaluate the performance of the developed models, seven different criteria were used. These criteria are Average Absolute Percent Error (MAPE), Root Mean Square Deviation (RMSE), Mean Absolute Deviation (MAD), Standard Error (SH), Correlation Number (R), Explanatory Coefficient (R2), Mean Square of Error (MSE). It is expected that the SH, MAD, RMSE, MSE and MAPE criteria will be close to 0 and the R and R2 criteria will be close to 1 [10]. Since it is used as a performance evaluation criterion in MSE regression models, it was preferred as a performance evaluation criterion in this study.

The data set obtained from the literature is divided into training and testing. 80% of the data set was used to train the model and 20% to test the created model (Table III). These data were then analyzed with decision trees.

Table III: Machine Learning Training Testing Process Distribution

Data Set	Training (%80)	Test (%20)	Total
Concrete Compressive Strength	824	206	1030

III. RESULTS

This study aims to develop an artificial intelligence-based system that can predict concrete compressive strength in a short time without cost.

The data set named Concrete Compressive Strength was used in the study, which was obtained from the UCI Machine Learning website. Using the Spearman Correlation algorithm, the effects of the concrete materials and age in the data set on the concrete compressive strength were determined (Table II). Model 1 and Model 2, which are decision tree models, were created by selecting the features that have the greatest effect on concrete compressive strength (Figure 2, 3).

Performance evaluation of Model 1 was made on seven criteria (Table IV). The models with the highest correlation value (R) according to the performance evaluation table were examined and the least number of features was selected to make the decision tree model more simple and readable, and the performance values of the model created with those features were written in bold letters. The mean absolute percent error (MAPE) of Model 1, which was created using four features, was determined as 17.93%, standard error value (SH) was 6.81, and correlation (R) value was 0.92. Model 1, which has an very good correlation value, has a complex structure and is difficult to read as its depth increases.(Figure 2)

Model 2, which is more straightforward and more readable than Model 1, was created based on seven selected features (Figure 3). The performance evaluation results of Model 2, which is evaluated over seven criteria, are in Table V.When the models with the best correlation value (R) according to the performance evaluation table were examined, it was observed that the most successful model was the model created with 7 features. The correlation (R) value was 0.80, the standard error (SH) value was 9.79, absolute percent error value (MAPE) was determined as 29.37%.

IV. DISCUSSION AND CONCLUSION

Concrete is one of the most used construction materials today with its advantages [1]. Determining the compressive

Table IV: Model 1 Performance Values

NoF	FP	MAPE	RMSE	MAD	SH	R	R2	MSE
1	12.5	39.41	12.40	9.63	12.46	0.66	0.44	153.68
2	25	24.48	9.41	7.10	9.45	0.85	0.72	88.48
3	37.5	20.01	7.85	5.85	7.89	0.88	0.78	61.63
4	**50**	**17.93**	**6.78**	**5.09**	**6.81**	**0.92**	**0.85**	**45.98**
5	62.5	17.74	7.08	5.05	7.12	0.91	0.83	50.14
6	75	16.60	6.71	4.58	6.74	0.92	0.85	44.99
7	87.5	17.18	6.98	5.08	7.01	0.92	0.85	48.65
8	100	16.16	6.94	4.68	6.97	0.92	0.84	48.10

NoF Number of Features, FP Feature Percentage

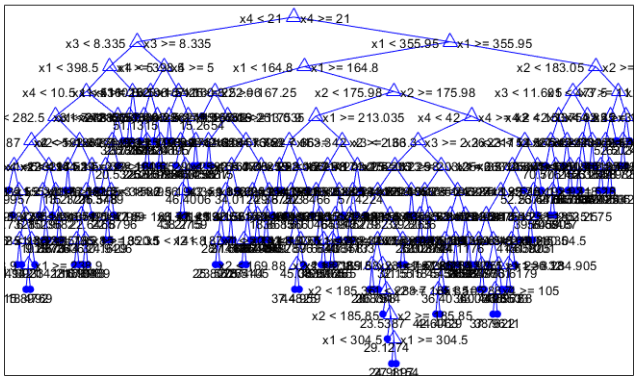

Figure 2: Model 1 Rules

Table V: Model 2 Performance Values

NoF	FP	MAPE	RMSE	MAD	SH	R	R2	MSE
1	12.5	39.62	12.46	9.71	12.52	0.66	0.44	155.34
2	25	28.56	10.56	8.12	10.61	0.80	0.64	111.46
3	37.5	31.05	10.07	7.93	10.12	0.78	0.60	101.44
4	50	30.93	10.26	8.01	10.31	0.78	0.61	105.18
5	62.5	30.93	10.26	8.01	10.31	0.78	0.61	105.18
6	75	30.93	10.26	8.01	10.31	0.78	0.61	105.18
7	**87.5**	**29.37**	**9.74**	**7.69**	**9.79**	**0.80**	**0.64**	**94.88**
8	100	29.37	9.74	7.69	9.79	0.80	0.64	94.88

NoF Number of Features, FP Feature Percentage

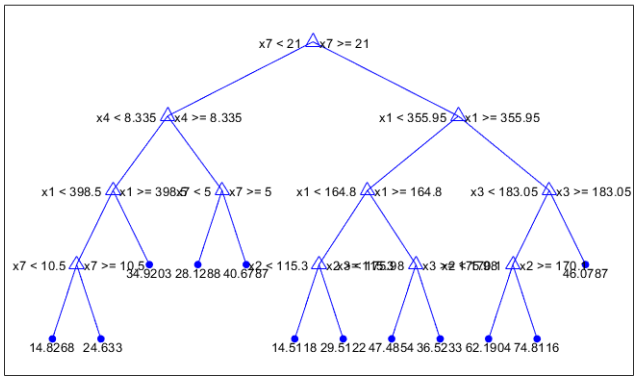

Figure 3: Model 2 Rules

strength, which is one of its advantages, takes both times and creates costs. For this reason, there is a need for systems that can reduce the cost and predict concrete compressive strength in a shorter time. When the literature is examined, it has been observed that there are studies that can predict concrete compressive strength with methods such as image processing techniques, ultrasonic sound wave velocity, and fuzzy logic [3], [4], [5]. When the studies were examined, it was seen that the success rates were high but it was not easy in practice. In studies in the literature, the Posso device is used for an ultrasonic sound wave [4], radiation source and armor are used in image processing techniques [3]. In this study, estimates are made on the amount and age of materials used in concrete production. Therefore, it is easier to implement by the engineer in the field.

This study aims to develop a system that can predict the compressive strength of concrete before and after production based on the amount of material used and the age of concrete. For this purpose, the effects of materials and age on concrete compressive strength were determined using Spearman Correlation Coefficient. This study examined the effects of eight properties on concrete compressive strength; concrete age, cement amount, superplasticizer and water amount were found to be the most effective properties on concrete compressive strength. It has been observed that the amount of fly ash is not very adequate on the concrete compressive strength. Decision tree models were created with the most influential parameters in concrete compressive strength. When both models are examined, Model 2 has less depth and better readability than Model 1. According to the performance evaluation results, Model 1 was more successful than Model 2.

The study showed that the compressive strength of concrete could be estimated with certain margins of error by using parameters such as the amount of cement contained in the concrete, the amount of blast furnace slag, the amount of fly ash, the amount of superplasticizer, the amount of fine aggregate, the amount of coarse aggregate, the amount of water and the age.

REFERENCES

[1] B. E. Demiryürek and B. Evren, "Türkiye'de hazır beton sektörü ve sektördeki büyüme," 2007, Accessed: Sep. 16, 2021. [Online]. Available: https://polen.itu.edu.tr/handle/11527/7244.

[2] Ö. SEVİM, "Concrete Quality In Existing Reinforced Concrete Structures In The First Seismic Zone In Turkey," Uluslararası Mühendislik Araştırma ve Geliştirme Derg., vol. 6, no. 2, pp. 21–26, Jun. 2014, doi: 10.29137/UMAGD.346075.

[3] C. BAŞYİĞİT, Ş. KILINÇARSLAN, and B. ÇOMAK, "Görüntü İşleme Tekniği ile Beton Basınç Dayanımının Tahmin Edilmesi," Süleyman Demirel Univ. J. Nat. Appl. Sci., vol. 16, no. 1, Jul. 2014.

[4] Z. Zebari, İ. Bedirhanoğlu, and E. Aydin, "Dicle Üniversitesi Mühendislik Fakültesi mühendislik dergisi Öz Beton basınç dayanımının ultrasonik ses dalgası yayılma hızı ile tahmin edilmesi."

[5] B. Basınç Dayanımının Bulanık Mantık Yöntemiyle Tahmin Edilmesi et al., "Estimation Of Compressive Strength Of Concrete Using Fuzzy Logic Method," Electron. J. Constr. Technol., vol. 6, no. 2, pp. 1–8, 2010, Accessed: Oct. 04, 2021. [Online]. Available: www.teknolojikarastirmalar.com.

[6] I-Cheng Yeh and Hsin Chu, "UCI Machine Learning Repository: Concrete Compressive Strength Data Set." http://archive.ics.uci.edu/ml/datasets/Concrete+Compressive+Strength (accessed Oct. 01, 2021).

[7] H. BUDAK, "Özellik Seçim Yöntemleri ve Yeni Bir Yaklaşım," Süleyman Demirel Univ. J. Nat. Appl. Sci., vol. 22, pp. 21–31, Oct. 2018, doi: 10.19113/sdufbed.01653.

[8] R. Alpar, Applied Statistic and Validation - Reliability. Detay Publishing, 2010.

[9] A. T. Azar and S. M. El-Metwally, "Decision tree classifiers for automated medical diagnosis," Neural Comput. Appl., vol. 23, no. 7–8, pp. 2387–2403, Dec. 2013, doi: 10.1007/s00521-012-1196-7.

[10] M. Akman, M. K. Uçar, Z. Uçar, K. Uçar, B. Baraklı, and M. R. Bozkurt, "Determination of Body Fat Percentage by Gender Based with Photoplethysmography Signal Using Machine Learning Algorithm," IRBM, Jan. 2021, doi: 10.1016/j.irbm.2020.12.003.

Harmonic Analysis of Input Current of 6-pulse and 12-pulse Rectifiers

A.DÖNÜK

Aydın Adnan Menderes University, Aydın/Turkey, adonuk@adu.edu.tr

Abstract **- In parallel with the advancing technology, power electronics circuits have been widely used in daily life, municipal services and industrial applications. Rectifiers are one of the most used structures of such circuits to satisfy ac-to-dc conversion. Due to the natural characteristics of switching semiconductor devices used in rectifiers, the ac supply current absorbed from the grid contains higher order harmonics. These harmonics may cause serious failures and damages in the power system equipment so there has been a great deal of attention at harmonic control in electric power systems. Therefore it is required to estimate the harmonic content produced by these rectifiers. This work presents the magnitudes and phase angles of harmonic components in the input current of 6 pulse uncontrolled, half-controlled and, of 6 and 12-pulse fully-controlled rectifiers with R and RL load at several firing angles via computer simulations. Harmonic levels of the rectifiers are discussed.**

Keywords **– Harmonics, rectifier, total harmonic distortion.**

I. INTRODUCTION

THREE phase rectifiers are one of the most used power electronics circuits in many applications in power systems. Semiconductor devices such as diodes and thyristors are used as switching elements in the rectifiers, as a result, these circuits draw non-sinusoidal ac currents with a high harmonic content. Harmonics in the line current cause power quality problems. In order to keep power supply quality at acceptable levels, harmonic limits are specified by the standards and the use of power factor correctors (PFC) is encouraged [1]. Harmonics may also cause serious failures and damages in the power system equipment. Harmonic heating became an important problem for transformers [2]. Both magnitude and phase angle of the harmonic content has a considerable effect on the transformer saturation [3]. Moreover, magnetic field intensities of harmonics may have an adverse health effect on people [4]. Therefore, it is required to precisely estimate the harmonic content produced by these rectifiers.

A control algorithm of the three-level rectifier in the three-phase voltage source converter, as well as a theoretical method for harmonic analysis of the input current rectifier has been presented in [5]. An approach to harmonic modeling of a power system and a case study was presented for harmonic reduction. Alternative plant power factor correction strategies were also presented with their pros and cons [6]. Input current harmonic analysis of single-phase fully controlled bridge rectifier was performed by mathematical derivation, computer simulation and practical application and total harmonic distortion (THD) is determined [7]. A fast time domain method was presented to analyze current and voltage harmonics of a single-phase uncontrolled bridge rectifier [8]. The current and voltage harmonic components in electrical networks with rectifying converter load in the distribution network of an oil producing enterprise and at the input supply of a railway traction were introduced and it is reported that THD can exceed the permitted value [9]. Simulation of 6, 12 and 18 pulse controlled converters for harmonic reduction was performed [10]. The studies in the literature mostly present the harmonic analysis of one type of topology, either single-phase or three-phase bridge configuration. Almost all studies consider the magnitude of the harmonic components, however they neglect the phase shift. In this work, magnitudes and phase angles of harmonic components in the input current of 6 pulse uncontrolled, half-controlled and, of 6 and 12-pulse fully-controlled rectifiers at several firing angles are obtained via computer simulations and harmonic levels of the rectifiers under consideration are discussed.

II. DEFINITION AND CALCULATION OF HARMONICS

Any periodic waveform may be shown to be composed of the superposition of a direct component with a fundamental pure sinewave component, together with pure sinewaves known as harmonics at frequencies which are integral multiples of the fundamental. A non-sinusoidal wave is often referred to as a complex wave and can be expressed mathematically as in (1) [11].

$$v = V_0 + V_1 \sin(\omega t + \emptyset_1) + V_2 \sin(2\omega t + \emptyset_2) + V_3 \sin(3\omega t + \emptyset_3) + \cdots + V_n \sin(n\omega t + \emptyset_n) \quad (1)$$

Where; v is the instantaneous value at any time t, Vo is the direct (or mean) value, V_1, V_2, and V_3 are the maximum value of the fundamental, second and third harmonic component, respectively. V_n is the maximum value of the nth harmonic component, Ø defines the relative angular reference, $\omega = 2\pi f$ is the angular frequency, where f is the frequency of the fundamental component.

In the input current of a p-pulse rectifier, harmonics exist in the order as given in (2) and their magnitude is 1/h times the fundamental component [11].

$$h = mp \pm 1 \quad (\mathrm{m} = 1,2,3,\mathrm{etc.}) \quad (2)$$

The amount of distortion in the input current waveform is called Total Harmonic Distortion (THD) and defined by (3) [12].

$$\%\,THD_i = 100 \times \frac{\sqrt{I_S^2 - I_{S1}^2}}{I_{S1}} \quad (3)$$

Where; I_s and I_{s1} are the rms values of the input (line) current and the fundamental component, respectively.

For a p-pulse fully-controlled rectifier general expression to calculate the mean load voltage is given in (4) [11].

$$V_{mean} = \frac{p\,V_{max}}{\pi}\ sin\ \frac{\pi}{p} \cos\alpha \quad (4)$$

For a 6-pulse half-controlled rectifier the mean load voltage can be calculated by (5) [11].

$$V_{mean} = \frac{3}{2\pi}\ V_{line(max)}(1 + \cos\alpha) \quad (5)$$

III. Computer Simulations

Figure 1 shows the circuit diagram for simulation of the 6-pulse fully controlled rectifier with a dc link filter capacitor (or smoothing dc capacitor) and resistive load. The rectifier circuit is supplied by a three-phase, 50 Hz, 0.4 kV (line-to-line) inductive voltage source with 1.5 mH line inductance and 10 mΩ line resistance. A phase-locked loop (PLL) based triggering unit is used to generate the thyristor gate signals as shown in Figure 2. Value of the firing angle (alpha) can be manually adjusted or automatically changed from an initial value to a desired final value throughout the simulation.

There are an infinite number of harmonics that make up a distorted wave. The amplitudes of these harmonics tend to decrease as the frequencies increase. The Fast Fourier Transform (FFT) is a short version of the Fourier analysis which limits the calculated number of harmonic components to 50 with insignificant error [13]. Therefore, magnitude and phase angles of the input phase current are obtained by Fourier series analysis via using FFT block. The simulation of other circuit topologies discussed in this paper are performed in the same manner.

The topologies under consideration are as follows:

- 6-pulse uncontrolled rectifier with R and RL load
- 6 pulse half-controlled rectifier with R and RL load
- 6 pulse fully-controlled rectifier with R and RL load
- 12 pulse fully-controlled rectifier with R and RL load

For controlled rectifiers the results are obtained at several firing angles, results of 30 and 60 degrees of firing angles are reported for comparison. For all circuits, up to thirty-first odd harmonic components are considered. For half-controlled topology up to tenth even harmonic components are also considered.

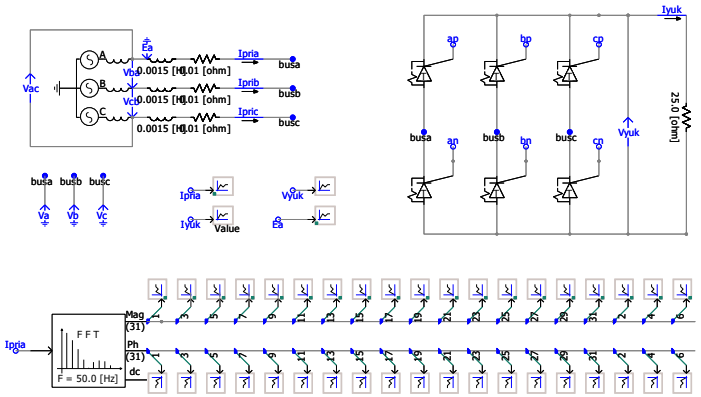

Figure 1: Simulation circuit for fully-controlled 6-pulse bridge topology

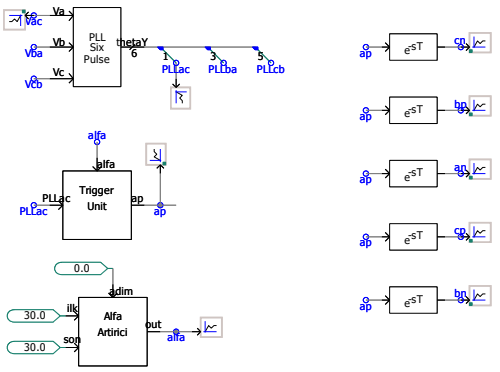

Figure 2: PLL circuit to generate the gate pulses for thyristors

IV. Results

Simulation results are given in Figure 3. The top window in each picture shows the line voltage and input line current drawn from the grid. Second window shows the output voltage and finally the third window shows the load current. Magnitudes and phase angles of each simulated circuit is given in the same figure.

Total harmonic distortion (THD) for each circuit is calculated by (4) and given in Table 1.

Table 1: Calculated THD values

Topology	THD (%)
6-p / un-controlled / R (25 Ω)	29.39
6-p / un-controlled / RL (25 Ω + 30 mH)	29.33
6-p / half-controlled / R / α=30	36.20
6-p / half-controlled / RL / α=30	34.91
6-p / fully-controlled / R / α=30	33.90
6-p / fully-controlled / RL / α=30	29.33
6-p / fully-controlled / R / α=60	32.93
6-p / fully-controlled / RL / α=60	29.32
12-p / fully-controlled / R / α=30	8.96
12-p / fully-controlled / RL / α=30	7.70
12-p / fully-controlled / R / α=60	10.21
12-p / fully-controlled / RL / α=60	5.08

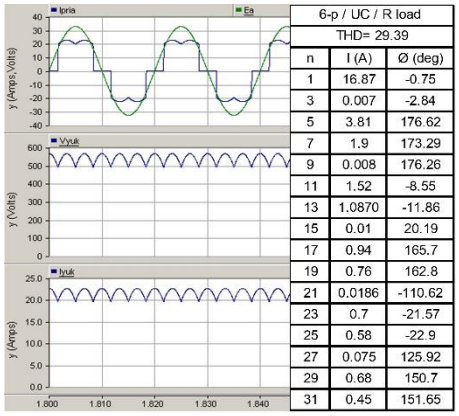

6-p / UC / R load — THD= 29.39

n	I (A)	Ø (deg)
1	16.87	-0.75
3	0.007	-2.84
5	3.81	176.62
7	1.9	173.29
9	0.008	176.26
11	1.52	-8.55
13	1.0870	-11.86
15	0.01	20.19
17	0.94	165.7
19	0.76	162.8
21	0.0186	-110.62
23	0.7	-21.57
25	0.58	-22.9
27	0.075	125.92
29	0.68	150.7
31	0.45	151.65

6-pulse un-controlled (R)

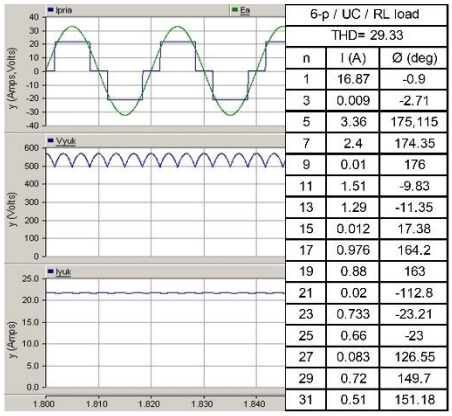

6-p / UC / RL load — THD= 29.33

n	I (A)	Ø (deg)
1	16.87	-0.9
3	0.009	-2.71
5	3.36	175,115
7	2.4	174.35
9	0.01	176
11	1.51	-9.83
13	1.29	-11.35
15	0.012	17.38
17	0.976	164.2
19	0.88	163
21	0.02	-112.8
23	0.733	-23.21
25	0.66	-23
27	0.083	126.55
29	0.72	149.7
31	0.51	151.18

6-pulse un-controlled (RL)

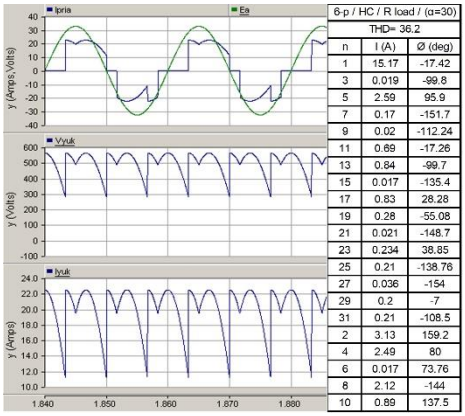

6-p / HC / R load / (α=30) — THD= 36.2

n	I (A)	Ø (deg)
1	15.17	-17.42
3	0.019	-99.8
5	2.59	95.9
7	0.17	-151.7
9	0.02	-112.24
11	0.69	-17.26
13	0.84	-99.7
15	0.017	-135.4
17	0.83	28.28
19	0.28	-55.08
21	0.021	-148.7
23	0.234	38.85
25	0.21	-138.76
27	0.036	-154
29	0.2	-7
31	0.21	-108.5
2	3.13	159.2
4	2.49	80
6	0.017	73.76
8	2.12	-144
10	0.89	137.5

6-pulse half-controlled (R/α=30)

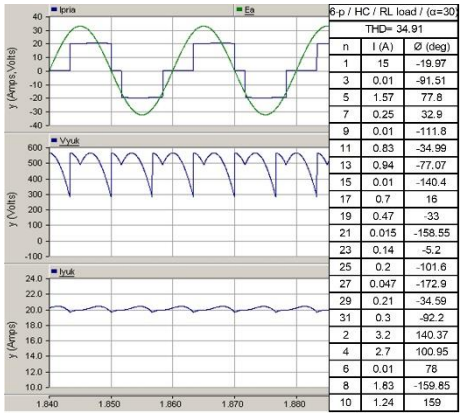

6-p / HC / RL load / (α=30) — THD= 34.91

n	I (A)	Ø (deg)
1	15	-19.97
3	0.01	-91.51
5	1.57	77.8
7	0.25	32.9
9	0.01	-111.8
11	0.83	-34.99
13	0.94	-77.07
15	0.01	-140.4
17	0.7	16
19	0.47	-33
21	0.015	-158.55
23	0.14	-5.2
25	0.2	-101.6
27	0.047	-172.9
29	0.21	-34.59
31	0.3	-92.2
2	3.2	140.37
4	2.7	100.95
6	0.01	78
8	1.83	-159.85
10	1.24	159

6-pulse half-controlled (RL/α=30)

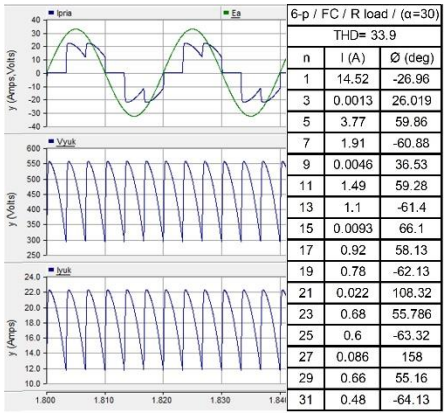

6-p / FC / R load / (α=30) — THD= 33.9

n	I (A)	Ø (deg)
1	14.52	-26.96
3	0.0013	26.019
5	3.77	59.86
7	1.91	-60.88
9	0.0046	36.53
11	1.49	59.28
13	1.1	-61.4
15	0.0093	66.1
17	0.92	58.13
19	0.78	-62.13
21	0.022	108.32
23	0.68	55.786
25	0.6	-63.32
27	0.086	158
29	0.66	55.16
31	0.48	-64.13

6-pulse fully-controlled (R/α=30)

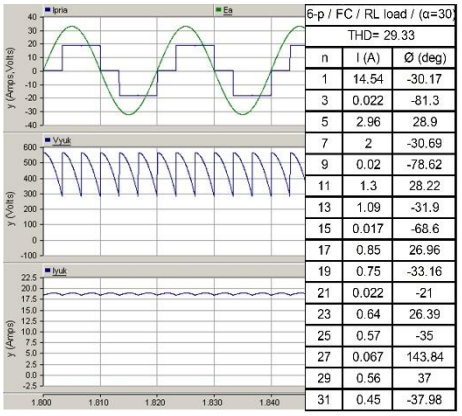

6-p / FC / RL load / (α=30) — THD= 29.33

n	I (A)	Ø (deg)
1	14.54	-30.17
3	0.022	-81.3
5	2.96	28.9
7	2	-30.69
9	0.02	-78.62
11	1.3	28.22
13	1.09	-31.9
15	0.017	-68.6
17	0.85	26.96
19	0.75	-33.16
21	0.022	-21
23	0.64	26.39
25	0.57	-35
27	0.067	143.84
29	0.56	37
31	0.45	-37.98

6-pulse fully-controlled (RL/α=30)

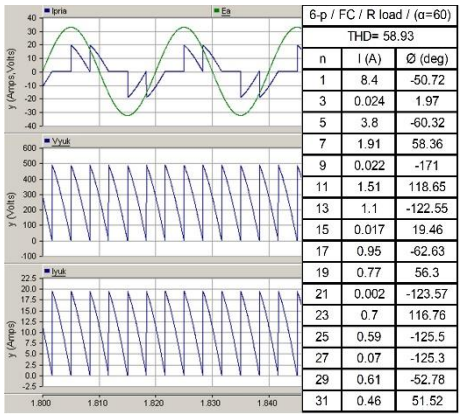

6-p / FC / R load / (α=60) — THD= 58.93

n	I (A)	Ø (deg)
1	8.4	-50.72
3	0.024	1.97
5	3.8	-60.32
7	1.91	58.36
9	0.022	-171
11	1.51	118.65
13	1.1	-122.55
15	0.017	19.46
17	0.95	-62.63
19	0.77	56.3
21	0.002	-123.57
23	0.7	116.76
25	0.59	-125.5
27	0.07	-125.3
29	0.61	-52.78
31	0.46	51.52

6-pulse fully-controlled (R/α=60)

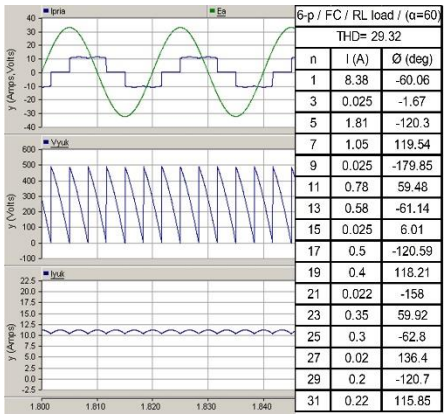

6-p / FC / RL load / (α=60) — THD= 29.32

n	I (A)	Ø (deg)
1	8.38	-60.06
3	0.025	-1.67
5	1.81	-120.3
7	1.05	119.54
9	0.025	-179.85
11	0.78	59.48
13	0.58	-61.14
15	0.025	6.01
17	0.5	-120.59
19	0.4	118.21
21	0.022	-158
23	0.35	59.92
25	0.3	-62.8
27	0.02	136.4
29	0.2	-120.7
31	0.22	115.85

6-pulse fully-controlled (RL/α=60)

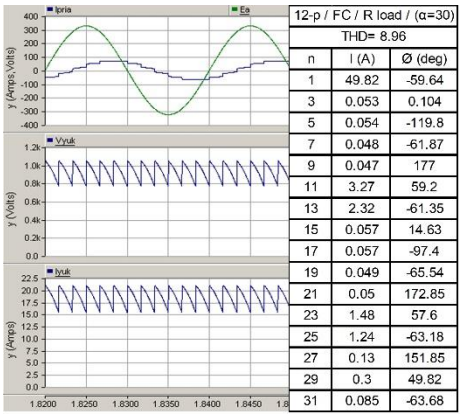

12-p / FC / R load / (α=30) — THD= 8.96

n	I (A)	Ø (deg)
1	49.82	-59.64
3	0.053	0.104
5	0.054	-119.8
7	0.048	-61.87
9	0.047	177
11	3.27	59.2
13	2.32	-61.35
15	0.057	14.63
17	0.057	-97.4
19	0.049	-65.54
21	0.05	172.85
23	1.48	57.6
25	1.24	-63.18
27	0.13	151.85
29	0.3	49.82
31	0.085	-63.68

12-pulse fully-controlled (R/α=30)

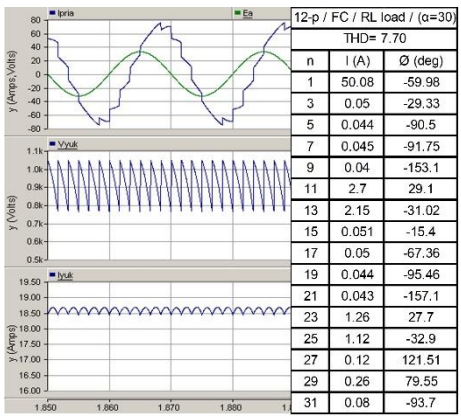

12-p / FC / RL load / (α=30) — THD= 7.70

n	I (A)	Ø (deg)
1	50.08	-59.98
3	0.05	-29.33
5	0.044	-90.5
7	0.045	-91.75
9	0.04	-153.1
11	2.7	29.1
13	2.15	-31.02
15	0.051	-15.4
17	0.05	-67.36
19	0.044	-95.46
21	0.043	-157.1
23	1.26	27.7
25	1.12	-32.9
27	0.12	121.51
29	0.26	79.55
31	0.08	-93.7

12-pulse fully-controlled (RL/α=30)

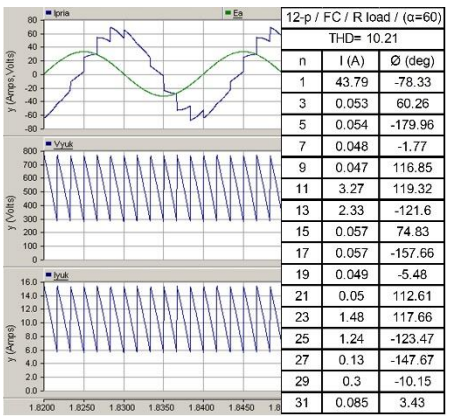

12-p / FC / RL load / (α=60) — THD= 10.21

n	I (A)	Ø (deg)
1	43.79	-78.33
3	0.053	60.26
5	0.054	-179.96
7	0.048	-1.77
9	0.047	116.85
11	3.27	119.32
13	2.33	-121.6
15	0.057	74.83
17	0.057	-157.66
19	0.049	-5.48
21	0.05	112.61
23	1.48	117.66
25	1.24	-123.47
27	0.13	-147.67
29	0.3	-10.15
31	0.085	3.43

12-pulse fully-controlled (R/α=60)

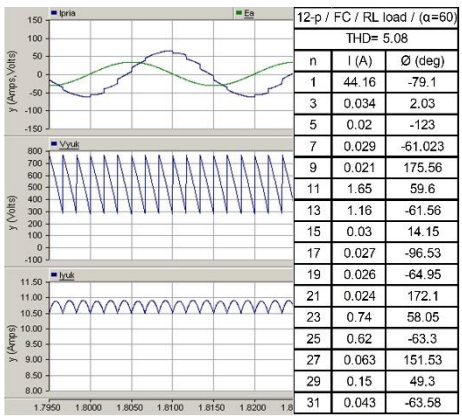

12-p / FC / RL load / (α=60) — THD= 5.08

n	I (A)	Ø (deg)
1	44.16	-79.1
3	0.034	2.03
5	0.02	-123
7	0.029	-61.023
9	0.021	175.56
11	1.65	59.6
13	1.16	-61.56
15	0.03	14.15
17	0.027	-96.53
19	0.026	-64.95
21	0.024	172.1
23	0.74	58.05
25	0.62	-63.3
27	0.063	151.53
29	0.15	49.3
31	0.043	-63.58

12-pulse fully-controlled (RL/α=60)

Figure 3: Input current and voltage, dc load voltage and load current waveforms, magnitude and phase shift of harmonic components.

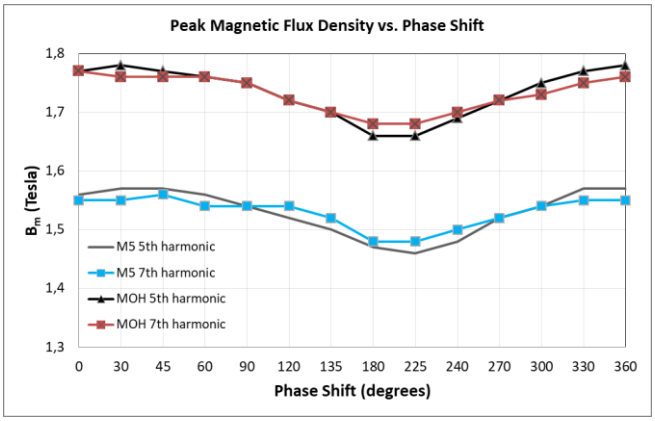

Figure 4: Variation in Bm for several phase shift between fundamental and harmonic component [3]

Studies in the literature show that not only the magnitude of the harmonic content in the supply voltage but also the phase angle has a considerable effect on the transformer saturation as shown in Figure 4 [3]. Therefore, for each simulated circuit phase angle of the harmonic components are also obtained and presented in Figure 3. Figure 5 shows the variation in phase angle of fundamental, fifth and seventh harmonic components against firing angle for 6-pulse fully-controlled rectifier. Line voltage zero crossing is taken as the reference point, so the value of the obtained phase angle represents the phase shift between the zero crossings of the line voltage and the harmonic component waveforms.

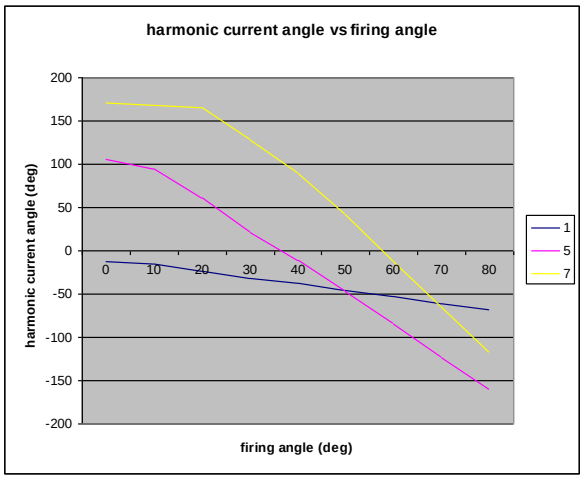

Figure 5: Variation in phase angle of fundamental, fifth and seventh harmonic components vs firing angle

V. Conclusion

Simulation results show that input current of rectifier converters contains significant harmonic components. As the pulse number increases harmonic content and THD decreases. The distortion in the current waveform for half-controlled topology is higher than fully-controlled case for the same firing angle due to the even harmonic components. Although the half-controlled topology is cheaper to apply, reversal of the mean load voltage is possible in a fully-controlled topology. The input current waveform resembles a square-wave and load current waveform ripple decreases as the value of the load inductance increases. Variation of phase angle of a harmonic component against firing angle shows that the worst case for the power system equipment design (such as transformers, etc.) should be considered for safe operation.

References

[1] R. Carbone, P. Corsonello and A. Scappatura, “A three-phase diode rectifier with low current harmonics,” 2003 *IEEE International Conference on Industrial Technology*, pp. 642-647.

[2] S. P. Kennedy, “Design and application of semiconductor rectifier transformers,” in *IEEE Transactions on Industry Applications*, vol. 38, no. 4, pp. 927-933, 2002.

[3] A. Dönük, “A laboratory application for teaching the effect of harmonics on transformer core saturation.” *The International Journal of Electrical Engineering & Education*, vol. 57, no. 3, pp. 191–201, 2020.

[4] K.B. Kuznetsov, A.R. Zakirova, “A Higher harmonic components of rectifiers magnetic fields and their adverse health effects,” *Procedia Engineering*, vol. 129, pp. 415–419, 2015.

[5] S. Brovanov, “Harmonic analysis and control strategy of a three-phase three-level rectifier,”*2007 The Int. Conference on "Computer as a Tool"*, pp. 2749-2753.

[6] R. G. Ellis, “Harmonic analysis of industrial power systems,” *IEEE Transactions on Industry Applications*, vol. 32, no. 2, pp. 417-421, 1996.

[7] M. McCarty, T. Taufik, A. Pratama and M. Anwari, "Harmonic analysis of input current of single- phase controlled bridge rectifier," *2009 IEEE Symposium on Industrial Electronics & Applications*, pp. 520-524.

[8] K. L. Lian and P. W. Lehn, "Harmonic Analysis of Single-Phase Full Bridge Rectifiers Based on Fast Time Domain Method," *2006 IEEE International Symposium on Industrial Electronics*, pp. 2608-2613.

[9] V. Vanin, A. Bulychov, M. Popov, O. Vasilyeva, M. Shakhova, “Measurement of currents and voltages non-sinusoidal parameters in power supply systems with rectifier load,” 2018 MATEC Web Conf. 245 06007.

[10] M. Saxena, S. Gupta, “Simulation of Multipulse Converter for Harmonic Reduction using Controlled Rectifier,” Int. Journal of Science and Research, vol. 2(4), pp. 260-264, 2013.

[11] C.W. Lander, *Power Electronics*. McGraw-Hill, 1993.

[12] N. Mohan, T.M. Undeland, W.P. Robbins, *Power Electronics Converters, Applications, and Design*. John Wiley&Sons, Inc., 2003.

[13] Henderson, R.D., and Patrick J. R. “Harmonics: the effects on power quality and transformers." *IEEE transactions on industry applications*” vol.30.3, pp. 528-532, 1994.

Simulation and Theoretical Analysis of a Digital Capacitance Measurement Circuit

M.DEMİRTAŞ[1], M.A.ERİŞMİŞ[2] and S.GÜNEŞ[3]

[1]Necmettin Erbakan University, Konya/Turkey, mdemirtas@erbakan.edu.tr,
[2]Necmettin Erbakan University, Konya/Turkey, maerismis@erbakan.edu.tr
[3]Konya Technical University, Konya/Turkey, sgunes@ktun.edu.tr

***Abstract* – This paper presents theoretical analysis and simulation of a digital capacitance measurement circuit. The capacitance measurement circuit setup consists of a digital signal processing unit and a transimpedance amplifier. An unknown capacitance is excited by an input signal generated by a digital signal processing unit. Transimpedance amplifier converts the current flowing on the unknown capacitance into a voltage value. This modulated voltage is sampled by an analog-to-digital converter. The digital lock-in amplifier can be built on the digital signal processing unit, and it outputs a voltage value proportional to the unknown capacitance. The effects of the transimpedance amplifier's analog noise and analog-to-digital converter's quantization errors are examined. Total noise, sensitivity, resolution, signal-to-noise ratio, settling time, response time and relative measurement error are the simulated performance metrics of the measurement circuit. 4.7 pF and 15 pF are chosen as the values of the unknown capacitance. The simulations are run for 50 kHz and 100 kHz excitation frequencies.**

***Keywords* – capacitance, digital lock-in amplifier, measurement, transimpedance amplifier.**

I. INTRODUCTION

LOCK-IN amplifiers (LIA) were introduced in the 1930s but they became popular after the 1950s. They are used to extract the phase and amplitude of a signal which is in a highly noisy environment [1]. Basically, a LIA circuit produces an output by multiplying the input signal with a reference signal and then filtering it through a low pass filter. In this way, the frequency of the wanted signal can be isolated from all other frequency components. The reference signal can be generated inside the LIA circuit, or it can be given from an external source. The waveform of the reference signal can be a sine wave or a square wave. LIAs are widely used in many applications such as AC phase meters, network and spectrum analyzers, phase detectors [2].

Digital lock-in amplifiers (DLIA) have the same structure as their analog counterparts [3], but they use a digital signal processing unit such as Field Programmable Gate Arrays (FPGA) [4], Digital Signal Processors (DSP) [5] and Complex Programmable Logic Devices (CPLD) [6]. This unit samples the input signal, generates internal reference signals and external driving signal, multiplies the reference signals with the input signal and filters out the unwanted signal components with a low-pass filter. Transimpedance amplifier (TIA) is connected in between the unknown capacitance and the digital signal processing unit [7]. The external driving signal flows through the unknown capacitance. TIA converts this current into a voltage signal which is processed in the digital signal processing unit. Several digital techniques are proposed in the literature [8] such as phase sensitive demodulation [9], recursive demodulation [10, 11], information filtering demodulation [12] to obtain an output voltage related to the unknown capacitance value.

Several metrics can be utilized to measure the performance of the digital capacitance measurement circuit [13]. Analog noise caused by TIA and analog-to-digital converter's (ADC) quantization errors are taken into consideration in this work to simulate the total noise of the system, sensitivity, resolution, signal-to-noise ratio (SNR), settling time and measurement errors.

II. DIGITAL CAPACITANCE MEASUREMENT CIRCUIT

A digital capacitance measurement circuit is shown in Figure 1.

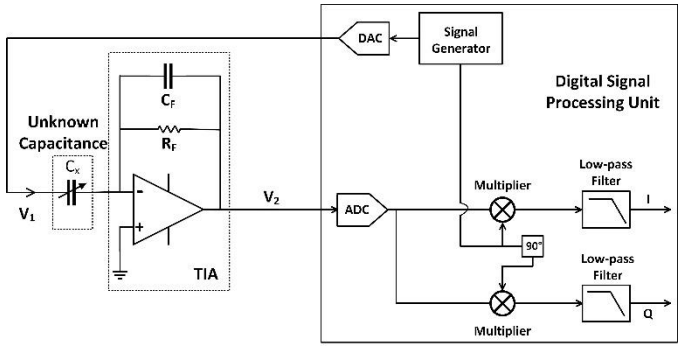

Figure 1: Digital capacitance measurement circuit.

The relationship between the excitation signal V_1 and the output of the TIA V_2 can be defined as follows.

$$\frac{V_2}{V_1} = \frac{-j2\pi f C_x R_F}{1 + j2\pi f C_F R_F} \tag{1}$$

where C_x is the unknown capacitance, f is the excitation frequency, C_F is the feedback capacitor and R_F is the feedback resistor. If the output of the TIA is defined as $V_2 = A\sin(2\pi f t + \theta)$ then ADC's discrete output voltage can be expressed as in (2).

$$V_{ADC}(n) = A\sin(2\pi\frac{f}{f_s}n+\theta), \qquad n = 0,1,\cdots M-1 \quad (2)$$

where f_s is the ADC's sampling frequency, M is the total number of samples which is equal to f_s/f and n is the sample index. Internal reference signals generated by the signal generator are given in (3) and (4).

$$i(n) = \sin(\frac{2\pi}{M}n), \qquad n = 0,1,\cdots M-1 \quad (3)$$

$$q(n) = \cos(\frac{2\pi}{M}n), \qquad n = 0,1,\cdots M-1 \quad (4)$$

The output of the ADC and internal reference signals $i(n)$ and $q(n)$ are multiplied by the multipliers and the following signals in (5) and (6) are obtained, respectively.

$$I = \sum_{n=0}^{M-1}\sin(\frac{2\pi}{M}n)\cdot A\sin(\frac{2\pi}{M}n+\theta) = \frac{A}{2}\sum_{n=0}^{M-1}\left[\cos\theta - \cos(\frac{4\pi}{M}n+\theta)\right] \quad (5)$$
$$= \frac{A}{2}M\cos\theta - \left\{\frac{A}{2}\sum_{n=0}^{M-1}\cos\left(\frac{4\pi}{M}n+\theta\right)\right\} = \frac{A}{2}M\cos\theta$$

$$Q = \sum_{n=0}^{M-1}\cos(\frac{2\pi}{M}n)\cdot A\sin(\frac{2\pi}{M}n+\theta) = \frac{A}{2}\sum_{n=0}^{M-1}\left[\sin\theta + \sin(\frac{4\pi}{M}n+\theta)\right] \quad (6)$$
$$= \frac{A}{2}M\sin\theta + \left\{\frac{A}{2}\sum_{n=0}^{M-1}\sin\left(\frac{4\pi}{M}n+\theta\right)\right\} = \frac{A}{2}M\sin\theta$$

The digital low-pass filters in Figure 1 act as a moving average filter. Their inputs are M samples coming from multipliers namely the signals expressed in (5) and (6). The LPF takes the average of its input signal by dividing it by the number of samples. Therefore, the following in-phase and quadratic-phase components can be obtained at the outputs.

$$I = \frac{A}{2}\cos\theta \quad (7)$$

$$Q = \frac{A}{2}\sin\theta \quad (8)$$

Using the equation in (7) and (8), $V_{ADC}(n)$ signal's amplitude and phase can be calculated as in (9) and (10), respectively.

$$A = 2\sqrt{I^2+Q^2} \quad (9)$$

$$\theta = \arctan(\frac{I}{Q}) \quad (10)$$

The output of the TIA V_2 can be found by the calculation of amplitude and phase. Since the values of the excitation signal V_1, excitation frequency f, R_F and C_F are all known, the unknown capacitance C_x can be calculated using equation (1).

III. Simulation Results

The overall performance of the measurement circuit is simulated using MATLAB 2017b. The amplitude of the excitation signal (V_1) is selected as 1.25 V. The output of the TIA is limited within ±0.5 V which is compatible with the ADC's input voltage range. The values of R_F and C_F are picked properly to comply with this voltage limitation. 4.7 pF and 15 pF are simulated values of C_x for two excitation frequencies $f = 50$ kHz and $f = 100$ kHz. A 12-bit with 1 MSPS sampling rate ADC is used.

If $C_x = 4.7$ pF is driven by a sinewave with amplitude of 1.25 V and frequency of 50 kHz, the input and output signals of the TIA can be shown as in Figure 2.

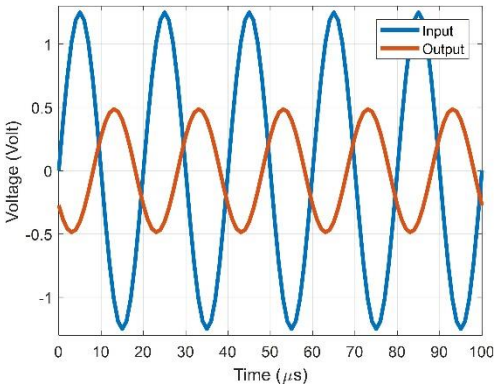

Figure 2: Input and output signals of the TIA ($C_x = 4.7$ pF).

The output voltage's amplitude is 0.486 V for the selection of $R_F = 470$ kΩ and $C_F = 10$ pF. TIA adds an analog noise on the output voltage. A generic operational amplifier with the selected R_F and C_F values cause around 91 μV_{RMS} analog noise [7]. Also, ADC's quantization error can be calculated [14] as given in (11).

$$e_n = \frac{q}{\sqrt{12}} \quad (11)$$

where e_n is the RMS value of the quantization error and q is equal to 1 least significant bit of the ADC's input signal. If both the analog noise and the quantization error is added on V_2, a total noise of 124.7 μV_{RMS} is calculated. The total noise is the main reason of the relative error between the simulated and real values of the unknown capacitance. The relative error (RE) is defined as in (12).

$$RE(\%) = \frac{|simulated\ value - real\ value|}{real\ value}\times 100 \quad (12)$$

The simulated value of C_x is found as 4.699456 pF which means a RE of 0.011573%. Table 1 lists the simulations of the amplitude of V_2, the analog noise, the total noise, the simulated value of C_x and the RE for different excitation frequencies.

Table 1: Simulation results of $C_x = 4.7$ pF and $C_x = 15$ pF for $f = 50$ kHz and $f = 100$ kHz.

	$C_x = 4.7$ pF		$C_x = 15$ pF	
	f=50 kHz	f=100 kHz	f=50 kHz	f=100 kHz
R_F (kΩ)	470	220	180	180
C_F (pF)	10	10	33	39
$\|V_2\|$ (V)	0.486	0.476	0.500	0.469
Analog noise (μV_{RMS})	91	91	87	85
Total noise (μV_{RMS})	124.7	125.2	117.9	124.5
Simulated C_x(pF)	4.699456	4.699504	15.001123	14.998839
RE (%)	0.011573	0.010545	0.007491	0.007740

Signal-to-noise ratio of an ideal ADC can be calculated [14] as in (13).

$$SNR = 6.02N + 1.76 \text{ (dB)} \quad (13)$$

where N is the number of bits of ADC. Thus, a 12-bit ADC's SNR is maximum of 74 dB. If there is a noise on the input signal (V_{noise}), the SNR value can be calculated as in (14).

$$SNR = 20\log\left(\frac{2}{3}\left(\frac{1}{2^N}\right)^2 + \left(\frac{2\sqrt{2}V_{noise}}{2^N}\right)^2\right)^{-\frac{1}{2}} \text{ (dB)} \quad (14)$$

Theoretically, SNR will decrease in proportional to the amount of analog noise.

Sensitivity is another simulated metric to evaluate the performance of the digital capacitance measurement system. It is defined as the ratio of the TIA's output's maximum voltage range to the value of the measured capacitance. Therefore, the sensitivity S can be calculated as follows.

$$S = \frac{|V_2|_{\max(pp)}}{C_x} \text{ (V/pF)} \quad (15)$$

Sensitivity is the amount of change in output voltage per capacitance change. Resolution, on the other hand, can be defined as the ability of the circuit to distinguish the smallest capacitance change. Resolution (R_{es}) is affected by the sensitivity and the total noise, and in this regard, it can be written with a formula as in equation (16).

$$R_{es} = \frac{e_n}{S} \quad (16)$$

where e_n is the RMS value of the total noise which consists of the analog noise and the quantization error.

The response time is the time it takes for the circuit to change the output signal in response to a change in the measured capacitance. The shortness of the response time indicates the high measurement speed of the circuit. It can be written as in (17).

$$t_{response} = t_{settling} + t_{DLIA} \quad (17)$$

where $t_{settling}$ is the TIA's settling time and t_{DLIA} is the digital demodulation time. The settling time is equal to $4.6R_FC_F$ and digital demodulation time is equal to $1/f$.

Table 2: SNR, sensitivity, resolution, and response time results of $C_x = 4.7$ pF and $C_x = 15$ pF for $f = 50$ kHz and $f = 100$ kHz.

	$C_x = 4.7$ pF		$C_x = 15$ pF	
	f=50 kHz	f=100 kHz	f=50 kHz	f=100 kHz
SNR (dB)	74.0517	74.0517	74.0517	74.0517
Sensitivity (V/pF)	0.207	0.203	0.067	0.063
Resolution(fF)	0.599	0.618	1.766	1.992
$t_{settling}$ (μs)	21.62	10.34	27.92	32.29
t_{DLIA}(μs)	20	10	20	10
$t_{response}$(μs)	41.62	20.34	47.92	42.29

Table 2 lists the simulations of the SNR, the sensitivity, the resolution, and the response time for two different excitation frequencies.

IV. Results and Discussion

The simulation results show that the excitation frequency of the system is an important parameter. The values of the R_F and C_F must be changed to make voltage V_2 compatible with the ADC's input range because of the frequency dependence as shown in equation (1). Simulations show that the sensitivity decreases as the amount of capacitance to be measured increases. As the amplitude of V_2 is tried to be kept constant approximately constant as given in Table 1, the amount of voltage per measured capacitance decreases. Similarly, the resolution also increases in proportion to the measured capacitance value because the total noise consisting of analog noise and quantization error is approximately similar for all measurement simulations. According to the simulated C_x values, the relative error was determined to be around 0.011% at most. On the other hand, the SNR values are almost the same because the most basic factor that affects this value is the resolution bit number of the ADC as given in (14). 12-bit resolution is assumed for all simulations. As can be seen in Table 2, the effect of noise on SNR is very limited. On the other hand, Table 2 demonstrates that R_F, C_F and f values are the parameters which determine the response time. High excitation frequency reduces the total response time. However, the settling time is only determined by the value of feedback resistor and feedback capacitor. Theoretical analysis proves that it is necessary to maximize the amplitude values of the input and output voltages of the TIA. However, in real-world applications, restrictions are necessary, as in the simulations in this work. In addition, as the resolution and sampling frequency of the ADC increase, it is possible to obtain higher SNR and lower relative error.

V. Conclusion

In this work, analysis of a digital capacitance measurement circuit is performed. Besides theoretical analysis, several simulations are run for different unknown capacitances. Noise

analysis, time analysis, error analysis, sensitivity analysis are carried out for 50 kHz and 100 kHz driving frequency values. Simulation results imply that many different parameters can be adjusted accordingly to make the measurement circuit work as intended.

REFERENCES

[1] K. Schultz, "Phase-sensitive detection in the undergraduate lab using a low-cost microcontroller," *American Journal of Physics*, vol. 84, no. 7, pp. 557-561, 2016.

[2] "Principles of lock-in detection and the state of the art," Zurich Instruments 2016, Available: https://www.zhinst.com/sites/default/files/li_primer/zi_whitepaper_principles_of_lock-in_detection.pdf.

[3] M. Demirtas, M. A. Erismis, and S. Gunes, "A Lossy Capacitance Measurement Circuit Based on Analog Lock-in Detection," *Elektronika ir Elektrotechnika*, vol. 26, no. 5, pp. 4-10, 2020.

[4] M. Carminati, A. Rottigni, D. Alagna, G. Ferrari, and M. Sampietro, "Compact FPGA-based elaboration platform for wide-bandwidth electrochemical measurements," in *2012 IEEE international instrumentation and measurement technology conference proceedings*, 2012, pp. 264-267: IEEE.

[5] S. Sun, Z. Cao, A. Huang, L. Xu, and W. Yang, "A High-Speed Digital Electrical Capacitance Tomography System Combining Digital Recursive Demodulation and Parallel Capacitance Measurement," *IEEE Sensors Journal*, vol. 17, no. 20, pp. 6690-6698, 2017.

[6] M. G. Tiapkin and A. P. Balkovoi, "High resolution processing of position sensor with amplitude modulated signals of servo drive," in *2017 IEEE Conference of Russian Young Researchers in Electrical and Electronic Engineering (EIConRus)*, 2017, pp. 1042-1047.

[7] M. Demirtaş, M. A. Erişmiş, and S. Güneş, "Analysis and design of a transimpedance amplifier based front-end circuit for capacitance measurements," *SN Applied Sciences*, vol. 2, no. 2, p. 280, 2020/01/28 2020.

[8] S. Sun, L. Xu, Z. Cao, and W. Yang, "Signal Demodulation Methods for Electrical Tomography: A Review," *IEEE Sensors Journal*, vol. 19, no. 20, pp. 9026-9035, 2019.

[9] L. Xu, H. Zhou, Z. Cao, and W. Yang, "A Digital Switching Demodulator for Electrical Capacitance Tomography," *IEEE Transactions on Instrumentation and Measurement*, vol. 62, no. 5, pp. 1025-1033, 2013.

[10] S. Sun, L. Xu, Z. Cao, and W. Yang, "A Recursive Demodulator for Real-Time Measurement of Multiple Sinusoids," *IEEE Sensors Journal*, vol. 18, no. 15, pp. 6281-6289, 2018.

[11] S. Sun, L. Xu, Z. Cao, A. Huang, and W. Yang, "Digital Recursive Demodulator Based on Kalman Filter," *IEEE Transactions on Instrumentation and Measurement*, vol. 66, no. 12, pp. 3138-3147, 2017.

[12] S. Sun, L. Xu, Z. Cao, H. Zhou, and W. Yang, "A high-speed electrical impedance measurement circuit based on information-filtering demodulation," *Measurement Science and Technology*, vol. 25, no. 7, p. 075010, 2014/05/29 2014.

[13] L. Xu, S. Sun, Z. Cao, and W. Yang, "Performance analysis of a digital capacitance measuring circuit," *Rev Sci Instrum*, vol. 86, no. 5, p. 054703, May 2015.

[14] W. Kester, "MT-001: Taking the mystery out of the infamous formula," snr= 6.02 n+ 1.76 db," and why you should care," pp. 10-03, 2005.

Design of a Digital Lock-in Amplifier using Xilinx System Generator

M.DEMİRTAŞ[1], M.A.ERİŞMİŞ[2] and S.GÜNEŞ[3]

[1]Necmettin Erbakan University, Konya/Turkey, mdemirtas@erbakan.edu.tr,
[2]Necmettin Erbakan University, Konya/Turkey, maerismis@erbakan.edu.tr
[3]Konya Technical University, Konya/Turkey, sgunes@ktun.edu.tr

***Abstract* – In this paper, a digital lock-in amplifier is designed using Xilinx System Generator. The designed digital lock-in amplifier is used to simulate values of the following nominal capacitances: 2.2 pF, 4.7 pF, 5.6 pF, 6.8 pF and 10 pF. The digital lock-in amplifier consists of an internal signal generator, two multipliers, 2 FIR low-pass filters and an ARCTAN block. The internal signal generator uses Direct Digital Synthesis to produce 50 kHz sine and cosine reference signals. The low-pass filters are designed using FIR Compiler blocks. The outputs of the low-pass filters are in-phase and quadrature components. CORDIC ATAN block converts in-phase and quadrature components into amplitude and phase values which are in proportional to the value of the measured capacitance. Analog noise and quantization error of analog-to-digital converter are added to obtain more realistic simulations. The digital lock-in amplifier in SIMULINK environment is compiled, and hardware description language bitstream is generated for Xilinx ZedBoard FPGA. The bitstream is downloaded into the FPGA and hardware-software co-simulation is performed. Relative errors are calculated for the nominal value and the measured value.**

***Keywords* – capacitance measurement, digital lock-in amplifier, FPGA, Xilinx System Generator**

I. INTRODUCTION

XILINX System Generator (XSG) is a tool which enables users to easily compile MATLAB/Simulink designs for hardware implementations [1]. Xilinx Blockset defined under Simulink library includes several digital signal processing blocks. The blocks can be used for system-level modelling design [2]. Moreover, XSG can be used to generate Hardware Description Language (HDL) for a certain type of FPGA based on the system-level model [3]. In the literature, XSG is employed in many applications such as image processing [4, 5], signal processing [6, 7], communication [8, 9], encryption [10, 11].

A digital lock-in amplifier (DLIA) can be used to obtain the phase and amplitude information of an input signal. A digital demodulation is executed inside the digital signal processing unit to recover the signal from noise [12]. Compared to analog lock-in amplifiers [13], DLIAs are advantageous in terms of accuracy [14]. A DLIA generally consists of a digital signal processing unit and an external circuit which supplies the modulated input signal. XSG can be utilized to design and implement a DLIA [15, 16]. Xilinx Direct Digital Synthesis (DDS) Compiler is used to generate internal reference signals. The multiplication of the input signal with the reference signals can be performed with the help of Xilinx Multiplier block. Also, digital low-pass filters (LPF) can be realized using Xilinx FIR block [17, 18]. The LPFs outputs in-phase and quadrature-phase components which can be converted into amplitude and phase values by Xilinx CORDIC ATAN. As the input signal contains information about the value of measured capacitance, the amplitude and phase values can be used to find the value of the capacitance.

II. CAPACITANCE MEASURING WITH DLIA

A capacitance measuring circuit with dual-phase DLIA's general circuit schematic is illustrated in Figure 1.

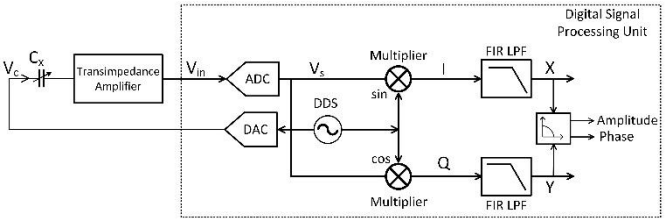

Figure 1: Capacitance measuring with DLIA.

The input signal of the unknown capacitance (V_c) and the output signal of the transimpedance amplifier (V_{in}) can be expressed as in (1) and (2), respectively.

$$V_c = A_c \sin(2\pi f t) \tag{1}$$

$$V_{in} = A \sin(2\pi f t + \theta) \tag{2}$$

If the transimpedance amplifier consists of an operational amplifier with a feedback resistor (R_F) and a feedback capacitor (C_F), then V_c and V_{in} voltages are related [19] as given in (3).

$$\frac{V_{in}}{V_c} = \frac{-j\omega C_x R_F}{1 + j\omega C_F R_F} \tag{3}$$

where C_x is the unknown capacitance and f is the operating frequency. If V_{in} is sampled by an ADC with a sampling rate of f_s, V_s is obtained as in (4). Also, the reference signals generated by DDS method are given in (5) and (6).

$$V_s(n) = A\sin(2\pi\frac{f}{f_s}n + \theta) \quad (4)$$

$$i(n) = \sin(\frac{2\pi}{M}n) \quad (5)$$

$$q(n) = \cos(\frac{2\pi}{M}n) \quad (6)$$

where $n = 0,1,\cdots M-1$ is the sample index and M is the number of samples. I and Q signals shown in Figure 1 can be obtained by multiplying (4) with (5) and (4) with (6), respectively.

$$I = \sum_{n=0}^{M-1} i(n)\cdot V_s(n) = \frac{A}{2}M\cos\theta \quad (7)$$

$$Q = \sum_{n=0}^{M-1} q(n)\cdot V_s(n) = \frac{A}{2}M\sin\theta \quad (8)$$

After low-pass filtering, X and Y signals are obtained as follows.

$$X = \frac{A}{2}\cos\theta \quad (9)$$

$$Y = \frac{A}{2}\sin\theta \quad (10)$$

Finally, the amplitude and phase of $V_s(n)$ can be calculated as in (11) and (12), respectively.

$$A = 2\sqrt{X^2 + Y^2} \quad (11)$$

$$\theta = \arctan(\frac{X}{Y}) \quad (12)$$

C_x can be computed using the equations (11), (12) and (3).

III. DLIA Design using Xilinx System Generator

A digital lock-in amplifier is designed using XSG according to the components shown in Figure 1. Firstly, the reference signals are chosen as 50 kHz sine and cosine waves. Their frequency can be determined by Xilinx DDS Compiler block using the following formula [20].

$$f_{DDS} = \frac{f_{system}\,M}{2^n} \quad (13)$$

where f_{system} is the system clock frequency of the used FPGA which is 100 MHz. M is the phase increment value and n is the total number of bits in the phase accumulator. The phase increment value can be calculated using (13) and the frequency of the reference signals can be obtained as intended. Figure 2 shows the generation of the reference signals using XSG.

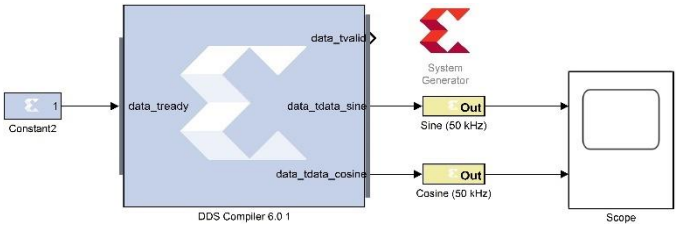

Figure 2: Generation of reference signals by XSG.

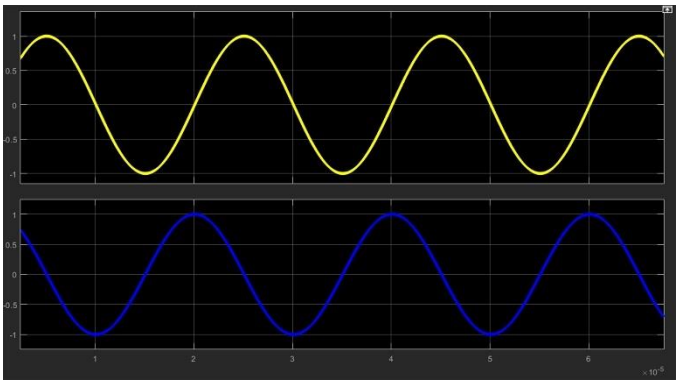

Figure 3: 50 kHz reference signals.

The graph of the 50 kHz reference signals obtained with DDS is shown in Figure 3. Xilinx Multiplier block is tested by multiplying the 50 kHz reference signals as shown in Figure 4. The result of the multiplication in which the amplitude is halved, and the frequency is doubled is shown in Figure 5.

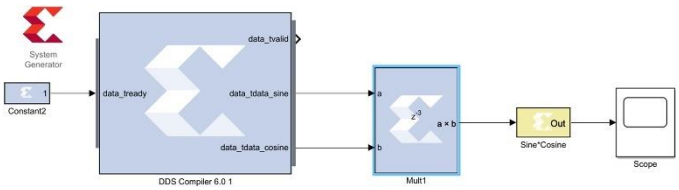

Figure 4: Test of the Xilinx Multiplier block.

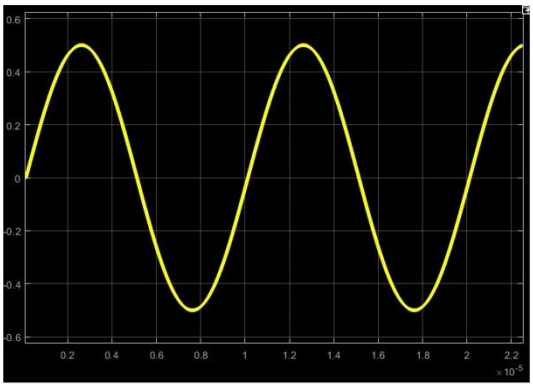

Figure 5: Multiplication of the reference signals.

The low-pass filters in DLIA is realized using Xilinx FIR Compiler block. It is possible to design high performance FIR filters whose parameters can be adjusted. Filter Design and Analysis Tool (FDATool) is used to adjust the FIR filters' parameters. The sampling frequency of the filter is chosen as 300 kHz which is more than two times the highest frequency component in the input signal. The passband ripple and the

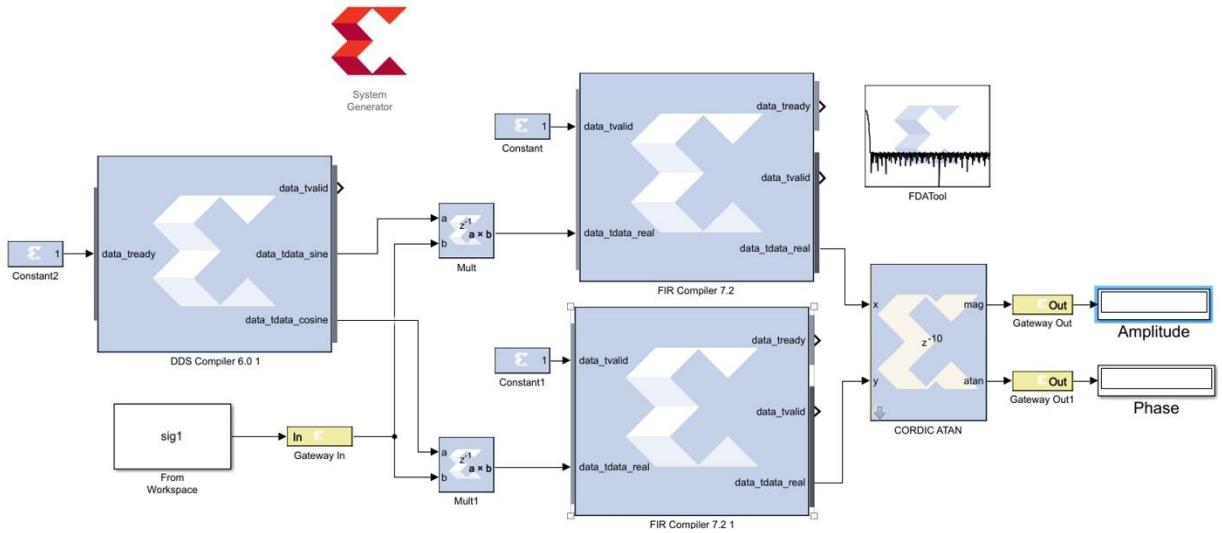

Figure 6: The designed DLIA using XSG.

stopband attenuation are adjusted as 0.5 dB and 80 dB, respectively. The stopband begins at 5 kHz. At the frequencies above 5 kHz, the filter's gain is less than -80 dB. Two 185th-order Direct-Form FIR low-pass filters are designed with equiripple method by FDATool. Then, 186 coefficients computed by FDATool is transferred to the FIR Compiler blocks. Xilinx CORDIC ATAN block is used to obtain the amplitude and phase values from the X and Y values formed at the output of the LPFs. This block allows converting Cartesian coordinates to polar coordinates.

The designed DLIA is shown in Figure 6. The System Generator panel is used to compile and generate the VHDL code of the designed DLIA circuit for ZedBoard Zynq Evaluation and Development Kit. Table 1 lists the resources that are used in FPGA for the designed circuit.

Table 1: The resource utilization of the designed circuit.

Block Name	BRAM	DSP	LUTs	Registers
Multiplier-1	-	1	-	-
Multiplier-2	-	1	-	-
FIR Compiler-1	1	3	147	181
FIR Compiler-2	1	3	147	181
DDS Compiler	0.5	3	76	243
CORDIC ATAN	-	-	1524	1275
Total	2.5	11	1894	1880

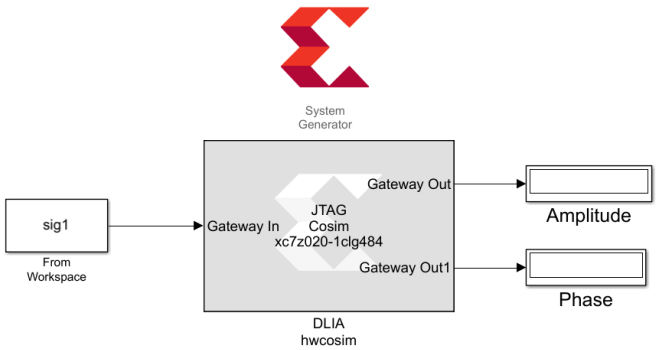

Figure 7: JTAG co-simulation block.

In order to implement this circuit in FPGA, the "Hardware Co-Simulation (JTAG)" option is selected in the System Generator control panel. XSG creates the JTAG co-simulation block after compiling the bitstream file required for the selected FPGA. JTAG co-simulation block which is illustrated in Figure 7 represents the ZedBoard FPGA board. It is used to synthesize the blocks between "Gateway In" and "Gateway Out" displayed in Figure 6. The bitstream file produced by XSG is sent to the ZedBoard card with the help of the USB port, so that the FPGA is configured. The outputs of the DLIA implemented in the FPGA can be transferred back to the software and displayed in the Display blocks shown in Figure 7.

IV. SIMULATION RESULTS

The input signal V_{in} of the designed circuit is supplied from the workspace. The analog noise of the transimpedance amplifier and the quantization error of analog-to-digital converter are added to input signal [19]. Therefore, a total 125 μV_{RMS} noise is added. If the unknown capacitance is chosen as 10 pF, the simulation in Simulink outputs an amplitude of 0.47002 V and a phase of -2.52854 rad/s. The simulated value of the unknown capacitance can be calculated as 9.901 pF using the equations (11), (12) and (3). Similarly, if the hardware-software co-simulation is implemented on ZedBoard, 0.47000 V amplitude and -2.52855 rad/s phase are obtained. C_x value can be found as 9.902 pF using these values. As a result, it is found out that the DLIA design implemented in ZedBoard works as expected.

Table 2: Simulation and implementation results for different capacitances

	Nominal value of the measured capacitance (pF)				
	2.2	4.7	5.6	6.8	10
Simulated value	2.030	4.450	5.425	6.662	9.901
Implemented value	2.032	4.452	5.426	6.664	9.902

Table 2 presents the simulated and implemented values of different capacitances. It can be observed from Table 2 that Simulink simulations and hardware realizations give similar measurement results. Table 3 lists the relative measurement errors for the measured capacitances. The relative error rate increases as the value of the measured capacitance decreases.

Table 3: Relative errors of simulation and implementation results.

	Nominal value of the measured capacitance (pF)				
	2.2	4.7	5.6	6.8	10
Simulated value relative error (%)	7.73 %	5.32 %	3.12 %	2.03 %	0.99 %
Implemented value relative error (%)	7.64 %	5.28 %	3.11 %	2.00 %	0.98 %

V. CONCLUSION

In this paper, a DLIA is designed, simulated in Simulink environment, and implemented in FPGA. DLIA is used to measure different capacitances. Possible noise sources are added to the input signal to make the simulations more realistic. Simulation and implementation results for capacitance measurement are presented. Also, corresponding relative errors are calculated.

REFERENCES

[1] "System Generator for DSP User Guide," 2012, Available: https://www.xilinx.com/support/documentation/sw_manuals/xilinx14_7/sysgen_user.pdf.

[2] L. Merah, P. Lorenz, A. Ali-Pacha, and N. Hadj-Said, "A Guide on Using Xilinx System Generator to Design and Implement Real-Time Audio Effects on FPGA," vol. 10, no. 3, 2021.

[3] K. Kintali and Y. Gu, "Model-based design with simulink, hdl coder, and xilinx system generator for dsp," 2012, Available: https://es.mathworks.com/content/dam/mathworks/tag-team/Objects/x/86457_92077_v01_Xilinx_WhitePaper.pdf.

[4] D. P. Guragain, P. Ghimire, and K. Budhathoki, "Implementation of FPGA Based Image Processing Algorithm Using Xilinx System Generator," *International Research Journal of Engineering Technology*, vol. 5, no. 01, pp. 2395-0056, 2018.

[5] T. Šušteršič, V. Milovanović, V. Ranković, N. Filipović, and A. Peulić, "Medical image processing using Xilinx system generator," in *International Conference on Computational Bioengineering*, 2019, pp. 104-116: Springer.

[6] K. Gaikwad and M. Chavan, "Design and Implementation of Digital Butterworth IIR filter using Xilinx System Generator for noise reduction in ECG Signal," *International Journal of Signal Processing*, vol. 2, 2017.

[7] U. Ghani *et al.*, "Efficient FIR filter implementations for multichannel BCIs using Xilinx system generator," *BioMed research international*, vol. 2018, 2018.

[8] D. Astharini, K. Azrina, D. Gunawan, D. I. Savitri, and O. N. Samijayani, "Design of visible light communication with DCT and M-ary PAM in Xilinx system generator," in *2018 IEEE 5th International Conference on Engineering Technologies and Applied Sciences (ICETAS)*, 2018, pp. 1-6: IEEE.

[9] D. S. Ibrahim and F. S. Hassan, "HARDWARE IMPLEMENTATION OF DCSK COMMUNICATION SYSTEM USING XILINX SYSTEM GENERATOR," *Journal of Engineering Sustainable Development*, vol. 24, no. Special Issue 2020, 2020.

[10] E. A. Hagras and M. Saber, "Low power and high-speed FPGA implementation for 4D memristor chaotic system for image encryption," *Multimedia Tools and Applications*, vol. 79, pp. 23203-23222, 2020.

[11] F. S. Hasan and M. A. Saffo, "FPGA Hardware Co-Simulation of Image Encryption Using Stream Cipher Based on Chaotic Maps," *Sensing and Imaging*, vol. 21, no. 1, pp. 1-22, 2020.

[12] A. A. Dorrington and R. Kunnemeyer, "A simple microcontroller based digital lock-in amplifier for the detection of low level optical signals," in *Proceedings First IEEE International Workshop on Electronic Design, Test and Applications' 2002*, 2002, pp. 486-488: IEEE.

[13] M. Demirtas, M. A. Erismis, and S. Gunes, "A Lossy Capacitance Measurement Circuit Based on Analog Lock-in Detection," *Elektronika ir Elektrotechnika*, vol. 26, no. 5, pp. 4-10, 2020.

[14] J. Gaspar, S. F. Chen, A. Gordillo, M. Hepp, P. Ferreyra, and C. Marqués, "Digital lock in amplifier: study, design and development with a digital signal processor," *Microprocessors and microsystems*, vol. 28, no. 4, pp. 157-162, 2004.

[15] Q. Wang, H. Zheng, and M. Jiang, "Implementation of digital lock-in amplifier based on system generator," in *2016 IEEE International Conference on Signal and Image Processing (ICSIP)*, 2016, pp. 636-640: IEEE.

[16] I. Muttakin, A. Yusuf, W. Widada, and W. P. Taruno, "Design and simulation of quadrature phase detection in electrical capacitance volume tomography," *Telkomnika*, vol. 13, no. 1, p. 55, 2015.

[17] E. Özpolat, B. Karakaya, and A. Gülten, "FIR Filtre Tasarımı ve FPGA Ortamında Gerçeklenmesi," *Fırat Üniversitesi Mühendislik Bilimleri Dergisi*, vol. 29, no. 2, pp. 269-275, 2017.

[18] A. Ghosh and D. Chakraborty, "Hardware Co-simulation of Reconfigurable FIR Filters on FPGA," in *Advances in Communication, Devices and Networking*: Springer, 2018, pp. 553-561.

[19] M. Demirtaş, M. A. Erişmiş, and S. Güneş, "Analysis and design of a transimpedance amplifier based front-end circuit for capacitance measurements," *SN Applied Sciences*, vol. 2, no. 2, p. 280, 2020/01/28 2020.

[20] "Fundamentals of direct digital synthesis (dds) " Analog Devices 2008, Available: https://www.analog.com/media/en/training-seminars/tutorials/MT-085.pdf.

Optimal reactive power dispatch using OBPSO algorithm

M. ÇEÇEN [1,2] and C. YAVUZ [2]

[1] Selcuk University, Ilgın Vocational School, Konya/Turkey, mehmet.cecen@selcuk.edu.tr
[2]Sakarya University, Electrical & Electronics Eng. Department, Sakarya/Turkey, cyavuz@sakarya.edu.tr

***Abstract* - In this study, OBPSO is proposed to find the optimal solution for optimal reactive power dispatch (ORPD) problems in power system. The proposed approach is used to find optimal control parameter values for ORPD. OBPSO is used to minimize power system losses and load bus voltage deviations. While the objective functions are minimized, they are run at the same time and in the same cycle with three frequently used optimization algorithms and the results are obtained. The performance of the proposed method has been tested on one of the standard test systems, IEEE 14 bus test system. In the study, cases with singular goal functions are discussed. Simulation results obtained from the proposed OBPSO approach indicate that OBPSO provides effective and give better results than other optimization techniques compared in the study.**

***Keywords* - OBPSO, Reactive power optimization, Real power loss minimization, Voltage deviation**

I. INTRODUCTION

The use of electrical energy continues to increase rapidly. To meet the increasing need, electricity must be produced in the most efficient way and delivered to the end user. The delivered electrical energy must constantly meet the power quality demands of the end user at the same standard. Reactive power flow in the power system cannot be prevented due to the inductive nature of many loads in the system, and devices that consume reactive power such as transformers and transmission lines from the network components, and it is not desired to be completely reset. Therefore, ORPD studies are important for the power system [1, 2].

Reactive power optimization is one of the important methods that ensure optimum operation of electrical power systems, power quality and system stability. This problem is solved by adjusting the generator voltages, transformer tap settings and reactive compensation devices to the most appropriate setting to minimize a certain objective function such as power loss, voltage deviation. While doing this, it also fulfills the equality and inequality constraints of the system. While transformer tap setting and reactive compensation devices are discrete values, bus voltage magnitudes and reactive power outputs are continuous variables. Therefore, the ORPD can be modeled with mixed integer nonlinear programming [3, 4].

Many techniques have been used in the past to solve ORPD in systems containing thermal power plants. Traditional methods such as quadratic programming [5], interior-point method [6], linear programming [7] and newton-rapson method [8] were used extensively in the early times. Later, methods such as stochastic, genetic algorithm (GA) [9], evolutionary strategy (ES) [10] were used. However, these methods are inefficient for nonlinear functions and systems with discrete variables [11].

Recently, with the development of meta-heuristic methods, they have given better results in solving ORPD. Commonly used methods are particle swarm optimization (PSO) [12, 13], gray wolf optimizer GWO [14], artificial bee colony ABC [15], harmony search algorithm HSA [16], gravitational search algorithm (GSA) [17], moth flame optimization (MFO) [18], seeker optimization algorithm (SOA) [19]. Later, researchers used improved methods and hybrid methods that gave better results than classical meta-heuristic methods to solve ORPD. These methods are gray wolf optimization-particle swarm optimization (GWO-PSO) [20], particle swarm optimization-gravitational search algorithm (PSOGSA) [21], comparative learning particle swarm optimization (CLPSO) [22], quasi-opposite differential evolution algorithm (QODE) [23].

In this paper, a new opposition-based particle swarm algorithm (OBPSO) is proposed to solve ORPD. With the proposed new method, the control parameters determined for ORPD will be optimized. Objective function results, control parameter values determined by the algorithm and reaching the result were examined. The objective function was run simultaneously with three different optimization algorithms in the same cycle and the results were obtained. Compared to other hybrid and enhanced optimization techniques, OBPSO is a method that is simple in its simplicity, efficiency, and application to problems as a tool. It also showed efficient performance against other optimization techniques. With the proposed new method, this paper focuses on finding the best control parameters that minimize power system losses and changes in load bus voltages. The proposed method has been applied to the IEEE 14 bus test system. In the study, cases where there is a singular objective function are discussed.

II. Problem Formulation

A. Objective Functions

In this article, the objective functions for ORPD are to minimize power losses and voltage deviation by considering equality and inequality constraints. The ORPD problem can be defined as the minimization of the function f(x,u) as follows:

$$\text{Min } f(x,u) \text{ Objective function: } \begin{matrix} g(x,u) = 0 \\ h(x,u) \le 0 \end{matrix} \quad (1)$$

The function f(x,u) is the objective function. g(x,u) and h(x,u) are the equality and inequality constraints, respectively. In the RGOP problem, the equality constraint is the power balance equations. Inequality constraints are generator voltage, transformer tap setting and reactive compensator size. x and u are vector of dependent variables and vector of control variables, respectively. The objective functions, the total power losses F1 of the transmission system and the voltage deviation F2 of the load bus, can be formulated as follows.

$$\text{F1}=P_{Loss}(x,u) = \sum_{L=1}^{Nl} P_{Loss} \quad (2)$$

$$\text{F2}=VD(x,u) = \sum_{i=1}^{Nd} |V_i - 1.0| \quad (3)$$

Nl represents the number of transmission lines while Nd is the number of load bus. V_i i. voltage of the bus and 1.0 pu is the reference voltage value.

B. Constraints

Equality Constraints:
The power equation of the load flow means that the difference between the power produced, and the power demand is equal to the power loss. The equality constraint equations can be expressed as:

$$P_{Gi} - P_{Di} = V_i \sum_{j \in N_i} V_j (G_{ij} cos\theta_{ij} + B_{ij} \sin\theta_{ij}) \quad (4)$$

$$Q_{Gi} - Q_{Di} = V_i \sum_{j \in N_i} V_j (B_{ij} cos\theta_{ij} - G_{ij} \sin\theta_{ij}) \quad (5)$$

V_i and V_j, respectively i. load bus and j. load bus voltages, B_{ij} and G_{ij} respectively i. bus and j expresses the susceptance and conductance between the bus. On the other hand, P_{Gi} and P_{Di} are active power generation and active load demand, respectively. Q_{Gi} and Q_{Di} represent reactive power generation and reactive load demand, respectively.

Inequality Constraints:
In optimization problems, the inequality constraints represent the operating constraints of the system.

Generator Constraints: Bus voltages as well as active and reactive power generation should be limited by the plant limits.

$$P_{Gi}^{min} \le P_{Gi} \le P_{Gi}^{max} \qquad i = 1, \dots \dots N_G \quad (6)$$

$$Q_{Gi}^{min} \le Q_{Gi} \le Q_{Gi}^{max} \qquad i = 1, \dots \dots N_G \quad (7)$$

$$V_{Gi}^{min} \le V_{Gi} \le V_{Gi}^{max} \qquad i = 1, \dots \dots N_G \quad (8)$$

N_G indicates the number of system generators.

Transformer tap setting: Transformer tap setting is limited as follows.

$$T_i^{min} \le T_i \le T_i^{max} \qquad i = 1, \dots \dots, N_T \quad (9)$$

N_T indicates the number of transformers.

Reactive compensator:

$$Q_{Ci}^{min} \le Q_{Ci} \le Q_{Ci}^{max} \qquad i = 1, \dots \dots, N_C \quad (10)$$

Displays the number of N_C reactive compensators.

III. Material Method

Particle swarm optimization (PSO)

The PSO algorithm was first proposed by Kennedy and Eberhart [24]. The idea of PSO is a simplified version of a flock of birds or flock of fish. PSO is a population-based algorithm. PSO can be viewed as a single solution to each particle problem. The position of each particle is denoted by X. PSO first solutions are chosen randomly, and then PSO constantly searches for the optimum value, updating the solutions at each iteration. The fitness value of the particle is related to the objective function. The velocity of the particles is denoted by V and is composed of the global best position and local best position components. Velocity shows the directions of all particles in the next iteration. The locally best-known position is the best solution obtained among each particle so far. The position that is best known globally is the best solution among all solutions achieved. The velocities and positions of the particles vary according to the equations given below.

$$V_i^{t+1} = wV_i^t + c_p r_p (pbest_i^t - x_i^t) + c_g r_g (gbest^t - x_i^t) \quad i=1,\dots,N \quad (11)$$

$$X_i^{t+1} = X_i^t + V_i^{t+1} \quad (12)$$

V_i and X_i respectively i. is the velocity vector and the position vector of the particle. N indicates the duration size. cp and cg are cognitive coefficients and social coefficients, respectively. $c_g=c_p=2$ are random numbers ranging from r_p to r_g [0,1]. The initial weight value w given above changes depending on the iteration as follows.

$$w = wMax - 1 * (\frac{wMax - wMin}{iter}) \quad (13)$$

For this study, wMax and wMin are 0.9 and 0.4, respectively, and iter is the number of iterations.

Opposition-based particle swarm optimization

Opposition-based learning (OBL) was first proposed by Tizhoosh [25]. OBL is an easy-to-implement technique for population-based algorithms. The OBL method was used for PSO development, opposition-based particle swarm optimization (OBPSO). OBL searches for the optimal point in a search area in the opposite direction to the current available search area. Its basic logic is that while searching for solutions in one direction, solutions in the opposite direction are considered. The OBL approach is about opposite numbers definition and is given in the following equation.

$$\breve{x} = a + b - x \tag{14}$$

x is a real number varying between [a, b]. $\breve{x}$ is the opposite number of x.

Reactive power optimization with OBPSO

The ORPD implementation of the proposed OBPSO method involves finding the optimum value of the control variables to minimize the objective functions, considering the system boundaries. The steps of applying the method to the problem are as follows:

1. Define the initial values for the PSO. A swarm of N particles is defined. Each particle contains control variables such as generator voltage, transformer tap setting, reactive power device value, which will minimize the objective function. Velocity, position, and objective function values are generated from the initial swarm. In the same way, a swarm of antiparticles consisting of N particles is created by using the equation numbered 14 for the OBL method. The speed, position and objective function values for the standard flock are created in the opposite swarm.
2. For each iteration, the load flow is run and the objective function for the standard swarm and the opposite swarm is obtained. Before the end of the iteration, the standard swarm objective function and the opposite swarm objective function are compared and the swarm with the smaller objective function and its values are determined as velocity, position, and objective functions.
3. During the iterations, standard PSO operations continue, that is, if there is an improvement in Pbest and Gbest values, the update is processed, otherwise the next step is taken.
4. If the maximum iteration is reached, the program is terminated and the results are obtained, otherwise, the operations from Step 2 are continued until the maximum iteration is reached.

IV. RESULTS

To demonstrate the effectiveness of the OBPSO algorithm in solving ORPD, simulations and optimization results were obtained using MATLAB based on Intel® Core™ i7-3630QM CPU @ 2.40GHz 8GB RAM Windows 8.1. The IEEE14 bus test system is the system used to demonstrate the effectiveness of the OBPSO algorithm. For load flows of test systems, the MATPOWER package program developed by Zimmerman et al. was used for the load flows of the test systems. [26].

IEEE 14 bus test system is one of the standard test systems. This system consists of 5 generators at bus 1, 2, 3, 6, and 8, 20 transmission lines, three on-load tap changer transformers and two shunt reactive power supplies at bus 9 and 14. Bus and line information is taken from the MATPOWER package program [26].

Using the IEEE 14 bus system, the OBPSO efficiency for four cases is given in comparison with other studies.

Case 1: Power loss minimization with 10 control variables without IEEE 14 bus system sensitivity analysis,
Case 2: Voltage deviation minimization with 10 control variables without IEEE 14 bus system sensitivity analysis,

Test system results

Case 1 results

Case 1 is the case where the ORPD solution is obtained without sensitivity analysis. The primary goal of this situation is to reduce the active power loss. Bus 9 and 14 have two capacitor banks. Table 1 shows the values taken by the control variable for power loss minimization using the OBPSO method. As can be seen from the table, the control variables are within the allowed limits. The optimum value of the active power loss was obtained as 12.2131 MW with the OBPSO algorithm.

Table 1: Comparison of results for IEEE 14 bus system (power loss).

Control Variables	Base Case	PSO	GWO	PSOGSA	WOA[28]	MGTLBO [27]	FJAYA [29]	OBPSO
V_1	1.06	1.10116	1.1	1.1	1.1	1.1	1.1	1.10112
V_2	1.045	1.08702	1.08694	1.086	1.0859	1.0791	1.0862	1.08698
V_3	1.01	1.05797	1.05762	1.0567	1.0566	1.0484	1.0571	1.05776
V_6	1.07	1.10004	1.09083	1.0892	1.0858	1.0553	1.0597	1.10005
V_8	1.09	1.08896	1.1	1.1	1.1	1.0326	1.1	1.04645
$T_{4\text{-}7}$	0.9467	0.980781	0.984181	0.975	0.95853	1.01	1	0.979664
$T_{4\text{-}9}$	0.9524	0.977991	0.982438	0.975	1.0453	1.01	1	1.0105
$T_{5\text{-}6}$	0.9091	1.00516	1.0207	1.025	1.0163	1.03	1.0545	1.00598
Q_{C9}	0.18	23.3403	13.9331	7.6045	12.497	0.3	2.9986	39.1006
Q_{C14}	0.18	5.94319	4.18364	7.027	8.0161	0.07	2.9999	5.9428
P_{loss}	13.393	12.2138	12.2457	12.2504	12.255	12.3105	12.2886	12.2131
% decrease	-	8.8046	8.5664	8.5313	8.497	8.0826	8.2461	**8.8098**

The power losses obtained with Case 1 were found to be 12.2138 MW with PSO, 12.2457 MW with GWO, 12.2504 MW with PSOGSA, 12.3105 MW with MGTLBO [27], 12.255 MW with WOA [28], 12.2886 MW with FJAYA [29]. These results prove that the proposed OBPSO algorithm shows the best performance with its efficiency (12.2131 MW) power loss against other algorithms compared. The graph of the convergence curves of these algorithms is given in Figure 1.

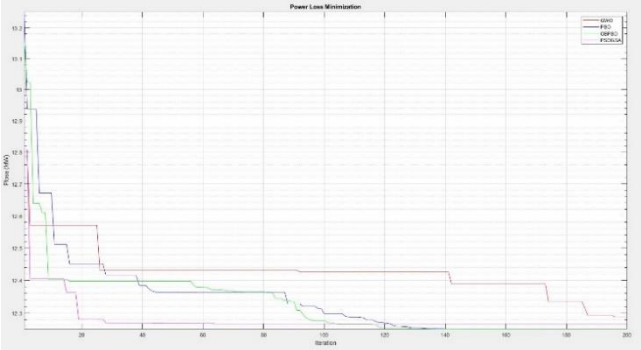

Figure 1: Power Loss Minimization.

Case 2 results

Case 2, the primary goal of this situation is to reduce the voltage deviation. Table 2 shows the values taken by the control variable for voltage deviation minimization using the OBPSO method. The voltage deviation optimum value was obtained as 0.044569 by the OBPSO algorithm.

With case 2, the voltage deviations were obtained as 0.044701 with PSO, 0.099047 with GWO, 0.079489 with PSOGSA, and 0.3826 with FJAYA. These results prove the effectiveness of the proposed OBPSO algorithm against other algorithms to which it is compared, as well as for voltage deviation. The graph of the convergence curves of these algorithms is given in Figure 2.

Table 2: Comparison of results for IEEE 14 bus system (voltage deviation).

Control Variables	Base Case	PSO	GWO	PSOGSA	FJAYA [29]	OBPSO
V_1	1.06	1.00003	0.999	1	1.1	1
V_2	1.045	0.99998	1.0212	1.03057	1.0862	1.00205
V_3	1.01	0.999982	1.0056	1	1.0571	1.00002
V_6	1.07	1.01279	1.0171	1.01513	1.0597	1.01284
V_8	1.09	1.00002	1.002	1	1.1	1.00001
T_{4-7}	0.9467	0.991354	0.97836	0.977209	1	0.98916
T_{4-9}	0.9524	1.02475	0.97596	0.975	1	1.025
T_{5-6}	0.9091	1.02485	1.025	1.025	1.0545	1.02502
Q_{C9}	0.18	26.0468	9.2207	1.48856	2.9986	26.8116
Q_{C14}	0.18	13.0796	5.0692	17.124	2.9999	12.5357
VD	0.3582	0.044701	0.099047	0.079489	0.3826	**0.044569**
% decrease	-	87.5207	72.3487	77.8088	-6.8118	87.5575

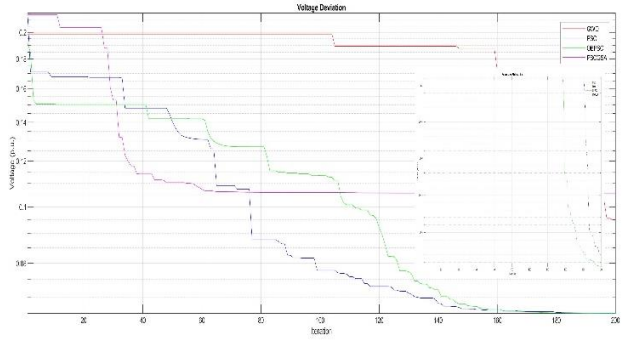

Figure 2: Voltage Deviation.

V. Conclusion

In this study, opposition-based particle swarm optimization algorithm is proposed for the solution of reactive power optimization problems. The obtained results were compared with the literature. The study with the proposed OBPSO algorithm give better results than the compared methods and studies. Reactive power optimization using the OBPSO algorithm provided 8.81% improvement for power loss in case 1 and 87.56% for voltage deviation in case 2. Considering the future, the proposed method using OBPSO algorithm is an efficient method that can be used for solving other optimization problems related to electrical power systems such as optimum capacitor placement, optimum distributed generation system placement.

References

[1] Enerdata, "Highlights from Enerdata's 2017 World Energy Trends Analysis," Enerdata, 2018. [Online]. Available: https://www.enerdata.net/system/files/publications/global-energy-trends-2017-publication.pdf

[2] S. Frank and S. Rebennack, "An introduction to optimal power flow: Theory, formulation, and examples," *IIE transactions*, vol. 48, no. 12, pp. 1172-1197, 2016.

[3] W. S. Sakr, R. A. El-Sehiemy, and A. M. Azmy, "Adaptive differential evolution algorithm for efficient reactive power management," *Applied Soft Computing*, vol. 53, pp. 336-351, 2017.

[4] D. T. Khanmiri, N. Nasiri, and S. T. Mobaraki, "Optimal reactive power dispatch by genetic algorithm and particle swarm optimization considering lost opportunities," *World Acad. Sci., Eng. Technol.*, vol. 62, pp. 871-876, 2012.

[5] V. Quintana and M. Santos-Nieto, "Reactive-power dispatch by successive quadratic programming," *IEEE transactions on energy conversion*, vol. 4, no. 3, pp. 425-435, 1989.

[6] J. Zhu and X. Xiong, "Optimal reactive power control using modified interior point method," *Electric Power Systems Research*, vol. 66, no. 2, pp. 187-192, 2003.

[7] K. Y. Lee and F. F. Yang, "Optimal reactive power planning using evolutionary algorithms: A comparative study for evolutionary programming, evolutionary strategy, genetic algorithm, and linear programming," *IEEE Transactions on power systems*, vol. 13, no. 1, pp. 101-108, 1998.

[8] R.-M. Jan and N. Chen, "Application of the fast Newton-Raphson economic dispatch and reactive power/voltage dispatch by sensitivity factors to optimal power flow," *IEEE transactions on energy conversion*, vol. 10, no. 2, pp. 293-301, 1995.

[9] S. Durairaj, D. Devaraj, and P. Kannan, "Genetic algorithm applications to optimal reactive power dispatch with voltage stability enhancement," *Journal-Institution of Engineers India Part El Electrical Engineering Division*, vol. 87, p. 42, 2006.

[10] Q. H. Wu and J. Ma, "Power system optimal reactive power dispatch using evolutionary programming," *IEEE Transactions on power systems*, vol. 10, no. 3, pp. 1243-1249, 1995.

[11] K. Ayan and U. Kılıç, "Artificial bee colony algorithm solution for optimal reactive power flow," *Applied soft computing*, vol. 12, no. 5, pp. 1477-1482, 2012.

[12] J. G. Vlachogiannis and K. Y. Lee, "A comparative study on particle swarm optimization for optimal steady-state performance of power systems," *IEEE transactions on power systems*, vol. 21, no. 4, pp. 1718-1728, 2006.

[13] B. Zhao, C. Guo, and Y. Cao, "A multiagent-based particle swarm optimization approach for optimal reactive power dispatch," *IEEE transactions on power systems*, vol. 20, no. 2, pp. 1070-1078, 2005.

[14] M. H. Sulaiman, Z. Mustaffa, M. R. Mohamed, and O. Aliman, "Using the gray wolf optimizer for solving optimal reactive power dispatch problem," *Applied Soft Computing*, vol. 32, pp. 286-292, 2015.

[15] S. Mouassa and T. Bouktir, "Artificial Bee Colony Algorithm for Discrete Optimal Reactive Power Dispatch," presented at the 2015 International Conference on Industrial Engineering and Systems Management (IESM), 2015.

[16] A. Khazali and M. Kalantar, "Optimal reactive power dispatch based on harmony search algorithm," *International Journal of Electrical Power & Energy Systems*, vol. 33, no. 3, pp. 684-692, 2011.

[17] S. Duman, U. Güvenç, Y. Sönmez, and N. Yörükeren, "Optimal power flow using gravitational search algorithm," *Energy conversion and management*, vol. 59, pp. 86-95, 2012.

[18] R. N. S. Mei, M. H. Sulaiman, Z. Mustaffa, and H. Daniyal, "Optimal reactive power dispatch solution by loss minimization using moth-flame optimization technique," *Applied Soft Computing*, vol. 59, pp. 210-222, 2017.

[19] C. Dai, W. Chen, Y. Zhu, and X. Zhang, "Reactive power dispatch considering voltage stability with seeker optimization algorithm," *Electric Power Systems Research*, vol. 79, no. 10, pp. 1462-1471, 2009.

[20] M. A. Shaheen, H. M. Hasanien, and A. Alkuhayli, "A novel hybrid GWO-PSO optimization technique for optimal reactive power dispatch problem solution," *Ain Shams Engineering Journal*, vol. 12, no. 1, pp. 621-630, 2021.

[21] N. H. Khan, Y. Wang, D. Tian, R. Jamal, M. Ebeed, and Q. Deng, "Fractional PSOGSA algorithm approach to solve optimal reactive power dispatch problems with uncertainty of renewable energy resources," *IEEE Access*, vol. 8, pp. 215399-215413, 2020.

[22] K. Mahadevan and P. Kannan, "Comprehensive learning particle swarm optimization for reactive power dispatch," *Applied soft computing*, vol. 10, no. 2, pp. 641-652, 2010.

[23] S. Rahnamayan, H. R. Tizhoosh, and M. M. Salama, "Quasi-oppositional differential evolution," in *2007 IEEE congress on evolutionary computation*, 2007: IEEE, pp. 2229-2236.

[24] R. C. Eberhart, Y. Shi, and J. Kennedy, *Swarm intelligence*. Elsevier, 2001.

[25] H. R. Tizhoosh, "Opposition-based learning: a new scheme for machine intelligence," in *International conference on computational intelligence for modelling, control and automation and international conference on intelligent agents, web technologies and internet commerce (CIMCA-IAWTIC'06)*, 2005, vol. 1: IEEE, pp. 695-701.

[26] R. D. Zimmerman, C. E. Murillo-Sánchez, and R. J. Thomas, "MATPOWER: Steady-state operations, planning, and analysis tools for power systems research and education," *IEEE Transactions on power systems*, vol. 26, no. 1, pp. 12-19, 2010.

[27] M. Ghasemi, M. Taghizadeh, S. Ghavidel, J. Aghaei, and A. Abbasian, "Solving optimal reactive power dispatch problem using a novel teaching–learning-based optimization algorithm," *Engineering Applications of Artificial Intelligence*, vol. 39, pp. 100-108, 2015.

[28] K. ben oualid Medani, S. Sayah, and A. Bekrar, "Whale optimization algorithm based optimal reactive power dispatch: A case study of the Algerian power system," *Electric Power Systems Research*, vol. 163, pp. 696-705, 2018.

[29] M. G. Gafar, R. A. El-Sehiemy, and H. M. Hasanien, "A novel hybrid fuzzy-JAYA optimization algorithm for efficient ORPD solution," *IEEE Access*, vol. 7, pp. 182078-182088, 2019.

Parallel Operation of Single-Phase Inverters in Islanded Microgrids

M. N. ISIK[1], M. UCAR[2], E. AVCI[3]

[1]Duzce University, Duzce/Turkey, muhammednurisik@gmail.com
[2]Duzce University, Duzce/Turkey, mehmetucar@duzce.edu.tr
[3]Duzce University, Duzce/Turkey, emreavci@duzce.edu.tr

Abstract **- In this study, a droop control method based active and reactive power sharing for parallel connected single-phase inverters in islanded microgrids is presented. The droop control is the optimal choice for wireless control of parallel connected inverter based distributed generators (DGs). However, conventional droop control is poor power sharing in islanded microgrids as the distribution lines impedance is largely resistive. Therefore, in this paper, $P-E$ and $Q-\omega$ droop control method is selected for the parallel operated single-phase inverters. In addition, the control technique of these inverters contains a current control loop and a voltage control loop to follow the reference voltage. Finally, PSIM simulation results are presented to show the active and reactive power sharing performance among parallel connected two 1 kVA single-phase inverters.**

Keywords **- Islanded microgrid, droop control, distributed generators (DGs), active and reactive power sharing, single-phase inverter.**

I. INTRODUCTION

Microgrids are small-scale distribution systems with distributed generation (DGs) units, storage devices and local loads [1]. Microgrids may be operated in grid-connected mode and islanded mode [2]. In grid-tied mode, the DG converters are grid-following for the current control. In islanded operation mode, the DG converters are grid-forming for the voltage control and the power sharing [3]. Line impedances of distribution networks vary according to voltage values. Table 1 shows typical line impedance values based on voltage level [4]. Generally, the line impedances are largely resistive in low voltage microgrids [5].

Table 1: Line impedances based on voltage values.

Line type	R [Ω/km]	X [Ω/km]	R/X
Low Voltage	0.642	0.083	7.7
Medium Voltage	0.161	0.190	0.85
High Voltage	0.06	0.191	0.31

Parallel operation of DG inverters is an important feature in microgrids [6, 7]. Droop control technique is a widely used for parallel operation of the inverters. The primary importance feature of the droop control method is that it does not use physical communication between inverters. Inverters have their own controller that only uses output current and voltage signals [8, 9]. The droop control has varied properties for the line impedance types. Active power-frequency $(P-\omega)$ and reactive power-voltage $(Q-E)$ droop control strategy is normally preferred in conventional grid for parallel operated distributed generation inverters [10, 11]. This coupling is acceptable in inductive distribution networks. However, mostly microgrids are mainly resistive for low-voltage distribution networks [4]. In resistive distribution grids, there is a natural coupling between P and E. Hence, active power-voltage $(P-E)$ drop controllers are preferred in resistive microgrids [12, 13]. Active power control in the $P-E$ droop controllers occur with the output voltage of the inverters.

In this study, $P-E$ and $Q-\omega$ droop control method is selected for load sharing in resistive microgrids. Two parallel operated inverters with resistive line impedances are demonstrated in Figure 1.

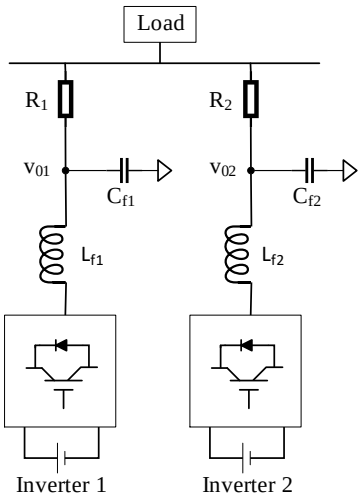

Figure 1: Parallel operation of the with resistive line impedances.

II. Droop Controlled Single-Phase Inverters

In general, interior impedance of an inverter is inductive for the large output inductor and the high inductive line impedance caused by the long distance between the parallel connected inverters. On the other hand, in low voltage microgrids the line impedance is essentially resistive [11, 13]. Two inverters operating in parallel with resistive line impedances are demonstrated in Figure 2.

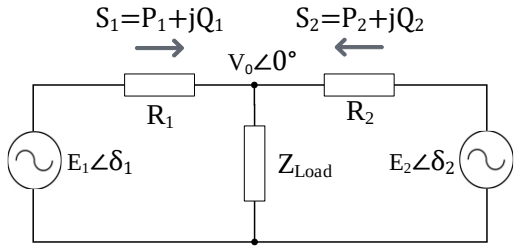

Figure 2: Two inverters operating in parallel with resistive line impedances.

Because the low voltage line impedance R/X ratio is high, the active and reactive power equations are simplified as in (1) and (2) [11]. In these equations, δ is the power angle among the output voltage amplitude E of the inverter and the common connection voltage V, and R is the simplified resistive output line impedance. There is a natural coupling between P and E in resistive distribution network.

$$P = \frac{V}{R}(E - V) \quad (1)$$

$$Q = -\frac{EV}{R} sin\delta \quad (2)$$

The $P - \omega$ and $Q - E$ droops are used for the inverter inductive output impedance. $P - E$ and $Q - \omega$ drops are also used for the inverter resistive output impedance. Thus, inverter frequency is controlled by the reactive power and the voltage amplitude is controlled by the active power in low-voltage single-phase microgrids [11, 14]. The active and reactive power control loops operate according to the resistive drop method and allows active and reactive powers to be shared among inverters in proportion to their rated values [11]. Droop control features with largely resistive line impedance is indicated in Figure 3.

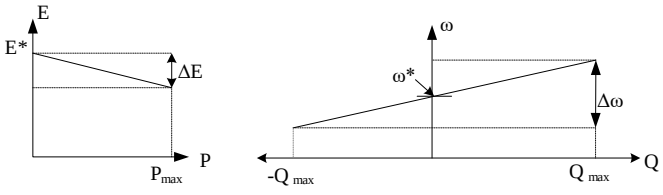

Figure 3: Droop control features with largely resistive line impedance.

Considering the line impedance is largely resistive, the drop control technique is expressed as in (3) and (4). In these equations E_o^* and ω_o^* are the reference output voltage amplitude and frequency of the inverters at no load condition and n and m are the droop coefficients for the voltage and frequency.

$$E = E_o^* - nP \quad (3)$$

$$\omega = \omega_o^* + mQ \quad (4)$$

III. Simulation Results

In this study, parallel operated single-phase inverters are simulated in PSIM software so as to validate load sharing. The single-phase inverters are a full bridge structure with switching frequency of 20 kHz and a LC filter with inductor of 3 mH, capacitor of 15 μF. The apparent power of the inverters is 1 kVA with input voltage of 650V dc, nominal output voltage of 230 Vrms and frequency of 50 Hz. The mainly resistive line impedances have equal values of 0.3+ j0.04 Ω. The inductive load is considered with apparent power of 1 kVA and power factor of 0.8. PSIM block diagram of main circuits is illustrated in Figure 4.

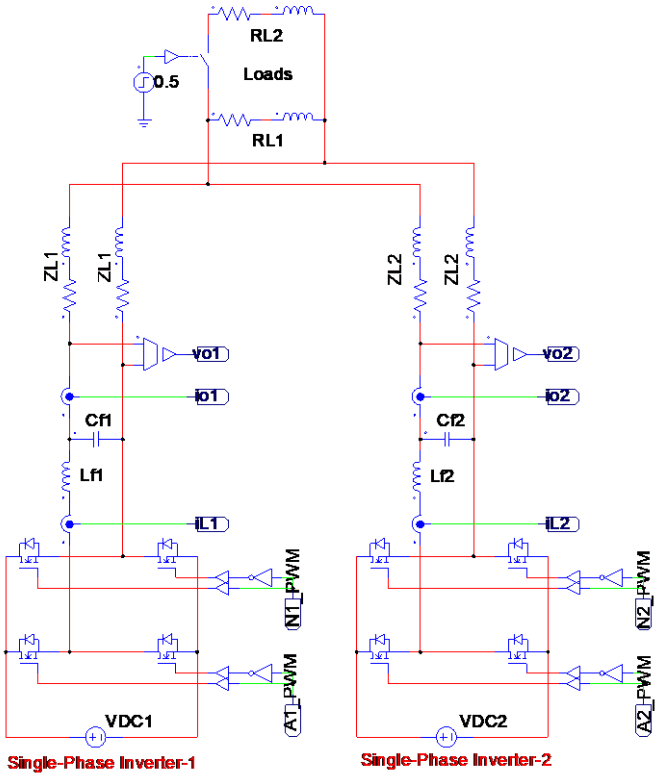

Figure 4: PSIM block diagram of main circuits.

PSIM circuit scheme of droop control is demonstrated in Figure 5. Average active and reactive power values are obtained with first-order low-pass filters with cut-off frequency of 20π rad/s.

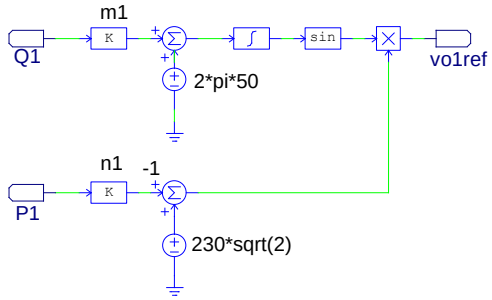

Figure 5: PSIM circuit scheme of droop control.

The inverters are controlled with cascaded proportional resonant (PR) based voltage control method [14, 15]. PSIM circuit diagram of cascaded voltage control technique is indicated in Figure 6.

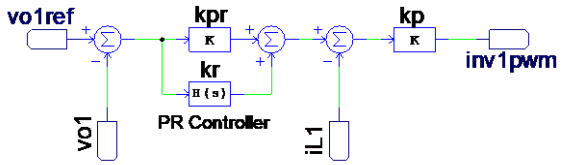

Figure 6: PSIM circuit diagram of cascaded voltage control method.

For the current control loop, a proportional controller with gain k_p is used. The k_p value is determined as to obtain resonance dumping. Also, the PR controller-based voltage control loop is used to provide output voltage regulation [16]. The PR controller transfer function is given (5).

$$G_{PR}(s) = k_{pr} + \frac{k_r \omega_c s}{s^2 + 2\omega_c s + \omega_1^2} \quad (5)$$

In this equation, k_{pr} is proportional gain, k_r is resonant gain and ω_c is the cut-off frequency. Where, k_{pr} adjusts controller speed, k_r reduces the steady-state error, and ω_c determines the bandwidth of resonant block [16]. General system parameters and values are given in Table 2.

Table 2: System parameters and values.

Parameter	Symbol	Value	Unit
Inverter power	S_{I1}, S_{I2}	1	kVA
Nominal amplitude	E_1^*, E_2^*	$230\sqrt{2}$	V
Nominal frequency	ω_1^*, ω_2^*	$2\pi 50$	Hz
$P-E$ coefficient	n_1, n_2	0.016	V/W
$Q-\omega$ coefficient	m_1, m_2	0.0031	(rad/s)/VAr
Line impedance	Z_{L1}, Z_{L2}	0.3 + j0.04	Ω
Load power	S_{L1}, S_{L2}	0.8 + j0.6	kVA

So as to demonstrate performance of the $P-E$ and $Q-\omega$ droop control method, parallel connected two single-phase inverter are simulated in the PSIM environment. The inverter reference voltage amplitudes and frequencies are shown in Figure 7. The active and reactive power waveforms provided by each inverter are demonstrated in Figure 8. Also, Figure 9 indicates the load voltage and current waveforms at the common bus.

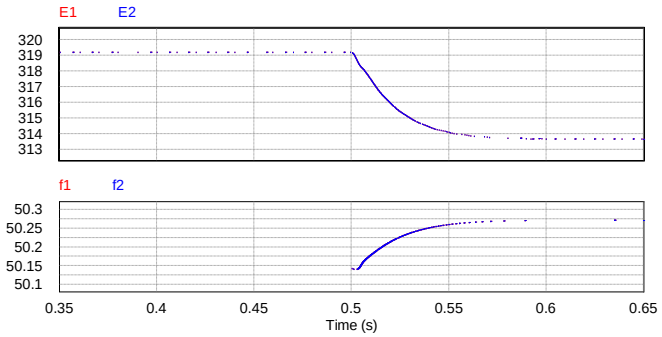

Figure 7: Reference voltage amplitude and frequency waveforms.

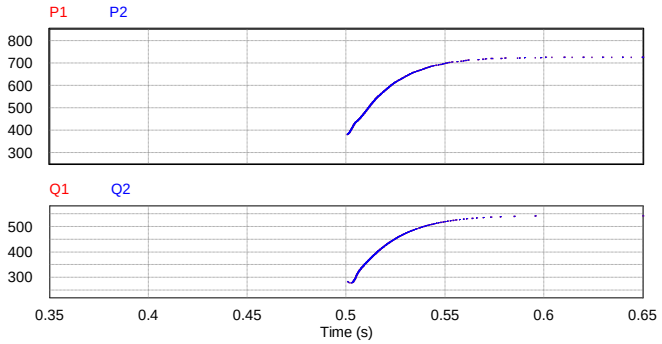

Figure 8: Provided active and reactive power waveforms.

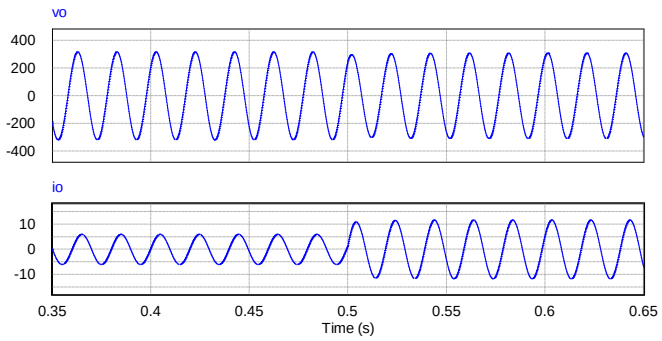

Figure 9: Load voltage and current waveforms.

As seen from the Figures obtained from the PSIM software when loads are activated, active powers increase and voltage amplitudes decrease. The reactive powers are increasing and the frequencies are also increasing. Thus, active and reactive powers are shared approximately equally among the two single-phase inverters connected in parallel.

IV. Conclusions

This paper presents the $P-E$ and $Q-\omega$ droop control method for parallel operated single-phase inverters in the condition of largely resistive islanded microgrids. Also, the cascaded control method is applied as an inner current control loop and an outer PR based voltage control loop in order to follow the reference voltage value. The obtained simulation results from the PSIM software verify the active and reactive power sharing among parallel operated two 1 kVA single-phase inverter for the low voltage islanded microgrid.

REFERENCES

[1] R. H. Lasseter and P. Paigi, "Microgrid: a conceptual solution," *IEEE 35th Annual Power Electronics Specialists Conference*, 2004, pp. 4285-4290 Vol. 6.

[2] S. Barsali, M. Ceraolo, P. Pelacchi and D. Poli, "Control techniques of Dispersed Generators to improve the continuity of electricity supply," *IEEE Power Engineering Society Winter Meeting*, 2002, pp. 789-794 vol.2.

[3] J. Rocabert, A. Luna, F. Blaabjerg and P. Rodríguez, "Control of Power Converters in AC Microgrids," in *IEEE Transactions on Power Electronics*, vol. 27, no. 11, pp. 4734-4749, Nov. 2012.

[4] A. Engler, "Applicability of droops in low voltage grids," *Int. J. Distrib. Energy Resour. Smart Grids*, no. 1, pp. 1–5, 2005.

[5] L. S. Araújo, D. I. Narváez, T. G. Siqueira and M. G. Villalva, "Modified droop control for low voltage single phase isolated microgrids," *IEEE International Conference on Automatica (ICA-ACCA)*, 2016, pp. 1-6.

[6] M. C. Chandorkar, D. M. Divan and R. Adapa, "Control of parallel connected inverters in standalone AC supply systems," *IEEE Transactions on Industry Applications*, vol. 29, no. 1, pp. 136-143, Jan.-Feb. 1993.

[7] A. Tuladhar, Hua Jin, T. Unger and K. Mauch, "Control of parallel inverters in distributed AC power systems with consideration of line impedance effect," *IEEE Transactions on Industry Applications*, vol. 36, no. 1, pp. 131-138, Jan.-Feb. 2000.

[8] K. De Brabandere, B. Bolsens, J. Van den Keybus, A. Woyte, J. Driesen and R. Belmans, "A Voltage and Frequency Droop Control Method for Parallel Inverters," *IEEE Transactions on Power Electronics*, vol. 22, no. 4, pp. 1107-1115, July 2007.

[9] H. Han, X. Hou, J. Yang, J. Wu, M. Su and J. M. Guerrero, "Review of Power Sharing Control Strategies for Islanding Operation of AC Microgrids," *IEEE Transactions on Smart Grid*, vol. 7, no. 1, pp. 200-215, Jan. 2016.

[10] J. M. Guerrero, J. Matas, L. Garcia De Vicunagarcia De Vicuna, M. Castilla and J. Miret, "Wireless-Control Strategy for Parallel Operation of Distributed-Generation Inverters," *IEEE Transactions on Industrial Electronics*, vol. 53, no. 5, pp. 1461-1470, Oct. 2006.

[11] J. M. Guerrero, J. Matas, L. Garcia de Vicuna, M. Castilla and J. Miret, "Decentralized Control for Parallel Operation of Distributed Generation Inverters Using Resistive Output Impedance," *IEEE Transactions on Industrial Electronics*, vol. 54, no. 2, pp. 994-1004, April 2007.

[12] L. Vandoorn, J. D. M. De Kooning, B. Meersman, J. M. Guerrero and L. Vandevelde, "Automatic Power-Sharing Modification of P/V Droop Controllers in Low-Voltage Resistive Microgrids," *IEEE Transactions on Power Delivery*, vol. 27, no. 4, pp. 2318-2325, Oct. 2012.

[13] Q. Zhong, "Robust Droop Controller for Accurate Proportional Load Sharing Among Inverters Operated in Parallel," *IEEE Transactions on Industrial Electronics*, vol. 60, no. 4, pp. 1281-1290, April 2013.

[14] X. Yu, A. M. Khambadkone, H. Wang and S. T. S. Terence, "Control of Parallel-Connected Power Converters for Low-Voltage Microgrid—Part I: A Hybrid Control Architecture," *IEEE Transactions on Power Electronics*, vol. 25, no. 12, pp. 2962-2970, Dec. 2010.

[15] G. M. S. Azevedo, M. C. Cavalcanti, F. A. S. Neves, P. Rodriguez and J. Rocabert, "Performance improvement of the droop control for single-phase inverters," *IEEE International Symposium on Industrial Electronics*, 2011, pp. 1465-1470.

[16] G. Mazzanti, M. Karimian, E. Chiodo, D. Lauria and A. Rabiee, "Accurate design of controllers in a parallel single-phase inverter system of distributed generators sharing linear and non-linear loads," *International Conference on Clean Electrical Power (ICCEP)*, 2015, pp. 1-8.

Design of a Synchronous Four Switch Buck-Boost Converter for Portable Communication Systems

O.TEK[1,2] and D.A.KOCABAŞ[3]

[1]Aselsan Inc., Ankara/Turkey, onurtek@aselsan.com.tr
[2]Istanbul Technical University, Istanbul/Turkey, tek19@itu.edu.tr
[3]Istanbul Technical University, Istanbul/Turkey, kocabasde@itu.edu.tr

***Abstract* - In portable industrial and military communication devices such as mobile phones, hand radios, satellite radios etc. batteries are used as power source. Digital, RF and other electronic circuits in these systems operate at a constant regulated DC voltage. Due to the variable voltage of the batteries (12 V DC – 35 V DC) a power electronic buck-boost converter is necessary to convert this variable input voltage to a constant regulated output voltage. With the increasing power demand in all around the world, electronic systems should be energy efficient especially in power electronic converters. In traditional two switch buck-boost converter topology, the stresses and losses are higher therefore the efficiency becomes lower. In order to reduce these high stresses and losses four switch synchronous buck-boost topologies are proposed. The buck-boost converters are operated in buck, buck-boost and boost modes with respect to the output voltage is higher or lower than or substantially equal to the input voltage. In this study, a four switch synchronous buck-boost converter was designed with 28 V DC constant output voltage, 250 W rated power and high efficiency and power density to be used in portable communication systems. Within the scope of the study, the design methodology, practical implementation of a buck-boost converter to be used in portable communication systems for a constant regulated 28 V DC output voltage was given. The converter was designed for 12 V DC – 35 V DC variable input voltage and the output voltage ripple is lower than 5% in buck, buck-boost and boost modes at full load. Also, in mode transitions and 10% to 90% of full load transitions voltage ripple is lower than 5% of the regulated output voltage. Besides, the effect of the change in switching frequency was also studied since it has major effect on circuit size, losses, efficiency and voltage ripple.**

***Keywords* - DC-DC converter, buck-boost converter, efficiency, ripple, switching frequency**

I. INTRODUCTION

ADVANCES in battery technologies have also led to the development of portable electronic devices. The most common industrial portable devices are mobile phones, navigation devices, power banks and in the military side handheld radios, software defined tactical radios and manpack satellite communication terminals can be given as examples [1]. There are many types of batteries with wide voltage range, the voltage range of batteries that used in military applications is 12 V DC to 16.8 V DC [2], [3]. In portable military communication systems, generally two batteries are used in series. When batteries are used as a power source, battery voltage decreases over time depending on the type of usage and the battery itself [4], [5]. In this case, a military portable communication system must have the capability to operate both when there is a single battery with a voltage drop decreased to 12 V DC and when two batteries are connected in series with a voltage increased up to 33.6 V DC.

Portable communication systems consist of many electronic circuits such as power distribution, digital, RF, antenna etc. and all of these electronic circuits operate with a constant regulated DC voltage. Therefore, in these systems there is a need for a power electronics circuit that converts the variable input voltage from the battery to a constant regulated output voltage. Commonly, buck-boost topologies are used where the output voltage is higher, lower or substantially equal to the input voltage [6]. In addition to buck-boost topologies, the single-ended primary inductance converters can be an alternative but because of the use of two inductors and two capacitors in this topology, the use of buck-boost topologies is more common in the view of its both cost effective and less number of the circuit elements [7].

Since the power source in portable communication systems is batteries, it is aimed to use the batteries for a longer time by efficient operation of the device. One of the most important parameters when designing a DC to DC power converter is efficiency. Non-ideal characteristics of the circuit elements, parasitics, switching and conduction losses in power switches directly affects the efficiency [8]. Another point to be considered is the output voltage ripple. Due to the sensitivity of the circuits to be supplied by the DC to DC converter, the output voltage ripple must be lower than a certain percentage of regulated output voltage set as the design target. In addition, the dynamic performance of the converter during mode transitions, instantaneous load and input voltage changes are the design aspects to be considered during the design.

In this paper, the design methodology of a four switch synchronous buck-boost converter (FSSBBC) to be used in portable communication devices is given and results for practical implementation are presented in comparison for different operational scenarios. A design with a low stress on the circuit elements serving a high efficiency is achieved and tested.

II. OPERATION

Conventional two switch non-inverting buck-boost converters consist of two MOSFETs and two diodes. Due to the structure of the diodes, the converter does not operate synchronously, relatedly, efficiency decreases especially in

the power loss of diodes. In a four switch non-inverting buck-boost converter, two diodes in two switch topology are replaced with the MOSFETs and the converter operates synchronously by controlling all of four switches. Since the conduction losses of the MOSFETs are lower than the diodes, the efficiency becomes higher than the two switch topologies. The structures of two switch and four switch non-inverting buck-boost converters are shown in Figure 1.

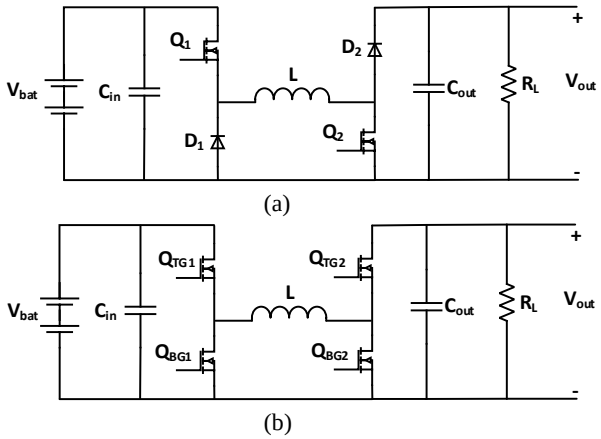

Figure 1: (a) Two Switch Non-Inverting Buck-Boost Converter (b) Four Switch Non-Inverting Buck-Boost Converter

When the output voltage is lower than the input voltage, the FSSBBC operates in buck mode. At the beginning of every switching cycle Q_{TG2} remains in conduction continuously while the Q_{BG2} is kept off. Q_{TG1} and the synchronous MOSFET Q_{BG1} are in switching mode with pulse-width modulation (PWM) method. When the output voltage is higher than the input voltage, the FSSBBC operates in boost mode. At the beginning of every switching cycle Q_{TG1} remains in conduction continuously while the Q_{BG1} is kept off. Q_{BG2} and the synchronous MOSFET Q_{TG2} are in switching mode with PWM method. When the output voltage is close to or substantially equal to the input voltage, the FSSBBC operates in buck-boost mode. In this case, all of four MOSFETs are in switching mode with PWM method. The waveforms of gate signals of the MOSFETs and the inductor current waveform for each mode are shown in Figure 2 [9].

In buck mode, duty cycle (D_{buck}), minimum inductance ($L_{min,buck}$), minimum capacitance ($C_{min,buck}$) are calculated as in (1), (2) and (3), respectively, where V_{out} is output voltage, V_{bat}, input battery voltage, R_{Lmax}, the maximum output load, f_s, switching frequency, $V_{cpp,}$ the voltage ripple across the capacitance.

$$D_{buck} = \frac{V_{out}}{V_{bat}} \tag{1}$$

$$L_{\min,buck} > \frac{R_{L\max}(1-D_{buck})}{2f_s} \tag{2}$$

$$C_{\min,buck} > \frac{(1-D_{buck})V_{out}}{8f_s^2 L_{buck} V_{cpp}} \tag{3}$$

In boost mode, duty cycle (D_{boost}), minimum inductance ($L_{min,boost}$), minimum capacitance ($C_{min,boost}$) are calculated are calculated as in (4), (5) and (6), respectively, where $I_{o,max}$ is maximum output current.

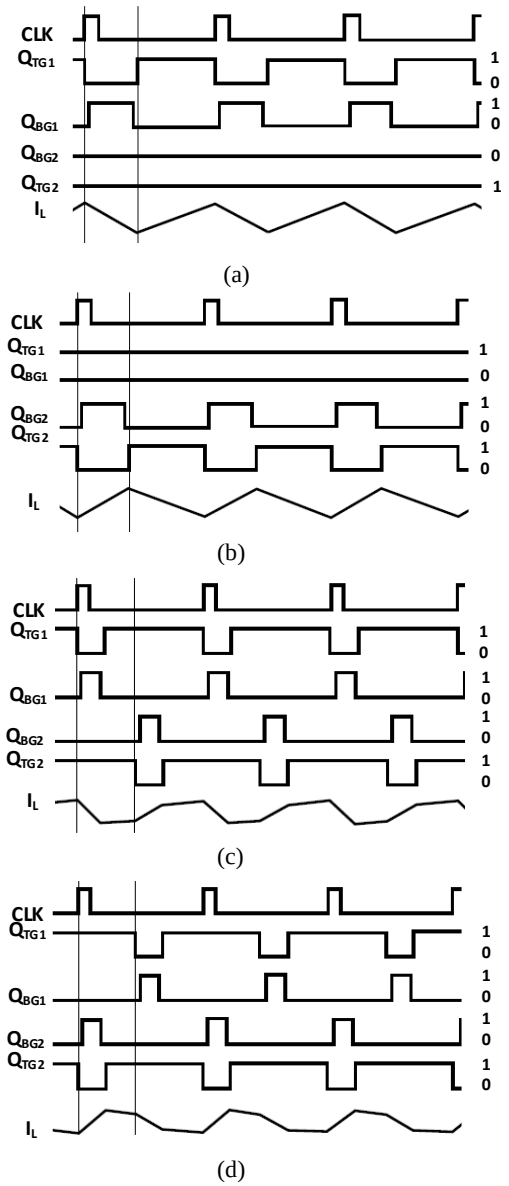

Figure 2: Switching and Inductor Current Waveforms (a) Buck Mode ($V_{out} < V_{bat}$) (b) Boost Mode ($V_{out} > V_{bat}$) (c) Buck-Boost Mode ($V_{bat} \geq V_{out}$) (d) Buck-Boost Mode ($V_{bat} \leq V_{out}$)

$$D_{boost} = \frac{V_{out} - V_{bat}}{V_{out}} \tag{4}$$

$$L_{\min,boost} > \frac{R_{L\max} D_{boost}(1-D_{boost})^2}{2f_s} \tag{5}$$

$$C_{\min,boost} > \frac{I_{o,\max} D_{\max}}{f_s V_{cpp}} \tag{6}$$

In FSSBBC topologies, essentially analog and digital based controllers are used to control the current and the voltage. In voltage mode control, the output voltage is compared with the reference voltage and an error voltage is obtained. This error voltage is amplified and compared with the saw-tooth waveform to generate the PWM signal. In current mode control, the amplified error voltage is compared with the inductor current mapped into a proportional voltage ramp instead of the saw-tooth waveform, then the PWM signal is generated. There are several current mode control techniques, but the most common one is fixed frequency peak current mode control with fixed slope compensation ramp [10].

The most important factor affecting the efficiency is the power losses due to the non-ideal characteristics of the circuit elements. Most of these losses consist of the conduction losses due to drain to source resistance of MOSFETs and switching losses due to the total gate charge of the MOSFETs. Also, the conduction losses due to the equivalent series resistances of switching inductor and capacitors exist. An additional power loss come from sensing resistors, printed circuit board traces, integrated circuit and diodes.

In (7)-(10), the power losses of Q_{TG1}, Q_{BG1}, Q_{BG2} and Q_{TG2} consisting of conduction and switching losses are given where $R_{ds(on)}$ represents the drain-source resistance of MOSFET while in conduction, ρ_τ represents the normalized on resistance of MOSFET varying with the junction temperature and t_{RF} represents the average of the switching node pin rise and fall times. The first parts of (7) and (9) refer the conduction losses and the seconds parts refer the switching losses. As seen in (8) and (10), the conduction losses of and are dominant [9].

$$P_{TG1} \cong \frac{V_{out}}{V_{in}} I_{out}^2 R_{ds(on)} \rho_\tau + V_{in} I_{out} f_s t_{RF1} \quad (7)$$

$$P_{BG1} \cong \frac{V_{in} - V_{out}}{V_{in}} I_{out}^2 R_{ds(on)} \rho_\tau \quad (8)$$

$$P_{BG2} \cong \frac{(V_{out} - V_{in}) V_{out}}{V_{in}^2} I_{out}^2 R_{ds(on)} \rho_\tau + V_{out}^2 I_{out} f_s \frac{t_{RF}^2}{V_{in}} \quad (9)$$

$$P_{TG2} \cong \frac{V_{out}}{V_{in}} I_{out}^2 R_{ds(on)} \rho_\tau \quad (10)$$

III. DESIGN, IMPLEMENTATION AND TEST RESULTS

The proposed FSSBBC specifications are given in Table 1. In accordance with the FSSBBC topology, the analog current mode control method was selected. For this purpose, the controller with part number LT8705A of Analog Devices was used [9]. Due to the high output power, all switching operations are in forced continuous mode. LTspice tool was used for the simulations.

Table 1: Design Specifications

Minimum Input Voltage	12 V DC
Nominal Input Voltage	24 V DC
Maximum Input Voltage	35 V DC
Output Voltage	28 V DC
Output Power	250 W
Switching Frequency	280 kHz
Voltage Ripple	<5%

In accordance with the design specifications and the equations (2) and (5) 5.6 µH inductor was selected. For the input and output capacitors 2x440 µF was selected in order to reduce the ripple. Since the current mode controller is used, the sense resistor which is used to sense inductor current was selected as 4mΩ to be used in two parallels.

In simulation, 12 V DC input voltage in boost mode, 28 V DC input voltage in buck-boost mode, 35 V DC input voltage in buck mode the output voltage waveforms under full load are shown in Figure 3. In order to reduce the simulation time, the soft start time of the controller is less than the experimental implementation.

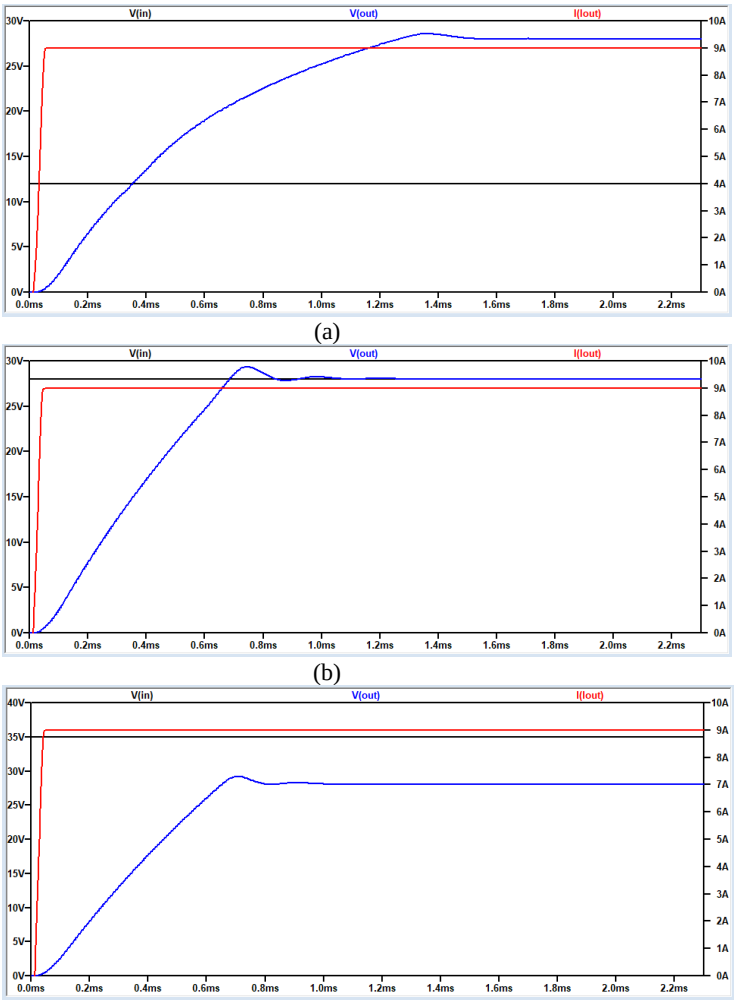

Figure 3: Output Voltage Waveforms (a) V_{in}=12 V DC (b) V_{in}=28 V DC (c) V_{in}=35 V DC

In order to meet the design specifications calculated for the experimental implementation, CSD18563Q5A 60V N-Channel MOSFET of Texas Instruments company was used as switching MOSFETs considering the silicon-type, low drain to source resistance and low gate charge [11]. For inductor IHLP6767GZER5R6M01 of Vishay company was selected considering low dimensions and volume, low equivalent series resistance, high rated and saturation currents [12]. For input and output capacitors A759MX447M1HAAE028 of Kemet company was selected considering the voltage, low dimensions, low equivalent series resistance and low change in equivalent series resistance with temperature [13]. In Figure 4, the switching waveforms are given for all three modes. The measured signals are consistent with the waveforms given in Figure 1. The difference in signal levels between Figure 1 and Figure 4 is related to the measurements which are taken as gate to ground instead of gate to source in the experiments. The targeted switching frequency in the design, 280 kHz, was measured at approximately 285 kHz in the experiments. The tolerances of the components and measuring devices can be considered as the reason for this difference.

In Table 2 shows that the experimental results of output voltage, efficiency and ripple for different input voltages under full load. The ripple is lower than the design target 5% of output voltage at all input voltages. At 24 V DC, 28 V DC and 35V DC input voltages, the efficiency is higher than

96% and the power loss is approximately 10W. At the 12 V DC input voltage, conduction losses become higher due to the high input current and the efficiency is approximately 91%. In this condition, the power loss of 25W is at a level that can be tolerated with the approximate thermal interface and cooling.

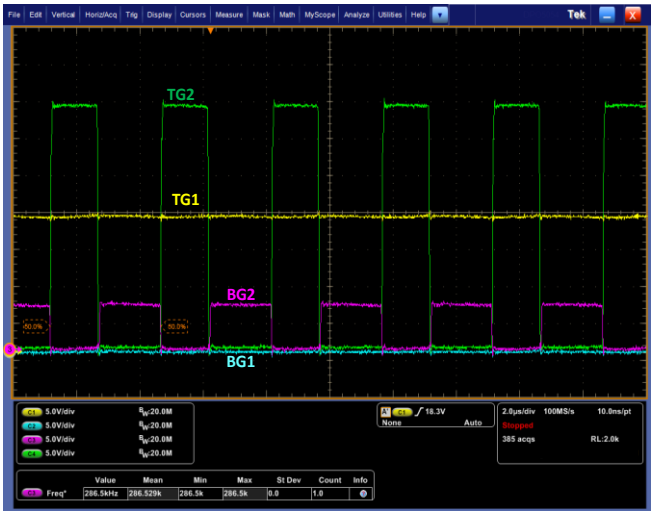

(a)

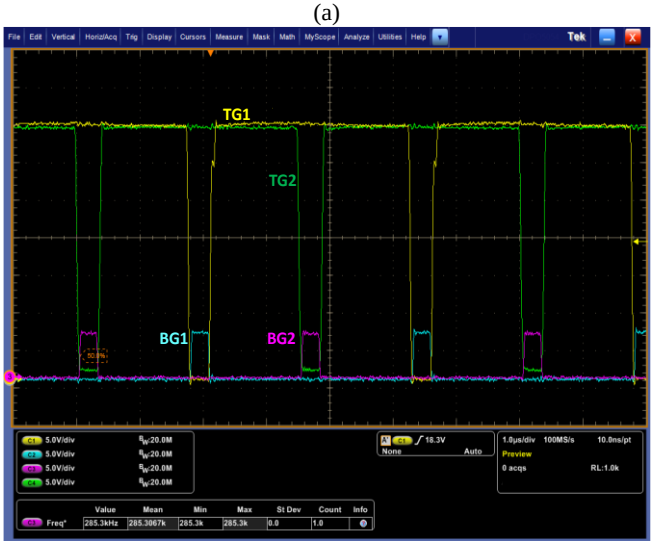

(b)

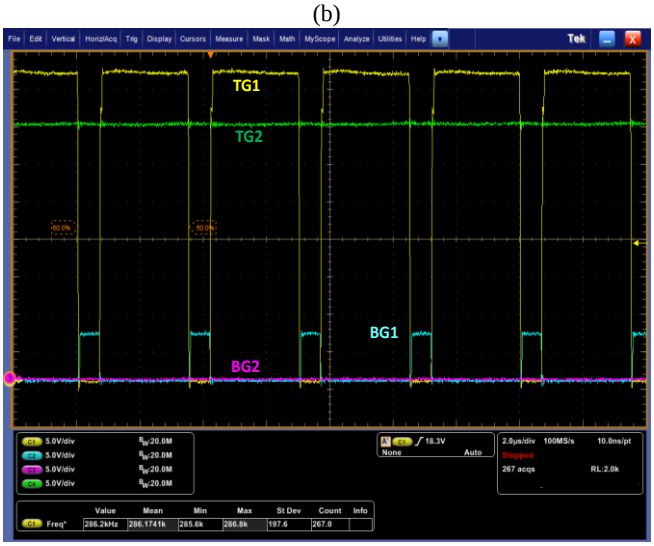

(c)

Figure 4: Switching Waveforms of MOSFETs (a) V_{in}=12 V DC (b) V_{in}=28 V DC (c) V_{in}=35 V DC

Table 2: Efficiency and Ripple Measurements

Input Voltage (V)	Output Power (W)	Output Voltage (V)	Efficiency (%)	Output Ripple (%)
12	250	28	90,85	2.04
24	250	28	98,05	0.72
28	250	28	97,49	1.20
35	250	28	98,37	0.33

At 12 V DC, 28 V DC and 35 V DC input voltages, the load response of the FSSBBC is measured from 0.9 A which is the 10% of the full load to 8.1 A which is the 90% of the full load with the duration of 10ms for each load value. In 35 V DC input voltage in DC coupling, output voltage in AC coupling and output current waveforms are shown in Figure 5.

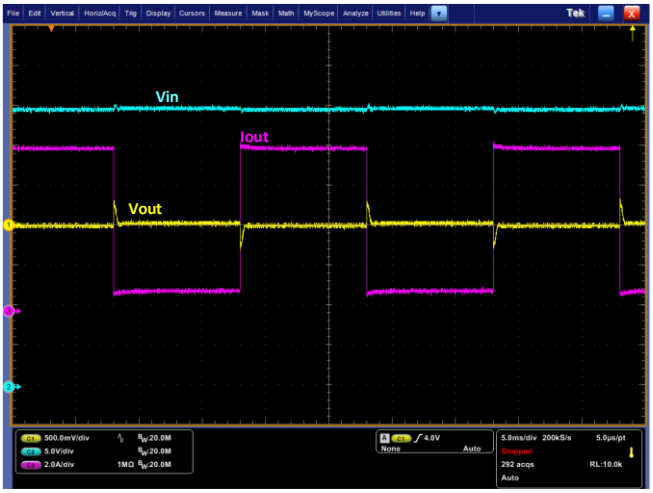

Figure 5: Load Change of FSSBBC

As given in Table 3, the peak to peak output voltage changes at load transition values at all input voltages are less than 5% of the output voltage.

Table 3: Load Change Measurements

Input Voltage (V)	Output Current Transition (A)	Peak to Peak Output Voltage Change at Load Transition (%)
12	0.9 to 8.1	2,29
12	8.1 to 0.9	1,96
28	0.9 to 8.1	2,03
28	8.1 to 0.9	1,45
35	0.9 to 8.1	1,12
35	8.1 to 0.9	1,00

In order to measure the instantaneous input voltage change of the FSSBBC, the input voltage was changed between 14 V DC, 28 V DC and 35 V DC under full load and peak to peak output voltage changes were measured. Due to the current limit of the programmable power supply that used during the experiments, measurements could be taken at minimum 14 V DC in this test. Input voltage changes, output voltage and the output current waveforms are shown in Figure 6.

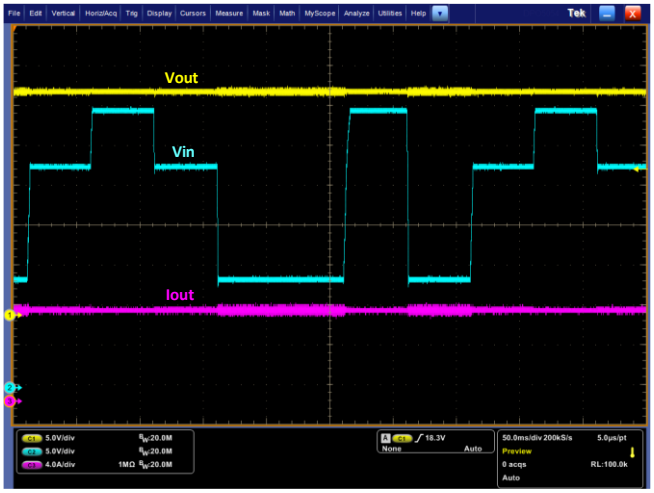

Figure 6: Input Voltage Change of FSSBBC

As given in Table 4, peak to peak output voltage changes at full load at the input voltage transitions are less than 5% of the output voltage.

Table 4: Input Voltage Change Measurements

Input Voltage Transition (V)	Output Power (W)	Peak to Peak Output Voltage Change at Voltage Transition (%)
14 to 28	250	1.90
14 to 35	250	2.01
28 to 14	250	2.00
28 to 35	250	1.50
35 to 14	250	2.59
35 to 28	250	2.32

In order to observe the effect of the switching frequency on the efficiency, the switching frequency of the FSSBBC was changed in 20 kHz steps between 230 kHz and 330 kHz and the efficiency was measured at each switching frequency at 12 V DC, 28 V DC and 35 V DC input voltages. As given in Figure 7, as the switching frequency increases, the FSSBBC efficiency decreases because the switching losses in MOSFETs increase. The highest efficiency of all three different input voltages was achieved at 230 kHz. According to (3) and (6), as the switching frequency increases the voltage ripple also increases. In this case, an optimum switching frequency should be selected considering the efficiency and the voltage ripple parameters. In our study, the switching frequency was selected as 280 kHz.

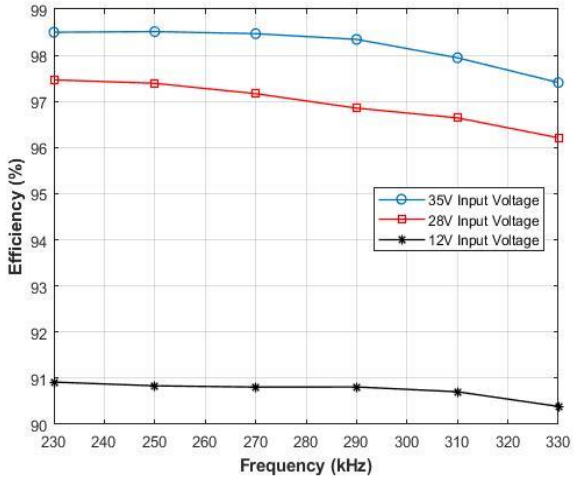

Figure 7: Switching Frequency vs. Efficiency

IV. CONCLUSION

In this study, a non-inverting four switch synchronous buck-boost converter for portable military communication devices with high power density and high efficiency was proposed. Proposed circuit performance for different modes was supported by both simulation and experimental data and the design targets was shown to be achieved and the results were presented in comparison. All-in-all, owing to the achievement of high efficiency levels, the proposed FSSBBC can increase the battery life and thus longer communication will be possible especially for portable communication systems where batteries are used as power source.

REFERENCES

[1] *Military Communication Systems Catalog*, Aselsan Inc., Ankara,2021

[2] *UBI-2590 LE SMBus Preliminary Technical Datasheet*, Ultralife Corp., NY, 2019

[3] A. Oudalov, T. Buehler, D. Chartouni, "Utility scale applications of energy storage," *IEEE Energy 2030 Conference*, 2008

[4] N.B. North, "Synthesis of battery – load operating characteristics," *IEEE Transactions on Aerospace*, vol. 2, issue 2, pp. 780-783, 1964

[5] T. Robbins, J. Hawkins, "Battery model for overcurrent protection simulation of DC distribution systems," *Proceedings of Intelec*, pp. 307-314, 1994

[6] J.G. Kassakian, M.F. Schlecht and G.C. Verghese, *Principles of Power Electronics*. Addison-Wesley, 1992

[7] B. Sahu and G.A. Rincon-Mora, "A low voltage, dynamic, non-inverting, synchronous buck-boost converter for portable application," *IEEE Transactions on Power Electronics*, vol. 19, no 2, pp. 443-452, 2004

[8] B. Arbetter, R. Erickson and D.Maksimovic, "DC-DC Converter Design for Battery-Operated Systems," *Proceedings of Power Electronics Specialist Conference*, pp. 103-109, 1995

[9] *LT8705A – 80V Vin and Vout Synchronous 4-Switch Buck-Boost DC/DC Controller*, Analog Devices Inc., Massachusetts, 2016

[10] M.K. Kazimierczuk, *Pulse-width Modulated DC-DC Power Converters*. Wiley, 2008

[11] *CSD18563Q5A 60 V N-Channel NexFET™ Power MOSFET Datasheet*, Texas Instruments Inc., Texas, 2016

[12] *IHLP-6767GZ-01 IHLP® Commercial Inductors, High Saturation Series Datasheet*, Vishay Intertechnology Inc., Pennsylvania, 2020

[13] *A759 Radial Solid Polymer Aluminum Capacitors Datasheet*, Kemet Corporation, Florida, 2021

Decision Trees Rule-Based Electroencephalography Signaling With Four Axis Control

Ahmet Burak Zor[1], Nazlı Sarıkaya [2], Emin Can BAYKAL[3], Hamza BOZKURT[4], Muhammed Kürşad UÇAR[5]
Elektrik-Elektronik Mühendisliği, Mühendislik Fakültesi, Sakarya Üniversitesi, Sakarya, Türkiye
[1]aburak.zor@ogr.sakarya.edu.tr, [2]nazli.sarikaya@ogr.sakarya.edu.tr,
[3]emin.baykal@ogr.sakarya.edu.tr [4]hamza.bozkurt@ogr.sakarya.edu.tr [5]mucar@sakarya.edu.tr

***Abstract*—Diseases such as Amyotrophic Lateral Sclerosis (ALS), stroke occur with nervous system problems. What causes some of these diseases is still unknown and is among the current study topics. Such diseases do not harm the brain functions of individuals but limit their daily activities. In this study, Electroencephalography (EEG) signals were taken and processed using an artificial intelligence-based program and classified as basic directional movements. EEG signals were filtered before classification due to the presence of noise. To make the classification more precise and detailed after filtering, first epoching and then feature extraction were done. With the extracted features, the decision trees method was used in the four-axis direction control process. For higher accuracy during classification, the data were divided into two groups as right-left and up-down. Performance evaluation criteria were obtained from the data classified using decision trees. The evaluation of the results was made based on the accuracy value, which is one of the performance criteria. As a result of the evaluation, the highest accuracy rate was found as 66in classification based on right and left grouped data, and the highest accuracy rate was 67in up and down grouped data. It is considered that the prepared system can be applied in practice.**

***Index Terms*—Amyotrophic Lateral Sclerosis, Electroencephalography, Artificial Intelligence, Signal Processing, Decision Tree Method.**

I. INTRODUCTION

In today's world, some health problems restrict the physical movement of individuals with that disease. While the root cause of some of these is still unknown today, the cause of some of them is based on cerebrospinal cord injury.

Amyotrophic Lateral Sclerosis (ALS), one of the diseases whose cause is not fully understood, is a neurological disease that occurs due to damage to the nerve cells responsible for controlling voluntary muscle movement. [1]

Stroke, an example of one of the disorders that occur due to cerebrospinal cord injury, occurs when the blood flow to the brain is cut off or reduced suddenly. This damage causes loss of function in some muscle groups in our body. [2]

In ALS and stroke-like diseases, there is usually no problem in the imagination and thinking functions of the brain. However, since some individuals with this disease cannot move at all, some have limited mobility as walking, speaking, holding, lifting, similar daily basic movements are also necessary for these individuals are limited. The basic movements imagined or thought of by individuals with the disease can be realized by using Electroencephalography (EEG) signals obtained as a result of monitoring the wave activities of the brain and artificial intelligence, making it possible to facilitate the daily lives of these individuals. By processing EEG signals from the thinking region of the brain, these people can be provided with opportunities such as movement, orientation, and selection.

In the literature researches, many studies involving EEG signals were found. The individuals with limited physical movement, studies have been carried out for mind-controlled wheelchairs. [3] When the algorithm of the study was examined, it was clear that it was specially designed and implemented for individuals. In this study, the algorithm created with the data obtained, unlike the study examined, is used for different individuals. In many literature studies, EEG signals were acquired from more than one point of the head, whereas in this study, signals were acquired from only 2 points. [9]

The aim of the study, like many studies in the literature, is to process EEG signals by passing them through signal processing processes and classify them as basic directional movements (right, left, down, up) and to control the thought by accelerating the classification process as the basics of direction. [7]

This study may be possible to perceive the patients' thoughts and facilitate their daily movements. Thus, patients can become able to perform their basic activities without being dependent on another person. The algorithm with the highest accuracy value was chosen for a realistic and applicable study at the classification.

II. MATERIALS AND METHODS

The application is planned according to the procedure in Figure 1. According to the flow chart, first, the data was collected, then filtered, and then the signals were divided into epochs. For extracting the characteristic features of the signals and increasing the classification success rate, feature extraction was performed, and then the classification, which is the final stage, was started.

Figure 1: Flow diagram

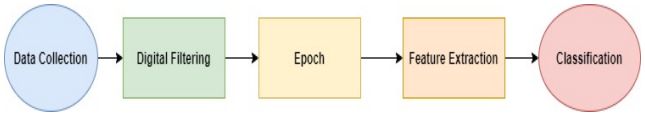

A. DATA COLLECTION

The database used in the study was created in Sakarya University Medical Electronics Laboratory with a total of 45 minutes of data at 15-minute intervals for each direction axis. The sampling frequency of the EEG signal was determined as 1000 Hz. The collected data distribution is shown in Table (I)

Table I: Number and distribution of collected data

Individual / Direction	Individual 1	Individual 2	Total
Up	759	757	1516
Down	757	763	1520
Total	1516	1520	3036
Right	758	725	1483
Left	751	753	1504
Total	1509	1478	2987

B. NUMERIC FILTER

In this study, numerical filtering processes were performed on MATLAB. The process of removing noise on the EEG signal is designed with a 0.1-100 Hz band gap filter Chebyshev Type 2. The sampling frequency is set at 1000 Hz. [10]

C. FEATURE EXTRACTION

The filtered EEG signal is split into 2-second segments for processing in MATLAB. Then, the signal segments are converted to a data matrix to use in feature extraction. The epoching process is applied for each direction axis. The feature extraction process determines the characteristic features of the epoched data matrices and the similarity between the data matrices. Twenty-five features were extracted from the EEG signal. These properties are used in classification processes. The 25 properties involved in the classification process are shown in Table (II) [4].

D. MACHINE LEARNING AND PERFORMANCE EVALUATION

After completing the necessary steps in processing EEG signals, classification was started as the last step. During the process, the data were grouped as right-left and up-down. As a result of the grouping, a numeric label was given to the axes for correct classification. The decision Trees (CTree) Method was used for this classification process.

Accuracy, sensitivity, specificity, precision, AUC, f-measurement parameters were used to evaluate model performances. [4] [5] [6]

III. RESULTS AND DISCUSSION

During the study process, the data groups of the individuals were combined then classified for the first and the second individuals. The classification was applied to the data grouped as right-left and up-down. The performance evaluation criteria

Table II: Table of features

Nu	Feature	Equation/ Formula
1	Kurtosis	$x_{kur} = \frac{\sum_{i=1}^{n}(x(i)-\overline{x})^4}{(n-1)S^4}$
2	Skewness	$x_{ske} = \frac{\sum_{i=1}^{n}(x_i-\overline{x})^3}{(n-1)S^3}$
3	IQR	$IQR = iqr(x)$
4	DK	$DK = (S/\overline{x})100$
5	Geometric Mean	$G = \sqrt[n]{x_1 + \cdots + x_n}$
6	Harmonic Mean	$H = n/(\frac{1}{x_1} + \cdots + \frac{1}{x_n})$
7	Hjorth - Activity Parameter	$A = S^2$
8	Hjorth - Mobility Parameter	$M = S_1^2/S^2$
9	Hjorth - Complexity Parameter	$C = \sqrt{(S_2^2/S_1^2)^2 - (S_1^2/S^2)^2}$
10	Maximum	$x_{max} = max(x_i)$
11	Median	$\underset{\sim}{x} = \begin{cases} x_{\frac{n+1}{2}} & : x \text{ odd} \\ \frac{1}{2}(x_{\frac{n}{2}} + x_{\frac{n}{2}+1}) & : x \text{ even} \end{cases}$
12	Mean absolute deviation (MAD)	$MAD = mad(x)$
13	Minimum	$x_{min} = min(x_i)$
14	Central moment	$CM = moment(x, 10)$
15	Mean	$\overline{x} = \frac{1}{n}\sum_{i=1}^{n} = \frac{1}{n}(x_1 + \cdots + x_n)$
16	Mean Value of Curve	$CL = \frac{1}{n}\sum_{i=2}^{n}\lvert x_i - x_{i-1}\rvert$
17	Mean Energy	$E = \frac{1}{n}\sum_{i=1}^{n} x_i^2$
18	Mean Square	$X_{rms} = \sqrt{\frac{1}{n}\sum_{i=1}^{n}\lvert x_i\rvert^2}$
19	Standard Error	$S_{\overline{x}} = S/\sqrt{n}$
20	Standard Deviation	$S = \sqrt{\frac{1}{n}\sum_{i=1}^{n}(x_i - \overline{x})}$
21	Shape Factor	$SF = X_{rms}/\left(\frac{1}{n}\sum_{i=1}^{n}\sqrt{\lvert x_i\rvert}\right)$
22	Singular Value Decomposition	$SVD = svd(x)$
23	25% KTrimmed Mean	$T25 = trimmean(x, 25)$
24	50% Trimmed Mean	$T50 = trimmean(x, 50)$
25	Mean Teager Energy	$TE = \frac{1}{n}\sum_{i=3}^{n}(x_{i-1}^2 - x_i x_{i-2})$

table of grouped individuals is shown by including the values of confusion matrix table (III, IV, V). [8]

Accuracy rates were taken into account during the evaluation process. According to this, when the analysis was made on grouped data, the highest accuracy rate is %67 from the individuals evaluated, was obtained from the up-down data. When the accuracy rate found was compared with the accuracy rate of the right-left directions from the grouped data, it was seen that there was no significant difference between them.

Table III: General type of a confusion matrix

Confusion Matrix	Actual	
Predicted	True Positive (TP)	False Positive (FP)
	False Negative (FN)	True Negative (TN)

Table IV: Confusion Matrix of up-down axis

Confusion Matrix	Actual	
Predicted	196	106
	89	214

Table V: Confusion Matrix of right-left axis

Confusion Matrix	Actual	
Predicted	206	96
	104	199

Table VI: Model performances of right-left and up-down axis control

Performance Evoluation Methods	Up - Down	Right - Left
Accuracy (ACC) %	67.76	66.94
Sensitivity (SEN)	0.68	0.66
Specificity (SPE)	0.66	0.67
Precision (PRE)	0.64	0.68
F - Measure	0.66	0.67
AUC	0.67	0.66

IV. CONCLUSION

The primary purpose of this study is to eliminate the physical limitations of individuals with ALS and stroke-like diseases and to make their daily lives easier by using the basic movements of individuals with ALS and stroke-like diseases, EEG signals obtained as a result of monitoring the wave activities of the brain, and artificial intelligence. For this reason, various methods were used to analyze and use the large number of data that we have and process them to solve the problem.

F-criterion is a criterion that provides a more accurate result by evaluating each of the sensitivity and precision criteria together. When examined in terms of all these performance values, the model performance is average compared to the literature.

The study's contribution to the literature is that it offers a technology that can be developed to eliminate the physical limitations of people with physical disabilities such as ALS and stroke and make their lives easier. It is thought that the proposed models can be put into practice and used.

REFERENCES

[1] Kjaergard, LiseL, Als-Nielsen, Bodil,Association between competing interests and authors' conclusions: epidemiological study of randomised clinical trials published in the BMJ, 2002

[2] C. André,G. R. De Freitas,M. M. Fukujima, Prevention of deep venous thrombosis and pulmonary embolism following stroke: a systematic review of published articles, 2007

[3] Mirza, I. A., Tripathy, A., Chopra, S., D'sa, M., Rajagopalan, K., D'souza, A., Sharma, N. (2015). Mind-controlled wheelchair using an EEG headset and arduino microcontroller. 2015 International Conference on Technologies for Sustainable Development (ICTSD), 1-5.

[4] D. M. W. Powers, "Evaluation: from precision, recall and F-measure to ROC, informedness, markedness and correlation," arXiv:2010.16061, pp. 37–63, 2020, [Online]. Available: http://arxiv.org/abs/2010.16061.

[5] M. K. Ucar, M. R. Bozkurt, C. Bilgin, and K. Polat, "Automatic detection of respiratory arrests in OSA patients using PPG and machine learning techniques," Neural Comput. Appl., vol. 28, no. 10, pp. 2931–2945, 2017, doi: 10.1007/s00521-016-2617-9.

[6] M. K. Ucar, M. R. Bozkurt, C. Bilgin, and K. Polat, "Automatic sleep staging in obstructive sleep apnea patients using photoplethysmography, heart rate variability signal and machine learning techniques," Neural Comput. Appl., vol. 29, no. 8, pp. 1–16, 2018, doi: 10.1007/s00521-016-2365-x.

[7] Naveen, R. S., Julian, A. (2013). Brain computing interface for wheel chair control. 2013 Fourth International Conference on Computing, Communications and Networking Technologies (ICCCNT), 1-5.

[8] Visa, Sofia Ramsay, Brian Ralescu, Anca Knaap, Esther. (2011). Confusion Matrix-based Feature Selection.. CEUR Workshop Proceedings. 710. 120-127.

[9] An asynchronous wheelchair control by hybrid EEG–EOG brain–computer interface Wang HLi YLong J et al. 2014

[10] S. V. Munkanpalli, S. P. Sagat, and M. D. Mali, "Design and development of EEG controlled mobile robots," 2016 IEEE Int. Conf. Adv. Electron. Commun. Comput. Technol. ICAECCT 2016, pp. 133–138, Jun. 2017, doi: 10.1109/ICAECCT.2016.7942569

Development of educational robot and user interfaces for robotic applications

A.K. ERDOĞMUŞ[1], B. YARIŞ[2], F. VATANSEVER[2], Y. UMUR[2], M.O. TAŞ[2] and H.S. YAVUZ[2]

[1]İnovasyon Mühendislik Ltd.Şti., Eskisehir/Turkey, kerem.erdogmus@inovasyonmuhendislik.com
[2]Eskisehir Osmangazi University, Eskisehir/Turkey, berkayyaris@hotmail.com
[2]Eskisehir Osmangazi University, Eskisehir/Turkey, fatihvsever@gmail.com
[2]Eskisehir Osmangazi University, Eskisehir/Turkey, yagizumur@hotmail.com
[2]Eskisehir Osmangazi University, Eskisehir/Turkey, motas@ogu.edu.tr
[2]Eskisehir Osmangazi University, Eskisehir/Turkey, hsyavuz@ogu.edu.tr

***Abstract* - There is a limited number of current resources that can be found on the internet or in books about Robot Operating System (ROS) and robotic programming. People trying to learn these platforms cope with various problems due to limited resources. In this study, we introduce a low cost modular education robot, called the Halikarnas Modular Education Robot (HAMER). The platform is equipped with some basic sensors and a visual camera. We designed experiments involving many ROS packages to introduce robotic programming concepts to users. These experiments have been arranged starting from basic level concepts to more complex robotic programming applications. In addition to the hardware design, a graphical user interface (GUI) for HAMER that can be executed on a personal computer has been developed to manage the learning outcomes in the study. The students can easily perform the experiments on the student screen of this interface and the teachers can follow and test the students' experiments on the teacher's screen to observe the outputs. This design not only contributes to the learning outcome, but also ensures that the learning process is effectively controlled and maintained. In this article, we present the hardware and software designs of the Halikarnas modular education robot. The main motivation of this study is to facilitate the learning of ROS applications through the designed educational robot and thus to inspire readers to create various mobile robot designs to fulfill specific tasks.**

***Keywords* – Education, Mobile robot, Robot operating system, Graphical user interface.**

I. INTRODUCTION

ROBOTS have been actively used for many years. Modular robots, a subclass of robots, are robots that can be controlled remotely or move autonomously with some algorithms, their parts can be changed easily and can adapt to the desired configurations according to the needs. These robots can work in space studies [1], transport operations [2] and many other fields [3].

With the developing technology, studies in the field of robotics are gaining momentum and people's interest in robotic technology is increasing. In this context, many education and research robots have been developed as open source or products and are available to people who want to work in the field of robotics. The educational robot presented in [4] enables the creation of two types of interactive education models with active participation of children, solving the problems given to them by a mobile robot and giving feedback to the robot. In the tests performed, it was reported that the robot had a positive effect on the education of children. Araújo et al. presented a simple education robot system with a minimalist design using Arduino in [5]. Erdogmus et al. developed education robots with ROS and containing lidar, camera, sonar and infrared sensors in [6]. Arvin et al. introduced an open source and low cost mobile robot that has been produced to be used for education and research in [7]. In [8], an Android and Arduino based mobile robot with internet connection was proposed for use in classrooms and laboratories. Another mobile robotic platform prototype including the simple robot parts to the students by using python and coding with blocks tools is presented in [9]. It enables students to combine the blocks consisting of these parts and work on the software. Guyonneau and Mercier presented the information about a modular robot and its structure, which is produced for use in education and research areas [10]. Gonzalez et al. introduced an Arduino-based modular mobile robot that aims to teach students programming, modeling, control and signal processing [11]. Guo et al. designed a modular mobile robot that aims to encourage students to develop innovative abilities and artificial intelligence technology [12].

In this study, we introduce the Halikarnas Modular Education Robot (HAMER), which is developed as an open source software and hardware. We also introduce the HAMER-GUI tool to make the robotic programming concepts to be used and understood by students in an efficient way. HAMER is designed as an alternative to previously developed mobile education robots. It helps to create basic robot systems and allows transfusing new designs into different robot variations. The aim of the study is to demonstrate that fundamental robotic applications can easily be performed through the specific experiments prepared for HAMER. The rest of the study is organized as follows: HAMER design is introduced in Section 2, the details of user interface is presented in Section 3, the prepared experiments are given in Section 4 and the conclusion is presented in the last section.

II. HAMER DESIGN

HAMER is a mobile robot designed to be compatible with the ROS Noetic system in Ubuntu 20.04 version, which has a camera with RGB-D feature, a 360-degree scanning LIDAR sensor and some other equipment. It includes some simulation tests in the Gazebo environment and a simple graphical user interface for users. While ROS is an open source software system where we can control robots or robot components via computer [13], Gazebo is an open source robot simulation environment that works in full harmony with ROS [14].

HAMER includes many ROS packages [15]. These packages are briefly described below.

hamer_description: It is the package that contains URDF contents, which are robotic description files of HAMER.

hamer_navigation: It is the package that contains the codes and ROS packages required for HAMER's autonomous navigation.

hamer_simulation: It is the package that contains the launch files which run HAMER in designed environments.

hamer_slam: It is the package that contains the launch files which enable HAMER to map the environment using SLAM (simultaneous localization and mapping) algorithm.

hamer_teleop: It is the package that contains the ROS node which provides the control of HAMER from the keyboard.

hamer_gui: It is the package that includes the graphical user interface of HAMER.

HAMER is designed as a modular model that can be developed specifically for many different working areas. For this purpose, it has been developed as a basic robot design with a software and hardware structure suitable for structural additions or configuration. This modularity makes the robot not just an educational robot, but a multi-purpose robot kit. The dimensions of the robot are (135×340×125) mm. There is a visual camera (RealSense D435) positioned in front of the robot and a LiDAR sensor positioned at the top of the robot. Skid Steering Drive [15] was used to enable it to move with four-wheel drive. The areas designed on the body are designed to be suitable for the camera that is intended to receive data from all angles and to be placed in the advanced designs of the robot by using sonar sensors to be used in the robot. The view of the robot in the simulation environment is given in Figure 1.

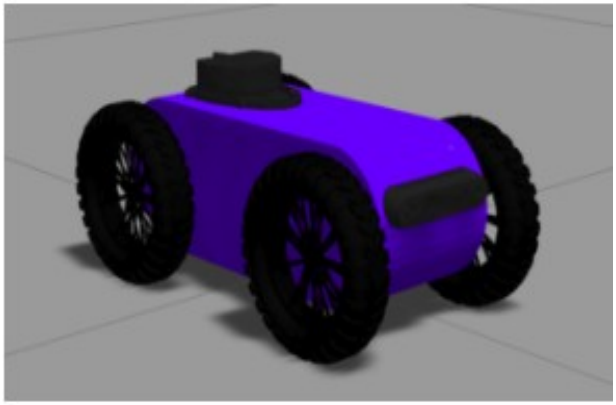

Figure 1: Halikarnas Modular Education Robot (HAMER)

III. GRAPHICAL USER INTERFACE DESIGN

An interface has been created to test, teach and develop HAMER's features and capabilities by users. The created interface was developed using PyQt5 [16]. PyQt5 is a Python link to the Qt library written in C ++ language for cross-platform application development.

The interface includes the stages of the tasks that the user has worked on the robot, and many information such as sensor data of the robot. Apart from these features, the interface includes some functions in order to minimize the time loss required for finding and coding many applications that need to be opened in the operating system. Therefore, it provides great convenience to students, teachers and ROS developers. The interface offers two different login options for teacher and student, as can be seen in Figure 2.

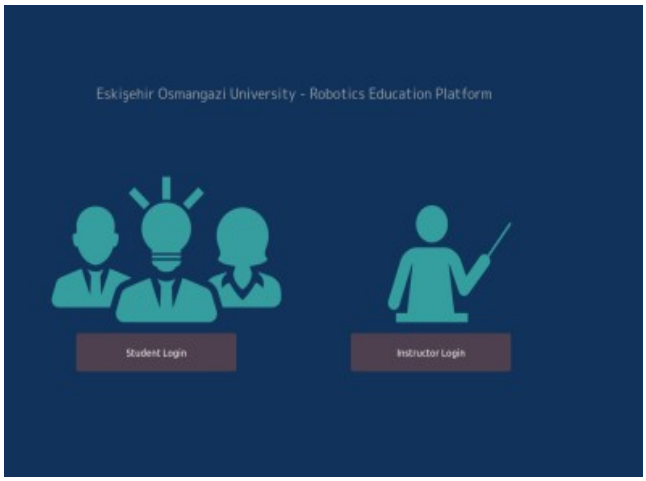

Figure 2: User selection screen

In the Student Interface Section given in Figure 3, the "Experiments" section allows selecting the desired experiment from the list of the experiments and showing the stages of the experiment. While the application to write Python codes is opened with the IDE button, hints about the experiment can be obtained with the Hints button. In the "Terminal" section, it is ensured that the commands required for the communication of the user with the shell are written over the interface. The "Camera Image" section shows the image from the robot camera. At the bottom of the section where the image from the camera is displayed, there are buttons for full-screen the image and taking pictures. In the "LIDAR Info" section, the data from the LIDAR sensor are taken to the user as right, left, front and back. When the distance to objects around the robot falls below a certain value, the sensor data turns red and the user is alerted. In the "Control Robot" section, the user is provided to move the robot with the arrow keys. Users can increase, decrease and zeroing the speed of the robot if they wish. In the "Robot Info" section, the current speed and position information of the robot is given to the user. Students who complete their experiments can save their codes with the Upload Script button and use the Logout button when they want to exit the system.

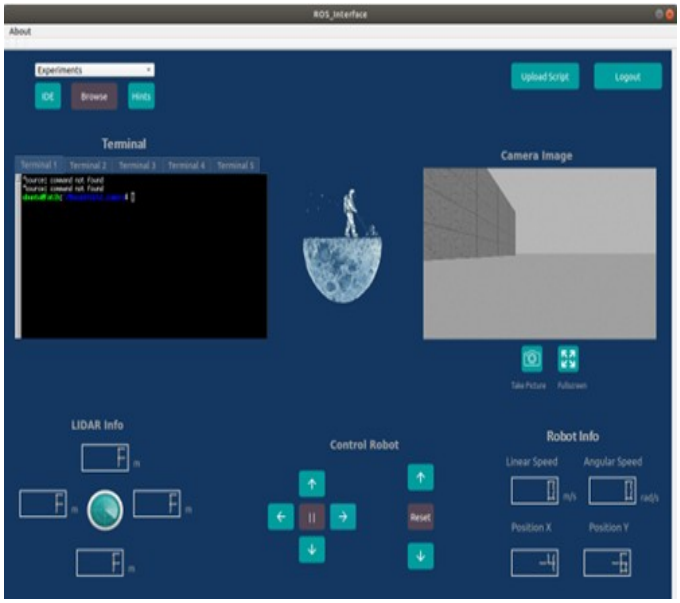

Figure 3: Student interface screen

In the Instructor Interface Section given in Figure 4, teachers can see the entrance and exit information of the students in the system and which experiment they have applied. Also, in this section, teachers can access original versions of the experiments and answer sheets. Finally, teachers can download and view the files sent by the students, and find out which steps they could or could not do in the experiments.

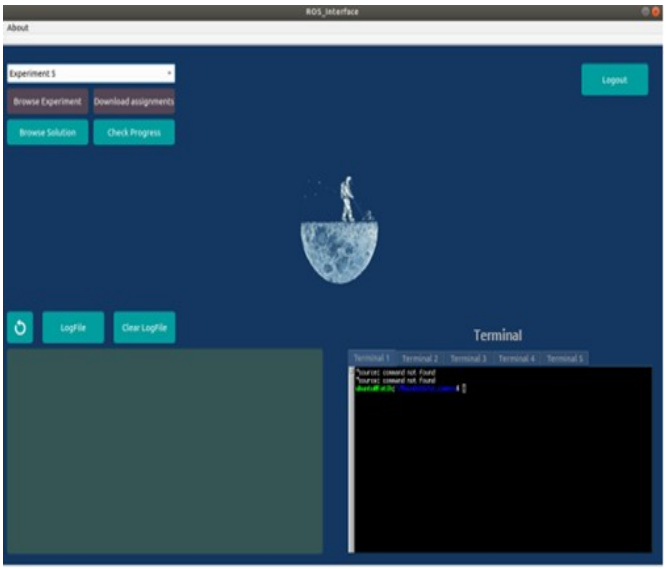

Figure 4: Instructor interface screen

IV. EXPERIMENTS

In this study, there are 15 experiments that provide students with basic information about the ROS and robotics and clearly indicate the stages of the tasks that need to be done. In these experiments, the student was provided to perform many applications from basic to advanced. Each experiment is briefly described below.

Experiment 1 – Sensor reading and control of the Robot with Keyboard: In this experiment, students are expected to practice reading data from the robot and controlling the robot from the keyboard.

Experiment 2 – Building Simulation Environment: In this experiment, students are expected to design a sample environment by using the Building Editor inside the Gazebo.

Experiment 3 – Draw Square Movement: In this experiment, students are expected to reinforce the Service-Client structure by moving the robot linearly and angularly and allowing the robot to move squarely.

Experiment 4 – Patrol Application: In this experiment, it is expected that the forward and backward movement of the robot will be made by using the Publisher-Subscriber and the ROS parameter structure.

Experiment 5 – Obstacle Avoidance Application with Bug0 Algorithm: In this experiment, as long as the robot does not reach the target or encounter an obstacle, the application that enables the robot to avoid obstacles and reach a target was added by using the Bug0 algorithm [18], which enables the robot to move towards the target point and, in case of encountering an obstacle, to reach the target by going around the obstacle [19].

Experiment 6 – Wall Follower Robot Application: In this experiment, using the distance information received from LIDAR sensor, it is expected to write a node that follows the wall without hitting the wall.

Experiment 7 – Voice Controlled Robot Application: In this experiment, it is expected to establish an algorithm that will provide voice control of the robot by using the Pocketsphinx ROS package [20], which enables the processing of the sound file sent by the user on the Python programming language.

Experiment 8 – SLAM and Navigation Application: In this experiment, it is expected that the gmapping ROS package [21] will be used to realize the simultaneous localization and mapping (SLAM) [22] and the robot will navigate autonomously over Rviz with the help of the environment map.

Experiment 9 – Autonomous Exploration of the Environment: In this experiment, it is aimed to use the exploration algorithm, which allows the robot to autonomously discovery in a region selected by the user, and autonomous building of the environment map [23] by using frontier_exploration ROS package [24].

Experiment 10 – Common Mapping for Multiple Robot Systems: In this experiment, it is expected to use the multirobot_map_merge ROS package [25], which allows multiple robots in the same environment to map and merge the environment simultaneously.

Experiment 11 – Travelling Salesman Problem with Genetic Algorithm: In this experiment, the student is expected to solve the Traveling Salesman Problem (TSP) with the help of Genetic Algorithm [26] for multi-point routing.

Experiment 12 – Visual SLAM: In this experiment, it is expected that the environment map will be built visually by using the rtabmap_ros package [27] of Real Time Appearance Based Mapping (RTAB-Map) algorithm, which is a visual

SLAM approach based on loop closure detection using an RGB-D camera with sensor providing 3D information [28].

Experiment 13 – Object Recognition Application with OpenCV: In this experiment, it is expected to perform object recognition application with find_object_2d ROS package [29], which is an object recognition package that can be applied by selecting the desired feature extraction methods such as SIFT, SURF, BRIEF, etc. in the OpenCV library.

Experiment 14 – Object Recognition Application with YOLO v3: In this experiment, it is expected to use darknet_ros package [30] for object recognition application with YOLO v3 [31], which is a very popular deep learning architecture.

Experiment 15 – Line Follower Robot Application: In this experiment, using image processing techniques, the robot is expected to autonomously follow a yellow line.

A sample application of an experiment from beginning to end can be viewed in the link presented in [32].

V. CONCLUSION

The development of robotic technology in the age we live has increased the interest in robotics. In this context, various researchers have presented many education and research robots. In this study, we introduced an open source modular education robot, called HAMER and a graphical user interface to manage and fulfil robotic experiments, called HAMER-GUI. It offers students to learn fundamental concepts of robotic programming based on ROS and to improve themselves. Within the scope of the study, we developed 15 experimental training applications at various difficulty levels. Interface elements, simulation environments and applications developed for this study serve as a robotics training kit. In future studies, we aim to increase the number of experiments in the training kit, to add additional features to the graphical user interface and to control the robot over the web.

ACKNOWLEDGMENT

This work was supported by TUBITAK 2209-B Industry Undergraduate Research Projects Support Program (2019/3).

REFERENCES

[1] Medina A., Pradalier C., Paar G., Merlo A., Ferraris S., Mollinedo L., and Didot F., A servicing rover for planetary outpost assembly. Astra, 2011.
[2] Groß R., Tuci E., Dorigo M., Bonani M., and Mondada F., Object Transport by Modular Robots that Self-assemble. ICRA, 2006.
[3] Murata S., Yoshida E., Kamimura A., Kurokawa H., Tomita K., and Kokaji S., M-tran: Self-reconfigurable modular robotic system. IEEE/ASME Transactions on Mechatronics, 2002, vol. 7, no. 4, pp. 431–441.
[4] Mitnik, R., Nussbaum, M., and Soto, A., An autonomous educational mobile robot mediator. Autonomous Robots, 2008, 25(4), 367-382.
[5] Araújo, A., Portugal, D., Couceiro, M. S., and Rocha, R. P., Integrating Arduino-based educational mobile robots in ROS. Journal of Intelligent & Robotic Systems, 2015, 77(2), 281-298.
[6] Erdogmuş, A. K., Tas, D. O., Karaca, M., and Yayan, U., Robot Operating System Compatible Mobile Robots for Education and Research. arXiv preprint arXiv:2012.12527, 2020.
[7] Arvin F., Espinosa J., Bird B., West A., Watson S., Lennox B., Mona: an Affordable Open-Source Mobile Robot for Education and Research. Journal of Intelligent & Robotic Systems, 2019, 94, 761-775.
[8] López-Rodríguez F. M., Cuesta F., Andruino-A1: Low-Cost Educational Mobile Robot Based on Android and Arduino. Journal of Intelligent & Robotic Systems, 2016, 81, 63-76
[9] Khamphroo M., Kwankeo N., Kaemarungsi K., Fukava K., MicroPython-based educational mobile robot for computer coding learning. In 2017 8th International Conference of Information and Communication Technology for Embedded Systems (IC-ICTES), 2017.
[10] Guyonneau R., Mercier F., IstiABot, an Open Source Mobile Robot for Education and Research. 12th International Workshop on Robot Motion and Control (RoMoCo), 2019.
[11] Gonzalez C., Alvarado I., Muñoz La Peña D., Low cost two-wheels self-balancing robot for control education. IFAC (International Federation of Automatic Control), 2017, 50-1, 9174–9179
[12] Guo T., Li M., Han Y., Lu G., Qie T., Zhang Q., Design of Educational Mobile Robot. Chinese Automation Congress (CAC), 2020
[13] Robot Operating System (ROS), URL: http://ros.org/, (Reached: April 28 2021)
[14] GazeboSim, URL: http://gazebosim.org/, (Reached: April 28 2021)
[15] HAMER (Halikarnas Modular Education Robot), URL: https://github.com/hamerrobots/hamer, (Reached: April 28 2021)
[16] PyQt, URL: https://riverbankcomputing.com/software/pyqt/intro, (Reached: April 28 2021)
[17] Shuang, G., Cheung, N. C., Cheng, K. E., Lei, D., and Xiaozhong, L., Skid steering in 4-wheel-drive electric vehicle. In 2007 7th International Conference on Power Electronics and Drive Systems, 2007, pp. 1548-1553.
[18] Bug0 ROS Implementation, URL: https://github.com/MohannedA/Bug0_ROS_Implementation, (Reached: April 28 2021)
[19] Yufka, A., Apaydin, A. and Aybar A., BUG-0,1,2 Algoritmaları ve Petri Ağı Modelleri. Eskişehir Teknik Üniversitesi Bilim ve Teknoloji Üniversitesi, 2018. p. 130
[20] PocketSphinx, URL: https://pypi.org/project/pocketsphinx/, (Reached: April 28 2021)
[21] gmapping. URL: http://wiki.ros.org/gmapping, (Reached: April 28 2021)
[22] Leonard, J. J., and Durrant-Whyte, H. F., Simultaneous map building and localization for an autonomous mobile robot. In IROS, 1991, Vol. 3, pp. 1442-1447.
[23] Yamauchi, B., A frontier-based approach for autonomous exploration. In Proceedings 1997 IEEE International Symposium on Computational Intelligence in Robotics and Automation CIRA'97.' Towards New Computational Principles for Robotics and Automation', 1997, pp. 146-151).
[24] frontier_exploration, URL: http://wiki.ros.org/frontier_exploration, (Reached: April 28 2021)
[25] multirobot_map_merge, URL: http://wiki.ros.org/multirobot_map_merge, (Reached: April 28 2021)
[26] Holland, J. H., Genetic algorithms. Scientific american, 1992, 267(1), 66-73.
[27] rtabmap_ros, URL: http://wiki.ros.org/rtabmap_ros, (Reached: April 28 2021)
[28] Labbé, M., and Michaud, F., Memory management for real-time appearance-based loop closure detection, Intelligent Robots and Systems (IROS), 2011, pp. 1271-1276.
[29] find_object_2d, URL: http://wiki.ros.org/find_object_2d, (Reached: April 28 2021)
[30] YOLO ROS: Real-Time Object Detection for ROS, URL: https://github.com/leggedrobotics/darknet_ros, (Reached: April 28 2021)
[31] Redmon, J., and Farhadi, A., Yolov3: An incremental improvement. arXiv preprint arXiv:1804.02767, 2018.
[32] Robotic Interface Experiment 5 Demo, URL: https://www.youtube.com/watch?v=oYt0xIoC70o, (Reached: April 28 2021)

A Study for the Improvement of Operating Capacity in Marine Generators

K. YİĞİT[1]

[1] Yildiz Technical University, Istanbul/Turkey, kyigit@yildiz.edu.tr

Abstract **- Most ships need diesel generators to meet their electrical energy requirements. Therefore, each improvement to be made in marine generators will increase energy efficiency in ship's power system. In this study, three scenarios for meeting the electrical energy requirement of a ship from diesel generators are examined. The switching ratio is set as 30%, 60%, and 90% of the generator's nominal capacities for Scenario I, Scenario II, and Scenario III, respectively. In each scenario, the operating conditions of the first, second, and third generators have been analyzed according to the determined switching ratios. Then the total fuel consumptions have been estimated for 10%, 20%, 30%, 40%, 50%, 60%, 70%, 80%, 90%, and 100% load demand of the total power capacity on board.**

The results show that maximum and minimum fuel consumption is occurred when the switching ratio is set to 30% and 90% of the generators' nominal capacities, respectively. The results also show that taking care to operate generators close to optimum load will increase the energy efficiency in the ship's electrical system to a certain rate.

Keywords **- Ship, Electrical energy, Marine generator**

I. INTRODUCTION

THE International Maritime Organization (IMO) focuses on operational and technical measures among other topics to increase the energy efficiency of ships. IMO prepares significant guidelines to support the implementation of compulsory measures and to increase energy efficiency activities on ships [1]. In short, it is aimed to increase energy efficiency, reduce carbon intensity, strengthen the energy performance indexes implemented on ships and ensure a sustainable maritime transport [2]. Numerous energy efficiency implementations and technologies for ships can be mentioned. The aft waterline extension and lightweight construction in the field of design, propeller modifications and contra-rotating propellers in the field of hydrodynamic, waste heat recovery and diesel-electric drive in the field of machinery, and solar-wind power in the field of alternative energy are just some of the energy efficiency activities on ships [3]. All technical and operational energy efficiency practices contribute to improving ship performance.

Electrical energy production and propulsion systems are one of the most important components on the ship structure. Diesel engines are widely used in almost all ships to provide both propulsion and electric power generation [4]. Therefore, diesel generators (DGs) have an important place in the improvement of ship electrical systems. DGs convert mechanical energy into electrical energy. It generally consists of the engine, alternator, fuel system, lubricating system, and control panel [5]. The specific fuel oil consumption (SFOC) is an also critical parameter for optimum operation of DGs. The more efficiently the generators are operated, the more it is possible to reduce the amount of fuel spent per electricity generation [6]. The load set point is also a critical parameter for optimal operation of each DG. The choice of the load set point will affect the fuel consumption, especially if several DGs on board are operating at the same time [7].

In this study, the fuel consumption that can occur when DGs are operated at different switching ratios on board has been analyzed. Thus, the importance of the load sharing approach in DGs and its potential effect on energy efficiency has been revealed. The aim of this study is to increase the energy efficiency in ship electrical power system by determining the best load set point for DGs among the scenarios.

II. MATERIALS AND METHODS

The conventional bulk carrier ship type was considered as an example to examine the performance and fuel consumption of its DGs. It is assumed that the ship consists of a main engine for propulsion and three identical main DGs (500 kW) to meet the electrical energy demand. The relationship between the SFOC and power characteristic of DGs was obtained from the literature and relevant SFOC values were derived from the 3rd order polynomial function [8]. The mean characteristic curve of SFOC for DGs can be given as an example in Figure 1.

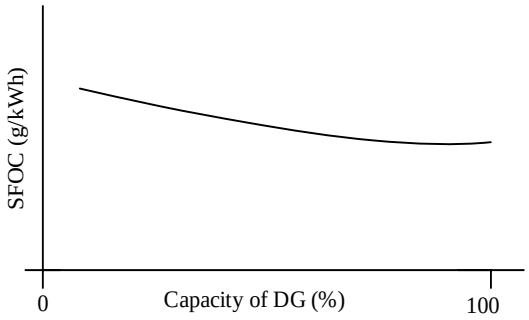

Figure 1: The mean characteristic SFOC curve.

The SFOC and fuel oil consumption functions can also be expressed by Equation 1 and Equation 2, respectively.

$$SFOC\ (P_i) = a(P_i)^3 + b(P_i)^2 + c(P_i) + d \quad (1)$$

$$FC\ (P_i) = SFOC\ (P_i) \times P_i \quad (2)$$

where SFOC is the specific fuel oil consumption (g/kWh) of i-th DG, FC is the fuel oil consumption (g/h) of i-th DG, P_i is the output power (kW) of i-th DG and a, b, c, and d are the polynomial coefficients of i-th DG.

As seen in Figure 1, the energy saving potential depends on the operating range of DGs. When DGs are operated at optimum load, the fuel consumption required for the ship's electrical energy generation will be minimal. Therefore, it is critical to decide both how many generators will run and how the load will be shared between the generators.

Three scenarios were considered to observe the performance of marine DGs under the different electrical energy requirements of the ship. In Scenario I, only DG1 was run up to 30% of its nominal capacity to supply the electrical energy. When the power requirement was higher than the certain capacity of DG1, DG2 was automatically switched on to produce electrical energy. DG1 and DG2 equally supplied the total load demand until their nominal capacities approach to 30%. DG3 was activated and synchronized, when the load demand exceeded the operating capacities determined for both DG1 and DG2. Thus, it was ensured that the total electrical energy need of the ship was met equally between DG1, DG2, and DG3. This procedure was applied in the same way for other scenarios. Only the switching ratio was set at 60% and 90% of DG's nominal power for Scenario II and Scenario III, respectively. Thus, in each scenario, the total fuel consumption caused by DGs under the different electrical energy requirements of the ship has been evaluated. The ship's power requirements have also been selected as 10%, 20%, 30%, 40%, 50%, 60%, 70%, 80%, 90%, and 100% of the total capacity of the DGs.

III. Results and Discussion

The total SFOC changes for active DGs under total power demand of the ship for each scenario are given in Figure 2.

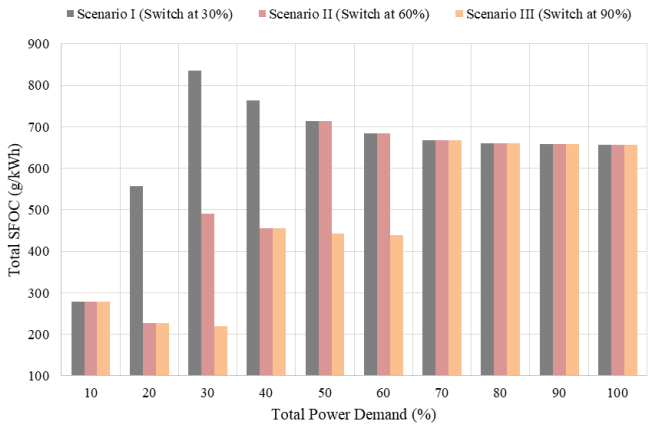

Figure 2: The total SFOC changes for active DGs under the different power requirements.

Figure 2 shows that when the power demand is 10% of the total capacity, the total SFOC from DGs is equal for each scenario. Because only one DG was operated in each scenario. In addition, when the power demand is 70%, 80%, 90%, and 100% of the total capacity, the equal SFOC values are obtained against the same load demand in each scenario. Because three DGs were operated in each scenario to meet the power demand of ship. On the other hand, when the power demand is 20% or 40% of the total capacity, the total SFOC is highest in Scenario I. Because while two DGs were operated at low load in Scenario I, only one DG was operated at high load in Scenario II and III. The total SFOC values were also equal in Scenario II and III. While the power demand is 30% of the total capacity, the total SFOC values are highest in Scenario I and lowest in Scenario III. Because, three DGs were operated at low load in Scenario I, two DGs were operated at low load in Scenario II, and one DG was operated at high load in Scenario III. In addition, when the power demand is 50% or 60% of the total capacity, the total SFOC is lowest in Scenario III. Because while all DGs were activated in Scenario I and II at lower load than Scenario III, only two DGs were operated in Scenario III at higher load than Scenario I and II. The total SFOC values were also equal in Scenario I and II.

The changes of total fuel consumption are also detailed in Figure 3, when the ship's power requirements are 10%, 20%, 30%, 40%, 50%, 60%, 70%, 80%, 90%, and 100% of its total capacity.

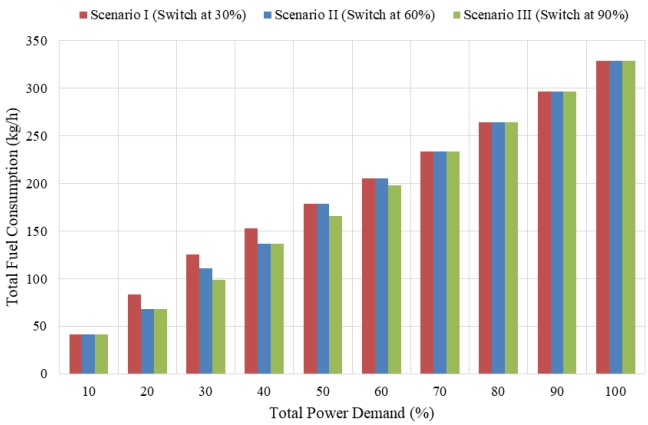

Figure 3: Total fuel consumption under different power requirements.

When the electrical load demand of ship is 10%, 70%, 80%, 90%, and 100% of the total power capacity, the total fuel consumption is equal in each scenario. Total fuel consumptions were realized as 42 kg/h, 234 kg/h, 264 kg/h, 296 kg/h, and 329 kg/h, respectively. While the load demand was 20% of the total capacity, the total fuel consumptions were 84 kg/h in Scenario I and 68 kg/h in Scenario II and III. While the power requirement was 30% of the total capacity, the total fuel consumptions occurred as 125 kg/h in Scenario I,

110 kg/h in Scenario II, and 99 kg/h in Scenario III. When the load demand was 40% of the total capacity, the total fuel consumptions were 153 kg/h in Scenario I and 137 kg/h in Scenario II and III. While the electrical energy requirement was 50% of the total capacity, the total fuel consumptions were 179 kg/h in Scenario I and II, 166 kg/h in Scenario III. While the power need was 60% of the total capacity, the total fuel consumptions were 205 kg/h in Scenario I and II, 198 kg/h in Scenario III.

Comparative analysis shows that fuel consumption decreases when the load rate of the generators reaches the optimum level. For this study, it can be said that operating the generators up to 90% of their nominal capacities will be more efficient in terms of fuel consumption than lower switching ratios.

IV. CONCLUSION

In this study, the effect of marine generator load set point on fuel consumption has been examined. In this context, three scenarios were performed to compare the performance of generators. The switching ratios of generators were set at 30%, 60%, and 90% of their nominal power for Scenario I, Scenario II, and Scenario III, respectively.

The results show that when the power requirement of the ship is 20%, 30%, 40%, 50%, and 60% of the total electrical energy capacity, the fuel consumption of the generators varies depending on the switching ratios. The SFOC values for each scenario are also equal when the electrical energy requirement is 10%, 70%, 80%, 90%, and 100% of the total power requirement. It can be said that the total fuel consumption for the same power requirement of ship is highest in Scenario I and the lowest in Scenario III.

As a result, diesel generators are an important parameter in the ship's electrical system. Generators will contribute positively to energy efficiency activities on ships when they are operated at optimum loading rates. Thus, a certain amount of economic and environmental savings can be achieved on ships.

REFERENCES

[1] IMO. International Maritime Organization. Available: https://www.imo.org/en/OurWork/Environment/Pages/AirPollution-Default.aspx

[2] T.-H. Joung, S.-G. Kang, J.-K. Lee, and J. Ahn, "The IMO initial strategy for reducing Greenhouse Gas(GHG) emissions, and its follow-up actions towards 2050," *J. Int. Marit. Saf. Environ. Aff. Shipp.*, vol. 4, no. 1, pp. 1–7, 2020.

[3] N. Rehmatulla, J. Calleya, and T. Smith, "The implementation of technical energy efficiency and CO2 emission reduction measures in shipping," *Ocean Eng.*, vol. 139, pp. 184–197, 2017.

[4] F. Vera-García, J. A. Pagán Rubio, J. Hernández Grau, and D. Albaladejo Hernández, "Improvements of a failure database for marine diesel engines using the RCM and simulations," *Energies*, vol. 13, no. 1, p. 104, 2019.

[5] What is the working principle of diesel generator? Available: https://www.generator.co.in/what-is-the-working principle of diesel generator/#:~:text=The%20functioning%20principle%20of%20a,uses%20diesel%20for%20its%20functioning

[6] S. I. Taheri, G. G. T. T. Vieira, M. B. C. Salles, and S. L. Avila, "A trip-ahead strategy for optimal energy dispatch in ship power systems," *Electric Power Syst. Res.*, vol. 192, no. 106917, p. 106917, 2021.

[7] A. Carlsen, "Diesel-electric generator load optimization," Master's thesis, Norwegian University of Science and Technology, Norway, 2014.

[8] V. Başhan, H. İ. Sönmez, and G. Gonca, "Bir yük gemisinin balast operasyonunun ekonomik ve ekolojik analizi," *1st International Congress on Ship and Marine Technology*, pp. 659-670, 2016.

Numerical Simulation of Diffraction Patterns with Different Illumination Laser Wavelength

M. SAYRAC[1]

[1]Department of Nanotechnology Engineering, Sivas Cumhuriyet University, Sivas/Turkey,
muhammedsayrac@cumhuriyet.edu.tr

Abstract **- In this study, a computer simulation program generating Fresnel diffraction patterns from the apertures by using the different illumination wavelength sources has been studied. Changing the aperture-screen distance and the illumination wavelength provides a clear transition of diffraction patterns from the Fresnel to the Fraunhofer region. The diffraction patterns obtained by the Fresnel integral method have been compared with those simulated by the Fraunhofer calculation. There is a good agreement between the results. Certain conditions have been investigated that Fresnel diffraction patterns approach the Fraunhofer diffraction patterns. The simulations have been performed using a personal computer with Matlab software.**

Keywords **– Diffraction, Optics, Numerical simulation, Micron/nano structures.**

I. INTRODUCTION

OPTICS is one of the important fields of physics that studies the properties of light. It plays an important role in technical applications such as communication and information sciences. In optics, the diffraction of light plays a paramount role in solving optical problems that do not usually reach an agreement with an exact solution. Therefore, numerical methods make it easy to investigate simpler cases. When the optical wave encounters an aperture, diffraction of light occurs [1]. Diffraction is classified known as Fraunhofer (far-field) and Fresnel (near-field) diffraction. The Fraunhofer diffraction pattern occurs when the aperture-observation screen distance is large. However, the Fresnel diffraction pattern appears when the aperture-screen distance is short [2, 3]. Diffraction and propagation of the optical field from an aperture were calculated by using Helmholtz-Kirchhoff [4] and Rayleigh-Sommerfeld integrals [5]. The Fresnel and Fraunhofer diffraction patterns were obtained by using the Fourier transform method [6] and two dimensional Fast Fourier transform method [7].

The calculation of the diffraction integral is possible with minimum effort due to the personal computer and packaged mathematical software. In this paper, the diffraction patterns have been obtained by using Matlab software (R2017b 9.3.0.713579 (x64)) [8] for different input parameters, i.e. wavelengths and aperture to screen distance. The Fresnel and Fraunhofer diffraction patterns have been simulated for micron size aperture by using the radiation source from 4nm to 600nm (corresponding to photon energy from ~310eV to 2eV) [1, 9]. This paper aims to study diffraction phenomena further for small-size structures by using short-wavelength radiation. The "soft x-ray region" of 4nm corresponds to the water window region in which water is transparent to extreme ultraviolet (XUV) radiations. Therefore, the wavelength region has a crucial role in viewing water-dominant biological samples, and the diffraction of light has a vital role in life science. On the other hand, this phenomenon is complex for studies at the short wavelength region, and it is not easy for laboratory experiments. For this reason, the simulation approaches facilitate viable alternatives and bring an idea for pre experiments studies. The contribution of the study to the literature is to investigate the diffraction phenomena by using small size structures at short wavelength regions, i.e. how does the diffraction phenomena behave in short wavelengths, which is important for life science studies?

Over the last 20 years, the optics field including coherent XUV beamlines has brought opportunities studied in several disciplines from biological imaging [10] to material science [11], and astrophysics [12] to high energy plasmas [13]. Also, it is useful to science and engineering students who deal with Fresnel diffraction, especially in short-wavelength regions. Therefore, the implementation of a diffraction model for a small-size aperture by using a short-wavelength source is important.

The diffraction patterns discussed the Fraunhofer diffractions of the single slit at the visible or infrared region, however, the diffraction patterns at the XUV region were not mentioned. The paper introduces a simulation for Fraunhofer and Fresnel diffraction at a wavelength range from XUV to the visible region. The simulation program is compiled by several input parameters, namely the aperture-screen distance and the illumination wavelength. The simulation program demonstrates how a diffraction pattern changes with varying input parameters from the Fraunhofer to the Fresnel region at the short wavelength region.

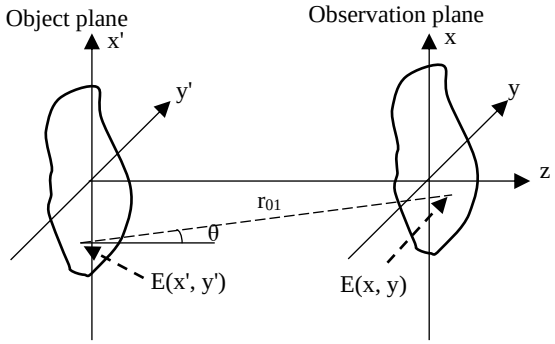

Figure 1 Schematic diagram of diffraction [1, 11]

II. BASIC DIFFRACTION THEORY

Light propagation and diffraction have been described by using the Huygens-Fresnel principle by several researchers [4, 7, 14, 15]. The fundamental calculation of Fresnel diffraction from a rectangular aperture is that a light wave passes through an aperture and the total electric field at any point in the xy-plane can be obtained by the Huygens-Fresnel Principle for rectangular coordinates, Fig. 1 [1, 9]. The diffracted light is observed on the screen located at distance. By using the Huygens-Fresnel principle, the total field (E(x, y)) in the xy-plane is integral of the fields of all the wavelets produced in each part of the aperture in the x'y'-plane [15]

$$E = \frac{-iE_u}{2}\left[C(u)+iS(u)\right]_{\alpha_1}^{\alpha_2}\left[C(v)+iS(v)\right]_{\beta_1}^{\beta_2} \qquad (1)$$

where E_u is the unobstructed electric field, and C and S are the Fresnel integrals, and two-dimensional variables are defined $u = y\left[\frac{2(r_{01}+P_0)}{\lambda r_{01}P_0}\right]^{0.5}$ and $v = z\left[\frac{2(r_{01}+P_0)}{\lambda r_{01}P_0}\right]^{0.5}$. λ is the wavelength, and r_{01} is a vector from an aperture point to a parallel screen, θ is the angle between r_{01} and the aperture surface x'. P_0 is the aperture to source distance. $E(x',y')$ and $E(x,y)$ are electric fields on the aperture and the screen, respectively. There are two approximations: (i) the dimensions of the diffraction geometry are larger than the illumination wavelength (λ). (ii) The observation screen distance is many wavelengths from the aperture ($r_{01} >> \lambda$)

Taking the square of the electric field, Eq. 1 gives

$$I = \frac{I_u}{4}\left\{\left[C(\alpha_2)-C(\alpha_1)\right]^2+\left[S(\alpha_2)-S(\alpha_1)\right]^2\right\}\times \times\left\{\left[C(\beta_2)-C(\beta_1)\right]^2+\left[S(\beta_2)-S(\beta_1)\right]^2\right\} \qquad (2)$$

I_u is unobstructed intensity corresponding to the square of E_u, and $\alpha = \sqrt{\frac{2}{\lambda z}}(x'-x)$ and $\beta = \sqrt{\frac{2}{\lambda z}}(y'-y)$ are coefficients.

The derivation of the Fresnel integral method is given in a detailed manner [15]. When the distance between the aperture to the observation screen is increased, the Fresnel diffraction region gradually approaches the Fraunhofer diffraction region. In the simulation part, the Fresnel diffraction integral has been used, Eq. 2. Input parameters namely the aperture to screen distance and the illumination wavelength have been changed, and the diffraction patterns vary with changing input parameters.

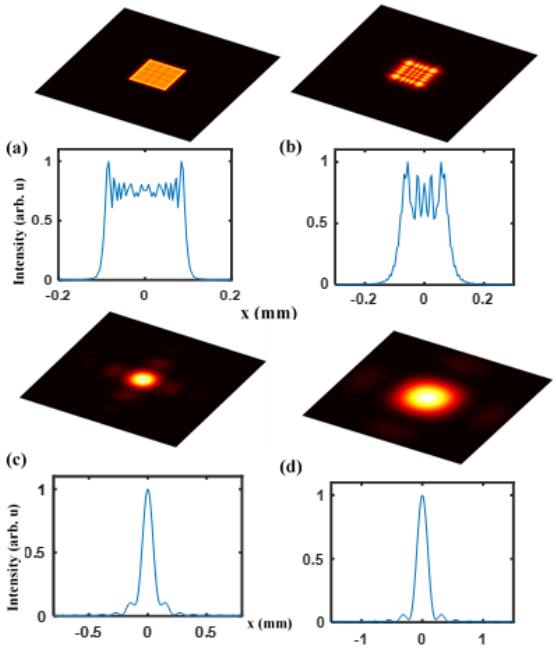

Figure 2 Diffraction patterns for increasing the aperture-screen distance. (a)10mm, (b)70mm, (c)700mm, (d)1400mm. The aperture size is 0.1mm×0.1mm, and the illumination wavelength is 32nm. In (a-d) the upper figures are for 2D diffraction patterns, and lower figures are for 1D normalized intensity distribution.

III. SIMULATION RESULTS

Figure 2 shows the diffraction patterns for the increasing aperture to screen distance. The illumination wavelength and the aperture size are 32nm and 0.1mm×0.1mm, respectively. When the aperture-screen distance is increased, the Fresnel diffraction pattern gradually changes into the Fraunhofer diffraction pattern. Aperture size is about 3100 wavelengths wide, and the screen has been placed from the aperture about 0.3million to 43million wavelength away, Fig. 2 (a) 0.3million, (b) 2.2million, (c) 22milllion, and (d) 43million. Upper figures in Figure 2 present 2D diffraction patterns while lower show the normalized 1D intensity distribution of the diffraction pattern.

Figure 3 presents diffraction patterns (upper figures Fig. 3 (a-d)) for fixed aperture size of 0.1mm×0.1mm and for the apertures to screen distance of 700mm. The illumination wavelength gradually increases from 4nm to 600nm wavelength. Thus, the aperture width varies from 25×10^3 to 160 wavelength size, and the distance between the aperture-observation screen changes from 175 to 1 million wavelengths away, Fig. 3 (a)-(d). When the aperture size and the aperture–screen distances are constant, the Fresnel diffraction patterns are generated at the short wavelength region. An increase in the illumination wavelength generates the Fraunhofer diffraction patterns, Fig. 3. Lower figures in Figure 3 are normalized-1D intensity distributions of diffraction patterns.

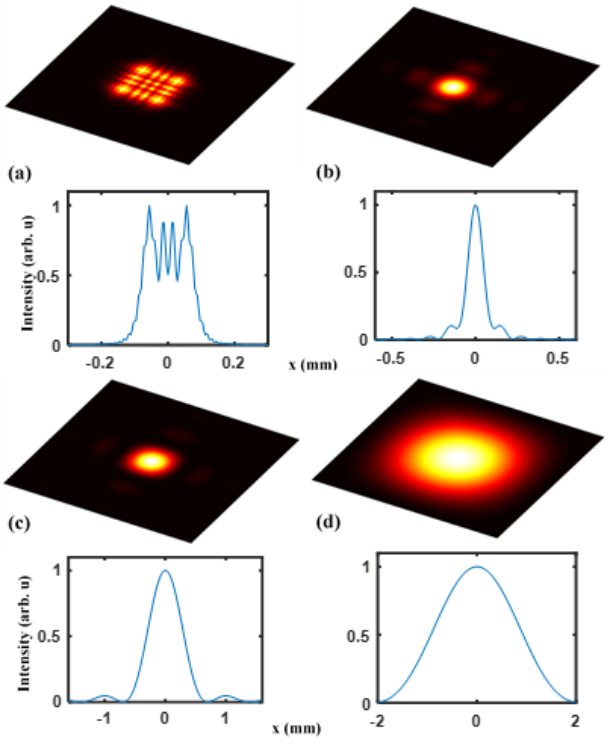

Figure 3 Diffraction patterns for increasing wavelength. (a) 4nm, (b) 32nm, (c) 200nm, (d) 600nm. The aperture size is 0.1mm×0.1mm, and the aperture-screen distance is 700mm. In (a-d) the upper figures are for 2D diffraction patterns, and lower figures are for 1D normalized intensity distribution.

Figures 2, 3 agree with the rule that the aperture-screen distance (r_{01}) and the illumination wavelength (λ) have effects on the diffraction patterns [1, 9]. A practical comparison, if a satisfies the relation of $r_{01} < a^2/\lambda$, the Fresnel diffraction occurs. The relation of $r_{01} > a^2/\lambda$ gives the Fraunhofer diffraction, where r_{01}, a, and λ are the aperture-screen distance, the aperture size, and the illumination wavelength, respectively.

IV. Conclusion

This study describes that the generated diffraction images in the Fresnel and the Fraunhofer region by using illumination wavelengths at different illuminating wavelengths and the aperture-screen distance. The basic diffraction theory is described. The simulated 2D diffraction images and 1D diffraction intensity distribution for small size aperture and different wavelength sources (from 4nm to 600nm) are presented in the results. The obtained diffraction result for 600nm illumination wavelengths in this paper is similar to the studies in Refs. [14, 15] which provides the simulated diffraction patterns for the visible wavelength region. The Matlab software simulates the diffraction patterns. The transition from the Fresnel to Fraunhofer region is observed with varying input parameters, namely the aperture-screen distance and the illumination wavelengths.

References

[1] J.W. Goodman, Introduction To Fourier Optics, McGraw-Hill Science, McGraw-Hill Science, 1996.
[2] Born M, W. E., Principles of Optics: Electromagnetic Theory of Propagation, Interference and Diffraction of Light, 7th ed. ed., Cambridge University1999.
[3] C.J. Ball, An Introduction to the Theory of diffraction, Pergamon Press,, New York, 1971.
[4] P.G. Rudolf, J.J. Tollett, R.R. McGowan, Computer modeling wave propagation with a variation of the Helmholtz-Kirchhoff relation, Appl. Opt., 29 (1990) 998-1003.
[5] J. Räsänen, K.M. Abedin, M. Kawazoe, K. Tenjimbayashi, T. Eiju, K. Matsuda, K.-E. Peiponen, Computer simulation of the scatter plate interferometer by scalar diffraction theory, Appl. Opt., 36 (1997) 5335-5339.
[6] S.A. Dodds, An optical diffraction experiment for the advanced laboratory, American Journal of Physics, 58 (1990).
[7] S. Trester, Computer-simulated Fresnel diffraction using the Fourier transform, Computing in Science & Engineering, 1 (1999) 77-83.
[8] MATLAB version 9.3.0.713579 (R2017b), The Mathworks, Inc., Natick, Massachusetts, 2017.
[9] E. Hecht, Optics, 5th ed., Pearson2016.
[10] T. Helk, M. Zürch, C. Spielmann, Perspective: Towards single shot time-resolved microscopy using short wavelength table-top light sources, Structural Dynamics, 6 (2019) 010902.
[11] D. Milathianaki, S. Boutet, G.J. Williams, A. Higginbotham, D. Ratner, A.E. Gleason, M. Messerschmidt, M.M. Seibert, D.C. Swift, P. Hering, J. Robinson, W.E. White, J.S. Wark, Femtosecond Visualization of Lattice Dynamics in Shock-Compressed Matter, Science, 342 (2013) 220-223.
[12] D.W. Savin, N.S. Brickhouse, J.J. Cowan, R.P. Drake, S.R. Federman, G.J. Ferland, A. Frank, M.S. Gudipati, W.C. Haxton, E. Herbst, S. Profumo, F. Salama, L.M. Ziurys, E.G. Zweibel, The impact of recent advances in laboratory astrophysics on our understanding of the cosmos, Reports on Progress in Physics, 75 (2012) 036901.
[13] M. Beye, S. Schreck, F. Sorgenfrei, C. Trabant, N. Pontius, C. Schüßler-Langeheine, W. Wurth, A. Föhlisch, Stimulated X-ray emission for materials science, Nature, 501 (2013) 191.
[14] D.E. Dauger, Simulation and study of Fresnel diffraction for arbitrary two-dimensional apertures, Computers in Physics, 10 (1996) 591-604.
[15] J.A. Díaz, Comment on "Computer simulation of Fresnel diffraction from rectangular apertures and obstacles using the Fresnel integrals approach", Optics & Laser Technology, 121 (2020) 105819.

Detection of Errors in Glass Products in Studio Environment with Image Processing and Deep Learning Methods

Ali Burak ULAŞ [1] and Filiz SARI[2]

[1] Aksaray University, Engineering Faculty, Electrical and Electronics Engineering Department, Aksaray Turkey, aliburak44@gmail.com
[2] Aksaray University, Engineering Faculty, Electrical and Electronics Engineering Department, Aksaray Turkey, filizsari@aksaray.edu.tr

***Abstract* - It is difficult to detect defects on the surfaces of glass products due to its transparent structure, sensitivity to reflections and being affected by dust and dirt. In this study, surface defects, which are bubbles and wrinkle, were investigated for glass packaging products with curved surfaces (glass bottles, glass jars, etc.). In the first stage, suitable lighting conditions were examined for faulty/defect-free glass products supplied from the manufacturer. The images taken with a professional camera were analyzed with Faster R-CNN by changing the background of the studio environment and the apex angle. In the analyzes made, the highest accuracy rate was obtained as 82,817%, with the apex angle of -60° and white matte background. After determining the appropriate lighting environment, the color space conversion methods HSV and CIE-Lab Luv were applied to the obtained images, and the overall accuracy rate was obtained as 89,577% for the V channel of CIE-Lab Luv. In order to improve the system performance, the results were analyzed by applying adaptive histogram equalization to the color space transformations and the overall accuracy was 90,423%.**

***Keywords* - Quality Control on Glass Surface, Image Processing, Deep Learning, Pixel Based Image Segmentation.**

I. INTRODUCTION

FOOD is an essential need for human life. It is critical for the production of foods sold in markets and other businesses with commercial titles to have a long shelf life and to be packaged in order not to deteriorate after the production process for the access of end-users. In packaged foods, food contact materials consist of materials such as paper, glass and metal, mainly plastics.

Glass products produced for the purpose of storing food are healthier when compared to paper, plastic and metal storage containers due to the low migration level, that is, the transition from packaging material to food [1]. However, glass products with high breakage sensitivity cause accidents due to errors that occur during production. For this reason, quality control in the production process is of great importance.

From time to time, surface defects occur in the produced glass products due to the mold and the raw material used. General errors in the production of glass; surface and edge defects, various cracks and chips, bubbles (bubbles), wrinkles (wavelets), holes and dirt [2]–[7]. These errors must be controlled by an operator and separated from the production line. Since traditional human-based visual inspection methods are insufficient and time-consuming, digital image processing techniques and machine learning algorithms are used to improve quality [5], [8], [9].

The reason why machines are preferred over human power is that, in addition to their low cost in the long run, the machine does not get tired, can react instantly and the mistakes made with human power are eliminated. In Figure 1, the visual of the quality control stage made with manpower and machines is presented.

Figure 1: Quality control process by the operator.

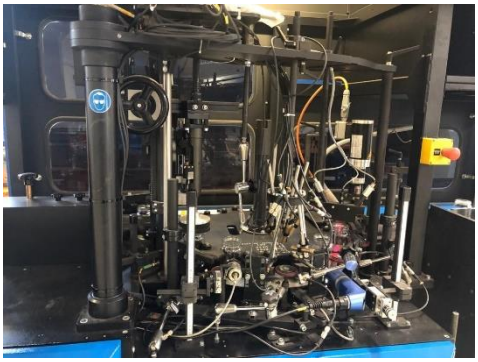

Figure 2: Quality control process by machine.

Glass, which is a transparent component, has some difficulties in detecting defects. These; The uneven distribution of light on the glass, the image taken very close to the background, small error sizes and irregular shape [6]. Therefore, a fixed lighting system is needed. Lighting is an essential component of the image capture process and its main function is to minimize reflection by making the desired features of an object or surface visible. For this purpose, lighting systems using dual cold cathode fluorescent lamps [5] and fluorescent lamps [9], [10] were applied to the production line. Afterwards, images taken on glass surfaces with a digital camera and processed by image processing algorithms.

To extract the attributes of the received images and to detect errors; color space transform [8], binary feature histogram [11], grayscale distribution map [12], edge detection, gray color space and adaptive histogram technique [13], wavelet transform with Shannon threshold method [14] and discrete Fourier transform [15], image processing methods have been applied to glass products.

In addition to digital image processing methods, classification techniques such as artificial intelligence, machine learning and deep learning have also been adapted to the glass industry. For flat glasses, fuzzy-logic based segmentation [9], fuzzy support vector machine (SVM), quadratic discriminant and middle tree classifiers [16] methods are used. SVM [17] and the deep learning methods, ResNET 101 Convolutional Neural Network (CNN), [18] methods were used to classify glass bottles.

In this study, bubble and scratched defects, which are frequently encountered on glass jar surfaces, were investigated. In general, there are studies for flat glasses and glass bottles in the literature, this study examined the determination of lighting conditions for glass with curved surfaces and combining the color space conversion method with deep learning. For this purpose, taking into account the slope of the glass jar surface, the studio environment was determined and images were taken with a professional camera in order to determine the correct lighting conditions. It has been applied to Faster Region Based Convolutional Neural Network (Faster R-CNN) by using color space conversion and adaptive histogram equalization methods from image processing techniques.

II. Material and Method

This study is carried out based on the information obtained from a company that produces glass packaging (glass bottles, glass jars) for food products.

The architecture in which reflection and glare can be eliminated so that the defects on the surface of the glass packages coming out of the glass production furnace can be detected by deep learning modeling instead of traditional quality control is shown on Figure 3.

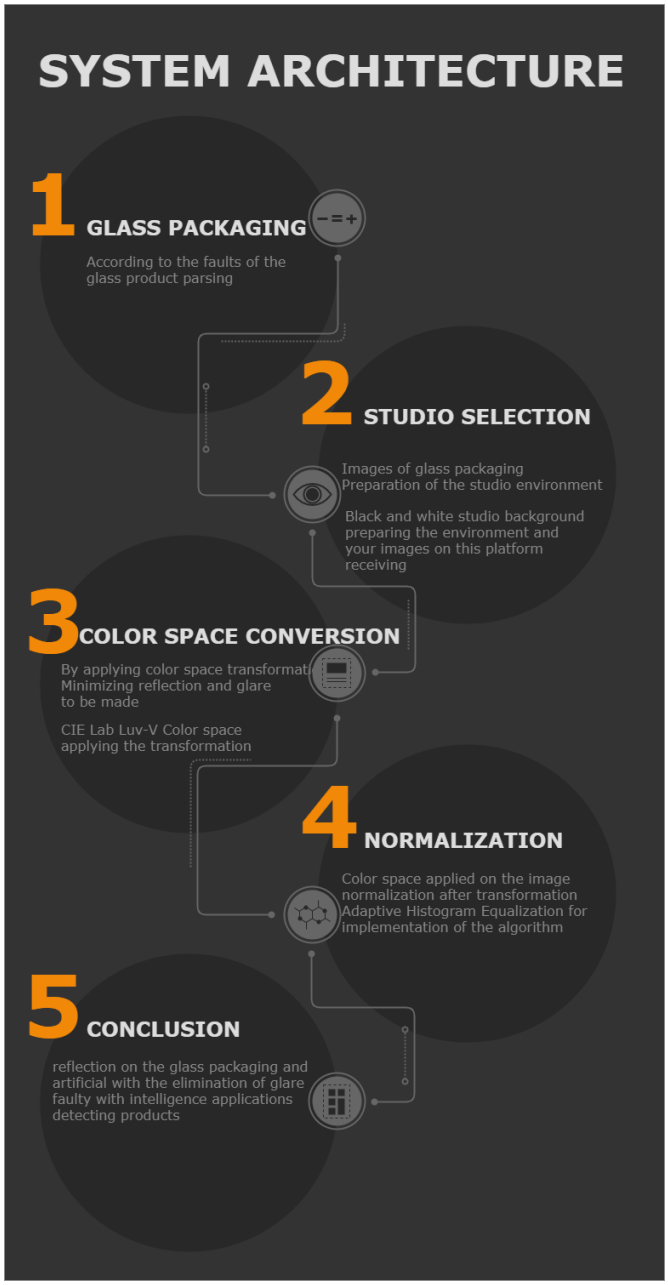

Figure 3: System Architecture.

In line with the manufacturer's reports, studies were carried out on the most common and critically important fault types in the production line. These errors are Bubble and Wrinkle errors. In the study planned for the machine to be designed for the production line, the images of the glass jars with the rough and

wrinkled defects were taken from the company in a studio environment with a black and white (matte/glossy) background. When the images stored in the database were examined, it was observed that there were reflections due to the transparency of the imaged product.

Bubble error occurs when air bubbles remain in the glass raw material pressed into the molds during production. The fluctuations that occur with the incomplete or adhered area when leaving the mold are called wrinkles. Bubble and Wrinkle errors used in the study are given in Figure 4.

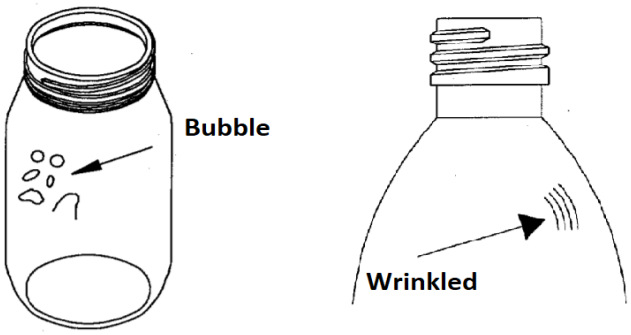

Figure 4: Errors used in the study; Bubble and Wrinkle.

In the study, Faster R-CNN was applied by applying CIE Lab-LUV - V transformation on the images taken on different backgrounds by changing the backgrounds of glass packaging products taken from the manufacturer.

III. Determining the Studio Environment

In this study, it is aimed to determine the suitable studio for use, where reflection and glare are at a minimum level. In the studio selection, photographs were taken for 4 backgrounds: black glossy, white glossy, black matte and white matte. The studio environment is given on Figure 5.

Figure 5: Studio environment and background.

Another element as important as the background in the studio set for reflection and glare is the lighting angle. Illumination angles are tested according to the camera angle. The studio images were recorded as 710 pixels horizontally and 1280 pixels vertically with the professional camera that can take 12 MP color images. A database consisting of 400 different images was created. Figure 6 presents the images obtained for the natural environment, black background and white background.

Figure 6: Natural Environment- Black Background- White Background.

A. *Image Processing Color Space Conversion*

In the study, image processing algorithms were used for preprocessing on the images taken from reflection and glare on the glass packaging.

Color images consist of three image parts: red (R), green (G), and blue (B). The RGB color model is the most popular model for processing digital images because it is insensitive to image rotation, translation, and scale change, and has strong robustness, but the RGB model is affected by density changes. Color space is a model used to represent color values in intensity and is converted from the RGB model using a linear/non-linear transformation matrix.

Numerous color spaces are available, from which a specific color space is selected depending on the application. Some of the color patterns are YUV, YIQ, HSV, HIS, HSL, Lab, Luv, LCH, YCbCr, etc. [7], [19], [20].

The HSV (Hue, Saturation, Value) color model is a popular model for computer graphics. The hue (H) of an image represents a pure color and ranges from 0-3600, where each value corresponds to a color. Saturation (S) is the intensity of the color and value (V) is the measurement of the brightness of the color [20].

L: , U: , V: defined as CIE Lab-Luv. With the color space transformation applied in the areas determined on the image together with the algorithm used, reflection and glare were eliminated [21] and new images were recorded as data.

Figure 7: CIE Lab Luv-v applied image.

B. Adaptive Histogram Equalization

Adaptive histogram equalization was applied to improve the contrast value by increasing the color space conversion algorithm on the data [13]. The image of the glass product taken after the process is given in Figure 8.

Figure 8: Image with CIE Lab Luv-v and Adaptive Histogram applied.

In Figure 8, it is aimed to label the image on which CIE Lab Luv-V transform is applied, by normalizing with adaptive histogram equalization, eliminating reflection and glare completely.

C. Faster R-CNN

Faster R-CNN [22] is referred to as the combination of Region Proposal Network (RPN) [23] and Fast R-CNN [24] models.

The Region Proposal Network (RPN) is a deep convolutional neural network for suggesting regions as the first stage. Here, the RPN takes input of any size and generates square suggestions that may belong to a set of objects based on the object score. It does this by shifting a small mesh created by the convolutional layer while creating these suggestions on the feature map. These calculations produced by RPN are inserted into the Fast R-CNN architecture and the class of the object is estimated with the help of a classifier and the bounding boxes are estimated with the regressor. As a result of the separate operations and the search for the desired object with separate operations in the specified boxes, the average training period was 84 hours, while the test duration was approximately 47 seconds.

In the Faster R-CNN model used in the study, the input image is passed through the convolutional neural networks and the feature map is extracted and the RPN is created. Zone suggestions are made on this network without any further processing. After the network regions are determined, classification is made on the determined regions. With the CNN architectures running simultaneously on the boxes created here, more than one object can be scanned in the box content, while the average training time is 8.75 hours, while the test time is approximately 0.4 ms.

The average accuracy value is an evaluation criterion used to measure the accuracy of deep learning algorithms and is the average of the accuracy magnitudes corresponding to different sensitivity values. Equations of accuracy and sensitivity values are presented in (1) and (2).

$$Accuracy = \frac{True\ Positive}{True\ Positive + False\ Positive} \quad (1)$$

$$Sensitivity = \frac{True\ Positive}{True\ Positive + Received\ Negative} \quad (2)$$

IV. Research Results and Discussion

Labeled and preserved products were obtained from the manufacturer in order to carry out R&D studies and improve production, Figure 9.

Figure 9: Labeled Data.

The number and features of images used for the diagnosis and classification of bubble and wrinkle are given in Table 1.

Table 1: Number of images used and their features.

Error Type	Number of Images	Resolution	Image Format
Bubble	450	710 x 1280	.png
Wrinkled	401	710 x 1280	.png
Sturdy	330	710 x 1280	.png

70% of the available image data was used for training deep learning models and 30% in the testing phase.

Measurements were made for different backgrounds of the studio, which received intense sunlight for Faster R-CNN modelling. At this stage, no preprocessing has been applied on the data, the aim is to determine the background that gives the best results with the raw data. The results are presented in Table 2.

Table 2: Studio Background Results.

Peak Angle/ Background	Sturdy (99)	Bubble (135)	Wrinkled (121)	Accuracy Rate (%)
Black Glossy	80	122	66	75.07
White Glossy	83	91	97	76.471

Black Matte	82	112	81	77.465
White Matte	86	101	96	79.718
-60° Black Matte	78	113	95	80.563
-60° White Matte	87	109	98	82.817

Table 2 presents the Faster R-CNN results for the selected background, the highest accuracy achieved on a white matte background at -60° apex angle.

After selecting the suitable background, color space transformation was applied to the images. Figure 10 presents HSV and CIE-lab LUV images.

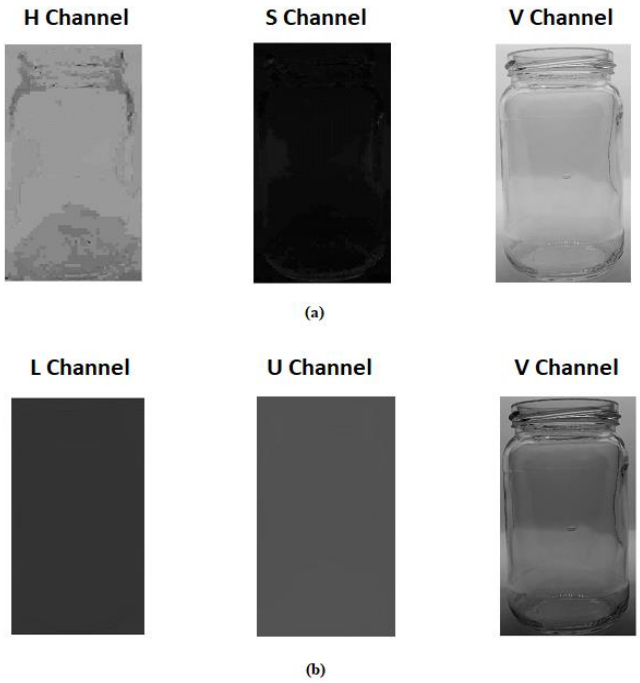

Figure 10: (a) HSV, (b) glass image treated with CIE-Lab Luv.

As shown in Figure 10, V channels for HSV and CIE-Lab Luv were chosen because they provide a suitable environment for labeling for deep learning modelling.

In this preprocessing-based process, the data received in the 'V' channel was labeled as Bubble and Wrinkled on Image Labeler with MATLAB for processing in deep learning modelling. The determination of the most healthy studio environment on the output obtained after the processes was concluded on the applied deep learning modeling. Finally, on the images taken in the studio environment, faulty/defective glass separation was carried out on the application. According to the error type (Bubble yellow, wrinkled red) it is directly enclosed in a rectangle and the operator is informed. In Figure 11, the defect types of a defective glass package are separated and given together with their accuracy rates.

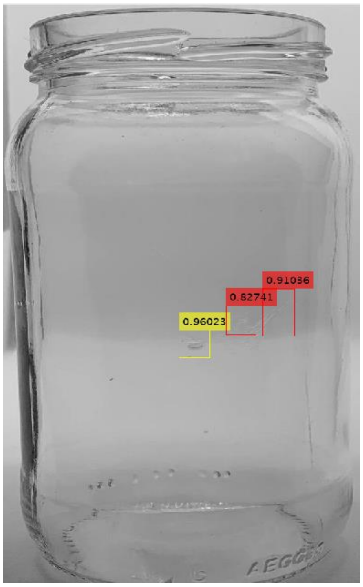

Figure 11: Bubble and Wrinkle Detection (Application).

The glass packaging error detection, which was printed in Figure 11, was carried out within 58 ms by manually selecting the file path.

The results from Faster R-CNN modeling run on preprocessed images for V channels for HSV and CIE-Lab Luv are given in Table 3.

Table 3: Faster R-CNN results for V channels for HSV and CIE-Lab Luv.

Confusion Matrix of Faster R-CNN model for HSV V Channel		Prediction			
		(0) Sturdy	(1) Bubble	(2) Wrinkled	Sens.
Real	(0) Sturdy	89	6	4	89.899
	(1) Bubble	15	112	8	82.963
	(2) Wrinkled	6	7	108	89.256
	Sens.	80.909	89.6	90	OA: 87.042
Faster R-CNN for CIE-Lab Luv V channels		Prediction			
		(0) Sturdy	(1) Bubble	(2) Wrinkled	Sens.
Real	(0) Sturdy	92	4	3	92.929
	(1) Bubble	9	119	7	88.148
	(2) Wrinkled	9	5	107	88.43
	Sens.	83.636	92.969	91.453	OA: 89.577

While the overall accuracy (OA) for the HSV-V channel was 87,042 %, the CIE Lab Luv-V channel achieved 89,577 % accuracy. In order to improve the results obtained, the image color space transform was trained and tested by applying adaptive histogram equalization to the data. Obtained results are

presented in Table 4.

Table 4: Faster R-CNN results for the adaptive histogram equalization method.

HSV V Channel and adaptive histogram equalization		Prediction			
		(0) Sturdy	(1) Bubble	(2) Wrinkled	Sens.
Real	(0) Sturdy	91	5	3	91.919
	(1) Bubble	9	119	7	88.148
	(2) Wrinkled	6	7	108	89.256
	Sens.	85.849	90.84	91.525	OA : 89.577
CIE Lab Luv V Channel and adaptive histogram equalization		Prediction			
		(0) Sturdy	(1) Bubble	(2) Wrinkled	Sens.
Real	(0) Sturdy	92	3	4	92.929
	(1) Bubble	7	123	5	91.111
	(2) Wrinkled	11	4	106	87.603
	Sens.	83.636	94.615	92.174	OA: 90.423

As presented in Table 4, the overall accuracy percentages for the V channels of HSV and CIE-Lab Luv increased and converged with the adaptive histogram method. The maximum accuracy achieved was 93%, while the overall accuracy was 90,423%.

V. Conclusion

This study was done with a deep learning library on the MATLAB platform. In the study, firstly, studio environments were classified. As a result of the analyzes made in different studio environments, the best result was obtained with a peak angle of -60 and a white matte background. Taken images in the determined studio environment were preprocessed with color space transformations on MATLAB. HSV and CIE-Lab Luv color space conversions were applied to taken images. When the results were examined, it was seen that the most healthy images that directly affect the reflection and can be used for deep learning modeling were created in V channels for both algorithms. The V channels of HSV and CIE-Lab Luv were applied to the Faster R-CNN algorithm. For this purpose, 70% of the data was used for training and 30% for testing. The highest accuracy rate was obtained in the CIE-Lab Luv –V channel. The adaptive histogram equalization technique was applied to the V channels in order to increase the overall accuracy. An overall accuracy increase of 2% for the HSV – V channel and 1% for the CIE-Lab Luv – V channel was observed. The maximum accuracy achieved is 93%. For the deep learning algorithm in the study, the average training time was 8.75 hours, while the test time was approximately 0.4 ms.

References

[1] P. ÇİNİBULAK, "Gida Ambalajlarinda Migrasyon,", Yüksek Lisans Tezi, 2010.

[2] N. and S. Agrawal, "Glass Defect Detection Techniques using Digital Image Processing – A Review," Spec. issues IP Multimed. Commun., pp. 65–67, 2011, [Online]. Available: https://www.ijcaonline.org/specialissues/ipmc/number1/3750-ipmc014.

[3] S. S. Tiwana and Sukhpreet Kaur, "Study on Various Glass Defect Using Glass Edge Detection Methods," vol. 2, no. May, pp. 82–85, 2013.

[4] C. Jian, J. Gao, and Y. Ao, "Automatic surface defect detection for mobile phone screen glass based on machine vision," Appl. Soft Comput. J., vol. 52, pp. 348–358, 2017, doi: 10.1016/j.asoc.2016.10.030.

[5] Y. Jin, Z. Wang, L. Zhu, and J. Yang, "Research on in-line glass defect inspection technology based on Dual CCFL," Procedia Eng., vol. 15, pp. 1797–1801, 2011, doi: 10.1016/j.proeng.2011.08.334.

[6] J. D. D. Cabral and S. A. Araújo, "Computer Vision System for Automatic Quality Inspection of Glass Products Used for Food Packaging," Int. Conf. Ind. Eng. Oper. Manag., pp. 1–10, 2012.

[7] W. Ming et al., "A comprehensive review of defect detection in 3C glass components," Meas. J. Int. Meas. Confed., vol. 158, p. 107722, 2020, doi: 10.1016/j.measurement.2020.107722.

[8] Nishu and S. Agrawal, "Glass Defect Detection Techniques using Digital Image Processing–A Review," Spec. issues IP Multimed. Commun., vol. 1, no. October, pp. 65–67, 2011, [Online]. Available: http://www.ijdacr.com/sites/default/files/may13/paper1015.pdf.

[9] Ş. Öztürk and B. Akdemir, "Fuzzy logic-based segmentation of manufacturing defects on reflective surfaces," Neural Comput. Appl., vol. 29, no. 8, pp. 107–116, 2018, doi: 10.1007/s00521-017-2862-6.

[10] S. S. Martínez, J. G. Ortega, J. G. García, A. S. García, and E. E. Estévez, "An industrial vision system for surface quality inspection of transparent parts," Int. J. Adv. Manuf. Technol., vol. 68, no. 5–8, pp. 1123–1136, 2013, doi: 10.1007/s00170-013-4904-2.

[11] J. Zhao, Q. J. Kong, X. Zhao, J. Liu, and Y. Liu, "A method for detection and classification of glass defects in low resolution images," Proc. - 6th Int. Conf. Image Graph. ICIG 2011, no. March, pp. 642–647, 2011, doi: 10.1109/ICIG.2011.187.

[12] X. Li and Y. Shu, "Research on glass surface quality inspection based on machine vision," Aust. J. Mech. Eng., vol. 16, no. sup1, pp. 98–104, 2018, doi: 10.1080/1448837X.2018.1545479.

[13] R. Kumar, N., Kaur, "Detection of Defects in Glass Using Edge Detection with Adaptive Histogram Equalization," Int. J. Innov. Res. Comput. Commun. Eng., vol. 1, no. 6, pp. 1321–1327, 2013.

[14] B. Akdemir and Ş. Öztürk, "Glass Surface Defects Detection with Wavelet Transforms," Int. J. Mater. Mech. Manuf., vol. 3, no. 3, pp. 170–173, 2015, doi: 10.7763/ijmmm.2015.v3.189.

[15] Hongxi Zhang, Zhenduo Guo, Zegang Qi, and Jiuge Wang, "Research of glass defects detection based on DFT and optimal threshold method," in 2012 International Conference on Computer Science and Information Processing (CSIP), Aug. 2012, vol. 3, pp. 1044–1047, doi: 10.1109/CSIP.2012.6309035.

[16] Ç. C. BÜKÜCÜ and L. GÖKREM, "a New Prototype That Performs Real-Time Error Detection in Glass Products," Uluslararası Muhendis. Arastirma ve Gelistirme Derg., pp. 510–519, 2020, doi: 10.29137/umagd.681653.

[17] H. Liu, Y. Wang, and F. Duan, "An empty bottle intelligent inspector based on support vector machines and fuzzy theory," Proc. World Congr. Intell. Control Autom., vol. 2, pp. 9739–9743, 2006, doi: 10.1109/WCICA.2006.1713895.

[18] Q. Liang, S. Xiang, J. Long, W. Sun, Y. Wang, and D. Zhang, "Real-time comprehensive glass container inspection system based on deep learning framework," Electron. Lett., vol. 55, no. 3, pp. 131–132, 2019, doi: 10.1049/el.2018.6934.

[19] A. S. Narote and L. M. Waghmare, "Performance evaluation of different color models used in color iris authentication," 2016 Int. Conf. Adv. Comput. Commun. Informatics, ICACCI 2016, pp. 2736–2739, 2016, doi: 10.1109/ICACCI.2016.7732475.

[20] S. Agrawal, "Automated Inspection of Defects in Glass by proper Color space selection and Segmentation Technique of Digital Image processing," vol. 3, no. June, pp. 1058–1063, 2012.

[21] R. W. G. Hunt, The Reproduction of Colour. Chichester, UK: John Wiley & Sons, Ltd, 2004.

[22] S. Ren, K. He, R. Girshick, and J. Sun, "Faster R-CNN: Towards Real-Time Object Detection with Region Proposal Networks," IEEE Trans. Pattern Anal. Mach. Intell., vol. 39, no. 6, pp. 1137–1149, 2017, doi: 10.1109/TPAMI.2016.2577031.
[23] R. Girshick, J. Donahue, T. Darrell, J. Malik, U. C. Berkeley, and J. Malik, "Rich feature hierarchies for accurate object detection and semantic segmentation," Proc. IEEE Comput. Soc. Conf. Comput. Vis. Pattern Recognit., vol. 1, p. 5000, 2014, doi: 10.1109/CVPR.2014.81.
[24] R. Girshick, "Fast R-CNN," Proc. IEEE Int. Conf. Comput. Vis., vol. 2015 Inter, pp. 1440–1448, 2015, doi: 10.1109/ICCV.2015.169.

Sensor Based Dairy Animal Health Monitoring and User Notification System

M.K. TURKES[1], M.M. YURDAKUL[1] and H. AKCA[2]

[1] Istanbul Gelisim University, Istanbul/Turkey, mktrks1@gmail.com, m.m.yrdkl@gmail.com
[2]Ege University, Izmır/Turkey, hakan.akca@ege.edu.tr

Abstract - **Within the scope of the study, an animal health monitoring system was promoted and the terms of efficiency and quality has been made measurable by monitoring some activities especially health in animals; heat, giving birth, nourishment, rumination etc. A smart system has been designed that can follow up disease and rutting by comparing the data gathered from a neck collar which is tied to the animals' neck with reference value in the computers by virtue of the formed algorithms. The neck collar with communication system will be on the animal. There is a station setting designed for data processing and user information and an enhanced system for data reporting and conveying to users. Problems will be occurred with this system will be conveyed to users and instant solutions will be provided.**

Keywords **- Animal monitoring system, disease detection, sensor, smart system**

I. INTRODUCTION

Being an agricultural country- our country has an important place in dairy farming. Thanks to the government policy supported contributions in relating to dairy farming, this sector gradually develops. In the matter of this issue, various support programs contributed by ministry of agriculture and forestry are found. In general, these contributions provide with large capacity and more modern facilities. By this means, it encourages animal breeding to be more fruitful, qualified and smarter. As a consequence, some developments are improved on the subjects of appropriate nutrition of the animals, animal health [1], milk yield and birth rate etc.

Because it causes the decrease of milk yield, mastitis is the most expensive disease of dairy animals. This disease cause expenses like treatment costs and reduction of milk production after treatment. Because of the fact that this disease reduces the quality of milk and increases the infection in the animal shelter it causes massive economic loss in food industry. [2]

With the improving life standards people's demand of milk increases day by day and consequently milk quality comes forward. To meet the market demand, it is useful to increase the milk yield and long the lactation processing and additionally it promotes the economic benefit. For this reason; it is really important to check the dairy cows' rutting timing in a correct way. [1]

Accurate rutting description may help the farmers identifying the rutting degree and the insemination time so that the cow can procreate in the planned time. Furthermore; it can prevent the negative consequences such as longing the breeding time, raising the procreation cost and reducing the procreation. [1]

It is important that aforementioned yield and quality are measurable and this occurs thanks to these smart systems. [3,4,5] With the neck collar system carried out within the scope of project, the terms of efficiency and quality has been made measurable by monitoring some activities especially health in animals; heat, giving birth, nourishment, rumination etc.

By enhancing a smart neck collar within the scope of the study, the terms of efficiency and quality in the matter of milk yield [2] and calf efficiency [6] etc. have been made measurable by monitoring some activities in animals especially health, heat, giving birth, nourishment, rumination etc. Thus, the general performance of the farm could be measured.

Neck collar system is preferred because of its advantages in terms of time, cost, workforce etc. Consequently, these products' setup cost is high because these are imported. Within the scope of the study, this smart system is developed with completely local facility.

The targeted outputs for the neck collar system developed in the study were planned to form a whole system. The system can be classified as the neck collar to be found on the animal in general, the computer system where the data is collected and recorded and the information system where the user is informed.

Neck collar -the first developed system- has a physical and ergonomic design that does not discomfort the animal. This neck collar has a resistant form to mechanical and physical effects from outside. Electronic card could continue working in any condition and export the datum appropriately. When a problem occurred, the system detected it and warned the user.

The second developed system is a computer environment that the datum were gathered via receiver and analyzed. In this

part there is a receiver that can import the data without interruption from the neck collar at every distance. Thus, by enhancing the data continuousness no problem occurred in animals was missed out. The datum in the computer environment have been used to identify the problems with the help of algorithms to be used. For instance, by using the datum of all animals and relevant animals, comparing these datum and looking into the values of the terms of body fewer, heat and rumination number it was detected whether there was any problem.

In the last part of the study, there is a system for reporting these results and communicating them to the user. The problems occurred with this system were instantly communicated to the user and instant solutions were provided. If case of not facing with a problem, the system has a capacity to work continuously.

Panchal and his colleagues claim that the mastitis disease causes significant economic loss in the food industry because of the fact that it is the most expensive disease of dairy animals because it causes to decrease of the milk production and after the treatment it includes drying and early drying, it decreases of the milk yield and increases the infection in the animal shelters.[2] J.Li and his colleagues state that with the healing life standards the demand of the milk increases day by day. Thus, in the milk purchasing process the quality of the milk comes forward. They stated that in order to meet this increasing demand of the market, it would be beneficial for the farmers to increase the milk yield of their cows and prolong the lactation period of their cows and they would provide economic benefits, and therefore it is very important to control the heat timing of dairy cows appropriately.

Additionally these scientists cite that the appropriate heat definition can help farmers to determine the heating process and insemination timing and consequently cows can procreate in the planned time thus prevent some negative consequences that cause cows to procreate abnormally such as prolonging the lactation time , increasing the cost of procreation and decreasing the procreation.[1] In the study conducted by L. Jindi and Z. Huaji, it has been observed that in the heat time the body temperature rises by 1-2°C and the moves of the cow significantly increases. [3]

Jihong Yan made a study on the working principle of the sensors and stated that the measurement accuracy may vary depending on the distance or the measured object. [7,8]

II. MATERIAL

The system is examined in two parts as hardware and software. Hardware, is exhibited in two separate terms as mechanic and electronic design. In the realization of electronic design; the general diagram was formed using arduino uno card, infrared temperature sensor, pulse sensor, wi-fi module and power supply. Mechanic design formed the design of the neck collar. The software part, on the other hand, processes the data received from the sensors and formed the informative stage to the user through the communication module.

2.1. General Design of The System

The mechanical part of the developed system has been completed firstly. After the mechanical design, electronic devices were placed in the designed system. After this process, the tests were carried out by enhancing the programing process to fulfill the planned functions. The structure for the design and the experimental application of the system was formed of the components showed in the Figure 1. The system is composed of two separate parts -the neck collar environment and the station. The neck collar, which has a communication system that measures body values such as body temperature, rumination number, pulse rate in the animal and transfers the data to the outside, was located on the animal.

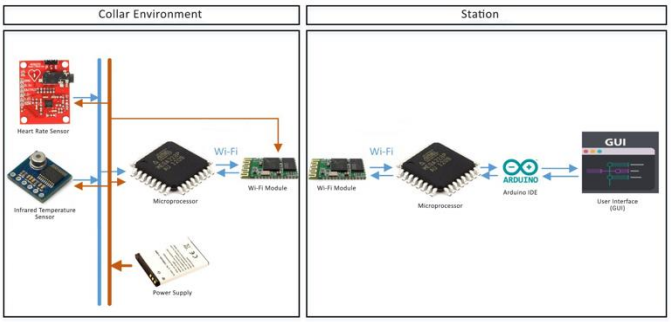

Figure 1: Flow Diagram.

As it can been seen in the Figure 1, the datum gathered by temperature and pulse sensor were transferred to the computer environment through wi-fi module. These measurements can be followed thanks to the user interface through an electronic device that has internet connection by means of the computer environment or web interface. Thanks to the sensors on the system, the data of the animal can be instantly transmitted to the user by means of relevant commands after receiving the data regularly and evaluating it on the microcontroller.

2.2. Mechanical Design

In the scope of the study, the neck region of the animal was determined as the most appropriate environment for data exchange of the neck collar design. A box design was made with reference to the materials to be used in this scope. The visuals of the design are mentioned below in details. Because of the fact that this part will be on the animal body, it may be exposed to both heavy physical and chemical (dash, rain, snow, pollution, sun light etc.) impacts.

Regarding these circumstances, suitable materials were chosen and this part was made. A modular approach was

adopted in neck collar design to support the usage scenarios like working in harmony with the animals of different groups such as neck related charging, repairing, different ages, sex etc. Neck collar was designed with a modular form in order to support the usage scenarios such as charging, repairing, and using in animals with different features.

Figure 2: Visual of the designed neck collar – front face (left) and back face (right).

2.3. Electrical Design

In this section, the electronic modules used in the system, the features of the modules and the undertaken missions at the robot are explained. In the electrical design of the robot, Arduino uno control card, infrared temperature sensor, pulse sensor, ESP8266 wi-fi module and the battery were used. The simplified electrical design of the system is shown in the Figure 3.

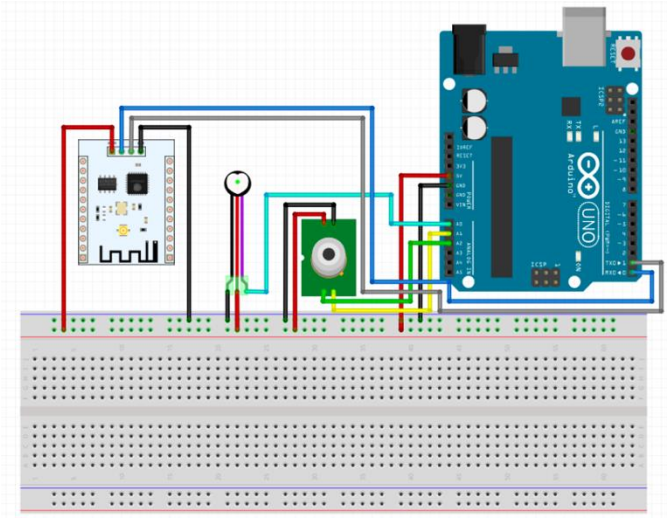

Figure 3: General circuit diagram of the system.

Arduino Uno Control Card: Arduino Uno is an ATmega328 based microcontroller. It has 14 digital input/output pins as 6 PWM outputs, one 16 MHz ceramic resonator, one ICPS header, 6 analogue inputs, one power input and one reset button. Arduino Uno is different from all other cards. It does not use FTDI USB-serial driver chip but has Atmega16U2 which is programmed as a USB-serial converter. [9,10,11]

The processor is one of the most important components in this study. The processor used in the neck collar generally works in collecting the information coming from the sensors, transferring this information to the computer through the communication unit in a suitable way and processing data. In the study; because of the both facts that it can be found easily and is easy to program, it was planned to use Arduino developing cards as a processor which uses Atmel ATMega microprocessor as a basis. Atmel ATMega 328 (UNO) processor is used as processor. Values such as flash memory, EEPROM, RAM, operating speed, operating voltages match the reference values specified for this study. [12,13]

Infrared Temperature Sensor: Failure to contact properly in contacted sensors and contamination of the contacted point over time may cause an error in the temperature to be read. For this reason, infrared temperature sensors that can read temperature without any contact were used in the project. The working principle of infrared sensors is as follows: Infrared temperature sensors work based on opaque body radiation. Since there are particles moving in any material with a temperature above absolute zero, the molecules move faster in the same direction as the temperature rises. As the molecules move fast, they emit infrared radiation, the temperature rises and increases in this direction and emits even more radiation. Therefore, the heated metal emits a red or white colored glow. Infrared sensors detect and measure this radiation. In order for the infrared sensors to work properly, a suitable detection point design has been made on the box. [14]

In this context, 2 different infrared temperature sensors, which are thought to be suitable for measuring body temperature, have been determined. The sensors identified include temperature measurement accuracy, temperature measurement range and size difference. By evaluating performance and cost, it was determined that the most efficient sensor was the MLX90614 infrared temperature sensor, which can measure between -70<t<+270 °C and has a sensitivity of 0.01 °C.

Heart Rate Sensor: It consists of a very bright red LED and a light sensor. The LED light needs to be very bright because too much light must be emitted on the surface and detected by the detector. When the heart pumps blood, the vessel surface becomes slightly more opaque and less light reaches the sensor. The sensor signal changes with each heartbeat. This diversity is converted into an electrical signal. This signal is amplified and triggered by an amplifier that outputs a +5V logic level signal. [15]

In this study, heart rate sensors belonging to 2 different manufacturers, which are thought to be the most suitable for the reference specifications we have determined, were determined. As a result of these evaluations, necessary tests were made for both sensors and the most efficient sensor was used.

Wi-fi Module: Wi-fi is one of the standards used for wireless communication. This module provides data exchange by connecting the internet. It enables the data transfer to web servers by using standard HTTP protocol through Arduino. Although it has the capability of carrying out a fast speed data

transfer, it has a low power consumption and productivity. [16,17]

In this study, as a wi-fi module ESP8266 module was used. This device is one of the most developed and extensive devices for connecting to internet. Without any need to a controller ESP8266 can run independently also. The version used in the study is commonly used in the studies that need less input/output port. [18,19]

When the ESP8266 is ready, it connects to the wireless network and data is read from the sensors connected to the analogue pins on the microcontroller. By converting this read data into information, the data on the web is gets updated and thus the users are delivered the updated data. This updating process is carried out in 10-minute periods. To save the data received from the animal, a channel was opened in the website https://thingspeak.com. Data saved here is simultaneously seen by user in the designed interface. This interface was developed in the scope of the present study.

Power Supply: When the designed system is examined, a battery model that will meet the power need for a long time is preferred. Li-ion battery model was used because it is advantageous in terms of expanded battery life, outstanding usable capacity values, not having a voltage lose, weight depending on size and size itself, being charged quickly, having a high climate resistance and having few maintenance needs. [20,21]

Since the day it was launched, lithium-ion battery group has been used in the portable electrical devices and projects with electrical substructure. During discharge process, lithuium ions in this battery group, negatrons (negative electrons) move toward positrons (positive electrons) and during the charge process they turn back in this direction. [22]

2.4. Neck collar Softwares

The software designed for the neck collar can be examined in two parts. The first one is the one that processes the data received from the sensors and the second one is the one that takes heart rate and body temperature measurements from the sensors and sends them to the web module through the wi-fi module.

2.4.1. Processing Data Received from The Sensors

The data of the animal received by the sensors placed in the neck collar environment were transferred to station environment through communication systems. The disease was detected as a result of processing the transferred data in comparison with the reference values of animal health by means of the algorithms written on Arduino IDE development environment.

The storage of the data will provide an immediate access to animal health record and reporting features will provide preventing mistakes and time loss in the animal monitoring.

The multilayered and modular architecture of the software enables the components that make up the software to be reutilized in other sensor-based applications. General system components are shown in the Figure 4.

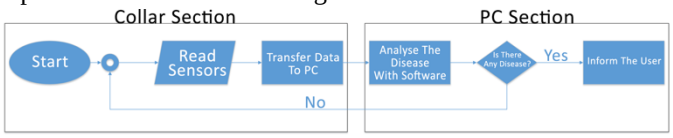

Figure 4: System Components.

2.4.2. Sending Sensor Data Through Wi-Fi Module

When the system is powered, wi-fi module connects to internet through the information downloaded in the software aforetime.

```
unsigned long myChannelField = 938423; // Channel ID
const int ChannelField = 1; // Which To Field Write
const char * myWriteAPIKey = "P547J32BTK08DOZO"; // Write API Key
```

The channel composed in *ThingSpeak* and the zone to be written are introduced with the command prompt. Data from the sensors are read. In order to send these read data to the web module by way of wi-fi, it gets connected to the server via the undermentioned command prompt.

```
Serial.begin(115200);
WiFi.mode(WIFI_STA);
ThingSpeak.begin(client);
```

The IP address in this command line belongs to the website thingspeak.com. ThingSpeak is an IoT analyze platform that allows to cumulate, visualize and analyze the live data flow in the cloud. ThingSpeak provides immediate visualization of the data send by the devices to ThingSpeak. Within the scope of this study, a channel has opened in the site.

if (Serial.available() > 0) With the command lines, data is reported to the ESP8266 module. If the module is suitable, with these commands,

```
“while (Serial.available() > 0)
  {
   int inChar = Serial.read();
   value += (char)inChar;” data flow becomes ready. Then the wi-fi connection of the device is check with these commands,
if (WiFi.status()!= WL_CONNECTED)
 {
  while (WiFi.status()!= WL_CONNECTED)
  {
   WiFi.begin(ssid, pass);
   delay (5000);
```

Here, in case of failure to connect with the delay command, it is ensured that it waits for 5 seconds and does not enter a vicious circle. If the conditions are appropriate,

ThingSpeak.writeField(myChannelField, ChannelField, value, myWriteAPIKey);

value = "";

with the command, the data are written in the fields specified in ThingSpeak. The value received through the sensors are dynamically inserted into the program. The data transferring process can be followed as shown in Figure 5 on the serial port screen of the Arduino IDE environment.

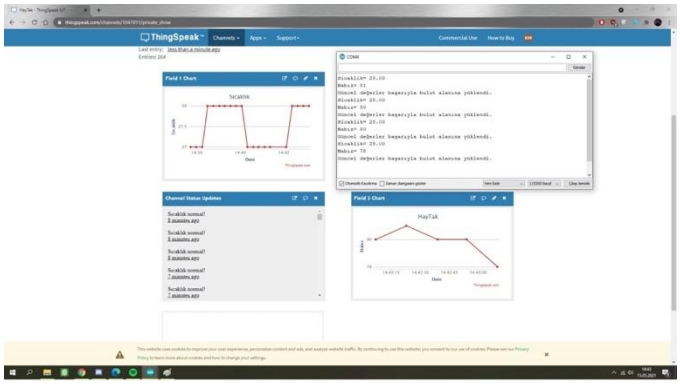

Figure 5: Monitoring the data transfer process through wi-fi on the serial port screen.

Designed user interface and the recorded display of received data are shown in the Figure 6.

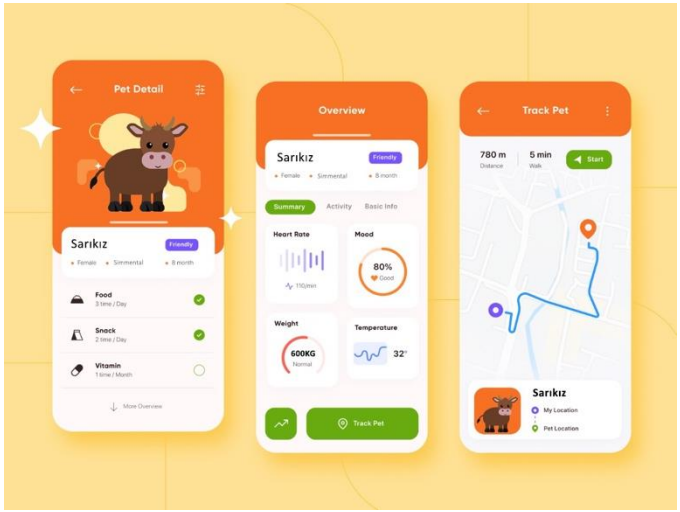

Figure 6: User Interface.

III. FINDINGS

The developed neck collar system can be evaluated in two titles. The first one is the neck collar carrying out appropriate measurement through the sensors. The most difficult part of engaging this process is that the used temperature and pulse sensors do not give consistent data. In order to avoid this obstacle infrared temperature and pulse sensor with high precision and wide range of measurement was used. Nevertheless, the sensors on the system did faulty measurement while reading once in 5-6 reading. To increase this faulty rates, sensors even higher precision can be used. This situation provides a more consistent working environment yet it also increases the cost in the same direction.

A set of tests were conducted to have the accuracy rate of the data comes from sensors. The chart is given in the table below. When the table is analyzed, it was observed that the temperature and pulse sensors transmit faulty data in regular base.

Test No	ID	Temperature	Pulse
1	Aa	38,5	30
2	Aa	38	77
3	Aa	38,5	80
4	Aa	37,5	85
5	Aa	38	65
6	Aa	37	70
7	Aa	33	73
8	Aa	38	87
9	Aa	38	55
10	Aa	37	80
11	Aa	37,5	83
12	Aa	38	--
13	Aa	39	67
14	Aa	35	75
15	Aa	37,5	86

Table 1: Test Content of the Data Read by Sensors.

The second evaluating can be done by having the measurements of the temperature and pulse sensors transmitting over wi-fi. At this point of view the system can transmit the data received from the sensors to the web module successfully when it is called for. One of the biggest problems here is the possibility of delays (10-20 secs.) in the time of notification of the web interface. Yet this delay can be avoided by using a local system or a more costed cloud system. Besides, before use, the wi-fi module should be updated for once otherwise there may be some problems during the data transmission or the module may not work.

IV. RESULTS

Being an agricultural country- our country has an important place in dairy farming. Thanks to the government policy supported contributions in relating to dairy farming, this sector gradually develops. In the matter of this issue, various support programs contributed by ministry of agriculture and forestry are found. In general, these contributions provide with large capacity and more modern facilities.

By this means, it encourages animal breeding to be more fruitful, qualified and smarter. As a consequence, some

developments are improved on the subjects of appropriate nutrition of the animals, animal health, milk yield and birth rate etc.

It is important that aforementioned yield and quality are measurable and this occurs thanks to these smart systems. With the neck collar system carried out within the scope of project, the terms of efficiency and quality has been made measurable by monitoring some activities especially health in animals; heat, giving birth, nourishment, rumination etc.

Thank to registering the data received from the sensors to the web environment and user interface, it provides convenience to the vets in detection of the sickness.

With the lights of the developed tests, the neck collar system developed within the scope of the study reached the level of giving information to the user at intervals of 10 minutes by taking the data on the animal through the temperature and pulse sensors thanks to the algorithms created in the station environment.

V. RECOMENDATIONS

Sensors such as air quality sensor and environment temperature sensors can be added to the developed system consequently the data of the environment can be transmitted to the user. The user can breed more easily and beneficially thank to the environment data. Apart from that wi-fi module shall not be used where there is no internet infrastructure, data transmission can be carried out over this module by adding bluethoot module.

ACKNOWLEDGEMENTS

The present study with name of "*Hayvan Sağlığı İzleme Sisteminin Geliştirilmesi"* and 1919B011901859 numbered project was supported under Tübitak 2209-A the University Students Research Projects Support Program. We thank to Tübitak for their supports in this context.

REFERENCES

[1] J. Li, J. Fang, Y. Fan, and C. Zhang, "Design on the Monitoring System of Physical Characteristics of Dairy Cattle Based on Zigbee Technology."

[2] I. Panchal, I. K. Sawhney, and A. K. Sharma, "Identifying healthy and mastitis sahiwal cows using electro-chemical properties: A connectionist approach," 2015 International Conference on Computing.

[3] Andonovic I., et al. : Wireless Sensor Networks for Cattle Health Monitoring. In: Danco D., Jorge M.G. (eds.): ICT Innovations 2009, Springer Berlin Heidelberg, (2010) 21-31.

[4] Sikka, P., Corke, P., Valencia, P., Crossman, C., Swain, D., Bishop-Hurley, G. : Wireless ad hoc sensor and actuator networks on the farm. Information Processing in Sensor Networks, IPSN 2006. The Fifth International Conference on, (2006) 492-499.

[5] Mayer, K., Ellis, K., Taylor, K.: Cattle Health Monitoring Using Wireless Sensor Networks, In: Proc. of CCN, Cambridge, Massachusetts, USA, (2004).

[6] L. Jindi and Z. Huaji, "Outlier detection in dairy cows estrus based on density clustering," 2017 3rd IEEE International Conference on Computer and Communications, ICCC 2017, vol. 2018-Janua, pp. 2291–2294, 2018.

[7] Jihong Yan (2015). Machinery Prognostics and Prognosis Oriented Maintenance Management. Wiley & Sons Singapore Pte. Ltd. p. 107. ISBN 9781118638729.

[8] Dincer, Can; Bruch, Richard; Costa-Rama, Estefanía; Fernández-Abedul, Maria Teresa; Merkoçi, Arben; Manz, Andreas; Urban, Gerald Anton; Güder, Firat (2019-05-15). "Disposable Sensors in Diagnostics, Food, and Environmental Monitoring". Advanced Materials: 1806739.

[9] A. M. Thomas, J. Joseph, R. Mathew, "Mobile Application for Automobile Management System", Journal for Research, 2(2), 66- 68, 2016.

[10] A. J. Lubbe, P. Kluge, "Development and Testing of a Wireless Controlled Car Using the Internet as Communication Medium", South African Journal of Industrial Engineering, 19(1), 137-147, 2008.

[11] A. M. Thomas, J. Joseph, R. Mathew, "Mobile Application for Automobile Management System", Journal for Research, 2(2), 66- 68, 2016.

[12] J.Sarik, I. Kymissis, "Lab kits using the Arduino prototyping platform", in IEEE Frontiers in Education Conference, Washington, 1-5, October 27 – 30, 2010.

[13] O. Güngör, "Kaçak Elektrik Kullanımının GSM Aracılığıyla Takibi", T, 4(8), 29-33, 2015.

[14] Melexis MLX90614 infrared sensor, https://www.melexis.com/en/product/mlx90614/digital-plug-play-infrared-thermometer-to-can

[15] Sparkfun SEN-11574 heart rate sensor, https://www.sparkfun.com/products/11574

[16] A. Djajadi, M.Wijanarko, "Ambient Environmental Quality Monitoring Using IoT Sensor Network", Internetworking Indonesia Journal, 8(1), 41-47, 2016.

[17] D. Jalamkar, A.A. Selvakumar, "Use of Internet of Things in a Humanoid Robot - A Review", Advances in Robotics & Automation, 5(2), 2016.

[18] R. S. Rosli, M. H. Habaebi, and M. R. Islam, "Characteristic Analysis of Received Signal Strength Indicator from ESP8266 WiFi Transceiver Module," Proceedings of the 2018 7th International Conference on Computer and Communication Engineering, ICCCE 2018, pp. 504–507, 2018.

[19] ESP8266 Wifi module, https://www.espressif.com/sites/default/files/documentation/0a-esp8266ex_datasheet_en.pdf

[20] Ballon, Massie Santos (14 October 2008). "Electrovaya, Tata Motors to make electric Indica". cleantech.com. Archived from the original on 9 May 2011. Retrieved 11 June 2010.

[21] Development of Lithium-Ion Batteries, https://www.energy.gov/science/articles/charging-development-lithium-ion-batteries

[22] Eftekhari, Ali (2017). "Lithium-Ion Batteries with High Rate Capabilities". ACS Sustainable Chemistry & Engineering. 5 (3): 2799–2816.

Design and Performance Analysis of a LoRaWAN Protocol Based Network for Data Communication with Smart Water-Meter Devices: Bursa Case Study

Ö. YILDIZ[1] and S. E. KARLIK[2]

[1] Bursa Uludag University, Bursa/Turkey, 511905009@ogr.uludag.edu.tr
[2] Bursa Uludag University, Bursa/Turkey, ekarlik@uludag.edu.tr

***Abstract* – The internet of things (IoT) subject became widespread during the last decade while 25 billion connected devices will dominate the life by 2030 due to statistical expectation reports. In smart cities, sensors mostly use wireless communication facilities involving huge energy consumption risk. Long range wide area network technology is one of the main solutions inside the low power consumption wide technologies era that are called LoRa and LoRaWAN.**

In this case study, there are totally 232 water-meters in the research area. Water-meters are deployed in a three-blocks-apartment in city of Bursa. We selected one water-meter from every floor. Totally 56 LoRaWAN supporting water-meters selected for performance analysis. Network design and performance analysis are studied focusing on received signal strength indicator (RSSI), signal-to-noise ratio (SNR), spreading factor (SF) and message transmission number by debugging the LoRa gateway logs. Best RSSI values are created by the Block B water-meters which are nearest end-devices (EDs) to gateways (GWs) while Block A and C values are already better than the theoretical limits. Also, in comparison to SNR values, Block B has better results. In conclusion, it is detected that Block A uses SF12, Block B uses SF7 and Block C uses SF12 values mostly.

***Keywords* – LoRa, LoRaWAN, Smart metering, Smart City, LPWAN, IoT**

I. INTRODUCTION

TODAY, internet of things (IoT) is a main domain for smart cities and it plays an important role for implementing smart city technologies [1]. IoT allows to sense real time situation of a case within the cities. Also, IoT can be used in various scenarios by wireless sensor network (WSN) implementations [2]. There are many wireless sensors covering cities while battery life of a sensor becomes a compulsive issue [3]. Low power consumption wide area network (LPWAN) which focuses on efficient battery usage is a new option that makes sense in communication technologies like Long Range (LoRa), Sigfox, Bluetooth Low Energy (BLE), and Narrow-Band IoT (NB-IoT) [4]. LoRa, is a reference to the extremely long-range data links that this technology enables. LoRa is a novel LPWAN communication technique with some unique features and widely used free wireless technology. LoRa has exemplary applications in many fields such as agriculture, energy, water management and transportation [5]. Long-range wide-area network is called the LoRaWAN technology which is preferred especially in large areas with energy infrastructure and harsh facility environments. It is becoming more and more widespread day by day for remote reading and management of water-meters, parking sensors, smart garbage collection, airport facility both in Turkey and in the world [6, 7]. LoRa uses 780-915 MHz frequency band range in European Union (EU) and 902 MHz frequency for United States (US) geographical area. LoRa gateways (GWs) also have advantage of a high sensitivity of received signals; almost -137 dBm [8]. Furthermore, there is 30-50 kbps uplink data rate in EU and 250.000 end nodes can be supported by one GW. The last important feature of the LoRa is 10-years-long battery life similar to the case in SigFox and DASH7 which are other industrial and open protocol IoT technologies [7].

In this research, a LoRaWAN network has been analyzed in city of Bursa including water-meters, GW, network servers and dashboard. Performance analysis has been evaluated over 70 days. In second section, theoretical information is given about LPWAN, LoRa and LoRaWAN technologies. In the material and method section, the basic installation features used in the research and the physical characteristics of the research area are explained. In the fourth chapter, the signal specifications like Received Signal Strength Indicator (RSSI), Signal-to-Noise Ratio (SNR) and Spreading Factor (SF) and transmitted message number results, which are obtained from the research area, are analyzed. Finally, performance of the LoRaWAN system is discussed and future works are given.

II. LORA AND LORAWAN

A. LoRa

LoRa is an RF modulation technology for LPWANs. The name LoRa provides for long-range communications: up to 5 kilometers in urban areas, and up to 15 kilometers or more in rural areas due to line of sight [7]. The key point of the LoRa-based solutions is ultra-low power consumption which allows the battery-operated devices to work up to 10 years. LoRaWAN protocol is perfect for applications that need long-

range or indoor communication among many devices which have low power requirements and that collect small amounts of data [9]. LoRa is the physical (PHY) layer, i.e., the wireless modulation used to create the long-range communication link [6]. The LoRa technology is generally divided into two different layers: the physical layer, which uses the chirp spread spectrum (CSS) and is called the LoRa modulation technique, and the medium access control (MAC) layer, which is called LoRaWAN protocol [10]. A LoRaWAN network can handle millions of messages by GW, but the number of messages supported in any deployed network depends on the number of implemented GWs. A single 8-channel GW can support up to 1.5 million messages in a day. One GW can support up to 60,000 devices whether each end-device (ED) sends hourly messages [9].

LoRa is based on Chirp Spread Spectrum (CSS) modulation, a rather classical technique in radar systems, which was proposed in 1962 for communication systems at first [5]. A chirp is a signal with a frequency that moves up or down at different speeds. The speed of the chirp is determined by the SF. The chirp rate depends only on the bandwidth: one chirp per second per Hertz of bandwidth. This means that an increase in one of the SFs will divide the frequency span of a chirp by two because two SF chirps covering the entire bandwidth will multiply the duration by two. Therefore, SF is an important parameter in CSS modulation. The higher the SF value, the wider is the wireless communication range. The SF value ranges from SF7 to SF12. The LoRa wireless communication distance can be extended to more than 30 km [11]. CSS uses a continuously varying carrier frequency to spread the signal modulated by chirp pulses (frequency varying sinusoidal pulses). CSS improves resilience and robustness against interference, Doppler effect and multipath [12].

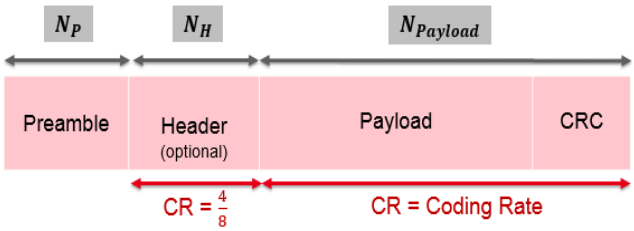

Figure 1: LoRa packet structure

The LoRa packet structure is shown in Figure 1. A packet starts with the preamble, programmable from 6 to 65535 symbols. The preamble is followed by an optional header that describes the length and Forward Error Coding (FEC) rate of the payload and indicates the presence of an optional 16-bit Cyclic Redundancy Check (CRC) for the payload. The header is always transmitted with a 4⁄8 FEC rate and has its own CRC. After the optional header, there is the payload, which can contain 1 to 255 bytes. At the end of the payload an optional 16-bit CRC may be included [5].

SF is the ratio between symbol rate and chip rate. A higher spreading factor increases the SNR, and thus sensitivity and range, but also increases the airtime of the packet. The number of chirps per symbol is calculated as 2SF. For example, with an SF of 12 (SF12) 4096 chirps/symbol are used. Each increase in SF halves the transmission rate and, hence, doubles transmission duration and ultimately energy consumption. Radio communications with different SFs are orthogonal to each other and using different SFs is possible [6].

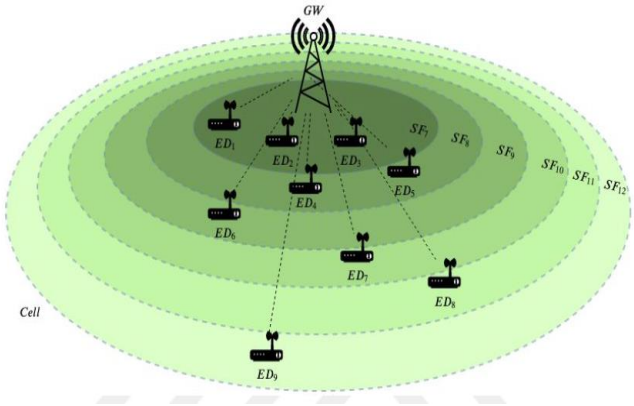

Figure 2: SF-ED distribution in LoRa

Figure 2 shows LoRaWAN SF example in the Cell of the ED. ED $_{[1-3]}$ use SF7, ED $_{[4-5]}$ use SF_8, ED_6 uses SF_9, ED_7 uses SF_{10}, ED_8 uses SF_{11}, and ED_9 uses SF_{12} [13].

Table 1: Data rates in EU ISM band

Data rate	Spreading factor	Channel width (kHz)	Code rate	PHY bit rate (bps)	RF sensitivity (dBm)
0	12	125	4/6	250	-137
1	11	125	4/6	440	-136
2	10	125	4/6	980	-134
3	9	125	4/6	1760	-131
4	8	125	4/6	3125	-128
5	7	125	4/6	5470	-125
6	7	250	4/6	11000	-122

Table 1 shows data rates of the Industrial, Scientific and Medical (ISM) band in EU region [8]. Table 2 shows lower limits of SF for RF sensitivity and SNR values in Semtech's SX1276 transceiver produced for LoRa modulation [14].

Table 2: Lower limits of RF sensivity and SNR values of SX1276 transceiver

SF	Receiver Sensitivity (dBm)	SNR (dB)
SF7	-123	-7.5
SF8	-126	-10
SF9	-129	-12.5
SF10	-132	-15
SF11	-133	-17.5
SF12	-136	-20

When a GW forwards a data packet from an ED to a network server, it also adds information regarding the quality of the reception (SNR) between the ED and the GW, which is a very useful information for Adaptive Data Rate (ADR). The server uses this information to manage the bit rates for each node individually and asynchronously. This is achieved by varying the SF for each ED depending on the quality of the connection between node and the base station [15]. Each ED distributes its transmissions evenly over the different available GW channels. A LoRa GW can receive data on the same channel from multiple nodes at the same time if the bit rates are different, which is its main advantage. This increases the capacity of EDs in a LoRa network. If two nodes sharing the same spreading factor transmit on the same channel at the same time, the most powerful message will be received correctly by the GW given that there is a minimum 3 dB difference, and the other messages are not received. Since a higher bit rate leads to a shorter time on air, the message frequency will vary between the nodes depending on the SNR. Nodes which are far away will only be able to transmit occasionally but nodes closer to a GW will be able to transmit more frequently due to the use of a lower spreading factor, according to the duty cycle restrictions posed by the region of operation. The reliability of the network depends on the EDs using an appropriate spreading factor based on the SNR. If an application does not need a constant bit rate, leaving the adjustment of the spreading factor to the server will improve the reliability of the system through ADR. However, if there is a demand for a certain fixed bit rate that prevents the server from using different spreading factors, the network will be less reliable, and the Packet Delivery Ratio (PDR) is reduced. As for errors in the data stream, the forward error correction will reduce the number of bit errors [6].

LoRa has 3 operational classes: Class A, Class B and Class C [16]. In this case study, Class A has been implemented. This Class A operation is the lowest power ED system for applications that only require downlink communication from the server shortly after the ED has sent an uplink transmission. Downlink communications from the server at any other time will have to wait until the next scheduled uplink. The main difference among A, B and C classes is their power consumption.

B. LoRaWAN

LoRaWAN is an open networking protocol that delivers secure bi-directional communication, mobility, and localization services standardized and maintained by the LoRa Alliance [15].

Table 3: LoRaWAN frequency bands in regions

Region	Frequency band
China	779-787 MHz
EU	863-870 MHz, 443 MHz
US	902-928 MHz

LoRaWAN is working on the LoRa RF modulation method. Table 3 shows regional bands like EU, US or Asian spectrum and allowed frequencies also [15]. LoRaWAN protocol stack is deployed into the EDs and the Network Server (NS) as the MAC and PHY layers. However, GW is not aware of LoRaWAN MAC protocol, and its only task is to deliver the data between the ED and the NS that is shown in Figure 3 [6]. LoRaWAN network topology has main nodes like end nodes, GW, LoRa enabled network server, application server, join server that are shown in Figure 4 [16]. A LoRaWAN-enabled end node is a sensor or an actuator which is wirelessly connected to a LoRaWAN network through radio GWs using LoRa RF modulation sensing smoke, water-meter, gas etc.

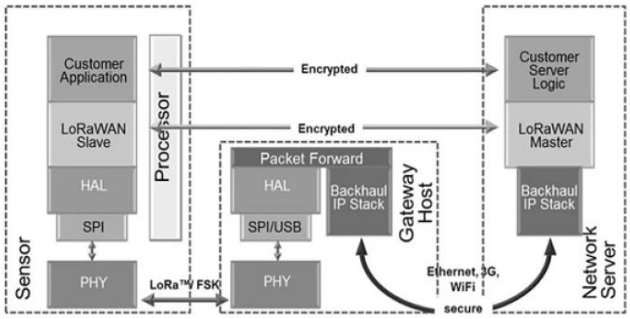

Figure 3: LoRaWAN protocol stack

In most applications, an ED is an autonomous, often battery-operated sensor that digitizes physical conditions and environmental events. Typical use cases for an actuator include street lighting, wireless locks, water valve shut off, leakage prevention among others.

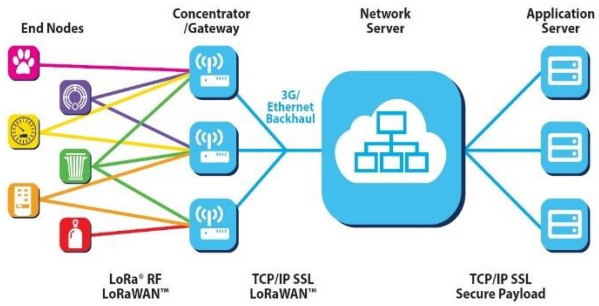

Figure 4: LoRaWAN network topology

When they are being manufactured, several unique identifiers are assigned to LoRa-based devices. These identifiers are used to securely activate and administer the device, to ensure the safe transport of packets over a private or public network and to deliver encrypted data to the cloud.

LoRaWAN GW receives the message from ED in listening distance and sends data messages to the server as called LoRaWAN network server (LNS). There is not a continuous link between an ED and a GW which occurs all the time. On the other hand, same ED can be served by multiple GWs. All GWs in the coverage area receive all ED messages as illustrated in Figure 4. This situation reduces packet error rate

and give chance to locate ED with a low-cost [9]. Connection between GW and network server can be via cellular connection, Wi-Fi or wired ethernet. GW operates at physical layer and only forward the LoRa radio messages. On the downlink side of the communication, GW forwards messages coming from LNS to the EDs without any additional operation. While multiple GWs receive message from the same ED, LNS evaluates all messages according to RSSI levels. LNS select the GW which has the best RSSI value for a specific ED [16].

Generally, LNSs use features like device address checking, frame authentication and frame counter management, acknowledgements of received messages, adapting data rates using the ADR protocol, responding to all MAC layer requests coming from the device, forwarding uplink application payloads to the appropriate application servers, queuing of downlink payloads coming from any Application Server to any device connected to the network and forwarding Join-request and Join-accept messages between the devices and the join server [9].

III. MATERIAL AND METHOD

A. Physical Conditions and Installation

Smart water-meters have been installed to three separate apartment blocks, i.e. Block A, Block B and Block C, with two GWs. There are totally 232 LoRaWAN featured smart water-meters installed in the research area. We have selected one water-meter from every flat randomly and 56 water-meters have created our cluster. Due to network configuration every ED has Class A specification and has been programmed to send hourly messages to GW. LoRa GWs have been installed at the rooftop of Block B. Figure 5 shows the positions of the water-meters by each block. Network has been designed with all possible SF values: 7, 8, 9, 10, 11 and 12.

B. Performance Analysis Method

We have analyzed the RSSI, SNR, SF values and periodic message count for every apartment block, i.e. Block A, B and C. RSSI is measured in dBm and is a negative value and it is the measurement of the power present in a received radio signal. Inside SNR and RSSI analyses, we have focused on the average SNR and RSSI values and compared them with number of EDs that have better RSSI and SNR values within all blocks. Average SNR and RSSI values for three blocks have been calculated for 70 days.

Table 4: Uplink messages sent by EDs

Block	Days	EDs	Number of messages sent
A	70	18	9261
B	70	19	11245
C	70	19	9088
Total	70	56	29594

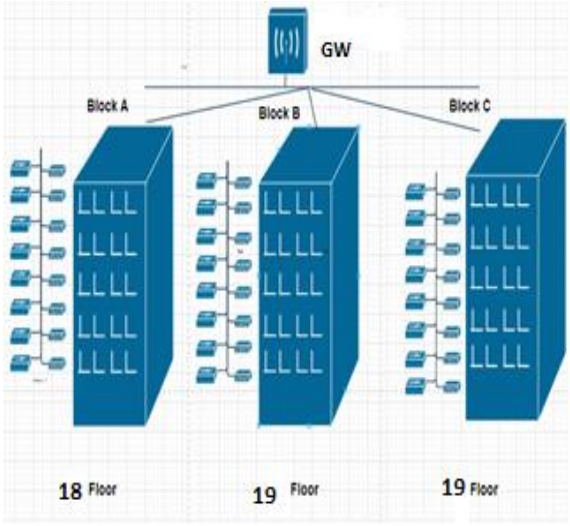

Figure 5: Physical installation scheme

Additionally, the SF usage times have been matched with used SF numbers defined previously for every block. The number of messages sent by every ED has been calculated and a message success rate table has been created.

IV. RESULTS AND PERFORMANCE ANALYSIS

Table 4 shows results about uplink messages sent by 56 EDs. We have focused on the GW message forwarding performance by this table. Table 5 shows average RSSI values for each block and total cluster which is another key performance indicator (KPI) for the network. Additionally, Table 6 gives average SNR values which are lower than zero and compatible with the values given in Table 2. We have computed the SF values used during the uplink communication of EDs. Tables 7-9 show the SF usage times by blocks A, B and C, respectively. Tables 7-9 also give the SF distribution and show the most used SF values for all blocks, i.e. given in bold values. Considering the results of RSSI, SNR, SF usage and sent message analyses, new tables have been created. Table 10 created from Tables 7-9, gives the most used SF values within blocks. Table 11 shows the message sending success rate while Table 12 and Table 13 display number of EDs exhibiting better RSSI and SNR than the average values, respectively.

Table 5: Average RSSI for each block and overall

Block	Average RSSI (dBm)
A	-109.22
B	-105.46
C	-109.82
Total	-108.16

Table 6: Average SNR for each block and overall

Block	Average SNR (dB)
A	-8.19
B	-0.26
C	-9.16
Total	-5.87

Table 7: SF usage times for Block A

Block	Used SF	Usage times
A	7	2237
A	8	372
A	9	360
A	10	377
A	11	1955
A	**12**	**3960**
Total	7, 8, 9, 10, 11, 12	9261

Table 8: SF usage times for Block B

Block	Used SF	Usage times
B	**7**	**7507**
B	8	1167
B	9	1063
B	10	639
B	11	128
B	12	741
Total	7, 8, 9, 10, 11, 12	11245

Table 9: SF usage times for Block C

Block	Used SF	Usage times
C	7	1513
C	8	371
C	9	586
C	10	1021
C	11	1838
C	**12**	**3759**
Total	7, 8, 9, 10, 11, 12	9088

Table 10: Most used SF values and their usage percentages by block

Block	Most used SF value	Usage times of this value	Usage times of all SFs	Usage percentage (%)
A	12	3960	9261	42.75
B	7	7507	11245	66.75
C	12	3759	9088	41.36

Table11: Message success rates

Block	ED	Number of sent messages	Number of expected messages	Ratio (%)
A	18	9261	30240 (1680*18)	30.63
B	19	11245	31920 (1680*19)	35.23
C	19	9088	31920 (1680*19)	28.47
Total	56	29594	94080 (1680*56)	31.46

Table12: Number of EDS with better RSSI than the average value

Block	Average RSSI (dBm)	EDs with better RSSI than the average value
A	-109.22	7
B	-105.46	9
C	-109.82	3

Table13: Number of EDS with better SNR than the average value

Block	Average SNR	EDs with better SNR than the average value
A	-8.19	6
B	-0.26	9
C	-9.16	6

The distance to GW is similar for Block A and Block C and hence they both use SF12 mostly with around 42 % and 41 % usage percentages, respectively, as shown in Table 9. However, Block B which is near to LoRaWAN GW uses the SF7 value mostly with a usage percentage of around 66 %. SF7 means the biggest bandwidth and payload during LoRa messaging. Also it has the smallest RF sensitivity. The results are in good agreement with the distribution given in Figure 2.

As shown in Table 10, all 56 EDs should have sent 94080 messages within the testing period but only 30 % of the total expected messages have been sent. Fading, obstacles and building construction equipment are probable causes for that improper result. This issue will be researched furtherly with future works debugging the message drop counts and their reasons in LNS and other servers.

Table 12 and 13 emphasize that average and block-based RSSI and SNR values are within the limits mentioned in Tables 1and 2. Block B has better values for both average RSSI and SNR than that of Block A and Block C which are standing closely. In Block B almost half of the water-meters' RSSI values are better than the average value while only 3 of 19 and 7 of 18 water-meters have better RSSI values than the average value in Block C and Block A, respectively, as shown Table 12. Similar to the results given in Table 12, it is obvious in Table 13 that Block B has better values than Block A and Block C, whose values are again standing closely to each other, both for average SNR and number of EDs with SNR values laying over the average.

V. CONCLUSION

This research shows that basic water consumption parameters can be daily and remotely monitored by using LoRaWAN technology, which is implemented among metropolitan city area with a necessary optimization. RSSI, SNR, SF and ED uplink messages are the main parameters in analyzing the network performance of LoRaWAN. Therefore, optimization has to focus on these parameters. Average RSSI value has been determined as -108.16 dBm and average SNR value has been found as -5.87 dB in our research. Those

values are similar to the values given in [17]. Furthermore, in [18], which focuses on indoor performance analysis with SNR, RSSI results and SF usage behaviors, SNR values are in the range of -10 – 0 dB while RSSI range is -105 – -100 dBm. SF7, SF9 and SF12 are mostly used SFs in [18]. Those results are also in good agreement with the results obtained in this research. The results given in [19], i.e. RSSI values around -120 dBm and SNR values in -7 – -2 dB range, also show that our research results are compatible with the results in the literature.

Furthermore, there are actions to be taken as future works, e.g. analyzing the low message transmission percentage and clarifying the missing part for the existing network. Else, performance optimization can deal with different point of views like coverage, line of sight with a bigger area or GW re-positioning. On the other hand, outdoor installation and performance analysis are planning to be done in the next step of this research to compare indoor and outdoor results.

In conclusion, this research gives a valuable support for usage of LoRaWAN technologies in smart city applications with real field research on water-meters.

VI. Acknowledgement

This research was achieved with BUSKI (Bursa Metropolitan Municipality Water and Wastewater Management Authority) permission in 2021.

VII. ABBREVIATIONS

AES: Advanced Encryption Standard
ADR: Adaptive Data Rate
CRC: Cyclic Redundancy Check
CSS: Chirp Spread Spectrum
ED: End Device
FEC: Forward Error Correction
GW: Gateway
IoT: Internet of Things
ISM: Industrial Scientific Medical
LNS: LoRaWAN Network Server
LPWAN: Low Power Wide Area Network
LoRa: Long Range
LoRaWAN: Long Range Wide Area Network
MAC: Medium Access Layer
RSSI: Received Signal Strength Indicator
SF: Spreading Factor
SNR: Signal-to-Noise Ratio

References

[1] R.P. Janani, K. Renuka, A. Aruna, K. Lakshmi Narayanan, *IoT in Smart Cities: A Contemporary Survey*. Global Transitions Proceedings-Science Direct, 2021.

[2] R. Asorey-Cacheda, A. J. Garcia-Sanchez, F. Garcia-Sanchez, J. Garcia Haro, and F. J. Gonzalez-Castano, "On maximizing the lifetime of wireless sensor networks by optimally assigning energy supplies," Sensors Journal, Basel, Switzerland, vol. 13, pp. 10219–10244, 2013.

[3] J. de C. Silva, J. J. P. C. Rodrigues, A. M. Alberti, P.Solic, A. L. L. Aquino, "LoRaWAN - A Low Power WAN Protocol for Internet of Things: a Review and Opportunities," 2017 2nd International Multidisciplinary Conference on Computer and Energy Science (SpliTech), pp. 1-6, 2017.

[4] W. Kassab, K. A. Darabkh, "A–Z survey of Internet of Things: Architectures, protocols, applications, recent advances, future directions and recommendations," Journal of Network and Computer Applications, Volume 163, 2020.

[5] M. C. Bor, "Towards the Efficient use of LoRa for Wireless Sensor Networks," Ph.D. dissertation, Dept. Comp. Sci., Lancaster University Lancaster, UK, 2020.

[6] S. H. Dunnala, "Design, Implementation and Testing of Paper-Printed LoRa Modules: Enabling the Internet of Things," MSc. dissertation, Dept. Elect. Eng., State University of New York at Buffalo, NY, 2018.

[7] I. C. R. Tardy, N. Aakvaag, B. Myhre, R. Bahr. (2017, March). Comparison of wireless techniques applied to environmental sensor monitoring. SINTEF Report: A27942. [Online]. pp 15-16. Available: https://sintef.brage.unit.no/sintef-xmlui/bitstream/handle/11250/2436270/SINTEF%2bA27942.pdf?sequence=2&isAllowed=y

[8] D. Bankov, E. Khorov and A. Lyakhov, "On the Limits of LoRaWAN Channel Access," International Conference on Engineering and Telecommunication (EnT), pp. 10-14, 2016.

[9] Technical Paper, Semtech Corportation (2019, December). LoRa® and LoRaWAN®: A Technical Overview. [Online]. Available: https://lora-developers.semtech.com/library/tech-papers-and-guides/lora-and-lorawan/

[10] B. Myagmardulam, R. Miura, F. Ono, T. Kagawa, L. Shan, T. Nakayama, F. Kojima, and B. Choijil, "Performance Evaluation of LoRa 920 MHz Frequency Band in a Hilly Forested Area," Electronics, vol. 10, no. 4, p. 502, Feb. 2021.

[11] J. Petäjäjärvi, K. Mikhaylov, M. Pettissalo, J. Janhunen, J. Iinatti, "Performance of a low-power wide-area network based on LoRa technology: Doppler robustness, scalability, and coverage," International Journal of Distributed Sensor Networks. March 2017.

[12] F. Adelantado, X. Vilajosana, P. Tuset-Peiro, B. Martinez, J. Melia-Segui and T. Watteyne, "Understanding the Limits of LoRaWAN," in IEEE Communications Magazine, vol. 55, no. 9, pp. 34-40, Sept. 2017.

[13] G. Yapar, "Improving the Performance of LoRaWAN IoT System", MSc Thesis, Dept. Comp. Eng., Middle East Technical University, Ankara, 2015.

[14] Semtech Corporation, SX1276/77/78/79 Datasheet,Rev7. [Online]. Available:https://semtech.my.salesforce.com/sfc/p/#E0000000JelG/a/2R0000001Rbr/6EfVZUorrpoKFfvaF_Fkpgp5kzjiNyiAbqcpqh9qSjE

[15] A. Yegin,(2021, September). LoRaWAN: Long Range and Low Power Communication for Enabling Massive IoT. [Online] Available: https://ninova.itu.edu.tr/en/courses/faculty-of-electrical-and-electronic-engineering/9839/ehb-453e/ekkaynaklar?g1624784

[16] What is LoRaWAN® Specification? (2021, September) [Online] Available: https://lora-alliance.org/about-lorawan, 2021.

[17] M.T. Büyükkaşlar, "Performance Analysis of LoRa and LoRaWAN Technologies," MSc dissertation, Dept. Comp. Eng., Istanbul Univ., Istanbul, 2018 (in Turkish).

[18] G. Dogan, "Study of LoRaWAN Wireless Communication Protocol and an IoT Application," MSc dissertation, Dept. Comp. Eng., Fırat Univ., Elazıg, 2019 (in Turkish).

[19] M.A. Amin, "Wolff: A Lora-Based Network Architecture to Extend Internet Service in Remote Areas," MSc dissertation, Dept. Comp. Eng, Northern Arizone Univ., Arizona, 2020.

A 6-Bit Two-Channel TI ADC in Si-Ge HBT BICMOS Technology

V. ABBASOVA[1] and A. TANGEL[1]

[1] Kocaeli University, Kocaeli/Turkey, 195103018@kocaeli.edu.tr
[1] Kocaeli University, Kocaeli/Turkey, atangel@kocaeli.edu.tr

***Abstract* – This paper presents design steps of a 6-bit two-channel time-interleaved (TI) ADC in 0.25µm Si-Ge HBT BiCMOS technology. Two 6-bit flash ADC cores are used in both time-interleaved channels. In digital parts of the design, standard CMOS logic gates are preferred since a low power consumption value is one of the main targets of this work. Transistor sizes are selected carefully to be able to obtain as high as possible speed performance, which is another main goal of this study. The main core design blocks of the complete TI ADC are sample/hold circuit, 6-Bit Flash ADC, a 6-bit 2x1 digital multiplexer, and a control pulse generator. BiCMOS analog comparator architecture is preferred in the analog part of flash ADC since BiCMOS technology combines the advantages of CMOS and Bipolar technologies. The power consumption value is 653 mW under a single DC power supply voltage of 3.3V. The simulation results include 7Gs/s sampling rate, 0,174 LSB of INL and 0,113 LSB of DNL values. The simulation results are compared to similar works in the literature. For the time being, the complete design is realized using Cadence IC design platform in schematic level only. However, the physical layout design and post-layout simulation steps are ongoing research of us.**

***Keywords* – TI ADC, Si-Ge HBT BICMOS, Flash ADC, VLSI**

I. INTRODUCTION

IN recent years, high speed and low power analog-to-digital converters (ADC) have important role in new generation signal processing and communication systems. There are several different types of ADC architectures in the literature, depending on the type of application. Typically, the serial ones have very high resolution, yielding higher accuracy whereas parallel ones operate at very high frequencies but have relatively low resolution. The flash ADC architecture is known as the fastest one among high speed ADCs since the conversion speed is only one clock cycle.

In the last decade, however, popular ADC architectures to satisfy the requirements of new generation RF communication systems are pipeline and time interleaved (TI) type of ADCs. The performance of TI-ADC is affected by mismatches among the interleaves, especially the mismatches of sampling time, gain and offset [1]. On the other hand, pipeline ADCs require calibration and correction logic additionally. To obtain desired resolution and accuracy levels are tedious work. Therefore, timing of controlling clock pulses for more than two pipelining stages are very critical for pipeline ADC case. For this reason, TI -ADC architecture is chosen in this study.

TI-ADC is used to increase the sampling rate of a specific core ADC, which is either Flash or SAR architecture in general. If the speed is the major concern, then Flash ADC core is inevitable as explained above. A traditional TI ADC architecture consists of N number of Sample and Hold (S/H) circuits, N number of core ADCs, a digital multiplexer and a digital pulse generator to produce the critical timing clock signals as shown in Figure 1. Here, N indicates the number of interleaving channels.

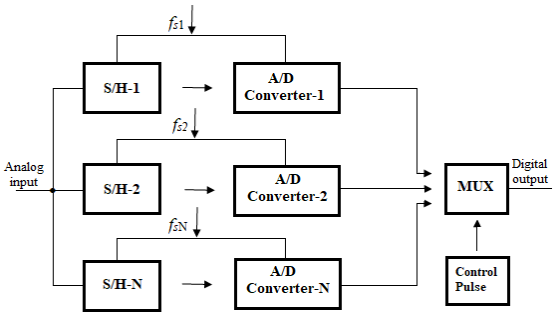

Figure 1: Block diagram of N–channel TI ADC

The sampling clock phases of each ADC cores are very important in TI-ADCs as mentioned above. The sampling rate of a TI ADC is given by F_s=N/T, where N is the number of channels and T is the minimum sampling period of a single ADC core. For instance, if four-channel TI_ADC is designed, and maximum sampling rate of each core ADC is assumed as 2Gs/s, then the final TI-ADC is supposed to have a sampling rate of 8GS/s. Timing diagram of an N channel TI-ADC is depicted in Figure 2 [2].

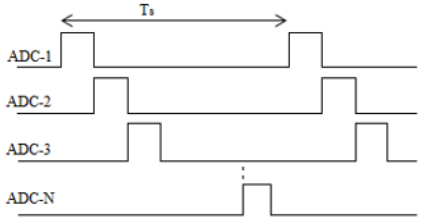

Figure 2: Timing diagram of N–channel TI ADC

The S/H circuits in TI ADC architecture are used to create an analog de-multiplexer circuit, which decides which ADC channel will work in which timing interval. Because the analog input signal is only one signal. The binary converted digital output data for a quantized input level is obtained from the core ADC outputs. Then, each ADC channel output is connected to

a specific digital multiplexer input. The resolution of the multiplexer inputs and the core ADCs are the same. The control pulse generator produces the sampling clock pulses at the input and the select control pulses of the digital multiplexer. The multiplexer is responsible for transferring the binary outputs of ADC cores in correct order to the final digital output port [3]. The timing and the synchronization issue of this operation is the most critical and difficult part of a TI-ADC design in general. In this study, a BiCMOS comparator based 6-bit Flash ADC core is decided for each channel to design a 6-bit TI-ADC in 250 nm BiCMOS technology using Cadence IC Design tools.

The rest of the paper is organized as follows: Section II describes all design steps of the proposed BiCMOS TI ADC. The circuit schematics of all design blocks are shown and explained in detail. The simulation results are given and discussed in Section III. Finally, Section IV concludes the study.

II. Design Steps of The Proposed Time Interleaved ADC

The proposed TI-ADC consists of the following core designs: S/H circuit, 6-bit Flash ADC, 2x1 multiplexer having 6-bit inputs and pulse generator. The following sub-sections describe them in detail.

A. *The Sample and Hold Circuit*

In this study, a simple CMOS analog switch with a hold capacitor at the output is used as a S/H circuit core as shown in Figure 3. The S/H circuit affects the speed performance and the accuracy of a TI-ADC. In fact, very high performance BiCMOS S/H circuits are available in the literature. However, the design of them is not an easy task. S/H circuit is responsible for sampling the analog input signal at a specific time and holding the corresponding input voltage level across the hold capacitor at the output. There are two S/H circuits in this work since the number of channel is chosen as two.

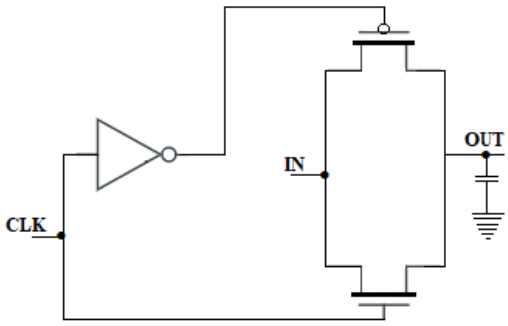

Figure 3: The sample and hold circuit

B. *The Flash ADC Core*

Full-flash ADC works in fully parallel fashion which makes it the fastest one among other ADCs. It consists of two main blocks as the analog part and the digital part. The analog part consists of a resistor array to produce quantization voltage levels for comparison purpose at the comparator array inputs, and comparator array. In this study, 6-bit resolution is aimed. Therefore, 64 number of resistors and 63 number of BiCMOS comparators form the analog part of the Flash ADC core of the proposed TI-ADC. The block diagram of the flash ADC core is shown in Figure 4.

Figure 4: The Flash ADC block diagram

a) The BICMOS Comparator Circuit

The comparators are the most important parts of Flash ADC architectures since their throughput and power consumption values are almost entirely depend on the comparator performance. In this study, a silicon-Germanium (Si-Ge) technology is chosen for its speed advantage over fully silicon CMOS circuits.

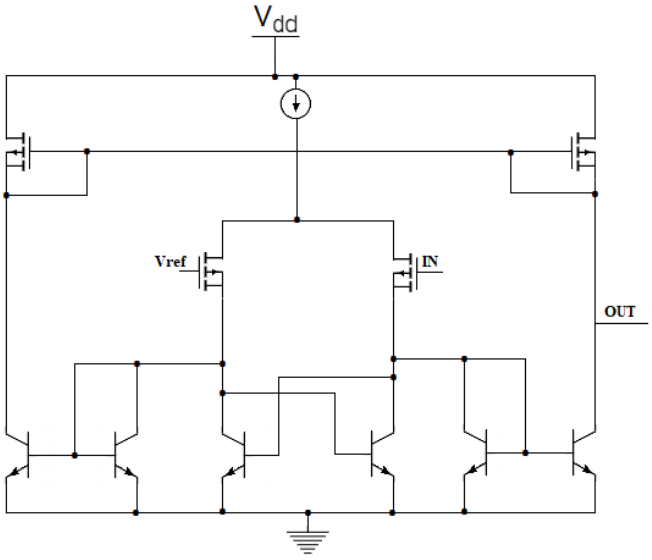

(a)

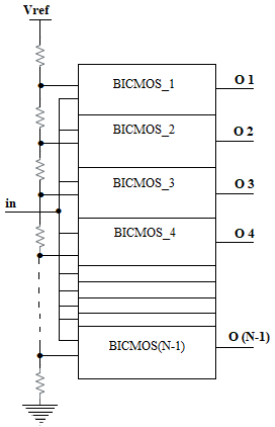

(b)

Figure 5: (a) The BICMOS comparator (b) The BICMOS comparator array

The BiCMOS comparator schematic used in this work is shown in Figure 5(a). This circuit is called as dynamic latch

comparator with push-pull output stage in [4]. However, optimum device sizes are reached after several transient simulations to obtain a higher speed and gain. The power supply voltage is a single 1.5 V. The complete comparator array structure is depicted in Figure 5(b).

The DC voltage transfer characteristic and transient analysis result are shown in Figure 6(a) and 6(b), respectively. The transient results and DC results of the complete analog part are also depicted in Figure 7(a) and Figure 7(b), respectively. As can be seen, 63 of transition levels are obtained almost with same distances in between.

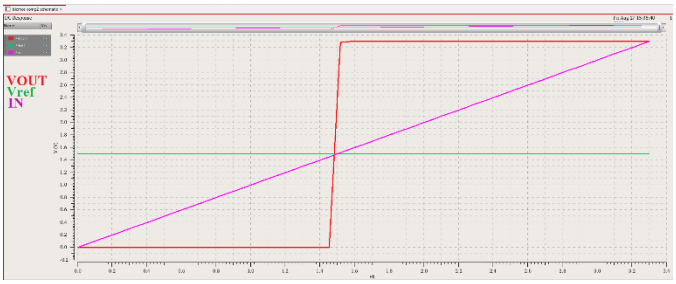

(a)

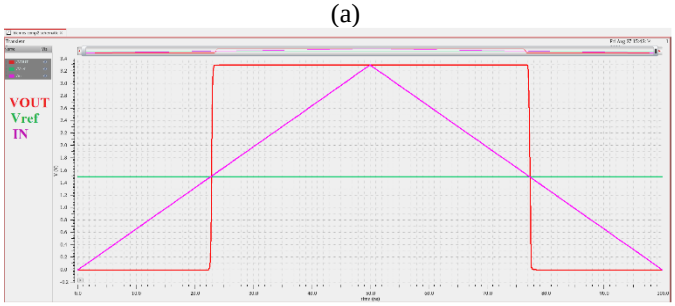

(b)

Figure 6: (a) DC simulation result of the BiCMOS comparator (b) Transient simulation result

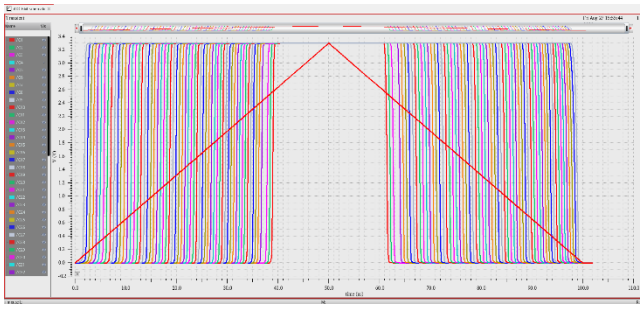

(a)

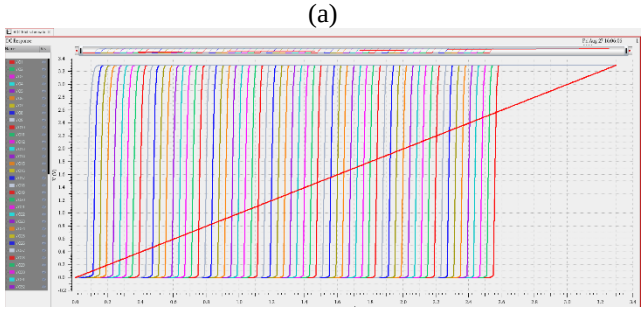

(b)

Figure 7: (a) Transient results of the complete comparator array (b) DC analysis results

b) The Dynamic Latch Circuit

The dynamic latch array is the first stage of digital part of Flash ADC. It keeps the logic output of the comparator array outputs (namely thermometer code) for a while to relax the rest part of the digital part until the final binary output is obtained. Since the analog input signal is continuous, the digital code belongs to an instantaneous input voltage can never be obtained at the same time due to the propagation delay of the digital part. Therefore, a dynamic latch circuit is necessary for ADC designs in general. The thermometer code is kept during the controlling CLK is logic "0". The period of the latch clock pulse defines the digital sampling rate of the Flash ADC. The circuit schematic of the dynamic CMOS inverter is shown in Figure 8 [5].

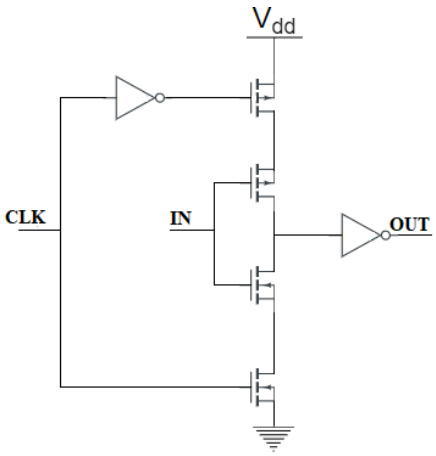

Figure 8: The dynamic latch circuit schematic

c) The 1-of-N Decoder Block

The thermometer code is converted to so-called 1-of-N code, which is necessary for the final stage, PLA-ROM circuit. The outputs of the 1-of-N decoder block shown in Figure 9 include only one logic "1", but the rest is all logic "0". This array block has a unit cell realizing F= $\bar{A}B$ function as shown in Figure 9(a).

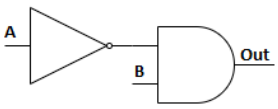

a)

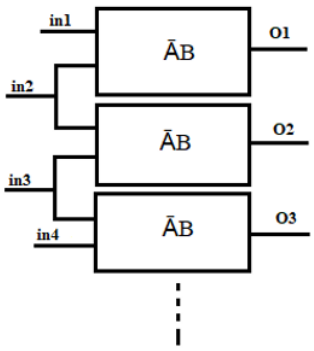

b)

Figure 9: (a) $\bar{A}B$ logic circuit (b) 1-of-N decoder block

d) PLA-ROM Circuit

The PLA-ROM circuit shown in Figure 10 is responsible for converting 1-of-N code to n-bit binary code. The final 6-bit binary output data of the Flash ADC is obtained at the outputs of this circuit. The basic cell of this structure is a PMOS load inverter. There are 6 columns and 63 rows here. NMOS transistors on each row are arranged according to the corresponding digital output code. The CMOS inverters at the output are used not only for logic inversion but also for gain boosting and buffering purposes. The complete schematic of the Flash ADC core is shown in Figure 11 after realizing each sub-blocks.

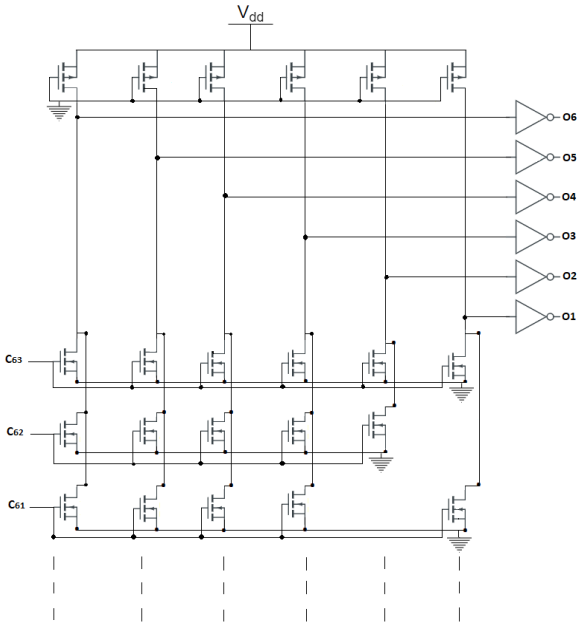

Figure 10: The PLA-ROM circuit

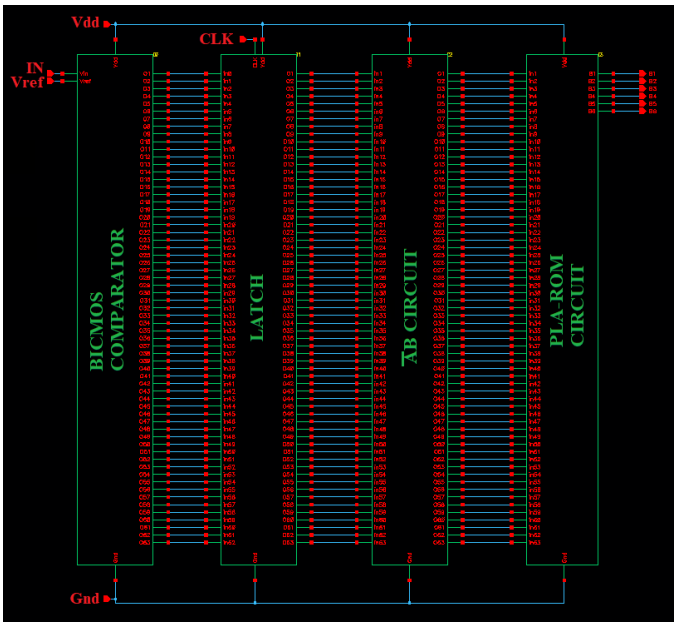

Figure 11: The complete Flash ADC schematic

C. The 2x1 Multiplexer Circuit

There are six 1-bit 2x1 CMOS multiplexers used in this block. The schematic of each 1-bit 2x1 multiplexer unit is shown in Figure 12 [6]. Timing of the select terminal of this multiplexer block is very important for a proper operation. The digital multiplexer block of the complete TI -DC must work at faster speed than that of each Flash ADC core. The control pulse generator circuit produces the system clock pulses, and coordinates the all critical timing and synchronization process.

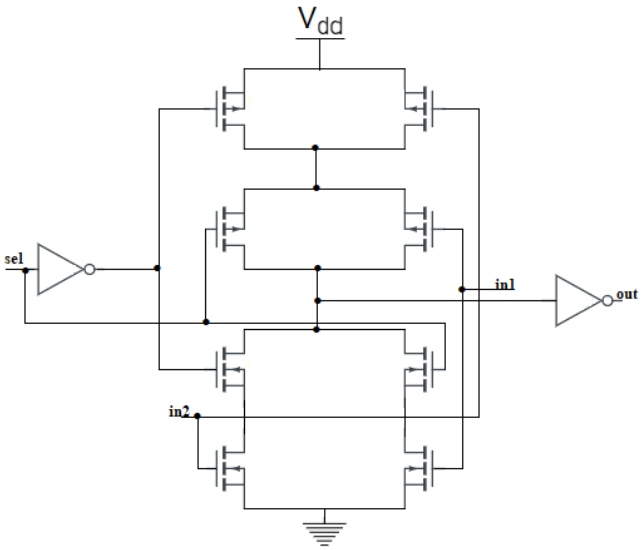

Figure 12: The multiplexer circuit [6]

D. Pulse Generator

The sampling control pulses of the analog de-multiplexer unit, the latch clock signals and select control pulse of the digital multiplexer are generated by this unit. The schematic of the pulse generator shown in Figure 13 is chosen from the literature [7], and the transistor aspect ratios are modified inside it. The speed performance of this circuit must be satisfying. Although the circuit schematic is simple, to obtain non-overlapping clock pulses with critical time delays is a tedious work. If the number of channels are increased, then this task become more difficult. There are four and even 8 channel TI-ADC examples can be found in the literature. Therefore, controlling pulse generation schemes are different in general. After all sub-blocks of the TI-ADC are finished, they are integrated carefully to realize the complete TI-ADC. The complete schematic of the 6-bit two-channel BiCMOS Flash ADC is depicted in Figure 14.

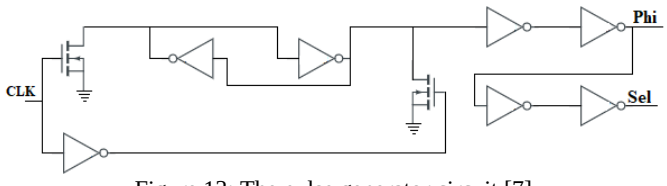

Figure 13: The pulse generator circuit [7]

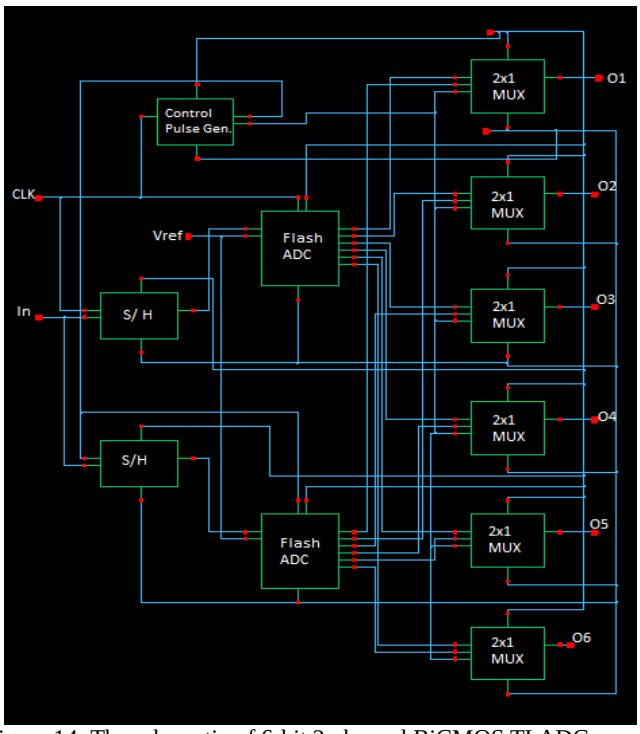

Figure 14: The schematic of 6-bit 2-channel BiCMOS TI ADC

III. Simulation Results

Schematics and simulations of the design are conducted using 0.25µm Si-Ge HBT BICMOS process parameters in Cadence IC Package Platform. Figure 15 and Figure 16 shows the transient simulation results of Flash ADC core and the complete TI ADC, respectively. As seen, there is almost no missing output code even for TI-ADC.

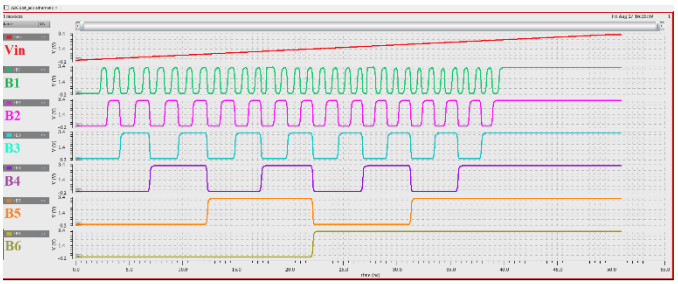

Figure 15: Transient results of the Flash ADC core

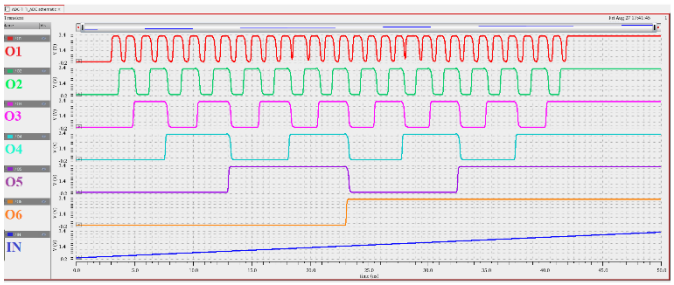

Figure 16: Transient results of the 6-bit 2-channel TI ADC

Figure 17 (a) and (b) shows the INL and DNL plots, respectively. The worst case INL value is 0.174 LSB, while DNL value is -0.113 LSB. Since all of the non-linearity measures are below 0.5 LSB, a monotonic converter operation is obtained. The design summary and a performance comparison is done in Table 1.

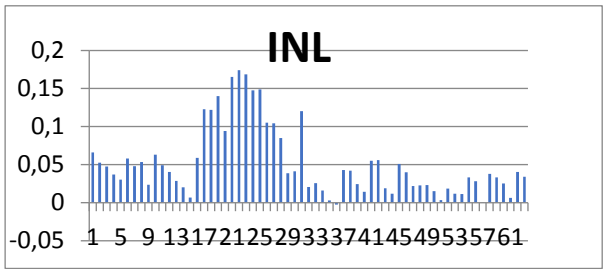

(a)

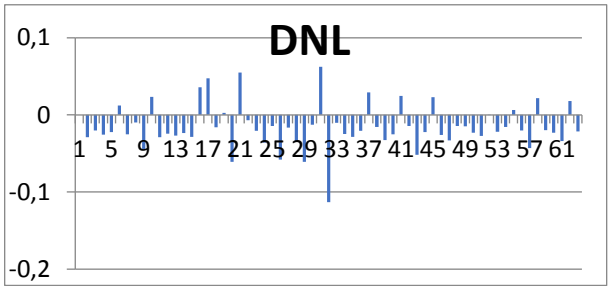

(b)

Figure 17: (a) INL Plot ,(b) DNL Plot

Table 1: Performance summary and comparison of the proposed TI-ADC

Parameters	This work	[2]	[8]	[9]
Design Technology	0.25µm Si-Ge HBT	0.25µm CMOS	0.65 µm CMOS	0.18 µm Si-Ge BICMOS
Resolution (bit)	6	4	6	6
Supply Voltage(V)	3.3	±1.5	1.5	3.3V-4.5V
INL (LSB)	-0.0022/ 0.174	+0.01/ -0.44 (f_{in}=100 MHz)	-0.4/0.7	-0.4/0.4
DNL (LSB)	-0.113/ 0.062	+0.26/ -0.22) (f_{in}=100 MHz)	-0.5/0.6	-0.2/0.2
Power Consumption (mW)	633.4	270	435	8.5W
Sampling Frequency (GHz)	7	10	16	30
Channel count	2	4	8	4
Core ADC	BICMOS Flash	CMOS Flash	CMOS Flash	SAR

IV. Conclusions And Future Works

In conclusion, a 6-bit TI-ADC was realized in 250nm Si-Ge HBT BiCMOS technology. A BiCMOS Flash ADC core was chosen in each interleaving channel. Cadence IC design platform was used during design and simulation processes. The

simulation results include 633,4 mW of ac power at 7GS/s operation under 3.3V power supply voltage, 0.74 LSB of INL, -0.113 LSB of DNL. When compared to other similar designs in the literature, this work is better in terms of linearity measures. The power consumption is lower than that of [9], but higher than others due to relatively higher supply voltage and Si-Ge HBT usage in the analog part. The sampling rate is lower than others since the number of channel is only two. As a future work, more ac performance measures will be obtained such as SNR and ENOB values. Also, post layout simulations will be conducted after completing the physical layout of the design. Moreover, the number of channel can be increased to four to obtain a higher sampling rate, which will require design of a new pulse generator circuit. In fact, this task requires a very high performance S/H or track and hold (T/H) amplifier circuit designs such as in [10]. Also, it is believed that more HBT usage in other sub-blocks as well in addition to the comparator circuit will increase the speed performance. It should be noted here that this work was the first attempt of an ADC design using Si-Ge BiCMOS technology of our VLSI research team.

V. REFERENCES

[1] F. Solis, A. F. Bocco, D. Morero, M. R. Hueda, B. T. Reyes, "Background Calibration Techniques of time interleaved ADC for optical coherent receivers using error backpropogation techniques", *2020 IEEE International Symposium on Circuits and Systems (ISCAS)*,2020

[2] O. Aytar, A. Tangel, E. Afacan, "A 10 GS/s time-interleaved ADC in 0,25 micrometer CMOS technology", *Journal of ELECTRICAL ENGINEERING, VOL 68, NO6, 415-424*,2017.

[3] L. B. Yurekli, E. Akdere, A. Tangel, "130 nm CMOS Teknolojide 2 Kanallı Zaman Ayrışmalı ADC Tasarımı", *ELECO-2018, pp.242-248*, Bursa,Turkey ,2018.

[4] B. R. Sissons, "Silicon Germanium BİCMOS Comparator Designed for Use in An Extreme Environment Analog to Digital Converter," MsC thesis dissertation, University of Arkansas, May 2017.

[5] Y. Talay, O. Aytar "4 Bit Flash Tabanlı Zaman Sayısal Dönüştürücü Tasarımı" *Düzce Ünversitesi Bilim ve Teknoloji Dergisi, 7 52-62*, 2019.

[6] T. Dua, A. Rajput, "2:1 Multiplexer Using Different Design Styles: Comparative Analysis", *Journal of Advancements in Robotics*, vol.7 no 3, pp . 2455-1872, 2020.

[7] B.Nowacki, N. Paulino, J. Goes, "A Simple 1 GHz Non-Overlapping Two-Phase Clock Generators for SC Circuits", *20th International Conference "Mixed Design of Integrated Circuits and Systems*, Gdynia, Poland, June 20-22, 2013.

[8] C. Huang, C. Wang, J. Wu, "A CMOS 6-Bit 16-GS/s Time-Interleaved ADC Using Digital Background Calibration Techniques," *in IEEE Journal of Solid-State Circuits, vol. 46, no. 4, pp. 848-858,* April 2011.

[9] X. Zhui, D. Wu, L. Zhou, Y. Huang, J. Wu, X. Liu, "A four-channel time-interleaved 30-GS/s 6-bit ADC in 0.18 μm SiGe BiCMOS technology", *Science China*, vol. 60, Dec. 2017

[10] H. Ding, D. Wu, X. Zheng, L. Zhou, T. Chen, F. Lv, J. Wang, B. An, J. Wu, X. Liu, "A Low-Distortion 20 GS/s Four-Channel Time- Interleaved Sample-and-Hold Amplifier in 0.18 μm SiGe BiCMOS" *Electronics*, vol. 9(20), 2020.

Propagation Characteristics of Low-Terahertz Band Channels

D. BORAN[1] and S. M. ÇÜRÜK[1]

[1] Iskenderun Technical University, Hatay/Turkey, didemboran.mfbe19@iste.edu.tr
[1] Iskenderun Technical University, Hatay/Turkey, selva.curuk@iste.edu.tr

***Abstract* - In recent years, due to the increasing need for high speed data transfer, wireless communication systems face difficulties in handling the demand. One of the suggested solutions to overcome these difficulties includes using the terahertz (THz) frequency band in the electromagnetic spectrum. THz band communication is among the promising technologies in reaching high data rates because of its wide bandwidth. Unfortunately, THz band is frequency selective with high path loss and molecular absorption. As known, transmission channel should be known for fast and reliable communication, but models used in low-frequency systems are not suitable for THz waves. In this study, after giving a brief information about the THz band, the free space path loss and molecular absorption loss that affect the propagation characteristics of the channel are examined for low THz band.**

***Keywords* – Channel characteristics, free space path loss, molecular absorption loss, path loss, terahertz communication.**

I. INTRODUCTION

The increase in the use of mobile communication devices such as wireless phones, computers and tablets creates high density data traffic in wireless networks. Studies have shown that wireless data rates double every eighteen months [1]. According to the International Telecommunication Union (ITU), data rate demand is expected to reach Terabits per second by 2030 [2, 3]. The spectral bandwidth of radio waves used in today's wireless systems is limited and cannot support data rates of more than a few giga bits per second [4], thus they are insufficient to meet this increasing demand. Terahertz (THz) band, which is located in the region of 0.1-10 THz band, between microwave and infrared waves in the electromagnetic spectrum, is among the promising frequency bands. THz waves may increase the data rate because of the high bandwidth [5]. For this reason, in 2008, THz Interest Group was established by IEEE for investigating the THz band and developing related 802.15 standard. Following in 2014, a group called The Task Group 3d (TG3d) was formed to update this standard and increase the data rate to 100 Gbps [6, 7]. In 2017, the first IEEE standard, 802.15.3d-2017, was approved at 300 GHz [6]. Today, studies on THz communication continue without slowing down.

THz waves have advantages in high rate wireless communication, but they have also difficulties mainly because the device technology required to generate THz frequencies is limited. However, the developments in technology of nano materials, such as grapheme, has made the generation of high frequency signals possible [8]. Another challenge faced in THz communication is the limited transmission distance due to the short wavelength. Further, THz waves have high path losses, which also restrict the transmission distance, because they are affected seriously from atmospheric conditions such as rain, wind and fog. The absorption of THz waves by water vapor and oxygen molecules is high. In order to increase the transmission distance, high gain directional antennas are used [9].

The increasing interest for communication in the THz band has accelerated the studies for high performance systems. As it is known, channel is the most important factor that affects the performance of the communication i.e., for an efficient, fast and reliable communication system, the effect of the transmission channel should be determined. THz band is known to be frequency selective and also because they are subject to high path loss and molecular absorption, therefore the models used in low-frequency systems are not suitable for THz waves. Thus, analyzing and characterizing the THz band channels realistically is the priority.

Due to the capabilities of the current state of the signal generators and because of the frequency response, most of the researches focus on the band below 300 GHz, in low THz band. In this study, we have presented the propagation characteristics of THz channel in the 275-400 GHz band for a line-of-sight (LoS) indoor scenario. The path loss and molecular absorption loss are examined in detail.

II. THZ CHANNEL

THz channels, similar to the other wireless channels, are modeled by characterizing both large- and small-scale fading. Then, the channel h includes information about the losses, large-scale fading includes the blockage and shadowing effects, and multipath fading. Then it is formalized as [10]

$$h = h_{pl}.h_{bl}.h_{sh}.h_{mis}.h_{mf} \quad (1)$$

where h_{pl}, h_{bl}, h_{sh}, h_{mis}, and h_{mf} are path loss, blockage, shadowing, misalignment and multipath fading, respectively. Path loss gives propagation characteristics of the channel and fading symbolizes all small-scale fading occurs because of movements and reflections. In case of short-range communication, i.e., the transmitter and the receiver are stable and see each other, a LoS path exists, therefore large scale and multipath fading may be ignored.

In THz communication, path loss depends not only on frequency and distance, but also on the variations of temperature and water vapor concentration. Then, the path loss of the channel is:

$$h_{pl} = h_{fspl}.h_{ma} \quad (2)$$

where h_{fspl} is free space path loss (FSPL) and h_{ma} is molecular absorption. In free space, the received power is a function of distance, which is given by Friis formula as [11]

$$h_{fspl}(f) = \frac{c\sqrt{G_T.G_R}}{4.\pi.f.d} \quad (3)$$

where c represents the speed of light, d is the transmission distance between transmitter and receiver, G_T , G_R are the gain of transmitter and receiver, respectively and f is frequency.

Molecular absorption loss is one of the main attenuation factors in the THz band, because the electromagnetic wave is affected by the atmospheric conditions. Water vapor is the most effective factor that affects absorption loss [12]. The molecular absorption loss can be described by the Beer-Lambert law [12, 13].

$$h_{ma}(f) = \exp\left\{-\frac{1}{2}k_a(f).d\right\} \quad (4)$$

where $k_a(f)$ refers to the molecular absorption coefficient. It depends on the temperature, pressure and molecular coefficient of the channel. It can be found with the help of spectroscopic databases such as High Resolution Transmission Molecular Absorption (HITRAN) database. However, a simplified absorption model has been developed, which is available at 275-400 GHz band [14]. According to this simplified model, first absorption lines are identified, then absorption coefficient is calculated:

$$h_{ma}(f) = \exp\left\{-\frac{d}{2}(\sum_i y_i(f,\mu) + g(f))\right\} \quad (5)$$

where y_i is an absorption coefficient for the i-th absorption line. In the 275-400 GHz band, there exists two absorption lines [10, 14, 15],

$$y_1(f,\mu) = \frac{A(\mu)}{B(\mu)+(\frac{f}{100c}-c_1)^2} \quad (6)$$

$$y_2(f,\mu) = \frac{C(\mu)}{D(\mu)+(\frac{f}{100c}-c_2)^2} \quad (7)$$

where $c_1 = 10.835$ cm^{-1} and $c_2 = 12.664$ cm^{-1}. $g(f)$ is an equalization factor which is calculated by a polynomial [10, 14, 15].

$$g(f) = p_1.f^3 + p_2.f^2 + p_3.f + p_4 \quad (8)$$

where $p_1 = 5.57\ 10^{-37}$ Hz^{-3}, $p_2 = -3.94\ 10^{-25}$ Hz^{-2}, $p_3 = 9.06\ 10^{-14}$ Hz^{-1}, and $p_4 = -6.36\ 10^{-3}$.

$$A(\mu) = 0.2205\ \mu\ (0.1303\ \mu + 0.0294) \quad (9)$$

$$B(\mu) = (0.4093\ \ \mu + 0.0925)^2 \quad (10)$$

$$C(\mu) = 2.014\ \mu\ (0.1702\ \mu + 0.0303) \quad (11)$$

$$D(\mu) = (0.537\ \mu + 0.0956)^2 \quad (12)$$

μ is the volume mixing ratio of water vapor,

$$\mu = \frac{\phi}{100}.\frac{p_w(T,p)}{p} \quad (13)$$

where ϕ represents relative humidity, p is pressure and T is temperature in centigrade degree. $p_w(T,p)$ is the saturated water vapor partial pressure p in temperature T.

$$p_w(T,p) = 6.1121\ (1.0007 + 3.46\ 10^{-6}\ p)\exp\left\{\frac{17.502\ T}{240.97+T}\right\} \quad (14)$$

Path loss is the decrease in the power of a signal as it travels from the transmitter to the receiver. The received power is given by [2].

$$P_R = P_T.|h(f,d)|^2 \quad (15)$$

P_T, P_R are the transmitted and the received power, respectively. Then, total path loss in decibel is

$$PL(dB) = 10.\log\frac{P_T}{P_R} \quad (16)$$

which is equal to

$$PL(dB) = 10.\log\frac{1}{|h(f,d)|^2} \quad (17)$$

Then, for an indoor low THz band LoS channel

$$PL(dB) = 20.\log_{10}\frac{4\pi fd}{c} + k_a(f).d.\log_{10} e \quad (18)$$

III. Results and Discussion

Numerical results are obtained using computer simulation based on the MATLAB software.

Figure 1 gives the FSPL (in dB) versus transmission distance for two different frequency, 275 GHz and 400 GHz. As seen from the figure, FSPL increases when the transmission distance increases, which means that transmission distance is a factor that limits the path gain in the free space. Note that, path loss in the THz band is large compared to other communication bands due to the high frequency.

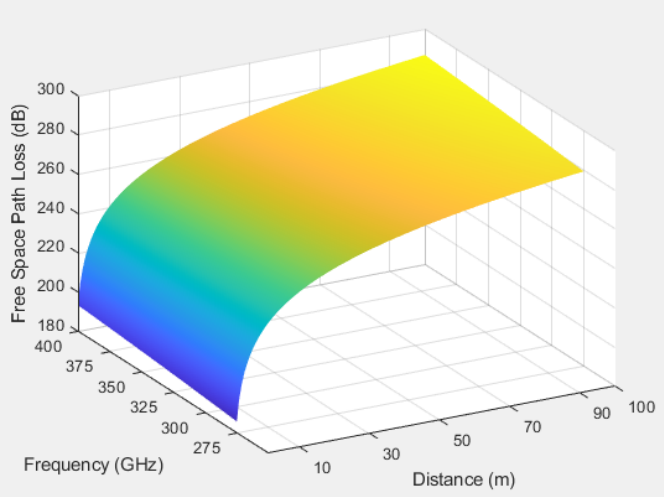

Figure 1: FSPL for 275 GHz and 400 GHz frequencies.

Figure 2 gives the molecular absorption loss versus frequency graphs for different transmission distances (1 m, 10 m, 100 m), under the standard pressure, 25°C temperature and 40 % humidity. As seen from the figure, the absorption loss increases as the distance increases. Further, there exist peaks in two frequencies, comparing with Figure 1, it is evident that absorption loss is less serious compared to FSPL.

The total path loss versus frequency is given in Figure 3, for the same THz band and transmission distances where G_T and G_R are *1 W*. The same result is also seen in this figure; thus the total loss increases as the distance increases.

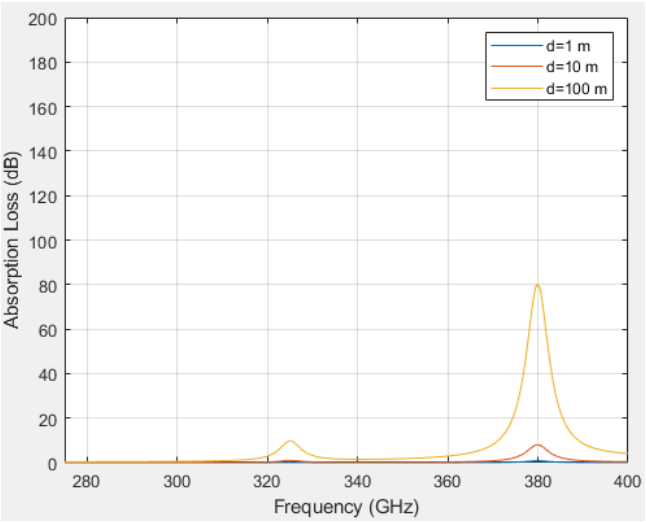

Figure 2: Molecular absorption loss, 25°C and 40 % humidity.

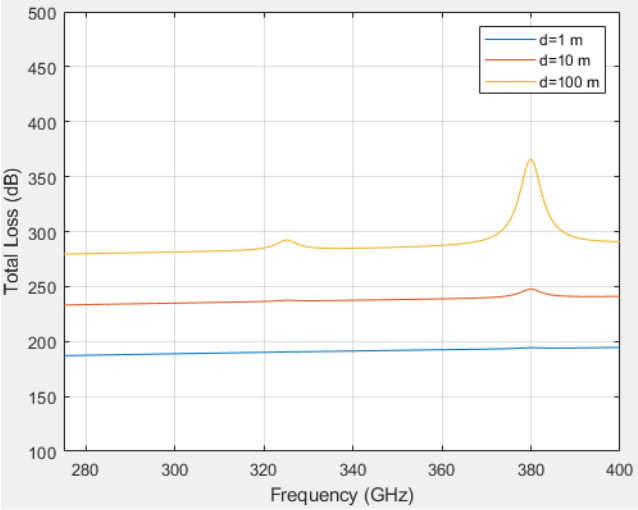

Figure 3: Total path loss (G_T=G_R=*1*), 25°C and 40 % humidity.

THz waves are highly sensitive to humidity and temperature, as given in the previous section. Therefore, we examined how the total loss is affected in Hatay, which is located in the Mediterranean region: hot weather most of the year with high humidity. According to the General Directorate of Meteorology, in this region the average temperature is 32°C and the humidity is around 70 % in summers. Note that FSPL will remain the same, however molecular absorption changes as given in Figure 4, whose effects is also seen in total loss (Figure 5). Comparing the figures, it is observed that molecular absorption (and also total path loss) is increasing if the temperature and humidity increase.

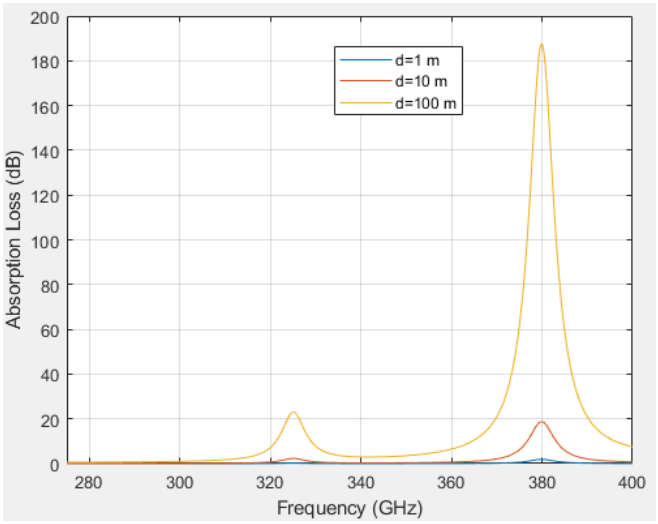

Figure 4: Molecular absorption loss, 32°C and 70 % humidity.

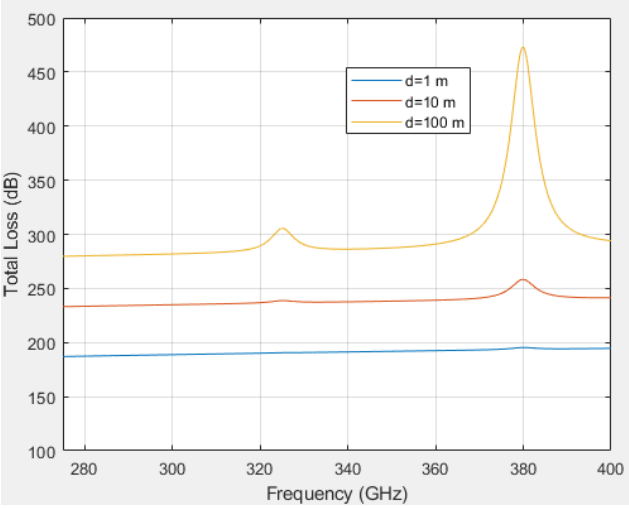

Figure 5: Total path Loss (G_T=G_R=1), 32°C and 70 % humidity.

IV. CONCLUSION

In this study, the propagation characteristics of low-THz band waves are investigated. As known, the transmission distance in THz communication is short due to the high frequency and the influence of atmospheric conditions. FSPL and molecular absorption loss are the most important factors of the propagation characteristics in an indoor LoS channel. FSPL is a distance and frequency dependent loss. Molecular absorption loss also depends on distance and frequency as well as pressure, temperature and humidity. This dependence may be critical in regions with high temperature and humidity, as in Hatay. It has been shown that the molecular absorption loss increases dramatically, especially in the frequencies where peaks are observed, for a rise of 7°C in temperature and 30% in humidity. The trace of this rise is also observed in the total path loss.

REFERENCES

[1] C. Han, Y Chen, "Propagation modeling for wireless communications in the terahertz band," *IEEE Communication Magazine*, vol. 56, pp. 96-101, 2018.

[2] N. Khalid, O. B. Akan, "Wideband THz communication channel measurements for 5G indoor wireless networks," *IEEE International Conference on Communications*," pp. 1-6, May 2016.

[3] S. Liu, X. Yu, R. Guo, Y. Tang, and Z. Zhao, "THz channel modeling: consolidating the road to THz communications," *China Communications*, vol. 18, pp. 33-49, 2021.

[4] R. Piesiewicz, T. Kleine-Ostman, N. Krumbholz, D. Mittleman, M. Koch, J. SchoebeI, and T. Kürner, "Short-range ultra-broadband terahertz communications: concepts and perspectives," *IEEE Antennas and Propagation Magazine*, vol. 49, pp. 24-39, 2007.

[5] M. A. Akkaş, "Terahertz teknolojisi uygulamaları ve terahertz dalgalarının kablosuz haberleşme için elektromanyetik modellemesi," *Afyon Kocatepe Üniversitesi Fen ve Mühendislik Bilimleri Dergisi*, vol. 18, pp. 190-200, 2018.

[6] H. Elayan, O. Amin, R. M. Shubair, and M. S. Alouini, "Terahertz communication: the opportunities of wireless technology beyond 5G," *In 2018 International Conference on Advanced Communication Technologies and Networking*, pp. 1-5, April 2018.

[7] V. Petrov, T. Kurner, and I. Hosako, "IEEE 802.15. 3d: first standardization efforts for sub-terahertz band communications toward 6G," *IEEE Communications Magazine*, vol. *58*, pp. 28-33, 2020.

[8] Z. Hossain, C. Mollica, and J. M. Jornet, "Stochastic multipath channel modeling and power delay profile analysis for terahertz-band communication," *In Proceedings of the 4th ACM International Conference on Nanoscale Computing and Communication*, vol. 32, pp. 1-7, September 2017.

[9] I. F. Akyıldız, and J. M. Jornet, "Realizing ultra-massive MIMO (1024x1024) communication in the (0.06–10) terahertz band," *Nano Communication Networks*, vol. 8, pp. 46-54, 2016.

[10] A. A. A. Boulogeorgos, E. N. Papasotiriou, and A. Alexiou, "Analytical performance assessment of THz wireless systems," *IEEE Access*, vol. *7*, pp. 11436-11453, 2019

[11] P. Tang, J. Zhang, H. Tian, Z. Chang, J. Men, Y. Zhang, L. Tian, L. Xia, Q. Wang, and J. He, "Channel measurement and path loss modeling from 220 GHz to 330 GHz for 6G wireless communications," *China Communications*, vol.18, pp. 19-32, 2021.

[12] J. M. Jornet, and I. F. Akyıldız, "Channel modeling and capacity analysis for electromagnetic wireless nanonetworks in the terahertz band," *IEEE Transactions on Wireless Communications*, vol 10, pp. 3211-3221, 2021.

[13] J. Kokkoniemi, J. Lehtomäki, and M. Juntti, "A line-of-sight Channel Model for the 100–450 Gigahertz Frequency Band," *EURASIP Journal on Wireless Communications and Networking*, pp. 1-15, 2021.

[14] J. Kokkoniemi, J. Lehtomäki, and M. Juntti, "Simplified molecular absorption loss model for 275–400 gigahertz frequency band," *In 12th European Conference on Antennas and Propagation*, pp. 1-5, April 2018.

[15] E. N. Papasotiriou, J. Kokkoniemi, A. A. A. Boulogeorgos, J. Lehtomäki, A. Alexiou, and M. Juntti, "A new look to 275 to 400 GHz band: channel model and performance evaluation," *In 2018 IEEE 29th Annual International Symposium on Personal, Indoor and Mobile Radio Communications*, pp. 1-5, September 2018.

Comparison of Optical OFDM Techniques in Visible Light Communication

S. M. ÇÜRÜK[1]

[1]Iskenderun Technical University, Hatay/Turkey, selva.curuk@iste.edu.tr

Abstract **- Already crowded radio frequency spectrum struggles to cope with the uncontrollable increase in wireless data traffic. A promising candidate for high speed data transmission is Visible Light Communication (VLC), whose widespread use is relatively easy because it uses currently exist illumination setup for communication. Orthogonal Frequency Division Multiplexing (OFDM) is a powerful technique used in VLC systems, as in other wireless communication systems, because of its resilience to inter symbol interference. But the conventional OFDM, which outputs complex valued time domain samples, should be adopted to be used in optic communication, because intensity modulation requires real positive signals. In this paper, we examine three optical OFDM techniques given in the literature, namely Direct Current Biased Optical OFDM, Asymmetrically Clipped Optical OFDM and Unipolar OFDM. These techniques all use hermitian symmetry to obtain real signals, but bipolar to unipolar conversion is done with various approaches: The signals are made positive by adding simply a dc bias or by asymmetrically clipping or positive and negative values are send separately. In this paper, these techniques are questioned with respect to their performance, spectral efficiency and complexity.**

Keywords **- Orthogonal Frequency Division Multiplexing, Asymmetrically Clipped Optical OFDM, Direct Current Biased Optical OFDM, Unipolar OFDM, Visible Light Communication**

I. INTRODUCTION

There is a tremendous amount of increase in wireless data traffic due to the rise in the number of mobile users with demands of high speed communication for internet based services such as social media, video streaming services, and cloud storage services. Wireless systems using radio frequency band become more and more saturated every day. Visible Light Communication (VLC), a kind of optic communication, has many advantages such as license free wide band, high data rate, high security and no interference to RF band and seems to be a strong candidate for future wireless communication [1]. VLC systems use already existing Light Emitting Diode (LED) based illumination infrastructure for communication, and as LEDs become widespread, the health friendly, low cost VLC systems seem to increase rapidly with many interesting indoor and outdoor applications. i.e., high speed data transmission in houses and offices, communication in hospitals and airplane cabins, traffic management and underwater communication.

Optical communication systems, as well as VLC systems, use Intensity Modulation / Direct Detection (IM/DD) technique [2]. Thus, the intensity of light is modulated with LED's input current which is controlled by modulated signal. In the receiver, after transmission of the signal in optical medium, demodulation process is carried out by an optical detector, generally a photodiode, which outputs an electrical signal related to the detected light intensity.

Orthogonal Frequency Division Multiplexing (OFDM), a Multicarrier Modulation technique, is attractive for high data rates in wireless communication, with its resilience to Inter Symbol Interference (ISI). OFDM may be a good choice for the VLC channel, which are proven to be frequency selective, especially in multisource case [3]. However, the output signals of a conventional OFDM have complex and bipolar structures and cannot be applied to optical communication systems directly because input of IM/DD block should be real and unipolar. Various approaches are proposed in the literature to solve the problem. The well-known solution is forcing hermitian symmetry on the data subcarriers for obtaining real signals and following, bipolar signals are made unipolar, by adding a bias or by clipping, or sending positive and negative values separately [4-6]. In this paper, we investigate the performance of these optical OFDM techniques, based on spectral efficiency, complexity and Bit Error Rate (BER).

The remainder of this paper is organized as follows. First, optical OFDM is introduced. Then a basic comparison of these techniques is demonstrated by simulations. Finally, conclusions of the study are given.

II. OPTICAL OFDM

Block diagram of an optical OFDM based VLC system is given in Figure 1. Note that, the receiver side of the optical OFDM is same as the conventional one, but the transmitter differs in some steps [4]. As known, independent of applied mapping, the output of Inverse Discrete Fourier Transform (IDFT) is complex (and bipolar), unless hermitian symmetry is exist in the input. Therefore, mapped signals together with their hermitian symmetries are fed to the IDFT block for obtaining real signals. Following, cyclic prefix (CP) is added to mitigate the effect of ISI, where the length of CP is selected to be at least equal to the length of channel impulse response. Finally, bipolar to unipolar conversion is done by an appropriate technique before IM.

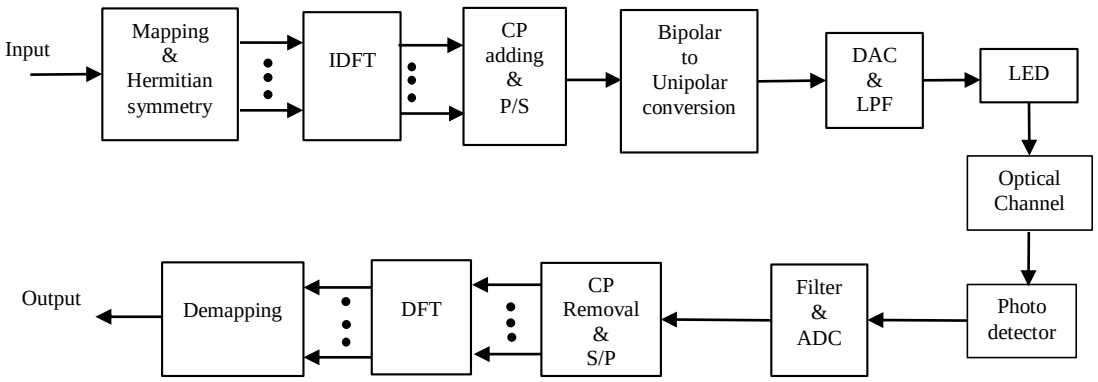

Figure 1: OFDM based VLC system block diagram.

The input of IDFT is given below [7]:

$$X_0 = X_{N/2} = 0 \tag{1}$$

$$X_{N-k} = X_k^* \qquad k = 1, 2, \dots, \frac{N}{2} - 1 \tag{2}$$

$$\boldsymbol{X} = [0, X_1, X_2, \dots, X_{\frac{N}{2}-1}, 0, X_{\frac{N}{2}-1}^*, \dots, X_2^*, X_1^*] \tag{3}$$

where N is number of subcarriers, X_k is serial to parallel converted mapped signals and X_k^* denotes the complex conjugate of it. The time-domain samples, which are transmitted during one OFDM symbol such that $x_1, x_2, \dots, x_{N-1}$ are obtained from $X_1, X_2, \dots, X_{N-1}$ through the IDFT operation. DFT equation is known to be

$$X_k = \frac{1}{\sqrt{N}} \sum_{n=0}^{N-1} x_n . \exp\left(\frac{-j2\pi kn}{N}\right), \quad k = 0, 1, 2, \dots, N-1 \tag{4}$$

where n is subcarrier indices. Then, the output IDFT is given by:

$$x_n = \frac{1}{\sqrt{N}} \sum_{k=0}^{N-1} X_k . \exp\left(\frac{j2\pi kn}{N}\right), \quad n = 0, 1, 2, \dots, N-1 \tag{5}$$

Note that because of the hermitian symmetry given in (3), it can easily be shown that (5) simplifies to,

$$x_n = \frac{1}{\sqrt{N}} \left[\sum_{k=1}^{\frac{N}{2}-1} 2X_{real,k} . \cos\left(\frac{2\pi nk}{N}\right) \right], n = 0, 1, \dots, N-1 \tag{6}$$

Thus, the output of IDFT block is real so that it can be transferred via IM/DD after bipolar to unipolar conversion.

Following, real but bipolar OFDM signals are made unipolar for optic communication. Three prominent techniques found in the literature are Direct Current Biased Optical OFDM (DCO-OOFDM), Asymmetrically Clipped Optical OFDM (ACO-OFDM) and Unipolar OFDM (U-OFDM) [8-14]. In DCO-OFDM, simply an appropriate dc bias is added to the signal and then all remaining negative peaks are clipped at zero. The dc bias added signal is [8],

$$x_{DC}(t) = x_{cp}(t) + B_{DC} \tag{7}$$

where $x_{cp}(t)$ is the CP added bipolar OFDM signal and B_{DC} is the dc bias. Adding a constant dc bias is a choice but selecting a dc bias related to the power of the signal will be more appropriate [8]:

$$B_{DC} = k \sqrt{E\{(x_{cp}(t)^2\}} \tag{8}$$

where k is the proportional constant of clipping factor and E{} denotes statistical expectation. Then the energy dissipation of DCO-OFDM increases approximately by (in decibel):

$$B_{DC,dB} = 10 \log_{10}(k^2 + 1) \tag{9}$$

All negative parts may not be eliminated even after adding the dc bias, therefore clipping at zero is applied:

$$x_{DCO}(t) = \begin{cases} x_{DC}(t), & x_{DC}(t) \geq 0 \\ 0, & x_{DC}(t) < 0 \end{cases} \tag{10}$$

DCO-OFDM is simple and easy to implement, but high positive peaks may be observed which requires high power. Thus, Peak to Average Power Rate (PAPR) increases which lowers the power efficiency and PAPR reduction techniques are needed [7].

ACO-OFDM is introduced as a power efficient technique, where only odd subcarriers are used for data transmission and even subcarriers are set to zero to ensure OFDM signals non negativity [5, 7]. Hermitian symmetry is again used for real signals. Then, in an ACO-OFDM system, the input vector of IDFT is expressed as [9]

$$\boldsymbol{X} = [0, X_1, 0, X_2, \dots, X_{\frac{N}{2}-1}, 0, X_{\frac{N}{2}-1}^*, 0, X_{\frac{N}{2}-3}^*, \dots, 0, X_1^*] \tag{11}$$

It can be shown that, since only the odd subcarriers are modulated all of the intermodulation caused by clipping falls on

the even subcarriers and does not affect the data-carrying odd subcarriers [9]. Finally, negative parts are clipped:

$$x_{ACO}(t) = \begin{cases} x_{cp}(t), & x_{cp}(t) \geq 0 \\ 0, & x_{cp}(t) < 0 \end{cases} \quad (12)$$

In U-OFDM, hermitian symmetry is used as in DCO-OFDM for obtaining real signals, then a simple transformation is applied to the time-domain signal in order to make it unipolar with no biasing requirements [10, 11]: Each bipolar frame is split into two separate frames, and transmitted one after the other. The first frame (positive frame) holds the positive time-domain samples and set zeros in the places of negative ones. The second frame (negative frame) holds the absolute values of the negative samples and set zeros in the places of positive ones. At the receiver, original bipolar frame is recovered by subtracting the samples in the negative frame from the samples in the positive frame. Note that, this combines the AWGN at both frames and leads to a signal-to-noise ratio (SNR) penalty.

The illustration of OFDM symbol structures of related schemes for the same amount of sending data is given in Figure 2. Note that, the use of hermitian symmetry results with $N/2$ independent complex input values for an N point IDFT in DCO-OFDM. Then Spectral efficiency of DCO-OFDM with M level of mapping is calculated by [14],

$$\eta_{DCO} = \frac{N-2}{2.(N+N_{cp})} log_2(M) \quad (bits/sec/Hz) \quad (13)$$

In ACO-OFDM, hermitian symmetry and the use of only odd subcarriers result with $N/4$ independent complex input values for an N point IDFT, spectral efficiency of ACO-OFDM is [14],

$$\eta_{ACO} = \frac{N-2}{4.(N+N_{cp})} log_2(M) \quad (bits/sec/Hz) \quad (14)$$

In U-OFDM, transformation halves the achievable data rate and effectively halves the spectral efficiency which becomes [10]:

$$\eta_{U} = \frac{N-2}{4.(N+N_{cp})} log_2(M) \quad (bits/sec/Hz) \quad (15)$$

where N_{cp} is the length of the cyclic prefix. As seen, spectral efficiency is halved in ACO-OFDM compared to DCO-OFDM, whereas Unipolar-OFDM spectral efficiency is equal to spectral efficiency of ACO-OFDM. However, they have a significant energy advantage over DCO-OFDM.

CP	DCO-OFDM signal		
CP	ACO-OFDM signal	CP	ACO-OFDM signal
CP	U-OFDM positive part	CP	U-OFDM negative part

Figure 2: Illustration of the structure of the transmitted signals for DCO-OFDM, ACO-OFDM and U-OFDM.

III. RESULTS AND DISCUSSION

Numerical results are obtained using computer simulation based on the MATLAB software, via Monte Carlo simulations. Note that Quadrature Amplitude Modulation (QAM) is generally used for mapping in an optic OFDM system, as is done in these simulations. The number of subcarriers is selected to be 128.

Examples of transmitted DCO-OFDM (6 dB bias, k=1.7266), ACO-OFDM and U-OFDM symbols with 16-QAM mapping are given in Figure 3. The amplitudes of DCO-OFDM, ACO-OFDM and U-OFDM have means of 1.5185, 0.2821, 0.4156 and maximums of 3.9545, 2.0060, 2.4625, respectively. DCO-OFDM has high positive peaks and requires higher power compared to the others. ACO-OFDM needs the lowest power, and U-OFDM power is close to it.

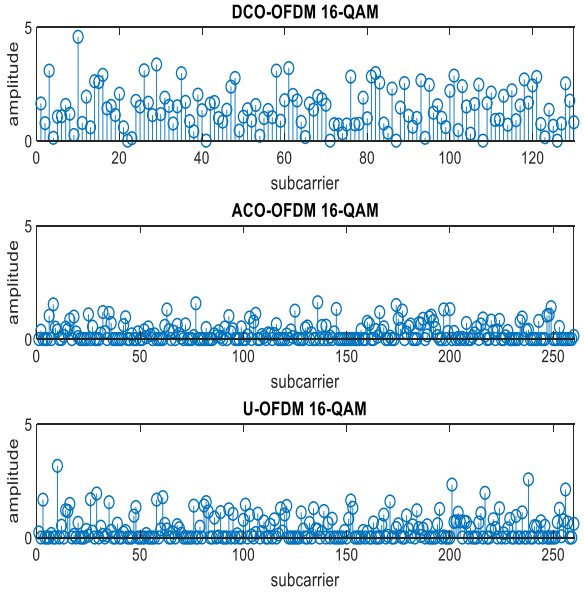

Figure 3: Examples of DCO-OFDM (6 dB bias), ACO-OFDM and U-OFDM symbols.

The geometric model of the indoor environment is not considered in the simulations, and only the line-of-sight path is assumed, which results with additive white Gaussian noise (AWGN) channel, as is commonly used in optical wireless systems in literature. Examples of cancellation diagrams of DCO-OFDM, ACO-OFDM and U-OFDM for 16-QAM mapping and 25 dB SNR are given in Figure 4.

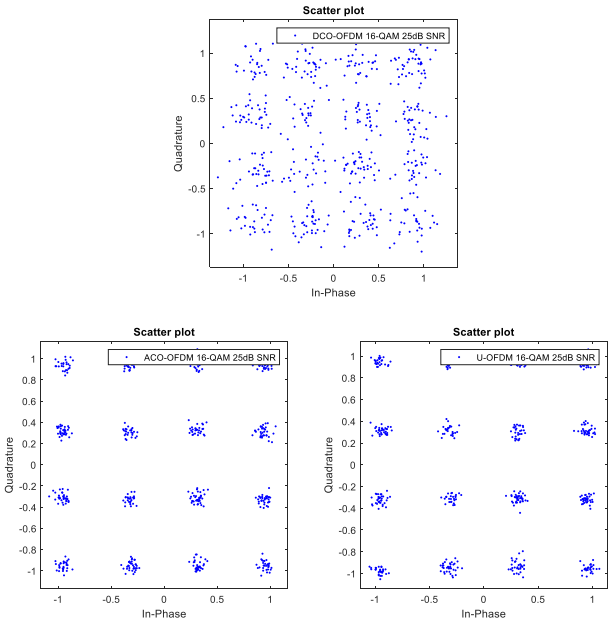

Figure 4: Cancellation diagram of DCO-OFDM (5 dB bias), ACO-OFDM and U-OFDM, 16-QAM mapping and 25 dB SNR.

The BER graphs of DCO-OFDM as a function SNR, with 4-QAM and under AWGN channel assumption, is given in Figure 5. The added dc biases are selected to be 5 dB, 9 dB and 13 dB. As seen, adding larger dc bias increases the BERs. For high levels of bias the clipping noise is negligible. Similar graphs for 16-QAM and 64-QAM constellations are given in Figure 6 and Figure 7, respectively. Comparing the figures, it is seen that as the modulation level increases, the BER also increases, as expected. Adding larger dc biases also increase the BERs in these graphs. But note that adding 5 dB bias results with larger BERs compared to 9 dB bias when SNR is larger than 22 dB. This is the case when dc bias is not sufficient which results with higher clipping error. It is concluded that the added bias is critical for the performance. Increasing the bias increases the power but reduces the clipping noise.

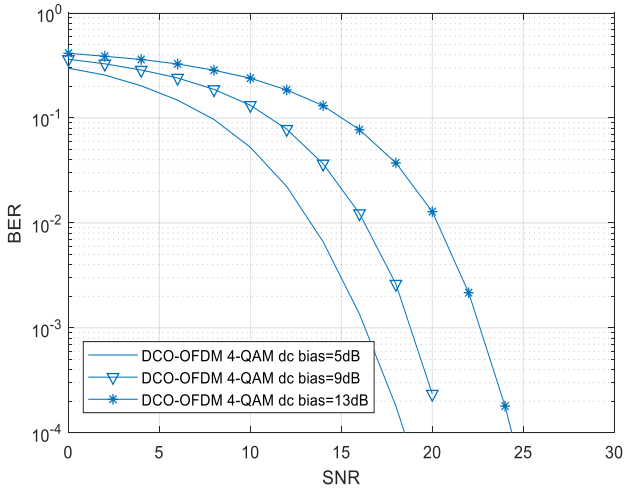

Figure 5: BER graphs of DCO-OFDM, 4-QAM.

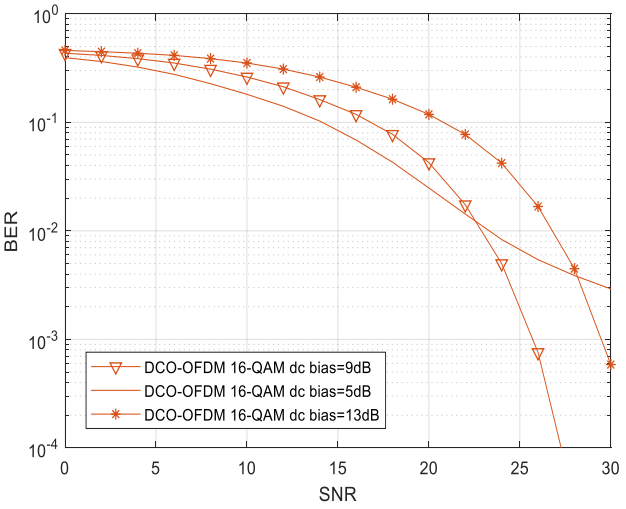

Figure 6: BER graphs of DCO-OFDM, 16-QAM.

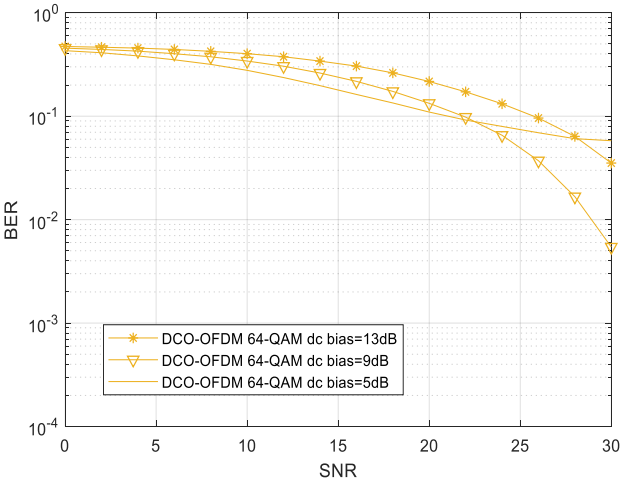

Figure 7: BER graphs of DCO-OFDM, 64-QAM.

Figure 8 and Figure 9 show simulation results for the BERs of ACO-OFDM and U-OFDM as a function SNR for different M-QAM constellations and AWGN channel. Comparing the BER graphs, it is seen that the performance of ACO-OFDM and U-OFDM is very close. Although DCO-OFDM performance depends on the selected dc bias, but it is worser than the other two optic OFDM techniques even in the best case.

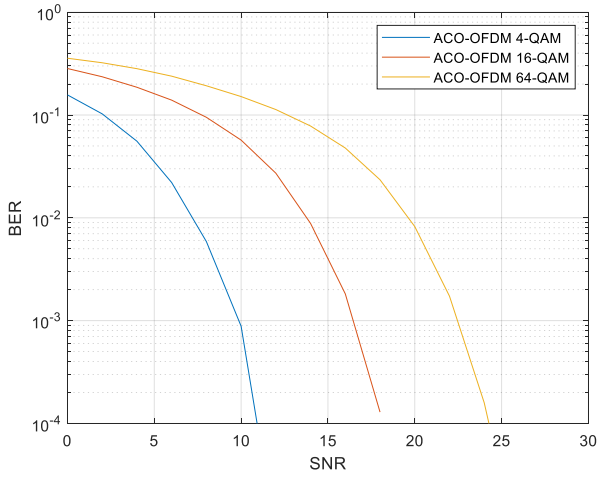

Figure 8: BER graphs of ACO-OFDM.

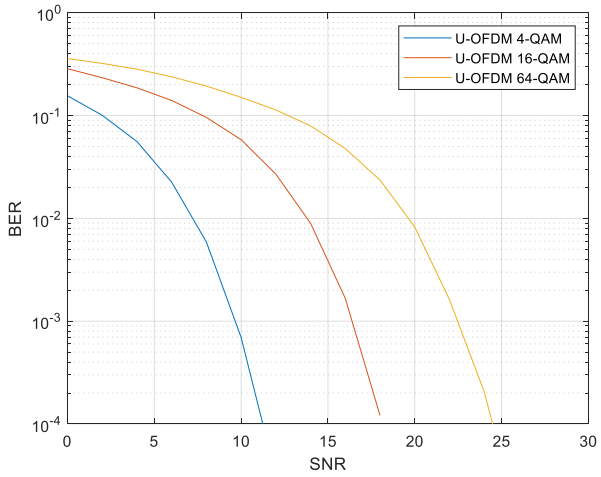

Figure 9: BER graphs of U-OFDM.

IV. CONCLUSIONS

The promising candidate, VLC, uses optical OFDM for high speed data transmission. In this paper, we examine three optical OFDM techniques given in the literature, namely DCO-OFDM, ACO-OFDM and U-OFDM. These techniques all use hermitian symmetry to obtain real signals, but bipolar to unipolar conversion is done by adding a dc bias or by asymmetrically clipping or by a transformation that sends positive and negative values separately. In this paper, these techniques are questioned with respect to their BER performance, spectral efficiency and complexity. DCO-OFDM has the best spectral efficiency with simple structure but high power requirement and low BER performance are the disadvantages. Further, the added dc bias level is critical for BER performance, i.e., high dc bias increases the power but reduces the clipping noise. ACO-OFDM and U-OFDM have similar performances in means of spectral efficiency and BER performance, but ACO-OFDM comes forward with its relatively simple structure.

REFERENCES

1. M. Saadi, T. Ahmad, M. K. Saleem, L. Wuttisittikulkij, "Visible light communication - An architectural perspective on the applications and data rate improvement strategies", *Transactions on Emerging Telecommunication Technologies*, vol. 30, no. 2, pp. 1-21, 2019.
2. S. M. Çürük, M. Kimyacı, "The impact of configuration on channel characteristics in Visible Light Communication", in *IEEE Global Power, Energy and Communication Conference*, pp. 56-61, 2019.
3. M. Kimyacı, S. M. Çürük, "Channel in multiple transmitter Visible Light Communication", *Academic Platform Journal of Engineering and Science*, vol. 9, no. 1, pp. 10-18, 2021.
4. J. Armstrong, "OFDM for optical communications", *Journal of Lightwave Technology*, vol. 27, no. 3, pp. 189-204, 2009.
5. F. A. Dahri1, S. Ali, M. M. Jawaid, "A review of modulation schemes for Visible Light Communication", *IJCSNS International Journal of Computer Science and Network Security*, vol.18, no.2, pp. 117-125, 2018.
6. H. Kazemi and H. Haas, "On the performance of single side-band OFDM for band-limited Visible Light Communication", in *IEEE International Conference on Communications Workshops*, pp. 1-6, 2020.
7. A. A. Sharifi, "A new post-coding approach for PAPR reduction in DC-biased optical OFDM systems", *Optoelectronics Letters*, vol.15, no.4, pp. 302-305, 2019.
8. J. Armstrong and B. J. C. Schmidt, "Comparison of asymmetrically clipped optical OFDM and DC-biased optical OFDM in AWGN", *IEEE Communications Letters*, vol. 12, no. 5, pp. 343-345, 2008.
9. J. Panta, P. Saengudomlert and K. Sripimanwat, "Performance improvement of ACO-OFDM indoor optical wireless transmissions using partial pre-equalization", *ECTI Transactions on Electrical Engineering, Electronics, and Communications*, vol. 14, no. 1, pp. 1-11, 2015.
10. D. Tsonev and H. Haas, "Avoiding spectral efficiency loss in unipolar OFDM for optical wireless communication," in *IEEE International Conference on Communications (ICC)*, pp. 3336–3341, June 2014.
11. R. J. Godwin, K. Veena, D. S. Kumar, "Performance analysis of direct detection Flip-OFDM for VLC system", in *2016 International Conference on Emerging Trends in Engineering, Technology and Science (ICETETS)*, pp. 442-446, 2016.
12. R. Alindra; M. O. Fauzan; R. Ramadhan; S. Rahardjo, "Performance analysis of DCO-OFDM and ACO-OFDM for Visible Light Communication system", in *3rd International Seminar on Sensors, Instrumentation, Measurement and Metrology (ISSIMM)*, pp. 84-90, 2018.
13. V. K. Singha, U. D. Dalala, "Investigation of LED non-linearity on DCO-OFDM and ACO-OFDM in VLC systems using multichip RGB LEDs for indoor applications", *Procedia Computer Science*, vol. 143, pp. 852–859, 2018.
14. M. P. Bhadoria, G. Pandey, A. Dixit, "Performance Eevaluation of Visible Light Communication for DCO and ACO Ooptical OFDM techniques", in *National Conference on Communications (NCC)*, pp. 1-6, 2019.

A New Approach to Increasing the Efficiency of Solar Panels

A. S. ÇABUK[1]

[1] Electrical & Electronics Eng. Faculty, Electrical Engineering Dept. Istanbul Technical University
Istanbul/Turkey, ascabuk@itu.edu.tr

Abstract **- Obtaining electricity from solar panels, which is one of the renewable energy sources, is very important today. Obtaining the highest level of energy from solar panels is one of the main issues that researchers focus on. One of the methods that helps to increase the efficiency of solar panels is panel cleaning. This paper presents a new approach to increase the efficiency of solar panels. In the study carried out on three solar panels of 10W, one of the panels is covered with stretch film, another panel is covered with rain-slip solution and the other panel does not have any coating. These three panels were exposed to the same ambient conditions and efficiency values and operating parameters were compared.**

Keywords **– Solar panel, efficiency, photo voltaic system, cleaning PV.**

I. INTRODUCTION

RENEWABLE energy sources have played a very important role in energy production in recent years. Of these, solar energy has a large share in energy production. It is predicted that the sun, which is an inexhaustible energy source, will have a large share in energy production in the future [1,2]. Photovoltaic (PV) cells are used to generate electricity from solar energy. These are designed to generate electrical energy from the radiation from the sun. The most important problem in PV systems is the efficiency issue due to the inability to use the sun effectively. The reasons that affect the efficiency are due to production or use. Among the reasons arising from use, not having the same sun angle every hour of the day or the panel not being as clean as in the first production can be listed [3,4]. Solar panels, like other surfaces in the external environment, are polluted. These are environmental pollution dust, sand and bird droppings. The result of this pollution causes a decrease in the amount of sunlight transmitted to the panel and therefore the efficiency of the solar panel is low. This efficiency reduction is approximately 35-40% and this causes a decrease in the power produced by the solar panel [5].

Periodic maintenance is required to minimize these effects. These increases operating and maintenance costs. In recent years, researchers have focused on studies that reduce the effects of reducing the efficiency of solar panels, such as dust accumulation [6]. These studies are on self-cleaning coating materials used in the manufacture of solar panels and cleaning the panel with a mechanism [7-9].

Most research for solar panels efficiency improvement is for the development of new panel manufacturing. Studies for existing systems are on cleaning systems with a mechanism or human power. This seriously affects the maintenance costs of existing systems. This study presents a simple and inexpensive method for increasing the efficiency of existing solar panels. 10W polycrystalline panels were used in this study. Three identical solar panels with the same power and electrical parameters were examined.

II. PHOTOVOLTAIC CELL

Photovoltaic cell is semiconductor material that transform sunlight into electric energy. A semiconductor is a simple substance that can conduct electricity and control its current under suitable conditions. Silicon material is the most widely used semiconductor in photovoltaic cells. Besides, it is used in semiconductor materials such as gallium phosphide, gallium arsenide, aluminum phosphide, aluminum arsenide) and indium phosphide. These semiconductors are of two types, p and n type. A photovoltaic cell consists of combining p-type and n-type semiconductors [10-12].

Efficiency is very important in photovoltaic systems. Researches both in production and use are on the increase of productivity. The efficiency of the energy produced by a photovoltaic cell; wavelength of sunlight, panel surface temperature, surface reflectivity and recombination of electrons holes and holes.

One of the most important problems in solar panels is efficiency. PV cell efficiency;

$$\eta_{PV} = P_{PV}/(G.A) \quad (1)$$

$$P_{PV} = U_m I_m \quad (2)$$

where P_{PV} is PV module power, G is solar radiation, A is PV array area, U_m is maximum PV module voltage and I_m is maximum PV module current [13, 14].

Factors affecting PV cell efficiency are environmental factors, PV module and PV installation design. Local pollution, dust, rainfall, ambient temperature and humidity are environmental factors. Material choice, self-cleaning glass and glass transmittance are PV module factors. Solar reflector,

water sprinklers and sun-tracking devices are PV installation design factors [11].

This study focuses on environmental factors affecting the efficiency of panels. Pollution such as dust effect causes a decrease in the electrical energy produced by the PV system. This is a negative effect on the total gain from the solar panel. Therefore, solar panel cleaning is important. There are automatic or manual systems for that and they affect the maintenance cost expenses. It is quite difficult to determine the correct time intervals for panel cleaning. Because natural weather conditions are predicted and its effect on the panel cannot be determined. Panel cleaning planning directly affects the gain from solar panels. When the energy obtained from the solar panel is considered as a commercial activity, the panel cleaning interval directly affects the cost per unit of energy. The total cost of this lost energy of the solar panel is found by adding the cost of the cleaning process to the cost of the lost energy. The cleaning interval can be defined as t_{clean} and the value of energy lost due to contamination during this interval can be defined as W_{clean} [15, 16]. According to this

$$W_{clean} = \int_0^{t_{clean}} R\,(t)P(t)L_s(t)dt \quad (3)$$

where $R(t)$, $P(t)$ and $L(s)$ are tariff of electricity, power produced by the panel at time interval t_{clean} and the power loss due to soiling, respectively [15, 16]. The sold value of the energy generated by the solar panel is

$$W_{sold} = \int_0^{t_{clean}} R\,(t)P(t)[1 - L_s(t)]dt \quad (4)$$

III. Experimental Setup

The outdoor test bench is located in Electrical Engineering Department at Istanbul Technical University in Istanbul, Turkey (at coordinates 41°06'17.1"N 29°01'29.2"E). The test bench consists of 3 solar panels. All solar panels are 10W polycrystalline silicon panel as shown Figure 1. The electrical specifications of solar panels are as given in Table 1. One of the solar panels is covered with stretch film, another panel is covered with rain-slip solution and the other panel does not have any coating. The panels were then coated as specified.

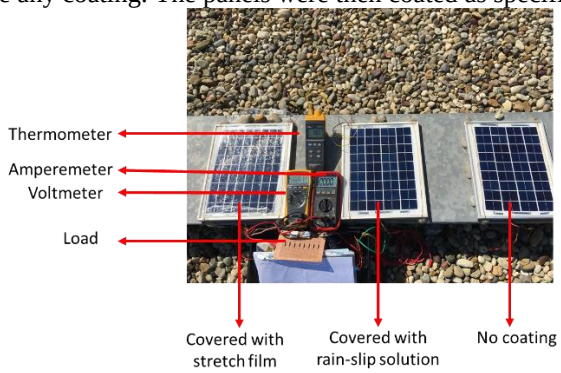

Figure 1: Experimental solar panels

Table 1: Electrical and physical specifications of the solar panels

Parameters	Value
Rated Maximum Power (Pmax) [W]	10
Power Tolerance Range [%]	5
Open Circuit Voltage (Voc) [V]	22.10
Maximum Power Voltage (Vmp) [V]	18.00
Short Circuit Current (Isc) [A]	0.67
Maximum Power Current (Imp) [A]	0.56
Maximum System Voltage [V]	1000
Maximum Series Fuse Rating [A]	10
Weight [kg]	1.3
Dimensions length (L) × width (W) × thickness (T) [mm]	300x300x20

Experimental work was started in August and electrical measurements of solar panels were carried out periodically once a week. These measurements continued for 3 months. The uncoated solar panel was taken as the reference panel and used for comparison with other coated panels.

Before starting the measurement studies, the contamination times of the panels in the Istanbul Technical University Ayazağa Campus, where the study was carried out, were found. Solar panels were placed on the roof of the Faculty of Electrical and Electronics and it was determined that the pollution level of the panels reached the highest level in a 2-week period. In addition, the effect time of the rain-slip solution was determined. It was found that this period corresponds to approximately 12 days. It has been observed that the resistance of the stretch coating material on the panel to outdoor conditions (excluding bird attacks) is approximately 1 month. During the measurement studies of the panels, the change of the stretch film and the renewal of the rain-slip solution were carried out by paying attention to the specified times.

IV. Results

The study was started by taking the measurement values for the situation that we will call the nominal production condition after the solar panels were cleaned. Measurements were taken at the same time and in the same weather conditions for consistency. The data obtained with the coating of the panels are as in Table 2. The panel called PV A is a solar panel covered with stretch film, the panel called PV B is a solar panel covered with rain-slip solution, and the panel called PV C is solar panels without any coating.

Table 2: Results of solar panels for clean situation.

Solar Panel	Open Circuit Voltage [V]	Voltage with Load [V]	Current with Load [mA]	Temperature of Solar Panel [ºC]
PV A	21.07	19.3	0.98	38.4
PV B	21.1	20.35	1.02	38.4
PV C	21.15	20.7	1.05	38.4

The data at the end of the 2nd week are as in Table 3. This period is when the pollution on the solar panels is at the

maximum level. The initial states of the solar panels and the states after 2 weeks are shown in Figure 2.

Table 3: Results of solar panels for dirty-clean situation.

	Solar Panel	Open Circuit Voltage [V]	Voltage with Load [V]	Current with Load [mA]	Temperature of Solar Panel [ºC]
Dirty	PV A	20.48	20.4	1.03	37.2
	PV B	21.1	20.5	1.03	37.2
	PV C	19.93	19.17	0.96	37.2
Clean	PV A	21.17	21.1	1.07	37.2
	PV B	21.1	20.9	1.05	37.2
	PV C	20.54	20.45	1.04	37.2

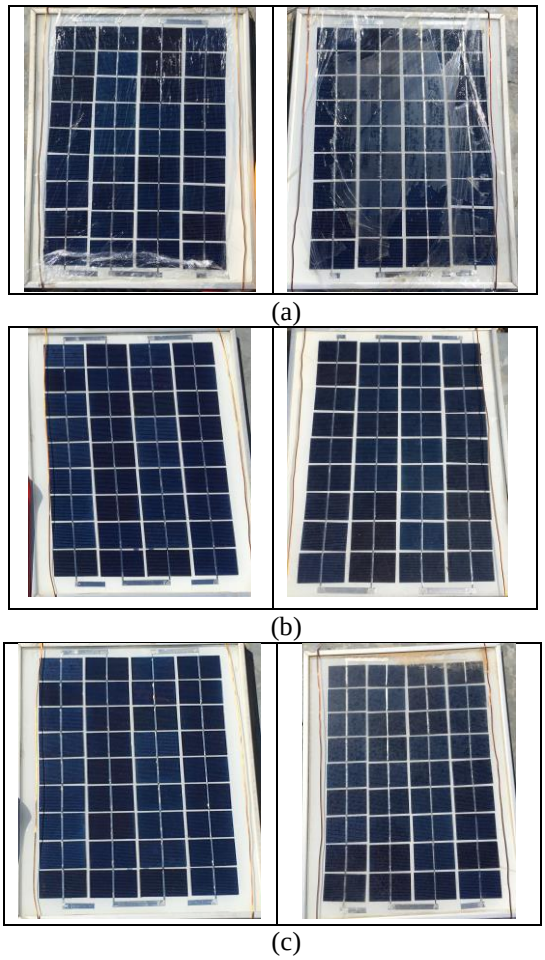

(a)

(b)

(c)

Figure 2: State of the polluted PV modules (a) stretch film coated (b) rain-slip coated (c) no coated.

As can be seen in Figure 2, pollution has occurred on the stretch film covered panel and the stretch film has been damaged. On the other hand, the panel on which rain-slip solution is applied has very little pollution. On the panel without any coating, the pollution is at the maximum level.

The change and comparison of the measured voltage values under load with the contamination of the solar panels due to weeks is as in Figure 3.

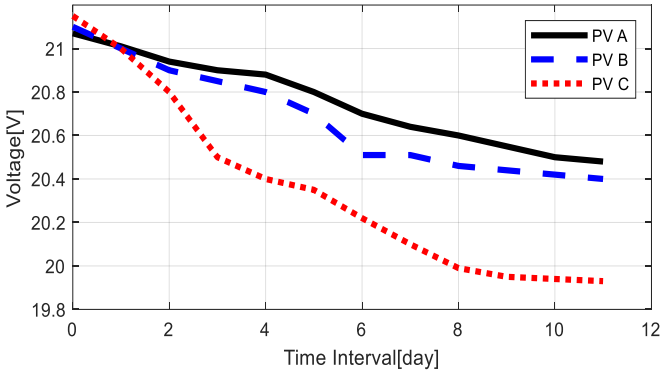

Figure 3: Compare voltage value of solar panels

.

The efficiency change obtained according to the measured electrical values of the solar panels is as seen in Figure 4.

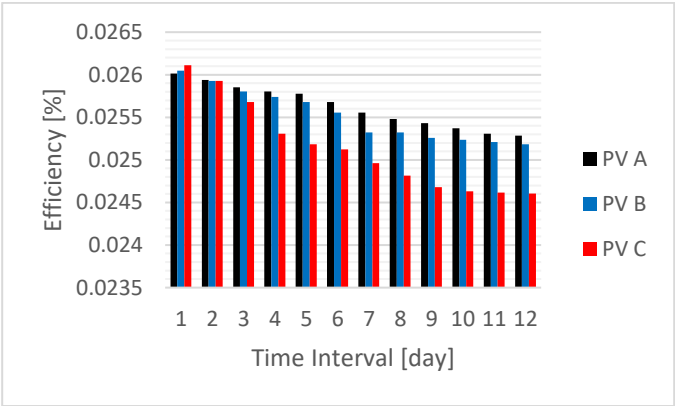

Figure 4: Compare efficiency of solar panels

V. CONCLUSION

This study is on the comparison of solar panels with the same electrical parameters. it also proposes a method to ensure that the energy they produce is greater. Three solar panels were examined using different coating materials. One of the panels is covered with stretch film, another panel is covered with rain-slip solution and the other panel does not have any coating. These 3 panels were exposed to the same ambient conditions and efficiency values and operating parameters were compared. It is seen that the voltage value obtained from the solar panels using stretch-coated film and rain-slip solution is much better than the uncoated solar panel. When the solar panel without any coating material is exposed to pollution, there is a decrease of approximately 5.77% in its efficiency. In the stretch film covered panel, which is exposed to the same pollution conditions, this yield decrease is 2.79%. The same situation is 3.32% in the solar panel with rain-slip solution.

The energy gain obtained from this efficiency obtained with the coating material and the cost of the coating material should be compared and a cost analysis should be done. It is planned to examine these economic values in detail in future studies.

.

REFERENCES

[1] S. A. Marathe and B. P. Patil, "Performance of Solar Panel in Presence and Absence of Dust," *2021 International Conference on Intelligent Technologies (CONIT)*, 2021, pp. 1-5.

[2] R. Majeed, A. Waqas, H. Sami, M. Ali and N. Shahzad, "Experimental investigation of soiling losses and a novel cost-effective cleaning system for PV modules", *Solar Energy*, vol. 201, pp. 298-306, 2020.

[3] O. Steven, M. Peter and W. Cyrus, "Effect of Enhanced Heat Transfer on Photovoltaic/ Thermal Collector Efficiency," *2021 IEEE PES/IAS PowerAfrica*, 2021, pp. 1-5.

[4] B. Abhilash and A. K. Panchal, "Self-cleaning and tracking solar photovoltaic panel for improving efficiency," *2nd International Conference on Advances in Electrical, Electronics, Information, Communication and Bio-Informatics (AEEICB)*, 2016, pp. 1-4,

[5] T. P. Pawale, R. Motekar, R. L. Chakrasali, P. Hugar and S. B. Halabhavi, "Implementation of a Novel Self-Cleaning Roof Top PV Cells using Protective Film Coating," *Third International Conference on Smart Systems and Inventive Technology (ICSSIT)*, 2020, pp. 455-459.

[6] M. Gostein et al., "Soiling measurement station to evaluate anti-soiling properties of PV module coatings," *2016 IEEE 43rd Photovoltaic Specialists Conference (PVSC)*, 2016, pp. 3129-3131.

[7] H. Nakagawa, K. Mathuoka and H. Yonemori, "A study about the self-cleaning of a PV module surface using photocatalyst," *2014 IEEE Region 10 Humanitarian Technology Conference (R10 HTC)*, 2014, pp. 82-87.

[8] M. Despeisse et al., "Engineering of Thin-Film Silicon Materials for High Efficiency Crystalline Silicon Solar Cells," *2018 IEEE 7th World Conference on Photovoltaic Energy Conversion (WCPEC) (A Joint Conference of 45th IEEE PVSC, 28th PVSEC & 34th EU PVSEC)*, 2018, pp. 3888-3889.

[9] R. Tejwani and C. S. Solanki, "360° sun tracking with automated cleaning system for solar PV modules," *35th IEEE Photovoltaic Specialists Conference*, 2010, pp. 002895-002898.

[10] K.V. Vidyanandan, "An Overview of Factors Affecting the Performance of Solar PV Systems", *Energy Scan (A house journal of Corporate Planning, NTPC Ltd.)*. vol. 27, pp 2-8.

[11] M. Mani, R. Pillai, "Impact of dust on solar photovoltaic (PV) performance: Research status, challenges and recommendations", *Renewable and Sustainable Energy Reviews*, vol. 14 (9), 2010, pp. 3124-3131.

[12] N. Santhosh and B. Prasad, "Efficiency improvement of a solar PV-panel through spectral sharing by combination of different panels," *IEEE Students' Conference on Electrical, Electronics and Computer Science (SCEECS)*, 2016, pp. 1-4.

[13] S. S. Konjare, R. L. Shrivastava, R. B. Chadge and V. Kumar, "Efficiency improvement of PV module by way of effective cooling - a review," *2015 International Conference on Industrial Instrumentation and Control (ICIC)*, 2015, pp. 1008-1011.

[14] S. Dubey, J. N. Sarvaiya and B. Seshadri, "Temperature Dependent Photovoltaic (PV) Efficiency and Its Effect on PV Production in the World A Review", *Science direct Energy Procedia*, 2013, vol. 33, pp. 311 – 321.

[15] R. K. Jones et al., "Optimized Cleaning Cost and Schedule Based on Observed Soiling Conditions for Photovoltaic Plants in Central Saudi Arabia," *IEEE Journal of Photovoltaics*, vol. 6, no. 3, pp. 730-738, May 2016.

[16] A. Bianchini, M. Gambuti, M. Pellegrini, and C. Saccani, "Performance analysis and economic assessment of different photovoltaic technologies based on experimental measurements," Renewable Energy, vol. 85, pp. 1–11, Jan. 2016.

Application Example of Deep Echo State Neural Networks
Case Study: Prediction of Mobile Hydraulic Crane's Pressure and ECU Temperatures

K. KARAGÖZLER[1] and S. CANAN[2] and M. CEYLAN[3]

[1] Elfatek Elektronik Co. Ltd., Konya/Turkey, kerim.karagozler@elfatek.com.tr
[2]Elfatek Elektronik Co. Ltd., Konya/Turkey, suleyman.canan@elfatek.com.tr
[3]Konya Technical University, Konya/Turkey, mceylan@ktun.edu.tr

***Abstract* - Real data taken from the field can be used as design parameters in engineering studies. Alternatively, the calculated and analyzed values should be verified by field tests. However, waiting for data from the field for design parameters can sometimes take a very long time. This makes engineering solutions too long or impossible. In the same way, there may be tests that are difficult to test in design verifications, require cost, and create security problems. This study sought solutions to the problems described using the DESN model in two different data sets. In the study, deep Echo State neural network analysis was performed on two different data sets. As data, the pressures formed in the cylinder during the lifting and lowering of 6 different loads by a truck-mounted mobile crane and the 4-month device temperature of the electronic control unit in an overhead crane were recorded. Echo State Network application was made on these records with deep learning. After training with 80% of the data, the DeepESN model was tested with 20%, and these results were evaluated.**

***Keywords* – Deep ESN, ECU Temperature Prediction, Mobile Crane Lifting Pressure Prediction.**

I. INTRODUCTION

After ANN and CNN, RNN made a quick introduction to the world of neural networks. Problems such as zeroing or overgrowth of weights over time have been observed in the use of RNN. Many new learning algorithms have been developed under the name of RNN [1]. It is an RNN-based artificial neural network model in an echo state network. RNN-based network structures are dynamic systems. In other words, if the data in the environment is constantly changing, it can adapt quickly. Ideal for time-dependent series predictions. Its most significant feature is that it learns quickly and requires less processing power compared to similar systems.

II. ECHO STATE NEURAL NETWORK

There are three layers in the ESN structure: input, neuron pool (reservoir), and output. While the input and pool weights are fixed, the weight in the output layer is updated according to the iteration. The neurons in the pool are initially given a random weight, and these weights are not changed. The second issue is that the connection of neurons in the pool does not have to be as in classical methods. It can be selected in a random connection.

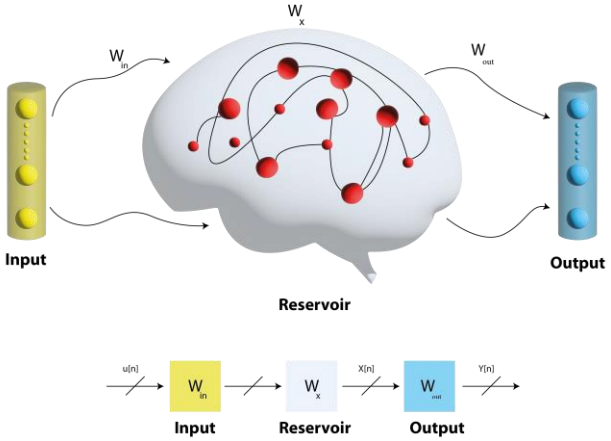

Figure 1: Echo State Network model.

The ESN model is shown in Figure 1. As seen in this model, there are three layers. It is seen that the neurons seen in the reservoir part make a random connection instead of a sequential connection. Weights are named Win for the input, Wx for the Reservoir, and Wout for the output.

Input and reservoir weights are randomly generated. These weights are fixed and cannot be changed. Only the Wout in the output layer is updated. Wx and Win are not updated, so mathematical operations are high-speed. It can be done with less processing power than other models. The ESN model gives better results for predictions moving along the time axis. Therefore, applying time-dependent data will give better results. The calculation of the input and reservoir weights is shown in (1). Then, the reservoir output is calculated according to Equation (2).

$$x[n+1] = f^{res}\left(w_{in}\,u[n+1] + w_x u[n]\right) \quad (1)$$

$$w_{out} = (YX^t)(XX^t)^{-1} \quad (2)$$

In the formulation, "u" is the ESN input. Then, the inputs and neurons multiplied by the weights are summed and passed

through the activation function. Generally, the following steps are performed for the Esn model [1].

1. At the beginning, random Win, Wx weights are determined for input and output.
2. The first data set to be used is applied to the input.
3. The reservoir is calculated according to the formula (1)
4. The reservoir output is saved as a data set.
5. Steps 2 to 4 are performed for each data set, respectively.
6. Output weight is calculated according to the obtained data.
7. Weights with outputs are calculated by the formula (2)

In formulation (3), the reservoir outlet is found by multiplying the outlet weight and passing it through the activation function.

$$y[n+1] = f^{out}(w_{out}\, x[n+1]) \quad (3)$$

ESNs are very successful in autonomous predictions as they use the previous data set in the following input set. The initial randomly determined weights are important for the Esn model to work correctly. The strength of Esn is that they learn quickly. Because it is made with a linear calculation with fixed weights. It is very successful in predictions in the one-dimensional time domain. In 2012, Sutskever stated that RNN would work more effectively if the weights were used with the Esn method at the beginning [2]. DESN is one of the topics of the last decade. It is used to execute specific tasks in fields such as industrial, medical, financial, and robotics.

Many reservoir models for the Deep Echo State neural network structure are still under investigation. The neurons within the reservoir can be connected as a ring, or they can be connected randomly. Different results are obtained according to each reservoir shape.

More than one reservoir is used in the application in Esn for deep learning. That is, the output of one reservoir is connected to the other. The reservoir layer, shown as a single layer in Figure 1, is connected to more than one reservoir layer, as seen in Figure 2.

Figure 2: Deep ESN model.

Since each reservoir output is connected to the other's input, they are transmitted one after the other. Therefore, the fixed random weight determination step valid in Esn is also valid for other reservoirs. From the last layer to the output layer, the previously mentioned calculations apply.

III. DATASET DESCRIPTION

Two different datasets were used for the application.

A. *Pressure data set of the mobile crane lifting cylinder*

This data set was obtained by working on the 115TM model, which has a lifting capacity of 32 tons, of the company MPG A.Ş, which manufactures mobile cranes in Konya. In Figure 3, there is a drawing showing how the mobile crane collects data. By connecting the pressure sensor to the cylinder part of the crane, the pressure created by the load in the cylinder was measured in bar. First, the load at the boom tip is raised and lowered from the ground. Then, a different load was taken, and the load was lifted and lowered. In this way, six different loads were lifted and lowered, and cylinder pressure was measured every 50 ms. (Records during the connection and disconnection of different loads have been neglected.) In summary, in this data set, the pressure in the cylinder during the lifting and lowering of 6 different weights by a mobile crane is recorded according to time. A data set was created by recording 15793 pressure data in 13.1 minutes in total.

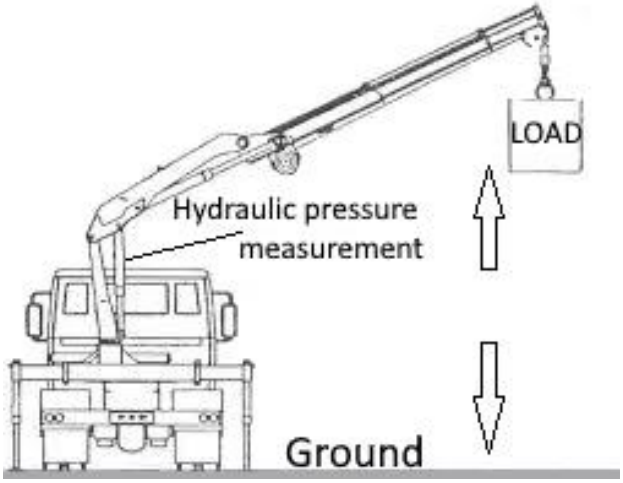

Figure 3: Mobile Hydraulic Crane.

An equivalent image is shown in Figure 3. The weights are respectively 4500kg, 5160kg, 6520kg, 8360kg, 10240kg, 19240kg.

B. *ECU Temperature data set*

The other data set was obtained by working in the workshop of a factory producing overhead cranes in Konya in 2020. The data set was created by recording the internal temperature of the control unit produced by Elfatek Elektronik every 30 seconds from September to December. In total, 291976 data records were taken.

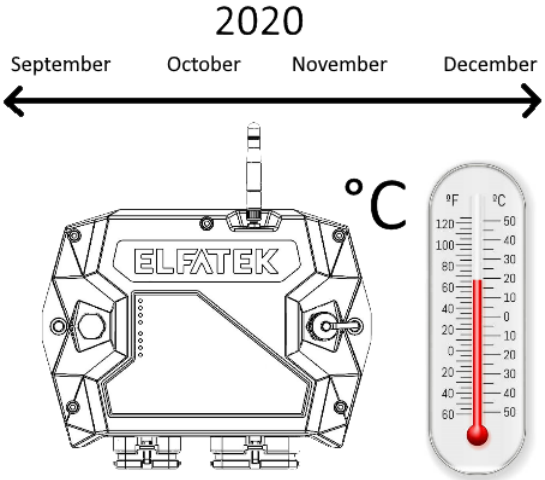

Figure 4: ECU (Electronic Control Unit)

In Figure 4, there is a visual of the electronic control unit where data is recorded.

IV. RESULTS

The data were run on the Jupiter platform in the Python environment. The training was performed in 80% of each data set, and tests was carried out for the remaining 20%.

A. *Mobile crane data prediction*

The graph in Figure 5 shows a visual of the pressure data set received at 50ms of the mobile crane. The vertical column shows the pressure created by the load in the cylinder, and the horizontal column shows the rank of the recorded data according to time. Six different peaks in the graph correspond to six different loads.

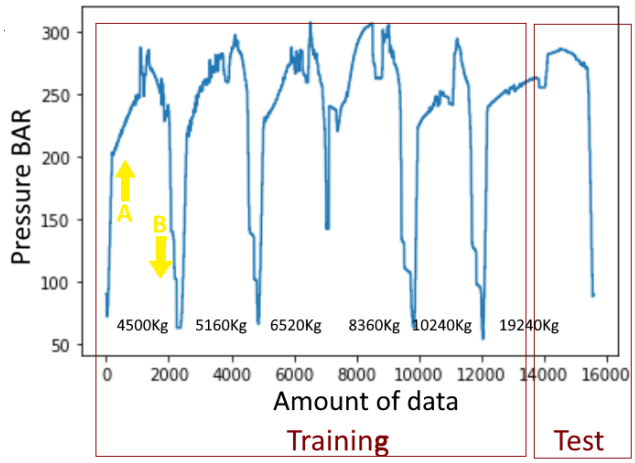

Figure 5: Pressure data graph for different loads.

The yellow arrow indicated by A indicates the recordings during the lifting movement, and the arrow indicated by B indicates the recordings during the lowering movement.

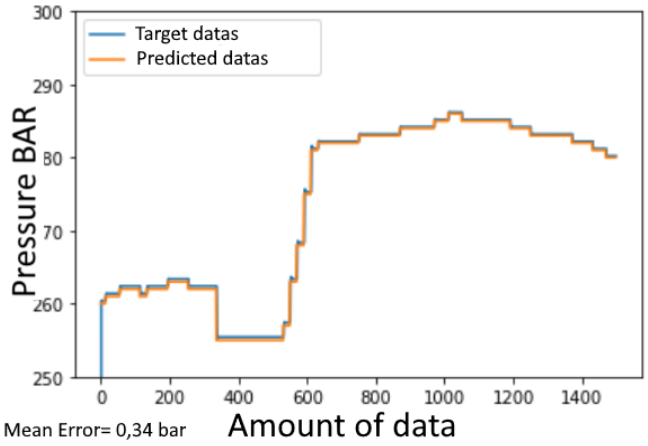

Figure 6: Comparison of predicted and actual data.

In Figure 6, there is a graphical representation of the test part of the input data set. The vertical column of the graph in Figure 6 shows the pressure created by the load in the cylinder, and the horizontal column shows the order of the values according to time. The mean error was 0.34bar.

There may be fluctuations of 4-5 bar in mobile cranes due to the flapping or shaking of the load. Error values between min 0.2 and max 5 bar were obtained when the estimation algorithm was run repeatedly. This shows us the range of the estimation. These different values are due to the random assignment of the reservoir neuron model and initial weights. Connection patterns within the Esn reservoir are still the subject of ongoing research.

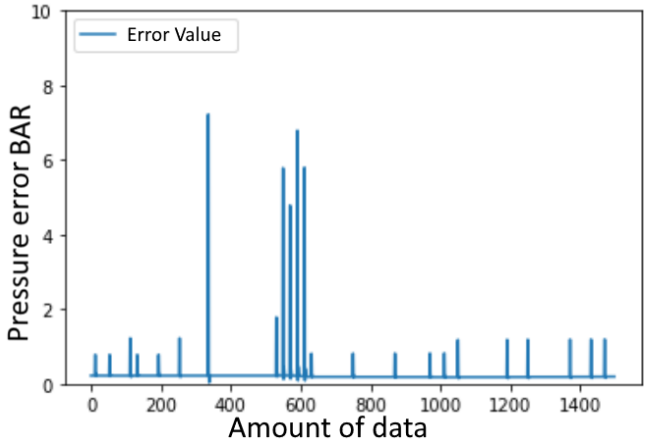

Figure 7: Time distribution of predicted pressure error.

The graph in Figure 7 shows the error values resulting from comparing the test data with the actual value. The vertical column shows the difference between the actual and the estimated pressure. The horizontal column shows the order of the values taken over time. When the graph is examined, major instantaneous errors can be seen. However, there is an average error of 0.34bar.

B. *ECU Temperature data set*

Figure 8 is seen as a graphed version of the 4-month temperature value of an electronic control unit, which is the second data set.

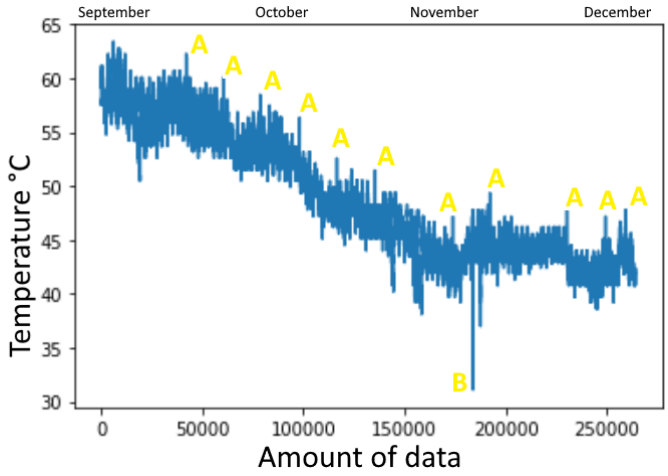

Figure 8: Four-month ECU temperature dataset.

The vertical column shows degrees Celsius, the horizontal column shows the order of data by time. It is seen that there are different values between 30°C and 65°C. At the same time,

it is seen that the seasonally based average temperature decreases towards December.

The instantaneous peaks where the yellow letter A is in the graph indicate the heating caused by the system's excessive effort to record the log. The rapid decrease in the part with the yellow letter B is due to the reset of the system.

In Figure 9, the values predicted by the model are drawn in orange on the test data. The vertical column shows the temperature value, the horizontal column shows the order of the data against time.

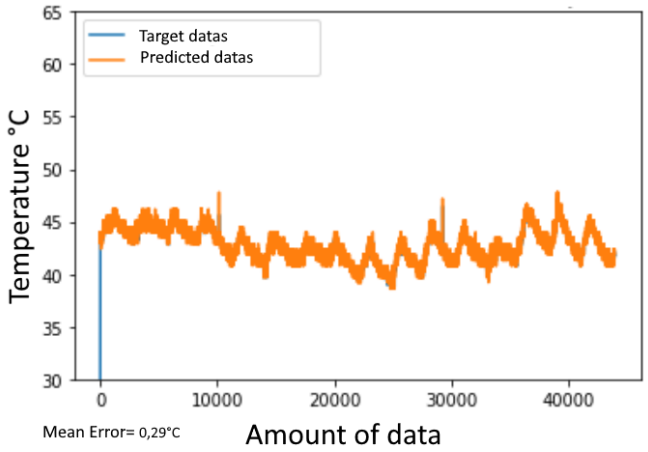

Figure 9: Tahmin edilen ile gerçekleşen verinin karşılaştırılması.

Figure 10 shows the graphic form of the error values. The vertical column shows the estimated temperature difference with the actual value, the horizontal column shows the order of the data by time. The average error is 0.29°C. Thus, 5°C error is seen at two points.

Figure 10: Time distribution of predicted temperature error

V. Conclusion

The calculated and analyzed values in mobile crane designs are confirmed by design verification. In design verification, trials are carried out on many different loads. In particular, the values above or near the capacity also brought the risk of test accidents. In this study, it has been shown that by taking the value of five different loads in the field, a comparison can be made by estimating without taking the sixth load. In this case study, values below capacitance are taken to demonstrate accuracy. Thanks to this estimation, time can be saved in the design validation process. Accident risks are reduced.

The second temperature data set shows an example of the time loss problem in using the data taken from the field as a design parameter. In the four-month (120-day) data set, the last 24 days of temperature data are estimated. Therefore, with this estimation, a 24-day time gain has been achieved. Considering the data set ten times larger than this data set will provide a time advantage of about 1 year.

In summary, learning is very fast as the Echo state model adapts quickly to changes. As a result, it gives outstanding results in the estimation of time-dependent data. Making these results with a bit of processing power is one of the important features of this model.

Neuron models suitable for separate interrelated but time-dependent data structures are new topics for researchers. Therefore, it is recommended that new researchers investigate the system performances that occur in the combination of the Esn model with different neuron models.

References

[1] Kudithipudi, D., Saleh, Q., Merkel, C., Thesing, J., & Wysocki, B. (2016). Design and analysis of a neuromemristive reservoir computing architecture for biosignal processing. Frontiers in neuroscience, 9, 502.

[2] Naima Chouikhi, Boudour Ammar, Amir Hussain, Adel M. Alimi, Bi-level multi-objective evolution of a Multi-Layered Echo-State Network Autoencoder for data representations,Neurocomputing,.

[3] J. Dai, G. K. Venayagamoorthy and R. G. Harley, "An Introduction to the Echo State Network and its Applications in Power System," 2009 15th International Conference on Intelligent System Applications to Power Systems, Curitiba, 2009, pp. 1-7, doi: 10.1109/ISAP.2009.5352913.J. Williams, “Narrow-band analyzer (Thesis or Dissertation style),” Ph.D. dissertation, Dept. Elect. Eng., Harvard Univ., Cambridge, MA, 1993.

[4] Claudio Gallicchio, Alessio Micheli, Deep Reservoir Neural Networks for Trees, Information Sciences, Volume 480, 2019, Pages 174-193, ISSN 0020-0255,

[5] Lyudmila Grigoryeva, Juan-Pablo Ortega, Echo state networks are universal, Neural Networks, Volume 108, 2018, Pages 495-508, ISSN 0893-6080,

[6] Jiang F., Berry H., Schoenauer M. (2008) Supervised and Evolutionary Learning of Echo State Networks. In: Rudolph G., Jansen T., Beume N., Lucas S., Poloni C. (eds) Parallel Problem Solving from Nature – PPSN X. PPSN 2008. Lecture Notes in Computer Science, vol 5199. Springer, Berlin, Heidelberg. https://doi.org/10.1007/978-3-540-87700-4_22

[7] Bozhkov, L., Koprinkova-Hristova, P., & Georgieva, P. (2016). Learning to decode human emotions with Echo State Networks. Neural Networks, 78, 112-119.

[8] Hart, A. G., Hook, J. L., & Dawes, J. H. (2021). Echo state networks trained by Tikhonov least squares are l2 (μ) approximators of ergodic dynamical systems. Physica D: Nonlinear Phenomena, 421, 132882.

[9] Liang, Y., Gao, Z., Gao, J., Wang, R., & Zhao, H. (2018). Data fusion combined with echo state network for multivariate time series prediction in complex electromechanical system. Computational and Applied Mathematics, 37(5), 5920-5934.

[10] Park, J., Lee, B., Awan, A. U., & Kim, H. J. (2013). Application of echo-state networks to the position control of shape-memory alloys. IFAC Proceedings Volumes, 46(11), 712-717.

Implementation of 802.11s Mesh Network Attacks on an 802.11ac Based Wireless Testbed Environment

O.YUKSEL[1] and M. ALANYALI[2]

[1]TOBB University of Economics and Technology, Ankara/Turkey, ozanyuksel@etu.edu.tr
[2]TOBB University of Economics and Technology, Ankara/Turkey, malanyali@etu.edu.tr

***Abstract* – Today, IEEE 802.11 wireless network technology has reached the point where it can provide a considerable amount of wide bandwidth at the physical layer. It has a wide range of usage to cover personal, industrial and military applications. At this level reached in wireless technologies has also made other 802.11 standards become more usable and popular. IEEE 802.11s Wireless Mesh Networking, one of those standards, has stood out with the flexibility and scalability that brings to wireless networks. 802.11s presents ease of use and deployment, distributed wireless network architecture, dynamic and intelligent routing ability which is essential to sustainability of Wireless Mesh Networks (WMN) via using Hybrid Wireless Mesh Protocols (HWMP) and Mesh Peering Management (MPM). Based on these concepts, this paper presents an implementation of Mesh Authentication, Path Diversion, Blackhole attacks on 802.11s wireless mesh networks and reports results obtained on an 802.11ac based wireless testbed.**

***Keywords* – 802.11s, 802.11ac, HWMP, wireless security, wireless attacks, wireless mesh networks, campus networks**

I. INTRODUCTION

Wi-Fi technologies provide users reliable, consistent, and secure experience they have come to expect in daily, industrial and military applications, and represent more than USD3 trillion in global market share[1] while carrying more than half of all internet traffic through thirteen billion devices[2].

With recent amendments such as 802.11ac, Wi-Fi physical layer bandwidth has pushed beyond 7 Gbps[3]. Along with the complementary mesh networking standard IEEE 802.11s, these data rates make Wi-Fi a viable alternative for more demanding applications that involve network architectures beyond the conventional Basic Set Service (BSS) architecture that is constructed on an Access Point (AP) and Stations (STAs) connected to it.

IEEE 802.11s standard involves layer-2 specification of a flexible and scalable architecture for multihop wireless mesh networks (WMNs) that are dynamically self-organized, self-configured and capable of automatically establishing and maintaining mesh connectivity without human intervention. These features entail important advantages such as low up-front cost, easy network maintenance, robustness, and reliable service coverage[4]; thereby significantly leveraging link layer capabilities of Wi-Fi.

While WMNs has many advantages, they are also prone to cyber attacks, especially those that manipulate the broadcast nature of radio communications. It is plausible to expect that the potential damage caused by such attacks will increase significantly with the capabilities and proliferation of WMNs. There are many comprehensive studies on 802.11 in the literature such as [5,6]. Along with the theoretical infrastructure of these studies, there are also studies supported by many open source tools and software for training and testing purposes[7]. However, as a result of the compilation of studies, there were no noticeable attack studies covering the concept of 802.11s. For this reason, the purpose of this article is to contribute by analyzing researches on these deficiencies in the literature. The attacks are constructed by doing research on the basic principles of Mesh Discovery, Mesh Peering and HWMP.

The rest of this paper is structured as follows: Section II summarizes main features of 802.11ac, 802.11s, 802.11s-based WMN and HWMP protocols. Section III describes the testbed and the experimental setup of this study. A detailed description of the attack types and their implementation methods considered here is given in section IV. The paper concludes with main observations and final remarks in the conclusion section.

II. BACKGROUND

This section presents a brief explanation of the IEEE 802.11ac, IEEE 802.11s, 802.11s-based WMN and HWMP Routing Procotol. The advantages and use cases of implementing IEEE802.11s-based WMN are summarized.

A. IEEE 802.11ac

802.11 WLAN (Wireless Local Area Network) standards developed by IEEE, are mainly used for local wireless communications in the 2.4 and 5 GHz unlicensed frequency bands. IEEE 802.11ac is an emerging very high throughput (VHT) WLAN standard that could achieve phy data rates theoretically reach almost 7 Gbps for the 5 GHz band[3]. Behind the data rates achieved, there are following important key features of 802.11ac standard.

RF channel bandwidths

One of the significant improvements in 802.11ac is using a wider RF channel bandwidth. Wider channels bring higher throughput in proportion to their width. The 40 MHz channels of 802.11n which is predecessor of 802.11ac is extended to 80

MHz and 160 MHz in 802.11ac standard. 80 MHz channels are two adjacent 40 MHz channels but with subchannels in the middle filled in. 160-MHz channels are defined as two 80-MHz channels[8].

Spatial streams

Spatial streaming is a Multiple Input Multiple Output (MIMO) technique that is used to transmit independent streams to single or multiple receivers simultaneously. By the help of this principle, throughput can be folded respectively quantity of spatial streams such as 2x2, 3x3, 4x4. Four spatial streams defined in the 802.11n standard, reach up to eight spatial streams in 802.11ac standard[3,8]. Today 802.11ac products support up to four spatial streams. A divergence between chips and equipment for APs and clients will occur due to cost, physical size and power constraints. APs will grow by adding antennas, while clients will become more capable by implementing multiple spatial streams and beamforming features behind a smaller number of antennas. This divergence will create opportunities for multi-user MIMO, where a high-capacity AP can communicate with multiple, lower-throughput clients simultaneously.

Multi-user MIMO (MU-MIMO)

With 802.11n, a device can transmit multiple spatial streams at once, but only directed to a single address or broadcast. For individually addressed frames, this means that only a single device (or user) gets data at a time. We call this Single-User MIMO (SU-MIMO). With the advent of 802.11ac, a new technology is defined, called multiuser MIMO (MU-MIMO). A new feature allows an AP to transmit different streams to several targeted clients simultaneously and AP is able to use its antenna resources to transmit multiple frames to different clients, all at the same time and over the same frequency spectrum[8].

Modulation and coding

With last amendment of 802.11ac standard and new technologies on designing semiconductor radios which aims to increase more accurate and more powerful digital processing continues to exploit the limits of modulation and coding techniques. By the leaping from 64 quadrature amplitude modulation (QAM) to 256-QAM, 3/4 and 5/6 code rates are added as optional modes which correspond modulation and coding scheme (MCS) 8 and 9. For the basic case of one spatial stream in a 20 MHz channel, this extends the previous highest rate of 802.11n from 65 Mbps (long guard interval) to 78 Mbps and 86.7 Mbps respectively, a 20% and 33% improvement [8].

802.11ac Frame Format

802.11ac frame format is shown as figure below.

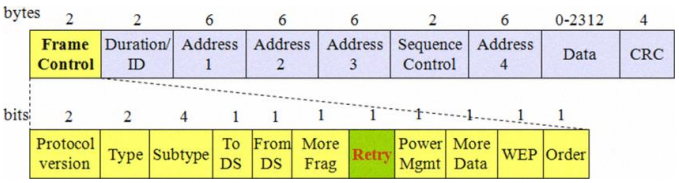

Figure 1: 802.11ac Frame Format

As seen in the figure, with the help of ToDS and FromDs fields which are in 802.11ac frame, four address frame structure can be provided for connection and data transfer between WLAN clients and APs.

B. IEEE 802.11s and 802.11s Based WMN

802.11s

With the development of wireless technologies at the physical layer, especially 802.11ac, it has become very popular to use wireless technologies to cover the areas such as general public, a campus, outdoor industrial or military where cable connections are not possible or efficient. At this point, those situations bring the 802.11 working group together and they defined the concept of a Wireless Distribution System as a mechanism for wireless communication. IEEE 802.11s, Wireless Mesh Networking, become prominent to has rapid deployment with lower-cost backhaul, self-healing, self-forming, resilient and expandable features[4].

802.11s Frame Format

802.11s frame format is shown as figure below.

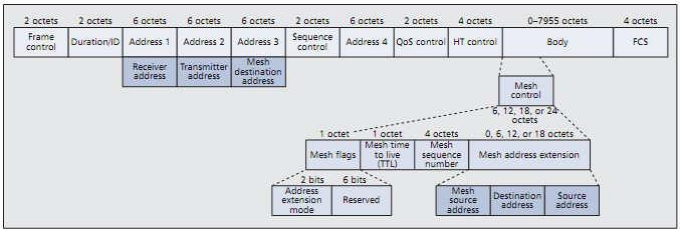

Figure 2: 802.11s Frame Format

There are slight differences between the 802.11s and 802.11ac frame types. Six address frame formats are useful in payload with the help of two additional address fields and based on this concept the hopping mechanism is provided.

802.11s Based Wireless Mesh Networking

802.11s Based WMN is a Distributed System(DS) created using the 802.11s protocol between MPs. Additional to conservative BSS architecture which is basically a network topology that allows all wireless devices to communicate with each other through a common medium, MBSS is defined to connect BSS via DS. The mesh facility is simply the set of features, functions, and frame formats that enable mesh operation[9].

In order to create MBSS, firstly, all mesh points have to discover each other. The most important feature for the execution of discovery phase is the "*Mesh ID*" which is identifier of all mesh points. Mesh stations participating in an MBSS send beacons and answer to probe requests with probe responses via using their own IDs. After the discovery process,

MPs move on to the next phase which is Mesh Peering Management (MPM) [10]. After the completion of the Mesh Peering Management phase, the details of which will be given in section IV, MPs create a MBSS to which they are connected each other.

Devices use MBSS structure to interconnect BSSs. They can also provide the gateway service required for switching to the wired network. In figure below, general MBSS architecture is shown.

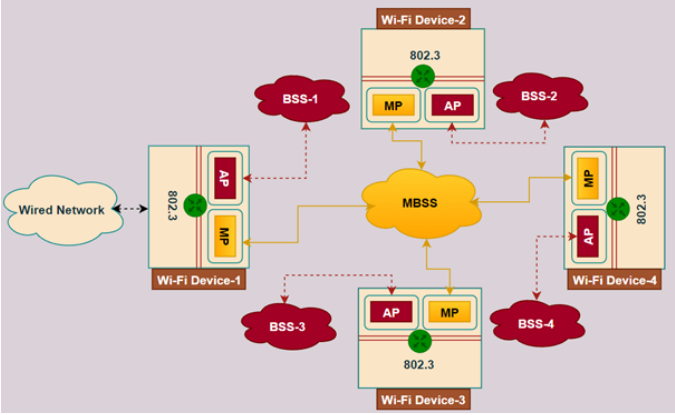

Figure 3: An example of MBSS Architecture

It can also be used as a range extender as it is known from daily life, as another derivative of connecting BSSs to each other. The following figure shows stations out of range of a BSS.

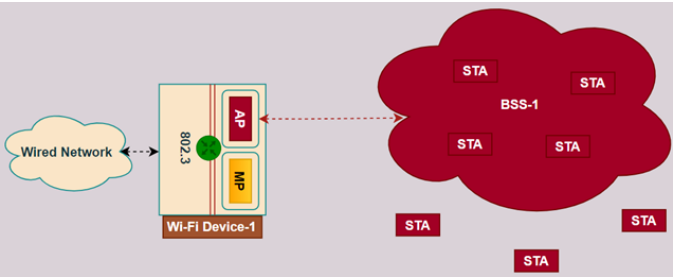

Figure 4: An example of BSS Architecture includes STAs out of coverage

By positioning the Mesh Points to places outside the coverage area, range extender can be done.

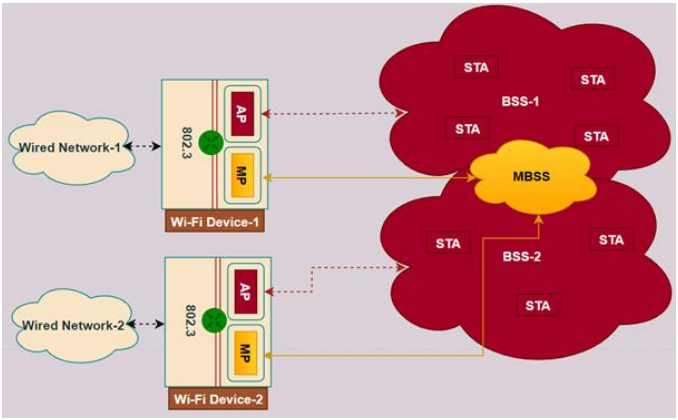

Figure 5: An Example of MBSS Architecture MPs used for Range Extender

C. Hybrid Wireless Mesh Protocol

Although there are vendor specific methods can be used in 802.11s, Hybrid Wireless Mesh Protocol (HWMP) must be supported as default routing protocol. HWMP provides both proactive path selection and reactive path selection. Reactive path selection is based on Ad Hoc On-Demand (AODV), proactive is based on Tree-Based Routing. A mesh station that needs to transmit a frame to an unknown destination can dynamically discover the shortest path to this destination. Mesh stations can also proactively discover the MBSS and determine shortest paths to any point of the mesh network before needing to send any data frame.

HWMP Frame Format

There are four types HWMP frames including Path Request (PREQ), Path Reply (PREP), Path Error (PERR), and Root Announcement (RANN). The definitions of these frames are shown below [11].

PREQ: It can be a unicast or broadcast packet that asks destination Mesh Points to form a reverse route to the originator.

PREP: It is a unicast packet that forms a forward route to the originator and confirms the reverse route.

PERR: It is a broadcast packet that tells receiving Mesh Points that originator no longer supports certain routers.

RANN: It is a broadcast packet that tells Mesh Points about presence and distance of Root MP. [12]

802.11s frame format is shown as figure below.

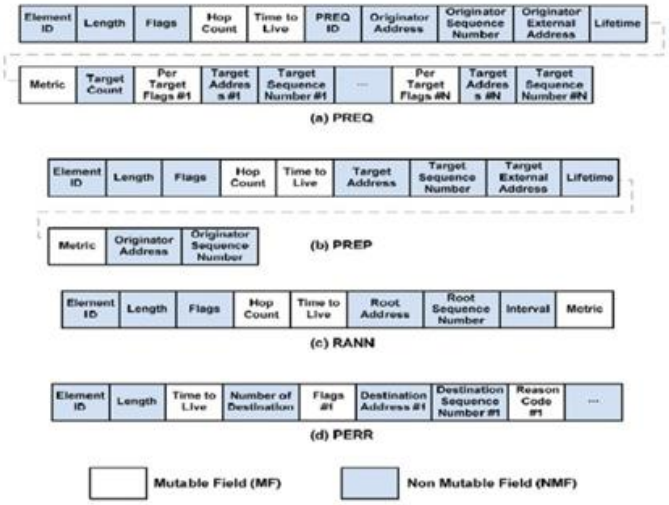

Figure 6: HWMP Frame Format

III. TESTBED ENVIRONMENT

In this section, all the components that make up the infrastructure of the testbed environment will be explained in order to be able to make the attacks and set up the topologies intended by the paper.

A. Wi-Fi Hardware

The device used in this study as a Wi-Fi hardware, is a custom made design. WMN topologies that is created for attack surface established by using this Wi-Fi hardwares. Wi-Fi Devices support to 802.11ac phy and capable to provide service both AP and MP modes. Key notes for this device explained following;

- Atheros QCA9880 chipset based Radio Module
- Compatible for 802.11b/g/n/ac
- Supports 5GHz, 3x3 MIMO OFDM Technology, up to 1300Mbps physical data rate
- Supports 802.11s

Wi-Fi device has two Wi-Fi Radio module; first module is set as AP, other module set as MP. Wi-Fi Radio modules connect to mainboard via PCI-e interface and all Wi-Fi activities are controlled by Linux Operating System via using Ath10k Linux Wi-Fi driver. In addition, it is possible to connect to this operating system from the debug interface. The basic embedded architecture of Wi-Fi Device mentioned before explained in the Figure 7 below.

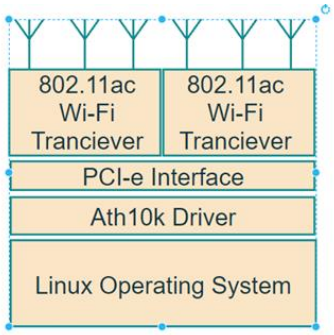

Figure 7: The Basic Architecture of Wi-Fi Device

B. USB Wi-Fi Adapter

In the study, to sniffing and injecting packets into the respective network, commercial off the shelf USB Wi-Fi Adapter product is used. This product is ALFA AWUS036ACH. Reason for choosing this USB Wi-Fi Adapter is that it is highly capable to packet injection and packet monitoring. In the addition that, this hardware supports 802.11ac standard which is operating spectrum of wireless testbed environment. It is connected to the computer via the USB port and the attack scripts prepared to be sent to the network will be sent through this USB Wi-Fi Adapter.

C. Attacker PC

The PC described as the attacker is the device that contains attack scripts to manipulate the network. Further, USB Wi-Fi Adapter connection is made to this device and attack scripts are sent using this hardware. Kali Linux[13] is one of the most recommended and suitable operating systems for packet injection and monitoring. Therefore, it is preferred that the Attacker PC runs on 20.04 release version Kali Linux. While it provides easy to use the monitoring mode option, it is compatible with variety of open source driver that removes the restrictions on hardware of USB Wi-Fi adapter.

D. RF Attenuators

RF Attenuators are components that reduce the amplitude level of an incoming signal. The main using goal is to protect systems from receiving a signal with a power level that is too high to process.

RF attenuators can have variable attenuation level such as 10 dB, 20 dB. It can be created wireless network topology that we can control and adjust every RF link between Wi-Fi Radios by using this different step size attenuators. In this manner, it can be simulated real word topologies in testbed; creating mesh topologies that it is desired path and metric combinations.

E. RF Cables

RF cables are a type of coaxial cable that is used to send radio frequency signals. It can be plugged to RF ports of Wi-Fi Devices and combined with RF attenuators. In this study, these are used for connects Wi-Fi radios each other that have variety of RF links for provide connectivity.

F. Experimental Setup

With the help of components that is explained previous sections, variety of wireless network topology can be established in simulation environment in 802.11ac based wireless testbed. Wi-Fi Radio modules of Wi-Fi Device can be set as AP and MP mode. Module set as AP, provide connectivity their STAs called BSS. This is a service that we often use in daily life. On the other hand, module set as MP, provide connectivity to other Wi-Fi devices. This connection is compatible with the 802.11s standard and the structure formed in this network is expressed as MBSS. Wi-Fi Devices in MBSS are capable of many forwarding and hopping abilities. They provide the basis of forwarding and hopping mechanisms with the HWMP protocol described in the previous section. MAC addresses are used to make these decisions, and each device has a unique factory default MAC address. In addition, IP assignment can be made to each wireless interface of the devices via the operating system. The frequency assignment that the radio modules will operate can also be adjusted via the operating system (in this study channel 149 (5745 MHz) is selected). Since studies will be conducted on the MBSS network created with 802.11s, the topologies described are limited in this direction. Under favor of RF attenuators and RF cables, different topologies which includes direct and undirect connections can be created. Under normal conditions, devices are used with antennas as expected. In the laboratory environment, RF components are used in order to precise arrangement the signal strength of wireless links and to easily prepare the desired topologies. Otherwise, in order to use these topologies and conduct controlled experiments, it is necessary to keep a great deal of distance between devices, and the ability to conduct controlled experiments will decrease as much. The figure below shows the most inclusive topology set up in the testbed environment, which will be used in most of our work.

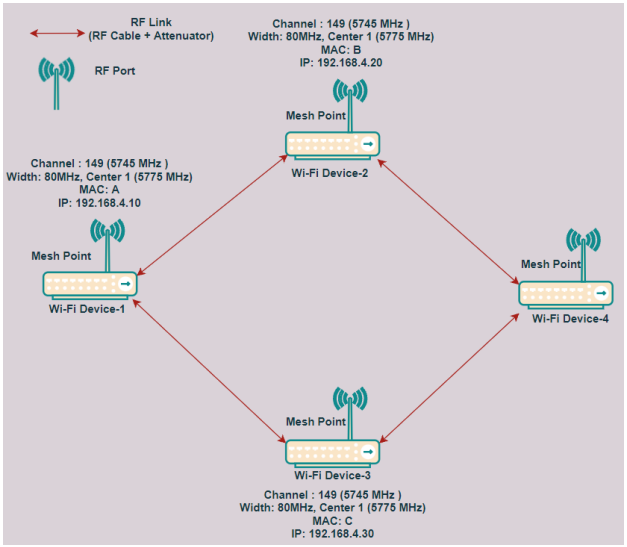

Figure 8: An Example Of Topology Created In Testbed

The attacker PC and the USB Wi-Fi adapter connected to it, which creates the attacks by monitoring and injecting packets, can be located anywhere in the network and attack any Wi-Fi device.

Related to this explanation, in addition to Figure 11, the established topology is shown below.

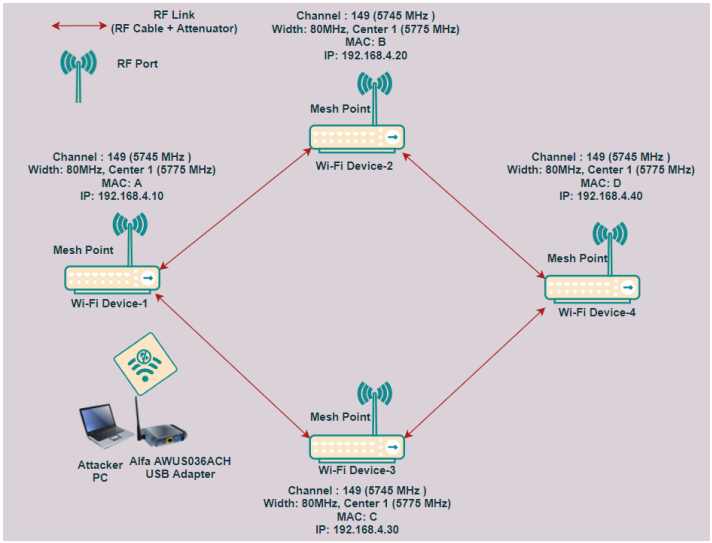

Figure 9: An Example of Topology Created In Testbed With Attacker

IV. Attack Definitions and Implementations

In this section, attack definitions and implementation methods that form the basis of the study are explained in detail. Attack scripts are implemented in the Python programming language. In order to operations of packet management and analysis, Pyshark[1] library which is Python wrapper for Tshark[2], allowing Python packet parsing using Wireshark[3] dissectors is used.

[1] https://github.com/KimiNewt/pyshark/
[2] https://www.wireshark.org/docs/man-pages/tshark.html
[3] https://www.wireshark.org/

Another important library is Scapy[4], which is used to simulate and inject packets into the target network.

Along with previous information, this section discusses three types of attacks related to the 802.11s standard.

A. Mesh Authentication Attacks

In this part, it is aimed to establish a fake authentication with any Mesh Point of Wi-Fi Device without any extra privileges. Before the attack implementation, working principles of Mesh Peering Management are explained.

There are three packet types in MPM. These packet types are described below.

Mesh Peering Open: It is a unicast packet that is used for to offer a peering request to discovered Mesh Point.

Mesh Peering Confirm: It is a unicast packet that is used for to accept peering request from initiator Mesh Point.

Mesh Peering Close: It is a unicast packet that is used for to terminate mesh peering sequence for some reason.

The flowchart of an ideal scenario related Mesh Peering Management sequence between two MPs is shown in the figure below.

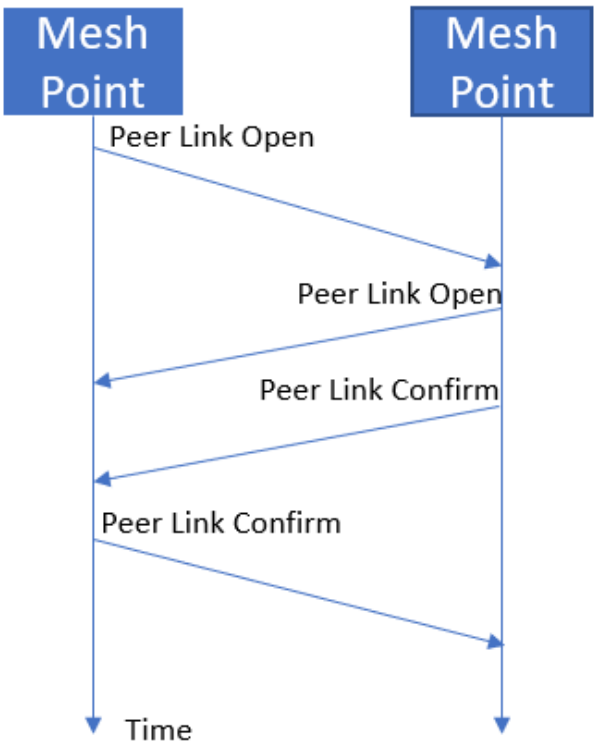

Figure 10: An Example Of MPM Flow

With the detailing of Figure 13, the step-by-step processes are explained as follows.

The MPM sequence starts when any mesh point triggers the process. The MP that initiates the process sends frame which type is "action" and action code “Mesh Peering Open”. Frame also includes "*Source MAC Address*" (address of initiator), "*Destination MAC Address*" (address of promoter MP) and "*Local Link ID*" (id of initiator MP) in the IEEE 802.11 Wireless Management header. Later on, promoter MP response this frame with same action type which is “*Mesh Peering Open*”. This packet also includes “*Source MAC Adress*” (address of promoter MP), “*Destination MAC*” (address of initiator MP) and “*Local Link ID*” (id of promoter MP). After that, promoter MP sends Mesh Peering Confirm frame to initiator MP and put own id into this frame as a “*Local Link ID*” and initiator MP id as a “*Peer Link ID*”. In final step, initiator MP also sends Mesh Peering Confirm frame to promoter MP with putting own id as a “Local Link ID” and promoter MP id as a “Peer Link ID” for finishing MPM sequence.

The topology set up in the testbed environment to analyze this process is shown in the figure below.

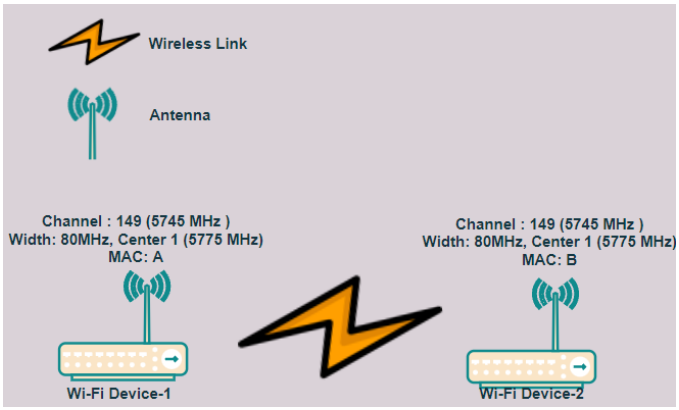

Figure 11: An Example of Topology Created In Testbed For Analyzing MPM Sequence

The Wi-Fi adapter connected to PC is set to monitor mode for sniffing related MPM sequence. Corresponding frames captured by Wireshark. All outputs of the process are shown in the figures below respectively.

[4] https://scapy.net/

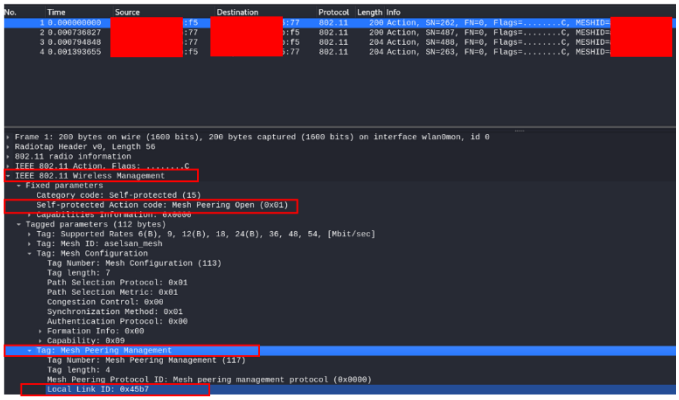

Figure 12: First Mesh Peering Open Frame from Initiator MP

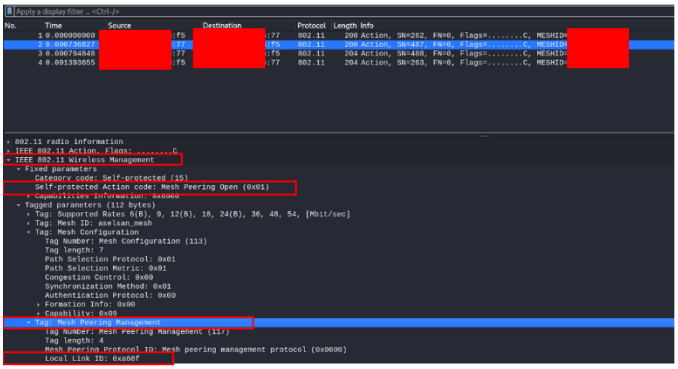

Figure 13: Response Mesh Peering Open Frame Response From Promoter MP

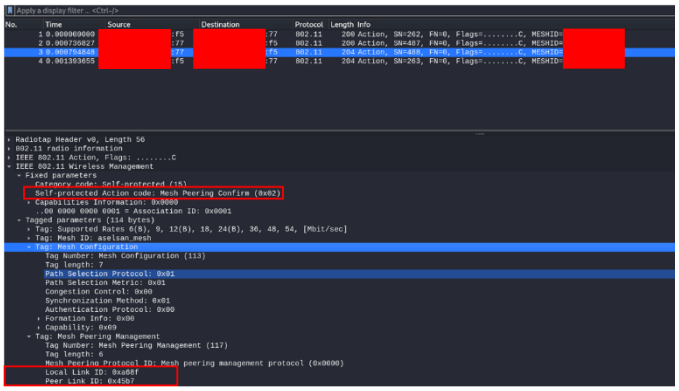

Figure 14: First Mesh Peering Confirm Frame From Promoter MP

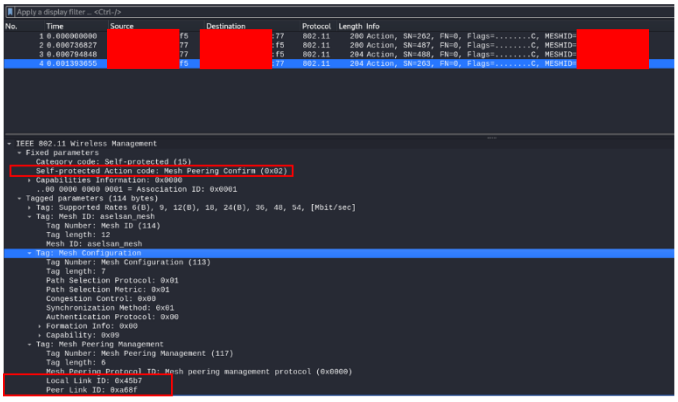

Figure 15: Mesh Peering Confirm Frame Response From Initiator

After this sequence, any MPs can be authenticated with each other. For the checking of this peering process, debug interface of the operating system in which the devices are running is used. With the help of "*iw ~mesh~ station dump*" command, information of stations that are connected each other can be dumped.

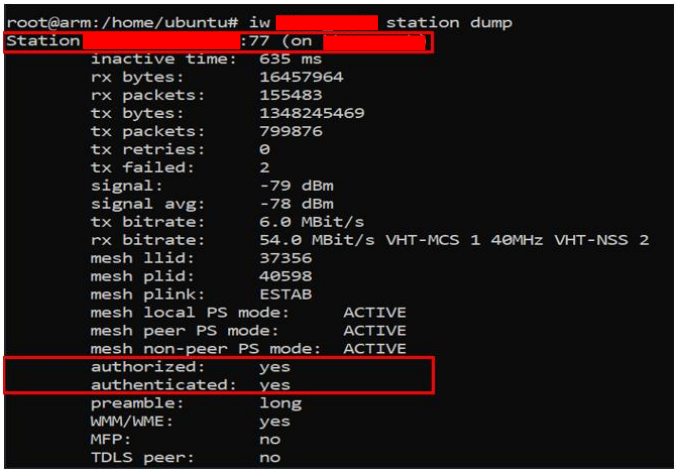

Figure 16: Output of "iw *mesh* station dump" command from Initiator MP

After this stage, the topology shown in the figure below is created in the testbed environment in order to attack on the relevant sequence.

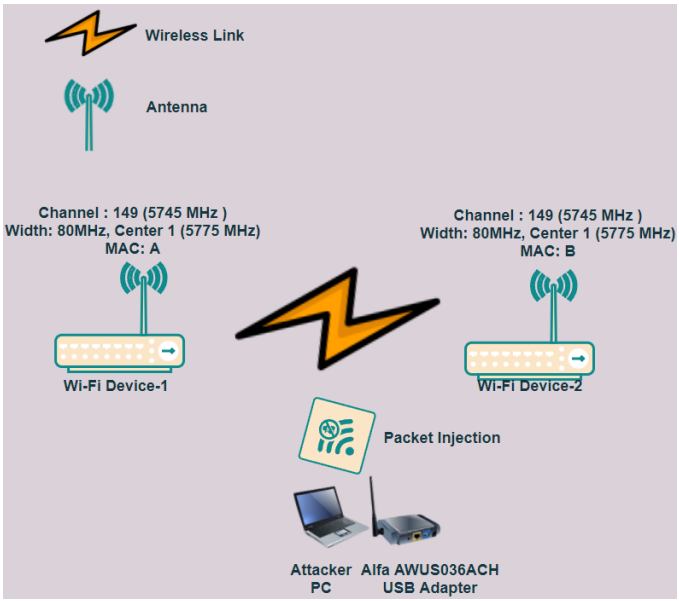

Figure 17: An Example of Topology Created In Testbed For Manipulation MPM Sequence With Attacker

Fundamental principle of behind of this attack is to impersonate this session in proper way. First of all, it is necessary to tune on the correct frequency band to analyze the packets which flow between Wi-Fi devices placed in the test environment. In order to detect to the RF activities in the network, the frequency band within the scope of 802.11ac is scanned with the USB Wi-Fi adapter. After detection, USB Wi-Fi Adapter tunes in the frequency band where network activity is detected. After the

tuning step, sniffing and capturing processes are started. After detailed sniffing process, all MAC addresses of MPs are found. As has just been explained, as a result of these sniffing, attacking processes are started according to the details of the MPM sequence.

In order to the designed attack scripts running on attacker PC sends the Mesh Peering Open frame with its own Local Link ID(it is generated randomly) to the MP under attack in a way that impersonates MPM sequence and for the start of sequence. The device under attack responds normally to this appropriate packet in order to continue the MPM sequence. In the last stage, the adapter that correctly extracts local id of MP under attack. and sends the peer link id in the incoming response finishes the process. One of the most important points here is to extract the response very quickly during the listening process and send the right packet. For this reason, the designed attacks can perform these operations with the help of the parallel processing. These processes must be finished as fast as possible due to manufacturer-dependent timeout (~1 sec). Otherwise, the process will be terminated by an MP along with the mesh peering close frame. After the successful attack process, the adapter is able to authenticate to the MP.

All Wireshark output are shown as Figure 21 below.

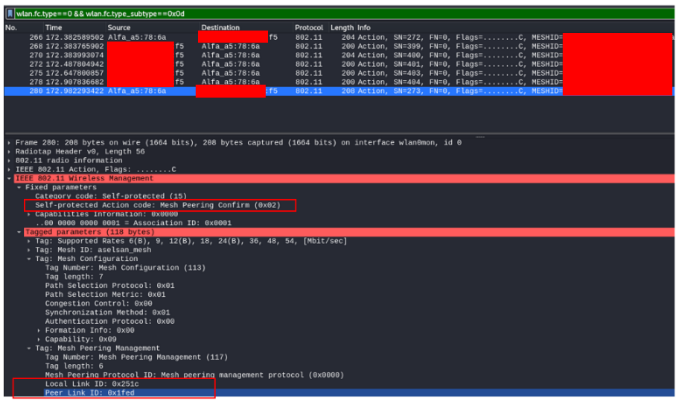

Figure 18: MPM Sequence Between Wi-Fi Device And Attacker

For the checking whether the attack is successful, so that, whether the adapter successfully authenticate with the MP, *"iw mesh station dump*" command can be executed again.

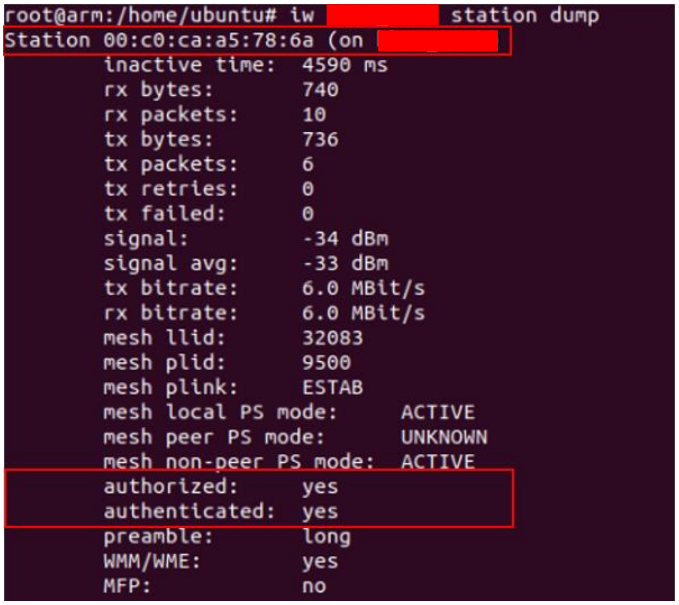

Figure 19: Output of "iw *mesh* station dump" command from Initiator MP (The adapter has been successfully authenticated.)

B. Path Diversion Attack

This attack is based on manipulation of PREQ packets by the attacker[11]. In order to the Wi-Fi Device process PREQ packets, the sequence number of those packets must be up to date from other packets on the network. Thus, the attacker increases the sequence number of the PREQ packet, allowing the Wi-Fi device to process these packets. It also sends packets to the network by changing the metric information of these packets, for which it changes the sequence number. Thus, the routing table of the Wi-Fi device can be differentiated at the desired path for the target device.

In 802.11ac based wireless testbed, the topology given below is created by using Wi-Fi devices. With the help of the attenuators, the topology is established so that the "*PATH-1*" is the shortest path. In order for *PATH-1* to be selected the shortest path, RF attenuators which have more attenuation capability are used in *PATH-2*. (10 dB attenuation for in every link of *PATH-1*, 30 dB for every link of *PATH-2*)

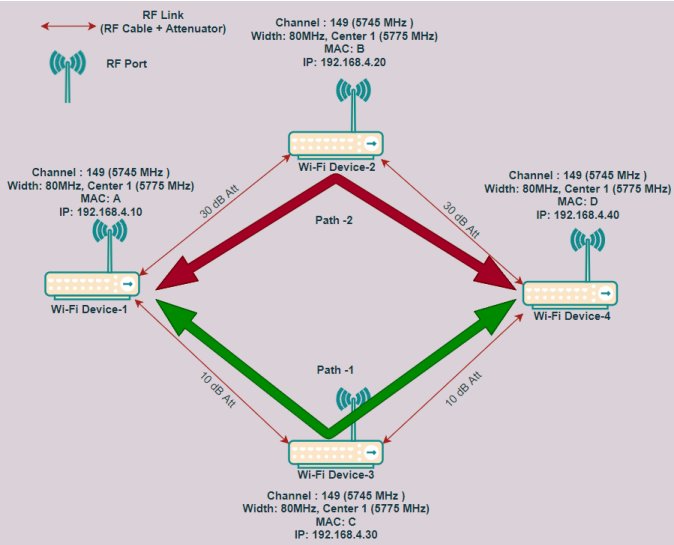

Figure 20: An Example of Topology Created In Testbed For Analyzing Path Selection and Packet Forwarding

As expected, when the data flow from Wi-Fi Device-1 to Wi-Fi Device-4 which do not have a direct connection between each other, "*Path-1*" is selected as a shortest path. Which path the devices choose is controlled by the debug interface that we access through the operation system. As mentioned before, the shortest path selection in this topology is made by HWMP, which is the default protocol of 802.11s. With the help of PREP, PREQ, RREP frames spread to the environment in the mesh network, the forwarding table of each device is created in an optimized way.

In this attack, it is aimed to manipulate forwarding table of Mesh Point that is under attack by creating fake metric by attacker. Scripts running on Attacker PC and sending via USB Wi-Fi adapter. The topology established for this in the testbed environment is shown below.

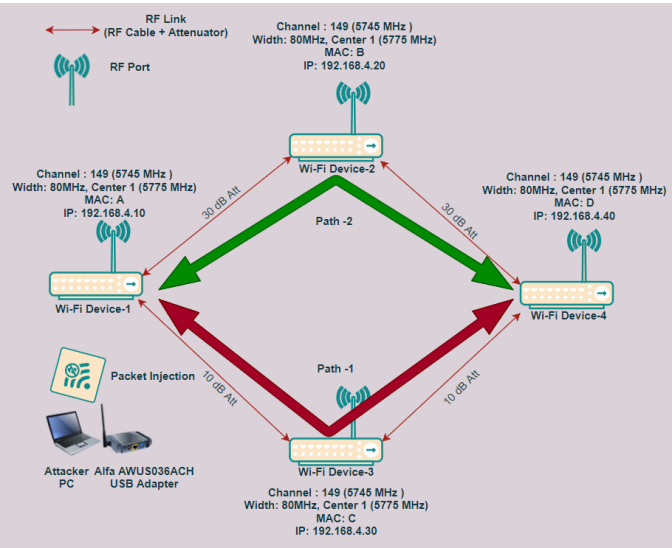

Figure 21: An Example of Topology Created In Testbed For Manipulating Path Selection and Packet Forwarding

As in the first section, first of all, the frequency where there is mobility is determined and the relevant frequency is tuned by Wi-Fi Adapter. HWMP packets transmitted periodically during communication are sniffed and captured. The recorded frames are standard HWMP frames and the fields in them can be changed as desired. HWMP frames are manipulated via attack scripts. The content of this manipulation shows the MAC address of the non-shortest route as the shortest path address to the attacked device. Thus, Wi-Fi Device-3 is said to be the shortest path to go from Wi-Fi Device-1 to Wi-Fi Device-4. Wi-Fi Device-1 continues to choose PATH-2 as it processes these fake packets sent by the adapter.

At the end of steps that is explained just before, "*Path 2*", which is not the shortest path, is chosen by the devices to the desired extent. In this manner, the desired path diversion can be made successfully by sending the attack codes prepared by us to the network via the adapter.

C. Blackhole Attack

This attack also is based on manipulation of PREQ packets by the attacker [11, 14]. The most important step to take before starting this attack will be for the attacker who will create a blackhole to establish a relationship with the relevant MP using the attack described in the first part. This attack is formed by the principle that the attacker, who is included in the network outside the desired network topology, takes and terminates the traffic on itself.

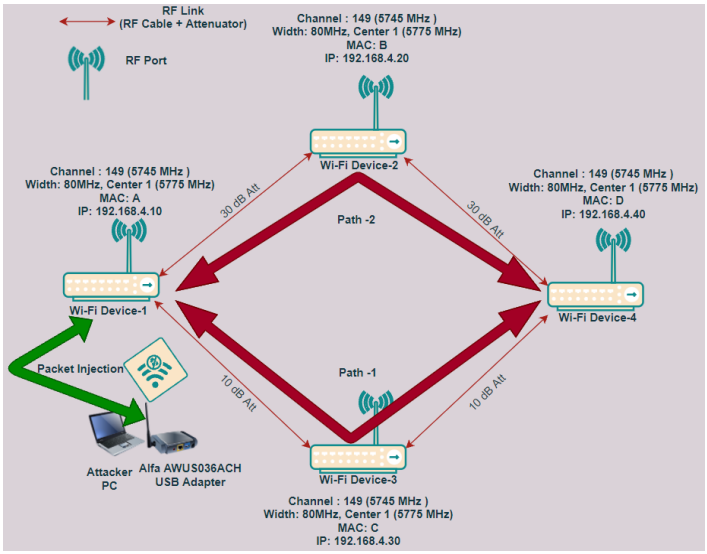

Figure 22: An Example of Topology Created In Testbed For Execution of Blackhole Attack

In the nature of Wi-Fi device architectures, in order to process HWMP packets, related MAC addresses (this part, it is an attacker MAC address) have to be authenticated to Wi-Fi Device under attack. Therefore, section IV-A attack process must be executed before starting Blackhole Attack.

As seen in the figure, fake PREP messages are sent to the node where the traffic is initiated via USB Wi-Fi Adapter. These messages contain the fake information and metrics that the first

hopping route to any destination in the network is from itself and it has the shortest path. That being so, as the device processes these messages, it always tends to forward packets to the attacker, and network traffic becomes inoperable while the attack continues.

V. CONCLUSION

This study collects, describes and survey some of the most common attacks in the IEEE 802.11s standard and explains the working principles behind them. It demonstrates how the attack scripts designed for methods are developed and applied to WMNs and shows how to manipulate WMNs using the basic principles of MPM and HWMP. Thus, it is aimed to contribute to field of 802.11 attacks, which is maturing technical area in the literature. In the light of all information related this paper, a security mechanism can be applied to protect from such attacks for future studies.

REFERENCES

[1] Wi-Fi Alliance 2020 Annual Report
[2] Cisco VNI, 2020
[3] Ong E. H.; Kneckt J.; Alanen O.; Chang Z.; Huovinen T.; Nihtila T, "IEEE 802.11ac: Enhancements for Very High Throughput WLANs", 2011 IEEE 22nd International Symposium on Personal, Indoor and Mobile Radio Communications.
[4] Akyildiz, F.I.; Wang, X.; Wang, W. Wireless mesh networks: A survey. Comput. Netw. ISDN Syst. 2005, 47, 445–487.802.11s
[5] C. Kolias, G. Kambourakis, A. Stavrou, and S. Gritzalis, ``Intrusion detection in 802.11 networks: Empirical evaluation of threats and a public dataset," *IEEE Commun. Surveys Tuts.*, vol. 18, no. 1, pp. 184_208, 1st Quart., 2016, doi: 10.1109/COMST.2015.2402161.
[6] Thing, L. L. V. "IEEE 802.11 Network Anomaly Detection and Attack Classification: A Deep Learning Approach"
[7] https://www.aircrack-ng.org/
[8] Gast S. M. "802.11ac A Survival Guide", O'REILLY
[9] E. Sisinni, F. Tramarin, "IEEE 802.11s performance assessment: From simulations to real-world experiments", Conference Paper · May 2017, DOI: 10.1109/I2MTC.2017.7969752
[10] R.C. Carrano, L. C. S. Magalhanes, C.M.Saade, C.V.N.Albaquerque IEEE 802.11s Multihop MAC: A Tutorial" , 2011
[11] W.K.Tan, S.G Lee, J.H. Lam and S.M.Yoo, "A Security Analysis of the 802.11s Wireless Mesh Network Routing Protocol and Its Secure Routing Protocols", 2013
[12] A.O. Lim, X. Wang, "IEEE 802.11s wireless mesh networks: Framework and challenges", Ad Hoc Networks, 2007
[13] https://www.kali.org/
[14] Yi, P.; Wu, Y.; Zou. F.; Liu, N. A survey on security in wireless mesh networks. IETE Tech. Rev. 2010, 27, 6–14.

Renewable Energy Guarantees of Origin System in Turkey: A preliminary assessment

A.SENTURK[1] and M.OZCAN[2]

[1] Kocaeli University, Kocaeli/Turkey, azrassenturk@gmail.com
[2]Kocaeli University, Kocaeli/Turkey, mustafa.ozcan@kocaeli.edu.tr

Abstract **- Renewable energy certificates (RECs) are market-based mechanisms that are awarded to certify the generation of 1 MWh of electricity from renewable energy sources (RESs-E). Participation in the RECs system is provided entirely on a voluntary basis and RECs support renewable energy generation. Turkey launched its national renewable energy certification system, the Renewable Energy Guarantees of Origin (YEK-G or RES-G), on June 01, 2021. In this study, the performance analysis of YEK-G has been carried out using determined performance indicators. The maximum YEK-G issuance was performed from hydro plants during the analysis period. There is no YEK-G issuance originating from solar plants. The lack of solar YEK-G issuance was caused by unlicensed power plants not being included in the YEK-G system. Despite the high amounts in the issuances, the redemption amounts for all plants were quite low. The most YEK-G redemption realized from geothermal plants. The overall consumption of electricity from renewable plants by using YEK-G reached 36,660 MWh at the end of the analysis period. During the analysis period; the quantities of matches in the organized YEK-G market and bilateral agreements in the over-the-counter YEK-G market increased. In order for the YEK-G system to succeed, unlicensed power plants must be included in the YEK-G system. The YEK-G system that has been established in line with the Association of Issuing Bodies' (AIB) standardized system of energy certification should be joined with AIB. Large-scale energy consumers should be obliged to consume RES-E in order to activate the YEK-G demand and ensure continuity.**

Keywords **- Renewable Energy, Renewable Energy Guarantees of Origin System (YEK-G), Renewable Energy Certificate, Organized YEK-G Market**

I. INTRODUCTION

Each one megawatt hour (MWh) of electricity from renewable energy sources (RESs) can be electronically documented and tracked with Energy Attribute Certificates (EACs). EAC is a certificate that provides information about the environmental attributes of one MWh of electricity. EACs allow that companies to report lower Scope 2 emissions while demonstrating demand for renewable energy generation. Companies can also use EACs to report lower Scope 1 emissions. Global EAC standards for renewable claims are Guarantees of Origin (GOs) in Europe, Renewable Energy Certificates (RECs) in North America, Renewable Energy Guarantees of Origin (REGOs) in the United Kingdom (UK), International RECs (I-RECs) and Tradable Instruments for Global Renewables (TIGRs) across the rest of the world [1].

Additionally, to the above mentioned EACs systems and registries, other national systems do exist, for example, Taiwan Renewable Energy Certificate (T-REC), China Green Energy Certificate (C-GEC), Japan's Green Power Certification System and Turkey's Renewable Energy Guarantees of Origin (YEK-G).

Due to the global climate crisis concerning the whole of our world, countries have started to take different measures within the framework of the United Nations Framework Convention on Climate Change (UNFCCC) and certain mechanisms have been developed for the parties to the UNFCCC to execute their obligations. Carbon markets exist under both mandatory and voluntary markets. Of these, the Emissions Trading systems and carbon tax are mandatory markets while carbon offsets and RECs are the mechanisms that constitute voluntary markets. Participation in voluntary carbon markets, is provided on a voluntary basis.

RECs are market-based mechanisms and represent that energy has been generated from RESs. RECs are issued for every MWh of electricity generated and delivered to the electric grid from RESs. RECs usually include the type of renewable plants producing the electricity, the vintage of the date when the RECs were created, the location of generation, and the RECs' eligibility for certification or renewable portfolio compliance [2].

RECs are a renewable energy product that companies can purchase to reduce the environmental impact of their business activities. A REC represents the environmental attributes—for example, avoided CO_2 emissions—that are created when electricity is generated using RESs instead of using fossil fuel sources. RECs can be sold separately from their associated electricity and thus enable customers to purchase the environmental attributes of renewable power generation independently of their retail power supply. Purchasing RECs, therefore, can be an effective means for a company to "green" the electricity it consumes. RECs provide many benefits to companies. They can help corporations reduce their Greenhouse gas (GHG) emissions, meet renewable energy targets, strengthen stakeholder relations, and differentiate products and brands [3].

GO are a type of EAC, which is an electronic document that guarantees that one MWh of electricity has been produced from a specified RES. GOs enable companies to credibly claim electricity from the consumption of RESs(RESs-E) and report lower Scope 2 emissions. Each GO is issued to that MWh with a special serial number. This serial number traces the GO from generation to issuance, transfer, then redemption, to provide a

robust system that meets unique demand criteria. The validity of a GO expires 12 months after issuance [4].

The I-REC system is managed by the International Renewable Energy Certificate Foundation. This internationally recognized certificate combines the best practices in European GO and North American REC systems to enable the registration of renewable energy produced and consumed outside Europe and North America. Each electronic certificate produced within this scope corresponds to 1 MWh production and can be used by both energy producers and energy consumers for certifying the use of the renewable energy [5].

The I-REC code provides the blueprints for a standardized tracking system that can be implemented in any country or region. Standardization allows for simplified consumer claims and the elimination of double claiming, double counting, and double certificate issuance. The I-REC attribute tracking system supports tracking compliance with governmental renewable energy requirements, also the voluntary consumers for tracking and verifying the progress towards their environmental goals. This gives all I-REC system participants the ability to track attributes of renewable electricity production from its location of generation to its place of consumption [6].

In this study, the performance analysis of YEK-G, Turkey's national renewable energy certification mechanism, was realized using the determined performance indicators. These performance indicators are: "Amount of Issued YEK-G Certificates", "Amount of Redemption Transactions", "Organized Market YEK-G Matching Quantities" and "Bilateral Contract Quantities".

This study consists of four sections. In the second section of the study, YEK-G performance analysis has been carried out. The third section is the conclusion section. The last part is the recommendations section. In this section, recommendations were made for the improvement of the YEK-G system.

II. YEK-G SYSTEM AND MARKET STRUCTURE

In Turkey, it has been possible for the consumers to purchase renewable energy within the scope of bilateral contracts signed with electrical power producers who have a generation portfolio consisting of only RESs. However, there is a need for a mechanism to register the purchased energy as renewable energy. In order to meet this need, Turkey has taken a national step and published the YEK-G regulation. As a result of the studies carried out by examining international examples in order to develop a green certification system in line with the European Union (EU) standard, the name of the system in question was determined as the YEK-G system [7].

YEK-G trading is carried out in the organized and over-the-counter (OTC) markets through bilateral contracts. Organized YEK-G market is the market that is organized and operated by Energy Exchange Istanbul (EXIST) and where the YEK-G certificate is traded among market participants. In the organized YEK-G market, the contracts that oblige to receive or deliver the YEK-G document equal to the matching quantity of the YEK-G document at the matched price are opened by the EXIST in accordance with the continuous trade model. The YEK-G certificate issued within the scope of certifiable production amount is processed in contracts opened with the type of the production source. Market participants can bid and/or sell the contracts that are open during the session. During the market, the maximum and minimum prices are determined by EXIST, and market transaction collateral is taken against the financial risks that may arise regarding the invoice payments of the transactions that are carried out by the market participants. Market participants can trade in the Organized YEK-G Market as much as the current market transaction collateral amounts. YEK-G certificates will be tradeable through bilateral contracts in the OTC market [8, 9].

2.1. YEK-G PERFORMANCE ANALYSIS

The YEK-G system became operational on June 01, 2021. The performance analysis of the YEK-G has been performed by using these performance indicators: "Quantity of Issued YEK-G Documents", "Amount of Redemption Transactions", "Organized Market YEK-G Matched Quantity" and "Bilateral Contract Quantity". According to the data received from the EXIST transparency platform between 01.06.2021 and 31.08.2021 (analysis period), issuance volumes by plant type are given in Table 1.

Table 1. Issuance volumes by plant type [10].

	Wind (MWh)	Solar (MWh)	Hydro (MWh)	Geothermal (MWh)	Biomass (MWh)	Total (MWh)
June	39,532	-	5,758,768	440,299	16,739	6,255,338
July	9,857	-	391,157	94,848	12,174	508,036
August	32,683	-	238,827	233,541	7,087	512,138
Total	82,072	-	6,388,752	768,688	36,000	7,275,512

Following the application of the producers in the YEK-G system, YEK-G certificate is created by EXIST for each 1 MWh energy production from a specified RES and transferred to the account of the relevant producer. During the analysis period, a total of 7,275,512 YEK-G certificates were issued. During the analysis period, hydro plants were responsible for most of the YEK-G issuance. Hydro plants represented 88% of the volumes issued during the analysis period.

As seen in Table 1, the most YEK-G redemption was realized from hydro plants. Issuance volumes during the analysis period for hydro, geothermal, wind, and biomass were determined as 6,388,752 MWh, 768,688 MWh, 82,072 MWh, and 36,000 MWh respectively. There is no YEK-G issuance originating from solar plants.

Redemption in the YEK-G mechanism is the process of electronically ending a YEK-G document in the account in the registry database, in order to be associated with certain renewable energy consumption and used for disclosure purposes, in such a way that it is prevented from being transferred to another account by the EXIST upon the request of the account holders [11]. During the analysis period, redemption volumes by plant type are given in Table 2.

Table 2. Redemption volumes by plant type [12].

	Wind (MWh)	Solar (MWh)	Hydro (MWh)	Geothermal (MWh)	Biomass (MWh)	Total (MWh)
June	4	-	22	6,867	-	6,893
July	20	-	221	7	1	249
August	12	-	6,212	23,294	-	29,518
Total	36	-	6,455	30,168	1	36,660

As seen in Table 2, the most YEK-G redemption was realized from geothermal plants. Redemption volumes during the analysis period for geothermal, hydro, wind, and biomass were determined as 30,168 MWh, 6,455 MWh, 36 MWh, and 1 MWh respectively.

The issuance and redemption quantities in the YEK-G Market are given in Figure 1 [10, 12].

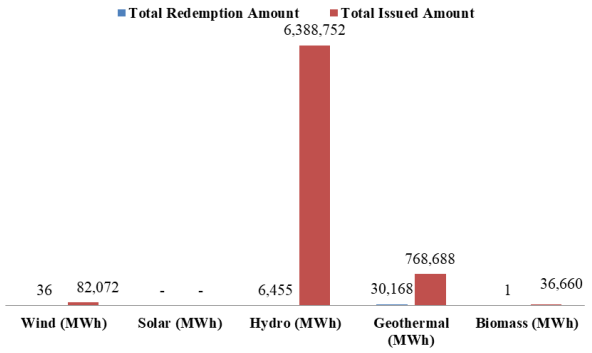

Figure 1. Comparison of issuance and redemption quantities in the YEK-G market.

As seen in Figure 1; the redemption quantities for all plants are quite low despite the high issuance quantities. While the total quantity issued was 7,275.512 MWh, the total amount redeemed was 36,660 MWh. Total redemption rate was 0.5%. Redemption rates for wind, hydro, geothermal plants were found as 0.043%, 0.10% and 3.9% respectively. Only 0.0002% of the issued quantity originating from biomass plant was redeemed.

For the analysis period; matching quantities of organized YEK-G market by plant type are given in Table 3 [13].

Table 3. Matching quantities in the Organized YEK-G market.

	Wind (MWh)	Solar (MWh)	Hydro (MWh)	Geothermal (MWh)	Biomass (MWh)	Total (MWh)
June	635	-	2,045	29	1	2,710
July	301	-	2,779	1	-	3,081
August	12	-	18	5,800	-	5,830
Total	948	-	4,842	5,830	1	11,621

As seen in Table 3, the quantities of matches in the organized YEK-G market are increasing. In the YEK-G system, the matching quantities realized in the Organized Market session in June was 2,710 MWh. In July, a match of 3,081 MWh was realized with an increase of 13% compared to June. In the organized market session of August, 5,830 MWh was matched with a 90% increase compared to the July session. When the matched quantities are analyzed by plant type, the most matched was from the geothermal plant with 5,830 MWh. Quantities for hydro, wind, and biomass plants were 4,842 MWh, 948 MWh, and 1 MWh respectively. The total trading volume in the organized market was 11,621 MWh.

The OTC YEK-G Market bilateral contract quantities, for the analysis period, are given in Table 4 [14].

Table 4. Bilateral contract quantities in the OTC YEK-G market [14].

	Wind (MWh)	Solar (MWh)	Hydro (MWh)	Geothermal (MWh)	Biomass (MWh)	Total (MWh)
June	-	-	994	1,006	-	2
July	-	-	10,848	-	-	10,848
August	-	-	12,360	-	-	12,360
Total	-	-	24,202	1,006	-	25,208

As seen in Table 4, the number of bilateral contracts in the OTC YEK-G market is increasing. In the YEK-G System, the number of bilateral contracts realized in the OTC YEK-G market in June was 2,000 MWh. In July, the quantity of bilateral contracts reached 10,848 MWh. In the OTC market in August, 12,160 MWh bilateral contracts were signed, with an increase of 12% compared to July. In the OTC YEK-G Market, the highest quantity of bilateral contracts was from hydro plants with 24,202 MWh. This plant is followed by the geothermal plants with 1,006 MWh. In other plants, however, no bilateral contracts were made.

The total transaction volume in the YEK-G market is the sum of the "bilateral contract quantities" and the "OTC Market YEK-G Matching quantities". Accordingly, the total trading volume of the YEK-G Market is 36,829 MWh. The total volume of the YEK-G market by plant type is given in Table 5 [13,14].

Table 5. Total volume of YEK-G market.

	Wind (MWh)	Solar (MWh)	Hydro (MWh)	Geothermal (MWh)	Biomass (MWh)	Total (MWh)
OTC Market	-	-	24,202	1,006	-	25,208
Organized YEK-G Market	948	-	4,842	5,83	1	11,621
Total YEK-G Market Trading Volume	948	-	29,044	6,836	1	36,829

For the analysis period; the change in the weighted average prices by plant type in the organized YEK-G market is given in Table 6.

Weighted average prices of I-REC by plant type as of the end of 2021 are given in Table 7 [16]. The prices in Table 7 show the wholesale trade prices. Redemption and other costs are not included in transactions realized on the I-REC platform. Prices also vary widely in volume sales. For this reason, it is not possible for consumptions of 50,000 MWh and below to trade at these prices [16].

Table 6. Organized YEK-G market's weighted average price change [15].

Date	Plant Type	Weighted Average Price (TRY/MWh)	Weighted Average Price (USD/MWh)	Weighted Average Price (EUR/MWh)
21.06.2021	Hydro	0.38	0.04	0.04
21.06.2021	Geothermal	3.34	0.39	0.32
21.06.2021	Wind	0.44	0.05	0.04
21.06.2021	Biomass	5	0.58	0.48
29.07.2021	Hydro	0.39	0.05	0.04
29.07.2021	Geothermal	0.5	0.06	0.05
29.07.2021	Wind	0.25	0.03	0.02
20.08.2021	Wind	1	0.12	0.1
20.08.2021	Geothermal	0.45	0.05	0.05
20.08.2021	Hydro	0.29	0.03	0.03

If the organized YEK-G market's weighted average price change in Table 6 and the weighted average prices of I-REC in Table 7 are compared, it is seen that the weighted average prices of I-REC in TRY at the end of September are higher than the organized YEK-G market's weighted average price.

Table 7. Weighted average prices of I-REC [16].

Plant Type	Weighted average prices (TRY/MWh)
Hydro	1.35
Geothermal	1.4
Wind	2
Solar	2.25
Biomass	1.5

The OTC market depends on the contract between the buyer and the seller. After the bilateral contracts between the buyer and the seller are agreed between the two participants, only the quantity parts are processed from the system. Therefore, the price of the bilateral contract does not know, including EXIST[14].

The quantities of issuance and redemption of I-REC certificates by year are given in Table 8.

Table 8. The quantities of issuance and redemption of I-REC certificates by year (GWh) [11].

Year	Issuance	Redemption
2016	100	100
2017	50	50
2018	100	100
2019	510	260
2020	825	350
Since the beginning of 2021	4,200	1,000

When the I-REC issuance and redemption quantities are analyzed by year, it is seen that the quantities issued and redeemed in the last five years are in parallel with each other. The issue quantity was 825 GWh in 2020, and approximately 42% of this amount (approximately 350 GWh) was redeemed. The quantity of I-REC issued since the beginning of 2021 is 4,200 GWh, and 23,8% (1,000 GWh) of this quantity has been redeemed. According to the data we have within the YEK-G analysis period, the YEK-G transaction volume is 36,829 MWh. When compared in terms of transaction volumes, it is seen that the performance of YEK-G is lower than that of I-REC in the current situation. Although it is not possible to compare for similar periods in the light of the data, the general picture proves the accuracy of this result.

III. CONCLUSION

During the analysis period, most of the YEK-G issuances were realized from hydro plants. The second most YEK-G issued plant is the geothermal. Wind and Biomass plants follow the geothermal, respectively.

During the analysis period, there was no YEK-G issuance originating from solar plants. A significant part of the solar power plants installed in Turkey consists of unlicensed power plants. It is thought that the lack of YEK-G issuance originating from solar plants is due to the fact that unlicensed power plants are not included in the YEK-G system. In the period of June 2021, the installed power from solar plants was determined as 6,572.33 MWh, among the unlicensed electricity installed capacity. Accordingly; the ratio of the installed power of unlicensed solar power plants to the total installed power of unlicensed plants is 91.70%[17]. While the share of unlicensed solar power plants in the installed power is high, their inclusion in the YEK-G system has limited the number of certificates that can be issued and therefore redeemed. Being local and the source of energy is important in fulfilling the renewable energy consumption obligations of companies. Solar energy is the first preferred type of RES by companies that want to use renewable energy. This plant is followed by wind and hydro, respectively [4]. In this case, it is expected that the tendency for the issuance of YEK-G certificate will be a predominantly solar plant, but the expected situation has not materialized due to unlicensed power plants that are not included in the YEK-G system being implemented.

During the analysis period, the most YEK-G redemption was realized from geothermal plants. The quantity of YEK-G redemption realized from the geothermal plants are 30,168 MWh. It is followed by hydro with 6,455 MWh, wind with 36 MWh and biomass with 1 MWh. It has been observed that the redemption quantities for all plant types are quite low, despite the high quantities in the issuance quantities. While the total quantities issued was 7,275.512 MWh, the total quantity redeemed was 36,660 MWh. Only 0.5% of the total amount issued has been redeemed and 0,043% of the issued amount from the wind plant was redeemed. For the Hydro plant, the redemption rate is 0.10% of the issuance rate. For the geothermal plant, the redemption rate is only 3.9% of the issuance rate. 0.0002% of the issued amount originating from Biomass plants were redeemed.

The redemption process is the process of using a YEK-G document in the account in the registry database with specific renewable energy consumption and using it for disclosure purposes. This transaction is carried out by the EXIST at the request of the account holders. YEK-G System users (account holders) might have to wait for a certain period of time for the disclosure of their documents. The reason for the quantity of the

redemption being lower compared to the issuance could be related to this issue.

The total volume of the YEK-G market during the analysis period is 36,829 MWh. When analyzed in terms of plant types, hydro plants (29,044 MWh) constitute a large part of the total volume. The volumes for geothermal, Wind, and Biomass were 6,836 MWh, 948 MWh, and 1 MWh respectively.

In the light of all these data, it is clearly seen that the most preferred plant type for issuance during the analysis period is hydro. When prices are analyzed on the basis of plants, the most affordable plant was hydro (0.38 TRY/MWh) in June. In July, Wind was the most affordable plant (0.25 TRY/MWh). The most affordable plant in August was again Hydro (0.29 TRY/MWh). When we compare YEK-G and I-REC on a price basis, it can be said that the YEK-G system is more affordable than the I-REC system in TRY. It can be predicted that YEK-G's affordable price will be an important reason for its preference in the Turkish market.

Taiwan and China have a national REC system similar to Turkey. For the certification system to be successful, the issued certificate and the rate of certificates traded must be proportional to each other. When the REC mechanisms used in Taiwan and China are examined, it is seen that the REC issues are disproportionate. The large difference between the number of certificates issued and the number of certificates traded indicates that the trade volumes of the certification systems used in Taiwan and China are low. Its limitation with only onshore wind and solar in China appears as a factor limiting the trade volume [18,19,20].

The roadmap planned by Energy Market Regulatory Authority (EMRA) includes Turkey's membership in the Association of Issuing Bodies (AIB), which sets the energy certificate standards in the EU, and its inclusion in the European Energy Certificate System (EECS) scheme. By this means, it is aimed to make the certificates in Turkey valid in the EU and to expand the trade opportunities. In the medium term, these certificates are thought to be an instrument that can be used in the EU carbon tax obligations [4].

IV. Recommendations

For the YEK-G System to be successful, unlicensed power plants must be included in the system. Studies on this subject should be accelerated in order to ensure adequate supply. Solar power plants are the first preferred plant by companies that want to use renewable energy. The fact that unlicensed solar power plants are not included in the YEK-G System has limited the number of certificates that can be redeemed.

The fact that the certificates are valid for 12 months (validity) may cause problems for the consumer. In the first place, it may be appropriate for the validity of the certificates to continue for a while for the market to revive and the demand to continue. The validity period in the REC mechanism used in India is 1095 days (approximately 3 years) days from the date of issuance [15,21].

The documents in the YEK-G market must be acceptable to the EU. This acceptability is also important for the competition between YEK-G and I-REC. An important reason for the preference of the I-REC certificate by international companies is acceptance of the I-REC certificate by the GHG Protocol and the Carbon Disclosure Project (CDP). In order to stimulate demand and ensure continuity, large-scale energy consumers should be obliged to consume renewable energy.

References

[1] Natural Capital Partners, *Energy Attribute Certificate Factsheet*, . Available:https://assets.naturalcapitalpartners.com/downloads/Energy_Attribute_Certificate_Factsheet.pdf

[2] EPA's Green Power Partnership, *Renewable Energy Certificates*, Available: https://www.renewablemarketers.org/pdf/resources/EPA%20-%20REC%20101.pdf

[3] Hanson and Van Son, World Resources Institute, *Renewable Energy Certificates: An Attractive Means For Corporate customers to purchase renewable energy* Available: http://pdf.wri.org/gpmdg_corporate_guide_05.pdf

[4] Natural Capital Partners, *Guarantees of Origin (GOs)*, Available: https://assets.naturalcapitalpartners.com/downloads/GO_Factsheet.pdf

[5] The International REC Standard, *I-REC GUIDE – HOW I-REC WORKS*, Available: https://www.irecstandard.org/about-us/#/

[6] SHURA Energy Transition Center, (2021, March). *Renewable Energy Supply and Certification in Turkey*, Available:https://www.shura.org.tr/wp-content/uploads/2021/03/turkiyede_yenilenebilir_enerji_tedariki_ve_belgelenmesi.pdf

[7] EPDK, "*The green certificate market is coming*", Available: https://www.epdk.gov.tr/Detay/Icerik/2-9224/RECil-sertifika-piyasasi-geliyor

[8] Turkey's Energy Exchange Istanbul (EXIST), *YEK-G System and Organized Market Introduction*, Available: https://www.epias.com.tr/yek-g-piyasasi/yek-g-sistemi-ve-organize-yek-g-piyasasi-tanitimi/

[9] Turkey's Energy Exchange Istanbul (EXIST)(2021). *What is YEK-G?* Available: https://yekgnedir.com/

[10] Turkey's Energy Exchange Istanbul (EXIST) (2021a). *YEK-G System and Organized Market, Transparency platform* Available: https://seffaflik.epias.com.tr/transparency/piyasalar/yekg/ihrac-edilen-yekg-belge-sayisi.xhtml

[11] Renewable Energy Source Guarantee Certificate Regulation in the Electricity Market (2020, November). Official Gazette (No: 31304), Available: https://www.resmigazete.gov.tr/eskiler/2020/11/20201114-2.htm

[12] Turkey's Energy Exchange Istanbul (EXIST) (2021b). *YEK-G System and Organized Market, Transparency platform* Available:https://seffaflik.epias.com.tr/transparency/piyasalar/yekg/itfa-edilen-yekg-belge-sayisi.xhtml

[13] Turkey's Energy Exchange Istanbul (EXIST) (2021c). *YEK-G System and Organized Market, Transparency platform* Available:https://seffaflik.epias.com.tr/transparency/piyasalar/yekg/eslesme-miktari.xhtml

[14] Turkey's Energy Exchange Istanbul (EXIST) (2021d). *YEK-G System and Organized Market, Transparency platform* Available:https://seffaflik.epias.com.tr/transparency/piyasalar/yekg/ikili-anlasma-miktarlari.xhtml

[15] Turkey's Energy Exchange Istanbul (EXIST) (2021e). *YEK-G System and Organized Market, Transparency platform* Available: https://seffaflik.epias.com.tr/transparency/piyasalar/yekg/agirlikli-ortalama-fiyat.xhtml#

[16] Can Arslan, Foton Energy, Meeting Date: 28.09.2021

[17] EPDK, *Electricity Market Sector Report*, (2020, June). Available: https://www.epdk.gov.tr/Detay/Icerik/5-11444/2021-yili-haziran-ayi-sektor-raporlari-yayimlanmi

[18] Climate Group, *Technical Assessment Report*, (2020, August). Green Electricity Certificate (GECs) of China, Available: https://www.there100.org/sites/re100/files/2020-10/Chinese%20GEC%20Paper_RE100_2020%20FINAL.pdf

[19] Dr. Jules Chuang, Asian Power Market & Renewable Energy Options, (2020, January). Mt.Stonegate Green Asset Management Ltd, Available: https://www.renewable-ei.org/pdfdownload/activities/05_JulesChuang_MtStonegate.pdf

[20] Renewable Energy Institute, Renewable Electricity Procurement Guidebook, Available: https://www.renewable-ei.org/pdfdownload/activities/REI_RE_Procurement_Guidebook_EN_201902.pdf

[21] Indian Energy Exchange, IEX Market:An Overview May, 2019, Accessed: https://www.iexindia.com/Uploads/Presentation/24_05_2019Renewable_Energy_Certificates.pdf

Design of a Miniaturized Frequency Selective Surface Based Rasorber

M. MALKOÇ[1] and S. ÜNALDI[1]

[1]Bilecik Şeyh Edebali University, Bilecik/Turkey, muhammed.malkoc@bilecik.edu.tr
[1]Bilecik Şeyh Edebali University, Bilecik/Turkey, sibel.unaldi@bilecik.edu.tr

Abstract **- This study presents a single layer FSS based rasorber by using FR-4 substrate with 1.2mm thickness. The presented design has an absorber with a copper hexagon loop shape on the front surface and a Frequency Selective Surface on the back surface of the designed structure. The given rasorber has one reflection band. This reflection band has 0.25 dB insertion loss between 3.85 GHz and 4.23 GHz. In the process of the optimizing the parameters of the rasorber, the absorption frequency of the FSS is adjusted so that it may act as a metallic surface. One of the aims of this study is to reduce the unit cell's thickness compared to other studies in the literature. In order to minimize the overall dimension of the unit cell, optimization is made and the size of the designed structure is determined as 22 mm x 22 mm. Also proposed rasorber structure has stable transmission characteristic for both TE and TM polarizations under oblique incidence from 0° to 30°.**

Keywords **- Frequency Selective Surface, Frequency Selective Rasorber, Insertion Loss, Transmission, Absorber**

I. INTRODUCTION

FREQUENCY Selective Surfaces (FSSs) usually consist of metal patches with a periodic arrangement of random geometry or patch-like aperture elements in metal [1]. Many studies on FSS based absorber has been taken place in recent years because of the important role of the FSS based absorber in stealth technology [2]. In 2009, the complete conceptual multilayer rasorber design was proposed [3]. Also, in some studies in the literature, it is called Absorptive/Transmissive Frequency Selective Surface (ATFSS) [4], [5].

The Frequency Selective Rasorbers (FSRs) have attracted attention in the last decade because of their perfect filtering properties [6]. The zero transmission in the FSS based absorbers is provided by metallic layer [7]. One of the reasons that FSRs have gained wide popularity in the past years is that they have transmission properties as well as absorber properties [8].

Several FSS based rasorber studies have been reported recently. As reported in [9], the FSR design consists of two absorption bands along with a transmission window at 6.3 GHz with the insertion loss of 0.6dB windows. In addition to its broadband absorption window, they achieved a transmission window [10]. It's also utilizing the combination of a lossless and lossy layers to obtain the transmission window [10].

In this study, a dual-band absorption bandwidth is obtained with a single-layer, thin FSS-based rasorber design. The given unit cell contains a hexagon-shaped absorber on its front surface and FSS on its rear surface.

II. RASORBER UNIT CELL DESIGN AND ANALYSIS

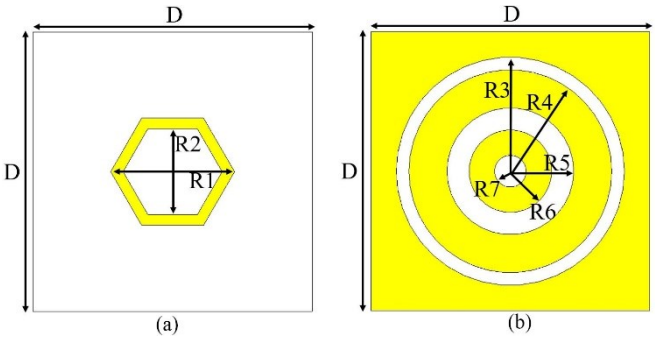

Figure 1: Proposed Unit Cell (a) Front view (b) Back view

The front view and the back view of the designed FSS based rasorber structure are depicted in Figure 1. The design parameters of the presented structure are detailed in Table 1. All the units are used as millimeters in design.

Table 1: Unit Cell Design Parameters

Parameter	Value(mm)	Parameter	Value(mm)
D	22	R4	8
R1	8.44	R5	5
R2	6.75	R6	3.25
R3	9	R7	1.25

The unit cell view of presented rasorber, illustratted in Figure 1, is designed on a single layer FR-4 dielectric substrate. As seen in Figure 1, the yellow sections represent copper and the white sections represent the dielectric substrate. In the proposed unit cell design, a hexagon-shaped absorber can be found on the front surface. The back surface of the layer contains an FSS which has three concentric rings subtracted from the fully metal. The unit cell was designed using an FR-4 dielectric layer with a dielectric permeability of $\varepsilon = 4.3$ and a dielectric loss of $\tan\delta = 0.025$.

The design stages for the proposed rasorber initially consist of the analysis of the structure on the front surface, then the analysis of the FSS on the back surface. The design consists of three stages. Firstly, we focused on designing the absorber which has a completely metallic background, then we designed the FSS.

The goal is to make the reflection coefficient of the absorber at the same frequency as the reflection of the FSS. The main purpose here is to make the FSS acts like a fully metallic surface. So, in the last step, we placed the FSS background of the absorber and took it out of the complete metallic background.

The reflection coefficient simulation result of the absorber which is located on the front surface of the presented design is depicted in Figure 2. The reflection and transmission coefficients simulation result of the FSS on the back surface is as seen in Figure 3. In Figure 3, the designed FSS unit cell shows the characteristic of a bandpass filter on 6.52 GHz.

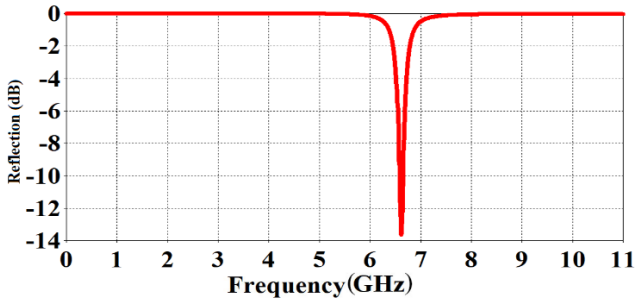

Figure 2: Absorber Reflection Coefficient

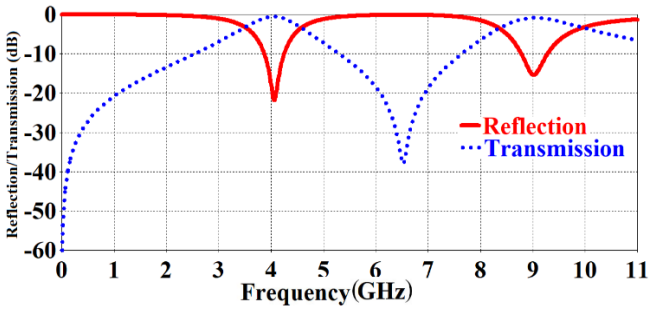

Figure 3: FSS Reflection/Transmission Coefficient

The design parameters of the presented unit cell are optimized in such a way that the FSS should have the maximum reflection at the absorption frequency of the presented absorber. After these optimizations, the structure is analyzed in the CST Microwave Studio software.

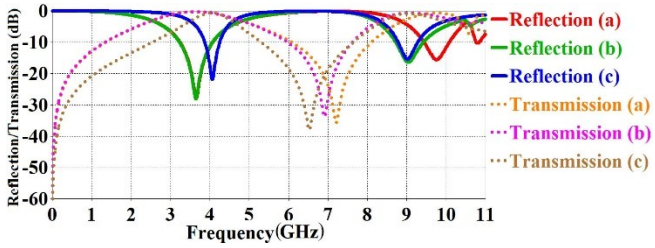

Figure 4: Optimizing the FSS

Different parameters for the FSS design are examined. The cases called a, b and c are included in Table 2 and each case contains different values of some design parameters of R3, R6 and R7. In case a, the operating frequency of the transmission for the FSS is acquired around 7.25 GHz, which is not matching with the operating frequency of the reflection.

Table 2. FSS with the different parameters

Parameter/ Case	R3	R6	R7
a	10.75	2.65	0.4
b	10.75	3.25	0.25
c	9	3.25	1.25

After changing the value of R6 and R7 the operating frequency of the transmission for the FSS is obtained around 6.95 GHz, in the last case, with the change of R3 R6 R7 parameters the goal was achieved, and FSS's the operating frequency of the transmission is obtained around 6.5 GHz. The simulation results for both reflection and transmission coefficients for each case are given in Fig. 4. The obtained best result can be seen in Figure 5.

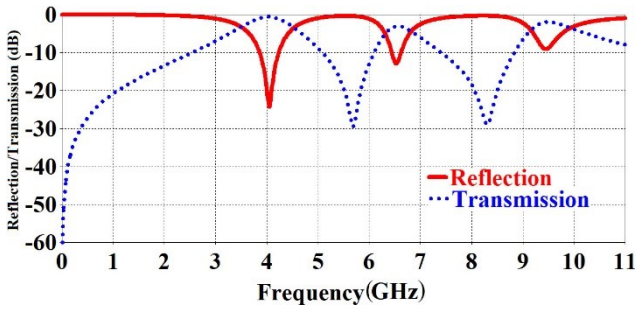

Figure 5: Reflection/Transmission Coefficients of the Proposed Design

The simulation results for TE - TM polarizations under oblique incidence are illustrated in Fig. 6 and Fig. 7. As seen in Fig. 6 and Fig. 7, the stable transmission characteristic of the designed rasorber is obtained when the angle of incidence changes from 0° to 30°. The Reflection characteristics of the rasorber are stable in frequencies that lower than 9 GHz with the incident angle ranging from 0° to 30°. They are both the same in TE and TM polarization.

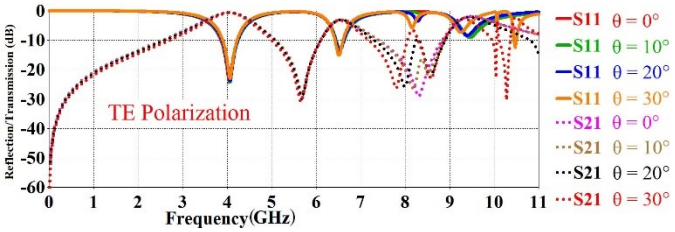

Figure 6: Simulated transmission coefficient and reflection coefficient under an oblique incidence (TE Polarization).

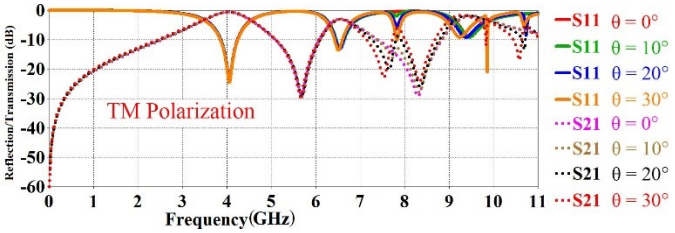

Figure 7: Simulated transmission coefficient and reflection coefficient under an oblique incidence (TM Polarization).

The simulation results of the proposed structures are given in the Figure 5, which is obtained from the CST microwave simulation software. As indicated in Figure 5, the FSS based absorber has one transmission band and a narrowband absorption window. This reflection band has 0.25 dB insertion loss between 3.85 GHz and 4.23 GHz. The thickness of the proposed unit cell is $0.016\lambda_L$ (λ_L is the free space wavelength at lowest frequency of -10 dB reflection). The unit cell's size is obtained as $0.28\ \lambda_L\ x\ 0.28\ \lambda_L$. Compared to the studies in the literature, as seen in [10]: a study with $0.04\lambda_L$ unit cell thickness and less than 1 dB of insertion loss, our study has improved both on insertion loss and thickness. The comparison of the unit cell to the other studies in terms of absorption bandwidth, transmission frequency and thickness is given in Table 3.

Table 3. Performance comparison of proposed FSS based rasorber.

Refer-ence	Lower Bandwidth	Insertion Loss	Transmission Frequency	Thickness
[9]	1.9GHz – 5.1GHz	0.6 dB	6.3 GHz	$0.104\lambda_L$
[10]	4.8GHz – 6.81GHz	Less than 1dB	1.5 GHz	$0.04\lambda_L$
[11]	4.02GHz – 6.27GHz	2.30 dB and 1.69 dB	7.2 GHz – 13.05 GHz	$0.107\lambda_L$
[12]	Not Specific	0.68 dB	4.42 GHz	$0.108\ \lambda_L$
This Work	3.85 GHz – 4.23 GHz	0.25 dB	6.52 GHz	$0.016\lambda_L$

λ_L = wavelength of free space at lowest operation frequency.

III. CONCLUSION

This study, presents a single-layer FSS based rasorber. The proposed unit cell consists of an absorber placed on the back surface of the dielectric layer and FSS placed on the front surface. The reflection bandwidth of the designed structure is between 3.85 GHz – 4.23 GHz with the 0.25dB insertion loss. Also, the operating frequency of transmission is achieved at 6.52 GHz. The thickness of the proposed unit cell is $0.016\ \lambda_L$ in free space wavelengths at the lowest reflection frequency. In addition to these properties the designed rasorber has stable transmission characteristic for both TE and TM polarizations under oblique incidence from 0° to 30°.

REFERENCES

[1] S. Ünaldı, "İnce Tabakalı Çift Bant Durduran Frekans Seçici Yüzey Tasarımı" M. thesis, Yıldız Teknik Üniversitesi Fen bilimleri Enstitüsü, İstanbul, 2014.

[2] M. Guo, T. Guo, Q. Cheng, Y. Zheng, Y. Fu, "Frequency Selective Rasorber with Anisotropic Transmission Band" IEEE Antennas and Wireless Propagation Letters, Vol. 20, I.2, 2021, pp.155-159.

[3] B. A. Munk, Metamaterials: Critique and Alternatives, Hoboken, NJ, USA: Wiley, 2009.

[4] Q. Guo, Z. Li, J. Su, L. Y. Yang, and J. Song, "Dual-polarization absorptive/transmissive frequency-selective surface based on tripole elements," IEEE Antennas Wireless Propag. Lett., vol. 18, no. 5, pp. 961-965, May 2019.

[5] Q. Chen, D. Sang, M. Guo, J. Bai, and Y. Fu, "Frequency selective rasorber with inter absorption band transparent window and interdigital resonator," IEEE Trans. Antennas Propag., vol. 66, no. 8, pp. 4105-4114, Aug. 2018.

[6] W. F. Bahret, "The beginnings of stealth technology," IEEE Transactions on Aerospace and Electronics system, vol. 29, Issue 4, pp. 1377-1385,

[7] M. M. Zargar, A. Rajput, K. Saurav, S. K. Koul, "A Polarization Insensitive Frequency SelectiveSurface Based Rasorber with Narrow Band

[8] Absorption Between Two Transmission Bands" in Proceedings of the 50th European Microwave Conference, 2021, p. 503-505.

[9] Y. Shang, Z. Shen, and S. Xiao, ''Frequency-selective rasorber based on square-loop and cross-dipole arrays,'' IEEE Trans. Antennas Propag., vol. 62, no. 11, pp. 5581–5589, Nov. 2014

[10] W. Yu, G. Luo, Y. Yu, W. Cao, Y. Pan, and Z. Shen, "Dual-polarized band-absorptive frequency selective rasorber using meander-line and lumped resistors," IEEE Trans. Antennas Propag., vol. 67, no. 2, pp.1318- 1322, Feb. 2019.

[11] [M. Guo, Q. Chen, Z. Sun, D. Sang and Y. Fu, "Design of Dual-Band Frequency-Selective Rasorber," IEEE Antennas and Wireless Propagation Letters, vol. 18, no. 5, pp. 841-845, May 2019.

[12] W.S. Arceneaux, R.D. Akins, and W.B. May, "Absorptive/transmissive radome," US. Patent 5,400,043, May 21, 1995. (2002) The IEEE website. [Online]. Available: http://www.ieee.org/

Determination of Effective Thermal Conductivity of Composites by Literature Models

E. CANLI[1] and H. SEPETCIOGLU[2]

[1] Selcuk University, Technology Faculty, Mechanical Engineering Department, Konya/Turkey, ecanli@selcuk.edu.tr

[2] Selcuk University, Technology Faculty, Metallurgy and Material Engineering Department, Konya/Turkey, harunsepet@selcuk.edu.tr

***Abstract* - In this work, literature was surveyed in order to find convenient models of effective thermal conductivity for composites. Five different common models were compared with each other in terms of their consistency by using the same model inputs. Three levels of matrix thermal conductivities, three levels of filler thermal conductivities, and three levels of volume fraction ratios were used as inputs. Obtained trends were graphically plotted against each other. It is seen that models including effects solid-solid interface thermal resistance are giving results distinguishing from models excluding the effects of the interface thermal resistance. It is also understood that models dealing with the thermal conductivity of composites are becoming more complex by considering filler geometries, surface properties, and other interface interactions.**

***Keywords* – Composite, effective thermal conductivity, filler geometry, mathematical modeling.**

I. INTRODUCTION

THERMAL conduction in terms of isotropic single-phase materials is relatively easily classified and quantified by engineering disciplines. Thermal conduction can be analyzed analytically for such substances. However, determination of thermal conductivity values for composites is a more challenging task. Composites may have several different solid materials in a specific geometry, which may disperse regularly or irregularly. Additionally, the geometry of composite itself can impose liquid or gas phases originating from the environment into the main geometry volume. As it will be stated by the below literature survey, temperature jumps are realized between different materials and phases. In practice and real-world applications, most engineering materials cannot be classified as pure substances or homogenous structures. Therefore, in terms of heat conduction, determining an overall heat conductivity is important for engineers regarding design purposes. Accordingly, this proceeding aims to present some literature evaluations on the subject and give quantitative comparison of some available algebraic models.

The present study is mostly inspired by the review work of Pietrak and Wisniewski [1]. The authors reviewed empirical, analytical, and numerical models that try to interpolate effective thermal conductivity of composite materials or materials having more than one phase. The problem of determining effective thermal conductivity of a real-world material for engineering purposes is identified as a more complex task compared to averaging constituent thermal conductivities according to volume percentages. Authors stress that solid-solid interfaces and interfaces between different phases pose an additional thermal resistance, analogue to different conduction phenomena such as electrical conduction. Two different components of interfacial thermal resistances are mentioned in their report, i.e., irregularities at the material interfaces and temperature jump due to material properties. The authors also emphasize that early models did not consider interface thermal resistances in terms of conductivity. As a general conclusion, considering thermal conductivities of constituents in a composite material, together with volume fractions, is not sufficient to determine an effective thermal conductivity for the material. Nevertheless, some basic and special arrangements can benefit from early simpler models. Additionally, porosity and higher volume fractions in composites leading to percolation are mentioned as other factors that make calculating or predicting an effective thermal conductivity for the material. It is understood from the review work that early models assumed simple geometrical setups including filler geometries and distributions in order to make analytical analyses. Later more complex models incorporated empirical constants and blended analytical models with them. Of course, the authors mention more recent numerical analysis tools such as Finite Element Method (FEM). Last but not least is the silica aerogel emphasis of the authors as one of the most effective thermal insulation materials.

The remaining part of the introduction section presents a brief literature survey in chronological order.

Nieberlein reported a study on improving thermal conductivity of a composite of epoxy and filler options by obtaining a higher effective thermal conductivity [2]. The author considered a geometrical model for unit composite, in which two hemispheres connect with each other representing the matrix, and a circular cylinder passes through the centers of the two hemispheres representing the filler. After the

arrangement of an analytical model, the author tried to calculate the effective thermal conductivity. However, it is understood that an experimental point data is needed to obtain a correction factor. Therefore, this work can be regarded as a hybrid empirical/analytical modeling. During the development of the analytical expression, the author considered packing density of spheres, then non-spherical nature of the filler particle aggregates. The paper shows that increasing volume fraction of fillers increases effective thermal conductivity of the matrix linearly to a point, in case of high thermal conductivity of filler than the matrix, and then, the effective thermal conductivity increases asymptotically. The critical volume fraction seems to start at 28 to 56 percent based on filler geometry. It is also seen that filler thermal conductivity has a lower effect on effective thermal conductivity compared to the effect of filler volume fraction. In the last part of the paper, the author emphasizes that exceptions are especially valid for conductive paths of fillers at high volume fraction rates and constituent conductivities similar to each other.

Yamada and Ota conducted experimental measurements for determining effective thermal conductivity of mixtures by dispersing substances having different principal geometries into matrices [3]. The dispersed materials also have different thermal conductivities. They tried several effective thermal conductivity models from the literature, assessed them, and then prepared their own. They claim a wider range of applications for their proposed model, while the wide range is in terms of dispersed material volume fraction. The tried substances by the authors are lead, copper, and aluminum oxide while the tried shapes are sphere, parallelopiped, cylinder, and irregular geometries. The test data consist of volume fraction ratios up to 50%. Most of the literature models they tried are accurate for low volume fractions while the error grows bigger as volume fraction increases. Therefore, they proposed their own mathematical expression in order to correlate thermal conductivity of the constituent dispersed substance, volume fraction, and shape to effective thermal conductivity. They claim that the proposed expression can give accurate results with an error band of 15% for constituent thermal conductivity ratio bigger than unity and volume fraction is smaller than 50%.

Bigg reported a comprehensible work on increased thermal conductivity of polymers by preparing composites of them [4]. The author tried steady and transient thermal conductivity determination tests and shares the obtained experience. Especially, it is stated that there are several challenges relating to the type of thermal conduction testing, which can change obtained experimental results to vary from the literature significantly. The author reminds that the thermal conductivity concept is a bulk property definition. Therefore, the author suggests that changes in thermal conductivity of materials or effective thermal conductivity of composites due to anisotropy are milder than other conductivity types such as electricity, though thermal and electrical conductivities are regarded analogue to each other. The author also tried to determine coefficients of a literature model by means of experimentally determined results. It is stated that literature model can predict effective thermal conductivity accurately up to a volume fraction ratio. After that threshold, the model overpredicts the results. In the tried model, maximum packing concentrations were considered. Some maximum packing values are 0.6 and 0.74 for spherical fillers and 0.78 and 0.9 for fibers.

Agari et al. proposed a model for predicting and interpolating effective thermal conductivity of polymer composites [5]. The authors used polyethylene as matrix and several different fillers, i.e., graphite, copper, and aluminum oxide. Experimental means were also employed in order to assess the model. Fillers were mixed to see if the proposed method is valid for such cases. Two different heat flux modes are defined as parallel and series material stacking. The volume content of particles is up to 30%. The authors claimed that their proposed model is able to capture the experimental data.

Agari et al. extended their previous work to very high-volume fractions of fillers [6]. The main purpose of the extended work is to avoid voids and increase volume fraction of the fillers to their maximum levels. Experiments were conducted and a new model for two-phase material effective thermal conductivity was proposed. In the extended work, two different types of polymers, that are polyethylene and polystyrene were used. Filler particles were selected as quartz and aluminum oxide. Another aspect of the work is the fractional void values, which have effects on the effective thermal conductivity values.

Matt and Cruz conducted a theoretical numerical analysis on three-dimensional fillers in matrices for effective thermal conductivity values, involving interfacial thermal resistance phenomenon [7]. An iso-parametric second-order finite element discretization method was employed by the authors in order to numerically analyze a model three-dimensional cell containing fillers and matrix constituents. Fillers were regarded as ordered and disordered dispersions or arrangements in the numerical models. The filler geometries were designed as spheres, prolate ellipsoid of revolution, and circular cylinders. Numerical results obtained from the numerical scheme were compared to results from analytical expressions of the literature. In the final part of their work, a disordered multiple geometry filler dispersion was numerically analyzed. They used the Biot number for indicating constituent thermal conductivities and parameter levels. Authors emphasize that fiber-matrix interface thermal resistance has a major effect on effective thermal conductivity. Another favorable aspect of the numerical FEM method is that voids in the composite can be considered. The authors indicate two major future goals for the literature, which are geometric modeling for flexible and universal modeling purposes and empirical modeling for reducing findings and tabulated data.

This proceeding presents a literature survey and some principal models for evaluating effective thermal conductivity of composites with relatively low filler concentrations. After models are introduced in the second section, they were compared to each other by hypothetical elemental thermal conductivity values and volume fractions of the constituents. In this way, only changes in trends are considered to reveal

differences between models. No real-world data providing is aimed.

II. Considered Effective Thermal Conductivity Models

In this part, selected models from the literature are obtained from reference [1]. Constituent thermal conductivities were selected as three levels that are 0.01, 1, and 100 W/m·K. The constituent thermal conductivities were selected as hypothetical values, just for their easy utilization and parameter levels that are increased a hundred times for each level. Therefore, the constituent thermal conductivity values do not represent specific materials. Matrix thermal conductivity is shown by "k_m" and filler thermal conductivity is shown by "k_l". The volume fraction of the filler is taken as 0.01, 0.05, and 0.25 as an additional parameter. The volume fraction of the filler is represented by "φ" symbol. The 0.25 limit for fraction was specifically selected since the tried early methods have a relevant limitation. The basic parameter pattern of the work is given in Table 1.

Table 1: This caption is centered.

k_m	k_l	φ
0.01	0.01	0.01
1	1	0.05
100	100	0.25

Effective thermal conductivity values (k_{eff}) of the hypothetical composites that are consisted of two phases indicated by Table 1 were calculated by literature models. Accordingly, 9 different effective thermal conductivity values were calculated for each model. Used models are introduced below.

The first model is named as Maxwell model (Model 1) and is given below in equation (1).

$$k_{eff} = k_m + \frac{3k_m\varphi}{\left(\frac{k_l + 2k_m}{k_l - k_m}\right) - \varphi} \tag{1}$$

The second model is named after Lord Rayleigh and has three versions depending on the distribution and shape of the fillers. The three versions are denoted with equation (2) – Model 2.1, equation (3) – Model 2.2, and equation (4) – Model 2.3, respectively.

$$k_{eff} = k_m + \frac{3k_m\varphi}{\left(\frac{k_l - 2k_m}{k_l - k_m}\right) - \varphi + 1.569\left(\frac{k_l - k_m}{3k_l - 4k_m}\right)\varphi^{\frac{10}{3}}} \tag{2}$$

$$k_{eff} = k_m + k_m\left(\frac{k_l - k_m}{k_m}\right)\varphi \tag{3}$$

$$k_{eff} = k_m + \frac{2k_m\varphi}{\left(\frac{k_l + k_m}{k_l - k_m}\right) - \varphi + \left(\frac{k_l - k_m}{k_l + k_m}\right)\left(0.30584\varphi^4 + 0.013363\varphi^8\right)} \tag{4}$$

Equation (2) is for random distribution while equation (3) is for ordered fillers spanning thoroughly the matrix in an axis for a parallel heat flux scenario. Equation (4) is for the same arrangement as equation (3) but for perpendicular heat flux scenario.

The third model has three mathematical expressions that are given below in equations (5)-(7). The model constants were selected for spherical filler case, in order to have a correspondence between Model 1.

$$k_{eff} = \frac{1 + 1.5B\varphi}{1 - B\psi\varphi} \tag{5}$$

$$B = \left(\frac{\frac{k_l}{k_m} - 1}{\frac{k_l}{k_m} + 1.5}\right) \tag{6}$$

$$\psi = 1 + \left(\frac{1 - 0.7405}{0.7405^2}\right)\varphi \tag{7}$$

Model 4, which is given below by equation (8), has two unknowns indicating particle radius "a" and boundary conductivity "h". The two unknowns were determined by least-squares fit of the Model 4 to Model 3. In this way, a composite with known effective thermal conductivity can be evaluated in terms of filler particle radius and boundary conductivity. Of course, those values would be bulk representative values.

$$k_{eff} = k_m\left[\frac{2\left(\frac{k_l}{k_m} - \frac{k_l}{ah} - 1\right)\varphi + \frac{k_l}{k_m} + \frac{2k_l}{ah} + 2}{\left(1 - \frac{k_l}{k_m} + \frac{k_l}{ah}\right)\varphi + \frac{k_l}{k_m} + \frac{2k_l}{ah} + 2}\right] \tag{8}$$

Finally, a similar approach with Model 4 and Model 3 was applied for Model 5. However, the "α" parameter in equation (9) is a dimensionless parameter for interface thermal resistance.

$$\left(1 - \varphi\right)^3 = \left(\frac{k_m}{k_{eff}}\right)^{(1+2\alpha)/(1-\alpha)}\left(\frac{k_{eff} - k_l\left(1-\alpha\right)}{k_m - k_l\left(1-\alpha\right)}\right)^{3/(1-\alpha)} \tag{9}$$

III. Results

Effective thermal conductivities from models are given in Figure 1. Qualitative evaluations are provided after the presentation of figures.

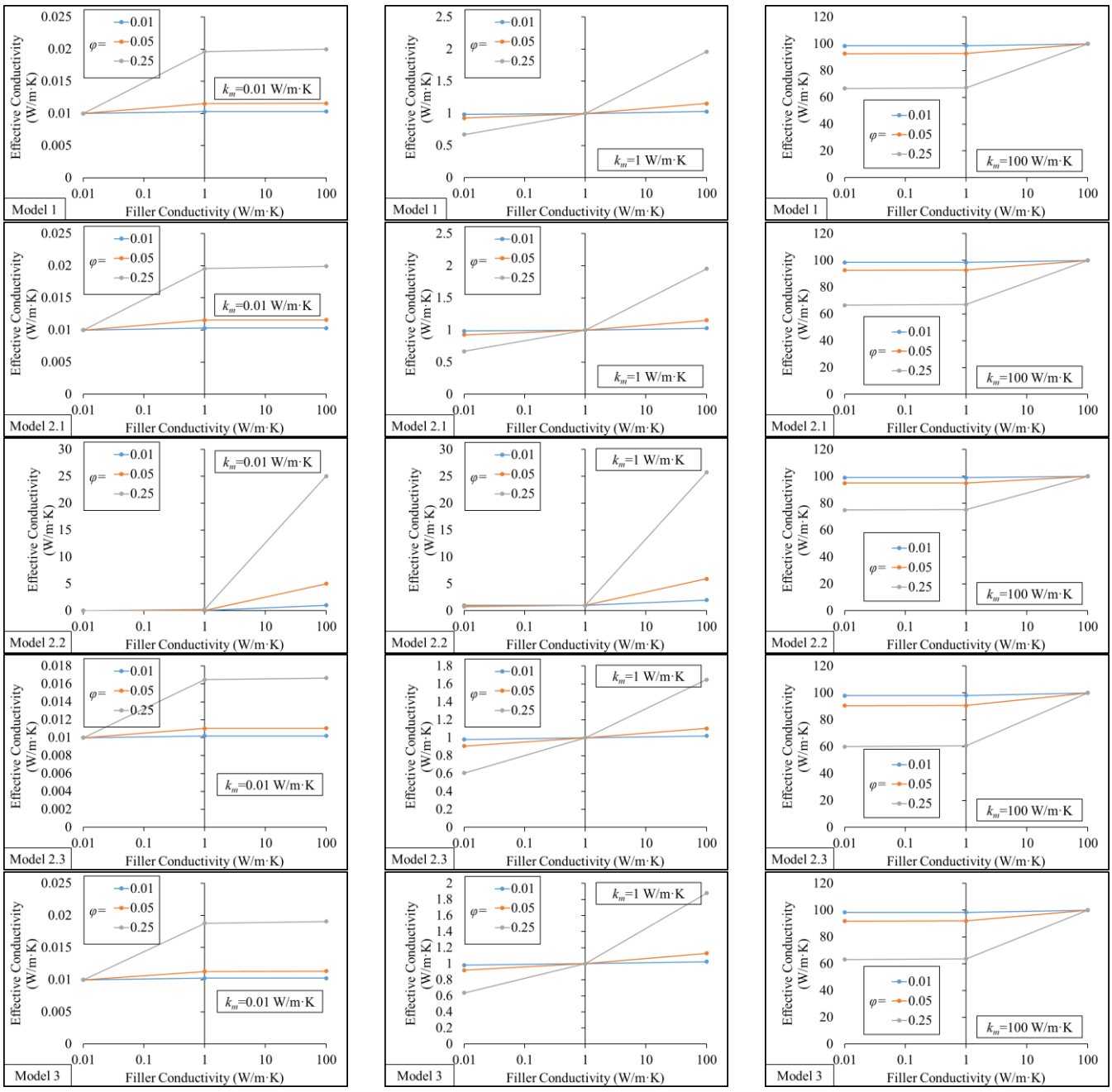

Figure 1: Effective thermal conductivities according to Models 1, 2, and 3.

Figure 1 shows that principal models for low volume fraction ratio composites (<0.25) can be predicted/calculated accurately by means of Models 1, 2, and 3. Only slight differences can be mentioned between model results. However, effective thermal conductivity values from Model 2.2 are clearly different from remaining since Model 2.2 is for fillers aligned with a certain axis of the composite material while the length of the fillers in the composite has the same length with the matrix at that axis. In the case of Model 2.2, heat flux is applied parallel to the filler orientation. This mode can be analogue to electrical current flowing in two separate wires.

Model 4 was fitted to Model 3 results with least squares. At that instance, parameter values of a and h become 1848.67 since they have the same effect on the model expression in terms of mathematics. However, particle size a should be much smaller in real-world applications. Therefore, when a is fixed to "0.01" value, h becomes a very large number, i.e., 341×10^6. Nevertheless, it can be reasoned that such small scales at the interfaces necessitate very big numerical values in order to simulate interface thermal resistance values.

In the case of Model 5, the α parameter for dimensionless interfacial thermal resistance was found about 0.0957 by fitting effective thermal conductivity results to Model 3 results.

IV. Conclusion

In this proceeding, literature was surveyed in order to compare mathematical models for determining effective

thermal conductivity values of composites for low volume fraction fillers. Three models were directly compared with each other by using hypothetical thermal conductivities of constituents and volume fractions up to 0.25. Two additional models were used in order to determine their unknown coefficients and constants by means of the effective thermal conductivities of Model 3. Following remarks can be given as results of the literature review and numerical trials.

i. The volume fraction of fillers has a major effect on effective thermal conductivity. There can be major differences when a threshold value of fillers is exceeded.
ii. Principal early models with their simple structures are sufficient for predicting and interpolating effective thermal conductivity values of composites for low volume fractions.
iii. The real engineering and research problem arises when volume fraction exceeds the percolation threshold since heat bridges can occur through fillers. In those instances, the literature suggests numerical approaches.

REFERENCES

[1] K. Pietrak, and T. S. Wisniewski, "A review of models for effective thermal conductivity of composite materials," *Journal of Power Technologies*, vol. 95, iss. 1, pp. 14, 2015.

[2] V. Nieberlein, "Thermal conductivity enhancement of epoxies by the use of fillers," *IEEE Transactions on Components, Hybrids, and Manufacturing Technology*, vol. 1, iss. 2, pp. 172-176, 1978.

[3] E. Yamada, and T. Ota, "Effective thermal conductivity of dispersed materials," *Wärme-und Stoffübertragung*, vol. 13, iss. 1, pp. 27-37, 1980.

[4] D.M. Bigg, "Thermally conductive polymer compositions," *Polymer composites*, vol. *7*, iss. 3, pp. 125-140, 1986.

[5] Y. Agari, M. Tanaka, S. Nagai, and T. Uno, "Thermal conductivity of a polymer composite filled with mixtures of particles," *Journal of Applied Polymer Science*, vol. 34, iss. 4, pp. 1429-1437, 1987.

[6] Y. Agari, A. Ueda, M. Tanaka, and S. Nagai, "Thermal conductivity of a polymer filled with particles in the wide range from low to super-high volume content," *Journal of Applied Polymer Science*, vol. 40, iss. 5-6, pp. 929-941, 1990.

[7] C.F. Matt, and M.E. Cruz, "Effective thermal conductivity of composite materials with 3-D microstructures and interfacial thermal resistance," *Numerical Heat Transfer, Part A: Applications*, vol. 53, iss. 6, pp. 577-604, 2007.

Fabrication of PVDF Membranes Modified with Dopamine/Zinc Oxide and Investigation of Lead Removal from Aqueous Solutions

I. S. UCEL[1] and E. DEMIREL[1]

[1] Eskisehir Technical University, Department of Chemical Engineering, Eskisehir/Turkey, iremsevimucel@eskisehir.edu.tr

[1] Eskisehir Technical University, Department of Chemical Engineering, Eskisehir/Turkey, elifyildiz@eskisehir.edu.tr

Abstract **- The global water challenge has been an important issue in the last decade as the world population and economies of developing countries expand and existing water and wastewater treatment technologies and infrastructure are becoming critical for providing adequate water quality to meet human and environmental needs. Ultrafiltration (UF) membranes have long been a leading separation technology with a strong historic track record for a wide range of applications such as treatment of ground water and wastewater. The fast development of techniques for producing nanostructured materials and nanoparticles has led to breakthroughs in membrane preparation. In the present work, polyvinylidene fluoride (PVDF) based nanocomposite membranes modified with zinc oxide (ZnO), polydopamine (PDA) and ZnO/PDA powders were fabricated using phase inversion technique. ZnO/PDA nanoparticles, which were synthesized via sol-gel method, were incorporated into membrane matrix by blending method and PDA powders were incorporated into PVDF membrane matrix by coating method. Surface and cross-sectional morphology, thermal behavior, and mechanical strength of the membranes were characterized using several analytical techniques and instruments. Membrane filtration performance was tested in terms of water flux, sodium alginate (SA) rejection and antifouling properties in comparison to those of pristine PVDF membrane. Moreover, lead (Pb^{+2}) removal of the prepared membranes from aqueous solutions complexed with chitosan was investigated. Although modification of pristine PVDF membrane using different powders could not lead to a significant improvement in water flux and SA rejections, anti-fouling properties could be enhanced markedly. PVDF/ZnO/PDA membrane was found to exhibit the best performance in filtration experiments with 92% flux recovery ratio and 97% SA rejection and had the highest lead removal (88.5%) from aqueous solutions.**

Keywords **- Membrane, nanoparticle, zinc oxide, dopamine, lead removal**

I. INTRODUCTION

Lead pollution in water has become a matter of great concern due to its high toxicity in the aqueous environment and easy accumulation in human body. Lead can damage the nervous system, kidneys and reproductive system, and excessive lead intake can cause stomach pain, headache, mental system damage, cancer and even death [1, 2, 3]. World Health Organization (WHO) determined the maximum contaminant level (MCL) of Pb^{+2} in drinking water to be 15 μg/L [3].

There are many technologies to separate lead from water such as chemical precipitation, coagulation-flocculation, adsorption, membrane technology, ion exchange, and electrochemical treatment [3]. The application of membrane separation processes to improve water quality and treatment capacity has become widespread. Membranes can be defined as semi-permeable barriers where selective separation and transport is carried out [4, 5]. Ultrafiltration (UF), which is one of the most common membrane processes applied especially for water purification, should be modified to ensure the separation of heavy metal ions from aqueous solutions [1, 6, 7]. Membrane fouling is the most common problem in membrane technologies, which can reduce the permeability and leads to considerable technical problems such as requirement for higher pressures and harsh cleaning processes. Incorporation of fillers into the membrane matrix by physical blending, chemical grafting and surface modifications improves the hydrophilicity, permeability and contamination resistance of the membrane [8]. Zinc oxide (ZnO) has been used as a membrane filler for its physical and chemical properties, including its antibacterial activity [9, 10]. Also, dopamine (DA), a bio-inspired substance that has been known to improve the properties of membrane has recently attracted the attention of scientists. DA is a very hydrophilic molecule and biocompatible with catechol and amino groups. It is a highly suitable material for surface modification since it self-polymerizes to polydopamine (PDA) under alkaline conditions on almost any surface regardless of its morphology or chemical composition [11, 12]. In addition, PDA coating brings advantages such as electrostatic attraction, chelation and covalent bonds with the surface [13].

In this study, polyvinylidene fluoride (PVDF) based nanocomposite membranes modified with zinc oxide (ZnO), polydopamine (PDA) and ZnO/PDA powders were fabricated using phase inversion technique. In this context, ZnO and ZnO/PDA powders were incorporated into the membrane

matrix in certain proportions by blending method, and PDA was added by coating method. Membrane characterization in terms of morphology, porosity, mean pore size, bulk thermal stability and mechanical strength were carried out using several equipments and analytical techniques and filtration performance of the nanocomposite membranes was determined in terms of water flux, solute rejection, and anti-fouling characteristics in comparison to those of pristine PVDF membrane. In addition, pristine PVDF membrane and fabricated nanocomposite membranes were tested for lead removal from aqueous solutions using polymer assisted ultrafiltration technique.

II. Materials and Methods

A. Chemicals

PVDF (MW = 534,000 g.mol^{-1}), polyethylene glycol (PEG, MW= 6,000 Da), 3,4-dihydroxyphenethylamine (dopamine hydrochloride), Tris(hydroxymethyl) aminomethane (Tris), ZnO (particle size <100 nm), chitosan (from shrimp shells, ≥75%) and sodium alginate (SA) were purchased from Sigma-Aldrich. 1-Methyl-2-pyrrolidone (NMP, >99%) and lead nitrate ($PbNO_3$) was supplied by Alfa Aesar and Carlo Elba, respectively. All the other chemicals were used as received without further treatment. Deionized (DI) water was produced by a Milli-Q system (Millipore, US).

B. Fabrication of PVDF membranes

Pristine PVDF, ZnO and ZnO/PDA doped nanocomposite membranes were fabricated using blending and phase inversion with immersion precipitation technique [12]. ZnO/PDA nanoparticles were prepared by the sol-gel method using ZnO and dopamine hydrochloride (DA) [12]. In order to prepare membrane casting solutions, ZnO or ZnO/PDA nanoparticles (0.5wt.% of PVDF) were added into NMP and stirred in ultrasonic bath for 3 and 1 hours, respectively. After the addition of PVDF and PEG, the resulting mixture was stirred at 70°C for 48 hours to get a homogenous solution. The casting solution was poured on a glass plate and cast into a film of 150 μm thickness using an adjustable casting blade and the thin film was immediately immersed into a coagulation bath of nonsolvent, i.e. water. After complete solidification, the membrane was moved into DI water to extract the residual NMP. All the membranes were dried in an oven at 50°C for 24 hours prior to characterization tests. To investigate the effect of PDA coating, pristine PVDF membrane was immersed into 2 g/L DA solution for 24 hours. For this purpose, 0.4 g DA was added into 200 mL ethanol-Tris-HCl buffer solution (1:1, v/v) and the pH was adjusted to 8.5. The solution was stirred at 25°C for 24 hours, and DA in the solution self-polymerized into PDA. Finally, nanocomposite membranes were washed with DI water and ethanol to remove the possible residual PDA particles [14].

The compositions of the membranes prepared either by blending and coating methods are listed in Table 1.

Table 1: The compositions of membranes

Membran	PVDF (g)	PEG (g)	NMP (g)	Additives (%wt.)
PVDF	9	0.5	40.500	-
PVDF/ZnO	9	0.5	40.455	0.5 ZnO
PVDF/ZnO/PDA	9	0.5	40.455	0.5 ZnO/PDA
PVDF/PDA	9	0.5	40.455	PDA

C. Characterization

The morphology of the top surface and cross-section of the pristine and nanocomposite membranes were determined by Scanning Electron Microscopy (SEM) (Hitachi Regulus 8230).

Membrane porosity was calculated based on the ratio of the total pore volume to the geometric volume of the membrane using the following equation [16].

$$\varepsilon = \frac{W_w - W_d}{\rho_w(\pi r^2 l)} * 100\% \quad (1)$$

where W_w and W_d are the weights of the wet and dry membranes (g), respectively, ρ_w is the density of the water at room temperature (g/cm^3), r is the radius (cm) and l is the thickness (cm) of the membrane.

Mean pore diameter of the membrane was calculated using the Guerout-Elford-Ferry equation below [17, 18].

$$a = \sqrt{\frac{(2.9 - 1.75\varepsilon) * (8\mu l Q_w)}{\varepsilon A \Delta P}} \quad (2)$$

where denotes the mean pore diameter (m), ε is the porosity, μ is the viscosity of the water to be filtrated at room temperature (Pa.s), l is the thickness of the membrane (m), Q_w is the water flux (m^3/s), A is the filtration area of the membrane (m^2), and ΔP is the transmembrane pressure (Pa).

The addition of ZnO and ZnO/PDA fillers and the effect of PDA coating on thermal behavior of the pristine membrane were investigated by thermogravimetric analysis (TGA, Perkin Elmer (STA) 6000). The mechanical stabilities of the membranes were determined using a single-column mechanical tensile tester (Instron 5944) and the results are reported in terms of Young modulus (MPa), tensile strength (MPa) and elongation at break (%).

D. Separation performance of membranes

Water flux values of the membranes were measured using a dead-end ultrafiltration system. A membrane sample was placed in a stirred cell (Millipore, Amicon Stirred Cell), which had an effective surface area of 28.7 cm^2 and a capacity of 200 mL. Each membrane was compacted at 0.21 MPa for 1 h prior to performing the ultrafiltration experiments. Then the pressure was lowered to 0.07 MPa and all the ultrafiltration experiments were carried out at this pressure. The solution in the cell was stirred at 400 rpm to minimize concentration polarization [16]. Permeate was weighed in one minute time intervals using a balance, and the data was collected using a software. The water flux was calculated using the following equation.

$$J_{w,1} = \frac{\Delta V}{A * \Delta t} \quad (3)$$

E-ISBN: 978-625-44427-7-3

where $J_{w,1}$ is the pure water flux (L/m^{2}h), ΔV is volume change of the permeate (L) in one minute interval, A is the membrane filtration area (m^2), and Δt is the permeation time (h).

Rejection tests of the fabricated membranes were carried out using SA solution with a concentration of 20 mg/L. Concentrations of the collected permeate and feed for each membrane were determined quantitatively using a TOC-L Analyzer (Shimadzu, Japan) and calculated using the following equation.

$$R(\%) = \left(1 - \frac{C_P}{C_f}\right) * 100 \quad (4)$$

where C_p and C_f are the concentrations of the permeate and feed solutions, respectively.

In order to determine the anti-fouling property, the membrane sample was subjected to SA solution for 4 hours, washed with DI water and the flux was measured again. The anti-fouling property was interpreted in terms of flux recovery ratio (FRR), which was calculated using the equation below.

$$FRR\ (\%) = \frac{J_{w,2}}{J_{w,1}} * 100 \quad (5)$$

where $J_{w,1}$ and $J_{w,2}$ denote the pure water flux and water flux after the SA fouling test (m^3/m^2.s), respectively.

E. Lead removal efficiency

The performance of the fabricated membranes was tested for Pb^{+2} removal efficiency from aqueous solutions using polymer assisted ultrafiltration method. The Pb^{2+} ions were filtered through the membranes by converting them into a chitosan-Pb complex using chitosan as chelating agent, which is a natural linear polymer [19, 20]. For this purpose, 10 ppm Pb^{+2}solution was added to chitosan solutions of different concentrations (500 ppm and 1000 ppm) in 0.4 vol% acetic acid and the resulting mixture is stirred for 24 hours to form a complex. pH was adjusted to the desired value using either 0.1 M NaOH or 0.1 M HNO_3 solutions. The concentrations of the permeate and the feed were determined using UV-Vis Spectrophotometer (Shimadzu, UV 2600/2700) at a wavelength of 200 nm.

III. Result and Discussion

A. Characterization of membranes

Morphology

The cross-section and surface morphology of the pristine and nanocomposite membranes were determined by SEM imaging analysis and the results are given in Figure 1 and Figure 2, respectively. The surface porosity of the pristine PVDF membrane was the highest and decreased with the addition of nanoparticles to the membrane matrix. A significant amount of ZnO clusters were observed on the surface of the PVDF/ZnO membrane, indicating that ZnO was not uniformly distributed in the matrix due to its poor interaction with PVDF [21]. However, incorporation of functional ZnO/PDA powders to the membrane matrix enhanced the interaction of PDA chains with PVDF, which in turn led to a uniform distribution of fillers in the matrix. As also shown in Figure 1c, no aggregates were observed on the membrane surface. PVDF/PDA membrane had the lowest porosity with significant amounts PDA clusters on the coating surface [22].

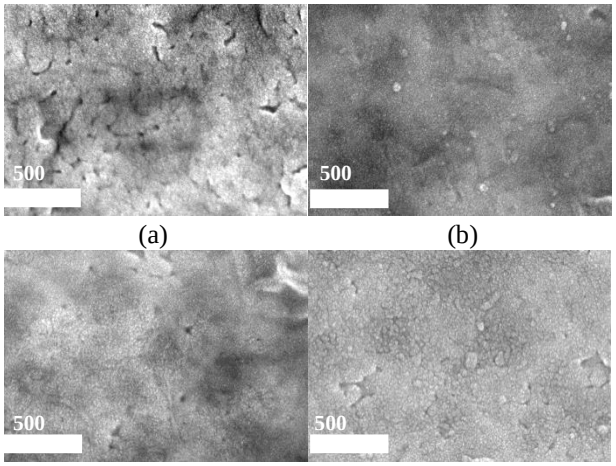

(a) (b) (c) (d)

Figure 1: SEM images of the surface of membranes
(a) PVDF, (b) PVDF/ZnO, (c) PVDF/ZnO/PDA, (d) PVDF/PDA

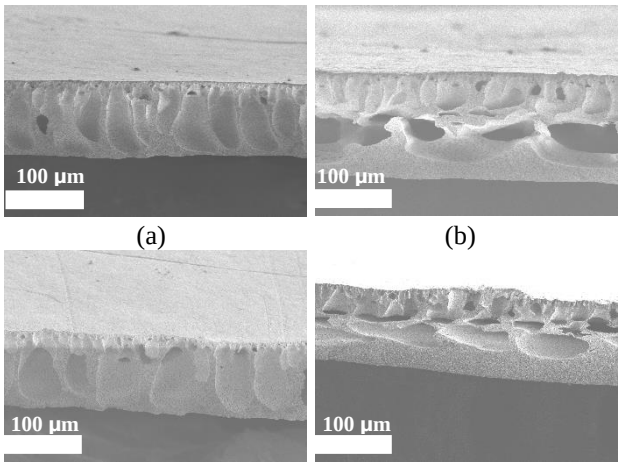

(a) (b) (c) (d)

Figure 2: Cross-section SEM images of the membranes
(a) PVDF, (b) PVDF/ZnO, (c) PVDF/ZnO/PDA, (d) PVDF/PDA

Table 2: Some morphological properties of membranes

Membran	Porosity (%)	Mean pore diameter (nm)	Thickness (µm)
PVDF	85.4	14.4	73
PVDF/ZnO	84.6	14.1	77
PVDF/ZnO/PDA	96.1	12.8	75
PVDF/PDA	93.3	10.5	74

As seen in Figure 2, all membranes consist of an active upper layer with a low pore density and a support layer consisting of larger macro pores. The finger-like structures of the pristine PVDF membrane extended along the membrane cross-section. However, with the addition of ZnO to the matrix, as the size of the finger-like pore sizes were shortened, macro porous gaps occurred in the lower sections. By adding

ZnO/PDA powders to the membrane matrix, the fingerlike pore sizes extended and expanded along the cross section, similar to that of the pristine PVDF membrane. Due to the non-uniform distribution of PDA powders, not enough finger-like pores have been detected in the cross-section of the PVDF/PDA membrane, and macro pore formation is observed at the membrane base.

As seen in Table 2, the porosity and mean pore diameter of the PVDF/ZnO nanocomposite membrane (84.6% and 14.1 nm, respectively) were similar to those of the pristine PVDF membrane (85.4% and 14.4 nm, respectively) since ZnO nanoparticles could not be distributed evenly over the membrane surface and finger-like pores. The PVDF/ZnO/PDA membrane had the highest porosity (96.1%) with comparatively smaller mean pore size indicating the existence of large number of smaller pores in the matrix. The mean pore diameter (10.5 nm) of the PVDF/PDA membrane was the lowest since a long coating time may have caused the formation of a thick PDA layer on the surface or probably PDA aggregates clogged the membrane pores [23]. Morphological properties of membranes were in good agreement with the water permeability values.

TG analysis

Thermal properties of the fabricated membranes investigated using TGA analysis are given in Figure 3. The degradation of the pristine membrane occurred at about 430-500°C with a mass loss of 65%. Due to the strong interaction of ZnO/PDA powders with the polymer chains, decomposition of the PVDF/ZnO/PDA nanocomposite membrane was observed in the range of 470-510°C [24, 25].

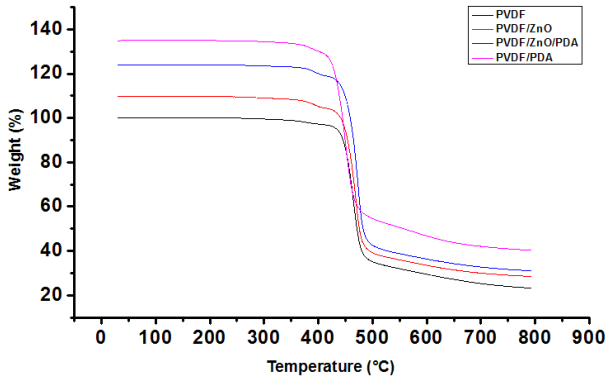

Figure 3: TGA thermograms of the fabricated membranes

Mechanical properties

The mechanical properties of the pristine PVDF and nanocomposite membranes were evaluated by Young's modulus (MPa), tensile strength (MPa) and elongation at break (%) and the results are given in Table 3.

Table 3: Mechanical properties of the membranes

Membrane ID	Young's modulus (MPa)	Tensile strength (MPa)	Elongation at break (%)
PVDF	67.1	1.89±0.35	14.5
PVDF/ZnO	117.8	2.23±0.49	10.4
PVDF/ZnO/PDA	98.9	2.15±0.43	19.0
PVDF/PDA	61.9	1.69±0.05	12.0

The mechanical properties of porous membranes depend mainly on porosity and mean pore diameter for porous membranes. As shown in Table 3, the Young modulus of the pristine PVDF membrane was 67.1 MPa and increased with the addition of ZnO and ZnO/PDA powders to the membrane matrix. The PVDF/ZnO membrane had the highest Young's modulus value, which might be attributed to its comparatively low porosity [26]. The tensile strength of the PVDF/ZnO and PVDF/ZnO/PDA membranes had higher values in comparison to that of pristine PVDF membrane since more energy would be required to break the bonds between ZnO and PVDF due to the fact that ZnO nanoparticles increased the rigidity of polymer chains [10]. The elongation at the break is an indicator of the elasticity of the material. Elongation at break of the PVDF membrane increased from 14.5% to 19.0% with the addition of ZnO/PDA powders into the membrane matrix since PDA was able to absorb energy during the tensile test, thereby leading to a decrease in the fragility of the membranes [27, 28]. Non-uniform distribution of PDA fillers on the surface caused the formation of weak stress zones, which in turn resulted in a poor mechanical stability of the PVDF/PDA membrane.

B. Separation performance of membranes

Separation performance of the fabricated membranes was determined in terms of water flux, rejection and anti-fouling properties.

Water flux and SA rejections of the fabricated membranes are shown in Figure 4.

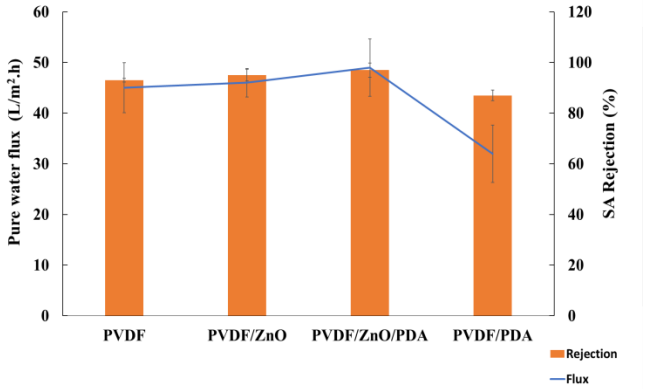

Figure 4: Water flux and SA rejections of the fabricated membranes

According to Figure 4, water flux values of pristine PVDF, PVDF/ZnO, PVDF/ZnO/PDA and PVDF/PDA membranes were determined as 45 L/m^{2}h, 46 L/m^{2}h, 49 L/m^{2}h and 32

E-ISBN: 978-625-44427-7-3

L/m^2h, respectively. This result showed that modification of PVDF matrix with nanoparticles resulted in no significant change in water flux, whereas surface coating resulted in a reduction in the flux. This was supported by SEM analysis and porosity calculations.

The SA removal of pristine PVDF membrane increased from 93% to 95% and 97%, respectively, with the addition of ZnO and ZnO/PDA fillers to the membrane matrix, which was attributed to the improved hydrophilicity of the matrix. The increase in hydrophilicity with the addition of fillers reduced the interaction between SA and the membrane surface, preventing the penetration of contaminant molecules through modified membranes during SA filtration [29, 30].

FRR values of the fabricated membranes are given in Figure 5. The FRR of the pristine PVDF membrane was as low as 51% due to the extremely hydrophobic nature of PVDF. Modification of membrane matrix with ZnO, PVDF/ZnO and PDA increased the FRR values to 57%, 92%, and 70%, respectively. The negatively charged groups (-OH) present in ZnO/PDA nanoparticles repel the negative ions in the SA foulant solution reducing adsorption of the particles onto the membrane surface and internal pores, and therefore the antifouling properties were enhanced [31]. In addition, hydration layer induced on the membrane surface due to the presence of hydrophilic fillers would prevent SA molecules from attaching to the membrane surface [32]. The FRR value of PVDF/PDA membrane was not as high as PVDF/ZnO/PDA membrane due to the uneven distribution of PDA fillers in the matrix.

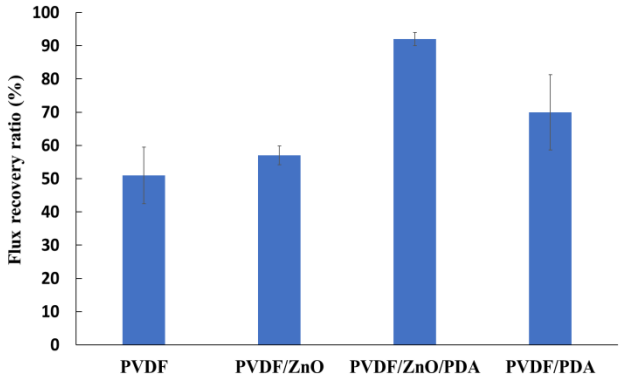

Figure 5: FRR values of the fabricated membranes after SA fouling

C. *Lead removal efficiency*

Since the pore sizes of the ultrafiltration membranes were not appropriate to separate Pb^{+2} ions with a high efficiency, chitosan as the chelating agent was used for binding the metal to form macromolecular complexes. The removal performances of the fabricated membranes using lead-chitosan complex solutions were investigated for a constant Pb^{+2} concentration of 10 ppm and a pH value of 9.0 for different Pb/chitosan ratios of 1:50 and 1:100. The results are given in Figure 6.

The formation of the chitosan-metal ion complex occurs primarily through the amino groups of chitosan, which act as ligands [33]. The interaction of metal ions with -OH and $-NH_2$ connects one or more chitosan chains. The complex structure formed has a larger diameter than the membrane pores, which allows the Pb^{+2} ions to be retained by the membrane [34, 35]. As seen in Figure 6, Pb^{+2} removal efficiency increased as a result of addition of different fillers into pristine membrane matrix. Moreover, doubling the concentration of chitosan led to a marked increase in the removal efficiency of Pb^{+2} from aqueous solutions in the case of all fabricated membranes. The lead removal performances of pristine PVDF, PVDF/ZnO, PVDF/ZnO/PDA and PVDF/PDA membranes were determined as 42%, 63.5%, 88.5% and 75.5%, respectively for a Pb-chitosan ratio of 1:100. Among the fabricated membranes, PVDF/ZnO/PDA membrane exhibited the highest Pb^{+2} removal efficiency, which was probably due to the combined effects of uniform distribution of ZnO/PDA nanoparticles on the membrane matrix, especially on the surface and the small pore diameter of the PVDF/ZnO/PDA membrane.

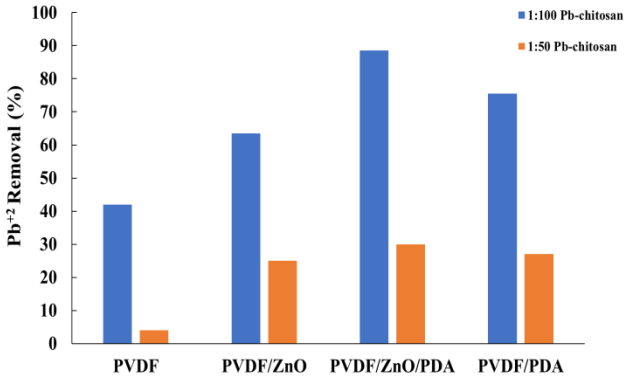

Figure 6 : Pb^{2+} removal performance of membranes at different Pb/chitosan ratios (pH:9)

REFERENCES

[1] Xu, W., Sun, X., Huang, M., Pan, X., Huang, X., & Zhuang, H. (2020). Novel covalent organic framework/PVDF ultrafiltration membranes with antifouling and lead removal performance. *Journal of Environmental Management*, *269*, 110758.

[2] Sheng, P. X., Ting, Y. P., Chen, J. P., & Hong, L. (2004). Sorption of lead, copper, cadmium, zinc, and nickel by marine algal biomass: characterization of biosorptive capacity and investigation of mechanisms. *Journal of colloid and interface science*, *275*(1), 131-141.

[3] He, J., Xiong, D., Zhou, P., Xiao, X., Ni, F., Deng, S., & Luo, L. (2020). A novel homogenous in-situ generated ferrihydrite nanoparticles/polyethersulfone composite membrane for removal of lead from water: Development, characterization, performance and mechanism. *Chemical Engineering Journal*, *393*, 124696.

[4] Mulder, M., & Mulder, J. (1996). *Basic principles of membrane technology*. Springer Science & Business Media.

[5] Aslan, M. (2016). Membran Teknolojileri. *T.C. Çevre ve Şehircilik Bakanlığı*. 57-218.

[6] Gebru, K. A., & Das, C. (2018). Removal of chromium (VI) ions from aqueous solutions using amine impregnated TiO_2 nanoparticles modified cellulose acetate membranes. *Chemosphere*, *191*, 673-684.

[7] Fang, X., Li, J., Li, X., Pan, S., Zhang, X., Sun, X., ... & Wang, L. (2017). Internal pore decoration with polydopamine nanoparticle on polymeric ultrafiltration membrane for enhanced heavy metal removal. *Chemical Engineering Journal*, *314*, 38-49.

[8] Bai, H., Wang, X., Zhou, Y., & Zhang, L. (2012). Preparation and characterization of poly (vinylidene fluoride) composite membranes blended with nano-crystalline cellulose. *Progress in Natural Science: Materials International*, *22*(3), 250-257.

[9] Ursino, C., Castro-Muñoz, R., Drioli, E., Gzara, L., Albeirutty, M. H., & Figoli, A. (2018). Progress of nanocomposite membranes for water treatment. *Membranes*, *8*(2), 18.

[10] Hong, J., & He, Y. (2012). Effects of nano sized zinc oxide on the performance of PVDF microfiltration membranes. *Desalination*, *302*, 71-79.

[11] Shi, H., He, Y., Pan, Y., Di, H., Zeng, G., Zhang, L., & Zhang, C. (2016). A modified mussel-inspired method to fabricate TiO2 decorated superhydrophilic PVDF membrane for oil/water separation. *Journal of Membrane Science*, *506*, 60-70.

[12] Zhang, Q., Cui, Z., & Li, W. (2020). High permeability poly (vinylidene fluoride) ultrafiltration membrane doped with polydopamine modified TiO_2 nanoparticles. *Chinese Journal of Chemical Engineering*, *28(12)*, 3152-3158.

[13] Wang, Z., Yang, H. C., He, F., Peng, S., Li, Y., Shao, L., & Darling, S. B. (2019). Mussel-inspired surface engineering for water-remediation materials. *Matter*, *1(1)*, 115-155.

[14] Gu, X., Zhang, Y., Sun, H., Song, X., Fu, C., & Dong, P. (2015). Mussel-inspired polydopamine coated iron oxide nanoparticles for biomedical application. *Journal of Nanomaterials*, 2015.

[15] Yue, Q., Wang, M., Sun, Z., Wang, C., Wang, C., Deng, Y., & Zhao, D. (2013). A versatile ethanol-mediated polymerization of dopamine for efficient surface modification and the construction of functional core–shell nanostructures. *Journal of Materials Chemistry B*, *1*(44), 6085-6093.

[16] Demirel, E., Zhang, B., Papakyriakou, M., Xia, S., & Chen, Y. (2017). Fe2O3 nanocomposite PVC membrane with enhanced properties and separation performance. *Journal of membrane science*, *529*, 170-184.

[17] Wu, G., Gan, S., Cui, L., & Xu, Y. (2008). Preparation and characterization of PES/TiO2 composite membranes. *Applied Surface Science*, *254*(21), 7080-7086.

[18] Vatanpour, V., Madaeni, S. S., Moradian, R., Zinadini, S., & Astinchap, B. (2012). Novel antibifouling nanofiltration polyethersulfone membrane fabricated from embedding TiO2 coated multiwalled carbon nanotubes. *Separation and purification technology*, *90*, 69-82.

[19] Llorens, J., Pujola, M., & Sabaté, J. (2004). Separation of cadmium from aqueous streams by polymer enhanced ultrafiltration: a two-phase model for complexation binding. *Journal of Membrane Science*, *239*(2), 173-181.

[20] Juang, R. S., & Chiou, C. H. (2000). Ultrafiltration rejection of dissolved ions using various weakly basic water-soluble polymers. *Journal of Membrane Science*, 177(1-2), 207-214

[21] Popa, A., Toloman, D., Stan, M., Stefan, M., Radu, T., Vlad, G., & Pana, O. (2021). Tailoring the RhB removal rate by modifying the PVDF membrane surface through ZnO particles deposition. *Journal of Inorganic and Organometallic Polymers and Materials*, *31*(4), 1642-1652.

[22] Syawaliah, S., Arahman, N., Riza, M., & Mulyati, S. (2018). The influences of polydopamine immersion time on characteristics and performance of polyvinylidene fluoride ultrafiltration membrane. In *MATEC Web of Conferences* (Vol. 197, p. 09007). EDP Sciences.

[23] Muchtar, S., Wahab, M. Y., Fang, L. F., Jeon, S., Rajabzadeh, S., Takagi, R., & Matsuyama, H. (2019). Polydopamine-coated poly (vinylidene fluoride) membranes with high ultraviolet resistance and antifouling properties for a photocatalytic membrane reactor. *Journal of Applied Polymer Science*, *136*(14), 47312.

[24] Ma, F. F., Zhang, N., Wei, X., Yang, J. H., Wang, Y., & Zhou, Z. W. (2017). Blend-electrospun poly (vinylidene fluoride)/polydopamine membranes: self-polymerization of dopamine and the excellent adsorption/separation abilities. Journal of Materials Chemistry A, 5(27), 14430-14443.

[25] Liebscher, J. (2019). Chemistry of polydopamine–scope, variation, and limitation. *European Journal of Organic Chemistry*, *2019*(31-32), 4976-4994.

[26] Manawi, Y. M., Wang, K., Kochkodan, V., Johnson, D. J., Atieh, M. A., & Khraisheh, M. K. (2018). Engineering the surface and mechanical properties of water desalination membranes using ultralong carbon nanotubes. *Membranes*, *8*(4), 106.

[27] Li, J. H., Ni, X. X., Zhang, D. B., Zheng, H., Wang, J. B., & Zhang, Q. Q. (2018). Engineering a self-driven PVDF/PDA hybrid membranes based on membrane micro-reactor effect to achieve super-hydrophilicity, excellent antifouling properties and hemocompatibility. Applied Surface Science, 444, 672-690

[28] Jiang, J. H., Zhu, L. P., Zhang, H. T., Zhu, B. K., & Xu, Y. Y. (2014). Improved hydrodynamic permeability and antifouling properties of poly (vinylidene fluoride) membranes using polydopamine nanoparticles as additives. *Journal of Membrane Science*, *457*, 73-81.

[29] Breite, D., Went, M., Prager, A., Schulze, A. (2015). Tailoring Membrane Surface Charges: A Novel Study on Electrostatic Interactions during Membrane Fouling. *Polymers*, **7**(10), 2017–2030.

[30] Rana, D., & Matsuura, T. (2010). Surface modifications for antifouling membranes. *Chemical Reviews*, 110(4), 2448-2471.

[31] Lalia, B. S., Kochkodan, V., Hashaikeh, R., & Hilal, N. (2013). A review on membrane fabrication: Structure, properties and performance relationship. *Desalination*, *326*, 77-95.

[32] Kumar, R., & Ismail, A. F. (2015). Fouling control on microfiltration/ultrafiltration membranes: Effects of morphology, hydrophilicity, and charge. *Journal of Applied Polymer Science*, 132(21).

[33] Krajewska, B. (2001). Diffusion of metal ions through gel chitosan membranes. *Reactive and Functional Polymers*, *47*(1), 37-47.

[34] Wang, X., Du, Y., Fan, L., Liu, H., & Hu, Y. (2005). Chitosan-metal complexes as antimicrobial agent: synthesis, characterization and structure-activity study. *Polymer Bulletin*, *55*(1), 105-113.

[35] Garba, M. D., Usman, M., Mazumder, M. A. J., & Al-Ahmed, A. (2019). Complexing agents for metal removal using ultrafiltration membranes: *Environmental Chemistry Letters*, 1-14.

E-ISBN: 978-625-44427-7-3

EFFECTS OF REDUCTION RATIO ON WIRE ROPE STRENGTH IN COMPACTED WIRE ROPE PRODUCTION

S.G. ESEN[1]

[1] Çelik Halat ve Tel Sanayii A.Ş, Kocaeli/TURKEY, sesen@celikhalat.com.tr

Abstract **- Compacted wire ropes have more load bearing capacities than the standard ropes with same diameters. Abrasion is less and expected life times are longer as they contact the reel surfaces in a larger area. The reduction ratio applied in the production of compacted wire rope affects the strength of the wire rope. In this study, the effects of different reduction ratios on steel wire rope strength were investigated. In this respect, the strength values of the rope in the 6x36WS IWRC composition compared to the pre-compact strength values and the different reduction ratios were compared.**

Keywords **- Compacted wire rope, High strength, Reduction ratio, 6x36WS IWRC**

I. INTRODUCTION

The compacted wire rope is obtained by die forming a standard rope or pressing it through a special machine. The compacting process applies to the outer strand of the wire rope to flatten the surface and increase the contact area of all strands [1]. The wires of the standard wire ropes are round, but after passing through the pressing, are flattened from the outside, and there is a softer wire rope with a smaller diameter [2].

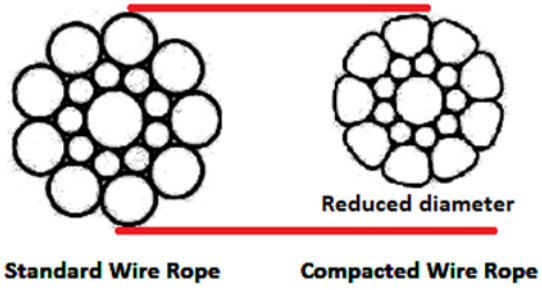

Figure 1: Standard wire rope and compacted wire rope [1]

The compacting process reduces the gaps between the wires of the wire rope and increases the metallic cross-sectional area so that a wire rope with a higher breaking load is obtained (Figure 1). Thus the compacted wire rope has a flat surface that provides a smoother and wider contact area. Because the wires and strands are more flat, they have more contact area with adjacent wires / strands and the increase of contact area reduces the force per unit area (Figure 2).

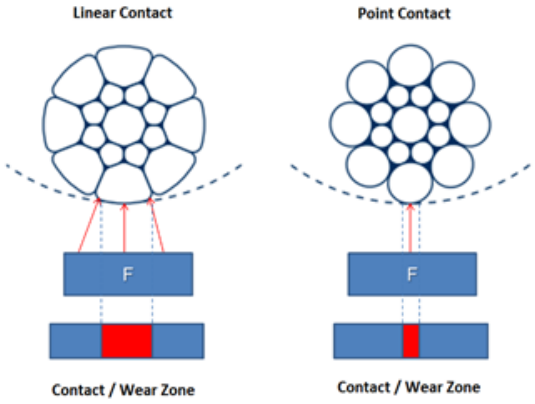

Figure 2: Linear and point contacts

Compacting of wire rope reduces the diameter while increasing strength, which means that a smaller diameter compacted wire rope will have the same strength and lifting capacity as a standard wire rope with a larger diameter (same construction) [1,2,3,4]. The smaller diameter also allows it to be used with smaller pulleys and drums and / or to reduce friction wear due to less contact with the pulley or drum. It also reduces the wear on the pulleys itself, thus extending the working life [5,6]. It is aimed to increase the wear resistance of the wire rope wires in contact with multilayer drums due to superposition (Figure 3).

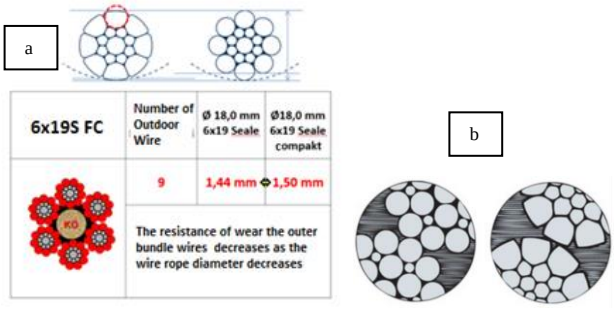

Figure 3: a)Diameters of standard and compacted wire ropes b) standard and compact ropes in the drum winding representations

In this study, the strengths of compacted ropes at different reduction ratios were investigated. Reduction ratios of 10%, 12% and 13% were applied in Ø32mm 6x36WS IWRC compacted steel wire rope production.

II. EXPERIMENTAL DETAILS

The steel material for the experimental studies were wt. 0.83% carbon composition wires (Table 1). After the application of the wire drawing process, the patented heat treatment was applied and the wires were drawing again to their final diameters.

Table 1: Steel chemical composition

C %	Mn%	Si%	P%	S%	Cu%	Cr%	Ni%	N%	V%
0.81	0.50	0.21	0.01	0.015	0.012	0.03	0.017	0.004	0.001

The properties of the wires and wire layers of the steel wire rope are given in Table 2. In the table, the wire rope composition shows the wire layers and the number of wires.

Table 2: Properties of wire of steel wire rope

Final Steel Wire Rope Diameter (mm)	Wire Place	Number	Steel Wire Rope Structure
32	1st Wire	1	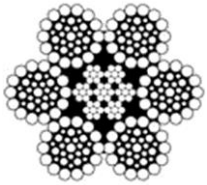
	2nd Wire	7	
	3rd Wire	7	
	4th Wire	7	
	5th Wire	14	

For the production of compacted steel wire ropes, the strands diameters must be determined. In this sense, as the reduction ratio increases, the diameter of the wires forming the strands increases. Wires and strands diameter according to reduction ratio are given in Table 3.

Table 3: Properties of wire of steel wire rope's strands

Wire Diameter Reduction 10% (mm)	Before 10% Reduction of Uncompacted Strand Dia. (mm)	Wire Diameter Reduction 12% (mm)	Before 12% Reduction of Uncompacted Strand Dia.(mm)	Wire Diameter Reduction 13% (mm)	Before 13% Reduction of Uncompacted Strand Dia. (mm)
2.2135619	10.90	2.2387637	11.03	2.2513647	11.09
1.5813103		1.5993138		1.6083156	
1.5813103		1.5993138		1.6083156	
1.1670765		1.1803639		1.1870076	
1.8824474		1.9038794		1.9145954	

The steel wire rope samples were tested at the universal tensile testing unit in accordance with EN 12185 - 1 standard. Subsequently, microstructures were observed in the stereo microscope (SM). Microscopic investigations were carried out at 100X magnification using a Nikon Eclipse stereo microscope.

III. RESULTS AND DISCUSSION

For Ø32.00 mm, 6x36WS IWRC compacted steel wire rope production, The final strand diameter is determined as 10.34 mm. At this point, 10.34 mm strands was reached by applying three different reduction ratios to three different strands diameter. These diameters were given in Table 4.

Table 4: Diameters of strands before and after reduction

Before 10% Reduction of Uncompacted Strand Diameter (mm)	Before 12% Reduction of Uncompacted Strand Diameter (mm)	Before 13% Reduction of Uncompacted Strand Diameter (mm)	After Reductions of Final Strand Diameter (mm)
10.90	11.03	11.09	10.34

The diameter increasing according to the reduction ratios is as indicated in Figure 4.

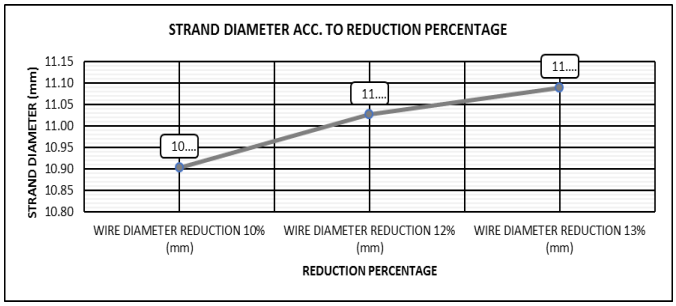

Figure 4: Strand diameter according to reduction percentage

The minimum breaking load of the uncompacted steel wire rope is 715 kN. Therefore, increasing the amount of metal in the cross-sectional area of the steel wire ropes that are compacted and the breaking load is provided increasing. The minimum breaking loads and the obtained percentage increasing of minimum breaking loads according to the applied reduction ratio are given in Table 5.

Table 5: Minimum breaking loads of compacted steel wire ropes

Reduction Percentage	MBL(kN)	Distinction Percentage
Uncompacted Steel Wire Rope	715	-
10%	843	18%
12%	862	21%
13%	897	25%

The minimum breaking load increases according to the compacting reductions are given in Figure 5. It is clearly seen that the rate of reduction load is proportional to the change of the breaking load. According to the results obtained in experimental studies, the breaking load of 897 kN is reached in 13% reduction ratio. Increase of the breaking load represents 25% strength increase compared to the

uncompacted steel wire rope.

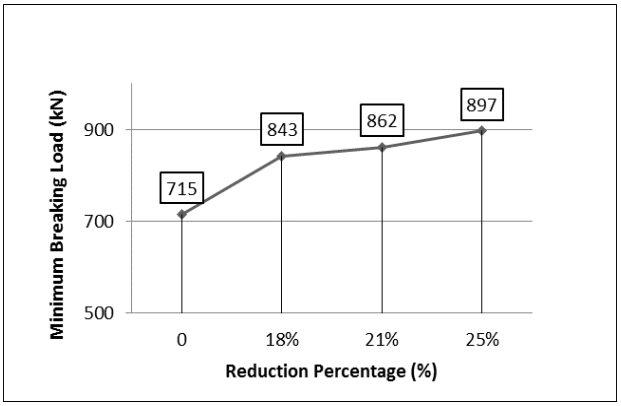

Figure 5: Minimum breaking loads of compacted steel wire ropes

Figure 6a shows that increased amount of metal in cross section area at strand that provides increase strength. Also, surface structure that provides abrasion resistance shows in Figure 6b. The compacted wire rope has a flat surface that provides a smoother and wider contact area. Because the wires and strands are more flat, they have more contact area with adjacent wires / strands and the increase of contact area reduces the force per unit area.

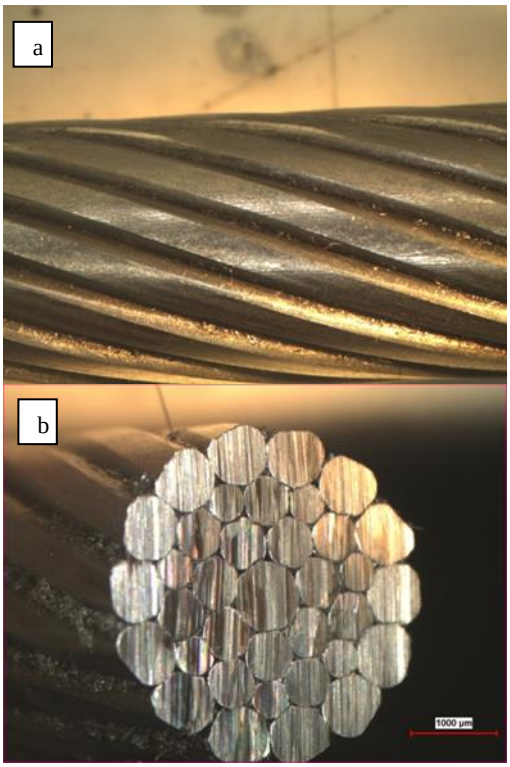

Figure 6: Microscopic examination of after compacted strand

IV. CONCLUSION

High strength properties and abrasion resistance are required that in steel wire ropes used in fishing, crane and drilling machines. In order to increase minimum breaking loads in steel wire ropes, various methods are used for compacting process. In this study, strength (minimum breaking load) changes were investigated by applying different reductions to the strands that forming the steel wire rope. For this purpose, 10%, 12% and 13% reduction was applied to the strands. The applied increasing reduction ratio has provided increased the breaking load.

A. References

Number citations consecutively in square brackets [1]. Multiple references should be numbered as [2, 3] or [1-4].

Abbreviations and Acronyms

Define abbreviations and acronyms the first time they are used in the text, even after they have already been defined in the abstract. Abbreviations such as SI, ac, and dc do not have to be defined. Do not use abbreviations in the title unless they are unavoidable (for example, “ICENTE 2017” in the title of this article).

ACKNOWLEDGMENT

The authors would like to thank the Çelik Halat ve Tel Sanayii A.Ş for providing laboratory facilities for this research.

REFERENCES

[1] K.Feyrer, Wire Ropes: Tension, Endurance, Reliability. Berlin: Springer-Verlag, 2007.
[2] V. F. Danenko, L. M. Gurevich, E. Y. Kushkina, E. B. Glaadskikh, “New applicaations compacted steel strands and wire rope”, Steel in translation, vol. 46, pp. 757-763, 2016.
[3] Y. Guo, D. Zhang, X. Yang, C. Feng, S. Ge, “Experimental research on effet of wire rope transverse vibration on transmission stability in friction hoisting system”, Tribology International, vol. 115, pp. 233-245, 2017
[4] I. Argatov, “Response of wire rope strand to axial and torsional loads. Asymtotic modeling of the effect of interwire contact deformation” International Journal of Solids and Structures, vol.115, pp:233-245, 2017
[5] D.K. Zhang, K. Chen, X. F. Jia, D. G. Wang, S. Q. Wang, Y. Luo, “Bending fatigue behavior of bearing ropes working around pulleys of different materials” Eng Fail Anal, vol.33, pp:37-47, 2013
[6] G. A. Costello, “Theory of Wire Rope”, New York, Springer-Verlag, 1990
[7] I. Herreraq, E. Romero, “Software design to calculate and simulate the mechanical response of electromechanical lifts”, J Phys Conf Ser IOP Publ, vol:721, 2016

Experimental Investigation on Torque-Rotation and Tensile Strength Behavior of Multistrand Rotation-Resistant Steel Wire Ropes

M. POLAT[1] and Z. Ş. SERDAROĞLU[1]

[1] Çelik Halat ve Tel Sanayi A.Ş., Kocaeli/Turkey, mpolat@celikhalat.com.tr
[1] Çelik Halat ve Tel Sanayi A.Ş., Kocaeli/Turkey, zserdaroglu@celikhalat.com.tr

Abstract **- Steel wire ropes are used as lifting equipment at different lifting heights and working areas. Steel wire ropes, which stand out with their high lifting capacity and optimum elongation, can be produced in different properties and constructions. Ropes are subject to rotation due to their helical structure. If the lifting height is more than 60 meters, the amount of rotation increases. Exposure of the wire rope to rotation during use causes various damages. These damages end the service life of the wire rope. In this study, the rotation performance of the wire rope with 34x7 construction will be examined. Within the scope of the study, specially designed wire rope production will be carried out. Then the tensile test and torque-rotation test will be applied to the samples. Test results will be compared with other wire rope constructions with rotation resistant. As a result of the tensile tests, it was determined that the the wire rope with 34x7 construction has 5% higher strength than the wire rope with 35x7 construction. 34x7 ropes provide 3 times higher extra torque resistance compared to 35x7 ropes. This study contains theoretical data on steel wire ropes.**

Keywords **- Steel wire rope, torque behavior, rotation resistant, multistrand**

I. INTRODUCTION

STEEL wire ropes are lifting equipment used in various fields such as fishing, marine, port, forestry, mining industries. Steel wire ropes, which stand out with their advanced flexibility and superior load-bearing feature, have different properties depending on the area of use.

Steel wire ropes are usually made of a single wire or many bundles stranded around a steel core. This steel core may consist of steel wires or may be a fibrous element. The design of wire rope sections continues until the late 1800s [1].

Depending on the application of use, steel wire ropes can be produced as fiber core (FC), independent wire rope core (IWRC) and wire strand core (WSC). While fibre core ropes are preferred in areas where flexibility and elongation capability are required, independent wire rope core and wire strand core ropes are preferred in applications requiring high strength. Core types used in steel wire ropes are given in Figure 1.

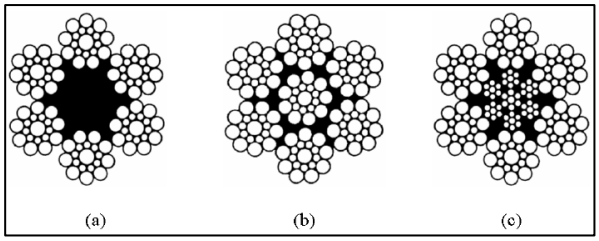

Figure 1. Core types of steel wire ropes; a)fibre core (FC), b)wire strand core (WSC), c)independent wire rope core (IWRC) [2]

Steel wire ropes have different contact points. These contacts are defined as linear contacts in the same layer and trellis contacts between layers[3].

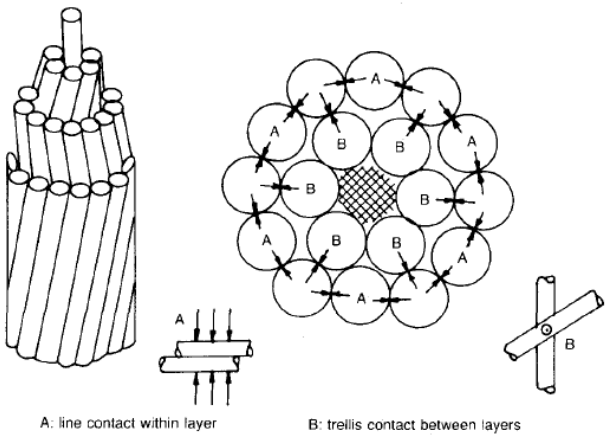

Figure 2. Typical contacts in steel wire ropes [3]

Steel wire ropes can be classified as monotron, single layer and multilayer. Multilayer steel wire ropes are defined as rotation resistant ropes. Multi-layer ropes are also known as multi-strand [4].

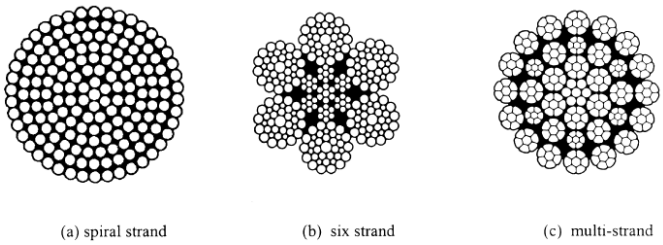

Figure 3. Typical rope constructions [4]

Steel wire ropes are subject to rotation under load due to their helical structure. In multistrand ropes, torque balance is provided and resistance to rotation is obtained. In addition, the strands are compacted to reduce stresses at the contact points [4].

Rotation behavior of steel wire ropes may vary depending on the rope's residual torsion and lay length. The rotation quantity can also vary depending on the design. Rotation behavior in torque-balanced ropes is variable. When the rope is under load, it balances itself by changing the direction of rotation. The rotational behavior graph is given in Figure 4 [4].

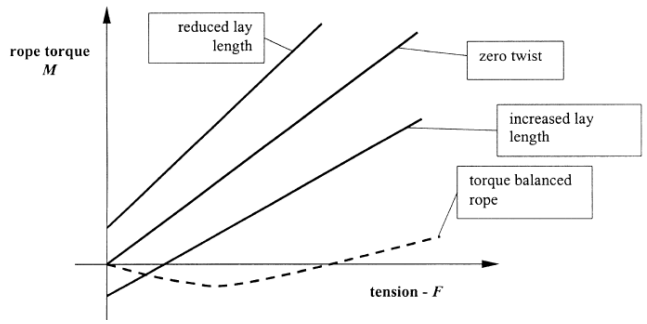

Figure 4. Rotation behavior of steel wire ropes

ISO 21669 standard is used to determine the rotation class of steel wire ropes. In the standard, they are subjected to rotation under free load on the vertical axis and are classified according to the angle of rotation. According to the standard, the test sample length should be at least 100 times the rope diameter. The amount of rotation obtained as a result of the test should be linearly proportional to the length value corresponding to 1000 times the rope diameter. As a result of the test, if the amount of rotation of the rope is between -360 and 360 degrees, it is defined as a rope with rotation resistant, between -1440 and 1440 degrees with semi-rotation resistant, and if it is more than 1440 degrees, it is defined as a rope with non-rotation resistance [5].

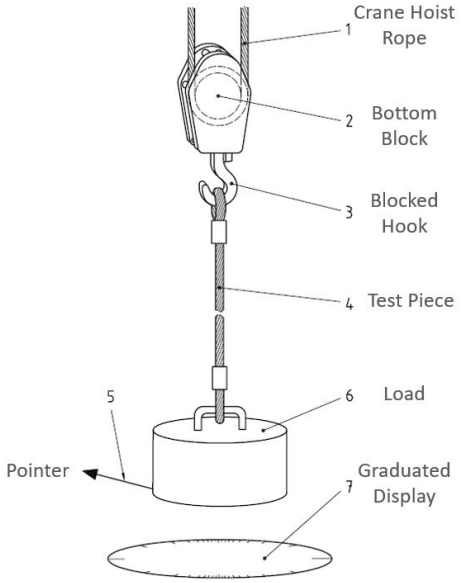

Figure 5. Typical test arrangement [5]

Torque-rotation tests can be done with the high technological test devices. As a result of applying a single axis load to the rope, the amount of rotation is determined with the help of torque and angle sensors. An example test device schematic is given in Figure 6 [6].

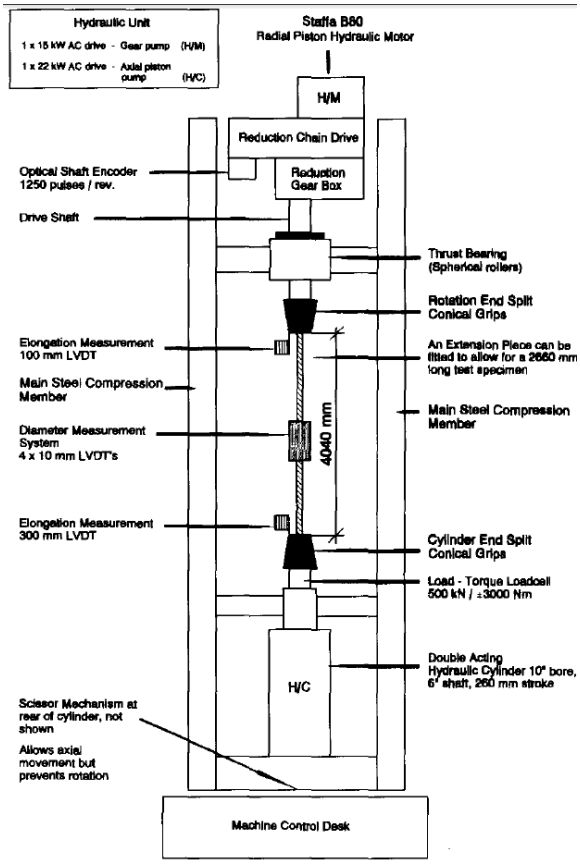

Figure 6. Schematic layout of torque-rotation test device[6]

II. MATERIALS AND METHODS

For the study, a wire strand core (WSC) multi-strand ropes of 34x7 and 35x7 constructions with diameter of 16 mm, wire strength of 1960 N/mm^2 was used. Detailed information about the samples is given in Table 1.

Table 1: Sample information to be used in the study

Sample No	Construction	Diameter (mm)	Tensile Grade (N/mm^2)	Minimum Breaking Load (kN)
1	34x7	16	1960	224
2	35x7	16	1960	213

For tensile tests, 1.20 meters samples were taken from the produced steel wire ropes. Both ends of the samples are terminated with a zinc head.Tensile tests were carried out in accordance with EN 12385-1 and ISO 6892-1 standards.

Torque-rotation tests are carried out in accordance with ISO 21669 standard. The schematic view of the test is given in

Figure 7. Samples are prepared at a length of 200 times the diameter of the rope.

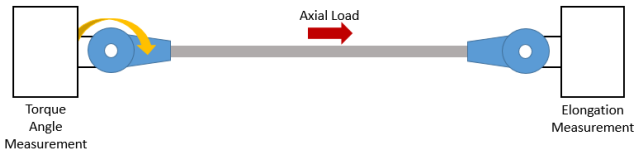

Figure 7. Schematic view of torque-rotation test

III. Results and Discussions

Tensile tests were carried out on steel wire ropes with 34x7 and 35x7 constructions. Tensile test results are given in Table 2.

Table 2. Tensile Test Results

Sample No	Construction	Diameter (mm)	Tensile Grade (N/mm^2)	Actual Breaking Load (kN)
1	34x7	16	1960	227.2
2	35x7	16	1960	218.1

Torque-rotation tests were carried out on steel wire ropes with 34x7 and 35x7 constructions. Test results are given in Table 3. Torque and torque factor diagrams are given in Figure 8.

Table 3. Torque-Rotation Test Results

Sample No	Construction	Diameter mm	Torque Factor	Torque N.m
1	34x7	16	-0,30	-1,30
2	35x7	16	-0,90	-5,90

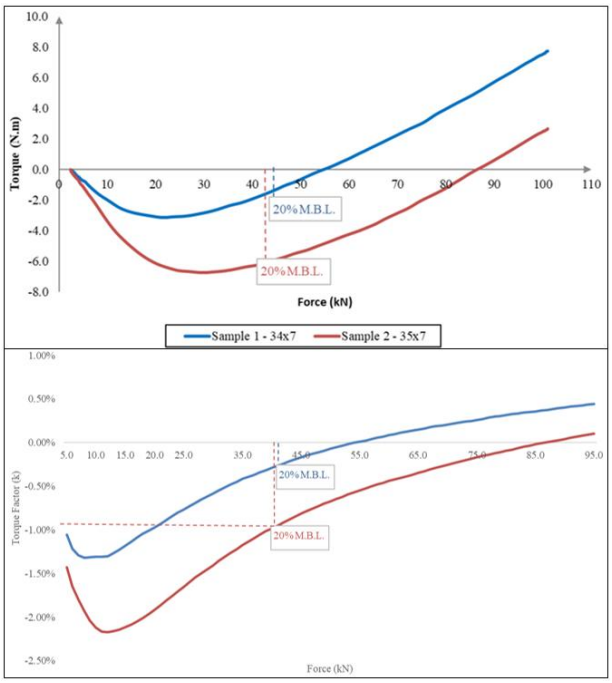

Figure 8. Torque-Rotation Test Diagrams

IV. Conclusions

Steel wire ropes are lifting equipments used in different industries. Steel wire ropes with helical structure are subject to rotation in applications higher than 60 meters. Multi-layer rotation resistant wire ropes have been developed for use in applications with lifting heights greater than 60 meters. In this study, the performance of steel wire ropes with 34x7 and 35x7 constructions was compared. As a result of the study, it was determined that 34x7 ropes have 5% higher breaking load and 3 times higher torque-rotation resistance than 35x7 ropes. All tests performed in the study were carried out under laboratory conditions and contain theoretical results.

Acknowledgment

This study was funded by The Scientific and Technological Research Council of Turkey (TUBITAK) project 3191439. Thanks to Çelik Halat ve Tel Sanayi A.Ş. for laboratory and test facilities in this project.

References

[1] D. Sayenga, *The birth and evaluation of the american wire rope industry. In: First AnnualWire Rope Proceedings, Engineering Extension Service*, Washington State University, Pullman, Washington, 1980.
[2] Anon. Steel Wire Ropes and Fittings. Bridon Ropes. 1992.
[3] M. Raoof, Simple formulae for spiral strands and multi-strand ropes, *Proc. Instn Civ. Engrs*, 88(2), pp. 527-542, December 1990.
[4] C.R. Chaplin, Torsional failure of a wire rope mooring line during installation in deep water, *Engineering Failure Analysis*, 6, pp. 67-82, October 1998.
[5] ISO 21669 Steel wire ropes – Determination of rotational properties, https://www.iso.org/standard/35962.html
[6] G. Rebel, M. Borello and H.D. Chandler, On the torsional behaviour of triangular-strand hoisting rope, The Journal of the South African Institute of Mining and Metallurgy, 96(6), pp. 280-288, November 1996.

The Effect of Core Material and Stretch Ratio on Pre-stretched Elevator Ropes

Z.ALTINIŞIK[1] and E. EFENDİ[2]

[1] Çelik Halat ve Tel Sanayii A.Ş., Kocaeli/Turkey, zaltinisik@celikhalat.com.tr
[2] Çelik Halat ve Tel Sanayii A.Ş., Kocaeli/Turkey, eefendi@celikhalat.com.tr

Abstract **- Elevator ropes are subject to permanent and elastic elongation due to their usage areas. One of these types of elongation, permanent elongation occurs during the use of the wire rope and the positions of the elevator car corresponding to the floors changes when the elevator stops at the floors, and this situation needs to be corrected with additional processes. For this reason, within the scope of this study, these permanent elongations that may occur during use have been pre-applied and secondary processes have been eliminated by pre-stretching the relevant wire ropes during their production. The related stretching process was carried out in a double drum production system with different speeds and the required force values were determined for the different applied stress values. In order to be able to make comparative tests and analyzes of the produced wire ropes, first of all, the production of non-pre-stretched ropes, followed by the production of ropes with 40% stretch value was completed. The produced ropes were subjected to the tensile test and the unit elongation amounts were compared by means of force-elongation curves.**

In the second phase of the study, as a result of the optimization studies and comparison tests carried out in the first phase of the study, the production with jute, polypropylene and sisal core was completed in order to determine the effects of the changes in the core material of the rope on the elongation performance of the rope. The tensile tests of the completed wire ropes were carried out and considering the sector demands; with the force-elongation curves obtained, the force value required for the stress value with the most optimum value, the rope core material to be used and process parameters were determined. These results are the experimental conclusions.

Keywords **- Elevator ropes, Wire ropes, Steel wire ropes, Pre-stretched ropes, Pre-stretched elevator ropes**

I. INTRODUCTION

Steel wire ropes have a helical structure and constitute a very important and large area of engineering elements. They are very important in terms of exhibiting the expected performances in lifting equipment such as cranes and elevators, which are areas where high load carrying capacity is expected. They are produced and tested in different constructions and forms in order to carry various lifting loads in these areas. When structural examination of steel ropes is made; they are made of high-strength steel wires. These steel wires are wound according to their intended use and determine the final shape of the rope. As can be seen in Figure 1, more than one wire is wound around a center wire to form strands, and these strands are closed around one or more strands to form the steel wire rope [1,2].

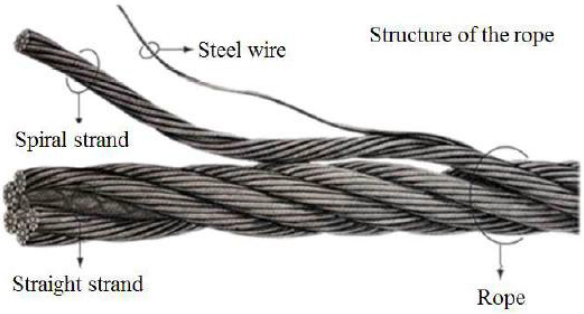

Figure 1 : A typical wire rope structure and its components [3]

The steel rope used in elevators, which has an important place among lifting equipment, has important features that it should have. Elevator ropes are produced with a certain construction and structural integrity in order to fulfill these important features such as high strength values in small diameters, bending and twisting in all directions, wear durability, easy maintenance, and superior life performance [4].

Mainly produced elevator rope constructions are produced in 6x19S+FC constructions that provide high abrasion resistance or 8x19S+FC constructions where abrasion and flexibility properties are more balanced, depending on the usage conditions [4]. Sectional images of these constructions are shown in Figure 2.

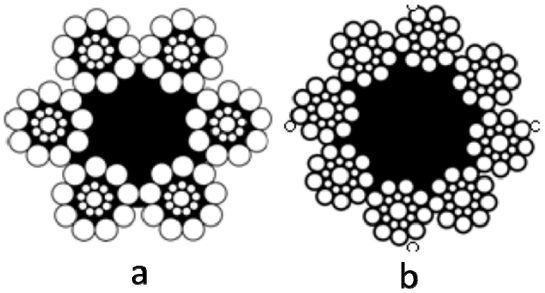

Figure 2 : a) 6x19S+FC, b) 8x19S+FC [4]

Elevator ropes are subject to permanent elongation during their working life and to structural permanent elongation when first hung before use. This type of elongation causes the elevator cars not to coincide with the floors as they should correspond to when they are started to be used, and creates the need for shortening with additional secondary operations. To eliminate this need, elevator ropes are pre-stretched prior to use with preloads corresponding to their permanent

elongation. This process is called pre-stretching. For these ropes produced in accordance with the ISO 4344 standard, it is said that pre-tensioning can be applied in the relevant parts of the standard, but this force should not be more than half of the minimum breaking strength. Pre-stretching process is applied in line with these boundary conditions in order to provide the structural permanent elongation to the users before use and to minimize the secondary processing requirements [5].

In elevator ropes with pre-stretching process, the core of the rope is directly effective on providing permanent elongation. Elevator ropes with fiber core structure have more effective permanent elongation rates compared to those with steel cores. Wire ropes with steel core, on the other hand, eliminate their permanent elongation effects during their transportation until the installation process. [6].

Within the scope of this study, the force values that should be applied against the desired tension values for the pre-stretch elevator ropes were determined and for comparison purposes, they were produced firstly without pre-stretch and then with 30-40% stretch.

Then, the elongation values of the ropes were determined as a result of the elongation tests specially applied to the elevator ropes in accordance with the DIN 51201 standard.

In the second phase of the study, the production of steel ropes with different cores was completed and the effect of the material type of the steel core on the permanent elongation value of the rope was investigated.

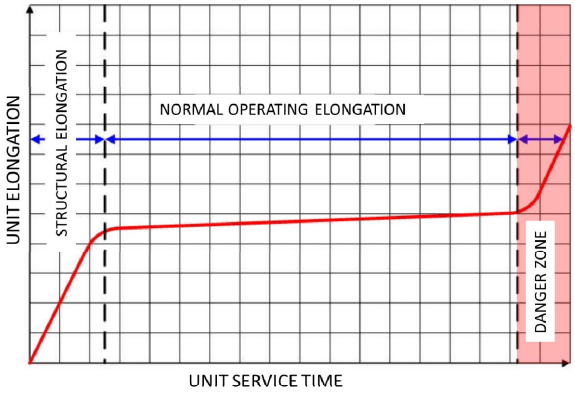

Figure 3: Elongation performances of elevator ropes during service life [4]

II. MATERIALS AND METHODS

Within the scope of the study, the production of elevator ropes with fiber core was completed. As seen in Figure 4, three different types of fiber cores, jute, sisal and PP, were used in the ropes produced. These ropes were produced with 10 mm diameter, 8x19S construction and with jute core in the first phase of the study and with three different cores in the second phase.

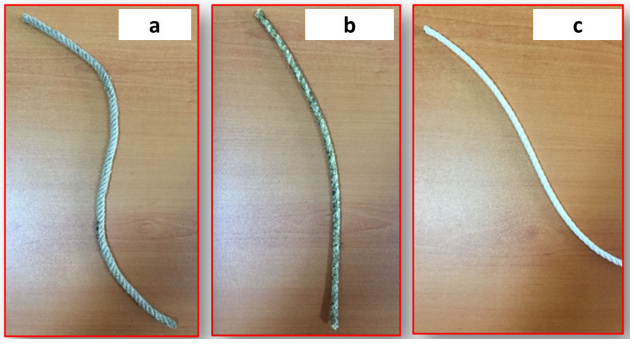

Figure 4: Fiber cores used in elevator ropes a) Jute core, b) Sisal core, c) PP (Polypropylene) core

Pre-stretched elevator ropes are produced by the stresses that occur on the rope as a result of the winding process of the rope at different speeds by two separate drums with different speeds. In the system shown in Figure 5, the main drum and rotor part get their power with the help of the cardan shaft coming from the main motor and turning the rotor, and therefore its speed is gradually increases. The other drum that applies stretch to the rope is shown in Figure 6. The motor system of this drum is different from the system of the machine drum and it has a separate speed system.

Figure 5: Main machine drum and rotor part

Figure 6: Pre-stretching drum

The working principle of the machine system is given in Figure 7. The pre-stretching drum has a higher linear velocity than the main drum. This situation creates a stretch on the rope and executes the structural elongation.

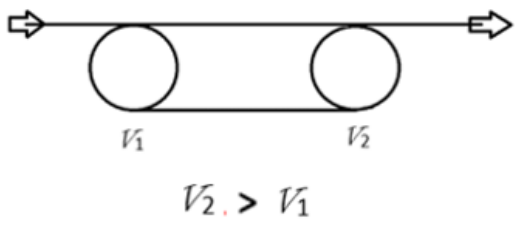

Figure 7: Basic working principle of pre-stretching

The load cell shown in Figure 8 was placed between the two drums to determine the stretch ratio on the rope. With the help of the force values in the load cell and the breaking load of the rope, the force values that should be applied for different stretching ratios were determined.

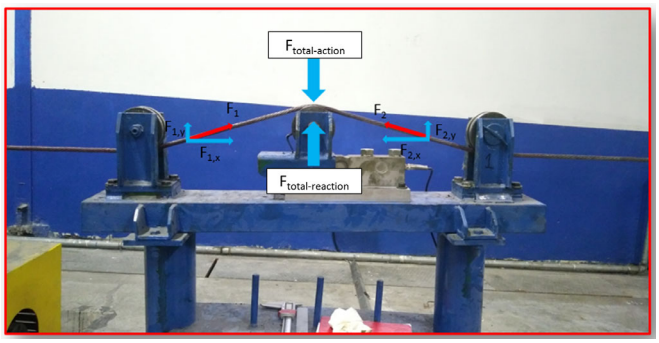

Figure 8: Loadcell installed for pre-stretching measurement

Within the scope of the study, non-prestretched and 40% pre-stretched ropes were first produced in order to compare the unit elongation values, and the elongation tests applied specifically to the elevator ropes were completed. In addition, the elongation tests were repeated 24 hours after the first elongation tests to simulate the elongation performance of the ropes, and then three weeks later. So that the change in the elongation performance over time was discussed.

In order to examine the effect of the rope core type, which is the second stage of the study, under maximum conditions, the elongation rates under 55% tension were determined and the appropriate core type that could provide the optimum conditions was decided. A final elongation test was performed for the determined core type and optimum tension and process conditions for the appropriate core type were determined.

III. Results and Discussion

The elongation test graphs of the 10mm 8x19S jute core rope, which is produced without pre-stretched and 40% pre-stretched, are given in Figure 9. As can be seen in the elongation diagram of the rope produced without pre-stretched here, the permanent elongation is 0.53%. On the other hand, the permanent elongation of the rope with 40% pre-stretched is seen as 0.45%. This shows that the pre-stretching process has effect of improving the elongation performance of the rope.

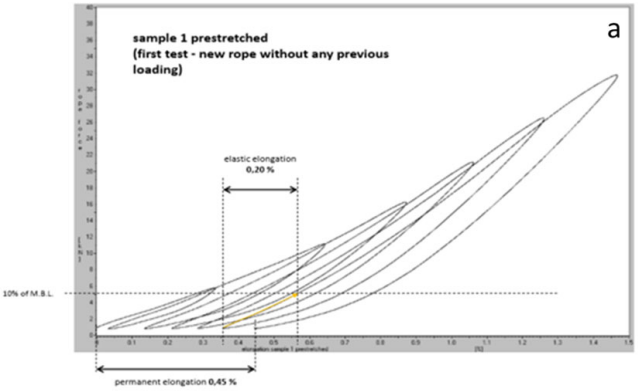

40% Pre-stretched – Sisal Core 10 mm 8x19S Steel Wire Rope Elongation Test Result

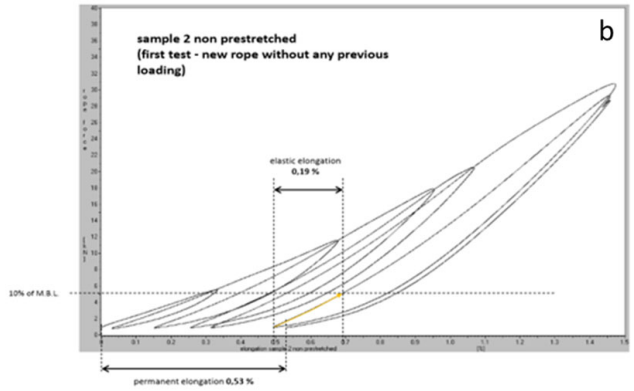

Non Pre-stretched – Sisal Core 10 mm 8x19S Steel Wire Rope Elongation Test Result

Figure 9: Initial elongation test results of non-pre-stretched and 40% pre-stretched jute core samples

Elevator ropes must have a maximum elongation of 0.4% in accordance with the ISO 4344 standard. These first test values obtained are close to the desired values. After the first tests to simulate this performance improvement, elongation tests were performed again after 24 hours and the results are given in Figure 10.

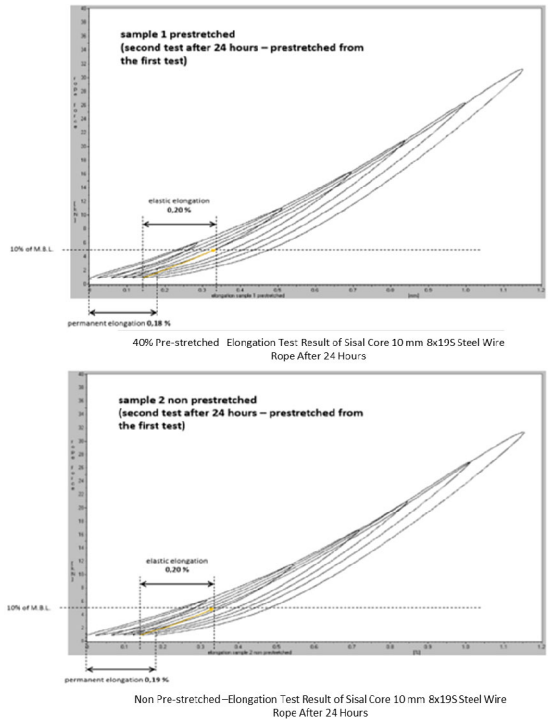

Figure 10 : Elongation test results after 24 hours of non-pre-stretched and 40% pre-stretched jute core samples

Within the scope of the study, an average of 30% decrease was observed in the elongation rates obtained as a result of the second elongation tests applied to the ropes produced with and without pre-stretching. Therefore, these reductions in permanent elongation values prove that the test forces applied in the first elongation test create a second stretching effect in the produced ropes. The permanent elongation values obtained as a result of the second elongation tests of the elevator rope produced without pre-stretching are 0.19%. The elongation value of the rope, which was both pre-stretched and re-elongation tested after 24 hours, was 0.18%. As can be seen, the elongation values of the ropes subjected to these two different loads are almost the same regardless of the pre-stretching process applied. As a result, the tests were applied again three weeks after the second elongation test in order to examine the change in the permanent elongation values over time in a longer period and the results are given in Figure 11. When the results were examined, a slight increase was observed in the permanent elongation values compared to the second tests. The permanent elongation values of the tests performed are summarized in Table 1.

Table 1: Summary Results of Tests Performed

Type of Core	State of Stretching	First Test	Second Test	Third Test
			After 24 Hours	After 3 Weeks
Jute	Pre-stretched	0.45%	0.18%	0.27%
	Non pre-stretched	0.53%	0.19%	0.23%

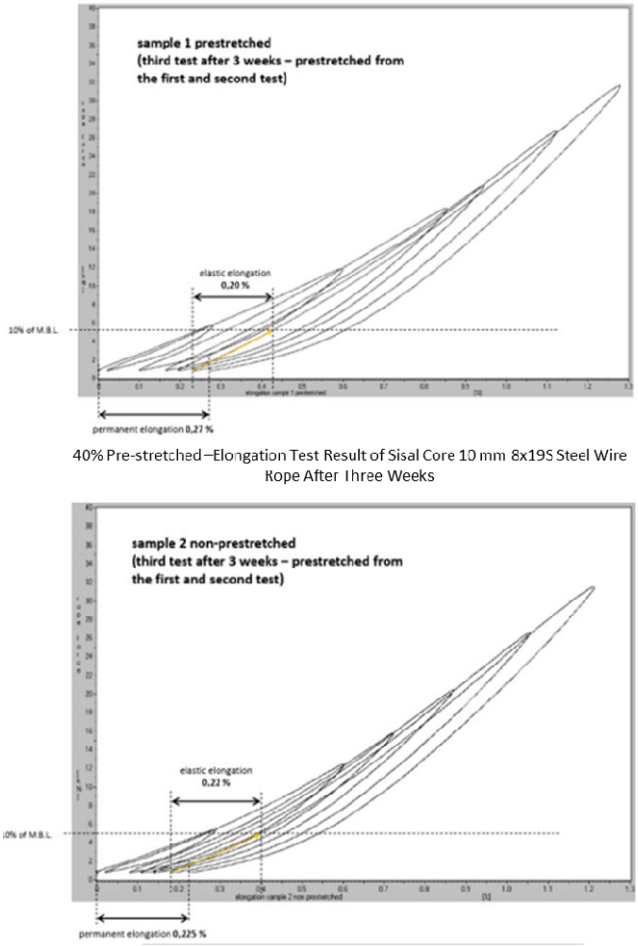

Figure 11 : Elongation test results after three weeks of non-pre-stretched and 40% pre-stretched jute core samples

In the second stage of the study, the tests were completed at 55% stretch rate in order to determine the effect of the core type used on the permanent elongation and to eliminate the inhomogeneities in the time-dependent permanent elongation, and the permanent elongation values were shared in Table 2.

Table 2: Elongation values of ropes with different core types

Percentage of Stretching	Types of Cores		
	Jute	PP	Sisal
55	0.28%	0.28%	0.24%

The elongation values of the ropes using different cores were close to each other. However, the elongation amount of sisal core is slightly better than the others. This is due to the fact that sisal core has a harder structure compared to others. For the jute core sample, the permanent deformation rate was 0.28%, and the desired value range could be achieved below the elongation value of 0.4% in accordance with the ISO 4344 standard. However, sisal core rope is preferred instead of jute

core rope in the sector. For this reason, a final elongation test at 40% stretching value was performed for sisal core rope and the results compared with 55% tensile value are shared in Table 3.

Table 3: Elongation behavior of sisal core rope at 40% and 55% stretching

Sisal Core	
Percentage of Stretching	Elongation Ratio
40	29%
55	24%

When all test results were examined, ropes with sisal core gave the best test result with a stretching value of 55%. However, the results of the samples of the same rope produced with 40% stretching were also obtained with a value of 0.29%, within the limit values given by the standard. Therefore, it was decided that the rope with sisal core produced with 40% stretching value is the most suitable rope in terms of the most suitable process parameter and rope core.

IV. Conclusions

Within the scope of this study, pre-stretched elevator ropes with a construction of 10 mm 8x19S were determined with the desired stretching ratios within the scope of ISO 4344 standard, and their production was successfully completed with different rope core materials. The elongation tests of the produced ropes were carried out and these tests were repeated at certain time periods and their elongation performances were examined depending on time. Within the scope of the study, the most suitable process parameters that determine the stretching ratios and the rope core material were determined. As a result; It has been observed that the pre-tensioning process applied to the rope has a positive effect on the reduction of the permanent elongation. The permanent elongation values achieved in the different rope core materials used are provided within the scope of ISO 4344 standard. Although the permanent elongation value of the jute core sample, whose trials were completed in the first stage of the study, is 0.28% at 55% stretching rate, within the scope of the standard, sisal core is predominantly preferred in the sector and the permanent elongation value of sisal core can be achieved with 0.29% value in the desired value range, even at 40% stretch rate. Therefore, sisal core and 40% tension ratio were determined as this optimum core and tension value.

Acknowledgment

The authors would like to thank the Dresden University of Technology for providing laboratory facilities for this work. We would also like to thank Çelik Halat ve Tel Sanayii for all the testing and laboratory opportunities.

References

[1] A. B. Seelam, M. S. Jawed, and Sachidananda Hassan Krishanmurthy, *Design and analysis of elevator wire ropes*. International Journal for Simulation and Multidisciplinary Design Optimization (IJSMDO), 2021.

[2] C. Erdem İmrak, and Ö. Salman, "TAŞIYICI HALATLARIN DENEYSEL GERİLME ANALİZİ," *Mühendis ve Makina*, vol. 51, pp. 23-29, July 2010.

[3] Z. Ren, Z. Lu, Q. Yu, and Y. Jiang, "Failure Analysis and Safety Protection of a Certain Type of Wire Ropes under High-Speed Impact Loads," *International Conference on Materials Applications and Engineering,* vol. 142, 2018.

[4] G. Kutay. (2012, July). Asansör Halatları. Available: http://www.guven-kutay.ch/Asansor/80-1-1a-AsansorHalatlari.pdf

[5] *Preifer Drako. (2019, September)* Elevator Products. Available: https://www.pfeifer.info/out/assets/PFEIFER-DRAKO_ELEVATOR-PRODUCTS_BROCHURE_EN.PDF

[6] *Draka, a brand of the prysmian group.* Pre-stretched and low-stretch elevatorropes.Available:https://it.prysmiangroup.com/sites/default/files/atoms/files/Tech-Tip-16.pdf

Investigation on Mechanical Properties of Swaged Wire Ropes via Construction Changes

E. EFENDİ[1] and Z. ALTINIŞIK[2]

[1] Çelik Halat ve Tel Sanayii A.Ş. Kocaeli/Turkey, eefendi@celikhalat.com.tr
[2] Çelik Halat ve Tel Sanayii A.Ş. Kocaeli/Turkey, zaltinisik@celikhalat.com.tr

Abstract – **In the current study, steel core and wire rope closing process was carried out with a new production one-step method using a special design and parallel wire rope closing on 12 cradle rope closing machines. It is observed approximately 3% improvement in the production process with the one-step production method. Wire rope breaking load tests showed increase by up to 15% in actual breaking load of the parallel swaged wire rope. In metallic cross sectional area 5 % enhancement was observed. Results are carried out under laboratory conditions and compared to literature.**

Keywords **– steel wire rope, swaged wire rope, parallel swaged wire rope, swaging, swaging process**

I. INTRODUCTION

Steel wire ropes consist of several strands of metal wire twisted into a helical form. Each strand occurred by many helical wires that are stranded to the wire core. The helical form of the wire strands enables high carrying and endurance capacity to the wire rope, which make it proper hoisting member in many areas such as elevators, cranes, excavation, surface and undergoing mining, marine, mine hoisting and bridges [1].

However, there have been some limitations in usage area of standard wire ropes which move on a pulley or drum; because of reduced contact point, resulting low contact surface, stress and friction. Increased friction over the wire contact area causes overheating, excessive wear and breakage of wires. In order to overcome such difficulties, swaged wire ropes are developed. Swaged wire ropes have been produced with flattening of outer wires of the outer strands by swaging operation with high deformation rates. Compression applied to the outer surface provides many advantages to the swaged wire rope such as higher strength and higher abrasion resistance, compared to the standard wire rope. Thanks to their advanced properties, swaged wire ropes are being used in areas mainly forestry, mining and port industry [2]. Figure 1 shows schematic image of swaged wire rope and standard wire rope.

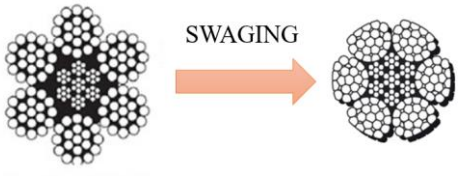

Figure 1: Standard wire rope and swaged wire rope

Selection of a suitable construction for the wire rope is an important issue. In a standard rope, all wires and strands have different lay lengths. The high stress concentration at the cross-over point leads to an early internal failure. In a parallel lay rope, all wires and strands have the same lay length. Linear contact of the wires provides optimal stress distribution. Furthermore, compacted parallel design leads to a higher fill factor and breaking strength. Figure 2 shows the difference between point contact pressure and linear contact pressure distribution [3].

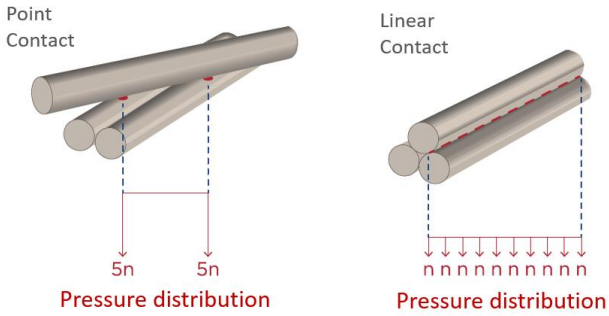

Figure 2: Different forms of contact pressure distributions

Swamy et al., designed roller swaging process to achieve higher swaging deformation rates, resulting with excess reduction in the diameter of the rope, which also contributes to the improvement of rope strength [4]. Erdönmez in his research, designed multi-layered 3D model of wire rope. Compacting process was carried out on the designed wire rope. Results showed that compacted wire ropes have increased wear resistance and tensile strength. With the compaction process, diameter of the wire rope decreases which results a decrease on the reaction moment also [5].

II. MATERIALS AND METHODS

In the current study, parallel swaged 6x26WS wire rope was designed in special wire rope design program, and then 2D and 3D drawings for visual verification was carried out by "Solidworks". Figure 3 shows 2D and 3D drawing images of the designed wire rope. Wire rope consists of (1+6) center strand, (1+6) outer strand of steel core and (1+26) outer strand.

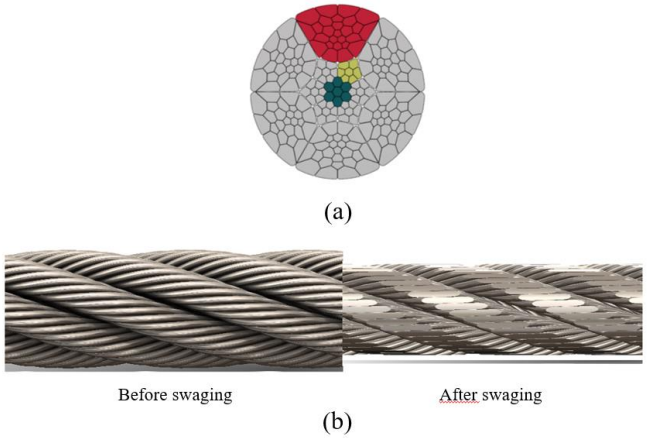

Figure 3: Solidworks drawings of wire rope (a) 2D and (b) 3D drawing images

After computer aided design process, wire production steps were determined. Initially, Ø 5.5 mm diameter wires were drawn with two phases, dry and wet drawing process. Steel wire material for the experimental study was selected with the composition of 0.75 % C wt. and 1960MPa strength. After wire production process, strand production process was carried out. 25 cradles wire rope machine was used for strand production. Two different rope closing processes were tested. First, conventional closing process consists of manufacturing process of the wires, and then strand the wires to create the final wire rope in two steps. This production process consists of steel core and steel wire rope production in different time and machines. In the second closing process, steel core and wire rope closing process was carried out with a new production one-step method using a special design on 12 cradles rope closing machine.

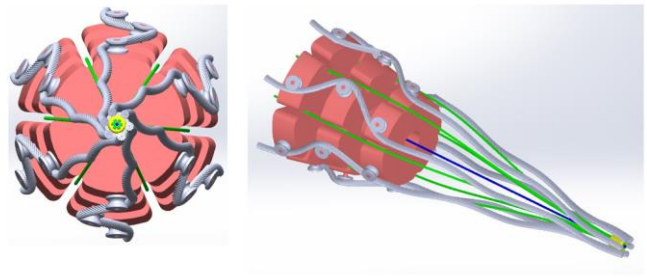

Figure 4: 3D drawing of special designed preforming head

Special preforming head was designed to enable one-step production method. Figure 4 shows 3D drawing of the preforming head. The design of the preform head provides to produce parallel lay wire rope by knitting strands together with steel core simultaneously.

In the current study, 6x26WS standard lay wire rope was selected as a reference material to compare with 6x26 parallel lay wire rope. All wire rope samples are swaged after production process. Tensile test was carried out in accordance with EN 12385-1 and ISO 6892-1 standards. 1.20 m length samples were cut from the wire rope and both ends of the samples terminated with a zinc head.

III. RESULTS AND DISCUSSION

The production process of the parallel lay wire rope has been successfully completed with 11.8 mm initial diameter. Rope diameter was reduced to 10 mm after swaging process. Breaking load test was carried out to both samples. Figure 5 shows the results of tensile tests.

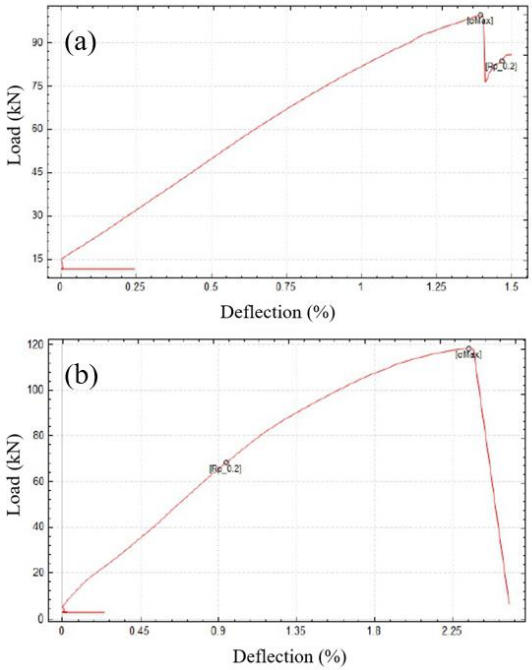

Figure 5: Breaking load test results of parallel lay wire ropes (a) before and (b) after swaging process.

Expected minimum breaking load for parallel lay 6x26WS wire rope is 97 kN. Tensile test results exhibited 99.5 kN actual braking load, before swaging process. Similarly, swaged wire rope tensile increased with swaging process. Expected minimum breaking load was 100.5 kN for parallel 6x26WS swaged wire rope. Actual tensile test results showed that breaking load increased to 115 kN. Wire rope strength tests showed increase by up to 15% in minimum breaking load of the parallel swaged wire rope.

Table 1. Comparison of breaking load test results of all samples

Sample No	Construction	Diameter (mm)	Actual Breaking Load (kN)
1	6x26WS (parallel lay)	11.80	99.5
2	6x26WS (parallel lay+swaged)	10	115
3	6x26WS (standard lay+swaged)	10	102

Table 1 shows difference between breaking test results of the samples. It can be seen that swaging process has a significant effect on the tensile properties. On the other hand, parallel lay construction has also substantial effect on the breaking load test results. When compared standard lay wire rope with parallel wire rope, there is a significant improvement in the breaking load of parallel lay wire rope construction. It is considered that improvement of tensile properties are related with metallic cros sectional fill rate enhancement.

Table 2: Comparison of different manufacturing process duration times

Manufacturing method	**Time (s)**
Conventional Process (standard lay wire rope)	4963
One-step Proces (parallel lay wire rope)	4860

Table 2 shows different manufacturing process duration times. In the conventional process, manufacturing process consist of two different steps as steel core and steel wire rope production in different time and machines. This process extends the production time. In one-step production method, steel core and wire rope closing process was carried out at the same time. This, reduced production time. Another advantage of one-step method, this production technique enables to produce parallel lay wire ropes which shows better tensile properties than standard lay wire rope.

IV. Conclusion

Steel wire ropes have many usage areas because of their high carrying and endurance capacity such as elevators, cranes, excavation etc. Many production techniques have been developed in manufacturing process of wire ropes. In the current study two production techniques, one-step production and conventional production were compared. When compared with conventional production method, one-step production consist of shorter periods. Another advantage of one-step method is that, it provides to produce parallel lay wire rope, which shows higher mechanical properties. Swaging process has also significant effect on the increase in mechanical properties of wire rope, rates due to the high amount of deformation rates applied to the surface of final wire rope.

Acknowledgment

This project was funded by Çelik Halat ve Tel Sanayii A. Ş. Thanks to Çelik Halat ve Tel Sanayi A.Ş. for laboratory and test facilities.

References

[1] Y. A. Onur, C. E. İmrak, and T. Ö. Onur, "Investigation on bending over sheave fatigue life determination of rotation resistant steel wire rope", *Experimental Techniques*, vol. 41(5), pp. 475-482, 2017.

[2] C. Erdönmez, "Computational design of the compacted wire strand model and and its behavior under axial elongation" *International journal of Precision Engineering and Manufacturing*, vol. 20(11), pp. 1957-1968, 2019.

[3] S. Yadav, G. R. Kesheorey, and A. Duggal, "Optimization of conductor wire rope for different testing and generation of common test set up", *International Journal for Research in Applied Science & Engineering Technology (IJRASET)*, vol. 9(3), pp. 298-303, 2021.

[4] R. P. Swamy, B. T. Ramesh, A. R. MAnjunatha, and J. Jaya Naik, "Analysis of roller swaging machine" *International Journal of Research & Development (IJRD)*, vol. 4 (6), pp. 71-82, June 2019.

[5] C. Erdönmez, "Analysis and design of compacted IWRC meshed model under axial strain", *International Journal of Precision Engineering and Manufacturing*, vol. 20(11), pp. 1957-1968, 2019.

Experimental Investigations On Mechanical Properties Of Steel Wire Ropes By Using Different Empregnated Thermoplastic Materials

Z. Ş. SERDAROĞLU[1] and M. POLAT[1]

[1] Çelik Halat ve Tel Sanayii A. Ş., Kocaeli/Turkey, zserdardoglu@celikhalat.com.tr
[1] Çelik Halat ve Tel Sanayii A. Ş., Kocaeli/Turkey, mpolat@celikhalat.com.tr

***Abstract* – Steel wire ropes are lifting equipment of produced in different constractions and strength values according to the place of use. In impregnated plastic core (EPIWRC), the plastic coating between the steel core and the outer strands increases the corrosion resistance and fatigue life of the steel core. The plastic impregnated core steel wire ropes have 10% higher strength than the independent wire rope core ropes (IWRC). In this study, plastic impregnated steel wire rope is aimed to examine the effects of polymer coating material on the targeted mechanical properties of steel core plastic impregnated steel wire ropes known as EPIWRC and the polymer selection methods. Empregnated plastic core (EPIWRC) steel wire ropes with 2 different plastic coating were examined. Polypropylene and high density polyethylene, which are plastic coating materials, were made mechanical, DSC and TGA analyzes. The differences between the plastic materials were analyzed by applying corrosion, tensile and fatigue tests to the steel wire ropes produced after the coating was applied. This study contains experimental data on different plastic material coat of steel wire rope of 8x26WS constraction.**

***Keywords* – steel wire rope, plastic filled, corrosion test, bending fatigue test**

I. INTRODUCTION

STEEl wire ropes are made up of individual steel wires spun into a strand. A number of strands are closed over a central core thus producing a rope. The number and size of wires must offer the best compromise possible between large wires for maximum corrosion protection and resistance to abrasion [1]. Because of load-bearing and high endurance capacity, wire ropes are used in many areas such as oil&gas and mining equipment, harbor cranes, bridges, offshore and aerial ropeway systems [2].

Steel ropes are produced with different core types according to their usage areas. The most commonly used three core types are jute, PP and steel core. Steel wire ropes produced using jute and PP are called "fiber core (FC)". The core formed by weaving steel bundles together is called "steel core (IWRC)". The type of core produced by impregnating the steel core with plastic is called "plastic empregnated plastic core (EPIWRC)" [3]. Core types used in steel wire ropes are given in Figure 1.

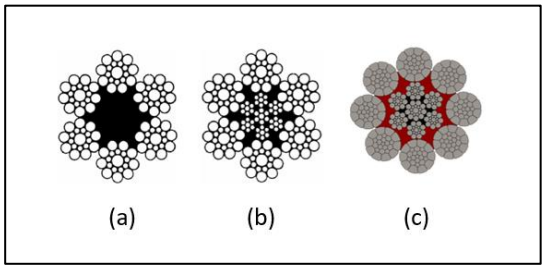

Figure 1: Core types of steel wire ropes; (a) fiber core (FC), (b) independent wire rope core (IWRC), (c) empregnated plastic independent wire rope core (EPIWRC)

Steel ropes are named according to the number of strand and the number of wires in the outer strands. Another concept used in naming is the configuration of the wires in the rope strand. There are four commonly used strand array types. These are Seale, Filler, Warrington and Warrington Seale [4]. Strand types used in steel wire ropes are given in Figure 2.

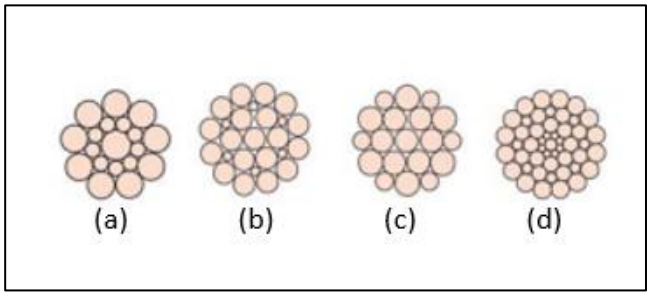

Figure 2: Strand types of steel wire ropes; (a)Seale (b)Filler, (c)Warrington, (d)Warrington Seale [4]

Steel wire ropes generally come across with challenging conditions during usage. Friction between individual wires, between strands, between rope coils, and between other surfaces and rope generally effect fatigue life of wire rope. Accordingly, the service life of steel wire rope is reduces. In addition, depending on the working environment, corrosion occurs in the ropes. Main reason for corrosion occurrence in wire rope is decreasing galvanized coating thickness and reduction of lubricant amount on the surface of the wire rope.

Corrosion is also a condition that reduces the life of the rope and may increase the risk of work accidents over time [5].

İmrak and Onur investigated theoretical and experiment fatigue performance of 10 mm diameter 6x36 WS steel wire rope. As a result of the study, they observed that when the pulley diameter decreases and applying force increases, service life of the steel wire rope decreases [6].

In this study, two different plastic materials are used, polypropylene and high density polyethylene. This prototype production ropes were investigated on corrosion test and fatigue life of steel wire ropes.

II. Materials and Methods

In this study, two steel wire ropes with different core types are produced. The first one is independent wire rope core (IWRC) and the second one is empregnated plastic independent wire rope core (EPIWRC) with 8x26WS construction and 22 mm diameter ropes. Two different thermoplastic material were used for plastic layers. Detailed information about the samples is given in Table 1.

Table 1: Technical details of produced samples

Sample No	Diameter (mm)	Construction	Core Type	Plastic Material Type	Core Construction	Lay Ratio
1	22	8x26WS	IWRC	-	7x7	6,50
2	22	8x26WS	EPIWRC	PP HDPE	6x17S	6.50

The technical drawings of the samples were prepared by "Solidworks". 3D drawings of Sample 1 and Sample 2 are given in Figure 3.

Figure 3: 3D designs of (a)Sample 1 (IWRC) (b)Sample 2 (EPIWRC)

Corrosion tests according to ASTM B117 were carried out in the salt spray test cabinet and continued until red rust was observed on 50 cm long samples. As a result of the test, the steel core outer surface of independent wire rope core (IWRC) and empregnated plastic independent wire rope core (EPIWRC) were examined.

According to the ISO 4309 standard, when the steel ropes are reduced in diameter or a certain wire fracture is reached, the rope service life is completed. In order to simulate bending fatigue effects, the working system is arranged with the help of drive sheave. Test was applied in a special bending fatigue test device designed for steel wire ropes. The bending fatigue test principle is given in Figure 4.

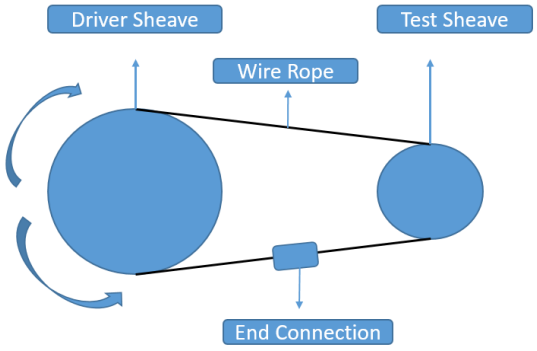

Figure 4: Test Principle of Bending Fatigue Test

After all the samples were produced and their tests were completed, all the information was shared in the results and discussion section.

III. Results and Discussion

The hardness test, tensile test and impact strength test of thermoplastic materials are given in Table 2.

Table 2: Mechanical test results of plastic materials

Sample	Hardness (Shore D)	Tensile Test (N/mm²)	Impact Strength (kj/m²)
Polyprophylene(PP)	67	23.7	7.68
High Density Polyethylene (HDPE)	63	20.8	2.29

Differential Scanning Calorimetry (DSC) is a thermal analysis technique that studies how the heat capacity (Cp) of a material changes with temperature. A sample of known mass is heated or cooled, and changes in heat capacity are monitored as changes in heat flux. DSC analyzes diagram is given in Figure 5.

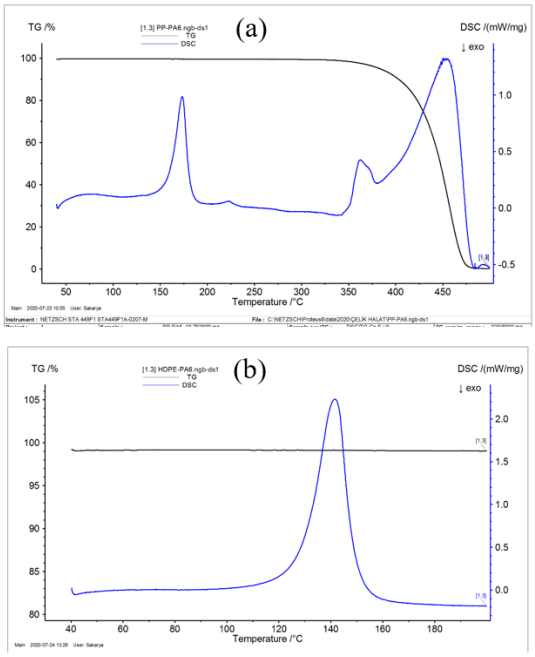

Figure 5: Differential Scanning Calorimetry (DSC) Analyzes of Sample (a)Polypropylene (b)High Density Polyethylene

Analyzes of glass transition temperature, melting point and chemical degradation temperature is given Table 3.

Table 3: Glass Transition Temperature, Melting Point and Chemical Degradation Temperature of Thermoplastic Materials

	Glass Transition Temperature (C°)	**Melting Point (C°)**	**Chemical Degradation Temperature (C°)**
PP	45	170	350
HDPE	40	140	200+

The corrosion test was applied to the steel wire ropes and the steel cores were compared after the test. While red rust was observed in the uncoated steel core, white rust was observed in the HDPE coated steel core and no corrosion initiation was observed in the PP coated steel core. Rust condition of steel core is given Figure 6.

Figure 6. Rust condition of steel core (a) IWRC, (b) PP, (c) HDPE

Bending fatigue tests were performed on the samples. The test results are given in Table 4.

Tablo 4. Results of Bending Fatigue Tests

Sample	**Diameter (mm)**	**Core Type**	**Load Level**	**Number of Bending Cycles**
1	22	IWRC	20% (Safety Factor 5)	38.868
2	22	PP	20% (Safety Factor 5)	56.833
3	22	HDPE	20% (Safety Factor 5)	40.198

IV. CONCLUSIONS

In this study, the differences between the rope with independent wire rope core (IWRC) and empregnated plastic independent wire rope core (EPIWRC) with two different thermoplastic materials were investigated. As a thermoplastic material, polypropylene (PP) and high density polyethylene (HDPE) were used. The corrosion resistance of coated and uncoated cores was investigated. In addition, bending fatigue was compared. Compared to steel core uncoated rope, plastic coated materials have more cycles in bending fatigue tests. The highest number of cycles was observed in the PP coated rope. All tests performed in the study were carried out under laboratory conditions and contain theoretical results.

ACKNOWLEDGMENT

This project was funded by The Scientific and Technological Research Council of Turkey (TUBITAK) project 3191466. Thanks to Çelik Halat ve Tel Sanayi A.Ş. for laboratory and test facilities in this project.

REFERENCES

[1] R. P. Singh, M. Mallick, and M. K. Verma, “Studies on failure behavior of wire rope used in underground coal mines”, *Engineering Failure Analysis*, vol. 70, pp: 290-304, 2016

[2] A. Güzey, “Demirsel teller üretim sürecinin incelenmesi” Msc thesis, Dept. Met. And Mat. Eng. Trakya University, Edirne

[3] Anon. Steel Wire Ropes and Fittings. Bridon Ropes. 1992.

[4] Usha Martin. Wire Rope Handbook. [online]. 2012[viewed in 2021-03 24]. Available from: http://www.ushamartin.com/wp content/uploads/2014/04/Wire-Rope-Handbook.pdf

[5] X. D. Chang, H. B. Huang, Y. X. Peng, and S. X. Li, “Friction, wear and residual strength properties of steel wire rope with different corrosion types”, *Wear*, vol. 458, pp.203425, 2020.

[6] Y. Onur, C. İmrak, “Experimental and Theoretical investigation of bending over sheave fatigue life of stranded steel wire rope”, *Indian Journal of Engineering & Material Sciences*. vol. 19, pp. 189-195, 2012.

Characterization Methods of Nano-particles Added to Industrial Lubricants

Onur Can SIRVAN[1], M. Huseyin CETIN[2], Babur OZCELIK[3]

[1] Konya Technical University, Konya/Turkey, ocsirvan@ktun.edu.tr
[2] Konya Technical University, Konya/Turkey, mhcetin@ktun.edu.tr
[3] Konya Technical University, Konya/Turkey, ozcelik@ktun.edu.tr

Abstract - **Lubricants used in mechanical systems are directly related to main factors such as energy consumption, material deformation and environmental pollution. With the additives added to the oils, the tribological performance of the oil can be increased. In recent years, the use of nano-particles as additives has become quite common. Nano-particles, which are especially effective in increasing the heat transfer coefficient, can reduce the friction coefficient by increasing the oil film strength, wettability and penetration of liquids. However, nano-particles must have specific characteristic properties to be used as oil additives and to be stable. In order to determine these properties, it is necessary to determine the characteristic properties of the synthesized nano-particles. In this paper, information will be given about these characterization stages.**

Keywords **- Nano-particle, Characterization, Colloidal Suspension, Zeta Potential, UV Absorbance**

I. INTRODUCTION

WITH the increase in parameters such as speed, pressure and temperature in mechanical systems, material losses due to friction and wear increase. Efficient lubrication systems are needed to reduce these losses. With the additives added to the oils, the tribological performance of the oils can be increased. In addition, with the development of nano lubricants, high-performance-oriented lubricants can be developed for applications in vehicle technologies [1]. Therefore, especially in the last few years, the interest in nanoscale new generation additives has increased.

Nano-particles form the basis of nano-technology with their size below 100 nm. For example, the diameter of a copper atom is 140 pm (picometer), or 0.14 nm. Nano-particles are used to improve the tribological properties of oils by adding them to lubricants to prevent corrosion and increase oil film strength and heat transfer coefficient.

Nano-particles with high thermal conductivity (Silver 406 W/mK, Copper 385 W/mK) reduce the friction coefficient by carrying the heat generated by friction in materials and cutting tools more efficiently. As the temperature in the friction zone decreases, adhesion wear can be prevented, and micro weld formations on the surface are minimized [2]. In addition, metals with antioxidant properties such as silver can prevent material loss due to tribo-corrosion by reducing oxidation [3].

It is predicted that nano-particle added oils have rolling friction formation, repair, polishing and protective film formation mechanisms [4]. Thanks to their spherical morphology, the nano-particles transform the sliding friction between the friction surfaces into rolling friction (ball bearing effect), significantly reducing the friction coefficient (Figure 1a). Nano-particles, which can easily penetrate even capillary cracks thanks to their size, can compensate for the loss of mass (repair effect) by filling the gaps when used in high concentrations (Figure 1b). Depending on the hardness values of the nano-particles, it can be claimed that they act like sandpaper on soft and notched surfaces with the effect of pressure, creating a polishing effect and reducing the surface roughness (Figure 1c). Due to their size, nano-particles have very high chemical instability and bond energies. For this reason, nano-particles can form a protective film layer on the surface by forming bonds when they come into contact with metallic surfaces (Figure 1d).

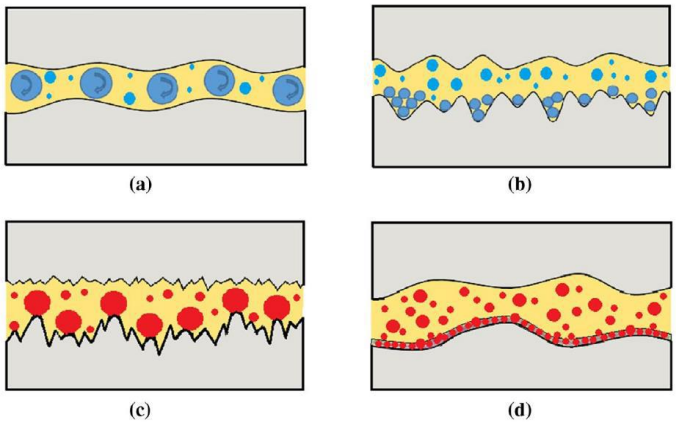

Figure 1: a) Rolling Mechanism b) Mending Mechanism, c) Polishing Mechanism, d) Protective Film [4]

The specified mechanical effects of nano-particles depend on their chemical stability. Since nano-particles have high free surface energy, they form bonds among themselves, causing aggregation and precipitation problems. In addition, the particles obtained by the chemical synthesis method can show different characteristics and morphological properties depending on the chemical reaction conditions. For this reason, it is important to determine the characteristics of nano-particles after the synthesis process.

In this study, the necessary methods for the characterization of colloidal suspensions formed by nano-particles and nano-particle added oils to be used as oil additives for tribological performance and how to interpret the results were

investigated. Explaining the necessity of the methods discussed in detail and discussing the conditions under which the results will be sufficient is unique for the literature. The study is a guide for academics who will study tribology-focused nano-particles.

II. Synthesis of Nano-Particles

Metallic nano-particles produced using physical, chemical and biological methods are of tribological importance. Green plants are used as natural reducing agents in biological nano-particle synthesis, and this method is generally preferred in medical research. Different methods such as condensation and evaporation are used in physical nano-particle synthesis. Since the physical method requires high energy, temperature, time, and pressure, it is preferred when a high amount of nano-particle synthesis is made. On the other hand, chemical nano-particle synthesis is usually carried out by the chemical reaction of a metal, which is found in nature as a compound with a reducing agent. Nano-particles synthesized by the chemical solution method have higher conductivity and stability than nano-particles produced by other methods. In addition, researchers prefer this method more because it is simple and inexpensive [5], [6].

The properties of nanofluids depend on the structure and shape of the nanomaterials. Particularly, nano-particles produced in circular form can reduce the friction coefficient by showing a rolling effect on surfaces subject to sliding friction [7]. On the other hand, nano-particles tend to clump together due to their high surface energy [8]. Therefore, when nano-particles are synthesized without applying ligand, they agglomerate and increase in size and act as an abrasive at the friction interface. Therefore, agglomeration tendency and colloidal stability of nano-particles are very important parameters for ensuring sustainable use. In order to minimize the aggregation behavior, the surfaces of nano-particles are coated with organic or polymer-based materials called ligands. As a ligand, organic agents such as PVA (polyvinyl alcohol), PVP (polyvinylpyrrolidone), gelatin and glucose are used.

III. Characterization of Synthesized Nano-Particles

Certain characterization processes are required after nano-particle synthesis. The generally preferred characterization methods in the literature are given in Figure 2. The most practical, fastest and most reliable method applied after synthesis is UV absorbance measurement. While the UV test determines the absorbance of the particles, the bandwidth gives information about the size of the particles. The basis of UV absorption spectroscopy is based on the absorption (absorption) of a beam of light passing through the object and the reduction of light intensity. Different compounds and molecules absorb different wavelengths. In the literature, it has been observed that the wavelength at which nano-gold molecules reach the highest absorbance value (peak) is ~543 nm, and nano-silver molecules are around ~430 nm [9]–[12].

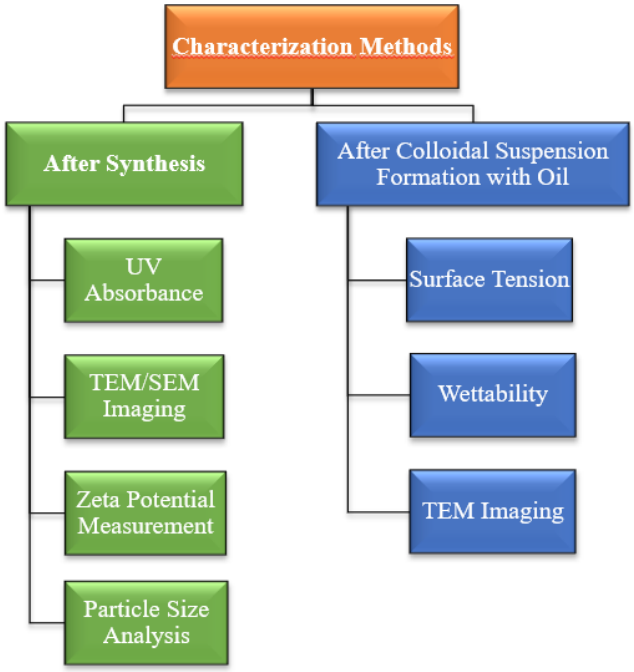

Figure 2: Characterization methods of nano-particles

When the bandwidth decreases in the UV Absorbance graph, the nano-particle sizes are monodisperse, and when it increases, it is polydisperse. It is understood that as the wavelength value increases (the peak value shifts to the right), the nano-particle size increases. When the nano-particle concentration increases, the absorbance value increases. Example UV Absorbance plots for nano-gold and nano-silver are given in Figure 3.

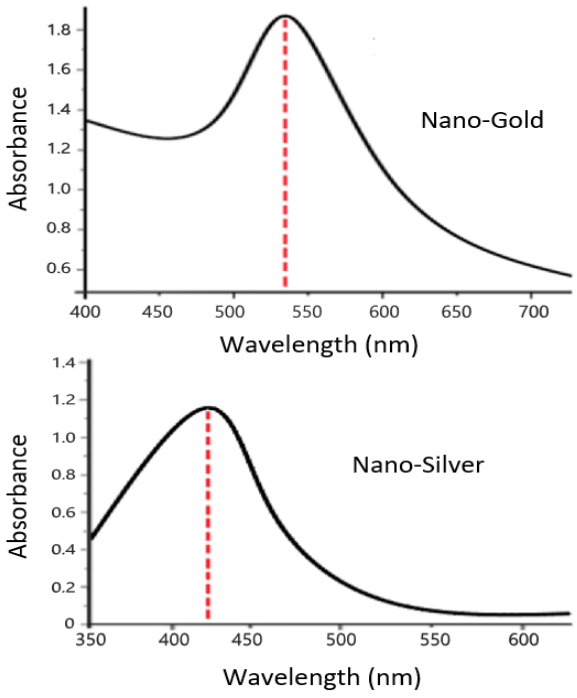

Figure 3: UV absorbance analysis for nano-gold and nano-silver

In Figure 3, it is seen that nano-gold peaks at ~540 nm and nano-silver peaks at ~425 nm. When these values are compared with the values in the literature, it is understood that nano-particle synthesis is successful.

The physical structures and dimensions (morphology) of nano-particles are determined visually by TEM analysis. When the TEM analysis image in Figure 4 is examined, it is seen that the particles are ~10 nm in size and spherical.

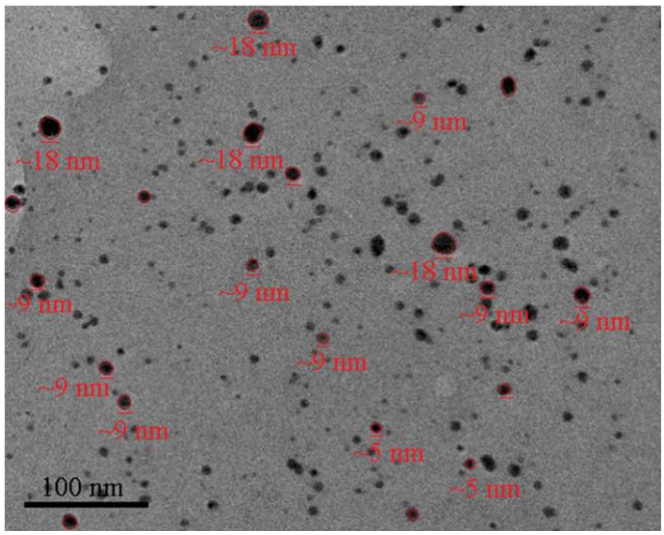

Figure 4: AgNP TEM Analysis [13]

With particle size analysis (PSA), the size distribution of nano-particles can be analyzed numerically. The PSA plot gives results according to the standard distribution curve. While the peak point of the resulting graph gives the average particle size, the graph changes depending on the variance (σ) value to the right and left. Dimensions with a value of ±1 σ indicate the size of 65% of the total nano-particles, those with a value of ±2 σ indicate the size of 95%, those with a value of ±3 σ indicate the size of 99%. For this reason, a narrow curve indicates that the size variability is minimal, and a wide curve indicates that nano-particles are synthesized in a high size range. It should not be forgotten that the standard deviation and mean values will be used together to analyze the curve. When the PSA graph example given in Figure 5 is examined, it is seen that the nano-particle sizes are approximately 10 nm in size. If the standard deviation value for Figure 5 is considered as σ=1, it is understood that the nano-particle ratio in the 9-11 nm range is 65%, the nano-particle ratio in the 8-12 range is 95%, and the nano-particle ratio in the 7-13 nm range is 99%.

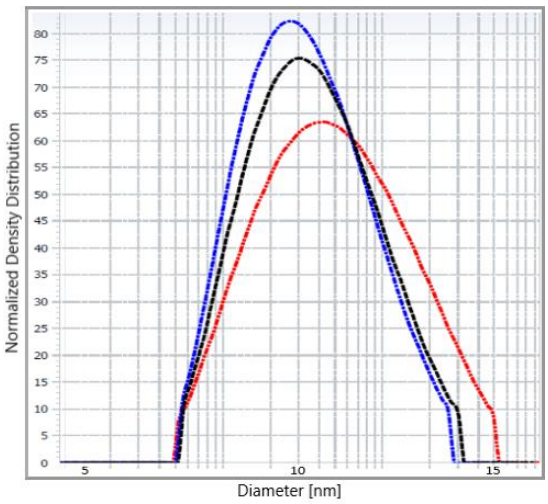

Figure 5: Particle size analysis (PSA)

Colloidal stability is achieved by the balance of attractive forces (Van der Waals) and repulsive forces (electrostatic charge) in nano-particles. Electrostatic charge values of nano-particles are measured by Zeta potential analysis. A Zeta potential test result of less than -30 mV or greater than +30 mV indicates that the nano-particles have a high degree of stability [14]. This is because the repulsive forces between the nano-particles overcome the Van der Waals (agglomeration) and gravity (precipitation) forces. When an exemplary Zeta potential analysis (Figure 5) is examined, it is seen that the ligand stability is high with a value of -38 mV.

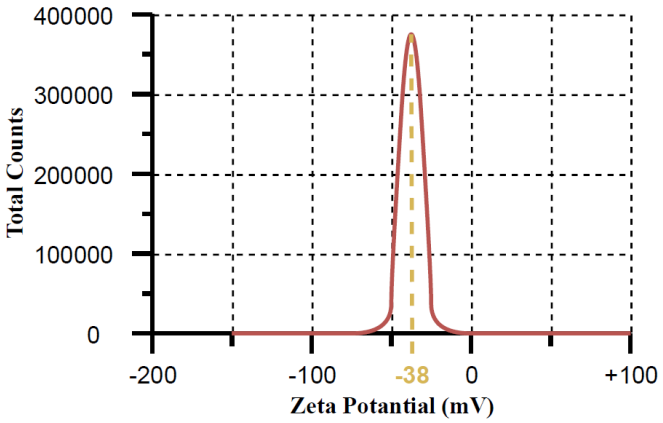

Figure 6: Zeta potential analysis

IV. Characterization of Nano-particles Forming Colloidal Suspension with Oil

Surface tension and contact angle affect the ability of liquids to penetrate the surface and the tribological performance of the oil. Surface tension is the resistance of liquids to an increase in their surface area. The angle formed by a liquid in contact with a solid surface is called the contact (wetting) angle. As the contact angle decreases, the surface energy and wettability increase [15]. Studies in the literature show that nano-particles added to oils reduce the surface

tension of oils [16]. When the surface tension of the oil decreases, the wetting angle decreases indirectly, and the area in which the oil contacts the solid material increases (Figure 7). Thus, it is expected that the tribological performance of the oil, which spreads and penetrates the surface better, will increase.

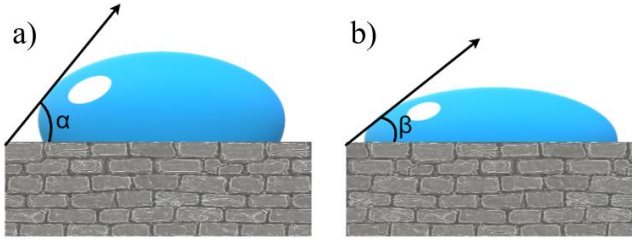

Figure 7: a) High surface tension, b) Low surface tension

V. Conclusion

In this study, post-synthesis characterization methods and evaluation methods of nano-particles added to industrial oils as oil additives were investigated. The ability of nano-particle added oils to provide high tribological performance depends on their high colloidal stability. The methods and analysis methods considered within the scope of the study are given below.

The wavelength value with the highest absorbance value in the **UV absorbance** test gives information about the type and size of the synthesized nano-particles.

The **TEM analysis** image shows the size and physical structure (morphology) of the particles.

With the **Zeta potential**, the repulsion forces of the nano-particles are measured. The zeta potential test is important for determining the aggregation tendencies of nano-particles in solution and forming a colloidal suspension. A Zeta potential value lower than -30 mV or higher than +30 mV indicates sufficient stability.

By **particle size analysis**, the dimensional distributions of the synthesized nano-particles are determined statistically.

Surface tension and **wetting angle** analyzes provide information on the ability of liquids to penetrate the surface. The penetrating ability of the liquid increases as the surface tension and wetting angle decrease.

When the characterizations of the synthesized nano-particles and the colloidal suspensions formed by the nano-particles with oil are performed exactly based on these tests, more accurate results are obtained about the tribological performance of the nano-particles on the lubricant.

References

[1] K. Lee *et al.*, "Understanding the role of nano-particles in nano-oil lubrication," *Tribol. Lett.*, vol. 35, no. 2, pp. 127–131, 2009, doi: 10.1007/s11249-009-9441-7.

[2] M. H. Cetin and S. Korkmaz, "Investigation of the concentration rate and aggregation behaviour of nano-silver added colloidal suspensions on wear behaviour of metallic materials by using ANOVA method," *Tribol. Int.*, vol. 147, no. February, p. 106273, 2020, doi: 10.1016/j.triboint.2020.106273.

[3] S. Korkmaz *et al.*, "A Comprehensive Investigation on Tribological Performance of Nano-Silver and Nano-Gold Additivated Fluids on Wearing Surfaces," *J. Tribol.*, vol. 142, no. 8, Apr. 2020, doi: 10.1115/1.4046570.

[4] A. Singh, P. Chauhan, and T. G. Mamatha, "A review on tribological performance of lubricants with nano-particles additives," *Mater. Today Proc.*, vol. 25, pp. 586–591, 2019, doi: 10.1016/j.matpr.2019.07.245.

[5] M. Alim-Al-Razy, G. M. A. Bayazid, R. U. Rahman, R. Bosu, and S. S. Shamma, "Silver nano-particle synthesis, UV-Vis spectroscopy to find particle size and measure resistance of colloidal solution," *J. Phys. Conf. Ser.*, vol. 1706, no. 1, 2020, doi: 10.1088/1742-6596/1706/1/012020.

[6] L. Wang and J. Fan, "Nanofluids research: Key issues," *Nanoscale Res. Lett.*, vol. 5, no. 8, pp. 1241–1252, 2010, doi: 10.1007/s11671-010-9638-6.

[7] L. Chang and K. Friedrich, "Enhancement effect of nano-particles on the sliding wear of short fiber-reinforced polymer composites: A critical discussion of wear mechanisms," *Tribol. Int.*, vol. 43, no. 12, pp. 2355–2364, 2010, doi: 10.1016/j.triboint.2010.08.011.

[8] N. Eltugral, H. Simsir, and S. Karagoz, "Preparation of nano-silver-supported activated carbon using different ligands," *Res. Chem. Intermed.*, vol. 42, no. 3, pp. 1663–1676, 2016, doi: 10.1007/s11164-015-2110-6.

[9] M. J. Wali M., Sajjad AS., Sumaira S., Muhammad N., Safia H., "Green Synthesis of Gold Nano-particles and Their Characterizations Using Plant Extract of Papaver somniferum," *Nano Sci Nano Technol*, vol. 11, no. 2, p. 118, 2017.

[10] S. Ibrahim, Z. Ahmad, M. Z. Manzoor, M. Mujahid, Z. Faheem, and A. Adnan, "Optimization for biogenic microbial synthesis of silver nano-particles through response surface methodology, characterization, their antimicrobial, antioxidant, and catalytic potential," *Sci. Rep.*, vol. 11, no. 1, pp. 1–18, 2021, doi: 10.1038/s41598-020-80805-0.

[11] M. N. Babu, V. Anandan, N. Muthukrishnan, and M.

Gajendiran, “Experimental process to evaluate the minimum quantity lubrication technique using copper nanofluids in turning process,” *Int. J. Mach. Mach. Mater.*, vol. 20, no. 6, pp. 497–512, 2018, doi: 10.1504/IJMMM.2018.096377.

[12] K. Anandalakshmi, J. Venugobal, and V. Ramasamy, “Characterization of silver nano-particles by green synthesis method using Pedalium murex leaf extract and their antibacterial activity,” *Appl. Nanosci.*, vol. 6, no. 3, pp. 399–408, 2016, doi: 10.1007/s13204-015-0449-z.

[13] M. H. Cetin and S. Kabave Kilincarslan, “Effects of cutting fluids with nano-silver and borax additives on milling performance of aluminium alloys,” *J. Manuf. Process.*, vol. 50, no. December 2019, pp. 170–182, 2020, doi: 10.1016/j.jmapro.2019.12.042.

[14] J. D. Clogston and A. K. Patri, “Zeta potential measurement.,” *Methods Mol. Biol.*, vol. 697, pp. 63–70, 2011, doi: 10.1007/978-1-60327-198-1_6.

[15] A. W. ADAMSON, “Physical Chemistry of Surfaces,” *Wiley Intersci.*, vol. pp 777, 1990.

[16] X. X. Tian, R. Kalbasi, R. Jahanshahi, C. Qi, H. L. Huang, and S. Rostami, “Competition between intermolecular forces of adhesion and cohesion in the presence of graphene nano-particles: Investigation of graphene nanosheets/ethylene glycol surface tension,” *J. Mol. Liq.*, vol. 311, p. 113329, 2020, doi: 10.1016/j.molliq.2020.113329.

Facile Preparation and Efficient Degradation Performance of ZnO/CuO Composite under Visible Light Irradiation

A.İ. VAİZOĞULLAR[1] M. UĞURLU[2] and S.İ.YILMAZ[3]

[1] Muğla Sıtkı Koçman University, Muğla/TURKEY, aliimran@mu.edu.tr
[2] Muğla Sıtkı Koçman University, Muğla/TURKEY, mehmetu@mu.edu.tr
[3] İstanbul University, İstanbul/TURKEY, yilmazilteris@istanbul.edu.tr

In the present study, ZnO/CuO composite photocatalyst were prepared via a chemical precipitation method and characterized with SEM, XRD, UV-DRS, and XPS analysis to explain photocatalytic performance and possible degradation mechanism. Crystallite structures of the samples were investigated with XRD analysis. The results confirmed that ZnO and CuO were hexagonal and monoclinic structure. The SEM results showed that ZnO nanorods and semi-spherical CuO were exhibited an aggregation state. To confirm the formation of heterojunction and changing of electronic states XPS analysis were performed and presented that the peak shifts were observed. Comparing with bare ZnO and CuO, ZnO/CuO composite was extends to visible region and displayed the higher photocatalytic degradation efficiency of bromine thymol blue. These findings suggested that ZnO/CuO composite has broaden light absorption and efficient electron/hole separation with p-n heterojunction. Possible degradation mechanism led that the photo-excited holes and superoxide radicals were dominant role for occurring the reactant intermediates and oxidation of brom thymol blue respectively.

Keywords: ZnO/CuO, Composite Phtocatalysts, Organic Pollutant, Material Characterization

1. INTRODUCTION

Persistent organic pollutants (POPs) are chemicals that can stay in nature for a long time. They are transported over long distances, accumulate in adipose tissue, and also pose a high risk to the environment and human health. As a result of their chemical properties, these chemicals, whose traces can be found not only in the place where they are produced, but also in places that are never produced or even used, are known as dangerous substances not only nationally but also globally. POPs are hazardous chemicals that occur unintentionally (unintentionally) as a result of conventionally produced pesticides, industrial chemicals and industrial activities. First, POPs are carbon-based compounds. The carbon chain is usually surrounded by hydrogen and oxygen atoms and halogens such as chlorine or bromine. Most POPs, which are known to the chemical industry due to their dependence on chlorine with numerous structural possibilities, belong to the organochlorine chemical group (eg DDT, Aldrin, Endrin, and chlordane) [1]

The concept of photocatalytic is increasing phenomenon in the world. It is a Nano technological product that does not harm organic materials and human health. It can maintain its performance for a long time when used once, and creates a chemical reaction by using light energy.

Chemical precipitation, filtration, electro deposition, ion exchanger adsorption and membrane systems are some of the traditional methods used in wastewater treatment. However, these methods are not very effective in the degradation of some persistent organic pollutants. In addition, these methods since their applications require expensive equipment, their use is limited [2]. Recently, the most used method for the removal of such toxic and stable pollutants from the environment is photocatalytic decomposition, which is an advanced oxidation method. [3]. this method is the excitation of a semiconductor.

II. MATERIALS AND METHOD

$Zn(NO_3)_2{\cdot}6H_2O$ (Zinc Nitrate Hexahydrate), $Cu(NO_3)_2{\cdot}3H_2O$ (Copper Nitrate Threehydrate) and hexamethylenetetramine, HMTA ($C_6H_{12}N_4$) as an agent for one-dimensional (1-D) growth were prepared with desire amount. All samples were synthesized with chemical precipitation method. Firstly, $Zn(NO_3)_2{\cdot}6H_2O$ and agent (HTMA) with 0,002M were dissolved in pure water. And then,

0,003M of $Cu(NO_3)_2 \cdot 3H_2O$ solution was added to previous solution. 0.01M of Ammonia (NH_4OH) solution was added to that solution drop by drop. The obtained precipitate was stirred for an hour. It was filtered and washed with water three times. The obtained particles were dried at 90°C and calcined at 350°C for 180 min.

III. RESULTS AND DISCUSSION

SEM results

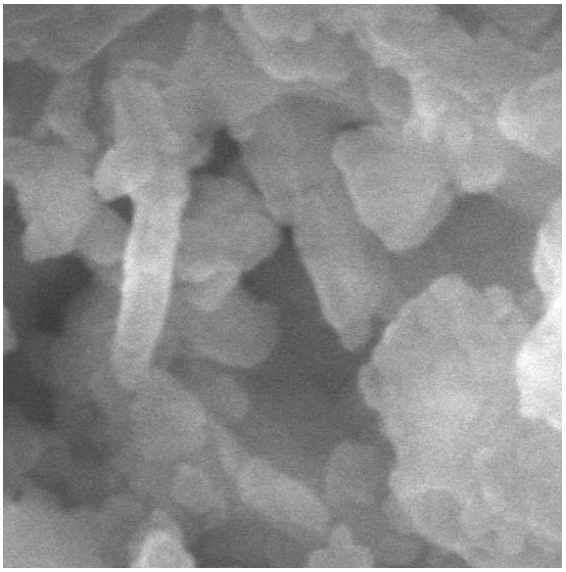

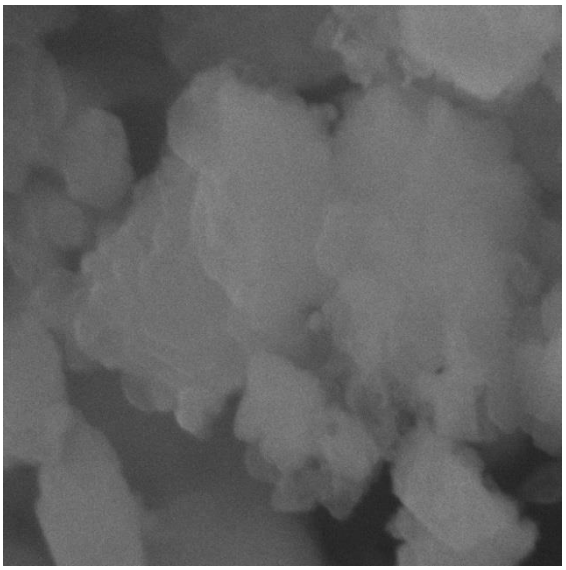

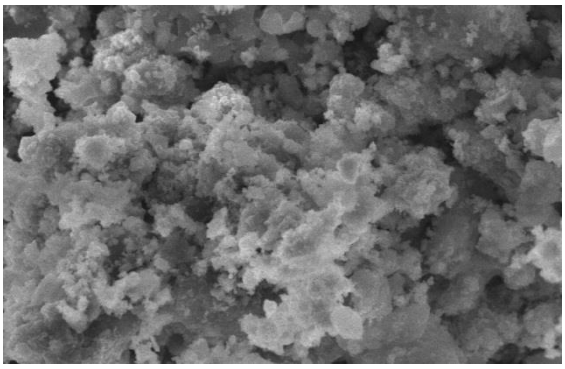

Figure 1. SEM images of the photocatalysts

The morphological structures of the as prepared ZnO/CuO composite were investigated by SEM and corresponding micrographs are presented in Figure 1. The ZnO/CuO sample shows rods and semispherical morphologies and therefore referred as ‘’rod/ball’’ particles. The both bare ZnO and CuO particles have more agglomerated. This is attributed to the calcination temperatures which favors the agglomerated particles due to the adhesion of particles through weak bonds (Cahinoet al). If less aggregation had been achieved, we could say that it was attributed to the CuO effect. We could even say that CuO has a regulating effect on the size and the controlled growth of ZnO particles [4].

XRD Analysis

Figure 2 represents the XRD patterns of ZnO, CuO and ZnO/CuO samples comparably. ZnO samples exhibited three main peaks at 31.5 (100), 34.7 (002) and 36.9 (101) planes with wurtzite structure (JPDS-36-1451). Also, two main peaks at 35.5 and 38.8◦appeared confirming the existence of the CuO phase (JCPDS No. 48–1548) [5,6,7]. There are some sharply peaks belong to the other possible phases of CuO for example $Cu(OH)_2$ or Cu_2O. We would also point out that the ionic diameters of copper and zinc are different from each other. Hence peak shifts can be observed in the XRD analysis. But here, we did not specify too much.

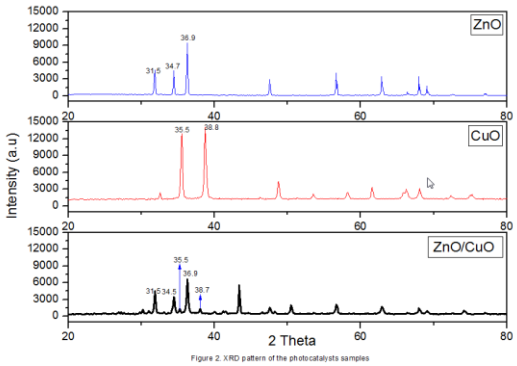

Figure 2. XRD pattern of the photocatalysts samples

Figure 2. XRD pattern of the photocatalsts samples

UV-DRS Analysis

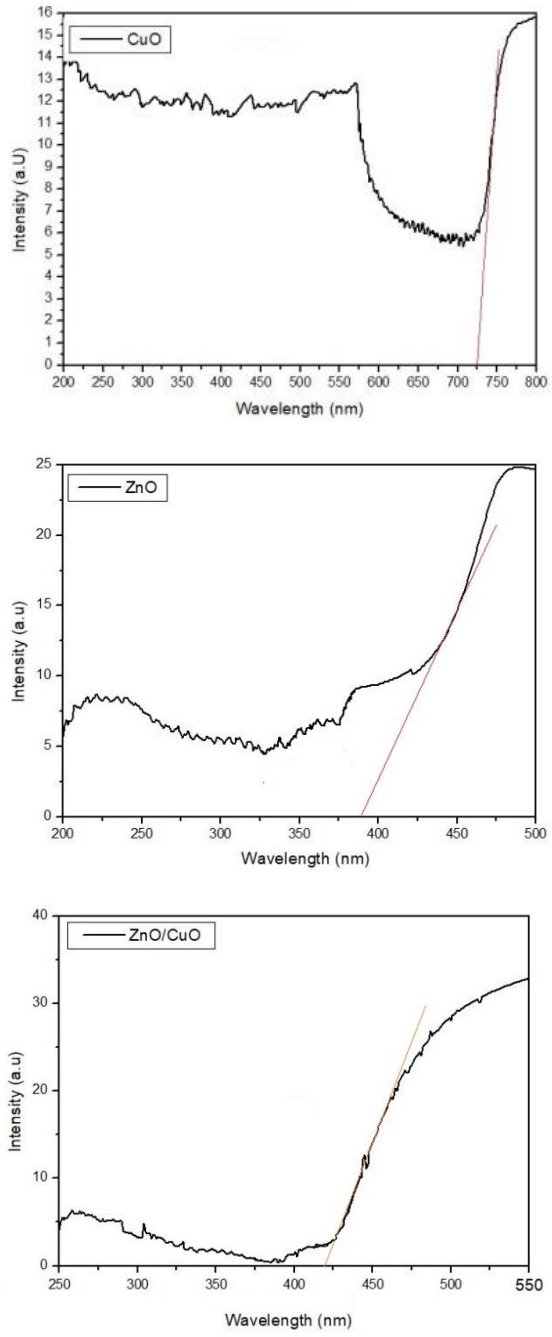

Figure 3. UV-DRS analysis of the photocatalsts samples

UV-DRS results of the samples were shown in Figure 3. As seen from the Figure 3, ZnO sample presented in the UV region absorbance with 388 nm while CuO sample showed visible absorption spectra with 725 nm. In addition, ZnO/CuO particles exhibited to visible region spectra with 425 nm. ıt can thus be suggested that the contact between ZnO and CuO enhanced the visible light absorption. The estimated band gap values of ZnO, CuO and ZnO/CuO composite is 3.88, 1.71 and 2.91 respectively. In bare ZnO, ($2p^6$) O^{2-} and ($3d^{10}$-4s) Zn^{2+} are valence and conduction band. When ZnO coupled with CuO an extra conduction band Cu^{2+} ($3d^9$-4s) occurred nearly to the Zn^{2+}. Therefore less differences of energy band at O^{2-} ($2p^6$)/Cu^{2+} ($3d^9$-4s) and O^{2-} ($2p^6$)/Zn^{2+} ($3d^{10}$-4s) confirming to enhanced visible light absorption and effective degradation under the visible light irradiation [5].

IV. PHOTOCATALYTIC RESULTS

The photocatalytic eperformances of the samples were investigated by BTM with 5 ppm under visible light irradiation for 90 min. Fig. 7(a) represents BTM degradation efficiency (C/C0) versus irradiation time for different samples.

As seen, bare ZnO presented low degradation efficiency (21%) due to limited charge separation. In addition ZnO/CuO composite exhibited a remarkable enhancing photocatalytic activity (64 %) compared to bare ZnO and CuO. Therefore ıt can be concluded that a significant photocatalytic performance of composite was higher visible light active band gap and effective inhibition of charge carries electron/hole. Several studies have been showed that the kinetics of organic dyes at liquid-solid interface under visible light follows a Pseudo-First-Order reaction model [8]. Based on the previous studies, the CB and VB band potential of samples and electronegativity of ZnO and CuO can be calculated as follows

$$E_{VB} = X\text{-}E^e + 0.5Eg$$

Where X is the electronegativity of the ZnO and CuO, Ee is the energy of free electrons in the hydrogen scale (~4.5 eV) and Eg is the energy bandgap of the semiconductor. The X values for ZnO and CuO are 5.78 and 5.83 eV The bandgaps of ZnO and CuO are 3.19 and 1.71 eV [9].

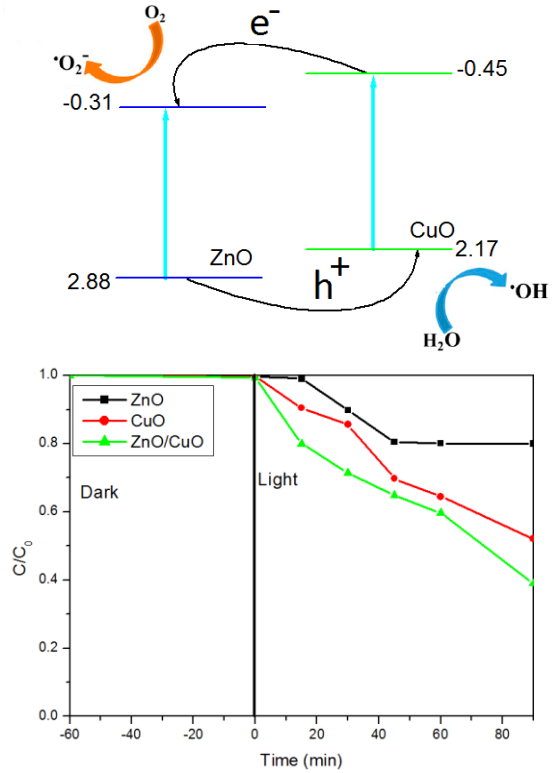

Firstly, under visible light irradiation, CuO is excited but ZnO is not. The photogenerated electrons of CuO transferred to CB level of ZnO.As the samely, the holes of ZnO migrates to the VB level of CuO. These steps limits the recombination of charge carries and thus inccrease the photocaralytic performance of composite [10].

V. CONCLUSION

ZnO, CuO and ZnO/CuO photocatalysts samples wewre presented a facile preperation method. ZnO/CuO composite dsplayed an effctive photocatalytic performance for BTM degradation. The improved degradation ability was basically descirbed to the electrical field between ZnO and CuO. This not only increased the catalytic activity, but also facilitated the charge transfer between the surfaces, providing an effective charge separation.

References

[1] Republic of Turkey Ministry of Environment and Urbanization https://onceliklikimyasallar.csb.gov.tr/kalici-organik-kirleticiler-i-5173

[2] A. Pohl, ''Removal of heavy metal ions from water and wastewaters by sulfur-containing precipitation agents'' *Water, Air, & Soil Pollution*, vol. *231*(10), pp. 1-17, 2020.

[3] E. M, Cuerda-Correa, M. F, Alexandre-Franco, C Fernández-González. ''Advanced oxidation processes for the removal of antibiotics from water''. An overview. *Water*, vol *12*(1), pp. 102, 2020.

[4] K. P, Sapkota, I, Lee, S, Shrestha, A, Islam, A, Hanif, J, Akter, J. R. Hahn, ''Coherent CuO-ZnO Nanobullets Maneuvered for Photocatalytic Hydrogen Generation and Degradation of a Persistent Water Pollutant under Visible-Light'' Illumination. *Journal of Environmental Chemical Engineering*, pp. 106497, 2021.

[5] M, Nami, A, Rakhsha, S, Sheibani, H.Abdizadeh, ''The enhanced photocatalytic activity of ZnO nanorods/CuO nanourchins composite prepared by chemical bath precipitation''. *Materials Science and Engineering: B*, vol. *271*, pp. 115262, 2021.

[6] Q, Meng, W, Liu, J, Jiang, & X.Zhang, (). Fabrication of novel p-CuO/n-ZnO heterojunction nanofibers by electrospinning for enhanced photocatalytic performance in the denitrification of fuel oil. *Ceramics International*. 2021

[7] A.M. Cahino, R.G. Loureiro, J. Dantas, V.S. Madeira, P.C.R. Fernandes, Characterization and evaluation of ZnO/CuO catalyst in the degradation of methylene blue using solar radiation, Ceram. Int. vol. 45 (11) pp. 13628–13636, 2019.

[8] H. Esmaili, A. Kotobi, S. Sheibani, F. Rashchi, Photocatalytic degradation of methylene blue by nanostructured Fe/FeS powder under visible light, Int. J. Miner. Metall. Mater. Vol. 25 (2), 244–252, 2018.

[9] Y. Xu, M.A. Schoonen, The absolute energy positions of conduction and valencebands of selected semiconducting minerals, Am. Mineral. Vol. 85, pp. 543–556, 2000

[10] Vaizogullar AI, ''Heterostructured MgO/ZnO photocatalysts: synthesis, characterization and UV light-induced photocatalytic activity using model pollutant 2,6-dichlorophenol''. Kinet Catal vol. 59(4), pp. 418–427, 2018

The use of an Agricultural Waste in the Sanitaryware Ceramics: Rice Husk Ash (RHA)

A. ODABAŞI [1], H.K. ODABAŞI[2*], E. KARİP[1], M. MURATOĞLU[1]

[1] Fırat University, Engineering Faculty, Metallurgical and Materials Engineering Department, Elazığ/Turkey
odabasia@firat.edu.tr, erdogankarip13@gmail.com, mehtug@firat.edu.tr

[2*]Fırat University, School of Civil Aviation, Dept. of Airframe and Powerplant, Elazığ/Turkey
hkodabasi@firat.edu.tr

Abstract— **Rice husk is known as an agricultural waste material containing high amounts of silicon dioxide (10-20%) depending on the soil in which the stalks grow. In this study, four different recipes (0%, 3%, 5% and 8 wt.% with rice husk ashes which is partially replaced by quartz) of sanitaryware ceramics were fabricated using the firing temperature of 1100 °C. The effects of rice husk ash addition on the firing shrinkage, water absorption, density, hardness and flexural strength of sanitaryware ceramics were investigated. The total shrinkage values of ceramics did not change to a great extent. The addition of 8 wt.% rice husk ash yielded high hardness values (29 HV) and dramatically lower bending strength compared to that of the base ceramic (0 wt.%).**

Keywords— **Sanitaryware, Rice Husk Ash, Physical properties**

I. INTRODUCTION

Rice husk is one of the most important by-products from the rice milling industry. The chemical composition of rice husk varies according to the geographical location in which it is grown and the specific growing practices. Rice husk (RH) is industrially burned at 600- 700 °C [1]. Burning of rice husk not only provides energy, but also produces rice husk ash which contains a high concentration of SiO_2 (85-98%) and can be used industrially. While the SiO_2 in the shell is in an inhomogeneous distribution, it is seen that there is a homogeneous distribution in the ash formed after combustion. Therefore, rice husk ash (RHA) is more suitable for obtaining homogeneously distributed silica particles.

Rice husk has found many potential uses in a variety applications (filler for a natural rubber and concrete, Li-ion battery, solar cell fabrication, biomedical applications) [2-4] since it is one of the most abundant natural resources rich in silica. Vanketasvaran et al. [3] synthesized silicon nanoparticles from nano silica produced from the RHA with high purity (~99%) by magnesiothermic reduction and they have applied this product in solar cell applications. Likewise, Wong et al. [4] incorporated Si nanoparticles obtained by magnesiothermic reduction of RHA based silica for battery applications. Anthinarayanan et al. [2] synthesized biogenic silica nanoparticles using RH as a precursor by an acid treatment and subsequent calcination method and evaluated their biocompatibility in vitro-cell. Several investigation have shown the successful utilization of RH as a raw material in the fabrication of different ceramic materials [5-7]. Mostari et al. [5] fabricated and characterized the porcelain ceramics prepared by incorporation of 25% RHA using a different sintering temperatures (950, 1050 and 1150 °C). Their results revealed that 1050 °C was an optimum temperature for sintering of 25 % RHA added porcelain by considering the mechanical and physical properties. The effects of rice husk ash addition (10 wt.%-50 wt.%) as a silica source on the mechanical properties, porosity and the microstructures of alumina ceramics were investigated by Ali et al [6]. Their findings revealed that the tensile strengths reduced at 10 wt.% RHA addition and after that increased at 30 wt.% and 50 wt.% RHA additions. Silva and his co-workers [7] fabricated low-cost and sustainable refractory ceramics using RHA and wollastonite microfibers. They have found that the partial replacement of the refractory clay by RHA resulted in an increase on the porosity and water absorption, associated with the incomplete mullitization reaction and the granulometric aspects.

In this study we investigate the effects of silica rich rice husk as used for replacing quartz in a standard sanitaryware composition on some technological properties (water absorption, linear firing shrinkage, bending strength) and microstructure changes of sanitaryware ceramics.

II. MATERIALS AND METHODS

In this study, four different sanitaryware ceramics were prepared containing different amount (0 wt.%, 3wt.%, 5wt.% and 8 wt.%) of rice husk ash as a silica source which partially replace by quartz. For the base sanitaryware ceramics, clay, kaolen, quartz and Na-feldspar (albite) were used as the starting materials. Raw materials were supplied from Kalemaden Company, Turkey. Rice husk came from Edirne/ Turkey. Rice husk were washed thoroughly with tap water several times and then with distilled water two times to remove impurities and other contaminants present in the raw material. After the pre-cleaning treatment, RH was dried at 80 °C for 12 hours in an vacuum oven. Rice husk was combusted at 600 °C for 6h in a graphite crucible using a melting furnace. Sodium silicate (0.5g) was used as a deflocculant. The XRF (Rigaku) analysis of rice husk ash pyrolized at 600 °C for 6h is presented in Table I. In addition, the designed four different compositions are shown in Table II. All of the compositions given in Table II were mixed in a distilled water using a

Heidolph mixer for 5 hours (Figure 1a). The slurries were prepared with a 70% in solids content.

TABLE I.
THE CHEMICAL ANALYSIS OF RICE HUSK ASH (WT.%).

SiO_2	Al_2O_3	Fe_2O_3	CaO	MgO
85.34	2.62	3.26	1.73	1.46
SO_3	K_2O	Na_2O	LOI*	
0.13	2.47	0.21	0.45	

The cylindrical specimens with a dimension of Φ 12mm×140 mm were prepared through the slip casting process (Figure 1 b) and then dried for 48h (Figure 1c), remaining 24h at ambient temperature and 24h in an electric oven at 100 °C. The pressed green bodies fired in electrical furnace (Nabertherm™) at 1100°C for 30 min.

TABLE II.
STUDIED SANITARYWARE CERAMIC (WEIGHT BASIS)

Sample	Clay	Kaolen	Feldspar	Quartz
Base	22	28	29	21
%3	23	28	29	18
%5	23	28	29	16
%8	23	28	29	13

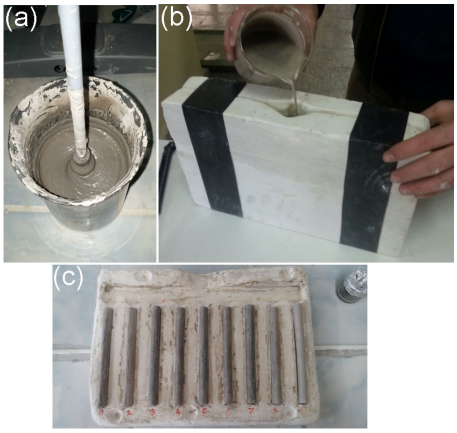

Figure 1: (a) slurry preparation (b) slip casting process (c) bar-shaped green ceramics

Some technological properties such as linear shrinkage during firing, water absorption, apparent density, Vickers hardness and flexural strength of ceramics were analysed after firing process. Bulk density was determined using the Archimedes method. The results presented are the average of those obtained for at least five samples. Water absorption was quantified according to the ASTM C373 standard [8]. The microstructure of the fired ceramics was examined by scanning electron microscopy (Zeiss Evo™). Before morphological characterization, the fired samples were polished and etched with a HF solution for 1 min. Flexural strength at room temperature was determined via three-point bending mode using a universal testing instrument (MTS criterion). Hardness measurements were carried out using a Vickers hardness instrument (Innovatest) by applying HV (0.2) to the sample surfaces for 10s.

III. RESULTS AND DISCUSSIONS

A. Physical Characteristics

The chemical compositions of raw materials is given in Table III. It was observed From Table I and Table III, RHA and quartz contain similar ceramic oxides, therefore, RHA can be used as a partial replacement for quartz in the ceramic mass. Figure 2 gives the drying shrinkage values of ceramics containing different amount of rice husk ash. It was observed from this Figure that the dry shrinkage value increased with the addition of 3% of rice husk ash to the ceramic. This value gradually decreased in samples with high addition of rice husk ash (5 wt% and 8 wt.%).

TABLE III.
CHEMICAL COMPOSITION FOR RAW MATERIALS UTILIZED (WEIGHT BASIS)

Raw Materials	SiO_2	Al_2O_3	TiO_2	CaO	Fe_2O_3
Clay 1	59.2	27	1.45	0.31	2.38
Clay 2	57.7	28.2	1.38	0.32	1.22
Kaolin 1	68.9	21.7	0.40	0.16	0.16
Kaolin 2	67.0	23.1	0.43	0.40	0.40
Quartz	95.2	2.4	-	-	-
Albite	71	17.8	0.32	0.60	0.05
Raw Materials	**MgO**	**Na_2O**	**K_2O**	**L.O.I***	
Clay 1	0.43	0.36	1.97	7.64	
Clay 2	0.49	0.37	2.1	7.99	
Kaolin 1	0.03	0.04	0.25	8.11	
Kaolin 2	0.01	0.03	0.10	8.39	
Quartz	-	-	0.1	1.2	
Albite	0.17	9.50	0.24	0.29	

L.O.I* loss of ignition

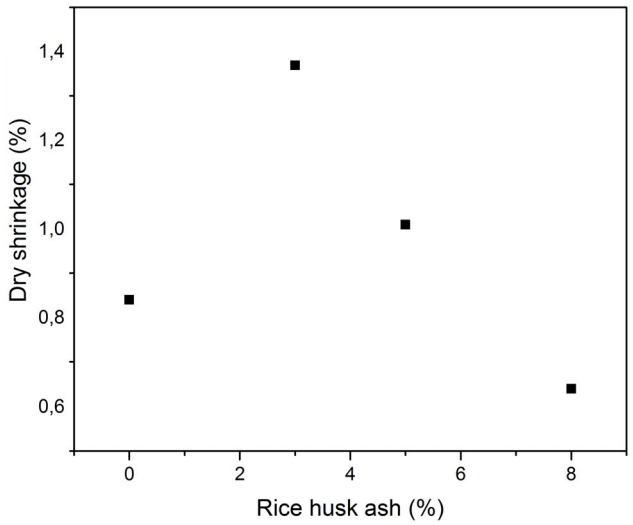

Figure 2: The changes in dry shrinkage percentage of the ceramic samples

In Figure 3 the variation of the linear shrinkage values of fired ceramics depending on the amount of rice husk ash is given. It is clear that linear shrinkage increases after addition of rice husk ash and reached the highest value in the ceramic containing 8 wt.% rice husk ash compared to the base ceramic (0 wt.%).

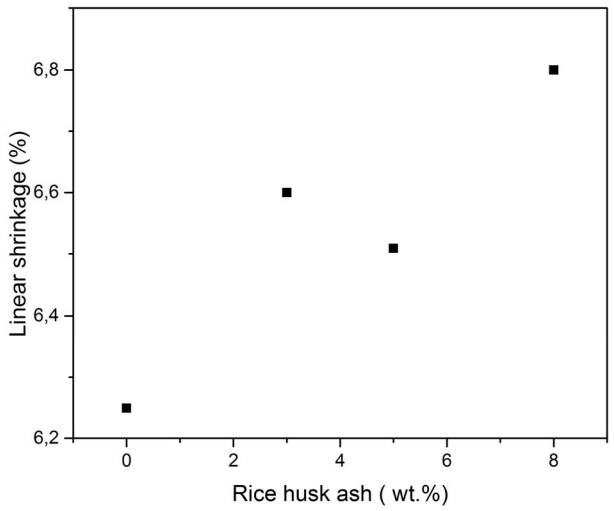

Figure 3: Variation of the linear firing shrinkage with the contents of rice husk ash.

An increase in linear firing shrinkage as the amount of the RHA was increased, which could be attributed to incorporation of a slightly lower quantity of SiO_2 in sanitaryware mixtures (Table III), considering the silica content in the chemical composition of RHA (Table II). Linear firing shrinkage at 1100 °C varied between 6.25-6.80% depending on the RHA content, which is in the compliance with the range (less than 12%) recommended sanitaryware ceramics [9]. Martini et al. [9] have found the linear firing shrinkage values between 12 and 13% at 1145-1175 °C for sanitaryware ceramics. They have reported that linear firing shrinkage is related to the pores removed or lost during sintering. An increase in the sintering temperature leads to higher shrinkage due to increasing the amount of molten materials filling the pores [9]. According to this statement, it is expected that when the linear shrinkage increases the water absorption (Figure 4) of the samples should be decreases. However in our case, water absorption increases with increase in substitution of quartz with RHA. This is probably due to enhanced pore formation properties of the RHA. The increment in the water absorption of the ceramic samples are also consistent with the decrease in density values given in Table III.

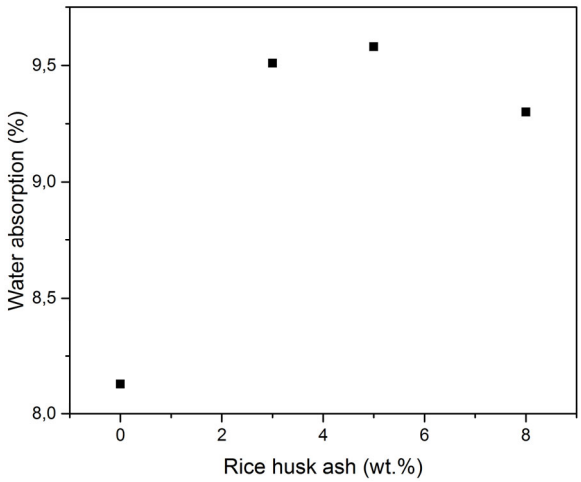

Figure 4: Variation of water absorption percentage depending on the rice husk ash amount.

Table IV shows the density and hardness values of the fired sanitaryware ceramics as a function of RHA content. The density values of samples vary between 2.43-2.13 g/cm^3. As can be seen from Table IV, density values of samples gradually decreases with RHA content.

TABLE IV.
CHARACTERIZATION RESULTS OF THE SANITARYWARE CERAMICS.

Sample name	Hardness (HV)	Bulk density (g/cm^3)	$\sigma_{e,max}$ (MPa)
Base	22.7±1.07	2.43	69.4±10.4
%3 wt.	23.8±0.85	2.33	27.1±0.15
%5 wt.	25.9±2.34	2.24	19.5±0.30
%8 wt.	29.5±1.90	2.13	19.3±0.14

Hardness values of the sanitaryware ceramics increases with the increase the amount of RHA contents. Higher hardness value was obtained as 29.5 HV when addition of 8 wt.% RHA, while this value was obtained 22.7 HV for the base ceramic. The increment in the hardness values of ceramics is related to the formation of the ceramic phases,

namely mullite, cristobalite, which have high value of hardness [6, 9]. Similar, enhancements in hardness of RHA added porous alumina ceramics were reported in the literature [6]. Major crystalline phases present in the sanitaryware ceramics fired at 1100 °C were as mullite (11-18%) and cristobalite (14-18%) phases and also minor amounts of feldspar and quartz were reported [7].

B. SEM Investigations and Bending properties

Figure 5 (a-d) reveal the SEM images of sanitaryware ceramics with different RHA contents (3 wt.%, 5 wt.% and 8 wt.%) fired at 1100 °C. As can be seen from the SEM images belonging to sanitaryware ceramics, an increase in the content of RHA leads to an increase in the porosity. Additionally, the additions of RHA causes change in the microstructure; i.e . quartz grains are getting smaller and the shape of the porosity changes from round shape (in base and 3 wt.% RHA samples) to more longitudinal shape. For example, the longitudinal shaped pores and quartz grains in the 8wt.% RHA containing ceramic sample can be clearly seen in Figure 5 (d). Similar microstructural features was also observed in the work of Ali et al. [6] who added 10wt%, 30 wt% and 50 wt.% RHA into alumina ceramics.

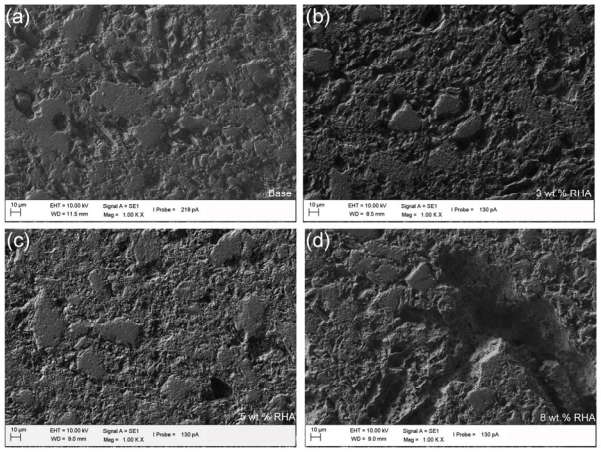

Fig. 5 SEM images of polished and etched ceramics (a) base, (b) %3 RHA, (c)5wt.% RHA, (d) 8 wt.% RHA containing samples.

The main factor affecting bending strength of samples is porosity as verified in SEM investigations (Figure 5). This is because as higher numbers of pores exist, there is much space to contribute to the fracture. Table IV shows a linear relationship between the density values of the ceramic samples with their bending strength. Additionally, the higher number of pores exist in RHA containing samples, act as stress concentrators, can be contribute to lower densification (Table IV) of the sanitaryware ceramics with a consequent decrease in bending strengths.

IV. CONCLUSIONS

In this study, sanitaryware ceramics with different compositions containing 3-8 wt.% RHA were fabricated at 1100°C and their properties were compared with the base ceramic (0 wt.% RHA). The effects of RHA contents on the dry shrinkage, linear firing shrinkage, water absorption, density, hardness and bending strength values of sanitaryware ceramics were investigated. Density values of samples gradually decrease with RHA content due to formation of porosities in the microstructures of sanitaryware ceramics. Likewise, the increment in the water absorption of the ceramic samples are also consistent with the decrease in density values. Approximately 29% increase in hardness values of ceramics were observed with the addition of 8 wt.% RHA compared with the base ceramics probably due to the lower amount of vitreous phase in the microstructures. The bending strength decrease with increasing the porosity of the sanitaryware ceramics as the RHA content increases from 3 wt.% to 8 wt.% also with substitution of quartz by RHA.

ACKNOWLEDGMENT

The authors grateful to BSc. students E. Yazıcı, O. İnce, H. Erkan who helps in carrying out of the experiments. The authors also thank for the Kaleseramik Technical Ceramic R&D center for supplying the raw materials.

REFERENCES

[1] H. D. Banerjee, S. Sen and H.N. Acharya "Effect of Addition of Talc on the Properties of Feldspar-Kaolinitic Clay Blends during Heating," *Materials Science Engineering*, vol. 52, pp. 173, 1982.

[2] J. Athinarayanan, V. Subbarayan Periasamy, M. Alhazmi, K. A. Alatiah, A. A. Alshatwi "Synthesis of Biogenic Silica Nanoparticles from Rice Husks for Biomedical Applications" *Ceramics International,* vol.41, 275–281, 2015.

[3] S. Venkateswaran, R. Yuvakkumar, V.Rajendran, "Nano Silicon from Nano Silica Using Natural Resource (Rha) for Solar Cell Fabrication" *Phosphorus, Sulfur and Silicon,* vol. 188, pp. 1178–1193, 2013.

[4] D. P. Wong, Rangaraj Suriyaprabha, d Rathinam Yuvakumar, V. Rajendran, Y-T. Chen, B-J.Hwang, L-C. Chen, K.-H. Chen, "Binder-free Rice Husk-based Silicon–Graphene Composite as Energy Efficient Li-ion Battery Anodes" *J. Mater. Chem. A*, vol. 2, 13437, 2014.

[5] M. S. Mostari, T. Zaman, A. Sen, M. R. Al Hassan, "Synthesis and Characterization of Porcelain Body Developed from Rice Husk Ash" *IJE Transactions A: Basics* Vol. 31, No. 1, 25-31, 2018.

[6] M. S. Ali, M. A. A. Hanim, S. M. Tahir, C. N. A. Jaafar, N.Mazlan, K. Amin Matori, " The Effect of Commercial Rice Husk Ash Additives on the Porosity, Mechanical Properties, and Microstructure of Alumina Ceramics" *Advances in Materials Science and Engineering* Volume 2017, Article ID 2586026, 10 pages, 2017.

[7] D. Silva, E. P., E. M., M. Tier , A. P. Garcia, "Effects of Rice Husk Ash and Wollastonite Incorporation on the Physical and Thermal Properties of Refractory Ceramic Composites" *Revista Materia*, vol. 25, no.3, 2020.

[8] ASTM C373-72 (1972) Water absorption, bulk density, apparent density, aparent porosity, and apparent specific gravity of fired whiteware products.

[9] E. Martini, D. Fortuna, A. Fortuna, G. Rubino, V. Tagliaferri 2 Sanitser, "An innovative sanitary ware body, formulated with waste glass and recycled materials" *Cerâmica* vol. 63 pp.542-548, 2017.

Correlation between Mechanical Proporties and Electrical Conductivity Values of Nordic Gold Alloy with Different Annealing Temperatures

R.G. IŞIK[1], Ç. YÜKSEL[2], A. KISASÖZ[3], Z.Y. CÖMERT[4], M. YILDIZ[5], and S. O. YILMAZ[6]
[1]Kayalar Bakır Alasımları, Tekirdağ/Turkey, rasim.isik@kayalarcopper.com
[2]Atatürk University, Erzurum/Turkey, cyuksel@atauni.edu.tr
[3]Kirklareli University, Kirklareli/Turkey, akisasoz@klu.edu.tr
[4]Yildiz Technical University, Istanbul/Turkey, zcomert@yildiz.edu.tr
[5]Kayalar Bakır Alasımları, Tekirdag/Turkey
[6]Namik Kemal University, Tekirdag/Turkey, oyilmaz@nku.edu.tr

Abstract **- Due to their superior corrosion and electrical conductivity properties, Nordic alloys are commonly utilized to produce coin blanks. Coining is a closed die forging method that involves applying pressure to the forging's surface to obtain tighter tolerances, smoother surfaces, and eliminate draft. Since the coining process mostly relies on mechanical properties, these properties are crucial for the coin blank industry. Although this procedure focuses mainly on microstructure refining, it can have significant effects on electrical conductivity. The effect of recrystallization on the mechanical properties and electrical conductivity properties of CuAl5Zn5Sn was examined in this work. The Nordic gold alloy was first cast as an ingot using the vertical semi-continuous casting method. The samples were obtained as-cast from the ingot and cut into square-shape samples with an abrasive cutter. Three of the samples were picked as reference samples, while the rest were annealed four by four at varied temperatures for the same duration of time. Samples were prepared for optical microscopy analysis, and microstructural investigations were performed using an optical microscope. The microhardness testing and analyses were and tensile tests were carried out and measured according to ASTM D638 and ASTM E384, respectively. The annealed samples' electrical conductivity was measured according to ASTM E1004 and reported in conductivity rate compared to the International Annealed Copper Standard (IACS). A relationship between annealing temperature, mechanical properties, and electrical conductivity for CuAl5Zn5Sn was investigated based on the results of the hardness and electrical conductivity tests.**

Keywords **- CuAl5Zn5Sn alloy, Annealing, Electrical Conductivity, Coining**

I. INTRODUCTION

COPPER-BASED alloys are used for a wide range of applications due to copper's excellent electrical and thermal conductivity. As a result, copper-based alloys are frequently used as coin blanks. Nordic gold alloys are well-known for having a good balance of physical and mechanical properties. It has electrical conductivity values that are suitable for the coin blank industry, as well as mechanical strength that is suitable for the coining process. Furthermore, nordic gold alloys were preferred over other alloys for use as coin blanks due to their golden shape color and lowest tarnish rates among coin blank alloys [1]. Although due to their high electrical conductivity, corrosion resistance, and formability, copper-based alloys are one of the most important commercial alloy groups. Copper-aluminum-nickel alloys are distinguished from other copper-based alloys by their excellent electrical conductivity and corrosion resistance. Although aluminum inclusion significantly improves the mechanical qualities of copper alloys, researchers have long known that it produces a significant loss in electrical conductivity [2]–[4]. Nestrovic et al. discovered in their study that the alloying element aluminum has a pronounced effect on the increase in the recrystallization temperature of copper, and they observe the anneal hardening effect in the Cu-Al alloy in the temperature range of 180–300 °C accompanied by an increase in electrical conductivity [5].

Severe plastic deformation processes, such as cold working with high deformation ratios, are used in the production of coin blanks. For the coin blank industry, hardness, microstructure, and mechanical properties are critical; the coining process depends solely on microstructure refinement, low hardness, and

ductility. For many years, previous studies have proven that plastic deformation and subsequent annealing can control the grain size and mechanical properties of copper-based alloys without compromising toughness [6]–[8].

During cold working, especially in alloys but not pure metals, strain hardening increases hardness while distortion of the lattice structure hinders electron passage and decreases electrical conductivity [9], [10].

To avoid this and continue cold work, re-crystallization annealing can solve a variety of issues. After cold forming, recrystallization annealing is a heat treatment method. This method, like stress-relief annealing, normalizing, or soft annealing, is an annealing process. Since grain boundaries migrate due to diffusion processes, grains can form anew during recrystallization annealing. When the grains return to their original shape, the material regains its ductility and ability to be formed. The biggest concern with recrystallization annealing is that it is frequently performed at high temperatures (600 – 700 ºC) for copper alloys.

In this paper, relatively low and relatively high annealing degrees are chosen to investigate the feasibility of relatively lower annealing degrees for recrystallization and how they affect electrical conductivity values and grain size. Due to this changes, a relationship between electrical conductivity and mechanical properties of the sample was investigated.

II. Experimental Studies

The experimental studies utilised CuAl5Zn5Sn. Table 1 summarizes the chemical composition of the alloy. The chemical composition of the alloy was given in Table 1. A CuAl5Zn5Sn ingot was cast using a vertical semi-continuous vertical mold. Eleven samples in the shape of dog-bone tensile rods were collected using a 100-tonne press machine. Three of the samples were used as reference samples and were not annealed.

Half of the remaining samples are annealed for 7 hours at 450°C, while the other four are annealed for 7 hours at 750°C. Due to microstructural analysis, all samples were ground and then polished with 1 m diamond paste for microstructural investigations. The microstructural evolutions of the samples were determined and examined using optical microscopy in comparison to the grain size of the alloys. Microhardness testing and analysis were conducted in accordance with ASTM E384 using microhardness tester, 30 kgf/mm^2 applied under three seconds and measured. The reported results were calculated as the average of 10 measurements taken from the sample surface and different sample regions Electrical conductivity measurements of the samples were performed in accordance with ASTM E1004 using the FISCHER Sigmascope SM330 device based on Eddy current principle. The measurements were reported in conductivity rate compared to International Annealed Copper Standard (IACS). In addition, to investigate the mechanical properties of the samples, tensile tests were applied and, yield strength and tensile strength values.

Table 1. Chemical composition of the Nordic Gold alloy.

Alloy	Cu	Al	Zn	Sn	Ni
%	88.7	5.01	Rest	1.10	0.002
Alloy	Fe	P	S	Si	As
%	0.025	0.005	0.005	0.004	0.001

III. Results

The test results of the electrical conductivity of the specimens and hardness values of the samples were given in Figure 1 and Figure 2 , respectively. As can be seen in Figure 1, the electrical conductivity values remained nearly constant with different annealing temperatures or without any annealing. The maximum electrical conductivity measured value was 15.95 %IACS which was almost the same as the electrical conductivity value of the as-cast sample, whereas the lowest value of electrical conductivity of all specimens was 15.92 %IACS.

However, as can be seen in Figure 2, hardness values were decrease from 80 HV to 60 HV.

Normally for pure copper, the electrical conductivity did not affect by crystal orientation and did not depend on grain size except for the losses due to dendritic microstructure. Raygan et al. reported that they increased the electrical conductivity by 32% by modifying the dendritic structure of pure and as-cast copper [3]. Exceptionally, the cold working process, one of the plastic deformation processes, of an annealed copper to about higher reduction rates can cause a small decrease in %IACS values of the alloys. The alloying of pure copper could reduce its electrical conductivity due to the occupation of the foreign atoms in the copper lattice, in addition, there is a cumulative effect of this scenario when more than one element is added into copper [11].

In Figure 3**Hata! Başvuru kaynağı bulunamadı.**, the hardness values of the samples and the electrical conductivity values of the samples were given together. The recrystallization process applied to the samples enabled the electrical conductivity values to reach the values in cast form. Basically, the same

electrical conductivity values were obtained in the cast and recrystallized samples. When the hardness values were examined, it was determined that the hardness values decreased significantly with the recrystallization process and the increasing process temperature accelerated the hardness decrease. It is known that the hardness values of cold rolled structures increase in the forming direction. With the applied recrystallization processes, the hardness values were reduced to values below the hardness of as cast sample In Figure 7, the microstructure of the samples were given. It was clearly seen that recrystallization occurs for both annealing temperature. It was observed that recrystallization can occur at low-temperature annealing such as 450 ºC for Nordic Gold alloys.

Elongation is a measure of the ductility of a material as determined by a tension test. It is the increase in the gauge length of a test specimen after fracture divided by its original gauge length. Higher elongation means higher ductility. Hardness, tensile strength, and modulus are inversely proportional to elongation. High tensile strength and modulus requires more force to stretch than a soft material with low tensile strength and modulus. Elongation values of the samples were given in Figure 4.

Copper alloys are mostly used as strips or plates and generally produce by cold or hot (less) rolling. Thus, the elongation values of the samples and their correlation between hardness and tensile strength were primarily investigated in this paper.

The average elongation values of the samples have been significantly increased when the annealing temperature changed. The average elongation value of the non-annealed sample has been measured at 13.46% (average of the three samples, maximum 22.43%, minimum 6.88%) where the 750 ºC -annealed samples at 38.54% (maximum 56.67%, minimum 23.12%).

In general, there is a notable increase is observed from 6.88% elongation values to 56.67% elongation values. However, there is no absolute change observed with non-annealed samples and 450 ºC -annealed samples. The average elongation value of the 450 ºC -annealed sample has been measured at 24.17% (average of the three samples, maximum 32.10%, minimum 18.12%) which is only a 10% change in the total.

The tensile strength and yield values of the samples are given in Figure 5 and Figure 6, respectively. On average, where tensile strength values of the samples remain almost the same with changing annealing temperature, yield strength values of samples significantly decrease. There is a known fact that yield strength of samples decreases with increasing temperature. This decrease in yield strength in samples is caused by recovery of dislocation pinning during thermal treatment, which results in easier plastic deformation at higher temperatures [12].

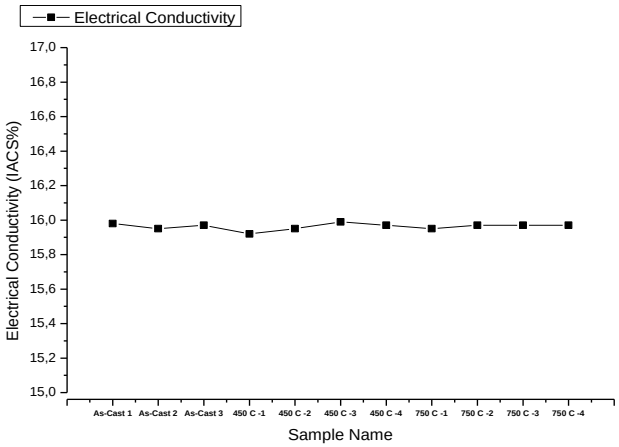

Figure 1. Electrical conductivity values of the samples.

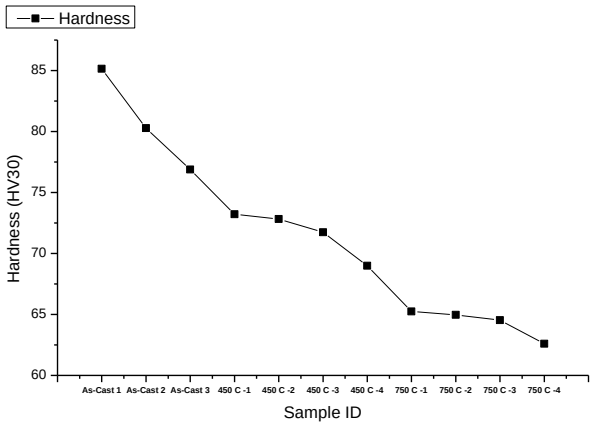

Figure 2. Hardness values of the samples.

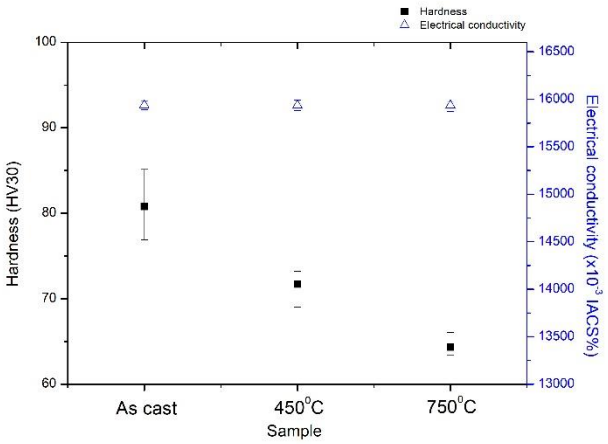

Figure 3. The hardness values and the electrical conductivity values of the samples; Black: Hardness, Blue: Electrical Conductivity

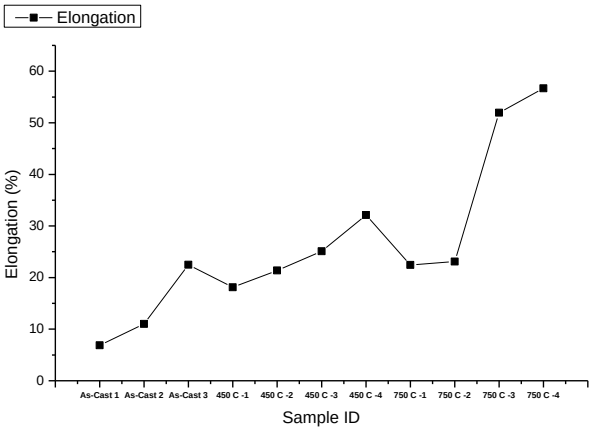

Figure 4. Elongation values of the samples.

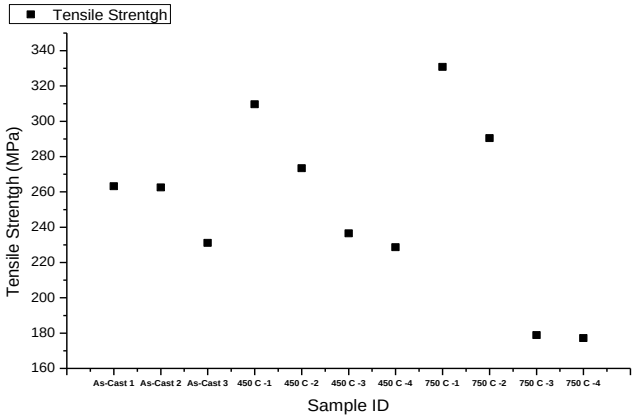

Figure 5. Tensile strength values of the samples.

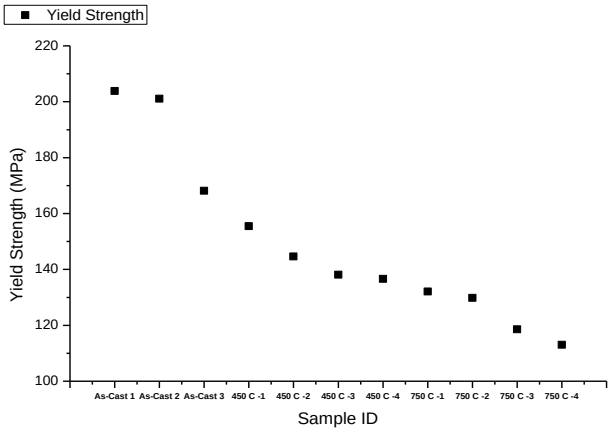

Figure 6. Yield strength values of the samples

.

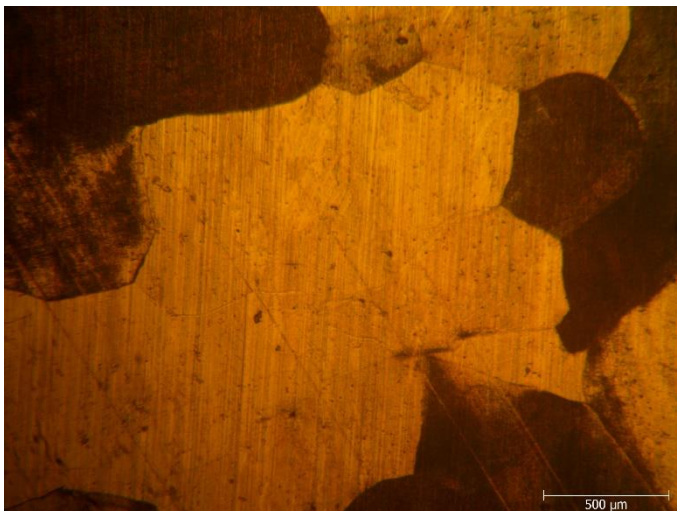

(a)

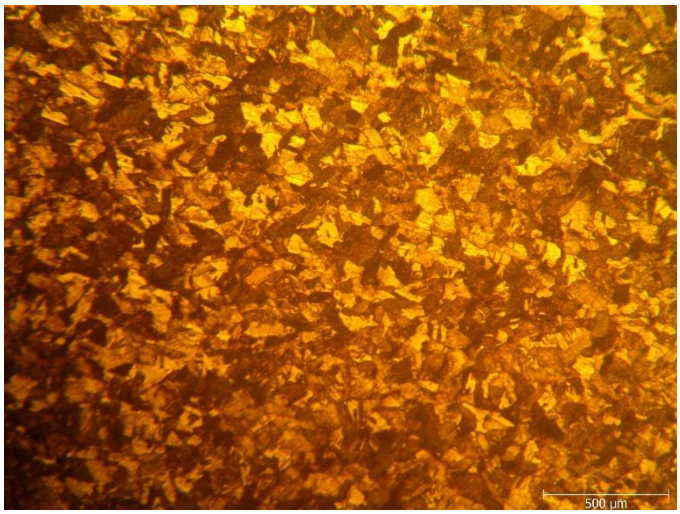

(b)

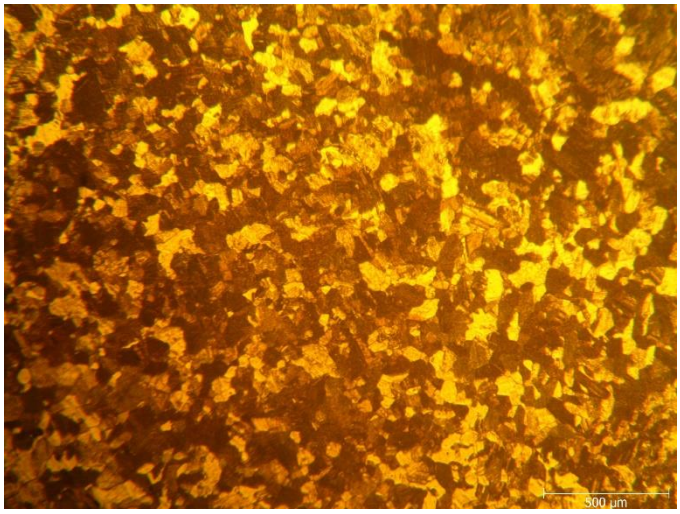

(c)

Figure 7. Microstructure of the samples;
(a) non-annealed, (b) 450 ºC, (c) 750 ºC.

IV. RESULTS

1) The recrystallization annealing has no obvious effect on electrical conductivity for CuAl5Zn5Sn alloy.
2) The hardness values of the samples decrease with higher annealing temperature due to recrystallization of grain structure.
3) The grain size of the samples decrease with annealing but then there is a small increase with 750˚C temperature annealing.
4) The elongation values of the samples increase with the increasing annealing temperature.
5) The tensile strength values of the samples remain closely the same with the increasing annealing temperature.
6) The yield strength values of the samples decrease with the increasing annealing temperature.

REFERENCES

[1] D. J. Horton, H. Ha, L. L. Foster, H. J. Bindig, and J. R. Scully, "Tarnishing and Cu Ion release in Selected Copper-Base Alloys: Implications towards Antimicrobial Functionality," *Electrochim. Acta*, vol. 169, pp. 351–366, Jul. 2015, doi: 10.1016/J.ELECTACTA.2015.04.001.

[2] A. Kisasoz, M. Türker, Z. Y. Comert, and K. A. Guler, "Experimental Research on Properties of Naval Brass Castings," *Prakt. Metallogr.*, vol. 53, pp. 24–36, 2016.

[3] S. Raygan, H. E. Mofrad, M. Pourabdoli, and F. K. Ahadi, "Effect of rolling and annealing processes on the hardness and electrical conductivity values of Cu-13.5%Mn-4%Ni alloy," *J. Mater. Process. Technol.*, vol. 211, no. 11, pp. 1810–1816, Nov. 2011, doi: 10.1016/j.jmatprotec.2011.06.002.

[4] I. J. Polmear, "The light metals," in *Light Alloys*, Elsevier, 2005, pp. 1–28.

[5] S. Nestorovic, D. Markovic, and L. Ivanic, "Influence of degree of deformation in rolling on anneal hardening effect of a cast copper alloy," *Bull. Mater. Sci.*, vol. 26, pp. 601–604, Oct. 2003, doi: 10.1007/BF02704322.

[6] S. Ma, L. Fu, X. Ma, and A. Shan, "Ultra-strong nickel aluminum bronze alloys with ultrafine microstructures by continuous heavy hot rolling," *Mater. Charact.*, vol. 158, p. 109986, Dec. 2019, doi: 10.1016/j.matchar.2019.109986.

[7] D. S. Schweckandt and M. del C. Aguirre, "Electrodeposition of Ni-Co Alloys. Determination of Properties to be Used as Coins," *Procedia Mater. Sci.*, vol. 8, pp. 91–100, Jan. 2015, doi: 10.1016/j.mspro.2015.04.052.

[8] A. Uniwersał, M. Wróbel, K. Wierzbanowski, S. Wroński, and A. Baczmański, "Rolling asymmetry effects on recrystallization process and on properties and microstructure of annealed copper," *Mater. Charact.*, vol. 153, pp. 136–147, Jul. 2019, doi: 10.1016/j.matchar.2019.05.001.

[9] D. P. Lu, J. Wang, W. J. Zeng, Y. Liu, L. Lu, and B. De Sun, "Study on high-strength and high-conductivity Cu–Fe–P alloys," *Mater. Sci. Eng. A*, vol. 421, no. 1–2, pp. 254–259, Apr. 2006, doi: 10.1016/J.MSEA.2006.01.068.

[10] V. Rontó, E. Nagy, M. Svéda, K. Tomolya, F. Varga, and B. Molnár, "Developing mechanical properties and electrical conductivity of Cu alloys by Jominy end-quench test," *Materials Science Forum*, vol. 537–538. pp. 55–62, 2007, doi: 10.4028/0-87849-426-x.55.

[11] J. R. Davis, Ed., *ASM Specialty Handbook® - Copper and Copper Alloys*. ASM International®, 2001.

[12] R. E. Smallman and A. H. W. Ngan, *Modern Physical Metallurgy: Eighth Edition*. Elsevier Inc., 2013.

The Influence of Mn Substitution and H_2S annealing on Cu2ZnSnS4 Thin Films

C.AYTUĞ AVA[1], Y. S OCAK[2] and O CELIK[2]

[1] Department of Physics, Institute of Natural Sciences, Dicle University Diyarbakir, Turkey, cananaytug@hotmail.com

[2]Smart-Lab, Dicle University, Diyarbakir, Turkey, yusufselim@gmail.com

Abstract **- Cu_2MnSnS_4 thin films were deposited by spin coating technique and annealed under 30 and 40 ccm H2S:Ar (1:9) flows to understand the influence of Mn atom content ratio and H2S flow rate during the annealing of thin films on morphological, structural and optical properties of Cu_2MnSnS_4 thin films. It was seen that the Mn content has a strong influence on structural and optical properties of the films. The crystal size of the films increase sharply for under 30 H2S:Ar (1:9) flows and start to decrease slowly again owing to the formation of high dislocation density and strain in the structures. For the films obtained under 40 ccm H2S:Ar (1:9) flows has very weak primary and secondary peaks with formation. The UV-Vis data showed the decrease of optical band gap from 1.4 to 1,17 eV with increase of H2S:Ar (1:9) flows in the structures.**

Keywords **–CZTS, Mn substitution, annealing condition**

I. INTRODUCTION

The rapid developing technology and industrialization, the increasing population and the global pollution brought about by them have become one of the most important problems recently. Traditional energy production methods are one of the important causes of environmental pollution today. Fossil fuels, which meet most of the energy needs, are decreasing day by day. Although the world is rich in renewable resources such as solar, wind, geothermal, biomass and hydro energy, renewable energies has not been produced sufficiently yet. As a renewable energy source, solar energy is the most popular.

The research on thin film photovoltaic is rapidly developing to meet the demand for sustainable green energy using non-toxic and low-cost materials. Various semiconductors have been used as absorber layer materials, such as CdTe and Cu(In,Ga)Se2 (CIGS).Many advantages including low cost and easy preparation processes, deposition of various substrates and flexibility make thin film solar cells very center of interest [1-2].Cu2ZnSnS4 (CZTS) is one of the most exiting alternatives as absorber layer in thin film solar cells [3]. It is found naturally in the earth, and the most common types are questerite and stannite. CZTS can be used as an absorber layer because it has a direct band of 1.4-1.5 eV and a high absorption of 10^4 cm^{-1}. Various alternative quaternary structures derived from CZTS structures (I2-II-IV-VI4 compounds) have been studied as absorber layers for thin film solar cells. It has been proved that the substitution of different metals in CZTS structure can modify the electrical and optical properties of the films [4].

For instance, it was shown that while the Cu2CdSnS4 (CCTS) structure obtained by substation of Cd instead of Zn in CZTS compounds decreased the optical band gap value from 1.51 to 1.37 eV , the formation of Cu2MnSnS4 structure formed by substation of Mn decrease this value up to 1.4 eV and 1.17 eV [5]. Some methods have been used to obtain quaternary semiconductor thin films including magnetron sputtering, thermal evaporation, spin coating, SILAR and ultrasonic spray techniques [6-7]. Among to others, the spin coating technique give opportunity to obtain low cost, high quality thin films. that solar cells with the highest power conversion efficiency (12.6 %) have been obtained by the spin coating method [19]. In this study, it is aimed to understand the influence of Mn atom content ratio and

E-ISBN: 978-625-44427-7-3

H_2S flow rate during the annealing of thin films on morphological, structural and optical properties of Cu2MnSnS4 thin films. For this purpose, Cu2MnSnS4 thin films deposited by spin coating technique and annealed under H2S:Ar (1:9) atmosphere under 30 and 40 ccm flow rates. The morphological, structural and optical properties of the films were analyzed by x-ray diffraction (XRD), scanning electron microscopy, atomic force microscopy and UV-vis.

II. EXPERIMENTAL PROCEDURES

Soda lime glasses (SLGs) were cleaned by detergent and ultrasonically vibrated for 10 min in methanol and acetone. 0.08 M Cupric chloride ($CuCl_2$), 0.04 M Manganese chloride ($MnCl_2$), 0.04 M tin (II) chloride dihydrate ($Cl_2Sn_2H_2O$) solutions in ethanol were used for Cu, Mn, Sn sources. During the preparation of solutions, MnCl2 solution was added to CuCl2 solution and finally $Cl_2Sn_2H_2O$ was added. 0.1 ml dietanolamin was added to mixed solution. The solution was stirred for 3 hours. 0.5 ml solutions were dropped on SLG substrates and the glasses spinned at 5000 rpm for 30 sn and heated 240 °C for 10 minutes. This process was repeated for 10 times. After deposition of Cu_2MnSnS_4 thin films on glasses, the thin films were annealed in a quartz furnace under 30 ccm and 40 ccm H_2S:Ar (1:9) flows for 2 hours. The structural properties of the films were studied using X-ray diffraction (XRD) measurements obtained from a Rigaku Ultima III diffractometer with monochromatic Cu-Ka Radiation (^= 0.154 nm), at 40 kV and 30 mA, the morphological properties were determined using an FEI Quanta 250 FEG scanning electron microscopy (SEM); EDX and Park System XE-100 atomic force microscopy (AFM), optical properties were executed using a Shimadzu UV-3600 spectrophotometer.

II. RESULT AND DISCUSSION

Figure 1 show the XRD patterns of Cu_2MnSnS_4 thin films annealed under 30 and 40 ccm H_2S:Ar (1:9) flows. This change is attributed the Mn substitution influence on crystal properties of the samples. the XRD peaks annealed under 40 ccm H_2S:Ar (1:9) flows are very weak. The 20kx scanning electron microscopy (SEM) images of the Cu_2MnSnS_4 thin films annealed under 30 ccm and 40 ccm Ar:H_2S flows are given in Fig.2a and . Fig.2b.

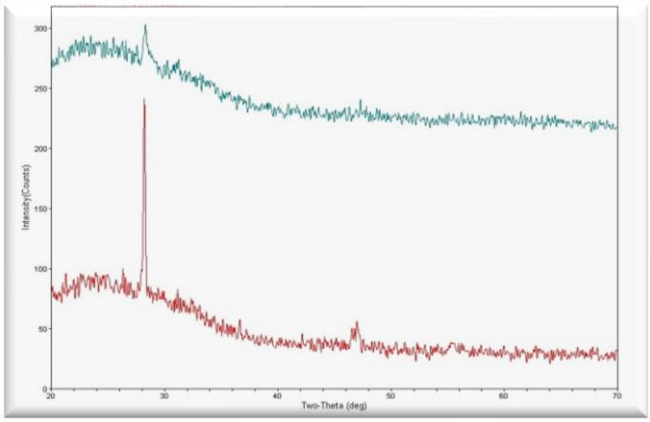

Figure 1. The XRD patterns of Cu_2MnSnS_4 thin films annealed under 30 (blue peaks) and 40 (red peaks) ccm H_2S:Ar (1:9) flows

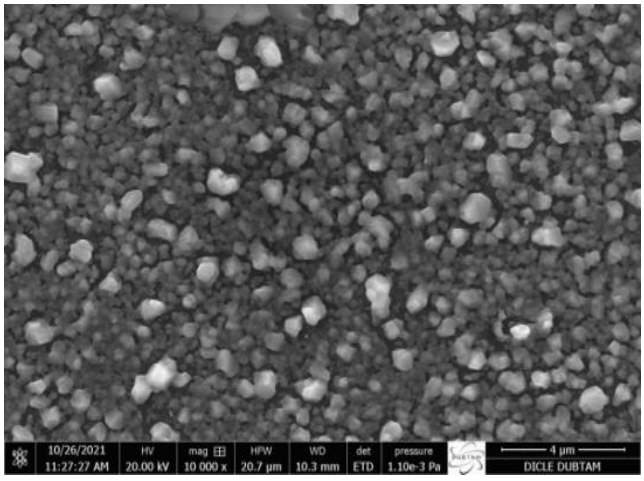

Figure 2a. The SEM images of Cu_2MnSnS_4 thin films annealed under 30 ccm H_2S:Ar (1:9) flows

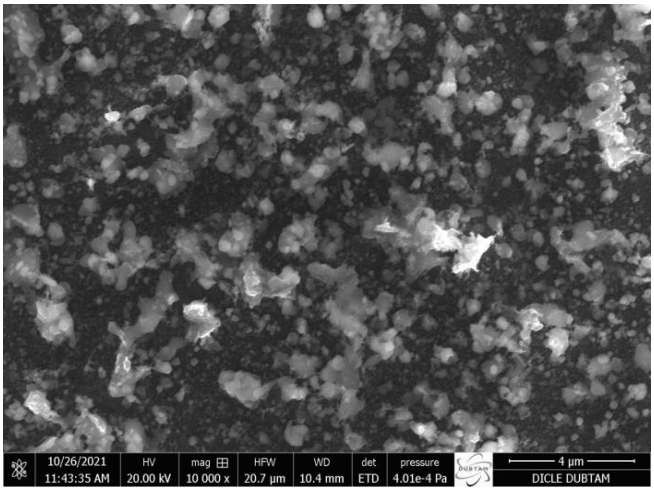

Figure 2b. The SEM images of Cu_2MnSnS_4 thin films annealed under 40 ccm H_2S:Ar (1:9) flows

E-ISBN: 978-625-44427-7-3

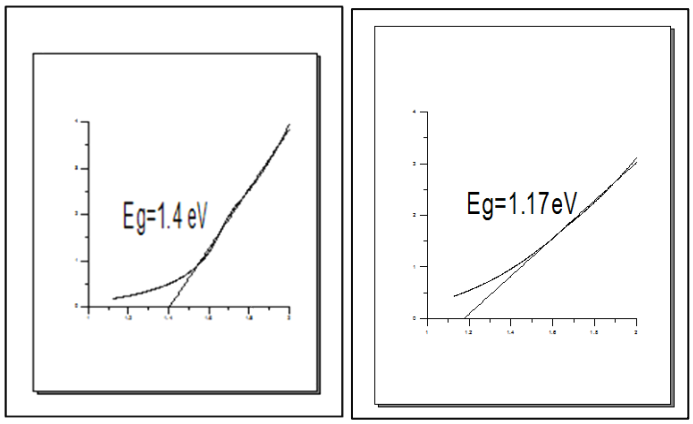

Figure 3. The band gaps of Cu2MnSnS4 thin films annealed under 30 and 40 ccm H2S:Ar (1:9) flows respectively

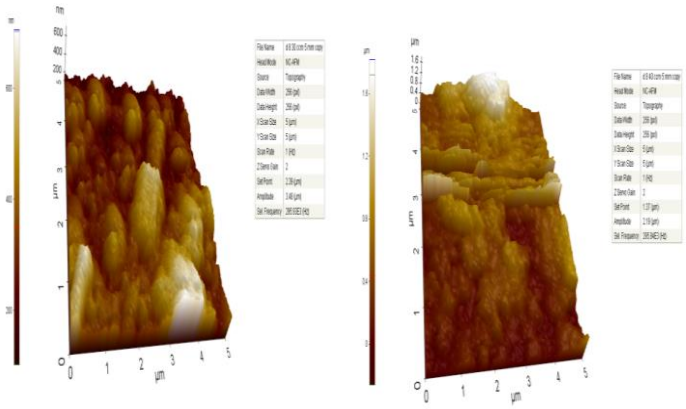

Figure 4. The AFM images of Cu2MnSnS4 thin films annealed under 30 and 40 ccm H2S:Ar (1:9) flows respectively

SEM images, it can be said that the surfaces of the films annealed under 30 ccm Ar:H2S flows are more homogeneous with respect to the ones annealed under 40 ccm Ar:H2S flows. It can be attributed the additional agglomeration on the surfaces owing to the more interactions between the films and H2S gas. Furthermore, the absorbance-wavelength of all films were analyzed using UV-vis data obtained between 300 and 1100 nm wavelength. The band gaps of all films were calculated by extrapolating (ah v)2- h v plot to energy axis. The obtained band gap values of both the films annealed under 30 and 40 ccm Ar:H2S flows are given in figüre 3. The AFM results show the changing of surface thin films at figure 4.

IV. CONCLUSION

In conclusion, we present the preparation of CMTS thin films by spin coating technique. The effects of annealing properities on the morphology, composition, structure and optical properties of CMTS thin films were investigated. The XRD measurements indicated that the as-prepared films were primarily composed of a CMTS phase but with poor crystallinity especially annealed for under 40 ccm Ar:H2S flows. Additionally, increasing the annealing flows, the surface morphologies of films became disordered in gradual and large grain size were obtained. The atomic force microscopy analysis show that under 40 ccm Ar:H2S flows thin film is surged. Efforts are underway to improve stoichiometry of CMTS films prepared at high flows by annealing in the presence of sulfur. CMTS thin films shows that the band gap energy values decreases from 1.4 to 1.17 eV .

V. REFERENCES

[1] Ma P, Li W, Yi C, Dai C, Luo H, Yang C. Investigation of Mo films deposited on high temperature polyimide substrate by magnetron sputtering for flexible CIGS thin film solar cells application. AIP Adv. 2019;9(4):045024

[2] Khalil MI, Bernasconi R, Lucotti A, Le Donne A, Mereu, RA, Binetti S., Hart JL, Taheri ML, Nobili L, Magagnin L. CZTS thin film solar cells on flexible Molybdenum foil by electrodeposition-annealing route. JApplElectrochem. 2021;57(2):209-218.

[3] Taskesen T, Neerken J, Schoneberg J, Pareek D, Steininger V, Parisi J, Gutay L. Device characteristics of an 11.4% CZTSe solar cell fabricated from sputtered precursors. Adv Energy Mater. 2018;8(16):1703295.

[4] Tombak A, Kilicoglu T, Ocak YS. Solar cells fabricated by spray pyrolysis deposited Cu2CdSnS4 thin films. Renew Energy. 2020;146:1465-1470.

[5] Courel M, Sanchez T, Mathews N, Mathew X. Cu2ZnGeS4 thin films deposited by thermal evaporation: the impact of Ge concentration on physical properties. J Phys D 2018;51(9):095107.

[6] Dalapati GK, Zhuk S, Masudy-Panah S, Kushwaha A, Seng HL, Chellappan V, Suresh V, Su Z, Bayabyal SK, Tan CC,Guchhait A, Wong LH, Wong TKS, Tripathy S. Impact of molybdenum out diffusion and interface quality on the performance of sputter grown CZTS based solar cells. Sci Rep. 2017;7(1):1-12.

[7] Henry J, Mohanraj K, Sivakumar G.Electrical and optical properties of CZTS thin films prepared by SILAR method, J Asian Ceram Soc. 2016;4(1):81-84.

Investigation of TIG Melting Influence on a Mechanically Alloyed High Entropy Alloy

M. KAFALI[1], K.M. DÖLEKER[1], S.E. SÜNBÜL[2], K. İÇİN[2]

[1] Ondokuz Mayıs University, Samsun/Turkey, mertcankafali55@hotmail.com
[1] Ondokuz Mayıs University, Samsun/Turkey, mert.doleker@omu.edu.tr
[2] Karadeniz Technical University, Trabzon/Turkey, sunbulsefa@ktu.edu.tr
[2] Karadeniz Technical University, Trabzon /Turkey, kursaticin@ktu.edu.tr

***Abstract* – High entropy alloys (HEAs) can be produced by different techniques such as arc melting, induction melting or powder metallurgy. In this study, AlCoCrFeNi HEA was produced via powder metallurgy (PM) technique. The produced equimolar HEA was exposed to TIG surface melting to get denser surface. The obtained analysis showed that Tungsten Inert Gas (TIG) melting seriously decreased the porosity of surface. After the TIG melting process, elemental distribution changed due to high arc temperature.**

***Keywords* – AlCoCrFeNi, High entropy alloy, Powder metallurgy, TIG surface melting.**

I. INTRODUCTION

HIGH entropy alloys (HEAs) compared to conventional alloys have unique properties. Steel is a conventional alloy that generally consists of dominantly Fe (principal element) and minor amount other elements. However, HEAs 5 or more principal elements (from 5% to 35% as atomic) include [1]. This leads to high mixing enthalpy compared to conventional alloys. High mixing enthalpy enables the formation of low amount of solid solution phases. HEAs exhibit attractive properties such as high corrosion resistance, high oxidation resistance, high hardness, high strength, and high wear resistance [2]. These properties are associated with HEAs' core effect (high entropy, cocktail, sluggish diffusion and lattice distortion). HEAs can be manufactured using different techniques such as melting, casting, coating or powder metallurgy etc. [3]. Casting and melting techniques can lead to segregation in the microstructure. Coating techniques does not provide dense and non-oxide microstructure [4]. In PM technique, metallic powders can be alloyed using ball milling and, this can enable better homogeneity depending on the sintering process.

PM is the technique of manufacturing, processing and combining fine powder particles to produce a solid part. For many years, the TM sector has been a sector where iron, copper and nickel-based materials are used intensively, while today many structural metals have become a state where powders can be produced [5, 6].

The production methods of powder metallurgy are completely different from other metal forming techniques and resemble the technology of ceramic part production. The process begins in both cases by compressing the powders in a mold. The formed figure is baked and given the necessary strength [7].

Mechanical alloying (MA) was developed by Benjamin in 1966 [8,9]. With this method, controlled, precise, homogeneously distributed alloy powders are produced with a high-energy mill containing balls [10]. Problems arising from known casting or solidification in materials produced with the obtained alloy powders do not occur [11]. Alloys that are difficult or impossible to produce by other methods, very complex and reinforced with oxides can be produced [12-14]. Iron-based alloys are used in environments that will be exposed to high temperatures (up to 1400 °C) for a very long time [15].

In order to change the surface properties of materials and to gain new engineering properties, material surfaces can be modified using some technologies. Nowadays, the importance of surface treatments based on both classical and modern technology continues to grow [16]. For example, laser melting, electron beam melting and TIG melting methods can be used to improve the surface properties of materials. Thermally sprayed coatings or porous surfaces can be densified using surface melting techniques.

The method of alloying with TIG, which is expressed as a surface modification, is based on the principle of melting alloy powders or powders with the appropriate composition on the surface of the substrate material. Melting occurs simultaneously in both materials, and the surface and the base metal, which are modified by rapidly solidifying, are connected metallurgically [17,18,19]. Fine-grained microstructures that solidify rapidly can contain hard carbide phases in some alloys or steels [20]. In the current study, AlCoCrFeNi HEA was produced using mechanical alloying and sintering. The alloy's surface was remelted using TIG. The occurred variations were investigated and characterized.

II. MATERIALS AND METHODS

Al, Co, Fe, Ni and Fe powders (99% purity, Alfa Aesar) have been used in the mechanical alloying (MA) process.

Each powder was weighed in an equiatomic ratio. 10 g powder mixture was exposed to ball milling process using WC balls (Ø10 mm). In the MA process, 10:1 ball-to-powder mass ratio, 400 rpm, 20 min. milling and 20 min. cooling has been subjected to powders for 24h. At the end of the milling, Ø10 mm pellets under 500 MPa pressure were molded via a uniaxial hydraulic press. The produced 3mm pellets have been exposed to 1200 °C for 6h under a vacuum ambient in an electric tube furnace. The produced HEA was exposed to TIG surface melting process. Its parameters were given in Table 1.

Table 1: TIG surface melting parameters

Current/Volt	45 A / 5 V
Speed	1.209 – 1.510 mm/s
Protective Gas	%99.9 Ar
Protective Gas Flow Rate	17 l/min.
Electrode	2% ThO_2 -Tungsten Electrode
Electrode Diameter	2.4 mm

The microstructure of the samples was investigated using scanning electron microscopy (SEM) (JEOL JSM-7001F, Japan) equipped with an energy dispersive X-ray spectrometer (EDS) (Oxford Instruments, X-max 80 AZtec). XRD analysis (Rigaku, CuKα, DMAX 2200, Japan) was performed to AlCoCrFeNi HEA to observe phase structure. The hardness values as Vickers were obtained by microhardness machine (Qness, Q10M, Austria) under a 300 g load for 15 s holding time. Five different measurements and their average were used to get the hardness values of the samples.

III. RESULTS AND DISCUSSION

Figure 1 shows the SEM image and EDX spectrum of AlCoCrFeNi HEA produced by PM. According to the SEM image, there are some boundaries in the microstructure like a grain boundary. Also, there are many porosities in these boundaries. To evaluate the elemental distribution, EDX analysis were subjected to denser regions. EDX analysis showed that almost equimolar elemental distribution was obtained. This shows a successful production of HEA. The boundaries (dark regions) are dominantly composed of alumina and pores.

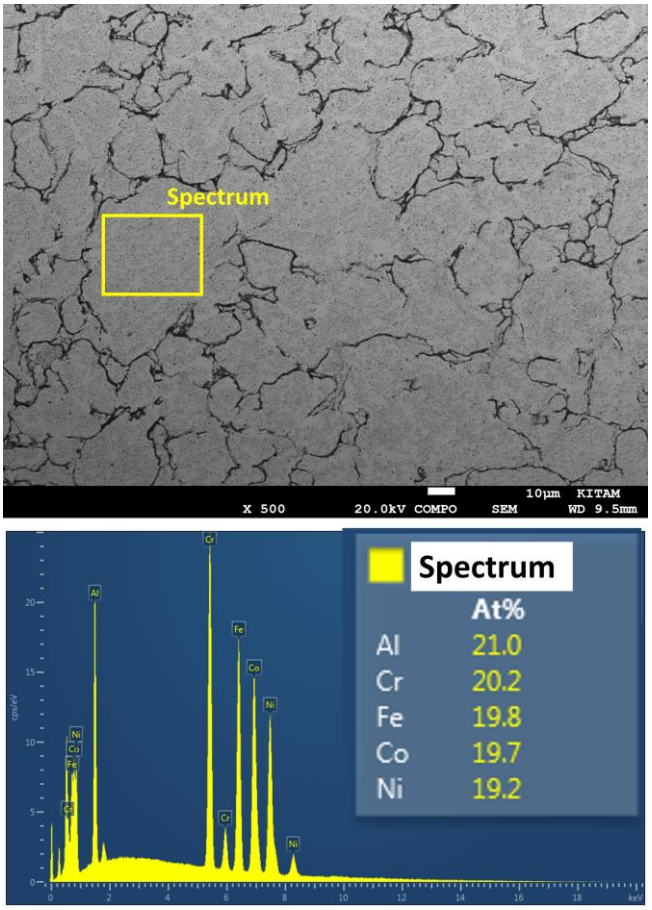

Figure 1: SEM and EDX analysis of AlCoCrFeNi.

In Figure 2, XRD pattern of AlCoCrFeNi HEA produced by PM was given. The sample consists of FCC, BCC, B2 and Al_2O_3 phases. Light gray regions belong to FCC phases structure while dark gray regions are BCC+B2 phases. Al_2O_3 formations were also seen in Figure 1.

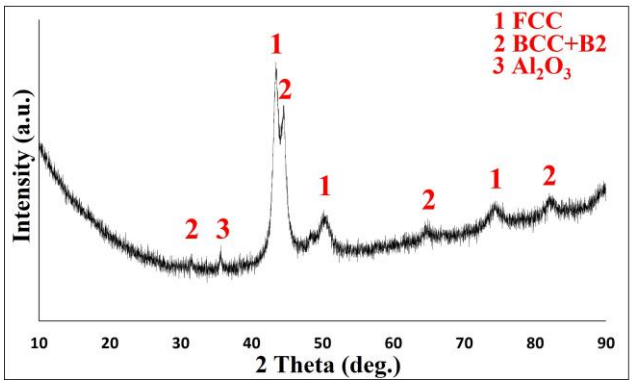

Figure 2: XRD pattern of AlCoCrFeNi.

Figure 3 shows the cross-sectional SEM image, EDX and mapping analysis of TIG surface melted AlCoCrFeNi. There is a significant decrease in porosity content on the surface of the alloy. However, there is no visible phase distribution on the surface of the alloy. At the interface, dark regions belong to Al_2O_3 phases according to elemental distribution. This may have occurred during the initial stage of the TIG melting

process. During the TIG melting, arc formation leads to high heat input on the surface of the alloy. In addition, the presence of pores in the alloy and the presence of oxygen in the ambient caused the oxide formation at the interface. Al_2O_3 formation brings about a decrease in Al content both TIG melted surface and the alloy. According to EDX analysis, Fe-rich phase formation is more dominant in both the alloy and TIG melted surface.

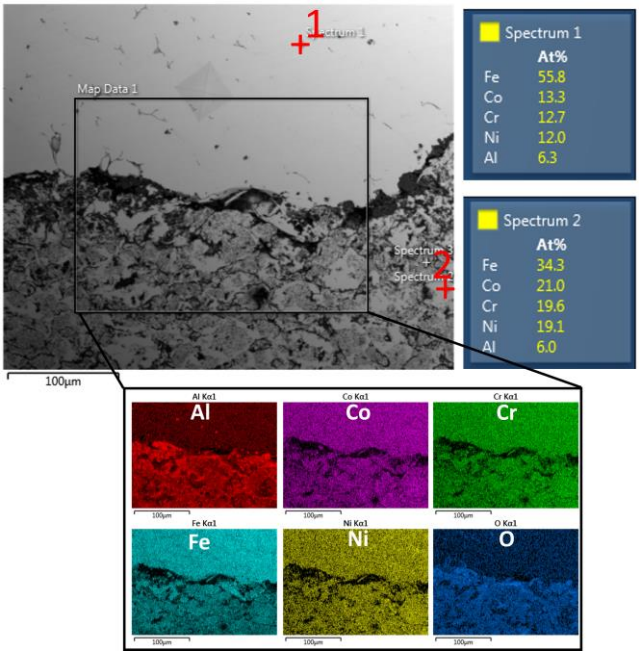

Figure 3: Cross-sectional SEM image, EDX analysis and elemental mapping image of the interface between the alloy and TIG melted surface

Figure 4 exhibits the SEM image of the TIG melted surface at higher magnification. Higher magnification reveals the phase distribution in the TIG melted surface. The obtained spectrum 1 (light gray regions) is poor in Al whereas dark gray regions are relatively rich in Al. However, dominant phase distribution in the TIG melted surface Fe-rich phases. These phases can be Fe-rich solid solutions.

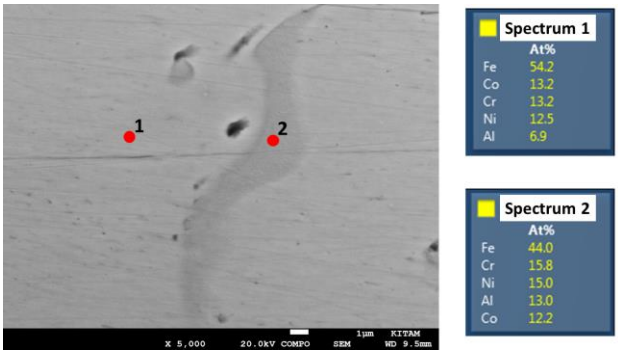

Figure 4: Cross-sectional SEM image and EDX analysis of TIG melted surface

After the hardness measurements, a relatively two-fold decrease was observed in TIG melted surface. TIG melted surfaces have approximately 260±30 HV, while the hardness of the alloy is found at about 440±25 HV. This hardness variation is directly related to the depletion of Al content on the surface since Al provides high hardness in the alloy due to its higher atomic radii and high bond effect with the other elements. Besides, high Al content in CoCrFeNi alloys leads to the formation of Al-rich intermetallics such as (Fe, Ni, Co)Al. The formation of these phases enables a significant increase in the hardness of the alloy.

IV. Conclusion

This study exhibits the TIG melting effect on AlCoCrFeNi produced by powder metallurgy technique. The microstructure and hardness changes were investigated before and after TIG melting in the alloy. The obtained results were summarized below:

1. Before the TIG melting process, the alloy dominantly consists of BCC and B2 phases.
2. The microstructure of the alloy contains a high amount of oxide and porosity.
3. After TIG melting process, TIG melted surface becomes significantly denser. However, the hardness of the surface decreased due to the Al depletion during the TIG melting.

Corrosion and wear behavior of AlCoCrFeNi HEA will be investigated before and after TIG surface melting in future studies.

References

[1] M.H. Tsai, J.W. Yeh, "High-entropy alloys: A critical review," *Mater. Res. Letters.* vol. 2, pp. 107–123, 2014.
[2] B.E. MacDonald, Z. Fu, B. Zheng, W. Chen, Y. Lin, F. Chen, L. Zhang, J. Ivanisenko, Y. Zhou, H. Hahn, E.J. Lavernia, "Recent Progress in High Entropy Alloy Research," *JOM*. vol.69, pp.2024-2031, 2017.
[3] P.D. Jablonski, J.J. Licavoli, M.C. Gao, J.A. Hawk, Manufacturing of High Entropy Alloys, *JOM*. 67 (2015) 2278–2287.
[4] A. Erdogan, S.E. Sunbul, K. Icin, K.M. Doleker, Microstructure, wear and oxidation behavior of AlCrFeNiX (X = Cu, Si, Co) high entropy alloys produced by powder metallurgy, Vacuum. 187 (2021) 110143.
[5] K.H. Roll, "Progress in Powder Metallurgy 1982" *MPIF /APMI*, 38 (1982),P.1
[6] J.A. Vaccari, American Machining, *Special Report*, 754, (1983), p.121
[7] I. and Steel, H., The effect of copper ratio on the mechanical properties of iron-based molybdenum, nickel, copper-doped powder metal alloys, *2. National Powder Metallurgy Conference*, 729-736, Ankara, (1999).
[8] J.S. Benjamin, 1988, *Proc. Conf. On New Materials by MA Tecniques*, ed.Eartzand L. Schultz, Calw-Girasu, Oct.,3.
[9] J.S. Benjamin, 1970, *Met. Trans.*, 1,2943.
[10] R.F. Singer, W.C. Oliver and D. Nix, 1980, *Met. Trans.*, 11A, 1985.
[11] Tank, E. ,1983, Proc. Conf. On Frontiers of High Temperature Materials II, *Inco Alloy International*, May 22-25, 251.
[12] P.S. Gilman and Benjamin, J. , 1983, *Rev.Mater. Sci.*, 13,279.
[13] Tien, J.K. and Howson, T.E., 1981, Advance in powder technology, *Paper Presented at the 1981 ASM Material Science Seminar*, 10-11 Oct. ,155, Lomissille, Kentuaky.
[14] L.R. Curwick, 1981, *Proc. Conf. On Frontiers of High Temperature Materials* I, Ed. by Benjamin, J.S. ,63. New York.
[15] C. S. Tassen, J.J. Fisher, G.D. Smith and M.J. Shaw, 1991, *Proc. Conf. On Heat Ressistance Materials*, 23-26 Sept. 105. Fontana, Wisconcin, U.S.A.

[16] M. Urgen, Modern Surface Treatment Technologies and Developments in Turkey, *9. International Metallurgical and Materials Congress*, Istanbul, p. 333-350, June 11-15 (1995).
[17] A. Hidouci, J.M. Pelletier, F. Ducoin, D. Dezert, R. Guerjouma, "Microstructural and mechanical characteristics of laser coatings", *Surf. Coati. Technol.*, Vol.123, pp.17-23, 2000.
[18] Korkut, M.H., Yılmaz, O., Buytoz, S., "Effect of aging on the microstructure and toughness of the interface zone of a gas tungsten arc (GTA) synthesized Fe–Cr–Si– Mo–C coated low carbon steel", *Surf. Coati. Technol.*, Vol.157, pp.5– 13, 2002.
[19] Khedkar, J., Khanna, A.S., Gupt, K.M., "Tribological behaviour of plasma and laser coated steels", *Wear*, Vol.205, pp.220-227, 1997.
[20] Mridha S., Ong H.S., Poh L.S., Cheang P., "Intermetallic coating produced by TIG surface melting", *J. Mater. Process. Technol.*, Vol.113, pp.516-520, 2001.

Absorption coefficient and refractive index change of exponentially confined $In_{0.52}Ga_{0.48}As$ quantum well

B. Ö. Alaydin[1,2]

[1] Sivas Cumhuriyet University, Nanophotonic Application and Research Center University, Sivas/Turkey, balaydin@cumhuriyet.edu.tr

[2] Sivas Cumhuriyet University, Faculty of Science, Department of Physics, Sivas/Turkey

***Abstract* – In this study, we have studied the optical properties of the exponentially confined $In_{0.52}Ga_{0.48}As/Al_{0.47}In_{0.53}As$ heterostructures. Zero external fields, $20\ kV/cm^2$ electric field and $20\ T$ magnetic fields are applied, wavefunctions and corresponding energy eigenvalues are found using the finite element method under effective mass approximations. It is shown that exponential confinement pushes energy states to lower energies. The overlapping probability of the E_{12} is low and this results in almost no absorption. However overlapping probability is high for E_{23} and E_{34} and very high absorption and considerable change in refractive index are observed.**

***Keywords* – Exponential confinement, $In_{0.52}Ga_{0.48}As$, $Al_{0.47}In_{0.53}As$, quantum well, optical properties**

I. INTRODUCTION

Nanoscale low dimensional systems have been intensively studied for the last couple of decades due to their crucial optical and electronic properties. In low dimensional systems, while quantum dots and quantum wires confine the carriers in three and two dimensions, quantum wells (QWs) provide one-dimensional confinement. It is well known in the literature that it is easier to grow quantum well heterojunctions owing to the more precise control of the growth during metal-organic vapor phase epitaxy and molecular beam epitaxy processes. This provides more frequent use of the QWs in the device structures therefore the studies create a new field in condensed matter physics which results in lots of potential applications for optoelectronic devices such as high-speed electron-optical modulators [1], field-effect transistors [2], infrared detectors [3] and semiconductor lasers [4]. Owing to the broad range of technological applications hydrostatic pressure, temperature, electric field, magnetic field, laser field, and different doping processes, etc. have been analyzed intensively for single and multiple quantum wells [5-9]. Subbands and corresponding wavefunctions are obtained under various circumstances as given above. Thus, eigenstates and eigenenergies are found in the quantum wells with confined carriers, this mostly results in more pronounced optical nonlinearity in the semiconductor structures than bulk semiconductors [10, 11].

In this study, exponentially confined $In_{0.52}Ga_{0.48}As$ QWs are studied under applied electric and magnetic fields. As a quantum barrier $Al_{0.47}In_{0.53}As$ is used and it provides exponential confinement. Electronic and optical properties of $In_{0.52}Ga_{0.48}As/Al_{0.47}In_{0.53}As$ heterostructure are examined for zero external fields, $20\ kV/cm^2$ electric field and $20\ T$ magnetic fields. Intraband transition energies, overlapping probability, linear absorption coefficients, nonlinear absorption coefficients, total absorption coefficients, linear refractive index changes, nonlinear refractive index changes, and total refractive index changes are found out numerically for E_{12}, E_{23} and E_{34} transitions. For numerical calculations, the effective mass approximation is used and the time-independent Schrödinger equation is solved by using the finite element method.

II. THEORY

In this paper, $In_{0.52}Ga_{0.48}As/Al_{0.47}In_{0.53}As$ exponentially confined QW heterojunction grown in the z-direction is studied. Quantum well and barrier are chosen as lattice-matched to InP. The electric and magnetic fields are set perpendicular to the growth surface as $\vec{F} = F\vec{z}$ and $\vec{B} = B\vec{z}$. Hamiltonian with external fields (electric and magnetic fields) is defined as [12];

$$H = \frac{\vec{p}^2}{2m^*} + V(z)\vec{z} + eF\vec{z} + \frac{e^2B^2\vec{z}^2}{2m^*} \quad (1)$$

In equation (1), m* describes the effective mass of the electron and it is taken as 0.07927 m_0, where m_0 is the free electron mass. p is the electron momentum operator, e is the electron charge and V(z) is the confinement potential. For $In_{0.52}Ga_{0.48}As/Al_{0.47}In_{0.53}As$ heterojunction, conduction band offset is taken as 0.6 and potential discontinuity V(z) is 0.45 meV. In numerical calculations, Hamiltonian is written in matrix formalism as;

$$H = \frac{\hbar^2}{2\ x\ 0.07927\ x\ {m_0}^*}\frac{d^2\psi(z)}{dz^2} + V(z) + eFz + \frac{e^2B^2z^2}{2\ x\ 0.07927\ x\ {m_0}^*} \quad (2)$$

where the exponentially confining potential is given by the following expression [13];

$$V(z) = \delta(A_1e^{-2z} - A_2e^{-z} + A_3e^{z}) \quad (3)$$

δ, A_1, A_2, and A_3 are real and dimensionless parameters. To solve equation (1), eigenfunctions of the infinite potential well is used as given below for well width L;

$$\psi_n(z) = \sqrt{\frac{2}{L}}\cos\left(\frac{n\pi z}{L}\right) \quad (4)$$

n is the number of eigenstates. After obtaining the energy levels and wave functions, linear and nonlinear absorption coefficients are calculated as follows [14]:

$$\alpha(w) = w\sqrt{\frac{\mu}{\varepsilon_r}}\frac{|M_{ij}|^2\sigma_v\hbar\Gamma_{ij}}{(\Delta E_{ij}-\hbar w)^2+(\hbar\Gamma_{ij})^2} \quad (5)$$

$$\alpha^{(3)}(w,I) = -2w\sqrt{\frac{\mu}{\varepsilon_r}}\left(\frac{I}{\varepsilon_0 n_r c}\right)\frac{|M_{ij}|^4\sigma_v\hbar\Gamma_{ij}}{((\Delta E_{ij}-\hbar w)^2+(\hbar\Gamma_{ij})^2)^2}$$
$$x\left(1-\frac{|M_{ff}-M_{ii}|}{|2M_{ii}|^2}\frac{(\Delta E_{ij}-\hbar w)^2-(\hbar\Gamma_{ij})^2+2\Delta E_{ij}(\Delta E_{ij}-\hbar w)}{\Delta E_{ij}{}^2+(\hbar\Gamma_{ij})^2}\right) \quad (6)$$

where w is the angular frequency, Γ_{ij} is the intersubband relaxation time, μ is the magnetic permeability, ε_r is the real part of the electrical permittivity, σ is the carrier number, I is the incident light intensity, ħ is the reduced Planck constant and ΔE_{ij} is the energy difference between final and initial energy levels of the electron. M_{ij} is the dipole matrix element and it is defined as;

$$M_{ij} = \int \psi_f(z)^*\,|e|\,z\,\psi_i(z)\;dz \quad (7)$$

Then total absorption coefficient is given as;

$$\alpha(w,I) = \alpha^{(1)}(w) + \alpha^{(3)}(w,I) \quad (8)$$

The linear and nonlinear refractive index change is expressed as [15]:

$$\frac{\Delta n(w)}{n_r} = \frac{|M_{ij}|^2\sigma_v}{2n_r^2\varepsilon_0}\left[\frac{\Delta E_{ij}-\hbar w}{(\Delta E_{ij}-\hbar w)^2+(\hbar\Gamma_{ij})^2}\right] \quad (9)$$

$$\frac{\Delta n^{(3)}(w,I)}{n_r} = -\frac{\mu c|M_{ij}|^2}{4n_r^3\varepsilon_0}\frac{\sigma_v I}{\left((\Delta E_{ij}-\hbar w)^2+(\hbar\Gamma_{ij})^2\right)^2}$$
$$x\left[4(\Delta E_{ij}-\hbar w)|M_{ij}|^2-\frac{(M_{ff}-M_{ii})^2}{\Delta E_{ij}{}^2+(\hbar\Gamma_{ij})^2}\{(\Delta E_{ij}-\right.$$
$$\left.\hbar w)\Delta E_{ij}(\Delta E_{ij}-\hbar w)-(\hbar\Gamma_{ij})^2(2\Delta E_{ij}-\hbar w)\}\right] \quad (10)$$

and finally, total refractive index change is given as;

$$\frac{\Delta n(w,I)}{n_r} = \frac{\Delta n^{(1)}(w)}{n_r} + \frac{\Delta n^{(3)}(w,I)}{n_r} \quad (11)$$

III. RESULT AND DISCUSSION

The parameters used in the study are as follow; $\delta = 0.01$, $A_1 = 15$, $A_2 = 55$, $A_3 = 0.001$, $I = 10\frac{MW}{m^2}$, $\mu = 4\pi\,x\,10^{-7}\,H\,m^{-1}$, $\sigma_v = 2.5\,x\,10^{17}\,cm^{-3}$, $\tau_{21} = 0.14\,ps$, $\tau_{32} = 2.4\,ps$, $\tau_{32} = 4\,ps$, $\Gamma_{ij} = \frac{1}{\tau_{ij}}$, and $n_r = 3.3$. In this part, numerical calculations have been done to obtain wavefunctions and corresponding eigenenergies for $In_{0.52}Ga_{0.48}As/Al_{0.47}In_{0.53}As$ exponentially confined quantum well for the zero external field, under electric field, and under magnetic field. A schematic representation of exponentially confined potentials and wavefunctions that correspond to the four lowest energy states are given in Figures 1-3 for the zero external field, under electric field, and under magnetic field. It is observed that there are four bounded states in the well for designed exponentially confined potential. The exponential confinement in the heterostructure causes a higher quantum barrier at boundaries. This results in a downward shift of energy states to lower energies. The same behavior is also observed by [12].

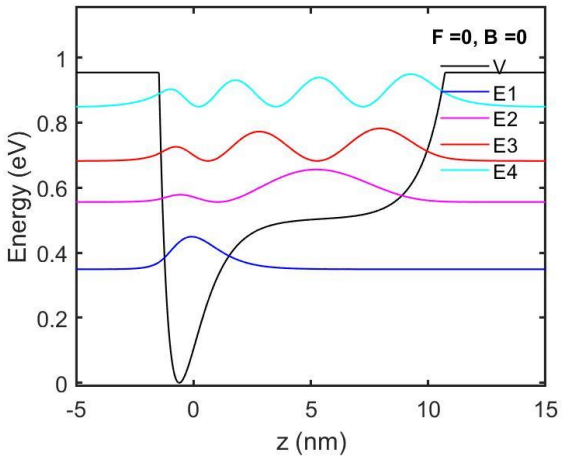

Figure 1: The variation of exponentially confining potential profile and corresponding wave functions for $F = 0\ kV/cm^2$ and $B = 0\ T$.

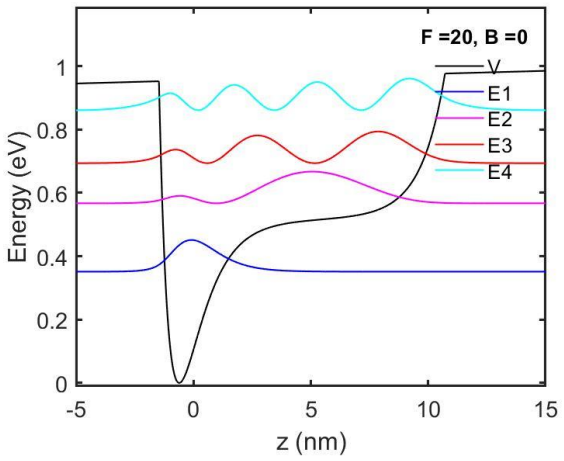

Figure 2: The variation of exponentially confining potential profile and corresponding wave functions for $F = 20\ kV/cm^2$ $B = 0\ T$.

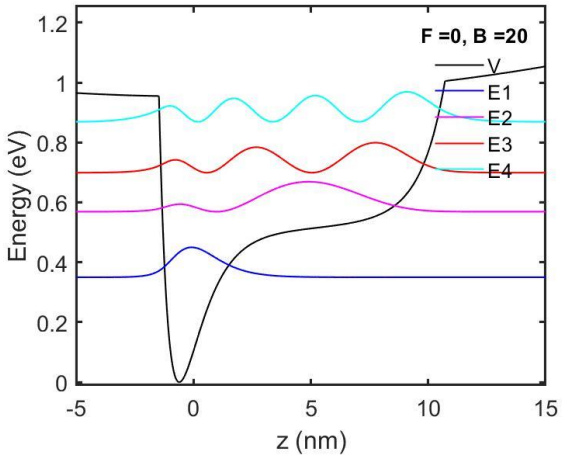

Figure 3: The variation of exponentially confining potential profile and corresponding wave functions for $F = 0\ kV/cm^2$ $B = 20\ T$.

Even though tilt and bowing at the edge of quantum barriers are observable for the applied electric and magnetic fields, contrary to the results of Altuntas external fields, electric and magnetic, have no remarkable effect on the intraband transition energies and wavefunction overlapping probability due to the exponentially confined quantum well and the bigger effective mass of InP than GaAs. Therefore, linear and nonlinear optical properties of the electric and magnetic fields are not given in the scope of this study for sake of the simplicity.

In Figure 4-6, the linear, nonlinear and total absorption coefficients of the E_{12}, E_{23} and E_{34} are given. It is seen that while there is a small amount of linear absorption, nonlinear absorption is zero for E_{12} transition owing to the low overlapping probability between ground and first excited states. However high overlapping probability between the first excited and second excited states results in 10 to the power 4 higher absorptions for E_{23} transition than E_{12} transition for linear, nonlinear, and total absorption terms. In addition, absorption at lower transition energies has higher absorption than higher transition energies as can be derived from equation 5. In Figure 4 and Figure 5, it is seen that E_{12} is bigger than E_{23}. Figure 6 shows the absorption coefficients of the E_{34} transition, we have seen that each absorption term (linear, nonlinear, and total) have higher absorption than E_{23}. Even though E_{23} transition energy is lower than E_{34}, the overlapping probability between the second excited state and the third excited state is a lot higher. Because of that, it can be said that overlapping probability is dominating. This is also observable from the value of the nonlinear term in Figure 6.

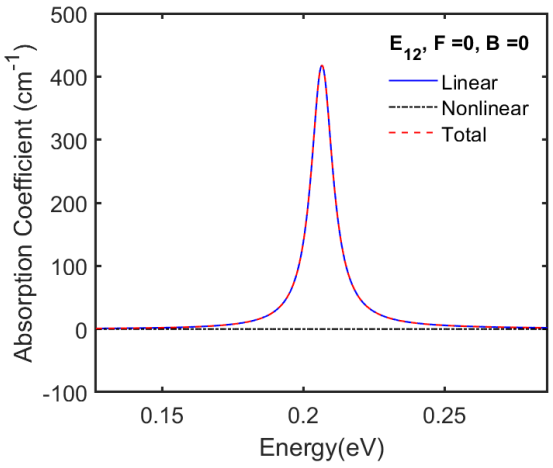

Figure 4: Variation of the absorption coefficient for E_{12} transition.

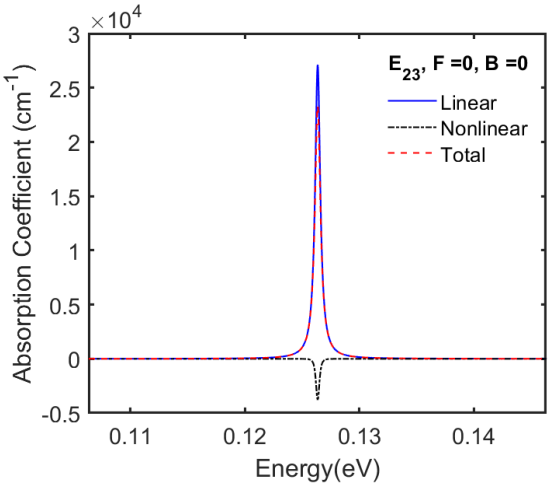

Figure 5: Variation of the absorption coefficient for E_{23} transition.

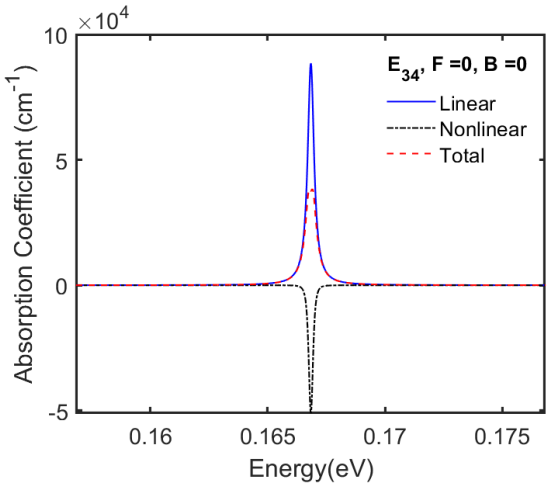

Figure 6: Variation of the absorption coefficient for E_{34} transition.

In this part of the paper, refractive index changes are given for the exponentially confined $In_{0.52}Ga_{0.48}As/Al_{0.47}In_{0.53}As$ quantum well. In figure 7, linear, nonlinear and total refractive index change of the E_{12} are shown. It is seen that while very incremental chage occurs for linear terms, it is zero for a nonlinear term which results in the same linear and total term. As a result of the higher overlapping probability of E_{23} than E_{12}, more meaningful variation is observed for linear, nonlinear, and total refractive index changes of E_{23} (Figure 8). As a perturbation term, nonlinear refractive index change is bigger and sharper than linear term. This results in an M-like (red dotted line in Figure 8) absorption trend for the total absorption coefficient and causes sharp refractive index changes in very small energy variations. In Figure 9, refractive index change for the E_{34} transition is plotted as a function of the transition energy. Refractive index change is one order bigger than E_{23} transition owing to the higher overlapping probability. Moreover, the nonlinear term is approximately 6 times higher than the linear term because of the high incident photon intensity. Even though higher nonlinear absorption, the absorption edge of linear and nonlinear terms are at the same energy which prevents sharp refractive index changes.

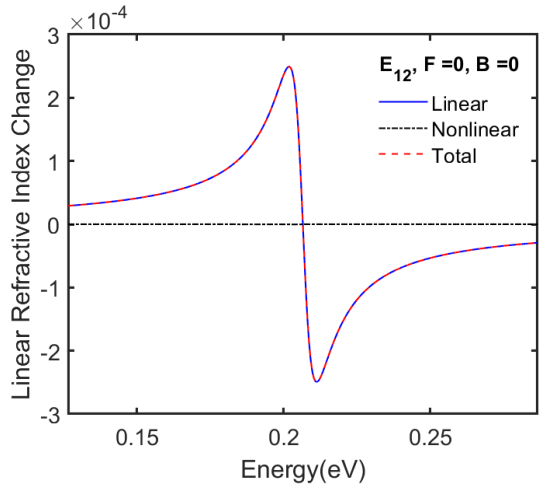

Figure 7: Variation of refractive index change for E_{12} transition.

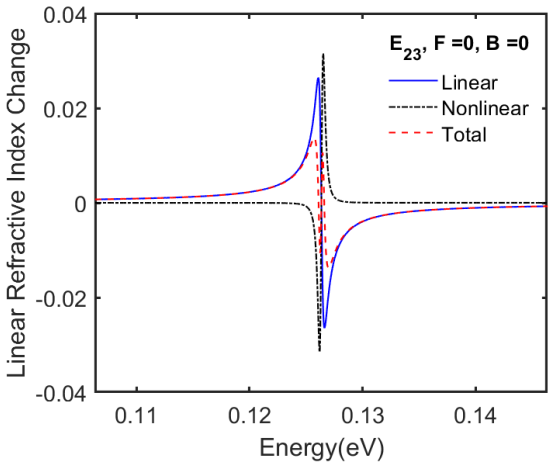

Figure 8: Variation of refractive index change for E_{23} transition.

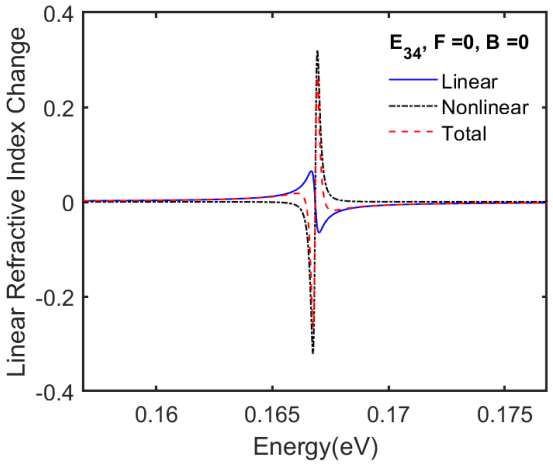

Figure 9: Variation of refractive index change for E_{34} transition.

IV. Conclusion

In conclusion, it is shown that exponential confinement results in deeper quantum well. This pushes down energy states to lower energies while transition energies are the same. It is seen that external fields have incremental effect on the exponentially confined quantum well due to deeper quantum well and bigger effective mass of InP. Because of that only zero external field results are given. Absorption coefficients of E_{12}, E_{23}, and E_{34} transitions are calculated. It is shown that absorption for E_{12} transition is comparatively lower than other possible transitions owing to the very low overlapping probability of the ground state and the first excited state. While absorption coefficients of E_{34} transition are approximately 4 orders higher than E_{12}, it is only one order bigger than E_{23} transition. As a result of the low overlapping probability of E_{12}, there is a very small refractive index change for E_{12} transition. However, refractive index changes of E_{23} and E_{34} transitions show more meaningful full values. The same as the absorption coefficients E_{34} is one order bigger than E_{23} while E_{23} has M-like refractive index change due to higher and sharper nonlinear term.

References

[1] A.D. Yoffe, Semiconductor quantum dots and related systems: Electronic, optical, luminescence and related properties of low dimensional systems, Advances in Physics, 50 (2001) 1-208.
[2] M. Vali, D. Dideban, N. Moezi, A scheme for a topological insulator field effect transistor, Physica E: Low-dimensional Systems and Nanostructures, 69 (2015) 360-363.
[3] M. Razeghi, B.-M. Nguyen, Band gap tunability of Type II Antimonide-based superlattices, Physics Procedia, 3 (2010) 1207-1212.
[4] D. Waldburger, S.M. Link, M. Mangold, C.G.E. Alfieri, E. Gini, M. Golling, B.W. Tilma, U. Keller, High-power 100 fs semiconductor disk lasers, Optica, 3 (2016) 844-852.
[5] H. Dakhlaoui, S. Almansour, E. Algrafy, Effect of Si δ-doped layer position on optical absorption in GaAs quantum well under hydrostatic pressure, Superlattices and Microstructures, 77 (2015) 196-208.
[6] İ. Karabulut, M.E. Mora-Ramos, C.A. Duque, Nonlinear optical rectification and optical absorption in GaAs–Ga1–xAlxAs asymmetric double quantum wells: Combined effects of applied electric and magnetic fields and hydrostatic pressure, Journal of Luminescence, 131 (2011) 1502-1509.
[7] J.C. Martínez-Orozco, M.E. Mora-Ramos, C.A. Duque, Nonlinear optical rectification and second and third harmonic generation in GaAs δ-FET systems under hydrostatic pressure, Journal of Luminescence, 132 (2012) 449-456.
[8] E.C. Niculescu, N. Eseanu, A. Radu, Heterointerface effects on the nonlinear optical rectification in a laser-dressed graded quantum well, Optics Communications, 294 (2013) 276-282.
[9] V.V. Tai, N.Q. Khanh, Transport properties of the two-dimensional electron gas in wide AlP quantum wells including temperature and correlation effects, Physica E: Low-dimensional Systems and Nanostructures, 67 (2015) 84-88.
[10] B.O. Alaydin, E. Ozturk, S. Elagoz, Interband transitions dependent on indium concentration in Ga1−xInxAs/GaAs asymmetric triple quantum wells, International Journal of Modern Physics B, 32 (2017) 1850052.
[11] B.O. Alaydin, E.S. Tuzemen, D. Altun, S. Elagoz, Comprehensive structural and optical characterization of AlAs/GaAs distributed Bragg reflector, International Journal of Modern Physics B, 33 (2019) 1950054.
[12] I. Altuntas, Effects of applied external fields on the nonlinear optical rectification, second, and third harmonic generation in a quantum well with exponentially confinement potential, The European Physical Journal B, 94 (2021) 177.
[13] A.D. Alhaidari, Exponentially confining potential well, Theoretical and Mathematical Physics, 206 (2021) 84-96.
[14] B.O. Alaydin, Effect of high bandgap AlAs quantum barrier on electronic and optical properties of In0.70Ga0.30As/Al0.60In0.40As superlattice under

applied electric field for laser and detector applications, International Journal of Modern Physics B, 35 (2020) 2150027.
[15] A.S. Durmuslar, C.A. Billur, A. Turkoglu, F. Ungan, Optical properties of a GaAs quantum well with new type of hyperbolic confinement potential: Effect of structure parameters and intense laser field, Optics Communications, 499 (2021) 127266.

Prototype and Modelling of Carrying Useful Load with Multicopters

Ö.F.SARI[1], M.M.SARITAŞ[2], A.ERHARMAN[3] and A.YAŞAR[4]

[1] Selcuk University, Konya/Turkey, omerfaruk.sari2@gmail.com
[2] Selcuk University, Konya/Turkey, mustafa.saritas@selcuk.edu.tr
[3] Selcuk University, Konya/Turkey, ahmet.erharman@selcuk.edu.tr
[4] Selcuk University, Konya/Turkey, aliyasar@selcuk.edu.tr

Abstract **- In this article describes the project and construction stages created to solve the problem of transporting useful cargo using Unmanned Aerial Vehicles. Our purpose is to keep both the aircraft and the payload stable along the entire trajectory and deliver the useful payload to the target, even if there are parametric uncertainties and measurement errors. The solution is considered an inconvenience for the system due to the load performed on the design, but software is used that prevents the system design and release. To verify the proposed control strategy, simulation and the results of real experiments are carried out.**

Keywords **- UAVs, Useful Loads, Real Time Point**

I. INTRODUCTION

UNMANNED aerial vehicles (UAV) are a type of flying vehicle in which there are no people inside. The most important and necessary component of UAVs is a communication system between a ground based on controller and an aircraft. UAVs are generally divided into two classes: those that fly by remote control, those that can move automatically [1].

UAVs produced for reconnaissance purposes are also used in many attack missions. Also, these vehicles can carry out many successful attacks in the defense industry. Additionally, it has also been used for fire extinguishing, cargo, health technologies. Recently, vehicles are produced different shapes, sizes, configurations and characters.

UAVs are reusable. It can fly at a certain altitude without stopping, being controlled without a crew or pilot.

1.1) Real-Time Precise Point Positioning

Global Navigation Satellite Systems (GNSS) are often used in everyday life, but they also take their place in many engineering applications that require high accuracy. Location determination with GNSS includes relative and absolute location determination methods. A minimum of two GNSS receivers are required for relative positioning [2]. The Precision Point Positioning (PPP) method is one of the absolute positioning methods, and the method uses undetected code and carrier phase measurements using a single receiver.[3,4]

Figure 1: Real-Time Point Position

1.2) Load Transportation with UAVs

Load transportation is between the many applications of attractive for Unmanned Aerial Vehicles. This task is extremely important in some missions such as search and rescue, surface exploration, military operations. With manual control aircraft usually require an experienced pilot to transport suspended loads through some trajectory while avoiding any accident with the load and the aircraft itself. On the other hand, autonomous UAVs are required to use more developed control abilities so as to achieve similar performances. Example of carrying load with UAV as it is seen in the figure 2.

Figure 2: UAV

II. SYSTEM MODELLING

Carbon fiber material was used for its mechanical structure and strength resistance, which can lift the load in the specified task. Considering the useful loads specified in the task, we need to have a ratio of engine thrust and propeller that can carry a load of about 3.5 kg. That is why the Sunny Sky V4014 drone engine was preferred. An EOLO 16*6 propellers made of carbon fiber was also selected as the propeller suitable for the engine. In the ability part, it is expected that by reducing the location accuracy to mm in determining GPS coordinates, people's health care material load will be delivered to the correct point.

2.1) Dimensional Parameters of the Design

The dimensional parameters and weight information used in the design of the Rotary Wing UAVs are given in Table 1.

Table 1: Material weight and balance table of rotary-wing UAV.

No	Part Name	Weight (gram)	Piece	Total Weight (gram)
1	Chassis	1000 g	1	1000 g
2	Motors	149 g	4	596 g
3	ESCs (Electronic Speed Control)	23 g	4	92 g
4	Battery	782g	1	782 g
5	Rotary-Wings	28 g	4	112 g
6	Navio2	23 g	1	23 g
7	Servo Motors	9 g	4	36 g
8	Telemetry	4 g	1	4 g
9	Load	240 g	4	240 g
10	Load Release System	200 g	1	200 g
11	Load Holding System	450 g	1	450 g
	TOTAL	2908 g	26	3355 g

2.2) Shaft and Mechanical Systems

The mechanical structure is formed by the vehicle body, wings and retaining mechanisms in which useful loads will be placed. The UAV body should be lightweight on the grounds that it does not provide a disadvantage in terms of stiffness and weight that can withstand the moments caused by high-speed engines. That is why the UAV chassis was created using carbon fiber composite material [5].

Figure 3: Mechanical System Design

2.3) Aerodynamics, Stability and Control Characteristics

A propeller is a tool that provides thrust or pulling power consisting of machetes placed on a rotating shaft and given a suitable aerodynamic or hydrodynamic shape. The four-rotor unmanned aerial vehicle used a Sunny Sky V4014 kv400 Brushless Direct Current Motor. According to the parameters of the engine used, a 16-inch carbon fiber propeller (1655 16*6) was preferred. The characteristics of the propeller are given in Table 2 below.

Table 2: Characteristic features of the propeller

Propeller diameter	16*6	Working Temperature	Between 40°C to 65°C
Weight	28gr	Degree of Safe keep	Between 10°C to 50°C
Material	CF + Epoxy	Average cycle	4000-6000 rpm
Surface Area	Polished	Thrust	7 kg

Propellers the typical behavior of a propeller can be defined by three parameters. Coefficient of thrust = C_T
Power coefficient = C_p
Propeller radius = r
These parameters allow calculating the thrust of a propeller.

$$T = c_T \frac{4\rho r^4}{\pi^2}\omega^2 \qquad (1)$$

Power = P_P

$$P_P = c_P \frac{4\rho r^5}{\pi^3}\omega^3 \qquad (2)$$

The thrust and power performance parameter of a selected propeller in the unmanned aerial vehicle is shown in figure 4.

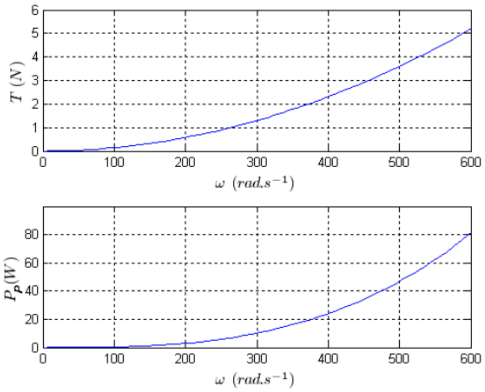

Figure 4: The thrust and power performance of the selected propeller are shown

III. FINAL DESIGN AND TASK PERFORMANCE

The four-rotor unmanned aerial vehicle has successfully performed flat, wide, vertical take-off and flight tests by combining mechanical and electronic equipment. As a result of the tests performed, the tasks of our load release system Task 2 were successfully performed. Also, the four-rotor

unmanned aerial vehicle remains in the air stably due to the configuration of the aircraft and the fact that its parts are designed to center the center force.

Figure 3.1 Final Test Stage

IV. CONCLUSION

In this modeling and paper, it was focused on the ability of unmanned aerial vehicles to carry useful cargo for different needs and to deliver certain points. Our work is designed for use in various fields. We will continue our efforts to advance this project, to provide ease of use and to multiply the areas of use.

V. ACKNOWLEDGMENTS

This work was supported by a research grant numbered 48348 from the Scientific and Technological Research Council of Turkey.

REFERENCES

[1] H. Eisenbeiss, and M. Sauerbier, "Investigation of UAV systems and flight modes for photogrammetric applications*." The Photogrammetric Record*, 2011.
[2] A. Altan, Ö. Aslan, and R. Hacıoğlu, "Real-time control based on NARX neural network of hexarotor UAV with load transporting system for path tracking", *IEEE Trans. CEIT*, 2018.
[3] L. Mervart, Z. Lukes, C. Rocken, T. Iwabuchi, "Precise point positioning with ambiguity resolution in real-time", *Proceedings of the 21st International Technical Meeting of the Satellite Division of The Institute of Navigation*, 2008.
[4] M. Elsobeiey, S. Al-Harbi, "Performance of real-time Precise Point Positioning using IGS real-time service." *GPS Solutions*, 2016.
[5] G. Chamayou, "A Theory of the Drone" *The New Press*, 2015.

Electromechanical Modeling of Energy Harvesting for FRP Composite Structures Coupled with Piezoelectric Transducers

H.UÇAR[1]

[1] Design Project Office, Istanbul/Turkey, hkucar@gmail.com

Abstract **-** Supplanting of metals by composites is on the rise for the last three decades in the aerospace, marine and automotive industry following the trend of electrification and indigenous design approaches. In parallel, piezoelectric (PZT) sensors and energy harvesters have gained significant attention due to their applicability and efficacy for microscale power generation systems. From a new perspective, embedding PZT sensors into composite structures will be beneficial in many aspects. Condition monitoring can be performed by using the sensing capability of PZTs while vibration can be controlled by means of its excitation capability. Besides, energy harvesting can be employed due to the mechanical forces exerted on the coupled structure. It is critical to create an accurate numerical modeling of electromechanical coupling for the investigation of efficiency of PZT sensors. In this paper, electromechanical modeling of a Fiber Reinforced Polymer (FRP) composite structure with an embedded PZT patch is presented and validated with an experimental setup. Afterwards, the energy harvesting capability of a PZT patch embedded in the FRP structure is investigated.

Keywords **– electromechanical modeling, piezoelectric, FRP, energy harvesting, finite element method.**

I. INTRODUCTION

LATELY, shortcomings in energy resources have made energy harvesting an important issue. Energy harvesting is basically the conversion of existing ambient energy into electrical energy. One of the most widely used materials for this purpose is piezoelectric material with its high power density, transduction capacity and functionality in high frequency applications [1]. Piezoelectric materials have the ability to convert mechanical energy into electrical energy as a result of mechanical deformation and vice versa. Thus, these materials are widely used as sensors [3, 4] and energy harvesters [5, 6]. On the other hand, by using the converse effect of the piezoelectric material, they can be used as actuators [7-9].

Piezoelectric energy harvesting is mainly applied for harvesting small-scale energy to be supplied for low power electronics [2]. In order to achieve a sufficient energy harvesting, the effectiveness of the PZT sensors must be well defined. For this reason, it is necessary to conduct energy harvesting experiments prior to the use on-site. However, these experiments pose significant costs and time consumption. Therefore, it has become crucial to conduct computer analysis with verified benchmarking studies for modeling the electromechanical coupling. Within this scope, analytical models such equivalent circuits [10], spring models [11] and thermal analogy [12] are applied for two-dimensional analysis. For three-dimensional analysis, Finite Element Method (FEM) is a convenient tool that provides detailed analysis of structures and predicts the behavior of electromechanical structures under real conditions at a lower cost and more quickly [13, 14]. In previous studies conducted on electromechanical modeling based on FEM, V. Nguyen et. al [15] presented the development of a three-dimensional finite element (FE) model for characterizing the piezoelectric actuators. In other study, the use of shell elements for electromechanical FE analysis of composite and sandwich multilayered structures [16]. S. Avdiaj et. al [17] investigated the piezoelectric effect using FEM and showed that FE model is applicable for microstructures.

In this study, the electromechanical modeling is of an Aramid FRP (AFRP) composite beam coupled with a PZT patch is introduced. FE model of the beam is created and direct effect of the piezoelectricity is presented. Results are validated with the experimental results. Once the electromechanical modeling is validated, energy harvesting capabilities of PZT patch embedded in the AFRP beam are investigated numerically.

The paper is organized as follows. Section 2 presents the theory of electromechanical modeling of the beam highlighting the governing equations. In Section 3, the numerical model of AFRP beam with a PZT patch and validation is introduced. Section 4 presents the energy harvesting capabilities and brief discussion of the results. Finally, Section 5 concludes the paper.

II. THEORY OF ELECTROMECHANICAL MODELING

For linear piezoelectricity, the interaction between stress, strain, electric charge and electric field is defined in the electromechanical constitutive equations [18], given as follows;

$$\sigma_{ij} = C^{E}_{ijkl}\,\varepsilon_{kl} - e_{ijk}\,E_k \tag{1}$$

$$D_i = e_{ikl}\,\varepsilon_{kl} + \epsilon^{S}_{ij}\,E_j \tag{2}$$

where σ_{ij} is the component of stress tensor; D_i is the component of electric displacement vector; ε_{kl} is the component of strain tensor; E is the electric field vector; C_{ijkl} is the elastic constant; ϵ_{ij} is the dielectric material constant and e_{ijk} is the piezoelectric constant. Subscripts $()_i$ and $()_{ij}$ represent the corresponding component of a vector and a matrix, respectively. Superscript E

stands for constant electrical field while S represents constant strain, where the elastic stiffness and permittivity parameters are obtained.

According to the electromechanical coupling defined in Equation (2), the mechanical strain is transformed to electrical charge. This is referred as direct piezoelectric effect and allows piezoelectric materials to be used as sensors and energy harvesters. On the contrary, the electromechanical coupling described in Equation (1) enables the conversion of electrical energy into mechanical energy, by which allows piezoelectric materials to be used as actuators.

Equation of motion of the electromechanical system can be derived according to the Hamilton principle along with the virtual work theory for a virtual displacement field δu_i and the potential δV. Electric field, in Equation (1) and (2) is associated with the electrical potential V as in Equation (3).

$$E = -grad\ V \tag{3}$$

In a FEM analysis, the domain is divided into a finite number of small elements having geometrically simple shapes. The unknowns in electromechanical model such as mechanical displacement, u, exciting force, f, electrical potential, V and the charge, q are determined and stored at the nodes of these elements.

The displacement field, $\{u\}$ and the electric potential, $\{V\}$ can be determined by establishing nodal solutions and corresponding shape functions defined as in Equation (4) and (5).

$$\{u\} = [N_u]^T\{u_i\} \tag{4}$$

$$\{V\} = [N_V]^T\{V_i\} \tag{5}$$

where $\{u_i\}$, $\{V_i\}$, $[N_u]$, $[N_V]$ is the nodal displacement, nodal electric potential, the matrix of displacement shape function and the matrix of electric potential shape function, respectively.

Strain vector, $\{\varepsilon\}$ and the electric field, $\{E\}$ can be related to the displacement field and potentials by implementing Equations (6) and (7).

$$\{\varepsilon\} = [B_u]\{u\} \tag{6}$$

$$\{E\} = [B_V]\{V\} \tag{7}$$

where

$$[B_u] = \begin{bmatrix} \frac{\partial}{\partial x} & 0 & 0 & \frac{\partial}{\partial y} & 0 & \frac{\partial}{\partial z} \\ 0 & \frac{\partial}{\partial y} & 0 & \frac{\partial}{\partial x} & \frac{\partial}{\partial z} & 0 \\ 0 & 0 & \frac{\partial}{\partial z} & 0 & \frac{\partial}{\partial y} & \frac{\partial}{\partial x} \end{bmatrix}^T \tag{8}$$

$$[B_V] = \begin{bmatrix} \frac{\partial}{\partial x} & \frac{\partial}{\partial y} & \frac{\partial}{\partial z} \end{bmatrix}^T \tag{9}$$

Elastic behavior of piezoelectric material is defined by Newton's law, as in Equation (10).

$$div\{\sigma\} = \rho \frac{\partial^2\{u\}}{\partial t^2} \tag{10}$$

where ρ is the density of the piezoelectric material. On the other hand, considering that there is no free volume charge through piezoelectric material, electrical behavior of the piezoelectric material is governed by Maxwell's equation.

$$div\{D\} = 0 \tag{11}$$

Composing Equations (1) to (11), the differential equation of motion can be formed and solved by appropriate mechanical and electrical boundary conditions, such as displacement and electrical potential or charge, respectively. However, Hamilton's variational principle, as given in Equation (12), can be extended to electromechanical couplings.

$$\delta \int_{t_1}^{t_2} (L + W)\ dt = 0 \tag{12}$$

where δ represents the first-order variation, t_1 and t_2 are the time interval. L, Lagrangian term is defined by the energies stored in the piezoelectric material whereas W *i*s the virtual work of the mechanical forces exerted on the system.

Using the Hamilton's variational principle and the finite element discretization, the coupled electromechanical equation of motion in matrix notation can be determined as in Equation (13).

$$\begin{bmatrix} [M] & 0 \\ 0 & 0 \end{bmatrix} \begin{bmatrix} \ddot{u} \\ \ddot{V} \end{bmatrix} + \begin{bmatrix} [C] & 0 \\ 0 & 0 \end{bmatrix} \begin{bmatrix} \dot{u} \\ \dot{V} \end{bmatrix} + \begin{bmatrix} [K_{uu}] & [K_{uV}] \\ [K_{Vu}] & [K_{VV}] \end{bmatrix} \begin{bmatrix} u \\ V \end{bmatrix} = \begin{bmatrix} \{F\} \\ \{Q\} \end{bmatrix} \tag{13}$$

where $\{F\}$ is the exciting force and $\{Q\}$ is the electrical charge vector. Here $[M]$, $[C]$, $[K_{uu}]$, $[K_{VV}]$, $[K_{uV}]$ is the mass matrix, damping matrix, structural stiffness matrix, dielectric conductivity matrix and piezoelectric coupling matrix, respectively and can be defined as Equation (14-20).

$$[M] = \sum_i [L_{ui}]^T \left[M^{(i)}\right] [L_{ui}] \tag{14}$$

$$[K_{uu}] = \sum_i [L_{ui}]^T \left[{K_{uu}}^{(i)}\right] [L_{ui}] \tag{15}$$

$$[K_{uV}] = \sum_i [L_{ui}]^T \left[{K_{uV}}^{(i)}\right] [L_{Vi}] \tag{16}$$

$$[K_{Vu}] = \sum_i [L_{Vi}]^T \left[{K_{Vu}}^{(i)}\right] [L_{ui}] \tag{17}$$

$$[K_{VV}] = \sum_i [L_{Vi}]^T \left[{K_{VV}}^{(i)}\right] [L_{Vi}] \tag{18}$$

$$\{F\} = \sum_i [L_{ui}]^T [f_i] \tag{19}$$

$$\{Q\} = \sum_i [L_{Vi}]^T [q_i] \tag{20}$$

III. AFRP Beam Case Study

A. Experimental Set-Up and Validation

In accordance with the statements of electromechanical theory, an AFRP beam coupled with an embedded PZT patch was created in order to validate the electromechanical coupling. Beam was clamped at the side of the embedded PZT patch to constitute a cantilever set-up. The setup is shown in Figure 1, and the corresponding material and physical properties of AFRP beam and PZT patch (PI Dura-act 876.A12) are presented in Table 1.

PZT patch is considered as anisotropic whereas the AFRP material is taken as isotropic. Thus, elastic, piezoelectric and dielectric constants of PZT, which are defined in Equations (1) and (2), are tabulated in Table 2.

Using the converse effect of the piezoelectric material, the structure is excited by the piezoelectric patch and the frequency responses are measured at the tip of the beam by the Laser Doppler Vibrometer (LDV).

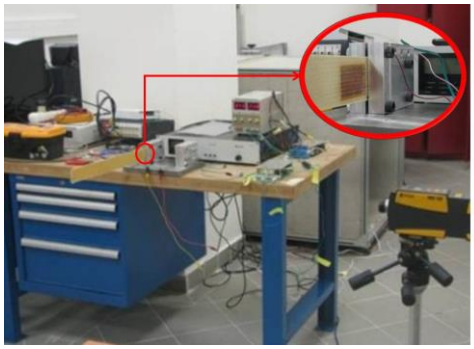

Figure 1: AFRP Cantilever Beam Set-Up

Table 1: Mechanical Properties of Set-Up.

Property	**AFRP Beam**	**PZT Patch**
Length (mm)	500	65
Width (mm)	50	31
Thickness (mm)	1	0.5
Elastic Modulus (GPa)	73.2	-
Poisson's Ratio	0.36	0.36
Damping Ratio	0.0176	-
Density (kg/m^3)	1250	7800
Relative Permittivity, $\varepsilon_{33}^T/\varepsilon_0$ $\varepsilon_{11}^T/\varepsilon_0$	-	1750 1650
Piezoelectric Voltage Coefficient, g_{31}, (10^{-3} Vm/N)	-	-11.3

Table 2: Electromechanical Properties of PZT Patch.

Elastic (GPa)		**Piezoelectric (C/m^2)**		**Dielectric (10^{-12} C/Vm)**	
C_{11}	123	e_{15}	11.91	ε_{11}	1649
C_{12}	76.7	e_{24}	11.91	ε_{22}	1649
C_{13}	70.25	e_{31}	-7.07	ε_{33}	1750
C_{22}	97.11	e_{32}	-7.07		
C_{33}	97.11	e_{33}	13.81		
C_{44}	22.26				
C_{55}	22.26				
C_{66}	23.15				

A finite element model of the experimental setup was created using the specified mechanical and electromechanical inputs. To verify the numerical model, the frequency response of the tip is calculated and compared with the experimental one. The numerical model and the comparison of the frequency responses are shown in Figure 2 and 3, respectively.

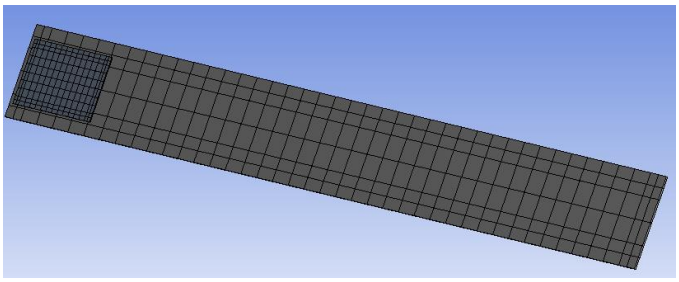

Figure 2: FE Model of AFRP Beam

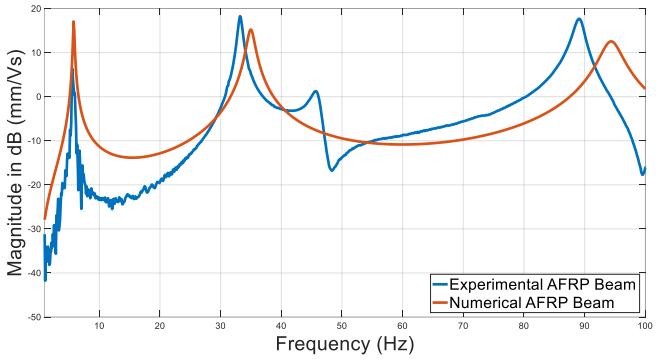

Figure 3: Frequency Response at Tip of AFRP Beam

As shown in Figure 3, the numerical frequency response catches the dynamic character of the experimentally measured one. It can be determined that there is a "bump" around 46 Hz of the experimental frequency response. Since the bump is a result of the effect of the constraint and has no significant meaning, this effect is not included in the numerical model. As a consequence, the numerical model of electromechanical model composed of AFRP beam and PZT patch is valid and the piezoelectric and composite material characteristics are quite correctly defined to be used for energy harvesting studies.

B. Energy Harvesting Study

In this part of the study, the energy harvesting capability of PZT patch was investigated. PZT patch is directly connected to a load resistance, R_L in order to obtain the electrical power. Using the expression of voltage across the resistive load, the output power generated by PZT patch can be calculated by employing

$$P(\omega) = \frac{V^2(\omega)}{R_L} \tag{21}$$

Electrical circuit of PZT patch can be represented by a voltage source, V in parallel with internal capacitance C_p and internal resistance, R_p. Thus, the equivalent circuit model of the

piezoelectric energy harvester with the resistive load is illustrated in Figure 4.

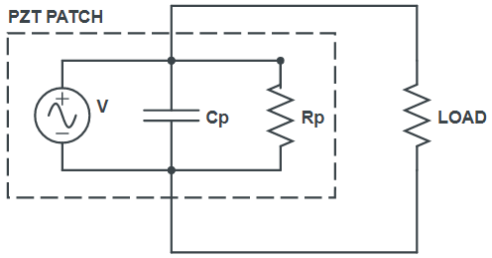

Figure 4: Equivalent Circuit Model

A unit force was applied at the tip of the beam and due to the direct effect of the piezoelectric material, electrical potentials were obtained based on the different values of resistors (from 100 Ω to 50 kΩ), as shown in Figure 5. It can be seen that generated output voltages increase with increasing resistive load values and maximum output voltages are generated at resonance frequencies. Output voltage exhibits an increasing trend with the increase of the resistance value and after a certain value of resistive load, which is about 10 kΩ, the generated voltage remains almost constant. In this condition, it can be stated that the open circuit is achieved and with a resistive load of 50 kΩ, a maximum voltage of 2.68 V is generated at 19.5 Hz, second resonance frequency of the beam.

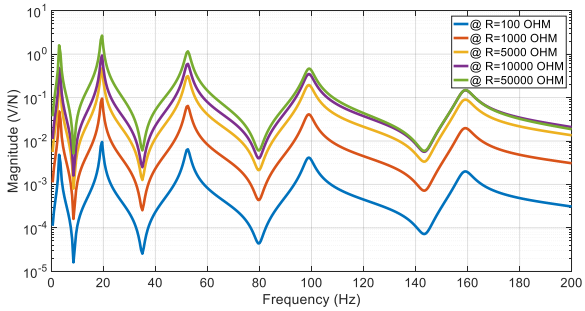

Figure 5: Voltage Outputs at Various Resistances

Output power was calculated by using Equation (21) and presented with respect to the resistive loads in Figure 6. As shown in the figure, maximum power was also obtained when connected to a 50 kΩ resistive load at 19.5 Hz with the value of 0.14 mW. However, it can be seen that same amount of voltage output can be achieved with the use of a resistive load of 50 kΩ and after the open-circuit condition, at higher frequencies the generated powers with respect to resistive loads become close to each other. Besides, the generated power can become lower with increasing the resistive load. In this case study, considering the higher frequencies, 10 kΩ resistive load is determined as the optimum value of the resistance.

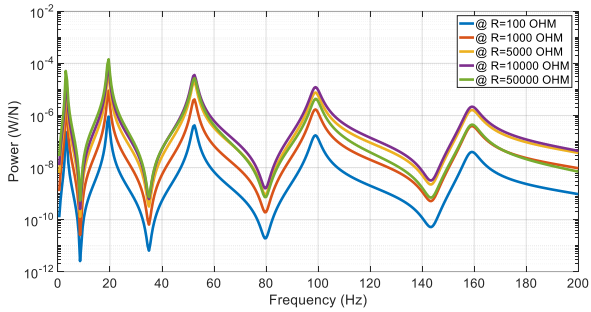

Figure 6: Power Outputs at Various Resistances

IV. Conclusion

In this study, electromechanical modeling of piezoelectric energy harvesting by means of the finite element methods was presented and a case study composed of a cantilever AFRP beam with the embedded PZT patch was conducted.

Modal behavior of the structure is leading for piezoelectric energy harvesting. It can be stated that maximum electrical outputs are obtained at resonance frequencies of the structure. Besides, the location of the PZT patch is also critical. PZT patches should be placed at the locations where considerable strain occurs. Thus, especially for complex structures numerical analysis should be performed in order to select the appropriate locations for PZT patches.

Selecting resistive load to be connected to the PZT patch is important in terms of electrical outputs. Output voltage increases with increasing resistive loads. In the case of power generation, maximum output power differs with respect to resistive load values and there exists an optimum value of resistive load at which the maximum power can be obtained. Thus, a numerical study should be performed prior to energy harvesting in order to determine the optimum value of the resistive loads.

Acknowledgment

The experimental setup was developed, and the experiments were carried out during author's academic study at Koc University. The author gratefully acknowledges the in-kind support from Professor İpek Başdoğan (Koc University) for the experiment setup and Yonca-Onuk Shipyard JV for composite structures.

References

[1] M. K. Stojčev, M. R. Kosanović, L. R. Golubović, "Power management and energy harvesting techniques for wireless sensor nodes." *9th Int. Conf. on Telecommunication in Modern Satellite, Cable, and Broadcasting Services (IEEE)*, 2009. https://doi.org/10.1109/TELSKS.2009.5339410

[2] M. Safaei, H. A. Sodano, and S. R. Anton, "A review of energy harvesting using piezoelectric materials: state-of-the-art a decade later (2008–2018)," *Smart Mater. Struct.* 28, pp. 62, 2019.

[3] L. Bruant, G. Coffignal, F. Lene, and M. Verge, "Active control of beam structures with piezoelectric actuators and sensors: modeling and simulation," *Smart Materials and Structures*, 2001, vol. 10, pp. 404-408.

[4] Y. Shen and A. Homaifar, "Vibration Control of Flexible Structures with PZT Sensors and Actuators," *Journal of Vibration and Control*, vol. 7, pp. 417-451, 2001.

[5] A. Erturk and D. J. Inman, "A Distributed Parameter Electromechanical Model for Cantilevered Piezoelectric Energy Harvesters," *Journal of Vibration and Acoustics*, 2008, vol. 130, pp. 041002-15.
[6] M. I. Friswell and S. Adhikari, "Sensor shape design for piezoelectric cantilever beams to harvest vibration energy," Journal of Applied Physics, 2010, vol. 108, pp. 014901-6.
[7] Y. Aoki, P. Gardonio, M. Gavagni, C. Galassi, and S. J. Elliott, "Parametric Study of a Piezoceramic Patch Actuator for Proportional Velocity Feedback Control Loop," *Journal of Vibration and Acoustics*, 2010, vol. 132.
[8] Y. Aoki, P. Gardonio, and S. J. Elliott, "Rectangular plate with velocity feedback loops using triangularly shaped piezoceramic actuators: Experimental control performance," *Journal of the Acoustical Society of America*, 2008, vol. 123, pp. 1421-1426.
[9] Y. Aoki, P. Gardonio, and S. J. Elliott, "Modelling of a piezoceramic patch actuator for velocity feedback control," *Smart Materials and Structures*, 2008, vol. 17, p. 015052.
[10] Z. Zyszkowski, *Podstawy Elektroakustyki; WNT*: Warszawa, Poland, 1984.
[11] J. G. Smits, S. I. Dalke, and T. K. Cooney, "The constituent equations of piezoelectric bimorph." *Sens. Actuators A Phys.* 1991, 28, 41–61.
[12] X. J. Dong, and G. Meng, "Dynamic analysis of structures with piezoelectric actuators based on thermal analogy method." *Int. J. Adv. Manuf. Technol.* 2006, 27, 841–844.
[13] H. Allik and T. J. R. Hughes, "Finite element method for piezoelectric vibration," *International Journal for Numerical Methods in Engineering*, 1970, vol. 2, no. 2, pp. 151–157.
[14] A. Benjeddou, "Advances in piezoelectric finite element modeling of adaptive structural elements: a survey," *Computers and Structures*, 2000, vol. 76, no. 1, pp. 347–363.
[15] V. Nguyen, P. Kumar, and J.Y.C. Leong, "Finite Element Modelling and Simulations of Piezoelectric Actuators Responses with Uncertainty Quantification", *Computation*, 2018, 6, no. 4: 60.
[16] E. Carrera, S. Valvano, and G. M. Kulikov, "Electro-mechanical analysis of composite and sandwich multilayered structures by shell elements with node-dependent kinematics." *Int. J. Smart Nano Mater.* 2018, 9, 1–33.
[17] S. Avdiaj, J. Setina, and N.Syla, "Modeling of the piezoelectric effect using the Finite Element Method", *Materials and Technology* 43, 2009, 6, pp. 283-291.
[18] IEEE Standard on Piezoelectricity ANSI/IEEE Std 176-1987, ed, 1988.

An application for the selection of steel sheet materials used in automotive construction with the MOORA method

B. ÖZAKIN[1]

[1] Kavak Vocational School, Samsun University, Samsun/Turkey, batuhan.ozakin@samsun.edu.tr

Abstract **- The new generation steel grades that can be used in automotive construction are increasing day by day and the material selection becomes very important both in the design and manufacturing processes due to the development in the materials. In this study, data on tensile strength, formability, load that weld joints can bear, fatigue stress, corrosion resistance and price criteria of high strength low alloy (HSLA), dual phase (DP), three phase (TRIP) and complex phase (CP) steel sheet materials used in the automotive industry were determined and a study was conducted for the material selection using the MOORA (Multi Objective Optimization on the Basis of Ratio Analysis) ratio approach. It was concluded that the selection of DP grade steel sheet material according to the MOORA ratio approach among the materials used in the study would be the optimum choice.**

Keywords **– Automotive construction, automotive sheet materials, steel sheet grades, material selection, MOORA method.**

I. INTRODUCTION

SIGNIFICANT progress has been made in the automotive industry in terms of safety, fuel economy, crash resistance and comfort, and in this direction, various steel sheet materials are used in vehicles. In order to achieve the stated targets, steel sheet manufacturers are introducing new generation steel grades every day and contributing to the development of the automobile [1]. The new generation steel grades used in the automotive industry, which show the tensile strength-elongation relationship of these steel grades and the usage areas of sheet materials in automobiles, are shown in Figure 1.

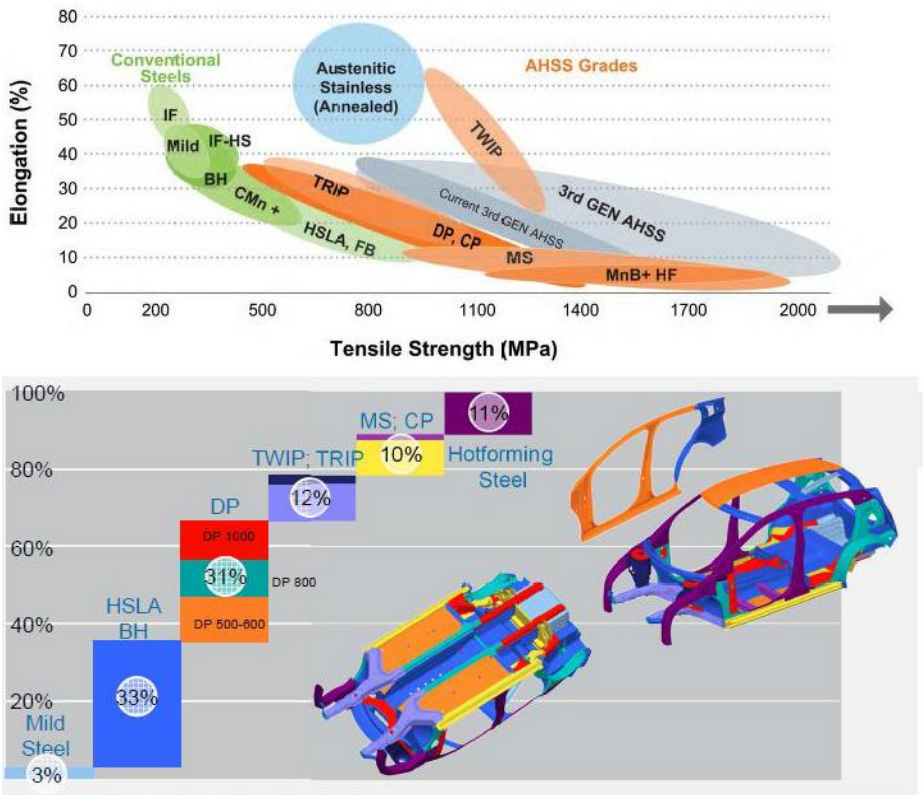

Figure 1: New generation steel grades used in the automotive industry [2-4].

Material selection plays a very important role in product design and development. Again, the selection of the right material is of great importance in the success of the manufacturers and it is necessary to choose the optimum material that achieves maximum performance and minimum cost in development [5-7]. Recently, effective solutions in material selection have been obtained by using multi-criteria decision making (MCDM) approach [8]. In the MCDM approach, there are various approaches according to the type of decision making. In the material selection made in these approaches, after the problem is defined, criteria are determined and evaluated and the best one is selected among the alternatives. Hambali et al., with AHP (Analytical Hierarchy Process) analysis, concluded that the most suitable material for automobile bumper is glass fiber reinforced epoxy material [9]. Mayyas et al. performed material selection among ten different materials used in automotive panels using QPD (Quality Function Distribution) and AHP methods [10]. Girubha and Vinodh made the material selection of an automobile part using the VIKOR (Vlse Kriterijumska Optimizacija Kompromisno Resenje) method [11]. Hasanzadeh et al., using AHP, TOPSIS (Technique for Order Preference by Similarity to Ideal Solution) and MOORA methods for automotive bumper, stated that the composite material containing 0.5% nano alumina among six different alternative composite materials would be the most appropriate choice [12]. Mondal et al., on the other hand, carried out material selection among magnesium alloys in automobile wheels in accordance with the MOORA method. They observed that among eight different magnesium alloys, the AZ91 grade was the most suitable for this selection [13]. Banerjee et al., among four different materials (carbon fiber/epoxy composites, steel, aluminum and titanium alloys) used in automobile parts (piston, wheel, brake disc, bumper, etc.), using the CODAS (Combinative Distance-Based Assessment) method, stated that the most suitable material is titanium alloy [14]. Steel sheet materials are used extensively in automotive construction (chassis, body, etc.). Also, considering that quite different types of sheet materials can be used in these regions, material selection comes to the fore. It has been observed that there are almost no applications in which material selection is made for steel sheet materials used in automotive construction and there is a gap in the literature.

In this study, data on tensile strength, formability, load that weld joints can bear, fatigue stress, corrosion resistance and price criteria of high strength low alloy (HSLA), dual phase (DP), three phase (TRIP) and complex phase (CP) steel sheet materials used in the automotive industry were determined and a study was conducted for the material selection using the MOORA (Multi Objective Optimization on the Basis of Ratio Analysis) ratio approach.

II. MATERIAL SELECTION METHOD

A. Alternative Materials and Properties

In the study, the properties of sheet materials were determined by using the technical information of the automotive steel sheet manufacturer company [15]. In this selection process, an orientation towards materials with high tensile strength and alternatives to each other from the new generation steel generations has been achieved in general. In this context, four different materials were determined. HSLA (high strength low alloy) steels are obtained by adding small amounts of titanium, niobium and vanadium to C-Mn steels, making the grain structure micro and thus gaining strength [16]. The properties of CR460LA grade sheet material were taken from these steels. DP (Dual Phase) steels are low carbon steels consisting of soft ferrite and hard martensite structure [17]. The properties of DP600 grade sheet material were taken from these steels. In TRIP (Transformation Induced Plasticity) steels, three phases containing bainite and residual austenite are present in certain proportions in a soft ferrite matrix in the microstructure [18]. The properties of TRIP700 grade sheet material were taken from these steels. CP (Complex Phase) steels are a type of steel with ferrite and martensite, as well as bainite and in some cases residual austenite [17]. The properties of CP600 grade sheet material were taken from these steels.

Multi-criteria properties of CR460LA, DP600, TRIP700 and CP600 steel materials were obtained. In the tensile strength criterion of the materials used in this study, the minimum tensile strength value was used for all materials from the catalog. In the formability criterion, major strain amounts corresponding to "0" minor strain amount in the forming limit curve were used. In the weldability criterion, the load values that the weld joint can carry under pure tensile load and tensile-shear load are determined. In the fatigue stress criterion, the maximum stress values obtained in 2×10^6 cycles under tensile-tensile loading were selected. In the price criterion, price information obtained from the internet is used [19]. The corrosion resistance criterion was determined by evaluating the alloy element amount and experience from a scale of 1-5 (1: very good, 2: good, 3: moderate, 4: bad and 5: very bad). In Table 1, materials and criteria used for material selection and material properties are given.

Table 1: Materials and criteria used for material selection and material properties.

Material	Price (USD/ton)	Corrosion resistance	Tensile strength (MPa)	Formability	Weldability (pure tensile load) kN	Weldability (tensile-shear load) kN	Fatique stress (MPa)
CR460LA	900	4	520	18.31	11.00	18.09	458
DP600	1000	2	590	26.27	13.10	22.30	503
CP600	1100	3	600	22.98	15.10	21.20	493
TRIP700	1200	3	690	42.65	6.70	13.00	560

B. MOORA Method

The MOORA method is a multi-criteria decision-making method developed by Brauers and Zavadskas [20] and used frequently recently. In this method, the interactions between the criteria are considered as a whole and material selection is made with weighted values. Although there are many methods in the MOORA method, the most used one is the MOORA ratio approach. The steps of this approach are as follows.

Stage 1: The decision matrix (K) is created. This matrix is obtained from the criteria determined at the beginning.

$$K = \begin{pmatrix} k_{11} & k_{12} & \cdots & k_{1m} \\ k_{21} & k_{22} & \vdots & k_{2m} \\ \vdots & \vdots & \ddots & \vdots \\ k_{n1} & k_{n2} & \cdots & k_{nm} \end{pmatrix} \qquad (1)$$

Stage 2: The decision matrix (K) is normalized. The normalized decision matrix (N) is created with the help of the equation 2 given below and the maximum or minimum objective in the selected criteria is not examined.

$$k_{ij}^{*} = \frac{k_{ij}}{\sqrt{\sum_{i=1}^{n} k_{ij}^{2}}}, i = 1,2,\dots.,n, j = 1,2,\dots.,m \qquad (2)$$

Stage 3: Performance of decision criteria (X); It is determined with the help of the equation 3 given below by subtracting the sum of performance values for minimization from the sum of performance values for maximization purposes.

$$X = \sum_{j=1}^{t} k_{ij}^{*} - \sum_{j=t+1}^{n} k_{ij}^{*}, i = 1,2,\dots.,n \qquad (3)$$

Stage 4: The resulting X values are sorted. As a result of the ranking, the material with the highest value is selected in the first place.

III. RESULTS AND DISCUSSION

The decision matrix (K) considered in the MOORA ratio approach for material selection is as indicated in Table 1. These values are converted to their normalized values with the help of the equation given in Stage 2. The values of the normalized decision matrix are given in Table 2.

Table 2: Values of the normalized decision matrix.

Material	Price (USD/ton)	Corrosion resistance	Tensile strength (MPa)	Formability	Weldability (pure tensile load) kN	Weldability (tensile-shear load) kN	Fatique stress (MPa)
CR460LA	0.426	0.649	0.431	0.315	0.463	0.476	0.454
DP600	0.474	0.325	0.489	0.452	0.551	0.587	0.498
CP600	0.521	0.487	0.498	0.396	0.609	0.558	0.488
TRIP700	0.568	0.487	0.572	0.735	0.282	0.342	0.555

While evaluating the performance of the decision criteria, it is desired that the tensile strength, forming ability, welding ability and fatigue strength criteria be maximum. At the same time, it is desirable that the criteria for price and corrosion resistance be minimal. When substituting for each material in the equation 3 given in Stage 3, the performance values of the decision criteria (X) are obtained. The performance values of the decision criteria given in Step 4 are listed and the ranking of the material selection is obtained. In Table 3, the material selection order obtained with the MOORA ratio approach is given.

Table 3: Material selection ranking obtained with the MOORA ratio approach.

	CR460LA	DP600	CP600	TRIP700
X	1.064	1.778	1.541	1.431
Sıralama	4	1	2	3

The MOORA ratio approach reveals very effective results in material selection among four materials that exhibit different microstructure properties but are close to each other in terms of tensile strength. In such a study, it is suggested that steels with martensite phase or DP grade should be generally preferred by using QPD and AHP material selection methods in automotive panels (eg A, B columns, doors, hood, etc.) [10]. Therefore, from the results obtained from this study, it is possible to say that it would be more optimum to prefer dual phase (DP) steel sheet materials.

IV. CONCLUSION

In this study, data on tensile strength, formability, load that weld joints can bear, fatigue stress, corrosion resistance and price criteria of high strength low alloy (HSLA), dual phase (DP), three phase (TRIP) and complex phase (CP) steel sheet materials used in the automotive industry were determined and a study was conducted for the material selection using the MOORA (Multi Objective Optimization on the Basis of Ratio Analysis) ratio approach. In the study, it was tried to select as many criteria as possible in the multi-criteria selection methods within the scope of this study, and when evaluated with the criteria of tensile strength, forming ability, welding ability, fatigue strength, price and corrosion resistance, it is possible to summarize the order in material selection among the four materials determined at the beginning of the study as follows. It is recommended to use DP grade steel sheet material first. This material is followed by CP grade steel sheet material and TRIP grade steel sheet material comes in third place. It was concluded that the last preferred material is HSLA grade sheet material.

REFERENCES

[1] D. Cornette, T. Hourman, O. Hudin, J. P. Laurent, and A. Reynaert, "High strength steels for automotive safety parts (No. 2001-01-0078)," *SAE Technical Paper*, March 2001.

[2] M. K. Singh, "Application of steel in automotive industry," *International Journal of Emerging Technology and Advanced Engineering*, vol. 6, issue. 7, pp. 246-253, July 2016.

[3] World Auto Steel, (2021, August). Available: https://www.worldautosteel.org/steel-basics/automotive-advanced-high-strength-steel-ahss-definitions/

[4] D. O. Hoffmann, "Steel lightweight materials and design for environmental friendly mobility,". in *2012 Industrial Technologies Conference*, Aarhus, Germany.

[5] H. Çalışkan, B. Kurşuncu, C. Kurbanoğlu, and Ş. Y. Güven, "Material selection for the tool holder working under hard milling conditions using different multi criteria decision making methods," *Materials & Design*, vol. 45, pp. 473-479, March 2013.

[6] P. Chatterjee, and S. Chakraborty, "Material selection using preferential ranking methods," *Materials & Design*, vol. 35, pp. 384-393, March 2012.

[7] A. Thakker, J. Jarvis, M. Buggy, and A. Sahed, "A novel approach to materials selection strategy case study: Wave energy extraction impulse turbine blade," *Materials & Design*, vol. 29, issue. 10, pp. 1973-1980, December 2008.

[8] S. S. Raju, G. B. Murali, and P. T. Patnaik, "Ranking of Al-CSA composite by MCDM approach using AHP–TOPSIS and MOORA methods," *Journal of Reinforced Plastics and Composites*, vol. 39, issue. 19-20, pp. 721-732, May 2020.

[9] A. Hambali, S. M. Sapuan, N. Ismail, and Y. Nukman, "Material selection of polymeric composite automotive bumper beam using analytical hierarchy process," *Journal of Central South University of Technology*, vol. 17, issue. 2, pp. 244-256, April 2010.

[10] A. Mayyas, Q. Shen, A. Mayyas, D. Shan, A. Qattawi, and M. Omar, "Using quality function deployment and analytical hierarchy process for material selection of body-in-white," *Materials & Design*, vol. 32, issue. 5, pp. 2771-2782, May 2011.

[11] R. J. Girubha and S. Vinodh, "Application of fuzzy VIKOR and environmental impact analysis for material selection of an automotive component," *Materials & Design*, vol. 37, pp. 478-486, May 2012.

[12] R. Hasanzadeh, T. Azdast, R. Eungkee Lee, and A. Afsari Ghazi, "Experimental polymeric nanocomposite material selection for automotive bumper beam using multi-criteria decision making methods," *Iranian Journal of Materials Science and Engineering*, vol. 14, issue. 3, pp. 1-10, 2017.

[13] S. Mondal, A. Ghosh, and N. V. Deshpande, "Automobile wheel material selection using Multi-Objective Optimization on the basis of ratio analysis (MOORA) method," *International Journal of Research Publications in Engineering and Technology [IJRPET]*, vol. 3, issue. 5, pp. 45-49, May 2017.

[14] S. Banerjee, S. Mondal, P. Chatterjee, and A. K. Pramanick, "An intercriteria correlation model for sustainable automotive body material selection," *Journal of Industrial Engineering and Decision Making*, vol. 2, issue. 1, pp. 8-14, May 2021.

[15] Arcelormittal, (2021, July). Available: https://automotive.arcelormittal.com/products/flat/product_catalogue

[16] E. Billur, B. Cetin, and M. Gurleyik, M. "New generation advanced high strength steels: developments, trends and constraints," *International Journal of Scientific and Technological Research*, vol. 2, issue. 1, pp. 50-62, 2016.

[17] F. Öztürk, S. Toros, E. Esener, and E. Uysal, "Otomotiv endüstrisinde yüksek mukavemetli çeliklerin kullanımının incelenmesi," *Mühendis ve Makina*, vol. 50, issue. 596, pp. 44-49, May 2009.

[18] F. Hayat, F. "TRIP çeliklerinin otomotiv endüstrisinde kullanımının incelenmesi," *Gazi Üniversitesi Mühendislik Mimarlık Fakültesi Dergisi*, vol. 25, issue. 4, 2010.

[19] Alibaba, (2021, July). Available: https://www.alibaba.com/

[20] W. K. Brauers, and E. K. Zavadskas, E. K. "The MOORA method and its application to privatization in a transition economy," *Control and Cybernetics*, vol. 35, pp. 445-469, 2006.

Comparing Nuclear and Solar Energy Options for Turkey

Sinem UZUN

Erzincan Binali Yildirim University, sinemuzun@erzincan.edu.tr

Abstract

Increasing energy needs and the quest for finding new energy sources worldwide, is also the case in Turkey. Nuclear energy technology has been gaining importance in recent years for developing countries such as Turkey to meet the ever increasing energy needs. Turkey's first nuclear power plant, Akkuyu Nuclear Power Plant is being under construction. Reviewing literature content, private sector in Turkey seems able to compensate a portion of energy needs of Turkey, by means of renewable energy systems. As a rising power, Turkey consumes more energy with its increasing population, daily life comfort expectations and industrialization. On the other hand, public opinion is partially negative about new energy investments such as nuclear energy. This situation should be eliminated by more effective introduction of nuclear technology. Public awareness should be raised. The aim of this study is to compare the costs and environmental factors of currently available energy options in Turkey. In order to make this comparison, a literature review about Akkuyu Nuclear Power Plant and solar power plants has been made and various numerical data have been compiled.

Keywords: LCOE, nuclear energy, solar energy, Turkey

1. INTRODUCTION

The need for energy and the search for energy resources for this need are increasing worldwide. However, in developing countries, it is difficult to meet this need due to socio-economic weaknesses, lack of technology and resources. In recent years, nuclear technology has gained importance in order to meet the energy needs of developing countries such as Turkey. Necessary permits were obtained for Mersin Akkuyu to build the 4800 MWe VVER-1200 technology, licensing activities were completed and a Cooperation Agreement was signed between the Russian Federation Government and the Republic of Turkey in 2010 for the construction of Mersin Akkuyu Nuclear Power Plant (NPP) [1]. Akkuyu Nuclear Power Plant construction project is the first NPP project in the world to be built with the "Build, Operate, Own" model. The construction phase of the first reactor of this power plant continues to be commissioned in 2023 [2].

There are many anti-nuclear energy discourses in Turkey and in the world. The main reasons for these occurrences are radiation emission, accident risk and cost [3]. However, due to the increasing world population, available resources have become insufficient, so the need for nuclear energy has become essential. According to the analyzes of some researchers for Turkey, renewable resources are sufficient to meet the country's energy needs. [4], [5].

Turkey's gross electricity consumption 303.7 (TWh) in 2019, respectively [6]. Turkey's total annual solar energy value was determined as 1527 kWh/m² (4.2 kWh/m² per day). According to 2018 data, the share of electricity generation from solar energy in total electricity generation was 2.56% and its share in renewable energy-based generation was 7.96% [7], [8]. Solar power plant to establish a convenient and annual sunshine duration square meter in 1650 kWh to be higher in Turkey and plant establishment of a suitable area (4,600 km^2), taking into account the electricity generating potential based on the solar year is estimated to be 380 billion kWh [9]. And according to these values, it will only be supplied from solar energy will not be enough for Turkey. However, if all renewable systems are considered together (wind, biomass etc.), it will be possible to reduce the dependency on foreign energy [10].

Emerging Turkey, population growth, rising standards of living, due to industrialization and orientation activities for new technologies every year is obliged to expend more energy [11]. In order to meet this energy need, the tendency to renewable resources has increased over time. The energy production from solar energy began in 2014 in Turkey. According to Solar Power Europe Turkey 2018 data, the change in the previous year's ranking in the new solar energy installation is in the top ten [12].

In the establishment of energy facilities, environmental factors are as important as economic factors. Especially in the use of resources beyond human control such as sun and wind, the cost also varies according to the changing parameters [13].

The most important point in energy production is cost analysis. If the benefit-cost ratio is taken into consideration, particularly the most useful method of power generation can be identified for developing countries such as Turkey. And this makes it possible to use more efficient energy at less cost.

The aim of this study is to compare the effects of environmental factors and cost of the currently existing solar power plants in Turkey with the Akkuyu nuclear power plant under construction.

2. TURKEY'S ELECTRICITY (INSTALLED CAPACITY)

Turkey is in the category of developing countries, energy production shows improvement over the year. The values

of the energy produced for the current demand for 2020 according to months and energy types are given in Table 1 [14]. Year 2020 Monthly Electricity production and consumption according to the report [14] renewable energy sourced electricity production in Turkey is very modest. Most of the energy is obtained from coal, natural gas, thermal and hydroelectric power plants. According to the data of EPDK (Energy Market Regulatory Authority), the natural gas import in 2016 alone was 46,352.17 million m^3. This is an indicator of foreign dependency in energy and high economic expense for energy supply. As Table 1 shows, Turkey's gross energy demand in 2020 was 304,835.7 GWh.

Table 1 :Monthly distribution of Turkey's gross electricity generation by primary energy resources

2020													
	JANUARY	FEBRUARY	MARCH	APRIL	MAY	JUNE	JULY	AUGUST	SEPTEMBER	OCTOBER	NOVEMBER	DECEMBER	TOTAL
Hard Coal + Imported Coal	6,653.4	5,817.1	5,229.4	2,916.6	3,556.7	5,922.2	6,641.2	6,683.9	6,398.3	5,785.6	6,085.9	6,414.7	68,105.2
Lignite	3,174.1	3,006.1	2,976.8	2,429.6	2,600.2	3,666.6	3,408.4	3,176.0	3,075.3	3,516.6	3,530.8	3,603.5	38,163.8
Liquid Fuels	27.7	25.5	25.3	23.1	25.2	24.3	28.1	28.4	26.9	26.9	25.6	25.8	313.0
Naturl Gas +Lng	7,474.4	4,859.2	2,494.9	1,536.9	1,718.4	3,632.5	6,628.5	7,398.7	8,142.4	8,243.9	8,284.9	8,916.5	69,331.1
Renew and Wastes	425.5	405.3	445.3	434.6	453.227	426.376	466.283	463.3	470.1	493.1	501.9	516.6	5,501.5
Thermal	17,755.1	14,113.3	11,171.8	7,340.8	8,353.7	13,671.9	17,172.4	17,750.3	18,113.0	18,066.2	18,429.2	19,477.0	181,414.7
Hydro	5,487.8	7,168.8	9,633.6	9,137.1	9,019.2	6,723.1	6,919.5	6,709.4	5,578.9	4,476.5	3,311.4	3,954.0	78,119.2
Geothermal + Wind+Solar	3,834.2	3,646.9	3,898.0	3,863.5	3,519.5	3,229.8	4,684.9	4,472.6	3,951.2	2,903.5	3,962.3	3,930.9	45,897.5
Gross Generation	27,077.1	24,929.0	24,703.4	20,341.4	20,892.4	23,624.8	28,776.9	28,932.3	27,643.1	25,446.2	25,702.9	27,361.8	305,431.4
IMPORTS	126.8	284.2	307.2	163.8	210.7	343.7	172.0	106.0	52.8	55.7	30.5	35.0	1,888.3
EXPORTS	227.5	184.3	190.9	163.2	120.7	56.2	139.5	152.9	218.6	320.0	372.0	338.1	2,484.0
GROSS DEMAND	26,976.4	25,028.9	24,819.6	20,342.0	20,982.4	23,912.2	28,809.4	28,885.4	27,477.3	25,181.9	25,361.4	27,058.7	304,835.7

Unit: GWh

Table 2 [14] shows the installed capacity of Turkey to the development of domestic energy resources over the years the share of the total installed capacity has been shown. According to accelerate the production of solar energy in Turkey has increased since 2014 and in 2019 reached 5,995.2 MW. However, in a high solar energy potential of the country such as Turkey, this solar-generated electricity production is quite low values.

Table 2:Annual development of domestic resources based installed capacity share in Turkey total installed capacity (2000-2019)

YEARS	HYDRO	GEOTERMAL	WIND	SOLAR	RENEW.WASTES + WASTE HEAT	LIGNITE	HARD COAL +ASPHALTITE	DOMESTIC RESOURCES INSTALLED CAPACITY	TOTAL INSTALLED CAPACITIY	DOMESTIC RESOURCES SHARE %
2000	11,175.2	17.5	18.9		23.8	6,508.9	335.0	18,079.3	27,264.1	66.3
2001	11,672.9	17.5	18.9		23.6	6,510.7	335.0	18,578.6	28,332.4	65.6
2002	12,240.9	17.5	18.9		27.6	6,502.9	335.0	19,142.8	31,845.8	60.1
2003	12,578.7	15.0	18.9		27.6	6,438.9	335.0	19,414.1	35,587.0	54.6
2004	12,645.4	15.0	18.9		27.6	6,450.8	335.0	19,492.7	36,824.0	52.9
2005	12,906.1	15.0	20.1		35.3	7,130.8	335.0	20,442.3	38,843.5	52.6
2006	13,062.7	23.0	59.0		41.3	8,210.8	335.0	21,731.7	40,564.8	53.6
2007	13,394.9	23.0	147.5		42.7	8,211.4	335.0	22,154.5	40,835.7	54.3
2008	13,828.7	29.8	363.7		59.7	8,205.0	335.0	22,821.9	41,817.2	54.6
2009	14,553.3	77.2	791.6		86.5	8,199.3	470.0	24,177.9	44,761.2	54.0
2010	15,831.2	94.2	1,320.2		107.2	8,199.3	470.0	26,022.1	49,524.1	52.5
2011	17,137.1	114.2	1,728.7		125.7	8,199.3	470.0	27,775.0	52,911.1	52.5
2012	19,609.4	162.2	2,260.6		168.8	8,193.3	470.0	30,864.3	57,059.4	54.1
2013	22,289.0	310.8	2,759.7		235.0	8,223.2	470.0	34,287.7	64,007.5	53.6
2014	23,643.2	404.9	3,629.7	40.2	299.1	8,281.3	470.0	36,768.4	69,519.8	52.9
2015	25,867.8	623.9	4,503.2	248.8	370.1	8,663.4	755.0	41,032.2	73,146.7	56.1
2016	26,681.1	820.9	5,751.3	832.5	496.4	9,126.5	755.0	44,463.7	78,497.4	56.6
2017	27,273.1	1,063.7	6,516.2	3,420.7	641.9	9,129.1	782.5	48,827.2	85,200.0	57.3
2018	28,291.4	1,282.5	7,005.4	5,062.8	818.9	9,456.1	782.5	52,699.6	88,550.8	59.5
2019	28,503.0	1,514.7	7,591.2	5,995.2	1,170.5	9,966.0	782.5	55,523.1	91,267.0	60.8

Unit: MW

3. NUCLEAR POWER IN TURKEY

Turkey is one of the countries that first introduction to nuclear technology [15]. Despite this, until recently, there has been no serious development in nuclear technology due to political instability, economic and social problems. However, the agreement signed with the Government of the Russian Federation in 2010, which will be Turkey's first nuclear power plant in Mersin Akkuyu Nuclear Power Plant construction began. The map of Turkey's planned nuclear power plants is shown in Figure 1 [16].

Figure 1: Turkey's planned nuclear power plants

Turkey's nuclear energy process [17] after Chernobyl, people in the wake of the country's economic problems, fears and induced a long time failed to show improvement [18]. There are those who advocate the view that if nuclear power plants can only be established according to international standards, with continuous quality controls that can be done by relevant experts or experts, radiation safety may be high, or accident probability is close to zero [19]. There are also those who advocate the view that this situation should be eliminated with the more effective introduction of nuclear technology and the public should be made conscious [20].

Many illuminating studies have been conducted in Turkey concerning nuclear energy [15], [21]–[23]. However, the environmental impacts of nuclear energy and especially the cost of installation are a matter of concern.

4. SOLAR POWER IN TURKEY

Turkey's current geographic location, for potential for solar energy is very efficient (Figure 2) [24]. Turkey's Solar Energy Potential Atlas of (GEPA) has been found to the annual 2,737 hours of sunshine duration (daily 7.5 hours), the annual total incoming solar energy 1,527 kWh / m² (daily 4.2 kWh / m²) [24].

There are many studies done about solar energy in Turkey [25]–[29]. In 2030, energy demand will be met from renewable energy in Turkey told that almost half of the studies [30] as it is, there are also studies claiming that renewable energy sources are inadequate.

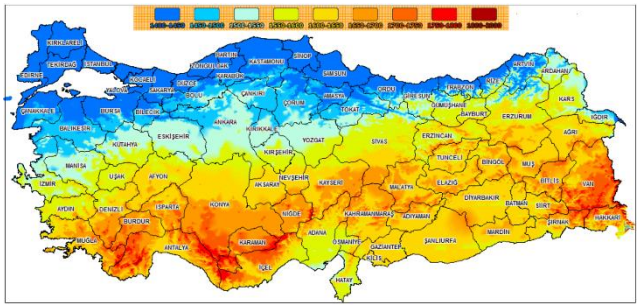

Figure 2: Turkey Solar Energy Potential Map

Turkey solar energy potential in Figure 2 [24] is shown. According to the current map, there is a serious solar potential especially in the eastern and southern parts of the country. And in order to use this potential, studies on solar energy have increased especially since 2014. Even in Turkey have also been studies that examined the city-based solar energy potential [27], [31], [32].

There are 81 provinces in Turkey and the establishment phase of the ongoing first nuclear power plant in Mersin (İçel) will be established in the province. When viewed from city-based perspective, solar energy potential for Mersin province is shown in Figure 3 [24].

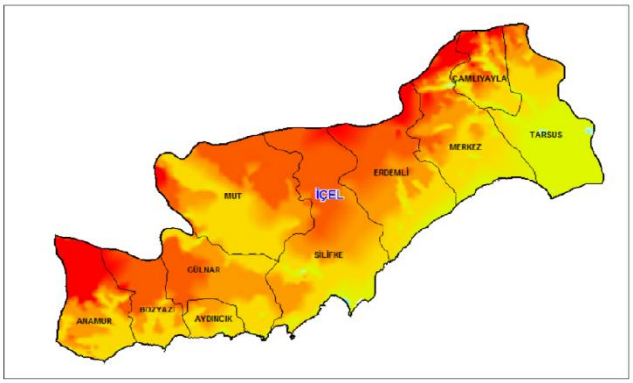

Figure 3: Solar energy potential in Mersin province

Table 3: List of SPP available in Mersin province

	SPP name	Installed Power
1)	Borusan EnBW Dayıcık SPP	6,00 MW
2)	Gülnar SPP	5,75 MW
3)	Mersin Gülnar SPP	5,53 MW
4)	Nar Solar SPP	5,00 MW
5)	Tiryaki Agro Mersin SPP	4,00 MW
6)	Kıvanç 2 SPP	3,88 MW
7)	Göl, Hörç ve Akova Tuluk SPP	3,00 MW
8)	Yayla Agro Gıda SPP	1,00 MW

9)	Özipek SPP	1,00 MW
10)	Cemile Bingül SPP	1,00 MW
11)	Ah-Fer SPP	0,97 MW
12)	Eren Tarım SPP	0,48 MW
13)	Opat Otomotiv Mersin SPP	0,15 MW
14)	Büyükeceli Camii	0,003 MW

The list and installed power of Solar Power Plants in Mersin province are given in Table 3 [33]. According to the table, the total installed power from SPP in Mersin is approximately 37.8 MW. It is predicted that Mersin province will consume approximately 4600 GWh of energy in 2023 [32]. Accordingly, existing solar power plants meet a small amount of the energy needs of 2023. However, with the Akkuyu Nuclear Power Plant, whose first unit is planned to be commissioned in 2023, it is expected that all energy needs will be met on Mersin basis and even energy surplus will be released.

5. COST COMPARISON

The most important criterion when comparing energy production methods is cost calculation. Especially for developing countries, it is very important to obtain the most efficient energy with the least cost.

LCOE (Levelized Cost of Energy) analysis is a method used to calculate the unit energy cost of power generation plants. The unit price of energy is calculated by taking into account the initial investment cost, operating and maintenance costs, and fuel expenses. Thus, the minimum price at which the energy should be sold can be calculated in order to avoid losses [34].

The levelled electricity cost represents the average revenue per unit of generated electricity required to recover the costs of building and operating a manufacturing facility and a battery storage facility during an assumed fiscal life and duty cycle, respectively [35].

According to studies [36] that have done LCOE analysis for a solar power plant, there has been a levelled reduction in electricity cost for a solar PV since 2018. As the system costs den SPP decreased, the total installed costs decreased and the change in the total installation cost ranged from 0.21 USD / W to 0.38 USD / W according to December 2019 data.

Basically, the unit energy price is obtained by dividing all costs on an annual basis by the electrical energy produced in a year. It can be calculated with many different approaches and formulas. One of the most common levelled energy cost formulas is shown in Eq. 1 and Eq 2.

$$LCOE = \frac{I_0 x\ GKO + M_Y + V_Y}{8760\ x P_T x KF} + F\ xH \quad (1)$$

$$GKO = \frac{D(1+D)^N}{(1+D)^N - 1} \quad (2)$$

In these equations, I_0 = Initial investment cost ($), GKO = Capital Recovery Rate, My = Annual Fixed Expenses ($), Vy = Annual Variable Expenses ($), P_T = Power Plant (kW), KF = Capacity factor, F = Fuel Cost ($ / BTU), H = Thermal Coefficient (BTU / kWh), D = Discount Rate, N = Estimated life of the plant (years).

LCOE is a method that allows a financial comparison of many different energy generation sources. It makes it possible to make comparisons by considering differences such as unequal working lifetimes, different initial investment and operating costs, and the size of projects.

Akkuyu nuclear power plant is a nuclear power plant whose construction started in 2018 by ROSATOM and the first unit of 1200 MW is planned to be commissioned in 2023. The total cost of this power plant has been calculated to be 18 billion euros and the price per kW hour has been determined as 4160 euro / kW [30].

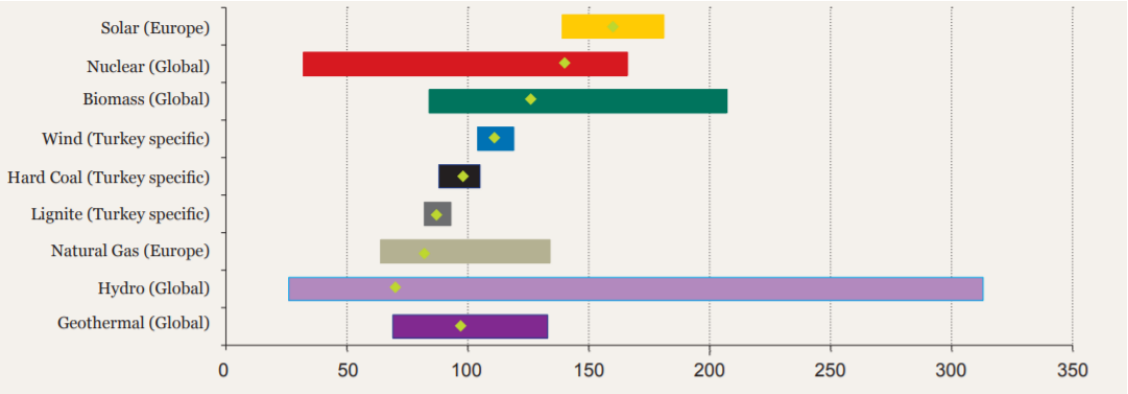

Figure 4: Levelized cost of electricity for various technologies in Europe, Turkey and globally, 2014 ($ / MWh)

LCOE is a scale used to compare different electricity generation methods. OECD has conducted a special study for this comparison and Figure 4 [37] shows the results of the comparison performed for thermal energy generation technologies (Vertical axis LCOE values, horizontal axis interest values; 3%, 7%, 10%). In this comparison, it is

clearly seen that when interest rates increase, the most affected electricity generation method is nuclear energy. This is due to the large initial investment requirement and long construction times. Therefore, timely construction of facilities in accordance with plans is critical for competitive energy generation in the nuclear field [38], [39].

6. EVALUATION AND CONCLUSION

Meeting the country's increasing energy needs has become an important issue for Turkey. Especially for Turkey, which is in the transition phase to nuclear technology, the questions of renewable energy or nuclear energy come up frequently. Although solar energy seems more appropriate at first in terms of cost, in the long term, the efficiency to be obtained from nuclear energy is much higher. In addition, nuclear energy, like the sun, is almost completely harmless to the environment, and contrary to what is generally believed, there is no radiation emission to the environment. Petroleum and natural gas based thermal power plants while they cause acid rain by emitting CO_2, NOx and SO_2 gases, nuclear power plants do not pollute the environment like coal, oil, and natural gas-based thermal power. Therefore, the energy is clean, safe, and economical energy production, nuclear energy has become almost obligatory for Turkey [40]. According to IEA data, the annual carbon emission reduction resulting from operating 1000 MWh NPP is approximately 2.5 million tons of CO_2 [41] .

The main purpose of this study is to compare the environmental and economic effects of solar and nuclear energies. In order to make these comparisons, LCOE analysis was requested. However, this analysis requires a lot of data. The study will be expanded further in the future, LCOE analysis will be made and economic comparison will be seen more clearly. Although it is known that solar and nuclear energy do not have negative effects on the environment, when the study is expanded, environmental effects will be mentioned more.

REFERENCES

[1] “Başbakanlık Mevzuatı Geliştirme ve Yayın Genel Müdürlüğü,” no. 3. pp. 1–10, 2016.
[2] Akkuyu Ngs, “http://www.akkunpp.com/.” .
[3] Anonymous, “Nükleer Santral Karşiti Bilim İnsanlari Bildirisi,” *Elektr. Mühendisliği*, pp. 105–107, 2007, [Online].
[4] Doğru, B., Recepoğlu, M., “Dumlupınar Üniversitesi Sosyal Bilimler Dergisi EY İ 2013 Özel Sayısı,” *Dumlupınar Üniversitesi Sos. Bilim. Derg.*, no. 2013 Eyi Özel Sayı, pp. 17–34, 2013.
[5] Mutlu, Y., “Türkiye’nin enerji potansiyeli ve yenilenebilir enerji kaynaklarının elektrik enerjisi üretimi açısından önemi,” *Ankara Üniversitesi Çevrebilimleri Derg.*, vol. 4, no. 2, pp. 33–54, 2012.
[6] Hakyemez, C., Yanık E., “Aylık Enerji Bülteni,” *Tskb*, 2020.
[7] Varınca, K. B. *et al.*, “Türkiye’de Günes Enerjisi Potansiyeli ve Bu Potansiyelin Kullanım Derecesi, Yöntemi ve Yaygınlıgı Üzerine Bir Arastırma,” *Muhendis ve Makina*, vol. 4, no. 42, pp. 33–54, 2012.
[8] Özgür, E., “Türkiye’de Güneş Enerjisi,” *Türkiye’nin Enerj. Görünümü*, pp. 297–316, 2020.
[9] Şenol,Tunç, “Türkiye İçin Güneş Enerjisi Politikası,” *Türkiye’nin Enerj. Görünümü*, 2016.
[10] M. Meclisinin, T. Plan, K. Enerji, T. K. Bakanl, and E. Bakan, “GelecekVizyonu,” 2020.
[11] H. Sosyal *et al.*, “Türkiye’nin nükleer enerji politikasi *,” pp. 421–438, 2016.
[12] Önal, M.,“Sürdürülebilir KalkinmaYenilenebilir Enerjinin Önemi:Türkiye Üzerine Bir Değerlendirme,” Turkish Bus. J., vol. 1, no. 1, pp. 78–97, 2020.
[13] Dong, M. *et al.*, “Uncertainty and global sensitivity analysis of levelized cost of energy in wind power generation,” *Energy Convers. Manag.*, vol. 229, no. January, 2021.
[14] TEİAŞ, “No Title,” *Türkiye Elektrik Üretim A.Ş.* https://www.teias.gov.tr/.
[15] L. U. Ankara, “Dünden Bugüne Türkiye ’ de,” 2020.
[16] ORDAF, “Ortadoğu ve Afrika Araştırmacıları Derneği.” https://ordaf.org/turkiyenin-sivil-nukleer-santral-projeleri-ve-nukleer-yayginlasma-endisesi/.
[17] Ergün, S., “Nükleer enerji ve Türkiye’ye yansimalari,” vol. 1, no. 2, pp. 34–58, 2012.
[18] Kok B., H. Benli, “Energy diversity and nuclear energy for sustainable development in Turkey,” *Renew. Energy*, vol. 111, pp. 870–877, 2017.
[19] Özel, M. E., “Türkiye’de Nükleer Enerjinin Durumu Ve Akkuyu Nükleer Enerji Santralimiz,” 2017.
[20] Temurçi, K., Aliağaoğlu, A., “Nükleer Enerji ve Tartışmalar Işığında Türkiye’de Nükleer Enerji Gerçeği,” *Coğrafi Bilim. Derg.*, vol. 1, no. 2, pp. 25–39, 2003, [Online].
[21] Özalp, M., “Türkiye’de Nükleer Enerji Kurulumunun Enerjide Dişa Bağimlilik Ve Arz Güvenliğine Etkisi,” *Cilt*, vol. 18, pp. 175–188, 2017.
[22] Kozak, N., “Türkiye’ de nükleer enerji sorgulanıyor ...” Anatolia, https://dergipark.org.tr/tr/download/article-file/1016739.
[23] Eren AlperYILMAZ, “Güvenlik Ve Ekonomik Boyutuyla Nükleer Enerji Tartışmaları”, Cumhuriyet Üniversitesi Edebiyat Fakültesi Sosyal Bilimler Dergisi, 2015.
[24] T.C., “T.C.Enerji ve Tabii Kaynaklar Bakanlığı.” https://enerji.gov.tr/.
[25] Yolcan O. And Köse R., “Türkiye’nin Güneş Enerjisi Durumu Ve GüneEnerjisiSantrali KurulumundaÖnemli Parametreler,” *Kırklareli Üniversitesi Mühendislik ve Fen Bilim. Derg.*, vol. 2, pp. 196–215, 2020.
[26] F. In, A. Bonding, D. For, and C. Structures, “Fundamentals In Adhesıve Bondıng Desıgn For,” *İleri Te*, Pp. 1174–1187.
[27] Gezer T., “Bir Güneş Enerjisi Santralinin Maliyet Analizi: Aydın İli Örneği,” *Tek. Bilim. Derg.*, vol. 9, no. 2, pp. 46–54, 2019, doi: 10.35354/tbed.574190.
[28] Dinçer, F. “Türkiye’de Güneş Enerjisinden Elektrik Üretimi Potansiyeli - Ekonomik Analizi ve AB Ülkeleri ile Karşılaştırmalı Değerlendirme,” *Kahramanmaras Sutcu Imam Univ. J. Eng. Sci.*, vol. 14, no. 1, pp. 8–17, 2011.
[29] Türk V. E., İ. Y. E. Dek, “Subsidies on renewable energy investments and current situation in turkey,” pp. 69–78.
[30] Berke M. O., "Turkey’s Renewable Power: Alternative Power Supply Scenarios for Turkey". 2014.
[31] Biçen T., “Güneş Panelleri İle Elektrik Üretiminin Teknik ve Ekonomik Analizi: Bursa Örneği,” p. 69, 2018, [Online]. Available: http://hdl.handle.net/11452/958.
[32] Tekin G., Erat S., and Zeren Y., “Mersin İlinin 2023 Yılına Kadar Elektrik Enerjisi İhtiyacının Hesaplanması” vol. 32, no. March, pp. 187–195, 2017.
[33] Enerji Atlası, “Enerji Atlası.” https://www.enerjiatlasi.com/.
[34] Electricport, “Seviyelendirilmiş Enerji Maliyeti Nedir?” https://www.elektrikport.com/teknik-kutuphane/seviyelendirilmis-enerji-maliyeti-nedir/22646#ad-image-0.
[35] EIA, “Levelized Cost of New Generation Resources in the Annual Energy Outlook 2013,” *US Energy Inf. Adm.*, no. January, pp. 1–5, 2013.
[36] Taylor M., “Renewable Power Generation Costs in 2019: Latest Trends and Drivers,” *Renew. Power Gener. Costs 2019 Latest Trends Drivers*, no. June, pp. 0–15, 2019.
[37] Report: Turkey’s Renewable Power, Alternative Power Supply Scenarios For Turkey, WWF, 2014.
[38] Bayram A., “Nükleer enerji ve Türkiye,” *Çevre Kongresi Bildir. Kitabı, Şanlurfa, s.*, pp. 617–624, 2000.
[39] OECD, “2015 Edition,” p. 215, 2015, [Online]. Available: https://www.oecd-nea.org/ndd/pubs/2015/7057-proj-costs-electricity-2015.pdf.
[40] Onural A. S., N. Doğdu, “Future Demand For Nuclear Energy In Turkey,” *Int. J. Energy Appl. Technol.*, vol. 4, no. 4, pp. 147–151, 2017, [Online].
[41] Toprak S., Dal S., “Akkuyu Nuclear Power Plant Cost & Benefit Analysis,” *Energy Policy Turkey*, no. 4, pp. 85–91, 2017.

Corrosion Resistance of Anodized Aluminum Alloys

Özlem Baran Acımert[1], Lynn Hopkins[2], Ayşenur Keleş Dayauç[3] and Emir Avcıoğlu[3]

[1] Erzincan Binali Yıldırım University, Erzincan/Turkey, obaran@erzincan.edu.tr
[2] Aprem Consulting and Machinery Manufacturing Industry Limited Company, Çorum/Turkey, lynnehopkins@gmail.com
[3] Hitit University, Çorum/Turkey, aysenurkeles@hitit.edu.tr
[3] Hitit University, Çorum/Turkey, emiravcioglu@hitit.edu.tr

Abstract **- Aluminum alloys are a preferred material in the defense industry due to their excellent mechanical properties and low density. However, in certain working conditions their corrosion resistance is insufficient. The anodization technique is the most effective technique for increasing the corrosion resistance of aluminum alloys. This technique is interesting because of its ease of use and cheapness. In this study, Al2024 and Al5083 alloys were anodized in different electrolyte solutions (Sulfuric acid, Oxalic acid and Sulfuric acid/Oxalic acid). Anodization was performed for 15 minutes at a current density of 25mA/cm2. Electrochemical testing was performed to determine the corrosion resistance of the alloys before and after anodization. Results have shown that the anodization process increased the corrosion resistance of both aluminum alloys. In addition, the properties reported for the Al-2024 alloy were superior to those of the Al-5083 alloy.**

Keywords **– Aluminum, Anodization, Hardness, Corrosion**

I. INTRODUCTION

Aluminum (Al) alloys, which are abundant in nature, are used in a wide variety of applications such as aerospace, sports, transportation and civil industries due to their advantages such as low specific gravity, high specificity, good conductivity, strength and ease of use [1]. An oxide (passive) film that naturally develops under normal atmospheric conditions forms on the surface of aluminum alloys. However, this oxide film provides a certain level of protection under normal conditions as it is not thin, compatible and homogeneous [2]. However, the easy occurrence of different types of local corrosion (pitting, intergranular, exfoliation and stress corrosion, etc.) in aluminum alloys limits the applications of these alloys to a large extent. Therefore, appropriate surface treatments are required to improve the corrosion resistance of these alloys [3]. The anodization process, which is an electrochemical process used to form oxide films on the surface of metals, forms hard, corrosion and wear resistant oxide films on aluminum alloys [4, 5]. Compared with the traditional single acid electrolyte, multiacid electrolyte systems have been used, which can help reduce the dissolution rate of the anodized layer and be beneficial in improving the surface properties of aluminum [5]. Therefore, in this study, Al2024 and Al5083 alloys were anodized in different electrolyte solutions (Sulfuric acid, Oxalic acid and Sulfuric acid/Oxalic acid) and determined the corrosion resistance of the alloys before and after anodization.

II. EXPERIMENTAL METHODS

In this study, Al2024 and Al5083 materials were used as the substrate. The samples were polished with 120-240-400-800-1200 mesh sandpaper. The substrates were polished to Ra 0.05µ before the anodization process. Al2024 and Al5083 alloys were anodized in different electrolyte solutions (Sulfuric acid, Oxalic acid and Sulfuric acid/Oxalic acid). The amount of each acid in 1 liter of solution was adjusted to 120g. Anodization was performed for 15 minutes at a current density of 25mA/cm^2. Graphite was chosen as a cathode material. The distance between the anode and the cathode is set to 2 cm. The hardness values of the samples before and after anodization were determined by the Knoop hardness method. The experiment was carried out under 10gf load for 15s. To determine the corrosion resistance of the samples before and after anodization, potentiodynamic polarization test (Versa Stat) experiments were performed. Potentiodynamic polarization test was performed between -2 and 3 mV and scanning speed of 1mV/s. The surface area is set to 1 cm^2.

III. RESULTS AND DISCUSSION

In order to determine the aluminum anode corrosion behavior in 3.5% NaCl solution, the polarization test method with the 3-electrode method was used. The best corrosion resistance of Al2024 and Al5083 alloy was obtained from the anodization process using a sulfuric acid/oxalic acid mixture. Potential dynamic curves of Al2024 and Al2024 anodized in sulfuric acid/oxalic acid solution are given in Figure 1. Potential dynamic curves of Al5083 and Al5083 anodized in sulfuric acid/oxalic acid solution are given in Figure 2. It can be seen in Figure 1 and Figure 2 that the anodized with sulfuric acid/oxalic acid solution on Al2024 and Al5083 samples showed more noble and less noble behavior, respectively [6]. In Figure 1 and 2, the aluminum substrates have a higher corrosion current density than the steel surface with hard anodic film protection. As can be seen, the positive

Ecorr value of Al2024 anodized in sulfuric acid/oxalic acid solution indicates that this material exhibits better pitting corrosion resistance in seawater. The difference in corrosion resistance of Al2024 and Al5083 may be related to the intermetallic particle properties present in the two alloys [7]. In summary, the anodization technique in Sulfuric acid/Oxalic acid electrolyte is much more useful to enhance the corrosion resistance of the Al2024 and Al5083.

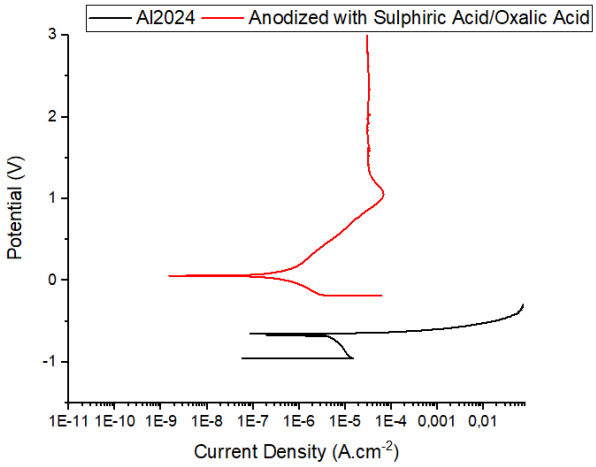

Figure 1: Potential dynamic curves of Al2024 and Al2024 anodized in sulfuric acid/oxalic acid solution

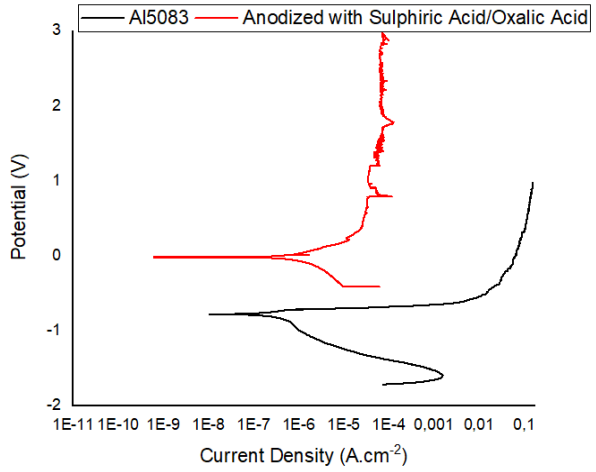

Figure 1: Potential dynamic curves of Al5083 and Al5083 anodized in sulfuric acid/oxalic acid solution

The hardness values and corrosion rates of samples are given in Table 1. The highest hardness was obtained from Al2024 anodized in sulfuric acid/oxalic acid solution. The hardness of the formed oxide was affected by the hardness of the base material. An increase in corrosion resistance was observed with increasing hardness value [8]. Better corrosion resistance was observed in aluminum alloys with lower icorr and more positive Ecorr values [9].

Table 1: The hardness values and corrosion rates.

Run Number	Hardness value (GPa)	Corrosion rate ($\times 10^{-6}$,mm·yr^{-1})
Al5083	0,9	0,000465425
Al2024	1,3	0,000203763
Anodized with Sulphiric Acid/oxalic Acid on Al5083	3,1	7,06934E-05
Anodized with Sulphiric Acid/oxalic Acid on Al2024	5,2	1,66337E-05

IV. CONCLUSIONS

In this study, Al2024 and Al5083 alloys were anodized in different electrolyte solutions (Sulfuric acid, Oxalic acid and Sulfuric acid/Oxalic acid). Corrosion resistances were observed before and after anodization. When the hardness values were examined, the highest hardness was obtained by anodizing the Al2024 alloy in Sulfuric acid/Oxalic acid. The base material was effective in the hardness value. When the corrosion resistances are examined, the best corrosion resistance was measured from the anodization of Al2024 alloy in Sulfuric acid/Oxalic acid. When the hardness values and corrosion rates were compared, it was observed that the lowest corrosion rate was obtained in the sample with the highest hardness. In summary, the best hardness and corrosion resistance were obtained in the anodization process in sulfuric acid/oxalic acid electrolyte. In addition, all anodization processes increased the corrosion resistance of aluminum alloys.

ACKNOWLEDGMENT

The authors would like to thank Erzincan Binali Yıldırım University and Hitit University for their work..

REFERENCES

[1] L. Feng, Y. Che, Y. Liu, X. Qiang, Y. Wang, Fabrication of superhydrophobic aluminium alloy surface with excellent corrosion resistance by a facile and environment-friendly method, Applied Surface Science 283 (2013) 367-374.
[2] H. Ezuber, A. El-Houd, F. El-Shawesh, A study on the corrosion behavior of aluminum alloys in seawater, Materials & Design 29 (4) (2008) 801-805.
[3] L. Shao, H. Li, B. Jiang, C. Liu, X. Gu, D. Chen, A Comparative Study of Corrosion Behavior of Hard Anodized and Micro-Arc Oxidation Coatings on 7050 Aluminum Alloy, Metals 8 (3) (2018).
[4] A.M.A. El-Hameed, Y.A. Abdel-Aziz, F.S. El-Tokhy, Anodic Coating Characteristics of Different Aluminum Alloys for Spacecraft Materials Applications, Materials Sciences and Applications 08 (02) (2017) 197-208.
[5] J. Lu, G. Wei, Y. Yu, C. Guo, L. Jiang, Aluminum alloy AA2024 anodized from the mixed acid system with enhanced mechanical properties, Surfaces and Interfaces 13 (2018) 46-50.
[6] M.P. Martinez-Viademonte, S.T. Abrahami, T. Hack, M. Burchardt, H. Terryn, A Review on Anodizing of Aerospace Aluminum Alloys for Corrosion Protection, Coatings 10 (11) (2020) 30.
[7] A. Aballe, M. Bethencourt, F.J. Botana, M.J. Cano, M. Marcos, Influence of the cathodic intermetallics distribution on the reproducibility of the electrochemical measurements on AA5083 alloy in NaCl solutions, Corrosion Science 45 (1) (2003) 161-180.
[8] I. Saefuloh, N. Kanani, F. Gumelar Ramadhan, Y. Rukmayadi, Y. Yusuf, S. Abdullah, S. Susilo, The Study of Corrosion Behavior and Hardness of AISI Stainless Steel 304 in Concentration of Chloride Acid Solution and

Temperature Variations, Journal of Physics: Conference Series 1477 (2020) 052058- 052066.
[9] W. Handoko, F. Pahlevani, V. Sahajwalla, Enhancing Corrosion Resistance and Hardness Properties of Carbon Steel through Modification of Microstructure, Materials (Basel) 11 (12) (2018).

Applicability of Reduced-Order Modeling Approach on Rapid Investigation of Airfoil Vibration Characteristics

C.TOLA[1]

[1] Aselsan Inc, Ankara/Turkey, ctola@aselsan.com.tr

***Abstract* – Structural dynamic behavior of lifting surfaces such as wing, tail, canard, fin is quite critical for the aircraft/missile design process since their natural frequencies determine the flight envelope of the vehicle. The aerodynamic efficiency of an aircraft can be maximized by preferring slender designs which leads to a decrement of the structural stiffness and so the natural frequencies of the structure. To satisfy both aerodynamic efficiency and structural strength, an iterative design process is applied during the preliminary design phase of the lifting surfaces. Application of reduced-order modeling approach on the structural model and modeling the lifting surfaces with shell elements instead of solid considerably shortens both modeling and solution time. This study aims to examine the applicability of the modeling approach by comparing the results of the shell models with solid ones. The applicability of the reduced-order modeling approach is tested for different wings designed from different airfoil sections having different taper ratios and sweep angles. Finite element models are prepared and solved in the Abaqus environment. Thickness distributions of the lifting surfaces are calculated and transferred to the Abaqus using an in-house Matlab script developed within the content of this research. According to the results, the reduced-order modeling approach provides accurate solutions as long as the number of elements in chordwise and in spanwise directions is high enough.**

***Keywords* – Reduced-order modeling, Airfoil vibration characteristics, Rapid investigation, Finite element method.**

I. INTRODUCTION

MODAL analysis is quite critical for the structural design process. It is possible to foresee the probable catastrophic failures such as resonance governing from the vibration characteristics of the design through the modal analysis. Accurate determination of natural frequencies has special importance especially for aerospace industry to determine the flutter velocity of the aerospace vehicles. The designers generally tend to produce the lightest possible lifting surface that can satisfy aerodynamic, aeroelastic, and structural requirements. An iterative design process or a multidisciplinary optimization process is applied to satisfy the requirements of different disciplines. Since numerical methods such as finite element analysis are generally preferred for structural analyses, usage of solid elements leads to a considerable increment of solution duration for the iterative design process. Application of reduced-order modeling to the finite element model will save a considerable amount of time in the design process.

Reduced-order modeling method was applied to various problems in literature. Carassale et al. modeled compressor blades using 1-D beam elements and validated their results with an accurate 3-D finite element calculation [1]. Dantulwar et. al. applied the reduced-order modeling technique in order to provide an efficient tool to investigate parachute behavior under different operating conditions [2]. Wilber used the parametric reduced-order modeling technique to construct a computationally efficient model of a complex bladed disk geometry [3]. Sun et al. proposed an accurate and efficient general shell model to predict the dynamic behavior of compressor blades [4]. Yuan et al. propose a reduced-order model technique in order to model the dynamic behavior of turbofan blades [5].

Within the content of this research, the applicability of the reduced-order modeling approach on a rapid investigation of airfoil vibration characteristics is examined by making a comparison between the natural frequency results of the solid and the shell wing models. To construct the shell wing models, a home-written Matlab script is prepared and variable thickness distribution following the airfoil coordinates are calculated with it.

The methodology used in the Matlab script to calculate the variable shell thicknesses in both chordwise and spanwise directions is explained in the Methodology section. Details about the finite element models are described in the Finite Element Model section. Then, a comparison of the results is carried out in the subsequent section.

II. METHODOLOGY

To convert a solid airfoil model into a shell, first of all, variable thickness distribution through the chordwise and the spanwise directions should be calculated. A Matlab script is prepared for this purpose. Input variables of the script are wingspan (b), root chord length (c_{root}), taper ratio (TR), sweep angle (λ), dimensionless airfoil coordinates (X_{AF},Y_{AF}), and dimensionless camber line coordinates (X_{CAM},Y_{CAM}). Figure 1 illustrates the top view of a sample backward swept wing.

Using geometric relations, the script calculates chord length values for each of the spanwise stations (c_i) as in (1).

$$c_i = \left((TR-1)\frac{c_{root}}{b}b_i\right) + c_{root} \quad (1)$$

where the taper ratio (TR) refers to the ratio of tip chord

length (c_{tip}) to the root chord length of the wing. b_i, corresponds to the location of the spanwise station.

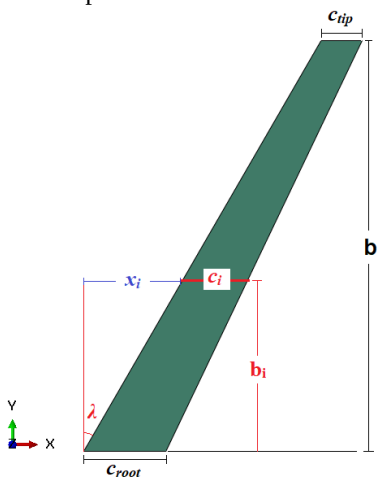

Figure 1: Parameters of a sample wing.

Leading-edge locations for each of the spanwise station (x_i) is calculated as in (2).

$$x_i = \frac{\tan^{-1}(\lambda)}{b_i} \quad (2)$$

Variation of the dimensionless thickness ($t_{c\_j\_0}$) in the chordwise direction is calculated by subtracting the y components of the airfoil coordinates from the top (y_{top_j}) to bottom (y_{bottom_j}) for each chordwise station as in (3).

$$t_{c\_j\_0} = y_{top\_j} - y_{bottom\_j} \quad (3)$$

Finally, the variation of thickness (t_{xyz}) value in the global coordinate system (X_i, Y_i, Z_i) is calculated as in (4), (5), (6), and (7).

$$X_i = x_i + c_i \cdot X_{AF} \quad (4)$$
$$Y_i = b_i \quad (5)$$
$$Z_i = c_i \cdot Y_{CAM} \quad (6)$$
$$t_{xyz} = c_i \cdot t_{c\_j\_0} \quad (7)$$

III. Finite Element Model

Finite element models of the solid and shell airfoils are prepared in Abaqus commercial software. Five different airfoils are used to make a comparison between the results of the solid and the shell models. Additionally, the effect of the taper ratio and the sweep angle on modal analysis results are also examined. Table 1 lists the design cases analyzed within the content of this research.

Table 1: List of the design cases.

Case	Airfoil	Taper Ratio	Sweep Angle
1	NACA 0008	0.5	30°
2	NACA 0008	1.0	0°
3	NACA 2408	0.5	30°
4	NACA 4412	0.5	30°
5	NACA 63415	0.5	30°
6	SC(2) 1010	0.5	30°

A. Geometry

Airfoil sections used in this work are illustrated in Figure 2.

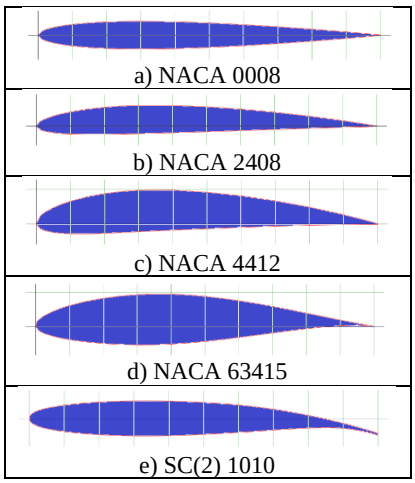

Figure 2: Airfoil sections used in this research [6].

For all configurations constant root chord length is 200 mm and span length is 1000 mm.

All design cases are modeled as solid and shell to examine the difference between their modal analysis results. During the construction of shell models, the shell surface is modeled through the camber line of the airfoil. Figure 3 illustrates sample solid and shell geometries.

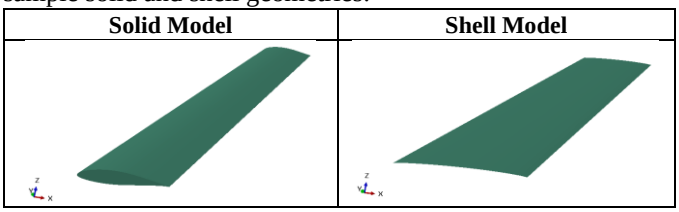

Figure 3: Solid and shell models prepared for NACA 63415

Variable thickness distribution of the shell is calculated using the Matlab script. Variation of the thickness concerning the airfoil coordinates is shown in Figure 4. Red represents the thickest and blue represents the thinnest locations.

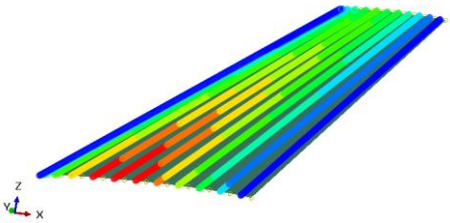

Figure 4: Variable thickness distribution of NACA 63415 shell.

B. Material Properties

Wings are made from Aluminum 7075 T6 alloy. Mechanical properties of the material are listed in Table 2.

Table 2: Mechanical properties of Al-7075 T6 [7].

Young's Modulus	71.8 GPa
Poisson's Ratio	0.33
Density	2810 kg/m^3

C. Boundary Conditions

Encastre boundary condition is applied from the root chord of the wings. Figure 5 illustrates the boundary conditions for the

sample solid and shell wing models.

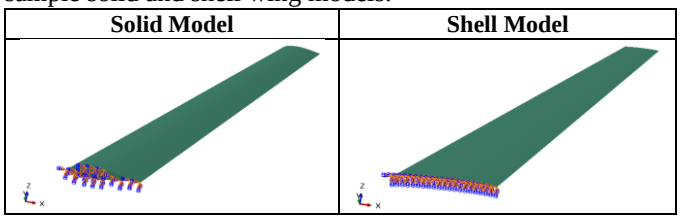

Figure 5: Boundary condition for NACA 63415 solid and shell.

D. Mesh

Shell models are constructed from quadratic quadrilateral elements having 8 nodes and reduced integration while solid models are constructed from quadratic hexagonal elements having 20 nodes and full integration. 8 mm approximate element size is used for solid models and 4 mm approximate element size is used for shell models. Table 3 lists the number of elements and nodes for each finite element model.

Table 3: Number of elements and nodes for all models.

Type	Airfoil	Taper Ratio	Sweep Angle	# of Elements	# of Nodes
Shell	NACA 0008	0.5	30°	19527	59286
		1.0	0°	17250	52389
	NACA 2408	0.5	30°	9975	30566
	NACA 4412	0.5	30°	10260	31423
	NACA 63415	0.5	30°	11928	36437
	SC(2) 1010	0.5	30°	28866	87369
Solid	NACA 0008	0.5	30°	20878	101046
		1.0	0°	20250	97948
	NACA 2408	0.5	30°	24708	119327
	NACA 4412	0.5	30°	21450	103777
	NACA 63415	0.5	30°	32318	148339
	SC(2) 1010	0.5	30°	22594	109239

Figure 6 shows mesh structures of sample solid and shell finite element models.

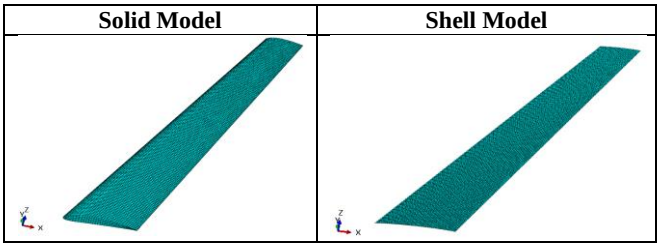

Figure 6: Mesh structures for NACA 63415 solid and shell.

IV. Comparison Of The Results

This section covers the comparison of modal analysis results between the shell and the solid finite element models corresponding to each of the design cases listed in Table 1.

A. Case-1

NACA 0008 airfoil having a 30° sweep angle and taper ratio of 0.5 is used for this case. The root chord length and the span length of the wing is taken as 200 mm and 1000 mm sequentially. The difference between the solid and the shell models is summarized in Table 4. A comparison of the mode shapes of the first 6 modes is shown in Figure 7.

Table 4: Case-1 comparison of the results.

Case	Solid	Shell	Difference %
Mass [kg]	3.593	3.573	0.547
Mode-1 [Hz]	11.171	11.127	0.394
Mode-2 [Hz]	47.211	47.016	-0.413
Mode-3 [Hz]	117.010	116.520	-0.419
Mode-4 [Hz]	122.480	122.290	-0.155
Mode-5 [Hz]	202.630	201.880	-0.370
Mode-6 [Hz]	220.840	219.900	-0.426

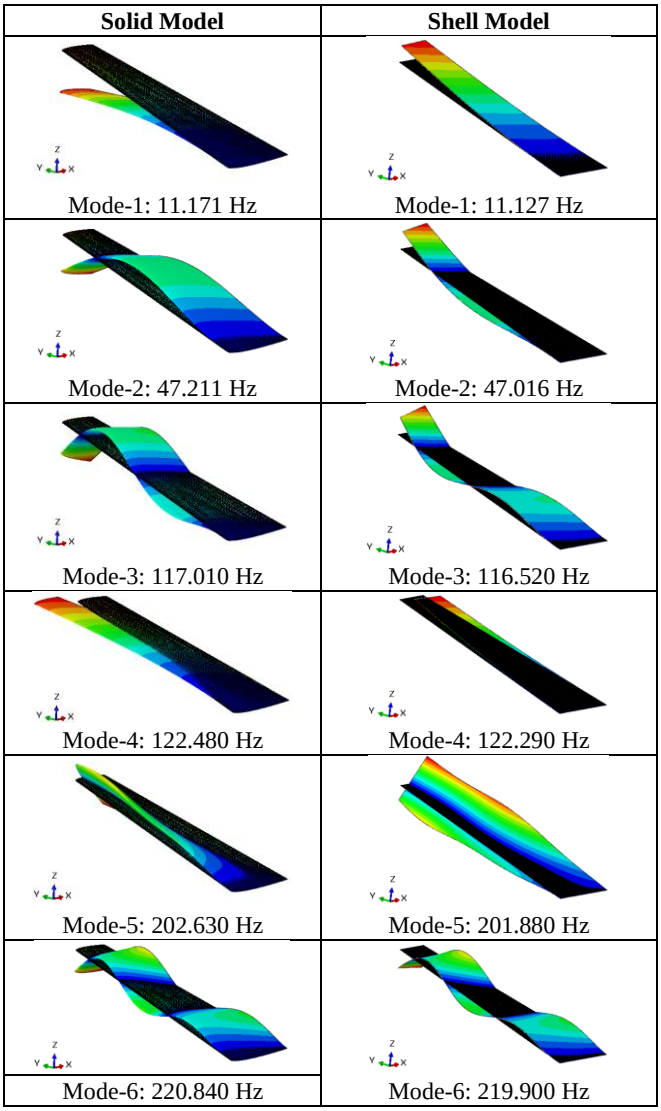

Figure 7: Case-1 comparison of the mode shapes.

B. Case-2

NACA 0008 airfoil without having any sweep and taper ratio is used for this case. The root chord length and the span length of the wing is taken as 200 mm and 1000 mm sequentially. The difference between the solid and the shell models is summarized in Table 5. A comparison of the mode shapes of the first 6 modes is shown in Figure 8.

Table 5: Case-2 comparison of the results.

Case	Solid	Shell	Difference %
Mass [kg]	6.160	6.130	0.480
Mode-1 [Hz]	10.980	10.935	0.410
Mode-2 [Hz]	68.437	68.156	0.411
Mode-3 [Hz]	129.460	129.020	0.340
Mode-4 [Hz]	130.770	130.520	0.191
Mode-5 [Hz]	190.180	189.390	0.415
Mode-6 [Hz]	368.360	366.800	0.423

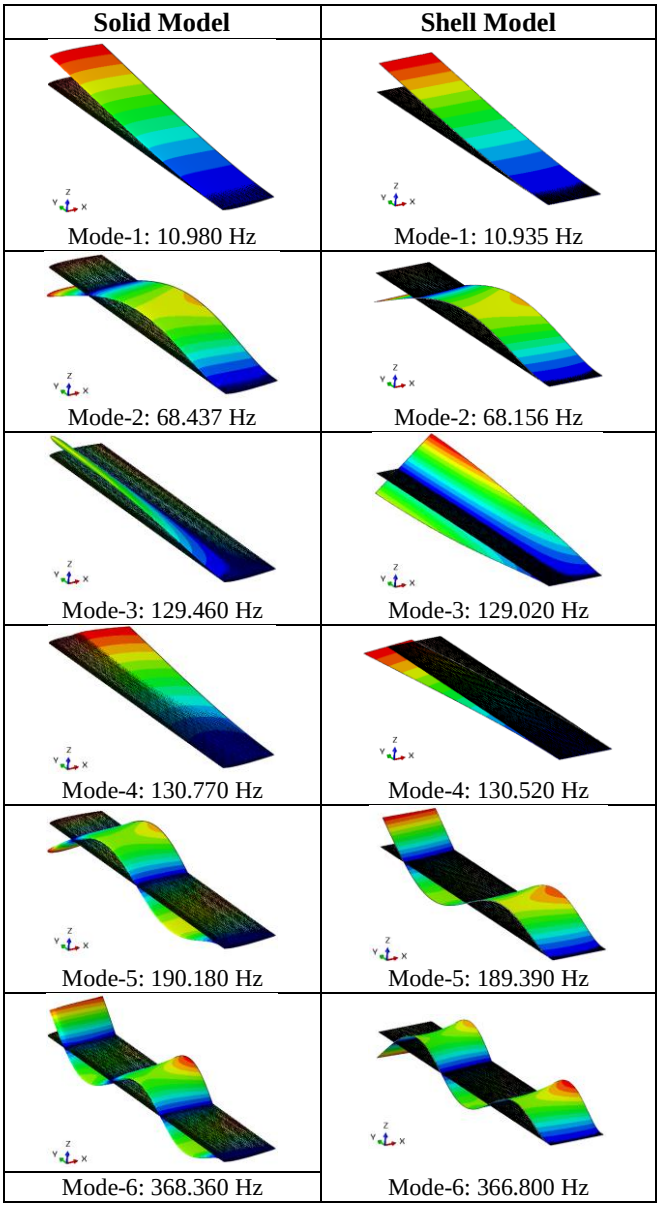

Figure 8: Case-2 comparison of the mode shapes.

C. Case-3

NACA 2408 airfoil having a 30° sweep angle and taper ratio of 0.5 is used for this case. The root chord length and the span length of the wing is taken as 200 mm and 1000 mm sequentially. The difference between the solid and the shell models is summarized in Table 6. A comparison of the mode shapes of the first 6 modes is shown in Figure 9.

Table 6: Case-3 comparison of the results.

Case	Solid	Shell	Difference %
Mass [kg]	3.596	3.575	0.581
Mode-1 [Hz]	11.508	11.443	0.565
Mode-2 [Hz]	48.611	48.330	0.578
Mode-3 [Hz]	120.130	119.490	0.533
Mode-4 [Hz]	122.700	122.440	0.212
Mode-5 [Hz]	202.660	201.880	0.385
Mode-6 [Hz]	226.820	225.530	0.569

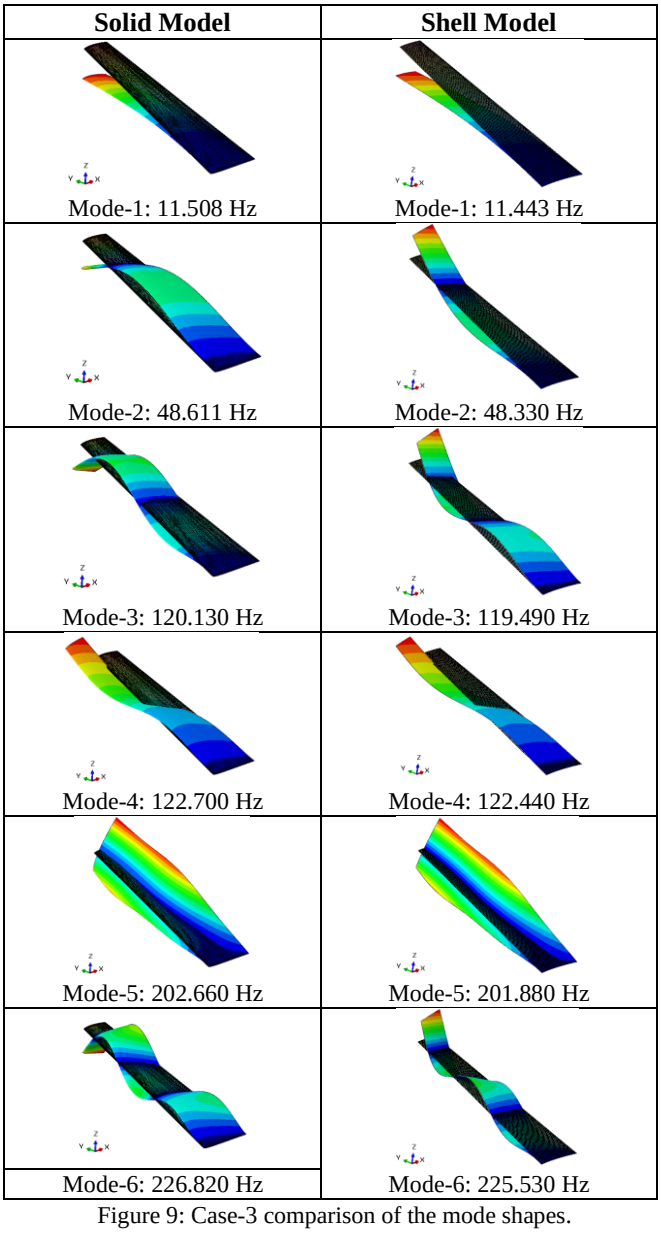

Figure 9: Case-3 comparison of the mode shapes.

D. Case-4

NACA 4412 airfoil having a 30° sweep angle and taper ratio of 0.5 is used for this case. The root chord length and the span length of the wing is taken as 200 mm and 1000 mm sequentially. The difference between the solid and the shell models is summarized in Table 7. A comparison of the mode shapes of the first 6 modes is shown in Figure 10.

Table 7: Case-4 comparison of the results.

Case	Solid	Shell	Difference %
Mass [kg]	5.410	5.399	0.213
Mode-1 [Hz]	17.619	17.491	0.726
Mode-2 [Hz]	74.357	73.812	0.733
Mode-3 [Hz]	122.620	122.620	0.000
Mode-4 [Hz]	183.960	182.630	0.723
Mode-5 [Hz]	299.020	297.590	0.478
Mode-6 [Hz]	345.680	343.220	0.712

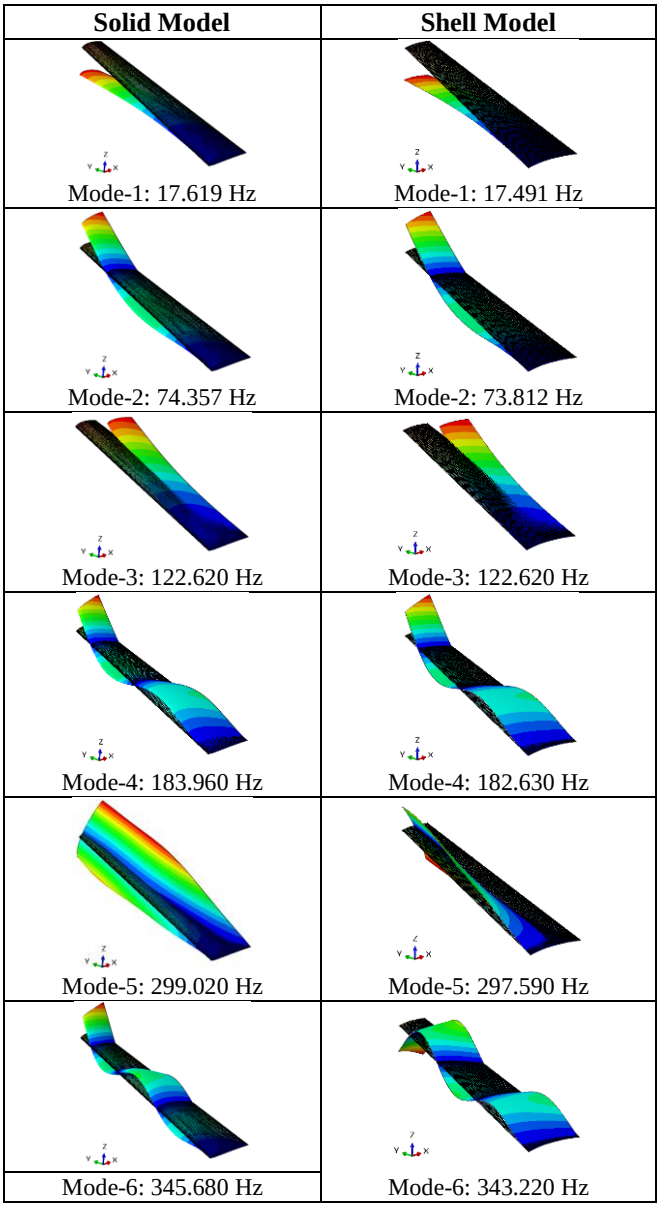

Figure 10: Case-4 comparison of the mode shapes.

E. Case-5

NACA 63415 airfoil having a 30° sweep angle and taper ratio of 0.5 is used for this case. The root chord length and the span length of the wing is taken as 200 mm and 1000 mm sequentially. The difference between the solid and the shell models is summarized in Table 8. A comparison of the mode shapes of the first 6 modes is shown in Figure 11.

Table 8: Case-5 comparison of the results.

Case	Solid	Shell	Difference %
Mass [kg]	6.152	6.141	0.184
Mode-1 [Hz]	20.796	20.698	0.471
Mode-2 [Hz]	87.821	87.394	0.486
Mode-3 [Hz]	112.370	112.650	0.249
Mode-4 [Hz]	217.440	216.370	0.492
Mode-5 [Hz]	394.780	390.850	0.995
Mode-6 [Hz]	410.840	408.480	0.574

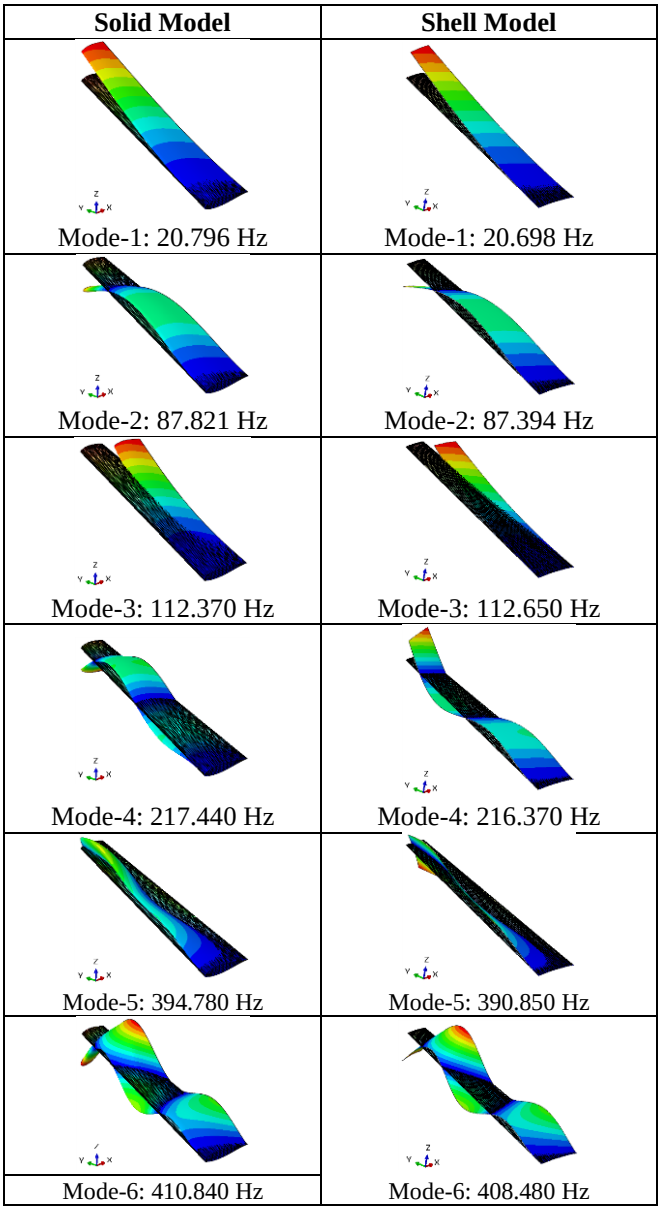

Figure 11: Case-5 comparison of the mode shapes.

F. Case-6

SC(2) 1010 supercritical airfoil having a 30° sweep angle and taper ratio of 0.5 is used for this case. The root chord length and the span length of the wing is taken as 200 mm and 1000 mm sequentially. The difference between the solid and the shell models is summarized in Table 9. A comparison of the mode shapes of the first 6 modes is shown in Figure 12.

Table 9: Case-6 comparison of the results.

Case	Solid	Shell	Difference %
Mass [kg]	4.385	4.387	0.049
Mode-1 [Hz]	14.268	14.258	0.070
Mode-2 [Hz]	60.302	60.254	0.080
Mode-3 [Hz]	117.900	118.020	0.102
Mode-4 [Hz]	149.460	149.330	0.087
Mode-5 [Hz]	262.980	262.000	0.373
Mode-6 [Hz]	282.420	282.100	0.113

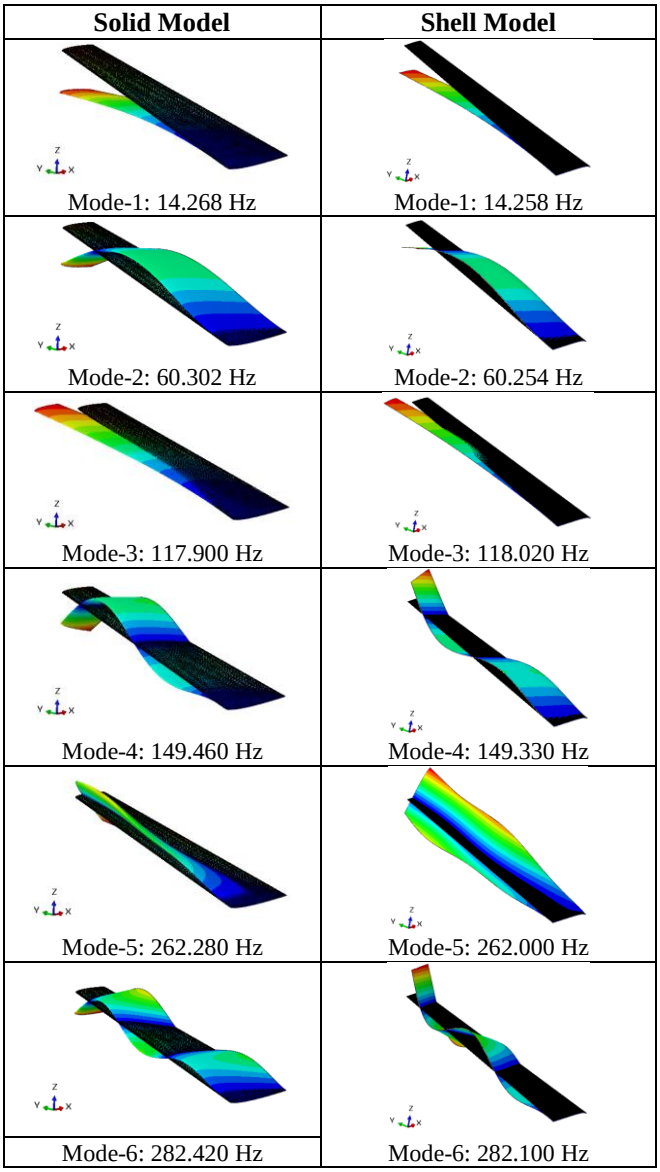

Figure 12: Case-6 comparison of the mode shapes.

According to the results, the difference between the solid and the shell models is less than 1% for all of the examined design cases. Therefore, conversion of solid airfoil models to shell models having a variable thickness not only lessens the duration of the solution but also provides results with satisfactory accuracy regardless of the airfoil type, the sweep angle, and the taper ratio.

To further increase the accuracy of the shell model, the number of the spanwise stations and the chordwise stations where the local thickness calculations are performed should be increased. Additionally, the number of nodes through the spanwise and the chordwise directions in the shell wing model should be increased.

V. CONCLUSION

The applicability of reduced-order modeling on a rapid investigation of airfoil vibration characteristics is examined by comparing the modal analysis results of solid and shell finite element models for different airfoils, sweep angles, and taper ratios. A home-written Matlab code is prepared and used to calculate the variable shell thickness for the reduced-order model preparation. If the number of spanwise stations where the thickness values are calculated is high enough, and if the size of the elements of the shell model is small enough, the difference between the natural frequency results of the solid and the shell models are quite low. Analysis results also showed that mode shapes of the solid and the shell models are compatible with each other. Thus, the offered reduced-order modeling approach can be applied to lessen the solution time of modal analysis with a little compromise in the accuracy of the results. Application of this modeling technique is not only critical for speeding up the optimization processes related to natural frequency maximization, but also significant for performing flutter analysis of the wings since modal analysis results are used as an input for the flutter solution process.

REFERENCES

[1] L. Carassale, M. Maurici, and L. Traversone "Reduced-order modeling of compressor blades by 1D finite elements," in *ASME Turbo Expo 2015: Turbine Technical Conference and Exposition*, pp. 1–7.

[2] R. Dantulwar, and M. Accorsi "Reduced order modeling of parachute systems using large scale finite element models," in *21st AIAA Aerodynamic Decelerator Systems Technology Conference*, pp. 1–18.

[3] R. Wilber, "Application of Parametric Reduced Order Models for Bladed Disks," thesis, 2017.

[4] J. Sun, I. L. Arteaga, and L. Kari, "General shell model for a rotating pretwisted blade," *Journal of Sound and Vibration*, vol. 332, pp. 5804–5820, October 2013.

[5] J. Yuan, G. Allegri, F. Scarpa, R. Rajasekaran, and S. Patsias, "Novel parametric reduced order model for aeroengine blade dynamics," *Mechanical Systems and Signal Processing*, vol. 62-63, pp. 235–253, October 2015.

[6] "Airfoil tools," Airfoil Tools. [Online]. Available: http://airfoiltools.com/. [Accessed: 10-Sep-2021].

[7] "Aluminum 7075-T6; 7075-T651," MatWeb. [Online]. Available: http://www.matweb.com/search/DataSheet.aspx?MatGUID=4f19a42be94546b686bbf43f79c51b7d&ckck=1. [Accessed: 10-Sep-2021].

Optimization of Machinability Parameters of S960QL Structural Steel by Finite Elements and Taguchi Method

R. BİNALİ[1], S. YALDIZ[1] and S. NEŞELİ[1]

[1] Selcuk University, Konya/Turkey, rustem..binali@selcuk.edu.tr, syaldiz@selcuk.edu.tr, sneseli@selcuk.edu.tr

Abstract **- In this study, three different feed rates, three different lateral depths and three different axial depths of S960QL structural steel material used as armor and structural steel, regardless of the cutting speed, were optimized for the most effective parameter on shear force, moment and temperature by Taguchi and finite element method. analyzed. In the finite element method, TiAlNi coated cutting tool is used for chip removal with the corner milling command. ANOVA and statistical analyzes based on the "lowest and best" objective function were performed with the Minitab 18 program. It was determined that the optimum cutting parameters obtained as a result of the study were 0.8 mm lateral depth, 4 mm axial depth and 0.08 mm/tooth feed rate. In addition, the lowest feed force value was obtained at $A_1B_1D_2$ and the highest feed force value was obtained at $A_3B_3D_1$ levels. In terms of moment and temperature values, the lowest value was determined at $A_1B_1D_1$ and the highest value at $A_3B_3D_3$ levels. Finally, according to the results of ANOVA analysis, the axial depth parameter was effective on the process feed force, and the axial depth parameter was effective on the moment and temperature.**

Keywords - S960QL, Milling, TAGUCHI Method, Feed Force, Torque, Temperature**.**

I. INTRODUCTION

THE process of bringing from the raw material to the final product is one of the oldest methods since the time of humanity. These processes have been carried out in different ways by people in every age. With the development of technology, the raw material has become the final product and the shaping of the products has begun to be carried out easier and more smoothly. The industrial revolution also contributed to the production stages. Various production stages can be sorted according to the processes performed. These are casting, forging, forming, welding and machining [1].

Machining is widely used in bringing the raw material to the final product. With the machining method, the desired final shape is given to the material or the undesirable parts of the material are removed. In this method, the cutting tool must be harder than the workpiece material for shaping operations to be accepted. The method includes milling, turning, drilling, etc. transactions [2].

Milling is the most widely used machining method and the most different cutting mechanics [3]. This is because the cutting process removes chips from tools with multiple cutting edges and from each axis of the coordinate plane. This method is used almost throughout the industry. With the milling process, inclined, planar, uncomplicated and circular parts can be processed. The final product desired to be obtained by using a cutting tool with more than one cutting edge can be produced within narrower tolerances [4,5].

In addition to the machine, cutting tool material and machining method, cutting parameters are also important in machining. These cutting parameters are cutting speed, feed rate and depth of cut. These cutting parameters also affect the cutting force, moment and temperature that occur during the process. For this reason, the selection of cutting parameters before machining is important [6,7]. Today, the finite element method has been widely used for the optimization of cutting parameters. Optimization processes with the finite element method provide information about the cutting force, moment and temperature that occur during the machining process [8]. Thus, physical experiments are avoided and cost and time savings are made. In addition, statistical (Taguchi, etc.) studies are carried out in order to obtain suitable cutting parameters and to determine the interactions between post-process output parameters [9].

In this study, the machinability of S960QL structural steel material by milling method was carried out using the finite element method. The values of feed rate per tooth, lateral depth and axial depth were evaluated as machinability parameters. As a result of the finite element analysis, the optimization processes of the parameters evaluated by the Taguchi method were examined. As a result of the optimization studies carried out, the optimum feed rate and cutting depths were determined depending on the lowest cutting force, temperature and moment value. In addition, signal-to-noise ratio (S/N) and analysis of variance (ANOVA) were examined at 95% confidence level, and the interactions of control factors with each other were evaluated.

II. MATERIAL METHOD

In experimental studies, milling was carried out using the finite element method. The Johnson-Cook model parameters of the material used for finite element analysis are given in Table 1. Johnson-Cook material model is given in equation 1 [8]. The materials and parameters used in the study are given in Table 2.

$$\sigma^0 = (A + B(\varepsilon^p)^n(1 + C ln\left(\frac{\dot{\varepsilon}^p}{\dot{\varepsilon}_n}\right))(1 - (\hat{T})^m) \quad (1)$$

Table 1. JC model parameters of S960QL material [10].

A (MPa)	B (MPa)	n	c	m (400 °C)	m (550 °C)	m (avg.)
1034	828	0,6539	0,015045	1,028	1,277	1,154

Table 2. Cutting parameters.

Material	Radial Deep of cut (mm)	Axial deep of cut (mm)	Feed rate (mm/tooth)
S960QL	0,8-1,2-1,6	4-6-8	0,08-0,12-0,16

The S960QL material used in the study is used in structural steel and military land vehicle systems. The chemical composition of the material is given in Table 3.

Table 3. Chemical composition of the material S960QL [11].

C	Si	Mn	P	S	Cr	Cu	Ni	Mo	B
0,2	0,5	1,6	0,02	0,01	0,8	0,3	2,0	0,7	0,005

III. TAGUCHI METHOD

The reason why machinability studies are difficult is the determination of combinations of cutting parameters. Depending on the parameters, the resulting process parameters can be time consuming and complex. This increases processing costs. For this reason, the TAGUCHI method allows to reduce the number of experiments in terms of cost reduction and is a widely used method [12,13]. In this method, the quality criterion is obtained by the actual value S (Signal) given by the system and desired to be measured, and the uncontrollable undesirable factors N (Noise) within the measured value. This is called the S/N ratio [14]. In the study, evaluations were made according to the smallest best S/N ratio given in Equation 2.

The smaller-the better: $S/N=-\log (1/n\sum_{i=1}^{n} y_i^2)$ (2)

In Equation 1, n represents the number of observations and y represents the observed data [15].

IV. EXPERIMENTAL RESULTS AND DISCUSSION

The experimental design used to determine the optimum values of the cutting parameters is given in Table 5. In order to determine the combinations of cutting parameters, a Taguchi orthogonal experimental design was carried out in order to distribute the effect levels of each parameter. However, not all array cells were used for the four factors in this study, only three factors were considered (lateral depth, axial depth, and rate of feed per tooth). Therefore, the third column (cutting speed factor) in the L9 orthogonal array is left blank in this study. Similar work was done by Vidal et al. [16]. In order to find the optimum points of the cutting parameters used in the study, the S/N ratios were determined by taking into account the smaller-the-better quality characteristic objective function (Table 6 and Table 7) [17].

Table 5. Experimental design.

Radial Deep of Cut (mm) (A)	**Axial Deep of Cut (mm) (B)**	**Cutting speed (m/min) (C)**	**Feed Rate (mm/tooth) (D)**
1	1	1	1
1	2	2	2
1	3	3	3
2	1	2	3
2	2	3	1
2	3	1	2
3	1	3	2
3	2	1	3
3	3	2	1

Table 6. Average S/N response for the feed force.

Level	Radial Deep of Cut (mm)	Axial Deep of Cut (mm)	Feed Rate (mm/tooth)
1	**-53,93**	**-50,94**	-56,39
2	-56,64	-56,15	**-55,88**
3	-57,96	-61,44	-56,26
Delta	4,03	10,50	0,51
Rank	2	1	3

Table 7. Average S/N response for torque and temperature.

Level	Radial Deep of Cut (mm)	Axial Deep of Cut (mm)	Feed Rate (mm/tooth)
1	**-8,822**	**-5,850**	**-9,448**
2	-11,168	-10,888	-10,958
3	-12,529	-15,781	-12,113
Delta	3,708	9,931	2,664
Rank	2	1	3

According to the average S/N values found in Tables 6 and 7, the highest value of Delta levels specified for each level has the greatest effect on feed force, moment and temperature. In the tables, the order of effects is given by rank. In this study, for the optimum feed force value, it was determined that the lateral depth of cut was 1, the axial depth of cut was 1 and the feed rate per tooth was 2. Likewise, for the optimum level of moment and temperature values, it was concluded that

the combination of cutting parameters was at 1 level in depth of cut, 1 in axial depth and 1 in feed per tooth.

The graphs of the S/N ratio responses for the feed force, moment and temperatures are given in Figures 1 and 2. The maximum points of the slopes in the graphs in the figure give information about the efficiency levels of the cutting parameters.

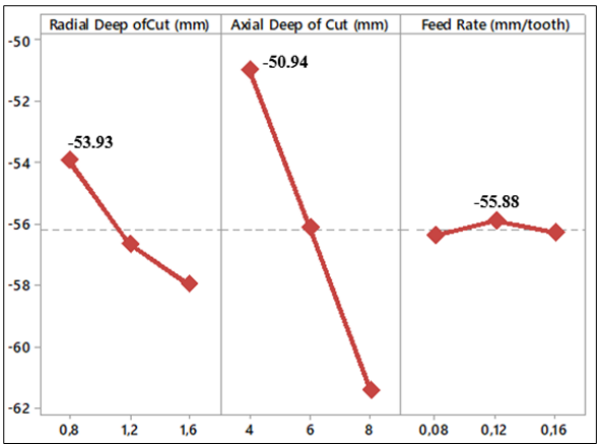

Figure 1. S/N chart for feed force.

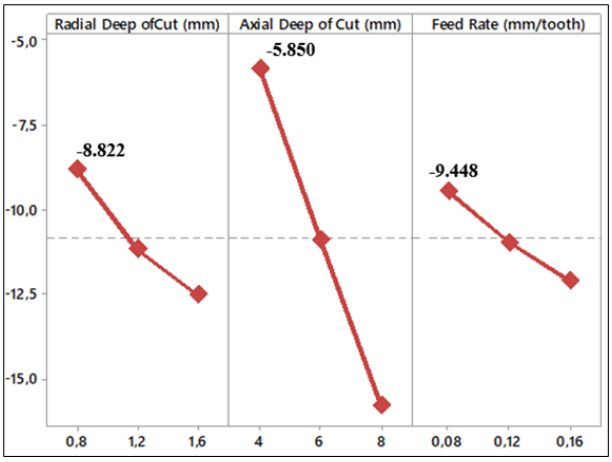

Figure 2. S/N chart for torque and temperature.

ANOVA (analysis of variance) method was used to determine and express the interaction of control factors with cut-off parameters numerically [15]. The results of analysis of variance for the feed force, moment and temperature values are given in Table 8 and Table 9.

Table 8. ANOVA for the feed force.

	DF	SS	MS	F	p	PCR (%)
Radial Deep of Cut (mm)	2	175934	87967	4,34	0,187	12,68
Axial Deep of Cut (mm)	2	1114402	557201	27,48	0,035	80,30
Feed Rate (mm/tooth)	2	56920	28460	1,40	0,416	4,10
Error	2	40553	20276			2,92
Total	8	1387809				100
R^2=%97.08						

Table 9. ANOVA for torque and temperature.

	DF	SS	MS	F	p	PCR (%)
Radial Deep of Cut (mm)	2	2,2256	1,1128	79,30	0,012	7,74
Axial Deep oof Cut (mm)	2	25,8044	12,9022	919,38	0,001	89,75
Feed Rate (mm/tooth)	2	0,6923	0,3461	24,67	0,039	2,41
Error	2	0,0281	0,0140			0,10
Total	8	28,7504				100
R^2=%99.90						

In Table 8 and Table 9, p values expressing the significance level on the results of each cut-off parameter, degrees of freedom (DF), sum of squares (SD), mean squares (MS), F values and percent effect ratios (PCR) are given. In the analysis of variance, the p value is checked to decide whether each cut-off parameter has an effect on each other. The responses of the cut-off parameters on the results are evaluated according to $p<0.05$, taking into account the 95% confidence interval. The effect of control factors can be determined by comparing the F values. The factor affecting the analysis result the most is the highest F value [18] In this context, by examining the data in Table 8, it was determined that the most effective parameter for the feed force was the axial cutting depth with a rate of 80.30%. It was concluded that the least effective parameter was the rate of feed per tooth with a rate of 4.10%. According to the data in Table 9, it was concluded that the most effective parameter on the moment and temperature was the axial cutting depth with a rate of 89.75%, and the least effective parameter was the feed per tooth with a rate of 2.41%. According to the analysis of variance, the error rate was determined as 2.92% in the feed force and 0.10% in the moment and temperature values. According to the data in Table 8 and Table 9, it was concluded that the most effective parameter in the process outputs is the axial depth of cut.

V. CONCLUSION

In this study, milling operations were carried out with the finite element method. In the study, corner milling process of

S960QL material was applied and optimum cutting parameters were determined by Taguchi method. Study results are summarized below.

1. The optimum cutting parameters for the feed force were obtained at $A_1B_1D_2$ and the highest feed force value at $A_3B_3D_1$ levels according to the experimental design.
2. The optimum cutting parameters for the torque and temperature values were determined at $A_1B_1D_1$, and the highest value at $A_3B_3D_3$ levels.
3. According to the results of the analysis of variance, it was determined that the most effective parameter for the feed force value was the axial cutting depth with a rate of 80.30%.
4. According to the results of the analysis of variance for the torque and temperature values, the most effective parameter was 89.75% of the axial depth of cut.
5. It was concluded that the finite element method is suitable for machinability tests in machining operations and Taguchi method is suitable for feed force, moment and temperature.

ACKNOWLEDGMENT

This study was supported by Selcuk University Scientific Research Projects Unit as a PhD thesis project. Project Number: 20111014.

REFERENCES

[1] D. L. Goetsch, *Modern Manufacturing Process.* Cengage Learning, 1991.

[2] R. Binali, H. Demir, S. Neşeli, and S. Yaldız, "*An Investigation of Factors Afeecting Machinability of Milling Toolox 44", International Conference on Engineering Technologies (ICENTE'20),* November 2020.

[3] T. S. Lee, and Y. J. Lin, "*3D Predictive Cutting-Force Model for End Milling of Parts Having Sculptured Surfaces",* Int. J. Adv. Manuf. Technol., (16), pp. 773-783, 2000.

[4] A. Gezgim, "*Prizmatik parçaların frezelenmesi esnasında kesici uç sayısının takım ömrü ve yüzey pürüzlülüğü açısından değerlendirilmesi", Yüksek Lisans Tezi,*Gazi Üniversitesi Fen Bilimleri Enstitüsü, 2007.

[5] M. Coşkun, İ. Çiftçi ve H. Demir, "*AISI P20S Kalıp Çeliğinin İşlenebilirliğinin İncelenmesi*", İmalat Teknolojileri ve Uygulamaları, pp. 1-9, 2021.

[6] M. C. Çakır, *Modern Talaşlı İmalatın Esasları*, Ankara: Nobel Yayın Dağıtımı, 2006.

[7] A. Duran ve A. Acır, HSS torna kalemindeki talaş açısının kesme kuvvetlerine etkisi, *Politeknik Dergisi*, 7(3), pp. 211-215, 2004.

[8] M. E. Korkmaz, T. Meral ve M. Günay, "*AISI 420 Martenzitik Paslanmaz Çeliğin Delinebilirliğinin Sonlu Elemanlar Yöntemiyle Analizi*", Gazi Mühendislik Bilimleri Dergisi, vol. 4, no. 3, pp. 223-229, 2018.

[9] İ. B. Toprak, F. M. Çağlar, O. Çolak, K. Kıran ve M. Bayhan, "*Ti-6Al-4V Süper Alaşiminin Yüksek Basinçli Soğutma Kullanilarak Frezelenmesinde Yüzey Pürüzlülüğünün Taguchi Yöntemi ile Optimizasyonu",* SDU International Technologic Science, vol. 4, no. 2, pp. 30-39, 2012.

[10] E. Cadoni, and D. Forni, "*Mechanical behaviour of a very-high strength steel (S960QL) under extreme conditions of high strain rates and elevated temperatures*", Fire Safety Journal, pp. 1-14, 2019.

[11] [Online] Available: https://www.ssab.com.tr/products/brands/strenx/products/strenx-960-e-f.

[12] T. Kıvak, "*Optimization of surface roughness and flank wear using the Taguchi method in milling of Hadfield steel with PVD and CVD coated inserts",* Measurement, 50, 19-28, 2014.

[13] K. Palanikumar, Experimental investigation and optimisation in drilling of GFRP composites, *Measurement*, 44(10), pp. 2138-2148, 2011.

[14] N. Masmiati andA. A. D. Sarhan, Optimizing cutting parameters in inclined end milling for minimum surface residual stress–Taguchi approach, *Measurement*, vol. 60, pp. 267-275, 2015.

[15] N. Mandal, B. Doloi, B. Mondal and R. Das, Optimization of flank wear using Zirconia Toughened Alumina (ZTA) cutting tool: Taguchi method and Regression analysis, *Measurement,* 44(10), pp. 2149-2155, 2011.

[16] C. Vidal, V. Infante and P. Vilaca, "Assessment of Improvement Techniques Effect on Fatigue Behaviour of Friction Stir Welded Aerospace Aluminium Alloys", *Procedia Engineering*, vol. 2, pp. 1605-1616, 2010.

[17] S. Neşeli, Tırlama titreşimleri üzerine süreç sönümleme etkisinin analitik olarak araştırılması ve tornalamada kararlı kesme derinliği ile süreç sönümleme değerlerine bağlı parametre optimizasyonu, Doktora Tezi, *Selçuk Üniversitesi Fen Bilimleri Enstitüsü*, 2013.

[18] E. Şirin, Ş. Şirin, Y. Turgut ve İ. Korkut, AISI D2 soğuk iş takım çeliğinin frezelenmesinde yüzey pürüzlülüğünün taguchi metodu ile optimizasyonu, *Düzce Üniversitesi Bilim ve Teknoloji Dergisi*, (3), pp. 132-144, 2015.

Effect of Line Search Conditions on Conjugate Gradient Method Performance in Nonlinear Least Squares Fitting of 2D Geometries

K. KIRAN[1]

[1] Suleyman Demirel University, Isparta/Turkey, kadirkiran@sdu.edu.tr

***Abstract* - This paper investigates influence of line search conditions including Backtracking (BC), Armijo-Backtracking (ABC) and Goldstein (GC) on the performance of the well-known conjugate gradient (CG) method (i.e., Fletcher-Reeves) while nonlinear least squares fitting of 2D primitive geometries (i.e., circle, ellipse, square, rectangle and triangle) profiles obtained from coordinate measuring machine (CMM). First, the five primitive geometries are built using 3D printer. Second, those geometries are scanned with CMM to acquire their 2D profiles. At the third stage of the work, the nonlinear least squares process is conducted by employing the above-mentioned CG-line search condition combinations to be able to reach best parameters that represent the measured data. During this fitting process, the maximum number of function evaluations for each combination are recorded when the combination in question satisfies the defined converge tolerance. Those data are later used to generate performance and data profiles which enable to assess the combination performance. By means of these profiles, it has been determined that the GC provides best performance for CG method. For the second best, the ABC stands out. All those results have shown that the line search conditions have a great importance on the performance of the CG method. Therefore, its selection requires a special attention for optimal performance.**

***Keywords* - Conjugate gradient method; nonlinear least squares fitting; performance profiles; data profiles; optimization**

I. INTRODUCTION

The conjugate gradient methods draw considerable interest in solving linear equations and nonlinear optimization problems. Within these scopes, they have been frequently utilized in many fields due to their simplicity and low computation requirements. For instance, Hu et al. [1] presented several modified Hestenes-Stiefel CG algorithms that are beneficial to large-scale nonlinear equations, nonsmooth optimization and image restoration. An application of the CG method on the inverse heat transfer problem was conducted by Helmig et al. [2]. In this study, they focused on investigating effect of the number of temperature measurements on the estimation of boundary conditions. Another inverse heat transfer problem was studies in [3] using a sequential CG method. The authors stated that the proposed method outperforms the traditional sequential function specification and CG methods with a high accuracy and a lower computation time. In other respects, the implementation of the CG methods on finite element analysis was revealed by Schwarz [4]. In [5], it was developed a neurocomputing model using CG method based backpropagation in artificial neural network. By means of this model, the authors predict average rainfall, and the CG method becomes beneficial. For an optimal rocket landing guidance, Li et al. [6] presented a CG method along with pseudospectral collocation scheme. It was mentioned that the converge speed of the presented algorithm is notably high. On the other hand, some improved CG methods for general applications have been also brought in the literature. Andrei [7], for instance, proposed a three-term CG method by modifying the Hestenes-Stiefel algorithm. The proposed method performance was tested on 750 unconstrained optimization problems and it was seen that it is slightly faster than the others. In addition to this study, Du et al. [8] was revealed four modified CG methods and they stated that the proposed algorithms are pretty efficient compared to existing ones. As summarized above, the CG methods are useful tools for optimization purposes and highly applicable in many areas. Considering these, in this study, the well-known Fletcher-Reeves CG method is implemented along with three line search conditions in nonlinear least squares geometry fitting. In other words, a performance evaluation of the Fletcher-Reeves CG method is completed by taking into account the line search conditions accommodating the BC, the ABC and the GC. To do that, a geometry fitting procedure of five primitive 2D geometries is carried out with three CG-line search condition combinations. For performance criterion, the total number of function evaluations when the combination in question converges the required term are used. With these data, the performance and data profiles are generated for the performance assessments of the combinations. The reminder of this paper is structured as follows: Section II explains the geometry fitting procedure as well as covers the 2D test geometries. In section III, the results and discussion on the fitting and performance evaluation are provided. Finally, section IV concludes the paper.

II. FITTING OF 2D GEOMETRIES

To investigate the effect of line search condition on Fletcher-Reeves CG method performance in nonlinear least squares geometry fitting, the five 2D geometries containing circle, square, triangle, ellipse and rectangle are chosen. Their parametric mathematical models [9] along with parameter vector are given in Table 1. First, all those geometries are built using 3D printer with PLA material. Secondly, they are scanned with the CMM in order to obtain their 2D profiles. It is then described a parameter dependent error function [10] as follows:

Table 1: 2D test geometries and their parametric mathematical models

Geometry number	Mathematical model	Parameter vector	Geometry
1	$x = r_c \cos(u) + x_c$ $y = r_c \sin(u) + y_c$	$p = [r_c\ x_c\ y_c\ u]$	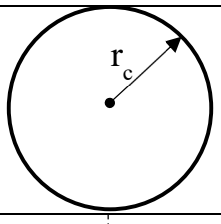
2	$x_u = \frac{w}{2}(\lvert\cos(u)\rvert\cos(u) + \lvert\sin(u)\rvert\sin(u))$ $y_u = \frac{h}{2}(\lvert\cos(u)\rvert\cos(u) - \lvert\sin(u)\rvert\sin(u))$ $x = x_u\cos(\theta) - y_u\sin(\theta) + x_c$ $y = x_u\sin(\theta) + y_u\cos(\theta) + y_c$	$p = [w\ h\ x_c\ y_c\ \theta\ u]$	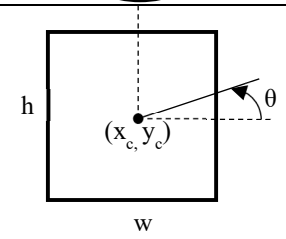
3	$r = \frac{h}{\cos\left(\frac{2}{n_s} arcsin\left(sin\left(\frac{n_s}{2}u\right)\right)\right)}$ $x_u = r\cos(u)$ $y_u = r\sin(u)$ $x = x_u\cos(\theta) - y_u\sin(\theta) + x_c$ $y = x_u\sin(\theta) + y_u\cos(\theta) + y_c$	$p = [h\ x_c\ y_c\ \theta\ u]$	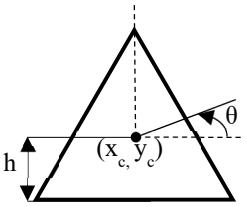
4	$x_u = a\cos(u)$ $y_u = b\sin(u)$ $x = x_u\cos(\theta) - y_u\sin(\theta) + x_c$ $y = x_u\sin(\theta) + y_u\cos(\theta) + y_c$	$p = [a\ b\ x_c\ y_c\ \theta\ u]$	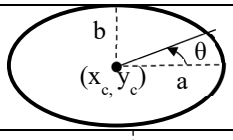
5	$x_u = \frac{w}{2}(\lvert\cos(u)\rvert\cos(u) + \lvert\sin(u)\rvert\sin(u))$ $y_u = \frac{h}{2}(\lvert\cos(u)\rvert\cos(u) - \lvert\sin(u)\rvert\sin(u))$ $x = x_u\cos(\theta) - y_u\sin(\theta) + x_c$ $y = x_u\sin(\theta) + y_u\cos(\theta) + y_c$	$p = [w\ h\ x_c\ y_c\ \theta\ u]$	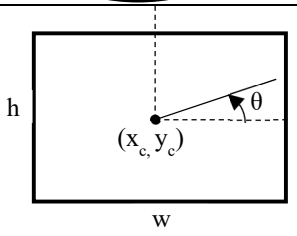

$$\epsilon^2(p) = \sum_{j=1}^{n}\left[x_j^{measured} - x_j^{modeled}(p)\right]^2 + \sum_{j=1}^{n}\left[y_j^{measured} - y_j^{modeled}(p)\right]^2 \quad (1)$$

This equation computes the sum of the squared error between the measured and modeled coordinates. Our task is to find the best parameter vector p, which minimizes this error function, for each geometry. To do that, a line search is conducted as follows:

$$p_{q+1} = p_q + \Omega_q d_q \quad (2)$$

where p_{q+1} is the next parameter vector, p_q is the current parameter vector, Ω_q is the step length and d_q is the search direction which is described to be:

$$d_{q+1} = -G(p_{q+1}) + \beta_{q+1} d_q \quad (3)$$

where $G = -J^T D$ is the objective function gradient, J is the Jacobian matrix of the objective function that is numerically calculated using finite difference method, $D = \begin{bmatrix} D_x \\ D_y \end{bmatrix}$ is the difference matrix, $D_x = x_j^{measured} - x_j^{modeled}(p)$ and $D_y = y_j^{measured} - y_j^{modeled}(p)$. β_{q+1} is the coefficient of the CG method. As mentioned before, in this study, the Fletcher-Reeves CG method is employed. Therefore, this coefficient [11] is:

$$\beta_{q+1} = \frac{G(p_{q+1})^T G(p_{q+1})}{G(p_q)^T G(p_q)} \quad (4)$$

It is noteworthy that the initial search direction is used to be $d_0 = -G(p_0)$ (i.e., opposite of the objective function gradient).

For the step length Ω_q computation, the three well-known line search conditions such as Backtracking (BC), Armijo-

Backtracking (ABC) and Goldstein (GC) are employed and they are mathematically described as follows [12]:

BC:

$$\epsilon(p_q + \Omega_q d_q) \leq \epsilon(p_q) \tag{5}$$

ABC:

$$\epsilon(p_q + \Omega_q d_q) \leq \epsilon(p_q) + \zeta \Omega_q G^T d_q \tag{6}$$

GC:

$$\epsilon(p_q) + (1-\nu)\Omega_q G^T d_q \leq \epsilon(p_q + \Omega_q d_q) \leq \epsilon(p_q) + \nu \Omega_q G^T d_q \tag{7}$$

In these equations, ζ and ν are the scalars and their values are 0.25 and 0.35, respectively. The iterative line search procedure with computed step lengths proceeds until the converge condition, $max|J^T D| \leq 10^{-3}$, is satisfied.

III. RESULTS AND DISCUSSION

The above-mentioned fitting procedure are completed for all the geometries using the three line search conditions. For an example, the completed circle fitting with CG-GC combination is illustrated in Figure 1. As seen from this figure, the circle fitting successfully represents the measured data. Note that there is slight difference between the actual and fitted circles. This is due to the manufacturing tolerance of the 3D printer used to build the geometries. From this perspective, it should be mentioned that the fitting procedure covered in this study can be used to identify the manufacturing tolerances of the 3D printers or other manufacturing machines.

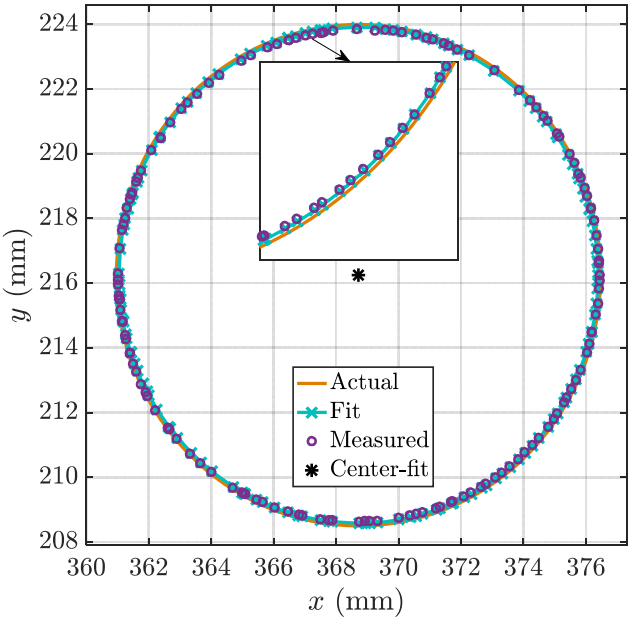

Figure 1: Circle fitting

While conducting fitting procedure, all the geometry parameters, step length, sum of the squared error, norm of the objective function gradient are monitored at each iteration, as shown in Figure 2. For a performance criteria of the line search conditions, the number of functions evaluations at each iteration are computed as well (see Figure 3). The total number of function evaluations when the fitting is completed are used for the performance assessment of the line search conditions.

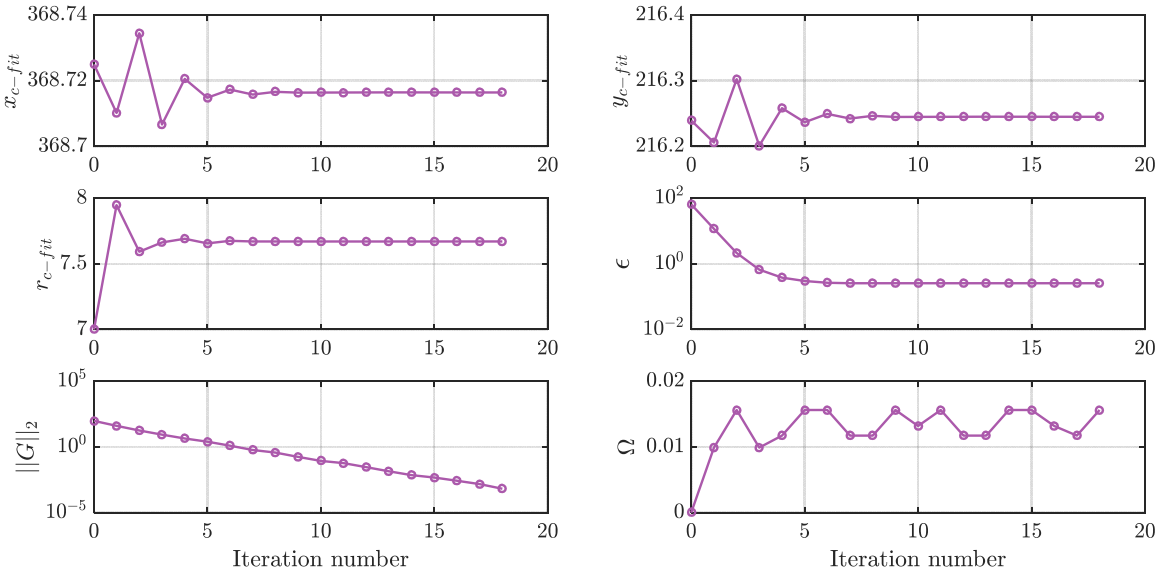

Figure 2: Line search outputs for each iteration

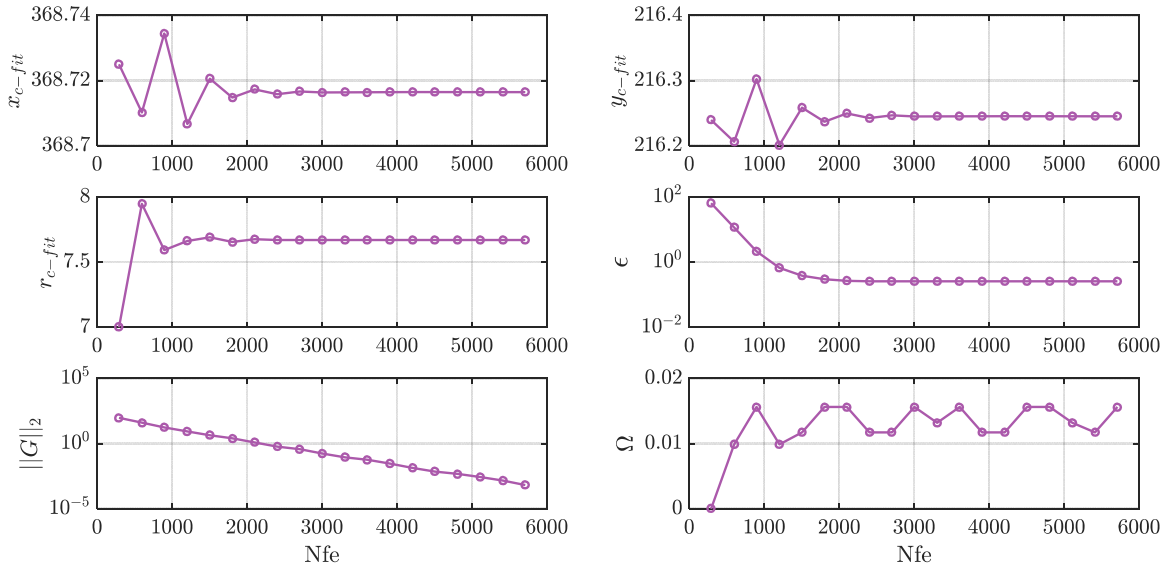

Figure 3: Line search outputs versus number of function evaluations corresponding each iteration

From Figures 2 and 3, one can notice that the sum of the squared errors and norm of the objective function gradient decrease as expected. This shows that the proposed algorithm works very well. The geometry parameters are quickly converged after a little bit fluctuation. Notice also that the step length Ω varies at eat iteration due to the line search condition that aims a significant progress toward the best parameters. This variation brings a computational burden. In other words, the step length computation may be conducted with different number of function evaluations depending on the line search condition being used. To analysis this fact, we generate the performance profiles [13] using the total number of function evaluations, as shown in Figure 4. Before elaborating this figure, it must be stated what the performance profiles provide. Generally speaking, the performance profiles fundamentally show us the success probability of the algorithm within the given factor. By adapting this approach to the current study, we aim to obtain the success probability of the line search conditions in geometry fitting process. From this point of view, Figure 4 indicates the success probabilities of the line search conditions (i.e., $P(\upsilon)$) within a factor range of $10^0 \leq \upsilon \leq 10^3$. By looking at $P(\upsilon = 10^0)$ values, we are able to determine the fastest line search condition, which is the GC with the probability at $P(\upsilon = 10^0) = 80\%$. More specifically, it completes the fitting on the 4 geometries out of 5 with the lowest number of function evaluations. For BC and ABC, to reach same probability, the factor υ have to be increased to 10.66 and 2.55, respectively. Since the performance profiles depend on each other, it is required to exclude first fastest one and regenerate the performance profiles with rest of them to identity the second fastest line search condition. This is done in Figure 5. Analogues to Figure 4, by looking at the $P(\upsilon = 10^0)$ values, the ABC stands out to be the second fastest line search condition with the probability $P(\upsilon = 10^0) = 60\%$. It means that the ABC beats the BC on fitting of 3 geometries. Obviously, the BC takes last place. This is attributed that it cannot provide sufficient decrease in the error function due to the lack of gradient term in the condition (see Equation 5).

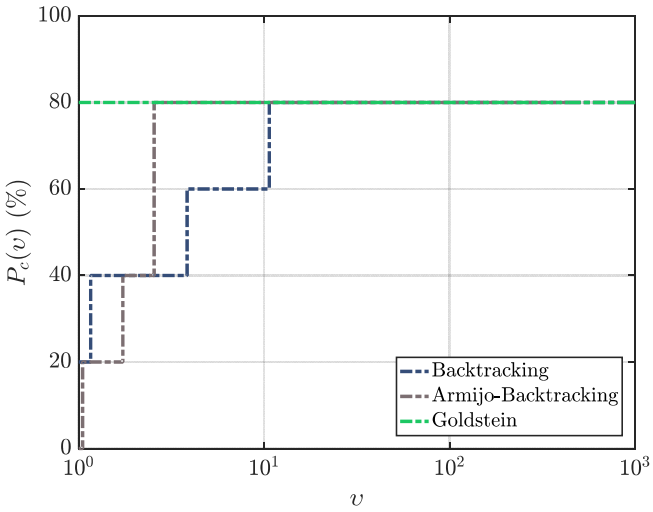

Figure 4: Performance profiles of line search conditions-1

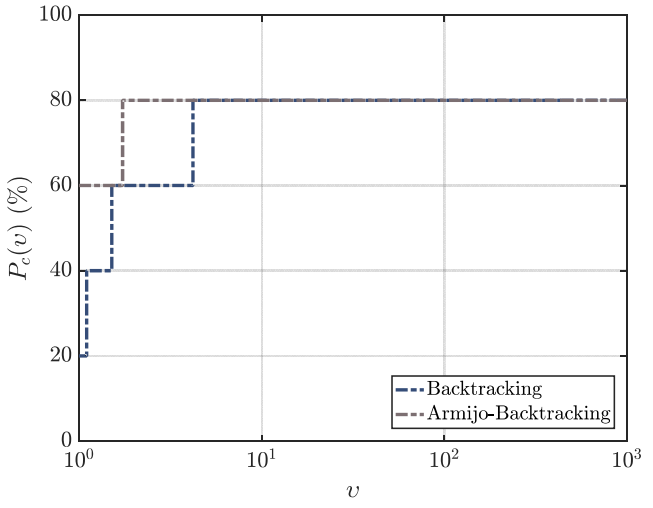

Figure 5: Performance profiles of line search conditions-2

In addition to the performance profiles, the data profiles [14] are generated as well, to evaluate the line search conditions in terms of computational budgets. Figure 6 shows the data profiles of line search conditions within the range of $10^3 \leq \psi \leq 10^7$ number of function evaluations.

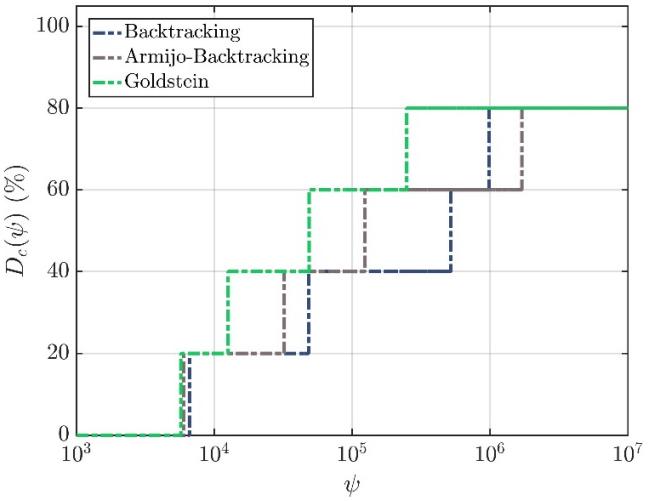

Figure 6: Data profiles of line search conditions

This figure enables us to select the line search condition or conditions that meet the given computational budget. We, for instance, are given $\psi \leq 2.5 \times 10^4$ number of function evaluations to fit at least 2 geometries. In these terms, the choice should be the GC because its probability within the range of $1.259 \times 10^4 \leq \psi \leq 2.5 \times 10^4$ is 40%. Another example: if $\psi = 1.85 \times 10^5$ and it is required to fit the geometries as much as possible. Then, we can choose either the ABC or the GC because they have same probability at this budget (i.e., $D(\psi = 1.85 \times 10^5) = 60\%$) and they are able to fit 3 geometries out of 5. As have been seen so far, the performance and data profiles are quite useful for analyzing of the line search conditions performances.

IV. CONCLUSIONS

This work has presented an analysis on the performance of Fletcher-Reeves CG method considering three well-know line search conditions in nonlinear least squares geometry fitting. The five primitive geometries were used in the fitting procedure. The total number of function evaluations when the fitting is completed are used as a performance criterion of the CG-line search condition combinations. Using these data, the performance and data profiles were generated to be able to carry out reliable assessments. As such, those profiles point out that the GC is the fastest line search condition. For the second fastest one, the ABC shows up. The BC is the latest one because it does not have gradient term, thereby it cannot guarantee a sufficient decrease in the error function value. All those results have shown that the step length computation techniques require a great deal of attention due to their effect on the performance and success of the CG method. For a remarkable success in the geometry fitting, an optimal line search condition, which is the GC in this study, has to be implemented.

ACKNOWLEDGEMENT

The author thanks Design and Manufacturing Technologies Research Laboratory, Innovative Technologies Application and Research Center, Suleyman Demirel University for experimental studies.

REFERENCES

[1] W. Hu, J. Wu, and G. Yuan, "Some modified Hestenes-Stiefel conjugate gradient algorithms with application in image restoration", *Applied Numerical Mathematics*, vol. 158, pp. 360–376, 2020.

[2] T. Helmig, F. Al-Sibai, and R. Kneer, "Estimating sensor number and spacing for inverse calculation of thermal boundary conditions using the conjugate gradient method", *International Journal of Heat and Mass Transfer*, vol. 153, pp. 119638, 2020.

[3] P. Xiong, J. Deng, T. Lu, Q. Lu, Y. Liu, and Y. Zhang, "A sequential conjugate gradient method to estimate heat flux for nonlinear inverse heat conduction problem", *Annals of Nuclear Energy*, vol. 149, pp. 107798, 2020.

[4] H. R. Schwarz, "The method of conjugate gradients in finite element applications", *Journal of Applied Mathematics and Physics*, vol. 30, pp. 342-354, 1979.

[5] S. Chattopadhyay, and G. Chattopadhyay, "Conjugate gradient descent learned ANN for Indian summer monsoon rainfall and efficiency assessment through Shannon-Fano coding", *Journal of Atmospheric and Solar-Terrestrial Physics*, vol. 179, pp. 202-205, 2018.

[6] Y. Li, W. Chen, H. Zhou, and L. Yang, "Conjugate gradient method with pseudospectral collocation scheme for optimal rocket landing guidance", *Aerospace Science and Technology*, vol. 104, pp. 105999, 2020.

[7] N. Andrei, "A simple three-term conjugate gradient algorithm for unconstrained optimization", *Journal of Computational and Applied Mathematics*, vol. 241, pp. 19-29, 2013

[8] X. Du, P. Zhang, and W. Ma, "Some modified conjugate gradient methods for unconstrained optimization", *Journal of Computational and Applied Mathematics*, vol. 305, pp. 92-114, 2016.

[9] https://www.desmos.com (Access date:16.05.2021).

[10] P. Jia, "Fitting a parametric model to a cloud of points via optimization methods," Ph.D. thesis, Syracuse University, New York, USA, 2017.

[11] R. Fletcher, and C.M. Reeves, "Function minimization by conjugate gradients", *The Computer Journal*, vol. 7(2), pp. 149-154, 1964.

[12] J. Nocedal, and S. J. Wright, *Numerical optimization*, 2nd ed., New York, USA: Springer Science & Business Media; 2006.

[13] E. D. Dolan, and J. J. More, "Benchmarking optimization software with performance profiles," *Mathematical programming,* vol. 91(2), pp. 201-213, 2002.

[14] J. J. More, and S. M. Wild, "Benchmarking derivative-free optimization algorithms," *SIAM Journal on Optimization,* vol. 20(1), pp. 172-191, 2009.

On the Effect of Cellular Periodicity of Acoustic Transmission Line Metamaterials with Visco-thermal Effects

T. BAYGÜN[1] and A. SEÇGİN[1,2]

[1] METADYNA Müh. San. Tic. A.Ş., İzmir/Turkey, baygun.tuba@hotmail.com
[2]Dokuz Eylül University, İzmir/Turkey, abdullah.secgin@deu.edu.tr

Abstract **- The study investigates the effects of cellular periodicity of acoustic transmission line metamaterials on acoustic performance parameters by considering visco-thermal effects of Kirchhoff model. Acoustic metamaterials (AMMs) are composed of different combinations of expansion chamber type unit cells with such arrangements as mean, linear and golden ratio increase. Transfer matrix method (TMM) is conducted for retrieving effective (homogenous) medium and acoustic performance parameters. The TMM models with and without visco-thermal effects are verified by Finite Element Method (FEM). Acoustic performance parameters such as sound transmission and absorption coefficients are determined using those homogenous parameters. The results showed that all unit-cell arrangements have single negative compressibility properties.**

Keywords **- Transmission line acoustic metamaterial, visco-thermal effects, cellular arrangements, effective parameters, transfer matrix method.**

I. INTRODUCTION

ENGINE exhaust systems, gas or fluid transmission lines, ventilation systems including pipes provides a guide for the noise propagation caused by the noise source such as engine, fan etc. Therefore, they transmit sound from the source to the environment through the ducts. For suppressing that noise, generally reactive or reflective mufflers by means of passive isolation are used besides making several design corrections. Works on these kinds of problems goes beyond 1920's [1]. These noise handling techniques are generally successful at higher frequencies. However, the problem for suppressing the noise with lower frequencies is still questioning.

In recent decade, a concept called acoustic metamaterial (AMM) inspired from electromagnetic metamaterials (EMMs) was emerged. The first theoretical study on metamaterials (MMs) was made by Veselago [2]. He stated that phase and group velocities may be opposite direction to each other in an electromagnetic environment. This promised that the EMMs have a great potential for scientific research and industrial applications such as cloaking, super lensing etc. The theoretical fundamentals of AMMs are based on the available information on electromagnetic metamaterials. AMMs are artificial structures made of periodic or non-periodic sub-wavelength units. Ma and Sheng [3], Haberman and Guild [4], Cummer et.al [5] and Haberman and Norris [6] presented very informative review papers on abilities of AMMs. There are numerous researches on AMMs in the last 20 years for various purposes. The main development of AMMs can be historically cited here. Liu et. al. [7] manufactured metal spheres coated with elastic silicon rubbers exhibiting local resonance frequency. Sheng [8] and Hirsekorn et al. [9] followed the work of creating local resonances by coated PCs. Lazarov and Jensen [10] used spring-mass oscillators to achieve band gap close to local resonance. Huang et.al [11] performed mass in mass lattice model to achieve the same purpose. Zhou and Hu [12] constructed an analytical model for effective mass density, bulk and shear modulus of elastic metamaterials composed of coated spheres embedded in a host matrix similar to the model of Liu et.al [7]. Fang et al. [13] designed an ultrasonic metamaterial with a negative compressibility consisting of a Helmholtz resonator series, and showed that phase and group velocity could be in opposite direction. Hu et al. [14] obtained analytically the effective medium parameters of a Helmholtz resonator in the fluid and supported the aforementioned findings of Fang et al. [13]. Lee et al. [15] created a negative compressibility by developing a different metamaterial with side holes in a pipeline. With this material, they have shown analytically and experimentally that they may prohibit sound transmission below 450 Hz. Lee et al. [16] developed another metamaterial with a negative effective density at resonance frequencies of membranes by placing very thin membranes in a pipe transmission line. Yang et al. [17] designed a different metamaterial by placing small masses on very thin membranes showing negative effective density which can be adjusted to desired frequencies. They confirmed their results by experimental studies. Yao et al. [18] shown experimentally that negative density can be achieved by oscillators consisting of a large number of small mass and spring systems. Beside that several simultaneously double negative metamaterials were designed including zero and /or negative mass and /or negative elasticity [19-22]. For example, Li and Chan [19] mathematically proved that Veselego's double negativity [2] is possible in AMMs too by using a model a soft rubber immersed in water.

For a realistic acoustic model of a transmission line, acoustic performance parameters such as sound transmission, reflection and absorption coefficients should be predicted by including

visco-thermal (v-t) effects. Theocharis et.al., [23] showed that those effects influence slow sound propagation in systems with side resonators. Moleron [24] experimentally investigated visco-thermal effects for the metamaterials composed of rigid slabs and demonstrated that visco-thermal effects should not be avoided for actual acoustic response. These effects are generally treated in the models by two manners; analytical and numerical. The theory of both method is based on full set of Navier-Stokes (N-S) equations. Tijdeman [25] states that approximate analytical models for circular ducts are generally grouped in two divisions. The first group formulates these effects based on Kirchhoff solutions to complex transcendental equations. The second group uses more basic governing equations known as Low Reduced Frequency (LRF) solution. Zwicker-Kosten model [26] is one of the well-known models of this kind. Finite element method is very flexible numerical tool to handle v-t effects [27]. In FE computations two methodologies are used based on the selection of field variables [28-30]; i)temperature variation, particle velocities, ii) temperature variation, particle velocities and sound pressure. Cordioli [31] showed that the latter presents more accurate results when compared with experiments, since it is capable of dissipation due to discontinuities.

Expansion Chambers (ECs) and Helmholtz Resonators (HRs) are very basic acoustic units which are widely used in muffler design with their different forms and combinations. Since they are easy to design, cheaper to produce, their theories are explicit and they can present higher transmission losses, they are still being attracted much by the design and analyses of AMMs [32-38]. When they are designed periodically with sub-wavelength units, they may compose so called a metamaterial. And then the material can show tuneable Bragg type and resonance band gaps.

In this study the effects of cellular periodicity of AMMs composed of several combinations of ECs on acoustic performance parameters are investigated. In this context, three different cellular arrangement with different number of cells regarding on their diameters of expansion are considered (with noting that all have the same acoustic cavity volume in total); i) cells with the same expansion diameters (mean), ii) cells with golden-ratio increasing diameters (golden ratio) and iii) cells with linear increasing diameters (linear). It is observed that all unit cell arrangements have single negative metamaterial properties. The study uses transfer matrix method (TMM) for computational tool by considering Kirchhoff model of visco-thermal effects and utilizes effective (homogenous) medium parameters in evaluations. The TMM models are verified by Finite Element Method (FEM). Effective medium parameters of these arrangements are also determined from acoustic performance parameters to test behaviour of those holding physical consistency. The results showed that all three arrangements exhibit single negative effective material property, and different transmission and absorption characteristics.

II. MATHEMATICAL BACKGROUND

2.1. TRANSFER MATRIX METHOD AND DETERMINATION OF EFFECTIVE MEDIUM PARAMETERS

Consider an acoustic transmission line metamaterial shown schematically in Fig 1,

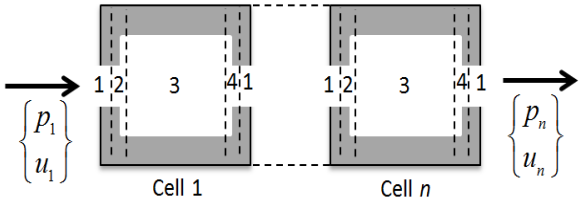

Figure 1. An acoustic transmission line metamaterial consists of n number of expansion chamber type metacells.

The two port parameters; p sound pressure and u particle velocity at ports 1 and n can be related by total transfer matrix T_m as [1];

$$\begin{Bmatrix} p_1 \\ u_1 \end{Bmatrix} = T_m \begin{Bmatrix} p_n \\ u_n \end{Bmatrix} \quad (1)$$

The T_m of the metamaterial can be obtained by the multiplication of the individual transfer matrices (TMs) of each acoustic segment; tube (1) - sudden expansion (2) -tube (3) - sudden contraction (4) – tube (1);

$$T_m = \prod_{i=1}^{n} (T_1 \cdot T_2 \cdot T_3 \cdot T_4 \cdot T_1)_i = \begin{bmatrix} T_{m,11} & T_{m,12} \\ T_{m,21} & T_{m,22} \end{bmatrix}, \quad (2)$$

where n is the number of cell in the transmission line. The transfer matrix of tubes 1 and 3 is given by [1]:

$$T_{1(3)} = \begin{bmatrix} cos\, k_0\, n_0 L_{1(3)} & jZ_0\, sin\, k_0\, n_0 L_{1(3)} \\ \frac{j}{Z_0} sin\, k_0\, n_0 L_{1(3)} & cos\, k_0\, n_0 L_{1(3)} \end{bmatrix} \quad (3)$$

and, the transfer matrix of sudden expansion and contraction including end corrections for stationary medium is given by [1]

$$T_{2(4)} = \begin{bmatrix} 1 & j\omega \left(1 - 1.25 \frac{r_1}{r_3}\right) 0.85 \frac{r_1}{S_1} \\ 0 & 1 \end{bmatrix}. \quad (4)$$

Here, for air medium $n_0 = 1$ is the refraction index of air, $k_0 = \omega/c_0$ is the wavenumber (ω is frequency of the propagation), $Z_0 = \rho_0 c_0$ (ρ_0 is the mass density, c_0 is the speed of sound) is the acoustic impedance, r_i and L_i are the radius and length of the i.th tube, respectively. S_1 is the cross-section are of the smallest tube (Tube 1) and j=$\sqrt{-1}$. Transfer matrix of an effective medium, can be written in terms of effective parameters;

$$T_e = \begin{bmatrix} T_{e,11} & T_{e,12} \\ T_{e,21} & T_{e,22} \end{bmatrix} = \begin{bmatrix} cos\, k_0\, n_{eff} L_{eff} & jZ_{eff}\, sin\, k_0\, n_{eff} L_{eff} \\ \frac{j}{Z_{eff}} sin\, k_0\, n_{eff} L_{eff} & cos\, k_0\, n_{eff} L_{eff} \end{bmatrix} \quad (5)$$

and effective medium parameters in the matrix can be found by equating Eq. (5) with Eq. (2), i.e.,

$$T_e = T_m. \quad (6)$$

For details of the determination of effective parameters, one can refer to [39]. Finally acoustic performance parameters; transmission, reflection and absorption coefficients are derived from effective medium transfer matrix, respectively as [23];

$$t = \frac{2}{T_{e,11}+\frac{T_{e,12}}{Z_0}+Z_0T_{e,21}+T_{e,22}}, \quad (7)$$

$$r = \frac{T_{e,11}+\frac{T_{e,12}}{Z_0}-Z_0T_{e,21}-T_{e,22}}{T_{e,11}+\frac{T_{e,12}}{Z_0}+Z_0T_{e,21}+T_{e,22}}, \quad (8)$$

$$\alpha = 1 - t^2 - r^2. \quad (9)$$

Then effective medium parameters are computed as follows [39];

$$n_{eff} = \frac{1}{k_0 L_{eff}} cos^{-1}(T_{11}), \quad (10)$$

$$Z_{eff} = Z_0 S \left(\frac{1-r}{1+r}\right) \quad \left[\frac{\text{kg}}{m^2 s}\right], \quad (11)$$

$$\rho_{eff} = \frac{n_{eff}}{c_0} Z_{eff} \quad \left[\frac{\text{kg}}{m^3}\right], \quad (12)$$

$$C_{eff} = \frac{n_{eff}}{c_0 Z_{eff}} \quad \left[\frac{1}{\text{MPa}}\right]. \quad (13)$$

.

2.2. KIRCHHOFF VISCO-THERMAL MODEL

As it is mentioned in the introduction section, two groups of analytical methods are generally applied for visco-thermal effects for circular tubes. The first group is based on Kirchhoff solution (KS) model and the second one is low reduced frequency (LRF) model. A comprehensive discussion on this issue can be found in Ref. [26]. For "wide" circular tubes, modifying Kirchhoff formulas [25], one can end up with the following wavenumbers corresponding to viscos and thermal losses;

$$k_{visc} = \frac{(1-j)}{R\sqrt{2}} d_{visc}, \quad (16)$$

$$k_{therm} = \frac{(1-j)}{R\sqrt{2}} (\gamma - 1) d_{therm}, \quad (17)$$

respectively. Here R is the radius of the circular duct and γ is heat capacity ratio and d_{visc} and d_{therm} are thicknesses of viscos and thermal boundary layers, and can be written as

$$d_{visc} = \sqrt{\frac{2\mu}{\rho_0 \omega}}, \quad (18)$$

$$d_{therm} = \frac{d_{visc}}{\sqrt{\text{Pr}}}, \quad (19)$$

respectively. Here μ is the dynamic viscosity. Pr is the Prandtl number for air medium. Defining shear wavenumber (also known as Stoke's number) as $s = R/d_{visc}$, for "very wide" tubes, $\lim_{s\to\infty} k = k_0$ being the solution of for a plane wave in the absence of viscos and thermal effects. For small values of shear wavenumber, Kirchhoff formula reduces to Rayleigh solution:

$$k \approx 2(1-j)\frac{\sqrt{\gamma}}{R} d_{visc}. \quad (20)$$

III. MODELLING AND SIMULATIONS

Here in this paper, circular expansion chamber type units as shown in Fig. 2 are considered in all analyses. This section is devoted firstly to present verification study of the TMM models by using finite element method. Then the effect of cellular arrangements of transmission line metamaterials on their acoustic performances are discussed based on the results of TMM simulations. Visco-thermal effects based on Kirchhoff model is adapted to the TMMs by making following replacements:

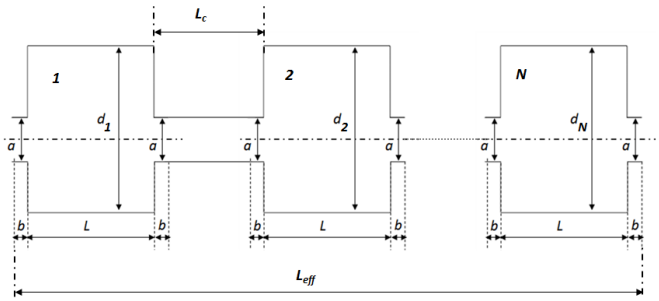

Figure 2. Schematic of a metamaterial composed of N number of expansion chamber type units

$$k_0 \rightarrow k_0(1 + k_{visc} + k_{therm}) \quad (21)$$

$$Z_0 \rightarrow Z_0(1 + k_{visc} - k_{therm}) \quad (22)$$

This section presents the verification of transfer matrix method (TMM) by using finite element method (FEM) via Comsol Multiphysics. Here, two material arrangements are considered; i) the material with single circular unit cell, ii) the material with three-unit cells composed of the same single cells. Each cell has the following properties; a=12.5 mm, b=5 mm, d=53.904 mm, L=40 mm, Pr=0.7491, $\mu = 1.78 \times 10^{-5}$Ns/m^2, $\rho_0 = 1.2$ kg/m^3, $\gamma = 1.4028$.

3.1. COMPARISION OF TMM MODELS WITH FEM

Comparisons are performed for the cases with and without v-t models. In analytical v-t modelling, KS model is used in TMMs, whereas Comsol® Multiphysics, Thermo-acoustics Physics (with isothermal case) with 2D axisymmetric modelling is used in FEM computations (Fig. 3). The theory behind FEM v-t model can be found in [27]. Since the v-t effects are generally considerable on peaks, FEM v-t computations are carried out only for certain frequency bands covering transmission peaks in order to reduce computational costs and memory usage. The amount and types of finite elements were determined by automatic convergence control of Comsol® "fine mesh" feature. Boundary conditions were applied to the input and output ends according to the plane wave theory and the left end is excited by 1Pa harmonic sound pressure. The $d_{visc} = 0.22\sqrt{100/f}$ (mm) is calibrated for 100 Hz for each frequency of interest f (Hz).

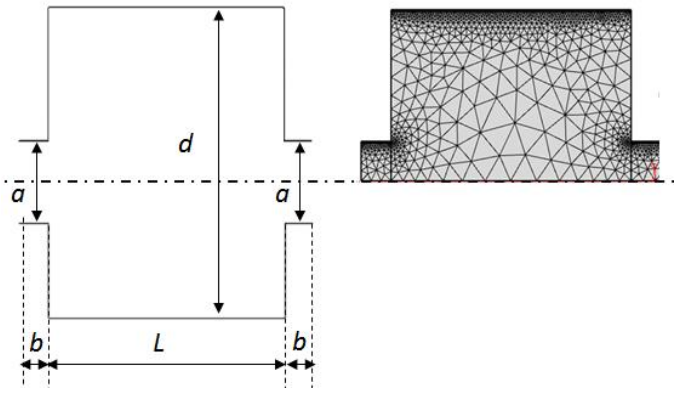

Figure 3. Schematic of a single circular expansion chamber type unit and its Comsol FE mesh of 2D axisymmetric model

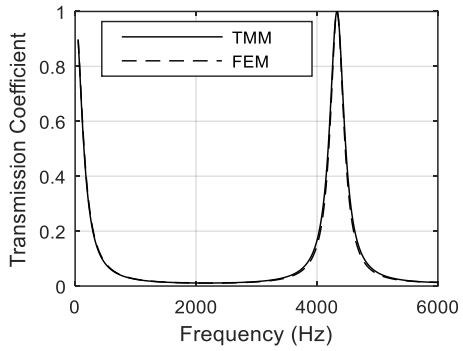

(a)

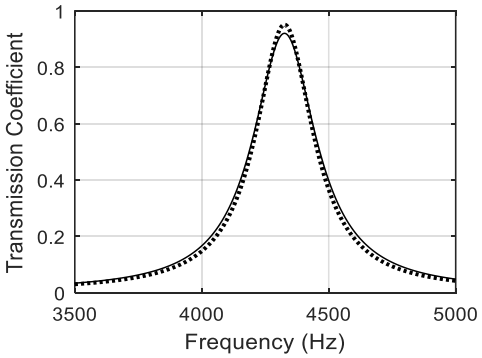

(b)

Figure 4. Verification of TMM by using FEM for the single unit case a) without v-t effects, b) with v-t effects (3500-5000 Hz)

Fig 4.a presents a perfect match between the TMM and the FEM when v-t effects are neglected for the single unit cell. The first peak corresponds the first plane wave mode of the expansion chamber analytically at $f = mc/2L = 4287.5$ Hz (where m=1) which is consistent with the FEM and TMM results. Besides, Fig 4.b shows very close results of TMM and FEM with v-t effects. The similar behaviours are also seen for the material with three-unit cell cases as shown in Fig 5. However, there are small discrepancies especially at higher frequency peaks in case of v-t effects are taken into consideration; this may be caused due to the differences of analytical and numerical v-t models adapted.

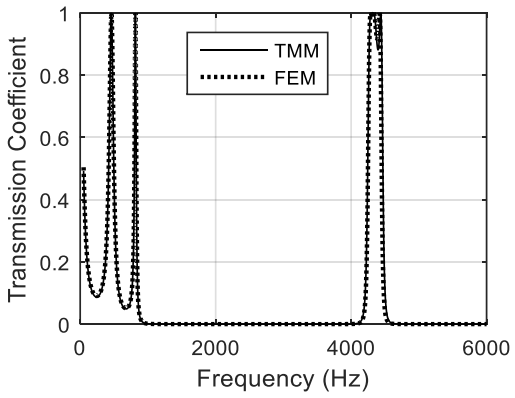

(a)

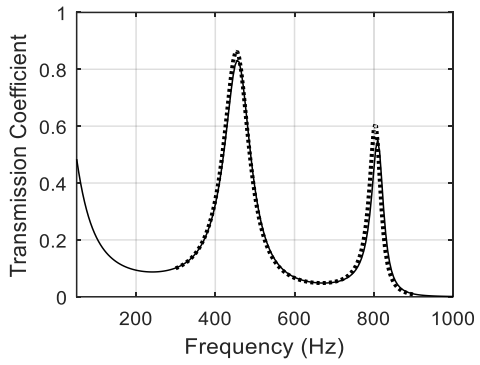

(b)

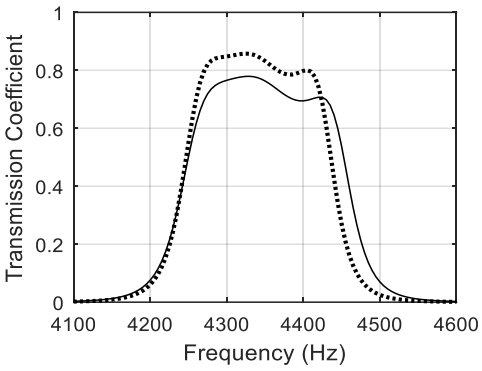

(c)

Figure 5. Verification of TMM by using FEM for the three-unit case a) without v-t effects, b) with v-t effects (50-1000 Hz), c) with v-t effects (4100-4600 Hz)

3.2. THE EFFECT OF CELLULAR PERIODICITY

In this section, as a main study, the effect of cellular arrangement of an acoustic transmission line metamaterial on the acoustic performance parameters is investigated by using TMM in case of visco-thermal effects are taken into account. For this purpose three different cellular arrangements, each of which have the same total expansion volume but changeable diameters, are designed. These metamaterials are composed of four circular expansion chamber type cells as schematically shown in Fig. 2 for 4 unit cells. The arrangements are made by changing the diameters of expansion; i) cells with the same expansion diameters ("mean"), ii) cells with golden-ratio increasing diameters ("golden ratio") and iii) cells with linearly increasing diameters("linear"). Table 1 tabulates the diameters of expansions.

Here, the analyses start with determining effective medium parameters of the metamaterial arrangements based on an inverse homogenization procedure [27]. It is known for a passive medium that, the conditions $\text{imag}(n_{eff}) \geq 0$ and $\text{real}(Z_{eff}) \geq 0$ must be satisfied for physical consistency. Fig 7.a and b show that all three arrangements satisfy these required physical consistencies. Besides, Fig 7.c presents that those materials present negative compressibility, i.e., $C_{eff} = n_{eff}/c_0 Z_{eff}(1/\text{MPa})$at certain frequency bands. This property makes these materials as "metamaterial".

Table1:Diameters of expansion of considered metamaterials shown in Fig.6 with noting that a=12.5 mm, b=5 mm, L=40 mm for each cell

Cellular Arrangements	d_1(mm)	d_2 (mm)	d_3(mm)	d4 (mm)
Arrangement 1 (Mean)	53.904	53.904	53.904	53.904
Arrangement 2 (Golden Ratio)	20.225	32.724	52.947	85.669
Arrangement 3 (Linear)	25.254	42.091	58.928	75.765
Total volume of expansion	3.6513×10^5 mm^3			

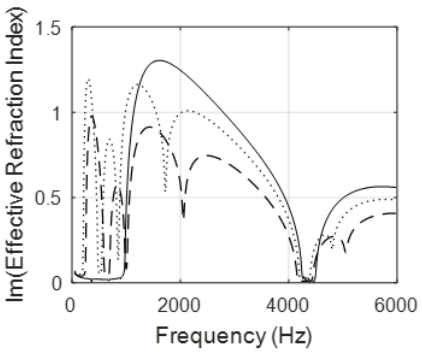

(a)

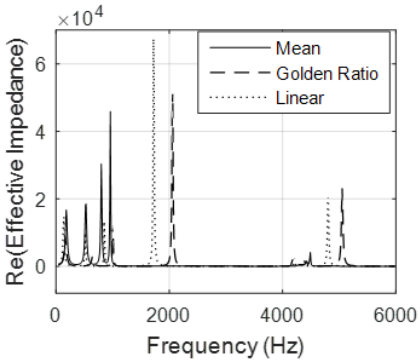

(b)

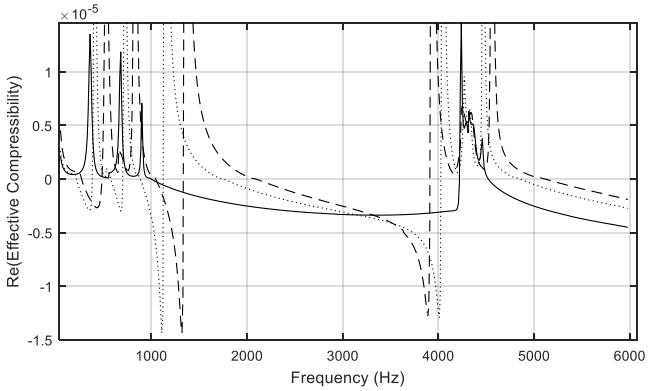

(c)

Figure 6. Effective parameters of three metacells arrangements: a)Imaginary part of effective refraction indices, b) Real part of effective impedances, c) Real part of effective compressibilities.

In Fig.6, all three arrangements are compared by themselves and with a single cell having the same total expansion volume. At first glance, it is seen that total volume bans the transmission of waves up to about 4000 Hz. This exhibits a pure reflective character of a single cell. However, the other arrangements let the waves transmit at certain frequencies called F-P frequencies. These behaviours improve absorption characteristics of periodic metamaterials as shown in Fig. 7, which is a required property from a metamaterial if they are specifically designed as absorption material.

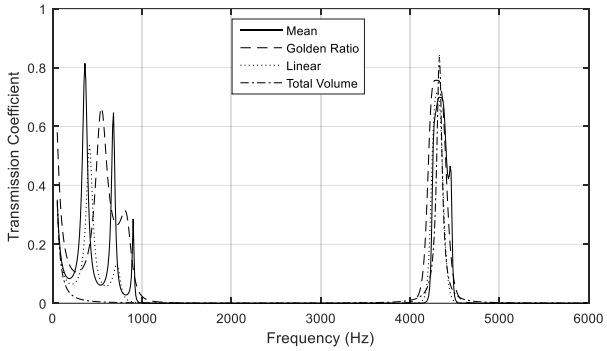

Figure 7.Transmission coefficients of different cellular arrangements

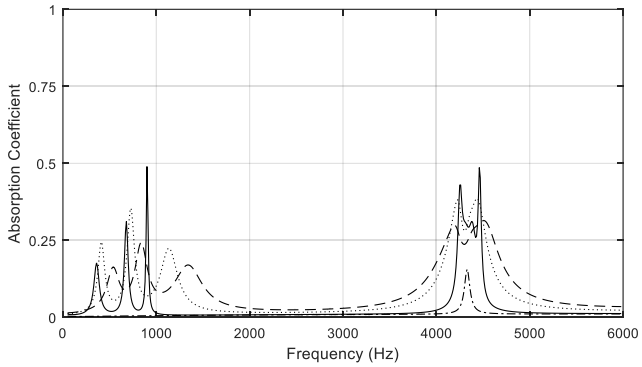

Figure 8. Absorption coefficients of different cellular arrangements

When Fig.7 and Fig. 8 are investigated, following conclusions can be drawn;

- The peaks up to 1000 Hz are caused due to Fabry-Perot frequencies and improve absorption around those peaks.
- A stop-band behaviour is observed between about 1000-4000 Hz. This shows that the materials exhibit a band pass filter.
- The peaks observed at 4000-4600 Hz show the resonance behaviour of each unit cells. This behaviour also improves absorption.
- Absorption limit is obtained as 0.5, as expected, since these kind of materials (single negative, cavity based) shows monopole behaviour. For details information one may refer to [4].
- "Mean" composition shows higher absorption values, however "golden ratio" composition have wider bandwidth.
- When considering higher absorption and wider bandwidth together, it seems that the best choice is "linear" composition.
- "Linear" composition also seems as the best choice among others for the transmission loss character, if one expects small transmission and higher absorption at a wide band.

IV. CONCLUSION

The study is concerned with an investigation on the effects of cellular arrangement of transmission line acoustic metamaterials on their acoustic performance parameters such as sound transmission and absorption. The Transfer Matrix Method together with the adaption of Kirchhoff visco-thermal models is used as analysing tool. Several verification studies are performed using finite element method. There different metamaterials, each one is composed of four expansion chamber type units are designed based on providing diameter increasing periodicity; "mean", "golden-ratio", "linear". Effective medium parameters of these metamaterials are firstly determined to test that these arrangements have physical consistency with regard to passive medium assumption. The results showed that all three arrangements present single negative effective material properties. It is concluded that for this kind of metamaterials, the periodicity designed by linearly increasing diameters are more effective as far as transmission and absorption enhancements are concerned. It is shown that the cellular arrangement is quite important factor for designing acoustic transmission line metamaterials.

REFERENCES

[1] M. L. Munjal, *Acoustics of Ducts and Mufflers*. John Wiley & Sons, 1987.

[2] V. G. Veselago, "The electrodynamics of substances with simultaneously negative values of μ and ε", *Soviet Physics Uspekhi*, vol. 10(4), pp. 509-514, 1968.

[3] G. Ma, P. Sheng, "Acoustic metamaterials: From local resonances to broad horizons", *Science Advances 2*, e1501595, 2016.

[4] M. R. Haberman, M. D. Guild, "Acoustic Metamaterials", *Physics Today*, vol. 69, pp. 42-48, 2016.

[5] S. A. Cummer, J. Christensen, A. Alù, "Controlling sound with acoustic metamaterials", *Nature Review Materials*, 1 16001, 2016.

[6] M. R. Haberman, A. N. Norris, "Introduction to the special issue on acoustic metamaterials" *Journal of Acoustic Society of America*, 139, 3239, 2016.

[7] X. Zhang, Z. Liu, "Negative refraction of acoustic waves in two-dimensional phononic crystals", *Applied Physics Letters*, vol. 85(2), pp. 341-343, 2004.

[8] P. Sheng, X. X. Zhang, Z. Liu, C. T. Chan, "Locally resonant sonic materials", *Physica B*, 338 201-205, 2003.

[9] M. Hirsekorn, P. P. Delsanto, N. K. Batra, P. Matic, "Modelling and simulation of acoustic wave propagation in locally resonant sonic materials", *Ultrasonics*, vol. 42(1), pp. 231-235, 2004.

[10] B. S. Lazarov, J. S. Jensen, "Low-frequency band gaps in chains with attached non-linear oscillators", *International Journal of Nonlinear Mechanics*, vol. 42, pp. 1186-1193, 2007.

[11] H. H. Huang, C. T. Sun, G. L. Huang, "On the negative effective mass density in acoustic metamaterials", *Internation Journal of Engineering Science*, vol. 47(4), pp. 610-617, 2009.

[12] X. Zhou, G. Hu, "Analytic model of elastic metamaterials with local resonances", *Physical Review*, vol. 79, 195109, 2009.

[13] N. Fang, D. Xi, J. Xu, M. Ambati, W. Srituravanich, C. Sun, X. Zhang, "Ultrasonic metamaterials with negative modulus", *Nature Materials*, vol. 5(6), pp. 452-456, 2006.

[14] X. Hu, K. M. Ho, C. T. Chan, J. Zi, "Homogenization of acoustic metamaterials of Helmholtz resonators in fluid", *Physical Review B*, vol. 77(17), 172301, 2008.

[15] S. H. Lee, C. M. Park, Y. M. Seo, Z. G. Wang, C. K. Kim, "Acoustic metamaterial with negative modulus", *Journal of Physics: Condensed Matter*, vol. 21(17), 175704, 2009.

[16] S. H. Lee, C. M. Park, Y. M. Seo, Z. G. Wang, C. K. Kim, "Acoustic metamaterial with negative density", *Physics Letters A*, vol. 373(48), pp. 4464-4469, 2009.

[17] Z. Yang, J. Mei, M. Yang, N. H. Chan, P. Sheng, "Membrane-type acoustic metamaterial with negative dynamic mass", *Physical review letters*, vol. 101(20), 204301, 2008.

[18] S. Yao, X. Zhou, G. Hu, "Experimental study on negative effective mass in a 1D mass–spring system", *New Journal of Physics*, vol. 10(4), 043020, 2008.

[19] J. Li, C. T. Chan, "Double-negative acoustic metamaterial", *Physical Review E*, vol. 70(5), 055602, 2004.

[20] Y. Ding, Z. Liu, C. Qiu, J. Shi, "Metamaterial with simultaneously negative bulk modulus and mass density", *Physical Review Letters*, vol. 99(9), 093904, 2007.

[21] Y. Cheng, J. Y. Xu, X. J. Liu, "One-dimensional structured ultrasonic metamaterials with simultaneously negative dynamic density and modulus", *Physical Review B*, vol. 77(4), 045134, 2008.

[22] F. Bongard, H. Lissek, J. R. Mosig, "Acoustic transmission line metamaterial with negative/zero/positive refractive index", *Physical Review B*, vol. 82(9), 094306, 2010.

[23] G. Theocharis, O. Richoux, G. V. Romero, A. Merkel, V. Tournat, "Limits of slow sound propagation and transparency in lossy, locally resonant periodic structures", *New Journal of Physics*, vol. 16, 093017, 2014.

[24] M. Molerón, M. Serra-Garcia, C. Daraio, "Viscothermal effects in acoustic metamaterials: from total transmission to total reflection and high absorption", *New Journal of Physics*, vol. 18, 033003, 2016.

[25] H. Tijdeman, "On the propagation of sound waves in cylindrical tubes", *Journal of Sound and Vibration*, vol. 39(1), pp. 1-33, 1975.

[26] C. Zwicker, C. Kosten, *Sound Absorbing Materials*. Amsterdam: Elsevier, 1949.

[27] W. M. Beltman, "Viscothermal wave propagation including acousto-elastic interaction" Ph.D. dissertation, University of Twente, Twente, 1998.

[28] N. Joly, (2008). Finite element modeling of thermoviscous acoustics in closed cavities. *Acoustics'08*. Paris, France, pp. 2469–2474.

[29] M. Malinen, M. Lyly, P. Råback, A. Kärkkäinen, L. Kärkkäinen, "A finite element method for the modeling of thermo-viscous effects in acoustics", *2004 Proceedings of ECCOMAS*.

[30] W. R. Kampinga, Y. H. Wijnant, A. de Boer, "Performance of several viscothermal acoustic finite elements", *Acta Acustica*, vol. 96, pp. 115-124, 2010.

[31] J. A. Cordioli, G.C. Martins, R. Jordan, P.H. Mareze, "A comparison of models for visco-thermal acoustic problems", *InterNoise*. Lisbon Portugal 2010.

[32] X. Wang, C. M. Mak, "Wave propagation in a duct with a periodic Helmholtz resonator array", *The Journal of Acoustical Society of America*, pp. 1172-1182, 2012.

[33] N. Jimenez, T.J Cox, V. R. Garcia, J. Groby, "Metadiffusers: Deep-subwavelength sound diffusers", *Scientific Reports*, vol. 7, 5389, 2017.

[34] T. Yamamoto, "Acoustic metamaterial plate embedded with Helmholtz resonators for extraordinary sound transmission loss", *Journal of Applied Physics*, vol. 123, 215110, 2018.

[35] S. B. Gebrekidan, H. J. Kim, S. J. Song, "Investigation of Helmholtz resonator-based composite acoustic metamaterial", *Applied Physics A*, vol. 125 (65), 2019.

[36] J. Lan, Y. Li, H. Yu, B. Li, X. Liu, "Nonlinear effects in acoustic metamaterial based on a cylindrical pipe with ordered Helmholtz resonators", vol. 381(13), pp. 1111-1117, 2017.

[37] B. Sharma, C. T. Sun, "Acoustic metamaterial with negative modulus and a double negative structure", arXiv:1501.02833, 2015.

[38] J. W. Jung, J. E. Kim, J.W. Lee, "Acoustic metamaterial panel for both fluid passage and broadband soundproofing in the audible frequency range", *Applied Physics Letters*, vol. 112, 041903, 2018.

[39] A. Seçgin, T. Baygün, "Determination of effective medium parameters of an in-line cavity based acoustic metamaterials with visco-thermal losses", *Material Research Express*, vol. 6, 065801, 2019.

Improving Level Measurement Techniques and Measurement Accuracy in Vehicle Fuel Tanks

Öner ATALAY[1*], Buse BELLİ[1,2], Oğuz SEZGİN[2]
[1]Pamukkale University, Denizli/Turkey, oatalay@pau.edu.tr
[2]NESAN Automotive, İzmir/Turkey, info@nesan.com.tr

Abstract **- Measuring the level and accurate transmission of the amount of fuel in vehicle fuel tanks is important in many ways. In vehicle warehouse designs, very different geometric shapes are encountered. Vehicle geometry and equipment placement cause warehouses to be produced in very different geometries. It is very important that information about the amount of fuel is transmitted to the driver in the most accurate way so that the driving safety and the car can travel safe distances. Shaking the fuel in the tank on a flat road, slope or off-road conditions may affect the display of the correct amount of fuel. In the study, the maximum and minimum production tolerance and geometry of the vehicle tanks, known as the mathematical model, the turbulence caused by acceleration of the float fuel measurement system in contact with the liquid placed in the tank, as well as the accuracy of the Up/Down movement of the level measurement float and the measurement of the fuel level as a result of the turbulence, were examined. Focusing on the shaking state of the measuring part on the float and preventive geometries.**

Keywords **– Fuel, Tank, Sloshing, Level Measurement**

I. INTRODUCTION

Many methods are used for level measurement in vehicle fuel tanks. The important thing here is that the correct measurement can be performed while cruising or standing. Pressure tanks in which the fuel needed for the operation of the car engine is stored are called "fuel tanks". Liquid contact/non-contact sensors or mechanical solutions can be used to measure the fuel tank level. Vertical movable float systems are usually preferred because they are more cost-effective.

Capacitive level sensors (Figure 1) usually use radio frequency technology. It uses the electrical characteristics of capacitors to detect the level of liquid, granules, cement-like materials in the container. The electrode (probe) in the clothed or naked state is immersed in the tank as the first conductive part of the capacitor. The metal body of the tank, on the other hand, will act as the other conductor. In non-metal and plastic tanks, double-electrode systems should be used in which the second electrode serves as the other capacitor conductor. The capacitive level sensor measures the change in capacity that occurs during the movement (increase or decrease) of the material inside the tank through the sensor probe. This capacity value can also be used for a linear measurement, as well as for obtaining level information at a certain point as a contact output[1].

Figure 1: Capacitive Level Sensor

The principle of operation of inductive level switches (Figure 2) is based on the method of measurement of magnetic field permeability (permeability). It is hardly seen outside of laboratory studies. It is not very practical to monitor the change of the tank impedance, it requires large amounts of energy. On the other hand, it is also possible to measure at least as a switch by changing the operating frequency (resonance frequency) provided by the system formed by the tank. This is also the principle of operation of metal detectors. However, its applicability in level measurement is poor[1].

Figure 2: Inductive Level Switches

Ultrasonic level sensors (Figure 3) use sound waves to detect the level. A piezoelectric crystal in a transducer placed on top of a tank converts non-electrical signals into sound energy that moves in waves through the medium at a certain frequency and constant speed. The sound waves propagate and return to the transducer as an echo. The device simply measures the time elapsed between the wave beginning to propagate and reflecting off the surface and decaying back. This time is directly proportional to the distance between the transducer and the surface of the material whose level dec to be measured, and can be used to measure the level of the material.

Ultrasonic level switches, especially for point level of low

viscosity liquids it is an alternative method for measuring. The transducer located on one side of the switch detects whether there is material between the crystal and the receiving crystal on the other side by the method of sound wave dec. This method is quite similar to the ultrasonic principle. Radar (Sometimes also called microwave.) in his method, high-frequency electromagnetic waves of the order of GHz are used, which are directed downward from the sensor placed on top of the container. The part of the sent energy reflected from the liquid surface, the level of which is to be measured, returns to the sensor. The commuting time of the signal (also called the flight time.) is the magnitude used for the determination of the level. No tubes or cables are used in the radar technology, which is called Non-Invasive. FMCW (Frequency Modular Continuous Wave) and pulse radar are two different non-invasive radar technologies, invasive radar technology uses a cable or rod extending from the sensor to the bottom of the tank to guide the wave[1].

Figure 3: Ultrasonic Level Sensor

Vibration probes, on the other hand, vibrate using a piezo-electric element located at the end. This piezo-electric element is set to a certain vibration frequency. With any material of the probe upon contact, the vibration is absorbed by the material. This change in vibration is felt by the sensor and converted into a relay output. Single-bar devices are only solid when used in materials, double-probe devices can be used in both liquid and solid materials. Vibration probes are typically placed on the top or side of the tank is mounted. Electronic level switches have two important advantages. The first is that they do not need any calibration for different materials. The second is that these probes can work smoothly even in very low density materials.

Light sensors use simple optical switching. The change in the amount of light in the sensor indicates that the level is at this point. It is not used frequently for level measurements due to the excessive need for maintenance (especially cleaning). Measurement insensitive to reference light change (pollution) is also possible, but its cost is quite high. This measurement method is more useful in pollution measurement applications than level measurement[2].

Level measurement with transparent pipes (Figure 4) basically, the principle of combined containers is used to view the liquid level in the tank. Since the level in the glass pipe mounted on the tank edge and the level of the material inside the tank are the same, the level can be easily monitored from outside the tank. With this method, only visual level control can be performed, since there is no mechanical or electronic interference with the system.

Figure 4: Level Measurement with Transparent Pipes

Level Measurement with a diaphragm is usually performed when the lever with a magnet approaches the body with a reed contact or micro-switch under the pressure of the material, and the level of the material is checked with the contact received. It is similar to the float principle, but it is advantageous to use solid materials in level control.

The different studies to be carried out will help both the literature and the employees in the application part of the subject. Below are the summaries of some of the studies related to the subject.

In their studies, they have refined the working principles of capacitive sensor, ultrasonic sensor, differential pressure transducer and vertical moving float used in liquid level measurement. It has been observed that the pressure and temperature value of the medium and the type of liquid in the tank from the material of the tank to be used and the environment to be used in the measurement of the sensor to be used are effective[3].

The reseacher used an ultrasonic sensor to measure the liquid level and performed the level measurement with a sound wave without direct contact with the liquid. It has achieved a successful measurement at levels in the range of 0-30 cm[4].

In other study, the turbulence in the fuel tanks was investigated. Two different tanks with and without curtains were observed with 50%-85% occupancy rates and warnings were given in different directions. In this study, it was seen that the turbulence caused sudden pressure changes. In the webbed tank design, it has been observed that the liquid is effective in reducing the pressure value during the turbulence[5].

A detailed study was conducted on the level measurement methods and they divided them into two groups as mechanical-based and electrical-based. They also used the ultrasonic measurement method to measure the level of liquid in a small tank. They concluded that successful measurement was obtained in the december of 0-20 cm levels in their experimental studies[6].

Theoretical and experimental studies have been carried out according to different design styles, refueling rate and direction

of linear movement of the fuel tank for the standard input value of the shaking event in the passenger car fuel tank. They examined the shaking event by making different designs such as fretless, fretless/float and fretted/float. They observed that the webbed/float tank structure has a more balanced pressure distribution and dampens turbulent movement[7].

The level control was carried out by processing the analog data obtained with the float and potentiometer. The purpose is for the centrifugal pump to work stably and to maintain the liquid level at the required levels. In the experimental study, fuel level measurement was performed not at all levels, but to the extent necessary to ensure that it exhibits a stable structure[8].

In a thesis study, a mechanical solution with a high-precision servo motor drive that can measure the lifting force of liquids and solids based on is investigated. As with any method, the type and temperature of the substance whose level is measured in this measurement method varies depending on parameters such as the pressure or opening of the tank to the atmosphere, the size and location of the tank. It has been seen that while this application provides high accuracy in measuring liquids, special attention should be paid to parameters such as smooth and accurate assembly in solids[9].

In addition to mechanical measurement methods, it is possible to measure liquid without liquid contact. The accuracy of measurements performed without liquid contact, without adding any measuring substance or device to the liquid, disappears over time and gives erroneous results. In this study, it is aimed to prevent this condition. The measurement system is used in a hybrid form with ultrasonic, temperature and humidity sensors, without being connected to a single sensor, the liquid level is measured, it can also be easily adapted to liquid tanks of different sizes and shapes[10].

II. MATERIAL AND METHODS

In this study, mainly the maximum and minimum production tolerance and geometry of the float fuel metering system in contact with the liquid placed in the tank in on-board tanks known as the mathematical model, the turbulence caused by acceleration and the accuracy of the upward/downward movement of the level metering float and the measurement of the fuel level as a result of the turbulence were examined. Design of the level measuring float part on the float (Figure 5) in an unprotected way together with the initial design works carried out; it has been found in the analysis and design processes that it is very affected by the turbulence that occurs in the fuel tank. In particular, it has been found that the turbulence level is too high in models with complex tank geometry (asymmetric), and when the vehicle is accelerated suddenly, the fuel fluid in the tank hits the float part with a shock effect (Figure 6).

Figure 5: The Float Part of the Level Measurement

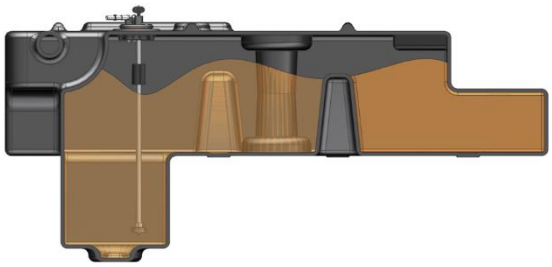

Figure 6: The Effect of Turbulence on the Level Meter

Another method is the breakwater mechanism to be added to the fuel tank(Figure 7). Parts of the fin structure that will be placed in the tank during the manufacture of a fuel tank can somewhat protect the float part in cases of sudden turbulence. However, this manufacturing method may not be suitable both from a technical point of view, from a production point of view, and from a cost point of view. Since the manufacturing processes of fuel tanks are produced with fairly large molds, it can be quite difficult to put the breakwater parts in the mold. It is hardly possible to add breakwater parts externally after manufacturing. In addition, even if the breakwater parts are somehow added to the tank, the distance to the float part will be far away, and it will not be able to restrict the turbulence at the expected levels over a large volume. In this case, it will still be affected by float turbulence and will be able to make level measurement errors.

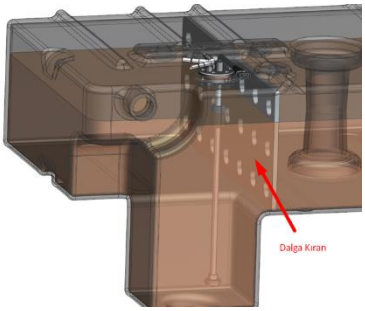

Figure 7: Breakwater Mechanism

In order to avoid such situations and reduce error modes to zero, it is possible to carry out a filtration design mechanically. In the current design, the float part is located in an unprotected structure on the float and therefore it can be affected very much by the turbulence. With the design made, a piece of housing was

thought out around the float and it was aimed to reduce these error modes to minimum levels by producing the housing to be monolithic with the float. This designed housing part (damper unit) takes the float on the float into a reservoir, creating a closed volume and protecting it from sudden turbulent effects (Figure 8).

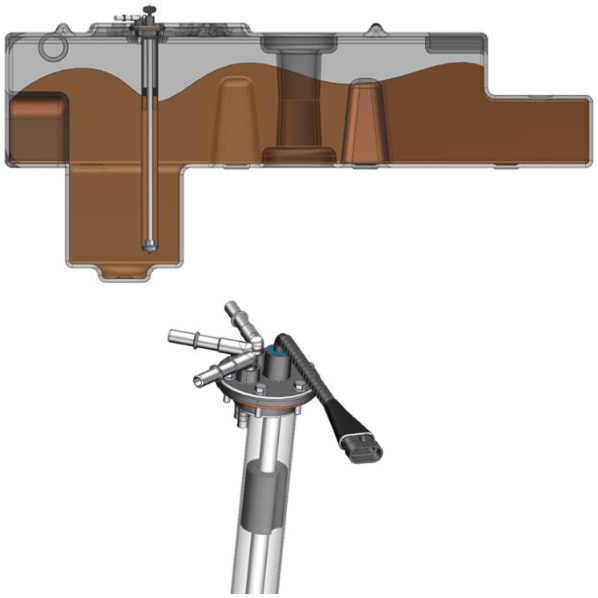

Figure 8: The Structure of the Housing Part on the Tank

However, in order for the float part to float in the fuel, small holes are also needed at the bottom of the housing part so that there is a fuel inlet into the closed volume through these holes and the float can continue to float in the liquid (Figure 9).

Figure 9: Placement of Fuel Inlet Holes on the Part

The dimensions of the housing part must be designed in accordance with the dimensions of the float part. The inner diameter and outer diameter of the housing part should be determined by conducting tolerance analyses of the outermost diameter dimension and inner diameter dimensions of the float part and applying code chain calculation. Otherwise, the float may overlap/rub with the inner diameter of the housing part and make an incorrect fuel level measurement. In addition, the vacuum-forming state of the casing part protection should also be evaluated in this mechanical filtration method. There should also be holes on the housing part with the same dimensions of the holes drilled to ensure the entry of fuel into the closed volume, as well as in areas where the maximum fuel level is (Figure 10).

Figure 10: Damper Breathing Hole

Otherwise, if there is no hole drilled on the top side, there will be no air intake into the closed volume, as the fuel level decreases, the fuel level in the closed volume will decrease very slowly, that is, it will vacuum. In this case, incorrect level measurement information will be read from the float.

III. RESULTS

As a result of the unprotected design of the float level measurement part on the float together with the initial design studies, it was found in the analysis and design processes that it was very affected by the turbulence that occurred in the fuel tank. In particular, it has been found that the turbulence level is too high in models with complex tank geometry (asymmetric), and when the vehicle is accelerated suddenly, the in-tank fuel liquid hits the float part with a shock effect.

In such cases floatin too much upward/downward moves and hence the lack of sensitivity in the measurement of level and faulty measurements by making vehicle electronic control unit (ECU) that sends the wrong level of analysis and design information in the environment have been identified. This incorrect information gives the user incorrect fuel level display information on the vehicle ECU, but it can also cause the hand on the level indicator to move up/down continuously. This error mode a delay can be created using the ‘delay’ function on the software on the car ECU. In this case, an intermediate measurement is made not by receiving continuous data from the float, but by dec decelerating it for the duration of the ‘delay’. Thanks to this method, the movements of the float part can be deafened, albeit somewhat. However, in the deafening technique performed with this method, the float can also give incorrect level measurement information to the vehicle ECU in some cases. Because, no matter how infrequently the measurement frequency is performed, in extremely turbulent situations, the up/down movement of the float can be captured at the wrong position point and incorrect level measurement information can be sent to the ECU.

The raw material details of the designed damper unit part are also important. Because it will constantly come into contact

with the fuel fluid, a raw material with a high corrosion resistance should also be selected. In addition, the inner diameter measurement and outer diameter measurement of the damper unit part will be designed depending on the float and float sensor head, so the wall thickness will also be thin. (december the range of 1-2 mm. In this context, it is appropriate to prefer aluminum raw materials, preferably aluminum 6061 or 6063 (tempered at T6 level) supports the design in a rigid structure[12].

IV. CONCLUSION

The above mentioned design conditions will be examined with real-time experimental studies to be carried out. By activating different acceleration and shaking simulations, the movement of the liquid will be monitored. The behavior of the liquid contained in the tank in different modes and the measurement results obtained will be compared. The results obtained will be included in subsequent studies.

ACKNOWLEDGMENT

This work is supported by Pamukkale University Scientific Research Projects(2020FEBE053) and NESAN Automotive Company

REFERENCES

[1] http://www.inverterlc.net/sens%C3%B6rler/seviye_%C3%B6l%C3%A7erler.html
[2] ÖLÇME TEKNİĞİ DERS NOTLARI, ONDOKUZ MAYIS ÜNİVERSİTESİ MAKİNA MÜHENNDİSLİĞİ BÖLÜMÜ,SAMSUN
[3] YUMUTRACI, M., & YABANOVA, İ. (2018). Sıvı Seviye Sensörlerinin İncelenmesi ve Su Seviyesi Ölçümü Uygulaması. AKÜ FEMÜBİD 18 (2018) 015202 (201- 207), 18, 201–207.
[4] ŞAHBAZLI, R. (2017). SU TANKLARINDA SIVI SEVİYE KONTROL SİSTEMİNİN GELİŞTİRİLMESİ.
[5] TOPÇU, E. E., KILIÇ, E., & ÇAVDAR, K. (2017). Bir Binek Araç Yakıt Tankının Çalkalanma Davranışının Deneysel İncelenmesi. Afyon Kocatepe University Journal of Sciences and Engineering, 17(1), 292–301. https://doi.org/10.5578/fmbd.54008
[6] KESKİN, M., & SARIBAŞ, D. (2017). Container Level Measurement Methods and Testing an Ultrasonic Level Sensor. International Advanced Researches & Engineering Congress-2017, November.
[7] KILIÇ, E. (2015). TAŞIT YAKIT DEPOSUNDA ÇALKALANMA OLAYININ ANALİZİ.
[8] ADIYAN, A. (2012). Sıvı Seviye Kontrolü için Scada Sistem Tasarımı.
[9] CEYLAN, İ. (2007). Mekanik Seviye Ölçüm Cihazı Tasarımı. 68–70.
[10] ARTAN, M., SOYDEMİR, M. U., & ŞAHİN, S. (2020). ARM Based Hybrid Measurement System Design for Liquid Level Measurement with High Accuracy under Vibrating Case. Avrupa Bilim ve Teknoloji Dergisi Özel Sayı, S. 381-388, Ağustos 2020, August, 381–388. https://doi.org/10.31590/ejosat.7802632
[11] https://www.gentekelektronik.com.tr/ultrasonik-seviye-sensoru/
[12] (https://www.kloecknermetals.com/blog/comparing-6061-vs-6063-aluminum/)

Evaluation of Free Vibration Analysis of EPS Filled Syntactic Foam Core

K. Ç. ÇIBIKÇI[1], M. F. ŞANSVEREN[2] and M.YAMAN[2]

[1] Erzincan Binali Yildirim University, Erzincan /Turkey, kubra.cibikci@erzincan.edu.tr
[2]Atatürk University, Erzurum /Turkey, f.sansveren@atauni.edu.tr
[2]Atatürk University, Erzurum /Turkey, myaman@atauni.edu.tr

Abstract **- Sandwich structures using foam as core material are widely used in engineering applications such as aircraft, automotive, marine and construction. Therefore, for the design of these engineering applications is in need of free vibration analysis results. In this study, free vibration behavior of new designed EPS filled syntactic foam core was investigated with experimental approach. Syntactic foam core was prepared using epoxy resin, glass microballoons (GMBs) and expanded polystyrene (EPS). The influences of density on the free vibration performance for new designed the core were evaluated. The natural frequencies and damping ratios of the samples were investigated under boundary conditions as fixed-free. The vibration tests were performed with the PULSE vibration measurement system using the impulse frequency response technique. Finally, the natural frequencies and damping ratio of EPS filled syntactic foam core were obtained and discussed.**

Keywords **- EPS filled syntactic foam, vibration analysis, natural frequencies, damping.**

I. INTRODUCTION

Sandwich structure is a type of composite material produced by placing a light core material between two thin and hard skin [1-2]. The most important feature of sandwich structures is to obtain the desired material by changing the core, thickness and material according to the needs. Different core designs can be made into sandwich structures to achieve the desired vibration behavior in the system [3]. Commonly used core materials are honeycomb [4], wood, open-closed cell foams, syntactic foams [5-6]. Sandwich structures are widely used in engineering applications such as aircraft, automotive, marine and construction [7]. Syntactic foams, low density, high acoustic and moisture insulation, insulating etc. with its properties, it has gained great importance as a core material in sandwich structures for these engineering applications [8-9].

Syntactic foams can be used as core material in sandwich structures due to their low density and high specific strength [10]. Syntactic foams are materials obtained by dispersing hollow particles in a matrix material [11-12]. The hollow particles may be made of polymer, ceramic, carbon or metal [13]. The use of glass microballoons is the most common due to their lower cost and higher strength [14]. Thermoset resins such as epoxy, polyurethane, phenolic, are generally used as binders [13]. Density of syntactic foams consisting of glass microballoons and polymer is between 200 kg / m^3 and 800 kg / m^3 [15-16-17]. For this reason, two-phase syntactic foams are not suitable for use in applications where lightness is desired due to their relatively high densities. Microballoons are not effective to reduce density. Expanded polystyrene beads (EPS) can both effectively reduce the foam density and obtain high-strength foam [18].

The present paper reports the results of a research study on the free vibration analysis of syntactic foam cores made with an epoxy resin randomly dispersed hollow glass microballoons and expanded polystyrene beads (EPS). The effect of the varying density of the core material on free vibration was investigated experimentally.

II. MATERİAL AND METHOD

In this study, EPS filled syntactic foams, which can be used as a core for sandwich structures, has been studied. The microstructure of EPS filled syntactic foam includes three components: microballoons, matrix material (polymer) and expanded polystyrene beads (EPS). Hollow glass microballoons (GMBs) with a nominal density of 220 kg/m^3 were used for the preparation of EPS filled syntactic foam. The properties of hollow glass microballoon are listed in Table 1. Epoxy resin Araldite GY 9513 and hardener TETA were used as the matrix materials and the elastic constants and densities of the matrix material and hardener are given in Table 2. As seen in Figure 1, three types of expanded EPS beads were used. Syntactic foams were produced by slowly mixing the filler and binder to minimize gas bubbles, pouring the mixture into a mold, curing and finishing [13-19]. The EPS filled syntactic foam was compression molded using an aluminum mold of 305x130x40 mm^3. Foams were cured for 48 hours at ambient temperature [20].

Table 1: Physical properties of S22 microballoon.

Properties	Type of mikroballoon [a]
	S22
Average particle density (kg/m^3)	220
Diameter (μm)	35
Wall thickness (μm)	0,521
Radius ratio	0,970

[a] Supplied by 3M Corp., under the trade name S22 mikroballoons

Table 2: Elastic constants and densities of epoxy resin and hardener materials.

Material [b]	Density (kg/m^3)	Poisson's ratio	Young's modulus (GPa)
Epoxy resin	1130	0,35	1,652
Hardener	9810	-	-

[b] Supplied by HUNTSMAN Co., under the trade name 'Araldite GY 9513 and TETA'

Figure 1: EPS beads with the density of 10 kg/m^3, 18 kg/m^3, 30 kg/m^3, respectively.

Foams were produced using expanded polystyrene beads (EPS) in different density. Samples of different densities used in the experiments are shown in Figure 2. The samples for the testing were cut using diamond saw. The overall length of the testing samples was 210 mm and thickness of 10 mm. Density value was obtained by measuring the weight of fabricated test samples with a digital balance and the dimensions with a digital caliper. Dimension and measured density of the samples produced for the experiment are listed in Table 3.

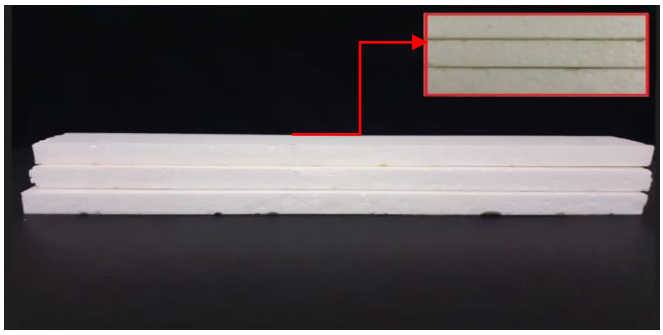

Figure 2: Samples of different densities used in the experiment.

Table 3: Structure parameters of samples used in the experiments.

Sample name	Thickness (mm)	Length (mm)	Width (mm)	Density (kg/m^3)
Epoxy	10	210	25	1130
Foam – I	10	210	25	948
Foam – II	10	210	25	469,02
Foam – III	10	210	25	482,06
Foam – IV	10	210	25	493,66

Note: Foam- I-syntactic foam with the GMBs density of 220 kg/m^3
Foam- II- syntactic foam with the EPS density of 10 kg/m^3
Foam- III- syntactic foam with the EPS density of 18 kg/m^3
Foam- IV- syntactic foam with the EPS density of 30 kg/m^3

Experimental results were obtained with the PULSE vibration measurement system (Brüel & Kjær Sound & Vibration Measurement A/S, Denmark), which is a computer-based multichannel analysis system. Vibration test system consisting of impact hammer, laser vibrometer and data recording system is shown in Figure 3. The test samples were excited with this impact hammer and the response of the samples to the effect was calculated using a laser vibrometer and the frequency response function (FRF) was obtained. In addition, the Fast Fourier Transform (FFT) algorithm is used to determine the natural frequencies by converting the time base to the frequency base. Using this non -destructive testing technique, damping rates and initial natural frequencies of specimens have been determined – based on the fixed-free boundary condition.

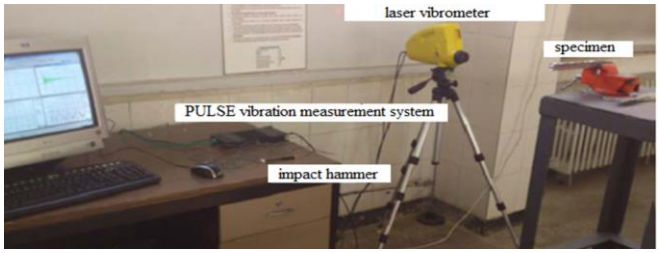

Figure 3: Experimental setup of the PULSE vibration measurement system.

The fixed ends of samples were fixed 80 mm inside the fixed. In addition, the samples were compressed with a constant torque of 8 Nm using a torque meter. During the experiments, the laser beam exposure distance and hammer excitation distance of all samples were kept constant. To ensure the reliability of the results, three samples of each samples type were prepared and free vibration tested. In addition, each samples was tested 3 times and averages were taken of the values obtained.

III. Result and Discussion

In this study, the vibration analysis behavior of EPS filled syntactic foam was investigated experimentally. Experiment were performed when samples are fixed at one end and free at the other end. In the study, analyzes were made for samples with different density. Also, samples of resin with hollow microballoons and only samples of resin without inclusion of hollow microballoons and expanded polystyrene beads (EPS) were made for comparative use. The obtained results are given in Table 4. The natural frequency and damping ratio of syntactic foam are also graphically shown in Figure 4 (a, b) and Figure 5 shows the variation of the damping ratio, natural frequency and density for produced samples.

According to the results shown in Figure 4 (a), if the density of the expanded polystyrene bead (EPS) used increases, the natural frequencies decrease, which can be easily explained by the natural frequency formula. As can be seen in Figure 4 (b), the damping ratio of the foam samples does not change significantly. The percentage damping ratio value and natural frequency value of the non-reinforced epoxy samples was 1,37 and 127, respectively. It was seen that there was a significant decrease in the damping ratio of

the samples as the reinforcement material was added to the neat epoxy.

In future studies, numerical studies can be carried out for verification and comparison purposes, as well as by changing the core thicknesses and increasing the density diversity, the analyzes can be made safer.

Table 4: Experimentally determined natural frequency and damping ratio of the samples.

Sample name	1st natural frequency (Hz)	1 st damping ratio (%)
Epoxy	127,00	1,37
Foam - I	140,67	1,13
Foam - II	158,00	1,10
Foam - III	149,00	1,07
Foam - IV	148,67	1,09

(a)

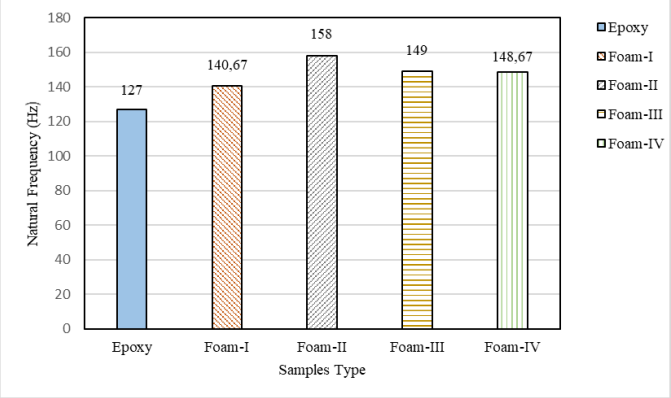

(b)

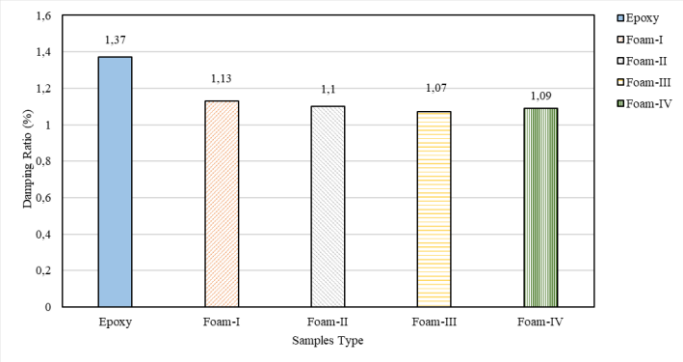

Figure 4: (a) Natural frequencies of syntactic foams in fixed-free boundary conditions (b) damping ratios of the syntactic foams in fixed-free boundary conditions.

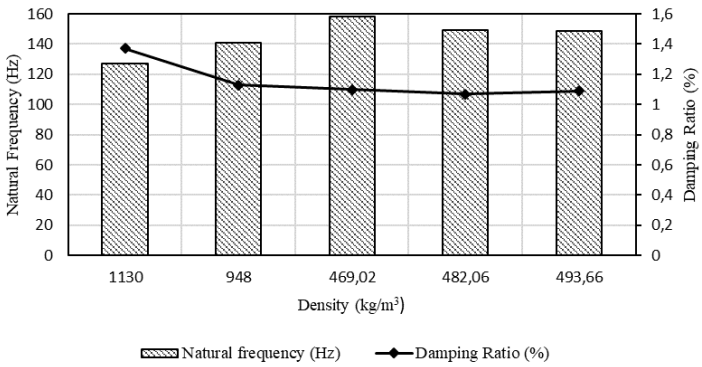

Figure 5: Variation of natural frequency, damping ratio and density values of different samples.

REFERENCES

[1] E. Ahmadi, A. Atrian, J. J. Fesharaki, H. Montazerolghaem, and S. Saberi, "Experimental and numerical assessment of high-velocity impact behavior of syntactic foam core sandwich structures," *Eur. J. Mech. A/Solids*, vol. 90, no. June, p. 104355, 2021, doi: 10.1016/j.euromechsol.2021.104355.

[2] A. Petras, "Design of sandwich structures," *Proc. Est. Acad. Sci.*, pp. 4–8, 1999, [Online]. Available: https://www.repository.cam.ac.uk/handle/1810/236995.

[3] S. Gürgen and M. A. Sofuoğlu, "Vibration attenuation of sandwich structures filled with shear thickening fluids," *Compos. Part B Eng.*, vol. 186, no. October 2019, 2020, doi: 10.1016/j.compositesb.2020.107831.

[4] J. Kee Paik, A. K. Thayamballi, and G. Sung Kim, "Strength characteristics of aluminum honeycomb sandwich panels," *Thin-Walled Struct.*, vol. 35, no. 3, pp. 205–231, 1999, doi: 10.1016/S0263-8231(99)00026-9.

[5] E. K. Njim, M. Al-Waily, and S. H. Bakhy, "A review of the recent research on the experimental tests of functionally graded sandwich panels," *J. Mech. Eng. Res. Dev.*, vol. 44, no. 3, pp. 420–441, 2021.

[6] R. D. Palacio, P. J. Negret, J. Velásquez-Tibatá, and A. P. Jacobson, *济無No Title No Title No Title*. 1967.

[7] P. M. Schubel, J. J. Luo, and I. M. Daniel, "Low velocity impact behavior of composite sandwich panels," *Compos. Part A Appl. Sci. Manuf.*, vol. 36, no. 10 SPEC. ISS., pp. 1389–1396, 2005, doi: 10.1016/j.compositesa.2004.11.014.

[8] O. Rahmani, S. M. R. Khalili, K. Malekzadeh, and H. Hadavinia, "Free vibration analysis of sandwich structures with a flexible functionally graded syntactic core," *Compos. Struct.*, vol. 91, no. 2, pp. 229–235, 2009, doi: 10.1016/j.compstruct.2009.05.007.

[9] N. Gupta, C. S. Karthikeyan, S. Sankaran, and Kishore, "Correlation of processing methodology to the physical and mechanical properties of syntactic foams with and without fibers," *Mater. Charact.*, vol. 43, no. 4, pp. 271–277, 1999, doi: 10.1016/S1044-5803(99)00039-X.

[10] S. Waddar, J. Pitchaimani, M. Doddamani, and E. Barbero, "Buckling and vibration behaviour of syntactic foam core sandwich beam with natural fiber composite facings under axial compressive loads," *Compos. Part B Eng.*, vol. 175, pp. 1–37, 2019, doi: 10.1016/j.compositesb.2019.107133.

[11] G. Hu and D. Yu, "Tensile, thermal and dynamic mechanical properties of hollow polymer particle-filled epoxy syntactic foam," *Mater. Sci. Eng. A*, vol. 528, no. 15, pp. 5177–5183, 2011, doi: 10.1016/j.msea.2011.03.071.

[12] K. Shahapurkar, C. D. Garcia, M. Doddamani, G. C. Mohan Kumar, and P. Prabhakar, "Compressive behavior of cenosphere/epoxy syntactic foams in arctic conditions," *Compos. Part B Eng.*, vol. 135, no. October 2017, pp. 253–262, 2018, doi: 10.1016/j.compositesb.2017.10.006.

[13] E. M. Wouterson, F. Y. C. Boey, X. Hu, and S. C. Wong, "Specific properties and fracture toughness of syntactic foam: Effect of foam microstructures," *Compos. Sci. Technol.*, vol. 65,

no. 11–12, pp. 1840–1850, 2005, doi: 10.1016/j.compscitech.2005.03.012.

[14] M. Ashby, *Materials selection in mechanical design: Fourth edition*, vol. 9780080952239. 2010.

[15] M. Porfiri and N. Gupta, "Effect of volume fraction and wall thickness on the elastic properties of hollow particle filled composites," *Compos. Part B Eng.*, vol. 40, no. 2, pp. 166–173, 2009, doi: 10.1016/j.compositesb.2008.09.002.

[16] L. Wang, X. Yang, J. Zhang, C. Zhang, and L. He, "The compressive properties of expandable microspheres/epoxy foams," *Compos. Part B Eng.*, vol. 56, pp. 724–732, 2014, doi: 10.1016/j.compositesb.2013.09.030.

[17] C. S. Karthikeyan, S. Sankaran, and Kishore, "Elastic behaviour of plain and fibre-reinforced syntactic foams under compression," *Mater. Lett.*, vol. 58, no. 6, pp. 995–999, 2004, doi: 10.1016/j.matlet.2003.08.012.

[18] Q. Yu, Y. Zhao, A. Dong, and Y. Li, "Mechanical properties of EPS filled syntactic foams prepared by VARTM," *Compos. Part B Eng.*, vol. 136, pp. 126–134, 2018, doi: 10.1016/j.compositesb.2017.07.053.

[19] S. J. Park, F. L. Jin, and C. Lee, "Preparation and physical properties of hollow glass microspheres-reinforced epoxy matrix resins," *Mater. Sci. Eng. A*, vol. 402, no. 1–2, pp. 335–340, 2005, doi: 10.1016/j.msea.2005.05.015.

[20] N. Gupta, Kishore, E. Woldesenbet, and S. Sankaran, "Studies on compressive failure features in syntactic foam material," *J. Mater. Sci.*, vol. 36, no. 18, pp. 4485–4491, 2001, doi: 10.1023/A:1017986820603.

Optimization of Cutting Parameters Affecting Cutting Force and Surface Roughness in Machining of AISI P20 Die Steel

M.AKGÜN[1] and B. ÖZLÜ[1]

[1] Aksaray University, Aksaray/Turkey,
mahirakgun@aksaray.edu.tr – barisozlu@aksaray.edu.tr

Abstract **- This study focuses on optimizing cutting parameters effective on cutting force (Fc) and surface roughness (Ra) in the machining of AISI P20 steel. The turning experiments have been performed in CNC lathe at three different cutting speeds (Vc) (120, 180, and 240 m/min), three different feed rates (f) (0.12 0.21 and 0.3 mm/rev), and three different depths of cut (a) (0.4, 0.8, and 1.2 mm) according to Taguchi L9 orthogonal array. The effect levels of the cutting parameters on Fc and Ra have been determined with analysis of variance (Anova). The analysis results indicate that the depth of cut is the most significant parameter affecting Fc while the feed rate is the most significant parameter affecting Ra. Moreover, the result analysis shows that cutting speed of 240 m/min, feed rate of 0.12 mm/rev, and depth of cut of 0.4 mm) factor levels were the optimum cutting parameters for the output parameters (Fc and Ra).**

Keywords **– AISI P20 steel, Cutting Force, Surface Roughness**

I. INTRODUCTION

In today's conditions, many mass-produced parts are created using molds and mold elements. In particular, considering the use of thermoplastics, the importance of the molding sector is understood. Moreover, the quality, cost and lead times of molds are critical to the economics of many industries. For example, in the automotive industry, it affects produce a large number of components, subassemblies, and assemblies. Therefore, it focuses on process modeling, rapid prototyping, rapid tooling, high-speed cutting and optimized toolpath creation for hard machining with the developing technology in this field [1,2].

AISI P20 steel, which is plastic mold steel, is used in applications such as plastic extrusion, plastic injection, and blow molding. The very important properties of these steels are hardness, strength, high toughness, very good polishability, weldability, and suitability for nitration. However, the formation of built-up edge (BUE) in the machining process of this steel seriously affects the cutting tool life and production efficiency [3]. Moreover, it is difficult to machine these steels, which are alloyed with strong carbide forming elements such as Mo and Cr [4]. on the other hand, in the mold manufacturing industry, it is desired to produce the molds with the best surface quality in a short time. Therefore, in order to obtain high cutting performance in mold production, optimum levels of cutting parameters should be selected. However, cutting conditions are generally determined by an operator's experience or practical knowledge [5]. Tooling cost and time loss are increased in this way. For these reasons, it is very important to define the most suitable cutting conditions in terms of surface quality and cutting forces, which are essential machinability criteria for production efficiency [6-9].

In this study, the machinability of AISI P20 mold steel, which is widely used in the mold industry, was evaluated in terms of main cutting force (Fc) and surface roughness (Ra). Machinability tests were carried out on a CNC lathe according to the Taguchi L9 index. S/N analysis and analysis of variance were used to determine ideal cutting conditions and the effects of cutting parameters on output parameters (Fc and Ra), respectively.

II. MATERIALS AND METHODS

In the study, AISI P20 steel with a diameter of 30 mm and a length of 300 mm was used as the workpiece material. Table 1 shows the chemical composition of the workpiece material used in the experiments. Turning experiments were performed on Johnford TC-35 CNC lathe under dry cutting conditions. Kistler 9257A type dynamometer and equipment's were used to measure the main cutting force (Fc).

Table 1: Chemical composition (%) of the workpiece material.

Elements	C	Si	Mn
Wt.%	0.1	0.3	2.5
	Cr	Ni	Mo
	3.00	1.00	0.3

In the turning experiments, carbide cutting tools, which were coated with $TiCN/Al_2O_3$ using the CVD method and produced by Kennametal in KCM15 quality and CNMG120408UP geometry, were used. The turning parameters and levels used in the experiments are given in Table 2.

Table 2: Cutting parameters and levels.

Code	Cutting Parameters	Units	Level 1	Level 2	Level 3
A	Cutting speed (Vc)	(m/min)	120	180	240
B	Feed rate (f)	(mm/rev)	0.12	0.21	0.3
C	Depth of cut (ap)	(mm)	0.4	0.8	1.2

Roughness measurements were made on the machined surfaces using the MAHR-Perthometer-M1 portable surface roughness (Ra) device. After each measure, the workpiece was rotated 90º on its axis, and the average Ra value was determined by taking the arithmetic average of the four measurements.

III. EXPERIMENTAL DESIGN AND OPTIMIZATION

In the manufacturing industry, different optimization methods are used in material processing to minimize product costs and increase efficiency [10]. Taguchi method, which is one of the optimization methods, is used to reduce the product development time and the relative costs [11]. In this study, Taguchi method was used in designing the experiments and determining the optimum cutting parameters. In this context, turning experiments were designed according to Taguchi's L9 (33) orthogonal array and the signal-to-noise (S/N) ratio was calculated to determine the optimum cutting parameters [12]. The "smallest best" approach in Eq. (1) was used to calculate the signal-to-noise (S/N) ratios because it was aimed to determine the optimum cutting parameters to obtain the lowest levels of Fc and Ra in the study.

$$n = \frac{S}{N} = -10 \log\left(\frac{1}{n}\sum_{i=1}^{n} y_i^2\right) \quad (1)$$

Moreover, analysis of variance (ANOVA) was applied to determine the effects of cutting parameters on the main cutting force (Fc) and surface roughness (Ra) values.

IV. RESULTS AND DISCUSSIONS

The values of the main cutting force and surface roughness obtained as a result of machining AISI P20 steel in different cutting parameters are given in Table 3. Moreover, the changes of Fc and Ra values depending on the cutting parameters are presented in Figure 1 and Figure 2.

When Figure 1 is examined, it is seen that the main cutting force increases depending on the increase in the feed rate in the machining of AISI P20 steel. The cutting force values obtained from the experiments carried out at 120 m/min cutting speed, 0.8 mm cutting depth, and three different feed speeds were compared. Consequently, the cutting force values increased by 30% and 45%, respectively, at 0.21 mm/rev feed rate and 0.30 mm/rev feed rate according to 0.12 mm/rev feed rate. It is thought that this situation is caused by the increase in the loads on the cutting tool as a result of the increase in the chip cross-section due to the increase in the feed rate [13].

Table 3: Experiment results.

Id No	Experiment Code	Fc (N)	SN-Fc (N)	Ra (µm)	SN-Ra (µm)
1	$A_1B_1C_1$	95.00	-39.5545	0.550	5.1927
2	$A_1B_2C_2$	160.50	-44.1095	0.670	3.4785
3	$A_1B_3C_3$	210.85	-46.4795	0.765	2.3267
4	$A_2B_1C_2$	148.24	-43.4193	0.620	4.1521
5	$A_2B_2C_3$	192.05	-45.6683	0.720	2.8533
6	$A_2B_3C_1$	115.90	-41.2817	0.765	2.3267
7	$A_3B_1C_3$	138.00	-42.7976	0.650	3.7417
8	$A_3B_2C_1$	87.00	-38.7904	0.500	6.0206
9	$A_3B_3C_2$	145.00	-43.2274	0.780	2.1581

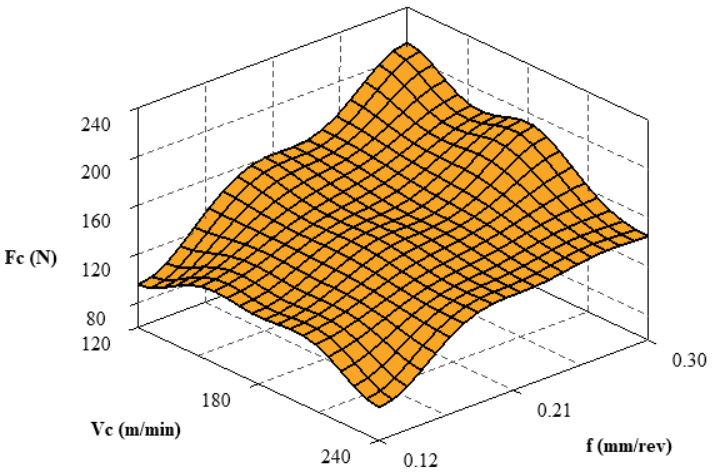

Figure 1: Effect of cutting parameters on Fc.

The S/N response table for the input parameters (Fc and Ra) is given in Table 4. According to Table 4, the ideal levels of cutting parameters for the Fc were determined as A cutting speed 240 m/min (level 3), B feed rate 0.12 mm/rev (level 1) and C depth of cut 0.4 mm (level 1). The Fc value was measured as 78N in the turning experiment performed in these parameters. Moreover, Analysis of variance was performed to determine the effects of cutting parameters on the main cutting force (Fc) and surface roughness (Ra) values and analysis result is given in Table 5. According to Table 5, the most critical parameter affecting the main cutting force was the depth of cut (ap), with an additive rate (PCR) of 74.6%.

When Figure 2 is examined, it is seen that the surface roughness values decrease with the increase in the cutting speed, but increase with the increase in the feed rate. The surface roughness values varied between 0.86-2.01µm. In particular, the lowest surface roughness value was measured as 0.412 µm as a result of the experiment performed at the highest level of cutting speed at the lowest levels of feed rate and depth of cut. This is a good result regarding the desired surface quality in the production of molds and mold elements.

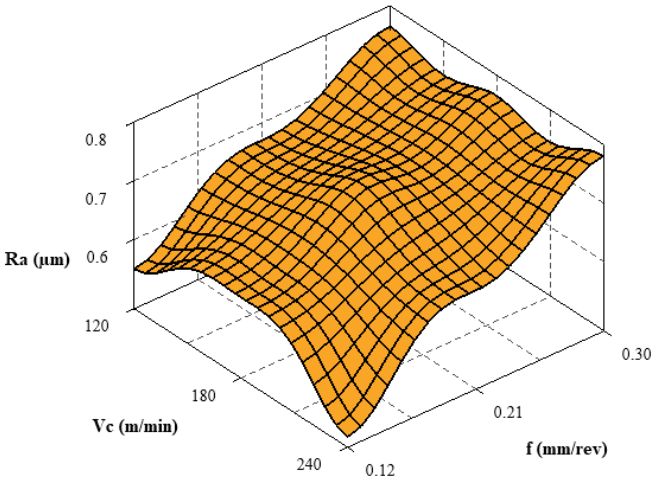

Figure 2: Effect of cutting parameters on Ra.

According to Table 4, the ideal levels of cutting parameters for the Ra were determined as A cutting speed 240 m/min (level 3), B feed rate 0.12 mm/rev (level 1) and C depth of cut 0.4 mm (level 1). The Ra value was measured as 0.412 µm in the turning experiment performed in these parameters. According to Table 5, the most critical parameter affecting the Ra was the feed rate (f), with an additive rate (PCR) of 59.39%. In a similar study, Gupta et al. reported that cutting speed of 160 m/min, nose radius of 0.8 mm, feed of 0.1 mm/rev, depth of cut of 0.2 mm and the cryogenic environment were the most favorable cutting parameters for high-speed CNC turning of AISI P-20 tool steel [14].

Table 4: Answer table for Fc and Ra.

Code	Factors	Level 1	Level 2	Level 3	Delta	Rank
Fc						
A	Vc	-43.38	-43.46	**-41.61**	1.85	2
B	f	**-41.92**	-42.86	-43.66	1.74	3
C	ap	**-39.88**	-43.59	-44.98	5.11	1
Ra						
A	Vc	3.666	3.111	**3.973**	0.863	3
B	f	**4.362**	4.117	2.271	2.092	1
C	ap	**4.513**	3.263	2.974	1.539	2

Table 5: Variance results for Fc and Ra.

Factors	DF	Seq SS	Adj MS	F-Value	P-Value	Contribution (%)
Fc						
Vc	2	1868.4	934.18	11.11	0.083	13.80
f	2	1403.2	701.61	8.35	0.107	10.36
ap	2	10103.6	5051.78	60.10	0.016	74.60
Error	2	168.1	84.05	-	-	1.24
Total	8	13543.2	-	-	-	100.00
Ra						
Vc	2	0.00533	0.00266	0.7	0.588	6.77
f	2	0.04682	0.02341	6.16	0.140	59.39
ap	2	0.19072	0.00953	2.51	0.285	24.19
Error	2	0.00760	0.00380	-	-	9.65
Total	8	0.07883	-	-	-	100

V. CONCLUSION

In this study, an experimental investigation was performed to analyze the effects of the cutting parameters on surface roughness (Ra) and cutting force (Fc) in the machining AISI P20 steel. Moreover, the optimum cutting conditions were determined by the Taguchi method. The following conclusions may be drawn from this study:

- Generally, with increasing feed rate, the surface roughness and the main cutting force (Fc) values were increased.
- According to the S/N ratios, it was concluded that the A3B1C1 (cutting speed 240 m/min, feed rate 0.12 mm/rev, and depth of cut 0.4 mm) factor levels were the optimum cutting parameters for the main cutting force and surface roughness. In turning experiments performed at optimum cutting parameters, the lowest Fc and Ra values were obtained as 78N and 0.412 µm, respectively.
- The variance results indicate that the depth of cut was the parameter affecting the main cutting force while the feed rate was the most significant factor affecting surface roughness with a percentage contribution of 74.6% and 59.39%, respectively.

REFERENCES

[1] Altan, T., Lilly, B. & Yen, Y. C. Manufacturing of Dies and Molds. CIRP Ann. 50, 404–422 (2001).
[2] Senevirathne, S. W. M. A. I. & Punchihewa, H. K. G. Reducing surface roughness by varying aerosol temperature with minimum quantity lubrication in machining AISI P20 and D2 steels. Int. J. Adv. Manuf. Technol. 94, 1009–1019 (2018).
[3] Ravi, S. & Gurusamy, P. Cryogenic machining of AISI p20 steel under liquid nitrogen cooling. Mater. Today Proc. 37, 806–809 (2021).
[4] Demir, H., Gündüz, S. & Erden, M. A. Influence of the heat treatment on the microstructure and machinability of AISI H13 hot work tool steel. Int. J. Adv. Manuf. Technol. 95, 2951–2958 (2018).
[5] Aslan, D. & Budak, E. Semi-analytical Force Model for Grinding Operations. Procedia CIRP 14, 7–12 (2014).
[6] Zeilmann, R. P., Nicola, G. L., Vacaro, T., Teixeira, C. R. & Heiler, R. Implications of the reduction of cutting fluid in drilling AISI P20 steel with carbide tools. Int. J. Adv. Manuf. Technol. 58, 431–441 (2012).
[7] Outeiro, J. C. Optimization of Machining Parameters for Improved Surface Integrity of AISI H13 Tool Steel. in Machines et Usinage a Grande Vitesse (MUGV) (2012).
[8] Kıvak, T. Optimization of surface roughness and flank wear using the Taguchi method in milling of Hadfield steel with PVD and CVD coated inserts. Measurement 50, 19–28 (2014).
[9] Kara, F. & Öztürk, B. Comparison and optimization of PVD and CVD method on surface roughness and flank wear in hard-machining of DIN 1.2738 mold steel. Sens. Rev. 39, 24–33 (2019).
[10] Nas, E. & Özbek, N. A. Optimization of the Machining Parameters in Turning of Hardened Hot Work Tool Steel Using Cryogenically Treated Tools. Surf. Rev. Lett. 1950177, (2019).
[11] Palanikumar, K. Experimental investigation and optimisation in drilling of GFRP composites. Measurement 44, 2138–2148 (2011).
[12] Asiltürk, İ. & Akkuş, H. Determining the effect of cutting parameters on surface roughness in hard turning using the Taguchi method. Measurement (2011) doi:10.1016/j.measurement.2011.07.003.

[13] Özlü, B., Demir, H. & Türkmen, M. The effect of mechanical properties and the cutting parameters on machinability of AISI 5140 steel cooled at high cooling rates after hot forging. Politek. Derg. 22, 879–887 (2019).
[14] Gupta, A., Singh, H. & Aggarwal, A. Taguchi-fuzzy multi output optimization (MOO) in high speed CNC turning of AISI P-20 tool steel. Expert Syst. Appl. 38, 6822–6828 (2011).H. Poor, *An Introduction to Signal Detection and Estimation*. New York: Springer-Verlag, 1985.
[15] S. Chen, B. Mulgrew, and P. M. Grant, "A clustering technique for digital communications channel equalization using radial basis function networks," *IEEE Trans. Neural Networks*, vol. 4, pp. 570–578, July 1993.
[16] G. R. Faulhaber, "Design of service systems with priority reservation," in *Conf. Rec. 1995 IEEE Int. Conf. Communications*, pp. 3–8.
[17] J. Williams, "Narrow-band analyzer (Thesis or Dissertation style)," Ph.D. dissertation, Dept. Elect. Eng., Harvard Univ., Cambridge, MA, 1993.
[18] *Motorola Semiconductor Data Manual*, Motorola Semiconductor Products Inc., Phoenix, AZ, 1989.
[19] R. J. Vidmar. (1992, August). On the use of atmospheric plasmas as electromagnetic reflectors. *IEEE Trans. Plasma Sci.* [Online]. *21(3).* pp. 876—880. Available: http://www.halcyon.com/pub/journals/21ps03-vidmar

INVESTIGATION ON REDUCING FUEL CONSUMPTION OF A TRUCK BY ADDING AERODYNAMICS STRUCTURES

N.VURGUN[1] and T.DAGDEVIR[1]

[1] Erciyes University, Kayseri/Turkey, nazmivrgn@gmail.com
[1]Erciyes University, Kayseri/Turkey, toygun@erciyes.edu.tr

Abstract - **In this study, numerical analyzes were carried out to both investigate and develop the aerodynamic characteristic of a truck by developing different aerodynamic structures by using computational fluid dynamic software. The investigated truck is selected as Mercedes Benz Actros, and the model is considered in 1:40 scale for experimental smoke test. Boundary conditions are arranged according to the scale. The combinations of the structures such as top deflector (TD), rear side wing (RSW) and boat tail (BT) are considered to reduce the fuel consumption of the truck in the study. As a result, the all considered structures on the truck show good result for reducing the fuel consumption. The results showed that the influence of the structures is CTD, BT and CRSW in ascending order. The numerical results are supported with conducting the smoke test.**

Keywords - **Fuel consumption, Drag coefficient, Aerodynamics design of the truck**

I. INTRODUCTION

Along with the sheet metal processing technology, which showed a rapid development as a result of the industrial revolution, important breakthroughs were made in technology and an important development was achieved in automotive technology. With the developing automotive technology, the speed and load carrying capacity of the vehicles have increased and the transportation time between distances has been shortened. The use of fossil fuel for the vehicles in the world has been increasing day by day. While there were 300 million automobiles in the 1970s, this number reaches to 1.3 billion today and nearly 100 million automobiles are still being produced daily. In addition, the fossil fuel reserves, which have limited reserves in the world, will run out in a few decades due to increased consumption, resulting in an increase in oil prices and global crises. Therefore, designers have been worked on aerodynamic designs in order to both reduce fuel consumption and enable the vehicle to reach higher speeds with lower fuel consumption.

The drag coefficient (C_d), which was between 0.80 ~ 1.00 in the early examples of vehicles, varies between 0.20 ~ 0.30 in passenger vehicles today. Aerodynamic improvements provide both more efficient fuel use and a quieter driving experience at high speeds in vehicles. The turbulence that develops due to the flow streams on the vehicle creates noise inside the vehicle. Today, many studies are carried out to improve the aerodynamics of the vehicle. Since wind tunnel tests require high cost and experience, a large part of the design is processed by CFD analysis [1-2].

In a study by Katz [3], in order to investigate the effect of downforce of racing vehicles on vehicle performance, front wing, rear spoiler, lower vortex generators with aerodynamic effects on the vehicle were designed and the changes in angle of attack and dimensional ratios were compared by analyzing them with the finite volume method. As a result of the research, it contributed to obtaining optimum lift and drag forces in the design of racing vehicles. In the study "Modelling the aerodynamic efficiency of a passenger car" by Ozen [4], the aerodynamic forces formed on the vehicle due to the air flow around the vehicle and the basic parameters forming these aerodynamic forces were investigated both experimentally and in the literature. In line with the data obtained, it was observed that the drag coefficient of the vehicle decreased by 2% and the road grip decreased significantly thanks to a diffuser channel opened to the rear of the vehicle.

Jeong Jae Kim et al. [5] developed 3 different designs that will be aerodynamically effective on the front cabin of a truck. These designs were simulated with the finite volume program and the relationship between the varying r/l ratios and the drag coefficient of the vehicle at varying Reynolds numbers was revealed. Current research in the literature has generally focused on improvements on a single point in vehicle design. For example, studies such as the contribution of only the cabin spoiler to the vehicle aerodynamics or the contribution of the differences in the vehicle rear diffuser design to the vehicle aerodynamics have been carried out.

In our study, unlike the existing studies in the literature, the combination of three different design structures on the truck are analyzed and compared according to the fuel consumption. Furthermore, the tunnel tests of the simplified and scaled model of the MERCEDES ACTROS model, which is a land vehicle, on the stock model were performed, and the drag coefficient values were obtained. These designs will be interpreted by comparing them with each other and a final design is recommended according to the fuel consumption.

II. Material And Method

A. Numerical Study

The analyses are performed by using student version of Ansys Fluent 16.0 as a computational fluid dynamics (CFD) software. The CFD software has advantageous due to low cost and saving time in the comparison with the experimental studies. The CFD uses the Navier-Strokes equations to calculate the pressure, velocity, density, and temperature of a moving fluid. The conservation equation of continuity (Eq. (1)) and the momentum (Eq. (2)) are solved by the CFD software [6].

Mass conservation equation:

$$\nabla(\rho \vec{V}) = 0 \tag{1}$$

Momentum conservation equation:

$$\nabla(\rho \vec{V} \vec{V}) = -\nabla P + \nabla(\mu \nabla \vec{V}) \tag{2}$$

A validation study is conducted to ensure the reliability of the numerical methodology. It is known that the Cd of a truck is in the range of 0.5-0.78 as shown in Fig. 1. [7]. In order to ensure the reliability of the numerical methodology, an analysis is run for the truck having one trailer. The model used in the study is selected as Mercedes-Benz Actross 2011 model truck, as modeled in Fig. 2a. The length (2416.18 mm), width (515.51 mm) and height (340.91 mm) of the truck is denoted with L, W and H, respectively.

The solution domain is arranged for preventing blockage effects with the dimensions, as depicted in the Fig. 2b. Velocity magnitude is given for the analysis as 2.5 km/h, which corresponds to 100 km/h for the truck in real size, since the model scale is 1:40. Outlet is defined as pressure outlet of 0 Pa, which means the outlet condition is same with atmospheric condition. The surface of the truck is defined as wall, which is no-slip boundary condition.

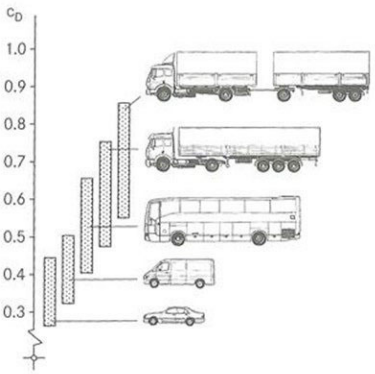

Figure 1: Drag coefficients for several vehicles. [7]

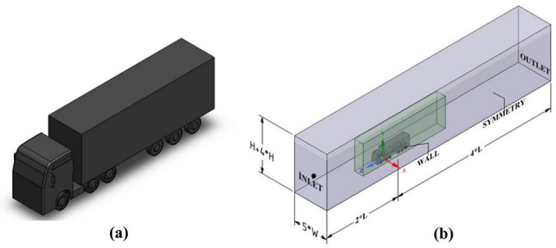

Figure 2: (a) The model truck and (b) solution domain and boundary types of the study.

The adopted mesh structure is given in Fig. 3. Patch independent was chosen as the mesh algorithm of the designed geometry and Tetrahedrons was chosen as the method. After the selected method and algorithm, mesh sizes in the model should be selected. Since the flow should be examined in detail in the regions close to the truck, it is necessary for the accuracy of the solution to be smaller in these regions than in the parts far from the vehicle. For this purpose, it is appropriate to determine the element size as 60 mm in regions that do not have any high impact on the vehicle, and as 30 mm in the region close to the vehicle.

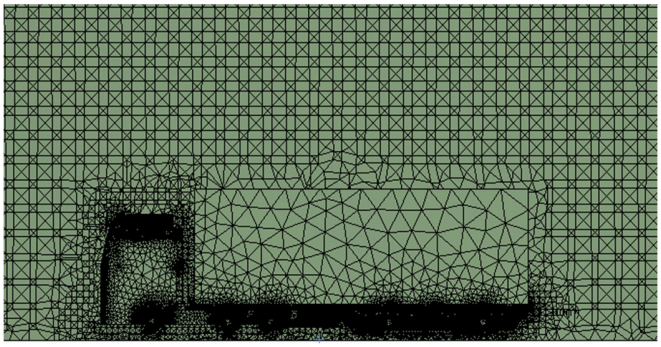

Figure 3: Mesh structure near the truck

In order to enhance the aerodynamic characteristic of the truck and reduce the drag force, three different aerodynamic parts are added onto the truck. The parts are top deflector (TD), rear side wing (RSW) and boat tail (BT) as illustrated in Fig. 4. The combinations of the parts investigated in the study are described in Table 1 whether the parts are used or not.

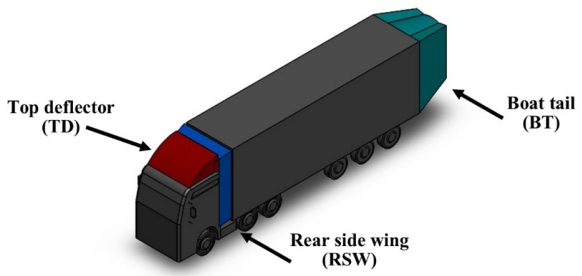

Figure 4: Used aerodynamics parts on the truck for the study.

Table 1: Description of the models whether the parts are used or not

Description	TD	RSW	BT
Model_000	Not used	Not used	Not used
Model_100	**Used**	Not used	Not used
Model_010	Not used	**Used**	Not used
Model_001	Not used	Not used	**Used**
Model_110	**Used**	**Used**	Not used
Model_011	Not used	**Used**	**Used**
Model_101	**Used**	Not used	**Used**
Model_111	**Used**	**Used**	**Used**

The SST k-ω turbulence model is used for the analysis to simulate the turbulent flow around the truck. Coupled which enables full pressure-velocity coupling is used for the algorithm scheme [6].

$$\frac{\partial}{\partial t}(\rho k)+\frac{\partial}{\partial x_i}(\rho k u_i)=\frac{\partial}{\partial x_j}(\Gamma_k \frac{\partial k}{\partial x_j})+\tilde{G}_k-Y_k+S_k \quad (3)$$

$$\frac{\partial}{\partial t}(\omega k)+\frac{\partial}{\partial x_i}(\rho \omega u_i)=\frac{\partial}{\partial x_j}(\Gamma_\omega \frac{\partial \omega}{\partial x_j})+\tilde{G}_\omega-Y_\omega+D_\omega+S_\omega \quad (4)$$

In these equations, $\tilde{G}_k$ represents the generation of turbulence kinetic energy due to mean velocity gradiens $\tilde{G}_\omega$ represents the generation of ω . Γ_k and Γ_ω represent the effective diffusivity of k and ω , respectively. Y_k and Y_ω represent the dissipation of k and ω due to turbulence, D_ω represents the cross-diffusion term. S_k and S_ω are user-defined source terms. Detail information is available in Fluent user guide [6].

B. Calculation of Fuel Consumption

In order to calculate the fuel consumption of the truck, the Cd (Eq. (5)) is calculated with data exported from the CFD software by surface integrals. Drag force, density of the air, projection area of the truck in direction of the flow and mean velocity of the air is represented with Fd, ρ, A and V, respectively. Methodology on calculating the fuel consumption (FC) is defined in the following equations from Eq. (6) to Eq. (9). Edrag represents the amount of energy which meets the drag force on the truck under the considered condition. D represents the distance traveled by the truck that is selected as 50,000 km. The net amount of energy (Enet) equals to Wdrag divided by efficiency of the truck (η) due to other losses such as thermodynamic losses, rolling losses by the tires, transmission loses, etc. is taken as 0.3 [8]. The amount of fuel (AF) is calculated with Eq. (8). The density (ρ_{fuel}) and the calorific value (CV) of the fuel and are taken as 0.80 kg/L and 4400 kj/kg, respectively [9],[10].
The price of fuel per liter (PF) is taken as 7.75 Turkish liras (TL). Finally, the fuel consumption (FC) is calculated with Eq. (9).

$$C_d=\frac{F_D}{\frac{1}{2}\rho A V^2} \quad (5)$$

$$E_{Drag}=F_D.D \quad (6)$$

$$E_{net}=\frac{E_{Drag}}{\eta} \quad (7)$$

$$AF=\frac{m_{fuel}}{\rho_{fuel}}=\frac{E_{net}/CV}{\rho_{fuel}} \quad (8)$$

$$FC=AF.PF \quad (9)$$

C. Smoke Test

In addition to numerical analysis, experimental smoke tests were conducted for the considered truck models, in order to observe the flow characteristic of the models. The truck models produced with a 3D printer is placed in a wind tunnel which is in similar physical conditions with the numerical solution domain.

III. Results and Discussions

Numerical analyses are conducted to reveal the drag coefficient and fuel consumption of various truck model combinations. The results obtained from the software are discussed model by model as in the following..

A. Model_000

A 1:40 scaled model of the truck model to be developed aerodynamically was drawn with CAD and meshing was performed. In order for the analysis result to be independent of the mesh, many different element numbers were tried and the error rate was adjusted not to exceed 5%. The results obtained from the software are given in Table 2. The C_d for the Model_000 is obtained as 0.76681. This result ensures that the numerical methodology is valid, since the C_d should be in the ranging from 0.5 to 0.78 stated by Chowdhury et al. [7].

Table 2: Results for the Model_000

Parameter found in the analysis	Value	Unit
Force by pressure	0.00144	[N]
Force by Viscous	0.00026	[N]
Total force	0.00170	[N]
C_d	0.76681	[-]
Annual fuel consumption	0.08080	[L/year]

As a result of the analysis, it is observed that the air flow leaving the upper part of the cabin of the vehicle creates a pushback force due to hitting the trailer. The air flow particles leaving here cause vortex formation between the cabin and the

trailer. As seen in Fig. 5. as a result of flow separation in the front cabin of the vehicle, an increase in speed occurs and the flow leaving here passes between the cabin of the vehicle and the trailer and creates turbulence here. As a result of the analysis, it is observed that the air flow leaving the upper part of the cabin of the vehicle creates a push back force due to hitting the trailer. The air flow particles leaving here cause vortex formation between the cabin and the trailer. The air flow flowing over the vehicle enters the negative pressure region formed in the rear region of the trailer during its transition to the rear region of the trailer. Air currents passing over the top of the trailer and the lower part of the vehicle collide in this negative pressure region and form a double scar. This vortex region shows a negative vacuum effect on the vehicle.

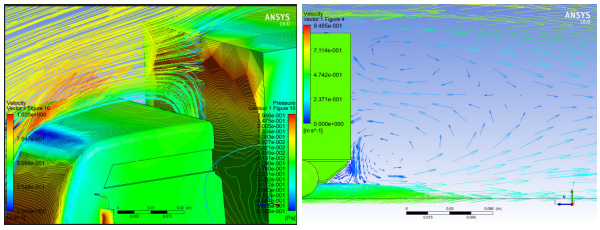

(a) (b)

Figure 5: Velocity vector contours around the Model_000 (a) on the truck cab and (b) back of the trailer.

B. *Model_100*

The first test to be made in aerodynamic development combinations is to direct the flow by regularizing the flow separation at the top of the cabin. For this purpose, a directing spoiler is designed on the cabin, starting from the point of departure of the current. As a design criterion, it is aimed to be at a curvature that will allow the flow to be directed and to be at a height that will prevent the separated flow from hitting the front of the trailer.

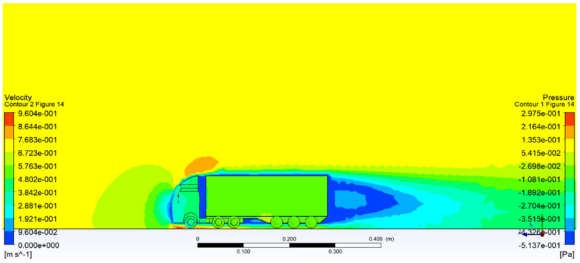

Figure 6: Velocity and pressure contours around the Model_100 side view.

As can be seen from the analysis, the aerodynamic "Top Deflector" (TD) added, as seen in Figure 7, prevents the flow separation in the upper part of the trailer and the direct impact of the vortex separated flow on the trailer. In Figure 8, it is seen that the velocity vectors hit the front of the trailer. Here, the front of the trailer behaves as if it were a flat plate and it reduced the speed of the air flow hitting it and created high pressure on the impact face at the point where the speed decreased. Here, the slowing air flow provided escape to the right, left, upper and lower regions with lower pressure. Low pressure (2,401e-001) was observed in the escape zones.

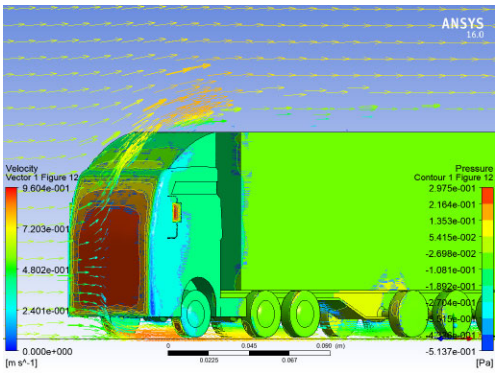

Figure 7: Velocity vector around the Model_100 ısometric view.

Table 3: Results for the Model_100

Parameter found in the analysis	Value	Unit
Pressure Force (N)	0.00113	[N]
Viscous	0.000306	[N]
Total	0.00143	[N]
Coefficient of pressure	0.50403	[-]
Viscous	0.13625	[-]
Total CD	0.64028	[-]
Improvement ratio	16.50%	[-]
Annual fuel consumption (L/year)	0.068162401	[L\year]

C. *Model_010*

One of the development combinations to be made to eliminate the aerodynamic deficiencies on the main model, as the second model, a piece that will close the intermediate area has been designed to prevent the region that passes between the cabin and the trailer of the truck and creates turbulent airflow there, as can be seen in Fig. 8.

Table 4: Results for the Model_010

Parameter found in the analysis	Value	Unit
Force by pressure	0.00129	[N]
Force by Viscous	0.00028	[N]
Total force	0.00157	[N]
Cd	0.70098	[-]
Improvement ratio	8.58%	[-]
Annual fuel consumption	0.074539801	[L/year]

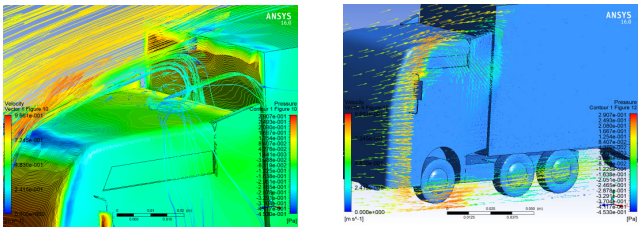

(a) (b)

Figure 8: Velocity and pressure gradients acting on the Model_010

and (b) air flow velocity vectors flowing from the side surface.

D. Model_110

Two different models have been designed in order to separate the current on the main model and to prevent the formation of vortex air flow between the cabinet. With these designed models, 8.5% and 16.5% improvement were achieved at a certain level. In this design, an aerodynamic design will be developed by using the combination of these two different combinations. As a result of the aerodynamic analysis, it was observed that the model's truck-top flow line was arranged and the vortex airflow escaping between the cabin and the trailer was prevented. As seen in Fig.9 in the Model_010 analysis of the flow behavior, it occurs as a result of the air flow hitting the trailer, and it is seen that the vortex formation is largely prevented and there is no flow separation. It is seen that the speed of the airflow hitting the front of the trailer almost approaches and the pressure is at the maximum value at this point. Low pressure is observed on the vehicle due to the slowing air flow in the front hood of the vehicle, escaping from the edges and increasing the flow rate in the edge regions.

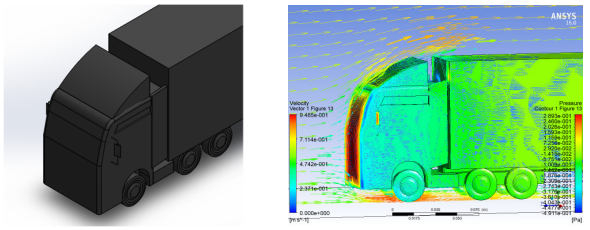

(a) (b)

Figure 9: (a) Model_110 cad model and (b) Velocity vector and pressure contour acting of the Model_110.

Table 5: Result for the Model_110

Parameter found in the analysis	Value	Unit
Force by pressure	0.00114	[N]
Force by Viscous	0.00030	[N]
Total force	0.00145	[N]
Cd	0.64831	[-]
Improvement ratio	15.45%	[-]
Annual fuel consumption	0.070523021	[L/year]

E. Model_001

As a result of the pressure drop in the trailer area, which is another problematic area on the vehicle, the drag force of the vehicle increases with the negative pressure that occurs as a result of the air flow coming from the lower and upper regions colliding and forming two vortexes. As a result of the researches carried out to solve this problem, it has been determined that the vortex region formed in the rear region of the vehicle is realized as far away from the vehicle body as possible, resulting in a decrease in the drag force. As a result of the design improvement trials, it was decided to add a nozzle-like aerodynamic part to the rear of the vehicle in the final design, which would make the vehicle resemble the drop geometry. As a result of the analysis, it has been determined that this design improves the vehicle aerodynamically. As seen in Fig.10. the formed swirl zone has been moved away from the back cover of the trailer by the length of the nozzle. In this way, the effect of the drag force that will be created by the vortex is prevented.

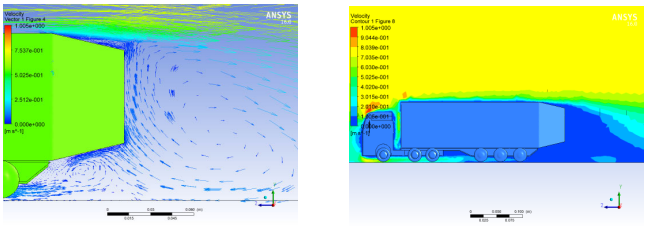

(a) (b)

Figure 10: (a) Velocity and pressure gradients acting on the aerodynamics part and (b) Velocity gradient.

Table 6: Result for the Model_001

Parameter found in the analysis	Value	Unit
Force by pressure	0.00141	[N]
Force by Viscous	0.00029	[N]
Total force	0.00169	[N]
C_d	0.75932	[-]
Improvement ratio	0.97%	[-]
Annual fuel consumption	0.080429176	[L/year]

F. Model_011

In the Model_011 configuration, aerodynamic parts have been added to the middle and rear parts of the vehicle. The purpose here is to move the rear area of the vehicle's scar formation area away and to prevent the air flow passing into the intermediate area of the trailer and the semi-trailer. As a result of the analysis, the air flow escaping between the trailer was prevented, but in Fig.11. the undesirable air flow in the 1st region directly hit the trailer and a vortex was formed between the front of the trailer and the trailer ceiling and high pressure was created on the trailer surface. As in the main model, the flow separations shown in regions 2 and 3 in Fig.12. are observed in this vehicle model. In Fig.12. in area 4, the design created the trace far away from the vehicle surface as desired.

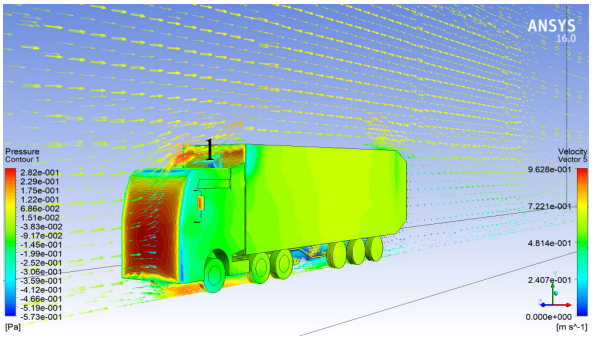

Figure 11: Velocity vector and pressure gradients acting on the Model_011

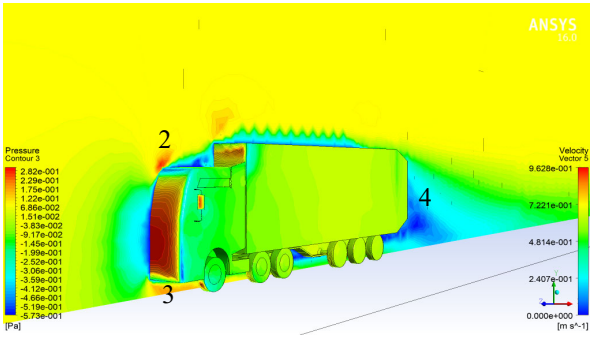

Figure 12: Velocity vector and pressure gradients acting on the Model_011

Table 7: Result for the Model_011

Parameter found in the analysis	Value	Unit
Force by pressure	0.00122	[N]
Force by Viscous	0.00029	[N]
Total force	0.00151	[N]
C_d	0.67542	[-]
Improvement ratio	11,91%	[-]
Annual fuel consumption	0.071831718	[L/year]

G. *Model_011*

One of the aerodynamic improvements in different combinations made on the main vehicle model is the addition of a wind-guiding aerodynamic part such as a windshield on the vehicle cabin and a nozzle at the back of the trailer. The main purpose of these designs is to make the vehicle look like a drop design.

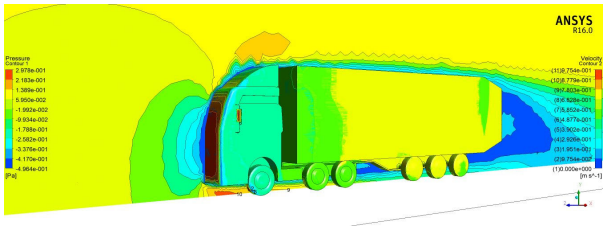

Figure 13: Velocity and pressure gradients acting on the Model_101

The speed of the air flow hitting the front of the truck slows down and causes an increase in pressure in the decelerated area. In Fig.13. The air flow that is separated by striking the surface is separated from the vehicle without creating flow separation and turbulence on the vehicle with the help of the aerodynamic wind director added on the cabin. With the aerodynamic nozzle piece added to the trailer, the air flow passing to the rear area ensures the formation of scars in the area far from the rear surface of the vehicle and reduces the negative pressure effect.

Table 8: Result for the Model_110

Parameter found in the analysis	Value	Unit
Force by pressure	0.00110	[N]
Force by Viscous	0.00031	[N]
Total force	0.00142	[N]
C_d	0.63258	[-]
Improvement ratio	15.84%	[-]
Annual fuel consumption	0.067335085	[L/year]

H. *Model_111*

All previous design improvements were used in the final design improvement combination. In this design, it is seen that the geometry of the vehicle resembles the shape of a drop. As a result of the aerodynamic analysis of the truck, the problem of flow separation in the front region, turbulence formation in the middle region and scar formation behind the trailer were prevented. Fuel analyzes made in the design have assumed that the vehicle travels 50 thousand km on an annual basis and the diesel unit price is 7.75 unit.

In Fig.14. it is seen that the upper deflector piece acts as a guide to the flow line in the 1st region. In Fig.15. it is seen that the airflow velocity lines flow smoothly and without turbulence with all the aerodynamic improvements. In this way, parameters such as undesired drag force or vibration did not occur.

In Fig.16. the air flow behaviors occurring in different regions on the vehicle are observed in the representation of the airflow velocity flowing over the truck with its contour. The speed of the air flow formed in the number 1 area hitting a flat surface and its speed approaching 0 and the pressure at this point increases. Speed increase due to airflow separation in zones 2 speed increase in the vortex region formed in region 3 deceleration of the velocity of the current striking the flat surface.

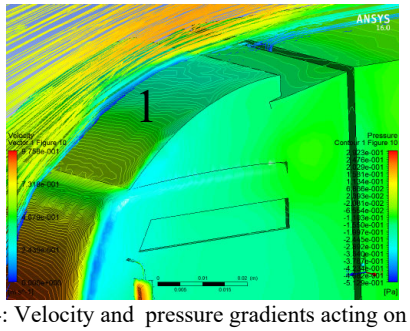

Figure 14: Velocity and pressure gradients acting on the (TD) Model_111

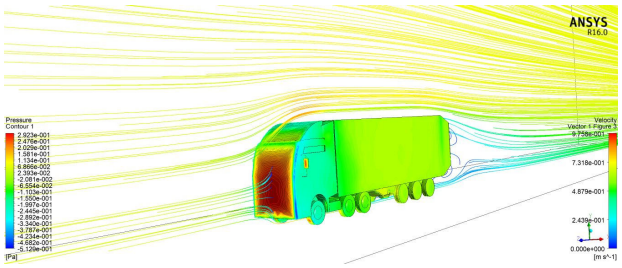

Figure 15: Pressure force and velocity streamlines acting on the Model_111

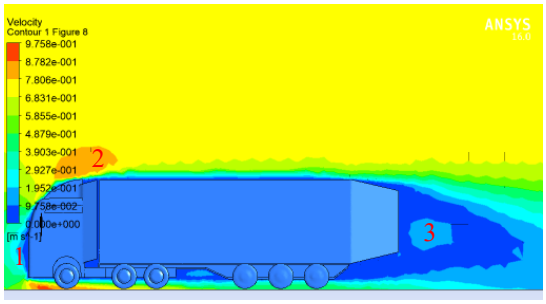

Figure 16: Velocity contours acting on the truck.

Table 7: Result for the Model_111

Parameter found in the analysis	**Value**	**Unit**
Force by pressure	0.00105	[N]
Force by Viscous	0.00032	[N]
Total force	0.00137	[N]
C_d	0.61331	[-]
Improvement ratio	20.04%	[-]
Annual fuel consumption	0.065289929	[L/year]

IV. CONCLUSION

With the combination of three different aerodynamic parts added, the aerodynamic improvements on the model were analyzed and compared. Here, it has been determined that the closer the design of the vehicle is to the drop model criterion, the lower the drag force. With this study, an idea has been created to reduce the fuel costs of the trucks that travel long distances annually and to increase the life of the vehicle parts that do extra work to overcome the drag force. Fig.16. shows the graph of calculated fuel consumption values, assuming that the aerodynamic improvements made on the vehicle will travel 50 thousand km per year. The values given here are independent of the size of the vehicle. This graph, which is prepared in line with the data taken at 1:40 scale, can give the fuel consumption values of the real-size vehicle with 1:1 scaling.

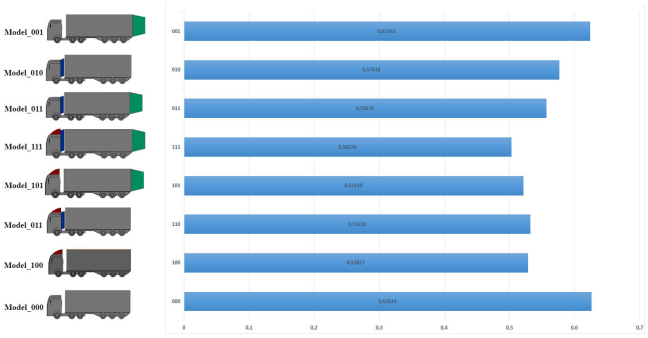

Figure 17: This caption is centered.

REFERENCES

[1] Wikipedia katılımcıları (2021). Otomobilin tarihi. Vikipedi, Özgür Ansiklopedi. Erişim tarihi 19.29, Ağustos 26, 2021 url://tr.wikipedia.org/w/index.php?title=Otomobilin_tarihi&oldid=26062176.
[2] Wikipedia katılımcıları (2021). Aerodinamik. Vikipedi, Özgür Ansiklopedi. Erişim tarihi 19.30, Ağustos 26, 2021 url://tr.wikipedia.org/w/index.php?title=Aerodinamik&oldid=24853481.
[3] Kartz Joseph Aerodynamics of Race Cars ,e Annual Review of Fluid Mechanics is online at, April, 2006.
[4] Özen, İsmail, 2015. Bir Binek Aracın Aerodinamik Etkinliğinin Modellenmesi, Fırat Üniversitesi, Yüksek Lisans Tezi, Elazığ, 109s.
[5] Jeong Jae Kima , Sangseung Leeb , Myeongkyun Kimb , Donghyun Youb,⁎ , Sang Joon Leea, Slient Drag Reduction of a Heavy Vehicle Using Modified Cab-Roof Fairings, Journal of Wind Engineering and Industrial Aerodynamics, 138-151, South Korea, 2017.
[6] Fluent, 'ANSYS Fluent User Guide'. New Hampshire, 2016.
[7] Chowdhury H., Juwono R., Zaid M., Islam R., Alam F., Loganathan B., An experimental study on of the effect of various deflectors used for light trucks in Indian subcontinent 2nd International Conference on Energy and Power, 13-15 Sydney, Australia 2018
[8] Gürbüz, Y. & Kulaksız, A. A. (2016). Elektrikli Araçlar ile Klasik İçten Yanmalı Motorlu Araçların Çeşitli Yönlerden Karşılaştırılması. Gümüşhane Üniversitesi Fen Bilimleri Enstitüsü Dergisi , 6 (2) , 117-125 . DOI: 10.17714/gufbed.2016.06.011.
[9] Wikipedia katılımcıları (2021). Kerosen. Vikipedi, Özgür Ansiklopedi. Erişim tarihi 20.46, Ağustos 26, 2021 url://tr.wikipedia.org/w/index.php?title=Kerosen&oldid=24995046.
[10] Karabektaş M., Saraç H., (2002). Alternatif Dizel Motor Yakıtı Olarak Biodizel Yakıtının Deneysel Olarak İncelenmesi SAU Fen Bilimleri Dergisi (2002) 6 (2),. http://www.saujs.sakarya.edu.tr/tr/download/article-file/193134 (Date of access : 25.08.2021)

Structural performance evaluation on aluminum plates retrofitted with composite: Impact of hybrid (bonded/bolted) joining methods under the flexural loading

H. ULUS[1] and H.B. KAYBAL[2]

[1] Selcuk University, Konya/Turkey, hasanulus@selcuk.edu.tr
[2]Amasya University, Amasya/Turkey, hburak@amasya.edu.tr

Abstract **- Engineering materials lose their mechanical performance due to environmental loadings during service, and they require reinforcement. Recently, externally jointed to metallic members have been regarded as an effective technique for strengthen structures due to the composites are light and have good mechanical properties. Although the traditional methods (bonded and/or mechanical joining) have been widely used for combining, hybrid joinings have recently become popular to take advantage of the load transfer efficiency of both techniques. On the other hand, it is essential to know which component the stress should be applied as a design criterion and how the damage behavior has changed accordingly. On the other hand, it is essential to know which component the stress should be applied as a design criterion and how the damage behavior has changed accordingly. Since the member below the neutral axis is subjected to tensile and the upper is subjected to compressive stresses during bending loading, it is essential to understand how structural behavior is affected by the reinforcement in both cases. This work investigated the flexural behavior of bolted/bonded hybrid jointed aluminum-basalt composite, in the case of composite is below the neutral axis and aluminum below the neutral axis. Different damage modes were observed depending on different loading conditions and used joining techniques. Experiments indicate that applying the hybrid joining technique enhanced load-carrying capacity significantly attributed to bolts' restriction of shear deformation. This paper extends the understanding of aluminum retrofitting with composites and provides valuable suggestions for the joining method.**

Keywords **– Aluminum, composite, bonded/bolted hybrid joint, epoxy, bending test**

I. INTRODUCTION

ENGINEERING structures lose their mechanical performance under service conditions for various reasons such as aging, corrosion, and ultraviolet radiation [1-6]. Essentially, the loss of strength and stiffness of metallic structures during service due to various environmental effects (fatigue loading and harsh conditions) result in the need for the retrofit, rehabilitate or rebuild [7]. In the retrofitting process, the damaged areas are usually repaired by bolting or welding steel plates. However, these plates are often heavy and susceptible to corrosion and fatigue. To rehabilitate deteriorated steel structures, composites with high mechanical properties and flexibility in adapting to other materials have recently received significant attention as external reinforcements [8]. Carbon fiber reinforced polymers (FRPs) have been widely used to reinforce metal structures thanks to their hardness, similar to steel [9-12].

The mechanical and adhesive bonding techniques are preferred for joining different materials. However, these techniques have some disadvantages. In mechanical joints, drilling processes cause materials damage and also leads to a weight increment. On the other hand, performance loss may occur in adhesive joints over time due to service conditions effects such as temperature and humidity. Hybrid (bolted/bonded) joints offer the opportunity to provide higher strength and longer service life with a synergistic effect by minimizing the disadvantages of both techniques and combining their advantages [13].

The difference in stiffness of the composite and metallic structures often leads to stiffness mismatch and debonding between metal/composite joints area. In addition, since shear stresses predominate at the metal-composite interfacial region in bending loading, ultimate failure occurs predominantly through delamination formations. From this point of view, it is thought that the bolted/bonded hybrid joining can potentially be advantageous can limit the propagation of interlayer damage.

Basalt fiber-reinforced polymer composites are economic and competitive materials that offer good mechanical performance in service conditions compared to fiber reinforced materials [14-16]. Basalt composites have a high potential to strengthen or reinforce aluminum structures, which is preferred in many industry (automotive, aerospace, marine, renewable energy) [17-19]. In the retrofitting process, the position of the reinforcement has an important role, especially in the bending load-carrying capacity of the structure. Because, if the composite reinforcement element is below the neutral axis (in the tensile zone) or above the neutral axis (in the compression zone), it provides a different strengthening mechanism. In the current research, the flexural behavior of basalt composite reinforced aluminum structure was investigated with three-point bending tests. The situation of basalt composite reinforcement both above and below the neutral axis was

evaluated separately. Additionally, the effectiveness of different joining techniques on bending load-carrying capacity was examined.

II. EXPERIMENTALS

The composite reinforcing, which consists of twelve layers of basalt fabric-epoxy laminates, was used for the retrofitted aluminum structure. The woven basalt fibers have an areal density of 300 $g.m^{-2}$ and were purchased from Tila Kompozit. The vacuum infusion method was conducted for composite manufacturing (details as can be seen in ref [4-6]). Aluminum 6061 components provided from Özen Metal. The epoxy adhesive (MGS L285 and MGS H285) was supplied from Momentive Hexion. The joining components were cut as dimensions of 3.5 x 25 x 100 mm^3. The surface preparation process, crucial to ensure good adhesion between adherents, is carefully performed according to ASTM standards. Hybrid surface treatment (sulfuric acid etching and phosphoric acid anodization) was applied to aluminum, and mechanical etching (sanding) was used to composite adherents. ASTM D2651 and ASTM D3933 for aluminum components and ASTM D2093-03 for composite components were followed. The adhesive was prepared according to the manufacturer's recommendations (75% by weight of epoxy resin and 25% by weight of hardener). M4 steel bolts, nuts, and washers are used for bolted joints. All samples were cured at room temperature for 24 hours and at 80 °C for 12 hours. Prepared joining configurations are presented in Figure 1.

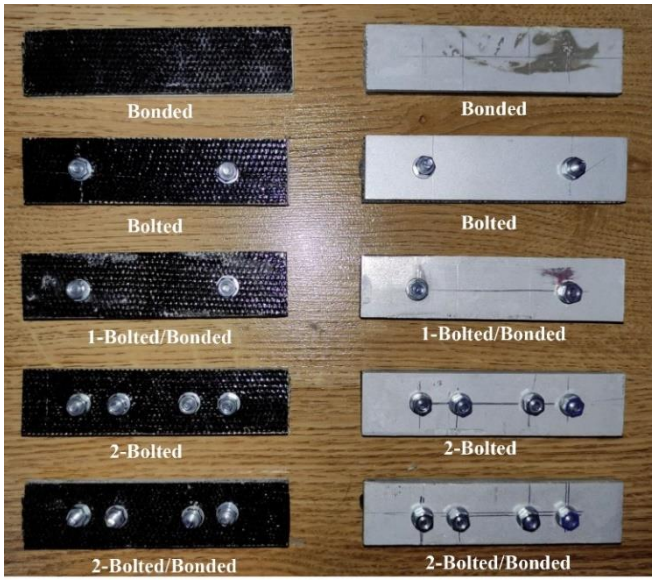

Figure 1: Prepared joining configurations

Three-point bending tests evaluated the performances of the produced structures. The bending tests were carried out at a displacement speed of 1 mm/min. The tests were conducted for two different loading conditions (Figure 2). In the first loading state (Loading 1), the aluminum is placed under the neutral axis, and force is applied to the composite surface (Figure 2.a). In the second case (Loading 2), the composite part is placed on the supports, and the loading is applied to the aluminum surface (Figure 2.b).

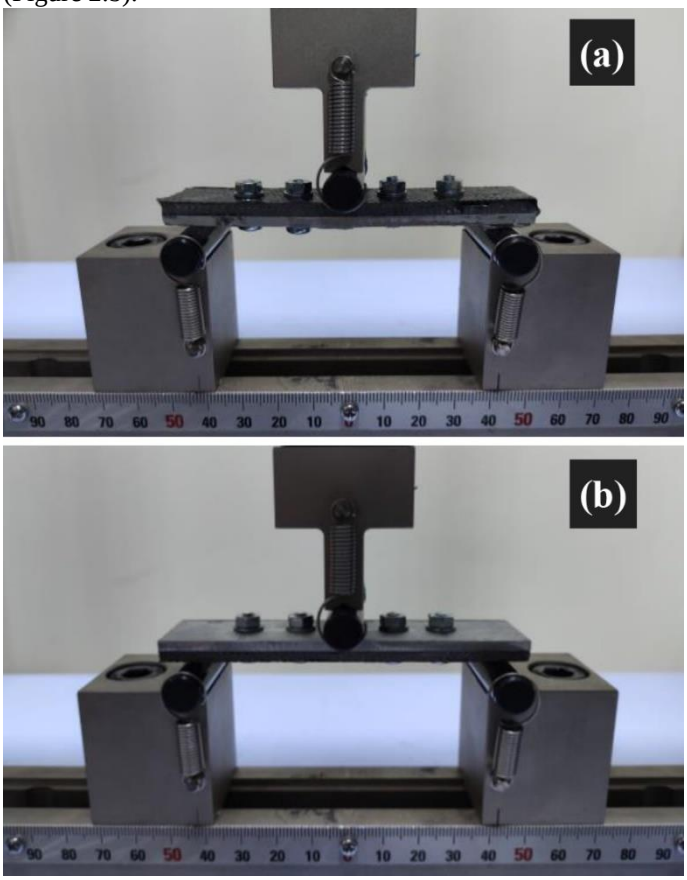

Figure 2: Loading conditions: a) loading apply on composite's top surface (Loading 1), b) loading apply on aluminum's top surface (Loading 2)

III. 3. RESULTS AND DISCUSSIONS

The load-displacement curves of the bending tests for the state of "loading 1" are given in Figure 3. It is seen that the load-carrying capacities of aluminum-composite structures after composite retrofitting increase dramatically compared to aluminum, but their deformation capabilities are relatively limited. The lowest flexural load carrying performance was obtained in the samples using one pair of bolts (1-Bolted), while the highest performance was obtained in the hybrid jointed samples with two pairs of bolts (2-Bolted/Bonded). Although the bolts have a significant effect on the load-carrying performance, it does not appear to affect the bending stiffness. On the other hand, it is clear that only bonded specimens perform better than only bolted specimens. It is seen that the load-carrying capacity and the deformation capability increase thanks to the bolts adding to the bonded specimens. Bending tests includes a complex loading involving tensile, compressive, and shear forces. Therefore, the interfacial region of the bonded adherents is subject to shear deformation in bending loading. Since bolts limit this shear deformation, hybrid jointed specimens perform enhanced bending performance.

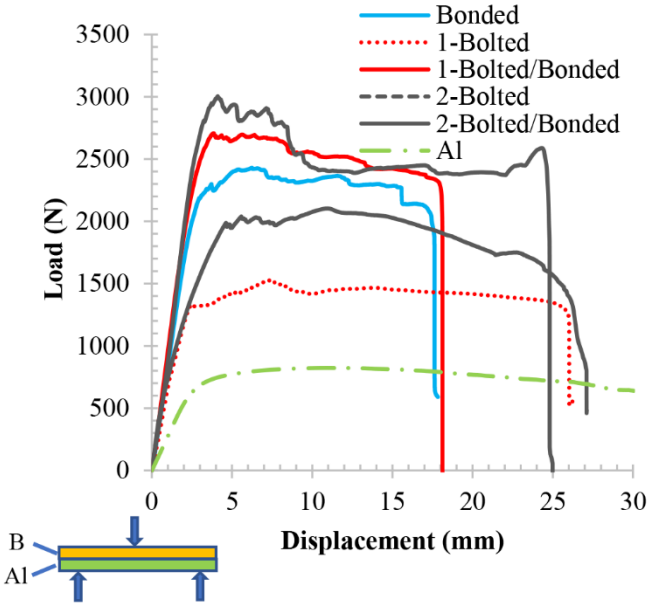

Figure 3: Load-displacement curves of jointed alumina-composite specimens for state of ''Loading 1''.

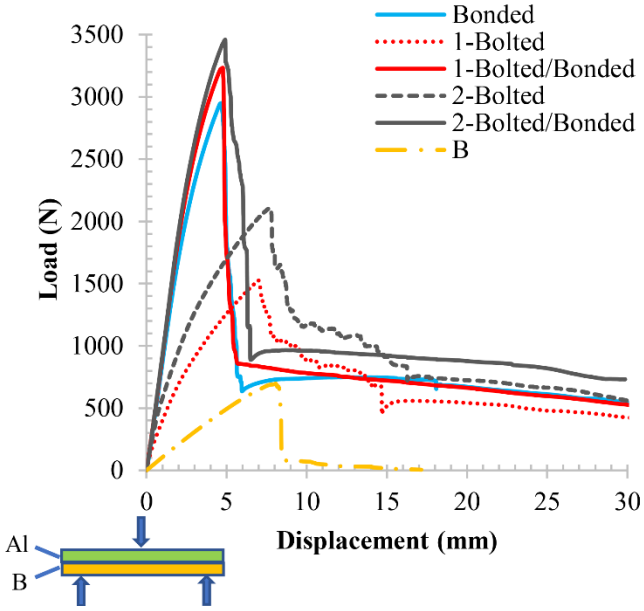

Figure 4: Load-displacement curves of jointed alumina-composite specimens for state of ''Loading 2''.

The load-displacement curves of the bending tests for the "Loading 2" condition are given in Figure 4. Two regions can be clearly identified corresponding to when the composite plate is not fully damaged and aluminum has yielded after composite has failed. In general, it is seen that all samples exhibit a sudden decrease after reaching a peak load value. This behavior actually very similar to the bending response of basalt composite. Basalt composite, below the neutral axis, fails under the influence of tensile stresses. Therefore, it is understood that the load drop is mainly caused by the damage of the basalt composite. The aluminum and basalt composite carry the applied load together until it reaches the peak loading, but when the composite is damaged, the force suddenly drops and transfers to the aluminum. The fact that the trend in the second region of the curves after the sudden decrease is similar to the aluminum curve presented in Figure 1 is clear evidence of this situation. The increase in the number of bolts enhances the peak load value in all sample groups. Bonded specimens perform better than only bolted specimens. On the other hand, it is seen that a synergistic effect occurs by combining the superior features of the two techniques in hybrid-jointed samples. Additionally, increasing the number of bolts (from one pair to two pairs) in the bolted specimens (without adhered) gradually increased the bending rigidity. However, flexural stiffness in adhesive joints does not affect the bolts.

The peak force values determined from the force-displacement curves for loading case 1 are presented in Figure 3. Only bonded specimens carried 1.6 and 1.15 times more load than 1-bolted and 2-bolted samples, respectively. Although increasing the number of bolts improves the performance, it does not increase the strength as much as the bonded joint. On the other hand, 1-Bolted/bonded specimen showed 1.7 and 1.1 times better strength than bolted and bonded specimens, respectively. 2-Bolted/bonded specimens offered 1.9 and 1.2 times improved performance than bolted and bonded specimens, respectively.

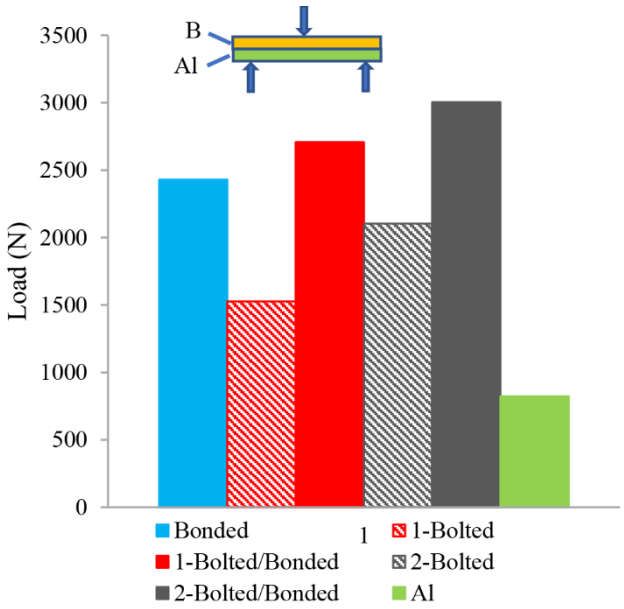

Figure 5: Bar graph of peak load values for state of ''Loading 1''.

The peak force values obtained from the force-displacement curves for loading case 2 are presented in Figure 6. The bonded sample carried 1.9 and 1.4 times more load than the 1-bolted and 2-bolted samples, respectively. Similarly, the addition of bolts improves performance. However, only bolted specimens do not exhibit as good strength as bonded specimens. On the other hand, 1-Bolted/bonded specimen showed 2.1 and 1.1 times better strength than bolted and bonded specimens, respectively. An additional pair of bolts, 2-Bolted/bonded specimens, offered 2.3 and 1.2 times improved performance than bolted and bonded specimens, respectively.

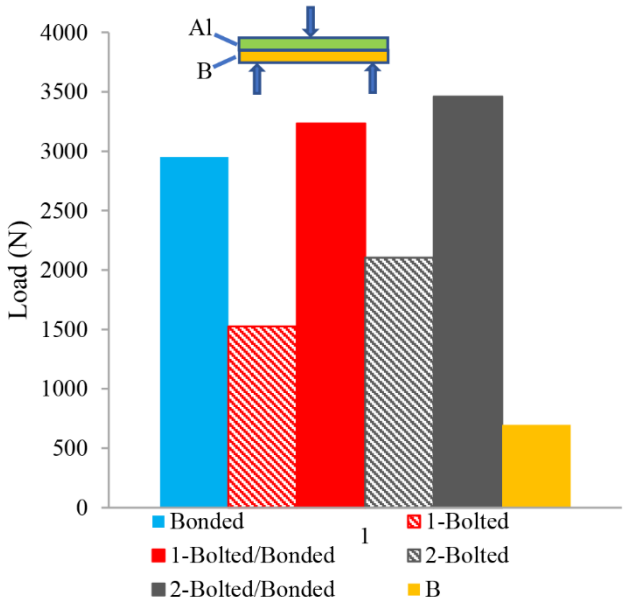

Figure 5: Bar graph of peak load values for state of ‘’Loading 2’’.

Damage images of specimens after tests specimens at the "Loading 1" condition are presented in Figure 6. In bonded specimens (without bolts), ultimate failure occurs with delamination damage governed by shear deformations (Fig. 6.a). Because, the crack seen on the aluminum surface has not yet progressed through the entire section. If the interface damage had not occurred, the transverse crack (seen in top view) would have traveled all the way through. In the case of hybrid joinings, it is seen that the components carry loads together thanks to the delamination restriction by bolts (Figure 6.d). So, the final damage is caused by the formation of transverse crack in the components. In using bolted joinings (without adhesive), composite breaking and delaminations occur, but no visible cracks occur in the aluminum (Figure 6.b-c). After the composite failure, ductile aluminum continues to deform.

Damage images of the tested specimens at the "Loading 2" condition are given in Figure 7. The ductility of aluminum is much higher than basalt/epoxy composite. When the composite layer is below the neutral axis, it is subject to tensile stresses. However, due to its low ductility, it cannot deform synchronously with aluminum. For this reason, first, the composite layer is broken, and then the load is transferred to the aluminum completely. It can be seen that the fracture of the composite caused the ultimate failure in all samples (Fig. 7.a-d).

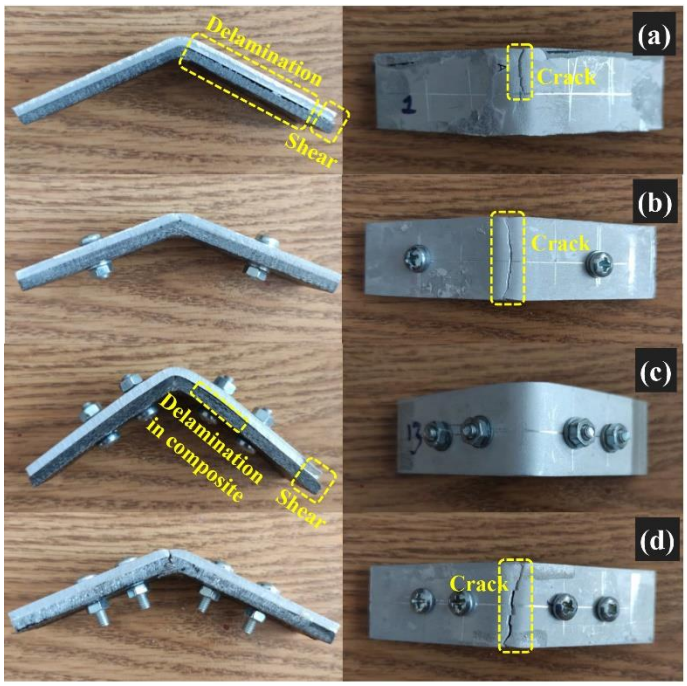

Figure 6: Damage images of tested specimens for state of ‘’Loading 1’’: a) bonded, b) 1-bolted/bonded, c) 2-bolted, d) 2-bolted/bonded

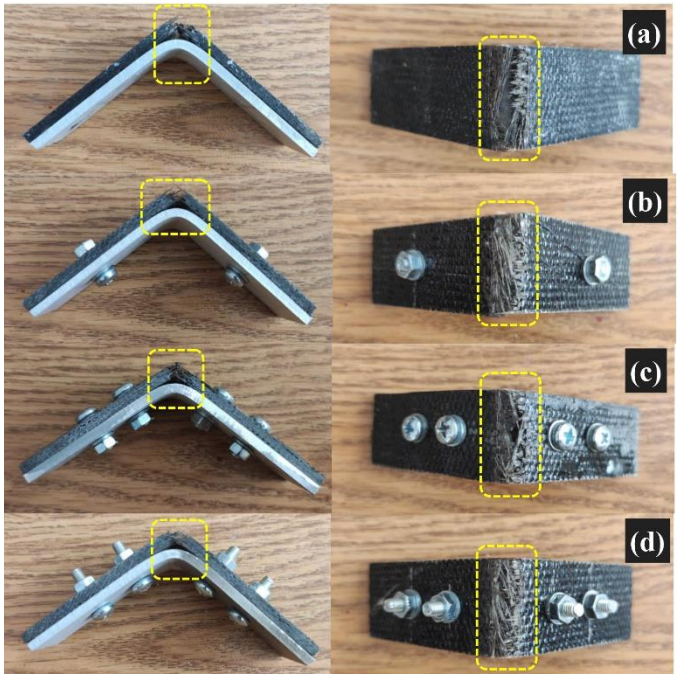

Figure 7: Damage images of tested specimens for state of ‘’Loading 2’’: a) bonded, b) 1-bolted, c) 2-bolted, d) 2-bolted/bonded

IV. CONCLUSIONS

In hybrid jointed specimens, interlaminar (aluminum-composite) shear deformation restricts by bolts, and so interlaminar shear strength increases. Thanks to the development of the interlaminar interaction, the components carry the applied load together. Thus, the load-bearing capacity of composite-aluminum structures improves with a hybrid joining technique for both loading conditions. The load values determined for both loading conditions in bolted samples are very close to each other shows that the bolted samples are not affected by the loading direction. In general, the fact that aluminum is below the neutral axis increases its deformation ability. However, when the basalt composite with lower deformation ability is below the neutral axis, after the loading reaches the peak force, the load-carrying capacity of the composite suddenly decreases with catastrophic damage.

ACKNOWLEDGMENT

The TUBITAK; The Scientific and Technologic Research Council of Turkey (project number:120M369) financially supported this investigation.

REFERENCES

[1] H. B. Kaybal, H. Ulus, and A. Avcı, "Seawater Aged Basalt/Epoxy Composites: Improved Bearing Performance with Halloysite Nanotube Reinforcement," *Fibers and Polymers*, pp. 1-10, 2021.

[2] H. B. Kaybal, H. Ulus, V. Eskizeybek, and A. Avcı, "An experimental study on low velocity impact performance of bolted composite joints part 1: Influence of halloysite nanotubes on dynamic loading response," *Composite Structures*, vol. 258, p. 113415, 2021.

[3] H. B. Kaybal, H. Ulus, V. Eskizeybek, and A. Avcı, "An experimental study on low velocity impact performance of bolted composite joints-part 2: Influence of long-term seawater aging," *Composite Structures*, p. 113571, 2021.

[4] H. Ulus, H. B. Kaybal, V. Eskizeybek, and A. Avcı, "Enhanced salty water durability of halloysite nanotube reinforced epoxy/basalt fiber hybrid composites," *Fibers and Polymers*, vol. 20, no. 10, pp. 2184-2199, 2019.

[5] H. Ulus, H. B. Kaybal, V. Eskizeybek, and A. Avcı, "Halloysite nanotube reinforcement endows ameliorated fracture resistance of seawater aged basalt/epoxy composites," *Journal of Composite Materials*, vol. 54, no. 20, pp. 2761-2779, 2020.

[6] H. Ulus, H. B. Kaybal, V. Eskizeybek, and A. Avcı, "Significantly improved shear, dynamic-mechanical, and mode II fracture performance of seawater aged basalt/epoxy composites: The impact of halloysite nanotube reinforcement," *Engineering Science and Technology, an International Journal*, vol. 24, no. 4, pp. 1005-1014, 2021.

[7] C. Wu, X. Zhao, W. H. Duan, and R. Al-Mahaidi, "Bond characteristics between ultra high modulus CFRP laminates and steel," *Thin-Walled Structures*, vol. 51, pp. 147-157, 2012.

[8] X.-L. Zhao and L. Zhang, "State-of-the-art review on FRP strengthened steel structures," *Engineering structures*, vol. 29, no. 8, pp. 1808-1823, 2007.

[9] S. Abdus, X. Cheng, W. Huang, A. Ahmed, and R. Hu, "Bearing failure and influence factors analysis of metal-to-composite bolted joints at high temperature," *Journal of the Brazilian Society of Mechanical Sciences and Engineering*, vol. 41, no. 7, p. 298, 2019.

[10] H. Liu, R. Al-Mahaidi, and X.-L. Zhao, "Experimental study of fatigue crack growth behaviour in adhesively reinforced steel structures," *Composite Structures*, vol. 90, no. 1, pp. 12-20, 2009.

[11] C. Wu, X.-L. Zhao, R. Al-Mahaidi, M. R. Emdad, and W. Duan, "Fatigue tests of cracked steel plates strengthened with UHM CFRP plates," *Advances in Structural Engineering*, vol. 15, no. 10, pp. 1801-1815, 2012.

[12] M. Tavakkolizadeh and H. Saadatmanesh, "Fatigue strength of steel girders strengthened with carbon fiber reinforced polymer patch," *Journal of structural engineering*, vol. 129, no. 2, pp. 186-196, 2003.

[13] B. Kumar, C. Sun, P. H. Wang, and R. Sterkenburg, "Adding additional load paths in a bonded/bolted hybrid joint," *Journal of Aircraft*, vol. 47, no. 5, pp. 1593-1598, 2010.

[14] A. Altalmas, A. El Refai, and F. Abed, "Bond degradation of basalt fiber-reinforced polymer (BFRP) bars exposed to accelerated aging conditions," *Construction and Building Materials*, vol. 81, pp. 162-171, 2015.

[15] P. Davies and W. Verbouwe, "Evaluation of basalt fibre composites for marine applications," *Applied Composite Materials*, vol. 25, no. 2, pp. 299-308, 2018.

[16] V. Dhand, G. Mittal, K. Y. Rhee, S.-J. Park, and D. Hui, "A short review on basalt fiber reinforced polymer composites," *Composites Part B: Engineering*, vol. 73, pp. 166-180, 2015.

[17] M. A. Wahid, A. N. Siddiquee, and Z. A. Khan, "Aluminum alloys in marine construction: characteristics, application, and problems from a fabrication viewpoint," *Marine Systems & Ocean Technology*, vol. 15, no. 1, pp. 70-80, 2020.

[18] R. Long, E. Boettcher, and D. Crawford, "Current and future uses of aluminum in the automotive industry," *JOM*, vol. 69, no. 12, pp. 2635-2639, 2017.

[19] P. Rambabu, N. E. Prasad, V. Kutumbarao, and R. Wanhill, "Aluminium alloys for aerospace applications," *Aerospace materials and material technologies*, pp. 29-52, 2017.

Investigation of the Effect of Diesel Fuel / JP8 Fuel Blends on the Emissions of a Common Rail Engine

Mehmet Selman Gökmen[1*], Hasan Aydoğan [2]

[1] *Necmettin Erbakan University, Seydişehir Vocational School, Konya, Turkey*
ORCID ID 0000-0001-5943-7504
[2] *Selçuk Üniversitesi, Faculty of Technology, Mechanical Engineering Department, Konya, Turkey*
ORCID ID 0000-0002-1448-8911
[*]*(msgokmen@erbakan.edu.tr)*

Abstract – Petroleum-based fuels have been used for power generation in internal combustion engines and in the industrial field for over 100 years. For this reason, oil has become one of the most important energy sources today, but emissions as a result of combustion affect the environment and human health negatively. For this reason, studies are carried out to reduce the exhaust emission values caused by vehicles used for passenger and cargo transportation in land, sea and air vehicles. In this study, the effect on emission values was investigated by mixing 5%, 10% and 15% JP8 fuel with standard diesel fuel in a diesel engine with 1.9 Multijet, Common rail injection system and turbocharger, which was produced for commercial use. As a result of the tests, it has been observed that fuel mixtures containing JP8 reduce CO, CO_2, HC, and NO emissions and increase O_2 emissions.

Keywords – JP8, Jet Fuel, Diesel Engine, Exhaust Emissions, Alternative Fuels

I. INTRODUCTION

As a result of the increase in the world population and technological and economic developments, the role of internal combustion engines in people's daily lives is increasing day by day [1], [2]. Internal combustion engines are widely used in transportation, industry, security and agricultural applications. Petroleum-based products are used as fuel in internal combustion engines [2]–[4].

Kerosene-based fuels are generally developed for use in aviation and military vehicles. Many kerosene-based fuel types have been produced from past to present, especially for jet-powered aircraft. These fuels are JET-A, JET-A1, JET-B, JP4, JP5, JP7 and JP8. [5]–[8].

After the Second World War, NATO countries thought that aviation fuel used for military purposes should be the only type. At this point, it was decided to use JP8 fuel [9]–[12]. Table 1 gives some properties of JP8 fuel and diesel fuel [4], [13]. When the table is examined, it is seen that the filter clogging point degree of JP8 fuel in the cold is quite low.

Table 1 Characteristics of Diesel and JP8 fuels

Property	**Diesel**	**JP8**	**Method**
Density (g/cm3)	0,8372	0,7950	ASTM D 1298
CFPP (°C)	-5	-48,5	ASTM D 2386
Flashing Point (°C)	73	41	ASTM D 93
LHV (kcal/kg)	10450	10200	ASTM D 2015
Cetane Number	54	45	ASTM D 976

Kerosene is obtained by distillation of petroleum between 150 °C and 270 °C [14]–[17]. The lower calorific values of JP8 and diesel fuel are very close to each other. However, the cetane number of JP8 fuel is lower than diesel fuel. This prolongs the ignition time [18], [19]. Common Rail fuel injection system is an electronically controlled fuel injection system used in diesel engines. The system has advantages such as reducing fuel consumption, lowering exhaust gas emissions and quieter operation. Fuel is injected into the cylinders by injectors at a pressure of more than 2000 bar [2], [14], [20].

In this study, the use of JP8 / diesel fuel mixtures in a turbocharged engine with a common rail fuel system was investigated. Changes in emission values were investigated.

II. MATERIAL AND METHOD

Fuel mixtures were obtained by mixing the standard JP8 fuel used in aircraft with 5% (JP8-5), 10% (JP8-10) and 15% (JP8-15) diesel by volume, and the results were compared with standard diesel fuel. The tests were carried out using a 1.9 Multijet 4-stroke and 4-cylinder diesel engine equipped with a turbocharger and common rail, with 500 rpm increments between 1000 and 3000 rpm. Measurements were made at full load using the BT-190 FR hydraulic dynamometer, which can provide 100 kW maximum power and 750 Nm maximum torque. The specifications of the test engine are given in table 2 and the test setup is given in figure 1. Emission values were measured with Bosch BEA 350 model exhaust emission device.

Table 2 Test Engine Specifications

Property	***Specification***
Model	*1.9 Multijet, 4 stroke, Common Rail*
Engine Volume	*1898 cm3*
Cylinder	*4*
Bore	*82 mm*
Stroke	*90.4 mm*
Engine Power	*77 kW (4000 rpm)*
Engine Torque	*200 Nm (1750 rpm)*

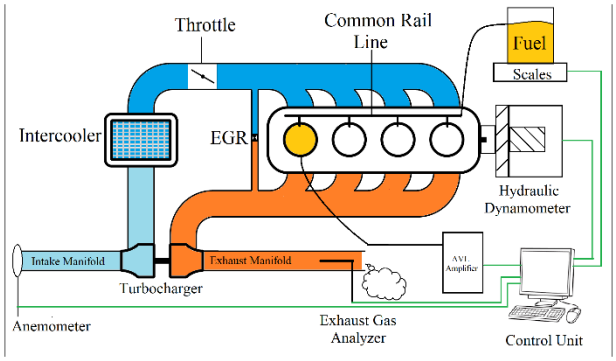

Figure 1 Test Setup

III. RESULTS

A. CO EMISSIONS

The contour curves given in Figure 2 show the variation of CO emissions depending on engine speed and JP8 ratioCO emissions decrease with increasing engine speed and JP8 ratio. The fact that the contour graphs behave parallel to the axis showing the JP8 ratio shows that the change in CO emissions varies more with engine speed compared to the JP8 ratio. Considering the curves, it is seen that CO emission is at its minimum value between 2100 and 2900 rpm, and it tends to increase again above 3000 rpm. In addition, the measurement results are given in Figure 3 as column charts. As a result of the measurements, it has been determined that the JP8 fuel mixture reduces CO emissions.

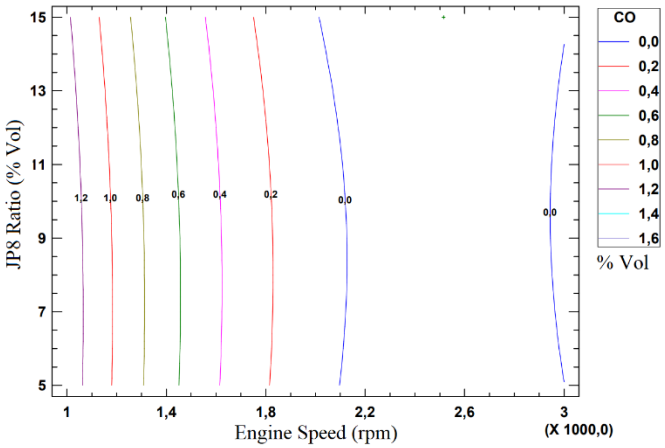

Figure 2 Variation of CO emissions depending on engine speed and JP8 ratio

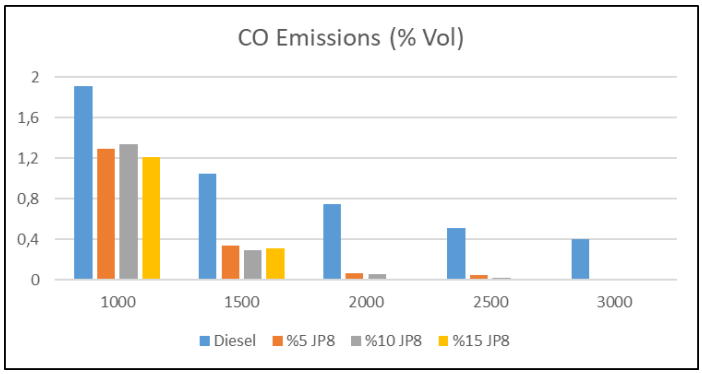

Figure 3 Measurement results of CO emissions

B. CO_2 EMISSIONS

The contour curves in Figure 4 show the variation of CO_2 emissions depending on engine speed and JP8 ratio. Although CO_2 emissions decreased depending on the JP8 ratio, it was observed that it continued to increase up to 2000 rpm and reached the highest value at 2000 rpm. In addition, the measurement results are given in Figure 5 as column charts. As a result of the measurements, it has been observed that JP8 fuel mixtures reduce CO_2 emissions compared to diesel fuel, but the emissions tend to increase as the JP8 ratio in the fuel mixture decreases in the range of 1600 - 2300 rpm.

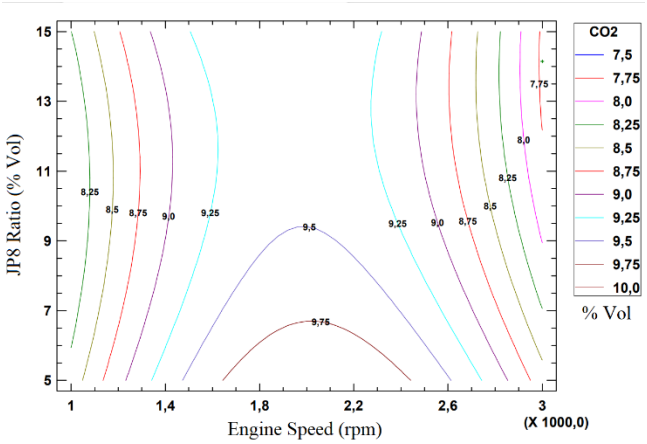

Figure 4 Variation of CO_2 emissions depending on engine speed and JP8 ratio

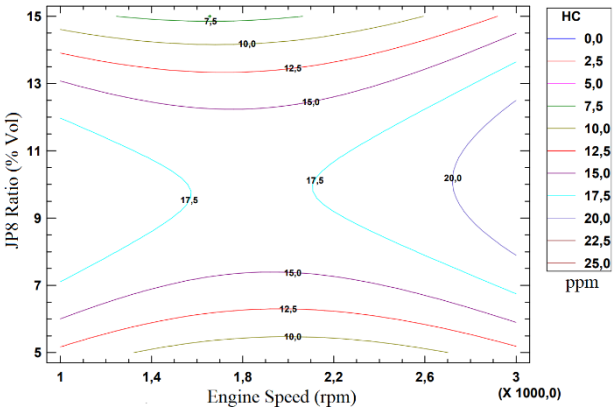

Figure 6 Variation of HC emissions depending on engine speed and JP8 ratio

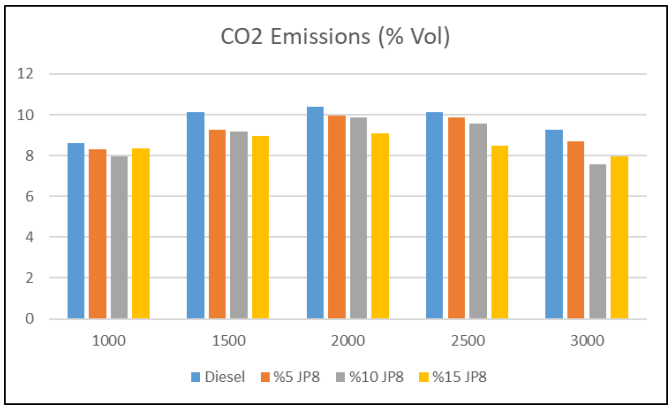

Figure 5 Measurement results of CO_2 emissions

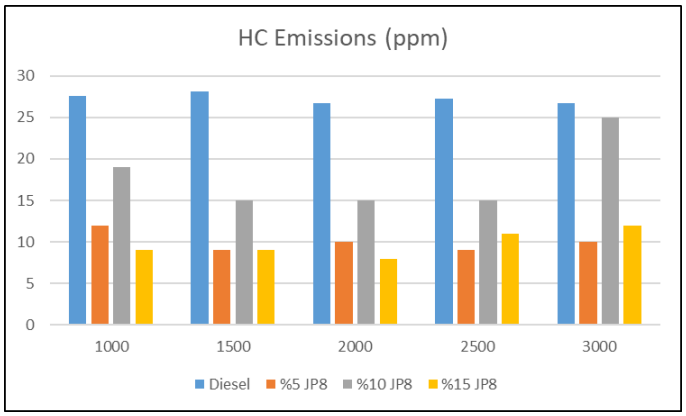

Figure 7 Measurement results of HC emissions

C. HC EMISSIONS

The contour curves given in Figure 6 show the variation of HC emissions depending on engine speed and JP8 ratio. JP8 fuel blends reduce HC emissions compared to diesel fuel, and it has been observed that the lowest values of HC emissions reach between 1000 – 2000 rpm with JP8-15 fuel. In addition, the measurement results are given in Figure 7 as column graphs. As a result of the measurements, it was seen that the use of JP8 fuel mixture at low engine speeds at high rates was more successful in reducing HC emissions.

D. O_2 EMISSIONS

The contour curves given in Figure 8 show the variation of O_2 emissions depending on engine speed and JP8 ratio. As can be seen from the contour curves, the O_2 emissions with the increasing JP8 ratio in the range of engine speed up to 1500 rpm are above the emission values obtained with diesel fuel. In the 2000 – 2500 rpm range, the values obtained with JP8-10 fuel gave the lowest emission results. Except for JP8-15 fuel, O_2 emissions of other fuel mixtures are lower than diesel fuel in the 2000 – 2500 rpm engine speed range. The measurement results are given in the form of column graphs in figure 9.

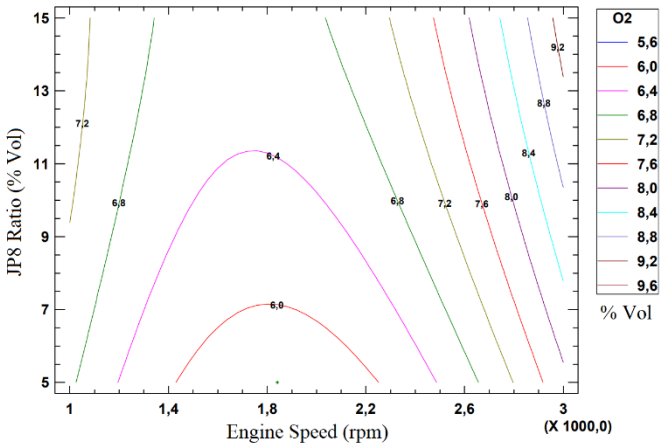

Figure 8 Variation of O_2 emissions depending on engine speed and JP8 ratio

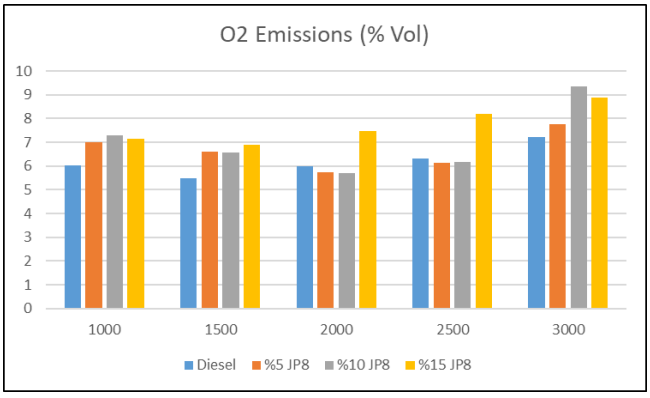

Figure 9 Measurement results of O_2 emissions

E. NO EMISSIONS

The contour curves given in Figure 10 show the variation of NO emissions depending on the engine speed and JP8 ratio. Similar to CO emissions, NO emissions form more parallel lines with the JP8 ratio. Considering the contour graphics, it is seen that increasing engine speed increases NO emissions. Considering the column charts given in Figure 11, it is seen that JP8 fuel mixtures have lower NO emission values compared to diesel fuel at all speeds below 3000 rpm engine speed, and the emission value increases in all fuels due to the increase in the in-cylinder temperature value as the speed increases.

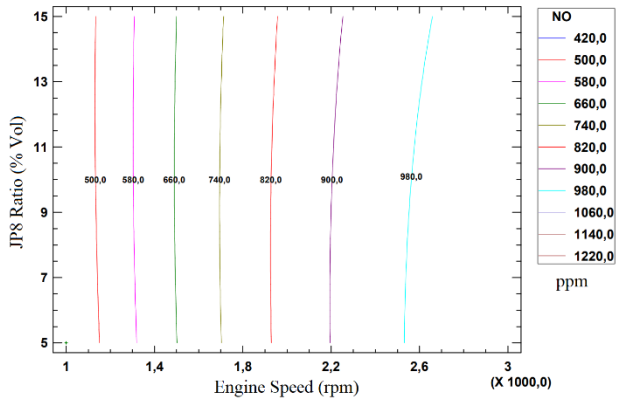

Figure 10 Variation of NO emissions depending on engine speed and JP8 ratio

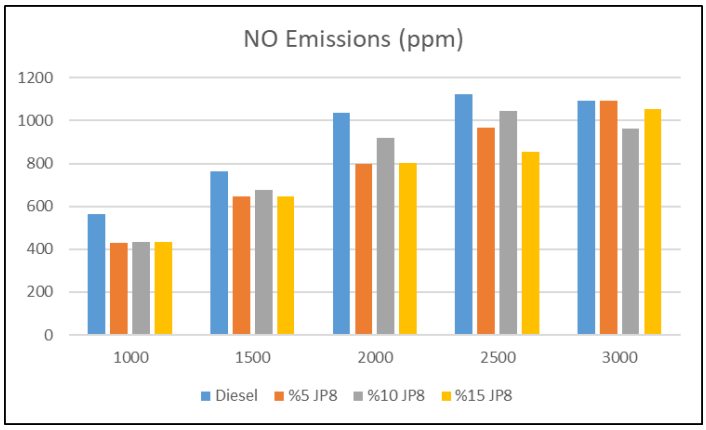

Figure 11 Measurement results of NO emissions

IV. CONCLUSIONS AND RECOMMENDATIONS

In this study, the fuels obtained by mixing kerosene-based JP8 fuel, which NATO countries accept as military fuel, with standard diesel fuel, were compared with diesel fuel and their emission values were examined. As a result of the study, it was observed that CO and HC emissions changed almost linearly according to engine speed in all ratios of JP8 fuel mixtures, while NO, CO_2 and O_2 emissions showed a curvilinear behavior depending on JP8 and engine speed. For this reason, in tests performed on a 1.9 Multijet, Common Rail and Turbocharged engine, which is frequently used in commercial vehicles, it has been observed that JP8-15 fuel mixture is more stable on emissions at all engine speeds, and JP8-5 fuel behaves similarly to JP8-15 fuel. According to the test results obtained with JP8-15 fuel, CO emission decreased by 36.70% at 1000 rpm engine speed

compared to diesel fuel. It was observed that CO_2, HC, and NO emissions decreased by 3.01%, 67.39% and 23.54%, respectively, in the same cycle, but O_2 emissions increased by 18.57%.

At 1500 rpm engine speed, CO, CO_2, HC, and NO emissions decreased by 70.73%, 11.28%, 67.97% and 15.58%, respectively, while O_2 emissions increased by 25.32%.

It was observed that CO, CO_2, HC, and NO emissions decreased by 98.92%, 12.50%, 70.04% and 22.61%, respectively, at 2000 rpm engine speed, but O_2 emissions increased by 18.57%.

As a result of the measurements made at 2500 rpm engine speed, it was observed that CO, CO_2, HC, and NO emissions decreased by 98.82%, 16.55%, 59.71% and 24%, respectively, while O_2 emissions increased by 30.16%.

At 3000 rpm engine speed, CO, CO_2, HC, and NO emissions decreased by 98.88%, 13.73%, 55.05% and 3.65%, respectively, but O_2 emissions increased by 22.99%.

As a result of the study;

- It has been observed that JP8/diesel fuel blends reduce CO, CO_2, HC, and NO emissions but increase O_2 emissions.
- It has been observed that the effect of JP8/diesel fuel mixtures on emissions is not in a linear relationship with the increasing JP8 ratio. Therefore, in further studies on the subject, the behavior of emission values depending on engine speed and JP8 ratio should be expressed mathematically by performing optimization studies.

REFERANCES

[1] J. Lee, H. Oh, and C. Bae, "Combustion process of JP-8 and fossil Diesel fuel in a heavy duty diesel engine using two-color thermometry," *Fuel*, vol. 102, pp. 264–273, Dec. 2012, doi: 10.1016/j.fuel.2012.07.029.

[2] M. A. Islam *et al.*, "Combustion analysis of microalgae methyl ester in a common rail direct injection diesel engine," *Fuel*, vol. 143, pp. 351–360, Mar. 2015, doi: 10.1016/j.fuel.2014.11.063.

[3] A. E. E. Khalil and A. K. Gupta, "Clean combustion in gas turbine engines using Butyl Nonanoate biofuel," *Fuel*, vol. 116, pp. 522–528, 2014, doi: 10.1016/j.fuel.2013.08.022.

[4] G. Üniv Müh Mim Fak Der *et al.*, "HAVACILIK YAKITI JP-8 VE DİZEL KARIŞIMLARININ TEK SİLİNDİRLİ BİR DİZEL MOTORUNDA PERFORMANS VE EGZOZ EMİSYONLARINA ETKİSİ," 2013.

[5] N. H. Pinkowski, S. J. Cassady, D. F. Davidson, and R. K. Hanson, "Spectroscopic inference of alkane, alkene, and aromatic formation during high-temperature JP8, JP5, and Jet-A pyrolysis," *Fuel*, vol. 269, Jun. 2020, doi: 10.1016/j.fuel.2020.117420.

[6] E. Schmidt, "'Air toxic& in combustion and gasification sys-tems: formation and removal," 1996.

[7] G. Labeckas and S. Slavinskas, "Comparative evaluation of the combustion process and emissions of a diesel engine operating on the cetane improver 2-Ethylhexyl nitrate doped rapeseed oil and aviation JP-8 fuel," *Energy Convers. Manag. X*, vol. 11, p. 100106, Sep. 2021, doi: 10.1016/j.ecmx.2021.100106.

[8] A. A. Yontar, "Injection parameters and lambda effects on diesel jet engine characteristics for JP-8, FAME and naphtha fuels," *Fuel*, vol. 271, Jul. 2020, doi: 10.1016/j.fuel.2020.117647.

[9] D. M. Korres, D. Karonis, E. Lois, M. B. Linck, and A. K. Gupta, "Aviation fuel JP-5 and biodiesel on a diesel engine," *Fuel*, vol. 87, no. 1, pp. 70–78, Jan. 2008, doi: 10.1016/j.fuel.2007.04.004.

[10] P. Arkoudeas *et al.*, "Study of using JP-8 aviation fuel and biodiesel in CI engines." [Online]. Available: www.elsevier.com/locate/enconman.

[11] J. Lee, J. Lee, S. Chu, H. Choi, and K. Min, "Emission reduction potential in a light-duty diesel engine fueled by JP-8," *Energy*, vol. 89, pp. 92–99, Sep. 2015, doi: 10.1016/j.energy.2015.07.060.

[12] K. E. Far, F. Parsinejad, and H. Metghalchi, "Flame structure and laminar burning speeds of JP-8/air premixed mixtures at high temperatures and pressures," *Fuel*, vol. 89, no. 5, pp. 1041–1049, May 2010, doi: 10.1016/j.fuel.2009.11.032.

[13] A. Uyumaz, H. Solmaz, E. Yilmaz, H. Yamik, and S. Polat, "Experimental examination of the effects of military aviation fuel JP-8 and biodiesel fuel blends on the engine performance, exhaust emissions and combustion in a direct injection engine," *Fuel Process. Technol.*, vol. 128, pp. 158–165, 2014, doi: 10.1016/j.fuproc.2014.07.013.

[14] C. Yao, P. Geng, Z. Yin, J. Hu, D. Chen, and Y. Ju, "Impacts of nozzle geometry on spray combustion of high pressure common rail injectors in a constant

volume combustion chamber," *Fuel*, vol. 179, pp. 235–245, Sep. 2016, doi: 10.1016/j.fuel.2016.03.097.

[15] P. K. Cheekatamarla *et al.*, "Design, integration and demonstration of a 50 W JP8/kerosene fueled portable SOFC power generator," *J. Power Sources*, vol. 193, no. 2, pp. 797–803, Sep. 2009, doi: 10.1016/j.jpowsour.2009.04.060.

[16] C. G. Tsanaktsidis, E. P. Favvas, G. T. Tzilantonis, and A. V. Scaltsoyiannes, "A new fuel (D-BD-J) from the blending of conventional diesel, biodiesel and JP8," *Fuel Process. Technol.*, vol. 127, pp. 66–71, 2014, doi: 10.1016/j.fuproc.2014.06.003.

[17] U. Žvar Baškovič, R. Vihar, T. Seljak, and T. Katrašnik, "Feasibility analysis of 100% tire pyrolysis oil in a common rail Diesel engine," *Energy*, vol. 137, pp. 980–990, Oct. 2017, doi: 10.1016/j.energy.2017.01.156.

[18] S. Gowdagiri, X. M. Cesari, M. Huang, and M. A. Oehlschlaeger, "A diesel engine study of conventional and alternative diesel and jet fuels: Ignition and emissions characteristics," *Fuel*, vol. 136, pp. 253–260, Nov. 2014, doi: 10.1016/j.fuel.2014.07.056.

[19] J. Lee and C. Bae, "Application of JP-8 in a heavy duty diesel engine," *Fuel*, vol. 90, no. 5, pp. 1762–1770, May 2011, doi: 10.1016/j.fuel.2011.01.032.

[20] M. D. Cárdenas, O. Armas, C. Mata, and F. Soto, "Performance and pollutant emissions from transient operation of a common rail diesel engine fueled with different biodiesel fuels," *Fuel*, vol. 185, pp. 743–762, Dec. 2016, doi: 10.1016/j.fuel.2016.08.002.

The influence of single-sided mounting material on longitudinal wave propagation in Ti6Al4V rod

Mehmet N. BALCI[1]

[1] Hacettepe University, Ankara/Turkey, mehmetbalci@hacettepe.edu.tr

Abstract **–This study examines the wave propagation, displacement and dynamic stress distribution within a solid Ti6Al4V rod mounted on a single side. Ti6Al4V alloy is used in some machine parts in automotive, aerospace/aeronautics, energy and biomedical applications. Due to its superior material properties and resistance to harsh environmental conditions, it is a future promising material. The influence of mounting material on displacement and stress behavior of Ti6Al4V rod is investigated by means of modelling one dimensional (1-D) wave propagation problem within the rod. Boundary conditions and initial condition is specified and governing partial differential equation (PDE) is solved computationally using an explicit scheme. Parametric analyses are performed to observe the effects of mounting material, mounting thickness and time on displacement and stress behavior. It is clearly observed that metallic mounting materials are efficient to delay stress and displacement waves without considerable reduction in their magnitude whereas rubber is very efficient in reduction of displacement and stress levels without considerable delay in displacement and stress waves.**

Keywords **– Wave propagation, Ti6Al4V rod, mounting material, explicit method, dynamic stress.**

I. INTRODUCTION

Titanium alloys have been recently used in many engineering applications. Ti6Al4V, also known as Ti64 is an $\alpha+\beta$ titanium alloy that has high strength, low density, high fracture toughness, excellent corrosion resistance and superior biocompatibility [1-3]. In the 1950s, Ti6Al4V alloy was designed for possible use in aircraft applications since this material withstands high loading conditions with less weight. Therefore, it is suitable for jet engines, gas turbines and many airframe components [4-7]. Moreover, Ti6Al4V has become an attractive material in other fields such as automotive, energy and biomedical. Bars and rod components have been widely used as machine components in many dynamic systems. For instance, the benefits of the utilization of Ti6Al4V alloy as connecting rod and crankshaft in a four-stroke engine are examined [8]. Viscous dampers and mounting materials are used to control and reduce the hazardous effects of impact loading on structures in dynamic systems. Jovanovic [9] presented a Fourier series solution for the longitudinal vibrations of a bar with viscous boundary conditions at both ends. Yüksel and Dalli [10] examined longitudinally vibrating elastic rod with locally and non-locally reacting damping, and optimal values for the external damping were determined. Lim [11] analyzed longitudinal wave speed in cylindrical auxetic rods with elastic constraint in the radial direction. Xu et al. [12] carried out a study on longitudinal vibration of elastically coupled multiple nano-rod system (MNRS) involving axial restraining springs. Sato [13] used finite-difference time-domain formulation for free boundary implementation in elastodynamics. Javanmardi et al. [14] reported that steel, aluminum, lead, and copper can be used as a metallic damper in structural systems subjected to various kinds of dynamic loading. In this study, an elastic rod made of Ti6Al4V has mounted on a single-side. Another side is subjected to displacement loading at the tip of right end at initial time $(t=0)$. Displacement distribution in the rod with respect to time is modelled by one-dimensional (1D) wave propagation equation. Then, this equation is numerically solved by means of the explicit method. Then, parametric analyses are conducted to reveal the influence of mounting material, mounting thickness and time on displacement and dynamic stress distribution.

II. PROBLEM DEFINITION AND FORMULATION

An elastic rod made of Ti6Al4V alloy is mounted at its left end. The right end is stress-free. The schematics of the problem is illustrated in Figure 1. This rod is subjected to initial tip displacement load at $t=0$ and it is free once displacement load is applied. Mounting material is considered as viscoelastic and Kelvin-Voigt material model is adopted [15, 16]. E, ρ show the elastic modulus and density of the rod. E_m, ρ_m, ξ_m and L_m denote elastic modulus, density, damping coefficient and thickness of mounting material, respectively.

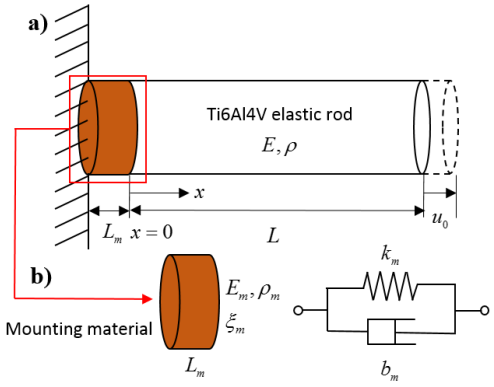

Figure 1: (a) The schematics of the elastic rod mounted at left end, (b) Kelvin-Voigt model for the mounting material.

$$E\,\frac{\partial^2 u(x,t)}{\partial x^2}=\rho\frac{\partial^2 u(x,t)}{\partial t^2},\ 0\le x\le L,\ t\ge 0, \tag{1}$$

$$\frac{\partial^2 u(x,t)}{\partial x^2}=\frac{1}{c^2}\frac{\partial^2 u(x,t)}{\partial t^2},\ 0\le x\le L,\ t\ge 0. \tag{2}$$

where $c=\sqrt{E/\rho}$ is the longitudinal wave propagation speed in elastic rod. Radius and length of the solid rod is assumed as 2 cm and 1m, respectively. The left end $(x=0)$ of the Ti6Al4V rod is mounted using various materials while right end of the boundary $(x=L)$ is stress-free. Therefore, following boundary conditions can be written:

$$E\,A_c\,\frac{\partial u(0,t)}{\partial x}=k_s\,u(0,t)+b_s\frac{\partial u(0,t)}{\partial t},\quad t\ge 0, \tag{3}$$

$$E\,A_c\,\frac{\partial u(L,t)}{\partial x}=0,\ t\ge 0, \tag{4}$$

Initial conditions are determined as:

$$u(x,0)=u_0\,\frac{x}{L},\ 0\le x\le L, \tag{5}$$

$$u_t(x,0)=0,\ 0\le x\le L. \tag{6}$$

The analytical solution for this wave equation can be performed using separation of variables as follows:

$$u(x,t)=X(x)T(t) \tag{7}$$

When Eq. (7) is substituted into Eq. (2), following solutions are obtained for $X(x)$ and $T(t)$.

$$X(x)=C_1\cos(\kappa x)+C_2\sin(\kappa x), \tag{8}$$

$$T(t)=C_3\cos(\kappa ct)+C_4\sin(\kappa ct), \tag{9}$$

The solution is written as:

$$\begin{aligned}u(x,t)=&D_1\cos(\kappa x)\cos(\kappa ct)+D_2\cos(\kappa x)\sin(\kappa ct)\\&+D_3\sin(\kappa x)\cos(\kappa ct)+D_4\cos(\kappa x)\sin(\kappa ct).\end{aligned} \tag{10}$$

Unknown constants D_1, D_2, D_3 and D_4 in Eq. (10) are determined using boundary and initial conditions provided by Eqs. (3)- (6). However, application of specified boundary and initial conditions to this PDE is not easy to handle since boundary conditions are not homogenous and analytical derivation in this case becomes very time consuming. Instead of analytical proceeding, computational method based on explicit scheme is adopted to get solution. Finite difference formulas are written based on the centered difference (CD) method. Then, longitudinal wave equation given by Eq. (2) is discretized in space and time domains.

$$\frac{\partial^2 u}{\partial x^2}\overset{CD}{\rightarrow}\frac{u_{i+1}^{\ j}-2u_i^{\ j}+u_{i-1}^{\ j}}{(\Delta x)^2}, \tag{11}$$

$$\frac{\partial^2 u}{\partial t^2}\overset{CD}{\rightarrow}\frac{u_i^{\ j+1}-2u_i^{\ j}+u_{i-1}^{\ j-1}}{(\Delta t)^2}, \tag{12}$$

After some mathematical manipulations, governing PDE given by Eq. (2) is obtained in discretized form as follows:

$$u_i^{\ j+1}=\frac{c^2\Delta t^2}{\Delta x^2}u_{i+1}^{\ j}+\left(2-\frac{2c^2\Delta t^2}{\Delta x^2}\right)u_i^{\ j}+\frac{c^2\Delta t^2}{\Delta x^2}u_{i-1}^{\ j}-u_i^{\ j-1}. \tag{13}$$

The solution for displacement indicated by $u_i^{\ j+1}$ depend on $u_{i+1}^{\ j}$, $u_i^{\ j}$, $u_{i-1}^{\ j}$ and $u_i^{\ j-1}$. Graphical demonstration of explicit method is provided in Figure 2. Horizontal line shows the spatial domain while vertical steps implies time marching towards next time step solutions.

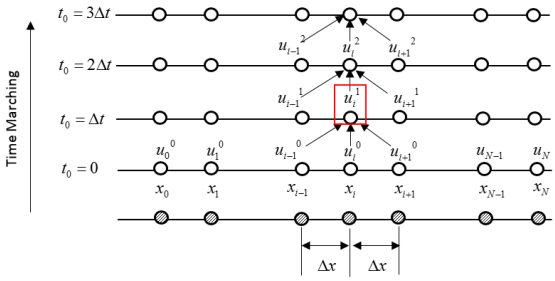

Figure 2: Graphical representation of explicit scheme.

Since boundary conditions are not homogenous and mixed type, it is necessary to obtain boundary conditions of the problem in discretized space and time steps. Boundary conditions can be discretized using centered difference (CD) scheme as follows:

$$E\,A_c\,\left.\frac{u_1^{\ j}-u_{-1}^{\ j}}{2\Delta x}\right|_{(x=0)}=-k\,u_0^{\ j}-b\frac{u_0^{\ j+1}-u_0^{\ j-1}}{2\Delta t}, \tag{14}$$

$$E\,A_c\,\left.\frac{u_{N+1}^{\ j}-u_{N-1}^{\ j}}{2\Delta x}\right|_{(x=L)}=0. \tag{15}$$

Displacement solution at left boundary $u(0,t)$ with respect to time is obtained in discretized form by means of mathematical manipulation of Eq. (14). Discretized equation is obtained for the left boundary where mounting material exists.

$$u_0^{\ j+1}=A\,u_1^{\ j}+B\,u_0^{\ j}-C\,u_0^{\ j-1}, \tag{16}$$

$$A=\frac{\left(\frac{2c^2\Delta t^2}{\Delta x^2}\right)}{\left(1-\frac{c^2\Delta t\,b_s}{E\,A_c\,\Delta x}\right)}, \tag{17}$$

$$B=\frac{\left(2+\frac{c^2\Delta t^2}{\Delta x^2}\left(\frac{2k_s\,\Delta x}{E\,A_c}-2\right)\right)}{\left(1-\frac{c^2\Delta t\,b_s}{E\,A_c\,\Delta x}\right)}, \tag{18}$$

$$C = \frac{\left(1+\frac{c^2\,\Delta t\,b_s}{E\,A_c\,\Delta x}\right)}{\left(1-\frac{c^2\,\Delta t\,b_s}{E\,A_c\,\Delta x}\right)}. \quad (19)$$

Eq. (15) requires that:

$$u_{N-1}{}^{j} = u_{N+1}{}^{j}. \quad (20)$$

Starter equation is derived by setting $j=0$ to governing discretized equation given by Eq. (13) and applying initial velocity condition $u_t(x,0)=0$ using centered difference (CD) formula. Therefore, this equation is shown as:

$$u_i^{1} = \frac{c^2\,\Delta t^2}{2\Delta x^2}u_{i+1}{}^{0} + \left(1-\frac{c^2\,\Delta t^2}{\Delta x^2}\right)u_i{}^{0} + \frac{c^2\Delta t^2}{2\Delta x^2}u_{i-1}{}^{0} \quad (21)$$

III. NUMERICAL RESULTS

Numerical results are obtained based on the displacement solution of discretized equation given by Eq. (13). Computer codes are developed in Matlab to generate results. Once displacement field within the Ti6Al4V rod is acquired, dynamic stress distribution is calculated using higher order forward, centered and backward difference formulas. Following relations indicate dynamic stress expressions. Since Ti6Al4V can be assumed as linear elastic material, Hooke's law is used based on general theory of elasticity.

$$\sigma = E\,\varepsilon_x. \quad (22)$$

where $\varepsilon_x = \partial u/\partial x$. Then, dynamic stress at left boundary $(x=0)$, interior $(0<x<L)$ and the right end boundary $(x=L)$ are calculated as:

$$\sigma(0,t) = \sigma_1{}^{j} = E\left(\frac{-u_3{}^{j} + 4u_2{}^{j} - 3u_1{}^{j}}{2\,\Delta x}\right), \quad (23)$$

$$\sigma(x,t) = \sigma_i{}^{j} = E\left(\frac{-u_i{}^{j+2} + 8u_i{}^{j+1} - 8u_i{}^{j-1} + u_i{}^{j-2}}{12\,\Delta x}\right), \quad (24)$$

$$\sigma(L,t) = \sigma_N{}^{j} = E\left(\frac{3u_N{}^{j} - 4u_{N-1}{}^{j} + u_{N-2}{}^{j}}{2\,\Delta x}\right). \quad (25)$$

$$\sigma_{Theoretical} = u_0\frac{E}{L}. \quad (26)$$

Material and dimensional properties of used Ti6Al4V alloy is provided in Table 1.

Table 1: Material and dimensional properties of Ti6Al4V rod [17].

Ti6Al4V	
Elastic modulus [GPA]	105.75
Density [kg/m^3]	4420
Radius [m]	0.02
Length [m]	1.0

Based on these material properties, the longitudinal wave propagation speed in Ti6Al4V alloy is 4891.35 m/s. Since length of the rod is 1m, wave propagates along the rod and hits left boundary (mounting) at t_{wr}. Reflection time (t_{wr}) can be found using following simple relation:

$$t_{wr} = \frac{L}{c} \quad (27)$$

Longitudinal wave due to the initial stretch applied at right end (stress free-end) hits to the left (mounting) boundary at $t_{wr} = 0.\,20444$ ms. Table 2 shows selected times in analyses and their propagation state (description) in the rod. $1/2\,t_{wr}$ and $3/2\,t_{wr}$ correspond to 1st wave propagation and return waves, respectively. In order to observe the influence of mounting material on the mechanical behavior of rod, larger time values are selected as $33/2\,t_{wr}$ and $35/2\,t_{wr}$, which respectively imply 9th propagation and return waves in the rod.

Table 2: Selected time values and illustration of their wave propagation state.

Selection	Time [ms]	Propagation State
$1/2\,t_{wr}$	0.10222	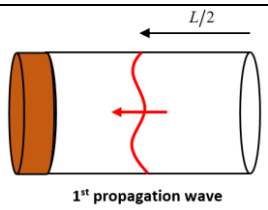
$3/2\,t_{wr}$	0.30666	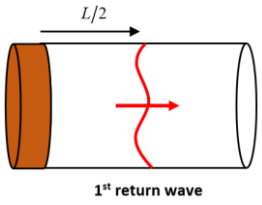
$33/2\,t_{wr}$	3.37326	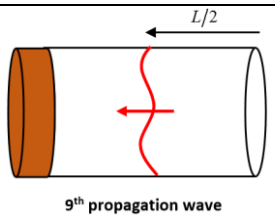
$35/2\,t_{wr}$	3.78214	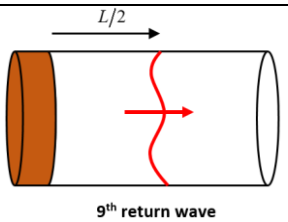

In analyses, as a mounting material, steel (St), aluminum (Al), brass (Br), copper (Co) and rubber are used. Mechanical and damping properties of these materials are given in Table 3. It can be seen that steel (St) has the highest elastic modulus while

rubber has the lowest one. Since density of the rubber is the smallest, the weight of mounting material at the same design volume is the minimum for rubber. Mounting stiffness and damping coefficient are found by [18],

$$k_s = \frac{E\,A_c}{L_m}, \tag{28}$$

$$b_s = 2\xi\sqrt{k_s\,m_m}, \tag{29}$$

where m_m is the mass of the mounting material and simply calculated by the formula $m_m = A_c\,L_m\,\rho_m$. Damping ratio for the rubber is the maximum as expected. Among other materials, copper (Co) and brass (Br) have higher damping ratio than those of steel (St) and aluminum (Al).

Table 3: Mechanical and damping properties of various mounting materials.

	Steel (St)	**Aluminum (Al)**	**Brass (Br)**	**Copper (Co)**	**Rubber**
Elastic Modulus	210 GPa	72 GPa	95 GPa	125 GPa	2.55 MPa
Density [kg/m^3]	7800	2700	8500	8900	1100
Damping ratio [-]	0.25x $(10)^{-4}$	6.5x $(10)^{-5}$	0.6x $(10)^{-3}$	2.0x $(10)^{-3}$	0.05

Figure 3(a)-(b) demonstrate the influence of mounting material on displacement and dynamic stress within the Ti6Al4V rod. At $t = t_{wr}/2$, 1st wave propagates towards the left end where mounting material exist. At this time, wave does not bump into the left end. Rigid mounting can be modelled by taking $k_s \to \infty$. Displacement profile in the rod is very similar for Rigid, St, Al, Br and Co mountings. However, displacement profile obtained for Rubber is very different throughout the rod. Dynamic stress value for Rigid, St, Al, Br, Co mountings is around 100MPa for $0 \le x \le 0.5\,\text{m}$, and significantly reduces to 0MPa for $0.5\,\text{m} \le x \le 1.0\,\text{m}$. However, dynamic stress value for the Rubber is 0 MPa at boundaries and 30 MPa in the middle of the rod. Theoretical stress at initial time $(t = 0)$ is calculated using Eq. (26) and displayed in grey color.

Figure 4(a)-(b) show the influence of mounting material on displacement and dynamic stress at larger time $t = 33t_{wr}/2$, which implies 9th propagation wave. While displacement for rigid mounting is exactly 0.5 mm for $0.5\,\text{m} \le x \le 1.0\,\text{m}$, displacement for St, Co, Br and Al is increasing at this section. Displacement for the rubber has a small decrease in the middle point and it is around 0.4 mm along the rod. While dynamic stress is suddenly drops at 0 MPa in the middle for rigid mounting, stress values for St, Co, Br and Al slowly reduces to 0 MPa at $0.5\,\text{m} \le x \le 1.0\,\text{m}$. Dynamic stress value for the rubber has the minimum value throughout the rod. It has around 0 MPa at boundaries and -30 MPa in the middle.

Figure 5(a)-(b) depict displacement and dynamic stress distribution in the rod for various values of mounting material thickness (L_m) .

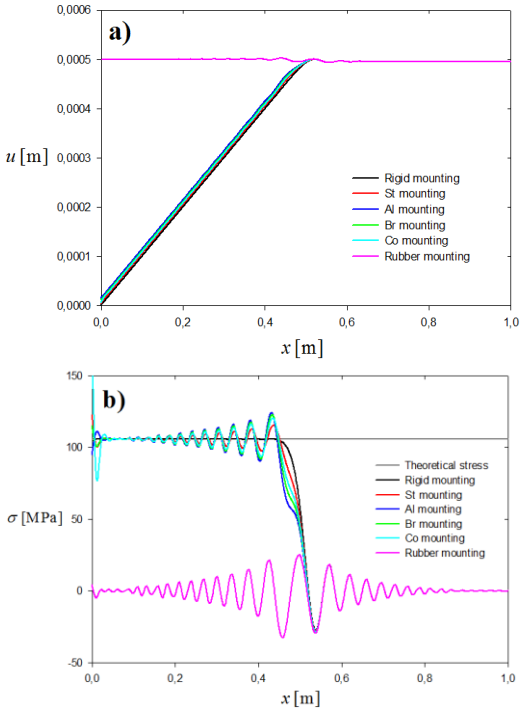

Figure 3: Influence of mounting material on (a) displacement, (b) dynamic stress distribution within Ti6Al4V rod at $t = t_{wr}/2$, $L_m = 0.01\,\text{m}$.

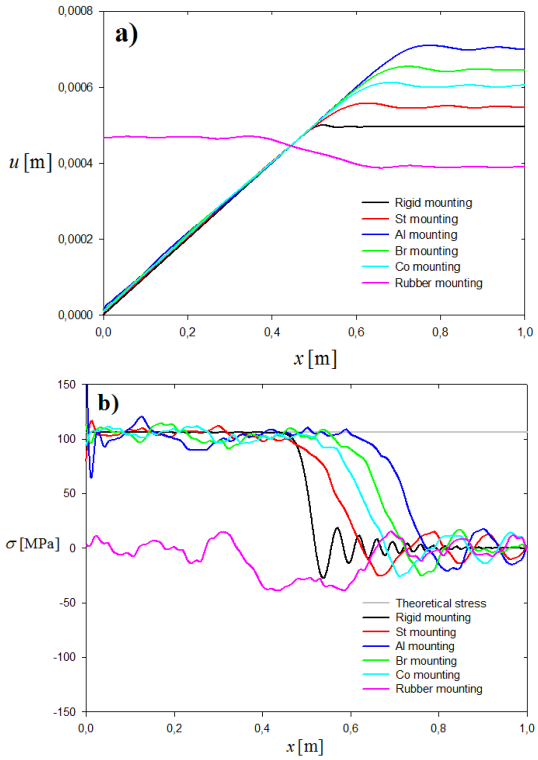

Figure 4: Influence of mounting material on (a) displacement, (b) dynamic stress distribution within Ti6Al4V rod at $t = 33t_{wr}/2$, $L_m = 0.01\,\text{m}$.

As the thickness of the mounting material (L_m) is increased from 5mm to 4 cm, the stiffness of the mounting is reduced at left boundary due to the relation given by Eq. (28). Indeed, as thickness is increased, damping coefficient remains the same due to the relation given by Eq. (29). As the thickness of the mounting material is increased, displacement values are increasing at section $0.5\,\text{m} \le x \le 1.0\,\text{m}$. Increase in the thickness leads to delay in reduction of dynamic stress within the rod. While dynamic stress reduces to 0MPa around $x = 0.58\,\text{m}$ for $L_m = 0.005\,\text{m}$, this location becomes $x = 0.62\,\text{m}$, $x = 0.70\,\text{m}$ and $x = 0.82\,\text{m}$ for $L_m = (0.01, 0.02, 0.04)\,\text{m}$, respectively.

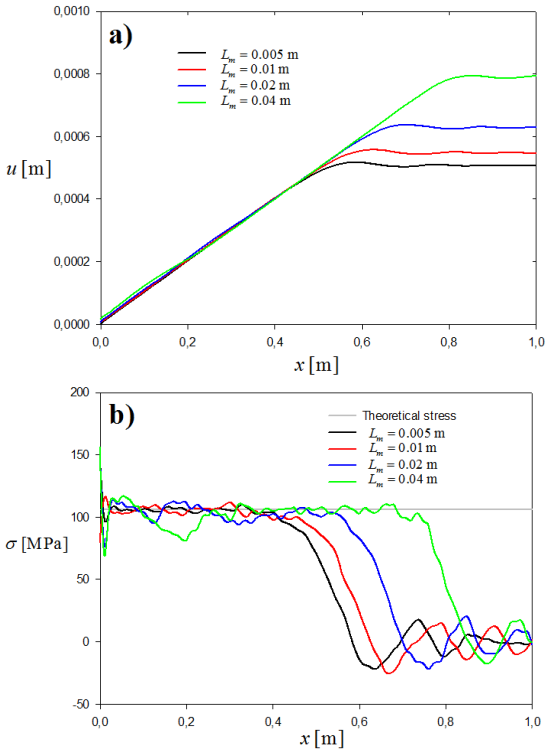

Figure 5: Influence of thickness of the steel (St) mounting on (a) displacement, (b) dynamic stress distribution within Ti6Al4V rod at $t = 33t_{wr}/2$.

Figures 6 presents displacement and dynamic stress distribution within Ti6Al4V rod mounted by aluminum material (Al) for various values of time such as $t = t_{wr}/2$, $t = 3t_{wr}/2$, $t = 33t_{wr}/2$ and $t = 35t_{wr}/2$. Wave reflection characteristic on displacement is obviously seen for Al mounting since stiffness value is high. At larger times such as $t = 33t_{wr}/2$ and $t = 35t_{wr}/2$ (9^{th} wave propagation and return), there is a delay in wave motion. This behavior is due to the stiffness of the mounting. Moreover, stress drop behavior tends to be smooth as time is increased.

Figure 7 depicts displacement and dynamic stress within Ti6Al4V rod mounted by rubber for different time values $t = t_{wr}/2$, $t = 3t_{wr}/2$, $t = 33t_{wr}/2$ and $t = 35t_{wr}/2$. For the rubber mounting, no significant delay in displacement and dynamic stress is observed since change occurs in the middle. However, due to large damping characteristics of rubber, displacement value is always positive and there is no sudden change within the rod. Dynamic stress value is around zero at ends, and it does not exceed ± 40 MPa in the middle.

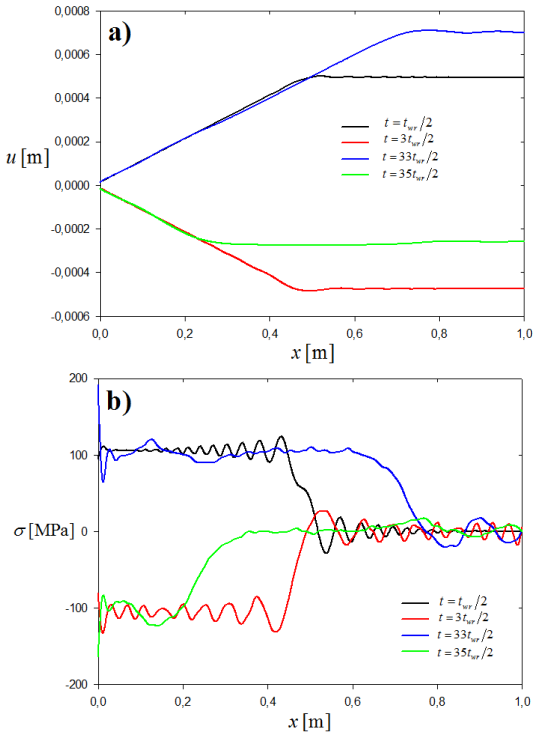

Figure 6: Influence of time on (a) displacement, (b) dynamic stress distribution in Ti6Al4V rod mounted by aluminum (Al) $L_m = 0.01\,\text{m}$.

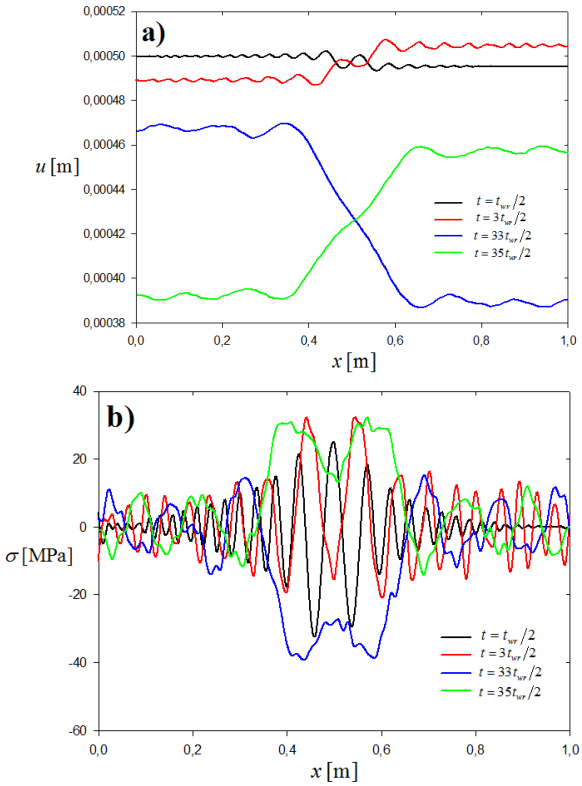

Figure 7: Influence of time on (a) displacement, (b) dynamic stress distribution in Ti6Al4V rod mounted by rubber mounting $L_m = 0.01\,\text{m}$.

IV. CONCLUSIONS

This study examines the wave propagation problem in solid Ti6Al4V rod mounted at single-side by various materials such as steel (St), aluminum (Al), copper (Co), brass (Br) and rubber. Ti6Al4V is used in many mechanical components in aerospace, aeronautics, energy and medical fields. Longitudinal wave propagation problem is modeled based on the 1-D wave propagation in solids. The mounting material at left boundary is modeled using Kelvin-Voigt material model, which includes stiffness and viscous damping parameter. Boundary conditions and initial condition is specified and governing partial differential equation (PDE) is solved by discretization in space and time domains using explicit scheme. Then, computational results are generated to assess the influence of mounting material, mounting thickness and time on displacement and dynamic stress distribution. Some conclusive remarks can be written as follows:

- Analyses conducted at first (1st) and ninth (9th) propagation and return waves showed that stiffness of the mounting materials are $k_s^{Rigid} > k_s^{St} > k_s^{Co} > k_s^{Br} > k_s^{Al} > k_s^{Rubber}$. Since metallic mounting materials have great stiffness and small damping, they lead to delay in displacement and stress without considerable drop in their magnitude.
- Maximum delay in displacement and stress is observed at Aluminum (Al) among metallic mounting materials. Sharp decrease in stress is seen in the middle of the rod for the rigid mounting. This sharp decrease tend to be softer for steel (St), copper (Co), brass (Br) and aluminum (Al) mountings.
- Rubber has small stiffness and high damping characteristics. Hence, it leads to significant decrease in displacement and stress level in Ti6Al4V bar without significant delay.
- Increase in mounting thickness leads to decrease in stiffness. Therefore, displacement and stress values have higher delay as thickness is increased.
- Since rubber has low stiffness and high damping property, it is useful to keep displacement with slight change in positive level. However, for aluminum (Al) mounting, displacement can be negative and wave reflection effect on dynamic stress is obvious. Stress level is significantly reduced for rubber mounting due to its high damping property.

References

[1] M. J. Donachie, "Titanium: A Technical Guide", second ed. *ASM International*, Materials Park, OH, 2000.

[2] C.Cui, B. Hu, L. Zhao, S. Lui, "Titanium alloy production technology, market prospects and industry development", *Materials & Design* 32(3), pp. 1684-1691, 2011.

[3] S. Liu, Y.C. Shin, "Additive manufacturing of Ti6Al4V: A review", *Materials and Design* 164, Article No: 107552, 2019.

[4] I. Inagaki, T. Takechi, Y. Shirai, N. Ariyasu, "Application and features of titanium for the aerospace industry", *Nippon Steel & Sumitomo Metal Technical Report*, pp. 22-27, 2014.

[5] R.R. Boyer, "An overview on the use of titanium in the aerospace industry", *Materials Science and Engineering A*, 213(1), pp. 103-114, 1996.

[6] P. Singh, H. Pungotra, N.S. Kalsi, "On the characteristics of titanium alloys for the aircraft applications", *Materials Today Proceedings*, 4(8), pp. 8971-8982, 2017.

[7] E. Uhlmann, R. Kkersting, T.B. Klein, M.F. Cruz, A.V. Borille, "Additive manufacturing of titanium alloy for aircraft components", *Proc. CIRP* 35, pp. 55-60, 2015.

[8] M. Hebzda, "Benefits of Using Ti6Al4V Alloy for Connecting Rod and Crankshaft of a Four-Stroke ICE", *Scientific Journal of Gdynia Maritime University*, 113(20), pp. 43-53, 2020.

[9] V. Jovanovic, "A Fourier series solution for the longitudinal vibrations of a bar with viscous boundary conditions at each end", *Journal of Engineering Mathematics*, 79, pp. 125-142, 2012.

[10] Ş. Yüksel, U. Dalli, "Longitudinally vibrating elastic rods with locally and non-locally reacting viscous dampers", *Shock and Vibration*, 12, pp. 109-118, 2005.

[11] T-C. Lim, "Longitudinal wave speed in cylindrical auxetic rods with elastic constraint in radial direction", *European Journal of Mechanics / A Solids*, 75, pp. 443-449, 2019.

[12] D. Xu, J. Du, Y. Zhao, "Longitudinal Vibration Analysis of Elastically Coupled Nanorods System with General Boundary Supports", *Sound & Vibration*, 53(2), pp. 16-28, 2019.

[13] M. Sato, "Comparing three methods of free boundary implementation for analyzing elastodynamics using the finite-difference time-domain formulation", *Acoustical Science & Technology*, 28(1), 2007.

[14] A. Javanmardi, Z. Ibrahim, K. Ghaedi, H.B. Ghadim, M.U. Hanif, "State-of-the-Art Review of Metallic Dampers: Testing, Development and Implementation", *Archives of Computational Methods in Engineering*, 27, pp. 455-478, 2020.

[15] J.A. Epaarachchi, "The effect of viscoelasticity on fatigue behavior of polymer matrix composites, Creep and Fatigue in Polymer Matrix Composites", *Woodhead Publishing Series in Composites Science and Engineering*, pp. 492-513, 2011.

[16] W. Flügge, "Viscoelasticity", Berlin, *Heidelberg: Springer Berlin Heidelberg*, 1975.

[17] http://www.matweb.com

[18] https://www.jpe-innovations.com/precision-point/structural-damping-properties-mechanical-systems/

Investigation of Usability of Canny Algorithm in the Field of Machinability

P. KARAKUS[1] and D. ZALAOGLU[2]

[1] Osmaniye Korkut Ata University, Osmaniye/Turkey, pinarkarakus@osmaniye.edu.tr
[2] Osmaniye Korkut Ata University, Osmaniye/Turkey, demetkayretli@osmaniye.edu.tr

Abstract **- Today, it is utilized from image processing methods in many fields. Edge detection is one of the basic and most important stages of image processing. In this study, the usability of the Canny algorithm, an extremely effective algorithm in edge detection method, is investigated in order to determine the cutting tool life, which is one of the important criteria in the interpretation of the machinability of the parts. For this purpose, during the milling process, two separate cutting tool inserts, being in a situation of eroded and usable, are used. The RGB images of the cutting insert have been converted to black-and-white and binary images. Then, the Canny edge detection algorithm is applied to these two different images and the results are compared. When both images results are evaluated, it is seen that the edges are determined better with the Canny algorithm applied to the binary image.**

Keywords **- Canny algorithm, Edge detection, Machinability.**

I. INTRODUCTION

Machining, which is one of the basic stages of production, is a widely used method [1]. Machinability is the most basic problem that is tried to be solved in machining processes. Although it does not have a very clear definition, machinability can be expressed as the relative ease or difficulty of shaping a material with machining methods by using appropriate cutting tools and cutting parameters [2].

In order to be able to comment on the machinability of a material, there are evaluation parameters such as cutting speed, amount of metal removal, tool life, cutting forces and surface quality [3]. In machining operations, tool life, which is one of the important parameters, is generally accepted as a scale for the wear of the cutting tool [4]. Tool wear is defined as the gradual loss of tool material that occurs on the surfaces of the workpiece in contact with the tool [5].

During machining, two different measuring methods on the point of being direct and indirect are used to determine tool wear [6]. Direct measurement methods are optical and image methods that aim to directly determine the wear on the tool during the cutting process and measure the geometric parameters of the cutting tool [7]. Indirect measurement methods, on the other hand, aim to evaluate the wear status of the tool by using signal properties such as measurable current, sensor. Indirect measurement methods are easier to apply than direct measurement methods, but they are less sensitive [8]. As indirect measurement methods; there are many studies in which machining forces, vibration, temperature, acoustic emission and signals from the feed motor and electrical power are used [9-20].

Edge detection is one of the most used analysis in the field of image processing [21]. Edge detection refers to the process of detecting and finding sharp discontinuities in an image [22]. Discontinuities are sudden changes in pixel density that characterize the boundaries of objects in a scene [23].

The edge indicates both the boundary between an object and its background and the boundary between overlapping objects. If the edges in the image can be accurately identified, it means that all objects can be positioned and key features such as area, perimeter, shape can be measured [24]. That is, incorrect results at this stage negatively affect subsequent analysis, as the edge forms the outline of the objects in the image [25].

Edge detection was first introduced by Marr and Hildreth in the 1980s. It has been seen that the edges of the image can be determined with Laplacian of Gauss [26]. Haralick [27] presented a method that searches for zero transitions in the direction of the gradient on the second derivative with the gradient value calculated by using the derivative value he found on the interpolation equation he applied on the pixels. Canny proposed a method based on the application of the operator obtained from the derivative of the Gaussian mask [28]. Canny edge detection algorithm is widely used in computer vision to find sharp intensity changes and find object boundaries in an image. The Canny edge detector classifies a pixel as an edge if the gradient magnitude of the pixel is larger than those of pixels at both its sides in the direction of maximum intensity change [29].

It is a fact that the Canny edge detection algorithm is used in many engineering fields today. Conversely, considering studies such as engineering applications [30], debugging in production automation [31], determining the dimensional parameters of rubber seals in the automotive industry [32], quality control of O-ring seals [33], dimensional control of complex shaped profiles [34], defect detection of valve guide [35], detection of cracks on the road [36], the feasibility of application of edge detection in machinability is considered. was found to be feasible. In this study, the usability of Canny edge detection algorithm as a different approach to direct measurement methods in Matlab program was investigated. For this purpose, two separate cutting tool inserts, which was on the situation of being of worn and usable situation during the milling process, was used. The color images of the insert were converted to black-and-white and binary images. Then,

the Canny edge detection algorithm was applied to these two different images and the results were compared. When the results of both images are evaluated, it is seen that the edges are determined better with the Canny algorithm applied to the binary image.

II. MATERIAL AND METHOD

A. Materials Used in the Study

In the study, the camera shown in the Figure 1 Sony ILCE-6000L DSLR digital camera was used. Sony 16-50mm f/3.5-5.6 OSS zoom lens is available. It has a 24.3 megapixel APS HD CMOS image sensor. Camera weight is 344 grams [37].

Figure 1: The camera used [37]

During the examinations, the triangular tool insert (Figure 2), that was not used in the milling process and was not exposed to any wear, was used with another triangular tool insert (Figure 3), that has completed the tool life when used sufficiently and has become unusable.

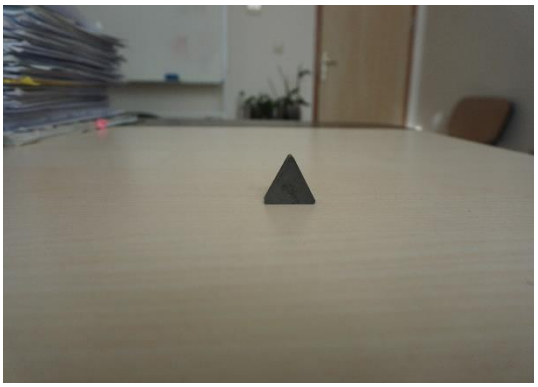

Figure 2: Crude cutting tool insert

Figure 3: Tool insert completing the tool life

B. Canny Edge Detection

Canny edge detection algorithm was developed by John F. Canny in 1986. Canny edge detection algorithm in general;

- Image smoothing (Smooth) with Gaussian filter to reduce noise
- Determine the gradient magnitude and gradient direction at each pixel.
- Suppression of Non-Maximum Points (Nonmaxima Suppression)
- Thresholding. [29, 38].

In the first step, images are obtained in a noisy manner due to the imperfection of the machine from which the image is obtained. In order for edge detection to be performed without error, the noise should be neutralized by passing a Gaussian filter to the image. The resulting blurred image is transferred as an input image to the next stage, where the direction and size of the gradient are determined [39,40].

In the next step, since edge detection takes place according to the places on the image where the gray scale density changes the most, the gradient value of the image needs to be calculated. For this, the gradient direction and value are calculated by means of a 3*3 Sobel filter [39,40]. At this stage, the gradient angles are calculated by equation (1);

$$\varphi = \arctan(G_y / G_x) \tag{1}$$

$$G_x = \begin{vmatrix} -1 & 0 & 1 \\ -2 & 0 & 2 \\ -1 & 0 & 1 \end{vmatrix} \qquad G_y = \begin{vmatrix} 1 & 2 & 1 \\ 0 & 0 & 0 \\ -1 & -2 & -1 \end{vmatrix} \tag{2}$$

$$|G| = |G_x| + |G_y| \tag{3}$$

In this equation, G is the gradient magnitude, which was on the point of being $|G_x|$ and $|G_y|$ the gradient vectors in the x and y direction.

In the third step, the blurred edges are sharpened with the help of the non-maximum suppression method. At this stage, two additional neighboring pixels in the direction of the gradient direction and angle value calculated in the previous stage are selected for each pixel, and the median pixel is desired to be higher than these. Pixels that do not meet this requirement are considered “0” and eliminated from the edge image. In this way, only pixels with maximum gradient values in the direction perpendicular to the edges are left in the edge image. In this way, suppression of non-maximums is ensured [34].

In the last stage, while some of the edges obtained in the previous process may be real edges, some may not be true edges due to various reasons. The purpose of double thresholding at this stage is to eliminate these non-edge pixels. Canny edge detection algorithm uses 2 threshold values, which is on the position of being high and low threshold. Pixels with an edge pixel density greater than the high threshold value are classified as “strong”, while pixels with a

low edge pixel density below the lower threshold value are suppressed. Pixels with a low edge pixel value between a low and a high threshold are classified as "weak" in case of edge [39]. Pixels classified as “strong” after double thresholding are determined as hard edges. Pixels, which is outside this classification and classified as “weak”, are taken if they are adjacent to pixels classified as “strong”. If it is not adjacent, it is not included in the sides by suppressing it [39].

III. RESULTS

In the images used during the studies, images were obtained with the tool inserts clear and the background blurred in order to determine the edges of the cutting tool inserts. In this way, only the details of the object to be studied are considered. As seen in Figure 2 and Figure 3, the pictures were taken with 6000 * 4000 pixels, 350 dpi, 16 mm focal length, 1/125 second exposure time, ISO 320.

The images taken in color were converted to black-and-white and binary format in MatLab program. Then, Canny edge detection algorithm is passed to both images. Thus, sharp edge details were obtained.

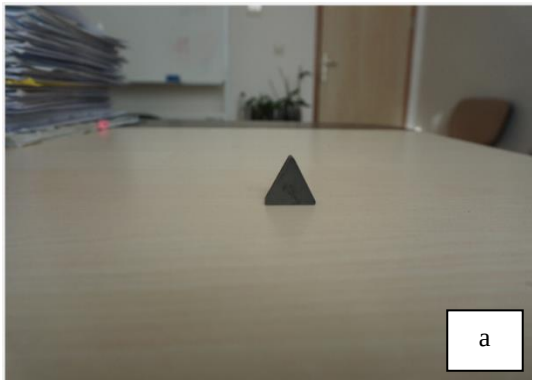

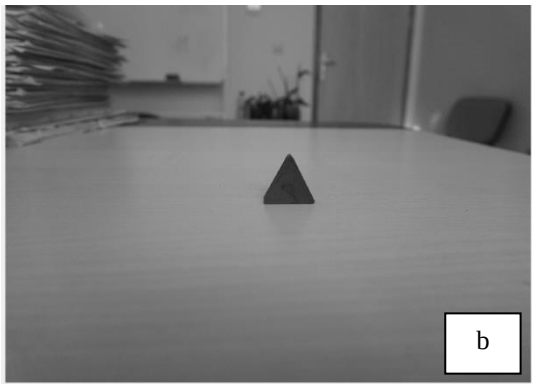

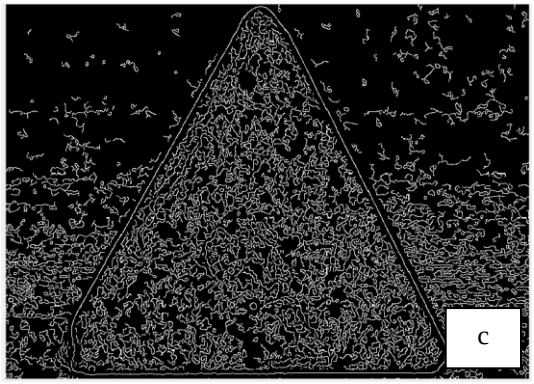

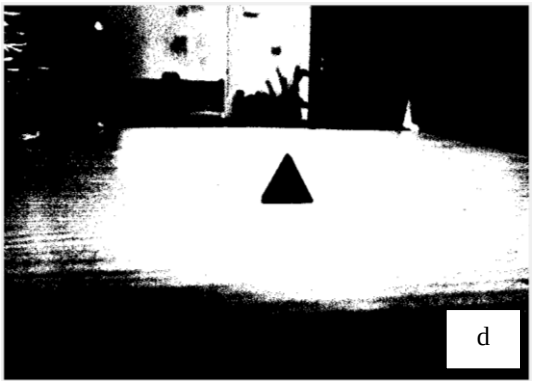

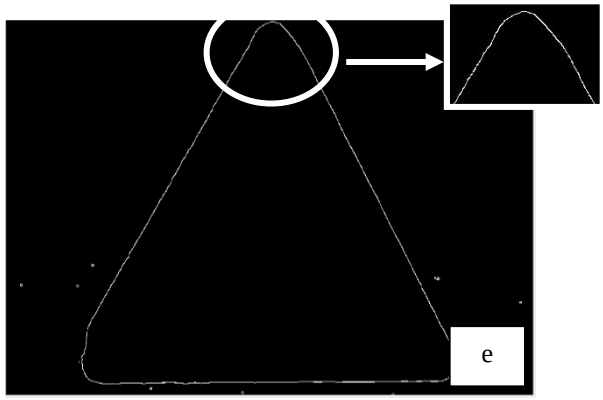

Figure 4: Crude cutting tool insert; a) original image, b) black and white image, c) canny algorithm applied to the black and white image, d) binary image and e) canny algorithm applied to the binary image

In Figure 4a, the raw image of the untreated cutting tool tip obtained in the Matlab program is given. Figure 4b shows the black and white image obtained in the Matlab program of this raw image, and the Canny algorithm applied to the black and white image in Figure 4c. When the results are examined, it is observed that the binary image and its canny algorithm are applied (Figures 4d and 4e, respectively) and that the images and edges are clearer and give better results.

In Figure 5a-5e, the raw image, black and white image, Canny algorithm applied to the black and white image, binary image and Canny algorithm applied to the binary image are given in the Matlab program of the tool tip that has completed its tool life, respectively, in Figure 5a-5e. In the images obtained, it is seen that better edge lines are obtained and how much the worn surface is eaten by passing the Canny

algorithm to the images converted to binary images.

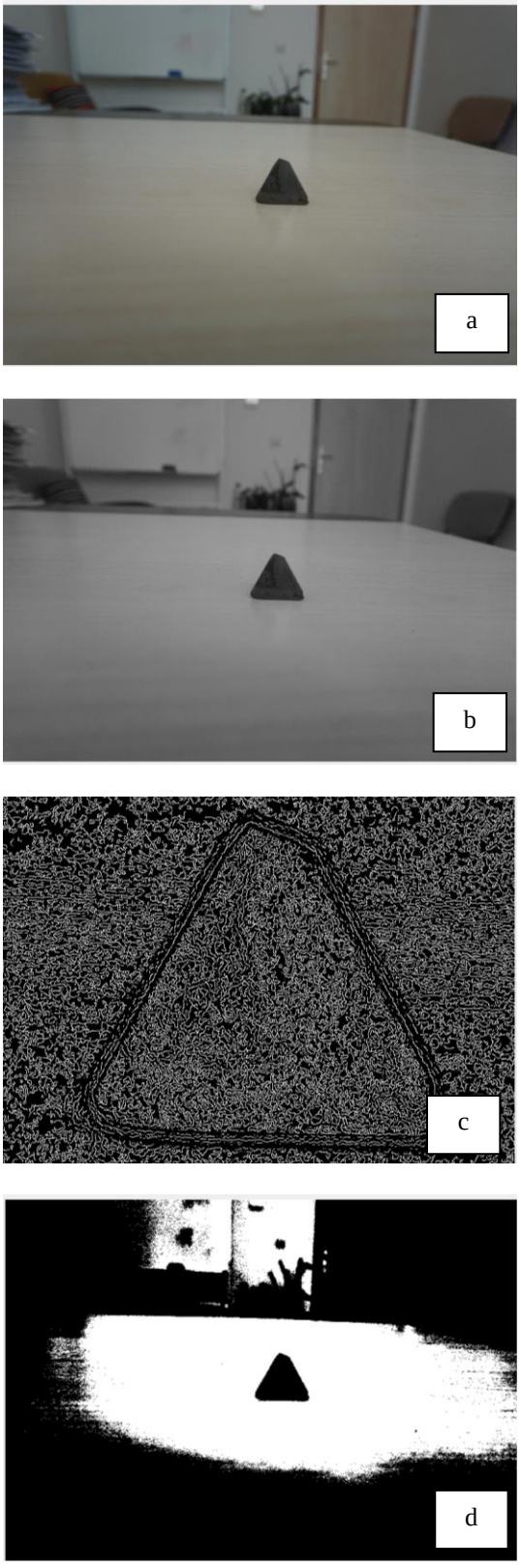

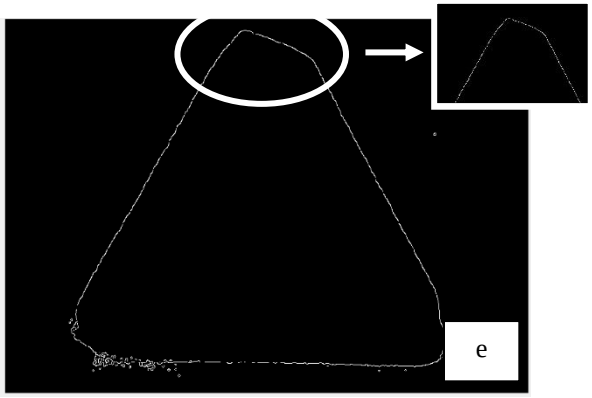

Figure 5: Tool insert completing the tool life; a) original image, b) black and white image, c) canny algorithm applied to the black and white image, d) binary image and e) canny algorithm applied to the binary imagea)

The results showed that the Canny algorithm, which is used extensively in image processing, is a practical method that can be used to visually determine the allowable wear amount on the lateral surfaces of the tool inserts. In addition, with the results obtained, it was determined that more accurate results were obtained by converting the color image used for removing the edges of the triangular cutting tool tips to binary image and then passing the Canny algorithm. For this purpose, it has been observed that for varying parameters (feed and rotation speeds, tool material and different materials to be machined), measurements can be made gradually up to the maximum amount of wear that will enable us to obtain a good surface, and in subsequent studies, the difference between the raw and machined parts of the tip can be expressed quantitatively. In addition, the usability of other edge detection methods in the determination of cutting tool insert wear will be investigated.

REFERENCES

[1] G. E. Dieter, *"SI metric edition (Mechanical Metallurgy),"* McGraw-Hill Education, London, UK, 1988.
[2] S. Coromant, *Modern Metal Cutting: A Practical Handbook*. Sweden: Sandvik Coromant, Sandviken, V1, 18-24, 1996.
[3] Y. Şahin, *Talaş Kaldırma Prensipleri 2*. Ankara: Nobel Yayın Dağıtım, 2001.
[4] L.A. Kendall, *"Friction and wear of cutting tools and cutting tool material, ASM Metal Handbook (Friction, Lubrication And Wear),"* Ohio, USA: ASM International, 1995.
[5] W. Koenig and K. Essel, *"New tool materials: wear mechanism and application"* Annals of CIRP, vol. 24, pp. 1, 1975.
[6] S. Jently, *"Measuring cutting tool wears online: some practical considerations,"* Manufacturing Engineering, pp. 55-60, 1984.
[7] K. Vehara, *"New attempts for short time tool-life testing,"* Annals of CIRP, vol. 22, pp. 23-24, 1973.
[8] B. Kıyak, A. Özer, H.S. Altundoğan, M. Erdem and F. Tümen*,"Cr (VI) reduction in aqueous solutions by using copper smelter slag,"* Waste Management, vol. 19, pp. 333-338, 1999.
[9] G. F. Micheletti, W. Koenig and H. R. Victor, *"In-process tool wear sensors for cutting operations,"* Annals of CIRP, vol. 25, pp. 483-496, 1976.
[10] S. M. Pandit, H. Suruhi and C. H. Kahng, *"Aplication of data depended systems to diagnostic vibration analysis,"* ASME Journal of Mech.des., vol. 102 (2), pp. 233-241, 1980.
[11] E. J. Weller, H. M. Schier and B. Wlichbradt, *"What sound can be expected from a worn tool,"* ASME Journal of Eng. for Ind., vol. 1, pp. 525, 1969.

[12] A. A. Zaharia and J. I. E. Gomayel,*"On the rehability of tutting temperatures for monitoring tool wear,"* Int. J. Mech. Tool. Des. Res., vol. 15, pp.195-208, 1975.
[13] G. Byrne, *"Thermoelectric signal characteristics and interfacial temperatures in machining of metals under geometrically defined conditions,"* Int. J. Mech. Tools Manufact., vol. 27 (2), pp. 215-224, 1987.
[14] L. V. Coolwel, *"Cutting temperature versus tool wear,"* Annals of the CIRP, vol. 24, pp. 73-76, 1975.
[15] F. Barrow, *"A review of experimental and theoritical techniques for assesing cutting temperatures,"* Annals of the CIRP, vol. 22, pp. 203-211, 1973.
[16] M. P. Groover, R. J. Karpovich and E. K. Levy, *"A study of the relationship between remote thermocouple temperatures and tool wear in machining,"* Int. J. Prod. Res., vol. 25, pp. 129-141, 1977.
[17] V. Solaya and D. Vukelya, *"Identification of tool wear rate by temperature variation of carbide tip,"* Annals of the CIRP, vol. 22, pp. 5-6, 1973.
[18] P. Srinivasa and P.K. Ramakrishna *"Acoustic emission analysis for tool wear monitoring in face milling,"* International Journal of Production Research, vol. 40, pp.1081– 1093, 2002.
[19] N. Ghosh, Y.B. Ravi, A. Patra, S. Mukhopadhyay, S. Paul, A.R. Mohanty and Y.B. Chattopadhyay, *"Estimation of tool wear during CNC milling using neural network-based sensor fusion,"* Mechanical Systems and Signal Processing, vol. 21, pp. 466–479, 2007.
[20] F.A. Al-Sulaiman and A.K. Baseer Ma Sheikh, *"Use of electrical power for online monitoring of tool condition,"* Journal of Materials Processing Technology, vol. 166, pp. 364–371, 2005.
[21] G. Jie and L. Ning, *"An Improved Adaptive Threshold Canny Edge Detection Algorithm,"* 2012, International Conference on Computer Science and Electronics Engineering, pp. 164-168,
[22] S. Vijayarani and M. Vinupriya, *"Performance analysis of canny and sobel edge detection algorithms in image mining"* International Journal of Innovative Research in Computer and Communication Engineering, vol. 1, pp. 1760-1767, 2013
[23] M. Raman and H. Aggarwal, *"Study and comparison of various image edge detection techniques,"* International Journal of Image Processing, vol. 1, pp. 1-11, 2009.
[24] E. Nadernejad, S. Sharifzadeh, and H. Hassanpour, *"Edge detection techniques: Evaluations and comparisons,"* Applied Mathematical Sciences, vol. 2, pp. 1507-1520, 2008.
[25] W. Rong, Z. Li, W. Zhang and L. Sun, *"An improved canny edge detection algorithm,"* 2014 IEEE International Conference on Mechatronics and Automation, pp. 577-582.
[26] D. Marr, and E. Hildreth, *Theory of Edge Detection*. Lodon, Proc. Roy. Soc., 1980.
[27] R. Haralick, "*Digital step edges from zero crossing of second directional derivatives*", IEEE Trans. Pattern Anal. Mach. Intell., vol.6, pp. 216-226, 1984.
[28] J. F. Canny, *"A computational approach to edge detection,"* IEEE Transactions on Pattern Analysis and Machine Intelligence, pp. 679-698, 1986.
[29] L. Ding, and A. Goshtasby, *"On the Canny edge detector,"* Pattern Recognition, vol. 34, pp. 721-725, 2001,
[30] M. Çetinel, *"Tersine mühendislik ile üç boyutlu cisimlerden grafik modeller için veri eldesi,"* MSc dissertation, Makine Mühendisliği Bölümü, Yıldız Teknik Üniversitesi, İstanbul, 2008,
[31] K. Balcı, *"Üretim otomasyonunda görüntü tabanli hata tanima sistemi,"* MSc dissertation., Elektirik Elektronik Mühendisliği Bölümü, Yıldız Teknik Üniversitesi, İstanbul, 2008.
[32] C. Liguori, A. Paolillo and A. Pietrosanto, *"An on-line stereo-vision system for dimensional measurements of rubber extrusions,"* Measurement, vol. 35, pp. 221-231, 2004.
[33] P. Peng, K. Lekadir, A. Gooya, L. Shao, S.E. Petersen, and A.F. Frangi, *"*A review of heart chamber segmentation for structural and functional analysis using cardiac magnetic resonance imaging*,"* Magnetic Resonance Materials in Physics, Biology and Medicine, vol. 29, pp. 155-195, 2016.
[34] M. Akdoğan, *"*Karmaşık şekilli mamullerin görüntü işleme teknikleri kullanılarak gerçek zamanlı boyut kontrolü*,"* Ph.D. dissertation, Makine Mühendisliği Bölümü, Selçuk Üniversitesi, Konya, 2018.
[35] A. Soni, M. Aghera, C. K. Modi and V. Chauhan, *"Machine vision based part inspection system using canny edge detection technique,"* 2010 Proc. of the 4th International Conference on Advances in Mechanical Engineering, pg: 531-535.
[36] Z. Othman, S. N. A. Zukfily, S. S. S. Ahmad and F. Kasmin, *"Road crack detection using modification of threshold values in canny algorithm,"* Proceedings of Mechanical Engineering Research Day 2020, pp. 184-186.
[37] (https://www.sony.com.tr/electronics/degistirilebilir lensli-fotograf-makineleri/ilce-6000-body-kit/specifications).
[38] Z. Xu, X. Baojie and W. Guoxin, *"Canny edge detection based on open CV,"* 2017 13th IEEE International Conference on Electronic measurement & Instruments (ICEMI), pp. 53-56.
[39] Y. İçer, *"*Kenar algılama algoritmalarının FPGA üzerinde gerçekleştirilmesi,*"* MSc dissertation, Elektirik Elektronik Mühendisliği Bölümü Bölümü, Fırat Üniversitesi, Elazığ, 2016.
[40] D.R. Sona, C. Rajabai, D. Dey, A. Jain, R.R. Das, S. Olabiyisi, *"A case study: edge detection techniques using hough transform and canny edge algorithm,"* International Journal of Mechanical Engineering and Technology, vol. 8, pp. 729-740, 2017.

Investigation Of Cutting Tool Overhang Length Effect on Surface Roughness of GGG70 Cast Iron

M.AYDIN[1] and M. TÜRKÖZ[1]

[1] Konya Technical University, Konya/Turkey, maydin@ktun.edu.tr
[1]Konya Technical University, Konya/Turkey, mturkoz@ktun.edu.tr

Abstract **- In machining processes, in order to obtain good surface qualities, it is very important to choose the cutting tool and cutting conditions. In addition, the rigidity of the cutting tool and workpiece fixture systems also majorly affects the surface quality. Numerous studies have been investigated the effect of cutting speed, feed and cutting depth parameters on the machining process. However, there are more limited studies investigating the effect of cutting tool overhang length. In this study, the effects of cutting tool overhang length on the surface roughness of austempered GGG70 cast iron material were investigated in the milling process. In this context, cutting speed, feed rate, cutting depth and number of passes were kept constant and milling was carried out at cutting tool overhang lengths of 2, 2.5, 3, 3.5, 4, 4.5 and 5 times the tool diameter (16 mm). The milling experiments performed with three repeated. As a result of experiments, the surface roughness obtained of 0.383 µm at 32 mm tool overhang length. The surface roughness increased to 0.547 at 80 mm tool overhang length. So, the surface roughness increased by 42.6% with the increase of the tool overhang length. In addition to the critical parameters, it has been observed that parameters such as tool overhang have a significant effect on the surface roughness.**

Keywords **– Cutting Tool Overhang Length, GGG70 Cast Iron, Milling, Surface Roughness**

I. INTRODUCTION

In machining processes, in order to obtain lower surface roughness and cutting force it is very important to choosing cutting and cutting tool condition. Several machining parameters, such as cutting speed, feed rate, workpiece material, and cutting tool geometry have significant effects on the process quality. Many researchers have studied the effect of these factors. The cutting tool overhang length affects the surface quality, especially during the turning and milling process [1]. Kiyak [1] was investigated the effects of tool overhang in the external turning process on both the surface quality of the work piece and tool wear. It was used work pieces of AISI 1050 material with diameters of 20, 30, and 40 mm. It was observed that the cutting tool deflection values increased as the tool overhang increased. Using a long tool length created excessive vibrations. It was concluded that, with a long tool length, the cutting variables were becoming important factors to control in order to significantly improve surface roughness. Kuram [2] investigated the effect of cutting tool overhang length on the tool wear, cutting forces during micro-milling process. Inconel 718 used for the Micro-Milling process. Three different values of cutting tool overhang length were selected, namely 10, 15 and 20 mm. According to experimental results, it was seen that the reduction in tool diameter increased with increasing cutting tool overhang length. As the cutting tool length was increased from 10 mm to 20 mm, the reduction in tool diameter increased from 3.74% to 7.15%. When the cutting tool overhang length was increased from 10 mm to 20 mm, the F_x force increased by 56.85% and the F_y force increased by 99.88%. Mishra [3] was determined optimum cutting tool overhang length for minimum surface roughness in turning operation. Also, the optimum machining parameters were found out for the situations where it is not possible to select an optimum tool overhang. In this context, the effect of spindle speed, depth of cut and feed rate on surface roughness were investigated. It is found that the surface roughness is found to be the minimum at tool overhang 14 mm. Sardar et al. [4] generated a finite element method (FEM) to understand the dynamics of tool shank overhang. They calculated the frequency at different tool overhang lengths, followed by experimental measurement of frequencies at these tool overhang lengths. They concluded that higher tool overhang length leads to more vibration in the machining process. Kassab and Khoshnaw [5] were investigated the surface roughness of the workpiece by selecting tool overhangs at 25, 30, 35, and 40 mm at different cutting conditions. In addition to the tool overhang length, the parameters of cutting speed, depth of cut and feed rate were also examined. The results showed that the feed rate had the greatest effect on surface roughness. It was clearly declared that as tool overhang length increase vibration and surface roughness increase directly. In all experiments, the surface roughness increased as the tool overhang increased. Similar studies are available in the literature on different cutting tips or different workpiece materials [6-9].

II. MATERIALS AND METHODS

In this study, the effect of cutting tool overhang on surface roughness was investigated. Austempered GGG-70 spheroidal graphite cast iron was used in the experiments. Chemical composition of the GGG-70 was given in Table 1. The workpiece sizes were specified as 300 mm x 50 mm x 50 mm

Table 1: Chemical Composition of GGG-70

C	Si	Mn	Cu	Mg	Ni	Mo
3.56	2.33	0.086	0.826	0.033	0.599	0.191

Before starting the experiments, the sample surfaces were milled to obtain planarity. Agma EA-600 CNC vertical machining center (Figure 1) in Konya Technical University was used in the experimental studies. For the milling process, a cutting tool produced by TeaguTec company was used. It has a diameter of 16 mm, which can be connected to two pieces of cutting inserts. Also, it has a fixed machining capacity with 90° cutting angle

Figure 1. CNC vertical machining center

The experiments were performed that dry process conditions. All experiments were performed in three repetitions. The cutting speed, feed rate and depth of cut were kept constant in the milling process. Constant parameters were given in Table 2. Experiments were performed that properly the cutting tool overhang was 2, 2.5, 3, 3.5, 4, 4.5 and 5 times of the diameter of cutting tool. 2PKT class AlTiN/TiN PVD coated tungsten carbide inserts from TeaguTec were used.

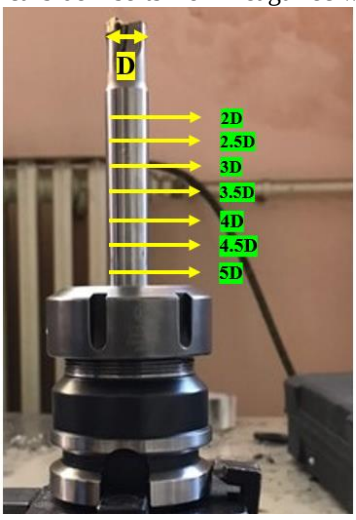

Figure 2. Cutting tool diameter and overhang lengths

Table 2: Constant values in machining process

Parameter	**Constant Value**
Cutting Speed (N)	2500 rpm
Feed Rate (f)	1000 mm/min
Cutting Depth (d)	0.3 mm

After each experiment, surface roughnesses were measured with the Mitutoyo surface roughness measuring device shown in Figure 3. Linear regression analysis was performed on the surface roughness measurement results. And the R squared value was calculated. Design of experiment were given Table 3.

Figure 3. Surface roughness measurement device

Table 1: Design of experiment

Exp.No/Parameters	**N**	**f**	**d**	**Overhang Length**
1	2500	1000	0.3	32
2	2500	1000	0.3	40
3	2500	1000	0.3	48
4	2500	1000	0.3	56
5	2500	1000	0.3	64
6	2500	1000	0.3	72
7	2500	1000	0.3	80

III. Results and Discussion

As a result of the experiments, the surface roughnesses were given in Table 4. The standard deviation was calculated for each experiment. It is clearly seen that as the tool length increased, the surface roughness values increased.

Table 4: Surface roughness values in machining process

Cutting Tool Overhang Length	Surface roughness (µm)			Mean	Std. Dev.
	Exp. 1	Exp. 2	Exp. 3		
2D (32 mm)	0.38	0.37	0.40	0.383	0.02
2.5D (40 mm)	0.39	0.41	0.40	0.400	0.01
3D (48 mm)	0.42	0.43	0.42	0.423	0.01
3.5D (56 mm)	0.47	0.47	0.48	0.473	0.01
4D (64 mm)	0.49	0.49	0.48	0.487	0.01
4.5D (72 mm)	0.48	0.5	0.51	0.497	0.02
5D (80 mm)	0.54	0.55	0.55	0.547	0.01

The maximum standard deviation between repetitions was calculated 0.02 micrometer. So, average surface roughness

was used for comparisons. The average surface roughness values were given in Table 4. The average surface roughness determined of 0.383 micrometer when the cutting tool overhang length was 2D (32 mm), this value increased 42.6% to 0.547 micrometer when the cutting tool overhang length was 5D (80mm). In finishing operations, the average surface roughness should be a maximum of 0.4 micrometers. So, during finishing cutting tool overhang length should not be used higher than 2.5 times the tool diameter.

The average surface roughness results are given graphically in figure 4. Linear regression analysis was performed on the surface roughness results. Analysis results shown in Table 6. The R-squared value is 97.85. It is seen that the increase in surface roughness with the increase in cutting tool overhang length is linear and significant.

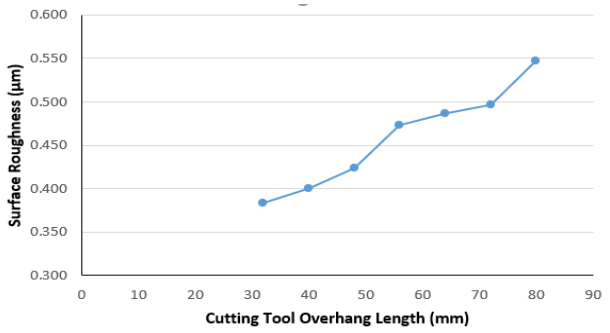

Figure 4. Surface roughness graph based on cutting tool overhang length

Table 6: Linear regression analysis results

Model Summary

S	R-sq	R-sq(adj)	PRESS	R-sq(pred)	AICc	BIC
0.0082873	97.85%	97.42%	0.0008672	94.56%	-35.59	-43.75

Also, normal probability and histogram graphs were plotted according to experiment results. It was observed that the frequency distribution of the results approached the normal distribution (Figure 5).

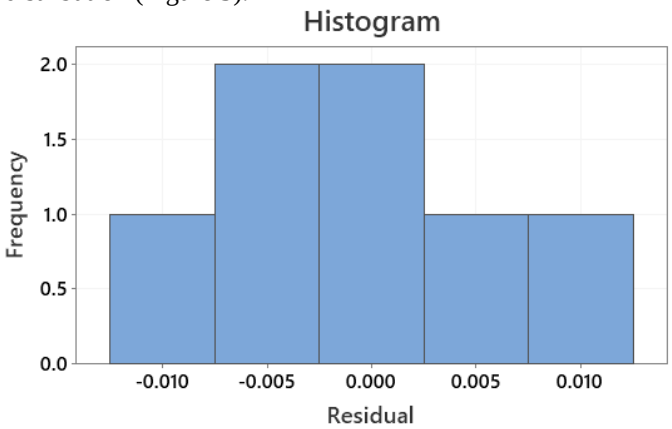

Figure 5. Histogram Graph-Normality Test Results

Figure 6 shows the normal distribution graph. It was seen that the marked points represent a line.

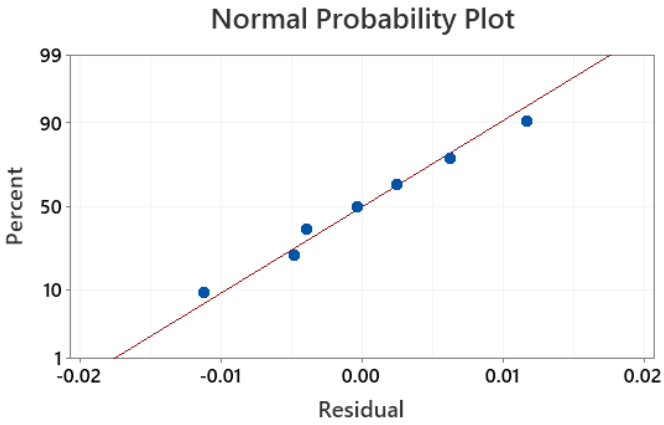

Figure 6. Normal probability plot of results

IV. CONCLUSIONS

In this study, the effect of cutting tool overhang length on surface roughness of Austempered GGG-70 were investigated. The outputs of the study are summarized below:

(1) Although the cutting conditions are constant, it has been understood that the parameters affecting the vibration, such as the cutting tool overhang length, are also very effective on the surface quality.

(2) As a result of the milling experiments, a significant increase was observed in the surface roughness values.

(3) According to the results, while the surface roughness was 0.383µm, this roughness value increased to 0.547 µm

(4) Up to 70% improvement in surface roughness was achieved by shortening the tool overhang length.

(5) In finishing operations, the average surface roughness should be a maximum of 0.4 micrometers. So, during finishing cutting tool overhang length should not be used higher than 2.5 times the tool diameter.

REFERENCES

[1] M. Kiyak, B. Kaner, I. Sahin, B. Aldemir, & O. Cakir, The dependence of tool overhang on surface quality and tool wear in the turning process. International Journal of Advanced Manufacturing Technology, 51(5–8), pp. 431–438. https://doi.org/10.1007/s00170-010-2654-y,2010

[2] E. Kuram, Effects of the Cutting Tool Overhang Length on the Tool Wear, Forces and Burr Dimension in Micro-Milling. Dokuz Eylul University- Faculty of Engineering Journal of Science and Engineering, Vol. 19, 55, pp229-237, 2017

[3] V. Mishra, G. S. Khan, K. D. Chattopadhyay, K. Nand, and R. V. Sarepaka, "Effects of tool overhang on selection of machining parameters and surface finish during diamond turning," Meas. J. Int. Meas. Confed., vol. 55, pp. 353–361, 2014, doi:10.1016/j.measurement.2014.05.019.

[4] Nabin S., Amiya B., Nirmal K.M., Modal Analysis and Experimental Determination of Optimum Tool Shank Overhang of a Lathe Machine, Sensors and Transducers, Vol. 99, Issue 12, December 2008, pp. 53-65

[5] Kassab SY, Khoshnaw YK, The effect of cutting toolvibration on surface roughness of workpiece in dry turningoperation. Eng Tech 25(7):879 – 889, 2017

[6] Clancy BE, Shin YC, A comprehensive chatter prediction model for face turning operation including tool wear effect. Int J Mach Tools Manuf 42(9):1035 – 1044, 2002

[7] Haddadi E, Shabghard MR, Ettefagh MM, Effect of different tool edge conditions on wear detection by vibration spectrum analysis in turning operation. J Appl Sci 8(21):3879 – 3886, (2008)

[8] Abouelatta OB, Madl J, Surface roughness prediction based on cutting parameters and tool vibrations in turning operations. J Mater Process Technol 118:269 – 277, 2001
[9] Kotaiah KR, Srinivas J, Sekar M, Prediction of optimal stability states in inward-turning operation using neurogenetic algorithms. Int J Adv Manuf Technol 45:679 – 689, 2009

Effect of Shrink Fit Process on Total Equivalent Stress and Total Amount of Material

M.AYDIN[1] and M. TURKOZ[1]

[1] Konya Technical University, Konya/Turkey, maydin@ktun.edu.tr
[1]Konya Technical University, Konya/Turkey, mturkoz@ktun.edu.tr

Abstract **- Pressure intensifier's, hydraulic cylinders and the extrusion containers are manufactured in compound layers in order to resist the stresses caused by the very high internal pressures. The assembly of the cylinder layers named "shrink fit" is done within certain shrinkage allowances. Thus, the compressive stresses created by the outer cylinder on the inner cylinder. Compressive stresses reduce the level of radial tensile stresses. In this study, the differences in stress levels of compound cylinders with different material pairs operating under ultra-high pressure were investigated. In addition, the lightest cylinder that can be obtained by determining the optimum dimensions in compound cylinders with the same stress value has been investigated. And the weight savings that can be achieved in case this stress value is carried with a single layer cylinder has been determined. The maximum equivalent stresses in the cylinders were determined by the Finite Element Method (FEM). In this context, material pairs of Aluminium-Steel, Steel-Steel and GGG40 (Cast Iron)-Steel were used. According to the results of the analysis, 716 MPa equivalent stress was calculated under 350 MPa pressure in a single layer cylinder. This equivalent stress was reduced to 579 MPa by using the same amount of material with the Steel-Steel shrink-fit process. The optimum cylinder diameter dimensions with the same stress were determined. The total amount of steel used was 6.65 kg in a single-layer cylinder, this value decreased to 3.46 kg in the compound cylinder with optimum diameters. So, up to 52% of the amount of material was saved with the shrink-fit process**

Keywords **– Container, Shrink-Fit, Hydraulic Cylinder, Material Weight Saving**

I. INTRODUCTION

In the industry, shrink fitting widely used assembly method. For example, extrusion containers, hydraulic piston, pressure intensifiers, autofrettage, industrial cleaning and high-pressure pasteurization processes, hydraulic presses, forging presses, power plants, gas storages, chemical and nuclear plants, military applications etc. [1]. Shrink fit is an assembly method in which heat is used, high radial stresses occur in cylindrical parts, and two or more cylinders with tolerances are combined. [2]. The heated metal cylinder will expand and grow, and the cold cylinder can be easily assembled inside the heated cylinder. Then the heated cylinder, which has cooled down, tries to return to its original size and applies radial pressure to the inner cylinder. [3]. Friction between the cylinders is very important in terms of torque transmission and safety of the assembly.

Miraje and Patil [1] investigated two- and three-layer cylinders to reduce the total amount of material. Steel was used for all layer materials. The stresses in the cylinders were calculated analytically and these values were compared with the FEA results. In the study, cylinder diameter ratios and shrinkage allowance were optimized. The difference between analytical results and ANSYS results is below 4%. 37974 mm^3 material was saved in the two-layer cylinder and 31778 mm^3 in the three-layer cylinder. Öztürk [3] investigated analytically and numerically the interference pressure of two cylinders designed with steel-steel and steel-aluminum materials at different shrinkage allowance in the shrink fit process. In addition, the stresses occurring along the thickness distribution in the shrink fit process were determined and verified with analytical values. In the study, it was stated that when the geometry of cylinders is simple, it may be sufficient to calculate the stress and interference pressures by analytical methods, but the finite element analysis results are more reliable in complex geometry assembly processes. Numerous studies investigated stresses formed in compound cylinders with FEA. And they were made verification of between analytic results and FEA results [4-9] Patil A. S., [10] used cylinders made of AISI 1020 steel with shrink fitted inner diameter 100 mm and outer diameter 153 mm. The cylinders were subjected to cyclic internal pressure between 0-250 MPa and the constant pressure applied to the outer surface. Both the cylinders were subjected to constant and non-constant amplitude loading. Fatigue analysis of compound cylinders was done by FEM. Due to the high number of cycles; the Stress-Life method was used. Analysis results showed that the outer cylinder was damaged earlier than the inner cylinder. It was stated that the contact surfaces, which are the most important region in the cylinders, fatigue faster than the other regions. Özel et al., [11] investigated the stress and deformations for different hub-shaft connections using FEM to determine the shrink fit between compound cylinders. It was stated that the ends of the cylinders are more dangerous than the center of cylinders.

In the literature, it is known that the radial stresses during occurring the shrink fitting process increase the fatigue life of the material and reduce the total stress on the material [13-16]. In this study, the effect of shrink-fit process on total equivalent stress and total amount of material were investigated. In this context, single-layer cylinder and compound-layer cylinders under 350 MPa pressure were compared in terms of maximum equivalent stress and total amount of material. The equivalent stress reduction in compound cylinders was calculated by FEM analysis. Comparison of the equivalent stresses under the same pressure in single-layer and double-layer cylinders was made. At the same stress level, optimum diameters of compound cylinder were determined. And material saving was calculated.

II. Materials and Methods

In this study, firstly total equivalent stress on the single layer cylinder determined by Finite Element Analysis (FEA). This stress value was used as the reference for comparing with shrink-fitted process. The effect of shrink-fit process on total equivalent stress and total amount of material in compound cylinders with different material-pairs operating under 350 MPa high pressure was determined.

A. Geometric Modelling

In the process, single and double layered cylinders were used (Figure 1). All cylinders have 60 mm inner diameter and 100 mm length. Selected diameter dimensions and analysis number were given in Table 1.

Table 1: Geometric Dimensions

Compound Cylinder	**1** (mm)	**2** (mm)	**3** (mm)	**4** (mm)	**5** (mm)
Inner Diameter	60	60	60	60	60
Middle Diameter	70	80	90	100	110
Outer Diameter	120	120	120	120	120
Shrinkage Allow.	0.05	0.05	0.05	0.05	0.05

The cylinders in the process were created in 3D in the Solidworks program. The shrinkage allowance is given in the FEA at the stage of defining the contact conditions. FEA's were performed using by Solidworks Simulation.

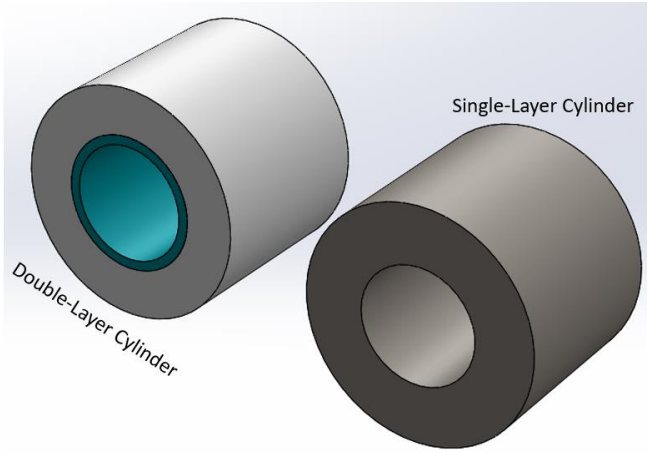

Figure 1: Single and Double-Layer Cylinders

B. Defining Material Properties

AISI 4140 steel material was used single layer cylinder. In compound cylinder, Al-St, GGG40-St and St-St material pairs were used. The mechanical properties of the materials given in Table .

Table 2: Mechanical properties of the material [17]

Material	Yield Strength	Tensile Strength	Elastic Modulus	Poisson Ratio
AISI 4140 (St)	835 MPa	952 MPa	210 GPa	0.29
Aluminum (Al)	345 MPa	485 MPa	72 GPa	0.33
GGG40	250 MPa	400 MPa	165 GPa	0.27

C. Contact Definitions

In the single layered cylinder, contact definition was not used. In compound cylinders, "Shrink-Fit" contact definition was used in Solidworks Simulation (Figure **2**).

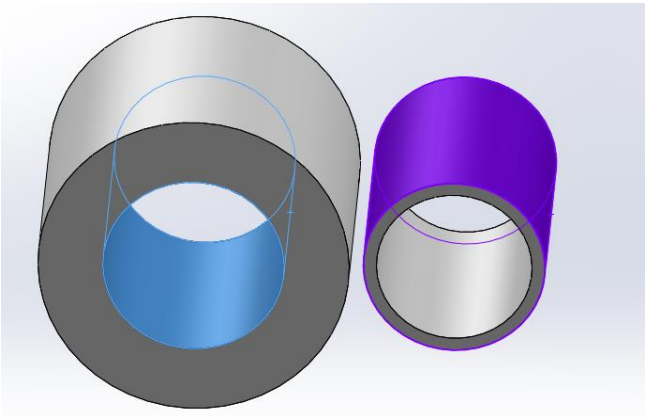

Figure 2: Shrink-fitted faces

D. Meshing

Curvature-based mesh type of maximum 6, minimum 4 mm sizes were used in the analysis. The model has 26304 elements and 41713 Nodes in total.

E. Defining Load and Boundary Conditions

Two boundary conditions and internal pressure were defined in the SEA model. Internal pressure of 350 MPa was applied inside the cylinder. The axial and rotational motion in z direction were limited (Figure 3).

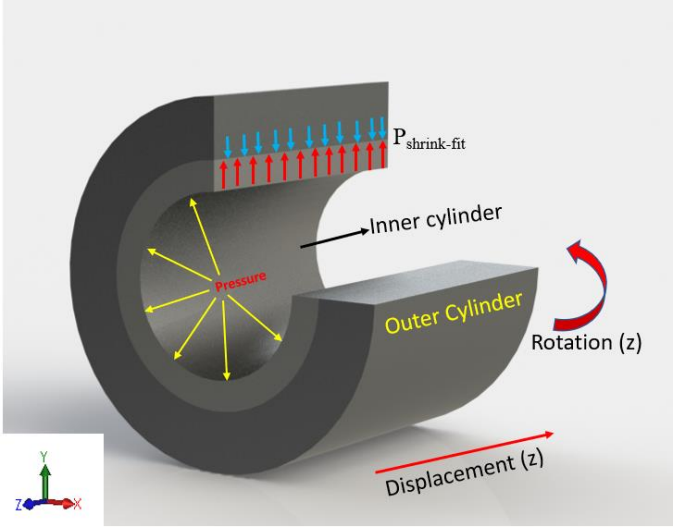

Figure 3: Boundary conditions

III. Results and Discussion

Firstly, single layer steel cylinder and compound St-St cylinders were compared. The average of the stresses on the inner surface of the inner cylinder (Figure 4) were given.

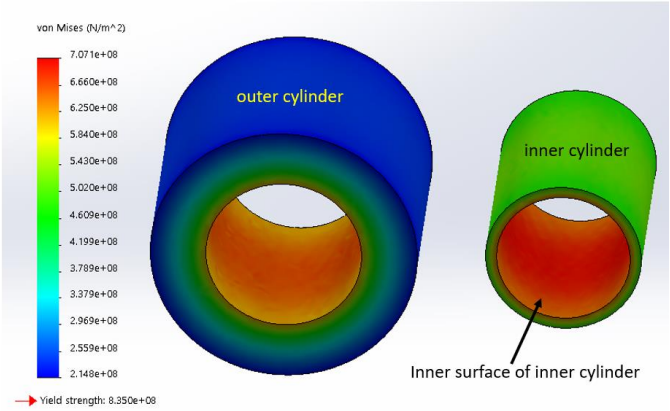

Figure 4. FEA result of compound cylinder

Total equivalent stresses of single layer cylinder and Steel - Steel compound cylinders under 350 MPa internal pressure were given Figure 5. In all dimensions of compound cylinders occurred less equivalent stress compared to single layer cylinder. The equivalent stress in the single-layer cylinder was 802 MPa. This stress was reduced to 579 MPa by the shrink fit process. With the shrink-fit process, the total equivalent stress was reduced by 38.5%.

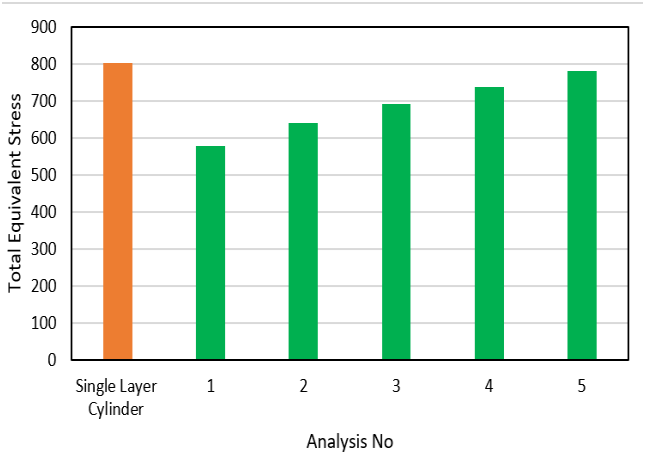

Figure 5: Total Equivalent Stresses of Single layered and St-St Compound Cylinder

As the inner diameter of outer cylinder increased, the equivalent stress on the inner cylinder increased. Because, pre-stress decrease while inner diameter of outer cylinder increase. The pre-stress that occurs in the shrink fit process create compressive stresses on the inner cylinder. These compressive stresses reduce the tensile stresses on the inner cylinder surface. The equivalent stress on the inner cylinder decreased as the pre-stress increased. Lower equivalent stresses were determined with the steel-steel material pair compared to the single-layer cylinder. In addition, a shrink-fit process was performed with outer cylinder made two different materials. These are Aluminum-Steel and GGG40 (Cast Iron)-Steel material pairs. All the results obtained from the analyzes are given in Table 3. Almost all the stresses in the Al-St compound cylinder were higher than the single-layer cylinder. On the other hand, in the GGG70-ST compound cylinder, total equivalent stress decreased.

Table 2: Total equivalent stress of single and compound cylinders

Compound Cylinder		1 (MPa)	2 (MPa)	3 (MPa)	4 (MPa)	5 (MPa)
Outer Cylinder	Inner Cylinder					
St	St	579	640	692	737	779
Al	St	1190	1001	858	830	779
GGG04	St	677	708	736	761	786
Single Layer Cylinder		802				

It is readily apparent that fewer stress occurs compound cylinders with St-St and GGG40-St materials under 350 MPa. While the improvement in the equivalent stress in the St-St compound cylinder was 38.5%, this value was maximum 18.5% in the GGG40-St layered cylinder. It was not observed an improvement in the Al-St compound cylinders.

The results were also compared in terms of the total amount of material used. The minimum diameter dimensions that give the same stress in St-St and GGG40-St compound cylinders are given in Table x, taking reference to 802 MPa (stress on the single layer cylinder). The equivalent stress was 802 MPa

when the inner diameter of the St-St layered cylinder was 60 mm, the middle diameter was 70, the outer diameter was 96 mm. Total amount of material (T.A.M.) decreased of 52% when using a compound cylinder instead of a single-layer cylinder. In the GGG40 - St compound cylinder, material savings could not be achieved at the same stress value (802 MPa). Since the Al-St compound cylinder did not have a significant effect on the equivalent stress, the total amount of material used was not investigated.

Table 3: Total amount of materials of Single and Compound Cylinder

Compound Cylinder	**T.A.M. (Inner Cylinder)**	**T.A.M. (Outer Cylinder)**	**T.A.M. Total**
Single Layer	6.65 kg	-	6.65 kg
St - St	0.8 kg	2.66 kg	3.46 kg
GGG40 - St	5.23 kg	1.41 kg	6.64 kg

As a result, it has been shown that less material is used when single-layer cylinders operating under high pressure are manufactured as compound cylinder. It is also seen that compound cylinders do not affect the same contribution for all material pairs.

IV. CONCLUSIONS

In this study, the effect of shrink-fit process on equivalent stress and total amount of Material were investigated. The outputs of the study are summarized below:

(1) As a result of the FEA's, a significant decrease was observed in the total equivalent stress on inner surface of inner cylinder.

(2) According to the results, while the total equivalent stress on the single layer cylinder was 802 MPa, this stress value could be reduced to 579 MPa with St – St compound cylinder.

(3) The improvement in the equivalent stress in the St-St compound cylinder was 38.5%.

(4) In addition to St-St compound cylinder, the equivalent stresses of compound cylinders with different two material pairs (Al-St and GGG40-St) were determined. It was not observed significant effect of Al-St compound cylinders.

(5) In the GGG40-St compound cylinder, the total equivalent stress was reduced maximum 18.5% but it had no effect on the total amount of material.

(6) By using the St-St compound cylinder, 52% was saved on the total amount of material used.

REFERENCES

[1] Miraje A. A., and Patil, S. A., Infinite fatigue life of three layer shrink fitted compound cylinder under fluctuating internal pressure. International Journal of Mechanical Engineering and Technology, Volume 3, Issue 1, 299-310, January 2012

[2] Truman, C. E. & Booker, J. D. Analysis of a shrink-fit failure on a gear hub/shaft assembly. Eng. Fail. Anal. 14, 557–572, March 2007.

[3] Ozturk, F. Finite-element modelling of two-disc shrink fit assembly and an evaluation of material pairs of discs. Proc. Inst. Mech. Eng. Part C J. Mech. Eng. Sci. 225, 263–273, March 2011.

[4] Y. Zhang, B. McClain, X.D. Fang, Design of interference fits via finite element method, Int. J. Mech. Sci. 42 (9) (2000) 1835–1850.

[5] Fahrettin Öztürk, W.O.O. Tse-Chien, Simulations of interference and Interfacial pressure for three disk shrink fit assembly, Gazi Univ. J. Sci. 23 (2) (2010) 233–236

[6] Manuel Paredes, Naoufel Nefissi, Marc Sartor, Study of an interference fit fastener assembly, in: IDMME. Bordeaux, France, 2010.

[7] Yiren Wang, Shih-Hao Lee, Design and analysis on interference fit in the hardwood dowel-glued joint by finite element method, Procedia Eng. 79 (2014) 166–172.

[8] I. Doležel, V. Kotlan, B. Ulrych, Numerical modelling of cylindrical induction shrink fits, Computing 95 (S1) (2013) 445–458

[9] H. Boutoutaou, J.F. Fontaine, Methodology for a computer-aided design of shrink fits that considers the roughness and form defects of the manufacturing process, J.

[10] Mech. Sci. Technol. 29 (5) (2015) 2097–2103.

[11] Patil, S. A. Fatigue analysis of compound cylinder subjected to repeated internal pressure. Am. Soc. Mech. Eng. Press. Vessel. Pip. Div. PVP 2006, 1–5, July 2006.

[12] Özel, A., Temiz, Ş., Aydin, M. D. & Şen, S. Stress analysis of shrink-fitted joints for various fit forms via finite element method. Mater. Des. 26, 281–289, September 2005.

[13] Özlü, T. Mikro Modüllü Dişli-Mil Sıkı Geçme Bağlantılarında Mil Çapı ve Delik Toleransının Gerilme Dağılımına Etkisi. *Eur. J. Sci. Technol.* 330–335, October 2019

[14] Chouchane, M., Fakhfakh, T., Daly, H. Ben, Aifaoui, N. & Chaari, F. Design and modeling of mechanical systems - II: Proceedings of the sixth conference on design and modeling of mechanical systems, Hammamet, Tunisia. 213–220, March 2015.

[15] Marouani, H. & Hassine, T. Finite element investigations of the shrink-fit assembly with radial cyclic load. *Lect. Notes Mech. Eng.* **789**, 213–220, 2015.

[16] Gaul, L. & Schmidt, A. Finite element simulation and experiments on rotor damping assembled by disc shrink fits. *Mech. Syst. Signal Process.* 127, 412–422, November 2019.

[17] SolidWorks, Solidworks, Dassault Systems, Version 2020.

Current Situations of Wind Energy Usage in the World and in Turkey

Faruk KOSE[1] and Suleyman KOSE[2]

[1] Department of Mechanical Engineering, Konya Technical University, Turkey, fkose@ktun.edu.tr
[2] Department of Mechanical Engineering, University of Sheffield, United Kingdom, skose1@sheffield.ac.uk

Abstract **- Among the renewable energy sources, wind energy has been the most increasing energy source in use around the world in recent years. Today, more than 100 countries in the world are producing electricity from wind energy. As the countries with the highest installed capacity of wind energy, China, the United States of America and Germany have been in the top 3 for a long time. According to the data from the year 2021, Turkey ranks 7th in Europe and 12th in the world in terms of installed wind power plant capacity. In this study, after examining the wind energy potentials and installed capacities of the other countries of the world and Turkey, their shares in the current electricity energy production and total energy consumption were examined. The conditions which would allow world consumption, including Turkey's, to be met entirely from renewable energy sources, and the possible contribution of wind energy to these renewable sources have been estimated. Additionally, possible expected future developments in wind turbine technology are also presented.**

Keywords**: Energy, Renewable Energy, Turkey Wind Energy Potential, Wind Energy, World Wind Energy Potential.**

I. INTRODUCTION

The rapid increase in the world population, industrialization and the intensive use of technological tools and equipment cause energy consumption to increase by 4-5% on average every year [1]. Environmental and health problems have occurred as a result of the long-term use of fossil-based energy sources, which are used to meet current and increasing energy needs. In addition, although there has not been much change in the reserve life of fossil energy resources (estimated reserve life 42-50 years for oil, 60-65 years for natural gas and 150-200 years for coal) in the last two decades, there is a concern that these resources will be depleted within 50-200 years. In recent years, this has accelerated the efforts to reduce the use of fossil-based energy sources and to find clean energy sources to replace them [2-4]. Within the scope of these studies, the use of natural gas, which is the least polluting and harmful among the other fossil fuels, has been increased as a near-term target, while the efforts to increase the use of renewable energy sources, which have no harmful emissions, have accelerated. It is known that the use of renewable energy sources such as solar, wind, geothermal and biomass for drying, grain grinding, heating and health purposes as conventional method, apart from electricity generation, is as old as human history. Today, utilization from renewable energy sources for electricity generation, which is the most effective form of their usage, is aimed to produce cleaner energy by reducing the usage of fossil resources.

The most widely engaged renewable energy sources; hydraulic, wind, solar, geothermal and biomass energies at the present time and their usage is increasing regularly. Wind energy, one of the most important renewable energy sources, occurs as a result of the different heating of the ground surfaces by the sun's rays. The difference in heating of the ground surfaces leads to a difference in the temperature, pressure and humidity of the air, and the pressure differences seen between the two different regions gives rise to the movement of air from high pressure to low pressure, leading to wind formation arises. Some advantages of wind energy are that wind energy is renewable and clean, does not require very high technology for energy production in some systems, and is free and abundant in the atmosphere. In order to make the most effective use of wind energy, which will exist as long as the sun and the world exist, it must be converted into electrical energy. Wind turbines are used for this purpose [1, 2]. In wind turbines, the kinetic energy of the wind is first converted to mechanical energy by the turbine blades and then to electrical energy by the generator. In recent years, developments in propeller type wind turbine technology (such as gearless turbines, with increased unit power and efficiency) have made wind energy competitive with fossil fuel energies by reducing the cost of electricity generation from wind energy.

Many studies are found in the literature on the situation of wind energy in Turkey and in the world. Şenel et al. [1] examined the wind energy potential in Turkey and the world, in addition to the development and usage status of wind energy systems as of the end of 2014. Köse [2] examined the formation and characteristic features of wind energy with Turkey's wind energy potential. Köse et al. [5] performed an analysis by using the wind energy measurement data which was obtained from measurements performed at the Alaaddin Keykubat campus of Konya Selcuk University and annual water data regarding Konya Altinapa dam. Their calculation showed that a wind power plant built in the region of Konya Akyokus and a water turbine power plant installed on the Akyokus purification plant can meet the annual electrical energy demand of the plant. In the report published by the International Renewable Energy Agency (IRENA), the statistical information about world total and each country's separately renewable energy potentials and their current situations associated with renewable energy usage for the year 2021 and before are given [6]. In the report published by Lee et al. [7] the statistical information about world total and each countries' separate wind energy potentials and their current situations associated with wind energy usage for year of 2020 and previous years are shared. According to the BP annual statistical report, electricity generation values for all countries of the world and the world total from 1985 to the end of 2020 using wind energy use are given [8]. Köse et al. [9] investigated the most suitable wind turbine and turbine tower height that can be built in the Konya Selcuk

University Alaeddin Keykubat campus region based on their wind energy measurements performed in this region. Their analysis showed that the proposed wind turbine would pay itself back in 6,5 years. Karabag et al. [10] examined the current and future status of renewable energy resources in light of large databases provided by national and international renewable energy institutions. They evaluated the latest situation in the world and Turkey in the transition to 100% renewable energy, and made predictions about how close to the target of 100% renewable energy the transition is.

The current study intends to systematically analyse the current situation of wind energy usage in the world and in Turkey. The outline of the paper is as follows: world wind energy potential and its usage is examined in detail in Section II. Turkey's wind energy potential and to what extent this potential is being utilized are discussed in Section III. The conclusion is provided in Section IV.

II. WORLD WIND ENERGY POTENTIAL AND ITS USAGE

Before examining the world wind energy potential and its current usage status, the world's total current energy use and the shares of different energy sources used for energy production should be examined. In Figure 1, between 1990 and 2019, the world's total energy uses are shown at 5-year intervals [11]. Based on the data provided by the International Energy Agency (IEA), this chart shows the highest energy supply is from oil with 187,364,800 TJ in 2019; coal with 162,375,732 TJ, third: natural gas with 140,784,380 TJ, fourth: biofuel and waste with 56,813,210 TJ, fifth: nuclear with 30,461,171 TJ, sixth: hydraulic power with 13,194,639 TJ and seventh: wind and solar with 13,417,236 TJ. As a result, the sum of all of them, 606,411,168 TJ, is the world's total energy consumption in 2019 [11]. The last three of these are renewable energies and they have a 14,1% share of the total, while the total of wind and solar power have a 2.21% share of the total.

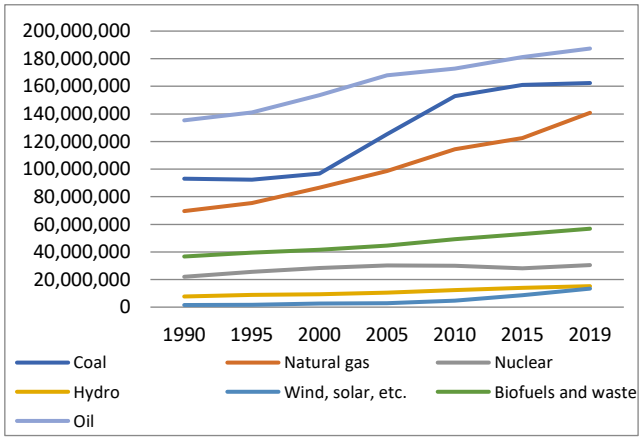

Figure 1: World 1990-2019 Total energy supply (TJ)[11]

Various studies have been carried out by the International Energy Agency (IEA) in order to determine the world wind energy potential. In these studies, the world technical wind potential was calculated as 53,000 TWh/year, based on the prediction that 4% of the regions with a wind capacity above 5.1 m/s would be used due to practical and social constraints [1]. In Figure 2, the comparison of technical wind potentials of world continents are illustrated. Wind energy potential is highest in North America with 14,000TWh/year and lowest in Oceania with 3,000 TWh/year. These data show that North America, Eastern Europe, Russia and Africa have 66% of the world wind energy potential.

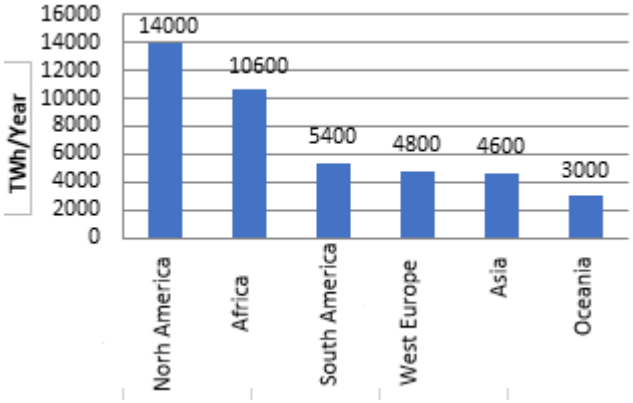

Figure 2: Technical wind potentials of world continents [1]

According to Lee et al. [7] as can be seen in Figure 3 a), by 2050, % 50 increases in global energy consumption is expected due to non–OECD economic growth and population increases. Furthermore, they claim that although liquid fuels are the largest primary source for energy production in the reference state, energy production from renewable sources also reaches about the same levels. In Figure 3 b), electricity generation from renewable sources has been converted to Btu at a rate of 8,124 Btu/kWh. When the total energy consumption of OECD member and non-member countries is analysed as it can be seen in Figure 3 a), it is noticed that energy consumption of non-OECD countries will increase tremendously due to increasing population and industrialization.

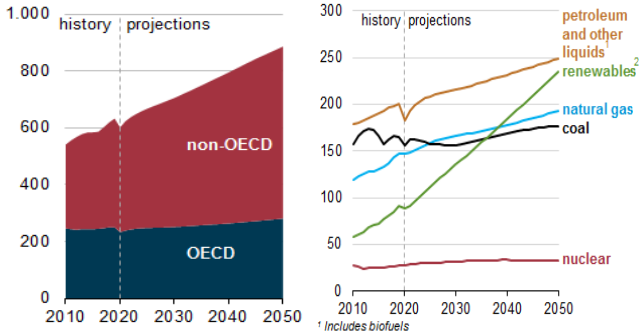

a) b) 8,124 Btu/kWh

Figure 3: 2010-2050 a) world energy consumption, b) world primary energy consumption by energy source, (quadrillion BTU) [7]

Total world electricity generation from wind power by the end of 2020 was 1591,2 TWh/year [6]. This value is approximately 3% of the world wind capacity given in Figure 2 and 5.3 times the electricity consumption of Turkey, which was 305 billion kWh/year in 2020. World total renewable energy production between 1999 and 2019 is given in Figure 4. Accordingly, it is seen that energy production from wind power has exceeded 50% of total renewable energy production in recent years.

For the global wind industry, 2020 was the best year in history with 53% annual growth. More than 93 GW of wind power was installed in a challenging year disrupting both the global supply chain and project processes [7]. World total wind power raises to 743 GW with 93 GW of new

installations as shown in Figure 5. This equals 1.1 billion tons of CO_2 reduction per year. New capacity installed in onshore wind increased by 59% (86,9 GW) compared to 2019. As can be seen from the Figure 6, China and the US increased their new onshore wind plant capacities by 56% and 19%, respectively.

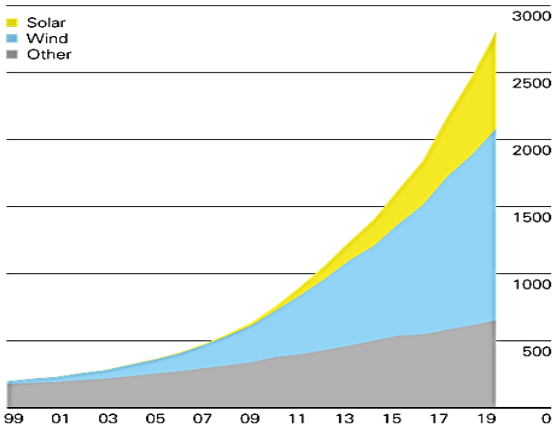

Figure 4: Renewable energy generation by source (TWh) [8]

World wind power installed capacity has nearly quadrupled in the last 10 years, making it one of the most cost competitive and durable energy sources worldwide as shown in Figure 5. At the regional level, 2020 was also a record year for onshore installations in Asia Pacific, North America and Latin America. These three regions obtained a total of 74 GW of new onshore wind capacity last year, which is equal to 76% growth compared to the previous year [7].

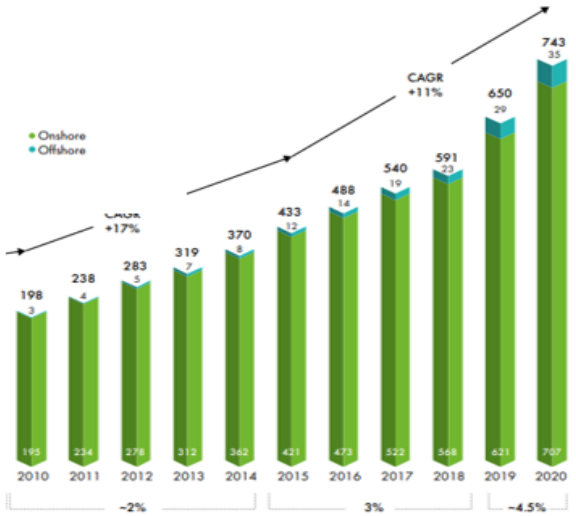

Figure 5: development in the world total wind installed power over a 10-year period [7]

As can be seen from Figure 6, when we look at the new wind installations, Turkey is seen among the top 10 countries on a global scale. In Turkey, there was a new wind capacity increase of 686 MW in 2019, and the increase in 2020 almost doubled the previous year with 1224 MW. The total wind capacity in Turkey increased to 9.559 MW in 2020. As an offshore wind farm, 6.1 GW of worldwide capacity was commissioned last year, making 2020 the second best year ever as shown in Figure 7. China has broken the record, achieving half of all new world offshore wind power installations. Steady growth was recorded in Europe. The Netherlands took the lead, followed by Belgium, England, Germany and Portugal. The remaining new offshore wind installations in 2020 were made by the US and South Korea. World offshore wind installation exceeded 35 GW in 2020 and represents 4.8% of total world wind capacity [7].

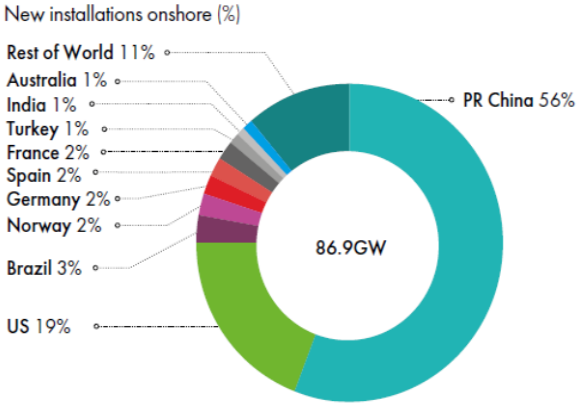

Figure 6: New onshore wind power installation rates by countries for 2020 [7]

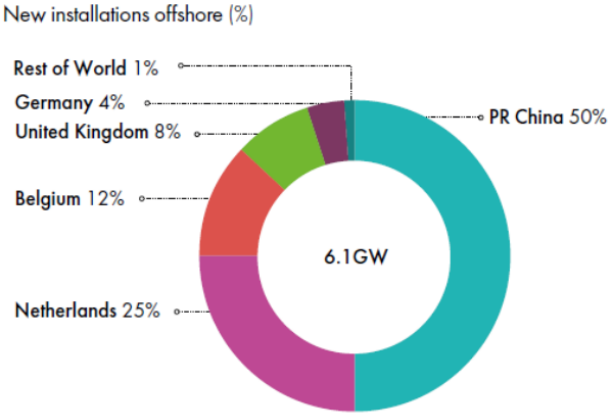

Figure 7: New offshore wind power installation rates by countries for 2020 [7]

The world and European wind installed power rankings taken into account considering 2020 values, China, USA and Germany are in the first three places in the world, respectively, and Germany, Spain and England are in the top three rankings in the European ranking. Turkey ranks 7th in Europe and 12th in the world with its 9.559 MW of installed power as presented in Table 1 [3, 6, 7].

Table 1: World and European wind installed power ranking

Rank	World Ranking Country	Installed Power (MW)	European Ranking Country	Installed Power (MW)
1	China	281.993	Germany	62.184
2	US	117.744	Spain	27.089
3	Germany	62.184	England	24.665
4	India	38.559	France	17.382
5	Spain	27.089	Italy	10.839
6	England	24.665	Sweden	9.688
7	France	17.382	**Turkey**	**9.559**
8	Brazil	17.198	Netherland	6.600
9	Canada	13.577	Denmark	6.235
10	Italy	10.839	Portugal	5.239
11	Sweden	9.688	Belgium	2.843
12	**Turkey**	**9.559**	Ireland	2.830
	Total	**707.517**	**Total**	**194.075**

Some scenarios and plans have been made by some international organizations such as IRENA, IEA and EWEA to produce the world's energy need from clean and renewable energy sources instead of fossil-based sources that disrupt the ecological balance and harm human health. Some of these are based on the 2015 Paris agreement targets, some are based on 2030 and some are based on 2050 [6-8]. According to IRENA's Energy Transition Scenario, world wind additional annual capacity increase would need to reach approximately 180 GW to meet the Paris agreement targets [6]. According to the IEA's Net Zero scenario by 2050, it needs to increase to 160 GW by 2025 and to 280 GW by 2030. This value corresponds to 3 times the increase in 2020 as illustrated in Figure 8. Total annual global investment in clean energy and efficient systems infrastructure should increase from US$380 billion in 2020 to US$1,6 trillion in 2030, according to the IEA [11].

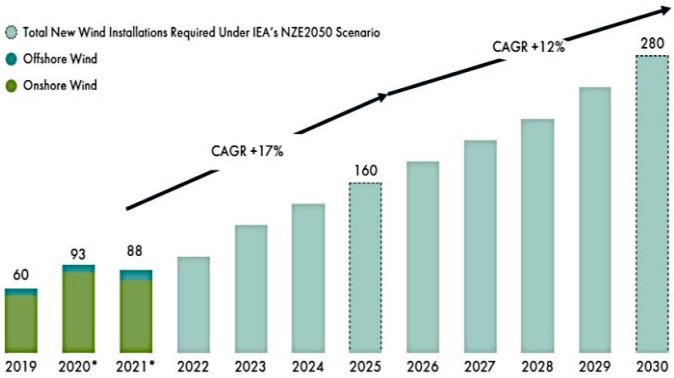

Figure 8: New global wind energy installations required by 2030 (GW)(CAGR: compound annual growth rate) [7]

To reach the net zero target, the wind market expects the addition of new onshore and offshore wind power with a capacity of over 469 GW in the next five years. That indicates around 94 GW of new installations per year by 2025, according to current policies [11]. Governments are expected to significantly increase their targets following COP26 (26th UN Climate Change Conference of the Parties) [7]. Combined with China's net zero target by 2060 and the United States' intention to reach net zero by 2050 are extremely important in terms of reducing the emissions of greenhouse gases because these countries adopt two-thirds of the global economy and represent 63% of global greenhouse gas emissions. By 2030, according to IRENA, the average LCOE (levellised cost of electricity) of both onshore and offshore wind electricity generation costs is projected to decrease by 25% for onshore and 55% for offshore, from 2018 levels. Annual wind installations must increase significantly to reach net zero by 2050 [6, 11].

III. TURKEY WIND ENERGY POTENTIAL AND ITS USAGE STATUS

There are different power estimations about the installed power of wind energy in Turkey depending on the annual average wind speeds at which power plants can be established. According to the Wind Energy Potential Atlas (REPA) [12] prepared by the Ministry of Energy and Natural Resources in 2007, the wind power plant that can be installed has been determined for the total country, regions and provinces based on the lands which is suitable for the establishment of a wind power plant having an altitude of 50 m with wind speed of 7,0 m/s and above as shown in Table 2 and Table3. According to these tables, the total capacity for terrestrial areas is 37.836 MW, and for offshore 10.013 MW, a total of 47.894 MW, which is approximately 48.000 MW. Among the regions, the Ege region has the highest value with 18.975 MW, followed by the Marmara region with 12.704 MW, which shows that there are too many wind farms established in these two regions today.

Table 2: Turkey's wind farm capacities for 50 m altitude and annual average wind speed of 7,0 m/s and above [12]

Wind Classification	Annual Power Density, W/m^2	Annual Average Wind Speed, m/s	Total Capacity, MW
4	400-500	7,0-7,5	29.259,36
5	500-600	7,5-8,0	12.994,32
6	600-800	8,0-9,0	5.399,92
7	>800	>9,0	195,84
Total Capacity			**47.894,44** terrestrial: 37.836 above the sea: 10.013

Table 3: Wind plant capacities of regions of Turkey for 50 m altitude and annual average wind speed of 7,0 m/s and above (MW) [12]

Region Name	Capacity (MW)
Marmara	12.704,0
Aegean	14.975,0
Mediterranean	5.335,0
Central Anatolia	914,0
Black Sea	2.472,0
Eastern Anatolia	986,0
Southeast Anatolia	0,0
Total Capacity	37.386,0

Although Turkey's wind potential values are determined as 48.000 MW based on the lands having 50 m altitude and wind speed of 7,0 m/s and above according to 2007 REPA values, when 100 m altitude and wind speed of 6.0 m/s and above areas are taken into consideration, the potential is 83.000 MW appears to be out. In recent city-based potential studies for larger powerful and more efficient wind turbines, it has been determined as 115.129 MW. Considering the rate at which this potential is used, the usage rate is 8,3% for the installed power of 9.559 MW according to the values of 2020, and 9,2% for the 10.585 MW power in October 2021. In Table 4, the 10 cities with the highest potential and current capacity utilizations status are given. The city with the highest potential is Balıkesir with 13.827 MW, followed by Çanakkale with 13.013 MW [1].

The development of Turkey's electrical installed power between 1980 and 2020 is given in Figure 9, and the power which was 5.118 MW in 1980 increased approximately 19 times and reached 95.890 MW after 40 years. The first wind farm in Turkey was established in 1998 in Izmir. Turkey's total electricity installed power values and electricity generation from renewable sources in 2020 are given in Table 5 and Table 6 respectively. As of the end of 2020, Turkey has 8.832 MW of installed wind power and the ratio

of this power to the installed electricity is 9,21% and the energy produced with this power is 24.828 GWh and its ratio to the total energy generation is approximately 8,1%. Some of the 269 power plants that have been commissioned have not yet reached the installed capacity of the license and their construction is still on going. With the full capacity commissioning of these power plants, an additional wind turbine with a capacity of 2.091 MW will be commissioned and the installed power will reach 11.650 MW.

In addition, the license capacity of 60 power plants, of which no units have been commissioned yet but progress has been made in their installation, is 165 MW. When all of these projects are completed, the installed capacity of Turkey's wind power plants will be 11.814 MW.

Table 4: 5 cities with the highest wind potential in Turkey [1]

City	Theoretical Potential MW	In operation MW	Under Constr. MW	licenced	Sub-license	Total Process	Process/ Theory Ratio
Balıkesir	13.827	1.294	87	0	0	1.382	10 %
Çanakkale	13.013	797	256	40	162	1.255	10 %
İzmir	11.854	1.680	55	0	23	1.758	15 %
Manisa	5.302	691	11	10	0	712	13 %
Samsun	5.222	48	4	9	0	61	1 %

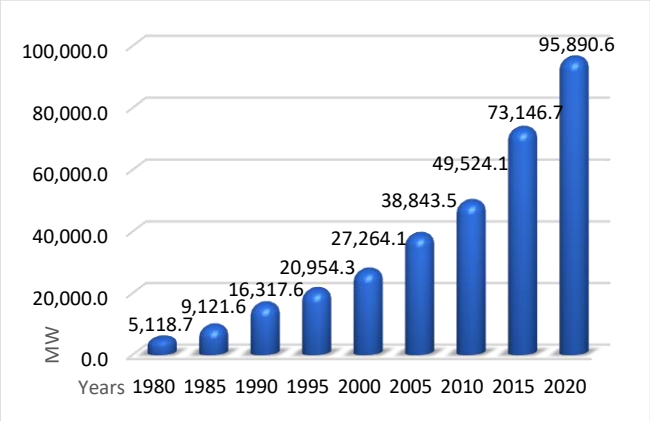

Figure 9: Development of Turkey's installed power over the years [13]

Table 5: Turkey's total electricity installed power values in 2020 [13]

SOURCE	INSTALLED POWER, MW	RATIO, %
IMPORT COAL	8.841,9	9,22
BITUMINOUS COAL	782,5	0,82
LIGNITE	9.988,7	10,42
LIQUID FUELS	189,4	0,20
MULTI-FUEL	4.889,1	5,10
WASTE HEAT	397,5	0,41
NATURAL GAS	21.599,4	22,53
RENEWABLE WASTE+WASTE	1.105,3	1,15
WIND	8.832,4	9,21
SOLAR	6.667,4	6,95
WATER DAM	22.925,0	23,91
WATER STREAM,LAKE	8.058,9	8,40
GEOTHERMAL	1.613,2	1,68
TOTAL	**95.890,6**	**100**

The share of wind energy in Turkey's total electricity installed power is approximately 10 percent, while wind energy has 19,3 percent of the total renewable energy installed power. When the wind energy capacity is evaluated on a city basis, İzmir has the highest capacity with approximately 1700 MW, followed by Balıkesir with 1300 MW, Çanakkale with approximately 850 MW, Manisa with 750 MW and Istanbul with 420 MW. In addition, Hatay and Kırklareli with 415 MW each, Aydın with 400 MW, Afyonkarahisar with 325 MW, Kayseri with 272 MW (10th), Osmaniye with 260 and Konya with 242 MW (12th), Muğla with 220 MW, Bursa with 205 MW and Mersin with approximately 200 MW installed wind capacity are among the 15 cities with the highest energy installed capacity.

Table 6: Turkey's electricity generation from renewable sources in 2020 [13]

SOURCE	GENERATION (GWh)	CONTRIBUTION (%)
RENEWABLE WASTE+WASTE	4.459,9	3,47
WIND	24.828,2	19,34
SOLAR	10.950,2	8,53
WATER DAM	57.463,9	44,77
WATER STREAM,LAKE	20.630,4	16,07
GEOTHERMAL	10.027,7	7,81
TOTAL	**128.360,4**	**100,00**
RENEWABLE %	----	**41,85**
TURKEY TOTAL	**306.703,1**	**100**

The installed power shares of different energy sources in Turkey's electricity production for the years 2010 and 2020 are given in Figure 10. These energy sources used for electricity production are hydroelectric, natural gas, coal (stone, lignite and imported coal), wind, diesel, liquid fuels, geothermal, biogas and solar The values given in Table5 is direct agreement with the 2020 values of Figure 10. Furthermore, the fact that the energy produced by hydroelectric power plants is higher than all the energy obtained by the use of fossil fuels in 2020 values, the rate of renewable energy approaching 50% and the rate of electricity generation from wind energy approaching 50% in renewable generation shows the importance of renewable and wind energy (Table 6).

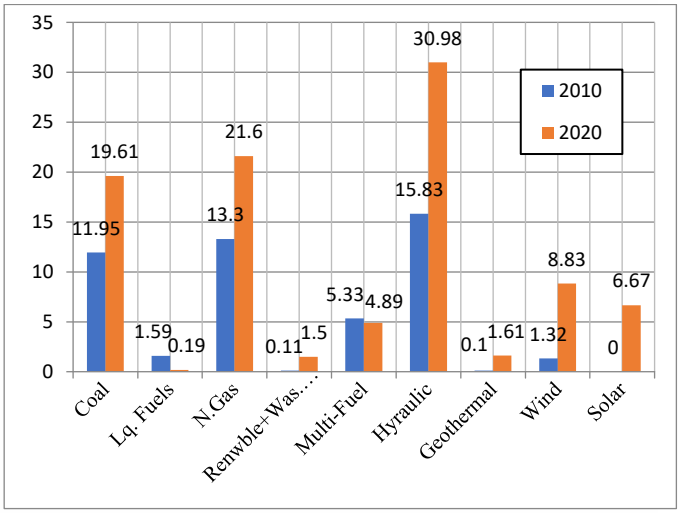

Figure 10: Electricity installed capacity of Turkey from primary energy sources in 2010 and 2020 (GW) [11]

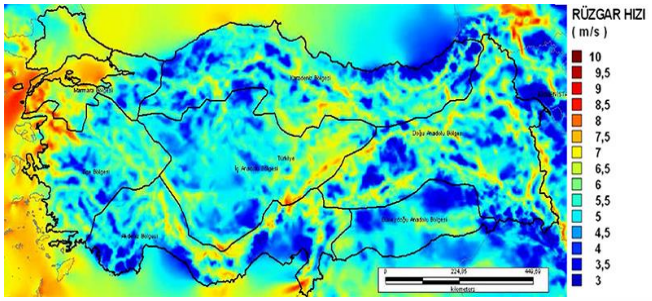

Figure 11: Turkey Wind Potential Map [14]

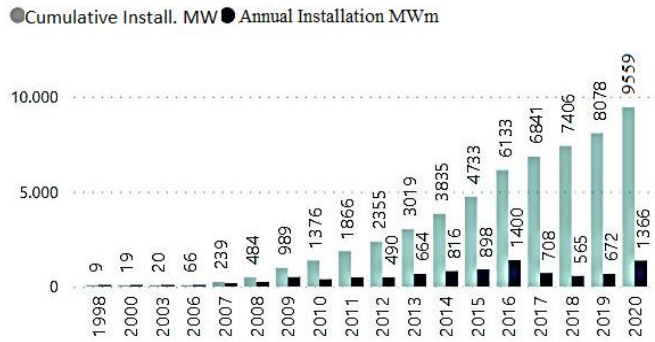

Figure 12: Development of Turkey's wind power over the years [15]

When the graph of Turkey's wind total installed power and annual installation amounts between (1998-2020) given in Figure 12 is examined, it is seen that the total installed power has increased approximately 7 times in the last 10 years and 2 times in the last 5 years. Annual installation amounts have grown rapidly after 2012, after reaching the highest value in 2016, it decreased slightly until 2018 and started to increase rapidly as of 2019..

In recent years, there have been significant developments in the technologies of wind turbines used to convert wind energy into electrical energy. The first of these developments has been achieved by the widespread use of turbines without gearbox and their getting cheaper. The second important development has been achieved by increasing the rotor diameter that is directly related with the turbine power, by constructing turbines with a power over 10 MW. While the first of these developments will increase the efficiency of the turbines, the second will increase the tower height of the turbine and increase the power coefficient value with higher wind speeds.

IV. CONCLUSION

In this study, first the energy needs and current energy usage status of the world and Turkey were determined, then the wind energy potentials were obtained and by using these wind energy potentials, it has been investigated to what extent the energy demands can be met. In addition, measures and scenarios were analysed to reduce the use of fossil-based energy, which has harmful effects on the ecological balance of the world and living health, and to increase the use of wind and other renewable energy resources to replace them. The results obtained in the study are summarized below.

Currently, 80% of the world's general energy needs and 85% of Turkey's total energy needs are met from fossil fuels. The share of wind energy in Turkey's total electricity installed power is approximately 10 per cent, while wind energy has 19,3 per cent of the total renewable energy installed power.

While the world's total electrical energy production in 2020 is 26.823,2 TWh/year, Turkey's production is 305,5 TWh/year. Energy production from renewable sources was 3.147,0 TWh/year for the world and 49,8 TWh/year for Turkey.

The total installed wind power of the world in 2020 is 743 GW, and the installed power of Turkey is 9,6 GW. With this power value, Turkey ranks 12th among world countries and 7th among European countries. As of the end of 2020, Turkey has 9.559 MW of wind power, which is 9,21% of the country's electrical installed power, and the energy generation by using this power is 24.828 GWh and its ratio to the total energy production is approximately 8,1%.

According to IRENA's Energy Transition Scenario, additional annual wind capacity increase would need to reach approximately 180 GW to have a chance to meet the Paris targets. According to the IEA's Net Zero scenario by 2050, it needs to increase to 160 GW by 2025 and to 280 GW by 2030. This value is 3 times the increase in 2020.

Developments seen in turbine technologies and the production of domestic turbines in Turkey will increase the use of wind energy, making wind electricity cheaper both in the world and in Turkey. As a result, it is estimated that it will be possible to reach the target of 100% zero emissions and 100% renewable energy production by using all renewable energy sources, even if not only with wind energy, until 2050 or 2070.

REFERENCES

[1] M. C. Şenel, E. Koç, 2015. "*Wind Energy in the World and Turkey Condition-General Evaluation"*, Journal of Engineers and Machinery, volume 56, issue 663, p. 46-56.

[2] F. Köse, *Renewable Energy Resources (and Systems)*, S.Unv. Faculty of Engineering and Architecture Lecture Note. Publication No: 51, Konya, 2002.

[3] Anonymous-1, "*Statistical Review of World Energy 2021*" 70th edition, 2021, (bp.com), BP p.l.c.1St James's Square London SW1Y 4PD/UK.

[4] bp *Statistical Review of World Energy 2007*, 56th edition.

[5] F., Köse, M.N., Kaya, (2013). "*Analysis on meeting the electric energy demand of an active plant with a wind-hydro hybrid power station in Konya Turkey Konya water treatment plant*." Renewable Energy, 55, 196-201.

[6] Anonymous-2, "IRENA (2021), "*Renewable Energy Statistics 2021*", The International Renewable Energy Agency, Abu Dhabi.

[7] J. Lee, F. Zhao, (2021), "*GWEC- Global Wind Report 2021*, Global Wind Energy Council, Rue Belliard 51-53, 1000 Brussels, Belgium.

[8] EWEA, "*Wind energy scenarios for 2030*", A report by the European Wind Energy Association, 2015. URL: ewea.org/

[9] F. Köse, M.H. Aksoy, M. Özgören (2014).,"*An Assessment of Wind Energy Potential to Meet Electricity Demand and Economic Feasibility in Konya, Turkey*", International Journal of Green Energy, 11(6), 559-576.,

[10] N. Karabağ, C. B. Çobanoğlu Kayıkcı, A. Öngen, (2021*), "%100 The World and Turkey on the Road to Renewable Energy Transition*,", European Journal of Science and Technology No.21, pp.230-240, 2021.

[11] Anonymous-3 (2021), URL1: https://www.iea.org/reports/world-energy-outlook-2021, Date of access: 27.10.2021.

[12] REPA,"Turkish Wind Energy Potential Atlas", Ministry of Energy and Natural Resources, 2007, Ankara.

[13] GWEA, "*Global Wind Energy Manifesto For Cop26*",18.10.2021, URL: www.windareyouin.com

[14] URL: https://enerji.gov.tr/eigm-yenilenebilir-enerji-kaynaklar-ruzgar

[15] TEİAŞ, 2021, Turkey Electricity Transmission Co., https://www.teias.gov.tr/, Date of access: 27.10.2021.

Asymptotic Sampling Regression with Machine Learning and Surrogate Modeling Techniques

G. BAYRAK[1] and E. ACAR[2]

[1] TOBB University of Economics and Technology, Ankara/Turkey, gbayrak@etu.edu.tr
[2] TOBB University of Economics and Technology, Ankara/Turkey, acar@etu.edu.tr

***Abstract* - Asymptotic sampling is an efficient simulation-based technique for estimating small failure probabilities of structures. The concept of asymptotic sampling utilizes the asymptotic behavior of the reliability index with respect to the standard deviations of the random variables. In this method, the standard deviations of the random variables are progressively increased using a scale parameter to obtain a set of scaled reliability indices. The collection of the standard deviation scale parameters and corresponding scaled reliability indices are called support points. Then, a regression is performed using these support points to establish a relationship between the scale parameter and scaled reliability indices. Finally, an extrapolation is performed to estimate the actual reliability index. In the previous studies, the relationship between reliability indices and support points has been established using nonlinear regression. In this study, we explored the use of more advanced machine learning (e.g., Gaussian process, support vector regression) and surrogate modeling (e.g., Kriging, linear Shepard) techniques, and compared the accuracies of these techniques to that of the nonlinear regression on six benchmark problems. It is found that using nonlinear regression yields more accurate results than machine learning and surrogate modeling techniques evaluated within the scope of this study.**

***Keywords* - asymptotic behavior, extrapolation models, Gaussian process, Kriging, linear Shepard, machine learning, reliability index, small failure probability, support vector regression, surrogate model.**

I. INTRODUCTION

Structural reliability is predicted using a limit state function (or performance function) that is used to separate the safe and failure regions of an input space. The probability of failure estimation requires calculation of the multi-dimensional integral of the joint probability density function of all the random variables over the failure region

$$P_f = \int \dots \int I[g(\mathbf{x}) \leq 0] \; f_{\mathbf{X}}(\mathbf{x}) d\mathbf{x} \qquad (1)$$

where I is the indicator function that takes the value of 1 when the condition is true and 0 when the condition is false, $f_{\mathbf{X}}(\mathbf{x})$ denotes the joint probability density function of the set of random variables $\mathbf{X}$, and $g(\mathbf{x})$ is the limit state function. For most real life structural problems, the analytical integration of this multi-dimensional function is not possible; therefore, analytical and simulation-based approaches have been proposed to estimate failure probability.

Analytical approaches require a small number of limit state function calculations; therefore, they are typically computationally inexpensive compared with simulation-based approaches. The most popular analytical methods are the first-order [1, 2] and second-order reliability methods [3, 4], which are based on the first order and second order expansions of the limit state function at the most probable failure point (MPP), respectively. Although the analytical approaches are computationally advantageous compared to other methods, they are not necessarily suitable for real-life problems which have complex and nonlinear limit state functions.

Simulation-based approaches can yield accurate results provided that a sufficient number of simulations are applied. The most popular simulation-based approach is the Monte Carlo simulation (MCS) method [5]. Unfortunately, MCS is computationally expensive for estimating small failure probabilities.

Extrapolation-based methods are used to overcome the disadvantages of other methods used in high-reliability systems. Asymptotic sampling is an extrapolation-based method for estimating small failure probabilities [6]. This method can reduce the computational cost for the estimation of the high reliability index due to the fact that the low reliability index can be estimated with lower computation. This method extrapolates from low reliability indices to the high reliability indices based on the asymptotic behavior of the failure probability with respect to the standard deviation of the variables. By using a scale parameter, the standard deviations of the random variables are progressively increased to obtain various (smaller) scaled reliability indices that can be predicted accurately using a small number of samples. Subsequently, with using least squares regression which is nonlinear regression analysis a relationship is established between the standard deviation inflation parameter and scaled reliability index values. Finally, extrapolation is performed to estimate the actual reliability index. Zhangchun et al. [7, 8] improved the accuracy of the asymptotic sampling method by using mean prediction of various extrapolation models.

This paper is organized as follows: The asymptotic sampling method is described briefly in the next section. The methods used for regression analysis and the findings from our previous study about asymptotic sampling are presented in Section III. The numerical examples used in this study are discussed in Section IV. The results obtained from these example problems are presented and discussed in Section V.

II. ASYMPTOTIC SAMPLING

In this method, the standard deviations of the random variables are artificially increased by using a scale parameter

to obtain smaller reliability indices, known as "scaled" reliability indices [6]. Subsequently, a functional relationship is established between the scale parameters and scaled reliability indices. Finally, the actual reliability index is predicted using the established functional relationship. Bucher first considered a problem involving a linear limit state function and suggested that this problem can be reduced to a single variable with standard deviation of σ via an appropriate coordinate transformation. Then, the reliability index can be formulated as

$$\beta(f) = \frac{\beta_f}{f} \tag{2}$$

where f is the scale factor and β_f is the scaled reliability index computed for the scaled standard deviation of the random variable $\sigma = \sigma/f$. The actual reliability index can be computed using $\beta_{act}{}^{f} = \beta(f = 1)$.

To obtain a good estimate for β_{act}, the reliability index for a larger value of σ (a smaller value of the scale factor f) can be computed using MCS, and then simply extrapolated by multiplying the result with f.

Based on the asymptotic behavior of the reliability index with respect to the standard deviation scale parameter, Bucher assumed the following functional relationship between the reliability index and the standard deviation scale parameter f

$$\beta = A\,f + \frac{B}{f} \tag{3}$$

To assign equal weights to all support points for the regression analysis, Eq. (3) can be rewritten in terms of a scaled reliability index as follows

$$\frac{\beta}{f} = A + \frac{B}{f^2} \tag{4}$$

Notice that as $f \to \infty$ (that is, as $\sigma_f \to 0$) the reliability index $\beta \to \infty$ so that the asymptotic behavior is ensured. Coefficients A and B are determined from least squares regression which is nonlinear regression analysis based on the estimates of β for different values of f smaller than 1. That is, a set of "support points" [f_i, $\beta(f_i)$] shown in Fig. 1 is used in the regression. Bucher [6] stated that five support points can be used. In his later studies, he used different numbers of support points [9]. They suggested that four or more support points to yield a more stable regression; however, this practice resulted in an increase in computational effort.

Bucher initiated the asymptotic sampling algorithm by using the scale parameter, f_0=1. The required number of samples in the failure domain is set to N_0=10 [6]. In the first step, the actual number of samples N_F in the failure domain was inadequate (less than N_0). Therefore, the parameter f was decreased by a factor of 0.9, and the simulation was repeated until N_F was equal to or exceeded N_0. The support points and regression curve obtained from the extrapolation process are shown in Fig. 1.

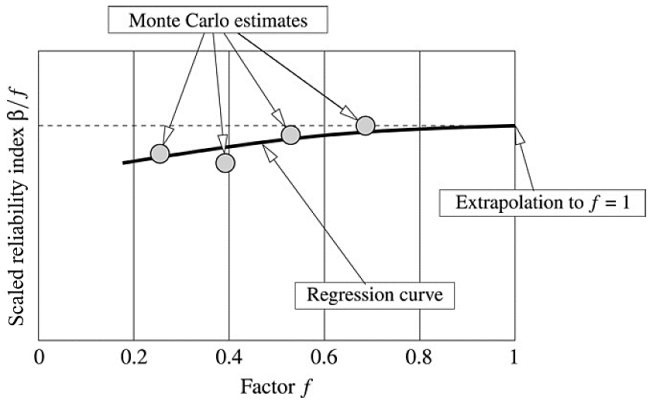

Figure 1: The concept of asymptotic sampling [6]

The asymptotic sampling method can decrease the computational cost for the evaluation of a high reliability index because the low reliability index can be estimated at a lower computational cost. However, Zhangchun et al. [7] discovered that the use of a single extrapolation model was not robust. They proposed to generate multiple extrapolation models and use the mean value of the reliability predictions of these models. Specifically, they proposed using 10-extrapolation models, as expressed in Eqs. (5) and (6).

$$\beta_t(f) = A_t f + \frac{B_t}{f^{q_t}} \quad \left(t = 1,2,3,4,5; q_1 = 3, q_2 = 2, q_3 = 1, q_4 = 0.5, q_5 = \frac{1}{3}\right) \tag{5}$$

$$\beta_t(f) = A_t f + \frac{B_t}{exp(f^{q_t})} \quad \left(t = 6,7,8,9,10;\ q_6 = 3, q_7 = 2, q_8 = 1, q_9 = 0.5, q_{10} = \frac{1}{3}\right) \tag{6}$$

where t = 1, . . ., 10 represents the extrapolation model index, q_t (t = 1, . . ., 10) is the exponent of the extrapolation model, and exp(.) is the exponential operation with natural base e as the base. The coefficients A_t and B_t are determined through least squares regression. Then, the actual reliability index is computed using the average of these 10 extrapolation models, expressed as

$$\beta(1) = \frac{1}{10}\sum_{t=1}^{10}\beta_t(1) = \frac{1}{10}\left(\sum_{t=1}^{5}(A_t + B_t) + \sum_{t=6}^{10}(A_t + B_t/e)\right) \tag{7}$$

In a follow-up study, Zhangchun et al. [8] proposed a new mean extrapolation technique that involves 6 extrapolation models to estimate the actual reliability index. In that study, only models corresponding to q_2, q_3 and q_4 in Eq. (5), and the models corresponding to q_7, q_8 and q_9 in Eq. (6) are used.

For this method, it is essential to use a sampling method that yields stable results. A typical choice is Latin hypercube sampling (LHS) method [10, 11]. Alternatively, pseudo-random sequences with low-discrepancy sampling methods such as Sobol sequences [12], Halton sequences [13] or Good lattice point sets [14] can be utilized. The accuracy and performance of the asymptotic sampling method are affected by various factors including the sampling method used, the

values of the scale parameters, the number of support points, and the formulation of extrapolation models.

III. METHODS USED

In our earlier study [15], to investigate the effects of various parameters (including the sampling method, values of scale parameters, number of support points, and extrapolation model formulations) on the performance of the asymptotic sampling method using various benchmark problems evaluated in a wide range of reliability index values (ranging from 4 to 6). In terms of sampling, we compared the use of LHS and Sobol sequences, and found that using Sobol sequences yielded better results. We also compared 6-model and 10-model mean extrapolation formulations and discovered that the 6-model mean extrapolation formulation was more accurate. Subsequently, we found that the initial scale parameter could be set between 0.3 and 0.4 for a reliability index range of 4 to 6. Finally, we also found that using 4 support points provided the best compromise between accuracy and efficiency, and if the reliability index is extremely high, we found that 5 support points can be used to achieve an acceptable level of accuracy. In this study, we used the optimum parameters, the most accurate sampling method and mean extrapolation formulation obtained for the asymptotic sampling method in our earlier study [15] for all example problems.

As noted earlier, Bucher [6] used the nonlinear regression analysis to establish a relationship between the standard deviation inflation parameter and reliability index values. In this study, we used more advanced machine learning techniques (Gaussian process regression (GPR) [16, 17] and support vector regression (SVR) [18, 19]) for regression analysis instead of the nonlinear regression. In addition, Zhang et al. [20] explored one-dimensional deterministic function extrapolation using surrogates. They proposed that Kriging (KR) [21, 22] and Linear Shepard (LSHEP) [23, 24] surrogates proved to be safer on challenging functions than polynomial response surfaces [25], support vector regression or radial basis functions [26]. Inspired by this study, the extrapolation was made with Kriging and Linear Shepard surrogate models. Then, we estimated the actual reliability indices. We used six structural mechanics example problems detailed in the next section to investigate the accuracy of regression analysis methods.

IV. NUMERICAL EXAMPLES

This section provides six structural mechanics example problems to compare the regression analysis methods of the asymptotic sampling method. To reduce random sampling effect, all asymptotic sampling processes are repeated 1000 times. The performances of the regression methods are evaluated by using root mean square error (*RMSE*) values obtained from 1000 different runs.

A. Connecting Rod Problem

The connecting rod problem under axial loading is illustrated in Figure 2. The problem is a two-variable simple problem involving the following linear limit state function

$$g = C - R \tag{8}$$

where R and C denote stress and strength, respectively, and both are random variables. The mean and standard deviation of the stress are taken as μ_R and 6, respectively, whereas the mean and standard deviation of the strength are set to 100 and 8, respectively. μ_R is varied to obtain various reliability levels as given in Appendix A.

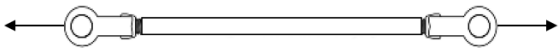

Figure 2: The connecting rod under axial loading

B. Cantilever Beam Problem

The cantilever beam problem is illustrated in Figure 3 [27]. The limit state occurs when the tip displacement exceeds the allowable, D_o.

$$g = D_0 - \frac{4L^3}{Ewt}\sqrt{\left(\frac{Y}{t^2}\right)^2 + \left(\frac{X}{w^2}\right)^2} \tag{9}$$

where the width w = 2.7" and thickness t=3.4" are the design variables. Random variables are: the modulus of elasticity E (mean 29×10^6 psi, standard deviation 1.45×10^6 psi), the random load X (mean 500 lb, standard deviation 100 lb), and the other random load Y (mean 1000 lb, standard deviation 100 lb). All random variables are normally distributed, and the allowable displacement D_0 is varied to obtain various reliability levels as given in Appendix A.

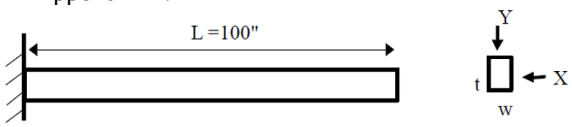

Figure 3: The cantilever beam under vertical and lateral bending [27]

C. Central Crack Problem

In this example [28], a rectangular plate of finite width W with a central through-thickness crack of length $2a$ loaded in tension with a uniform stress, S, is considered (see Figure 4). The limit state function for this problem can be written as

$$g = K_{IC} - \sqrt{sec\left(\frac{\pi a}{W}\right)}S\sqrt{\pi a} \tag{10}$$

where a is the half crack length, W is the plate width, S is the applied stress, K_{IC} is the fracture toughness, and all these variables are taken random. The probability distributions as well as the mean and the standard deviations of the random variables are given in Table 1. The mean value of the fracture toughness $\left(\overline{K}_{IC}\right)$ is varied to adjust the reliability level (see Appendix A).

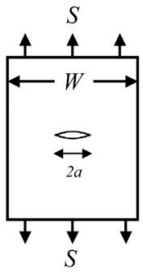

Figure 4: Central cracked plate with a finite width [28]

Table 1: Statistical properties of the random variables (RVs) in the central crack problem

Random variable	Distribution	Mean	Standard deviation
a [mm]	Normal	25	0.75
W [mm]	Normal	500	5
S [MPa]	Normal	100	10
K_{IC} [$MPa\sqrt{m}$]	Normal	$\overline{K}_{IC}$	$0.1\overline{K}_{IC}$

D. Fortini's Clutch Problem

The Fortini's clutch [29] is shown in Figure 5. The contact angle y is given in terms of the independent component variables, X_1, X_2, X_3, and X_4 as follows

$$y = arccos\left(\frac{X_1 + 0.5(X_2 + X_3)}{X_4 - 0.5(X_2 + X_3)}\right) \quad (11)$$

The statistical properties of the random variables are presented in Table 2. The limit state function of this problem is expressed in Eq. (12), where y_{crit} can be customized to obtain various reliability levels, as presented in Appendix A.

$$g = y - y_{crit} \quad (12)$$

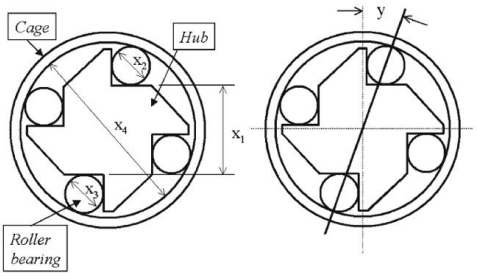

Figure 5: Fortini's clutch [30]

Table 2. Statistical properties of the RVs in the Fortini's clutch *

Random variable	Distribution	Mean	Standard deviation
X_1 [mm]	Lognormal	55.29	0.0793
X_2 [mm]	Normal	22.86	0.0043
X_3 [mm]	Normal	22.86	0.0043
X_4 [mm]	Extreme type I	101.6	0.0793

* For X_1 the scale parameter is λ = 4.01, and shape parameter is ζ = 0.0014. For X_4, the location parameter is μ = 101.6, and scale parameter is β = 0.062.

E. Roof Truss Problem

A roof truss subject to uniform loads is shown in Figure 6 [31]. The top boom and compression members are concrete, and the bottom boom is made of steel. The limit state function is expressed as follows

$$g = c - \left(\frac{ql^2}{2}\right)\left(\frac{3.81}{AcEc} + \frac{1.13}{AsEs}\right) \quad (13)$$

where c is the vertical deflection at the peak of the structure (node C in Fig. 6), q is uniform load, l is length, As and Ac are sectional areas and Es and Ec are the modulus of elasticity. The definitions of the random variables are presented in Table 3. The value of the vertical deflection c can be changed to arrange the reliability level of the problem as given in Appendix A.

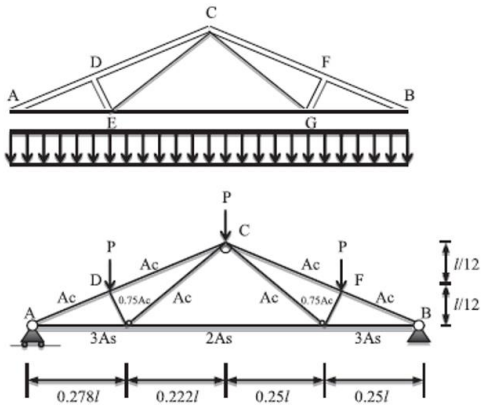

Figure 6: Roof truss [31]

Table 3. Statistical properties of RVs in the roof truss problem

Random variable	Distribution	Mean	Standard deviation
q [kN]	Normal	20×10^3	1400
l [m]	Normal	12	0.12
As [m^2]	Normal	9.82×10^{-4}	5.892×10^{-5}
Ac [m^2]	Normal	0.04	4.8×10^{-3}
Es [GPa]	Normal	1×10^{11}	6×10^9
Ec [GPa]	Normal	2×10^{10}	1.2×10^9

F. I Beam Problem

A simply supported I-beam subjected to a concentrated load is illustrated in Figure 7 [32]. This problem involves a limit state function, which is defined as the difference between the strength (S) and the maximum normal stress (σ_{max}) due to bending, expressed as follows

$$g = S - \sigma_{max} \quad (14)$$

$$\sigma_{max} = \frac{Pa(L-a)d}{2LI}; \quad I = \frac{b_f d^3 - (b_f - t_w)(d - 2t_f)^3}{12} \quad (15)$$

The statistical properties of the random variables in this example are listed in Table 4, where $\overline{S}$ is tailored to change the reliability level of the problem, as given in Appendix A.

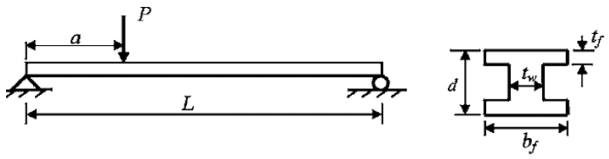

Figure 7: The cross section and loading for the simply supported I beam [32]

Table 4. Statistical properties of the RVs in the I beam problem

Random variable	Distribution	Mean	Standard deviation
P	Normal	6070	200
L	Normal	120	6
a	Normal	72	6
S	Normal	$\overline{S}$	$0.15\overline{S}$
d	Normal	2.3	1/24
b_f	Normal	2.3	1/24
t_w	Normal	0.16	1/48
t_f	Normal	0.26	1/48

V. RESULTS

In the first stage of the study, considering the optimum values for asymptotic sampling method explained in Section III, we obtained the support points required for the extrapolation and the corresponding reliability index values for each problem. As mentioned earlier, Bucher established a relationship between the support points and the reliability index values to obtain the actual reliability index and used the least square regression analysis to obtain the coefficients in this relationship.

Subsequently, we also applied SVR, GPR, KR and LSHEP methods, which are more advanced techniques that we think can estimate the actual reliability index more accurately, than Bucher's extrapolation method, to the example problems.

The support points and the corresponding reliability index values for the connecting rod problem of which the reliability index value of 4 and the regression lines generated in all the methods used for extrapolation are shown in Figure 8, separately. Since the points have a linear trend, the most accurate results have been obtained with the linear regression analysis. GPR and KR methods both perform exactly the same regression as they use Gaussian correlation (see Figure 8*b*).

Finally, for all reliability levels of each problem, we use the regression lines to obtain the actual reliability index values corresponding to the point where the support point is equal to 1. Comparisons of Bucher's nonlinear regression and the methods we used in the study at all reliability levels of each problem are given in Figure 9. When the support point is equal to 1, the reliability index value is expected to be around 4 for the connecting rod problem. However, this value is much lower than 4 for the LSHEP method (see Figure 8*c*). This situation proved to us that the regression analysis with the LSHEP function is not suitable for the asymptotic sampling method. Therefore, when the graphs in Figure 9 are examined, the regression analysis with the LSHEP model yields a rather large *RMSE* value compared to other methods. In addition, for all example problems, the *RMSE* values obtained from extrapolation with GPR were lower than those obtained with SVR. This shows that the performance of the GPR method is better than the SVR method.

As a result, considering the graphs in Figure 9, the extrapolation method with nonlinear regression yields the most accurate results for the asymptotic sampling method for all problems.

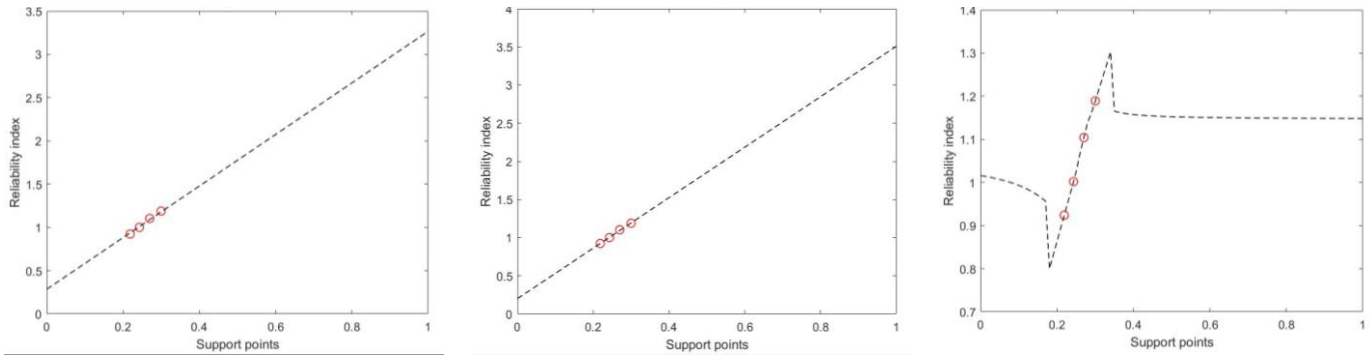

a. Support vector regression *b.* Gaussian process regression and Kriging *c.* Linear Shepard

Figure 8: The regression lines for extrapolation models

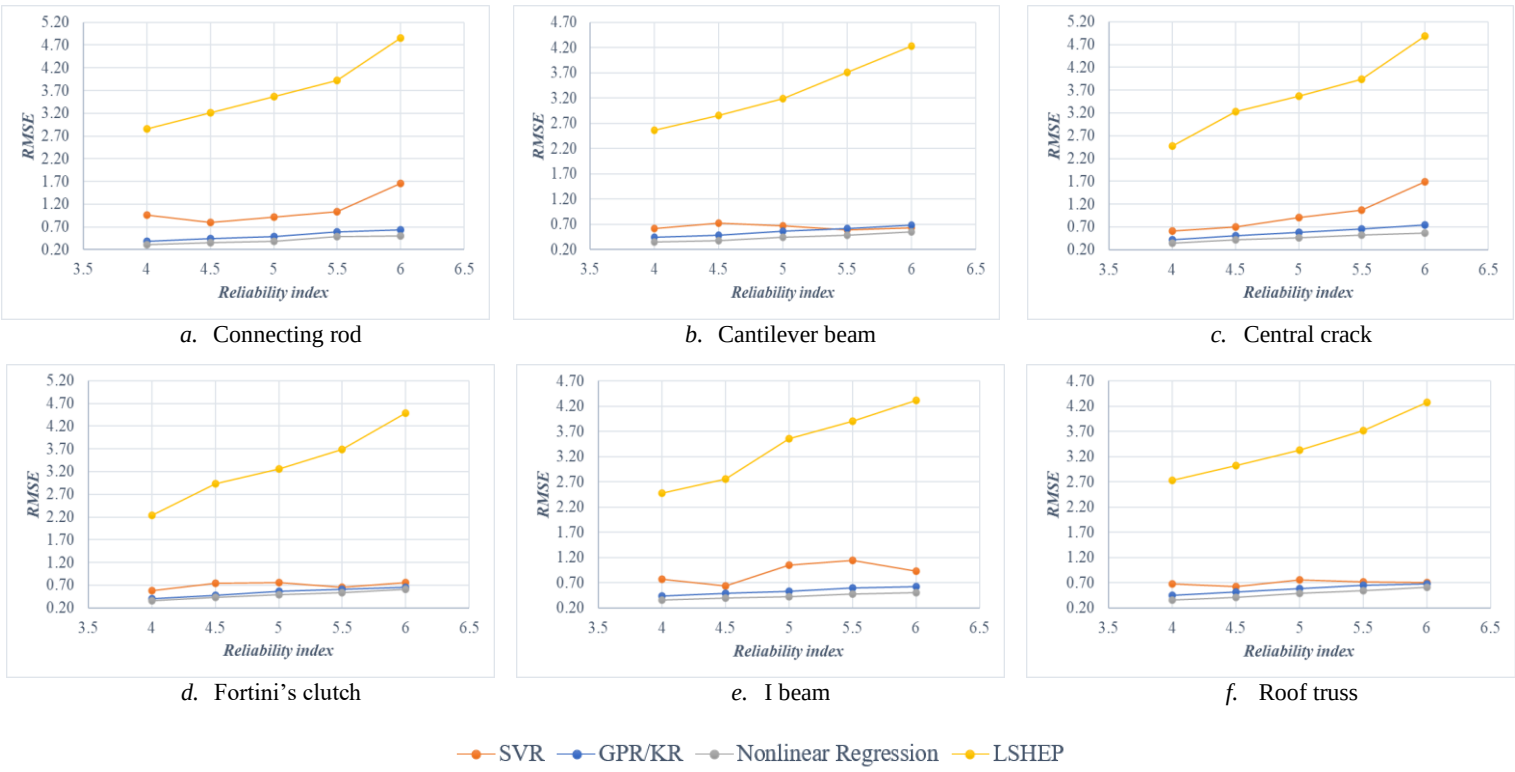

Figure 9: RMSE values corresponding to the extrapolation methods for example problems

VI. Conclusion

The performance of the asymptotic sampling method depends on various factors including the sampling method, formulation of extrapolation models, initial scale parameter, number of support points and regression technique used in extrapolation. To analyze the effect of regression techniques, we compared the performance of the least square method which is the nonlinear regression technique proposed by Bucher, with the performance of more advanced machine learning techniques such as Gaussian process regression, support vector regression, Kriging and Linear Shepard.

As a result of these comparisons, we determined that the most accurate results at all reliability levels of all problems have been obtained with the nonlinear regression proposed by Bucher. It has been also determined that the Linear Shepard method is not suitable for asymptotic sampling extrapolation due to the function it uses for regression.

Appendix

A. *Reliability Levels of the Numerical Example Problems*

For all numerical example problems, five different reliability levels are considered by changing a proper term in the limit state function (see Table A1). The reliability index values reported in Table A1 are predicted using crude Monte Carlo simulations with a sample size of 10^7, 10^8, 10^9, 10^{10}, and 10^{11} for reliability indices of 4, 4.5, 5, 5.5, and 6. Note that the reliability indices of 4, 4.5, 5, 5.5, and 6 correspond to the failure probabilities of 3.17×10^{-5}, 3.40×10^{-6}, 2.87×10^{-7}, 1.90×10^{-8}, and 9.87×10^{-10}, respectively.

Table A1: The reliability levels considered for the example problems

ID	Problem	Term	Value	β	Value	β	Value	β	Value	β	Value	β
1	Connecting rod	μ_R	60	4.00	55	4.50	50	5.00	45	5.50	40	6.00
2	Cantilever beam	D_0	2.50	4.03	2.62	4.51	2.75	5.00	2.89	5.54	3.04	6.05
3	Central crack	$\overline{K}_{IC}$	52	4.01	57	4.52	63	5.01	70	5.52	79	6.04
4	Fortini's clutch	y_{crit}	4.05	4.02	3.55	4.53	3.02	5.01	2.31	5.50	1.20	6.04
5	Roof truss	c	0.0360	4.07	0.0378	4.53	0.0400	5.01	0.0425	5.50	0.0466	6.07
6	I beam	$\overline{S}$	410×10^3	4.07	490×10^3	4.50	630×10^3	5.01	880×10^3	5.49	1700×10^3	6.06

REFERENCES

[1] Hasofer, A. M. (1974). An exact and invarient first order reliability format. *J. Eng. Mech. Div., Proc. ASCE*, *100*(1), 111-121.

[2] Rackwitz, R., & Flessler, B. (1978). Structural reliability under combined random load sequences. *Computers & Structures*, *9*(5), 489-494.

[3] Breitung, K. (1984). Asymptotic approximations for multinormal integrals. *Journal of Engineering Mechanics*, *110*(3), 357-366.

[4] Tvedt, L. (1990). Distribution of quadratic forms in normal space-application to structural reliability. *Journal of engineering mechanics*, *116*(6), 1183-1197.

[5] Rubinstein, R. Y., & Kroese, D. P. (2016). *Simulation and the Monte Carlo method* (Vol. 10). John Wiley & Sons.

[6] Bucher, C. (2009). Asymptotic sampling for high-dimensional reliability analysis. *Probabilistic Engineering Mechanics*, *24*(4), 504-510.

[7] Zhangchun, T., Zhenzhou, L., Wang, P., & Feng, Z. (2013). A mean extrapolation technique for high reliability analysis. *Applied Mathematics and Computation*, *222*, 82-93.

[8] Zhangchun, T., Zhenzhou, L., & Wang, P. (2014). Discussion on: Applications of asymptotic sampling on high dimensional structural dynamic problems: MT Sichani, SRK Nielsen and C. Bucher, Structural Safety, 33 (2011) 305–316. *Structural Safety*, (46), 8-10.

[9] Gasser, C., & Bucher, C. (2018). An optimized strategy for using asymptotic sampling for reliability analysis. *Structural safety*, *71*, 33-40.

[10] Iman, R. L., & Conover, W. J. (1982). A distribution-free approach to inducing rank correlation among input variables. *Communications in Statistics-Simulation and Computation*, *11*(3), 311-334.

[11] Florian, A. (1992). An efficient sampling scheme: updated latin hypercube sampling. *Probabilistic engineering mechanics*, *7*(2), 123-130.

[12] Bratley, P., & Fox, B. L. (1988). Algorithm 659: Implementing Sobol's quasirandom sequence generator. *ACM Transactions on Mathematical Software (TOMS)*, *14*(1), 88-100.

[13] Halton, J. H. (1960). On the efficiency of certain quasi-random sequences of points in evaluating multi-dimensional integrals. *Numerische Mathematik*, *2*(1), 84-90.

[14] Fang, K. T., Wang, Y., & Bentler, P. M. (1994). Some applications of number-theoretic methods in statistics. *Statistical Science*, 416-428.

[15] Bayrak, G., & Acar, E. (2021). A critical evaluation of asymptotic sampling method for highly safe structures. *Structural and Multidisciplinary Optimization*, https://doi.org/10.1007/s00158-021-03057-0.

[16] MacKay, D. J. (1998). Introduction to Gaussian processes. *NATO ASI series F computer and systems sciences*, *168*, 133-166.

[17] Daberkow, D., & Mavris, D. (2002, September). An investigation of metamodeling techniques for complex systems design. In *9th AIAA/ISSMO Symposium on Multidisciplinary Analysis and Optimization* (p. 5457).

[18] Gunn, S. R. (1998). Support vector machines for classification and regression. *ISIS technical report*, *14*(1), 5-16.

[19] Clarke, S. M., Griebsch, J. H., & Simpson, T. W. (2005). Analysis of support vector regression for approximation of complex engineering analyses.

[20] Zhang, Y., Kim, N. H., Park, C. Y., & Haftka, R. T. (2015). One-Dimensional Function Extrapolation Using Surrogates. In *11th World Congress on Structural and Multidisciplinary Optimization (WCSMO), Sydney, Australia, June* (pp. 7-12).

[21] Sacks, J., Welch, W. J., Mitchell, T. J., & Wynn, H. P. (1989). Design and analysis of computer experiments. *Statistical science*, *4*(4), 409-423.

[22] Martin, J. D., & Simpson, T. W. (2005). Use of kriging models to approximate deterministic computer models. *AIAA journal*, *43*(4), 853-863.

[23] Shepard, D. (1968, January). A two-dimensional interpolation function for irregularly-spaced data. In *Proceedings of the 1968 23rd ACM national conference* (pp. 517-524).

[24] Berry, M. W., & Minser, K. S. (1999). Algorithm 798: high-dimensional interpolation using the modified Shepard method. *ACM Transactions on Mathematical Software (TOMS)*, *25*(3), 353-366.

[25] Myers, R. H., Montgomery, D. C., Vining, G. G., Borror, C. M., & Kowalski, S. M. (2004). Response surface methodology: a retrospective and literature survey. *Journal of quality technology*, *36*(1), 53-77.

[26] Dyn, N., Levin, D., & Rippa, S. (1986). Numerical procedures for surface fitting of scattered data by radial functions. *SIAM Journal on Scientific and Statistical Computing*, *7*(2), 639-659.

[27] Wu, Y. T., Shin, Y., Sues, R., & Cesare, M. (2001). Safety-factor based approach for probability-based design optimization. In *19th AIAA applied aerodynamics conference* (p. 1522).

[28] Bayrak, G., & Acar, E. (2018). Reliability estimation using Markov chain Monte Carlo–based tail modeling. *AIAA Journal*, *56*(3), 1211-1224.

[29] Creveling, C. M. (1997). *Tolerance design: a handbook for developing optimal specifications*. Prentice Hall.

[30] Lee, S. H., & Kwak, B. M. (2006). Response surface augmented moment method for efficient reliability analysis. *Structural safety*, *28*(3), 261-272.

[31] Song, S., Lu, Z., & Qiao, H. (2009). Subset simulation for structural reliability sensitivity analysis. *Reliability Engineering & System Safety*, *94*(2), 658-665.

[32] Huang, B., & Du, X. (2006). Uncertainty analysis by dimension reduction integration and saddlepoint approximations. Journal of Mechanical Design, 28: 26-33.

A Procedure to Acquire Noise-Free Receptance Matrix for Receptance Coupling Substructure Analysis

K. KIRAN[1]

[1] Suleyman Demirel University, Isparta/Turkey, kadirkiran@sdu.edu.tr

***Abstract* – This paper proposes a procedure to eliminate measurement and calculation noises on the translational and rotational receptances for receptance coupling substructure analysis (RCSA). To this end, the holder-spindle subassembly direct and cross receptances are measured at three locations. For each measurement, a nonlinear least squares modal fitting approach is implemented with employing Levenberg-Marquardt method. By using those fitted receptances, the rotational receptances for the holder-spindle subassembly are derived through the synthesis method. It has been seen from the comparisons between the obtained rotational receptances via the proposed procedure and directly measured receptances that the proposed modal fitting approach entirely eliminates the measurement and calculation noises without using any filter and enables us to accurately obtain full receptance matrix for the RCSA. This will lead to improve the tool point receptance estimations with the RCSA.**

***Keywords* – Receptance coupling substructure analysis; modal fitting; chatter stability.**

I. INTRODUCTION

MACHINED part accuracy in the manufacturing industry may suffer from surface location errors [1-2] and chatter [3-4] during the machining. Those issues are directly related to the tool point or/and the workpiece frequency response functions or receptances. Measuring of those receptances for every tool, holder and machine spindle combinations are a great deal of work. To avoid this time-consuming work, researchers have presented the RCSA [5]. This technique allows us to predict the tool point receptances by coupling the tool, the holder and the spindle receptances. For this process, the individual component receptances can be obtained from measurements or models, which helps us to save a significant amount of time. Over the years, researchers have aimed to improve the RCSA. Schmitz and Duncan [6], for instance, presented a work on the RCSA to estimate the tool point receptances. In the work, they divided tool-holder-spindle assembly into three components. The spindle receptances were determined from the measurements and inverse RCSA whereas the tool and the holder receptances were obtained using Euler-Bernoulli and Timoshenko beam theories. The results have shown that the measured and predicted tool point receptances are in good agreement. In another study [7] completed by the same authors, a multiple-point RCSA was proposed to predict the receptances of the nested components with common neutral axis. On the other hand, Albertelli et al. [8] presented a new RCSA methodology. They provided a method to obtain the rotational receptances as well as acquired frequency dependent tool-holder interface contact matrix. Ji et al. [9] employed the same procedure with previous study for contact dynamics identification, but they proposed two new compensation strategies based on the one presented in [6] for accurately achieving rotational receptances. The authors reported that the proposed compensation strategies significantly enhance the RCSA predictions. In [10], the RCSA and structural modification methods were implemented to predict the tool point frequency response function for the chatter stability analysis. The mathematical model developed in the study includes spindle bearing dynamics and tool-holder contact dynamics. Other efforts on the RCSA can be found in [11-15] as well. Considering all those studies, it has been seen the importance of the computation of rotational receptances. Therefore, in this study, it is focused on improving accuracy of the rotational receptances by implementing a nonlinear least squares modal fitting approach. Henceforth, the paper is organized as follows: Section II covers a brief mathematical background of the RCSA. Section III includes proposed procedure for obtaining noise-free rotational receptances. Experimental work is presented in Section IV. In Section V, results and discussion are provided. Finally, Section VI concludes the paper.

II. RECEPTANCE COUPLING SUBSTRUCTURE ANALYSIS

Receptance coupling substructure analysis is a technique that computes assembly dynamics by combining dynamics of individual components. This technique has been frequently implemented in the literature to estimate tool-holder-spindle assembly receptances [1-15], which saves a significant amount of experimental time. A schematic view of the tool-holder-spindle assembly RCSA model is illustrated in Figure 1. This figure shows that the tool point receptances or tool-holder-spindle assembly (i.e., component III) at the location 1 can be obtained by conducting a damped-flexible coupling between the tool (i.e., component I) and holder-spindle subassembly (i.e., component II) by means of RCSA. That statement is mathematically described as follows [3]:

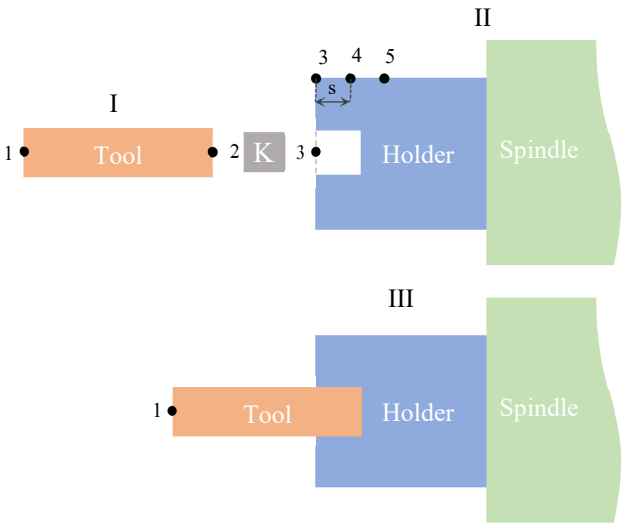

Figure 1: RCSA of tool-holder-spindle assembly

$$C_{III,11} = C_{I,11} - C_{I,12}\left(C_{I,22} + C_{II,33} + [K]^{-1}\right)^{-1} C_{I,21} \quad (1)$$

where $C_{III,11}$, $C_{I,11}$, $C_{I,22}$ and $C_{II,33}$ are the direct receptance matrices of the components III, I and II at the locations 1, 2 and 3, respectively. $C_{I,12}$ and $C_{I,21}$ are the cross receptance matrices of the component I. All those matrices include translational and rotational dynamics and they can be defined to be:

$$\begin{bmatrix} H_{I,11} & L_{I,11} \\ N_{I,11} & P_{I,11} \end{bmatrix}, \begin{bmatrix} H_{I,22} & L_{I,22} \\ N_{I,22} & P_{I,22} \end{bmatrix}, \begin{bmatrix} H_{I,12} & L_{I,12} \\ N_{I,12} & P_{I,12} \end{bmatrix}, \begin{bmatrix} H_{I,21} & L_{I,21} \\ N_{I,21} & P_{I,21} \end{bmatrix}, \begin{bmatrix} H_{II,33} & L_{II,33} \\ N_{II,33} & P_{II,33} \end{bmatrix}, \begin{bmatrix} H_{III,11} & L_{III,11} \\ N_{III,11} & P_{III,11} \end{bmatrix} \quad (2)$$

In Equation 2, H (m/N) is the displacement-to-force, L (m/Nm) is the displacement-to-couple, N (rad/N) is the rotation-to-force, P (rad/Nm) is the rotation-to-couple receptances. From these receptances, only displacement-to-force receptances can be experimentally acquired because it is not a straightforward task to measure rotational receptances. Therefore, a synthesis approach along with a nonlinear least squares modal fitting is used to indirectly obtain those receptances, which will be covered in next section. On the other hand, the damped-flexibility at the tool-holder interface is provided by the matrix:

$$K = \begin{bmatrix} k_x + i\omega c_x & 0 \\ 0 & k_\theta + i\omega c_\theta \end{bmatrix} \quad (3)$$

where k_x (N/m), k_θ (Nm/rad), c_x (Ns/m) and c_θ (Nms/rad) are the translational and rotational stiffness and damping terms, respectively.

III. PROPOSED PROCEDURE

As mentioned before, the rotational receptances of holder-spindle subassembly (i.e., $L_{II,33}$, $N_{II,33}$ and $P_{II,33}$) are difficult to measure. Therefore, we employ synthesis approach or second-order backward finite difference method [6] to derive them from displacement-to-force receptances. This approach requires three displacement-to-force receptances measurements, which are $H_{II,33}$, $H_{II,34}$ and $H_{II,35}$, on the holder-spindle subassembly. In performing these measurements, the response location (i.e., location 3) is kept same whereas the excitation locations are varied to be 3, 4 and 5, as shown in Figure 1. The $L_{II,33}$ is then computed as follows:

$$L_{II,33} = \frac{3H_{II,33} - 4H_{II,34} + H_{II,35}}{2s} \quad (4)$$

where s is the distance between measurement locations (see Figure 1.). From reciprocity, we can make the $N_{II,33}$ equal to the $L_{II,33}$. The remaining rotation-to-couple receptance is computed using Equation 5.

$$P_{II,33} = \frac{{L_{II,33}}^2}{H_{II,33}} \quad (5)$$

Now, we have the full receptance matrix for the holder-spindle subassembly. As can be followed, the synthesis approach is quite practical. However, the noise in the $H_{II,33}$, $H_{II,34}$ and $H_{II,35}$ measurements have a great deal of influence on the quality of the $L_{II,33}$, $N_{II,33}$ and $P_{II,33}$ due to subtraction and inversion during their computation. This is the significant drawback of this method. Therefore, in the literature, some efforts to avoid the measurements noises have been completed by applying some filters and compensation strategies. However, in this study, a nonlinear least squares modal fitting procedure is proposed. According to this procedure, the measured $H_{II,33}$, $H_{II,34}$ and $H_{II,35}$ receptances are subjected to modal fitting before computing the rotational receptances. By doing so, we achieve the noise-free and accurate rotational receptances. The proposed procedure is elaborated in the following.

First, the displacement-to-force receptance model [3] is described as follows:

$$H(\omega) = \sum_{q=1}^{n} \frac{1}{k_q}\left[\frac{\left(1 - {r_q}^2\right) - i\left(2\zeta_q r_q\right)}{\left(1 - {r_q}^2\right)^2 + \left(2\zeta_q r_q\right)^2}\right] \quad (6)$$

where q is the mode number, n is the number of modes, k_q is the modal stiffness, $r_q = \omega/\omega_{nq}$ is the frequency ratio, $\omega_{nq} = \sqrt{k_q/m_q}$ is the natural frequency, m_q is the modal mass and ζ_q is the damping ratio.

Second, parameter dependent sum of squared error function is defined to be:

$$\varepsilon(p) = \sum_{j=1}^{N} [Real(H^{measured}) - Real(H^{modeled}(p))]^2 + [Imaginary(H^{measured}) - Imaginary(H^{modeled}(p))]^2 \quad (7)$$

Here, this equation computes the sum of squared errors between the real and imaginary parts of measured and modeled

receptances. The modeled receptance is describes to be $H^{modeled}(p)$ because we aim to find best modal parameter vector, $p = (m_q \; k_q \; \zeta_q)$, that represents the measured receptances. To do so, an iterative line search procedure is performed with the aim of minimizing $\varepsilon(p)$ in Equation 8.

$$p_{k+1} = p_k + h \tag{8}$$

As seen from this equation, the parameter update is carried out with h that is computed using Levenberg-Marquardt method [16] to be:

$$h = \left(J^T J + \psi diag(J^T J)\right)^{-1} (J^T \Delta) \tag{9}$$

where J is the Jacobian matrix and it is approximated using finite difference method, ψ is the damping parameter and Δ is:

$$\Delta = \begin{bmatrix} \Delta_x \\ \Delta_y \end{bmatrix}$$

$$\begin{aligned} \Delta_x &= Real(H^{measured}) - Real\left(H^{modeled}(p)\right) \\ \Delta_y &= Imaginary(H^{measured}) \\ &\quad - Imaginary\left(H^{modeled}(p)\right) \end{aligned} \tag{10}$$

This iterative line search procedure proceeds until the converge term given in Equation 11 is satisfied.

$$max|J^T \Delta| \leq 10^{-8} \tag{11}$$

When the modal fit is completed using the above-mentioned procedure, the rotational receptances are computed with the same synthesis approach, but using the fitted or noise-free receptances as follows:

$$L_{II,33-fit} = \frac{3H_{II,33-fit} - 4H_{II,34-fit} + H_{II,35-fit}}{2s} \tag{12}$$

$$N_{II,33-fit} = L_{II,33-fit} \tag{13}$$

$$P_{II,33-fit} = \frac{{L_{II,33-fit}}^2}{H_{II,33-fit}} \tag{14}$$

IV. EXPERIMENTAL WORK

To measure the required holder-spindle subassembly displacement-to-force receptances, an experimental setup shown in Figure 2 was constituted. In this setup, an impact hammer (i.e., Kistler 9722A2000) was used to excite holder-spindle subassembly within a broad frequency range and the corresponding response was measured using an accelerometer (i.e., Kistler K-Shear Type 8702B500). For data recording, CUTPRO® MALTF module was employed.

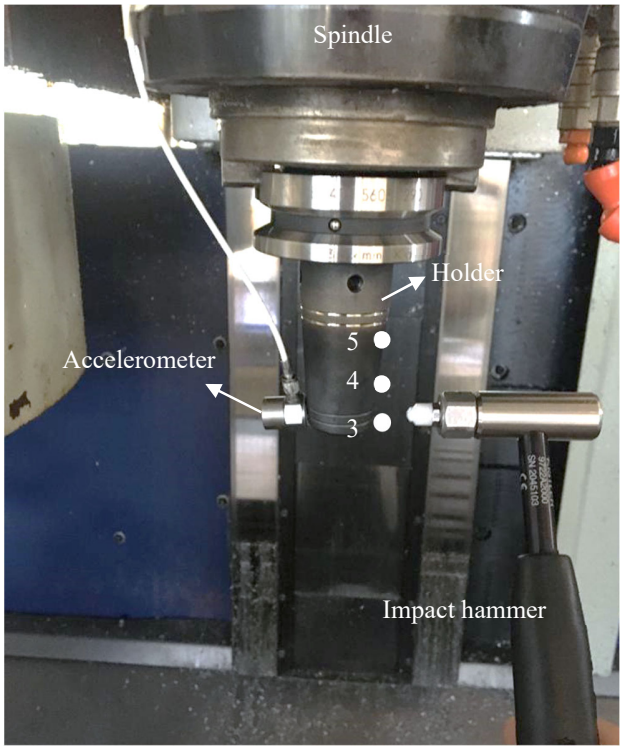

Figure 2: Experimental setup

As seen from Figure 2, the holder-spindle subassembly is excited at the locations 3, 4 and 5 while the response measurement location (i.e., 3) is kept same by not moving accelerometer. As such, we separately obtain the $H_{II,33}$, $H_{II,34}$ and $H_{II,35}$ receptances. Each receptance measurement was repeated three times and average of these three measurements was used in the fitting procedure and computing the rotational receptances. Note also that, in those measurements, a shrink fit tool holder (i.e., SECO E3414 5603 1290) was used on the Hartford CNC vertical machining center.

V. RESULTS AND DISCUSSION

Figure 3 compares the measured and nonlinear least squares modal fitted displacement-to-force receptances at the location 3 for the holder-spindle subassembly. Note that, in these receptances, the excitation and response locations are the same. By a closer look at this figure, one can observe that the nonlinear least squares modal fitting procedure works very well and the fitted receptance both real and imaginary parts satisfyingly are able to represent the measured ones. Totally, 10 modes are used in the modal fitting process. As seen, the most flexible modes are at the natural frequencies of 920.08 Hz and 1034.5 Hz. We put emphasis on these 2 modes of 10 because they are going to be more dominant than the others in obtaining tool point receptances. The same fitting procedure is completed for other measured displacement-to-force receptances (i.e., $H_{II,34}$ and $H_{II,35}$). As previously stated, those fitted receptances are used to compute the rotational receptance. By doing so, we obtain the noise-free full receptance matrix. Figure 4

comparatively shows the obtained full receptance matrices with the proposed procedure and directly using the measured receptances. In this figure, improvements in the rotational receptances with using proposed procedure are significantly obvious. The measurement and calculation noises are eliminated without employing any filter. Instead, the structural dynamics are considered. This will also improve the prediction of tool point receptances via the RCSA because the RCSA also performs frequency-by-frequency subtraction and inversion between receptances and any noise in the receptances may distort the prediction accuracy, which in turn poor stability analysis. On the other hand, it must be stated that the proposed procedure is pretty sensitive to the peaks at the natural frequencies. In other words, the modes, which are to be fitted, natural frequencies must be same for all displacement-to-force receptances measurements. Any frequency shift between them (i.e., $H_{II,33}$, $H_{II,34}$ and $H_{II,35}$) will lead to undesired peaks in the rotational receptances as been in directly using measured receptances (see Figure 4).

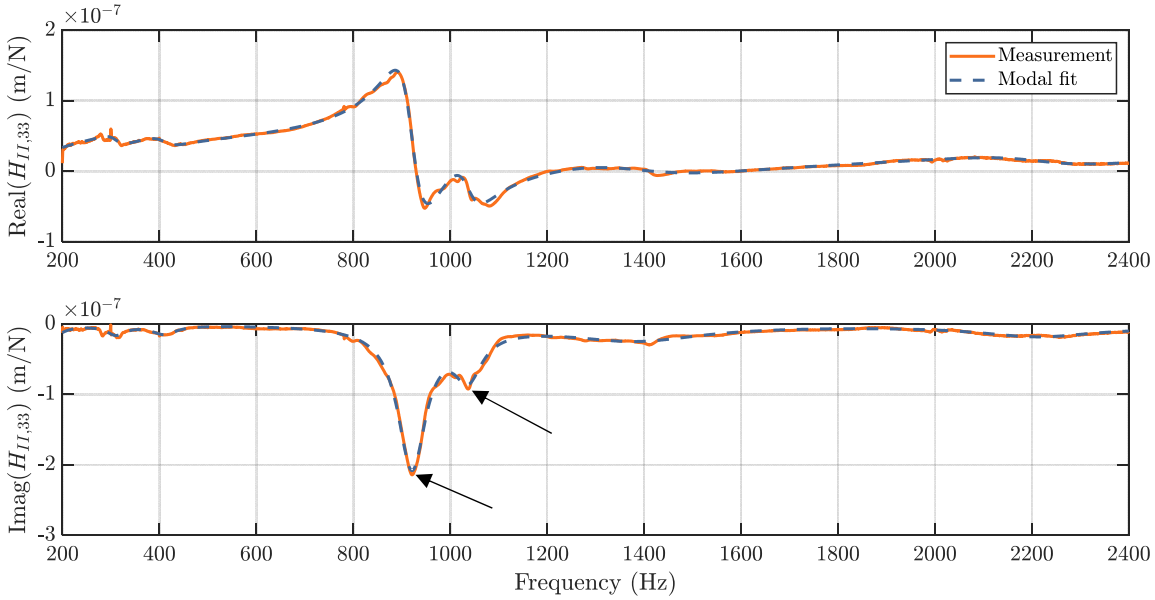

Figure 3: A comparison between measured and nonlinear least squares modal fitted displacement-to-force receptances at location 3 for holder-spindle subassembly

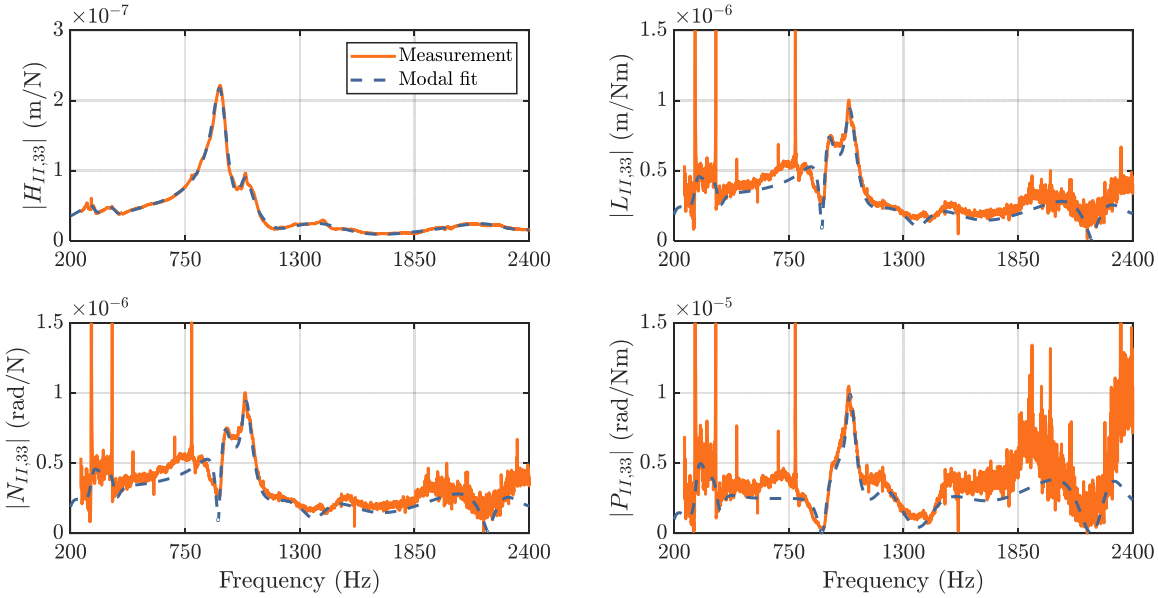

Figure 4: Comparison of full receptance matrices obtained from directly measurements and proposed procedure at location 3 for holder-spindle subassembly

VI. Conclusions

This paper has presented a nonlinear least squares modal fitting procedure to achieve noise-free receptances. Within this scope, the measured holder-spindle subassembly displacement-to-force receptances have subjected to a modal fitting procedure prior to computing rotational receptances with synthesis approach. By doing so, the measurement and calculations noises in the receptances have been completely eliminated without using any filter. In other words, the accuracy of the full receptance matrix for the RCSA has been remarkable improved. This will result in improving tool point receptance predictions with RCSA. For a future study, effect of this improvement on the tool point receptance predictions and the stability analysis will be studied.

Acknowledgment

The author thanks Design and Manufacturing Technologies Research Laboratory, Innovative Technologies Application and Research Center, Suleyman Demirel University for the experimental studies.

References

[1] T.L. Schmitz, and B.P. Mann, "Closed-form solutions for surface location error in milling", *International Journal of Machine Tools and Manufacture,* vol. 46(12), pp.1369–1377, 2006.

[2] K. Kiran, M. Rubeo, M.C. Kayacan, and T. Schmitz, "Two degree of freedom frequency domain surface location error prediction", *Precision Engineering*, vol. 48, pp. 234–42, 2017.

[3] T.L. Schmitz, and K.S. Smith, *Machining dynamics: frequency response to improved productivity*, 2nd ed., New York, USA: Springer Science & Business Media; 2019.

[4] Y. Altintas, *Manufacturing automation: metal cutting mechanics, machine tool vibrations, and CNC Design*, 2nd ed., Cambridge, Cambridge University Press; 2012.

[5] T.L. Schmitz, and R. Donalson, "Predicting high-speed machining dynamics by substructure analysis", *CIRP Annals*, vol. 49(1), pp. 303–308, 2000.

[6] T.L. Schmitz, and G.S. Duncan, "Three-component receptance coupling substructure analysis for tool point dynamics prediction", *J Manuf Sci Eng,* vol. 127(4), pp. 781–90, 2005.

[7] T.L. Schmitz, and G.S. Duncan, "Receptance coupling for dynamics prediction of assemblies with coincident neutral axes", *Journal of Sound and Vibration*, vol. 289(4-5), pp.1045-1065, 2006.

[8] P. Albertelli, M. Goletti, and M. Monno, "A new receptance coupling substructure analysis methodology to improve chatter free cutting conditions prediction", *International Journal of Machine Tools and Manufacture*, vol. 72, pp.16-24, 2013.

[9] Y. Ji, Q. Bi, S. Zhang, and Y. Wang, "A new receptance coupling substructure analysis methodology to predict tool tip dynamics", *International Journal of Machine Tools and Manufacture*, vol. 126, pp.18-26, 2018.

[10] A. Ertürk, H. N. Özgüven, and E. Budak, "Analytical modeling of spindle–tool dynamics on machine tools using Timoshenko beam model and receptance coupling for the prediction of tool point FRF", *International Journal of Machine Tools and Manufacture*, vol. *46*(15), pp.1901-1912, 2006.

[11] M. Postel, O. Özsahin, and Y. Altintas, "High speed tooltip FRF predictions of arbitrary tool-holder combinations based on operational spindle identification", *International Journal of Machine Tools and Manufacture*, vol. 129, pp. 48-60, 2018.

[12] Y. Yang, W.H. Zhang, Y.C. Ma, and M. Wan, "Generalized method for the analysis of bending, torsional and axial receptances of tool–holder–spindle assembly", *International Journal of Machine Tools and Manufacture*, vol. 99, pp. 48-67, 2015.

[13] S. S. Park, Y. Altintas, and M. Movahhedy, "Receptance coupling for end mills" *International Journal of Machine Tools and Manufacture*, vol. 43(9), pp. 889-896, 2003.

[14] M. M. Rezaei, M. R. Movahhedy, H. Moradi, and M.T. Ahmadian, "Extending the inverse receptance coupling method for prediction of tool-holder joint dynamics in milling" *Journal of Manufacturing Processes*, vol. 14(3), pp. 199-207, 2012.

[15] K. Kiran, and M. C. Kayacan, "Effect of material removal on workpiece dynamics in milling: Modeling and measurement", *Precision Engineering*, vol. 60, pp. 506-519, 2019.

[16] H.P. Gavin, "The Levenberg-Marquardt algorithm for nonlinear least squares curve-fitting problems" *Department of Civil and Environmental Engineering, Duke University*, pp. 1-19, 2019.

Optimization of Barrel Wall Thicknesses Used in Shotguns Through Finite Elements Method

A. UGUR[1], R. YAKUT[2,] H. DÜZCÜKOĞLU[1] and Ö. S. ŞAHİN[3]

[1] Selcuk University, Konya/Turkey, augur1990@gmail.com
[2]Batman University, Batman/Turkey, rifat.yakut@batman.edu.tr
[1] Selcuk University, Konya/Turkey, hayduzcukoglu@selcuk.edu.tr
[3]Konya Technical University, Konya/Turkey, ossahin@ktun.edu.tr

***Abstract* - Unrifled shotgun barrels are gun elements that have a certain wall thickness and are exposed to high pressures. When the barrel wall thickness is lower than the required amount in gas pressure-powered shotguns, the barrel gets heated and expands when consecutive shots are fired. The expansion of the barrel renders the system to be unable to perform shots in shotguns. As a solution to this problem, barrel wall thickness is unnecessarily increased, which causes the weight of the shotgun to increase. Barrel with more weight than the required amount is an undesired situation for shotguns. Barrel wall thickness should be adjusted to the most suitable values by considering the weight and expansion amounts. In this study, the optimization of design parameters was performed for barrel wall thicknesses used in shotguns as a result of the tests performed by using ANSYS response surface optimization. The study conducted enabled the revision of material choice of the main components in shotguns.**

***Keywords* - Shotgun, response surface method, material**

I. INTRODUCTION

SHOTGUNS are unrifled guns used in land hunting and shooting competitions [1, 3]. Shotgun industry has been increasing its production capacity in recent years, and different varieties of shotguns are being produced. As competition in the market demands better performance and products with longer life, the quality of shotguns becomes all the more important every passing day [4]. Firearms are used for different purposes such as in defense-war industry, hunting, sports and personal security [5, 6]. The part of the shotguns where they are handled is called the butt. The part pressed with finger in order to fire the shotgun is called the trigger, while the pointed edge that hits and fires the capsule at the bottom of the cartridge at the tip of the trigger is named the hammer. The steel bore that directs the pellets that gain speed due to gas pressure formed as a result of the firing and explosion of the gunpowder in the cartridge to the target is called the barrel, and the part at the head of the barrel in which cartridge can be loaded is named the chamber, and the conic part that connects the barrel to the chamber is named forcing cone [1]. There are a number of factors that affect the scattering of the pellets such as barrel length, pellet size, the shock condition of the shotgun, fuse structure, and environmental conditions [7]. Unrifled shotgun barrels are one of the important parts that are in different gauges and lengths, have a certain wall thickness, and are exposed to high pressure. It is highly important that the pressure forming in the gas-powered semi-automatic guns during the explosion is transferred to gas chamber holes. When this pressure is low, the system does not function properly and the gun misfires. When the pressure is higher than the pressure required for the system to work, it causes damage to the mechanical components [8]. In shots made with shotguns, there are many factors affecting the scattering of the pellets such as barrel length, the size of the pellet, shock degree, fuse structure, gun type, gunpowder amount and type, the elasticity and strength of the tissues, as well as wind, humidity, and temperature [9, 10].

Damage is defined as the components or parts that form various engineering systems becoming dysfunctional in the initial stages of their being put to service or during service, their inability to fulfill the performance expected from them, or leading to the occurrence of dangerous situations in case of continuing their use [11].

It is quite difficult to examine the interior ballistics of shotguns, and this examination is mostly related with the barrel component. While designing the barrel of a shotgun, it is highly important to determine the interior ballistic parameter correctly. When the gunpowder starts to fire in the barrel, very high pressure values are reached in just milliseconds. The high pressure value forming in the barrel drives the bullet forward with a high acceleration. In the meantime, with the effect of the pressure of the cartridge exploding in the barrel, there occur instant expansions, abrupt vibrations on the barrel, and flash temperatures. Due to this flash temperature increase, high temperature is formed on the inner surface of the barrel [12, 15].

II. MATERIALS AND METHOD

In the light of the data obtained from the test system prepared, optimization was performed on the barrel component by using ANSYS analysis program Response Surface Optimization module. With parametric optimization studies, improvements and developments were made in barrel design.

A. Barrel material

In the barrels used in the test system, SAE 4140 (42CrMo4) stress-relieved improved steel material was used. Table 1

presents the chemical properties, and Table 2 shows mechanical properties.

Table 1: Chemical properties [12].

C	Si	Mn	P	S	Cr
0,40	0,25	0,83	0,009	0,027	1,01

Ni	Mo	Cu	Al	Sn	V
0,12	0,18	0,22	0,022	0,016	-

Table 2: Mechanical Properties [12].

Hardness (HB)	Tensile Strength (MPa)	Yielding Strength (MPa)	Elongation (%)
302	1100-1200	750	11

B. Determination of pressure values

Pressure values were determined at measurement points observed on the barrel to which pressure sensor could be mounted through pressure sensors (Figure 1). The pressure of the position of the chamber is the pressure of the cartridge used. Chamber pressures are indicated on the cartridge by the manufacturing company.

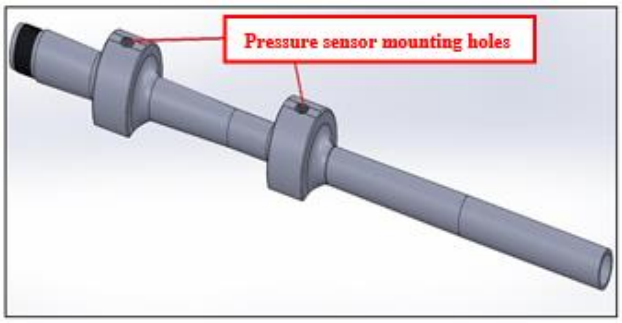

Figure 1: Barrel on which pressure sensor can be mounted

C. Determination of time values

Times are determined according to the movement of the bullet in the barrel after the shotgun is fired. The time that passes when the bullet is in the chamber position is 200 milliseconds. A speedometer was used, and the time that passed until the bullet reached the muzzle was determined to be 780 milliseconds.

D. Preparation of the analysis and acceptances

Acceptances for the analysis:

- As the elements were elastic, and in order for the stresses to be below the ratio limit, safety coefficient was determined between 1.25 and 1.65. While modelling, the barrel was modelled by dividing it into 5 different regions from the combustion chamber to the muzzle. As analysis of the division distance would be performed in 5 steps, analysis time for each step were determined, and pressure values were entered.
- Analyses were performed in Transient Structural.
- Barrel modal effects would be ignored (It was assumed that the shotgun would not be fired consecutively).
- It was assumed that the temperature of the barrel would be between 60-80 centigrade degrees in a single shot. The second shot was not fired directly after the first shot in order for the heat forming on the barrel to dissipate, and as the preparation period lasted approximately 4-6 minutes, shots were fired at the end of this period.
- After the bullet left the barrel, a certain amount of gas is left inside, and this remaining gas creates pressure. However, since this pressure formed was lower than the pressure formed at the moment of explosion, it was not considered while calculating the strength.
- 9806.6 MPa was applied to the barrel as standard gravitation acceleration.
- The barrel was modelled on quarter model as 3D. For this reason, the parameters provided during the optimization were taken as radius, and the barrel weight was calculated over a quarter barrel.

In the parametric optimization study, Response Surface Optimization add-on included in ANSYS analysis software was used. In this add-on, input parameters determined on geometry were assigned lower and upper values. Experiment designs were made according to these assigned values. A response surface was created for each output parameter. Finally, purpose functions and design criteria were determined. After all these procedures were completed, Response Surface Optimization add-on yielded the output parameters that provided design criteria and purpose functions and suggested input parameters. Parameter groups suggested by the add-on are called design points. Suggested design points were analyzed and confirmed one by one, and design optimization processes were completed.

Transient Structural analysis is used to determine the dynamic reaction of a structure under the effect of a load dependent on any general time. It is used to determine location changes, stresses, strains, and forces that change in time in a structure while it is responding to any temporary load.

Barrel modelling was realized in design models in ANSYS analysis software, and parameters were determined. While modelling was being carried out, barrel sections were divided into 5 different regions (Figure 2). Here, 3 important measurements that affect barrel weight were determined as input parameters. Regional representation of the barrel's input parameters is presented in Figure 3 and, and barrel input parameters are given in Table 3.

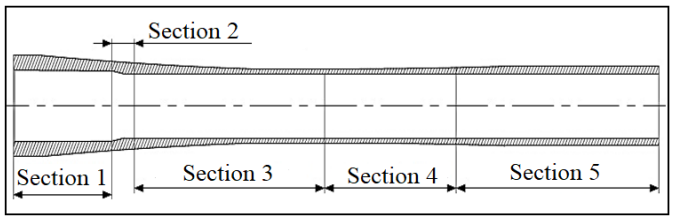

Figure 2: Barrel sections.

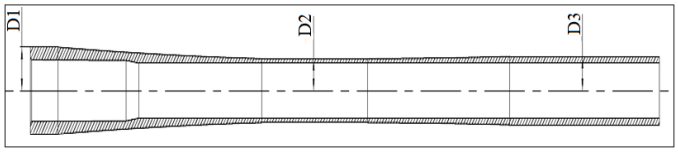

Figure 3: Regional representation of the barrel's input parameters

Table 3: Barrel input parameters.

D1 (mm)	D2 (mm)	D3 (mm)
15,5	10,75	11,5

In the geometrical design, quarter model was used in order for the analysis period to be shorter, meshing to be performed faster, and analysis points to be less. Figure 4 shows the face appearance of the quarter model geometrical design, and Figure 5 presents the side appearance of the geometrical design.

Figure 4: Face appearance of the geometrical design.

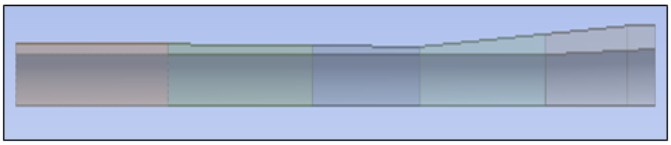

Figure 5: Side appearance of the geometrical design.

After the geometrical design was made, 0.159 kg, which was ¼ weight of the barrel, was determined as the output parameter. Barrel mesh size and mesh type were determined as quad/tri, and meshing was performed as 185272 nodes 35700 elements.

Average mesh quality was 89%, and average mesh skewness value was $3.3873x10^{-2}$. As a result of these values, it was seen that mesh quality was quite high. Skewness is the value that indicates whether there is skewness in the observed data. The closer to zero the skewness is, the higher the quality is.

In Figure 6., meshwork of chamber section is presented. In order to ensure the validity of the analyses, mesh number was chosen as more than three elements.

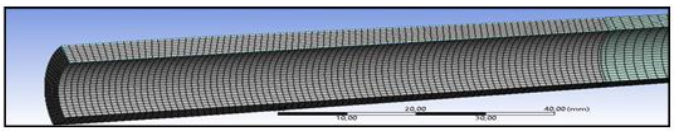

Figure 6: Chamber section meshwork.

Input parameters used in the analysis study are presented in Table 4. Analysis was performed in 5 steps.

Table 4: Analysis input parameters

Distance (mm)	Pressure (Bar)	Time (millisecond)	Section	Step
0	0	0	Position 0	
70	1200	200	Chamber position	Step 1
93,6	500	270	1st pressure measurement point	Step 2
241	225	475	2nd pressure measurement point	Step 3
343	120	640	Strain gauge position 1	Step 4
500	45	780	Muzzle position	Step 5

Figure 7 presents the strain values formed at each step as a result of the analysis.

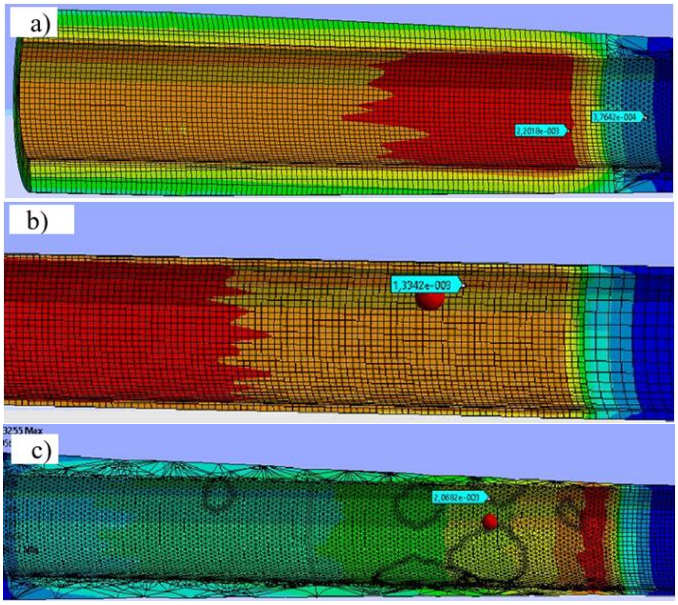

Figure 7: Strain results, a) strain gauge 3-4, b) strain gauge 3, c) strain gauge 1

The Maximum Stress Value Over Time of 438.67 MPa and ¼ weight of the barrel, which was 0.159 kg, were determined as parameters.

By entering the values presented in Table 5 in the design of experiments part of the ANSYS, the design parameters were determined and analysis was performed.

Table 5: Barrel lower-upper design points

	D1 (mm)	D2 (mm)	D1 (mm)
Upper value	16	11,6	12,65
Lower value	13,5	10,5	11
Current value	15,5	10,75	11,5

The experiment points obtained from the design points are presented in Table 6. These design points were analyzed in the software, and response surface was created. Genetic aggregation was chosen as response surface type.

Table 6: Experiment points of the barrel

No	D1 (mm)	D2 (mm)	D3 (mm)	Stress (Max)	Weight (kg)
1	14,25	11,05	11,825	432,47	0,19162
2	13,5	11,05	11,825	485,95	0,2197
3	15	11,05	11,825	453,53	0,16018

4	14,25	10,5	11,825	432,35	0,17314
5	14,25	11,6	11,825	432,69	0,21069
6	14,25	11,05	11	432,17	0,17347
7	14,25	11,05	12,65	432,19	0,21065
8	13,64	10,603	11,154	473,97	0,1851
9	14,86	10,603	11,154	491,09	0,13653
10	13,64	11,497	11,154	474,09	0,21506
11	14,86	11,497	11,154	436,77	0,16685
12	13,64	10,603	12,496	473,85	0,21494
13	14,86	10,603	12,496	487,56	0,16637
14	13,64	11,497	12,496	474,12	0,24568
15	14,86	11,497	12,496	436,71	0,19747

After the response surface was created, optimization was started. In the optimization stage, as purpose function, maximum stress was targeted to be lower than 500 MPa and maximum weight to be lower than 0.159 kg. By using this purpose function, the software determines the most suitable value for the design parameters of d1, d2, and d3.

As optimization method, MOGA (Multi-Objective Generic Algorithm) was used. While the software was carrying out the optimization, 3,000 primary samplings were conducted. 600 samples were determined per iteration. Finally, as a result of 20 iterations, 3 target parameters were determined.

As a result of the optimization, the software determined 3 target parameters. As these target parameters try to minimize the stress value, it does not meet our purpose of minimizing the mass. Mass minimization rates of these 3 target parameters with respect to each other are presented below, and the most ideal candidate for minimizing the mass among these target parameters is point 3. It was observed that mass gain was achieved more at point 3 at a rate of 5.47% in respect to point 1, 3.41% in respect to point 2, and 6.35% in respect to the current design of the barrel. In Table 7, 8, and 9 below, target parameters are presented.

Table 7: Point 1 target parameters.

Ref.	D1 (mm)	D2 (mm)	D3 (mm)	Stress (MPa)	Ref. Change (%)	Weight (kg)	Ref. Change (%)
◉	14,288	10,507	11,001	434,03	0	0,15398	0
○	14,298	10,611	11,001	432,93	-0,25	0,15704	1,99
○	15	11,247	11,007	444,75	2,47	0,1489	-3,3

Table 8: Point 2 target parameters.

Ref.	D1 (mm)	D2 (mm)	D3 (mm)	Stress (MPa)	Ref. Change (%)	Weight (kg)	Ref. Change (%)
○	14,288	10,507	11,001	434,03	0,25	0,15398	-1,95
◉	14,298	10,611	11,001	432,93	0	0,15704	0
○	15	11,247	11,007	444,75	2,73	0,1489	-5,18

Table 9: Point 3 target parameters.

Ref.	D1 (mm)	D2 (mm)	D3 (mm)	Stress (MPa)	Ref. Change (%)	Weight (kg)	Ref. Change (%)
○	14,288	10,507	11,001	434,03	-2,41	0,15398	3,41
○	14,298	10,611	11,001	432,93	-2,66	0,15704	5,47
◉	15	11,247	11,007	444,75	0	0,1489	0

Maximum and minimum stress values and weight values are presented in Table 10.

Table 10: Maximum and minimum stress and weight values.

Name	D1 (mm)	D2 (mm)	D3 (mm)	Stress (MPa)	Weight (kg)
Output Parameters (Min					
Stress	15	11,6	11,672	428,83	0,1759
Weight	15	10,5	11	488,31	0,12371
Output Parameters (Max)					
Stress	14,86	10,5	11	496,54	0,12985
Weight	13,5	11,6	12,65	479,31	0,25796

In the optimization made above, the maximum stress value of the material used in accordance with the purpose function is appropriate up to 500 MPa with respect to yield stress.

Figure 8 presents stress change with respect to weight. Vertical axis shows weight, and horizontal axis indicates stress.

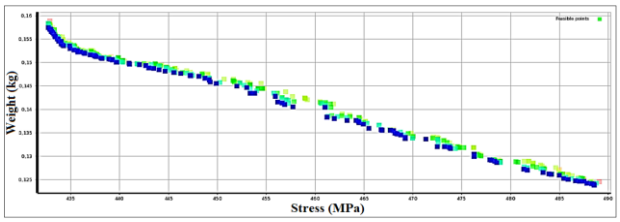

Figure 8: Weight – Stress graph

In Figure 8, the point where stress is high, was determined as target parameter. This process can be seen in detail in Figure 9.

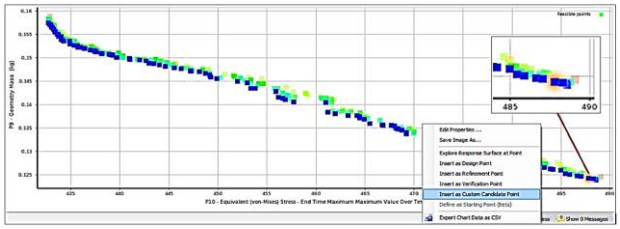

Figure 9: Target parameter selection.

Table 11 presents the data of the selected parameter point.

Table 11: Maximum and minimum stress and weight values.

Ref.	D1 (mm)	D2 (mm)	D3 (mm)	Stress (MPa)	Ref. Change (%)	Weight (kg)	Ref. Change (%)
○	14,288	10,507	11,001	434,03	-11,03	0,15398	23,91
○	14,298	10,611	11,001	432,93	-11,25	0,15704	26,37
○	15	11,247	11,007	444,75	-8,83	0,1489	19,82
◉	14,997	10,512	11,001	487,82	0	0,12427	0

The design differences of the barrel obtained from the optimization in comparison to its current design are presented in the following figures. The area shaded in black demonstrates the difference between the current design and the design obtained as a result of the optimization. The area shaded in red represents the design obtained as a result of the optimization. Chamber optimization difference (Figure 10),

Pressure sensor position 1 (Figure 11) and position 2 (Figure 12) measurement point optimization difference, Strain gauge position 1 (Figure 13) optimization difference, and muzzle optimization difference (Figure 14) are presented in relevant figures.

Figure 10: Chamber optimization difference.

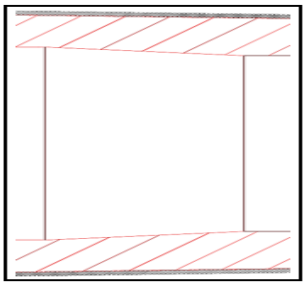

Figure 11: Pressure Sensor measurement point 1 optimization difference.

Figure 12: Pressure sensor measurement point 2 optimization difference.

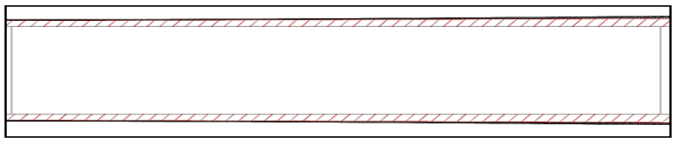

Figure 13: Strain gauge position 1 optimization difference.

Figure 14: Muzzle optimization difference.

III. CONCLUSION

- Barrel design made through trial and error method so far was made possible through optimization by using data.
- The strain value at the selected target parameter point is high with respect to other optimization values, but it is still within the range of safety coefficient. In addition, it was seen that mass gain at the target parameter point was achieved more by 19.9% in comparison to point 1, by 20.86% with respect to point 2, by 16.54% compared to point 3, and by 21.84% with respect to the current barrel design.
- During the barrel optimization, while more change was observed in D2 and D3 barrel input parameters, less change was observed in D1 barrel input parameter. The reason for this is the high pressure formed at the time of explosion in the chamber.
- As a result of the optimization studies, the current barrel weight of 0.636 kg was reduced down to 0.497 kg. With this result obtained, the barrel was made lighter by 21.84% in comparison to its current design.

REFERENCES

[1] F. Yücel Beyaztaş, "The determination of discharge distance with shotgun" *C. Ü. Tıp Fakültesi Dergisi*, vol. 25, no. 1, pp. 43-46, 2003.

[2] Ş. Demirci, K. H. Doğan, G. Günaydın ve Sermet Koç, "Av Tüfeği ile Ölümler" *Acta Turcica Çevrimiçi Tematik Türkoloji Dergisi*, vol. 1, no. 1, pp. 206-212, 2009.

[3] H. B. Üner, B. Şam, Ö. Kurtaş, C. Uysal, A. Çerkezoğlu, "The Factors that Effect on Dispersion of Shotgun Pellets", *The Bulletin of Legal Medicine*, vol. 5, no. 2, pp. 65-69, 2000.

[4] I. Doruk, R. Varol and M. Topçu, "Failure analysis of the semi-automatic shotgun locking block" *Scientific Research and Essays vol.* 5, no. 20, pp. 3134-3140, 2010.

[5] M. Karapirli, "Av tüfeği atışlarında ara hedeflerin saçma dağılımına etkisi", Uzmanlık tezi, Adli tip anabilim dalı, Tıp fakültesi, Marmara üniversitesi, İstanbul, 2007

[6] S. Bilgi, "Av tüfeği namlu uzunluğunun saçma dağılımına etkisinin değerlendirilmesi", Uzmanlık tezi, Adli Tip Anabilim Dalı, Tıp Fakültesi, Marmara üniversitesi, İstanbul, 2013.

[7] A. Çelikel, Y. Balcı, B. Üner, C. Bal, "The effect of barrel length on pellet dispersion and its importance in determination of range of fire", *Adli Tıp Derg.*, vol. 26, no. 2, pp. 115-123, 2012.

[8] A. Uğur, H. Düzcükoğlu, Ö. S. Şahin, Okan Uyar "Hafif silahlar için iç balistik sistem kurulumu ve sistemin sağlayacağı kazanimlar" *2019 Ereğli International Science and Academic Congress Ereğli Uluslararası Bilim ve Akademi Kongresi*, vol. 1, pp. 25-31.

[9] İ. Deniz, "12 ve 16 kalibrelik av tüfeklerinde yarım ve tam şokun saçma dağılımına etkisi" Tıpta Uzmanlık Tezi, Adli Tıp Anabilim Dalı, Meram Tıp Fakültesi, Selçuk Üniversitesi, Konya, 2009.

[10] F. Yücel and M. Örsal, "The determination of the dis charge distance after discharges done with different kinds of shotguns and cartridges" *Adli Tıp Derg.*, vol. 13, no. 1-4, pp. 27-35, 1997.

[11] H. Varol Özkavak and M. R. Usal, "Design Optimization of Lock Part of Shutgun and Improvement of Material Properties" *BEU Journal of Science* vol. 8, no. 4, pp. 1316-1326, 2019.

[12] A. Uğur, "Optimization of the meat thickness of barrel of the hunting rifle with the finete elements method" Master Thesis, Department of Mechanical Engineering, Institute of Graduate Studies, Konya Technical University, Konya, 2019.

[13] İ. H. Serdar, "Analysis of the forces on infantry rifle housing via finite element method", Master Thesis, Institute of Sciences, Sakarya University, Sakarya, 2016.

[14] T. Ablay Rutci, "Development of barrel material used in light weapons and investigations of manufacturing process parameters", Master Thesis, Institute of Sciences, Sakarya University, Sakarya, 2019.

[15] M. Akçay, "Internal and transitional ballistic solution for spherical and perforated propellants and verification with experimental results", *J. of Thermal Science and Technology*, vol. 37, no. 1, pp. 35-44, 2017.

A Test Scheme for Braking Performance Assessment of Tractor Trailer Combination Regarding Current Regulations

H. AYKAN[1], Ş. EKİNCİ[2], K. ÇARMAN[3]

[1]Selcuk University, Institute of Sciences, Konya/Turkey, hakanaykan_06@hotmail.com
[2]Selcuk University, Technology Faculty, Konya/Turkey, sekinci@selcuk.edu.tr
[3]Selcuk University, Faculty of Agriculture, Konya/Turkey, kcarman@selcuk.edu.tr

***Abstract* - The highest number of fatal occupational accidents in the world are experienced in the agricultural sector after the construction and mining sectors. Most of the occupational accidents in the agricultural sector are accidents with tractors and trailers. The increase in the speed of the tractor-trailer combination and the innovations in the braking system of the trailer significantly affect the co-operation performance of the trailer and the tractor. Today, studies on braking torque and braking acceleration in agricultural vehicles with advanced braking systems have begun to increase.**

This study presents an experimental procedure in order to evaluate braking strategies for agricultural tractor-trailer combinations. Tractor and trailer setup is introduced by visuals including photography and schematical sketching. Features of the tractor braking system and trailer braking system are specified. Loading work, braking circuits, transmission tools and additional measurement equipment are described. Two different experimental procedures for on road tests and bench tests are explained. Some preliminary results are given in order to exemplify the effectiveness of the described procedures. Also, jack-knifing phenomena and related travel speeds are discussed. Future work plan is introduced.

***Keywords* - Accident prevention, agricultural tractor trailer combination, braking, jack knifing, transportation.**

I. INTRODUCTION

AGRICULTURAL production had been boosted by means of agricultural mechanization in the past. Therefore, one of the leading roles on increasing effectiveness of the agricultural production is the agricultural mechanization. The principal power source of the agricultural mechanization is the agricultural tractor. One of the equipment that are used with the tractor is the trailer. Agricultural trailers are used in order to transport agricultural products from agricultural fields to depots, storages, or fields of processing facilities. Accordingly, the combination or the couple of agricultural tractor and trailer transmits function of the tractor to transportation. Recently, designs of agricultural trailer have been changing due to increasing travel speeds and improving capacities of agricultural tractors, improving road conditions, changing standards and regulations and infrastructures. Agricultural trailers grow bigger as they can carry more load and volume, their road equipment is being improved and their brake equipment are being enhanced.

Unfortunately, the second most dangerous work sector after mining is assumed as agriculture sector. Despite all the precautions, agricultural tractor takes the first place in agricultural accidents [1]. Approximately 50% of accidents in the last 8 years of the agricultural activities originated from agricultural tractor accidents according to an investigation that was done by English Health and Safety Commission [2]. Mukherjee and Ping [3] investigated work accidents in India and China regarding to agricultural machinery. They stated that the biggest factor of the accidents is the agricultural tractor usage.

The third most fatal occupational accident cases in Turkey are seen in agriculture sector after construction and mining. According to the study of Alçayır [4], 41.9% of work accidents in agriculture originates from accidents with agriculture tractor. This ratio is followed by accidents that involve agricultural trailer with a ratio of 20.9%. Fatal accidents in agriculture mostly due to the agriculture tractor trailer combination since people are transported in trailers.

Increases in tractor power and travel speed of tractor trailer combination necessitates innovation in brake systems of the agricultural trailers and affects cooperation performance of agricultural tractor trailer combination. During readings from literature, no paper has been encountered regarding braking effectiveness of agricultural tractor trailer combination with two axes four-wheel hydraulic braking of the agricultural trailer. Recently, hydraulic brake systems are replacing impact brake systems in agricultural trailers as the requirement of braking deceleration for agricultural trailers had been raised from 2.5m/s^2 to 3.5m/s^2.

People and economy of countries are negatively affected from injuries and deaths due to occupational accidents during agricultural activities. People suffer greatly and consequences of the deaths give various damages to economic and production aspects of countries. The most prominent reason for high human fatalities in agricultural activities is that agricultural employees are carried in tractors, trailers and in their combination.

It is understood that load condition, road condition, travel speed, road slope, braking, general maintenance and brake maintenance are very important in terms of agricultural tractor and trailer accidents in our country. Tractor involved accidents are mostly realized in types of rolling, falling to stockade, and crashing accidents in our country and in the world. In a

questionnaire work that was conducted in Karaman county for accidents in agriculture sector for 20 years period between 1973-1993, it was determined that 62% of total accidents were consist of tractor accidents and 65 people died in that accidents [5]. Reasons such as malfunctioning brake systems due to improper maintenance of tractor and not functioning brakes when frequent braking is done, are being effective in occurrence of accident risks in this way.

Brakes contribute to performances of automobiles, heavy duty vehicles, work machines and agricultural vehicles by providing deceleration, stopping, and fixing in a safely manner during parking. Brakes have crucial importance for vehicles themselves, transported living beings and everyone involved in traffic. Although excessive speed and driver faults are indicated as reasons of traffic accidents, another important cause is do not stopping vehicle in time or cannot control it. Therefore, high reliability and durability are expected from brake system of a vehicle. More emphasis is on brake systems and efforts for improving brake systems are increasing due to the upmost importance of the brake systems. Brake systems are made more effective and safer by adding additional power and control modules. A variety of brake systems are seen in vehicles. Generally common ones are hydraulic brake systems, pneumatic brake systems and mechanical brake systems.

In our literature survey, a work or report showing properness of agricultural tractor and trailer combination to legal regulations in terms of braking; evaluation of various brake system installations and strategies; assessment of current and recent real-world situation for braking at two trailer axles for four wheels coupled with tractor braking has not been encountered. Especially no work has been found on agricultural vehicles having hydraulic brake systems. The purpose of the present proceeding is to discuss an experimental procedure in order to determine brake effectiveness of agricultural tractor trailer combination for agricultural trailer with or without brake systems. The specific emphasis is on two axle balanced agricultural trailers. In conducted preliminary tests, such agricultural trailer was used with a hydraulic brake system. The main aim is to propose a test procedure in order to assess the brake system of the agricultural tractor trailer combination and in particular, the brake system of the trailer, in terms of relevant regulations in act. The proposed tests can further be employed to improve work safety regarding trailer involved duties. The proposed procedure can test modern tractors and trailers having hydraulic, pneumatic or mechanical brake systems for different loads, road types and for different braking strategies such as trailer front wheel braking trailer rear wheel braking, trailer all wheels braking. In this report, some preliminary results are given after the procedure is introduced.

II. Material and Method

In order to describe the procedure for assessing and evaluating braking performance and effectiveness of agricultural tractor trailer combination with a double axle balanced trailer having brake system, all concept is explained by means of preliminary tests with real world equipment. A NewHolland TD 110D branded agricultural tractor was used during experiments. Five oil bath brake disks exist in the hydraulic brake system of this tractor. The oil bath brake discs are connected to axis shaft of the differential box. Tractor brakes can be initiated with a single or separated brake pedals. Separated brake pedals can be merged with a pin or latch. Parking brake of the tractor uses the same system but operated by a hand lever. Technical specifications of the test tractor is given in Table 1.

Table 1: Technical specifications of the agricultural tractor.

Model	TD 110 D NewHolland
Fuel type/number of cylinders	Diesel / 4
Power / torque	110 BG/430 Nm
Cylinder volume	3908 cm^3
Clutch	Dry type double plates
Transmission	12 forward 12 backward ratios
Brake system	Lubricant bath 5 discs brake system
Weight	3900 kg
Distance between axes	2422 mm
Front / rear axles weights	1560 / 2340 kg

During the experiments, agricultural trailer that has 6 tons load capacity, double axles, rubber tires, mechanical brakes with hydraulic effect, the ability to unload by leverage towards backward, and that is drawn by the tractor was used (Figure 1). Hydraulic brake system equipment exists at each axis of the agricultural trailer. Technical specifications of the agricultural trailer are given in Table 2. Two piston-cylinder mechanisms exist in the brake equipment of the brake system at the two axles of the agricultural trailer, connected to braking levers/ratchets. Those mechanisms activate the braking systems on the two axles of the agricultural trailer simultaneously by means of the hydraulic pressure provided by the tractor hydraulic pump. Two-way directional control valves were mounted at each hydraulic circuit element on each axle of the agricultural trailer in order to arrange different trailer braking scenarios such as trailer front braking, trailer rear braking and trailer two axles braking. However, in this work, only two axles braking results are given as preliminary results. The hydraulic directional control valves are important in order to assess braking strategies as a further step for work safety and cost concerns since most of the operational trailers on the field are old and lack a brake system. In case of adaptation of external brake systems to old trailers, cost concern would be high and therefore, assessing several braking scenarios is crucial.

Table 2: Technical specifications of the agricultural trailer.

Total length	5800 mm
Total width	2100 mm
Total height	2180 mm
Track width	1550 mm
Casing dimensions without additions	4220x1920x600 mm
Distance between axes	2500 mm
Self-Weight	1950 daN
Front axis weight share	1000 daN

Rear axis weight share	950 daN
Brake lining length, width, thickness	320/50/6 mm

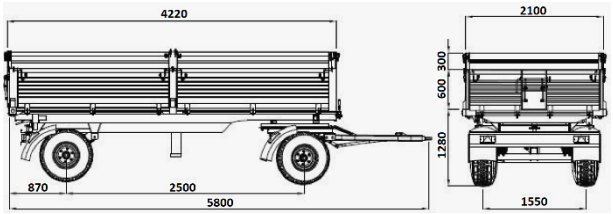

Figure 1: Dimensions of the agricultural trailer.

Determining static brake torque or moment can be done by means of a specific test setup that can easily be prepared by any test facility. In our proposed system, a moment arm of 1000 mm length is connected to the center of the wheel. When the wheel is braked at full hydraulic force, the other tip of the moment arm is held by a hoist. The connection between the hoist and the moment arm has a dynamometer, showing the mass corresponding to the weight force. In our specific setup, a digital screen dynamometer was used. To operate hoist easily, a hydraulic lever jack was also used. Schematical description of the explained static brake moment measurement system is given in Figure 2. This system measures the maximum static brake moment at initial rotation is observed at the wheel.

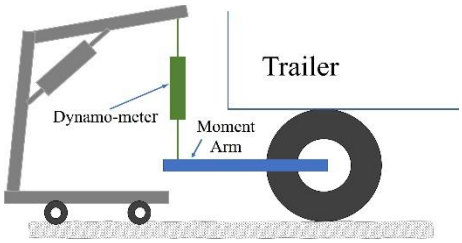

Figure 2: Schematic description of static wheel brake moment measurement system [6].

The static brake moment can also be calculated by the following formula [7]. This formula is an approximation, and the measured static maximum brake moment should be bigger than this value. Otherwise, brake equipment means improper for usage since it cannot be even used for parking.

$$M_d = 0.7 m_{et} R_{et} \quad (1)$$

Here;

M_d: The smallest of the wheel braking torque (Nm)

m: Weight per wheel (kg)

R_{et}: Effective static tire radius (m)

In case of dynamic brake tests, a chronometer was used in order to determine the brake time. Also, a Dickey John DJCMS200 branded velocity measurement device was utilized to record and monitor accurate travel speeds. Dynamic brake test is actually a travel simulation in which agricultural tractor trailer combination travels at a constant speed with a constant load. When the combination reaches a certain point on the road, braking is initiated. Time measurement is started simultaneously. When the combination stops completely, the chronometer is stopped. The travel distance is measured by means of an additional wheel that has rotation sensor on it. By that way, travel distance during braking, braking time and initial travel velocity values are known. Since travelled distance can also be measured by a scale between brake initiation point and stopping point, confidence level of brake distance and all measurements in general, is high. After measurement data is available, following expression is used to determine deceleration values.

$$a = \frac{\Delta V}{\Delta t} \quad (2)$$

The brake tests were conducted for empty agricultural trailer and for loads of 4200, 6000, and 7800 kg. After static brake moments were experimentally determined, same loads were applied to the combination and dynamic brake tests were done.

For the preliminary tests, initially, the travel speed of the combination was planned as 30 km/h. However, jack knifing phenomenon was observed during braking and therefore, travel speed was reduced to 25 km/h considering work safety. Dynamic braking effectiveness tests were conducted by 25 km/h initial maximum travel speed. Also, it is known that different road conditions change braking effectiveness results. Therefore, in order to exemplify different road conditions, two preliminary test results on asphalt and stabilized road conditions are reported in this work. Since this proceeding aims to propose proper test procedure for future works, Table 3 proposes different brake scenarios or strategies.

Table 3: The pattern for future trailer test plan

	Braking Strategy	**Load (kg)**
Braking by Tractor	No Trailer Braking	Empty
		4200
		6000
		7800
	Trailer Front Axle Braking	Empty
		4200
		6000
		7800
	Trailer Rear Axle Braking	Empty
		4200
		6000
		7800
	Trailer Double Axle Braking	Empty
		4200
		6000
		7800

It should be noted that a mass weighted average formulation can be used to determine the brake ratio of the agricultural trailer by using below expression [8]:

$$a_{ta} = \frac{W_k a_k - W_{tr} a_{tr}}{W_{ta}} \quad (3)$$

Here;

a_{ta}: Trailer braking deceleration (m/s^2)

W_k: Total mass of the combination (kg),

a_k: Deceleration of the combination (m/s^2),

W_{tr}: Tractor weight (kg),

a_{tr}: Tractor braking deceleration (m/s^2),

W_{ta}: The weight of the trolley is (kg).

Equation (3), however, is not a decisive expression and instead, it is a very rough approximation. Nevertheless, legal regulations are using this type of approximation for the evaluation of the agricultural trailer brakes.

For preliminary tests, and for proposed test procedure in general, markings on the test track were realized for the maximum travel speed point and brake initiation point. During the preliminary tests, two operators were on the tractor in order to initiate braking and chronometer simultaneously. Agricultural trailer brakes were also initiated by hydraulic valves.

In future test plans, totally 32 different parameter value combinations (2 different road conditions, 4 different braking strategies, 4 different trailer loads) can be tested. Therefore, analysis of variance can be an important indicator for evaluating test results. Generally, ANOVA tool of Minitab software is used for such task. In order to illustrate ANOVA in this proceeding, preliminary test variances were analyzed.

III. Research Result and Discussion

Based on principles and explanations in the previous section, experimental measurement were processed and reduced results are provided in this section. Comparison of experimental static brake moment with theoretical static brake moment is given in Figure 3.

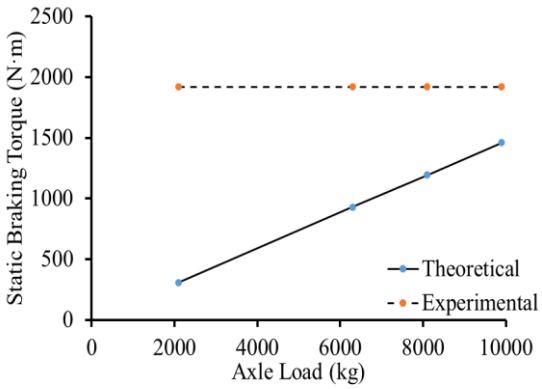

Figure 3: Comparison of experimental and theoretical static brake moment values.

Experimental static brake moment was found around 1920 Nm, which does not change with the load on the trailer. This is expected since the brake moment solely depends on the moment acting on moment arm and the brake equipment in the experimental static brake moment measurement. However, the approximate necessary static brake moment value increases with increasing trailer load per wheel. Nevertheless, it is seen that the static brake moment of the brake system of the trailer is able to withstand high loads without any trouble and has a safety margin according to the theoretical calculation.

Dynamic brake effectiveness test results are given in Figure 4. Brake deceleration values are lower for stabilized road conditions than the asphalt road conditions for all agricultural trailer loads. A linear decrease in braking deceleration is visible by reviewing Figure 4, based on the load of the trailer. A resembling case is visible in the literature [9]. However, that work is a theoretical one and there is difference between experimental results of the current work and the literature work, ranging between 25-50%. Experimental results have lower deceleration values as expected. This is due to the fact that experiments include all real-world effects while the theoretical ones ignore most of them.

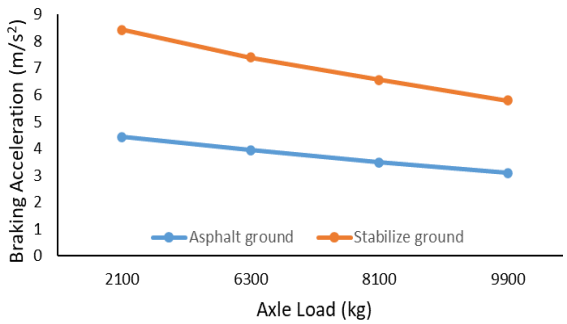

Figure 4: Comparison of brake deceleration values on asphalt and stabilized road conditions.

Table 4 presents parameters and results for an ANOVA instance. Variance analysis indicates that road condition has significant effect on braking effectiveness of the combination ($P<0.05$).

Table 4. Variance analysis results for brake decelerations results

Source	D.F.	M.S.	F-Value	P-Value
Ground (G)	1	1.44500	61.96	0.000**
Braking Type (BT)	3	3.28334	140.79	0.000**
Load	3	2.54442	109.10	0.000**
Error	24	0.02332	-	
General	31	-	-	

** Important at 1% level statistically ($P<0.05$)

G	BT	L
(A) 3.73313_A	(F_4) 4.32500_A	(L_1) 4.21125_A
(S) 3.30812_B	(F_3) 3.72375_B	(L_2) 3.69500_B
	(F_2) 3.15000_C	(L_3) 3.27875_C
	(F_1) 2.88375_D	(L_4) 2.89750_D

This proceeding also aims sharing experiences in the preliminary works. Figure 5 shows an undesired situation when the trailer was loaded unproperly. An accident occurred and welded sections on one of the trailer axles were broken. This would lead to a serious accident during braking. Therefore, authors of the present work suggest careful loading of agricultural trailers.

Figure 5: An instance showing broken axis of the agricultural trailer

IV. Conclusion

In this report, a general test approach was described including static and dynamic brake testing for the combination of agricultural tractors and trailers. The main and future aim is to assess several braking scenarios in order to see if current tractor trailer combinations are convenient for legal regulations. Accordingly, static brake moment determination is described in the text. Also, dynamic on road brake tests as preliminary results are given. Some principal results are briefly mentioned again below and remarks for future work are provided.

1. Proposed test setup is found feasible in terms of static braking moment measurement and dynamic braking effectiveness measurement.
2. Road surface significantly affects braking effectiveness.
3. Proper, uniform, and homogenous distribution of loading on the agricultural trailer is crucial for safe working.
4. Additional tests are required for producing results that can be used by decision makers regarding the agricultural trailers on the field. Improving brake conditions of the agricultural trailers on the field is very dependent to cost feasibility and therefore, braking effectiveness results can aid decision makers.

Acknowledgment

This proceeding was prepared from Master Thesis of Hakan AYKAN in Selcuk University, Institute of Sciences, Agricultural Machinery Department. Authors would like to acknowledge help of Dr. Eyub CANLI on the language of the proceeding.

References

[1] D. L. Hard, J. R. Myers and S. G. Gerberich, "Traumatic injuries in agriculture," *Journal of Agricultural Safety and Health*, vol. 8 (1), pp. 51-65, 2002.

[2] D. Trichopoulos, E. Petridou, T. Spyridopoulos and D. M. Alexe, "The magnitude and spectrum of farm injuries in the European Union countries," *European Union Health Safety Committee (HSC) Final Report*, Athens, Greece, 2004.

[3] A. Mukherjee and C. Ping, "Agricultural machinery safety–a perpetual theme of human society," *Global Agricultural Safety Forum*, Rome, Italy, pp. 1-11, 2008.

[4] A. Alçayır, "Konya ili Çumra ilçesi tarım işletmelerinde meydana gelen traktör ve tarım makineleri kaynaklı iş kazalarının belirlenmesi," MSc Thesis, Dept. Agri. Mach. and Tech. Eng. Selçuk Üniv., Konya, 2018.

[5] A. Peker and A. Özkan, "1973-1993 Yılları arasında Karaman yöresinde meydana gelen traktör ve tarım iş makineleri kazalarının değerlendirilmesi," 1994 *Tarımsal Mekanizasyon 15. Ulusal Kongresi Bildiri Kitabı*, pp. 475-484.

[6] F. Demir and K. Çarman, "Yerli yapım çift dingilli tarım arabalarının statik durumda frenleme etkinliğinin saptanması," *Selçuk Üniversitesi Ziraat Fakültesi Dergisi*, vol. 10 (12), pp. 106-113, 1996.

[7] M. N. Örnek and F. Demir, "İki dingilli tarım arabasının statik ve dinamik durumda frenleme etkinliğinin belirlenmesi," *Selcuk Journal of Agriculture and Food Sciences*, vol. 25 (3), pp. 104-109, 2011.

[8] M. N. Örnek, "Konya'da imal edilen iki dingilli tarım arabasının traktörle kombinasyonunda frenleme etkinliğinin belirlenmesi," MSc Thesis, Dept. Agri. Mach. and Tech. Eng. Selçuk Üniv., Konya, 1996.

[9] M. Nastasoiu and N. Ispas, "Comparative analysis into the tractor-trailer braking dynamics: tractor with single axle brakes, tractor with all wheel brakes," *Central European Journal of Engineering*, vol. 4 (2), pp. 142-147, 2014.

Effect of Adhesive Failure Geometry on Stress Behavior for Single Lap Joints

A. SAYLIK[1] and M.O. KAMAN[2]

[1] Mus Alparslan University, Mus/Turkey, a.saylik@alparslan.edu.tr
[2]Firat University, Elazig/Turkey, mkaman@firat.edu.tr

***Abstract* - In this study, the effect of adhesion damage geometry on the joint strength due to the lack of adhesive material in single-lap joints of fiber reinforced composite plates is numerically investigated. This damage in the adhesion zone is modeled as an adhesive volume void at the edge of the sheet. To define this region, a positive damage angle and starting point are defined relative to the direction of the fiber. While the left side of the joint is fixedly supported, the right side is subjected to equal displacement. Analyzes were made with *ANSYS APDL* using the finite element method. The effect of the variation of the damage angle and damage length at the overlap edge on the stress distribution under tensile load is presented with graphics. Increasing the damage angle by 35° increases the *von Mises* stresses by 52%.**

***Keywords* - Single lap joints, fiber reinforced composites, adhesive, finite element method, adhesive failure.**

I. INTRODUCTION

Today, structural adhesives; It is used in the assembly of parts in the aerospace, automotive and ship building industries. The fact that the plate mounting parts used in these application areas have planar surfaces allows the plates to be joined as single or double overlap using adhesive. The use of adhesives in the assembly of planar surfaces in industry provides significant advantages. Adhesive bonded composite structures are frequently preferred in industrial designs due to their easy manufacturability, light assembly weight, and low stress concentration, smoothness of load transmission, high fatigue and damage performances [1]. Machine elements such as bolts and rivets, which are used in the mechanical joining of heavy-duty materials, cause the weight of these structures to increase. Contrary to traditional joining methods such as bolts, rivets and welding, if adhesives are preferred, stress concentration is prevented due to the absence of holes and notches in the joint, and on the other hand, the strength/weight ratio can increase significantly. This provides a great advantage to the structure. For example, the 0.453 kg weight reduction to be achieved by choosing lightweight joints in the aviation industry means 1360 kg of fuel savings per year [2]. Structural damage sometimes occurs in adhesive joints, which are often preferred due to such advantages. General damages; *i*-damage in the composite layer, *ii*-damage in the adhesive, *iii*-interface damage between the composite layer and the adhesive.

Understanding and evaluating the damage that may occur in the structure in industrial application areas is very important for the life of the structures. Therefore, many numerical and experimental studies have been carried out for the types of damage to occur in composite structures. The effect of lap length in single-lap adhesive joints was compared experimentally and numerically by Ye et al. [3]. Al-Ramahi et al. [4] performed finite element analysis in order to reveal the understanding of stresses in the adhesive and the geometric parameters that determine the performance of the joint in single-lap adhesive joints. The thickness of the adhesive layer has no significant effect on the maximum load achieved, but greatly influences the tensile response at the attachment points [5]. A study was carried out to increase the strength of the joint by opening the adhesive notch in the single-lap adhesive joint by Bahrami et al. [6]. It has been found that the use of the adhesion notch can significantly increase the load bearing capacity of the joint. For example, a simple notch with a notch depth ratio of 20% increased the load carrying capacity by approximately 60%. The effect of layers on the damage mechanism of composites joined with a single-lap adhesive was investigated. It has been determined that the increase in adhesive stiffness and flexural strength delays the initiation of damage at the joint [7]. Experimental and numerical study was carried out to investigate the tensile performance of carbon fiber reinforced polymers bonded unilaterally with adhesive by Su [8]. Zhao et al. [9] aimed to develop two-dimensional material models for single lap joints with the finite element method. To validate the validity of the new material model, the shear and peel stress distribution in the middle of the adhesive layer obtained from the two-dimensional finite element analysis was compared with the *Tsai* and *Morton* results. When the damage analysis made for single-lap joints with adhesion notches is examined; it was determined that the improvement in the damage load from the notch was dependent on both the notch depth and the mechanical properties of the adhesive material [10]. In many studies examining the adhesive thickness change; it has been shown that increasing the adhesive thickness greatly reduces the strength of the joint [11-15].

In single-lap joint structures, the mechanical properties of the adhesive significantly affect the bond strength. During the joint, some irregularities due to manufacturing errors may occur in the bonding area. The most important and common of these is that the adhesive cannot spread homogeneously to the adhesion area and as a result, it cannot cover the adhesion surface. In this case, air gaps may appear in the adhesive area and these gaps may not be visible to the naked eye from the outer surface. In addition, even if the bonding process is done properly, bonding damage may occur on the overlap edges of the construction under load over time. This will also affect the bond strength. It is very important to know how this type of adhesion damage in the structure affects the stresses in the structure. In this study; unlike the studies in the literature, the effect of the change of

the geometry of the adhesive gap in the adhesive region on the stress behavior of the structure in single-lap joints was investigated numerically. The maximum *von Mises* stresses that will occur in the joint according to the changing gap geometry parameters were found by the finite element method and the obtained results were compared with each other.

II. MATERIAL AND METHOD

A. Problem Definition

The model created for the single-lap joint is shown in Figure 1. The bonded plates were selected as unidirectional carbon fiber reinforced composite material and the material properties are given in Table 1. The mechanical behavior of the composite material was chosen as linear elastic in the analyses. In addition, the fiber angles in the 150x40 mm composite plate are parallel to the $-x$ axis and are 0º. The mechanical properties of the adhesive material are presented in Table 2. As with the composite plate, the mechanical properties of the adhesive material are linear elastic. The total thickness of the adhesive layer is 0.2 mm. Damage zone geometry was defined at the overlap edge along the length n. According to Figure 1, overlap edge damage in the xz plane is shown in yellow. The blue area is the undamaged adhesive zone. The thickness of the damage gaps created is 0.1 mm. The gap damages in the xy plane are triangular. In order to generate the damages in the numerical model, the lap edge damage volume,

$$V_{damaged} = \frac{t}{2} n^2 \, tan\,(\alpha) = 0.05\, n^2 \, tan\,(\alpha) \quad (1)$$

subtracted from the total adhesive volume. Here t is the adhesive thickness. Therefore, the damaged areas are actually voids, as in the real damaged model. It is the angle α that defines the geometry of the edge void damage in the study. Analyzes were made for angle values 10º, 15º, 30º and 45º. The edge lengths are taken as n = 5, 10, 15, 20, 25 and 30 mm.

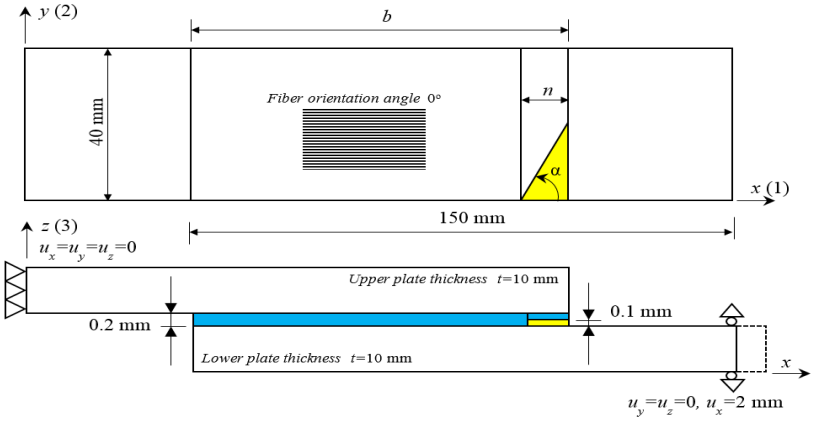

Figure 1: Problem dimensions.

B. Stress Analysis

ANSYS Mechanical program and *APDL* (Parametric Design Language) codes was used as the finite element analysis program. The left side of the joint is fixed ($u_x = u_y = u_z = 0$). It is given a total displacement of $u_x = 2$ mm along the longitudinal $-x$ axis ($u_y = u_z = 0$, $u_x = 2$ mm) to the edge nodes of the right-side surface. Thus, it is provided real application conditions in the numerical model. Linear elastic analysis was performed according to the material mechanical properties given in Tables 1 and 2.

Table 1. Mechanical properties of the unidirectional composite plate. (x −direction; y and z are the transverse and through-thickness directions, respectively)

Property	Value	Unit
Longitudinal elastic modulus (E_x)	100	GPa
Transverse elastic modulus (E_y)	50	GPa
Transverse elastic modulus (E_z)	50	GPa
Longitudinal (axial) shear modulus (G_{xy})	5.30	GPa
Longitudinal (axial) shear modulus (G_{xz})	5.26	GPa
Transverse shear modulus (G_{yz})	4.12	GPa
Major Poisson's ratio (v_{xy})	0.32	-
Transverse Poisson's ratio (v_{xz})	0.21	-
Transverse Poisson's ratio (v_{yz})	0.21	-

Table 2. Mechanical properties of the brittle adhesive.

Property	Value	Unit
Elastic modulus ($E_{adhesive}$)	60	GPa
Poisson's ratio ($v_{adhesive}$)	0.32	-

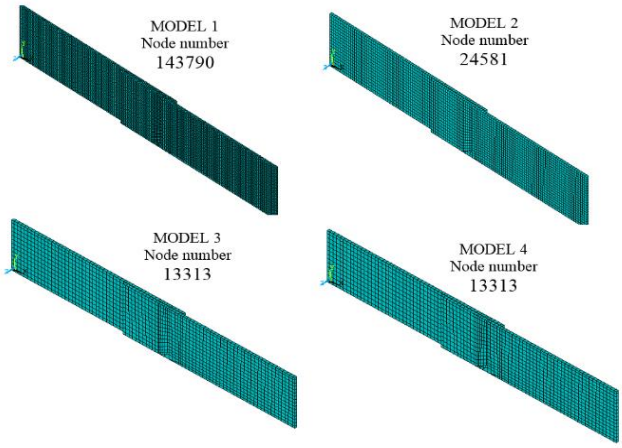

Figure 2: Finite element models generated for different node numbers.

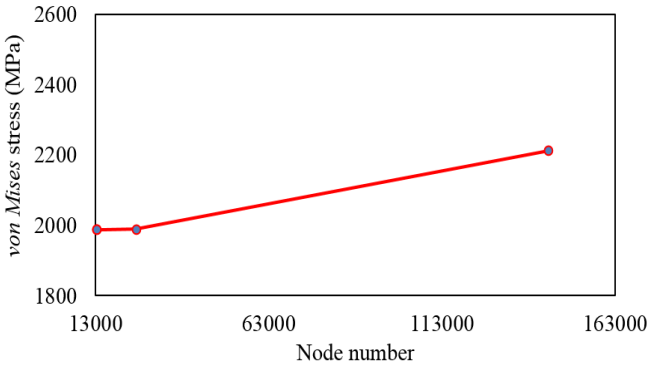

Figure 3: Variation of *von Mises* stresses with the node numbers.

Tetrahedral element *Solid186* is used in composite model mesh, and triangular element type is used in the adhesive region because it is quite small compared to the plate thickness. Before proceeding to the numerical solution, finite element mesh optimization was performed in order to determine the ideal number of elements and nodes. Different finite element models created to obtain the optimum number of nodes are shown in Figure 3. According to these analyzes, the optimum number of elements was determined as 2171 and the number of nodes as 13313 (Model 3, Figure 2).

As a result of the analysis, the maximum von Mises stresses obtained in the adhesive region were read and recorded in tables. The detail pictures of the adhesive volume and adhesion region in the three-dimensional finite element model used for analysis are given in Figure 4. The adhesive gap formed in the shape of a triangle was subtracted from the total adhesive volume with a thickness of 0.1 mm.

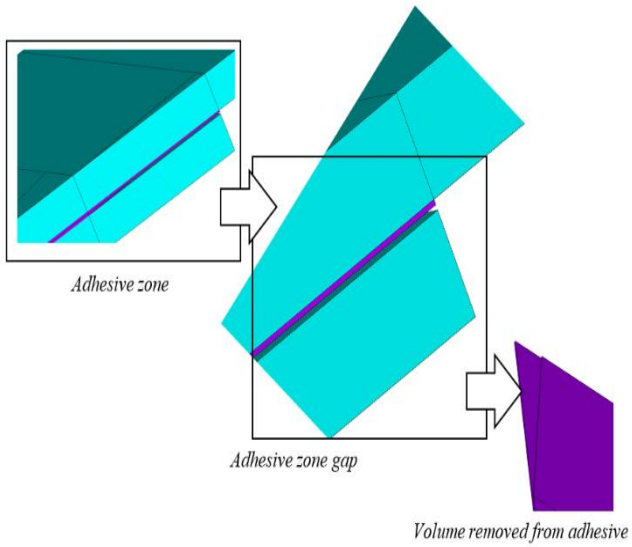

Figure 4: Detail pictures of adhesion zone and adhesive volume.

III. RESULT AND DISCUSSION

As shown in Figure 5, the effect of the variation of the plate overlap length on the maximum von Mises stress values was investigated. İt was concluded that the stress value increased as the value of the overlapping length of the bonded area of the plates increased. The maximum *von Mises* stress values were read over the adhesive volume. This increase is linear. For b =50 mm the stress is 1047 MPa, for b =60 mm it is 1185 MPa. Thus, for a 50% overlap length increase, a 13% increase in stress was obtained. The effect of the change of the α angle, which defines the geometry of the edge gap damage, on the *von Mises* stress value is examined in Figure 6.

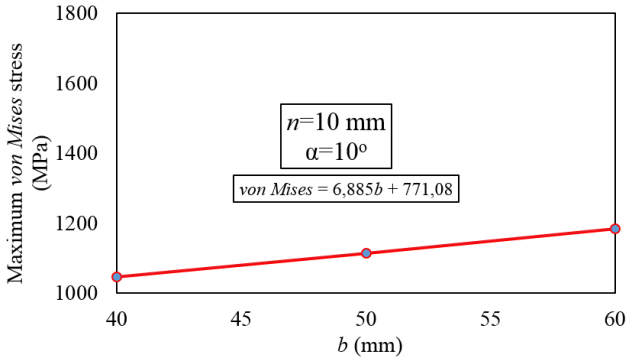

Figure 5: Variation of overlap length with maximum *von Mises* stress.

It can be seen that the stress values generally increase with the increase of α angle. In angle changes; it has been determined that the most stresses are in the angle change between 10° and 20° and increase up to 275 MPa. It was observed that the angle values with the least stress change were between 20° and 30°, and the stress change increased up to 10 MPa. It was determined that when the angle value is increased from 10° to 45°, the increase in stress is 52.4%. It is concluded that the damage will progress along the plate width depending on the increase in the angle. It has been shown that an adhesive damage that exists across the width of the plate rather than the central gap has much lower ultimate strength [16].

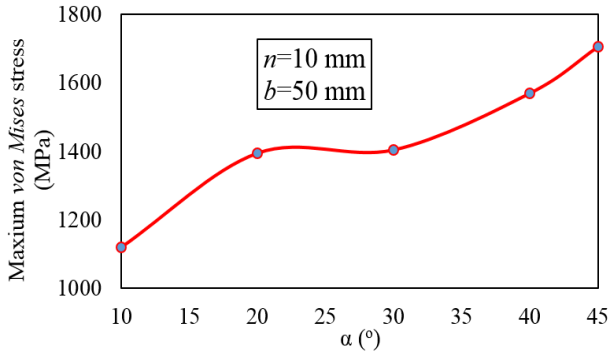

Figure 6: The effect of geometric damage angle α change on *von Mises* stress value.

The maximum *von Mises* stress values occurring in the model according to the length variation of the adhesion damage zone geometry defined at the overlap edge (along the n length) are presented in Figure 7. The stresses in the geometry created by keeping constant $\alpha = 10^o$, $b = 50$ mm and changing the n values were investigated. It was observed that the *von Mises* stress value increased between $n = 5$ mm and $n = 15$ mm values, while the values did not change between $n = 15$ mm and $n = 30$ mm and remained approximately constant. A similar study showed that in the case of high-strength steel bonding, an almost linear decrease in joint strength was observed as the defect size increased [17]. Ribeiro et al. [18] explained that the joints bonded with the adhesive have a brittle failure as soon as the limiting adhesive stresses are reached at the overlap ends. Thus, the presence of a defect centered in the adhesive layer is not so preponderant for the joints' strength.

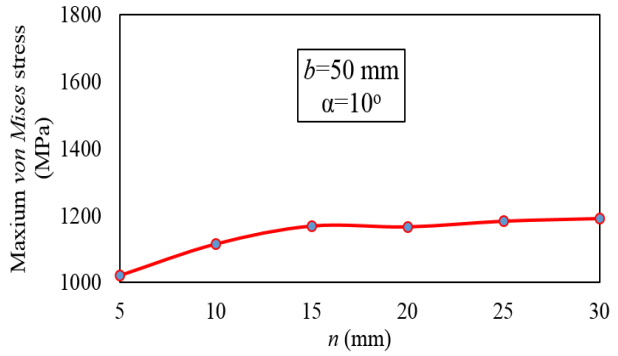

Figure 7: Variation of maximum *von Mises* stress value with n.

IV. Conclusion

In this study, the effect of changing the geometry of the adhesion damage zone defined at the overlap edge and at a certain angle on the stress behavior was investigated using the 3D finite element method. The obtained results can be briefly summarized as follows;

• Increasing the overlap length increased the stresses by 13%. The increase in lap length is related to the adhesive gap volume at the plate edge. As a result of the increase in the total volume of the adhesive with the overlap length, the damage geometry creates a crack effect, causing an increase in stress concentrations.

• The increase in the damage angle increased the stresses by 52.4%. Since the increase in the angle increased the void volume, it caused the adhesion surface to decrease along the edge.

• Increasing the damage length at constant angle is effective for $n < 15$ mm, but has no effect on adhesive stress at larger values. Depending on the increase in length, the damage on the edge moves away from the notch shape. Therefore, the increase in stresses does not change with the increase in length.

• Designers should pay particular attention to adhesive gap damage in adhesive joints. Especially long gap damages that may occur along the thickness of the plate increase the stress values in the adhesive. The progression of triangular notch-shaped spaces along the length, parallel to the loading direction, instead of the width, affects the stresses less.

References

[1] L. Kirkayak, "The effects of adhesive geometry on the stress distribution in bonded joints", *Pamukkale University Journal of Engineering Sciences*, 25(1), pp. 27-33, 2019.

[2] Oz, O., Ozer, H. 2016. "The effects of the hybrid adhesive-order on strength of the adhesively-bonded joint", *Muhendis ve Makina*, vol. 57, pp. 63-72, 2016.

[3] J. Ye, Y. Yana, J. Lia, Y. Honga and Z. Tiana, "3D explicit finite element analysis of tensile failure behavior in adhesive bonded composite single-lap joints", *Composite Structures*, vol. 201, pp. 261–275, 2018.

[4] N. J. Al-Ramahia, R. Joffea and J. Varna, "Investigation of end and edge effects on results of numerical simulation of single lap adhesive joint with non-linear materials", *International Journal of Adhesion and Adhesives*, vol. 87, pp. 191–204, 2018.

[5] M. Demiral and F. Kadioglu, "Failure behaviour of the adhesive layer and angle ply composite adherends in single lap joints: A numerical study", *International Journal of Adhesion and Adhesives*, vol. 87, pp. 181-190, 2018.

[6] B. Bahramia, M.R. Ayatollahia, M.J. Beigrezaee and L.F.M. da Silva, "Strength improvement in single lap adhesive joints by notching the adherends", *International Journal of Adhesion and Adhesives*, vol. 95, pp, 2019.

[7] J. Kupski, S. Teixeira de Freitas, D. Zarouchas, P.P. Camanhob and R. Benedictus, "Composite layup effect on the failure mechanism of single lap bonded joints", *Composite Structures*, vol. 217, pp. 14-26, 2019.

[8] L. Sun, C. Li, Y. Tie, Y. Hou and Y. Duan, "Experimental and numerical investigations of adhesively bonded CFRP single-lap joints subjected to tensile loads", *International Journal of Adhesion and Adhesives*, vol. 95, pp, 2019.

[9] L. Zhao, Y. Wang, T. Qın and J. Zhang, "A new material model for 2D FE analysis of adhesively bonded composite Joints", *Materials Science (Medziagotyra)*, vol. 20, 2014.

[10] B. Bahramia, M.R. Ayatollahia, B. Bahrami and L.F.M. da Silva, "Failure load analysis in single lap joints - effect of adherend notching", *Engineering Failure Analysis*, vol. 104, pp.75-83, 2019.

[11] R. Kahraman, M. Sunar and B.Yilbas, "Influence of adhesive thickness and filler content on the mechanical performance of aluminum single-lap joints bonded with aluminum powder filled epoxy adhesive", *Journal of Materials Processing Technology*, vol. 205, pp. 183-1889, 2008.

[12] L. F. M. da Silva , T. N. S. S. Rodrigues , M. A. V. Figueiredo, M. F. S. F. de Moura and J. A. G. Chousal, "Effect of Adhesive Type and thickness on the lap shear strength", *The Journal of Adhesion*, vol.82, pp.1091-1115, 2006.

[13] W. Xu and Y. Wei, "Influence of adhesive thickness on local interface fracture and overall strength of metallic adhesive bonding structures", *International Journal of Adhesion &Adhesives*, vol. 40, pp.158-167, 2013.

[14] L. F. M. da Silva , G.W. Critchlow and M. A. V. Figueiredo, "Parametric Study of Adhesively Bonded Single Lap Joints by the Taguchi Method", *Journal of Adhesion Science and Technology*, vol. 22, pp. 1477-1494, 2008.

[15] M. Lee , E. Yeo, M.Blacklock , M. Janardhana, S. Feih and C. H.Wang, "Predicting the strength of adhesively bonded joints of variable thickness using a cohesive element approach", *International Journal of Adhesion & Adhesives*, vol. 58, pp. 44-52, 2015.

[16] H.Y.Nezhad, D. Stratakis, D. Ayre, S. Addepalli and Y. Zhao, "Mechanical performance of composite bonded joints in the presence of localised process-induced zero-thickness defects", *Procedia Manufacturing*, vol. 16, pp. 91-98, 2018.

[17] E.F. Karachalios, R.D. Adams and Lucas F.M. da Silva, "Strength of single lap joints with artificial defects", *International Journal of Adhesion & Adhesives*, vol. 45, pp.69-76, 2013.

[18] F.M.F. Ribeiro, R.D.S.G. Campilho, R.J.C. Carbas and L.F.M. da Silva, "Strength and damage growth in composite bonded joints with defects", *Composites Part B*, vol. 100, pp. 91-100, 2016.

Digital Twin and Application of BTX Fractionation Section

O. KUTLU[1]

[1] Ege University, Solar Energy Institute, Izmir/Turkey, ozben.kutlu@ege.edu.tr

Abstract **- Virtual models of physical objects are created in a digital way to simulate their behaviors in real-world environments. Digital twins are software representations of assets and processes that are used to understand, predict, and optimize performance in order to achieve improved a process or systems. Digital twinning also known as using a digital copy of the physical system to perform real-time optimization.**

While real-time data is collected by sensors, that is transferred to be processed through mathematical models in process design. In recent years, the long downtime is unwanted situation for testing novel approach or uncovering the potential problems, especially in complex processes. Furthermore, the energy efficiency is of importance in terms of significantly decrease in the annual operating cost. Therefore, digital duplicates help to analyze, retrofit, or optimize these types of processes.

In this study, the flow diagram of the Benzene, Toluene, Xylene (BTX) fractionation section at aromatics process with real data was simulated in a comprehensive process simulation package. The effect of some parameters on the process performed at 60 ton/h feed capacity was investigated by sensitivity analysis and the digital twin infrastructure closest to the real data was obtained for adapting to other process steps.

Keywords **- Digital Twin, Industry 4.0, Modeling, Simulation, BTX Fractionation, Aromatics.**

I. INTRODUCTION

The digital twin (DT) is a method of Industry 4.0. From healthcare to the defense industry, the application of digital twins is spreading. AIAA Digital Engineering Integration (DEIC) Committee have essentially defined the digital twin as ‘‘a digital informational construct of a physical system as an entity on its own". Nowadays, the related ISO standard (ISO 23247-1:2021) has been published, and it has specified the requirements of digital twin framework. A digital twin replicates a physical product, process or service with the help of various IoT devices, matching the virtual and real worlds [1]. Even though the DT is not a new concept, the related studies as an innovative approach have increased rapidly after Internet of Things devices became widespread and cost-effective. But DTs should not be confused with digitization. The DT does not replace a physical item or process with a digital one to make it more accessible, efficient or secure. It creates a precise copy of the real item or process, creating a tool to test and monitor without needing to access it.

Velocity, resolution, and learning are three key factors of DT [2]. Internet of Things (IoT) devices creates the velocity, i.e. it can easily transfer collected immense volumes of data to a digital twin in almost real time. Resolution includes digital information that helps us get a close look at the finest details of physical process. In addition to these, machine learning algorithms can analyze gathered data and make predictions, refining the digital twin based on gathered information and calibrating the general model and its details.

A digital twin is a virtual representation of an object or system that spans its lifecycle, is updated from real-time data, and uses simulation, machine learning and reasoning to help decision-making [3]. Digital models are used both in simulations and digital twins to replicate a system’s various processes. The difference between digital twin and simulation is mostly a matter of scale. While a simulation typically studies one certain process, a digital twin can investigate multiple processes by running any number of significant simulations. Thereby, digital twins can study more issues far in broad perspective than standard simulations can to improve products and processes.

By analyzing DT studies, an increasing trend in last years could be observed even if the total number is not so high [4]. Due to the diffusion of Industry 4.0 paradigm, this phenomenon is clearly noticeable in the manufacturing sector (59%), where physical processes are integrating effectively with digital ones. Other interesting sector (12%) is the mobility systems that regard the safety of autonomous vehicles as well as self-driving cars [5].

The importance is highlighted that reconfiguration of DT is certainly a crucial supportive mechanism [6]. Zhang et al. [7] presents a five-dimensional DT modeling approach for manufacturing systems, which can some of the capabilities and dependencies of the DTs can be derived. After a reconfigurable strategy is proposed based on the expandable model structure and the reserved interfaces of objective functions and optimization algorithms, a prototype system is developed to demonstrate its performance.

Shao and Helu [8] highlight that there are several potential ways a product, process or system digital twin can be used at all production levels. Three examples of them have been stated below:

- Minimizing the impact of equipment downtime
- Optimizing production planning and scheduling
- Enabling virtual commissioning

As seen in Figure 1, while the process, parameter or equipment to be transferred to virtual environment changes depending on the selected purpose, the common point of all

three DTs is modeling, simulation, and analysis.

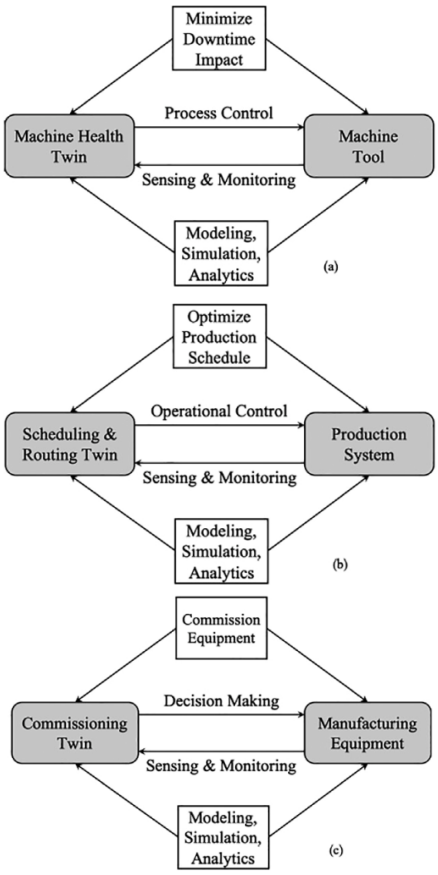

Figure 1: Three examples of the use of digital twins in manufacturing (adapted from Shou and Helu [8])

Considering a production plant, a comprehensive approach to the digital twin can improve process and control-system engineering from the earliest stages of project design. Virtualizing the commissioning steps can simplify factory acceptance testing, making the process more efficient and taking it off the critical path, eventually helping ensure projects stay on schedule [9]. Up to now, traditional simulation is used only during development and virtual commissioning of production systems, with the introduction of the DT, the use of simulation has gained prominence and have used for making decision support, system optimization and foresight of maintenance [10]. In this study, a chemical process simulation, that is the initial step of DT applications, was carried out due to the limited number of studies in the manufacturing sector. BTX fractionation section in an aromatics production process was chosen as the chemical process. By performing sensitivity analysis, the digital twin infrastructure closest to the real-time data was obtained.

II. Modelling of Process

In general, the selection of the appropriate components for accuracy of DT plays a critical role. For the simulation, the flowsheet of the fractionation section represents to the actual aromatic production facility. Appropriate changes and assumptions were made in the process, considering the privacy policy of the facility, in a way that would not distort the results. In the modeling of fractionation section has eight units which are Benzene and Toluene columns, one mixer, two condensers, two pressure regulators and cooler (Figure 2).

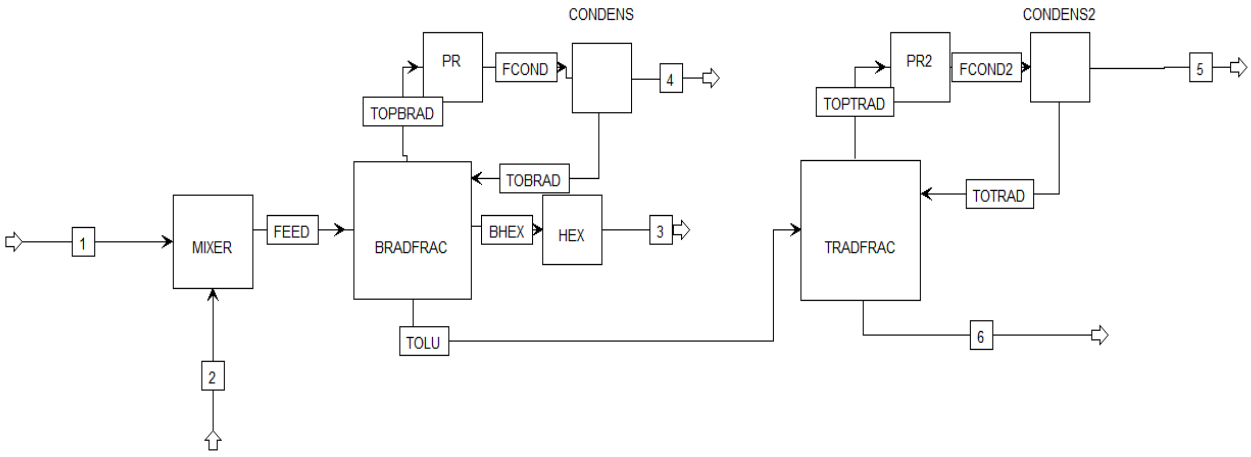

Figure 2: Block diagram of BTX fractionation section

As shown in Figure 2, two streams with high benzene and toluene concentrations coming from two different parts of the facility are first mixed in the mixer unit and the feed stream is prepared. By giving it to the benzene column, which is one of the two main columns of the fractionation section, the benzene is primarily separated. Pure benzene in the vapor phase is taken from the fifth tray of the column, condensed in the heat exchanger and sent to the storage tank. The bottom stream of the benzene column enters the toluene column, and from this second important column, it is aimed to separate the toluene from xylene. While xylene is taken from the bottom stream of the column, toluene is drawn from the upper stream, condensed in the condenser unit of the column at a certain rate, and sent to the storage tank.

The cascaded units are simulated in Aspen Plus V12 software package. The sequential simulation is performed on the boundary of each unit. RK-SOAVE property method as the most suitable model for petrochemical applications is chosen [11]. As a rigorous distillation model, Petrofrac Stripper model was selected, and the necessary auxiliary equipment (such as pressure regulator, separator) was added to the design. For some of components most fitted components were chosen from ASPEN database depending on their boiling points and molecular weights.

After the simulation of process, the effect of reflux ratio and feed temperature on benzene composition is investigated by sensitivity analysis to assess more effective operating conditions. The variable feed temperatures (Table 1) at two reflux ratios were set to assess the desired benzene efficiency.

Table 1: The different feed temperature set selected for sensitivity analysis

Feed Temperature	
Stream 1 (°C)	**Stream 2 (°C)**
64.4	70
84.4	90
104.4	110
124.4	130
150.0	160

III. Results and Discussion

The simulation of the flow diagram has been drawn in Figure 3. The simulation could also be designed with Radfrac distillation model being compact model. Because it needs less data, unfortunately sufficient sensitivity of model cannot be obtained for the digital twin by using this model. Although the flowsheet with Stripper column model was more complicated, the results were considerable similar to real-time data.

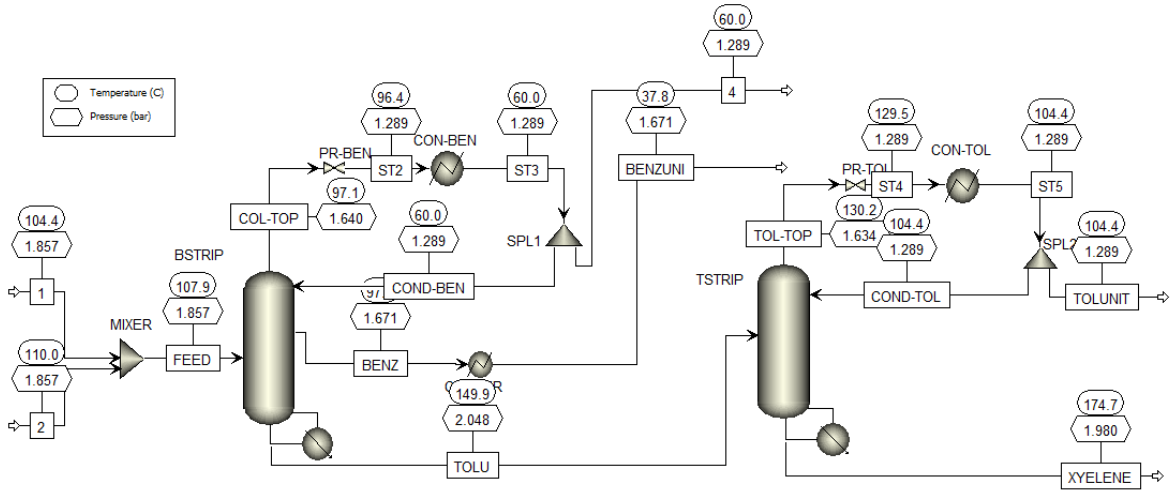

Figure 3: The simulation model of BTX fractionation section flowsheet

Table 2: Stream Data of Model Results

Stream ID		1	2	4	BENZ	BENZUNI	COL-TOP	COND-BEN	COND-TOL	FEED	ST2
Temperature	C	104.4	110.0	60.0	97.8	37.8	97.1	60.0	104.4	107.9	96.4
Pressure	bar	1.857	1.857	1.289	1.671	1.671	1.640	1.289	1.289	1.857	1.289
Vapor Frac		0.000	0.000	0.000	1.000	0.000	1.000	0.000	0.000	0.000	1.000
Mole Flow	kmol/hr	264.694	376.958	9.979	199.812	199.812	838.998	829.019	518.234	641.652	838.998
Mass Flow	kg/hr	21983.652	37268.118	779.558	15608.395	15608.395	65542.392	64762.833	47766.785	59251.771	65542.392
Volume Flow	cum/hr	27.988	47.360	0.932	3536.375	18.167	15109.084	77.468	60.702	75.440	19363.344
Enthalpy	Gcal/hr	3.006	1.156	0.128	4.261	2.429	17.852	10.628	3.070	4.162	17.852
Mole Flow	kmol/hr										
BENZE-01		174.878	34.845	9.969	199.754	199.754	838.138	828.169	< 0.001	209.723	838.138
TOLUE-01		86.722	184.930	trace	< 0.001	< 0.001	< 0.001	< 0.001	517.482	271.652	< 0.001
O-XYL-01		2.517	104.735	trace	trace	trace	trace	trace	< 0.001	107.252	trace
ISOPR-01			46.266	trace	trace	trace	trace	trace	trace	46.266	trace
1-MET-01			6.114	trace	trace	trace	trace	trace	trace	6.114	trace
METHY-01			0.068	0.010	0.058	0.058	0.860	0.850	trace	0.068	0.860
N-OCT-01		0.354		trace	trace	trace	trace	trace	0.674	0.354	trace
N-PRO-01		0.223		trace	trace	trace	trace	trace	0.077	0.223	trace

Stream ID		ST3	ST4	ST5	TOL-TOP	TOLU	TOLUNIT	XYELENE
Temperature	C	60.0	129.5	104.4	130.2	149.9	104.4	174.7
Pressure	bar	1.289	1.289	1.289	1.634	2.048	1.289	1.980
Vapor Frac		0.000	1.000	0.000	1.000	0.000	0.000	0.000
Mole Flow	kmol/hr	838.998	790.263	790.263	790.263	431.861	272.029	159.832
Mass Flow	kg/hr	65542.392	72840.305	72840.305	72840.305	42863.818	25073.520	17790.298
Volume Flow	cum/hr	78.401	19776.512	92.565	15462.490	57.542	31.863	24.339
Enthalpy	Gcal/hr	10.756	11.782	4.681	11.782	2.017	1.611	0.078
Mole Flow	kmol/hr							
BENZE-01		838.138	0.001	0.001	0.001	< 0.001	< 0.001	trace
TOLUE-01		< 0.001	789.117	789.117	789.117	271.652	271.634	0.017
O-XYL-01		trace	0.001	0.001	0.001	107.252	< 0.001	107.252
ISOPR-01		trace	trace	trace	trace	46.266	trace	46.266
1-MET-01		trace	trace	trace	trace	6.114	trace	6.114
METHY-01		0.860	trace	trace	trace	trace	trace	trace
N-OCT-01		trace	1.028	1.028	1.028	0.354	0.354	< 0.001
N-PRO-01		trace	0.117	0.117	0.117	0.223	0.040	0.183

The stream results of the simulation are given in Table 2. While the desired benzene and toluene streams are obtained in one-to-one real-time data, it is determined that the concentrations of other impurities in the stream varied. For example, whereas the paraffin impurity in toluene streams should be 0.023 kmol per hour in real-time data, it is able to simulate as 0.04 kmol per hour by this model. Although a deviation of 74% was calculated, this deviation was not considered since there was no significant stream that would affect the total mass flow.

Certain temperatures through distillation column should be captured to achieve the desired separation. Benzene, Toluene and Xylene are known to have different boiling points. For this reason, the main purpose in the Benzene column is to obtain Benzene as the top product and Toluene and Xylene as the bottom product. To obtain pure products, suitable temperature profiles as desired and appropriate separation have been observed (Figure 4).

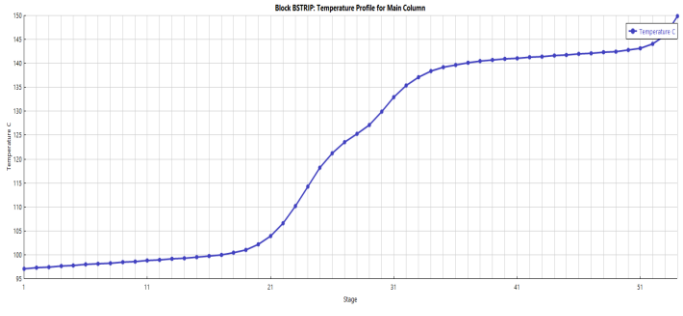

(a)

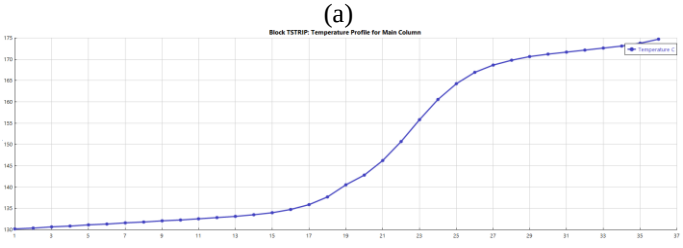

(b)

Figure 4: Temperature profile in benzene (a) and toluene (b) column

The effect of reflux ratio and feed temperature on benzene composition is investigated by sensitivity analysis to assess more effective operating conditions. The reflux ratio of benzene column at the actual process is at 3.9. By using sensitivity analysis, it was investigated whether reflux ratio can be decreased. When benzene mass purity in main stream, i.e the outflow from column, is %99.95, the reflux ratio is decreased to 2,13. Although the loss of benzene by the bottom stream is increased to 0.013 kmol per h, it is still between acceptable levels.

On the other hand, the actual reflux ratio of Toluen column is found as 1.9. Whereas the loss of Toluene with Xylene stream is 0.164 kmol per h, it is not significant amount and can be neglected. In case Toluene mass purity in Toluene stream is %99.8, the reflux ratio is increased to 3.06, and the loss of toluene with Xylene stream is decreased to 0.064 kmol per h. However, high reflux ratio is not preferred due to affect the column design and the recycled Toluene composition by adjusting reflux ratio is also the negligible level. For that reason, it can be said that the actual operating reflux ratio is suitable for toluene column.

Other important parameter in the distillation is the temperature of column that effect the mole flow of desired product in both Benzene and Toluene Columns. The feed temperature affects the degree of separation on fractionation column.

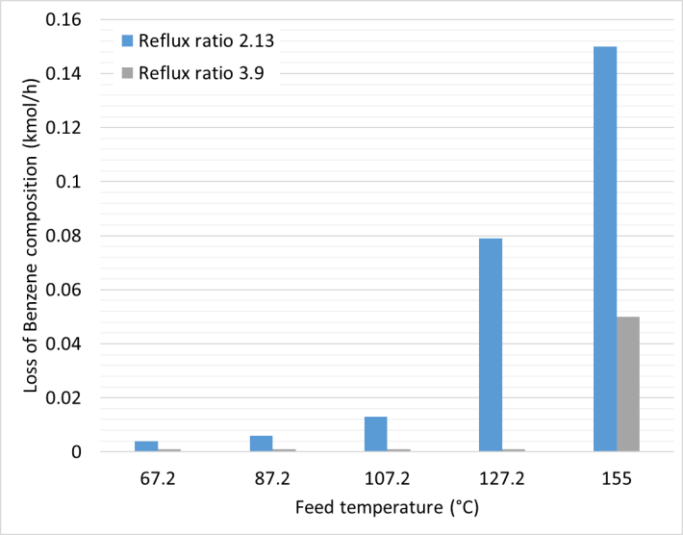

Figure 5: The distribution of benzene concentration in bottom stream by variable average feed temperatures and reflux ratios

Technically, high reflux ratio is known to be good for getting pure product. In this assessment, the high reflux ratio also allows to get more pure benzene stream, so causes less loss of benzene (Figure 5). At the average temperature assessment, it is observed that low temperature is suitable for high benzene concentration. Considering the temperature profile through the column, it is fluctuated by the increase in feed temperature (127.2 and 155°C) and the separation efficiency is decreased. In this study, the optimum conditions are obtained at low feed temperature with high reflux ratio. As seen in Figure 4, the optimum condition for benzene column is found at feed temperature of 67.2 ℃ with reflux ratio of 3.9. At this point, it has been determined that real-time reflux rates are the most suitable parameters for the BTX fractionation section, and the decrease in feed temperature can provide efficient production without significantly affecting the separation process.

IV. Conclusion

In this study, main purpose was to virtualize a chemical process by real-time data in order to create digital twin of it. BTX fractionation section in an aromatics production process was chosen as the chemical process. By performing sensitivity analysis, the digital twin infrastructure closest to the real-time data was obtained. It was determined that the feed temperature of Benzene column could be decreases 67.2 °C without significantly affecting the separation process. With the introduction of the ISO 23247-1:2021 standard, the general perspective of the manufacturers on the digital twin concept has changed. In aromatics production having importance in the world, innovative changes will always continuous, and digital twin of process will be predicted to widespread day by day.

References

[1] Q. Qi, and F. Tao, Digital Twin and Big Data Towards Smart Manufacturing and Industry 4.0: 360 Degree Comparison, *IEEE Access*, Vol 6, 2018, 3585 - 3593

[2] O. Martynova, Digital Twin Technology: A Guide for Innovative Technology, 2020, [Online] Available: https://intellias.com/digital-twin-technology-guide/

[3] Anon, What is Digital Twin? 2021, [Online] Available: https://www.ibm.com/topics/what-is-a-digital-twin

[4] Cimini, C., Pirola, F., Pinto, R., & Cavalieri, S. (2020). A human-in-the-loop manufacturing control architecture for the next generation of production systems. *Journal of Manufacturing Systems*, 54, 258–271.

[5] G. P. Agnusdei, V. Elia and M. G. Gnoni, "A classification proposal of digital twin applications in the safety domain" *Computers & Industrial Engineering* 154, 2021, 107137

[6] Datta S P A. Emergence of digital twins, *MIT Auto-ID Labs, Massachusetts Institute of Technology*, 2016 [Online] Available: https://dspace.mit.edu/handle/1721.1/104429

[7] C. Zhang, W. Xu, J. Liu, Z. Liu, Z. Zhou, D. T. Pham, A Reconfigurable Modeling Approach for Digital Twin-based Manufacturing System, *Procedia CIRP* 83, 2019, 118–125.

[8] G. Shou and M. Helu, Framework for a digital twin in manufacturing: Scope and requirements, *Manufacturing Letters* 24, 2020, 105–107

[9] M. Berutti, Defining Digital Twin Seven Essential Steps, *The Institution of Civil Engineers (ICE)*, 2019, United Kingdom

[10] T. Jung, P. Shah, M. Weyrich, Dynamic Co-Simulation of Internet-of-Things-Components using a Multi-Agent-System, *Procedia CIRP* 72, 2018, 874–879

[11] Aspen Physical Property System, 2013, USA

Investigation of Torsional Performance of Carbon Fiber Composite Driveshaft with Different Stacking Sequence and Fiber Orientation

M.S. OKUTAN[1] and K. GENEL[1]

[1] Sakarya University, Sakarya/Turkey, msaidokutan@sakarya.edu.tr
[1]Sakarya University, Sakarya/Turkey, kgenel@ sakarya.edu.tr

Abstract **- As is known, the design of shafts operating under the effect of torsion is made by considering the risk of resonance during operation as well as strength expectation, and the weight limitation of the part may cause some restrictions in both cases. Due to the advantage of composite materials in terms of lightness and strength, the application area is expanding, and it is seen that the studies on composite shaft design have continued with increasing interest for the last 30 years. The fact that there are many variables affecting composite part performance, damage conditions, fiber winding angle, stacking sequence, and layer thickness with respect to loading type makes it difficult to generalize the design rule. Within the scope of this study, the stiffness, bending natural frequency, and critical buckling moment values of carbon fiber tubes consisting of ten layers were examined analytically for a constant torsion moment. Twenty-five different array combinations for various winding angles (0, 45, and 90) were considered. Appropriate combinations have been determined according to the performance values. The finite element method was also used in the studies.**

Keywords **- composite driveshaft, torsional strength, fiber orientation, finite element method.**

I. INTRODUCTION

As it is known, composite tubes can be used in power transmission parts. These materials come to the fore in many applications due to their remarkable specific strength and specific stiffness values. In addition to mechanical properties, vibration damping and excellent corrosion resistance are among its essential advantages. Composite shafts are an important application area where lightness is prominent, especially in the automotive industry, aerospace, and defense industries.

Compared to composites, it is often impossible for a monolithic shaft to achieve the natural bending frequency in high-density metallic materials; therefore, composite shafts are preferred to metallic shafts. Besides, ease of assembly and low maintenance costs are among the advantages of composites. On the other hand, the lightness provided by composite materials also plays a vital role in reducing carbon emissions.[1]

The main constraints of the design are the natural bending frequency, the critical buckling moment, and the torque transmission capacity of the composite shaft. Kim et al. [2] stated that medium-weight vehicles should have a torque capacity of 3500 Nm and a natural bending frequency higher than 153.3 Hz. Carbon, glass, or other fibers alone take place in composite shafts, whereas these fibers are used together in hybrid structures. Also, there are hybrid structures obtained by using these fibers with metal tubes. [3-5]

The parameters affecting the performance of the composite shafts are fiber orientation angle, stacking sequence, layer thickness, and the number of layers. Badie et al. [6] studied the effects of fiber orientation angle and stacking sequence on torsional stiffness, buckling, natural bending frequency, fatigue life, and failure modes. They expressed that 0 degrees give the maximum value for natural frequency, 45 degrees for torque transmission, and 90 degrees for buckling. It was concluded that the stacking sequence also influenced the cases examined above. Abu Talib et al. [7] found that as the fiber orientation angle increases from 0 to 90, the natural bending frequency decreases. Moreover, it was reported that there is a 46% difference in buckling moment between the best and worst stacking sequences. In the study of Mutasher [8] by winding glass and carbon fiber on an aluminum tube, the effect of fiber angles, stacking sequence, and the number of layers on torque capacity was investigated. It has been experimentally observed that the torque capacity is best at 45 degrees and increases with the increasing number of layers.

The fact that many variables affect composite part performance, such as damage conditions, fiber orientation angle, stacking sequence, and layer thickness with respect to loading type, makes it difficult to generalize the design rule. Within the scope of this study, the stiffness, bending natural frequency, and critical buckling moment values of carbon fiber tubes consisting of ten layers were examined analytically for a constant torsion moment. Furthermore, twenty-five different array combinations for various winding angles (0, 45, and 90) were considered for ten layers. Appropriate combinations have been determined according to the performance values. The finite element method was also used in the studies.

II. LAMINATED STRUCTURE ANALYTICAL SOLUTION

Composite laminates are not like isotropic homogeneous materials; the stiffness of the lamina may vary depending on the fiber, matrix, or the point to be selected at the fiber-matrix interface. Since these differences complicate the modeling, analyses are made according to the average properties and assume that the lamina is homogeneous.

The material properties of the composite shaft were analyzed by classical lamination theory. The theory deals with the linear elastic response of the composite under a plane stress condition. Accordingly, for a composite structure with fiber angles and material properties, Q_{ij} reduced stiffness matrix is:

$$Q_{ij} = \begin{pmatrix} Q_{11} & Q_{12} & 0 \\ Q_{12} & Q_{22} & 0 \\ 0 & 0 & Q_{66} \end{pmatrix} \quad (1)$$

$$Q_{11} = \frac{E_1}{1-\upsilon_{12}\upsilon_{21}} \ , \ Q_{22} = \frac{E_2}{1-\upsilon_{12}\upsilon_{21}} \ , \ Q_{12} = \frac{\upsilon_{12}E_1}{1-\upsilon_{12}\upsilon_{21}}$$

$$Q_{66} = G_{12} \ , \ \upsilon_{21} = \upsilon_{12}\frac{E_1}{E_2} \quad (2)$$

where E is the modulus of elasticity, G is the modulus of shear, and ν is the Poisson's ratio. Calculations (stiffness matrix) are made for each layer, considering the material properties given in Table 1. A transformed stiffness matrix according to fiber angles is obtained for the calculation of stresses in the global direction. (c=cosΘ ve s=sinΘ).

$$\overline{Q}_{ij} = \begin{pmatrix} \overline{Q}_{11} & \overline{Q}_{12} & \overline{Q}_{16} \\ \overline{Q}_{12} & \overline{Q}_{22} & \overline{Q}_{16} \\ \overline{Q}_{16} & \overline{Q}_{26} & \overline{Q}_{66} \end{pmatrix} \quad (3)$$

$$\begin{aligned} \overline{Q}_{11} &= Q_{11}c^4 + 2(Q_{12}+2Q_{66})s^2c^2 + Q_{22}s^4 \\ \overline{Q}_{12} &= (Q_{11}+Q_{22}-4Q_{66})s^2c^2 + Q_{12}(s^4+c^4) \\ \overline{Q}_{22} &= Q_{11}s^4 + 2(Q_{12}+2Q_{66})s^2c^2 + Q_{22}c^4 \\ \overline{Q}_{16} &= (Q_{11}-Q_{12}-2Q_{66})sc^3 + (Q_{12}-Q_{22}+2Q_{66})s^3c \\ \overline{Q}_{26} &= (Q_{11}-Q_{12}-2Q_{66})s^3c + (Q_{12}-Q_{22}+2Q_{66})c^3s \\ \overline{Q}_{66} &= (Q_{11}+Q_{22}-2Q_{12}-Q_{66})s^2c^2 + Q_{66}(s^4+c^4) \end{aligned} \quad (4)$$

By obtaining the transformed stiffness matrices for each different angle, the following equation is obtained:

$$\begin{pmatrix} \sigma_x \\ \sigma_y \\ \tau_{xy} \end{pmatrix} = \begin{pmatrix} \overline{Q}_{11} & \overline{Q}_{12} & \overline{Q}_{16} \\ \overline{Q}_{12} & \overline{Q}_{22} & \overline{Q}_{16} \\ \overline{Q}_{16} & \overline{Q}_{26} & \overline{Q}_{66} \end{pmatrix} \begin{pmatrix} \varepsilon_x \\ \varepsilon_y \\ \gamma_{xy} \end{pmatrix} \quad (5)$$

with this equation, stresses are calculated for laminas.

A. Calculation of Laminate Modules

To calculate the modulus values of the laminated structure, the extensional matrix A is calculated as follows.

$$A_{ij} = \sum_k^n [\overline{Q}_{ij}]_k (h_k - h_{k-1}) = \sum_k^n [\overline{Q}_{ij}]_k t_k \quad \text{i=1,2,6; j=1,2,6} \quad (6)$$

$$E_x = \frac{1}{hA'(1,1)} , E_y = \frac{1}{hA'(2,2)} , G_{xy} = \frac{1}{hA'(1,1)} \quad (7)$$

where t is the thickness of a layer, h is the total thickness of the laminated structure, and A' is the inverse of the matrix. In addition, E_x, E_y, and G_{xy} are the longitudinal, transverse, and shear moduli, respectively.

B. Calculation of Critical Buckling Moment

Since composite shafts are long, thin, and hollow structures, they can buckle under torque. The buckling expression for thin-walled shafts is:

$$T_{cr} = (2\pi r_m h)(0.272)(E_x E_y{}^3)^{1/4}(\frac{h}{r_m})^{3/2} \quad (8)$$

In this expression, the mean radius of r_m and h represents the total laminate thickness.

C. Calculation of Natural Bending Frequency

First mode frequency calculation:

$$f_n = \frac{\pi}{2}\sqrt{\frac{E_x I}{mL^4}} \quad (9)$$

where m is the weight per unit length, *I* is the moment of inertia, L is the shaft length. The expression calculates the moment of inertia:

$$I = \frac{\pi}{2}(r_o{}^4 - r_i{}^4) \quad (10)$$

where r_o is the outer radius and r_i is the inner radius. [9,10]

D. Torque Carrying Capacity

The torque carrying capacity of a laminated structure can be obtained by evaluating the maximum loads that each layer can carry within that structure. Whether each lamina can safely bear the stress on it is determined by the factor of safety chosen. As part of the study, the safety factor and the maximum torque that the structure can bear were calculated for each lamina, taking the maximum stress values into account.

Table 1: Material properties of carbon fiber (T300/5208 type) [11]

E_1 [GPa]	E_2 [GPa]	G_{12} [GPa]	ν_{12}	ρ [g/cm³]	$(\sigma_1)_{ult}^t$ [MPa]	$(\sigma_1)_{ult}^c$ [MPa]	$(\sigma_2)_{ult}^t$ [MPa]	$(\sigma_2)_{ult}^c$ [MPa]	$(\tau_{12})_{ult}$ [MPa]
136.0	9.80	4.70	0.28	1.54	1550	1090	207	128	75

III. FINITE ELEMENT ANALYSIS

Finite element models of the composite shaft were created and analyzed in ABAQUS version 2020. In the model created, the thickness of each layer is 0.25 mm, the shaft length is 70 cm, and the inner diameter is 12.5 mm. By creating a 3-dimensional model, a mesh structure consisting of 4200 elements was created with the quadratic quadrilateral S8R5(an 8-node double thin curved shell, reduced integration, using five degrees of freedom per node) mesh type. As shown in Fig. 1, one end of the shaft is restricted for movement in all degrees of freedom (fixed support), while the other end is limited to rotating only in the axis given the torque. Then, a torque of 3500 Nm was applied to the reference point assigned to the midplane of the shaft. Due to the thin-walled cylindrical structure of the composite shaft, it tends to buckle under torque. The conditions used in the static torque analysis and the mesh properties were considered in examining this behavior.

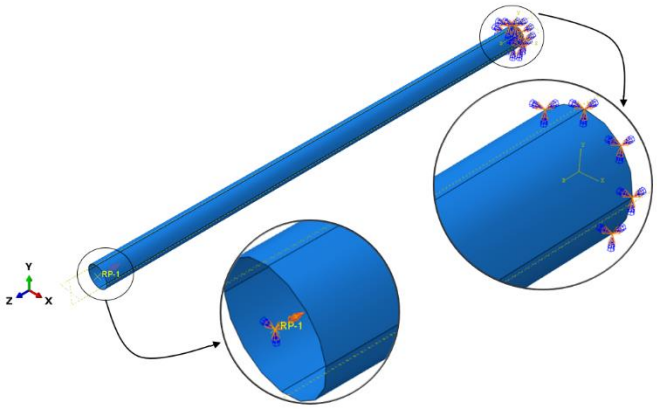

Figure 1: Loading and fixed support of composite shaft model

IV. RESULT AND DISCUSSION

A. *Effect of Fiber Orientation Angles on Laminate Modules*

Considering equations 8 and 9, it is seen that the expression $(E_x E_y^{\,3})^{1/4}$ for critical buckling and the indication $\sqrt{E_x}$ for natural frequency effect regardless of the part geometry. From this point of view, to examine the effect of fiber angles on the shaft design, the modulus values of the 10-layer structures with $[0]_{10}$, $[\pm 15]_{10}$, $[\pm 30]_{10}$, $[\pm 45]_{10}$, $[\pm 60]_{10}$, $[\pm 75]_{10}$ and $[90]_{10}$ arrays with a lamina thickness 0.25 mm were calculated. The graph given in Fig. 2 was created.

When examining the graph, in terms of critical buckling value, it is understood that 90-degree fiber orientation gives the maximum outcome, while the natural frequency value gives the maximum outcome of 0-degree. From this point, the results are in accordance with the literature [6,7].

It is seen that the torque carrying capacity of the composite shaft has reached the maximum value of 45 degrees by making deductions from the G_{xy} shear module.

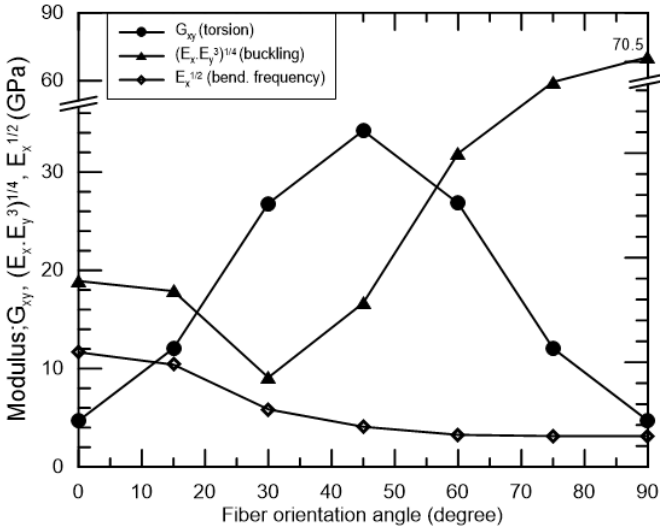

Figure 2: Effect of fiber orientation angle on modulus.

Fig. 2 is not enough to decide the design parameters with a single orientation. Based on these data, 10-layer composite shafts given in Table 2 were analyzed to reveal the effect of stacking sequence on buckling, frequency, and torque.

Table 2: Combination and Stacking Sequence

0-45	**90-45**	**0-45-90**
$[0/0/0/0/0]_s$	$[90/90/90/90/90]_s$	$[45/-45/45/-45/45]_s$
$[45/-45/45/-45/0]_s$	$[45/-45/45/-45/90]_s$	$[0/45/-45/45/90]_s$
$[45/-45/45/0/0]_s$	$[45/-45/45/90/90]_s$	$[90/45/-45/45/0]_s$
$[45/-45/0/0/0]_s$	$[45/-45/90/90/90]_s$	$[0/45/-45/90/90]_s$
$[0/45/-45/45/-45]_s$	$[90/45/-45/45/-45]_s$	$[90/90/45/-45/0]_s$
$[0/0/0/45/-45]_s$	$[90/90/90/45/-45]_s$	$[0/0/45/-45/90]_s$
$[0/45/-45/45/0]_s$	$[90/45/-45/45/90]_s$	$[90/45/-45/0/0]_s$
$[0/45/-45/0/0]_s$	$[90/45/-45/45/90]_s$	$[0/90/0/90/0]_s$
		$[90/0/90/0/90]_s$

B. *Effect of Fiber Orientation Angles and Stacking Sequence on Critical Buckling Moment*

In Fig.3, it is seen that the lowest critical buckling value is at 45-degree angles, as expected. On the other hand, while it is anticipated that the structure formed at only 90 degrees will reach the highest torsion value, on the contrary, it is noteworthy that the highest value is obtained for the $[90/0/90/0/90]_s$ sequence. This shows that the value of E_x is important as well as the value of E_y in the calculation of the critical buckling value. As seen in Fig. 3, eight of the given sequence combinations, in which 90 degrees are in the majority, can provide the critical buckling moment value.

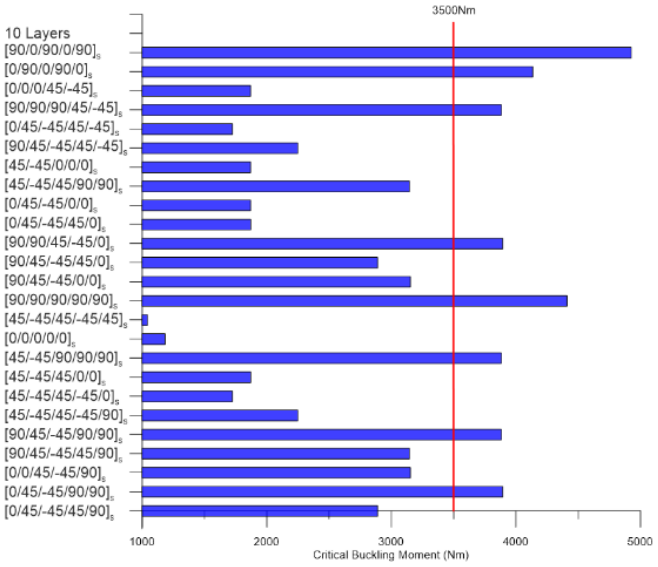

Figure 3: Critical buckling moments for twenty-five combinations

C. Effect of Fiber Orientation Angles and Stacking Sequence on Natural Bending Frequency

The calculated natural frequency values for the studied combinations are given in the figure below (Fig. 4). The targeted frequency value could not be achieved for combinations of 90 and 45 degrees. The best value is 0 degrees maximum as expected, and the value decreases with increasing angle. Therefore, it takes its minimum value in combination with 90-degree windings. It is clearly revealed that the stacking sequence does not affect the frequency.

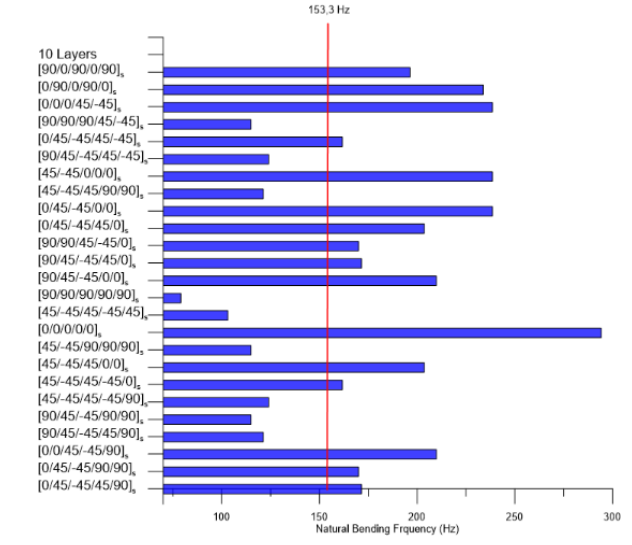

Figure 4: Natural bending frequency for twenty-five combinations

D. Torque Carrying Capacity

Combinations examined in Table 2, the torque that can be carried is calculated by taking the safety factor as one, and the graph shown in Fig. 5 is obtained. As can be seen, none of these structures designed can carry a moment of 3500 Nm. As expected, only 45-degree layers have maximum moment transmission capacity. However, regardless of the orientation angle, the torque value decreases with the increase of the number of layers different from 45 degrees. It takes the minimum value for 0 and 90 orientations. The maximum torque carrying capacity of 45 degrees is in line with previous studies. [8,12]

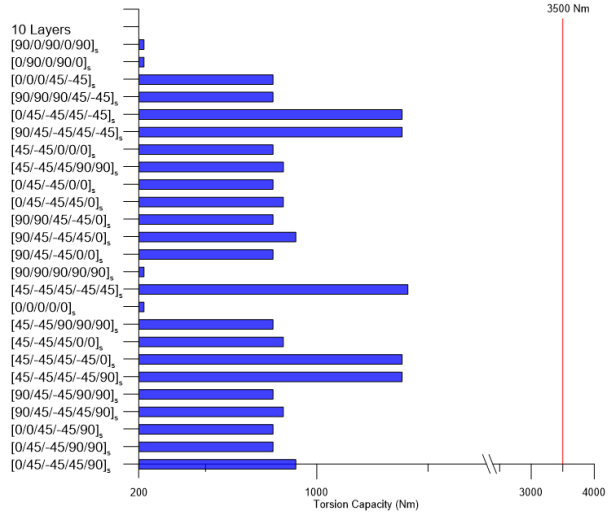

Figure 5: Torque carrying capacities for twenty-five combinations

As a result, considering the three criteria above for these 10-layer combinations, combination $[0/45/-45/45/90]_s$ and $[90/45/-45/45/0]_s$ sequence, in which three orientation angles are used, and 45 degrees are predominant, come to the fore. According to this, the number of layers has been increased to obtain the composite shaft that will provide the targeted torque. In Fig. 6, the variation of the torque value that can be obtained for cases where the number of layers is between 12 and 24 is given.

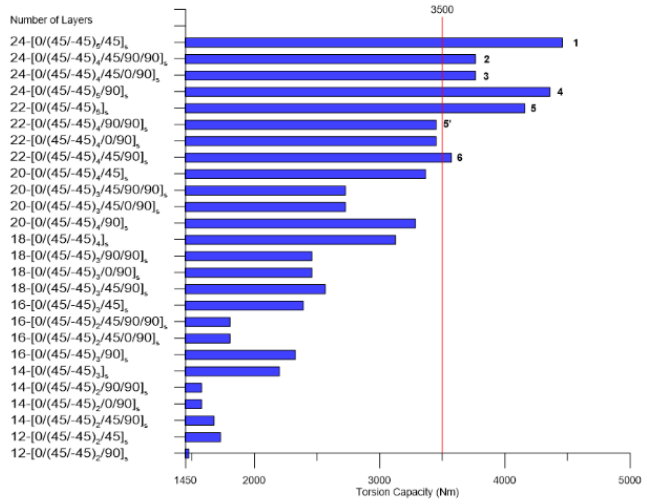

Figure 6: Torque carrying capacities for various stacking and number of layers.

Only six within the combinations given in Fig. 6 can carry 3500 Nm. Numbers 2, 3, 4, and 6 of these six combinations also provide the buckling and frequency requirements (Fig. 7 and 8).

Although the 6th combination has fewer layers than the others, it has the same performance as them. This makes it possible to obtain lighter structures if the orientation angle and stacking sequence are optimized.

The stress and safety factors of the 5 and 5' combinations indicated in Fig. 6 are given in Table 3. The normal stresses developed in the 5' structure are below the safety stress values of the material (Table 1); however, the shear stress is above the safety stress (75 MPa) and is 76 MPa for both 0 and 90 degrees, and the minor factor of safety is calculated for shear stress (0.98). On the other hand, the stresses calculated for the 5th combination were below the safety stress and thus safe.

Table 3: Comparison of two sequences for the safety factor.

Stacking Sequence	Stress	0 °	S	45 °	S	-45 °	S	90 °	S
5 $[0/(45/-45)_5]_s$	σ_1	0		897.9	1.72	-897.9	1.21		
	σ_2	0		-47.6	2.68	47.6	4.34		
	τ_{12}	**62.9**	**1.19**	0		0			
5' $[0/(45/-45)_5/90_2]_s$	σ_1	0		1083.3	1.43	-1083.3	1.06	0	
	σ_2	0		-57.4	2.22	57.4	3.6	0	
	τ_{12}	**76.0**	**0.98**	0		0		**-76.0**	**0.98**

Note: Stresses were obtained based on the local coordinate system (the materials axes) .The unit of all stresses is MPa. $(\sigma_1)_{ult}{}^t$=1550, $(\sigma_1)_{ult}{}^c$=1090, $(\sigma_2)_{ult}{}^t$=207,$(\sigma_2)_{ult}{}^c$=128, $(\tau_{12})_{ult}$ =75

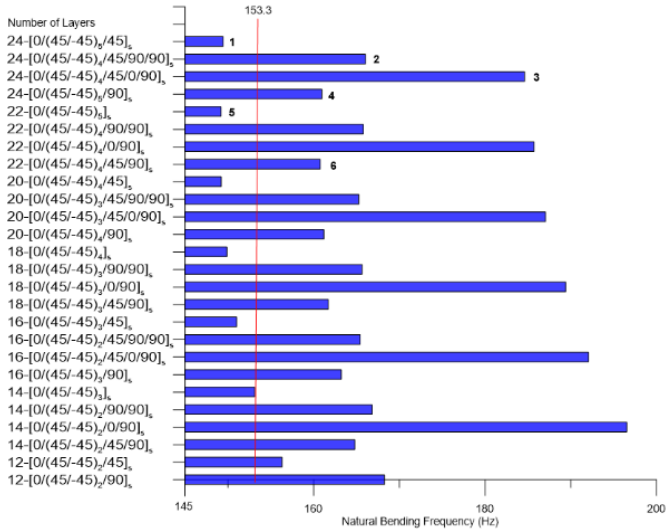

Figure 7: Natural bending frequency of 12 to 24 laminated structures

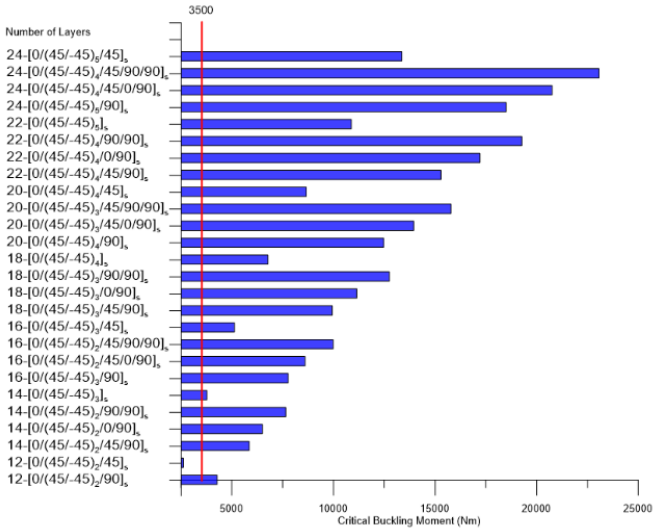

Figure 8: Critical buckling moments of 12 to 24 laminated structures

E. Finite element analysis results

The analysis of the structure (number 6 $[0/(45/-45)_4/45/90]_s$) selected among the 22-layer combinations in Fig. 6, which is sufficient in terms of torsion performance, was carried out using the finite element method, and the results, along with the analytical method, are given in Fig. 9 according to the stacking sequence number. Noted that τ_{xy} values in Fig. 9 were obtained in the global coordinate system(off-axes). It was determined that there was an acceptable deviation (10-20%) between the shear stress results obtained using both methods. However, with increasing wall thickness, it is noteworthy that the finite element results show a slightly increasing trend, contrary to the results obtained by the analytical method.

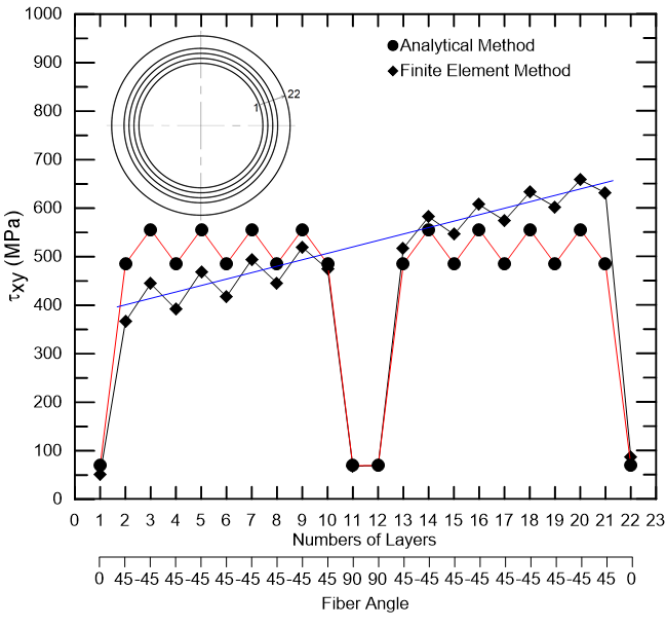

Figure 9: Comparison of analytical method and finite element method in shear stress

The graph comparing the critical buckling moment with the finite element and analytical method is given in Fig. 10. In the graph, structures with 22 and 24 layers, respectively $[0/(45/-45)_4/45/90]_s$ and $[0/(45/-45)_5/90]_s$ sequences that provide the design criteria are taken into account. It has been determined that the results obtained by the analytical method are in agreement with the results obtained by the finite element method, and a maximum deviation of 5% occurs between both ways.

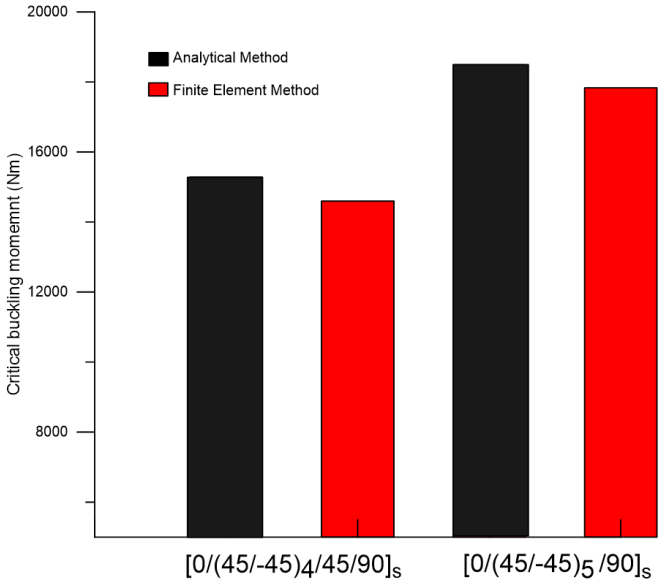

Figure 10: Comparison of analytical method and finite element method in critical buckling

Fig. 11 shows the cross-section view (relative to the z-axis) of the buckling analysis of the sequence $[0/(45/-45)_4/45/90]_s$. In the section, deformations that may occur under the effect of buckling are striking.

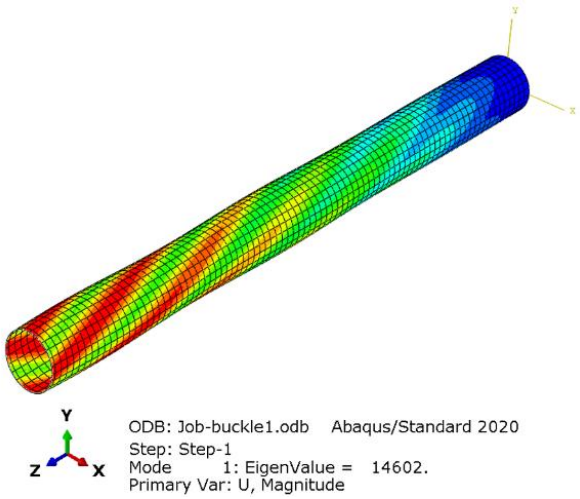

Figure 11: Buckling analysis of $[0/(45/-45)4/45/90]_s$

V. CONCLUSION

It has been confirmed that especially the 45-degree orientation is decisive in torque transmission. 0 and 90 degrees are the other two parameters considered in shaft design in terms of frequency and torsional moment, respectively.

The results revealed that the fiber orientation angle and the layer arrangement can significantly affect the part weight and thus the cost. With a proper fiber orientation and stacking sequence, lightweight and high-performance structures can be obtained.

It has been seen that practical and acceptable shaft design is possible with the analytical method, but finite elements can be used in detailed research.

REFERENCES

[1] Rastogi N. Design of composite driveshafts for automotive applications. SAE, technical paper series, 2004-01-0485; 2004.

[2] Kim HS, Kim BC, Lim TS, Lee DG. Foreign objects impact damage characteristics of aluminum/composite hybrid drive shaft. Compos Struct 2004; 66:377–89.

[3] Khalid Y A, Mutasher SA, Sahari B B and Hamouda AMS 2007 Bending fatigue behavior of hybrid aluminum/composite drive shafts Mater. Des. 28 329–34

[4] Suresh G, Srinivasan T, Bernard SS,Vivek S, Akash RM, Baradhan G, Anand B., Analyzing the mechanical behavior of IPN composite drive shaft with E-glass fiber reinforcement, Materials Today: Proceedings 2020: https://doi.org/10.1016/j.matpr.2020.03.198

[5] Shokrieh MM, Hasani A, Lessard LB. Shear buckling of a composite drive shaft under torsion. Composite Structure 2004; 64:63–9.

[6] Badie MA, Mahdi E, Hamouda AMS. An investigation into hybrid carbon/glass fiber reinforced epoxy composite automotive drive shaft. Mater Des 2011; 32:1485–500.

[7] Abu Talib AR, Ali A, Badie MA. Azida Che Lah N, Golestaneh AF. Developing a hybrid, carbon/glass fiber-reinforced, epoxy composite automotive drive shaft. Mater Des 2010; 31:514–21.

[8] Mutasher SA. Prediction of the torsional strength of the hybrid aluminum/composite drive shaft. Mater Des 2009; 30:215–20.

[9] Kaw, Autar K. Mechanics of Composite Materials. Boca Raton: CRC Press, 2006.

[10] Barbero, Ever J. Introduction to Composite Materials Design. Boca Raton: CRC Press, 2018

[11] Barbero, Ever J. Finite Element Analysis of Composite Materials Using Abaqus:Boca Raton:CRC Press, 2013

[12] Soykok IF, Ozcan AR, Tas H., Evaluation of the failure responses of filament wound and pre-preg wrapped glass fiber/epoxy composite tubes under quasi-static torsional loading, Mater. Res. Express 6 (2019) 055307

1D Analysis of Thermal Performance of a Double Pipe Heat Exchanger

H. BAYRAM[1]

[1] Department of Mechanical Engineering, Engineering Architecture Faculty, Amasya University, Amasya, Turkey, halil.bayram@amasya.edu.tr

Abstract **- In this study, a double pipe heat exchanger was modeled considering the conditions obtained from the reference study, and the thermal performance of the heat exchanger was numerically investigated under different Reynolds number and inlet temperature conditions by using the developed three-dimensional CFD and 1D models. Water was selected as a working fluid and counter flow conditions were considered for all analyses. Reynolds number values varied between 10000 and 40000 in increments of 5000 and were kept constant and the same for inner tube and annulus sides. In addition, the inlet temperature difference values were selected as 20, 40, and 60 °C. The results obtained from the analyses were compared to the reference study. All the other performed analyses were compared to each other in terms of thermal performance. It can be concluded that CFD and 1D analysis can be used with a high confidence level for double pipe heat exchangers for Re interval of 10000-40000. In addition, while more comprehensive results can be obtained by using the CFD models, the results of the 1D model were obtained much faster.**

Keywords **– CFD, Double pipe heat exchanger, Thermal performance, 1D analysis**

I. INTRODUCTION

The heat exchangers are devices to perform the heat transfer between the different temperature zones and used in different industries such as chemical, food, automotive, etc. [1-4]. Double pipe heat exchangers have a simple construction and consist of two or more concentric tubes. The heat exchange occurs through the cylindrical tube walls. The double pipe heat exchangers are fairly cheap and can be also operated under high pressure conditions. But these types of heat exchangers have higher volumes than other types for the same thermal capacity [5-8]. The thermal performance of the double pipe heat exchanger can be increased in several ways such as surface coating or roughness, extend the heat transfer surface areas, etc. [9-12]. The thermal performance studies were carried out experimentally and numerically. In numerical studies, CFD (Computational Fluid Dynamics) analyses have a big role and a lot of CFD studies can be found in the literature. In addition, the values such as temperature, velocity, pressure, etc. can also be observed by using the CFD method. A developed 1D mathematical model allows the analysis of dynamic behaviors of the problem under different conditions. In addition, the 1D models show the results much faster than the CFD method due to not contain a geometry as in the CFD method.

In this work, the thermal performance of a double pipe heat exchanger was investigated numerically under different Reynolds numbers and temperature conditions. The CFD analyses were performed by using Ansys Fluent package software program. On the other hand, the 1D analyses were performed by using the Amesim package software program. The results of both analyses that performed under the same conditions of the reference study were compared to the reference data to the validation process [13].

II. MATERIALS AND METHODS

The dimension specifications of the double pipe heat exchanger model used in the analyses were listed in Table 1. The working fluid was selected as water for both annulus and inner tube sides. The material of the inner pipe of the heat exchanger was copper. The outer pipe did not include to the heat exchanger model. But the outer surface of the annulus side water was assumed as adiabatic. The thermophysical properties of water and copper were given in Table 2

Table 1: Dimensions of the double pipe heat exchanger

Inner tube inside diameter	15	mm
Inner tube thickness	2	mm
Outer tube inside diameter	32	mm
Tube length	1000	mm

Table 2: Thermal properties of water and copper

	λ (W/m.K)	ρ (kg/m^3)	Cp (j/kg.K)	μ (kg/m.s)
Water	0.6	998.2	4182	0.001003
Copper	387.6	8978	381	-

Turbulence flow conditions were considered during all the analyses due to the Reynolds number varying between 10000 and 40000 in increments of 5000. k-epsilon turbulence model was selected considering the performed similar studies from the literature. In addition, different water inlet temperature values were selected to examine the temperature effects on the thermal performance of the heat exchanger. The detailed boundary conditions of the performed analyses can be shown in Table 3. And all the analyses were carried out under counter flow conditions until the steady-state conditions were obtained.

The hot and cold water flows through the inner tube and annulus sides, respectively. The total heat transfer rate between the hot and cold water streams can be calculated by using Equations 1 and 2, respectively. The walls of the heat exchanger contact the surrounding air were assumed as adiabatic.

$$Q_h = (\dot{m}c_p)_h (T_{h,i} - T_{h,o} \quad (1)$$

$$Q_c = mc_p{}_c \; T_{c,o} - T_{c,i} \quad (2)$$

The hydraulic diameter can be calculated by using Equation 3 and in this equation, A and P represent the net cross-sectional area for flow and the wetted perimeter, respectively.

$$D_{hydraulic} = \frac{4A}{P} \quad (3)$$

Table 3: Performed boundary conditions of the performed analyses

		Inlet temperature [°C]	
Case No	**Reynolds number**	**Hot side**	**Cold side**
Case-1.1	10000	70	10
Case-1.2		60	20
Case-1.3		50	30
Case-2.1	15000	70	10
Case-2.2		60	20
Case-2.3		50	30
Case-3.1	20000	70	10
Case-3.2		60	20
Case-3.3		50	30
Case-4.1	25000	70	10
Case-4.2		60	20
Case-4.3		50	30
Case-5.1	30000	70	10
Case-5.2		60	20
Case-5.3		50	30
Case-6.1	35000	70	10
Case-6.2		60	20
Case-6.3		50	30
Case-7.1	40000	70	10
Case-7.2		60	20
Case-7.3		50	30

In the double pipe heat exchangers, the hydraulic diameter of the inner tube was equal to the diameter of the inner tube (Equation 4). But on the annulus side, the hydraulic diameter can be calculated by using Equation 5. *Di* and *do* represent the outer tube inside diameter and inner tube inside diameter, respectively.

$$D_{hydraulic,hot} = D_i \quad (4)$$

$$D_{hydraulic,cold} = \frac{4\left(\frac{\Pi D_i^2}{4} - \frac{\Pi d_o^2}{4}\right)}{\Pi D_i + \Pi d_o} \quad (5)$$

Reynolds number was calculated by using the Equation 6 and ρ, u and μ represent the density velocity and dynamic viscosity of the working fluid, respectively.

$$Re = \frac{\rho u D_{hydraulic}}{P\mu} \quad (6)$$

The generated mesh structure used in the CFD analyses is shown in Figure 1 and the total element number is approximately 1.3 million.

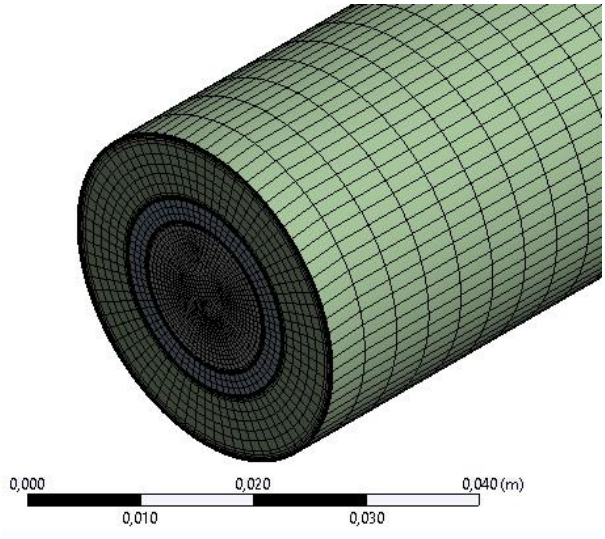

Figure 1: Mesh structure of the heat exchanger

The developed 1D model of the equivalent double pipe heat exchanger is shown in Figure 2. In this model, the working fluid and the material of the solid were selected as water and copper as in the CFD analyses. The 1D model was created by using the LMS Imagine Lab Amesim software that program can model and analysis of one-dimensional systems and also quickly estimate the effects of the variable parameters [14].

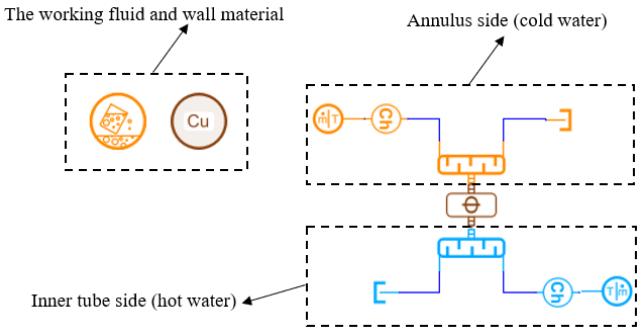

Figure 2: The developed 1D heat exchanger model

III. Results and Discussions

The comparison of the total heat transfer rate between the results of the reference study and the results of the performed analyses under the same conditions were given in Figure 3. The hot and cold water inlet temperature values of the reference study were 60 and 20 °C, respectively. According to the results, the difference between the reference study and the analyses was increased by rising the Reynolds number and all the results showed the same tendency for all cases. In addition,

the total heat transfer rate values obtained from the CFD and 1D analyses were calculated nearly the same for all cases.

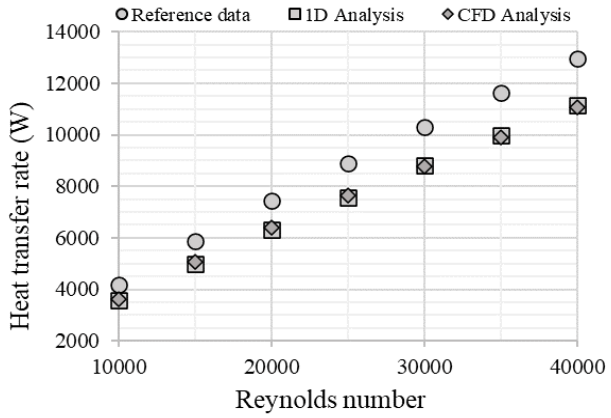

Figure 3: The comparative results of the total heat transfer rate

In general, when the total heat transfer rate values are examined under all Reynolds numbers and inlet temperature conditions, it can be easily seen from Figure 4 that the results obtained from the CFD and 1D analyses were calculated very close to each other. According to the results obtained from the performed analyzes under the difference between the inlet temperatures of the hot and cold water is 60 °C conditions, it is seen that the difference is slightly higher than in the other case. At the same time, the difference between the results was increased with rising Reynolds numbers and the value of the CFD analyses was calculated higher than the 1D ones. The total heat transfer rate was about 1800 W at a low Reynolds number and minimum inlet temperature difference. This value was about 5600 W at a low 40000 Reynolds number condition. On the other hand, the total heat transfer rate was calculated as about 16300 W at the highest Reynolds number and inlet temperature difference conditions. All the detailed results obtained from the analyses were also given in Table 4

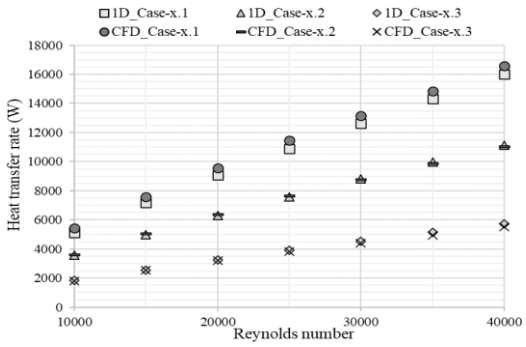

Figure 4: The total heat transfer rate values for all cases

Table 4: The total heat transfer rate values for all cases

Case No	Reynolds number	1D Analysis	CFD Analysis	Temp. Dif.
Case-1.1	10000	5095.97	5428.16	60
Case-1.2		3561.52	3619.35	40
Case-1.3		1832.19	1810.44	20
Case-2.1	15000	7147.74	7573.9	60
Case-2.2		4977.10	5049.45	40
Case-2.3		2560.58	2524.94	20
Case-3.1	20000	9054.28	9582.63	60
Case-3.2		6307.92	6388.61	40
Case-3.3		3245.52	3194.59	20
Case-4.1	25000	10874.20	11466.21	60
Case-4.2		7578.84	7643.94	40
Case-4.3		3899.69	3822.14	20
Case-5.1	30000	12627.80	13160.51	60
Case-5.2		8803.77	8773.44	40
Case-5.3		4530.22	4386.61	20
Case-6.1	35000	14327.80	14857.43	60
Case-6.2		9991.61	9904.73	40
Case-6.3		5141.70	4952.30	20
Case-7.1	40000	15983.10	16593.82	60
Case-7.2		11148.50	11062.16	40
Case-7.3		5737.28	5530.88	20

IV. CONCLUSIONS

In this study, a double pipe heat exchanger was modeled considering the conditions obtained from the reference study, and the thermal performance of the heat exchanger was numerically investigated under different Reynolds number and inlet temperature conditions by using the developed three-dimensional CFD and 1D models. The results of the analyses and reference study showed the same tendency under all Reynolds numbers. The total heat transfer rate values of the reference study and performed analyses varied between about 4200-13000 W and 3600-11000 W, respectively. In addition, the developed numerical models were performed under different inlet temperature values of both inner tube and annulus sides. The results of the analyses were calculated very close to each other, and the values varied between about 1800 and 16000 W. It can be concluded that CFD and 1D analysis can be used with a high confidence level for double pipe heat exchangers for Re interval of 10000-40000. In addition, while more comprehensive results can be obtained by using the CFD models, the results of the 1D model were obtained much faster.

REFERENCES

[1] Kakac, S., Liu, H. and Pramuanjaroenkij, A. (2020). Heat exchangers: selection, rating, and thermal design. CRC press.

[2] Bayram, H. and Sevilgen, G. (2017). Numerical Investigation of the Effect of Variable Baffle Spacing on the Thermal Performance of a Shell and Tube Heat Exchanger. Energies, 10(8), p.1156.

[3] Raj, K. and Ganne, S. (2012). Shell side numerical analysis of a shell and tube heat exchanger considering the effects of baffle inclination angle on fluid flow using CFD. Thermal Science, 16(4), pp.1165–1174.

[4] Shah, RK. and Sekulic, DP. (2003). Fundamentals of heat exchanger design: John Wiley & Sons.
[5] Bergman, TL., Incropera, FP., DeWitt, DP. and Lavine, AS. (2011). Fundamentals of heat and mass transfer: John Wiley & Sons.
[6] Kumar, S., Karanth, V. K. and Murthy, K. (2015). Numerical study of heat transfer in a finned double pipe heat exchanger. World Journal of Modelling and Simulation, 11(1), pp. 43-54.
[7] Chen, W.-L. and Dung, W.-C. (2008). Numerical study on heat transfer characteristics of double tube heat exchangers with alternating horizontal or vertical oval cross section pipes as inner tubes. Energy Conversion and Management, 49(6), pp.1574–1583.
[8] Syed, KS., Ishaq, M., Iqbal, Z. and Hassan, A. (2015). Numerical study of an innovative design of a finned double-pipe heat exchanger with variable fin-tip thickness. Energy Conversion and Management, 98, pp.69–80.
[9] Dewan, A., Mahanta, P., Raju, KS. and Kumar, PS. (2006). Review of passive heat transfer augmentation techniques. Proceedings of the Institution of Mechanical Engineers, Part A: Journal of Power and Energy, 218, pp.509-27.
[10] El Maakoul, A., Feddi, K., Saadeddine, S., Ben Abdellah A. and El Metoui, M. (2020). Performance enhancement of finned annulus using surface interruptions in double-pipe heat exchangers. Energy Conversion and Management, 210, pp.112710.
[11] Kind, M., Martin, H., Stephan, P., et al. (2010). VDI Heat Atlas. Springer.
[12] Balaras, CA. (1990). A review of augmentation techniques for heat transfer surfaces in single-phase heat exchangers. Energy,15, pp.899-906.
[13] Gomez A, (2017). Thermal Performance of a Double-Pipe Heat Exchanger with a Koch Snowflake Fractal Design, Master dissertation, Georgia Southern University.
[14] Simcenter Amesim 16 User's guide – LMS Imagine.Lab Amesim 16

Groundwater Flow Simulation with High Order Finite Difference Method

A. GHAREHBAGHI

[1] Hasan Kalyoncu University, Gaziantep /Turkey, amin.gharehbaghi@hku.edu.tr

Abstract - **This paper has introduced a numerical model for predicting the behavior of unsteady, one-dimensional groundwater flow. An analytical model and one set of experimental data are used to assess the results of the proposed model. The Boussinesq equation, which is the governing equation in this domain, is linearized and solved. The fourth-order finite difference method is employed to discretize the equations. Moreover, the numerical results of the offered model compared with the outcomes of the second-order finite difference method. The calculated results of the introduced model showed well agreement with the results of analytical and laboratory experiment data.**

Keywords **- Groundwater, Finite Difference Method, Second-Order, Fourth-Order, Boussinesq Equation**

I. INTRODUCTION

Groundwater is one of the most vital water resources, which has a great impact on human life, especially in arid regions. In addition, groundwater has a very significant role in the transport of underground pollution. Meanwhile, simulation of groundwater flow is crucial for understanding the variations in groundwater recharge and drainage. Consequently, calculating the motion of water through porous media has various benefits for groundwater resource management. One of the popular and effective research methods in this field is numerical method. The finite difference method (FDM) is one of the most widely used numerical methods in science and engineering. Thus, this technique has been used in this research to solve the governing equation.

This paper aims to develop an effective numerical model based on the fourth-order finite difference method (FOFDM) for solving the 1D time-dependent Boussinesq equation for predicting the behavior of groundwater flow. This equation is solved with two groundwater problems. In the first numerical experiment, an analytical solution introduced by Liang & Zhang [1] for 1D transient groundwater flow from a divide to a river in an unconfined aquifer is solved. In the second case, laboratory experiment, which was conducted by Hung et al. [2], is selected to predict the water table fluctuations above an inclined leaky layer due to ditch recharge with constant boundary conditions.

II. GOVERNING EQUATION

The general equation for 1D unsteady groundwater flow, called the Boussinesq equation, is given as follows (Olsen et al. [3]):

$$\frac{\partial}{\partial x}(h\frac{\partial h}{\partial x})-\tan\theta\frac{\partial h}{\partial x}=\frac{S}{k\cos^2\theta}\frac{\partial h}{\partial t}-\frac{R}{k\cos^2\theta} \quad (1)$$

where h is the depth of the groundwater table, θ is the angle of the sloping bed with respect to horizontal, R is the rate of surface recharge, k is the hydraulic conductivity, and S is the specific yield of the aquifer.

III. NUMERICAL AND LABORATORY EXPERIMENTS

To evaluate the correctness of the established model, one analytical solution and one laboratory experiment are applied. Meanwhile, the numerical model has developed in MATLAB software.

IV. TEST CASE ONE

Liang & Zhang [1] employed a hypothetical case and recommended a general analytical expression for problems related to drainage and recession from an unconfined aquifer. In this case, they assumed the values of the distance, computational time, hydraulic conductivity, recharge rate, the initial height of the water table, the angle of the sloping bed with the horizontal, and surface recharge, as 100 *m*, 10 *days*, 2 *m/d*, 0.01 *m/d*, 10 *m*, 0, and 0, respectively. The sketch of this case is shown in Fig (1). Liang and Zhang [1] did not mention soil types because they presented the analytical expression in a general form. However, by considering their and other's research, we selected the amount of specific yield (S) as 0.2. By implementing the assumptions of the angle of the sloping bed with the horizontal, and surface recharge, the following form of Eq. (1) can be extracted.

$$\frac{\partial}{\partial x}(h\frac{\partial h}{\partial x})=\frac{S}{k}\frac{\partial h}{\partial t} \quad (2)$$

The widely used method for dealing with the nonlinearity of the Boussinesq equation is to fit it in a linear format. In this study, the assumption of $h\approx\bar{h}$ is applied to linearize Eq. (2).

$$\beta\frac{\partial^2 h^2}{\partial x^2}=\frac{\partial h^2}{\partial t} \quad (3)$$

Where β is $k\bar{h}/S$. Also, $\bar{h}$ is the average depth of water table above the aquifer bottom. In this test case, the constant head at the river is presumed to predict the value of $\bar{h}$ (i.e. $\bar{h} = h_0$).

The dimensionless form of Liang & Zhang's analytical solution is expressed as:

$$h' = \sqrt{1+\alpha\cos(\frac{\pi}{2}x')\exp(-\frac{\pi^2}{4}t')}\ ;\quad h' = \frac{h}{h_0}\ ;\quad x' = \frac{x}{L}\ ;\quad t' = \frac{\beta}{L^2}t \qquad (4)$$

Where α is $32R_rL^2/(kh_0^2\pi^3)$ and R_r is a constant recharge rate. By some simplification, the following expression can be extracted.

$$\frac{h}{h_0} = \sqrt{1+\alpha\cos(\frac{\pi}{2}\frac{x}{L})\exp(-\frac{\pi^2}{4}\frac{\beta}{L^2}t)} \qquad (5)$$

In this case the following initial and boundary conditions are enforced.

$$h(x,0) = f(x) \qquad \left.\frac{\partial h}{\partial x}\right|_{x=0} = 0 \qquad h(L,t) = h_0 \qquad (6)$$

where $f(x) = h_0\sqrt{1+\alpha\cos(\frac{\pi}{2}\frac{x}{L})}$.

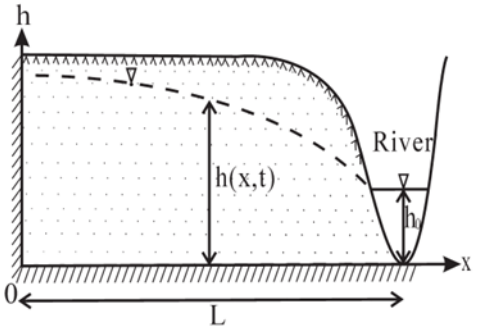

Figure 1: groundwater flow Sketch from a divide to a free surface water (Liang & Zhang [1])

V. Test Case Two

Ditch recharge is one of the effective methods to raise the groundwater table. Nevertheless, the leaky layer exerts its effect on the recharge when an aquifer is lying on it. As a second case, we have used data from the experimental study of Hung et al. [2], which handled this problem with a sandbox model. By Considering a zero-equal surface reload rate, a leaky bed, and the linearized form of Eq. (1) similar to the previous case, the following form of equation is extracted.

$$\frac{\partial^2 h^2}{\partial x^2} - \frac{\tan\theta}{\bar{h}}\frac{\partial h^2}{\partial x} = \frac{S}{\bar{h}k\cos^2\theta}\frac{\partial h^2}{\partial t} + \frac{2k^*}{\bar{h}bk\cos^2\theta}h^2 + \frac{2k^*}{k\cos^2\theta} \qquad (7)$$

where b and k^* are the vertical depth of the leaky bed, and vertical hydraulic conductivity, respectively. To provide a simpler form of Eq. (7), the following form and parameters are suggested.

$$\frac{\partial^2 h^2}{\partial x^2} - B\frac{\partial h^2}{\partial x} = C\frac{\partial h^2}{\partial t} + Dh^2 + Q \qquad (8)$$

Where $B = \frac{\tan\theta}{\bar{h}}$, $C = \frac{S}{\bar{h}k\cos^2\theta}$, $D = \frac{2k^*}{\bar{h}bk\cos^2\theta}$, and $Q = \frac{2k^*}{k\cos^2\theta}$.

However, in this case to get a more accurate approximation, the $\bar{h}$ value was calculated as $\bar{h} = 0.5(h_0(t) + h_L(t))$. Furthermore, the initial and boundary conditions are written as follows:

$$h(x,0) = h_{ic}(x) \qquad h(0,t) = h_0 \qquad h(L,t) = h_L(t) \qquad (9)$$

where $h_{ic}(x)$ is the initial depth (or height) of the water table. The value of h_0 is 17.8 cm. The illustration of this experimental setup, is demonstrated here.

They carried out the Laboratory tests on a sandbox model with 15 *cm* wide ×70 *cm* high × 240 *cm* long. The model was constructed with acrylic plates, and these plates had 5 *cm* thick. The side walls of the sandbox contained two rows of 13 holes with a diameter of 1 *cm*. Two tanks were emplaced at the ends of each side of the sandbox. The aquifers were simulated by two sand materials. The general sketch of the sandbox model is given in Fig. (2). In this case, the values of distance, the computation time, hydraulic conductivity, specific yield, vertical hydraulic conductivity, the slope angle, and the vertical thickness of the leaky bed were 240 *cm*, 8 *min*, 0.2 *cm/s*, 0.18, 0.00025 *cm/s*, 3%, and 5 *cm*, respectively.

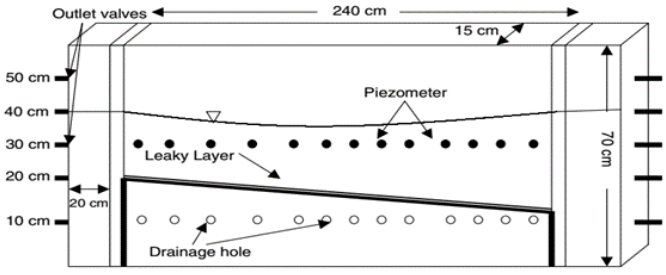

Figure 2: Illustration of the sandbox model (Hung et al., [2])

VI. Numerical Modeling

As highlighted earlier, in this paper, the second- and fourth-order schemes of FDM are employed for two groundwater problems.

VII. Numerical Modeling of Test Case One

We are implemented the following schemes:

Second-order accurate derivative in distance

$$\frac{\partial^2 h}{\partial x^2} = \frac{h_{i-1} - 2h_i + h_{i+1}}{\Delta x^2} \tag{10}$$

Fourth-order accurate derivative in distance:

$$(\frac{\partial^2 h}{\partial x^2})_i = \frac{-h_{i-2} + 16h_{i-1} - 30h_i + 16h_{i+1} - h_{i+2}}{12\Delta x^2} \tag{11}$$

First-order accurate derivative in time:

$$\frac{\partial h}{\partial t} = \frac{h_i^{t+1} - h_i^t}{\Delta t} \tag{12}$$

By replacing the second-order accurate derivative of distance and first-order accurate derivative of time in Eq. (3) the following equation can be obtained.

$$\frac{h^2{}_i^{t+1} - h^2{}_i^t}{\Delta t} = \beta \frac{h^2{}_{i-1}^t - 2h^2{}_i^t + h^2{}_{i+1}^t}{\Delta x^2} \tag{13}$$

Also by using Eqs. (11-12) the following equation can be extracted.

$$\frac{h^2{}_i^{t+1} - h^2{}_i^t}{\Delta t} = \beta \frac{-h^2{}_{i-2}^t + 16h^2{}_{i-1}^t - 30h^2{}_i^t + 16h^2{}_{i+1}^t - h^2{}_{i+2}^t}{12\Delta x^2} \tag{14}$$

Therefore, the eventual forms of second-order and fourth-order solutions in the explicit form are given as:

$$h_i^{t+1} = \sqrt{\Delta t\beta \frac{h^2{}_{i-1}^t - 2h^2{}_i^t + h^2{}_{i+1}^t}{\Delta x^2} + h^2{}_i^t} \tag{15}$$

$$h_i^{t+1} = \sqrt{\Delta t\beta \frac{-h^2{}_{i-2}^t + 16h^2{}_{i-1}^t - 30h^2{}_i^t + 16h^2{}_{i+1}^t - h^2{}_{i+2}^t}{12\Delta x^2} + h^2{}_i^t} \tag{16}$$

VIII. Numerical Modeling of Test Case Two

In this case, to develop the numerical model Eq. (8) has been implemented. Likewise, the first-order accurate derivative in the distance is employed as follows:

$$\frac{\partial h}{\partial x} = \frac{h_{i+1}^t - h_i^t}{\Delta x} \tag{17}$$

By substituting the derivatives of time and distance in Eq. (8) the following equation can be obtained.

$$\frac{h^2{}_i^{t+1} - h^2{}_i^t}{\Delta t} = \frac{1}{C}\frac{h^2{}_{i-1}^t - 2h^2{}_i^t + h^2{}_{i+1}^t}{\Delta x^2} - \frac{B}{C}\frac{h^2{}_{i+1}^t - h^2{}_i^t}{\Delta x} - \frac{D}{C}h^2{}_i^t - \frac{Q}{C} \tag{18}$$

Also, by using Eqs. (11-12-17) the following equation can be deduced.

$$\frac{h^2{}_i^{t+1} - h^2{}_i^t}{\Delta t} = \frac{1}{C}\frac{-h^2{}_{i-2}^t + 16h^2{}_{i-1}^t - 30h^2{}_i^t + 16h^2{}_{i+1}^t - h^2{}_{i+2}^t}{12\Delta x^2} - \frac{B}{C}\frac{h^2{}_{i+1}^t - h^2{}_i^t}{\Delta x} - \frac{D}{C}h^2{}_i^t - \frac{Q}{C} \tag{19}$$

Therefore, the final states of the second-order and fourth-order solutions are given as

$$h_i^{t+1} = \sqrt{\frac{\Delta t}{\Delta x^2 C}(h^2{}_{i-1}^t - 2h^2{}_i^t + h^2{}_{i+1}^t) - \frac{\Delta tB}{\Delta xC}(h^2{}_{i+1}^t - h^2{}_i^t) + h^2{}_i^t(1 - \Delta t\frac{D}{C}) - \Delta t\frac{Q}{C}} \tag{20}$$

$$h_i^{t+1} = \sqrt{\frac{\Delta t}{12\Delta x^2 C}(-h^2{}_{i-2}^t + 16h^2{}_{i-1}^t - 30h^2{}_i^t + 16h^2{}_{i+1}^t - h^2{}_{i+2}^t) - \frac{\Delta tB}{\Delta xC}(h^2{}_{i+1}^t - h^2{}_i^t) + h^2{}_i^t(1 - \Delta t\frac{D}{C}) - \Delta t\frac{Q}{C}} \tag{21}$$

IX. Results and Discussion

In the research, the second-and fourth-order schemes of FDM have been applied. Hence, one analytical solution and one laboratory experiment have been used to analyze the established model. The details of case studies have given in Table (1). In the tables and figures below, the first case stands for drainage and recession from an unconfined aquifer, and the second case stands for water table fluctuations above an inclined leaky layer due to ditch recharge with a constant upper boundary condition. In this paper, for the problem domain, the uniform node distribution has been enforced. The outcomes of case studies are presented in Figs. (3-4) and tables (2-3). To evaluate the results of FDM and FOFDM schemes the Root Mean Square Error (RMSE) is used.

$$RMSE = \sqrt{\frac{\sum_{i=1}^{N}(x_i - \hat{x}_i)^2}{N}} \tag{22}$$

x_i : Calculated value

$\hat{x}_i$: Observed value

N: Number of points

Based on the results, it can be concluded that both schemes can determine acceptable results. Nevertheless, according to the RMSE, FOFDM provided more accurate results. Although the computation time of FOFDM is a little higher than FDM, the differences are negligible. Therefore, by using FOFDM we can calculate more accurate results in the almost same execution time.

Table 1. Table of parameters

	x	***t***	***k***	***k****	***Rr***	***h0***	**S**	**θ**	***R***
First case	100 m	10 days	2 m/d	-	0.01 m/d	10 m	0.2	0	0
Second case	240 cm	8 min	0.2 cm/s	0.000 25 cm/s	-	17.8	0.18	3%	0

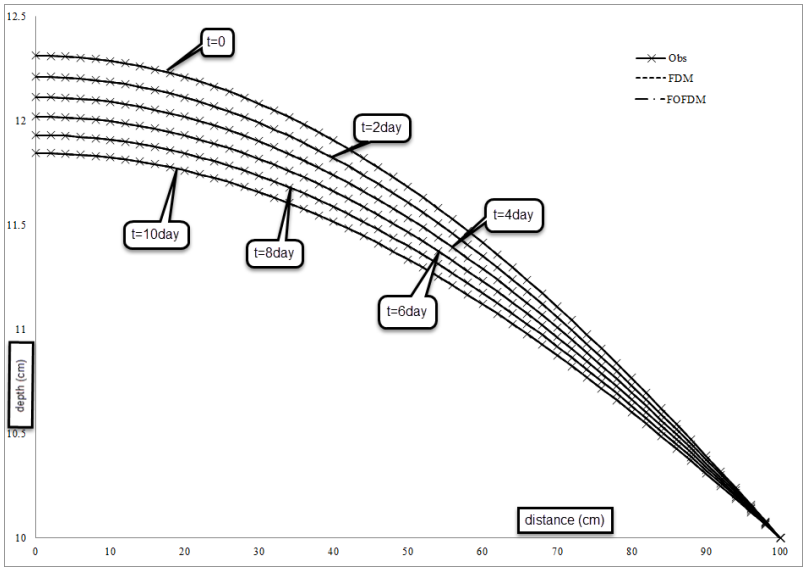

Figure 3: Illustration of results for the first case

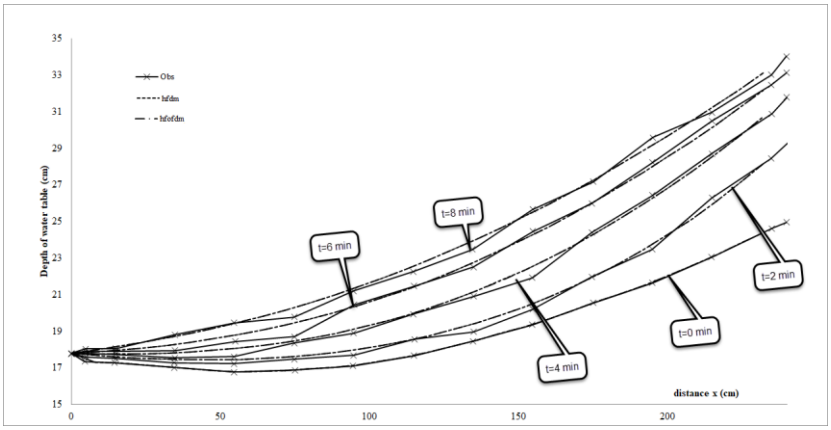

Figure 4: Illustration of results for the second case

Table 2. Table of RMSE in the first case

	schemes	**2th day**	**4th day**	**6th day**	**8th day**	**10th day**	**Execution time (s)**
dt=0.0033	FDM	3.2720e-04	5.7619e-04	7.6816e-04	9.1430e-04	0.0010	0.702964
dx=10	FOFDM	2.5630e-06	3.0271e-06	3.1584e-06	3.1883e-06	3.1679e-06	0.792303
dt=0.002	FDM	1.1677e-04	2.0514e-04	2.7323e-04	3.2494e-04	3.6333e-04	1.362367
dx=5	FOFDM	4.8364e-06	8.5278e-06	1.1313e-05	1.3369e-05	1.4844e-05	1.471358
dt= 0.0002	FDM	3.0698e-05	5.3859e-05	7.1688e-05	8.5236e-05	9.5289e-05	8.886940
dx= 2	FOFDM	9.0135e-07	1.5778e-06	2.0936e-06	2.4813e-06	2.7652e-06	13.092373

Table 3. Table of RMSE in the second case

	schemes	**2min**	**4min**	**6min**	**8min**	**10min**	**Execution time (s)**
dt= 0.06	FDM	1.2387	0.22865268	0.417261	0.379837608	0.26772449	1.166929
dx= 8	FOFDM	1.2387	0.22058401	0.416676	0.384616	0.26761358	1.209656
dt= 0.06	FDM	0.244693107	0.22100787	0.248524	0.274686048	0.2692351	1.176116
dx=4.8	FOFDM	0.244655	0.22072087	0.248307	0.274603	0.26918918	1.410299

X. CONCLUSION

In the current study, the Boussinesq equation is discretized with second-and fourth-schemes of FDM. Two numerical examples are presented as follows to demonstrate the effectiveness of the method: (i) Drainage and recession from an unconfined aquifer, and (ii) Water table fluctuations above an inclined leaky layer due to ditch recharge with a constant upper boundary condition. RMSE is used to evaluate the outcomes of the approaches. It has been observed that the calculated outcomes of the numerical method by using small and/or large time steps and the outcomes of the analytical method overlap with each other. Moreover, in the experimental test case, reliable results were determined. In spite of the fact that the required execution times in second-order FDM were less than the fourth-order FDM, nevertheless, the differences were insignificant. Thus by the same effort, the FOFDM has obtained more accurate results. In conclusion, the numerical results approved that the FOFDM can calculate satisfactory results in engineering and science applications.

REFERENCES

[1] Liang, X. & Zhang, Y.K., "Analytical solution for drainage and recession from an unconfined aquifer," Groundwater, vol. 50(5), pp. 793-798, 2011, Doi: 10.1111/j.1745-6584.2011.00867.x.

[2] Hung, C.J., Tan, Y.C., Chen, C.H., Chen, J.M. & Chang, PW., "Analytical solution of water table fluctuations above an inclined leaky layer due to ditch recharge," Hydrol. Process, vol. 20, pp. 1597–1609, 2006, Doi: 10.1002/hyp.5947.

[3] Olsen, J.S., Mortensen J. & Telyakovskiy A.S., "Polynomial approximate solutions of an unconfined Forchheimer groundwater flow equation," Advances in Water Resources, vol. 123, pp. 189–200, 2019.

Drought Assessment by Using Geographic Information Systems and Remote Sensing

Emre TOPÇU[1] and Şerife Pınar GÜVEL[2]

[1] Kafkas University, The Faculty of Engineering and Architecture, Civil Engineering Department, Kars/Turkey, emretopcu01@gmail.com

[2] General Directorate of State Hydraulic Works, 6th Regional Directorate, Information Technologies Department, Geographic Information Systems Section, Adana/Turkey, spinar.guvel@dsi.gov.tr

Abstract **– Drought is one of the natural disasters that has effects on water resources, socio-economic factors and environmental conditions on earth. Evaluation of drought hazard areas and drought risk mapping contribute management strategies and developments of natural resources. The use of geospatial information technology in monitoring and assessments of drought phenomenon provide estimations of drought prone areas, and prediction results can be considered in climate change adaptation works. In this study, a literature review on the use of Geographic Information Systems (GIS) and Remote Sensing (RS) on drought management is presented.**

Keywords **– Drought Analysis, Geographic Information Systems, Remote Sensing, Climate Change.**

I. Introduction

DROUGHT is a natural disaster as a climatic phenomenon which is defined as water scarcity and has some impacts on environment, living conditions of society, yield variability, agriculture (Hundera et al., 2016; Parmar et al., 2019), vegetation and economy. As drought is one of the problems caused by global warming and climate change, analysis of drought risk is of vital importance for both today and future generations.

Drought monitoring and drought risk assessment are the areas of interest for researchers to find solutions for environmental problems caused by drought impact. The use of geospatial information technology to support field surveys and assessments is a preferred method by various researchers in drought management.

Major categories on drought have been classified as meteorological, agricultural, hydrological and socio-economic drought (Patel et al., 2007; AghaKouchak et al., 2015; Acharya et al., 2019). In recent researches, types of drought have been considered and evaluated in regional or country scales. In the study conducted by Kumanlıoğlu and Fıstıkoğlu (2019), meteorological drought in Gediz Basin in Turkey was investigated. Liu et al. (2016) investigated feasibility of standardized stream index in Southwest China, temporal variations of drought indices were evaluated and drought assessment on the study site was presented. Paudel et al. (2021) studied agricultural drought risk of Tanahun district in Nepal. They prepared drought risk map of the study area, drought risk levels of five risk classes were also determined (Paudel et al., 2021).

The objective of this study is to present a literature review on the use of Remote Sensing (RS) and Geographic Information System (GIS) on drought assessment to support future drought-related researches and works.

II. Literature Review

Various studies have been carried out on drought risk assessment, drought monitoring, drought impacts or drought analysis in many countries around the world (Linglin Zeng et al., 2014; Mahajan and Dodamani, 2015; Hundera et al., 2016; Acharya et al., 2019; Cavus and Aksoy, 2019; Reis et al., 2020; Sun et al., 2020; Noichaisin et al., 2020; Kumar et al., 2021; Topçu and Karaçor, 2021; Oğuz et al., 2021; Paudel et al., 2021). In the study conducted by Önöz and Oğuz (1996), drought impacts on the water supply system of İstanbul was investigated for 1991-94 period by analyzing precipitation data.

Different drought indices have been used for analyzing drought phenomenon that changes upon meteorological and environmental conditions of a region or a country (Bhuiyan, 2004). Dikici and Aksel (2021) studied drought risk in the Ceyhan Basin comparing indices and as a result of their study a drought threat in the 20-year interval has been calculated for the basin. Wang et al. (2015) investigated droughts in the Luanhe River Basin between 1960 and 1989 by using standardized precipitation evapotranspiration index (SPEI), Standardized precipitation index (SPI) and the self-calibrating Palmer drought severity index (sc-PDSI), spatial changes of drought severity were analyzed and evaluated in their study.

One of the most preferred index methods for drought assessment in recent researches in the literature is Standardized Precipitation Index (SPI) (Sırdaş and Şen, 2003; Shah et al., 2015; Al-Mamun et al., 2018; Kumanlıoğlu and Fıstıkoğlu, 2019).

Cavus and Aksoy (2019) investigated spatial drought conditions of Seyhan River basin in Turkey, SPI was calculated by using precipitation data for 19 meteorological stations and spatial changes of drought characterization of Seyhan River basin were mapped and evaluated.

Patel et al. (2007) investigated usefulness of SPI for assessment of meteorological drought in Gujarat State which is located in India at seasonal scale, rainfall data in the period of

1981-2003 were used to compute SPI and drought severity maps were prepared.

Remote Sensing (RS) technology provides to monitor and collect information without any physical contact on the earth using satellites, airplanes, unmanned aerial vehicles, LIDAR or echosounders, etc. and has a wide application area in many disciplines concerning natural resources and events.

RS has advantages of providing to get data and information from hard-to-reach areas due to physical conditions. RS has benefits with time saving and labour saving abilities on monitoring disasters and environmental events, also supports decision-makers for disaster management strategies and application schedules.

Geographic information system (GIS) is a computer system that is used for storing data with location and feature information in the scope of analysis and management of resources with editing and analyzing capabilities to create digital models and thematic maps. Spatially referenced data in GIS environment provides to visualize distribution of various parameters from one location to another using interpolation methods and also to evaluate temporal changes of historical data.

GIS database is a storage area that stores spatial location and field attributes of data integrated and data is ready to perform analysis, to predict spatial and temporal distribution and support decision-making in various sectoral activities.

Some application fields of remote sensing and GIS are researches on water resources, land use, forestry, agriculture or meteorological events (Kite and Pietroniro, 1996; Chintapalli et al., 2000; Suresh Babu et al. 2012; Sisir and Balan, 2014; Roy et al., 2017; Piedelobo et al., 2018; Marshet Nigatu Gebeyehu, 2019). Kedirkan (2019) investigated current extent and also changes of water surface area for three lakes in Ethiopia between 2015 and 2018 by using Landsat image.

The issues on monitoring, assessment and management of drought and flood (Opolot, 2013) events are the significant fields that RS and GIS are used for.

RS and GIS have a key role in drought risk assessment (Abuzar et al., 2017). GIS tools contribute analysis and evaluation of drought risk with the ability of mapping spatial and temporal changes. Abuzar et al. (2017) investigated drought risks and severity in District Khushab in Pakistan by using Landsat images, meteorological data and GIS tools. In the study conducted by Hundera et al. (2016) in a study area in Ethiopia, agricultural drought risk maps were prepared by using RS and GIS.

In the study conducted by Badeghar and Jamadar (2019), a review study on evaluation of drought risks, drought risk areas, meteorological and agricultural drought by using RS and GIS was presented.

Giridhar M.V.S.S et al. (2017) presented assessments of drought analysis for the period between 2005 and 2009 by using GIS in Telangana Region in India, they prepared meteorological drought maps of the study area, drought classification has been made as heavy rain, normal rain, drought, moderate drought and severe drought in their study. It was indicated in the study that geomatic tools were to be effective in meteorological drought analysis.

In the study conducted by Changwony et al. (2017), water scarcity assessment has been carried out in Nakuru County in Kenya by using RS and GIS, the effects of rainfall and size of crop lands on yields were evaluated, when ground data was not available possibilities of using satellite data also evaluated.

III. Conclusion

In this study, the use and contribution of RS and GIS for assessment of drought risks is presented in order to point out the importance of contribution of advanced technologies on evaluation of drought characterization and drought impacts on water resources and environmental issues.

References

[1] Abuzar, M.K., Mahmood, S.A., Sarwar, F., Saleem, A.R., Khubaib, N., Malik, A.H., Khalil, T., Shaista, S. (2017). Drought risk assessment using GIS and remote sensing: A case study of District Khushab, Pakistan, 15th International Conference on Environmental Science and Technology, Rhodes, Greece, 31 August to 2 September 2017.

[2] Acharya et al. (2019). Monitoring Drought and its impact on Agriculture using Drought Indices and Geo-informatics Technology in Patan District, Gujarat, International Journal of Environment and Geoinformatics (IJEGEO), 6(2). 153-162. DOI: 10.30897/ijegeo.554465

[3] AghaKouchak, A., A. Farahmand, F. S. Melton, J. Teixeira, M. C. Anderson, B. D. Wardlow, and C. R. Hain (2015), Remote sensing of drought: Progress, challenges and opportunities, Rev. Geophys., 53, 452–480, doi:10.1002/2014RG000456.

[4] Al-Mamun A, Rahman MNF, Aziz MA, Qayum MA, Hossain MI, et al. (2018) Identification of Meteorological Drought Prone Area in Bangladesh using Standardized Precipitation Index. J Earth Sci Clim Change 9: 457. doi: 10.4172/2157-7617.1000457.

[5] Badeghar, A., Jamadar, B. (2019). Review on Drought Risk Assessment by using Remote Sensing and GIS, International Research Journal of Engineering and Technology (IRJET), Volume: 06 Issue: 07, July 2019.

[6] Bhuiyan, C. (2004). Various Drought Indices For Monitoring Drought Condition In Aravalli Terrain Of India, (https://www.isprs.org/proceedings/XXXV/congress/comm7/papers/243.pdf; access date: 04.08.2021)

[7] Cavus, Y., Aksoy, H. (2019). Spatial Drought Characterization for Seyhan River Basin in the Mediterranean Region of Turkey, Water 2019, 11, 1331; doi:10.3390/w11071331.

[8] Changwony, C., Sichangi, A.W., Ngigi, M.M. (2017). Using GIS and Remote Sensing in Assessment of Water Scarcity in Nakuru County, Kenya, Advances in Remote Sensing, 6, 88-102.

[9] Chintapalli, S.M., Raju, P.V., Abdul Hakeem, K., Jonna, S. (2000). Satellite Remote Sensing and GIS Technologies to Aid Sustainable Management of Indian Irrigation Systems, International Archives of Photogrammetry and Remote Sensing. Vol. XXXIII, Part B7. Amsterdam 2000.

[10] Dikici, M., Aksel, M. (2021). Comparison of Drought Indices in the Case of the Ceyhan Basin, International Journal of Environment and Geoinformatics 8(2):113-125 (2021).

[11] Giridhar M.V.S.S, Chandra Bose A.S, Viswanadh G.K (2017). Assessment of Meteorological Drought Using Spatial Information Technology, International Education & Research Journal (IERJ), Volume:3, Issue:5, May 2017.

[12] Hundera, H., Berhan, G., Bewuket, W. (2016). Remote Sensing and GIS Based Agricultural Drought Risk Assessment in East Shewa Zone, Central Rift Valley Region of Ethiopia, Journal of Environment and Earth Science, Vol.6, No.7, 2016.

[13] Kedirkan, NY. (2019). Water Surface Change of Lakes in the Central Rift Valley of Ethiopia, International Journal of Environment and Geoinformatics (IJEGEO), 6(3): 264-267. DOI: 10.30897/ijegeo.544770.

[14] Kite, G.W., Pietroniro, A. (1996). Remote sensing applications in hydrological modelling, Hydrological Sciences Journal, 41:4, 563-591, DOI: 10.1080/02626669609491526.

[15] Kumanlıoğlu, A. A., Fıstıkoğlu, O. (2019). Meteorological Drought Analysis of Upper Gediz Basin Precipitations, Dokuz Eylül University

Faculty of Engineering Journal of Science and Engineering, 21(62), 509-523, 2019. (in Turkish)
[16] Kumar, S., Roshni, T., Kumar, A., Jayakumar, D. (2021). GIS-Based Drought Assessment in Climate Change Context: A Case Study for Sone Command, Bihar, J. Inst. Eng. India Ser. A (March 2021) 102(1):199–213.
[17] Linglin Zeng et al. (2014). IOP Conf. Ser.: Earth Environ. Sci. 17 (2014) 012017.
[18] Liu, X., Xu, X., Yu, M., Lu, J. (2016). Hydrological drought forecasting and assessment based on the standardized stream index in the Southwest China, Procedia Engineering 154 (2016) 733-737.
[19] Mahajan, D.R., Dodamani, B.M. (2015). Trend Analysis of Drought Events Over Upper Krishna Basin in Maharashtra, Aquatic Procedia 4 (2015) 1250 – 1257.
[20] Marshet Nigatu Gebeyehu. (2019). Remote Sensing and GIS Application in Agriculture and Natural Resource Management. Int J Environ Sci Nat Res. 2019; 19(2): 556009. DOI: 10.19080/IJESNR.2019.19.556009.
[21] Noichaisin, L., Buranaprattheprat, A., Manthachitra, V. and Intarawichian, N. (2020). Drought risk area assessment using GIS in Sa Kaeo Province, Thailand. International Journal of Agricultural Technology 16(3): 655-666.
[22] Oğuz, K., Pekin, M.A., Çamalan, G. (2021). Drought Analysis of Muğla City for 1960-2018 Period, Journal of Natural Hazards and Environment, ; 7(1): 89-100, DOI: 10.21324/dacd.774955. (in Turkish)
[23] Opolot, E. (2013). Application of Remote Sensing and Geographical Information Systems in Flood Management: A Review, Research Journal of Applied Sciences, Engineering and Technology 6(10): 1884-1894, 2013.
[24] Önöz, B., Oğuz, B. (1996). İstanbul Su Temini Sistemi ve Kuraklık Analizi, İMO Teknik Dergi, 1996, 1083-1090, Yazı 83.
[25] Parmar, M., Shukla, S., Kalubarme, M.H. (2019). Impact of Climate Change and Drought Analysis on Agriculture in Sabarkantha District Using Geoinformatics Technology, Global Journal Of Engineering Science And Researches, 6(5): May 2019, ISSN 2348 – 8034.
[26] Patel, N.R., Chopra, P., Dadhwal, V.K. (2007). Analyzing spatial patterns of meteorological drought using standardized precipitation index, Meteorol. Appl. 14: 329–336 (2007).
[27] Paudel, P. R., Gautam, S., Joshi, S.P., Khatri, S., Parajuli, U. (2021). Agricultural Drought Vulnerability Assessment of Tanahun District, Nepal, FIG e-Working Week 2021, Virtually in the Netherlands, 21–25 June 2021.
[28] Piedelobo, L., Ortega-Terol, D., del Pozo, S., Hernández-López, D., Ballesteros, R., Moreno, M.A., Molina, J., González-Aguilera, D. (2018). HidroMap: A New Tool for Irrigation Monitoring and Management Using Free Satellite Imagery, International Journal of Geo-Information, 7, 220; doi:10.3390/ijgi7060220.
[29] Reis, G.A., Souza Filho, F.A., Nelson, D.R., Rocha, R.V., Silva, S.M.O. (2020). Development of a drought vulnerability index using MCDM and GIS: study case in São Paulo and Ceará, Brazil, Natural Hazards, https://doi.org/10.1007/s11069-020-04247-7.
[30] Roy, P.S., Behera, M.D., Srivastav, S.K. (2017). Satellite Remote Sensing: Sensors, Applications and Techniques, Proc. Natl. Acad. Sci., India, Sect. A Phys. Sci. (October–December 2017) 87(4):465–472.
[31] Shah, R., Bharadiya, N., Manekar, V. (2015). Drought Index Computation Using Standardized Precipitation Index (SPI) Method For Surat District, Gujarat. Aquatic Procedia 4 (2015) 1243–1249.
[32] Sırdaş, S., Şen, Z. (2003). Meteorolojik kuraklık modellemesi ve Türkiye uygulaması, İTÜDERGİSİ/d, Mühendislik, Cilt:2, Sayı:2,95-103, Nisan 2003.
[33] Sisir P, K Balan. (2014). Flood Risk Mapping of Kadalundi River Basin using GIS, International Journal of Scientific & Engineering Research, Volume 5, Issue 7, July-2014.
[34] Sun, C., Choy, S., Chua, Z., Aitkenhead, I.; Kuleshov, Y. (2020). Geographic Information System for Drought Risk Mapping in Australia-Drought Risk Analyser Web App, The International Archives of the Photogrammetry, Remote Sensing and Spatial Information Sciences, Volume XLIV-3/W1-2020, 2020, Gi4DM 2020 – 13th GeoInformation for Disaster Management conference, 30 November–4 December 2020, Sydney, Australia (online)
[35] Suresh Babu, A.V., Shanker, M., Venkateshwar Rao, V. (2012). Satellite Derived Geospatial Irrigation Performance Indicators for Benchmarking Studies of Irrigation Systems, Advances in Remote Sensing, 2012, 1, 1-13.
[36] Topçu E., Karaçor F., "Drought Analysis Of Erzurum Station By Using Standardized Precipitation Evapotranspiration Index And Aggregated Drought Index", Journal of Polytechnic, 24(2): 565-574, (2021). (in Turkish)
[37] Wang, K., Li, Q., Yang, Y., Zeng, M., Li. P., Zhang, J. (2015). Analysis of spatio-temporal evolution of droughts in Luanhe River Basin using different drought indices, Water Science and Engineering 2015, 8(4): 282-290.

The Non-symmetric Receding Contact Problem of Functionally Graded Layer Resting on Quarter Planes

G. Adıyaman[1] and E. Öner[2]

[1]*Karadeniz Technical University, Trabzon, Turkey, gadiyaman@ktu.edu.tr*

[2]*Bayburt University, Bayburt, Turkey, eonerbayburt.edu.tr*

Abstract

In this study, the non-symmetric receding contact problem of a functionally graded (FG) layer resting on two quarter planes (QPs) and loaded by a flat rigid block is considered. It is assumed that, the contact surfaces are frictionless and only compressive normal tractions can be transmitted through contact surfaces; the influence of the gravity is neglected in the solution of the problem. The problem is reduced into a set of singular integral equations in which contact distances and contact pressures are the unknowns using the theory of elasticity and Fourier integral transform techniques. By the help of corresponding Gauss-Chebyshev quadrature and an iterative scheme, the unknowns of the problem are found. A parametric study is carried out to investigate the influence of material properties, geometry and loading of the problem on the contact distances and contact pressures. Obtained results provide a deep insight into the non-symmetric contact mechanism between FG layer and QPs.

Keywords: non-symmetric contact, receding contact, functionally graded layer, quarter plane, Fourier integral transform

1. Introduction

Although the expressions of elasticity theory are complex and complicated, it gives better results compared to basic theory. The solution of strain and stress problems of engineering problems using elasticity theory has been increased parallel to the improvements in computer technology and numerical solution methods. Similarly, there has been a significant increase in contact mechanics problems.

In literature, the contact problems of layered mediums are approached generally in two ways. In the first way, the effect of the gravity is considered and the separation occurs in a finite zone. However, the effect of the gravity is neglected in the second way problems and the separation distance goes to infinite. These problmes are called receding contact in literature and this study is an example of this way. Some of the studies in the literature for receding contact can be summarized as follows.

The contact problem of an infinite layer resting on a half-plane and loaded with a distributed load was investigated by Keer at. al. [1]The contact problem of a layer resting on two quarter planes is studied by Ratwani and Erdogan [2]. A compressive load was applied to the layer through a frictionless rigid block. Dempsey at. al. [3] investigated the contact problem of layer on a Winkler foundation under different loadings. Birinci and Erdol [4] studied the frictionless contact problem of two layers resting on simple support. The contact problem for an anisotropic elastic medium consisting of a layer and a half plane is investigated by Kahya [5] et. al.. The contact problem of two layers lying on rigid foundation was investigated by Çömez et. al. [6]. The top of the medium was loaded using a rigid block.

The materials research community has recently been exploring the possibility of using new concepts in coating or layer design such as functionally graded materials (FGMs) in which material properties varies smoothly along a spatial direction, as an alternative to the conventional homogenous coating and layer [7]. These materials are used in various applications, including ball and roller bearings, gears, cutting edges, gas turbines, electromagnetic engineering and space vehicles, mostly to provide abrasion resistance and high-temperature endurance. Such a wide range of application has resulted in the inevitable use of FGMs in contact mechanics. Several studies have examined the contact problems of layers made from FGMs.

A receding contact plane problem for a functionally graded layer pressed against a homogeneous half space was analyzed by El-Borgi et al [7]. Rhimi et al. [8] considered the axisymmetric problem of a frictionless receding contact between an elastic functionally graded layer and a homogeneous half-space when the two bodies were pressed together and double receding contact between a rigid stamp of axisymmetric profile, an elastic functionally graded layer and a homogeneous half space. Chen and Chen [9] studied the contact behaviors of a graded layer resting on a homogeneous half space and pressed by a rigid stamp. Comez [10] considered a contact problem for a functionally graded layer loaded by means of a rigid stamp and supported by a Winkler foundation. Yan and Li [11]considered double receding contact plane problem between a functionally graded layer and an elastic layer. The receding contact of FG layer resting on quarter planes was investigated by Adiyaman et. al. [12]. Yan and Mi [13] examined double contact analysis of multilayered elastic structures involving functionally graded materials. The receding contact between a two-layer inhomogeneous laminate and a half-plane was considered by Liu et. al. [14].

Although the receding contact problem of a layered mediums have been studied, the problems in which the layers rest on quarter planes have not been adequately investigated and unsymmetrical contact problem of a FG layer problems including quarter planes has not been studied, yet. In this study, the unsymmetrical receding contact problem of a layer resting on a quarter planes is considered.

2. Definition of the Problem

As shown in Fig. 1, consider the unsymmetrical frictionless receding contact problem of infinitely long functionally graded (FG) layer resting on a quarter planes. Poisson's ratio of the FG layer ν is taken as constant and the shear modulus G depends on the depth of the FG layer y as follows:

$$G(y) = G_0 \exp(\beta y) \qquad (0 \le y \le h) \tag{1}$$

where G_0 is the shear modules at the bottom of the layer $y = 0$ and β_i is the non-homogeneity parameter controlling the variation of the shear module in the graded layer. Right and left quarter planes are homogenous and have constant Poisson's ratio ν_i and shear modulus G_i (i=R (right), L(left)). The top of the layer is subjected to a unsymmetrical concentrated load by means of a rigid flat block with a width of ($b_E - b_S$). The problem is investigated as a plane strain problem and the body forces are neglected.

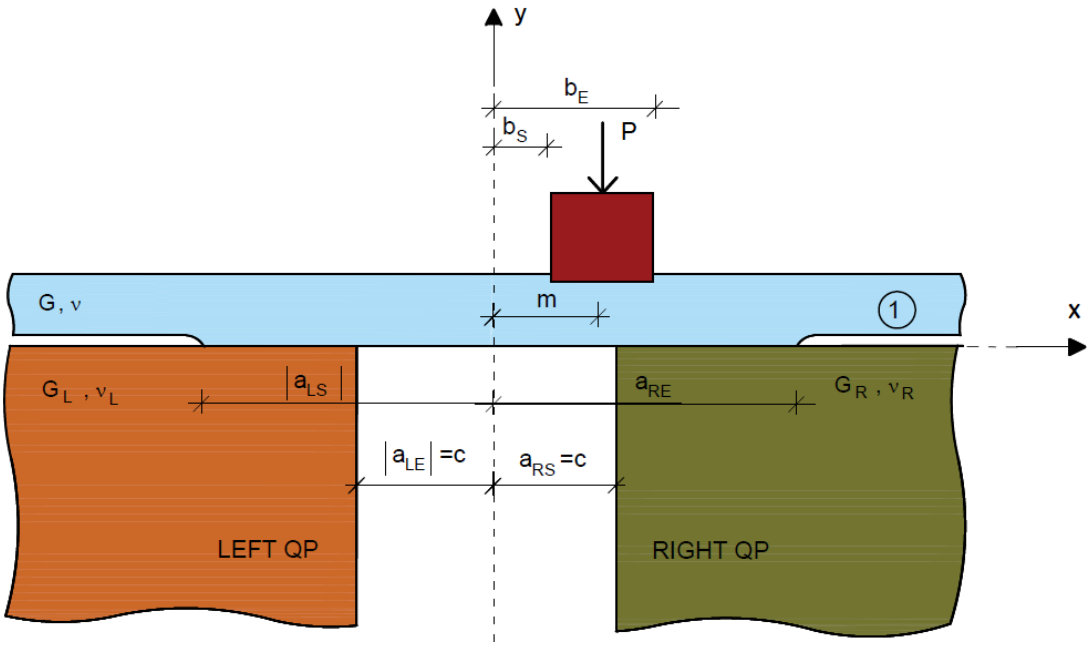

Figure 1. The geometry and loading case of the contact problem

Assuming that the FG layers are isotropic at every point, equilibrium equations, the strain-displacement relationships and the linear elastic stress-strain law, respectively, are given follows.

$$\frac{\partial \sigma_x}{\partial x}+\frac{\tau_{xy}}{\partial y}=0, \qquad \frac{\partial \tau_{yx}}{\partial x}+\frac{\partial \sigma_y}{\partial y}=0 \tag{2a,b}$$

$$\varepsilon_{xx}=\frac{\partial u}{\partial x}, \quad \varepsilon_{yy}=\frac{\partial v}{\partial y}, \quad \varepsilon_{xy}=\frac{1}{2}\left(\frac{\partial u}{\partial y}+\frac{\partial v}{\partial x}\right) \tag{3a-c}$$

$$\sigma_x=\frac{\mu(y)}{\kappa-1}\left[(1+\kappa)\varepsilon_{xx}+(3-\kappa)\varepsilon_{yy}\right], \ \sigma_y=\frac{\mu(y)}{\kappa-1}\left[(3-\kappa)\varepsilon_{xx}+(1+\kappa)\varepsilon_{yy}\right], \ \tau_{xy}=2\mu(y)\varepsilon_{xy} \tag{4a-c}$$

In Eq. (2-4), u and v are the x and y components of the displacement field, respectively; σ_x, σ_y and τ_{xy} are the components of the stress field in the same coordinate system; ε_x, ε_y and ε_{xy} are the corresponding components of the strain field; κ is a material property defined as $\kappa=3-4\nu$ for plane strain problems; and g is gravitational acceleration. Combining Eqs. (1)-(4), the following two-dimensional Navier's equations are obtained:

$$(\kappa+1)\frac{\partial^2 u}{\partial x^2}+(\kappa-1)\frac{\partial^2 u}{\partial y^2}+2\frac{\partial^2 v}{\partial x\partial y}+\beta(\kappa-1)\frac{\partial u}{\partial y}+\beta(\kappa-1)\frac{\partial v}{\partial x}=0 \tag{5}$$

$$(\kappa-1)\frac{\partial^2 v}{\partial x^2}+(\kappa+1)\frac{\partial^2 v}{\partial y^2}+2\frac{\partial^2 u}{\partial x\partial y}+\beta(3-\kappa)\frac{\partial u}{\partial x}+\beta(\kappa+1)\frac{\partial v}{\partial y}=0 \tag{6}$$

Eqs. (5) and (6) consist of partial differential equations. These equations can be converted into ordinary differential equations using Fourier integral transform techniques. The displacement components may be written as follows,

$$u(x,y)=\frac{1}{\sqrt{2\pi}}\int_{-\infty}^{\infty}\phi(\xi,y)e^{-i\xi x}d\xi, \qquad v(x,y)==\frac{1}{\sqrt{2\pi}}\int_{-\infty}^{\infty}\psi(\xi,y)e^{-i\xi x}d\xi \tag{7a,b}$$

where $\phi(\xi,y)$ and $\psi(\xi,y)$ are the Fourier transforms of u and v with respect to the x-coordinate, respectively. After substituting corresponding Fourier transforms of u and v into (5) and (6) and solving obtained ordinary differential equations, following displacement and stress components can be obtained for FG layer as follows.

$$u(x,y)=\frac{2}{\pi}\int_{-\infty}^{\infty}\sum_{j=1}^{4}A_j\,e^{n_j y}e^{-i\xi x}d\xi \tag{8}$$

$$v(x,y)=\frac{2}{\pi}\int_{-\infty}^{\infty}\sum_{j=1}^{4}A_j\,m_j\,e^{n_j y}e^{-i\xi x}d\xi \tag{9}$$

$$\sigma_x\ (x,y)=\frac{2\mu_0\,e^{\beta y}}{\pi(\kappa-1)}\int_{-\infty}^{\infty}\sum_{j=1}^{4}A_j\left[(3-\kappa)m_j n_j+\xi(\kappa+1)\right]e^{n_j y}e^{-i\xi x}d\xi \tag{10}$$

$$\sigma_y(x,y)=\frac{2\mu_0\,e^{\beta y}}{\pi(\kappa-1)}\int_{-\infty}^{\infty}\sum_{j=1}^{4}A_j C_j e^{n_j y}\ e^{-i\xi x}d\xi \tag{11}$$

$$\tau_{xy}(x,y)=\frac{2\mu_0 e^{\beta y}}{\pi}\int_{-\infty}^{\infty}\sum_{j=1}^{4}A_j D_j e^{n_j y}e^{-i\xi x}d\xi \tag{12}$$

in which, A_j ($j=1,\ldots,4$) are unknown coefficients; n_j, m_j, C_j and D_j are known functions and κ is a material constant defined as $\kappa=3-4\upsilon$ for plane strain problems. The boundary conditions of the problem can be defined as follows,

$$\sigma_y(x,y=h)=\begin{cases}-p & ; \quad (b_S\le x<b_E)\\ 0 & ; \quad other\end{cases} \tag{13}$$

$$\tau_{xy}(x,y=h)=0 \qquad (0\le x<\infty) \tag{14}$$

$$\sigma_y(x,y=0)=\begin{Bmatrix}-p_L & ; & (a_{LS}\le x<a_{LE})\\ -p_R & ; & (a_{RS}\le x<a_{RE})\\ 0 & ; & other\end{Bmatrix} \tag{15}$$

$$\tau_{xy}(x,y=0)=0 \qquad (0\le x<\infty) \tag{16}$$

$$\frac{\partial}{\partial x}v(x,y=h)=0 \qquad (b_S<x<b_E) \tag{17}$$

$$\frac{\partial}{\partial x}\left[v(x,y=0)-v_L(x,y=0)\right]=0 \qquad (a_{LS}<x<a_{LE}) \tag{18}$$

$$\frac{\partial}{\partial x}\left[v(x,y=0)+v_R(x,y=0)\right]=0 \qquad (a_{RS}<x<a_{RE}) \tag{19}$$

where, p , p_R and p_L are unknown contact pressures between the rigid block and layer, between layer and right quarter plane and between layer and left quarter plane, respectively; v_R and v_L are the displacement functions of the right and left quarter planes, respectively, and can be defined as in [12],

$$\frac{\partial v_i(x,0)}{\partial x}=-\frac{1}{\pi}\frac{(\kappa_i+1)}{4G_i}\frac{1}{x-c}\int_{a_{iS}}^{a_{iE}}p_i(t_i)\left\{\frac{1}{\log\left(\dfrac{x-c}{t_i-c}\right)}+K_i-\frac{\pi^2}{\pi^2-4}\right\}dt_i, \qquad i=R,L \tag{20}$$

in which, K_i 's (i=R,L) is known kernel function and κ_i is a material constant defined as $\kappa_i=3-4\upsilon_i$ for plane strain problems. The solution of the problem should also satisfy following equilibrium conditions,

$$\int_{-\infty}^{\infty}p(x)dx=\int_{b_S}^{b_E}p(t)dt=P \tag{22}$$

$$\int_{a_{LS}}^{a_{LE}}p_L(t_L)dt_L+\int_{a_{RS}}^{a_{RE}}p_R(t_R)dt_R=P \tag{23}$$

$$\int_{b_S}^{b_E}tp(t)dt+\int_{a_{LS}}^{a_{LE}}t_Lp_L(t_L)dt_L+\int_{a_{RS}}^{a_{RE}}t_Rp_R(t_R)dt_R=0 \tag{24}$$

Eqs. (21,22) are correspond to force equilibrium whereas Eq. (23) is correspond to moment equilibrium of the system.

Applying boundary conditions (**Hata! Başvuru kaynağı bulunamadı.**-16) to stress displacement fields (10-12), unknowns A_j (j=$1,\ldots,4$) in displacement and stress fields in terms of contact pressures and contact distances can be obtained (8-12). By the help of unused boundary conditions (17-19), three dimensionless singular integral equations, which will be used to find unknown contact distances and pressures, can be obtained as in the following form,

$$\int_{b_S}^{b_E}pK_i(t,x_i)dt+\int_{a_{RS}}^{a_{RE}}p_RK_{Ri}(t_R,x_i)dt_R+\int_{a_{LS}}^{a_{LE}}p_LK_{Li}(t_L,x_i)dt_L=0, \qquad (i=1,2,3) \tag{25}$$

in which, K_{ij} 's (i=$1,2$; j=$1,2$) are knowns kernel functions. Eqs. (22-25) can be converted into algebraic equation system which consists of $3N+2$ equations and $3N+2$ unknowns by the help of appreciate Gauss-Chebyshev integral formulations and unknowns of this system, which are the contact pressures ($3N$) and the contact

distances (*2*), may be found. Although obtained algebraic equation system is linear in term of contact pressures, contact distances cause a nonlinearity. Therefore an iterative solution method is needed to solve the system.

3. Numerical Results

The geometry and loading case of the problem are given in Fig. 1. Note that all quantities are given as dimensionless. In the solutions, a new parameter G_h is introduced such that G_h is the shear modules of the layer at $y = h$. In this case, non-homogeneity parameter can be described as follows.

$$\beta = \frac{\ln(G_h / G_0)}{h} \tag{26}$$

Table 1 shows that the variation of contact distances (a_{RE}/h, a_{LS}/h) for various loading positions ($m/h = \frac{b_E + b_S}{2}$) and the ratios of shear modulus of the quarter planes (G_R/G_L). As it is expected, the end of the contact for right quarter plane (RQP), a_{RE}/h, and the start of the contact for the left quarter plane (LQP), a_{LS}/h, moves to the right as the loading position, *m/h*, moves to the right. As the shear modules of the LQP is increased, the contact length between the layer and the LQP is also increased whereas the contact length between the layer and the RQP is decreased until the loading passes the corner of the LQP (*m=0.5*) and after that it also increases. For the symmetrical problem case ($G_R/G_L = 1,\ m/h = 0$), symmetrical contact distances are obtained.

The change in contact distances for different values of loading position and the ratios of the shear modulus at the top and the bottom of the layer (G_h/G_0) is given in Table 2. It can be seen from the table, the position change in loading cause a similar change as in the Table 1 in which, as the load move to the right, a_{RE}/h increases while a_{LS}/h decreases. If the shear modulus of the top of the layer is increased relative to the bottom, in other words, β increases, both of the contact distances a_{RE}/h and a_{LS}/h decrease. Since any change in the shear modulus of the layer does not affect the symmetry of the problem with respect to *x* axis, symmetrical loadings have reverse symmetrical contact distances, *e.g.* $a_{RE}/h\big|_{m=-0.5} = a_{LS}/h\big|_{m=0.5}$

Fig. 2 and 3 presents the variation of the contact stresses between the rigid block and the FG layer (p) and between the FG layer and quarter planes (p_R, p_L), respectively, for various ratios of the shear modules of the quarter planes (G_R/G_L) when the load is applied at the top of the edge of the RQP. It can be seen from the Fig.2 , the change in G_R/G_L ratio does no cause any significant change in stress distribution. It can be seen from Fig. 3 that G_R/G_L ratio is more effective in the distribution of p_L. The contact stresses between FG layer and RQP has a less steep descent at the near of the edge of the quarter plane because of the rigid block at the top of the layer. Since problem is unsymmetrical, the contact stress distributions are also unsymmetrical.

The change in the contact stresses between the rigid block and the FG layer and between the FG layer and quarter planes for the shear modules of the top and bottom of the layer (G_h/G_0) are shown in Fig 4 and 5, respectively, when the load is applied at the center of the gap between quarter planes. Similar to Fig. 2, G_h/G_0 also does not have a major effect on p. The variation of G_h/G_0 results in similar changes in contact stresses due to symmetry. Since both the loading and the material properties are symmetric with respect to *x=0* axis, p in itself and p_R and p_L among themselves have a symmetric stress distribution with respect to symmetry axis.

Table 1. The variation of contact distances for various loading positions and the ratios of shear modulus of the quarter planes ($G_0 / G_R = 1$, $\kappa = \kappa_R = \kappa_L = 2$, $b_E - b_S = 0.2$)

G_R / G_L	*m/h*									
	-1		-0.5		0		0.5		1	
	a_{RE} / h	a_{LS} / h	a_{RE} / h	a_{LS} / h	a_{RE} / h	a_{LS} / h	a_{RE} / h	a_{LS} / h	a_{RE} / h	a_{LS} / h
0.1	0.6278	-2.3251	0.7333	-1.8410	1.4373	-0.9132	1.8410	-0.7333	2.3251	-0.6278
0.5	0.7189	-2.3204	0.8879	-1.8243	1.4031	-1.1415	1.8243	-0.8879	2.3204	-0.7189
1	0.8225	-2.3150	1.0554	-1.8061	1.3703	-1.3703	1.8061	-1.0554	2.3150	-0.8225
2	10.090	-2.3051	1.3385	-1.7754	1.3227	-1.7227	1.7754	-1.3385	2.3051	-1.0090
10	20.362	-2.2541	2.6496	-1.6470	1.1729	-3.1124	1.6470	-2.6496	2.2541	-2.0362

Table 2. The change in contact distances for different values of loading position and the ratios of the shear modulus at the top and the bottom of the layer ($G_0 / G_R = 1$, $\kappa = \kappa_R = \kappa_L = 2$, $b_E - b_S = 0.2$)

G_h / G_0	*m/h*									
	-1		-0.5		0		0.5		1	
	a_{RE} / h	a_{LS} / h	a_{RE} / h	a_{LS} / h	a_{RE} / h	a_{LS} / h	a_{RE} / h	a_{LS} / h	a_{RE} / h	a_{LS} / h
0.25	1.0066	-2.6598	1.2963	-2.1574	1.6837	-1.6837	2.1574	-1.2963	2.6598	-1.0066
0.5	0.9022	-2.4773	1.1607	1.9707	1.5126	-1.5126	1.9707	-1.1607	2.4773	-0.9022
1	0.8225	-2.3150	1.0554	-1.8061	1.3703	-1.3703	1.8061	-1.0554	2.3150	-0.8225
2	0.7660	-2.1847	0.9818	-1.6760	1.2649	-1.2649	1.6760	-0.9818	2.1847	-0.7660
4	0.7296	-2.1002	0.9396	-1.5894	1.2001	-1.2001	1.5894	-0.9396	2.1002	-0.7296

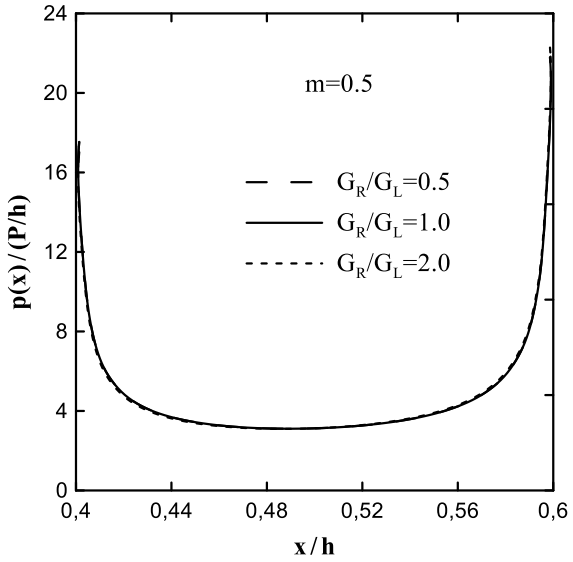

Figure 2. The variation of contact stresses between the rigid block and the layer for various ratios of the shear modules of the quarter planes ($G_0 / G_h = 1,\ G_0 / G_R = 1,\ \kappa = \kappa_R = \kappa_L = 2,\ b_E - b_S = 0.2$)

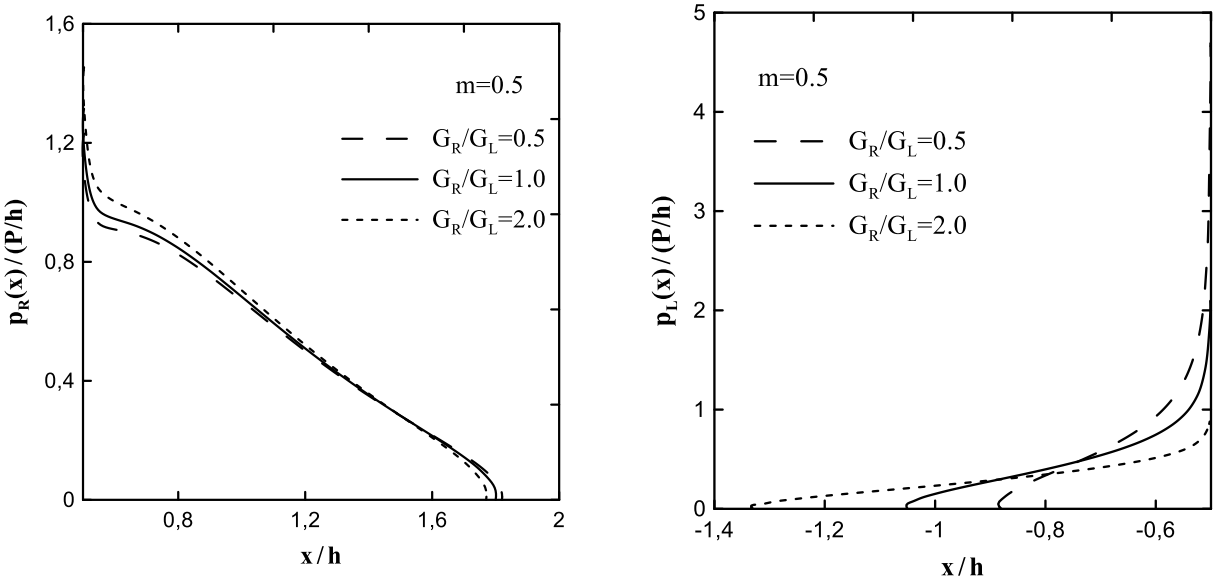

Figure 3. The variation of contact stresses between the layer and the RQP and LQP for various ratios of the shear modules of the quarter planes ($G_0 / G_h = 1,\ G_0 / G_R = 1,\ \kappa = \kappa_R = \kappa_L = 2,\ b_E - b_S = 0.2$)

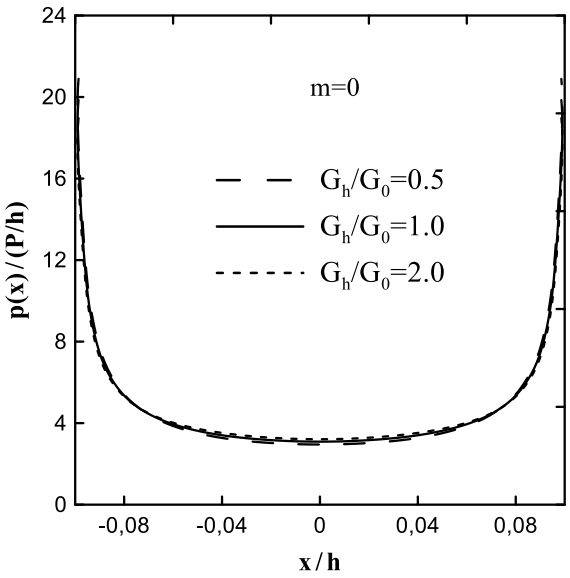

Figure 4. The variation of contact stresses between the rigid block and the layer (p) for various ratios of the shear modules of the top and bottom of the layer ($G_R / G_L = 1$, $G_0 / G_R = 1$, $\kappa = \kappa_R = \kappa_L = 2$, $b_E - b_S = 0.2$)

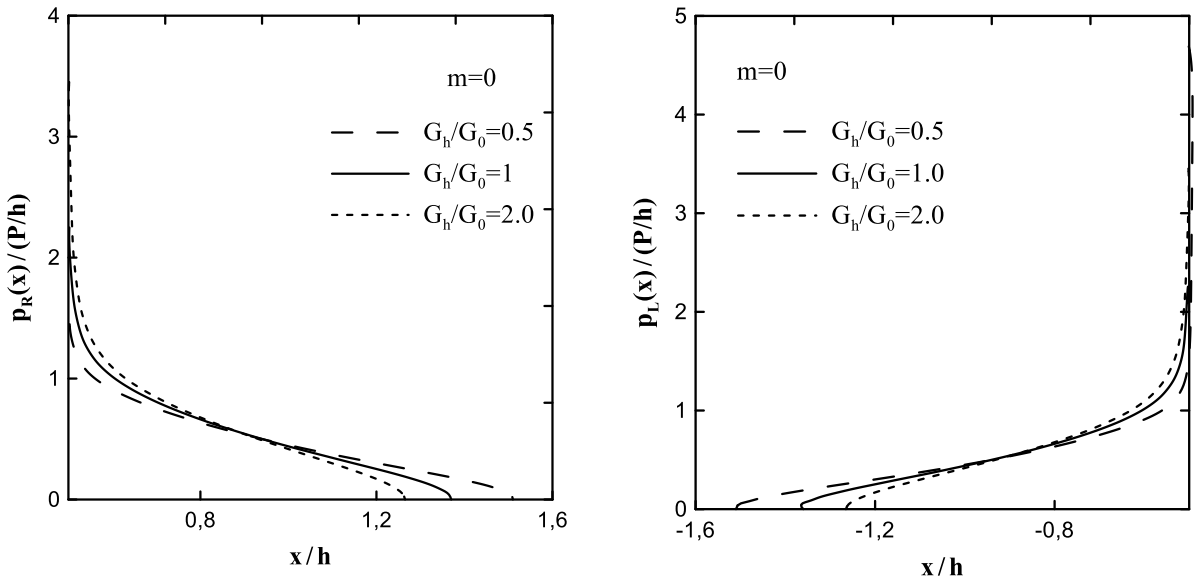

Figure 5. The variation of contact stresses between the layer and the RQP (p_R) and LQP (p_L) for various ratios of the shear modules of the top and bottom of the layer ($G_R / G_L = 1$, $G_0 / G_R = 1$, $\kappa = \kappa_R = \kappa_L = 2$, $b_E - b_S = 0.2$)

References

1. Keer LM, Dundurs J, Tsai KC (1972) PROBLEMS INVOLVING A RECEDING CONTACT BETWEEN A LAYER AND A HALF SPACE. J Appl Mech-Trans ASME 39 (4):1115-1120. doi:10.1115/1.3422839
2. Erdogan F, Ratwani M (1974) CONTRACT PROBLEM FOR AN ELASTIC LAYER SUPPORTED BY 2 ELASTIC QUARTER PLANES. J Appl Mech-Trans ASME 41 (3):673-678. doi:10.1115/1.3423369
3. Dempsey JP, Zhao ZG, Minnetyan L, Li H (1990) PLANE CONTACT OF AN ELASTIC LAYER SUPPORTED BY A WINKLER FOUNDATION. J Appl Mech-Trans ASME 57 (4):974-980. doi:10.1115/1.2897670
4. Birinci A, Erdol R (2001) Continuous and discontinuous contact problem for a layered composite resting on simple supports. Struct Eng Mech 12 (1):17-34. doi:10.12989/sem.2001.12.1.017
5. Kahya V, Ozsahin TS, Birinci A, Erdol R (2007) A receding contact problem for an anisotropic elastic medium consisting of a layer and a half plane. Int J Solids Struct 44 (17):5695-5710. doi:10.1016/j.ijsolstr.2007.01.020
6. Comez I, Birinci A, Erdol R (2004) Double receding contact problem for a rigid stamp and two elastic layers. Eur J Mech A-Solids 23 (2):301-309. doi:10.1016/j.euromechsol.2003.09.006
7. El-Borgi S, Abdelmoula R, Keer L (2006) A receding contact plane problem between a functionally graded layer and a homogeneous substrate. Int J Solids Struct 43 (3-4):658-674. doi:10.1016/j.ijsolstr.2005.04.017
8. Rhimi M, El-Borgi S, Ben Said W, Ben Jemaa F (2009) A receding contact axisymmetric problem between a functionally graded layer and a homogeneous substrate. Int J Solids Struct 46 (20):3633-3642. doi:10.1016/j.ijsolstr.2009.06.008
9. Chen PJ, Chen SH (2012) Contact behaviors of a rigid punch and a homogeneous half-space coated with a graded layer. Acta Mech 223 (3):563-577. doi:10.1007/s00707-011-0581-0
10. Comez I (2013) Contact problem of a functionally graded layer resting on a Winkler foundation. Acta Mech 224 (11):2833-2843. doi:10.1007/s00707-013-0903-5
11. Yan J, Li X (2015) Double receding contact plane problem between a functionally graded layer and an elastic layer. Eur J Mech A-Solids 53:143-150. doi:10.1016/j.euromechsol.2015.04.001
12. Adiyaman G, Birinci A, Oner E, Yaylaci M (2016) A receding contact problem between a functionally graded layer and two homogeneous quarter planes. Acta Mech 227 (6):1753-1766. doi:10.1007/s00707-016-1580-y
13. Yan J, Mi C (2017) Double contact analysis of multilayered elastic structures involving functionally graded materials. Arch Mech 69 (3):199-221
14. Liu ZX, Yan J, Mi CW (2018) On the receding contact between a two-layer inhomogeneous laminate and a half-plane. Struct Eng Mech 66 (3):329-341. doi:10.12989/sem.2018.66.3.329

Investigation Of The Use Of Teflon (Ptfe), Lead, Brass And Carbon Fiber Plates As Friction Pads In Rotational Friction Dampers

E. SUCİ[1] and N. KARA [1]

[1] Konya Technic University, Konya/Turkey, esuci@ktun.edu.tr, nkara@ktun.edu.tr

Abstract* - In terms of civil engineering buildings, earthquake mitigation is a rapidly developing new research area. In general, it is aimed to reduce the effects of earthquakes by consuming some of the earthquake energy acting on the buildings through various mechanisms, so that less earthquake energy will affect the building and smaller accelerations will occur in the building. One of these mechanisms, rotational friction dampers, are mechanisms that convert kinetic energy into thermal energy, work with a rotational deformation mechanism, and consist of steel plates and friction pads, which are clamped with high-strength bolts. In order to improve the damping behavior of these dampers operating according to the Coulomb friction law ($Ff = \mu \times N$), it is necessary to steadily increase the friction coefficient (μ) or the force acting perpendicular to the friction surfaces (N). The dampers should be stable in increasing displacements while operating, maintain their capacity under repetitive cyclic loads, dissipate sufficient energy and should not decrease in resistance. In our experimental study, different friction pad materials have been tried to improve the friction coefficient in rotational friction dampers. Energy dissipation behavior was observed by clamping the dampers formed with Teflon (PTFE), lead, brass and carbon fiber friction pads with bolts clamped at certain torques. By comparing the test results obtained, the suitability of the use of these materials as friction pads was determined.

Keywords* - Friction damper, friction pad, earthquake mitigation, energy dissipation.

I. INTRODUCTION

Although the subject of earthquake mitigation in terms of civil engineering structures is a relatively new research field, it is a rapidly developing field in recent years. The tragic consequences of the devastating earthquakes that Turkey has encountered from time to time due to its location on the Alpine-Himalayan seismic belt and the major earthquakes that occurred in other countries have revealed that the way buildings and bridges respond to earthquakes is of great importance, both in terms of human and economic factors. During the past years, great efforts have been made to develop various control approaches in the design of civil engineering structures to increase their safety and reliability against severe earthquakes. In general, seismic control techniques can be divided into two categories, these are strengthening methods and seismic mitigation methods. In strengthening methods, which is one of these approaches, it is possible to resist earthquake forces by increasing the rigidity of the structure. In the new approach, it is aimed to consume some of the earthquake energy acting on the structure with various mechanisms and methods, and to create less earthquake energy and smaller accelerations that affect the structure.

In recent years, various vibration control systems have been developed. These systems can be divided into 3 groups: active, semi-active and passive control. Active control systems are systems that require high technical knowledge, a large amount of energy to operate the system, and the presence of well-trained employees who can control the system after the system works. Active systems have sensors that read the information of an earthquake during an earthquake, and a computer that evaluates the data coming from the sensors and informs how the system should behave. In semi-active systems, less energy is required to operate the system and it is easier to use. Passive control systems, on the other hand, do not require external energy or operators. In passive control systems, devices are used to increase the rigidity and damping of structures. There are 3 main types of passive control. These are building base isolator systems, tuned mass dampers and energy distribution (damping) dampers, which include 4 main types. The types of dampers are listed as dampers containing viscous liquids, visco-elastic dampers, metallic yielding dampers and friction dampers.[2] In general for passive control systems, several conditions must be met for these systems to be acceptable:

- Must be stable for required design displacements,
- Its capacity should not decrease under repetitive cyclic loading,
- Must be able to distribute a sufficient amount of energy,
- Its resistance should not decrease under increasing displacements.

The friction damper is based on the Coulomb friction law, which expresses the general friction force by the formula 1.

$$Ff = \mu x N \tag{1}$$

The variable μ in the formula is the coefficient of friction and N is the normal force acting on the contact area.

According to this formula, it is necessary to overcome the frictional force Ff in order to move the two rubbing bodies into motion. Frictional forces resulting from the relative motion of two contacting surfaces are a source of energy dissipation. Sometimes, this phenomenon is an undesirable effect of design, but it can also be used intentionally to simply and cost-effectively increase the damping of a particular system. Friction-based dampers are mechanisms consisting of steel plates and friction pads, which are tightened with high-strength bolts with axial or rotational deformation mechanism, enabling the conversion of kinetic energy into thermal energy.

The development of friction dampers began with the invention of internal combustion engines in the 1880s and the spread of the automobile in the early 1900s with the discovery of the pneumatic rubber wheel. Before the invention of automobiles, elliptical and semi-elliptical leaf springs used in horse-drawn carriages provided a soft suspension, but these vehicles did not have a special device for damping. The friction between the steel plates arranged one after another in the leaf springs provided a natural damping (Figure 1). Since there were no roads developed for motor vehicles in the early days, an excessively rough wheel rolling surface caused too much vibration inside the vehicle for motor vehicles that were traveling relatively fast compared to horse-drawn carriages. Over time, as the speed of cars gradually increased, the excess of vibrations became an important problem both in terms of comfort and in terms of vehicle control, dampers began to be developed that would absorb high-frequency vibrations in addition to leaf springs. [1]

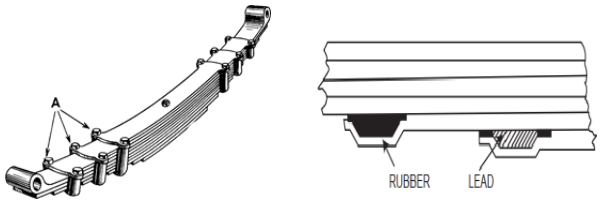

a) b)

Figure 1. a) Leaf springs, b) Detail parts placed to control friction in the leaf spring [1]

Friction dampers dissipate energy through friction at the interface between two rigid plates. One of the friction dampers is slot-bolt dampers, in which several steel plates are bolted together with a certain clamping force. [7;8,2] The compressive force is such that the slip occurs at a predetermined frictional force. Special materials can be used to obtain a constant coefficient of friction at the sliding interface between the plates. In the configuration known as the Pall friction damper, consists of a rectangular bolted plates mechanism connected in the center of cross braces. In the building frame under lateral load, two of the braces are deformed to be subjected to tension and the other two to compression. This causes the rectangular damper to deform into a parallelogram. As the damper changes shape, the friction between the plates causes energy dissipation in the bolted connections. [7;8,6] Another friction damper is a cylindrical friction damper where it dissipates energy through sliding friction between copper friction pads and a steel cylinder. Copper pads are impregnated with graphite to lubricate the sliding surface and maintain a constant coefficient of friction. [7;8]

Mualla (2000) designed a new friction damper device to dissipate the energy acting on the building in an earthquake to increase building safety. The friction damper can be used to retrofit existing buildings or to design new buildings. The friction damper has been tested to verify its characteristics and performance. This device consists of several steel plates rotating in opposite directions, creating friction between its parts. The friction damper mounted on the steel frame model undergoes geometric deformation when the frame makes lateral displacement, resulting in significantly controlled energy distribution. Different materials such as brass or composite friction pad material with a friction coefficient of 0.35-0.45 are used as friction pads at the interfaces between the internal parts of the device. This device showed a very stable hysteretic behavior without degradation over many cycles, especially when using composite friction pad material. Consequently, the use of additional damping provided by this friction damper dissipates a large amount of kinetic energy in a structure, thus eliminating the need for structural ductility while the structure remains undamaged elastic. [3-5]

II. MATERIAL AND METHODS

The phenomenon that most influences the role of the friction damper in consuming energy is the friction force. The friction force is proportional to the normal force acting on the friction surface and the coefficient of friction. The friction coefficient varies depending on the type of material and surface roughness. In previous studies, materials such as brass, bronze, brake disc composites, oily leather and wood were used as friction materials. [7] In the studies carried out in recent years, different materials have been tried in order to prevent the friction material from being affected by the heat caused by the friction that will occur during the earthquake and not to change the friction behavior. One of these materials is Teflon. It is also used as a friction pad in composite materials used in some patented systems and providing a stable friction coefficient range. [3-5]

Plates with different friction and heat dissipation properties were used in the friction pad, which is one of the most important parameters determining the behavior of the damper. A nut with the nut lock adhesive was used to ensure that the normal force on the bolt remains constant throughout the earthquake movement. A fitting sized washer was used to spread the force on the bolt as pressure on the plates. Conical

springs were used to flexibly maintain a continuous tension force on the bolt throughout the movement.

With four different materials, namely teflon (PTFE), carbonfiber, lead and brass plates were used as friction pads. The high-strength bolt, which creates normal force on the friction surfaces by holding together and compressing the steel plates and friction pads, gives different normal force values when clamped at different torques. Due to the normal force required for the produced friction damper to work efficiently, the clamping torques of the bolts were investigated.

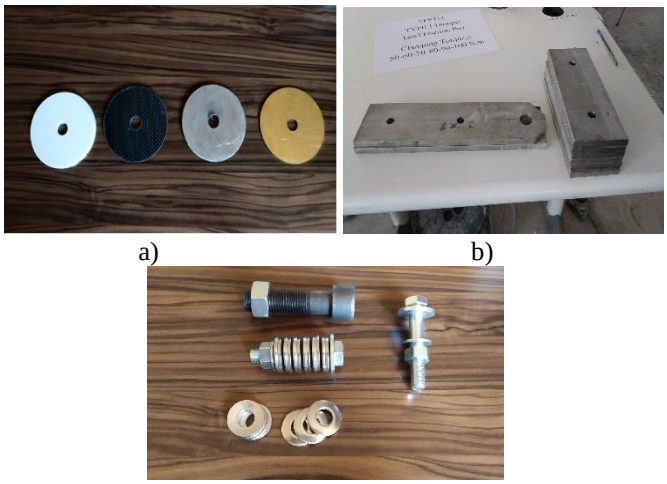

a) b)

c)

Figure 2. a) Teflon(PTFE), Carbonfiber, Lead and Brass Friction Pads b) Steel Plates used in dampers c) 12 mm and 20 mm diameter bolts, nuts, washers and conical springs

St 37 stainless steel plates are used in the production of the friction damper. The damper is formed as a single unit by attaching the 10 mm thick plate in the center and the 10 mm thick plates on both sides with 12 mm diameter high strength bolts. There are friction pads in the form of discs with an outer radius of 78 mm and an inner radius of 13 mm made of different types of materials (Teflon, lead, carbonfiber and brass pads) at the interface of the plates. Conical spring (Belleville washer) was used to obtain a constant coefficient of friction on the outer plate surfaces where the bolt head and the nut contact, and a pressure plate-washer was used to spread the pressure (Figure 2). The normal force acting on the friction surfaces on the damper and the friction coefficient on the friction surface are very important. In order to obtain a stable friction behavior, although the friction ratios cannot remain constant throughout the earthquake motion cycles, they must remain within a certain range. In previous studies, friction surfaces were treated in order to obtain a larger friction coefficient. Various processes can be applied to friction pads and frictional metal parts surfaces, such as impregnation with different chemicals, painting and coating the friction surfaces, chamfering the friction surfaces.[7] A similar procedure was not performed in this study. Conical springs will flexibly transfer the tensile force in the bolt during the rotation movement that will occur during the earthquake and will create a near-constant normal pressure force at the friction interfaces. Since the pressure on the friction surface will decrease outwardly from the center of the bolt, spreading the pressure as much as possible with the pressure plate-washer under the conical springs will create an efficient friction behavior. In order to create a certain normal force in the bolt, clamping was done with a digital torque wrench. After clamping at different torque values, the rigidity and energy distribution (hysteresis) curve of the damper were obtained with the tension-compression test setup (Figure 3). In this way, the most suitable rigidity values and energy dissipation capacities for the friction damper were obtained by trial-and-error method. Since the determined rigidity value will also be used in analytical studies, it is important to obtain the real behavior.

a) b)

Figure 3. a) clamping with a digital torque wrench, b) test setup

III. EXPERIMENT RESULTS

The energy consumption of friction pad materials was tested by manufacturing a single unit (consisting of 3 steel plates and 2 friction pads) single articulated test damper. Tensile-compression amplitudes of 30 mm and 50 mm were used as test amplitudes. In the experiment, a digital torque wrench with a capacity of 17-340 N.m was used to keep the normal force on the friction pad at a constant value. Energy dissipation graphs consisting of 10 cycles were obtained with bolt clamping torque values of 50-60-70-80-90-100 N.m for friction pads consisting of 4 different materials.

By examining the energy consumption graphs obtained, stiffness and energy consumption were calculated for each bolt clamping torque in 4 different friction pad materials. The approximate rectangle calculation was used while calculating the areas within the hysteresis curves. (Table 1) The graphic shape change caused by the moment arm change in the damper has been neglected. By examining the stiffness and energy consumption values, it was deemed appropriate to consider the maximum values at 100 N.m bolt tightening torque for a single-unit damper. The energy consumption obtained at 100 N.m of torque will be used in future frame tests.

Table 1. Amount of energy consumed by friction pads in a single cycle based on the calculation of approximate rectangular area (kg.mm)

Material	Teflon (PTFE)		Carbonfiber		Lead		Brass	
Amplitude (mm) / Clamping Torque (N.m)	30	50	30	50	30	50	30	50
50	5820	8900	8940	18700	12060	22400	14220	31900
60	5580	10000	15120	23700	12540	22800	18660	34500
70	7500	11000	17040	29200	13740	27800	20160	36600
80	7140	11600	18480	29000	17280	30800	23760	39400
90	8880	13700	18720	31600	20040	37800	27900	45400
100	8940	14100	20520	32800	23040	41500	29820	49200

IV. CONCLUSION

When the energy distribution graphs were examined, it was determined that the friction coefficient remained constant throughout the cycles for all pad materials, so the graphs repeated each other throughout the cycles. These results show that passive control systems meet the first two of the acceptability conditions for all 4 pad materials. (Figure 4,5)

As a result of the experiment, it was determined that the Teflon (PTFE) friction pad does not have sufficient energy distribution for its use in the damper device. It has been observed that Teflon (PTFE) friction pads do not consume enough energy and their resistance decreases due to the decrease in the friction coefficient by polishing the surfaces under increasing normal forces. This result shows that Teflon (PTFE) pad material cannot meet the third of the acceptability conditions of passive control systems. As can be seen from the graphs, although the normal force (Torque) on the friction pad has increased, the slope of the line has increased slightly. (Figure 6,7)

As a future study, 2 different types of damper are planned to be fabricated with carbonfiber, lead and brass friction pads to confirm their usefulness in reinforced concrete frames.

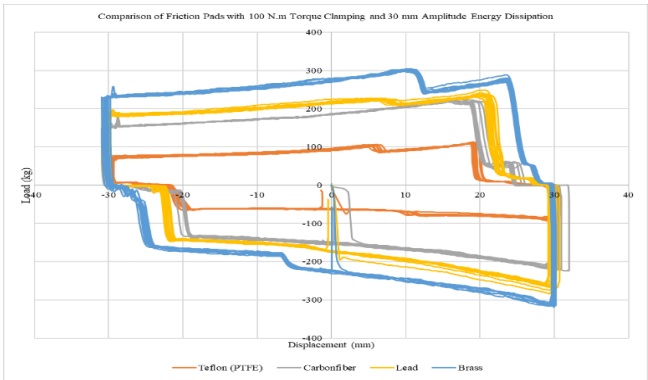

Figure 4. Comparison of friction pads with 100 N.m torque clamping and 30 mm amplitude energy dissipation

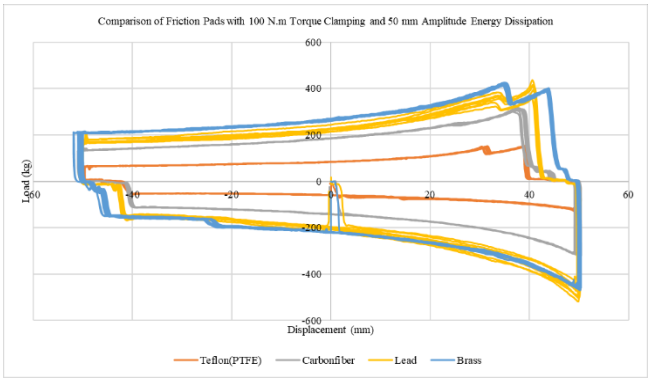

Figure 5. Comparison of friction pads with 100 N.m torque clamping and 50 mm amplitude energy dissipation

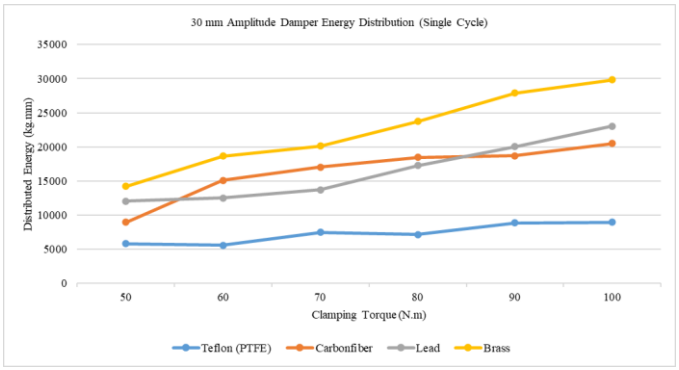

Figure 6. 30 mm amplitude damper energy distribution (single cycle)

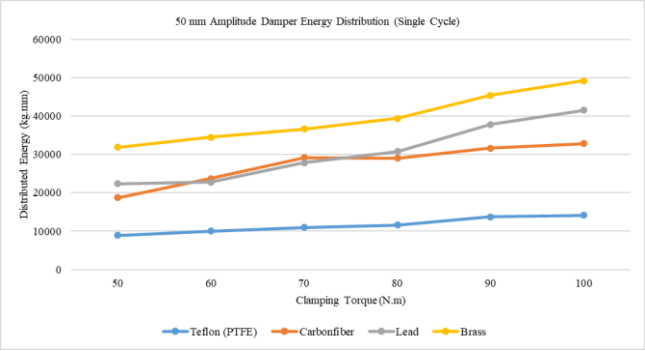

Figure 7. 50 mm amplitude damper energy distribution (single cycle)

ACKNOWLEDGMENT

This study was prepared by utilizing the Ph.D. thesis of Ensar SUCİ supported by the Konya Technic University Teaching Staff Training Program Research Projects (ÖYP) under grant number 2016-ÖYP-077.

REFERENCES

[1] Dixon J.C., "The Shock Absorber Handbook," John Wiley & Sons Ltd, UK, 2007.

[2] Grigorian, C. E., Yang, T. S., and Popov, E. P. "Slotted bolted connection energy dissipators." Earthquake Spectra, 93, 491–504, 1993.

[3] Mualla I. H., Belev B., "Performance Of Steel Frames With A New Friction Damper Device Under Earthquake Excitation," *Engineering Structures* 24 (2002), 365–371, 2002.

[4] Mualla I.H., "Experimental Evaluation Of New Friction Damper Device," 12th World Conference On Earthquake Engineering, Auckland, New Zeland, 1048, 2000.

[5] Mualla I. H., Nielsen L. O., Belev B., Liao W.I., Loh C.H., Agrawal A., "Numerical Predictions Of Shaking Table Tests On A Full Scale Friction-Damped Structure," *12th European Conference on Earthquake Engineering*, Elsevier Science Ltd, Paper Reference 190, London, UK, 2002

[6] Pall A. S., Marsh C., "Response of Friction Damped Braced Frames," *Proceedings of the American Society of Civil Engineers*, Vol. 108, No. ST6, 1982.

[7] Symans M.D., Charney F.A., Whittaker A.S., Constantinou M.C., Kircher C.A., Johnson M.W., McNamara R.J., "Energy Dissipation Systems for Seismic Applications: Current Practice and Recent Developments," *Journal of Structural Engineering*, 134(1), 3-21 (2008)

[8] Soong, T. T., and Dargush, G. F., "Passive energy dissipation systems in structural engineering," Wiley, Chichester, U.K, 1997.

Piezo-resistivity of Cement-based Mortars Doped with Carbon black and Carbon Fibers for Self-sensing Behavior

O.ÖZTÜRK[1], A. ÜNAL[1], M.KOÇER[1]

[1]Konya Technical University, Konya/Turkey, aunal@ktun.edu.tr
[1]Konya Technical University, Konya/Turkey, mkocer@ktun.edu.tr
[1]Konya Technical University, Konya/Turkey, oozturk@ktun.edu.tr

***Abstract* - The efficient use of carbon-based materials is of a challenge for the advanced self-sensing behavior of cement-based mortars. This study deals with the dispersion of the carbon-based materials and investigating the self-sensing response by using conductive fillers. To do this, carbon black (CB) and carbon fibers (CF) were used cement mortars to evaluate the piezo-resistivity response. Dispersion of the conductive fillers was achieved by using sodium hydroxide as surfactant. Reference specimens were produced and comparison was made with the specimens doped with CB and CF. Experimental work reveals that CB and CF enabled superior relative change in electrical resistivity of composites. However, CF was more promising than CB in terms of achieving higher piezo-resistivity. In addition to non-structural functionalities, mechanical properties of developed mixtures were also evaluated. The use of CF provided higher flexural strength compared to reference and CB-bearing specimens. On the other hand, carbon-based materials made a negligible contribution to the compressive strength of the cement-based mortars.**

***Keywords* – Carbon Black, Carbon Fiber, Cement Mortars, Self-sensing.**

I. INTRODUCTION

Structural health monitoring (SHM) is of great significance for the critical structures such as bridges, public buildings, airports, highways and port structures. There are different SHM methods comprising optical fibers [1], strain gauges [2] and impedance transducer [3]. However, SHM techniques require longer durability and service life together with compatibility in concrete structures. Therefore, structural concrete can be used as a sensor itself instead of integrating sensor-based apparatus. Efforts to develop structural concrete sensor itself are focused on the strain changes by tailoring the electrical response of the concrete. For this purpose, self-sensing concrete-like materials are introduced to literature a few decades ago [4]. "Self-sensing" of cement-based materials is mainly related to electrical response of whole material which is attributed to the piezo-resistive ability upon applied strain. On the other hand, electrical response of cement-based materials is weak and regarded as semiconductor [5]. Therefore, concrete matrix should be readdressed in terms of tailored piezo-resistivity. To that end, conductive fillers such as carbon black, carbon fiber, carbon nanotubes and other metallic fibers are used to change the electrical resistivity of the bulk material [6-9]. Conductive fillers are not only expected to improve electrical properties but they are also required to be compatible within the cementitious matrix. Therefore mechanical and volume stability of the mixtures doped with conductive fillers should be additionally addressed.

As carbon-based materials are inert and have dissimilar properties compared to ingredient of cement-matrix, dispersion of such materials should be handled reliably. For example, nanoscale carbon nanotubes lead to agglomeration due to their very high surface areas. On the other hand, microscale carbon fibers lead to entrained air into matrix and bundled forms of such materials are also difficult to disperse. To achieve a reliable electrically tailored matrix, surfactants are used with the conductive fillers and homogenously distribution makes the matrix piezo-resistive under the change of strain. In the case uniform distribution is provided for the matrix, conductive fillers can also contribute to mechanical properties besides electrical performance.

In this study, electrical properties of cement mortars are produced with different carbon-based materials. The aim of the investigation is to develop piezo-resistive cementitious composites that are capable of sensing the strain acting upon specimens. To do this, carbon black (CB) and carbon fiber (CF) were incorporated into cementitious matrix by using sodium hydroxide as a surfactant. Self-sensing ability of cement mortars was evaluated by calculating relative change in electrical resistivity under flexural loadings. 4-probe electrical resistivity measurements were applied for each specimen. Besides electrical performance, compressive and flexural strength of the specimens produced with CB and CF were assessed at 28 days.

II. MATERIALS

A standard Portland cement (PC) which is CEM II 32.5 R type and in conformity with EN 197-1 was used in the production of mixtures. Silica fume was used as mineral admixture at 10% by weight of total cementitious material. The chemical and physical properties of cement and silica fume were given in Table 1. Silica sand (<2 mm) was used as fine aggregate in the mortar mixture. As superplasticizer, polycarboxylate high range water reducer (HRWR) was added to mixture for modifying fresh properties. CFs had a specific gravity of 1.81 g/cc, length of 6 mm and 4200 MPa of direct tensile strength. On the other hand, CB had specific gravity of 1.73 g/cc and surface area of around 50 m^2/g. SEM and microscale images of CB and CF were given in Figure 1, respectively.

Table 1: Chemical and physical properties of Portland cement and silica fume

Chemical Composition (%)	PC	SF
SiO_2	19.80	91.0
Al_2O_3	4.82	0.60
Fe_2O_3	2.77	0.24
MgO	2.99	0.30
CaO	58.20	2.25
Na_2O	0.34	0.40
K_2O	0.32	4.30
Loss on ignition	9.20	1.85
Physical Properties		
Specific gravity	2.96	2.25
Blaine fineness (m^2/kg)	243	650

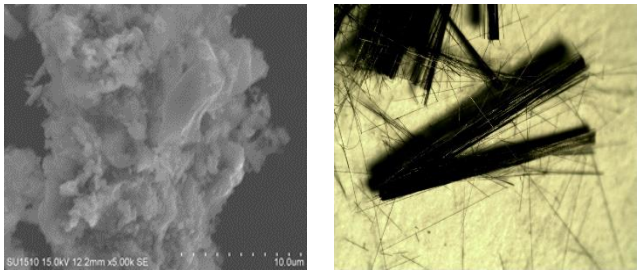

a) Carbon black b) Carbon fibers

Figure 1: Microscale carbon-based materials; a) carbon black (CB) b) carbon fibers (CF)

III. MIXING PROPORTIONS AND PRODUCTION

The mixture design of the study was given in Table 2. S/Ref., S/CB and S/CF refer to specimens of reference, carbon black and carbon fibers, respectively. Silica fume was used by around 10% of total binder and water to binder (w/b) ratio was 0.45. Carbon-based materials were used by 0.5% of total binder. As different carbon-based materials are used in the mixtures, workability properties were aimed to provide similar flow rate. Therefore different amount of HRWR was used in the mixture (Table 2).

Table 2: Mixture design (kg/m^3)

Mix-ID	PC	SF	W/B	Sand	CF	CB	HRWR
S-Ref.	560	56	0.45	1450	-	-	6.4
S-CB	560	56	0.45	1450	-	2.8	8.2
S-CF	560	56	0.45	1450	2.8	-	9.3

Mixing procedure was applied as following;

S-Ref.: Dry materials (sand, cement and silica fume) were mixed for two minutes in a traditional mortar mixer. Then, mixing water and half of the HRWR was added and mixing was continued for a minute. Then the other half of the HRWR was added and mixing was continued at high speed at 120 rpm (round per minute)

S-CB: Carbon-black was separately mixed in mechanical homogenizer. In this separate mixing, 0.2 M of sodium hydroxide (NaOH) was used together with the half of water and half of HRWR. NaOH, as alkaline material, acts as surfactant and lubricates the surfaces of CB powders thus providing uniform distribution. Besides separate mixing of CB, a traditional mixing was prepared similar to reference mixture. Firstly, dry materials (sand, cement and silica fume) were added and mixed for two minutes. Then, mixing with half of water and half of HRWR was made with additional mixing (a minute). Lastly, a prepared solution was added to ongoing traditional mortar mixer and a high speed mixing was performed for three minutes (120 rpm).

S-CF: Carbon fibers were separately mixed in a mechanical homogenizer. Similar to CB, dispersion of CF was also made with the use of NaOH (0.2 M) and similar procedure was followed. During the ongoing traditional mortar mixing (dry materials + half of the water + half of the HRWR), suspension of the CF was added to mixing and a high speed of mixing was made at 120 round per minute for three additional mixing.

After production of fresh mixtures, specimens were prepared with molds by dimension of 50×50×50 mm^3 (for compressive tests) and 40×40×160 mm^3 (for flexural tests). Cased fresh mixtures were covered with plastic sheets and ambient curing was provided at 50 ± 5% RH and 25 ± 2°C for 24 hours. Then, specimens were removed from molds and curing was applied at 25 ± 2°C until relevant curing ages.

IV. EXPERIMENTS

Specimens covering three different types of mixture (S-Ref. + S-CB + S-CF) were evaluated in terms of compressive (at 3 and 28 days) and flexural strength (at 28 days). Cubic (50×50×50 mm^3) and prism specimens (40×40×160 mm^3) were used by applying compressive (0.9 kN/second) and flexural load (0.05 kN/second) in universal test machine, respectively. Simultaneously with the flexural loading, electrical response of the specimens was assessed by using 4-probe electrical measurement. To that end, copper plates were used as electrodes which have dimensions of 60 × 15 × 1 mm (length × height × width). Inner electrodes were embedded from 2 cm inside from the two edges of the specimen while outer electrodes were embedded from 1 cm inside from the specimen (Figure 2). During electrical measurement, care was given to block any electrical contact between universal test machine and specimens.

Electrical measurement was carried out by using a 4-probe DC-Source meter and a digital voltmeter (with the accuracy

0.001 V). Recorded electrical impedance was continuously recorded to a computer for each second. Apply current (mA) was calculated from outer two electrodes and voltage (mV) was evaluated from the inner two electrodes (Figure 2). Ohm's law was considered and calculated electrical impedance (in ohm) was used by dividing the measured voltage over current [7]. Lastly, the calculated electrical data were converted to electrical resistivity data by using geometrical factors. The relevant equation was given as below:

$$R = \frac{V}{I} \times \frac{A}{L} \quad (1)$$

where, R, V, I, A and L equal to resistivity (Ω.m), voltage (V), current-DC (A), cross-sectional area of the contact area between electrodes and matrix of specimen (m^2), and the distance (m) between the internal electrodes, respectively. After an assessment, the relative factor in electrical resistivity (RFER, %) was taken into according to Equation given below:

$$RFER\ (\%) = \frac{ER_C - ER_I}{ER_I} \times 100 \quad (2)$$

where, RFER, E_{RC} and E_{RI} equal to relative factor in electrical resistivity (RFER), electrical resistivity recorded at each second and resistivity at initial stage, respectively.

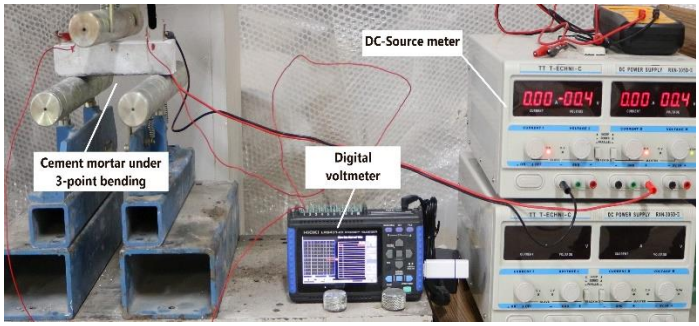

Figure 2: 4-probe measurement of piezo-resistive properties for cement mortars doped with CB and CF

V. RESULTS AND DISCUSSION

The average compressive and flexural strength of the mixtures were given in the Table 3. The compressive strength of the mixtures represents the average of six cubic specimens while an average of three prism specimens was given for flexural strength. Also, compressive strength of the 3- and 28-day-old specimens can be compared in Figure 3. As given in the results, compressive strength of the S-Ref., S-CB and S-CF was 22.63-54.02, 24.47-52.18, 26.37-58.70 MPa at 3 and 28 days, respectively. For example, 3-day-old S-Ref specimens had higher compressive strength than 3-day-old S-CB although this was vice versa for 28 day-old specimens. However, slight changes are within the range of standard deviation as given with red error bars in Figure 3. On the other hand, although results were similar to each other, slight changes were found especially for the CF-bearing specimens. As mixture matures between 3 days to 28 days, improved bond behavior between CF and cement matrix seems to have more contribution for compressive strength development. Compared to S-CB and S-Ref. mixtures, CFs were likely to participate as microcrack and pore bridging reinforcement thus modifying post-peak cracking and providing higher compressive strength [10]. Results clearly indicate that the dispersion of carbon-based materials (CF and CB) was achieved without compromising the compressive strength of developed mixtures at 3 and 28 days.

Table 3: Compressive and flexural strengths of mixtures (MPa)

Mix-ID	Compressive strength		Flexural strength (28 days)
	(3 days)	(28 days)	
S-Ref.	22.63	54.02	3.16
S-CB	24.47	52.18	4.05
S-CF	26.37	58.70	7.43

The average flexural strength of S-Ref, S-CB and S-CF was 3.16, 4.05, 7.43 MPa, respectively. The relationship between flexural strength of S-Ref and S-CF mixtures was similar to obtained results in compressive strength which showed similar behavior. Improved particle size distribution in the presence of CB can be related to slight increase of flexural strength for S-CB. On the other hand, the effect of CFs was highly pronounced on the flexural strength of mortars compared to reference and CB-bearing mortars. For example, CF incorporating specimens had 135% and 83.5% higher flexural strength than S-Ref. and S-CB specimens. As given in Table 3, increment of flexural strength is related to the high tensile strength of carbon fibers that act as crack bridging reinforment. This resulted in restricted or reduced crack width thus increasing the strength under tension zone. This can be also related to with the increased efficiency of carbon fiber distribution through dispersion method. For example, effect of NaOH could have provided more debundled CFs and homegenously distributed CFs may be more effective to provide crack-arresting capacity. However, this requires different mixing methods to compare with the aforesaid method in the presence of same amount of carbon fibers.

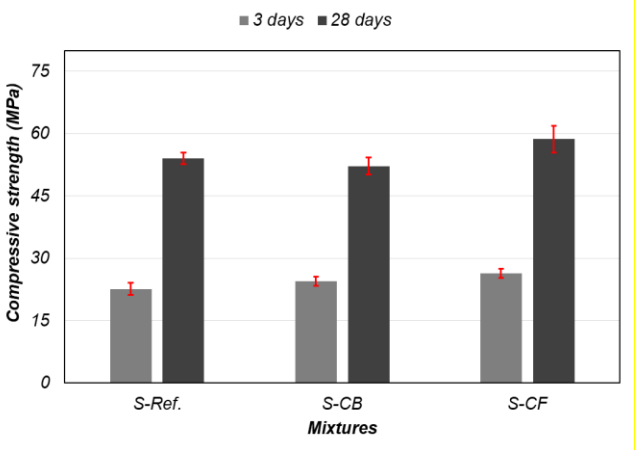

Figure 3: Compressive strength of specimens at 3 and 28 days

As temperature and humidity conditions influence the electrical properties, electrical resistivity (ER) of mortars was evaluated under constant environmental curing conditions. The self-sensing ability of three different mixtures was assessed

based on Equation (2) and piezo-resistive behavior of specimens was given with the applied load versus mid-span displacement, In Figure 4. RFER values of specimens were 101.9%, 1906% and 2002.4% for the reference, S-CB and S-CF mixtures, respectively. Ongoing hydration and pozzolanic effect of mixtures influence the pore chemistry and network together with pore solution [11]. As each mixture was identical except carbon-based material content, the piezo-resistive behavior can be only explained with the performance of individual electrical properties CB and CF that distributed in the matrix. As given in Figure 4, the highest electrical response was obtained from S-CF mixture after applied flexural loading. This was related to the CF effect providing electrically conductive ways in the cement matrix thus triggering higher and more consistent RFER in contrast to displacement. Also, tunneling barrier may be reduced with the use of fiber-like carbon-based materials (CF) and this may have led to shortened distance between adjacent CFs resulting in a more reliable piezo-resistivity. In addition, improved matrix-CF bond behavior (at 28 days) could be more effective to obtained higher RFER values as crack arresting of CFs may have been disturbed and this may have triggered higher self-sensing performance. On the other hand, CB particles also sustained considerable RFER values as CB particles may be efficient to fill microscopic gaps in cement matrix. However, reference mixture is far from guaranteeing electrical response under 3-point flexural loading with the RFER values of 101.9%. Having said that, combination of both carbon-based materials (CF and CB) would be more effective for obtaining consistent RFER values along with mid-span displacement.

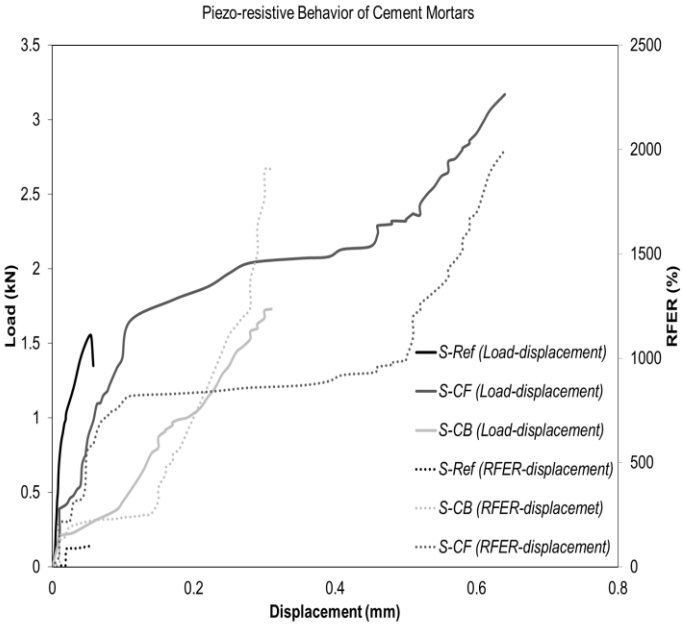

Figure 4: Self-sensing ability of cement mortars produced with carbon-based materials

VI. Conclusion

By using carbon-based materials (CF and CB), electrical and mechanical properties of cement mortars were investigated through evaluating relative factor in electrical resistivity, compressive and flexural strength. Based on the experimental work, following outcomes were reached:

- Carbon-based materials made a slight contribution for the compressive strength of specimens. Except S-CB mixture at 28 days, each experiment revealed that addition of CB or CF provided a limited increase for their compressive strength at 3 and 28 days. This shows that effective mixing method was achieved for both mixtures (S-CB and S-CF).
- The highest flexural strength was obtained in the mixtures of S-CF. S-CB mixtures were also promising to capture higher flexural strength compare to reference specimens although this increment was limited.
- For the self-sensing ability, both mixtures (S-CF and S-CB) were effective to capture electrical response under the change of strain. CF was more promising than S-CB in terms of providing consistent self-sensing behavior under post-yield region. On the other hand, no significant electrical response was available for the S-Ref mixtures.

References

[1] J.S. Leng, D. Winter, R.A. Barnes, G.C. Mays, G.F. Fernando, "Structural health monitoring of concrete cylinders using protected fibre optic sensors," *Smart Materials Structures,* Vol.15, pp. 302–308. 2006.

[2] H. De Backer, W. De Corte, P. A Van Bogaert, "Case study on strain gauge measurements on large post-tensioned concrete beams of a railway support structure". *Insight Non-Destructive Test Cond Monit.* Vol.45, pp. 822-830. 2003.

[3] H. Taha, R.J. Ball, K. Paine, "Sensing of Damage and Repair of Cement Mortar Using Electromechanical Impedance," *Materials (Basel)* Vol. 12 pp. 3925. 2019.

[4] P.W. Chen, D.D.L. Chung, "Carbon fiber reinforced concrete as an electrical contact material for smart structures," *Smart Materials Structures*, Vol. 2(3):181-188, 1993.

[5] D.D.L. Chung, "Electrical conduction behavior of cement-matrix composites," *Journal Materials Engineering Performance*, Vol 11. pp. 194–204. 2002.

[6] O. Öztürk, Ü.S. Keskin, M. Şahmaran, "Self-Sensing Fiber Reinforced Cement Mortars for the Monitoring Of Critical and Transport Infrastructures". Vol. 20, *EGU General Assembly Conference*, 2018.

[7] O. Öztürk, G. Yıldırım, Ü.S. Keskin Siad H, Şahmaran M. Nano-tailored multi-functional cementitious composites. *Composites Part B Engineering* Vol. 182 pp. 1-13. 2020.

[8] O. Öztürk, "Multifunctional behavior of CNT- and CB-based composite beams". *Construction and Building Materials* Vol. 296, 2021.

[9] O. Öztürk, M. Koçer, A.Ünal "Multifunctional Behavior of Composite Beams Incorporating Hybridized Carbon-based Materials under Cyclic Loadings" *Engineering Structures, (underreview).*

[10] Z.Tia, Y. Lia, J. Zheng S. Wang "A state-of-the-art on self-sensing concrete: Materials, fabrication and properties", *Composites Part B: Engineering*, Vol.177 pp. 107437. 2019

[11] RP Spragg, Y. Bu, K.A. Snyder, D.P. Bentz, J. Weiss "Electrical Testing of Cement-Based Materials: Role of Testing Techniques, Sample Conditioning, and Accelerated Curing". Transportation Research Program, Indiana Department of Transportation and Purdue University, West Lafayette, Indiana. 2013.

Mechanical and physical properties of glass fiber and fly ash added cement-bonded composites

Marwan ALITHAWI[1] and Arife AKIN[1]
[1]Konya Technical University, Konya/Turkey, mr1.ayad92@gmail.com
[1]Konya Technical University, Konya/Turkey, aakin@ktun.com

***Abstract*- In this study, the changes in the mechanical and physical properties of cement-bonded composites containing fly ash with different characters at high and low rates were investigated with varying proportions of glass fiber reinforcement. F and C class fly ash was added to the mixture in varying proportions (10%, 20%, 50%, 60%) by cement replacement method. In addition, 16 different mixtures containing fly ash were obtained by including glass fiber in two different ratios (10%, 20%).For control, fly ash was not used in the reference samples, and two different reference mixtures were prepared with two different fiber ratios. As a result of the experiments, it was observed that the strength properties were higher in the samples containing Class C fly ash. Depending on the changing glass fiber ratio, as the fiber ratio increased, an increase was observed in flexural strength, while a decrease incompressive strength was observed. In the permeability tests including water absorption tests, it was observed that the samples containing Class F fly ash generally gave better results than the samples containing Class C fly ash. In addition, the increase in permeability values due to the increase in the glass fiber ratio is among the results obtained.**

***Keywords* - glassfiber, flyash, mechanical properties, physical properties**

I. INTRODUCTION

In terms of sustainability, the effects of the construction industry are very important. It is considered as an effective solution for ensuring sustainability, especially for the structures produced to be durable and resistant to external effects, to be long-lasting and to choose the right building materials. Understanding the importance of the concept of sustainability and rapid developments in concrete technology have encouraged the use of pozzolanic materials in concrete production. For this purpose, fly ash (FA) is widely used as a waste material in the industry. From the past to the present, many studies have been carried out on the effects of the partial substitution of Portland cement in concrete and the use of FA[1-5].

In the rapidly developing world, the increase in structuring means that more cement is produced. As reported by Palomo, it is estimated that the annual concrete consumption worldwide will be around 18 billion tons by 2050[6]. Portland cement production processes release large amounts of carbon dioxide (CO_2), which significantly affects greenhouse emissions. One ton of cement production contributes to approximately one tonne of CO_2 production[7]. The role of CO_2 in global warming is about 65%[8].Davidovits suggested that waste materials such as fly ash containing aluminum (Al) and silicon (Si) can be used to produce environmentally friendly concrete. [9]. Fly ash, like natural pozzolans, is amorphous and fine-grained materials that contain high levels of silica. Thanks to these properties, they can show pozolanic properties. The addition of fly ash to concrete can have positive and negative effects. While the effect of some problems can be eliminated, it also reduces the porosity of concrete by making a micro-aggregate effect. Thus, the durability of concrete against external effects increases, and it also increases the workability of fresh concrete due to its spherical and smooth surface structure.[10].

Various kinds of fibers can be added to concrete in order to improve the strength and durability properties of concrete, to provide ductility and to control cracks. Fibers that are frequently preferred in practice; steel, polymer (polypropylene, PVA, etc.), glass and carbon-based fibers[11]. Factors such as fiber type and amount, slenderness ratio (fiber length/fiber diameter), homogeneous distribution of fibers in the mixture are the most important criteria affecting the concrete properties of the fibers. Glass fibers prevent the formation of shrinkage cracks in concrete and make the concrete more resistant to environmental abrasive effects in the long run. At the same time, it has positive effects on concrete such as preventing decomposition of fresh concrete, increasing its workability and bending strength.

In this study, the effects of increasing F and C class FA additions on some mechanical and physical properties of the composite in cement-bonded composites containing two different ratios of glass fiber were investigated. Depending on the changing parameters, a total of 18 different mixtures were prepared, 2 of which were reference mixtures. The blends are designed to have equal workability. Two different ratios (10% and 20%) of glass fiber were used in the reference blends, but no FA was used. Compression and bending tests for the determination of mechanical properties; In the determination of its physical properties, tests to determine the permeability properties such as water absorption tests were carried out. The positive and negative effects of FA included in the mixture in low and high ratios on the mechanical and physical properties of composites containing glass fiber in two different ratios have been revealed.

II. MATERIYAL AND METHOD

CEM I 42.5 R type cement was used as the binding material in the preparation of the mixtures. The cement used was supplied in bags by Konya Cement Industry. The specific gravity of CEM I 42.5 R type Portland cement is 3.06, and the Blaine specific surface is 3250 cm2/gr.

The FA used in the study are C type FA obtained from Manisa-Soma Thermal Power Plant and F type FA obtained from Zonguldak-Çatalağzı Thermal Power Plant. When the FA used are examined according to ASTM C 618, Manisa-Soma Thermal Power Plant ash is considered C class FA and Çatalağzı Thermal Power Plant ash is F class FA [12]. Chemical and physical properties of FAs are given in Table 1. Sand with grain size (0-4 mm) and silica sand with grain size (0-400 μ) were used as aggregates. Sand was obtained from Konya Region and silica sand was obtained from Pomza Export Madencilik Sanayi ve Ticaret AŞ. A phosphonate-based superplasticizer additive (SP) named Optima 100, produced by CHRYSO Construction Chemicals, was used to increase the workability of the mixtures. The properties of E-glass fiber used as fiber reinforcement are given in Table 2.

Table 1: Chemical and physical properties of fly ash used in mixtures [13]

Chemical Composition (%)	**FA (F)**	**FA (C)**
SiO_2	8.75	42.82
Al_2O_3	25.24	20.82
Fe_2O_3	5.76	4.57
S+A+F	89.75	68.21
CaO	1.46	23.45
MgO	2.22	1.74
SO_3	0.08	1.47
K_2O	4.05	1.31
Na_2O	0.60	0.32
Physicalproperties		
SpecipicWeight (g/cm^3)	2	2.27
Fineness (cm^2/g)	2900	3060

Table 2: Mechanical and chemical properties of E-glass fiber used in mixtures[14]

Properties	**Unit**	**E-Glass Fiber**
Intesity	gr/cm^3	2,56
Flexural Strength	MPa	3445
Modulus of elasticity	GPa	76
Elongation at rupture	%	2,75
Fiber diameter	μm	10-13
Length	mm	3
Chemical Composition		
SiO_2		52,4
Al_2O_3		14,4
B_2O_3	%	10,6
MgO		4,6
CaO		17,2
Others		0,8

Two different types of FA (10%, 20%, 50%, 60%) were used in the mixtures as F and C classes, and fly ash was not used in the reference mixtures. A total of 18 different mixtures were prepared by adding two different fiber ratios to each mixture. In the study, a total of 108 beams, 108 cubes and 36 cylinder samples were produced. For each mixture, 6 50x75x360 mm beam samples, 6 50x50x50 mm cube samples and 2 Φ100/200 mm cylinder samples were prepared. In the preparation of the mixtures, 25 lt. capacity planetary mixer is used. In Table 3, the mixture codes and the amount of materials used are given. As an example, the name (F-FA 10-10) was used for the mixture containing 10% F class FA and 10 g glass fiber. First of all, dry materials (aggregates, cement and FA) are dried at 100 rpm. speed for 1 minute, then water was added and 150 rpm. was mixed for an additional 1 minute. Then, superplasticizer was added to the mixture and mixing was continued for 3 minutes at the same speed. Finally, the fibers were added to the mixture and 150 rpm. 1 minute at speed, 300 rpm additionally. The mixing process was completed by mixing at high speed for 3 minutes. The mixtures were placed in pre-oiled molds and removed from their molds at the end of 24 hours and placed in a water-filled curing pool. At the end of the 7th and 28th days, compressive, bending and water absorption tests were performed on the samples taken from the pool.

Table 3: Amount of material in mixtures in grams (for 1 dm3)

Mix. ID	Cement	F-FA	C-FA	Silica Sand	Sand	Water	Fiber	SP
R-10	450	-	-	338	1012	225	10	4.6
R-20	450	-	-	338	1012	225	20	4.8
F-FA 10 -10	405	45	-	338	1012	225	10	4.2
F-FA 10 -20	405	45	-	338	1012	225	20	4.4
F-FA 20 -10	360	90	-	338	1012	225	10	3.8
F-FA 20 -20	360	90	-	338	1012	225	20	4.0
F-FA 50 -10	225	225	-	338	1012	225	10	3.4
F-FA 50 -20	225	225	-	338	1012	225	20	3.6
F-FA 60 -10	180	270	-	338	1012	225	10	3.0
F-FA 60 -20	180	270	-	338	1012	225	20	3.2
C-FA 10 -10	405	-	45	338	1012	225	10	6.2
C-FA 10 -20	405	-	45	338	1012	225	20	6.4
C-FA 20 -10	360	-	90	338	1012	225	10	6.6
C-FA 20 -20	360	-	90	338	1012	225	20	6.8
C-FA 50 -10	225	-	225	338	1012	225	10	7.0
C-FA 50 -20	225	-	225	338	1012	225	20	7.2
C-FA 60 -10	180	-	270	338	1012	225	10	7.4
C-FA 60 -20	180	-	270	338	1012	225	20	7.6

III. EXPERIMENTS

Compressive and flexural strength tests were carried out to determine the mechanical properties. Compressive tests were carried out on 50x50x50 mm cube specimens and bending tests were carried out on 50x75x360 mm beam specimens. For the permeability tests carried out to determine the physical properties, Ø100×200 mm cylindrical samples were prepared. The permeability properties of cylindrical samples were investigated by water absorption test.

A. Compressive Strength Test

On the 7th and 28th days, the pressure test was applied on the cube samples removed from the cure. Compressive strength test was carried out in accordance with ASTM C39 standard[15].

B. Flexural Strength Test

The bending test was carried out in accordance with ASTM C293[16] as a three-point bending load.

C. Water Absorption Test

The water absorption tests were carried out according to the ASTM C642 standard[17]. In order for the cylindrical samples taken out of the water on the test day to become completely dry, they were allowed to dry in an oven at 50 0C for 3 days. At the end of 3 days, the weights of the samples taken out of the oven were measured and recorded as dry weight (Wk), then the samples were kept in water for at least 2 days in order to become saturated. After removing the coarse water on the surfaces of the samples removed from the water, they were weighed on the balance (Ws). The water absorption rate (Sa) is calculated from Equation 1.

$$\text{Sa}\ (\%) = \frac{Ws - Wk}{Wk} . 100 \quad (1)$$

IV. EXPERIMENT RESULTS

A. Compressive Strength Test Results

The 7 and 28-day strength values obtained as a result of the pressure tests are given in Table 4. Graphs of comparison of compressive strengths of composites containing Class F FA and glass fiber are given in Figure 1, and Class C in Figure 2.

Table 4: Compressive strengths test results at 7 and 28 days

Mix ID	Compressive Strength (MPa)	
	7 days	28 days
R-10	54,36	59,92
R-20	51,01	52,35
F-FA 10 -10	46,57	50,36
F-FA 10 -20	43,70	46,01
F-FA 20 -10	36,54	38,37
F-FA 20 -20	34,63	36,06
F-FA 50 -10	26,15	27,88
F-FA 50 -20	24,97	26,85
F-FA 60 -10	22,50	23,54
F-FA 60 -20	20,55	21,55
C-FA 10 -10	50,84	53,37
C-FA 10 -20	47,90	50,12
C-FA 20 -10	43,68	46,36
C-FA 20 -20	41,29	44,04
C-FA 50 -10	37,14	40,04
C-FA 50 -20	32,81	36,77
C-FA 60 -10	29,89	34,41
C-FA 60 -20	23,87	27,17

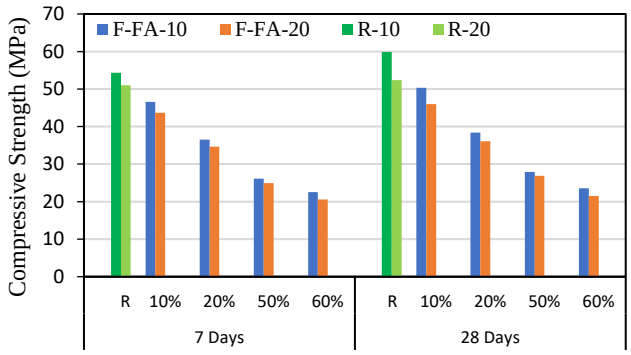

Figure 1: Comparison of compressive strength of samples containing F-FA and glass fiber in different ratios

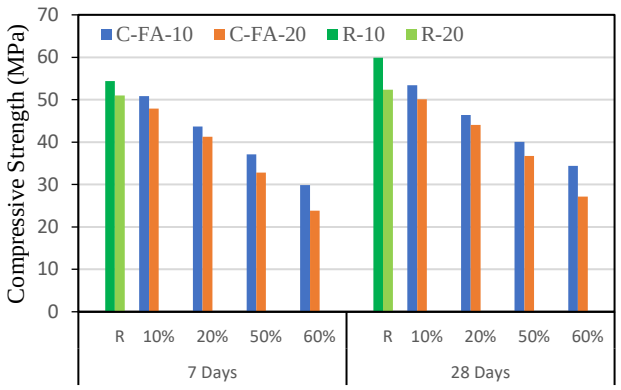

Figure2: Comparison of compressive strength of samples containing C-FA and glass fiber in different ratios

When Table 4 and Figure 1-2 are examined, the results obtained as a result of the compressive strength tests are given as items. These;

- It was observed that R-10 and R-20 had higher strength values than samples containing FA.
- It has been observed that samples containing 10% FA have higher compressive strengths than samples prepared with other FA ratios. The results obtained show parallelism with the results obtained from the literature studies. As it is known, the addition of the FA additive and/or the increase in the amount causes the strength values of cement-binding composites to decrease.
- When the strength values of the mixtures obtained after 7 and 28 days of curing are compared, it is seen that the highest strength values are obtained from the C-FA 10-10 mixture. This result can be associated with the fact that Class C FA has a finer grained structure compared to Class F FA and has higher pozzolanic activity. However, since the percentage changes depending on the age of the samples given in Table 4 were examined, no consistent change was recorded depending on the change in the amount of FA and fiber, but the highest change was obtained from the C-FA 60 -10 samples. As it is known, the contribution of pozzolanic materials such as FA to the strength usually occurs in later ages. In this study, it has been observed that there may be significant increases in strength values in advancing ages with the high use of FA.
- It has been determined that the compressive strength decreases as the amount of FA is kept constant and the amount of glass fiber increases. It can be said that the reason for this is that the fibers increase the void ratio in the matrix and the compressive strength of the fibers is lower than the matrix strength.

B. Flexural Strength Test Results

The strengths obtained as a result of bending tests are given in Table 5. Comparison curves of flexural strength values given according to different criteria are given in Figure 3-4. Figure 3 shows the graphs of the comparison of flexural strengths of composites containing Class F and Class C FA and glass fiber in Figure 4.

Table 5: Flexural strengths test results at 7 and 28 days

Mix ID	Flexural Strength (MPa)	
	7 days	28 days
R-10	9,50	9,81
R-20	10,22	10,30
F-FA 10 -10	7,79	7,90
F-FA 10 -20	7,93	8,02
F-FA 20 -10	7,56	7,82
F-FA 20 -20	7,74	7,85
F-FA 50 -10	7,13	7,42
F-FA 50 -20	7,36	7,73
F-FA 60 -10	5,94	6,46
F-FA 60 -20	6,14	6,63
C-FA 10 -10	8,41	9,36
C-FA 10 -20	8,51	9,77
C-FA 20 -10	7,79	8,98
C-FA 20 -20	8,10	9,04
C-FA 50 -10	7,34	8,38
C-FA 50 -20	7,91	8,61
C-FA 60 -10	7,02	7,39
C-FA 60 -20	7,12	8,08

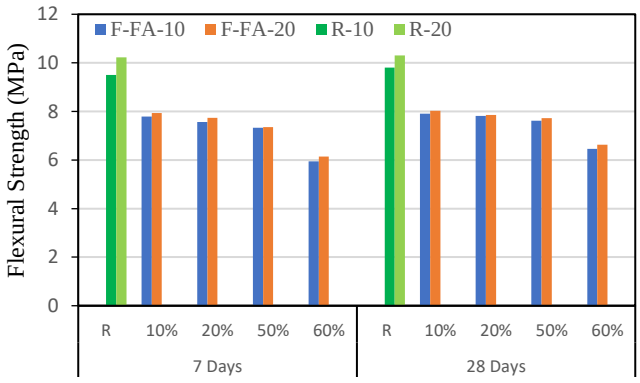

Figure 3. Comparison of flexural strength of samples containing F-FA and glass fiber in different ratios

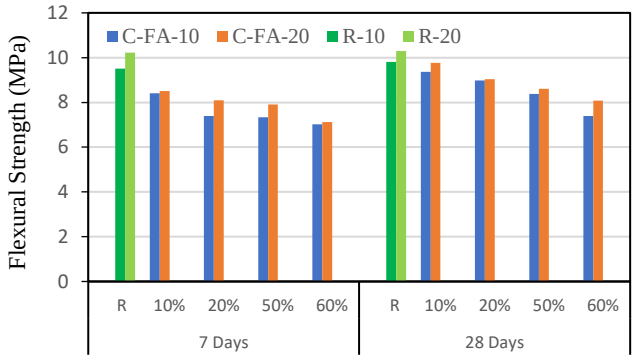

Figure 4. Comparison of flexural strength of samples containing C-FA and glass fiber in different ratios

When Table 5 and Figure 3-4 are examined, the results obtained are given as items.

- The increase in FA ratios negatively affected the flexural strength values in bending.
- Higher results were obtained in mixtures containing Class C FA in varying proportions compared to mixtures containing Class F FA.
- The flexural strength was higher as the amount of FA was kept constant and the amount of glass fiber increased. Among the mixtures containing FA, the highest flexural strength was obtained from the C-FA10-20 mixture.
- The percentage of increase in flexural strengths depending on the sample age was higher in samples containing C class FA. The reason for this can be explained by the fact that C class FA with high pozzolanic activity is also finer in structure and therefore its cementing ability is higher than F class FA.

C. Water Absorption Test Result

The water absorption test was performed on Ø100×50 mm cylindrical samples on the 7th and 28th days, the results are given in Table 6 and the comparison curves of the water absorption values according to different criteria are given in Figure 5-6.

Table 6: Water absorption test results at 7 and 28 days

Mix. ID	Water absorption (%)	
	7 days	28 days
R-10	2,79	1,30
R-20	2,99	1,45
F-FA 10 -10	2,78	1,87
F-FA 10 -20	2,80	1,93
F-FA 20 -10	3,05	2,08
F-FA 20 -20	3,10	2,20
F-FA 50 -10	3,12	2,40
F-FA 50 -20	3,20	2,60
F-FA 60 -10	3,23	2,69
F-FA 60 -20	3,55	3,01
C-FA 10 -10	2,84	2,21
C-FA 10 -20	2,91	2,25
C-FA 20 -10	3,21	2,43
C-FA 20 -20	3,32	2,64
C-FA 50 -10	3,43	3,00
C-FA 50 -20	3,45	3,06
C-FA 60 -10	3,61	3,15
C-FA 60 -20	3,63	3,20

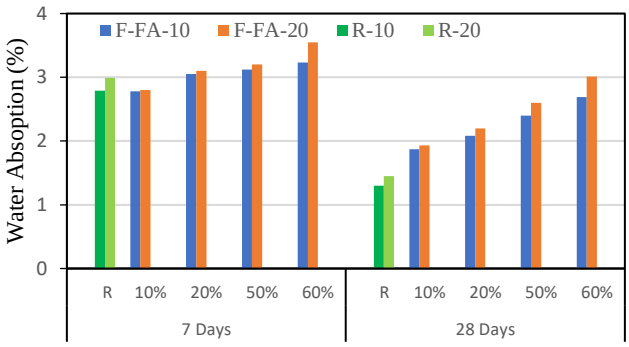

Figure 5: Comparison of water absorption values of samples containing F-FA and glass fiber in different ratios

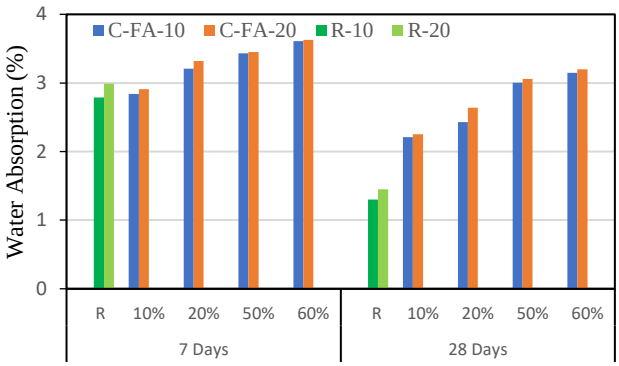

Figure 6: Comparison of water absorption values of samples containing C-FA and glass fiber in different ratios

When Table 6 and Figure 5-6 are examined, the results obtained as a result of the water absorption tests are given below.

- It was observed that the amount of water absorption increased as the amount of FA was kept constant and the amount of glass fiber increased. This can be explained by the fact that the fibers increase the void volume in the matrix.
- It was observed that the water absorption results increased as the amount of FA increased.
- When the decrease values in water absorption values of the samples given in Table 6 are examined depending on their age, the decrease recorded after the advancing curing periods in the mixtures containing F class FA is higher than the samples containing C class FA.
- As a result of the water absorption tests performed after 7 and 28 days of curing, it was observed that the water absorption values of the samples containing Class C FA were higher than the samples with Class F FA. This result can be explained by the fact that C class ash particles negatively affect the workability of the mixture due to their more angular and non-uniform physical

structures, and as a result, the composite has a more hollow structure.

V. RESULTS

The results obtained as a result of the experiments carried out within the scope of the study, in which the mechanical and physical properties of glass fiber added cement-bonded composites formed by using different types and amounts of FA were investigated, are presented below.

1) With the increase in the fiber content in the sample, the compressive strength values decrease. This can be attributed to the fact that the fibers increase the void ratio in the sample. A slight increase was observed in the flexural strength values as the fiber ratio increased. This shows the contribution of fibers with high ductility capacities to the bending behavior of the composite.
2) Regardless of the FA class of the composites, the maximum compressive and flexural strengths were obtained from samples containing 10% FA. With the use of FA, the decrease in the amount of cement causes the hydration reactions to slow down and the early wet strength values of the composite to decrease.
3) It was observed that the amount of water absorption increased as the amount of FA in the samples was kept constant and the amount of glass fiber increased. It can be said that this is due to the fact that the fibers increase the void ratio. At the same time, it was observed that the water absorption values increased as the fiber content was kept constant and the FA ratio increased. It is thought that this may be due to the fact that the experiments were carried out after a short curing period of 28 days, and therefore the hydration event could not be completed in mixtures containing large amounts of FA.
4) It has been observed that the water absorption values gradually decrease in the experiments performed after the 28-day curing period. This shows that the void structures of the samples decreased during curing.
5) Reducing the amount of cement to be used as binding material by using FA has many positive results. By using large amounts of FA, it is possible to obtain more green concrete, and at the same time, a waste material is effectively brought to the industry. As a result, the effects of ash on environmental pollution are reduced and the cost of storage is eliminated.

REFERENCES

[1] İ. B. Topçu and M. Canbaz, "Uçucu kül kullanımının betondaki etkileri," *Eskişehir Osmangazi Üniversitesi Mühendislik ve Mimarlık Fakültesi Dergisi,* vol. 14, no. 2, pp. 11-23, 2001.

[2] H. Aruntaş, "Uçucu Küllerin Inşaat Sektöründe Kullanim Potansiyeli," *Gazi Üniversitesi Mühendislik Mimarlık Fakültesi Dergisi,* vol. 21, no. 1, 2006.

[3] M. Thomas, *Optimizing the use of fly ash in concrete*. Portland Cement Association Skokie, IL, 2007.

[4] A. Bilodeau and V. M. Malhotra, "High-volume fly ash system: concrete solution for sustainable development," *Materials Journal,* vol. 97, no. 1, pp. 41-48, 2000.

[5] P. Wankhede and V. Fulari, "Effect of fly ash on properties of concrete," *International journal of emerging technology and advanced engineering,* vol. 4, no. 7, pp. 284-289, 2014.

[6] A. Palomo, M. Grutzeck, M. J. C. Blanco, and c. research, "Alkali-activated fly ashes: A cement for the future," vol. 29, no. 8, pp. 1323-1329, 1999.

[7] E. M. S. Mulapeer, "Cam elyaf ile takviyeli uçucu kül esasli jeopolİmer kompozitinin dayanim ve geçİrİmlİlİk özellİkleri," Yüksek Lisans Tezi, İnşaat Mühendisliği, Hasan Kalyoncu University, 2016.

[8] M. Robert, "Climate change and the cement industry," vol. 15, p. 19, 2002.

[9] J. Davidovits and J. Orlinski, *Proceedings Geopolymer'88*. Geopolymer Institute, 1988.

[10] K. Akçaözoğlu and Ş. E. GÜLDÜR, "Mikronize Kalsit ve Uçucu Kül Katkısının Beton Özelliklerine Etkisinin Araştırılması," *Afyon Kocatepe Üniversitesi Fen ve Mühendislik Bilimleri Dergisi,* vol. 17, no. 2, pp. 658-668, 2017.

[11] H. YAPRAK, O. ŞİMŞEK, and Ö. Aydın, "Cam ve çelik liflerin bazı beton özelliklerine etkisi," *Politeknik Dergisi,* vol. 7, no. 4, pp. 353-358, 2004.

[12] ASTM C618 "Standart Specification for Coal Fly Ash and Raw or Calcined Natural Pozzolan for Use as a Mineral Admixture in Concrete", 2000.

[13] V. Akyüncü, "F ve C tipi uçucu küllerin çimento İle İkame edilmesiyle üretİlen betonlarin mekanİk ve dayaniklilik özelİklerİnİn karşilaştirilarak İncelenmesİ," Doktora Tezi, İnşaat Mühendisliği, Sakarya Üniversitesi, 2012.

[14] H. İpek, "Cam elyaf takviyeli kestamid matrisli kompozitlerin üretimi ve mekanik özelliklerinin İncelenmesi," Yüksek Lisans Tezi, Metalurji Ve Malzeme Mühendisliği, 2011.

[15] ASTMC39, "ASTM C39, Standard test method for compressive strength of cylindrical concrete specimens, American Society for Testing and Materials, West Conshohocken, Pa.," ed, 2012.

[16] ASTM C293, Standard Test Method for Flexural Strength of Concrete (using simple beam with center-point loading), American Society for Testing and Materials, West Conshohocken, Pa, 1979.

[17] ASTMC642-13, "ASTM C642-13, Standard test method for density, absorption, and voids in hardened concrete, American Society for Testing and Materials, West Conshohocken, Pa," 2013.

The Comparison of the Approaches for Determining the Actual Embedment Depth of Cantilever Sheet Pile Walls

R.AKAN

Suleyman Demirel University, Isparta/Turkey, recepakan@hotmail.com

***Abstract* – Designing cantilever sheet pile walls is one of the most significant and complicated projects in geotechnical engineering because the complicated interaction between wall movement and earth pressure determines the distribution of earth pressure on the submerged part of the wall. Therefore, there are many approaches that relies on various assumptions and simplifications to modify the basic form of the pressure distribution to discover a solution. In this paper, the embedment depths of the cantilever sheet pile walls in the sand are calculated by using the simplified method(SM) and full method(FM) considering different safety approaches in order to determine the effect of the earth pressure and safety approaches to the embedment depths are examined.**

***Keywords* – Cantilever sheet pile, Embedment depth, Full method, Simplified method, Factor of safety**

I. INTRODUCTION

Cantilever sheet pile walls rely merely on a sufficient depth of embedment for their stability; they are not supported in any other way. The embedded cantilever wall can bear the pressure of the retained soil by producing resistant earth pressures on the immersed section of the wall. As long as the sheet pile is strong enough to bear the structural bending force, they tend to fail by rotation around a pivot point at the lower end [1]. Cantilever sheet-pile walls are often used for excavations that are 6 meters or fewer in height above the dredge line. Because of the various variables, methodologies, and ideas involved in limit equilibrium analysis, designing cantilever sheet pile walls is one of the most significant and complicated projects in geotechnical engineering.

The complicated interaction between wall movement and earth pressure determines the distribution of earth pressure on the submerged part of the wall. Many approaches for evaluating and constructing embedded cantilever walls have been proposed, and Bica and Clayton[2] have assessed them. Each approach assumes a distinct distribution of earth pressure on the wall as well as a varied deflection or movement of the wall. Many academics, including Blum[3], Krey[4], Rowe[5], Hansen[6], Bransby and Milligan[7], Padfield and Mair[8], Lyndon and Pearson[9], Bowles[10], and King[11], have carried out model studies on embedded walls.

Many investigations have contrasted the embedment depths achieved by analytical methods described in the literature with regulations in recent years. Day[12] compared King's [11] approach for designing cantilever sheet piles to frequently used methods in practice in the United Kingdom and the United States. A fresh proposal was also made based on experimental data and an examination of the identical models using the finite element method.

Franklin and Olopade[13] studied the impact of the soil's internal friction angle(IFA),ϕ, on the cantilever sheet pile's embedment depth in cohesionless soils. For this purpose, he interpreted the data using the CECP2 and BS80002 design methods. Hassani et al.[14] used both classical and numerical methods to create an acceptable design method and theory for the Tuti-Bahri Bridge project's anchored sheet pile walls. Conte et al.[15] analyze computational and experimental data on internal forces in embedded cantilever retaining walls and provide a straightforward method for designing embedded cantilever retaining walls in cohesionless soils under static and seismic conditions. Sheth and Raghavani[16] used conventional methods and finite element analysis to examine the behavior of sheet pile walls employed in homogeneous soils that are both cohesionless and cohesive soil.

In this paper, the actual embedment depths for the cantilever sheet pile walls in the sand were determined using the net pressure method in the FM [4], [17] and the SM [6], [8] while taking into account safety recommendations such as increasing the unfactored embedment depth by a factor of 1.3 and decreasing the passive pressure coefficient by 1.5 and 2 as factory of safety (FOS). The variations and ratios of embedment depths to each other were displayed, analyzed, and assessed while utilizing various IFA of the sand, calculation methods, and safety approaches.

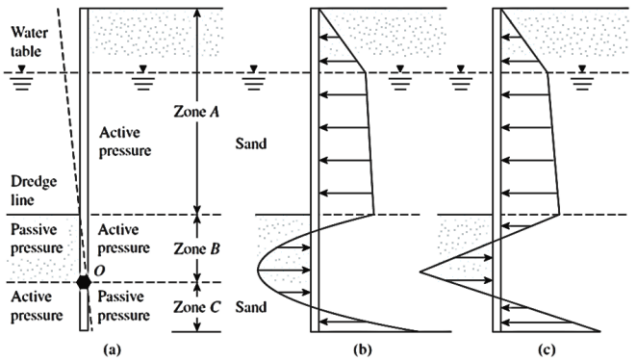

Figure 1: Cantilever sheet pile penetrating sand [17]

The actual deflection and net stress distribution and net idealized stress distribution of a sheet pile wall in the sand are shown in Fig. 1 [17]. The graphic depicts the sort of lateral yielding a cantilever wall experiences in the axis O below the dredge line. All of the primary limit equilibrium design and analysis methods employ this general shape and each approach relies on various assumptions and simplifications to modify the basic form of the pressure distribution to discover a solution.

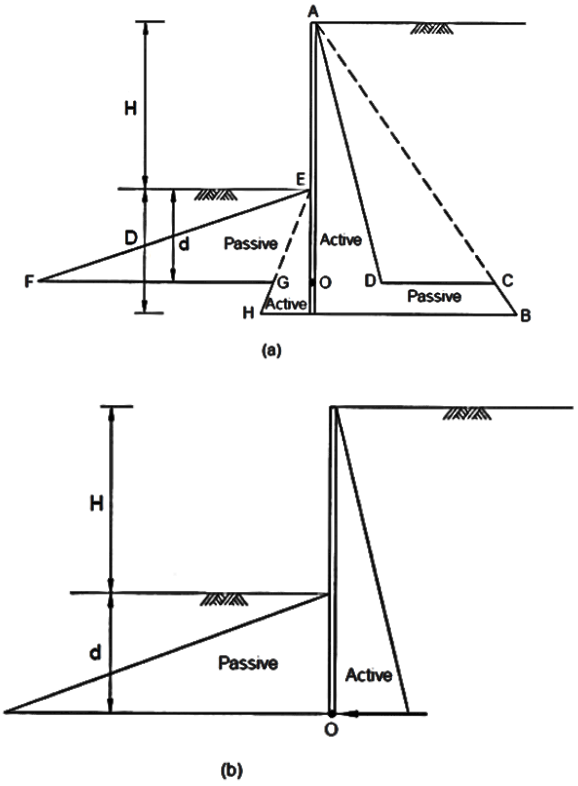

Figure 2: Pressure distribution based on a) FM b) SM [12]

Padfield and Mair[8] provide the "full method" and "simplified method" for cantilever retaining wall analysis. The two methods are based on the pressure diagrams depicted in Figure 2.

A. Full Method(FM)

This is a modernized version of a Krey-proposed method from Bowles[10] and King[11]. This method is widely utilized in the United States. Construct the equations for determining the adequate depth of sheet piles embedded into granular soil as well as the retained soil above the dredge line is granular. L_1 are the water table depth below the top of the wall and the sand's effective friction angle is ϕ'. The active pressure at L_1 depth is,

$$\sigma_1' = \gamma L_1 K_a \quad (1)$$

where,
K_a = Rankine active pressure coefficient = $tan^2(45 - \phi'/2)$
γ = Unit weight of soil above the water table

Similarly, for the depth of $H = L_1 + L_2$, the active pressure is,

$$\sigma_2' = (\gamma L_1 + \gamma' L_2) K_a \quad (2)$$

where γ'=effective unit weight of soil = $\gamma_{sat} - \gamma_w$.

In the calculations, the unit volume weight of water (γ_w) was taken to be 9.81 kN/m^3.

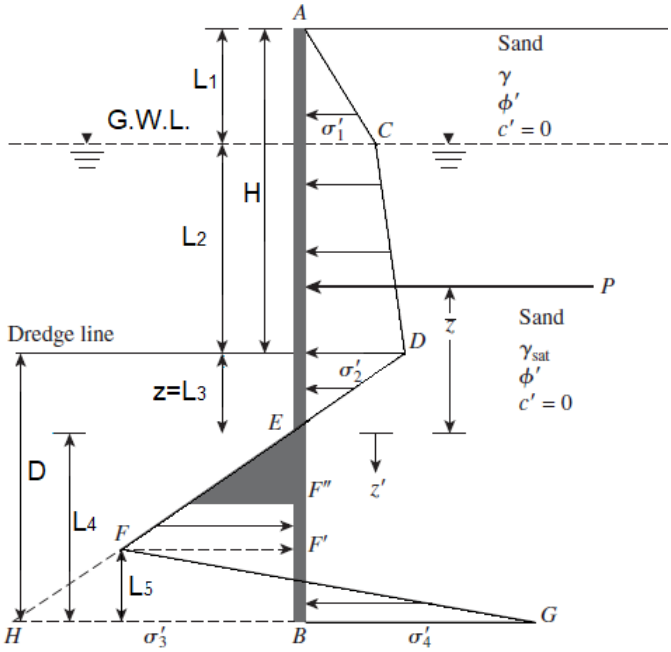

Figure 3: Variation of net pressure diagram in FM for a cantilever sheet pile penetrating sand[17]

Note that the hydrostatic pressures on both sides of the wall are the same magnitude for all levels and cancel out, therefore they are disregarded. To estimate the net lateral pressure below the dredge line up to the point of rotation, O, an engineer must assess both passive and active pressures working from the left side toward the right side of the wall, as illustrated in Figure 2a [12] and may use the net soil pressure as shown in Figure 3 and follow calculation steps below. At a depth of (H+z), the active pressure is,

$$\sigma_a' = [\gamma L_1 + \gamma' L_2 + \gamma' z] K_a \quad (3)$$

And passive pressure at a depth z is,

$$\sigma_P' = \gamma' z K_P \quad (4)$$

where,
K_P=Rankine passive pressure coefficient=$tan^2(45 + \phi'/2)$.
The net lateral pressure is obtained by combining Eqs. 3-4.

$$\sigma' = \sigma_2' - \gamma' z (K_P - K_a) \quad (5)$$

At a depth of z below the dredge line, the net pressure, σ' equals zero. So,

$$z = L_3 = \frac{\sigma_2'}{\gamma'(K_P - K_a)} \quad (6)$$

$$\sigma_3' = \gamma' L_4 (K_P - K_a) \quad (7)$$

Passive pressure, σ_P', acts from the right toward the left side of the sheet pile, whereas active pressure acts from the left

toward the right side. So, at the depth of (H+D) is,

$$\sigma_P' = (\gamma L_1 + \gamma' L_2 + \gamma' D)K_P \quad (8)$$
$$\sigma_a' = \gamma' D K_a \quad (9)$$

As a result, at the bottom of the sheet pile, the net lateral pressure is,

$$\sigma_5' = (\gamma L_1 + \gamma' L_2)K_P + \gamma' L_3(K_P - K_a) \quad (10)$$
$$D = L_3 + L_4 \quad (11)$$
$$\sigma_4' = \sigma_5' + \gamma' L_4(K_P - K_a) \quad (12)$$

Statics principles may now be used to determine the wall's stability. As a result, Eq. 13 is obtained by adding the moment of all the forces around point B.

$$P(L_4 + \bar{z}) - \left(\frac{1}{2}L_4\sigma_3'\right)\left(\frac{L_4}{3}\right) + \frac{1}{2}L_5(\sigma_3' + \sigma_4')\left(\frac{L_5}{3}\right) = 0 \quad (13)$$
$$L_5 = \frac{\sigma_3' L_4 - 2P}{\sigma_3' + \sigma_4'} \quad (14)$$

The following fourth-degree equation (Eq. 15) is derived in terms of L_4 by combining Eqs. 7,10,13, and 14 and simplifying them further:

$$L_4^4 + A_1 L_4^3 - A_2 L_4^2 - A_3 L_4 - A_4 = 0 \quad (15)$$

In this equation,

$$A_1 = \frac{\sigma_5'}{\gamma'(K_P - K_a)} \quad (16)$$
$$A_2 = \frac{8P}{\gamma'(K_P - K_a)} \quad (17)$$
$$A_3 = \frac{6P[2\bar{z}\gamma'(K_P - K_a) + \sigma_5']}{\gamma'^2(K_P - K_a)^2} \quad (18)$$
$$A_4 = \frac{P(6\bar{z}\sigma_5' + 4P)}{\gamma'^2(K_P - K_a)^2} \quad (19)$$

B. *Simplified Method(SM)*

The earth pressure distribution is simplified in this method, as illustrated in Fig. 4. At point O, the force R, which represents the net force operating below point O, is supposed to act. The value of d necessary for stability is obtained by achieving moment equilibrium around O. Padfield & Mair[8] proposed that the critical embedment length(d) produced by the SM be raised by 20% to allow the growth of the force R, in order to adjust for the simple method's approximations. That is, utilizing the D=1.2d relationship, a FM estimate of the unfactored embedment depth(D) may be produced. In the United Kingdom, this method is widely utilized. The following are the main steps for calculation of the lateral soil pressures using the SM (Eqs. 20-23).

The active pressure at L_1 depth is,

$$\sigma_1' = \gamma L_1 K_a \quad (20)$$

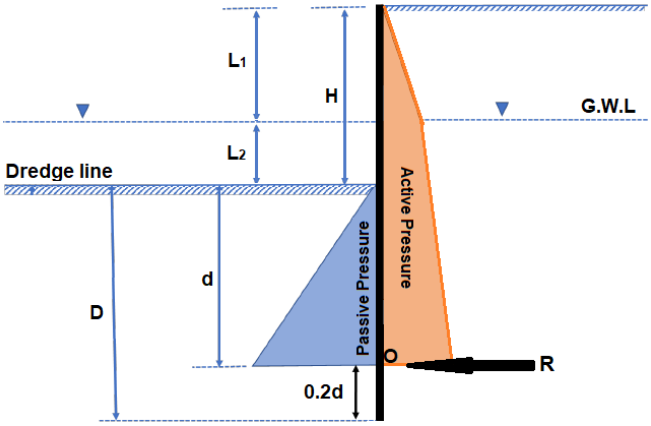

Figure 4: Pressure distribution of SM

Similarly, for the depth of $H = L_1 + L_2$, the active pressure is,

$$\sigma_2' = (\gamma L_1 + \gamma' L_2)K_a \quad (21)$$

The active pressure at the depth of (H+d) is,

$$\sigma_a' = [\gamma L_1 + \gamma' L_2 + \gamma' d]K_a \quad (22)$$

And passive pressure at depth z is,

$$\sigma_P' = \gamma' d K_P \quad (23)$$

The value of d, is derived by solving the third-order equation with the moment of all active and passive forces around point O summed and equalized to zero. Furthermore, to compute the unfactored embedment depth, D, the depth, d, must be raised by at least 20%.

The unfactored embedment depth is increased by about 20% to 30% for safety reasons. Also, as indicated below, some designers prefer to begin with a factor of FOS on the passive earth pressure coefficient, and then use the resulting $K_{P(design)}$ instead of K_P in the calculations above.

$$K_{P(design)} = \frac{K_P}{FS} \quad (20)$$

where FS is the factor of safety (usually between 1.5 and 2) [17].

The soil is sand that has 15.9 kN/m^3 and 19.33 kN/m^3 unit weights are natural and saturated, respectively. The excavation depth is 5m and the groundwater level is 2m below the surface on both sides of the wall. IFAs of sand vary 20 to 45 degrees and as a FOS, two different approaches were considered. One of these approaches is multiplying the embedment depth by 1.3 without reducing the passive earth pressure and the other one is reducing the passive earth pressure by both 1.5 and 2 as the FOS. The models are developed and the embedment depths of the cantilever sheet pile wall are calculated by using the SM and FM considering different safety approaches in order to determine the effect of the calculation methods and the approaches for safety to the embedment depths of the cantilever sheet pile walls in the sand are examined.

II. DISCUSSION

Fig. 5 and Fig. 7 show the variation of embedment depths obtained with the FM as a function of the IFA and the FOS, while Fig. 6 and Fig. 8 show the variation of embedment depths obtained with the SM as a function of the IFA and the FOS. Denotes are used in figures presented in the section of Appendix.

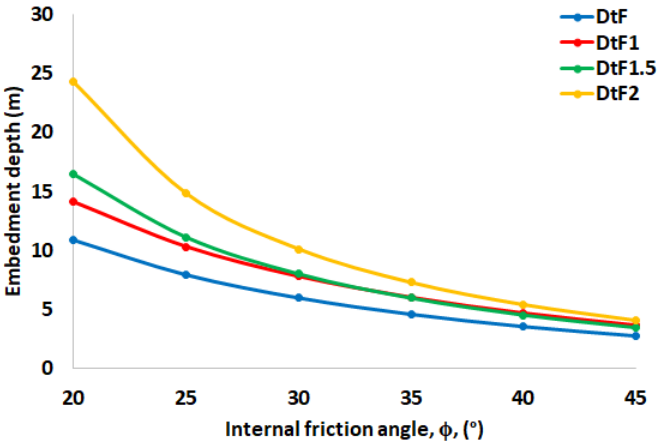

Figure 5: Variation of embedment depths with various factors of safety in the FM

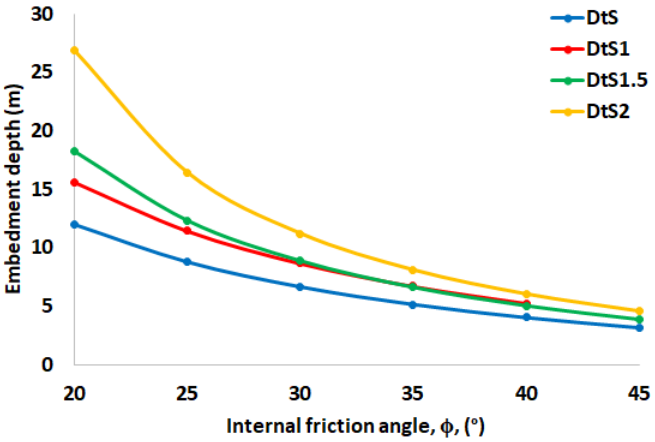

Figure 6: Variation of embedment depths with various factors of safety in the SM

The embedment depths in both SM and FM decrease as the IFA increases. For both methods, the effect of the IFA on embedment depth reduces as the IFA rises, whereas it rises as the FOS rises.

The embedment depths obtained by both the SM and the FM increase by 1.23 and 1.52 times for the IFAs of 45 and 20, respectively, if the FOS is taken as 1.5. If the FOS is taken as 2, the IFAs increase by 1.45 and 2.24 times for 45 and 20, respectively.

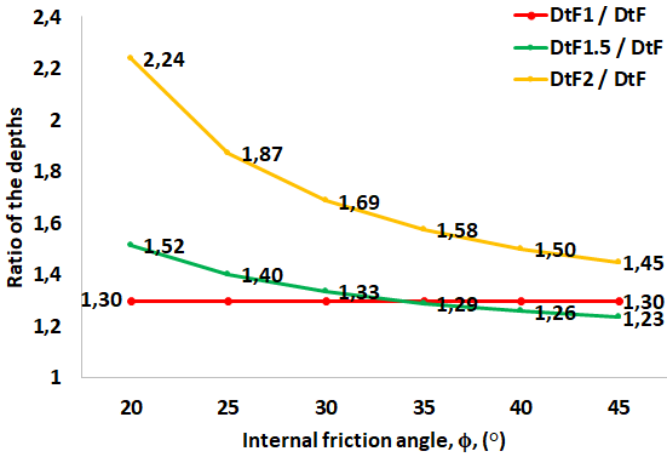

Figure 7: Variation ratios of embedment depths with various factors of safety based on unfactored embedment depths in the FM

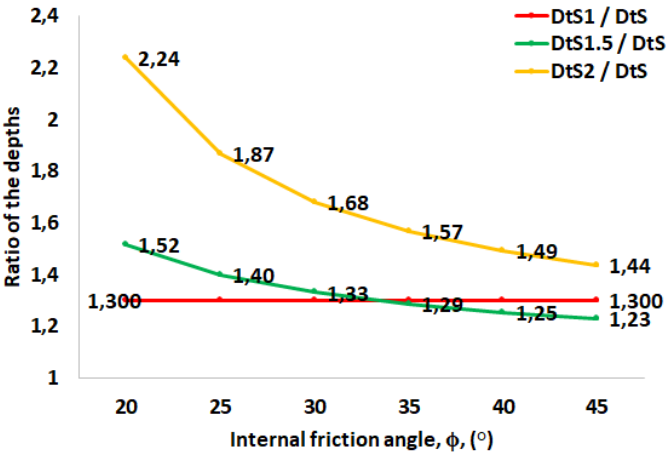

Figure 8: Variation ratios of embedment depths with various factors of safety based on unfactored embedment depths in the simplified method

In both methods, multiplying the embedment depths by 1.3 without reducing the passive stress coefficient by the FOS results in a lesser embedment depth than the cases that in the passive stress coefficient reduced by using the FOS as 2.

Multiplying the embedment depths by 1.3 without reducing the passive stress coefficient by the FOS results in a lesser embedment depth for the IFAs of 20 to 25 but greater embedment depths for the IFA of 35 and higher than the cases that in the passive stress coefficient reduced by using the FOS as 1.5.

In cases where similar factors of safety are used, the SM gives 10-12% greater embedding depths compared to the FM. The difference of depths obtained by different methods increases with the increase of the IFA, even if it is 2%.

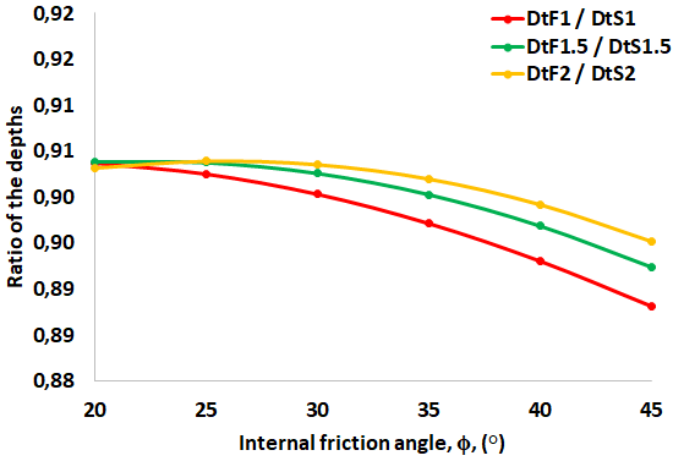

Figure 9: Ratios of embedment depths of the FM to SM with the various FOS

III. CONCLUSION

In this study, the models are developed and the embedment depths of the cantilever sheet pile wall are calculated by using the SM and FM considering different safety approaches in order to determine the effect of the used methods and the approaches for the safety to the embedment depths of cantilever sheet pile walls in the sand are examined. Consequently, the following conclusions can be drawn:

- The embedment depths decrease as the IFA increases.
- The effect of the IFA on embedment depth reduces as the IFA rises, whereas it rises as the FOS rises.
- The embedment depths increase in the range of 1.23 to 1.52 times for the IFA of 45 to 20 degrees in the case that the passive earth pressure is reduced by 1.5 as the FOS.
- The embedment depths increase in the range of 1.45 to 2.25 times for the IFA of 45 to 20 degrees in the case that the passive earth pressure is reduced by 2 as the FOS.
- Multiplying the embedment depths by 1.3 without reducing the passive stress coefficient by a FOS results in a lesser embedment depth than when the passive stress coefficient is reduced by using the FOS as 2.
- Multiplying the embedment depths by 1.3 without reducing the passive stress coefficient by a FOS results in a lesser embedment depth than when the passive stress coefficient is lowered by 1.5 for IFAs less than 35 degrees but not for higher angles.
- The SM gives 10-12% greater embedding depths compared to the FM.

APPENDIX

DtS: The embedment depth obtained from the simplified method before factored for safety

DtS1: The embedment depth that is multiplied by 1.3 obtained from the simplified method

DtS1.5: The embedment depth that is obtained by reducing the passive pressure by 1.5 as a factor of safety in the simplified method

DtS2: The embedment depth that is obtained by reducing the passive pressure by 2 as a factor of safety in the simplified method

DtF: The embedment depth obtained from the full method before factored for safety

DtF1: The embedment depth that is multiplied by 1.3 obtained from the full method

DtF1.5: The embedment depth that is obtained by reducing the passive pressure by 1.5 as a factor of safety in the full method

DtF2: The embedment depth that is obtained by reducing the passive pressure by 2 as a factor of safety in the full method

SM: Simplified method

FM: Full method

FOS : Factor of safety

IFA: Internal friction angle

REFERENCES

[1] W. Powrie, *Soil Mechanics: Concepts and Applications*. London, UK: E and FN Spon, An imprint of Chapman and Hall, 1997.

[2] A. V. D. Bica and C. R. I. Clayton, "Limit equilibrium design methods for free embedded cantilever walls in granular materials," *Proc. Instn Civ. Engrs Part 1*, vol. 86, pp. 879–989, 1989.

[3] H. Blum, *Einspannungsverhältnisse bei Bohlwerken*. Berlin, Germany: Ernst & Sohn, 1931.

[4] H. Krey, *Erddruck, Erdwiderstand und Traqjaliigkeit des Baugrundes*, 4th ed. Berlin, Germany: W. Ernst & Sohn, 1932.

[5] P. W. Rowe, "Cantilever sheet piling in cohesionless soil," in *Engineering*, 1951, pp. 316–319.

[6] J. B. Hansen, "Limit design and safety factors in soil mechanics," *Bulletin No. 1.*, Danish Geotechnical Institute, Lyngby, Denmark, 1956.

[7] J. E. Bransby and G. W. E. Milligan, "Soil Deformations near Cantilever Retaining Walls," *Geotechnique*, vol. 24, no. 2, pp. 175–195, 1975.

[8] C. Padfield and R. Mair, *Design of Retaining Walls Embedded in Stiff Clay*, no. 104. London, UK: Construction Industry Research & Information Assoc, 1984.

[9] A. Lyndon and R. A. Pearson, "Pressure Distribution on a Rigid Retaining Wall in Cohesionless Material," in *Proceedings of International Symposium on Application of Centrifuge Modelling to Geomechanics Design*, 1985, pp. 271–280.

[10] J. Bowles, *Foundation Analysis and Design*, 4th Editio. New York: McGraw-Hill, 1988.

[11] G. J. W. King, "Analysis of Cantilever Sheet-Pile Walls in Cohesionless Soil," *J. Geotech. Geoenvironmental Eng.*, vol. 121, no. 9, pp. 629–635, 1995.

[12] R. A. Day, "Net pressure analysis of cantilever sheet pile walls," *Géotechnique*, vol. 49, no. 2, pp. 231–245, Apr. 1999, doi: 10.1680/geot.1999.49.2.231.

[13] S. Oluyemi Franklin and A. Luqman Olopade, "Some Remarks on the Application of the Cecp2 and Bs8002 Methods for the Analysis and Design of Anchored Sheet Pile Walls," *IJRRAS*, vol. 11, no. 1, 2012, Accessed: Oct. 18, 2021. [Online]. Available: www.arpapress.com/Volumes/Vol11Issue1/IJRRAS_11_1_12.pdf.

[14] R. Hassani, R. Basirat, and N. Mahmoodian, "Classical Method and Numerical Modeling for Designing of Sheet Pile Wall (Case Study: Tuti-Bahri Bridge, Sudan)," 2016.

[15] E. Conte, A. Troncone, and M. Vena, "A method for the design of embedded cantilever retaining walls under static and seismic loading," *Geotechnique*, vol. 67, no. 12, pp. 1081–1089, 2017.

[16] A. K. Sheth and R. Raghavani, "Comparison of Conventional Method with Finite Element Analysis Using Plaxis 2D for Cantilever and Anchored Sheet Pile Walls," in *Proceedings of the Indian Geotechnical Conference 2019*, Springer Singapore, 2021, pp. 577–583.

[17] B. M. Das, "Solutions Manual for Principles of Foundation Engineering SI Edition 8th Edition," p. 12, 2016.

Hydrometeorological Trend Analysis for 1990-2017: A Case Study Sarız, Turkey

C. KOYCEGIZ[1*] and M. BUYUKYILDIZ[1]

[1*]Konya Technical University, Konya/Turkey, ckoycegiz@ktun.edu.tr
[1]Konya Technical University, Konya/Turkey, mbuyukyildiz@ktun.edu.tr

Abstract **- Climate change significantly affects the variability of hydro-meteorological parameters. Within the scope of this study, a trend analysis study was conducted for Sarız district in the Seyhan basin. Monthly data for the period 1990-2017 were provided for the parameters of flow, temperature, precipitation, relative humidity and wind speed. In the study, Mann Kendall (MK), Spearman's Rho (SRho) and Innovative Şen Trend (IŞT) methods were used for trend analysis. According to the results obtained, a significant trend in precipitation and temperature could not be determined. While there was a significantly decreasing trend in flow and wind speed, a significant increasing trend was revealed for relative humidity.**

Keywords– **Innovative Şen, Mann Kendall, Spearman's Rho, Sarız, Trend**

I. INTRODUCTION

Climate change and anthropogenic effects significantly affect the whole world. Many disasters occur with changing ecosystems and meteorological conditions. IPCC [1], states that climate change threatens not only water resources and ecosystems, but also many socio-economic structures. Conservation and development of water resources is vital given the increasing population. For this reason, researches on the development of water resources are important in terms of creating successful and sustainable strategies.

One of the basis hydro-meteorological studies is to determine the trends of the parameters and to get an idea about the future. Thus, available resources can be used efficiently. In addition, it is possible to take measures against disasters that may occur. Trend analysis methods are effective tools that are frequently used in hydrological studies. Important information about the behavior of the parameter can be obtained if its trend is determined. Among the trend methods, Mann Kendall, Spearman's Rho, Innovative Şen, Pettitt and Linear Regression methods are frequently used methods. There are many examples of trend studies in the literature [2-6].

The Seyhan Basin, determined as the study area, is located in the Mediterranean basin, which is one of the basins most affected by climate change [1]. In the basin, not only agricultural activities, but also animal husbandry and industrial activities are intense [7]. Also, the Seyhan Basin is a basin that transfers water between the basins. Hydrological studies in the Seyhan Basin reveal the effects of climate change [8]. For this reason, the examination of hydrological parameters, research and future predictions come to the fore.

Considering the socio-economic position of the Seyhan Basin and the water resources that have become fragile under climate change, hydrological studies to be carried out in the basin are very important. Kayseri province, Sarız district was determined as the study area. In this study, it is aimed to make a trend analysis of hydro-meteorological parameters (flow, precipitation, temperature, wind speed and relative humidity) for Sarız district in the Seyhan Basin.

II. MATERIAL AND METHODS

A. Study Area and Data

Seyhan Basin is a basin located in the south of Turkey, where agricultural and industrial activities are intense (Figure 1). Sariz district of Kayseri province, located in the Seyhan Basin, was chosen as the study area. Sariz district is a district where animal husbandry and agricultural activities come to the fore. Sariz is located at the intersection of Central Anatolia, Mediterranean and Eastern Anatolia regions. There are Binboğa Mountains in the east of the district and Tahtalı Mountains in the west. The district has a mountainous topography. The altitude is expressed as 1560 m. It has a terrestrial climate. Winters are cold and snowy, summers are dry and cool [9].

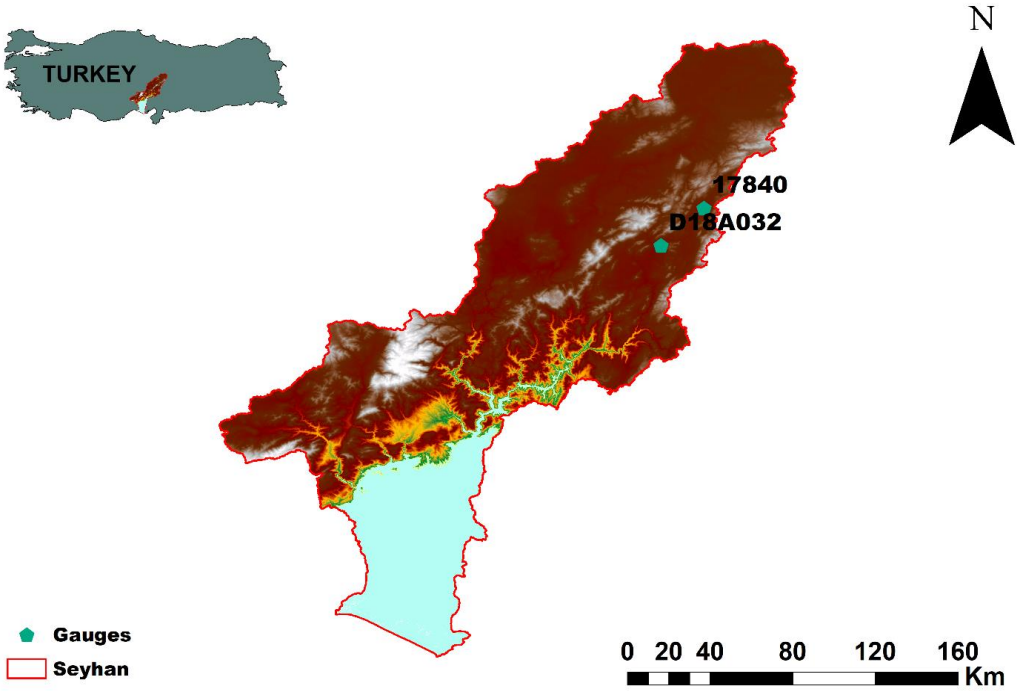

Figure 1: The locations of the stations where the data used in the study were obtained

The data of streamflow (Q) from station D18A032, total precipitation (P), average temperature (T), average wind speed (WS) and average relative humidity (RH) from station 17840, used in this study, were obtained from the State Hydraulic Works and Turkish State Meteorological Service. The data used in the study were obtained on a monthly scale for the period 1990-2017. In Table 1, the basic statistical properties of the studied parameters are given.

Table 1: Descriptive features of the data used in the study

	Min	Mean	Max	Std. Dev.	Skewness	Kurtosis
Q (m^3/s)	0.68	3.91	18.70	3.29	2.22	5.03
P (mm)	0.00	4.12	21.35	2.73	1.62	6.13
T (°C)	-9.30	7.61	22.80	8.41	-0.07	-1.22
WS (m/s)	1.10	1.95	5.10	0.54	1.46	3.85
RH (%)	34.00	60.05	83.60	9.62	0.13	-0.36

B. Trend Analysis Methods

In this study, three different trend analysis methods were used. These trend methods are Mann Kendall (MK) [10, 11], Spearman's Rho (SRho) [12], Innovative Şen Trend (IŞT) [13]. Trend methods are frequently used in time series of hydrology, meteorology and environmental data. Trend analysis methods were applied for 5 parameters obtained from two stations (D18A032 and 17840). For the MK and SRho tests, the critical value was ±1.96 at the 95% significance level. There are many studies in the literature about the trend analysis methods used in the study. The formulation is therefore not given here. For detailed information, references can be found in the literature [2, 14, 15].

III. RESULTS AND DISCUSSION

Hydro-meteorological data were obtained for Sariz district in the Seyhan Basin. Trend analysis was performed on the monthly data obtained for the period 1990-2017.

Table 2 shows the results of the MK and SRho trend tests. Temperature and precipitation parameters remain below the critical value of ±1.96. Therefore, it is not possible to talk about the existence of a significant trend. However, flow, wind speed and relative humidity have a significant trend. The trend direction of flow and wind speed is negative, while the trend for relative humidity is positive.

Table 2: MK and SRho trend analysis results

		Q	P	T	WS	RH
MK	**p-value**	0.0001	0.5845	0.1117	0.0000	0,0033
	z	-3.83	-0.55	1.59	-8.09	2.94
SRho	**p-value**	0.0001	0.6076	0.1065	0,0000	0,0021
	z	-3.92	-0.80	1.55	-8.97	3.02

The results of the IŞT method are given in Figure 2.While no significant trend is observed for low flows, an increasing trend is observed for high flows. No significant trend could be detected for precipitation and temperature. However, wind speed revealed a decreasing trend from low data to high data. Relative humidity has an increasing trend from low data to high data. According to the obtained IŞT results, while the trend in precipitation and temperature could not be determined, an increasing trend in flow and relative humidity and a decreasing trend in wind speed are observed.

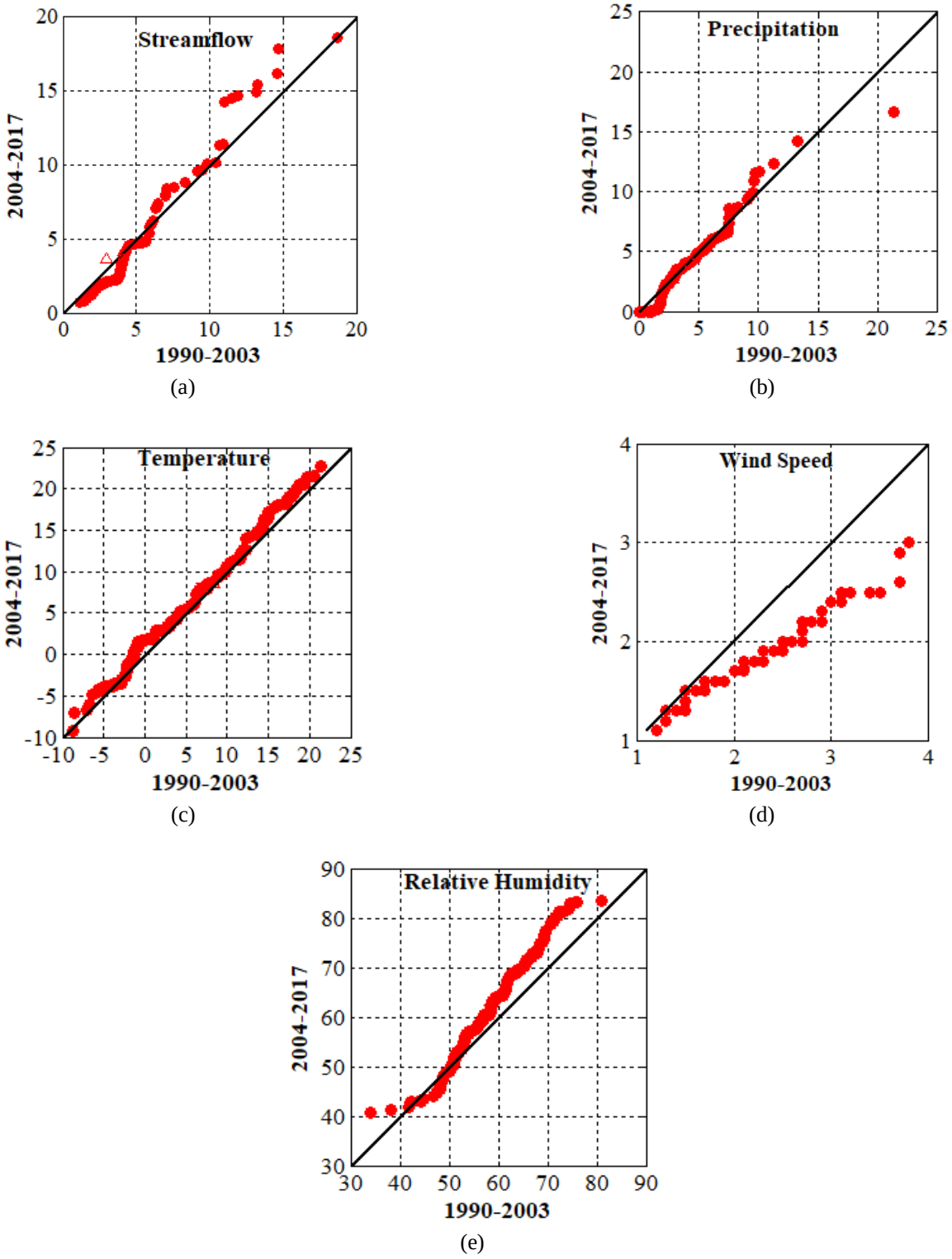

Figure 2: Innovative Şen Trend method results a) Streamflow, b) Precipitation, c) Temperature, d) Wind Speed, e) Relative Humidity

According to the results obtained, three trend analysis methods for temperature and precipitation indicate that there is no significant trend. For all methods, wind speed has a negative significant trend, while relative humidity has a positive significant trend. For flow data, IŞT does not reveal the existence of a significant trend, while MK and SRho indicate the presence of a negative significant trend.

IV. CONCLUSION

In this study, a trend analysis study was conducted for Sarız district, which is located within the borders of Kayseri province in Seyhan Basin. Flow, precipitation, temperature, wind speed and relative humidity parameters obtained for the study area were studied. MK, IŞT and SRho trend tests were applied to the monthly data for the period 1990-2017.

According to the results obtained, precipitation and temperature parameters do not have a significant trend. Even if precipitation and temperature are stable for the time period studied, the danger of climate change should not be ignored. A decreasing trend in flows may be one of the signs that the agricultural sector is in danger of drought. Also, it has been determined that the relative humidity has a significantly increasing trend in the strongly decreasing trend of wind speed.

REFERENCES

[1] IPCC. (2021). Climate Change 2021: The Physical Science Basis. Contribution of Working Group I to the Sixth. *Cambridge University Press*. [Online] Available: https://www.ipcc.ch/report/ar6/wg1/

[2] A. Z. Abiy, A. M. Melesse, W. Abtew, and D. Whitman, "Rainfall trend and variability in Southeast Florida: Implications for freshwater availability in the Everglades," *Plos One*, vol. 14(2), pp. 1-20, 2019.

[3] A. S. Bhatti, G. Wang, W. Ullah, S. Ullah, D. F. T. Hagan, I. K. Nooni, D. Lou, I. Ullah, "Trend in Extreme Precipitation Indices Based on Long Term In Situ Precipitation Records over Pakistan," *Water*, vol. 12, pp. 1-19, 2020.

[4] K. A. Elzopy, A. K. Chaturvedi, K. M. Chandran, G. Gopinath, K. Naveena, and U. Surendran, "Trend analysis of long-term rainfall and temperature data for Ethiopia," *South African Geographical Journal*, vol. 103(3), pp. 1-14, 2020.

[5] S. H. Pour, A. AbdWahab, S. Shahid, and Z. Bin Ismail, "Changes in reference evapotranspiration and its driving factors in peninsular Malaysia," *Atmospheric Research*, vol. 246, 2020.

[6] İ. Çiçek, and N. Duman, "Seasonal and Annual Precipitation Trends in Turkey," *Carpathian Journal of Earth and Environmental Sciences*, vol. 10, pp. 77-84, 2015.

[7] N. Talu, and H. Özüt, *Strategic Steps to Adapt to Climate Change in Seyhan River Basin.* Ankara: T.R. Ministry of Environment and Urbanization General Directorate of Environmental Management Department of Climate Change, 2011.

[8] T. B. Altın, F. Sarış, and B. N. Altın, "Determination of drought intensity in Seyhan and Ceyhan River Basins, Turkey, by hydrological drought analysis," *Theoretical and Applied Climatology*, vol. 139, pp. 95-107, 2020.

[9] Sariz District Governorship. (2019). The History of Sariz. [Online]. Available: http://www.sariz.gov.tr/sarizin-tarihcesi

[10] H. Mann, "Non-Parametric Test against Trend," *Econometrica*, vol. 13, pp. 245-259, 1945.

[11] M. Kendall, *Rank Correlation Methods*. London: Charles Griffin, 1975.

[12] E. L. Lehmann, *Nonparametrics, Statistical Methods Based on Ranks*. San Francisco, California, USA: Holden-Day, 1975.

[13] Z. Şen, "Innovative Trend Analysis Methodology," *Journal of Hydrologic Engineering*, vol. 17(9), 2011.

[14] A. Mondal, D. Khare, and S. Kundu, D. K. ArunMondal, "Spatial and temporal analysis of rainfall and temperature trend of India," *Theoretical and Applied Climatology*, vol. 122, pp. 143-158, 2015.

[15] C. Koycegiz, and M. Buyukyildiz, "Determination of Change Points and Trend Analysis of Annual Temperature Data in Konya Closed Basin (Turkey)," *Nigde Omer Halisdemir University Journal of Engineering Sciences*, vol. 9(1), pp. 393-404, 2020.

Investigation of the Use of Marble Powder in Production of High Strength Concrete

T.DEMİR[1] and K.E.ALYAMAÇ[1]

[1] Fırat University, Elazığ/Turkey, t.demir@firat.edu.tr
[1] Fırat University, Elazığ /Turkey, kealyamac@ firat.edu.tr

Abstract **- One of the aims of this study is to determine the amount of marble powder to be used in the optimum amount to high-strength concrete (HSC). The second is to contribute to the reduction of natural resources using marble powder from waste materials in HSC production. The fine aggregate was used by the marble powder with 0%, 8%, 16% and 24% . In concrete mixtures, the cement was added to the maximum use of the cement to increase the puzolanic activity and to ensure the maximum use of the marble powder. The slump experiment was applied to the mixed mixtures. Then fc-7., fc-28. and fc-90. days It has been kept in the curing pool to be subject to compressive strength test on the days. According to the results obtained from the compressive strength test, the amount of optimum marble powder was determined by taking into account the high strength value. It is also thought that the use of marble powder is positively contributed to the reduction of concrete compressive strength, natural resource consumption and environmental pollution.**

Keywords **- High strength concrete, marble powder, compressive strength, silica fume.**

I. INTRODUCTION

Concrete produced with traditional materials leads to the reduction of available natural materials (). In recent studies, approaches have been developed to include waste materials as an alternative to traditional methods in concrete production [1]. With the use of these waste materials, the negative effects on the environment are reduced, environmental efficiency is increased and solutions are found for the storage problems of wastes. Marble powder and silica fume are widely used in sustainable concrete mixes [2].

Marble powder comes out during the cutting process of marble stones and blocks. It does not have a pozzolanic feature, but by creating a filling effect in concrete mixtures, it provides more void-free concrete [3]. Thus, it affects the compressive strength of concrete positively. On the other hand, due to the small specific surface area of the marble powder, the concrete increases the water requirement. Therefore, the use of more than the optimum amount in concrete mixtures reduces the compressive strength [4]. Environmental benefits are also obtained by using marble powder in concrete mixtures [5]. The use of waste in concrete production provides many advantages. Because the accumulation of industrial wastes such as marble powder, silica fume, fly ash, slag also creates ecological problems, which creates environmental concerns with the occupation of lands [6]. The storage of these wastes, which are formed in large volumes, causes a lot of damage to the environment and living things in these areas [7]. Therefore, the safe use of these wastes is also of great importance for sustainability [8].

The first of the aims of this study is to determine the optimum amount of marble powder to be used in HSCs. The second is to contribute to reducing the use of natural resources by using marble powder from waste materials in the production of HSC. For this, fine aggregate was used by replacing marble powder at the rates of 0%, 8%, 16% and 24% by weight. In order to increase the pozzolanic activity in concrete mixes and to ensure the maximum use of marble powder, silica fume was added up to 10% by weight of the cement. The slump test was applied to the obtained mixtures. Then fc-7., fc-28. and fc-90. days, it was kept in the curing pool to be subjected to the compressive strength test. According to the results obtained from the compressive strength test, the optimum amount of marble powder was determined by taking into account the high strength value. In addition, it is thought that the use of marble powder contributes positively to the compressive strength of concrete, consumption of natural resources and reduction of environmental pollution.

II. MATERIALS AND METHODS

A. Materials

In this study, CEM I 42.5 R portland cement type produced in accordance with TS EN 197-1 standard was used [9]. Marble powder was used by replacing 0%, 8%, 16% and 24% fine aggregate. In order to increase the pozzolanic activity and to ensure the maximum use of marble powder, 10% by weight of silica fume was added to the cement. The physical and chemical properties of these materials are given in Table 1.

Table 1: Chemical and physical properties (%) of materials used in HSC.

Chemical Properties	Cement	Silica Fume	Marble

	(C)	(SF)	Powder (MP)
CaO	63.19	0.40	40.45
SiO_2	19.07	94.10	28.35
Fe_2O_3	3.72	1.50	9.70
Al_2O_3	4.82	0.90	0.17
SiO_3	2.94	94.10	0.02
Na_2O	0.39	0.40	0.05
K_2O	0.62	0.90	0.01
MgO	1.83	0.10	16.25
Cl	0.0101	-	-
Insoluble residue	0.56	-	-
Loss of ignition	3.43	-	4.84
Physical Properties			
Specific surface cm^2/g	3838		3920
Specific gravity g/cm^3	3.13	2.20	2.71
Initial setting time (min)	135	-	-
Final setting time(min)	215	-	-
Total volume exp. (mm)	1	-	-

In the study, andesite aggregate, which has a high compactness, was used. This type of aggregate is dark colored, non-absorbent, non-dispersible and highly compact. At the same time, andesite aggregate contains 52-63% quartz [10,11]. The maximum aggregate particle diameter (Dmax) used in experimental studies is 16 mm. Aggregates are divided into 4 different groups as 0-2, 2-4, 4-8, 8-16 mm. Aggregates separated by sieve classes are given in Figure 1.

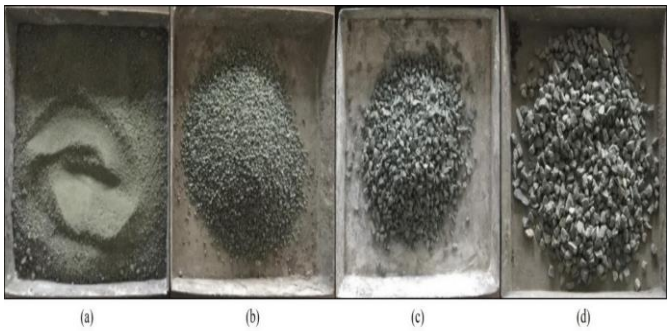

Figure 1: Aggregate grain diameters a) (0-2) mm, b) (2-4) mm, c) (4-8) mm, d) (8-16) mm

B. *Preparation of Samples*

It In the experiments, 4 series of concrete mixtures with different mixing ratios were prepared. Cement dosage was taken as 500 kg/m3 and water/binder ratio was 0.30 in the mixtures. Marble powder was used by replacing 0%, 8%, 16% and 24% fine aggregate. Silica fume was used as a mineral additive by replacing 10% by weight with cement. Due to the high water absorption properties of the materials used, Optima 280 SC3 chemical additive was used at the rate of 1.4% by weight of the cement to provide a fluid consistency in the concrete. The coding and ratios of these samples are presented in Table 2.

Table 2. Proportions of the concrete mixtures (kg/m^3)

Mix Code	Cement	Water	Mikro silis	(0-2) mm	(2-4) mm	(4-8) mm	(8-16) mm	Chemical Additive
S500-1	475	150	35.1	545	359	358	535	6.65
S500-2	475	150	35.1	523	345	358	535	6.65
S500-3	475	150	35.1	501	330	358	535	6.65
S500-4	475	150	35.1	480	316	358	535	6.65

The slump test, which is one of the fresh concrete tests, was applied to the concrete mixtures in the first stage. Afterwards, the prepared concrete mixture was placed in molds of 100x100x100 mm. The samples, which were cured by waiting in the laboratory environment for 24 hours, were removed from the molds and left in the curing pool. In order to determine the hardened concrete properties, the samples were subjected to standard compressive strength tests on the 7th, 28th and 90th days.

III. CONCLUSIONS AND EVALUATION

A. *Compressive Strength*

In this study, it is aimed to determine the amount of marble powder to be used in the optimum amount for HSC based on the compressive strength. For this, 4 series of concrete mixes were prepared and fc-7., fc-28. and fc-90. Compressive strength test was applied. The numerical results of the S500 dosed sample groups are shown in Figure 2 as graphics.

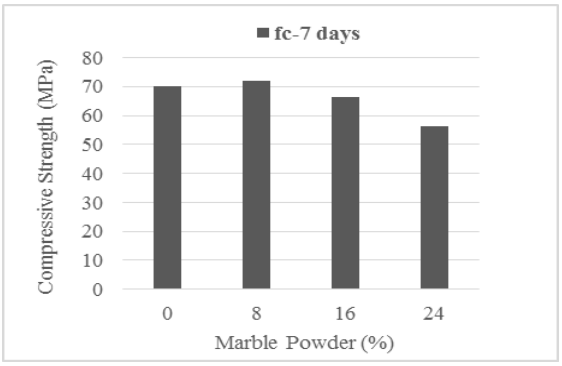

(a)

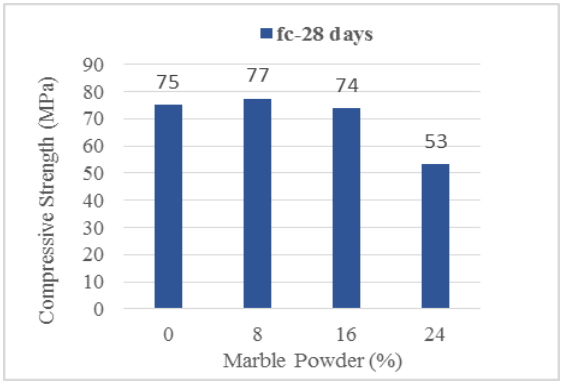

(b)

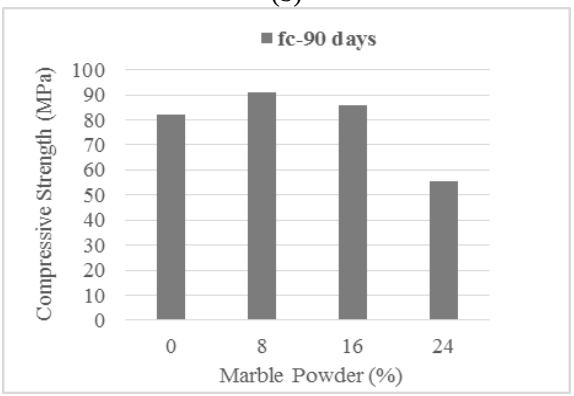

(c)

Figure 2: (a) fc-7 days compressive strength values (b) fc-28 days compressive strength values (c) fc-90 days compressive strength values

When Figure 2. is examined in terms of compressive strength, the compressive strength value was found to be high in the series in which 8% of marble powder was used in general. Due to the filling effect of the marble powder, the compressive strength value in the 1st series, in which marble powder is not used, was lower than in the 2nd series. On the other hand, due to the low machinability of the 3rd and 4th series in which marble powder is used at 16% and 24%, it is thought that the compressive strength of the materials used in the mixture cannot be homogeneously mixed and lumped and placed in the molds well [12]. Therefore, as a result of the data obtained from the experiments, it was seen that the optimum amount of marble powder for HSC was 8%.

The use of more than optimum amount of marble powder complicates the mixing, placing and compaction of concrete due to the increasing water demand. This adversely affects the compressive strength [13]. On the other hand, it is thought that the use of marble powder in HSC mixtures will contribute to the environment and economy.

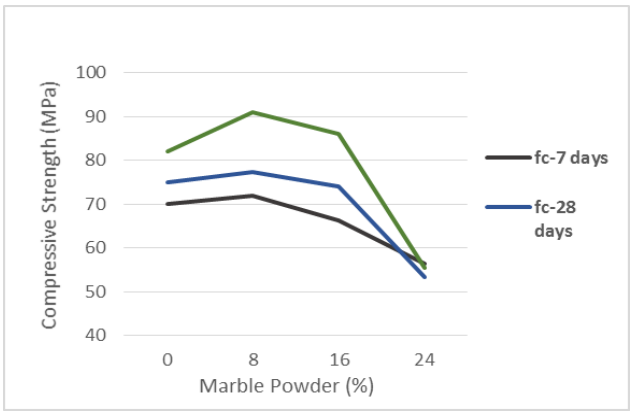

Figure 3: Comparison of fc-7, fc-28, and fc-90 days compressive strength values

Figure 3 shows the comparison of fc-7, fc-28 and fc-90 daily compressive strength values of all series. When the graph is examined, when the increase in compressive strength of fc-7 and fc-28 days is compared with the increase in compressive strength of fc-28 and fc-90; The increase after fc-28 days was greater. The reason for this increase is the addition of silica fume with high pozzolanic activity to the mixture [14]. In parallel with the literature, it is seen that silica fume in concrete mixtures shows a great increase in strength at advanced age and final age values [15]. Likewise, it is clearly seen that the highest value in the compressive strengths of marble powder on the 7th, 28th and 90th days is 8%.

IV. CONCLUSIONS

In this study, the amount of marble powder that can be used at the optimum rate in HSCs was determined and its effect on the performance of concrete was compared. For the study, 4 series of concrete mixes were prepared. Series slump experiments with fc-7, fc-28 and fc-90. Compressive strength tests were carried out. The data obtained and the variation of the marble powder ratio were compared. The general results of the study are given below:

- Since proper workability could not be achieved in concrete mixtures with high marble powder content, a decrease in the compressive strength value was observed.
- It has been determined that high strength is obtained with the use of optimum marble powder and silica fume.
- From the data obtained as a result of the experiments, it was observed that the pozzolanic activity of the silica fume continued for a long time.

As a result of the experiments, the optimum marble powder ratio was determined. In future studies, it is planned to make trial mixtures for HSC at different dosage values at intervals where the marble powder is 8% +/-2%. As a result of the study, it is aimed to produce more environmentally friendly concrete.

REFERENCES

[1] R. Zhong, K. Wille, and R. Viegas, "Material efficiency in the design of UHPC paste from a life cycle point of view," Constr. Build. Mater., vol. 160, 2018.

[2] S. Abbas, A. M. Soliman, and M. L. Nehdi, “Exploring mechanical and durability properties of ultra-high performance concrete incorporating various steel fiber lengths and dosages,” Constr. Build. Mater., 2015.
[3] D. K. Ashish, “Concrete made with waste marble powder and supplementary cementitious material for sustainable development,” J. Clean. Prod., vol. 211, pp. 716–729, 2019.
[4] K. E. Alyamac, E. Ghafari, and R. Ince, “Development of eco-efficient self-compacting concrete with waste marble powder using the response surface method,” J. Clean. Prod., vol. 144, pp. 192–202, 2017.
[5] K. E. Alyamac and A. B. Aydin, “Concrete properties containing fine aggregate marble powder,” KSCE J. Civ. Eng., vol. 19, no. 7, pp. 2208–2216, 2015.
[6] A. A. Thakare, A. Singh, V. Gupta, S. Siddique, and S. Chaudhary, “Sustainable development of self-compacting cementitious mixes using waste originated fibers: A review,” Resour. Conserv. Recycl., p. 105250, 2020.
[7] R. Kumar, S. Singh, and L. P. Singh, “Studies on enhanced thermally stable high strength concrete incorporating silica nanoparticles,” Constr. Build. Mater., vol. 153, pp. 506–513, 2017.
[8] J. Wang, Y. Wang, Y. Sun, D. D. Tingley, and Y. Zhang, “Life cycle sustainability assessment of fly ash concrete structures,” Renew. Sustain. Energy Rev., vol. 80, pp. 1162–1174, 2017.
[9] P. and C. C. Cement - Part 1: General Cements, Composition, “TS EN 197-1,” Turkey, 2012.
[10] O. Soykan, Ö. Cengiz, and Ö. Cenk, “Investigation of the Usability of Slate and Andesite as Concrete Aggregate,” J. Suleyman Demirel Univ. Grad. Sch. Nat. Appl. Sci., vol. 19, no. 1, 2015.
[11] A. D. Öcal and M. Dal, “Decays in natural stones,” Archit. Found. Econ. Enterp. Istanbul, 2012.
[12] N. M. Azmee and N. Shafiq, “Ultra-high performance concrete: From fundamental to applications,” Case Stud. Constr. Mater., vol. 9, 2018.
[13] V. Singhal, R. Nagar, and V. Agrawal, “Use of marble slurry powder and fly ash to obtain sustainable concrete,” Mater. Today Proc., vol. 44, pp. 4387–4392, 2021.
[14] S. Chithra, S. R. R. Senthil Kumar, and K. Chinnaraju, “The effect of Colloidal Nano-silica on workability, mechanical and durability properties of High Performance Concrete with Copper slag as partial fine aggregate,” Constr. Build. Mater., vol. 113, 2016.
[15] [S. A. Khedr and M. N. Abou-Zeid, “Characteristics of silica-fume concrete,” J. Mater. Civ. Eng., vol. 6, no. 3, pp. 357–375, 1994.

WAYFINDING SOLUTION AS STRENGTHENING METHOD FOR SCHOOL BUILDINGS IN CYPRUS

N. Bilsel[1*], I. Safkan[2]

[1] *Architecture Department, European University of Lefke, Lefke, Northern Cyprus, TR-10, Mersin, Turkey*

[2] *Civil Engineering Department, European University of Lefke, Lefke, Northern Cyprus, TR-10, Mersin, Turkey*

(* Corresponding author's email: nbilsel@eul.edu.tr)

Abstract

The island of Cyprus faced many fatal earthquakes throughout its history. Yet, the application of decent seismic design codes is rather recent. A significant number of school buildings in Cyprus were built between 1950-1980s, where the gravity load design and poor material properties were dominant. The school buildings have a prominent role in the education of students, for earthquake preparedness. This study, suggests a methodology where the seismic strengthening process demands the least social intervention on the school environment. Furthermore, the old type reinforced concrete buildings also suffer fire resistance deficiency. In case of an earthquake or fire, as part of the evacuation process, students in the building will face a significant crowd flow towards the way out. Any intervention applied for strengthening the school buildings, will affect the wayfinding characteristics of the school environment. For this purpose, a case study school building is analysed at a densely populated area of the capital city Nicosia. The case study building was built in 1950's with reinforced concrete frame with non-load bearing walls. Gravity load design by the British Standard CP114 dominated the era. Initially, a seismic assessment was conducted on a current frame structure and several strengthening intervention alternatives were applied. As a result, a multidimensional judgment was considered for the selection of strengthening measures. The innovative design procedure is believed to guide the region for a safer urban regeneration.

Keywords: Seismic Strengthening, Sustainable Design, School Buildings

Introduction

Destructive earthquakes hit the island of Cyprus through last centuries and resulted significant loss (1). On the other hand, the use of comprehensive seismic design code begins on late 1990s. During the British colonial rule in Cyprus, the government initiated a variety of unprecedent school designs for over 80 years. Significant number of school buildings were built before the major revision on seismic design code was done. Recent studies (2-5) on evaluation of seismic performance of buildings in Cyprus, argue significant deficiency against the expected event. Therefore, in current situation, significant number of school buildings require strengthening measures in order to achieve required performance level.

The demand on earthquake preparedness is growing with the increased knowledge on vulnerability potential of buildings. Today the education on disaster preparedness is an essential process at schools. Among other public buildings schools are one of the most imperative buildings in an event of evacuation. Students are educated on escape routes and meeting points on a regular basis.

Intervention on structural system often result in changes of architectural layout. Re-utilization of spaces on the other hand, might help the students` understanding especially for school buildings, where the earthquake preparedness form an important component of school education. Strengthening process of the old-type buildings often ignores the architectural layout and damage the existing spatial properties. This study aims to suggest a solution framework for the strengthening process of the old-type reinforced concrete school buildings.

General characteristics of old-type reinforced concrete buildings

Several reinforced concrete design codes were utilised in Cyprus were mainly based on same assumptions, some design rules differed. Table 1 shows the CP114 (6) code suggested concrete and steel material properties. According to the studies based on the statistical investigation of material strength in Cyprus (4), approximately similar cylinder strength (16MPa) was suggested for the same construction period of time.

Table 1. Material Properties of CP114 code (6)

Minimum Cube Strength, MPa	Mild Reinforcement Characteristic Yield Strength, MPa
21	250

Often low-rise school buildings dominate in island. Upon investigation of old structural drawings, code specified minimum reinforcement usage was detected on these buildings. Table 2 presents the code suggested minimum reinforcement ratio for both beam and columns.

Table 2. Comparison of structural detailing specifications

	Minimum Rebar Ratio Beams	Minimum Rebar Ratio Columns
CP114	0.0025	0.008

Most of the buildings in the region that belongs to the era were observed to have Φ6/25cm configuration for stirrups. Although the longitudinal rebar ratio was utilized may be adequate for relatively bigger sections, the inadequate confinement is expected to result in brittle failures.

Seismic Safety of School Buildings in Cyprus

Ribbed bars as well as decent confinement conditions were first observed on post Turkish Earthquake Code 1998 applications (5). This major seismic detailing revision was first initiated in early 2000s and the majority of the existing school buildings belong to the pre-code period. Strengthening these vulnerable buildings is essential and require significant attention due to the existing brittle behavior characteristics.

Several studies were conducted (2,5,7) on seismic assessment and strengthening of school buildings in Cyprus. Significant effort was made on strengthening both beams and columns for achieving the required

base shear demand of these buildings. It is often argued that the shear wall addition solution is inevitable for such deficient reinforced concrete buildings.

Fire Safety of School Buildings in Cyprus

An increased attention was recently drawn by structural engineers on fire safety of reinforced concrete buildings. Design manuals and codes are currently available for use which help achieving safe period of time for evacuation in case of fire. However, the current building stock suffer significant deficiency in fire resistance. In such case, the occupants should be evacuated rapidly. Eurocode method of analysis on fire resistance (8) suggests a method for analyzing fire resistance of structural members. The method is used later to assess the current situation of case study members.

Case Study

Ataturk elementary school was built in 1957 in capital city Nicosia of Cyprus. The building is one of the first reinforced concrete school buildings built in Cyprus. The layout, new materials and façade details marks the building as a pioneering modern architecture dedicated to education of the island. The building embodies almost all features of 20^{th} century modern architectures manifests. The massive building is rising on pilotis, creating both an unusual playground for the children and an unfamiliar architectural approach regarding the precedent school buildings of the island. Figure 1 demonstrates the positive response of this design feature on Mediterranean climate. The pilotis however weakens the general structure of the building making it more vulnerable to horizontal forces during an earthquake (soft story effect). It is suggested to strengthen these pilotis by inclusion of steel braces or by filling in between the columns. The outcome of this will be twofold. First, the covered surfaces will in return create different opportunities for the usage. The infilled spans can be used as semi open classroom. On the other hand, the drawback of this transformation is the difficulties it may cause during a rapid evacuation of the building by using the existing staircases.

The wide longitudinal layout of the building is interrupted with three segments of setback by the staircases. Although the number of staircases is adequate considering the overall meter square, the design of the

stairwell indicates a future probability of inclusion of an elevator system. Nevertheless, this shaft affects overall fragility of the possible escape routes. The setbacks break the monotonous appearance of the wide span building but it delivers a negative impact in the inner layout. The building is majorly occupied by elementary level children. The interrupted corridor by setbacks results in interrupted horizontal visual connectivity therefore both wayfinding, evacuation and control of the corridor is challenged by this fragmentation of the horizontal circulation.

The corridor circulation axis is significantly ample, leaving it possible for inclusion of shear wall strengthening by keeping it possible to maintain a healthy circulation space after the additions made.

Figure 1. Ataturk elementary school building façade

Analysis

A method for brittle building assessment which proposed by Safkan et al., (3) was adopted in this study. A two fold strengthening methodology was adapted herein. First the reinforced concrete shear wall addition to the selected frames were utilized. Alternatively, steel X braces allowing circulation was

designed. Shear wall solution will alter the current circulation layout and the X brace system is expected to keep existing layout. However, the difficulty arises when the X brace system interferes the existing infill walls. Due to that reason, significant amount of existing walls will be demolished, which then will help reducing the global mass of the building. The steel design also requires eccentrically connected braces in the middle due to the circulation corridors.

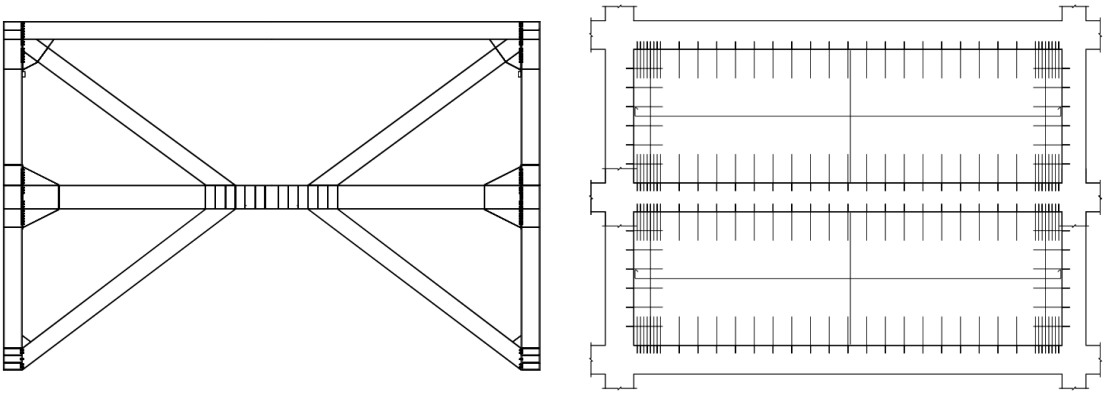

Figure 2. Steel X brace shear wall on the left and reinforced concrete shear wall on the right as two strengthening alternatives

Significant deficiency on expected shear demand was observed when the original frame was assessed. Brittle behavior of the column sections is evident for both flexure and shear demands. Due to the limited deformation capacity of frame, only additional stiffness such as shear wall addition was considered as the strengthening intervention. Pushover analysis was then conducted on both x-braced and shear wall strengthened frame models. Significant increase in base shear capacity was achieved with the additional stiffness (Fig 3). However, the deformation capacity is remained constant after the intervention, as the ductility properties of existing sections were not modified.

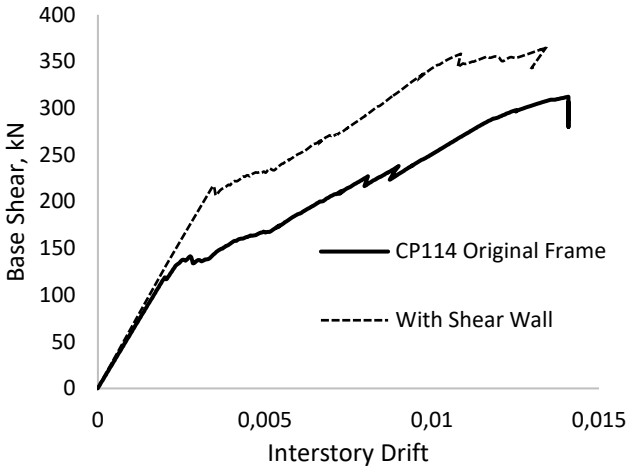

Figure 3. Pushover analysis results

Agent Analysis

Agent based analysis, is a commonly used method for obtaining variables which may have social significance. The agent analysis, assesses the likelihood of the human movement within the given space by considering the visibility of spaces (9). An opensource software tool DepthmapX (10) was utilized for conducting the parametric analysis. The method was formerly proposed by Braaksma and Cook (11) and further developed by Turner and Penn (12) and Turner et al. (13). The method is often used to determine the visibile connections of environments both building and urban scale.

The agent-based model virtually mimics artificially the human circulation in a defined space. It takes the visibility of the given space into consideration to develop a map of concentrated probable navigation pattern. This is an essential tool to understand the likelihood of pupil concentration on site and the building. Visibility of spaces increases the chance of navigation as well as the attained activities of which takes place in those particular spaces. By knowing the concentrated human circulation, the likelihood of congestion can be decreased. A study by Helvacioglu and Olgunturk (14) assessed the wayfinding characteristics of schools environments in Turkey. This study applied agent analysis on case study school building at initial and at post strengthened form.

The analysis was simulated with the average students and staff numbers. The results are presented in building scale and indicates significant reduction in circulation connection with the application of shear wall addition. Alternatively, the steel X brace strengthening method on the other hand allowed limited circulation for the users. Figure 4 shows agent analysis results of initial layout, shear wall intervention and x brace intervention.

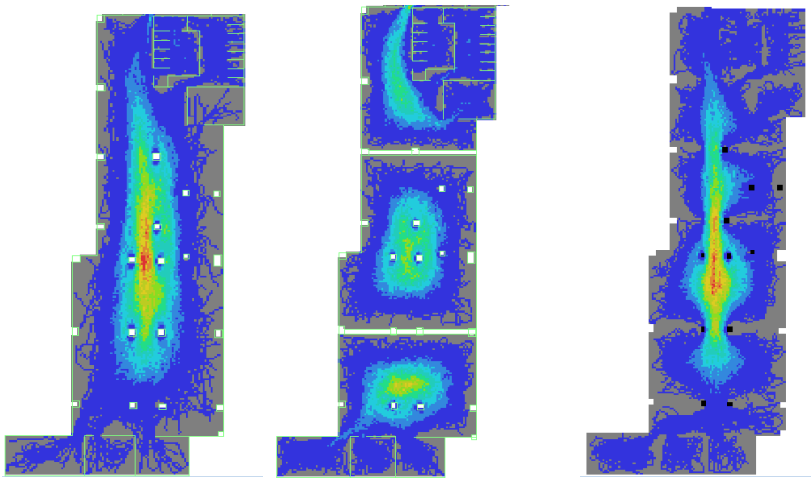

Figure 4. Agent analysis of ground floor original plan (left), after shear wall strengthening intervention (middle) X brace strengthening intervention (rigth)

Fire resistance

Structural members have shallow concrete cover, great diameter sparse reinforcement bars and relatively low confinement properties when compared with nowadays seismically designed sections. Although the density of longitudinal bars are small however, the diameter respect to concrete cover is significantly big. The structural members were evaluated by using Eurocode method of analysis on fire resistance (8) which suggests, the reinforced concrete columns of the case study building, can only resist the fire for 30 minutes. On the other hand, the building was covered recently with the highly flammable PVC insulation material (Fig. 1), which increases the fire potential of the building. In this case, significant effort is needed for

allowing the shortest evacuation route for the occupants. For this purpose, the plan was revisited and fire escape stairs were suggested by utilizing the inspection rooms that are currently out of use. (Fig. 5).

Figure 5. Current and proposed floor plans with fire exit stairs

Conclusions

As a result of the study, several strengthening alternatives were considered and a selection criteria was highlighted. Stiffness addition scheme was found to be the most convenient way of strengthening such old-type frame buildings. From the comparative analysis results, the selection of shear wall location was parametrically assessed and the location allowing the best evacuation route was chosen. The methodology allows designers to consider, the consequences of strengthening methods in order to allow the best evacuation route. Several conclusions are given below;

- A brittle behavior is expected from such mid-century reinforced concrete buildings, where the sections are poorly confined with limited ductility characteristics. Due to the global deficiency in rotational capacity, additional stiffness strengthening methodology solution was best utilized in such old type buildings.

- As result of comparative study on strengthening methodologies, the bare shear wall solution was found to obstruct the current pedestrian flow and expected to reduce the evacuation period. On the other hand, steel X brace strengthening methodology, allow easy access along the frames and minimize the pedestrian flow obstruction.
- The architectural consequence of the proposed seismic retrofit is twofold. The visual characteristics of the building will inevitable altered. On the other hand, the space beneath the building mass will have more definition and an increased possibility of usage will be offered due to new inclusion of vertical surfaces.
- The overall assessments indicate that, in case of a rapid evacuation need, the two story building does not deliver adequate safety measures for primary level students. For in such buildings, the additional fire exit staircase is essential.

References

1 Earthquake Report. Cyprus Historical Loss Database. Accessed online https://earthquake-report.com/2014/05/04/important-historic-earthquakes-in-cyprus/

2 Chrysostomou, C. Z., Kyriakides, N., Papanikolaou, V. K., Kappos, A. J., Dimitrakopoulos, E. G., & Giouvanidis, A. I. Vulnerability assessment and feasibility analysis of seismic strengthening of school buildings. Bulletin of Earthquake Engineering, 13(12), 3809-3840, 2015.

3 Safkan, I., Sensoy, S., & Cagnan, Z. Seismic behaviour of the old-type gravity load designed deteriorated RC buildings in Cyprus. Engineering Failure Analysis, 82, 198-207. 2017.

4 Safkan, I. Eastern Mediterranean University. PhD Thesis 2018

5 Safkan, I. Seismic safety of school buildings in Cyprus. International Civil Engineering and Architecture Conference, Turkey, 2019

6 British Standards Institution. CP114 Code of Practice for the Structural Use of Concrete. BSI.1948

7 Yalciner, H., Sensoy, S., & Eren, O. (2015). Seismic performance assessment of a corroded 50-year-old reinforced concrete building. Journal of Structural Engineering, 141(12), 05015001.

8. The Concrete Centre (2015), Concrete Design Guide. No. 6: Fire design of concrete columns and walls to Eurocode 2. The Institution of Structural Engineers, volume 93 issue 6, 2015

9 Turner, A. Depthmap: a program to perform visibility graph analysis. In Proceedings of the 3rd International Symposium on Space Syntax Vol. 31, pp. 31-12.2001

10 DepthmapX development team. (2017). depthmapX (Version 0.6.0) [Computer software]. Retrieved from https://github.com/SpaceGroupUCL/depthmapX/1

11 Braaksma, J P and Cook, W J, 1980, Human orientation in transportation terminals. Transportation Engineering Journal 106 (TE2) 189-203

12 Turner, A., Penn, A. (1999) Making isovists syntactic: isovist integration analysis. Proceedings of the 2nd International Space Syntax Symposium, Universidade de Brasília, Brasilia, Brazil, 29 March – 2 April 1999.

13 Turner, A., Doxa, M., O'Sullivan, D., Penn, A. (2001) From isovists to visibility graphs: a methodology for the analysis of architectural space. Environment and Planning B: Planning and Design 28(1) 103-12

14. Arslan, D. H. and Koken, B (2016). Evaluation of the Space Syntax Analysis in Post- strengthening Hospital Buildings. Architecture Research. 6(4): 88-97. doi:10.5923/j.arch.20160604.02

Use of F-type Fly Ash in Cement Mortar with Alternative Mixing Methods

A.AKIN[1] and M. ALITHAWI[1]

[1]Konya Technical University, Konya/Turkey, aakin@ktun.edu.tr
[1]Konya Technical University, Konya/Turkey, mr1.ayad92@gmail.com

Abstract **- In this study, it is focused on the use of fly ash, which is one of the industrial wastes, as a partial replacement of cement and fine aggregate in cement mortar. The feasibility of using fly ash as an alternative to cement and fine aggregates in concrete was determined by examining its effect on strength and durability properties in composites. Fly ash was used in the mixtures with three different mixing methods. These is the simple substitution method, addition method and the partial substitution method. In each method, 10%, 20% and 30% of the material was removed by weight, and a total of ten different mixtures were prepared by adding fly ash instead. As a result of the experiments to determine the properties of the mixtures in fresh and hardened state, the inclusion of fly ash in the mixtures improved the workability, freeze-thaw resistance, water absorption and capillary water absorption rate increased with the increase of the fly ash content. The results obtained in terms of the methods used in the study; in the pressure, water absorption and capillary water absorption experiments, the addition method gave better results than the other methods, and according to the bending and cylinder splitting test results, the mixtures prepared with the partial substitution method were found to be higher than the other mixing methods.**

Keywords **– Fly ash, simple substitution method, partial substitution method, addition method, mechanical properties, freeze-thaw, permeability properties**

I. INTRODUCTION

Concrete is the most used building material worldwide. The use of cement and aggregate in concrete composition causes rapid depletion of natural resources and environmental pollution. Replacing any of these materials with industrial waste materials has a positive impact on the environment as it reduces the problem of waste disposal, intensive use of energy and natural resources. The durability of concrete is an important consideration to ensure a long service life in aggressive environments. Although Portland cement is one of the main components used in concrete production, it is a relatively high cost material that has no alternative in the construction industry. A large amount of cement production causes environmental problems and also consumes a lot of energy. It causes about 7% of the total greenhouse gas emissions in the world [1]. In this situation, engineers and scientists are faced with the crucial decision to either destroy the ecosystem by continuing concrete production or to seek an alternative methodology to conserve natural resources by reducing CO_2 emissions [2]. They can be used as alternative sources in concrete as they can help solve some environmental concerns such as the use of industrial waste materials as recycled materials, the problem of waste disposal, and the intensive use of energy and natural resources. There are many industrial waste products that have the potential to replace aggregate and cement in concrete, such as plastic, fly ash, rubber, steel slag and leather waste. Fly ash (FA), which is one of these industrial wastes, can be partially used instead of cement thanks to its pozzolanic structure, thus reducing the carbon emissions and industrial waste amount resulting from cement production. Class F FA contains a small amount of lime. Thus, the increase in the amount of FA in the concrete causes a decrease in the compressive strength. However, the pozzolanic activity of FA increases the compressive strength in advancing curing times [3]. As a result of the pozzolanic reaction, the increase in strength lasts longer than conventional concrete [4].

The voids in the concrete affect the transport of environmental fluids. In their study, Supit and Shaikh observed that with the addition of FA to concrete, the void volume decreased by 6-11% compared to conventional concrete [5]. On the other hand, in the study reported by Mardani-Aghabaglou et al. it was reported that the durability performance was adversely affected as the FA ratio increased with the replacement of FA with cement [6].

FA can be used in concrete with three different mixing methods [7]. These; simple substitution method, addition method and partial substitution method. In the simple substitution method, a certain amount of cement is removed from the mixture and replaced with the same amount of FA. Concretes produced by this method have low strength at early ages. The main purpose of using the simple substitution method is to reduce the heat of hydration and increase the workability in mass concrete production. In addition, this method can be evaluated environmentally and economically. In the addition method, fine aggregate is removed from the mixture without changing the amount of cement in the mixture and FA is added instead. Thus, the amount of binder in the mixture increases. The main purpose of using this method is to increase the strength of concrete in later ages and to obtain a more impermeable concrete with a denser microstructure. In the partial replacement method, FA is substituted for the cement and fine aggregate removed from the mixture. In this method, it is aimed to provide optimum benefit from the positive features provided by the two methods mentioned above. In this study, three different ratios of FA were added to the mixtures with three different mixing methods and their effects on the fresh and hardened mortar properties were investigated. In the literature, FA is widely used in mortar by replacing cement [8]. In this study, the effects of FA on mixture properties were investigated by substituting both cement and aggregate in equal proportions. Various tests were

carried out to determine the consistency and unit weight values of fresh mixtures and the strength, permeability and durability properties of hardened samples. Compressive, flexural and cylinder splitting strength tests in the determination of mechanical properties; water absorption and capillary water absorption in determining permeability properties; In the determination of durability properties, freeze-thaw tests were carried out.

II. MATERIAL AND METHOD

A. Materials

In the study, CEM I 42.5 R type cement, F class FA according to ASTM C618 [9] standard and sand obtained from local sources with 0-4 mm grain size were used. Chemical and physical properties of cement and FA are given in Table 1.

Table 1: Chemical and physical properties of cement and fly ash

Chemical Composition (%)	Cement (C)	Fly Ash(FA)
SiO_2	20.8	50.98
Al_2O_3	5.42	13.11
Fe_2O_3	2.98	9.74
S+A+F	29.2	73.83
CaO	61.53	11.82
MgO	2.39	3.91
SO_3	2.4	3.94
K_2O	0.75	1.91
Na_2O	0.21	2.71
Physical Properties		
Specific weight (g/cm^3)	3.06	2.36
Fineness (cm^2/g)	3250	2900

B. Preparation of Mixtures and Experiments

When designing the mixtures, three different methods were used for incorporating FA into the mixture. In this way, a total of 10 different mixture sets were created, FA was not used for the control mixture(FA(0)). 9 different mixtures were obtained by using 3 different ratios of FA in 3 different methods. Mixing codes and material ratios are given in Table 2.

In the preparation of the mixtures, 25 lt. capacity planetary mixer is used. First of all, dry materials (aggregates, cement and FA) are processed at 100 rpm. was mixed at speed for 1 minute. Then water was added and 150 rpm. speed for 1 minute, finally 300 rpm. The mixing process was completed by mixing at high speed for 3 minutes. Prepared mixtures were placed in pre-lubricated molds and a vibrator was used for compaction. After 24 hours, the samples were taken out of their molds and placed in a pool filled with lime-saturated water. One of the tests applied to determine the fresh state properties of the mixtures, the unit weight test was carried out according to the ASTM C138 [9] standard. With this method, it was determined how much the weight of FA, which has a lower unit volume weight than cement, can be reduced compared to the control mixture by using different proportions and different methods in the mixtures. In order to determine the fresh state properties of the mixtures, the spreading table test was carried out in accordance with the ASTM C230[10] standard. . The mortar taken from the mixing bowl to the tray was placed in the mold on the spreading plate so that it was half filled, and after it was hit 25 times with the mallet, the other part of the mold was filled and another 25 strokes were applied. After the upper surface of the mold was cleaned and smoothed with a trowel, the handle of the test tool, which was taken by pulling the mold, was rotated 5 times in 15 seconds, the diameter of the spread mixture was measured with the help of a meter in 2 different axes and the average of the readings was recorded.

Mechanical and permeability tests were carried out on the hardened samples at the end of the 7th, 28th and 90th days following production, and the freeze-thaw test was performed at the end of the 28th day. Compressive strength test was carried out on 50x50x50 mm cube samples in accordance with ASTM C39[11] standard. The flexural strength test was carried out on beam specimens of 40x40x160 mm in 3-point bending model in accordance with ASTM C293[12] Cylinder specimens of Ø100/200 mm size were used in the cylinder splitting tests and the tests were carried out in accordance with ASTM C496. Freeze-thaw test was carried out in accordance with TSE CEN/TR 15177 standard. 40x40x160 mm beam specimens were produced for the experiments, and flexural and compressive strengths were determined by taking the average of the three specimens on the 28th day. In the freeze-thaw test according to the TSE CEN/TR 15177 standard, the samples are frozen at -20 ^{0}C for 18 hours and then left in the air for 30 minutes. Then it is expected to dissolve in water at 20 ^{0}C for 2 hours. In this way, a freeze-thaw cycle is performed. Within the scope of the experimental studies, a total of 30 cycles were applied and the compressive and flexural strengths of the samples were determined after the cycles and the changes that occurred before and after freezing-thawing were examined. Permeability tests are important tests applied to have an idea about the void character and amount of voids of the samples. Significant durability problems arise in materials with permeable voids. In the study, two different test methods were used to determine the permeability properties of the samples. For these experiments, Ø100/200 mm sized cylindrical samples were produced, and the samples extracted from the curing water on the day of the experiment were cut using a diamond saw to obtain Ø100×50 mm sized samples. Water absorption tests were carried out according to ASTM C642[13], capillary water absorption tests were carried out according to ASTM C1585 [14] standards.

Table 2: The amount of material in the mixtures in grams (in grams for 1 dm3).

Mix. ID	Cement (C)	F-FA	Sand(S)	Water
FA(0)	450	-	1350	225
FA(C10)	405	45	1350	225
FA(C5+A5)	427.5	90	1282.5	225
FA(A10)	450	135	1215	225
FA(C20)	360	90	1350	225
FA(C10+A10)	405	180	1215	225
FA(A20)	450	270	1080	225
FA(C30)	315	135	1350	225
FA(C15+A15)	382.5	270	1147.5	225
FA(A30)	450	405	945	225

III. EXPERIMENT RESULTS

A. *Unit Volume Weight Test*

The average unit volume weight values of the fresh mixtures are shown in Figure 1. In the simple substitution method in which FA is replaced by cement, unit weight values were lower than the control mixture. In other methods, it was observed that the unit volume weight was higher, especially at low FA ratios, and the values decreased depending on the increase in FA ratio.

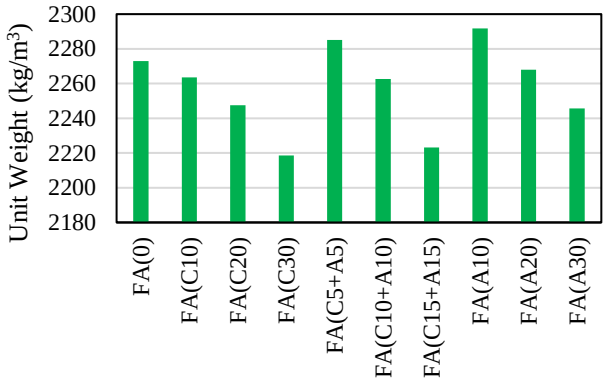

Figure 1: Average unit volume weight values of mixtures

B. *Spreading Table Test*

The average spreading values of the fresh mixtures are shown in Figure 2. To understand the effect of fly ash on the workability of concrete, the water content was adjusted to be constant for all mixtures. When the spreading test results were examined, the mixture dispersion increased as the fly ash ratio increased. In addition, it is noticed that the mixtures formed by the simple substitution method (using an equal amount of FA instead of cement) are more workable than the mixtures prepared by other methods.

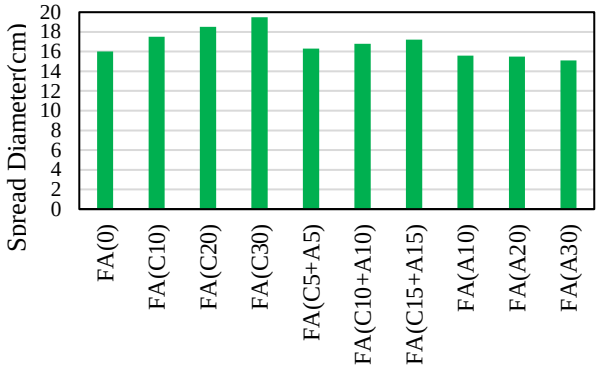

Figure 2: Average spreading diameter values of mixtures

C. *Compressive Strength Test*

The compressive strength test on the hardened samples was carried out on the 7th, 28th and 90th days following and the results are given graphically in Figure 3.

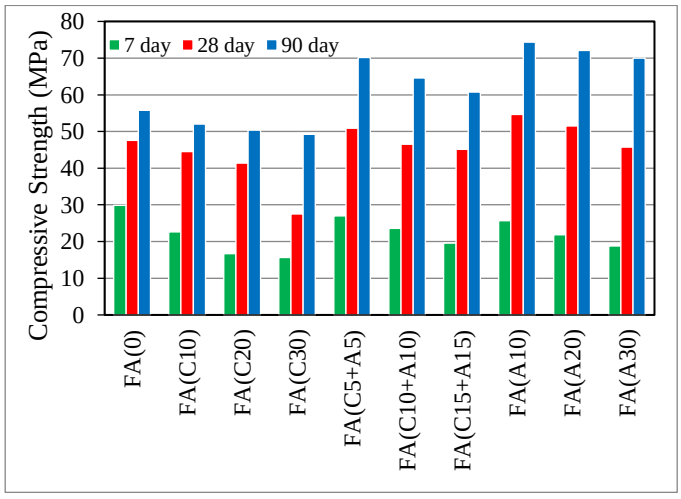

Figure 3: Comparison of compressive strength of samples

- It was observed that mixtures containing 10% FA at different ages had the highest compressive strength among all FA mixtures. When the existing literature studies are examined, it is seen that the use of FA in concrete reduces the mechanical properties of concrete.
- Increases in compressive strength were observed in all mixtures with advancing age. However, the increase in the 90-day compressive strength of the samples prepared in partial replacement and addition methods is quite evident. The amount of cement removed from the mixtures in these

two methods is less than in simple replacement methods. The hydration property of cement is higher than FA. However, the use of FA instead of aggregate caused an increase in the amount of binder in the mixture. Thanks to the pozzolanic character of the FA, the long-term continuation of the hydration event has led to an increase in strength in advancing ages. This can be explained by the positive contribution of pozzolanic activity on compressive strength in later ages.

- When the strength values obtained after the 7, 28 and 90 days curing periods of the mixtures are compared, it is seen that the highest strength values are obtained from the FA(A10) mixture.

D. Flexural strength test

The comparison graph of the 7, 28 and 90 days flexural strength values of the samples is given in Figure 4.

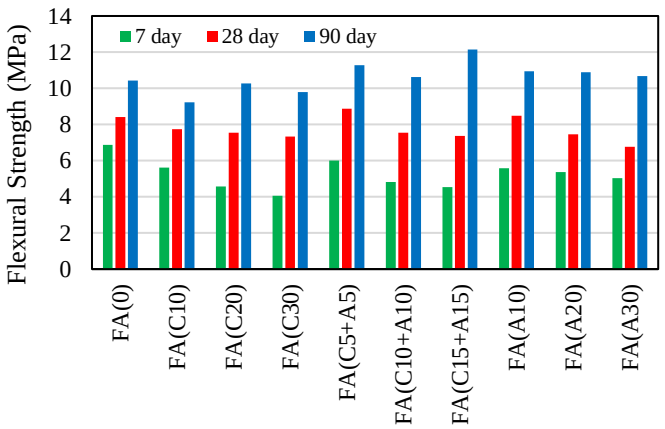

Figure 4: Comparison of flexural strengths of samples

- The flexural strength of the samples prepared by the simple substitution method at increasing FA ratios was lower than the values obtained from the control samples at different ages. In the samples prepared with the partial replacement method and the addition method, only 7-day flexural strength values were lower than the control samples, and the 28 and 90-day strength values were generally higher than the control sample. According to this result, the replacement of FA with cement only decreases the flexural strength values, partial replacement with cement and aggregate or only with aggregate causes an increase in flexural strengths in advancing ages.
- It has been observed that the increase in flexural strength of FA added samples in advancing ages is less than the increase in compressive strength. At the end of 90 days, the increase in flexural strength was at most 17%, and the increase in compressive strength was 33%.

E. Cylinder splitting strength test

The results obtained from the experiments are given in Figure 5. According to the results of the splitting tensile strength test performed on the cylindrical samples, it was observed that the splitting strength values decreased as the FA content increased. The cylinder splitting strength of the FA added mixtures is lower than the control samples, only the 90-day values of the FA(C15+A15) mixture were found to be greater.

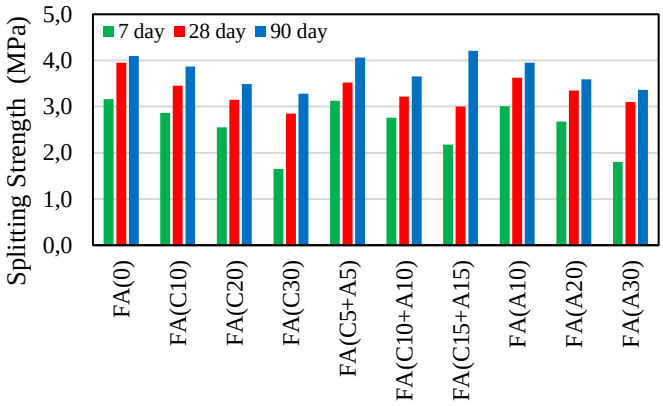

Figure 5: Comparison of cylinder splitting strength of samples

F. Freeze-Thaw test

The compressive and flexural strength results of the FA substituted and control samples with Freeze-Thaw (F-T) cycle and the comparison samples stored in the standard curing are given in Table 3.

Table 3: Strength drops under Freeze-Thaw effect

Mixture ID	No Cycle		30 F-T Cycle		Strength Change	
	Compressive strength (MPa)	Flexural strength (MPa)	Compressive strength (MPa)	Flexural strength (MPa)	Compressive strength (%)	Flexural strength (%)
FA(0)	56.65	11.16	52.93	9.83	7	12
FA(C10)	49.27	11.01	46.20	9.95	6	10
FA(C20)	47.16	10.17	44.70	9.60	5	6
FA(C30)	42.38	9.72	40.59	9.44	4	3
FA(C5+A5)	60.54	11.50	57.20	10.58	6	8
FA(C10+A10)	55.55	10.50	53.17	9.86	4	6
FA(C15+A15)	51.17	9.98	49.80	9.68	3	3
FA(A10)	64.51	11.41	61.81	10.79	4	5
FA(A20)	61.76	10.73	60.26	10.25	2	4
FA(A30)	57.87	10.31	57.16	10.20	1	1

When Table 3 is examined, it is seen that the compressive and flexural strength values decrease as the amount of FA increases, similar to the mechanical strength tests. However, when the percentage changes in the strength losses of the samples are examined, it is seen that the decrease in the strength of the control samples without FA is greater than the decrease in the strength of the samples containing FA. The addition method showed less loss in compressive and flexural strengths.

G. Water absorption test

The water absorption test was performed on Ø100×50 mm cylindrical samples on the 7th, 28th and 90th days and the percent water absorption values of the samples are given in Figure 6.

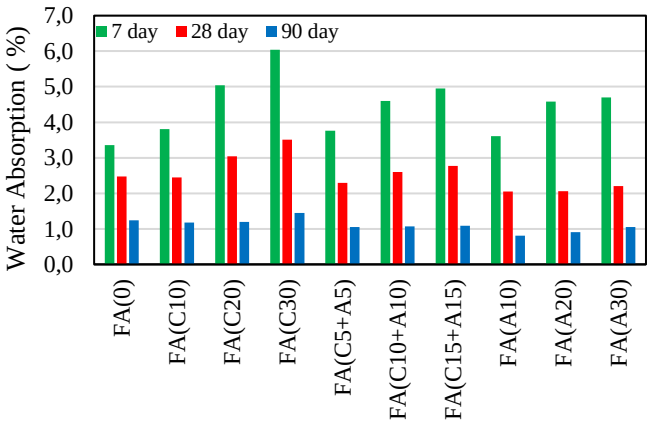

Şekil 6: Comparison of the water absorption values of the samples

- It is observed that as the amount of FA replacement increases, the amount of water absorption in the samples also increases. After 28 and 90 days of curing, it was observed that the water absorption values gradually decreased. This shows that the void structures of the samples decrease during curing.

H. Capillary water absorption test

The change in the permeability properties of the samples as a result of the capillary water absorption test is given in Figure 7.

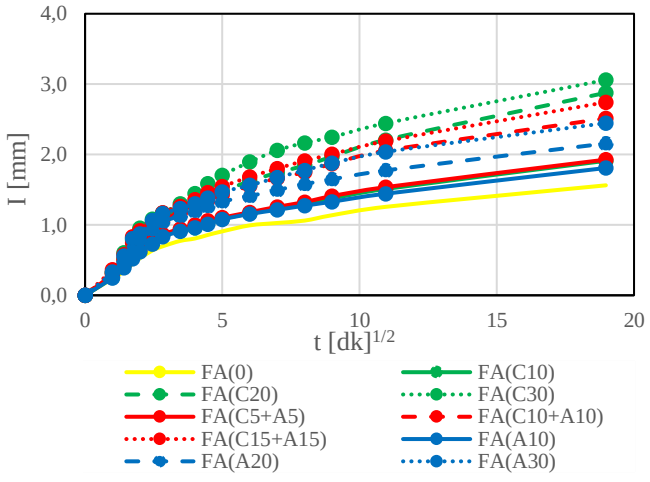

a) 7 days

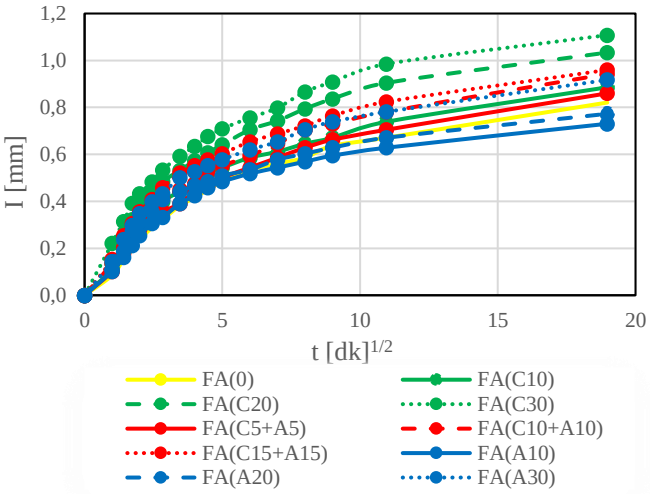

b) 28 days

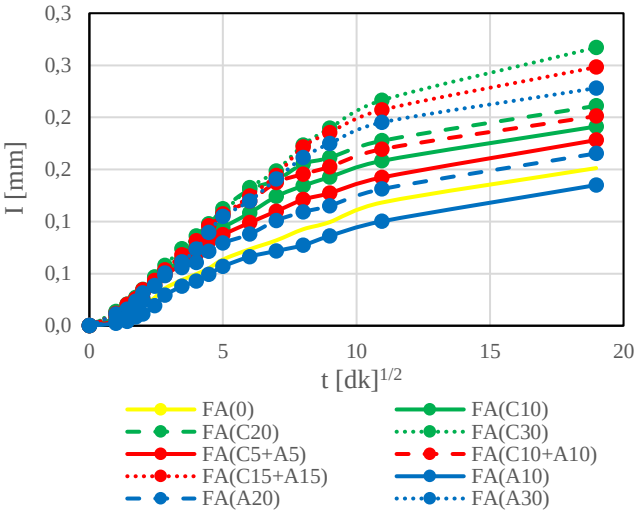

c) 90 days

Şekil 7: Change in capillary absorption values of samples

- Similar to the water absorption experiments, it was observed that the capillary water absorption results increased as the amount of FA increased, but this increase gradually decreased with advancing age, especially according to the 7-day test results. One of the most important factors affecting the void amount of the samples is the hydration of the cement. As the hydration progresses, the binder paste formed fills the capillary water absorption gaps and disconnects them. Similarly, additional C-S-H gels are formed as a result of the reaction of FA with $Ca(OH)_2$, which is formed as a result of the hydration of the main components of the cement, and this reduces the amount of capillary space. It was observed that the capillary water absorption values gradually decreased after 28 and 90 days of curing due to the slower hydration reaction of the FA.
- In the experiments performed at different ages, it was observed that the lowest capillary water absorption value was obtained from the FA(A10) samples, and the highest values were obtained from the FA(C30) samples.

IV. SONUÇLAR

In this study, FA was used in mixtures with three different mixing methods. Slump and unit weight tests were performed to determine the fresh properties of the mixtures, and mechanical, durability and permeability tests were performed to determine the hardened properties. The results obtained as a result of the experiments carried out are presented below.

1) Regardless of the rate of substitution for all mixes, the inclusion of FA improved the workability of concrete due to the fineness and spherical shape of its particles.
2) It has been observed that the use of large amounts of FA in concrete adversely affects the mechanical properties of the concrete. It is understood that the mechanical properties of mixtures containing 10% FA develop better. However, it was observed that the strength development accelerated in the samples prepared by the addition method or partial replacement method after the advancing curing periods and the FA additive had a positive effect on the behavior.
3) Decreases in flexural and compressive strength values of control samples after freeze-thaw cycles were higher than those of FA substituted samples. Accordingly, it can be said that as the FA content increases, the resistance of the samples to freeze-thaw increases. This can be explained by the fact that FA fills the voids in the sample better and increases the freeze-thaw resistance.
4) As a result of the permeability tests, the permeability properties of the samples prepared by the addition method were generally lower than the other mixing methods. According to this, it is understood that the replacement of FA with aggregate instead of cement has a positive effect in terms of reducing the amount of voids in the samples.
5) The use of FA as a binder material and reducing the amount of cement has positive results in many ways. By replacing FA with cement, it is possible to obtain more economical and environmentally friendly concrete. In addition, it is thought that the use of some FA instead of fine aggregate used in concrete will contribute to the efficient use of FA, which is a waste material, to the industry, and to reduce its effects on environmental pollution and storage costs.

ACKNOWLEDGMENT

This study was produced from Marvan Al-Ithawi's master's thesis.

V. REFERENCES

[1] A. K. Saha, "Effect of class F fly ash on the durability properties of concrete," *Sustainable environment research*, vol. 28, no. 1, pp. 25-31, 2018.
[2] J. Rissanen, K. Ohenoja, P. Kinnunen, and M. Illikainen, "Partial replacement of portland-composite cement by fluidized bed combustion fly ash," *Journal of Materials in Civil Engineering*, vol. 29, no. 8, p. 04017061, 2017.
[3] R. Siddique, "Performance characteristics of high-volume Class F fly ash concrete," Cement and Concrete Research, vol. 34, no. 3, pp. 487-493, 2004.
[4] A. K. Saha and P. K. Sarker, "Sustainable use of ferronickel slag fine aggregate and fly ash in structural concrete: Mechanical properties and leaching study," Journal of Cleaner Production, vol. 162, pp. 438-448, 2017.
[5] S. W. M. Supit and F. U. A. Shaikh, "Durability properties of high volume fly ash concrete containing nano-silica," Materials and structures, vol. 48, no. 8, pp. 2431-2445, 2015.
[6] A. Mardani-Aghabaglou, Ö. Andiç-Çakir, and K. Ramyar, "Freeze–thaw resistance and transport properties of high-volume fly ash roller compacted concrete designed by maximum density method," Cement and Concrete Composites, vol. 37, pp. 259-266, 2013.
[7] E. E. Berry and V. M. Malhotra, Fly ash in concrete. Energy, Mines and Resources Canada, CANMET, Ottawa, pp. 223-229., 1986.
[8] V. Akyüncü, "F ve C tipi uçucu küllerin çimento ile ikame edilmesiyle üretilen betonların mekanik ve dayanıklılık özelliklerinin karşılaştırılarak incelenmesi," 2012.
[9] A. C618, "Standard specification for coal fly ash and raw or calcined natural pozzolan for use in concrete," in American society for testing and materials, 2003: ASTM international West Conshohocken, PA, USA.
[10] C. ASTM, "230, Standard specification for sample and testing fly ash or natural pozzolan for use as a mineral admixture in Portland cement," Annual Book of ASTM Standard, vol. 4, p. 172, 1997.
[11] ASTMC39, "ASTM C39, Standard test method for compressive strength of cylindrical concrete specimens, American Society for Testing and Materials, West Conshohocken, Pa.," ed, 2012.
[12] ASTM C293, Standard Test Method for Flexural Strength of Concrete (using simple beam with center-point loading), American Society for Testing and Materials, West Conshohocken, Pa, 1979.
[13] ASTMC642-13, "ASTM C642-13, Standard test method for density, absorption, and voids in hardened concrete, American Society for Testing and Materials, West Conshohocken, Pa," 2013.
[14] ASTM C1585-13,Standard Test Method for Measurement of Rate of Absorption of Water by Hydraulic-Cement Concretes, American Society for Testing and Materials, West Conshohocken, Pa, 2013.

Computer Aided Determination and Comparison of Earthquake Damage Scores of RC Buildings in Turkey by Rapid Assessment Methods

M. ÖZDEMİR[1] and M.MUVAFIK [2]

[1] Agrı Ibrahim Cecen University, Agrı/Turkey, mozdemir@agrı.edu.tr
[2] Van Yüzüncü Yıl University, Van/Turkey, muvafik@yyu.edu.tr

Abstract **- In this paper, 7 different rapid evaluation methods which are used to determine the performance of buildings under the influence of earthquakes in a fast and practical way are examined. These methods were used to determine the earthquake performance behaviors (risky or safe) of buildings according to each method by using the parameters of 50 buildings that were collapsed or severely damaged in Van earthquake that occurred in 2011. Accurate estimation percentages of the methods on the buildings were calculated by comparing the obtained earthquake performance behaviors with the current situation of the buildings. The most suitable method has been tried to determine for 50 buildings related to these calculations. At the same time, a computer program called EPA (Earthquake Performance Analysis) was developed in order to evaluate the parameters of the related data set faster, easier and without error. The results show that rapid assessment methods are quite successful and worth using in estimating earthquake damage scores of buildings.**

Keywords **– Damage score, Earthquake performance, Rapid assessment methods, RC buildings**

I. INTRODUCTION

Since the existence of the Earth, earthquakes have been occurring all over the world due to the movement of the earth's crust. In one of the countries most affected by the earthquake, Turkey. Located on the Alpine-Himalayan earthquake zone, which is one of the active earthquake zones, the country has been affected by large earthquakes in which thousands of lives and millions of dollars were lost before. According to the Earthquake Zones Map, 92% of the country is in earthquake zones and 95% of the country's population lives under earthquake hazard [1]. Between the years 1903-2014 in Turkey occurred in the range of M = 6.0-11.0 magnitude 119 earthquake. These earthquakes resulted in an average annual loss of 748 lives, 5291 damaged buildings and economic loss of $ 721,610 dollars. These results clearly show the effect of earthquakes that may occur naturally and inevitably, unless the necessary measures are taken [2].

Experience and statistics have shown the importance of determining the behavior of buildings under earthquake impact. Therefore, many studies have been carried out to determine the behavior of buildings under earthquake effects and these studies have been classified into three categories. These categories can be listed as street survey methods (SSM), preliminary assessment methods (PAM) and detailed analyzes. Street survey methods are quite simple and fast. In this method, some parameters such as number of stories, irregularity information, structural system are obtained by making observations from outside without entering the building and then performance of the building against the earthquake effect is determined. PAM, which is another method, includes some different parameters which should be taken from the inside the building (material information, structural system element dimensions, etc.) in addition to the parameters used in SSM. Although this method (PAM) takes a little longer time-consuming than SSM, accuracy ratio is higher. The third and last method used to determine earthquake performance is detailed analysis. This method determines the performance of buildings against earthquake effects by performing linear and nonlinear analyzes. Although This method are highly accurate ratio, it take too time. When considering the thousands of buildings in which earthquake performance behavior should be determined, researchers have done many studies on SSM and PAM methods, which are called rapid assessment methods. The main purpose of these methods (SSM and PAM) is to determine the buildings that need detailed analysis by determining the risk distribution of the buildings.

There are 2 main goal of this paper. The first of these goals is to develop a computer program that can determine the earthquake performance status (damage scores) of buildings in a much shorter time and error without. Secondly, by selecting the most common 7 of the existing many rapid assessment methods (3 of them SSM and 4 of them PMA), to evaluate these methods according to the parameters of 50 buildings that have collapsed or severe damage in the earthquake in Van in 2011 and is to find the most suitable method for these buildings.

In this context, the parameters of 50 buildings were transferred to the developed EPA (Earthquake Performance Analysis) program and the earthquake performance status (risky or safe) of the buildings were determined according to the 7 rapid assessment methods selected. At the same time, earthquake performance graphs, earthquake performance maps and earthquake performance reports of all buildings were also created within the EPA program.

II. MATERIAL AND METHODS

In this chapter, the details of the 7 rapid evaluation methods examined in the study, the parameters used in these methods, the effects of the parameters on the earthquake performance of buildings and the details of the developed EPA computer program are explained.

A. Parameters used in methods

Rapid assessment methods have many different parameters that can significantly affect the earthquake performance of buildings such as architectural, structural system, soil class, earthquake zone of the region where they are created. While some of these parameters are used in almost all rapid assessment methods, some parameters are important for several methods. These parameters can be classified under 5 main headings. These are the structural parameters resulting from the building characteristics of the building, the ground parameters resulting from the ground where the buildings are located, the earthquake parameters resulting from the seismicity status of the buildings, the irregularity parameters resulting from the irregularities of the building and the other factors that affect the buildings.

Table 1. Parameters used in rapid assessment methods

Structural Parameters	Irregularity Parameters	Ground Parameters	Earthquake Parameters	Other Parameters
Number of stories	Soft story	Local soil conditions	*Sds (Design spectral acceleration factor)	Year of construction
Structural system type (Frame or frame and shear walls)	Short column	Topographic effects		Post-Benchmark
Pounding	Plan Irregularity	*Peak Ground Velocity (PGV)		Material properties (steel and concrete)
Apparent building quality	Vertical Irregularity			
*Redundancy (Frame Irregularity)	Heavy Overhangs (like balconies)			
Ground floor area				
Size of vertical members (column and shear wall)				

B. Methods

This study doesn't provide a new rapid assessment method for determining the earthquake performance of buildings. This study presents a computer program which combines seven different rapid evaluation methods under one roof and the comparison of these methods in computer program. Therefore, it is important to understand these 7 rapid assessment methods. Without giving details of the methods, only the names of the methods, basic application steps and references are given.

1. Street survey methods (First Level Methods)

1. FEMA P-154 (Rapid Visual Screening of Buildings for Potential Seismic Hazards) [4]
2. PRINCIPLES FOR DETERMINATION OF RISK STRUCTURES / Simplified Methods for Determining Regional Earthquake Risk Distribution of Buildings [5]
3. Simple Survey Procedures for Seismic Risk Assessment in Urban Building Stocks (Level-1) [6]

Features

- These methods are the most practical methods used to determine the earthquake performance of buildings.
- The number of parameters of these methods is less than other earthquake performance determination methods. As a result, accuracy ratio of methods is also lower.
- The main purpose of the method is to calculate the performance of the building against the earthquake force by observing from outside without entering the building whose performance will be determined.
- The basis of the method depends on statistical data.
- After earthquakes, the researchers go to the region to examine the state of the buildings and correlate the performance of the earthquake with the parameters of the building (short column, heavy overhangs, soft stories, etc.).
- As a result of statistical studies, the importance of related parameters is determined. Scores are given to the parameters of buildings according to these grades. Afterwards, earthquake performance formulas are developed by establishing relationships between these scores.

2. Preliminary assessment methods (Second Level Methods)

1. Simple Survey Procedures for Seismic Risk Assessment in Urban Building Stocks (Level-2) [6]
2. Preliminary Seismic Vulnerability Assessment of Existing RC Buildings in Turkey [3]
3. Preliminary Seismic Performance Assessment Procedure for Existing RC Buildings [7]
4. MVP Interaction Based Seismic Vulnerability Assessment of RC Buildings [2]

Features

- These methods are the most common rapid assessment methods used to determine the earthquake performance of buildings.
- Thanks to this method, earthquake performance scores of buildings can be found both in a short time and with high accurate result percentages.

- In addition to SSM, these methods depend on the parameters that must be entered by entering the building. These parameters can be collocate as structural system element dimensions (column, shear wall, wall), ground floor area, building weight, concrete and reinforcement strengths. The processing steps of these methods are similar to SSA methods.

C. Earthquake Performance Analysis Computer Program

EPA computer program was developed in C # programming language. Through this program, the earthquake performance damage scores of buildings can be calculated according to different rapid assessment method (RAM), Results can be compared, the appropriate RAM can be determined for the building, buildings can be displayed on the map and can generate earthquake performance reports. The main application menus included in the EPA program are listed as parameters input screen, database screen, earthquake performance maps, earthquake performance graphs and earthquake performance reports.

1. Parameters input screen

Rapid assessment methods have different parameters and different calculation steps. So, EPA program provides a different parameter input screen for each method. The parameters of the building whose earthquake performance score will be determined are selected on the input screens and the earthquake performance status can be easily determined according to any rapid assessment method.

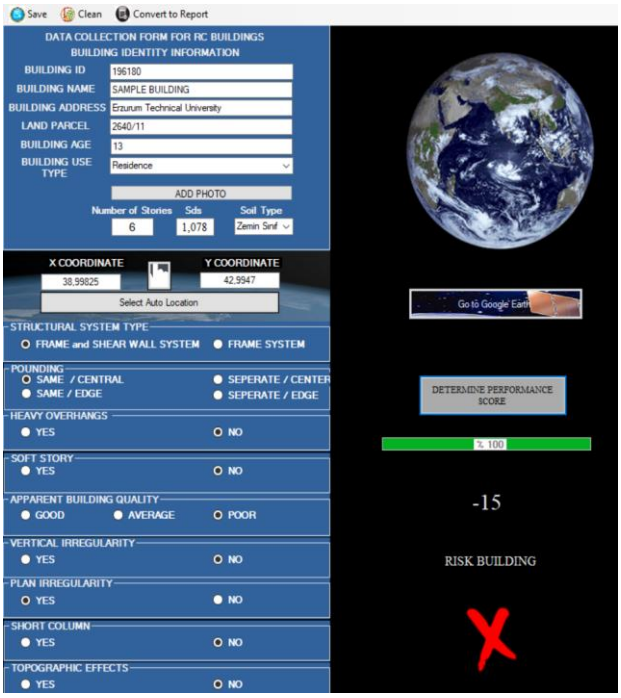

Figure 1: Sample parameter input screens for Street Survey

2. Database screen and earthquake performance maps

After the parameter information of the buildings whose earthquake performance is to be determined are defined to the EPA program, all information about the building is transferred to the database in the program through the save button on the parameter input screens. In the database, all saved buildings can be viewed. These buildings can be easily found or classified in thousands of buildings by searching through number of stories, type of method used and building names. In addition, using the database screen, building earthquake performance results can be sent to excel, earthquake performance maps and earthquake performance graphs screens.

Any data (building) or any data set is transferred from the database to the application menu of earthquake performance maps. Earthquake performance maps are generated by using geographic coordinate data of buildings in the parameter input screens. It shows the earthquake performance status of buildings (Risky building, Safe building) on the map and shows the earthquake performance distributions of buildings on the map. By assigning red point on risky buildings and green point on safe buildings, earthquake performance maps are easily understood.

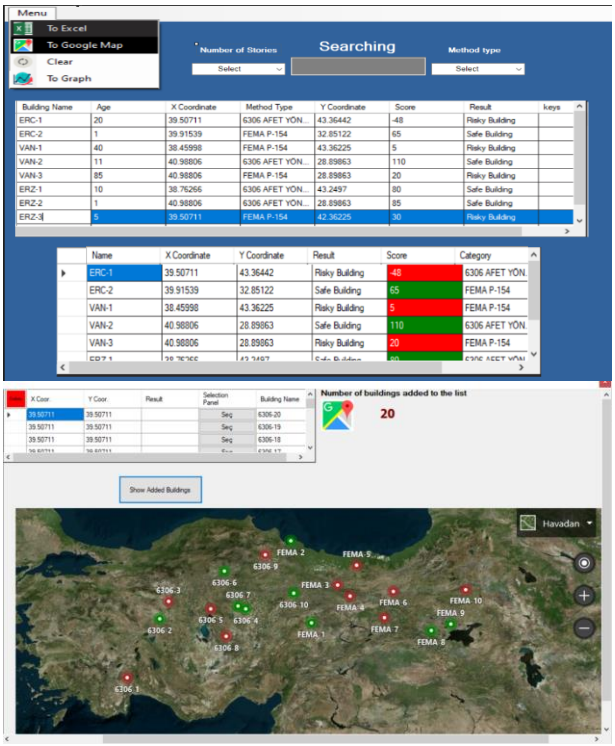

Figure 2: Database screen and earthquake performance maps

3. Earthquake performance graphs and earthquake performance reports

One of the main goals of this study is to find a rapid assessment method suitable for buildings. In order to find the suitable method, it is necessary to select the method with the highest accuracy rate by evaluating the data sets examined in different rapid evaluation methods. Using earthquake performance graphs, the accuracy percentage of any data set to be analyzed can be easily found by all methods. Then, the most suitable method for the data set is selected by comparing the accuracy percentages of the methods.

The last application menu presented by the EPA program is the earthquake performance reports menu. This application menu generates reports in Microsoft Word by using the parameters of the buildings that the earthquake performance evaluation had been made and the score equivalents of these parameters.

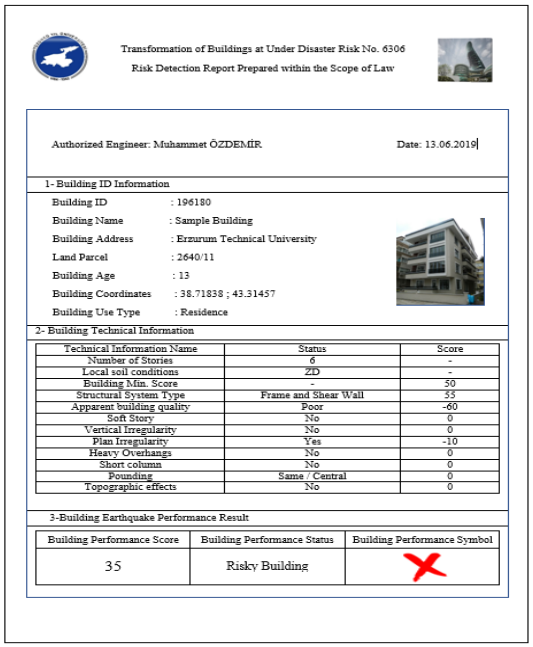

Transformation of Buildings at Under Disaster Risk No. 6306
Risk Detection Report Prepared within the Scope of Law

Authorized Engineer: Muhammet ÖZDEMİR Date: 13.06.2019

1- Building ID Information

Building ID : 196180
Building Name : Sample Building
Building Address : Erzurum Technical University
Land Parcel : 2640/11
Building Age : 13
Building Coordinates : 38.71838 ; 43.31457
Building Use Type : Residence

2- Building Technical Information

Technical Information Name	Status	Score
Number of Stories	6	-
Local soil conditions	ZD	-
Building Min. Score	-	50
Structural System Type	Frame and Shear Wall	55
Apparent building quality	Poor	-60
Soft Story	No	0
Vertical Irregularity	No	0
Plan Irregularity	Yes	-10
Heavy Overhangs	No	0
Short column	No	0
Pounding	Same / Central	0
Topographic effects	No	0

3-Building Earthquake Performance Result

Building Performance Score	Building Performance Status	Building Performance Symbol
35	Risky Building	

Figure 3: Earthquake performance Report

III. RESULTS

Earthquake performance damage score and earthquake performance behavior of 50 buildings in the data set were determined according to 7 different rapid assessment methods using EPA program. Using the obtained performance scores, earthquake performance graphs showing the success percentages of the methods and earthquake performance maps of the related data set were created according to the methods.

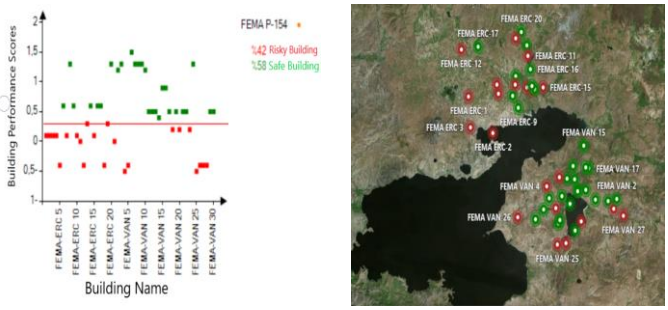

Figure 4: Earthquake performance graphs (left) and earthquake performance maps according to FEMA P-154 (right)

According to the earthquake performance graph obtained by EPA program, 42% of the buildings in the data set were found to be risky and 58% as safe. Since all of the buildings in the dataset are collapsed or heavily damaged, the success rate of this method can be said to be 42%. When the earthquake performance status of all buildings in the data set is evaluated according to the methods, the following table is revealed.

Table 2. Percentage of performance estimation on buildings in the data set of methods

	Street Survey Methods			**Preliminary Assessment Methods**			
	6306 RYY	FEMA P-154	S&Y Level 1	S&Y Level 2	Özcebe	Yakut	MVP
Right Guess (%)	74	42	28	38	32	86	82
Wrong Guess (%)	26	58	72	62	68	14	18

According to the obtained earthquake performance graphs, the percentage of buildings that are estimated correctly by all methods is 4 %. The percentage of buildings that the methods created with the data in Turkey (except FEMA P-154) accurately predicts is 22 %. All buildings that are right predicted have the majority of irregularities (plan irregularity, soft story, heavy overhang).

Among the street survey methods, the method that accurately predicts the earthquake performance behaviour of buildings at the highest rate (74%) is the Regulation on Risk Structures (6306), which is officially used in Turkey. This rate is quite high for a street screening method and can be used to identify buildings with priority risk. Among the preliminary assessment methods, Yakut method is the method that accurately predicts the earthquake performance behaviour of buildings at the highest rate (86%). It was also found that the methods using the concrete quality parameter had a much higher (approx. 40%) accurate estimation percentage than the methods without concrete quality parameter.

IV. DISCUSSION

As a result of the studies, three important questions have arisen. These;

1. Are street screening methods and preliminary assessment methods safe enough to determine earthquake performance status of buildings? Which is the most reliable street screening and pre-assessment method?
2. How has changed the success percentage of the pre-assessment methods obtained using more parameters according to street screening methods?
3. What is the most important parameter that affects the success rate of Rapid Evaluation Methods?

The answers to these questions are given below in order of earthquake performance graphs obtained from EPA program.

The most successful method of street survey methods was 6306 RYY with 74% accurate estimation, and the most successful method of preliminary assessment with 86% accurate prediction was Yakut method. It was observed that earthquake performance behaviours of buildings can be estimated accurately by using rapid assessment methods and priority buildings (unsafe buildings) can be determined by creating earthquake risk maps.

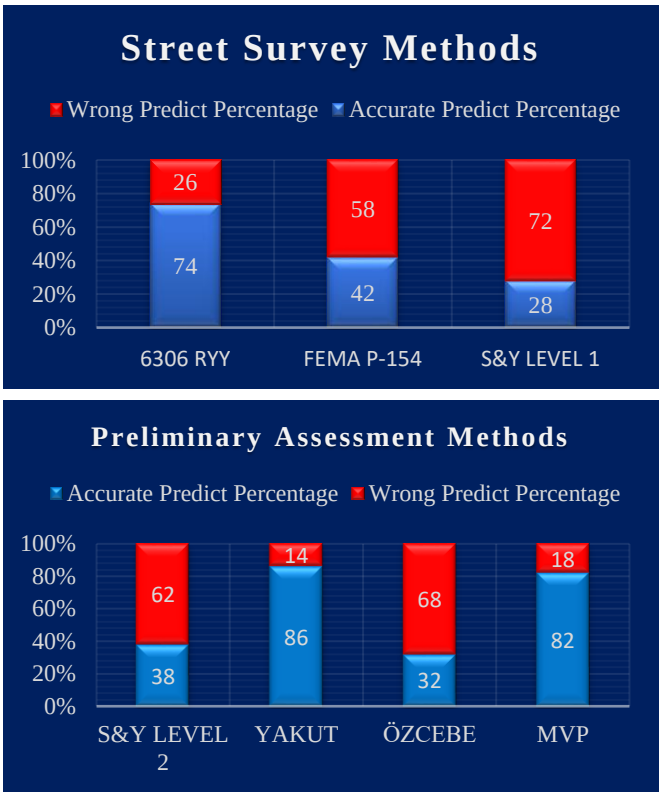

Figure 5: Percentage of wrong and accurate estimation on buildings in the data set of Street survey and Preliminary assessment methods

According to Figure 6, preliminary assessment methods accurately predicted the earthquake performance behaviour of buildings by 24% higher using 55.5% more parameters than street survey methods. The parameters that make up the difference between the number of parameters and accuracy percentages of the methods can be listed as structural system element (column, shear wall) dimensions, concrete compressive strength, ground floor area, frame discontinuity, reinforcement detail information.

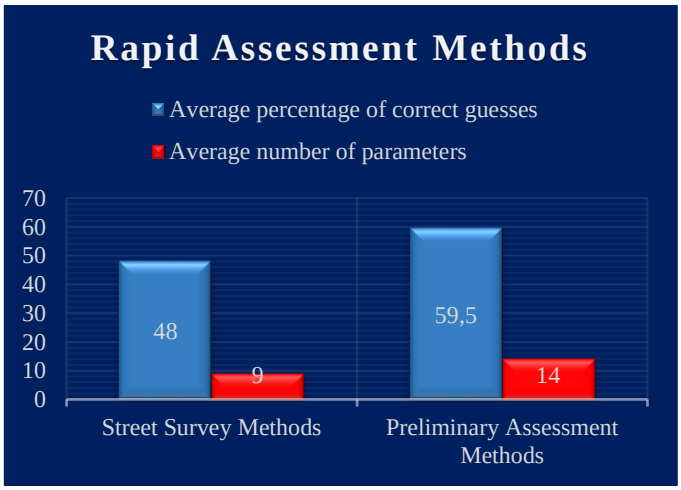

Figure 6: Average accurate estimation percentages and average parameter numbers of rapid evaluation methods.

Concrete compressive strength is not the only reason for this great difference between methods that use and do not use concrete compressive strength. Other parameters in the methods greatly affect this rate. However, the concrete strength is directly used in the calculation of the shear force capacity of the bearing elements. It is known that earthquake forces cause serious additional shear forces in buildings. In other words, the concrete strength and the damage of the earthquake effect on the buildings are directly related. For this reason, it is very difficult for methods that do not use concrete strength to accurately predict the earthquake performance behavior of buildings.

It can be said that together with the concrete compressive strength, the number of floors, load-bearing element dimensions, weak storey irregularity and torsional irregularity parameters are the most important factors affecting the earthquake performance status of the buildings.

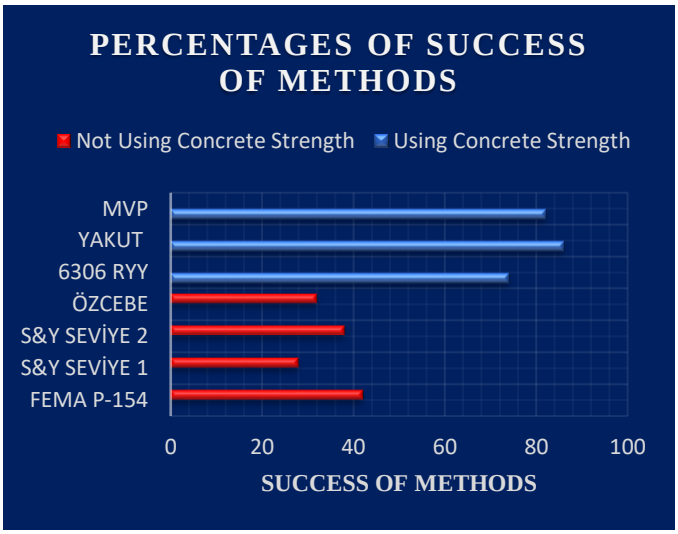

Figure 7: Comparison of success rates of Rapid Evaluation Methods according to concrete strength parameter

V. CONLUSION

The rapid assessment methods, which are divided into street survey and preliminary assessment methods, are used to determine the performance of buildings against earthquakes affects quickly and practically. The main purpose of the methods is to determine the buildings that need detailed analysis by determining the risk distribution of the buildings. Since these methods are created by using the data of a particular region, the success percentages of the methods in different regions may decrease. Therefore, in this study, the success rates of rapid evaluation methods were compared by using the data of buildings in Van. The results can be listed as follows.

1. The determination of earthquake safety of existing structures constitutes the technically most critical part of earthquake mitigation strategies. Although there are various assessment methods developed for buildings, these methods can't be applied to hundreds of

thousands of buildings. For this reason, there is a need for methods that provide fast and accurate results with less number of parameters and programming this method.

2. A sample data set was examined on the EPA program and the success rates of the methods were calculated. According to the results, the most successful method of street survey methods is 6306 RYY with 74% accurate estimation, and the most successful method with 86% accurate prediction percentage is Yakut.
3. Preliminary assessment methods used 55.5% more parameters than street survey methods to accurately predict earthquake performance behaviour of buildings at a rate of 24%.
4. It was found that the most important parameter for the methods was the compressive strength of concrete and therefore it was recommended to use Test (Schmidt) hammer for accurate determination of this value.
5. It has been observed that earthquake performance behaviour of buildings can be predicted accurately by using rapid assessment methods and by using earthquake risk maps can be established to determine priority buildings (unsafe buildings) easily and practically.

ACKNOWLEDGMENT

I would like to express my gratitude to the Scientific Research and Projects Coordination Unit (BAP) of the Yüzüncü Yıl University and to the university authorities for enabling this for supporting this study with the project number FYL-2019-8283.

REFERENCES

[1] KRDAE, 2019. Boğaziçi University Kandilli Observatory and Earthquake Research Institute http://www.koeri.boun.edu.tr/simo/2/deprem-bilgileri/buyuk-depremler/. Date of Access: 05.04.2019.

[2] Erdil B., Ceylan H., "Comparison of Walk-Down Procedures in Evaluating Seismic Vulnerability of RC Buildings in Turkey", 3rd International Mediterranean Science and Engineering Congress (IMSEC 2018), Adana, Turkey, 24-26 Ekim 2018, pp.357-361

[3] Özcebe, G., Yücemen, M. S., Aydoğan, V., Yakut, A. 2003. Preliminary Seismic Vulnerability Assessment of Existing Reinforced Concrete Buildings in Turkey. Seismic Assessment and Rehabilitiation of Existing Buildings, 29-42.

[4] FEMA 154, 2015. Rapid Visual Screening of Buildings for potential seismic hazards: A Handbook, Federal Emergency Management Agency, Washington DC, USA.

[5] TEC2018 (Turkish Earthquake Resistant Code) (2018) "Deprem Etkisi Altında Binaların Tasarımı İçin Esaslar (Specifications for Buildings to be Designed under Seismic Effect)", Turkish Ministry of Public Works and Settlement, Ankara, Turkey.

[6]Sucuoglu H, Yazgan U. (2003). "Simple survey procedures for seismic risk assessment in urban building stocks." In: Wasti ST, Özcebe G, editors. Seismic assessment and rehabilitation of existing buildings, earth and environmental sciences, Vol. 29. London:Kluwer Academic Publishers; 97–118.

[7] Yakut A., (2004). "Preliminary Seismic Performance Assessment Procedure for Existing RC Buildings." Engineering Structures, 26, 1447-1461.

[8] Özdemir M., Muvafık, M. (2019). "Computer aided quick determination of earthquake performance of buildings by using street survey and preliminary assessment methods, Van Yüzüncü Yıl University Institute of Science, VAN

[9] ATC 21, 2015. Rapid Visual Screening of Bıildings for Potential Seismic Hazards: A Handbook Second Edition, ATC-21, Applied Technology Council, USA

[10] Altıner, M., 2008. Rapid Evaluation Methods for Determining the Risk of Collapse of Reinforced Concrete Buildings Under the Impact of Earthquakes (master's thesis, unpublished). Istanbul Kultur University, Institute of Science and Technology, Istanbul.

[11] Coşkun, A., 2007. Determination of Structural Performance of Existing Reinforced Concrete Buildings Under the Impact of Earthquake (master's thesis, unpublished). Istanbul Technical University, Institute of Science and Technology, Istanbul.

[12] JBDPA, 2001. The Japan Building Disaster Prevetion Association "Standard for Seismic Evalaution of Existing Reinforced Concrete Buildings (Version 11). Japanese

A Numerical Study on Perforated Cold-Formed Steel Square Hollow Section Members Under Axial and Eccentric Compression Loading

SULEYMAN I. COSGUN[1] and M. EMIN AKCAN[2]

[1] Erzincan Binali Yıldırım University, Erzincan/Turkey, sicosgun@erzincan.edu.tr
[2] Erzincan Binali Yıldırım University, Erzincan/Turkey, mehmetakcan2424@gmail.com

Abstract - **Cold-formed Hollow Steel Sections (HSS) are widely used in the construction industry. These members are perforated for various reasons, such as ductwork, connection to other members, creating aesthetic form, geometric optimization to produce lightweight structural members, and accommodation of many services like plumbing, electrical cables, wires, heating, etc. However, the existence of the perforations is likely to impact the structural stability and performance of columns. Therefore, finite element analysis (FEA) was performed in this study to examine the load-carrying capacities and behaviors of perforated cold-formed square hollow steel stub columns under axial and eccentric compression loading. The perforations have a circular form located at column mid-height and, the diameter of perforation to cross-section width ratio was constant in all models with the value of 0.44. In addition, to investigate the eccentricity of the circular perforations, stub columns were modeled with the ratio of the transverse displacement of the circular perforation to the section width was 0.20, and both axial and eccentric compression loading was applied separately. The analysis results showed that the most critical case occurred when the circular perforation and the eccentricity of the compression load were on the same side.**

Keywords **Cold-formed, Finite element, Eccentric compression loading, Circular perforation**

I. INTRODUCTION

In the construction industry, cold-formed Hollow Steel Sections (HSS) are commonly used. These members are perforated for ducting, connection to other members, aesthetic shape, geometric optimization to generate lightweight structural members, and accommodation of numerous utilities such as plumbing, electrical cables, wiring, and heating. The presence of holes is likely to influence performance of columns and the structural stability. Several studies have been carried out in this area. Some of the studies carried out, especially in the last decades, were summarized below. Gao et al. [1] studied the load-carrying capacity of thin-walled box-section stub columns fabricated by high-strength steel. In the scope of the study, uniaxial compression loading, was applied to test specimens of different sizes. Gardner et al. [2] presented a comparative experimental study of hot-rolled and cold-formed rectangular hollow sections. An experimental program consisted of tensile coupon tests produced from flat and corner regions, residual stresses and geometric imperfections and column tests, and beam tests were introduced. The results of the tests have been combined with other available test data on square and rectangular hollow sections and analyzed. Peen et al. [3] investigated the effects of the ratio of circular shape perforations and arrangements of the perforations on the structural behavior of cylindrical hollow sections (CHS). A total of eleven models consisting of one cylindrical hollow section without perforation as the reference model and ten simplified equivalents perforated CHSs modeled using a finite element software. Umbarkar et al. [4] studied the effect of various geometrical parameters of circular shape single perforation on the critical/ultimate buckling load of a circular lean duplex stainless steel (LDSS) stub column axially loaded numerically. The effect of perforation eccentricity, diameter, and column thickness was studied on the critical buckling load capacity. Ghazijahani et al. [5] investigated the effect of circular openings (perforations) on the fatigue behavior of CHS members. The perforations were made close to the area of maximum tensile stress of tube specimens. The failure modes of the members, as well as the fatigue life, was explored. Vaz et al. [6] performed experimental and numerical studies to obtain the ultimate strength of tubular structures with circular perforated damage under axial compression loading. The experimental program comprised fifteen tubular scaled specimens are tested and the results were compared. Singh and Singh [7] made an experimental study to predict the stub columns capacity of cold-formed square (SHS) and rectangular hollow sections (RHS) containing two opposite central circular shape perforations at column mid-height. Peen et al. [8] presented the verification study of finite element modeling simulation with test results. A control model and the circular hollow section penetrated with 12 circular shape perforations arrangement were selected for the verification process. Both test specimens and FEA models were subjected to different loading types (compression, flexural and torsional loads). Ma et al. [9] carried out an experimental investigation on cold-formed high-strength steel (CFHSS) (members had the

nominal proof stresses of the test specimens were between 700 and 900 MPa) under combined loading (compression and bending) case. The test specimens comprised five square hollow section sizes and two rectangular hollow section sizes. Devi and Singh [10] performed a numerical study to investigate the effects of stiffened perforation on the torsional capacity of perforated slender LDSS semi-elliptical hollow section members. Four different stiffener arrangements (square, horizontal, vertical) were considered for single circular perforation on the flat part of the member. Effects of geometric parameters of members such as width, thickness, anchorage length, etc. on single circular form perforated member torsional capacity were studied. Sangeetha et al. [11] studied to examine the flexural strength, failure mode, load-deflection, and load-strain behavior of the cold-formed steel hollow beams with or without web perforations under flexure. Singh and Chan [13] presented a systematic finite element-based numerical parametric study to assess the buckling capacity of perforated cold-formed and hot-rolled steel column members. The effects of main geometric parameters such as eccentricity of perforation, perforations forms (square, circular, hexagonal), sizes (width/diameter), and height of perforation; and thickness on the buckling performance cold-formed and hot-rolled steel stub columns were investigated. Singh and Singh [14] made a numerical investigation on the performance and design of cold-formed steel squares (SHSs). Moreover, rectangular hollow sections (RHSs) stub columns have two opposite central circular perforations located at column mid-height. The numerical models were developed and validated against the researchers' experimental findings on perforated cold-formed steel stub columns. The many experimental and numerical column capacities, collected from previous experimental studies and present parametric study, were compared with the design strengths predicted by known code limitations. In this study, finite element analysis (FEA) was performed to investigate the load-carrying capacities and behaviors of perforated cold-formed square hollow steel stub column members under axial and eccentric compression. The perforations were circular and were located at column mid-height. The diameter of the perforation to cross-section width ratio was 0.44 in all configurations. In addition, stub columns were modeled with a ratio of the circular perforation's transverse displacement to the section width of 0.20. Both axial and eccentric compression loading was applied separately to study the eccentricity of the circular perforations. In this study, 100 mm loading eccentricity (e), which was the cross-section width or height, was preferred for SHS columns.

II. NUMERICAL STUDY

In this study, finite element analysis (FEA) was performed with ABAQUS/CAE [15] commercial software. Finite element models were constructed to obtain each SHS member's load-carrying capacities and behaviors under axial and eccentric compression loading. The classical metal plasticity (CMP) material model was used to define the steel material properties of the stub columns. The material properties of the steel were defined with the bilinear stress-strain relationship with a hardening branch for S235JRH. The bilinear stress-strain curve for S235JRH was given in Figure 1.

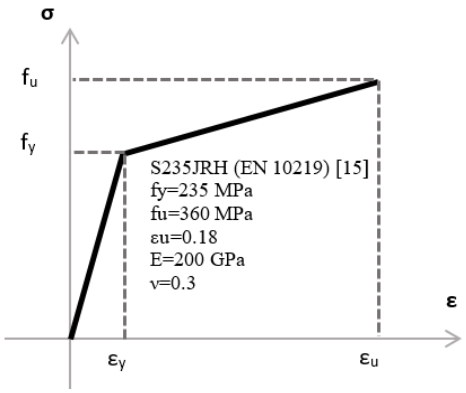

Figure 1: The bilinear stress-strain curve for S235JRH

The S4R finite element that is a shell-type element, was used to model SHS members. The mesh convergence study was carried out to determine the relatively accurate results. According to the study, the finite element size of the SHS was selected as 3.00 mm. The unique meshing technique was used for the perforation region (Figure 2).

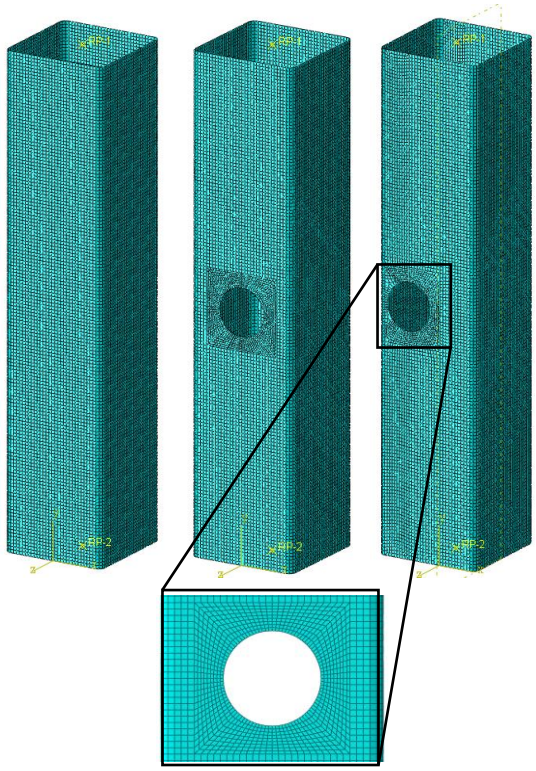

Figure 2: The finite element mesh model of perforated SHS stub column members

SHS members with nominal cross-section dimensions of 100x100x2.50 mm and a height of 450 mm were modeled with a boundary condition that allows the ends of the specimens to rotate freely in the bending plane. Numerical studies consist of two main stages. The first stage is the linear buckling analysis to determine the Eigenvalue and elastic buckling mode shapes

(Figure 3). The second stage is the nonlinear buckling analysis, which considers the defects defined using the obtained linear buckling modes. The summary of the mentioned modeling steps was given as a flowchart diagram in Figure 4.

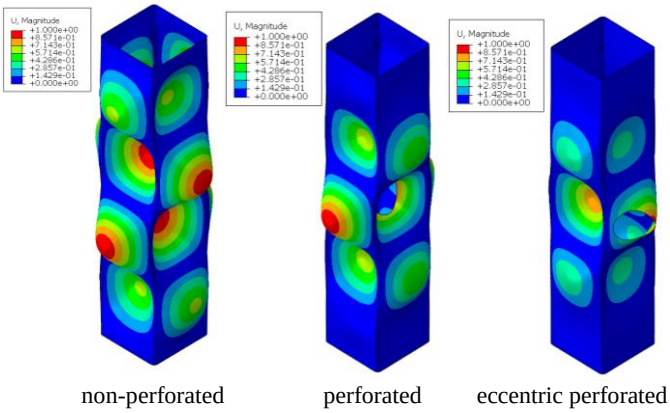

Figure 3: First linear buckling mode shapes obtained from linear buckling analysis

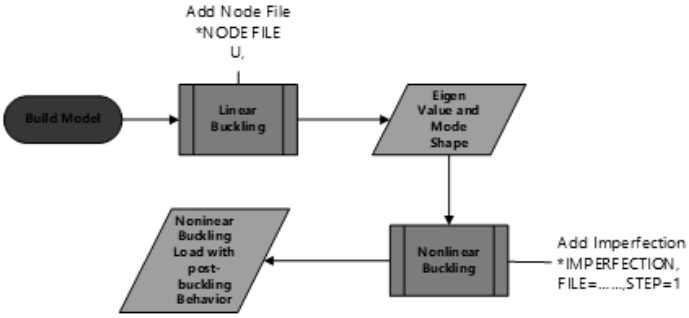

Figure 4: Nonlinear buckling modeling process in ABAQUS

The perforations have a circular form located at column mid-height. The diameter of the perforation to cross-section width ratio was constant in all models with the value of 0.44 (the ratio of the perforation diameter to the flat part of the section width is 0.50). In addition, to investigate the eccentricity of the circular perforations, stub columns were modeled with the ratio of the transverse displacement of the circular perforation to the section width was 0.20, and both axial and eccentric compression loading was applied separately. The section and three-dimensional schematic drawings of SHS members with symbol definitions were given in Figure 5. Detailed illustrations of the loading cases were depicted in Figure 6 and 7.

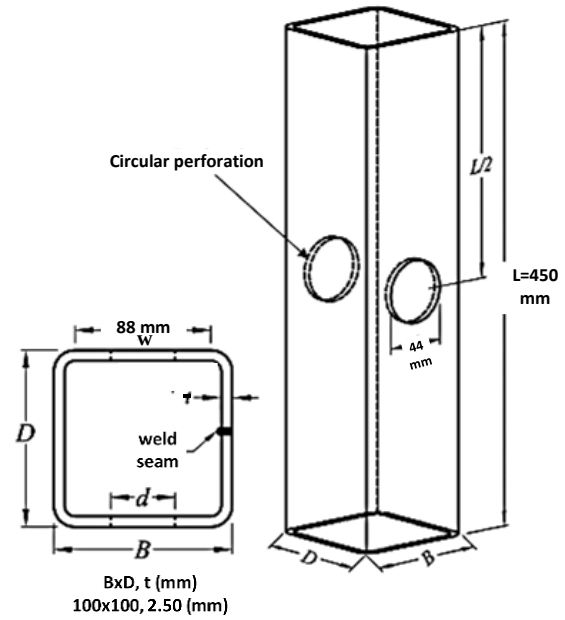

Figure 5: The section and three-dimensional schematic drawings of SHS members with symbol definitions [12]

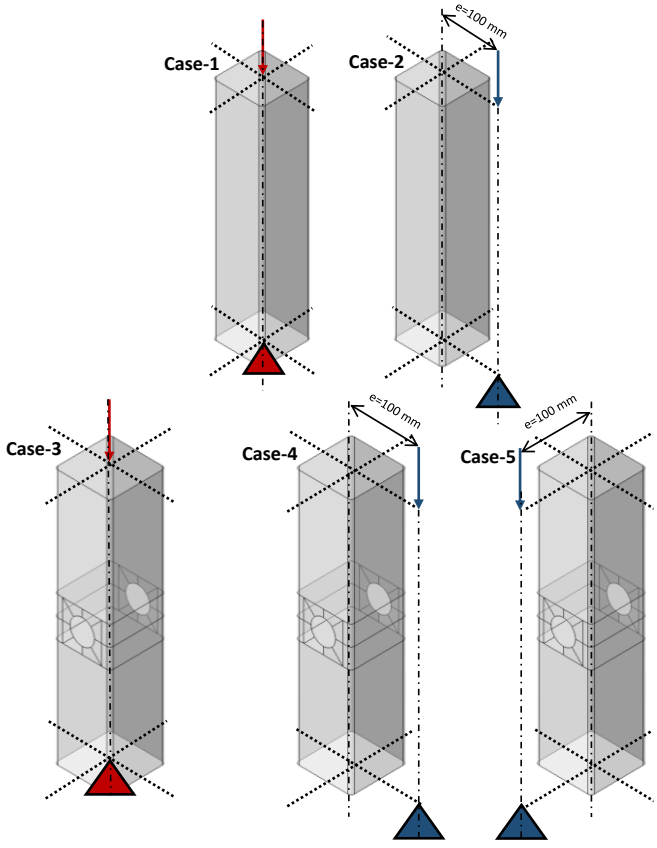

Figure 6: Loading cases

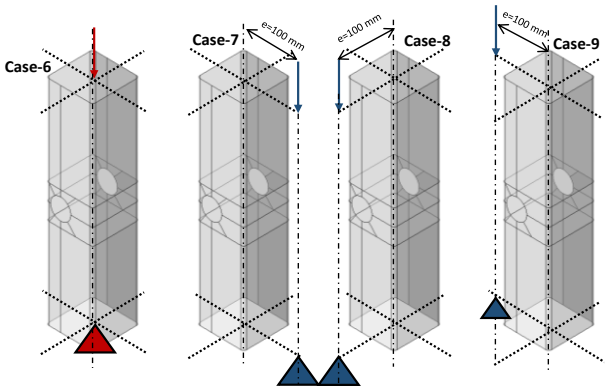

Figure 7: Continuation of Figure 6

III. RESULTS AND DISCUSSIONS

In this numerical study, non-perforated and circular perforated SHS stub columns with nominal cross-section dimensions of 100x100x2.50 mm and a height of 450 mm were modeled with a boundary condition that allows the ends of the specimens to rotate freely in the bending plane. The end-shortening versus load curves obtained from FEAs were given in Figure 8. Summary of numerical results for SHS stub column members also was given in Table 1. Local buckling deformations of the SHS stub columns along with Von-Mises stress contour was also given in Figure 9 and 10.

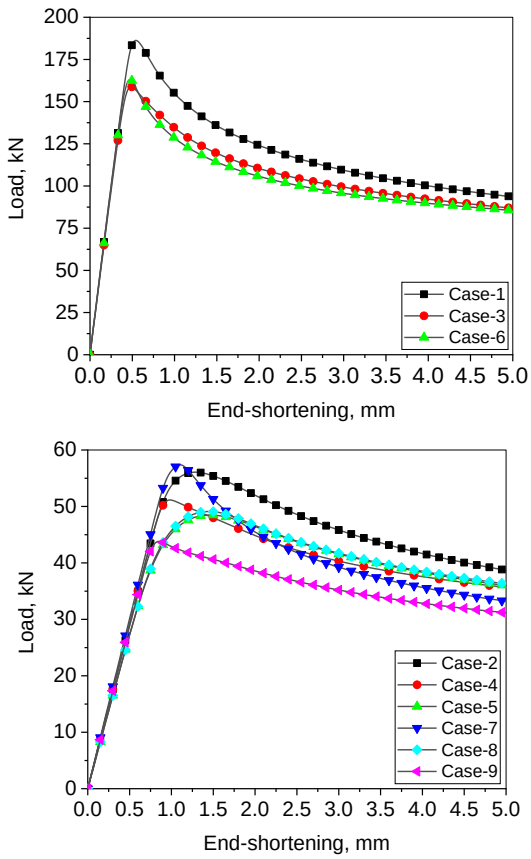

Figure 8: The end-shortening versus load curves

Table 1: Summary of FEA results

Loading Cases	Maximum load (kN)	Displacement at maximum load (mm)
1	186.3	0.54
2	56.0	1.29
3	158.9	0.48
4	51.2	0.99
5	48.5	1.45
6	163.1	0.48
7	57.4	1.11
8	49.1	1.45
9	43.8	0.85

As can be seen from Figure 8 and Table 1, the highest load-carrying capacity (186.3 kN) was obtained under the axial compressive loading of the non-perforated element representing the control member (Case-1), as expected. In Case-3 and Case-6, where perforated SHS members were subjected to axial compression loading, the difference between maximum loads was obtained less than 3%. It showed that in the case of axial loading, perforation affected the load-carrying capacity, but perforation location was negligible. When the results obtained from Case-3 and Case-6 were compared with the results of Case-1, it was seen that the maximum load value decreased by 12.5% and 14.65%, respectively. When the results obtained for eccentric compression loading cases were examined, the minimum capacity was obtained (43.8 kN) when the load and perforation were on the same side (Case-9). The highest load (57.4 kN) was obtained when the compression load and perforation were located on opposite sides (Case-7). The maximum load value obtained in Case-7 is 31% higher than the load value obtained in Case-9. Also, the maximum load value obtained from the control member under eccentric compression loading (Case-2) was 56 kN and was approximately the same as the maximum load value obtained in Case-7. This situation occurred because the part of the cross-section that resisted the load was not affected by the perforation. The opposite situation was valid for Case-9. When the findings obtained from Cases-4,5, and 8 were examined, the maximum loads under the mentioned loading conditions were 51.2 kN, 48.5 kN, and 49.1 kN, respectively. In particular, approximately the same maximum load values were obtained from Cases-5 and 8. These findings showed that the effect of perforation position was negligible if the point of application of the load in eccentric loading was the same as shown in these loading cases (see Figures 6 and 7). In the case of a superficial examination of Figure 9 and 10, the first striking situation was that, unlike all loading cases, in Case-2, the local buckling behavior occurred approximately 180 mm below the loading point of the SHS stub column (Figure 11). However, in other cases, local buckling occurred in the mid-height of stub columns. This situation was due to the weakening of the section at the mid-height due to the generated perforations.

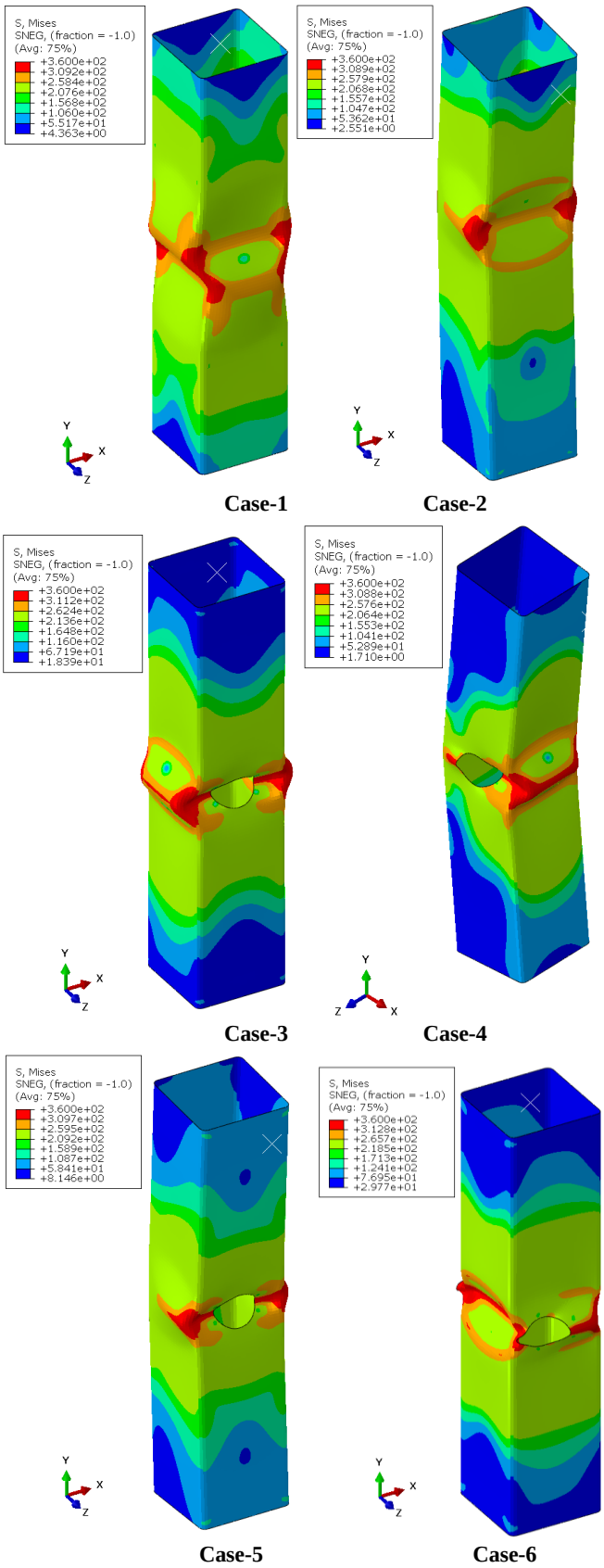

Figure 9: Local buckling deformations of SHS stub column along with Von-Mises stress contour

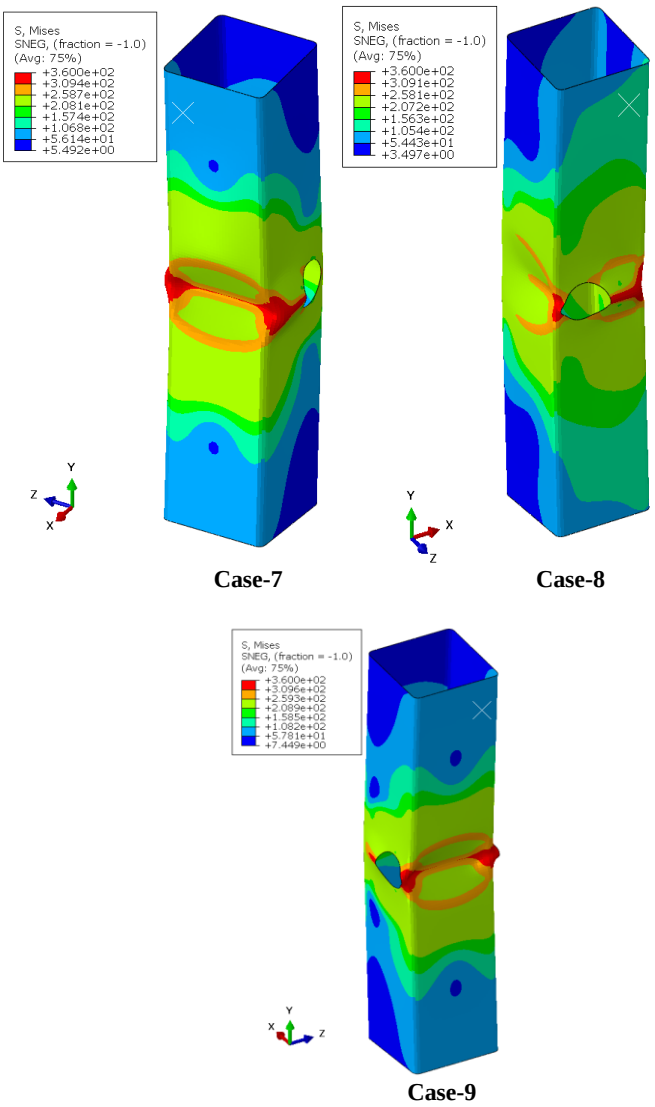

Figure 10: Continuation of Figure 9

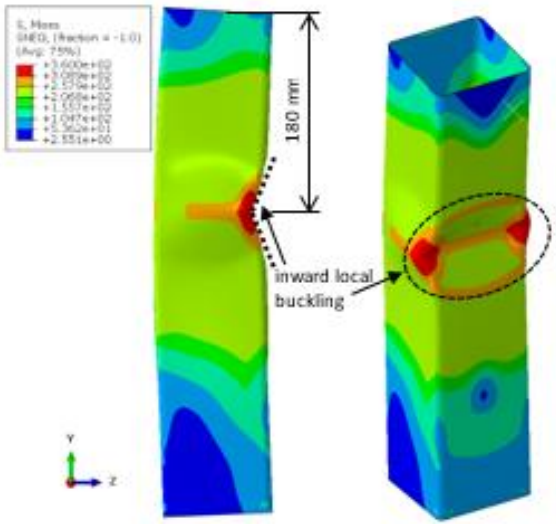

Figure 11: Local inward buckling of SHS stub column (Case-2)

IV. CONCLUSION

In this study, FEA was performed to investigate the behavior of perforated cold-formed square hollow steel stub column members under axial and eccentric compression loads. The perforations were circular and were located at column mid-height. The diameter of the perforation to cross-section width ratio was 0.44 in all configurations. In addition, stub columns were modeled with a ratio of the circular transverse displacement of perforations to the section width was 0.20. Both axial and eccentric compression loading was applied separately to study the eccentricity of the circular perforations. In this study, 100 mm loading eccentricity (e) was selected, which was the width or height of the cross-section. Based on this study, the following conclusions can be drawn:

- The highest load-carrying capacity (186.3 kN) was obtained under the axial compressive loading of the non-perforated (control) element (Case-1).
- In Case-3 and Case-6, where perforated SHS members were subjected to axial compression loading, the difference between maximum loads was obtained less than 3%. It showed that in the case of axial loading, perforation affected the load-carrying capacity, but perforation location was negligible.
- When the results obtained for eccentric compression loading cases were examined, the minimum capacity was obtained (43.8 kN) when the load and perforation were on the same side (Case-9).
- The maximum load value obtained from the control member under eccentric compression loading (Case-2) was 56 kN and was approximately the same as the maximum load value obtained in Case-7. This situation occurred because the part of the cross-section that resisted the load was not affected by the perforation. The opposite situation was also valid for Case-9.
- The approximately same maximum load values were obtained from Cases-5 and 8. These findings showed that the effect of perforation position was negligible if the point of application of the load in eccentric loading was the same as shown in these loading cases.
- In the case of a shallow examination, the first striking situation was that, unlike all loading cases, in Case-2, the local buckling behavior occurred approximately 180 mm below the loading point of the SHS stub column members. However, in other cases, local buckling occurred in the mid-height of stub columns. This situation was due to the weakening of the section at the mid-height due to the generated perforations.

In particular, it should be noted that a comprehensive literature review and numerical studies, and experimental studies should be conducted to obtain more precise and realistic results.

REFERENCES

[1] Gao, Lei, et al. "Load-carrying capacity of high-strength steel box-sections I: Stub columns." *Journal of Constructional Steel Research* 65.4 (2009): 918-924.

[2] Gardner, L., N. Saari, and F. Wang. "Comparative experimental study of hot-rolled and cold-formed rectangular hollow sections." *Thin-walled structures* 48.7 (2010): 495-507.

[3] Yian Peen, Woo, Chua Yie Sue, and Choong Kok Keong. "Effect of Perforation Area and Arrangement Pattern on Structural Behaviour of Nature Inspired Perforated Hollow Structure." *Iranian (Iranica) Journal of Energy & Environment* 4.3.

[4] Umbarkar, Kunal R., Longshithung M. Patton, and Konjengbam Darunkumar Singh. "Effect of single circular perforation in lean duplex stainless steel (LDSS) hollow circular stub columns under pure axial compression." *Thin-Walled Structures* 68 (2013): 18-25.

[5] Ghazijahani, Tohid Ghanbari, Hui Jiao, and Damien Holloway. "Influence of a cutout on circular steel hollow sections under cyclic loading." *Journal of Constructional steel research* 100 (2014): 12-20.

[6] Vaz, Murilo A., et al. "Experimental and numerical analyses of the ultimate compressive strength of perforated offshore tubular members." *Marine Structures* 58 (2018): 1-17.

[7] Singh, Tekcham Gishan, and Konjengbam Darunkumar Singh. "Experimental investigation on performance of perforated cold–formed steel tubular stub columns." *Thin-Walled Structures* 131 (2018): 107-121.

[8] Peen, Woo Yian, Choong Kok Keong, and Omid Hassanshahi. "Behaviour of hollow circular section with multiple perforations under compression, flexure and torsion." *Latin American Journal of Solids and Structures* 16 (2019).

[9] Ma, Jia-Lin, Tak-Ming Chan, and Ben Young. "Cold-formed high-strength steel rectangular and square hollow sections under combined compression and bending." *Journal of Structural Engineering* 145.12 (2019): 04019154.

[10] Devi, Sanasam Vipej, and Konjengbam Darunkumar Singh. "Finite element study of the stiffening effects on torsional capacity of perforated stainless steel slender semi-elliptical hollow section members." *Structures*. Vol. 26. Elsevier, 2020.

[11] Sangeetha, P., Revathi, S. M., Sudhakar, V., Swarnavarshini, D., & Sweatha, S. (2021). Behaviour of cold-formed steel hollow beam with perforation under flexural loading. *Materials Today: Proceedings*, *38*, 3103-3109.

[12] Singh, Tekcham Gishan, and Tak-Ming Chan. "Effect of access openings on the buckling performance of square hollow section module stub columns." *Journal of Constructional Steel Research* 177 (2021): 106438.

[13] Singh, Tekcham Gishan, and Konjengbam Darunkumar Singh. "Design of perforated cold-formed steel hollow stub columns using direct strength method." *Thin-Walled Structures* 168 (2021): 108265.

[14] Simulia, D. (2017). Abaqus 6.17 Documentation, Provid. RI, USA DS SIMULIA Corp.

[15] European Committee for Standardization (CEN). "Cold formed welded structural hollow sections of non-alloy and fine grain steels–part 1: technical delivery conditions." (2006).

Effects of Molds of Different Depths on Microbial Carbonate Precipitation

S. ÇELİK[1] H. AKOĞUZ[2] Ö. BARIŞ[3]

[1] Atatürk University, Erzurum/Turkey, scelik@atauni.edu.tr
[2]Erzincan Binali Yıldırım University, Erzincan/Turkey, hakoguz@erzincan.edu.tr
[3]Atatürk University, Erzurum/Turkey, ozlembaris@gmail.com

Abstract **- Microbially Induced Calcite Precipitation (MICP) has emerged as an alternative to the soil improvement methods used today. In our study, the effects of different mold heights on permeability and calcite percentage were investigated in the improvement of sand soils by using the MICP technique. In this context, the soils were placed in molds with a relative density of 45%. Afterward, the culture medium for 24 hours and the cementing solution for 96 hours was applied to the soils. As a result, the increase in die heights increased the permeability. Calcite percentage results were similar. It has been determined that the mold height is especially effective on the permeability in the improvement of soils with MICP.**

Keywords **- MICP, Viridibacillus arenosi, Ground Improvement, Biologically Soil Improvement, Calcite Content**

I. Introduction

There are many different methods used to improve soils. However, with the use of these methods, the pH level of the soil often changes, and the toxic and dangerous substances in it pollute the soil and groundwater [1,2].

In this context, as an alternative to existing soil improvement methods, soil improvement with the MICP method has emerged. Today, studies on MICP are increasing considerably. Bacillus pasteurii [3-8] bacteria are mostly used in the improvement of soils with MICP. In this study, unlike the literature, Viridibacillus arenosi bacteria were used.

MICP technique involves the formation of ammonium and carbonate ions as a result of the hydrolysis of the urease enzyme by including aerobically grown bacteria with high urease enzymes into the soil. The chemical reaction in this process is given in (1)

$$CO(NH_2)_2 + 2H_2O \Rightarrow 2NH_4^+ + CO_3^{2-} \quad (1)$$

In the presence of a calcium source (usually calcium chloride, $CaCl_2$), calcium carbonate ($CaCO_3$, calcite) is formed throughout the soil matrix, as in the chemical reaction given in (2) [9].

$$Ca^{2+} + CO_3^{2-} \Rightarrow CaCO_3\,(s) \quad (1.2)$$

Within the scope of this study, the effects of molds at different heights on the reaction of sand soils improved with MICP were investigated by permeability and calcite percentage analysis.

II. Materials and Methods

A. Microorganism and Culture Mediums

Viridibacillus arenosi K64 (GenBank Acceptance No: KR873397) obtained from stock production from Ataturk University, Faculty of Science, Department of Biology. Bacterium is Gram positive, rod shaped, endospore forming, motile, aerobe and urease active. A liquid growth medium (500 ml) consisting of Tryptic Soy Broth, 30 g / L; Urea 20 g / L; $MnSO_4 \bullet H_2O$, 12 mg / L and $NiCl_2 \bullet 6H_2O$, 24 mg/L was adjusted to pH 8.0 by HCl or NaOH [10].

B. Soil

Soil grain size distribution curve is given in Figure 1 according to the sieve analysis made according to ASTM E 11 standard, and the sieve analysis results are given in Table 1.

Table 1: Index Properties of the Poorly Graded Sand Soil Used in the Tests

Property	Unit	Value
Specific gravity, G_s[a]	-	2.65
D_{10}[b]	mm	0.18
D_{30}[b]	mm	0.20
D_{60}[b]	mm	0.22
C_u[b]	-	1.22
C_c[b]	-	1.01
Unified Soil Classification System (USCS)	-	SP

[a]ASTM D854-14, [b]ASTM D2487-11

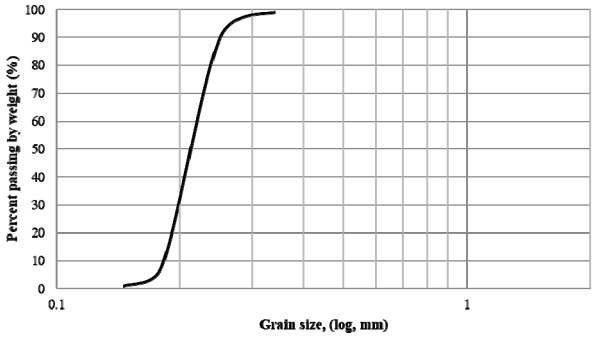

Figure 1: Grain size distribution of the sand soils in the tests

C. Preparation of Samples and Implementation Details

The soils had placed in PVC molds (Figure 2) of different height (38, 48, 58, 68 mm) with a radius of 38 mm and the

same relative densities (45%). Gravel filter and sponge had used on the lower and upper parts of the soil. In practice, using peristaltic pumps, first, the culture medium had given to the soils for about 24 hours, and then the cementing solution (0.75 M $CaCl_2$ + 1.5 M Urea) was given to the soils for 96 hours. When the cycles were completed, the samples were kept for 14 days in the oven set at 60 °C [11].

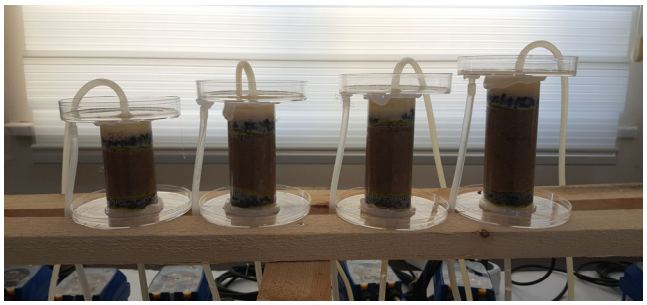

Figure 2: MICP implementation images

D. Calcite Content Determination

In this study, washing method was used to determine the calcite content [12].

E. Permeability

The permeability test was performed out in a PVC mold by using the constant level permeability method [13]. In addition, for the samples that were not treated, the permeability coefficient was determined to use a constant level permeability test for soil.

III. Results

A. Permeability Test Results

According to the constant level permeability test results, the permeability coefficient of soil which was not applied was determined as 0.0125 cm / sec. In Table 2, shows the permeability coefficients obtained after 4 days of application. According to the permeability test results, it was observed that the permeability decreased when the mold height decreased (Figure 3). Increasing the mold height affected the permeability negatively.

Table 2: Permeability coefficient in treated samples

Sample (mold height)	Flow Rate	Permeability coefficient (cm/sec)
38 mm	0.400 ml/sec	1.33 x10^{-3}
48 mm	0.400 ml/sec	3.36 x10^{-3}
58 mm	0.400 ml/sec	4.06 x10^{-3}
68 mm	0.400 ml/sec	4.16 x10^{-3}

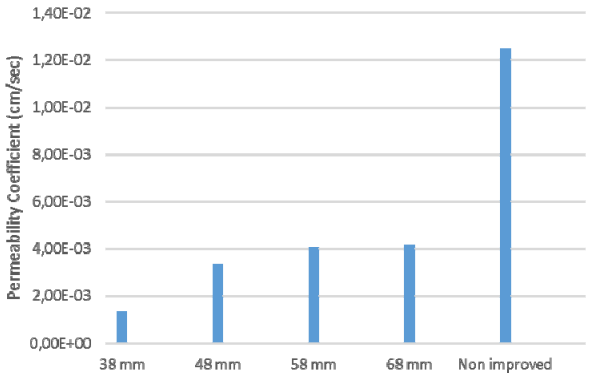

Figure 3: Permeability coefficient of improved and non-improved soil samples

B. Calcite Percentage Results

Figure 4 shows the improved soil samples and calcite percentages. Calcite percentages were determined in soil samples from the top, middle, and lower parts of the treated samples. In control samples where no culture media had been used, the calcite percentage found to be 0.38%. As a result of the application, calcite formation in all soil samples was observed mostly in the upper part and least in the lower part [14,15].

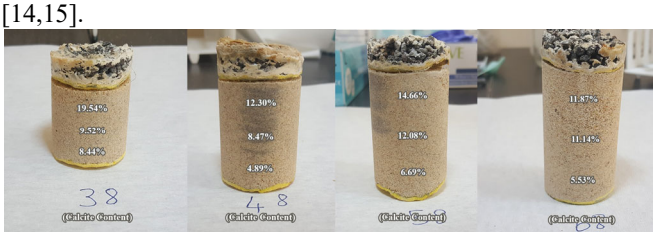

Figure 4. Improved soil samples and calcite percentages

IV. Conclusion

In this study, the effects of different mold heights on permeability and calcite percentages were investigated. Mold height was not very effective on calcite percentages, but it did affect permeability. Permeability increased with die height. It has been evaluated that taking into account the height of the mold in the studies to be conducted here may be effective in the application results.

References

[1] K. H. Reuben, "Chemical grouting and soil stabilization." Marcel Dekker New York, 2003.

[2] J. T. DeJong, M. B. Fritzges, and K. Nüsslein, "Microbially induced cementation to control sand response to undrained shear," J. Geotech. Geoenvironmental Eng., vol. 132, no. 11, pp. 1381–1392, 2006.

[3] S. S. Bang, J. K. Galinat, and V. Ramakrishnan, "Calcite precipitation induced by polyurethane-immobilized Bacillus pasteurii," Enzyme Microb. Technol., vol. 28, no. 4, pp. 404–409, 2001.

[4] G. D. O. Okwadha and J. Li, "Optimum conditions for microbial carbonate precipitation," Chemosphere, vol. 81, no. 9, pp. 1143–1148, 2010.

[5] V. S. Whiffin, L. A. van Paassen, and M. P. Harkes, "Microbial carbonate precipitation as a soil improvement technique," Geomicrobiol. J., vol. 24, no. 5, pp. 417–423, 2007.

[6] E. Salifu, E. MacLachlan, K. R. Iyer, C. W. Knapp, and A. Tarantino, "Application of microbially induced calcite precipitation in erosion mitigation and stabilisation of sandy soil foreshore slopes: A preliminary investigation," Eng. Geol., vol. 201, pp. 96–105, 2016.

[7] N.-J. Jiang, K. Soga, and M. Kuo, "Microbially induced carbonate precipitation for seepage-induced internal erosion control in sand–clay mixtures," J. Geotech. Geoenvironmental Eng., vol. 143, no. 3, p. 4016100, 2017.
[8] M. Sharma, N. Satyam, and K. R. Reddy, "Effect of freeze-thaw cycles on engineering properties of biocemented sand under different treatment conditions," Eng. Geol., vol. 284, p. 106022, 2021.
[9] L. Cheng, R. Cord-Ruwisch, and M. A. Shahin, "Cementation of sand soil by microbially induced calcite precipitation at various degrees of saturation," Can. Geotech. J., vol. 50, no. 1, pp. 81–90, 2013.
[10] B. Li, "Geotechnical properties of biocement treated sand and clay." 2015.
[11] H. Rong, C.-X. Qian, and L. Li, "Study on microstructure and properties of sandstone cemented by microbe cement," Constr. Build. Mater., vol. 36, pp. 687–694, 2012.
[12] Y. Xiao et al., "Restraint of particle breakage by biotreatment method," J. Geotech. Geoenvironmental Eng., vol. 146, no. 11, p. 4020123, 2020.
[13] J. Chu, V. Stabnikov, and V. Ivanov, "Microbially induced calcium carbonate precipitation on surface or in the bulk of soil," Geomicrobiol. J., vol. 29, no. 6, pp. 544–549, 2012.
[14] N. K. Dhami, M. S. Reddy, and A. Mukherjee, "Significant indicators for biomineralisation in sand of varying grain sizes," Constr. Build. Mater., vol. 104, pp. 198–207, 2016.
[15] A. Nafisi, S. Safavizadeh, and B. M. Montoya, "Influence of microbe and enzyme-induced treatments on cemented sand shear response," J. Geotech. Geoenvironmental Eng., vol. 145, no. 9, p. 6019008, 2019.

STATIC RESPONSE OF STEEL BEAMS WITH RECTANGULAR WEB OPENINGS

Fahrettin KURAN[1] and Ahmad Reshad NOORI[1]

[1] Istanbul Gelisim University, Istanbul/Turkey, fkuran@gelisim.edu.tr
[1]Istanbul Gelisim University, Istanbul/Turkey, arnoori@gelisim.edu.tr

***Abstract* - Steel beams are widely used in many engineering applications as structural members, therefore understanding their static behaviors is an important case. In this research, the finite-element method (FEM) is used to examine the static response of steel I-beams with rectangular web openings subjected to uniformly distributed loads. The finite-element software package, SAP2000 is used in the analysis. Results are obtained by using the thick shell and thin shell elements and comparisons are presented. The influence of the location of the rectangular web openings on the maximum vertical deflections and stresses is carried out for a clamped - clamped steel I-beam. The location of the web openings is determined to acquire the best performance of the beam under the same distributed load and fixed support conditions. Also, a parametric study is carried out to obtain the appropriate mesh of finite elements.**

***Keywords* – Steel beams, web openings, static response, stress, finite element method.**

I. INTRODUCTION

Due to their durability, high strength-to-weight ratio, and architectural appearance steel structural elements have been used widely in many construction projects. One of the most commonly used sections of the steel structural elements is the I section. Recently engineers prefer to use the I beams with web openings because these beams can have a significant contribution to the reduction of construction weight. Therefore, the static bending response of these important structures has been studied by various researchers.

Liu and Chung [1] examined the structural characteristics of steel beams with various web openings. They used the finite element method in their study. Chung et al. [2] investigated steel beams with web openings having different shapes and sizes, especially with an elaborate focus on their structural characteristics. The purpose of the Morkhade and Gupta's [3] study was to investigate the strength of a steel beam with rectangular web openings with different experiments on steel beams with rectangular mesh openings. Their findings indicated that there was a serious stress concentration in the corner regions of the openings.

Rodrigues et al. [4] put forward finite element models using ANSYS software. The aim was to examine the structural response of steel beams with web openings in terms of stress distributions, failure load magnitude and related failure modes. The research also included simulations of beams with a series of openings over their entire length. Al-Rifaie et al. [5] conducted experiments to investigate the response of steel beams under impact loads used to validate the FE models of steel-filled beams. Furthermore, the impact behavior of steel beams with rectangular web openings was investigated using these models. The effects of strain rate, ductility and shear damage were taken into account in the modeling. The influences on the impact response of steel beams with rectangular web openings were investigated by various parameters. There was better flexural impact resistance in the beams with narrow mesh openings than wide beams with an equivalent area.

Morkhade and Gupta [6] conducted experiments on beams with various web openings configurations and web openings areas to check their failure. It was seen that web post-buckling failure was the most common one in the study. Also, openings should be avoided in the shear dominant region but not in the bending region. The research by Shanmugam et al. [7] aimed to investigate the behavior and ultimate load of plate girders with web openings by using a finite element model. A method was introduced by Najafi and Wang [8] to analyze the capacity of steel members in various shapes and sizes joining axial compression, bending moment and shear force. The study by Panedpojaman and Theochatri [9] analyzed 408 cellular beams with 3-D finite elements to indicate how the cellular beam configuration might affect the deflection and presented that the stiffness of the analytical load-deflection curve would be influenced by cross-section dimension, beam slenderness, opening size and opening spacing. Doori and Noori [10] studied the bending response of steel beams with cellular and hexagonal web openings via 3D finite element analysis.

The literature survey indicates that most of the current works are focused on the shape of the web openings of I beams. To the best of the authors' knowledge, the influence of the location of the rectangular web openings on the static response of the considered structures has not been reported yet by using SAP2000.

In this study, the bending behaviors of the I steel beams with rectangular openings are examined. To obtain consistent results in SAP2000 a parametric study is carried for the appropriate mesh size. The impact of thick and thin shell elements on the maximum vertical displacements is examined and discussed. The importance of the location of the web openings is presented by giving several stress results. All the numerical results are obtained for clamped-clamped beams subjected to uniformly distributed loads.

II. FINITE ELEMENT MODELING IN SAP2000

The thick shell and the thin shell elements are used as finite elements to generate the model of the I beam with rectangular web openings in SAP2000 [11]. All translations and rotations at both ends of the beam are prevented.

To acquire the appropriate mesh size a parametric study is presented by considering seven different mesh cases for a solid I beam given in Figure 1. The details of the mesh size properties are listed in Table 1.

Table 1: Mesh size properties.

Model Number	Model Name	Mesh Size	
		Flange	Web
1	SW1BM1	20 x 2	20 x 2
2	SW1BM2	20 x 2	20 x 4
3	SW1BM3	20 x 2	20 x 8
4	SW1BM4	40 x 2	40 x 2
5	SW1BM5	40 x 2	40 x 4
6	SW1BM6	40 x 2	40 x 8
7	SW1BM7	40 x 2	40 x 16

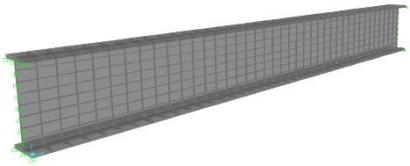

Figure 1: Solid I beam model

To analyze the I beam with rectangular web openings SW1BM6 mesh size is implemented. Results of the static response are obtained for several locations of the web openings (Figure 2) while their total area is considered to be constant.

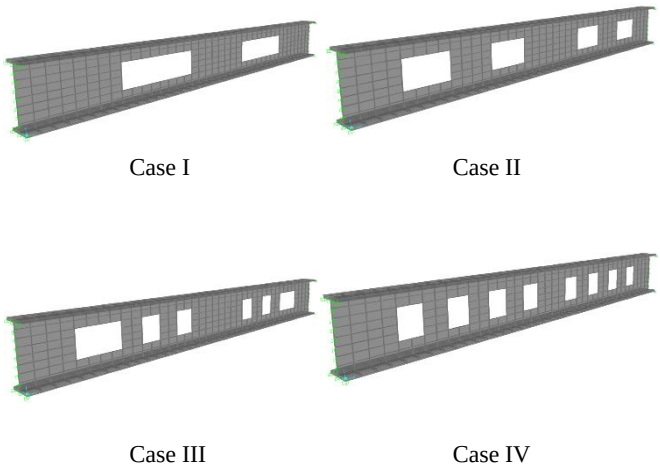

Figure 2: I beam with rectangular web openings

III. RESULTS AND DISCUSSION

In this section, numerical results are carried out to obtain the appropriate mesh size and to investigate the static response of I beams with rectangular web openings. A clamped-clamped isotropic I beam, shown in figure 3 is now considered under a uniformly distributed load of 0.1 ton/cm^2. Material properties are considered to be, Poisson's ratio, ν =0.3, mass density, ρ=7850 × 10^{-6} kg/cm^3, and modulus of elasticity, E= 2.1 × 10^6 kg$_f$/cm^2.

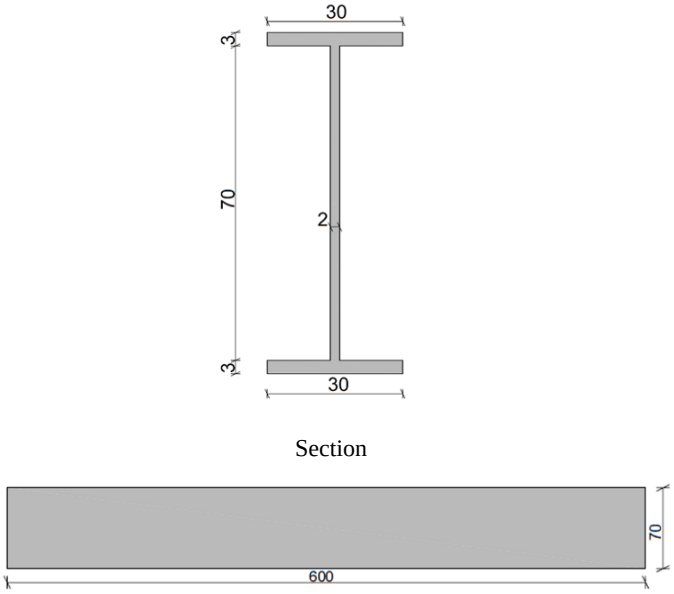

Figure 3: Geometric properties of Solid I beam model

The maximum vertical displacements obtained by various mesh sizes given in Table 1 are listed in Table 2.

Table 2: Maximum vertical displacement

Model Number	Model Name	Maximum vertical displacement (cm)	
		Thin Shell	Thick Shell
1	SW1BM1	-2.833834	-2.833814
2	SW1BM2	-2.841723	-2.844240
3	SW1BM3	-3.661633	-3.665918
4	SW1BM4	-2.843078	-2.835674
5	SW1BM5	-2.853536	-2.852954
6	SW1BM6	-3.679553	-3.682727
7	SW1BM7	-3.682888	-3.688136

The comparison given in Table 2 demonstrates that the mesh size has a significant effect on the bending response of I sections in the modeling process with the shell elements. The results of thick and thin shells are close to each other because the thickness of the shell elements is thin so the Kirchhoff theory can be implemented. Unless expressly provided otherwise, the SW1BM6 model will be used in the proceeding examples. In order to ascertain the impact of the location of the web openings on the displacement results of the considered structure, various cases for the web of the beam are presented in Figure 4.

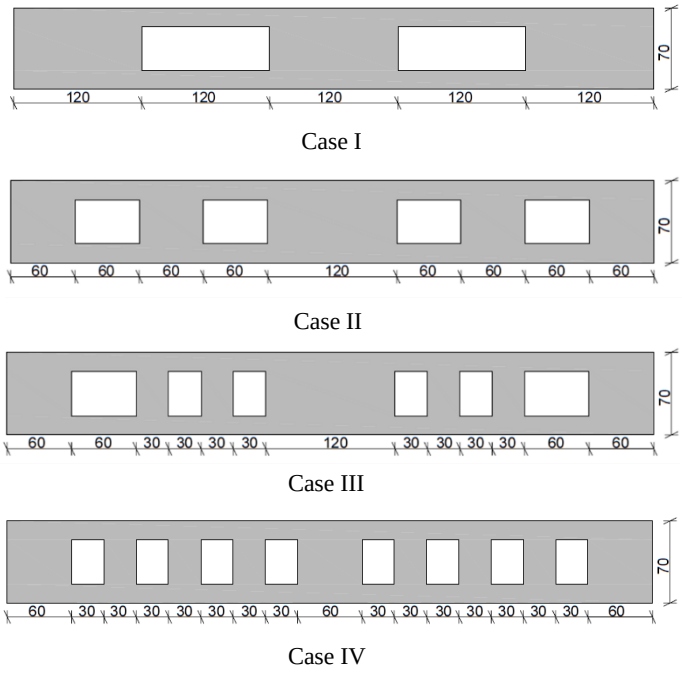

Figure 4: Geometric properties of rectangular web openings

Comparisons of the maximum vertical displacements are presented in Table 3 for the above cases of the web openings.

Table 3: Comparison of the maximum vertical displacement

Case	Model Name	Total Area of the web openings (cm^2)	Maximum vertical displacement (cm)
Solid Case	SW1BM6	-	-3.67960
Case 1	HW1BM1	8400	-12.4085
Case 2	HW1BM2	8400	-8.00190
Case 3	HW1BM3	8400	-7.87400
Case 4	HW1BM4	8400	-6.15670

It is apparent from Table 3 that the lowest vertical displacement occurs in the HW1BM4 model, while the largest vertical displacement occurs in HW1BM1. Results of HW1BM2 and HW1BM3 are closer to each other compared with other cases.

In the next step, the stress analysis of the considered I beam with rectangular web openings will be carried out with the help of the SAP2000. First, values of the Von Mises are illustrated for all of the web opening cases in Figure 5.

The comparison given in Figure 5 demonstrates that the values of the Von Mises stress have the largest value in model HW1BM1 and the lowest value in model HW1BM4. The Von Mises Stress diagrams of HW1BM2 and HW1BM3 are similar to each other.

The values of the maximum principal stresses are obtained and compared for the considered cases. The comparison is given in Figure 6.

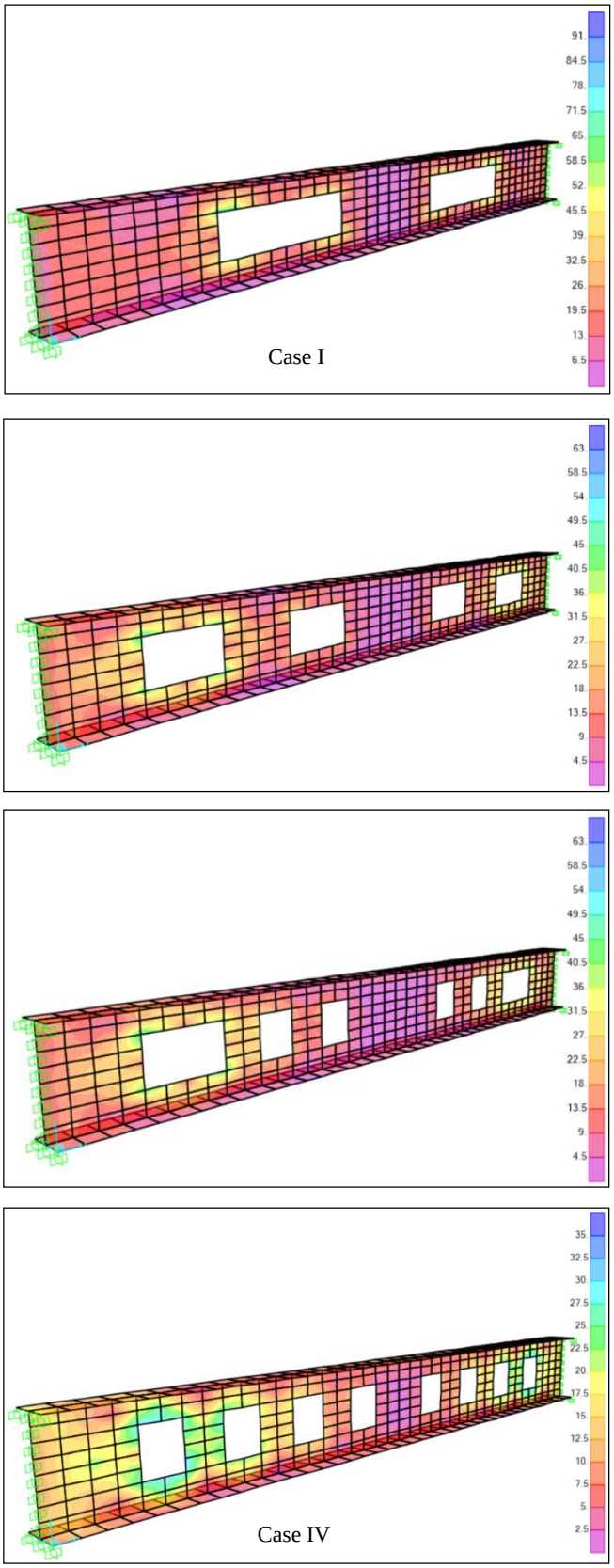

Figure 5: Von-Mises stress values (ton/cm^2) of fixed supported I beam with various rectangular web openings

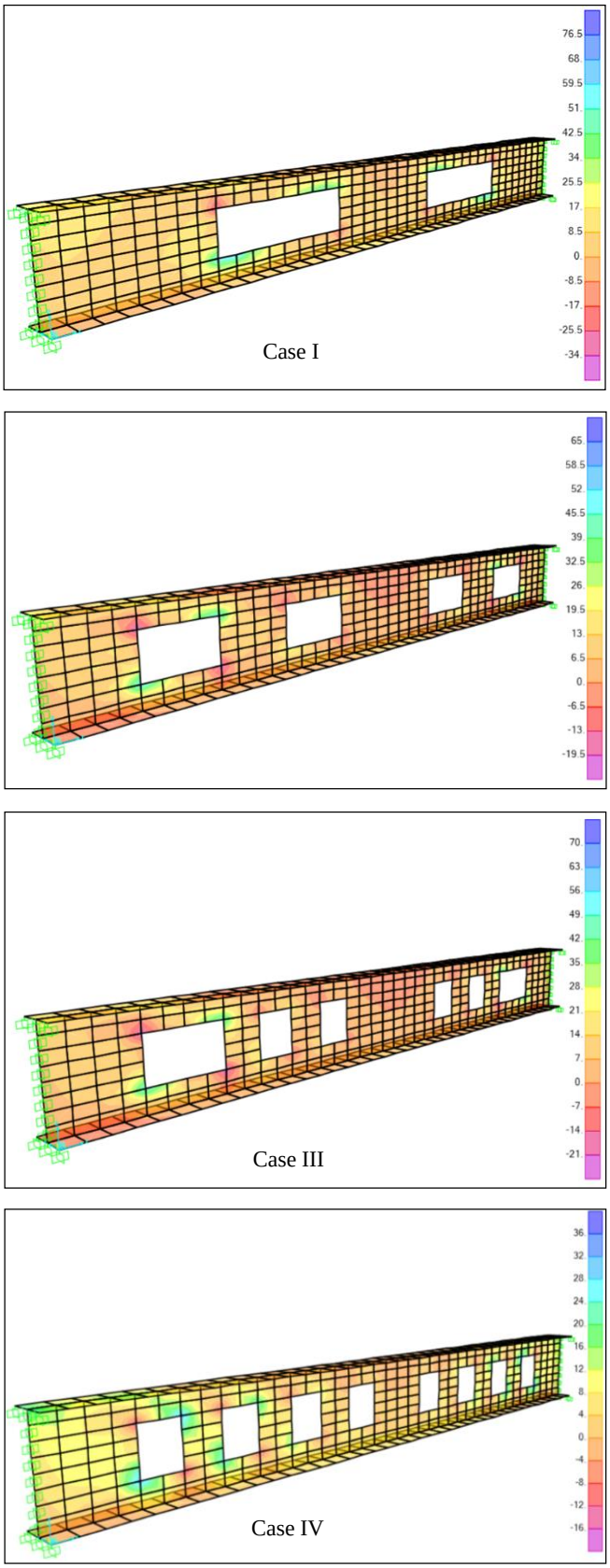

Figure 6: The maximum principal stress values (ton/cm^2) of fixed supported I beam with various rectangular web openings

Figure 6 clearly represents that the lowest values of maximum principal stress are generated in the model HW1BM4. Also, it is found that the highest values of maximum principal stress occur in Case 1.

IV. Conclusion

In this research, the bending response of I beams with rectangular web opening subjected to uniformly distributed static loads is examined via the finite element method. Stress and deflection results are acquired for several cases. Some important observations of this research can be summarized as follows:

- Based on the parametric study presented in this research, the proper finite element mesh is 40 x 2 for the flanges and 40 x 8 for the web of the I beam.
- The lowest transverse displacement occurs in HW1BM4, while the largest transverse displacements occur in HW1BM1.
- Comparison of the Von Mises and maximum principal stresses demonstrates that the most appropriate rectangular web opening is the HW1BM4 among the considered models.

References

[1] T.C.H. Liu and K.F. Chung, "Steel beams with large web openings of various shapes and sizes: finite element investigation," *Journal of Constructional Steel Research*, vol. 59, pp. 1159–1176, February 2003.

[2] K.F. Chung, C.H. Liu, and A.C.H. Ko, "Steel beams with large web openings of various shapes and sizes: an empirical design method using a generalised moment-shear interaction curve," *Journal of Constructional Steel Research*, vol. 59, pp. 1177–1200, February 2003.

[3] Samadhan G. Morkhade, and Laxmikant M. Gupta, "Analysis of steel I-beams with rectangular web openings: experimental and finite element investigation," *Engineering Structures and Technologies*, 7:1, 13-23, December 2015.

[4] Flavio Rodrigues, Pedro C. G. da S. Vellasco, Luciano R. O. de Lima, and Sebastião A. L. de Andrade, "Finite Element Modelling of Steel Beams with Web Openings," *Engineering*, 6, 886-913., December 2014.

[5] Ali Al-Rifaie, Alaa S. Al-Husainy, Tariq Al-Mansoori, and Ali Shubbar, "Flexural impact resistance of steel beams with rectangular web openings" *Case Studies in Construction Materials*, Volume 14, June 2021.

[6] Samadhan. G. Morkhade and L. M. Gupta, "Ultimate load behaviour of steel beams with web openings" *Australian Journal of Structural Engineering*, Pages 124-133, April 2019.

[7] N.E. Shanmugam, V.T. Lian, and V. Thevendran, "Finite element modelling of plate girders with web openings" *Thin-Walled Structures*, Volume 40, Issue 5, Pages 443-464, May 2002.

[8] M. Najafi and Y.C.Wang, "Behaviour and design of steel members with web openings under combined bending, shear and compression" *Journal of Constructional Steel Research*, Volume 128, Pages 579-600, January 2017.

[9] Pattamad Panedpojaman and Thaksin Thepchatri, "Finite Element Investigation on Deflection of Cellular Beams with Various Configurations Pattamad" *International Journal of Steel Structures*, Vol 13, No 3, 487-494, September 2013.

[10] Doori, S. and Noori, A. R., "Finite Element Approach for the Bending analysis of Castellated Steel Beams with Various Web openings" *ALKÜ Fen Bilimleri Dergisi*, Vol 3, No 2, 38-49, August 2021.

Effect Of Liquid Medium and Different Application Used in MICP On Some Properties of Cemented Soils

H.AKOĞUZ[1] and S.ÇELİK[2]

[1] Erzincan Binali Yıldırım University, Erzincan/Turkey, hakoguz@erzincan.edu.tr
[2]Atatürk University, Erzurum/Turkey, scelik@atauni.edu.tr

Abstract **- There are many different techniques used today in the improvement of soils. However, many of them contain components that are harmful to the environment. Improvement of soils with MICP (Microbially Induced Calcite Precipitation) emerges as an environmentally friendly technique. Our study investigated the effects of different liquid media and application techniques on soil improvement using the MICP technique. It was determined that different media were effective on bacterial densities. With the increase of the application time, better results were obtained in soil improvement. It has been determined that the application times and different media are effective in improving the MICP technique.**

Keywords **– MICP, Ground improvement, Biological soil improvement, Microbially induced calcite precipitation, *Viridibacillus arenosi***

I. INTRODUCTION

Today, many different methods are used to improve soils. Since many of these methods are harmful to the environment, different soil improvement methods have been sought. In this context, studies on soil improvement with MICP are increasing. Improvement using MICP promises us a promising future as a green, sustainable and eco-friendly technique. [1].
MICP occurs as a result of a series of reactions. This technique involves the formation of ammonium and carbonate ions due to the hydrolysis of the urease enzyme by incorporating aerobically grown bacteria with high urease enzyme into the substrate. The chemical reaction in this process is given in (1).

$$CO(NH_2)_2 + 2H_2O \Rightarrow 2\ NH_4+ + CO_3^{2-} \quad (1)$$

In the presence of a calcium source (usually calcium chloride, CaCl2), as in the chemical reaction given in (2), calcium carbonate (CaCO3, calcite) is formed throughout the soil matrix. [2].

$$Ca^{2+} + CO_3^{2-} \Rightarrow CaCO_3\ (s) \quad (2)$$

Many factors have been found in the studies that affect the calcium carbonate reaction. These include pH, liquid medium, temperature, urea activity, bacteria, soil type, etc. can be listed as.

Nutrients are the energy sources of bacteria, so nutrients have an important place for bacteria that produce calcite. Nutrients must be provided for the bacteria during the application to the substrate and the culture phase. [3]. Necessary nutrients for bacteria are generally CO_2, N, P, K, Mg, Ca, Fe et al. includes [4]. In the study [5], two different liquid mediums and different ambient conditions were used to evaluate the control of the reaction rate. In the [6] studies, 5 different liquid media were used. In our study, using 4 different liquid media, the most suitable medium was determined as a result of the analysis.
In the improvement of soils with MICP, the application method has an impact on the results. In our study, the results were evaluated using different applications.

II. MATERIALS AND METHODS

A. Microorganism

Viridibacillus arenosi K64 (GenBank Acceptance No: KR873397) obtained from stock production from Ataturk University, Faculty of Science, Department of Biology. Bacterium is Gram positive, rod shaped, endospore forming, motile, aerobe and urease active.

B. Soil

Soil grain size distribution curve is given in Figure 1 according to the sieve analysis made according to ASTM E 11 standard, and the sieve analysis results are given in Table 1.

Table 1 : Index Properties of the Poorly Graded Sand Soil Used in the Tests

Property	Unit	Value
Specific gravity, G_s[a]	-	2.65
D_{10}[b]	mm	0.18
D_{30}[b]	mm	0.20
D_{60}[b]	mm	0.22
C_u[b]	-	1.22
C_c[b]	-	1.01
Unified Soil Classification System (USCS)	-	SP

aASTM D854-14, bASTM D2487-11

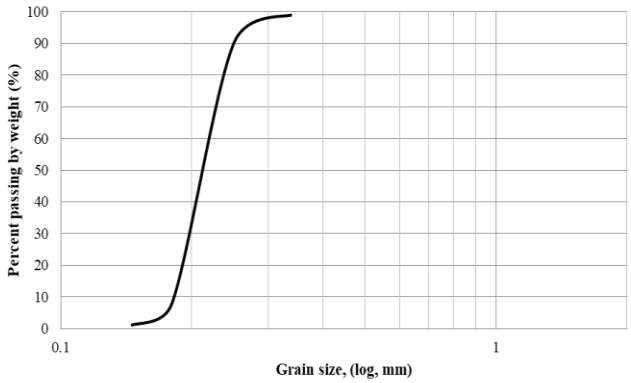

Figure 1: Grain size distribution of the sand soils in the tests

C. Liquid Medium

As liquid medium, liquid medium containing Tryptic Soy Broth, 30 g/l; Urea, 20 g/l; $MnSO_4 \cdot H_2O$, 12 mg/l; $NiCl_2 \cdot 6H_2O$, 24 mg/l and used in [7] study was used. While preparing this liquid medium, other chemicals except urea were sterilized in autoclave. Urea was added to the mixture through a 0.45 µm filter. The materials were weighed so that the mixture was 1 L and then combined in an aseptic environment. In order to compare with other media, 4 different media in Table 2 were used.

Table 2: Different liquid mediums used in the calcium carbonate precipitation reaction [8]

Name	Compound		pHa	References
	Nutrients	Concentration		
SF[b,c]	Nutrient broth	3 g l^{-1}	6	[9]
	Urea	20 g l^{-1}		
	$CaCl_2.2H_2O$	1.4-5.6 g l^{-1}		
	NH_4Cl	10 g l^{-1}		
	$NaHCO_3$	2.12 g l^{-1}		
Growth Medium (DB)	Yeast extract	20 g l^{-1}	7	[10]
	Urea	20 g l^{-1}		
Biodeposition (DB)	Urea	20 g l^{-1}	7	[11]
	$CaCl_2.2H_2O$	50 g l^{-1}		
TSB	Tryptic Soy Broth	30 g/l		[7]
	Urea	20 g/l		
	$MnSO_4 \cdot H_2O$	12 mg/l		
	$NiCl_2 \cdot 6H_2O$	24 mg/l		

D. Spectrophotometer Analysis

In order to determine the liquid medium to be used in our study, spectrophotometer analysis was performed on the culture media created with different liquid mediums at different times. As a result of this analysis, it was decided which medium to use.

E. Treatment Method

The soil is placed in PVC molds with a diameter of 38 mm. The cementing solution was applied cyclically by means of peristaltic pumps (Figure 2). Application results were evaluated by using different cementing solutions (Different molar $CaCl_2$ or $CaCl_2$+Urea) and different application times.

Figure 2: The experimental setup

III. RESULTS AND DISCUSSION

A. Effect of Different Implementations

Culture medium prepared with SF medium was applied to the soils in cycles for 1 hour using peristaltic pumps. Afterward, $CaCl_2$ (5 g/l) was applied for 6 hours, and the soil was left to dry. The soil obtained as a result of the application is given in Figure 3.

Figure 3: Application results

In the application, the $CaCl_2$ stock solution density was adjusted as 140 g/l and given to the soil. The application results are given in Figure 4.

Figure 4: Application results

As a result of the change in the stock solution, no difference was observed in the sample results. In the literature, it has been stated that prolonging the application period positively affects improvement. Similar to the method used in the study of [7], the effect on the results was evaluated. The medium used in the study of [7] and containing Tryptic Soy Broth, 30g/l; Urea, 20 g/l; $MnSO_4 \cdot H_2O$, 12 mg/l; $NiCl_2 \cdot 6H_2O$, 24 mg/l was prepared as 1 L. At the end of the 48 hour incubation period, the culture medium was precipitated in 50 ml tubes in the centrifuge (3000 rpm, 4°C, 10 min). The resulting pellet was made up to 50 ml by adding 9 g/L NaCl. The ground and 50 ml of bacterial solution were mixed in a sterile container and placed in a PVC container. For approximately one day, 200 ml of 50 mM $CaCl_2$ was cycled with a peristaltic pump. Afterward, the prepared 240 ml (0.75 M $CaCl_2$ and 1.5 M urea) solution was cycled for five days. After the cycle was finished, the soil was left to dry, and better results were obtained on the applied floor compared to other applications (Figure 5).

Figure 5: (a) liquid medium, (b) 48-hour culture medium, (c) pellet precipitated in centrifuge, (d) application result

As a result of the analyzes, it was determined that the liquid medium and the application time were effective in improvement. Spectrophotometer analyzes were performed for a more detailed analysis of liquid media.

B. Spectrophotometer Analysis Results

Biodeposition (DB), Growth medium (DB), $SF^{b,c}$ and TSB liquid media, the contents of which are given in Table 2, were used. *V. Arenosi* was inoculated into the prepared liquid mediums (Figure 6) and their density was measured with a spectrophotometer every 24 hours for 4 days.

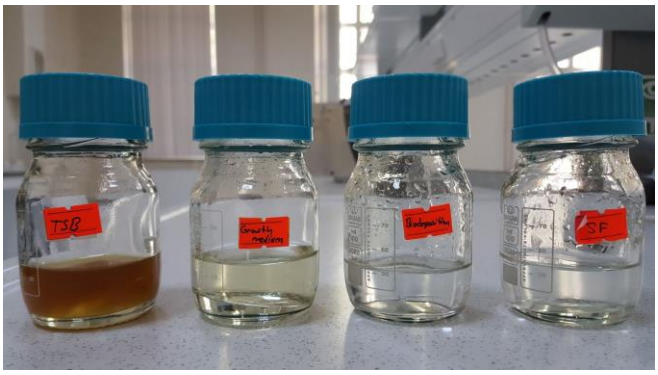

Figure 6: Prepared culture media (1 day)

In the analyzes, two containers were prepared from each medium, the culture medium was added to one of them and not to the other. After all the media were placed in the shaker, the media were removed every 24 hours and filled into tubes under aseptic conditions for analysis (Figure 7).

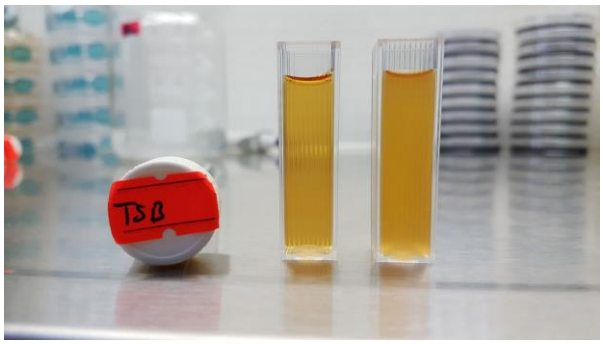

Figure 7: Tubes prepared for spectrophotometer analysis

The tubes prepared in an aseptic environment were analyzed by spectrophotometer for four days, and the results are given in Table 3.

Table 3: Spectrophotometer analysis results

Liquid medium	1 Day (%)	2 Day (%)	3 Day (%)	4 Day (%)
Biodeposition (DB)	101.4	101.4	101.3	101.6
Growthmedium (DB)	97.2	48.5	53	55.3
SF^{bc}	99.5	97.7	95.6	100.2
TSB	7.2	13.4	15.9	17.5

Table 3 shows the results of the spectrophotometer analysis. Since the analyzes continued at the same intensity after the 4th day, they were discontinued. When the analysis results are

examined, it is seen that the highest bacterial density is in TSB broth.

IV. Conclusions

As a result of the applications, it is understood that both the liquid medium and the application method affect the results. It has been evaluated that considering the liquid medium and application method in MICP improvement applications will positively affect the results.

Acknowledgment

The study was produced based on the doctoral dissertation study carried out at the School of Sciences at Atatürk University Investigation Of The Effects Of Some Variables In Biological Improvement Of Soils By Using Microbial Induced Calcite Precipitation. The dissertation study was carried out with the support provided by the Scientific Research Project coded 2019/6880 at Atatürk University. We would like to thank Atatürk University for the support received and their contributions.

References

[1] A. Sharma and R. R., "Study on effect of Microbial Induced Calcite Precipitates on strength of fine grained soils," Perspect. Sci., vol. 8, pp. 198–202, 2016, doi: 10.1016/j.pisc.2016.03.017.

[2] L. Cheng, R. Cord-Ruwisch, and M. A. Shahin, "Cementation of sand soil by microbially induced calcite precipitation at various degrees of saturation," Can. Geotech. J., vol. 50, no. 1, pp. 81–90, 2013.

[3] W.-S. Ng, M.-L. Lee, and S.-L. Hii, "An overview of the factors affecting microbial-induced calcite precipitation and its potential application in soil improvement," World Acad. Sci. Eng. Technol., vol. 62, pp. 723–729, 2012.

[4] J. K. Mitchell and J. C. Santamarina, "Biological considerations in geotechnical engineering," J. Geotech. Geoenvironmental Eng., vol. 131, no. 10, pp. 1222–1233, 2005.

[5] F. Kalantary and M. Kahani, "Evaluation of the Ability to Control Biological Precipitation to Improve Sandy Soils," Procedia Earth Planet. Sci., vol. 15, pp. 278–284, 2015.

[6] F. M. Helmi, H. R. Elmitwalli, S. M. Elnagdy, and A. F. El-Hagrassy, "Calcium carbonate precipitation induced by ureolytic bacteria Bacillus licheniformis," Ecol. Eng., vol. 90, pp. 367–371, 2016, doi: 10.1016/j.ecoleng.2016.01.044.

[7] B. Li, "Geotechnical properties of biocement treated sand and clay." 2015.

[8] W. De Muynck, N. De Belie, and W. Verstraete, "Microbial carbonate precipitation in construction materials : A review," vol. 36, pp. 118–136, 2010, doi: 10.1016/j.ecoleng.2009.02.006.

[9] S. Stocks-Fischer, J. K. Galinat, and S. S. Bang, "Microbiological precipitation of CaCO3," Soil Biol. Biochem., vol. 31, no. 11, pp. 1563–1571, 1999.

[10] V. S. Whiffin, "Microbial CaCO3 precipitation for the production of biocement." Murdoch University, 2004.

[11] N. De Belie and W. De Muynck, "Crack repair in concrete using biodeposition," in Proceedings of the International Conference on Concrete Repair, Rehabilitation and Retrofitting (ICCRRR), Cape Town, South Africa, 2008, pp. 291–292.

Coastline Change Analysis in Iznik Lake with Geographic Information Systems and Remote Sensing Methods

T.ALKAN[1] and S.S.DURDURAN[1]

[1] Necmettin Erbakan University, Konya/Turkey, tansualkan93@gmail.com
[1]Necmettin Erbakan University, Konya/Turkey, durduran2001@gmail.com

Abstract **- Iznik Lake, a tectonic freshwater lake, is the largest lake in the Marmara Region. It is also Turkey's fifth largest natural lake. In this study, it is aimed to determine the coastline change of Iznik Lake over time. Landsat satellite images of the years 1985, 2000, 2010, 2020 were used to determine the coastline change of Iznik Lake. Satellite images were analyzed using Geographic Information Systems and the coastline of Iznik Lake for the years 1986, 2000, 2010 and 2020 was determined. The lake area for the years 1986, 2000, 2010 and 2020 is 301.185 km^2, 300.082 km^2, 299.077 km^2 and 297.860 km^2, respectively. According to the results obtained, it was determined that there was decrease in the lake area.**

Keywords **- Iznik Lake, Remote Sensing, Geographic Information Systems, Coastline Change, Analysis**

I. INTRODUCTION

Today, the number of water resources and water bodies that are decreasing or disappearing due to climatic changes, increasing water demand and the impact of human activities is increasing [1]. Changes in these water bodies are effective on ecosystem and socioeconomic activities. Lakes and wetlands are bodies of water that are affected by climate change and human activities [2]. For this reason, it is necessary to act consciously for the protection of wetlands and the continuation of sustainability in these areas [3].

Remote Sensing (RS) and Geographic Information System (GIS) techniques are widely used to monitor changes in wetlands [4]. Wetlands that need to be protected and benefited can be examined by temporal variation analysis [5]. Because the images obtained on different dates reflect the changes that occur naturally or with human activities [6]. With the use of RS and GIS techniques, it is possible to protect and monitor water resources and to evaluate optimum usage conditions. The use of these techniques gives users and decision-makers quickness and flexibility in the decision-making process [7].

In this study, the temporal variation of the surface area of Iznik Lake was investigated using RS and GIS techniques. Landsat satellite images of 1986, 2000, 2010 and 2020 were used. Supervised classification was made on satellite images using ArcGIS software and the surface area of the lake was obtained. The results obtained were examined and the change in the coastline and surface area of the lake was determined.

II. MATERIAL AND METHOD

The study area is the Iznik Lake in the Marmara Region (Figure 1). Iznik Lake is the largest lake in the Marmara Region and the fifth largest lake in Turkey in terms of area. While Iznik Lake is located within the borders of Bursa province, some parts of the lake's basin are within the borders of Kocaeli and Yalova provinces. There are Samanlı Mountains and Karlık Mountains in the north, Avdan-Gürle Mountains in the south and Erikli Mountain and Gemlik Bay in the west of the Iznik Lake Basin [8].

Figure 1: Iznik Lake.

In this study, Landsat satellite images were used as remote sensing data. Landsat satellite images are free data sources used to analyze spatial and temporal changes in water bodies and land cover. Landsat satellite images were downloaded from the Earth Explorer portal of the United States Geological Survey (USGS). In 1986, 2000, 2010 and 2020, the coastline and areal changes of Iznik Lake were examined at four different times, representing the spring and summer months.

In this study, supervised classification method was applied

to satellite images. In this method, a sufficient number of sample regions describing the features of the earth are used. For each region to be classified, feature classes with defined spectral features are created. These classes are applied to satellite images. Each image element is assigned to the class it is most similar to according to the calculated probability values. ArcGIS software was used in this study. Two different classes, land and water, have been defined and supervised classification method has been applied to satellite images. Thus, the surface area of Iznik Lake was obtained and the changes in the coastline were determined.

III. RESULTS

The surface area of Iznik Lake, obtained using the satellite image of 1986, is 301.185 km^2 (Figure 2).

Figure 2: Iznik Lake area in 1986.

The surface area of Iznik Lake, obtained using the satellite image of 2000, is 300.082 km^2 (Figure 3).

Figure 3: Iznik Lake area in 2000.

The surface area of Iznik Lake, obtained using the satellite image of 2010, is 299.077 km^2 (Figure 4).

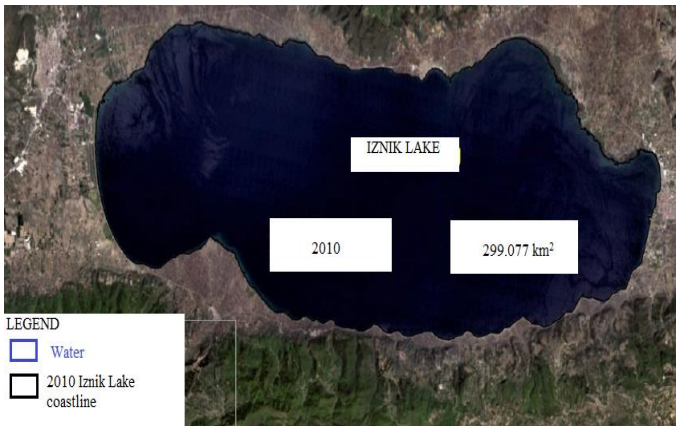

Figure 4: Iznik Lake area in 2010.

The surface area of Iznik Lake, obtained using the satellite image of 2020, is 297.860 km^2 (Figure 5).

Figure 5: Iznik Lake area in 2020.

When the surface areas obtained by the supervised classification of Landsat satellite images of 1986, 2000, 2010 and 2020 are examined, it has been determined that there are decreases.

There have been temporal changes in the use of the coastline of Iznik Lake. At the beginning of these changes is the filling works carried out to create usage areas such as transportation and recreation areas. Other causes of change are climate change, agricultural irrigation and human activities.

The temporal changes of coastline and surface area in Iznik Lake were determined using RS and GIS techniques. According to the data obtained, reductions have occurred in the lake. Measures should be taken to protect the lake and ensure its sustainability.

The existence of water resources is necessary for life to continue. Water resources should be used efficiently and strategies should be developed for their management. The most effective method to follow the changes in wetlands is the use of RS and GIS technologies. With the use of RS and GIS techniques, changes in wetlands are quickly detected and plans

are made for these changes. RS and GIS are techniques that are used effectively in many fields and provide accurate and reliable information.

IV. CONCLUSION

Changes occur in wetlands as a result of climate change and human activities in recent years. In order to ensure sustainability in wetlands, these changes should be determined and necessary measures should be taken. For this purpose, temporal changes in Iznik Lake were evaluated using RS and GIS techniques. Free downloadable Landsat satellite images were used. Supervised classification was applied to satellite images for four different times, 1986, 2000, 2010 and 2020, using ArcGIS software. Obtained results are given in Figure 6.

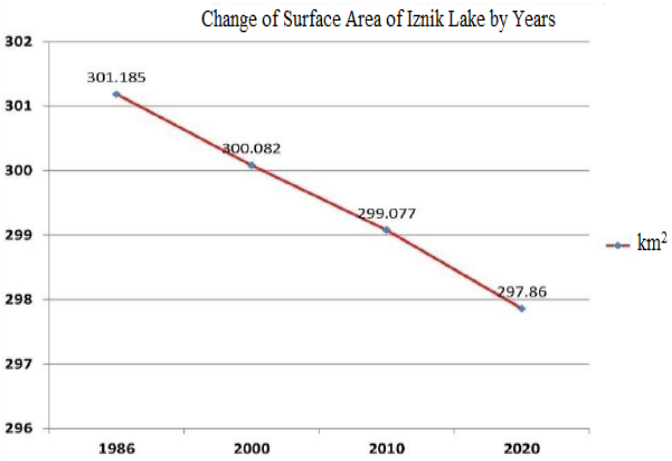

Figure 6: Change of surface area of Iznik Lake by years.

As given in Figure 6, the lake area has decreased over time. The lake area for the years 1986, 2000, 2010 and 2020 is 301.185 km^2, 300.082 km^2, 299.077 km^2 and 297.860 km^2, respectively. Human activities should be limited and strategies should be developed to protect the lake. As in this study, it is possible to monitor and manage wetlands by using RS and GIS technologies.

REFERENCES

[1] L. Kiage, and P. Douglas, "Linkages between land cover change, lake shrinkage, and sublacustrine influence determined from remote sensing of select Rift Valley Lakes in Kenya," *Science of the Total Environment*, vol. 709, 136022, 2020.

[2] B. Chang, K. He, R. Li, Z. Sheng, and H. Wang, " Linkage of climatic factors and human activities with water level fluctuations in Qinghai Lake in the northeastern Tibetan Plateau, China," *Water*, vol. 9, 552, 2017.

[3] M. Bayrak, "Analysis of Marmara Lake (Manisa) spatial change with RS and GIS," VII. Remote Sensing-GIS Symposium, 2018.

[4] C. Yurteri, and T. Kurttaş, "Analysis of temporal changes on the surface area of the Seyfe Lake (Kırşehir) using remote sensing and GIS techniques," *Gümüşhane University Journal of Science and Technology Institute*, vol. 11 (4), pp. 1115-1128, 2021.

[5] Ş. Bozduman, "Analysis of wetland exchange using classification methods: A case study of Dipsiz Lagoon example," *Turkish Journal of Remote Sensing*, vol. 1(1), pp. 16-20, 2019.

[6] Y. Güney, and S. Polat, "Coastline change detection using remote sensing data: the case of Aliağa and Çandarlı," *Journal of Aeronautics and Space Technologies*, vol. 8(1), pp. 11-17, 2015.

[7] N. Günal, and Y. Özdemir, "Determination of surface change of Neyriz Lake (Iran) by using multitemporal satellite imagery," *III. Remote Sensing - GIS Symposium*, 2010.

[8] N. Garipağaoğlu, and M. Uzun, "The effects of natural environment conditions, changes and possible risks on watershed management and planning in Basin of Iznik Lake," *Eastern Geographical Review*, vol. 24(42), pp. 1-24, 2019.

Coastline Change Analysis in Seyhan Dam Lake with Geographic Information Systems and Remote Sensing Methods

T. ALKAN[1] and S.S. DURDURAN[1]

[1] Necmettin Erbakan University, Konya/Turkey, tansualkan93@gmail.com
[1]Necmettin Erbakan University, Konya/Turkey, durduran2001@gmail.com

Abstract **- Seyhan Dam is an earth-fill type dam constructed 15 km above the old Adana to save 850,000 decares of land and Adana from flooding that may be caused by the Seyhan River. In this study, the coastline change of Seyhan Dam Lake was determined using Remote Sensing and Geographic Information Systems techniques. In this context, Landsat satellite images of 20 August 2010, 18 August 2015 and 15 August 2020 were used for the analysis of the coastline change of the Seyhan Dam Lake. These satellite images were evaluated with ArcGIS software and the changes in the coastline were examined using the controlled classification method. The lake area for the years 2010, 2015 and 2020 is 49.981 km^2, 49.340 km^2 and 44.626 km^2, respectively. According to the results obtained, it was determined that there was decrease in the lake area.**

Keywords **- Seyhan Dam Lake, Remote Sensing, Geographic Information Systems, Coastal Change, Analysis.**

I. INTRODUCTION

Wetlands are very important areas with their natural beauties, ecological importance and contribution to economic life [1, 2]. Due to global climate change and increasing world population, the need for water is increasing day by day. For this reason, limited water resources are constantly under pressure and risk in terms of both quantity and quality [3]. In addition, in parallel with the developing world conditions, the sectors that need water are diversifying and the competition between these sectors is increasing. In this case, the correct use and management of water resources is important for sustainability. In order to meet the developing water demands for purposes such as drinking, irrigation and industry, studies on the management of wetlands are required.

Wetlands are the richest and most productive ecosystems on earth [4]. These areas are natural systems that serve in a wide range from local people to the whole country and have a significant function and value compared to other ecosystems on earth [5-10]. Therefore, the management of sustainable water resources becomes even more important.

It is necessary to determine and monitor the past and current situation temporally, spatially, quantitatively and qualitatively in order to ensure the sustainability of the decreasing water resources due to the ongoing climate change effects both globally and in our country [11]. Depending on these, the determination of future scenarios will be the basis for the development of effective planning and policies in the management of water resources. In this context, Remote Sensing (RS) and Geographic Information Systems (GIS) technologies are used. Thanks to these technologies, it is possible to provide continuous and easy data, to analyze and evaluate data. In addition, more accurate and detailed information can be accessed much faster, more economically and more effectively.

The temporal and spatial analysis of changes occurring anywhere using RS and GIS techniques is quite common in national and international literature [2]. Satellite images with different temporal and spatial scales are selected in accordance with the purpose and contribute to the solutions of spatial problems with various image processing techniques [12]. RS and GIS are the most preferred methods in coastline change analysis.

In this study, the changes in the shoreline and surface area of the Seyhan Dam Lake were investigated using RS and GIS techniques. Landsat satellite images of 2010, 2015 and 2020 were used. Supervised classification was applied to Landsat satellite images in five-year periods using ArcGIS software. The results obtained were examined and the change in the coastline and surface area of the lake was determined.

II. MATERIAL AND METHOD

Seyhan Dam is an earth-fill type dam covering an area of 850,000 decares, 15 km above the old Adana. It was built with the aim of saving Adana from the flood that may be caused by the Seyhan River. This dam, which was put into service on April 8, 1956, was completed in 974 days. With the construction of the Seyhan Dam and the development of agricultural techniques, there have been great developments in agricultural productivity. Seyhan Dam Lake also hosts important sports organizations.

Figure 1: Seyhan Dam Lake.

In this study, Landsat satellite images were used. Landsat satellite images are free download data that are used effectively to determine the temporal changes in the coastline and surface areas of lakes. These data were downloaded from the Earth Explorer portal of the United States Geological Survey (USGS). In this study, Landsat 4-5 TM and Landsat-8 OLI/TIRS images of Adana Seyhan Dam Lake representing the dates of 20 August 2010, 18 August 2015 and 15 August 2020 were used.

The bands and characteristics of Landsat 4-5 TM and Landsat-8 OLI/TIRS satellite images are given in Tables 1 and 2.

Table 1: Landsat 4-5 TM satellite characteristics

Landsat 4-5 TM		
Bands	Wavelength (μm)	Resolution (m)
Band 1-Blue	0.45 - 0.52	30
Band2-Green	0.52 - 0.60	30
Band 3-Red	0.63 - 0.69	30
Band 4-Near Infrared	0.76 - 0.90	30
Band 5-Mid Infrared	1.55 - 1.75	30
Band 6-Thermal Infrared	10.40 - 12.50	120 * (30)
Band 7-Shortwave Infrared	2.08 - 2.35	30

Table 2: Landsat 8 OLI/TIRS satellite characteristics

Landsat 8 OLI/TIRS		
Bands	Wavelength (μm)	Resolution (m)
Band 1-Coastal Aerosol	0.43 - 0.45	30
Band 2-Blue	0.45 - 0.51	30
Band 3-Green	0.53 - 0.59	30
Band 4-Red	0.64 - 0.67	30
Band 5-Near Infrared	0.85 - 0.88	30
Band 6-SWIR-1	1.57 - 1.65	30
Band 7-SWIR-2	2.11 - 2.29	30
Band 8- Panchromatic	0.50 - 0.68	15
Band 9- Cirrus	1.36 - 1.38	30
Band 10- TIRS-1	10.6 - 11.19	100 * (30)
Band 11- TIRS-2	11.50 - 12.51	100 * (30)

In this study, supervised classification method was applied to satellite images. Supervised classification is a method applied under the control of the user. In this classification, the user specifies the sample classes that are already known on the image. Specified sample classes are called training sets. Then, the spectral distinguishability of these classes is examined. The classification algorithm examines all cells in the image by way of comparison, depending on the spectral characteristics of the cells in the training set. Thus, with this method, all of the images are classified according to the specified classes. In this study, supervised classification method was applied to Landsat satellite images using ArcGIS software. The temporal change was analyzed by determining the coastline and surface area of the Seyhan Dam Lake.

III. RESULTS

The surface area of Seyhan Dam Lake, obtained using the satellite image of 2010, is 49.981 km^2 (Figure 2).

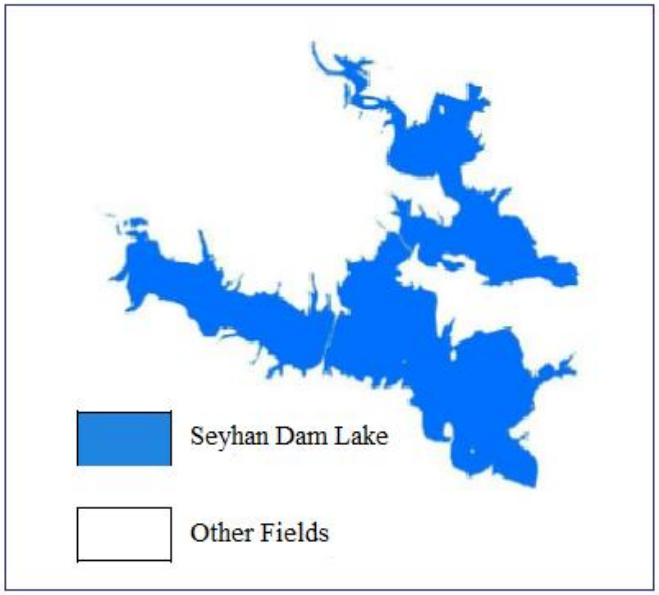

Figure 2: Seyhan Dam Lake area in 2010.

The surface area of Seyhan Dam Lake, obtained using the satellite image of 2015, is 49.340 km^2 (Figure 3).

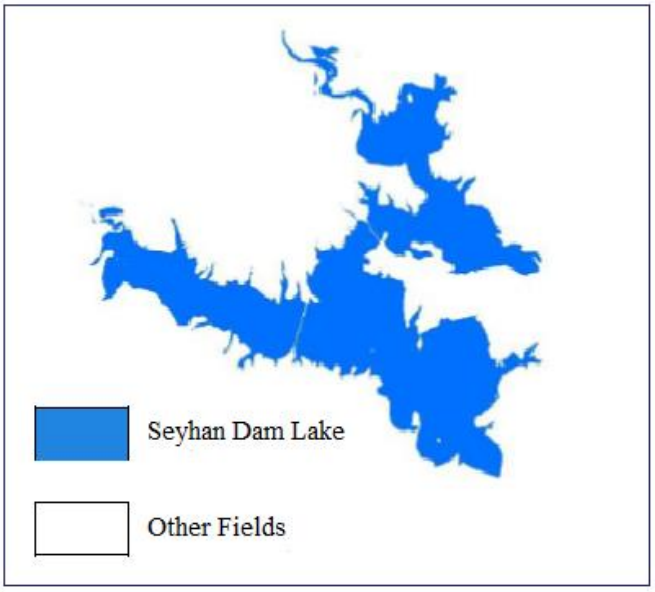

Figure 3: Seyhan Dam Lake area in 2015.

The surface area of Seyhan Dam Lake, obtained using the satellite image of 2020, is 44.626 km^2 (Figure 4).

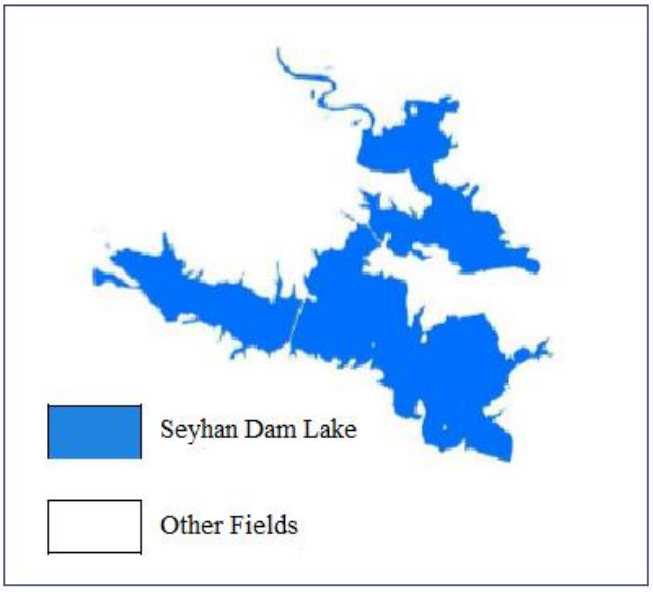

Figure 4: Seyhan Dam Lake area in 2020.

IV. CONCLUSION

It is necessary to follow the changes in water resources due to increasing population and climate change. The efficient and correct use and management of water resources is important for sustainability. In this study, the temporal change in the Seyhan Dam Lake was investigated by using Landsat satellite images that can be downloaded for free. Supervised classification method was applied to Landsat satellite images. The change in the Seyhan Dam Lake over time was analyzed using GIS technologies. Obtained results are given in Figure 5.

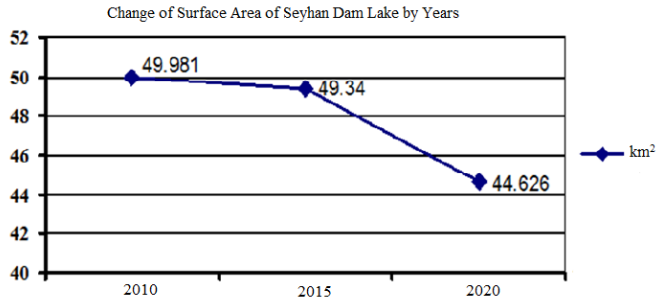

Figure 5: Change of surface area of Seyhan Dam Lake by years.

The lake area for the years 2010, 2015 and 2020 is 49.981 km^2, 49.340 km^2 and 44.626 km^2, respectively. According to the results obtained, it was determined that there was decrease in the lake area.

REFERENCES

[1] M. Karabulut, M. Gürbüz, Y. Kızılelma, E. Ceylan, M. Topuz, " Determination of misuse of land in Göksu Delta using GIS and Remote Sensing techniques," *III. National Geomorphology Symposium*, 2012.

[2] M. Topuz, and M. Karabulut, "Investigation of the temporal changes and their ecological effects in the Sarikum lake (Sinop)," *The Journal of International Social Research*, vol. 11(60), 2018.

[3] M.A. Akgül, and M. Çetin, "Estimation of reservoir water elevation in man-made lake by using Landsat 8 image data," *Dicle University Engineering Faculty Journal of Engineering*, vol. 9(1), pp. 493-502, 2018.

[4] Ö. A. Kaya, and G. Kaplan, "Determination of Burdur Lake`s area changes using Remote Sensing techniques," *Journal of Natural Hazards and Environment*, vol. 7(1), pp. 1-12, 2021.

[5] T.D. Acharya, A. Subedi, D.H. Lee, "Evaluation of machine learning algorithms for surface water extraction in a Landsat 8 scene of Nepal," *Sensors*, vol. 19(12), 2019.

[6] T. Aksoy, S. Sarı, A. Çabuk, "Determination of water index by Remote Sensing within the scope of wetlands management, Lakes Region," *GSI Journals Serie B: Advancements in Business and Economics*, vol. 2(1), pp. 35-48, 2019.

[7] M. Anderson, F. Gao, K. Knipper, C. Hain, W. Dulaney, D. Baldocchi, E. Eichelmann, K. Hemes, Y. Yang, J. Medellin-Azuara, "Field-scale assessment of land and water use change over the California Delta using Remote Sensing", *Remote Sensing*, vol. 10(6), 2018.

[8] R.E. Emanuel, "Climate change in the Lumbee River watershed and potential impacts on the Lumbee tribe of North Carolina," *Journal of Contemporary Water Research & Education*, vol. 163(1), pp. 79-93, 2018.

[9] C. Giardino, M. Bresciani, P. Villa, A. Martinelli, "Application of Remote Sensing in water resource management: the case study of Lake Trasimeno, Italy," *Water Resources Management*, vol. 24(14), pp. 3885-3899, 2010.

[10] G. Kaplan, Z.Y. Avdan, U. Avdan, T. Jovanovska, "Remote Sensing techniques for monitoring shared international waters; study case - Dojran Lake," *International Disaster and Resilience Congress*, pp. 413-418, 2019.

[11] M.A. Erdoğan, F. Sönmez, S. Berberoğlu, "The estimation and monitoring of dam lake water level with the support of Remote Sensing and GIS: In the case of Adana Seyhan Dam Lake," *V. Remote Sensing-GIS Symposium*, 2014.

[12] Y. Kızılelma, M. Karabulut, M. Gürbüz, M. Topuz, E. Ceylan, "An analysis of temporal changes of Nigde city and surrounding areas using Remote Sensing and GIS," *I. International Niğde Language, Culture and History Symposium*, 2012.

A Brief Study on the Compressive Strength and Flexural Strength of Fly Ash and Ground Granulated Blast Furnace Slag Geopolymer Mortar

H. ALTAWIL[1] and M. OLGUN[2]

[1] Konya Technical University, Konya/Turkey, dr.htawil@gmail.com
[2] Konya Technical University, Konya/Turkey, molgun@ktun.edu.tr

Abstract **- The effect of sodium concentration ratio (Na) on the compressive and flexural strength of fly ash mortars activated with sodium hydroxide (NaOH) was studied. Compressive strengths and flexural strengths of geopolymer mortars obtained by using F class fly ash and Ground-granulated blast furnace slag (GGBFS) mixtures at different rates of NaOH were determined at constant water content. 40 40 160 mm prismatic samples prepared from alkali-activated fly ash to obtain geopolymer mortar samples for the study. At the end of the 28-day curing period, the C3 mixture at molarity= 12 (12M) reached a compressive strength of 28.22 MPa, while the C1 (10M) mixture reached a compressive strength of 23.8 MPa. Concrete samples with a concentration of 12 M NaOH produced the highest compressive strength.**

Keywords **–Class F fly ash, Ground-granulated blast furnace slag GGBFS, Geopolymer, compressive strength, flexural strength.**

I. INTRODUCTION

In 1978, Davidovits proposed that an alkaline solution could be used to react with the aluminium (Al) and the silicon (Si) in an origin material of geological source or in by-product materials such as fly ash to produce binders. Fly ash is classified as class F and class C according to the percentage of chemical component (ASTM C618, 1998) [1].

Class F fly ash is generally preferred for geopolymer production. Geopolymer resources usually include silicon and aluminum, which are natural materials that are heat activated and formed.

Since the chemical reaction, which occurs in this case, is a polymerization process, it is invented the term 'Geopolymer' to represent these binders [2].

Geopolymer concrete is a material that may be used as an alternative to cement-based binders in the production of high-performance composite materials in recent years and is classified as synthetic aluminosilicate. Geopolymers belong to an inorganic polymer family.

The most commonly used aluminosilicate materials in the production of geopolymer concrete are fly ash and ground-granulated blast furnace slag [3].

Aluminosilicates are materials whose principal oxides are aluminum oxide (Al_2O_3) and silicon oxide (SiO_2), which have amorphous structure as a result of natural or post-thermal treatment.

It may be said that the Geopolymer materials have several advantages in concrete building technology, environmental friendliness, and resistance to environmental effects, fire resistance, mechanical properties and high durability. Geopolymers could be seen as potential materials for applications in many areas such as thermal insulation, fire resistance and other high-temperature applications [4].

Palomo et al. (2004) reported the manufacture of concrete rail sleepers based on fly ash. They found that the concrete structural elements of the geopolymer could be readily produced using today's concrete technology without any significant change. The performance of the products were excellent, and the drying shrinkage was very low [4,5].

Previously, [4,6] reported on the use of geopolymer composites to reinforce concrete structures as well as the coating of geopolymers to protect transport infrastructure. They stated that the geopolymer composites were successfully applied to reinforce the reinforced concrete beams. Geopolymers had better performance than organic polymers in terms of fire resistance, ultraviolet light durability and no toxic substances.

Concrete's durability depends mainly upon its permeability properties. Lower permeability results in greater resistance to aggressive ions entering the concrete and thus reduces the extent of deterioration of the concrete. Heat-hardened fly ash geopolymer concrete is highly compressive and tensile strength with low effective porosity, all of which good for concrete in an aggressive environment [7].

Most previous studies have been carried out on thermosetting geopolymer concrete, which is considered ideal for prefabricated concrete elements. However, geopolymer concrete produced without utilizing high thermal for curing will expand its application to zones beyond prefabricated elements [7].

Hence, the aim and objectives of this study are to produce geopolymer concrete suitable for ambient curing condition and to determine the change in compressive strength of geopolymer-based samples prepared by using different ratios of fly ash and chemical solutions.

II. MATERIAL

- **Fly Ash:**

Class F fly ash used in the study was brought from Seyitömer Thermal Power Plant and its general properties are given in Table 1.

Table 1. Chemical properties of Seyitömer fly ash used in experiments.

Oxides	Weight percent (%)
SiO_2	54.5
Al_2O_3	20.6
Fe_2O_3	9.27
S+A+F	84.34
CaO	4.3
MgO	4.48
K_2O	2.0
KK	3.0

- **Chemicals (NaOH, Na2Sio3):**

Sodium Silicate and Sodium Hydroxide liquid were obtained from local suppliers. NaOH solution is prepared by dissolving it in water.

- **Sand:**

Sand with a maximum grain diameter of 2 mm was used to obtain the geopolymer concrete mortar.

- **Slag (GGBFS):**

Slag (GGBFS) was used as mixing material with alumina silicate in the production of geopolymers in order to improve the properties of the fresh binder and the geopolymer binder. The major chemical component of slag GGBFS is CaO-SiO2-MgO-Al2O3 and GGBS is a coarse glass material with untreated particles larger than 4.5 mm as shown in Table 2 [8].

Table 2: Chemical composition of slag GGBFS

Oxides	Weight percent (%)
SiO_2	29.96
Al_2O_3	12.25
Fe_2O_3	0.52
CaO	40.45
MgO	7.50
SO_3	4.48
LOI	2.39
TiO_2	0.46

III. EXPERIMENTAL

For mortar mixes, sand/binder ratio was determined, as 2.67, water/binder ratio was determined as 0.39 and 0.56.

In the experiments, sand with a maximum grain diameter of 2 mm was used as fine aggregate. The rate of fly ash used in mortar production was 75% and the rate of GGBFS was selected as 25%. The produced mortar samples were cured at room temperature 25 C^o for 24 hours (Table 3).

Table 3. Basic Mixing Ratios (F class fly ash –Slag GGBFS)

Trial Mix	Contents	
	Molarity M	Water / Binder W/C
C1	10	0.39
C2	10	0.56
C3	12	0.39
C4	14	0.39
C5	16	0.39

In the study, Six prismatic specimens of 40×40×160 mm was prepared with alkali-activated F fly ash and slag GGBFS to produce geopolymer mortar.

First, a single point bending test (for flexural strength) and then compressive strength tests were carried out on the split parts (Figure 2&3).

A hydraulic pressure/bending press was used to determine the compressive strength and flexural strength of the samples prepared in 40x40x160mm dimensions (Figure 1).

Figure 1. Compressive strength test of geopolymer mortar

Test sand (fine aggregate) was placed in the concrete mixing machine and mixed with fly ash for about 90 seconds. Then, slag GGBFS was added to the mixer and mixing was continued for 90 seconds.

Finally, the prepared alkaline activator solution was added to the mixture and mixed again for approximately 180 seconds until the mixture became homogeneous and poured into molds with internal dimensions of 40x40x160mm (Figures 2).

Figure 2. Concrete mixer machine

IV. Results and Discussion

1. Compressive Strength

Table 4: Results of comresssive strength (Fly ash = %75 and (Slag) GGBFS =%25)

	Curing Time (day)	Compressive Strength (MPa)
C1	7	16.15
	14	16.76
	28	23.80
C2	7	18.59
	14	20.46
	28	27.88
C3	7	24.41
	14	23.96
	28	28.22
C4	7	19.55
	14	22.22
	28	27.13
C5	7	24.81
	14	25.11
	28	26.90
Max. Compressive Strength (28 days)		28.22

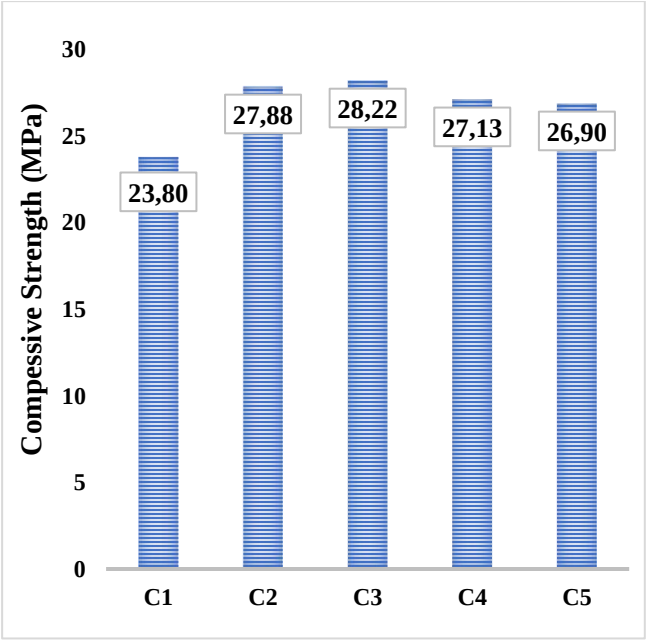

Figure 3. Fly ash – (Slag) GGBFS mixture Compressive strength values.

At the end of the 28-day curing period, the mixture C1 (10M) reached a compressive strength of 23.8 MPa, while the C2 (10M) mixture at the same molarity was 27.88 MPa. Higher water content resulted in a significant decrease in compressive strength (Table 4 and Figure 3).

The water in the mixture seems to be able to hydrate the silicates, which leads to an improvement in the compression force of the geopolymer.

A significant increase in the compressive strength was observed when the material in the geopolymer concrete, formed by reacting with 12M and cured at 25°C (Table 4 and Figure 3).

As shown in (Table 4 and Figure 3), It is clear from the study that higher molarity of NaOH does not improve the compressive strength properties. This is because more alkaline solution can interfere with the polymerization process as they form a thin layer on the binder particles that delay the polymerization process and leave few non-reactive particles.

NaOH 10M is not enough to complete the fly ash reaction; 12M NaOH is needed to ensure reaction with fly ash and slag GGBFS.

The improvement of strength of fly ash and slag-blended geopolymer concrete is due to the increase of calcium bearing compound in the dissoluted binder, which produced reaction product from both slag and fly ash.

2. Flexural Strength

The flexural strength of the fly ash-based geopolymer increased from 3.3MPa to 4.3MPa when the NaOH content was increased from 10 to 16M (Table 5 and Figure 4).

The results indicate that the bending strength of geopolymer concrete is greater than expected using current design equations for Portland cemented concrete of similar compression forces

(Table 4 and Figure 3).

Table 5. Flexural strength results (F class fly ash – Slag GGBFS)

	Curing Time (day)	Flexural Strength (MPa)
C1	7	3.4
	14	3.4
	28	3.3
C2	7	3.5
	14	3.6
	28	3.6
C3	7	3.2
	14	3.5
	28	3.7
C4	7	3.4
	14	3.5
	28	3.7
C5	7	4.0
	14	4.0
	28	4.3
Max. Flexural Strength (28 days)		4.3

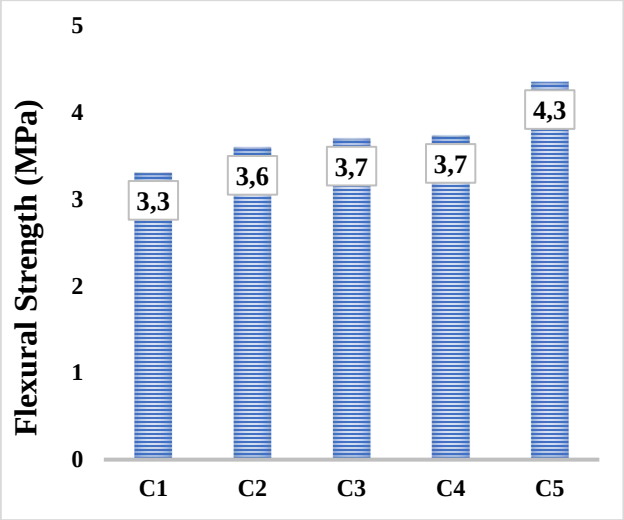

Figure 4. Flexural strength values for Fly ash – Slag GGBFS mixtures

According to the test results, the highest flexural strength value (4.3MPa) was obtained at M=16. The flexural strength of the specimens ranged from 13 to 15% of the compressive strength (Table 5 and Figure 4).

[10] Stated a similar trend, but on a larger scale, with the flexural strength varying between 9 and 26% of the compressive strength.

V. Conclusion

Based on the experimental results reported in the paper, the following conclusions are drawn:

a. The observed compressive and flexural strengths ranged from 23.8 to 28.22 MPa and 3.3 to 4.3 MPa, respectively.
b. The compressive strength of geopolymer concrete varies with the age of concrete.
c. Longer curing time improves the compressive strength.
d. There is very little difference in compressive strengths of specimens cured at 14 days and specimens cured at 28 days.
e. Water content plays an important role in determining the compressive strength of the fresh geopolymer concrete as well as of Ordinary Portland Cement (OPC) concrete.
f. It has been shown that it is possible to produce hardened geopolymer mortar cured at room temperature with class F fly ash and Ground-granulated blast furnace slag (GGBFS) binder.
g. Based on the test results, the flexural strength of the samples was between 13 and 15% of the compressive strength.

Acknowledgment

This paper is in the scope of "Performance (Installation) and Experimental Investigation of Factors Affecting on the Performance of Geopolymer Piles" Doctoral Thesis Project and BAP Project (Project Number: 211104034). The authors are grateful to, Konya Technical University and BAP for their support.

References

[1] American Society for Testing and Materials. "ASTM C 618-Standard specification for coal fly ash and raw or calcined natural pozzolan for use in concrete." West Conshohocken: ASTM, 2012.
[2] Davidovits, Joseph. "Properties of geopolymer cements." First international conference on alkaline cements and concretes. Vol. 1. Kiev State Technical University, Ukraine: Scientific Research Institute on Binders and Materials, 1994.
[3] Tuyan, M., Çakır Ö., Boyacı O. C. and Ramyar, K. (2017), Uçucu Kül Esaslı Geopolimer Betonların Mekanik Özelik Ve Yüksek Sıcaklık Dirençlerinin Araştırılması, Conference: Beton 2017 Hazır Beton Kongresi ve Beton, Agrega, İnşaat Teknolojileri ve Ekipmanları Fuarı, (13-14) Nisan, At Istanbul. Alınan https://www.researchgate.net/publication/325218322.
[4] Hardjito, Djwantoro, and B. Vijaya Rangan. "Development and properties of low-calcium fly ash-based geopolymer concrete." (2005).
[5] Palomo, A., et al. "Precast elements made of alkali-activated fly ash concrete." International Conference on fly ash, silica fume, slag and natural pozzolans in concrete. USA. 2004.
[6] Balaguru, P., Stephen Kurtz, and Jon Rudolph. "Geopolymer for repair and rehabilitation of reinforced concrete beams." St Quentin, France, Geopolymer Institute 5 (1997).
[7] Barbosa, Valéria Figueiredo Felisbino, Kenneth JD Mackenzie, and Clelio Thaumaturgo. "Synthesis and characterisation of sodium polysialate inorganic polymer based on alumina and silica." Geopolymer'99 International Conference, France. 1999.
[8] Olivia, Monita and Nikraz, H.R. "Corrosion performance of embedded steel in fly ash geopolymer concrete by impressed voltage method." (2011).
[9] McCabe, S., et al. "Innovative developments in the light of bond philosophy." Bulletin-Fédération internationale du béton (2000): 396-422.
[10] Diaz-Loya, E. Ivan, Erez N. Allouche, and Saiprasad Vaidya. "Mechanical properties of fly-ash-based geopolymer concrete." ACI materials journal 108.3 (2011): 300.

Moving People Effect On Indoor Mobile Node Location Estimation Based On Wi-Fi Signals

N. BANDIRMALI ERTURK

Department of Computer Engineering, Bandirma Onyedi Eylul University, Balikesir, Turkey
nerturk@bandirma.edu.tr

***Abstract* – The presented work focuses on an approach related to minimization of moving people effects for indoor mobile node location estimation (MNLE) methods and navigation solutions. It is of high importance considering the widespread deployment of localization techniques utilizing received signal strength indicator (RSSI) values especially in mobile application integrated web systems. Based on a proposed model for accurate RSSI reading and its simulation study explored in this paper, the preliminary results show that it is possible to reduce the negative impacts of moving people with mobile devices and to improve location estimation performance, especially with the effective utilization of available mobile device built-in hardware features such as gyroscope for specifying a user's heading direction.**

***Keywords* - Indoor Mobile Nodes, Location Estimation, Moving People, Mobile Device Features.**

I. INTRODUCTION

MOVING people effects (MPEs) are nowadays crucial issues within the scope of indoor mobile node location estimation (MNLE) methods, which have an ever-increasing importance in recent years with regard to customized services offered and managed in real-time web or mobile applications. This presented work focuses on fining MNLE performance based on mobile device built-in sensor features, modelled in a simulation environment that indeed aims to assure validation process accuracy and efficiency as well as to eliminate time-consuming expensive experimental setups.

In recent years, there have been sustainable changes and significant new developments in the field of mobile indoor positioning and navigation, which include technologies based on Wi-Fi, Bluetooth Low Energy (BLE), Ultra Wideband (UWB) and RFID. Hybrid approaches are also at the center of research and development efforts targeting at more accurate, precise and efficient methods in order to find the real-time position of the mobile nodes inside a kind of people-crowded environments like hospital, factory, plant, mall, shop, school etc. [1]. MNLE can be one of the most important components of diverse mobile applications for serving, monitoring, tracking or navigating [2]. Considering the complexity of indoor environments, signal interference & reflection, behavior & position of moving people or stationary objects and unreliable communication links, most of the classical localization approaches fail to meet contemporary needs of on-demand services provided through mobile or web applications with a current market value over US$ 10 billion globally. As a challenging point in this paper, modelling & decreasing the effects of moving people in MNLE methods is focused for improving poor localization results.

Developments in the MNLE accuracy are mostly related to obstacles resulting in fluctuations in the received signal strength indicator (RSSI) values obtained at the end point nodes [3]. Although several research studies have rather revolved around static indoor obstacles so far, human body presence and especially moving people with mobile devices are hot topics with this regard and yet to be challenging research issues in order to achieve a highly accurate mobile indoor localization.

In the following sections, first of all, MNLE, moving people effect on MNLE and employing mobile device built-in sensors in MNLE approaches are explained with respect to indoor applications. After that the proposed indoor MNLE simulation model utilizing a common hardware feature available with most of the smartphones in order to refine the critical moving people effects on the localization accuracy is presented together with the obtained results, followed by final remarks.

II. INDOOR MOBILE NODE LOCATION ESTIMATION (MNLE)

With the rapidly increasing number of smartphones in daily & business life, astonishingly widespread mobile applications and developments in built-in sensor technologies, mobile indoor positioning methods keep attracting the attention of researchers. This is nowadays an actual user & service provider-driven issue with regard to the increase in times that people spend indoors [4]. Traditional Wi-Fi mobile indoor localization methods utilizing signal propagation models have been replaced by the Wi-Fi-based fingerprinting technique, which stands out among the most common and accurate mobile indoor positioning technologies, is fundamentally based on a two-step approach; namely, offline training followed by real-time estimation. A virtual fingerprinting map is first created by using the obtained RSSI values of the Wi-Fi signals for the indoor area divided into the cells. It fundamentally relies on the respective signals from multiple (at least 3) reference access points. Based on it, the mobile users then can estimate their real-time location [3, 4]. It is clear that any physical change in the indoor environment, including people moving around, distorts the fingerprinting map; therefore, makes the consequent location estimation results inaccurate and sometimes useless for the specific application or service provided to the mobile users.

There are many well-known and researched sources of RSSI variations including the one about human presence. As the main focus of this presented work, it is certain that the presence of moving people significantly affects the RSSI values obtained at the receiver point, and the attenuation directly varies depending on both the number of people and the speed of movement of the people (Figure 1).

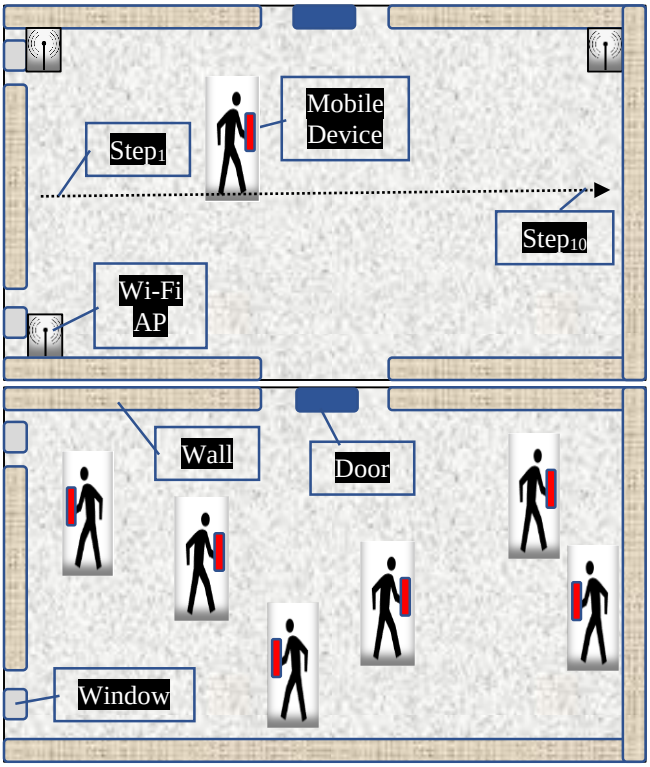

Figure 1: Indoor wireless networking environment including moving people.

A. *Indoor MNLE Based on Wi-Fi Signals*

There are many good reasons for the universal use of indoor MNLE systems based on Wi-Fi signals. Considering the facts that all most all of the smartphones have Wi-Fi modules and access points are now present everywhere, localization is easily achievable and a computational & cheap matter of making use of measured RSSI values from the access points, incorporating an indoor propagation model in addition to well-known trilateration or triangulation algorithms [1].

The International Telecommunication Union (ITU) indoor propagation model has been globally preferred as the fundamental radio propagation model for estimating indoor path loss (inside a room or a closed area inside a building). It is utilized in this presented work and simulation model. The ITU site-general model for path loss prediction in an indoor propagation environment is given by [5] as follows:

$$L_{Total} = 20\log_{10}(f) + N\log_{10}(d) + Lf(n) - 28 \text{ dB},$$

where f is the frequency (MHz), N is the distance power decay index, d is the distance ($d > 1$ meter), Lf(n) is the floor penetration loss factor and n is the number of floors between the receiver and the transmitter.

Triangulation method, utilized also in this presented work and simulation model, uses the fundamental properties of geometry and trigonometry, in which a position is determined by forming triangles to the point from known or reference points. It has two parts named lateration and angulation. The former refers to calculating the distance from reference points while the latter refers to calculating the angle to a certain position from reference points.

Assuming a mobile device (MD) location to be estimated and the RSSI values (P_{Ri}) are obtained at N different positions with respect to different access points (x_r, y_r , z_r), the distance is given by:

$$d_i = [(x_r - x_i)^2 + (y_r - y_i)^2 + (z_r - z_i)^2]^{1/2}$$

where $1 \geq i \leq N$. Following equation can be used for modeling the RSSI values (dBm):

$$P_{Ri} = K - 10n \log_{10}(d_i/d_0) + X_\sigma$$

where K is a constant term depending on antenna characteristics and average channel attenuation, d_0 is the reference distance, X is a Gaussian random variable with zero mean, σ is standard deviation by shadowing and n is the path-loss exponent [1, 4, 5].

B. *Moving People Effects on Indoor MNLE*

In literature, there are a few classical device-free indoor localization methods proposed to monitor and analyze any change in RSSI levels caused by human movement to finely locate the mobile nodes or people in a wireless networking environment. They do not conceptually make use of any hardware-based features of the mobile devices or built-in sensors of the smart-phones, assuming that their computational localization algorithms can overcome the unwanted side-effects up to a certain acceptable level or else could indeed ignore them, resulted from the presence of moving people or any other physical object around. However, many emerging applications require to precisely obtain especially the location of mobile devices or people so that the on-demand or limited services can be offered efficiently.

A device-free indoor MNLE method is given in [6] for better understanding of the human movement effects on RSSI levels. The work presented is based on an experimental study. It focuses on human presence effect with regard to the RSSI level while changing the distance within the wireless link. The results show that the RSSI values with different patterns are characteristically affected by the human presence and movement. The proposed model in this paper is different and produce much more accurate results as it makes use of gyroscope data in line with the MNLE deployed.

C. Indoor MNLE Using Mobile Device Built-in Sensors

Gyroscope is one of the common built-in sensors deployed in mobile devices and smartphones. It is originally designed to determine movement in a three-dimensional space. It is utilized in the proposed model in conjunction with the indoor MLNE method in order to obtain highly accurate localization results. The data obtained from mobile device built-in gyroscope is primarily used to decide direction changes.

A research work presented in [7] proposes a smartphone indoor positioning method together with its mobile application based on both built-in gyroscope and accelerometer usage. However, it assumes that a map and calibration marks are already available built-in. Similar to the one presented, the work also relies on gyroscope usage in the core method but differs mainly from the model proposed in this paper in that it disregards human presence and movement indeed.

In another effort for a mobile cleaning robot localization application based on a low-cost MEMS gyroscope states that an angular error compensation is well achieved by utilizing a constrained Kalman filtering approach [8].

III. The Proposed Indoor MNLE Model Incorporating With Mobile Device Gyroscope For Eliminating Moving People Effect

This section first describes the components of the proposed approach, especially the use of the gyroscope direction detection function with regard to human movement effect in the chosen MNLE as well as its simulation model by using MATLAB. The ITU indoor propagation model and the ERLAK method [9] have been utilized as the core structure for the indoor MNLE in the simulation study. The results for localization of mobile nodes are presented and evaluated with respect to the proposed approach based on utilizing real-time direction change information obtained from the mobile device gyroscope.

As the basis of the proposed approach in this paper, an experimental pre-study in the laboratory environment (Figure 1) has proclaimed that a moving human passing through a room (7m x 5m) in the indoor wireless link causes a varying non-linear deviation of ±4.5 dBm on the RSSI values, merely relying on the human's movement and heading direction parameter. A basic algorithm based on this empirical outcome is utilized in the indoor MNLE in line with the proposed direction-centered approach (Figure 2) in order to model the human movement effect on real-time RSSI readings and then to achieve a precise mobile node location estimation.

This presented work, about the validation and evaluation of the proposed approach with initial experimental and subsequent conceptual simulation model studies, will be also analytically studied in detail and presented in the literature, with its finest state of the art design as well as artificial intelligence and machine learning algorithms at its ultimate phase, which afterwards can be fully ready for common use in real-time mobile and/or web applications.

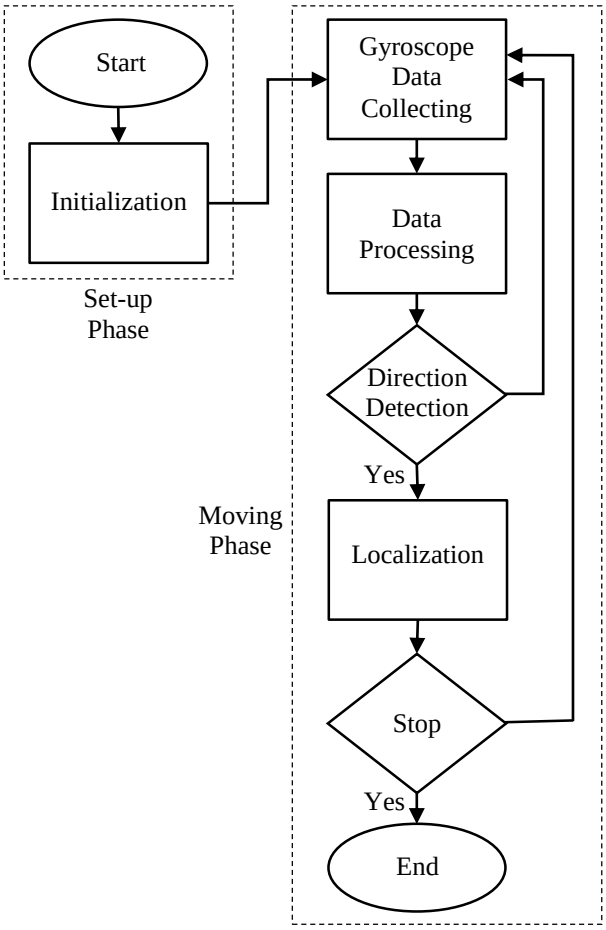

Figure 2: Proposed MNLE system flow-chart based on human moving direction.

A. Model and Simulation

The simulation model is based on a wireless network with 2.4 GHz, IEEE 802.15.4 technology. It includes a mobile node with a built-in gyroscope sensor, carried by the moving people in an indoor networking environment without any other physical obstacle or signal interference in the room. The person with mobile device walks at a constant speed of about 1 m/s (Figure 1). The distance error is computed as the distance between the estimated position and the real target position, and ten specific points (steps) on almost all a straight line through which the person walks by are considered for the testing.

B. Results

In this section, preliminary results of the proposed model taking into account the moving people effect for improving the location estimation performance are compared to those of the classical MNLE method with regard to the real mobile node locations.

Figure 3 shows the mean distance error ratios with respect to the real mobile node location both for the classical MNLE and the proposed MNLE with gyroscope reading-based human direction information.

Considering the simulation environment and the person's

movement in the specified trajectory, the former has produced location estimation results worse than those of the real ones, varying between 9.1% and 23.3%. On the other hand, the latter has location estimation results also worse than those of the real ones, varying between 3.9% and 10.7%. It is clear that both methods do not give the real node location exactly; however, the proposed approach improved the location estimation accuracy up to 2.3 times compared to its rival. It can be concluded from these results that the use of mobile device gyroscope for direction cooperative location estimation decreases the negative aspects of the human movement on RSSI readings for a certain level.

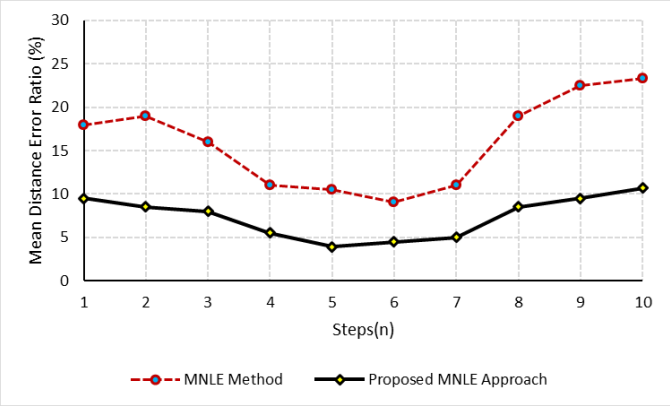

Figure 3: Localization performance comparison.

IV. Conclusion

A new approach, based on direction information, for reducing the moving people effect on indoor localization is proposed in this paper. It well achieves estimating position of mobile devices with less error compared to the traditional method based on using trilateration and ITU indoor path loss model.

The simulation study shows that it is possible to reduce the negative impacts of moving people with mobile devices and to improve indoor MNLE performance, especially with the effective use of mobile device built-in sensors such as gyroscope for specifying a person's heading direction. One of the concluding results is that decreasing the mean distance error ratio to 3.9% is well achievable.

There are still intensive worldwide researches being carried out on exact indoor localization techniques although the some new challenging issues, as the one focused in this paper, are also emerging for both fine results and diverse practical difficulties. Further work on analytical modeling of the proposed approach as well as its common use in commercial applications will be next considered.

References

[1] S. S. Sana "A survey of indoor localization techniques," *IOSR Journal of Electrical and Electronics Engineering*, vol. 6, no. 3, pp. 69-76, 2013.

[2] G. Gartner, F. Ortag and H. Huang, "A survey of mobile indoor navigation systems," *Cartography in Central and Eastern Europe*. Springer Berlin Heidelberg, pp. 305-319, 2010.

[3] F. Firdaus, N. A. Ahmad and S. Sahibuddin, "Accurate indoor-positioning model based on people effect and ray-tracing propagation," *Sensors*, doi:10.3390/s19245546, vol. 19, no. 5546, pp. 1-27, 2019.

[4] A. I. P. Sari and A. Z. Rakhman, "Indoor localization using accelerometer and gyroscope smartphone based," *Jurnal Teknik Informatika (JUTIF)*, vol. 2, no. 2, pp. 119-126, 2021.

[5] T. Chrysikos, G. Georgopoulos and S. Kotsopoulos, "Site-specific validation of ITU indoor path loss model at 2.4 GHz," IEEE International Symposium World Wireless Mobile Multimedia Network Workshops, pp. 1-6, June 15-19, 2009.

[6] Y. Sasiwat, N. Jindapetch, D. Buranapanichkit and A. Booranawong, "An experimental study of human movement effects on RSSI levels in an indoor wireless network," Biomedical Engineering International Conference, pp. 1-5, Thailand, November 19–22, 2019.

[7] H. H. Hsu, W. J. Peng, T. K. Shih, T. W. Pai and K. L. Man, "Smartphone indoor localization with accelerometer and gyroscope," *International Conference on Network-Based Information Systems*, pp. 465-469, Italy, September 10-12, 2014.

[8] H. Myung, H. K. Lee, K. Choi, S. Bang, Y. B. Kim and S. Kim, "Mobile robot localization using a gyroscope and constrained Kalman filter," *SICE-ICASE International Joint Conference*, pp. 2098-2103, Korea, October 18-21, 2006.

[9] N. Bandirmali and M. Torlak, "ERLAK: On the cooperative estimation of the real-time RSSI based location and K constant term," *Wireless Personal Communications*, vol. 95, no: 4, pp. 3923-3932, 2017.

Propagation of Gaussian Beam in Atmospheric Turbulence

Gamze Nur Secilmis[1] and Kholoud Elmabruk[2]

[1] Defense Technologies Program, Institute of Graduate Studies, Sivas University of Science and Technology, Sivas, TURKEY, 190102022@sivas.edu.tr

[2]Electric and Electronic Engineering Department, Sivas University of Science and Technology, Sivas, TURKEY, elmabruk@sivas.edu.tr

Abstract

The effect of system parameters on the intensity profile of Gaussian beams propagating in atmospheric turbulence is analyzed utilizing a random phase screen model. The intensity profile properties are assessed against the changes of operating wavelength, receiver aperture side length, and source size parameters. The results show that Gaussian beams with a bigger source size are able to keep their original profile and spreading less while propagating in a turbulent atmosphere. Increasing the receiver aperture side length does not have a noticeable effect on Gaussian beams. The beams operating at higher wavelengths suffer from more beam spreading.

Keywords **- Gaussian Beam, Turbulence, Random Phase Screen, Laser Beam Propagation, Optical Communication**

I. INTRODUCTION

Recently, the use of optical beams is of great importance due to the need for large bandwidths and high-speed data transfer [1-3]. Especially among these optical beams, the Gaussian beam is widely used since it is the simplest among the rays. The propagation medium of the optical beams used in applications namely free-space optical communication, laser radar systems, and remote sensing is the atmosphere. In the atmosphere, weather conditions such as rain, snow, wind, and fog cause three main phenomena that adversely affect the propagation of the beam through the atmosphere. These are absorption, scattering, and refractive index fluctuations [4]. The random changes in the atmospheric refractive index give rise to atmospheric turbulence which significantly limits the range and performance of free-space laser communication systems. The optical phase random distortions caused by atmospheric turbulence result in a decrease of the received density and potentially lead to higher system bit error rates [5]. In the literature, many research groups work on minimizing the turbulence-induced degradation in optical communication applications and increasing the system performance. Although, many different types of laser beams including Gaussian beams are investigated in the literature, to the best of our knowledge the effect of beam parameters on the received intensity of Gaussian beam has not been studied yet.

In this paper, we examine the effects of system parameters such as source size, wavelength, and aperture size on the intensity of the Gaussian beam propagating in a turbulent atmosphere.

II. THEORETICAL FORMULATIONS

The source field expression of Gaussian beam can be written in the Cylindrical coordinates system as follows;

$$u_s(s,\emptyset_s) = A_c\, exp\,(-k\alpha s^2) \tag{1}$$

where, $\mathrm{s} = (s,\emptyset_s)$ is the source plane transverse coordinates, A_c is the amplitude coefficient, $k = 2\pi/\lambda$ represents the wavenumber with λ is the operating wavelength, $\alpha = (1/k{\alpha_s}^2) + 0.5j/F_s$ where we have α_s, and F_s represent the radial Gaussian source size and the focusing parameter respectively.

Wave-optics are used to model the laser beam propagation through atmospheric turbulence. This approach models the atmosphere by the combination of Fourier transform and random phase screen model. Fourier transform evaluates the propagation of laser beams in free-space [5]. Thus, the turbulent medium effects are modeled by dividing the propagation link into intervals of ΔL length which are separated by phase screens.

The propagation of Gaussian beam in a turbulence-free medium (free-space) can be expressed by the Huygens–Fresnel integral, where the received field of the beam after propagating a distance L presented as [8]

$$u_{r_{fs}}(\mathbf{r},L) = \frac{-jk}{2\pi L} exp(jkL) \int_{-\infty}^{\infty}\int_{-\infty}^{\infty} u_s(\mathbf{s}) exp\left[\frac{jk}{2L}(\mathbf{r}-\mathbf{s})^2\right] d^2\mathbf{s} \tag{2}$$

where $r = (r_x, r_y)$ is the receiver plane transverse coordinates, L is the on-axis receiver plane location.
Since equation 2 has two-dimensional Fourier transform parts, it can be rewritten in the following equation [5-8]

$$u_{r_{fs}}(\boldsymbol{r},L) = F^{-1}\left[F(u_s(s))F(h(r))\right] = F^{-1}[U_s(\mathbf{f})H(\mathbf{f})] \tag{3}$$

where $h(r)$ represents the transfer function, F is the Fourier transform operator, F^{-1} is the inverse Fourier transform, $\mathbf{f} = (f_x, f_y)$ refers to the spatial frequency and H(f) is the

transfer function of the free-space propagation which is expressed as,

$$H(\mathbf{f}) = \exp\left[jL\left(k - \frac{2\pi^2}{k}|\mathbf{f}|^2\right)\right] \quad (4)$$

The utilized random phase screen model represents the effect of the turbulence through the division of the propagation distance into N_s intervals ($\Delta L = L/N_s$) separated by thin phase screen planes. Thus, the received field on the nth plane is expressed as [6-8]

$$u_r(\mathbf{r}, nL) = F^{-1}\left[F\left[u_s(\mathbf{r}, (n-1)\Delta L)\exp\left(j\emptyset(\mathbf{r})\right)\right]H(\mathbf{f})\right] \quad (5)$$

where $\emptyset(\mathbf{r})$ denotes the individual screens' phase power spectral density. The power spectral density of the Von-Karman spectrum is expressed by [5-8]

$$\Phi_\emptyset(\mathbf{f}) = \frac{0.0036LC_n^2k^2L_0^{11/3}}{(L_0^2|\mathbf{f}|^2+1)^{11/6}}\exp[-1.1265l_0^2|\mathbf{f}|^2] \quad (6)$$

where C_n^2 represents the refractive index structure constant, on the other hand, L_0, l_0 represent the outer and inner scales of the turbulent medium respectively.
Consequently, the averaged received field intensity of the beam can be calculated by the multiplication of the received field with its complex conjugate as follows,

$$\langle I_r(\mathbf{r}, L)\rangle = \frac{1}{N_r}\sum_{i=1}^{N_r} u_r(\mathbf{r}, L)u_r^*(\mathbf{r}, L) \quad (7)$$

where < > denotes the averaging, and $I_r(\mathbf{r}, L)$ represents the received field intensity. The upper averaging limit (N_r) in equation 7 theoretically approaches infinity, yet, practically it depends on the turbulence level and setting it to 500 is sufficient to get reliable results [6-8].

III. NUMERICAL RESULTS

The reliability of the presented results is achieved by dividing the propagation distance into 30 phase screens each with a grid size of 512×512. These settings are chosen according to the constraints stated in [9,10]. The averaged received beam intensity is presented in 3D plots. The averaging is set to 500 runs which is sufficient to meet the theoretical condition. The Gaussian beam under consideration propagates in an atmospheric medium with a constant of refraction index structure of $10^{-14}\ m^{-2/3}$, while traveling for 5 km. The tested beam operates at the widely used wavelength (1550 nm). The Von-Karman spectrum inner scale and outer scale are set to zero, and infinity respectively. The effects of the source size, aperture side length and operating wavelength on the Gaussian beam propagating in atmospheric turbulence are assessed and analyzed by comparing the received intensity of these beams with the ones propagating in free-space under the same circumstances.

The variation of Gaussian beam profile against the source size (α_s) is illustrated in figure 1 and figure 2. The figure compares Gaussian beams propagating in moderate atmospheric turbulence with the ones propagating in free-space. Both beams travel for 5 km with an operating wavelength of 1550 nm. As the figures show, beams with bigger source sizes keep their original profiles and faces less spreading, which is in a good agreement with the literature. As turbulence eddies in the atmosphere cause more degredation to beam with small sizes [11].

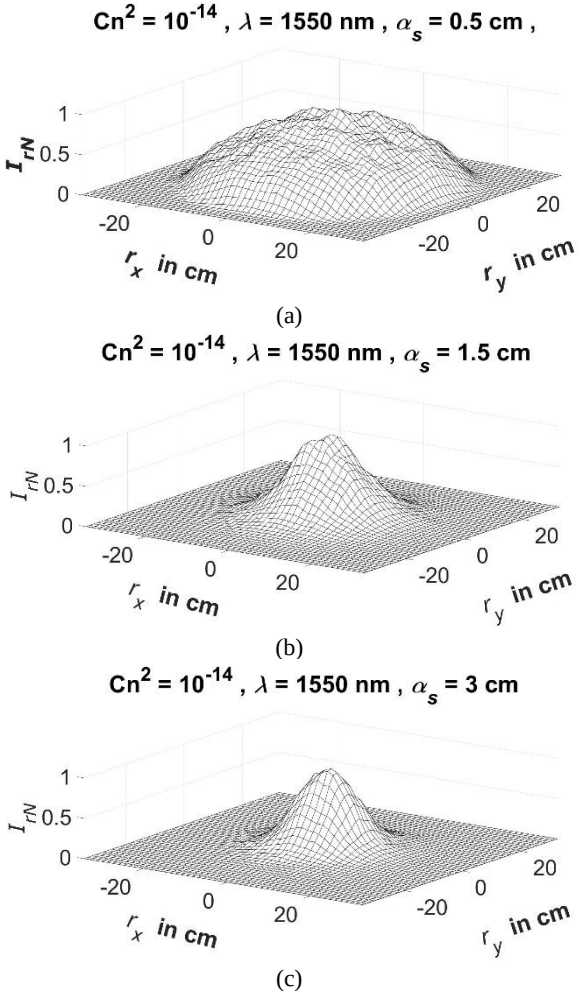

(a)

(b)

(c)

Figure 1: 3D Received normalized average intensity of Gaussian beam propagating in atmospheric turbulence with different source sizes

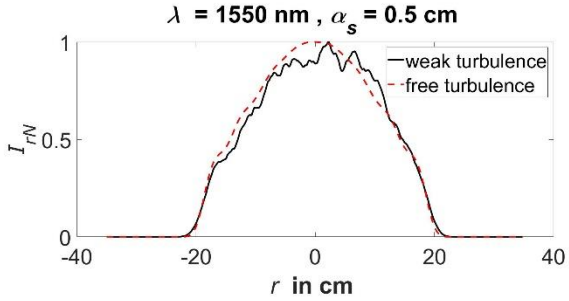

(a)

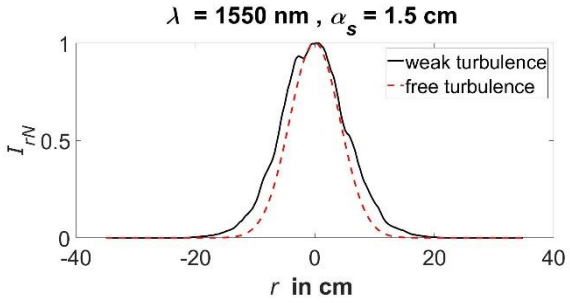

(b)

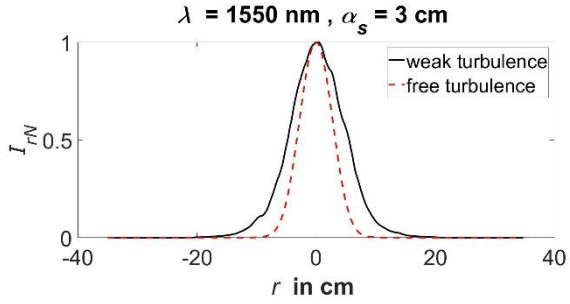

(c)

Figure 2: 2D Received normalized average intensity of Gaussian beam propagating in atmospheric turbulence vs. the one propagating in free-space with different source sizes

Since operating wavelength plays an important role in the communication links, its effect on Gaussian beam propagating in atmospheric turbulence is investigated. In this context, figure 3 and figure 4 illustrate that Gaussian beams operating at higher wavelengths suffer from beam spreading more than the ones at lower wavelenghts after propagating 5 Km in the atmosphere. Under such circumstances, diffractive effects are dominating rather than turbulence effects. These observations are in conformity with the other cases that are analyzed in the literature [12].

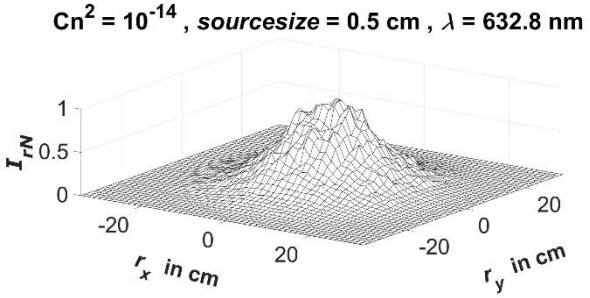

(a)

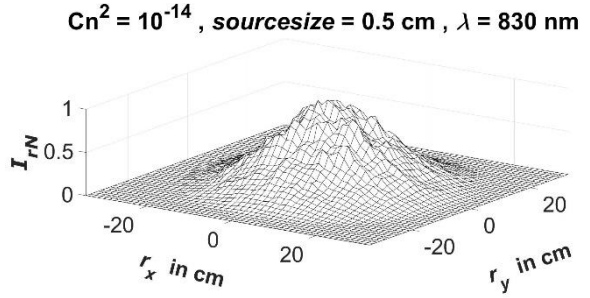

(b)

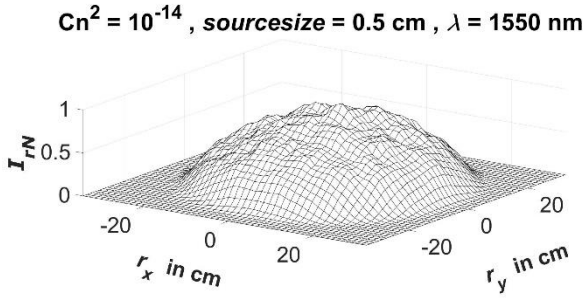

(c)

Figure 3: 3D Received normalized average intensity of Gaussian beam propagating in atmospheric turbulence with different operating wavelengths

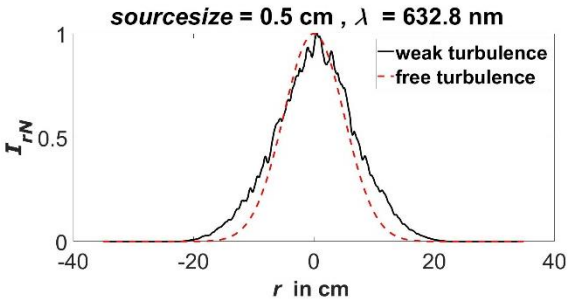

(a)

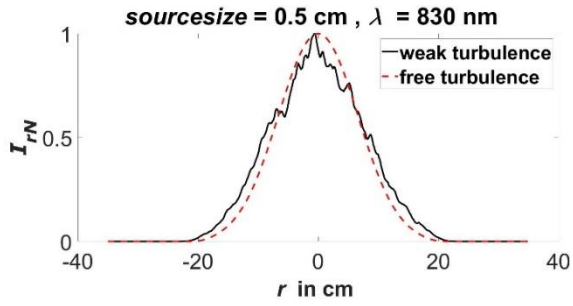

(b)

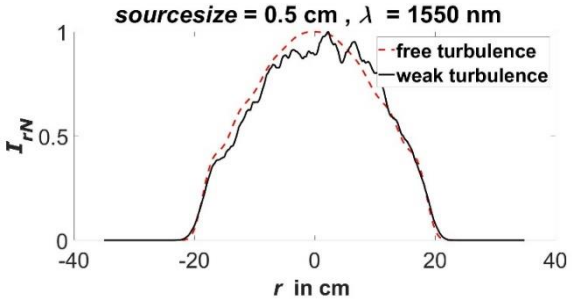

(c)

Figure 4: 2D Received normalized average intensity of Gaussian beam propagating in atmospheric turbulence vs. the one propagating in free-space with different operating wavelengths

Actually, as can be observed from figure 5 and figure 6 the tested receiver aperture side length values do not have a noticeable effect on reducing the beam spreading of the Gaussian beam that propagated 5 Km in atmospheric turbulence. On the other hand, having a high receiver aperture side length helps the beam to keep its original profile as it can be understood by comparing the beam profile propagating in turbulence with the one propagating in free-space. Since, having higher receiver aperture side length allows the system detecting more wandering charge [13].

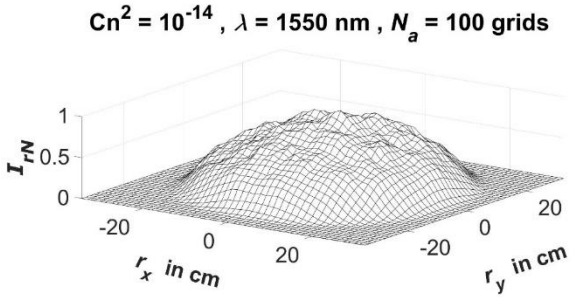

(a)

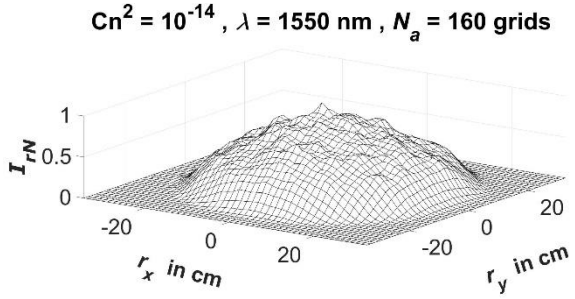

(b)

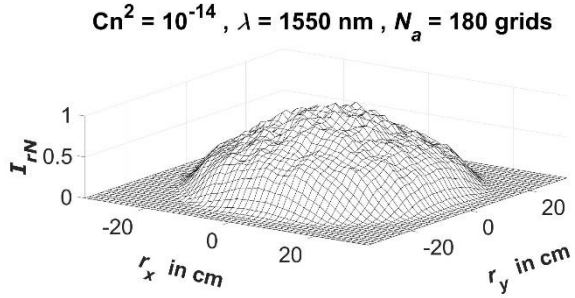

(c)

Figure 5: 3D Received normalized average intensity of Gaussian beam propagating in atmospheric turbulence with different aperture sizes

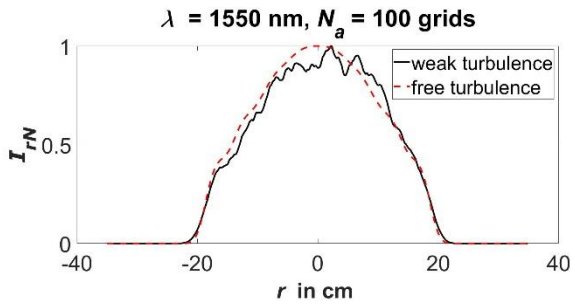

(a)

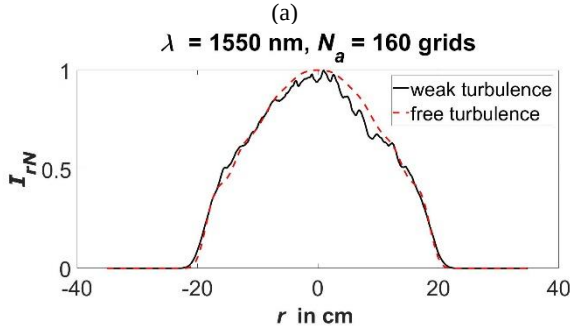

(b)

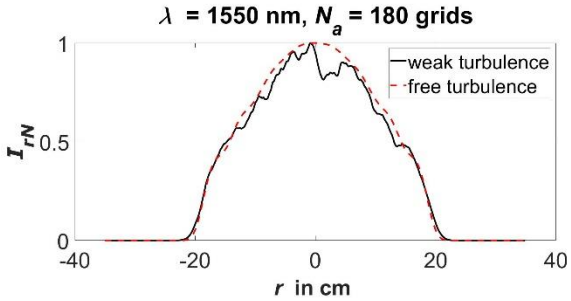

(c)

Figure 6: 2D Received normalized average intensity of Gaussian beam propagating in atmospheric turbulence vs. the one propagating in free-space with different aperture sizes

IV. CONCLUSION

The propagation of Gaussian beam in atmospheric turbulence is analyzed using a random phase screen model. The effect of beam parameters on the intensity of Gaussian beam propagating in a turbulent atmosphere is investigated for the first time in the literature, to the best of our knowledge. Accordingly, beams with bigger source sizes suffer less from the turbulence effects. Operating at higher wavelengths causes more beam spreading. The presented results are in good agreement with the analytical expectations in the literature. Consequently, we believe that the findings of this study have great importance for analyzing and designing the optical communication links used in a wide range of applications.

REFERENCES

[1] M. Z. Chowdhury, et. al. "A Comparative Survey of Optical Wireless Technologies: Architectures and Applications", IEEE ACCESS, 9819-9840, 2018.
[2] I. Alimi, et. al. Challenges and Opportunities of Optical Wireless Communication Technologies, Chapter, 2017, http://dx.doi.org/10.5772/intechopen.69113.
[3] H. Kaushal, et. al. "Overview of Wireless Optical Communication Systems", DOI: 10.1007/978-81-322-3691-7_1, 2017
[4] M.R. Chatterjee, A. Mohamed and F.S. Almehmadi, "Secure free-space communication, turbulence mitigation, and other applications using acousto-optic chaos," Appl. Opt. 57(10), C1-C13, 2018.
[5] L.C. Andrew and R.L. Phillips, *Laser Beam Propagation through Random Media*, SPIE Press: Bellingham, WA, 2005.
[6] H.T. Eyyuboğlu, "Estimation of aperture averaged scintillations in weak turbulence regime for annular, sinusoidal and hyperbolic Gaussian beams using random phase screen," Opt. Laser Technol. 52, 96–102, 2013.
[7] H.T. Eyyuboğlu, D. Voelz and X. Xiao, "Scintillation analysis of truncated Bessel beams via numerical turbulence propagation simulation," Appl. Opt. 52, 8032-8039, 2013.
[8] H.T. Eyyuboğlu, "Scintillation analysis of hypergeometric Gaussian beam via phase screen method," Opt. Comm. 309, 103–107, 2013.
[9] R. Rao, "Statistics of the fractal structure and phase singularity of a plane light wave propagation in atmospheric turbulence," Appl. Opt. 47, 269–276, 2008.
[10] J.D. Schmidt, Numerical simulation of optical wave propagation with examples in MATLAB, SPIE Press: Washington, DC, Chapters 7, 8 and 9, 2010.
[11] F. Yildiz and H. Kurt, "Analysis and Simulation of Turbulence Effects on Gaussian Beam Propagation Based on Generalized Modified Atmospheric Spectrum," Acta Materialia Turcica, 4, 32-38, 2020.
[12] H.T. Eyyuboğlu and Y. Cai, "Hypergeometric Gaussian beam and its propagation in turbulence," Opt. Comm. 285, 4194–4199, 2012.
[13] K. Elmabruk and H.T. Eyyuboğlu, "Analysis of flat-topped Gaussian vortex beam scintillation properties in atmospheric turbulence," Optical Engineering 58(6), 066115, 2019.

Effect of Nanofluids on Heat Transfer in a Zigzag Channel with Central Wings

S. AKCAY[1]

[1]Cankiri Karatekin University, Cankiri/Turkey, selmaakcay@karatekin.edu.tr

***Abstract*– In this study, effects of Al_2O_3-water nanofluid on heat transfer and friction factor are investigated numerically in a zigzag channel with central wings. In simulations, mass, momentum and energy equations are discretized with finite volume approach and iterations are solved with SIMPLE algorithm. In the study, Reynolds number ($200 \leq Re \leq 1200$), and nanoparticle volume ratio ($0.01 \leq \varphi \leq 0.05$) are changed, and other parameters kept constant. The lower and upper zigzag walls of the channel are kept at constant temperature, and the Nusselt number and friction factor along the channel are calculated. In order to observe the effects of the parameters examined, the contours of velocity and temperature in the channel are obtained. In addition, the results of the study are compared with the based fluid. The numerical results show that the nanofluidsand wings contribute significantly to the heat transfer enhancement while the friction factor increases slightly.**

***Keywords*–Nanofluid, Zigzag channel, Central wings, Heat transfer, Friction factor.**

I. INTRODUCTION

In engineering applications, heat transfer improvement is an important research area as it contributes to the efficiency of thermal devices. Passive and active methods are widely used to increase heat transfer without reducing the overall efficiency of these devices. Passive methods are applications such as inchannel baffles, wings, bent band, vortex generators and special surface geometries.These applications, which do not require an external power, are preferred in evaporators, condensers, gas turbine cooling, nuclear reactors, heat exchangers, solar air heaters. This methodis economical and reliable compared to other techniques as it has no moving parts and does not require any external energy [1-6]. Promvonge et al. [7] experimentally investigated the heat transfer performance in a channel where inclined horseshoe baffles were used and reported that the heat transfer increased by approximately 92-208% and the friction factor increased by 1.76-6.37 compared to straight channels. Kumar et al. [8] experimentally studied the heat transfer behavior of the solar air channel using multiple *V*-type baffles. Sahel et al. [9] reported that the different baffle design in a rectangular channel improved heat transfer by 65%.

Fluids containing water, ethylene glycol, and oil widely used in industrial applications, have low thermal properties. New technologies are used to improve the thermo-physical properties of such conventional coolants. One of these techniques is the addition of nano-sized solid particles with high thermal conductivity to the base fluid. Some researchers have used nanofluids together with other passive techniques [10-12]. Manca et al. [13] examined the heat transfer for the $20000 \leq Re \leq 60000$ of Al_2O_3-water nanofluid at different rib heights, at 0% to 4% nanoparticle volume ratios in a channel. As a result, they reported that as the Reynolds number and particle volume ratio increased, the heat transfer improved and at the same time an increase was observed in the pumping power.Heshmati et al. [14] numerically studied the mixed convective heat transfer in the $50 \leq Re \leq 400$ with the baffles of different geometries at varying particle volume ratios ($0.01 \leq \phi \leq 0.04$) of different nanofluids. It has been shown that nanofluids with high particle volume ratios and small nanoparticle diameter significantly improve heat transfer.Ajeel et al. [15] numerically studied the flow and heat transfer properties of ZnO-water nanofluid for turbulent flow with *L* -shaped baffles in a curved corrugated channel and reported that baffles and nanofluids increase heat transfer.Menni et al. [16] carried out the dynamic and thermal behaviors of nanofluids in turbulent flow conditions by using baffles at different angles in the channel and reported that the highest thermal improvement was obtained when vertical baffles were used at high Reynolds numbers.

There are many studies in the literature examining the combined effect of passive heat transfer applications. However, the high number of parameters used increases the efforts to find the optimum parameters and new studies are needed on this subject.Therefore, in this study, the effects on heat transfer and friction factor of Al_2O_3-water nanofluid in a zigzag channel with central wings were numerically investigated.

II. NUMERICAL STUDY

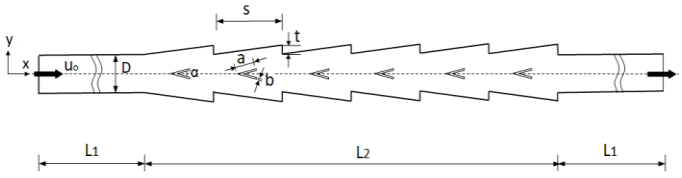

Figure 1: The geometry of the numerical model.

In Figure 1, the geometry of the zigzag channel with central wings used in the study is given. At the entrance and exit of

the channel, there is an unheated flat section L_1 = 0.1 m. The height of the channel (D) is 19 mm and the total length of the zigzag channel is L_2 = 0.171 m. The length of zigzag section is considered as S = 1.5D and the thickness as t = 3.8 mm. The length of the wings is a = 4 mm, b =1.5 mm and the angle between wings is α = 14 degree. Other geometric parameters were kept constant in the study.

Al_2O_3-water suspension was considered as the nanofluid, and three different nanoparticle volume fractions (φ = 1%, 3% and 5%) are used. Simulations are applied for a certain range of Reynolds number ($200 \leq Re \leq 1200$) under laminar flow conditions.

The flow in the channel is considered to be fully developed, laminar, incompressible, two-dimensional, steady, Newtonian type and single-phase. The heat transfer with gravity and radiation has been neglected. The equations used according to these assumptions are given below;

$$\frac{\partial u_i}{\partial t} + \nabla(\rho u) = 0 \tag{1}$$

$$\frac{\partial u_i}{\partial t} + \frac{\partial (u_i u_j)}{\partial x_i} = \frac{\partial p}{\partial x_i} + \frac{1}{\mathrm{Re}} \nabla^2 u_j \tag{2}$$

$$\frac{\partial T}{\partial t} + u_i \frac{\partial T}{\partial x_i} = \frac{1}{\mathrm{Re\,Pr}} \nabla^2 T \tag{3}$$

Fluent 15.0 [17] program was used for Computational Fluid Dynamics (*CFD*) based numerical solution. The pressure velocity coupling was solved using the SIMPLE algorithm and the terms convection and diffusion were discretized using a second order upwind scheme. The convergence criterion was taken as 10^{-6} for all residuals. Various tests were applied for grid independence for cell numbers of 42624, 75346, 106820, 137114, 185793.106820 cell number is used in this study since the change in Nusselt number is less than 2%.

Density, specific heat, thermal conductivity and viscosity were obtained by Equations (4-7) among the thermo-physical properties of nanofluids [18].

$$\rho_{nf} = (1-\varphi)\rho_{bf} + \varphi\rho_{pt} \tag{4}$$

$$c_{nf} = (1-\varphi)c_{bf} + \varphi c_{pt} \tag{5}$$

$$k_{nf} = k_{bf} \frac{\left[k_{pt} + 2k_{bf} - 2\varphi(k_{bf} - k_{pt})\right]}{\left[k_{pt} + 2k_{bf} + \varphi(k_{bf} - k_{pt})\right]} \tag{6}$$

$$\mu_{nf} = \mu_{bf}(123\varphi^2 + 7.3\varphi + 1) \tag{7}$$

The water is used as the base fluid. Thermo-physical properties of Al_2O_3 nanoparticle and water are given in Table 1.

Table 1: Thermo-physical properties of Al_2O_3 nanoparticle and water

	ρ [kg/m^3]	c [j/kgK]	k [W/mK]	μ [kg/ms]
water	998	4182	0.613	0.001003
Al_2O_3	3970	765	37	-

The fluid temperature at the channel inlet is T_o = 293 K. At the channel entrance, the "velocity inlet" boundary condition was defined. Fully developed flow was accepted at the outlet and "outflow" boundary condition was applied. The lower and upper surfaces of the zigzag channel are preserved at a constant temperature of T_w = 350 K and the non-slip boundary condition for the channel walls was defined. A non-slip and adiabatic boundary condition was applied for the straight section at the entrance and exit of the channel.

III. Discussion and Results

A. Validation of the Study

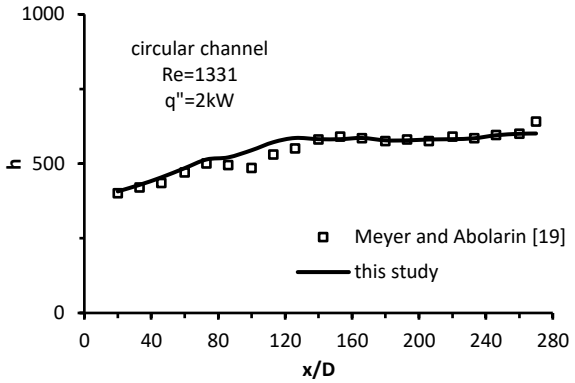

Figure 2: The validity of the numerical solution.

For the validity of the numerical solution,this study were compared with the experimental result of Meyer and Abolarin [19]. In a straight channel with a diameter of 19 mm and a constant heat flux of q''= 2 kW applied to the surface, for Re = 1331, the heat transfer coefficient was calculated with x / D distances along the channel. The agreement between the results of both studies is shown in Figure 2.

In this section, the velocity and temperature distributions are obtained in the channel to explain the flow and heat transfer mechanism.

In Figure 3, velocity contours are given for different Reynolds number at a constant particle volume fraction (φ=0.01). In Figure 4, temperature contours are shown for same parameters. It can be seen that the zigzag channel structure and central wings significantly affect the flow and temperature fields depending on the Reynolds number. It has been observed that the wings cause flow oscillation within the channel. Increasing Reynolds number leads to heat transfer enhancement by increasing flow oscillating.

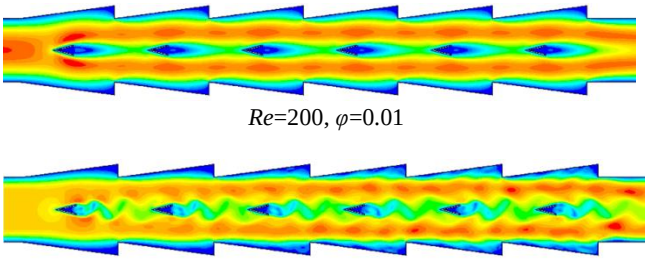

Re=200, φ=0.01

Re=1200, φ=0.01

Figure 3: The velocity contours for different Re (φ=0.01).

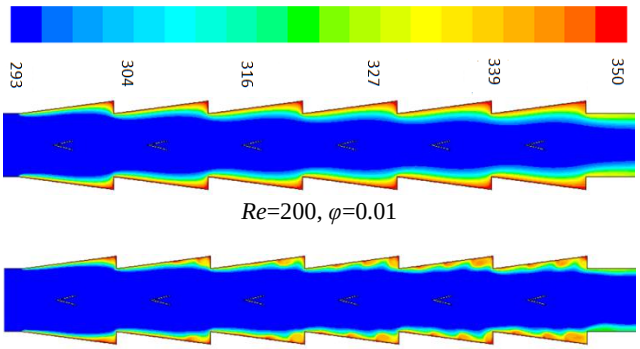

Re=200, φ=0.01

Re=1200, φ=0.01

Figure 4: The temperature contours for different *Re* (φ=0.01).

In Figure *5*, the temperature structures are given for different particle volume fraction at *Re* = 800. It is seen that the temperature in the channel walls decreases with the increase of the particle volume fraction.

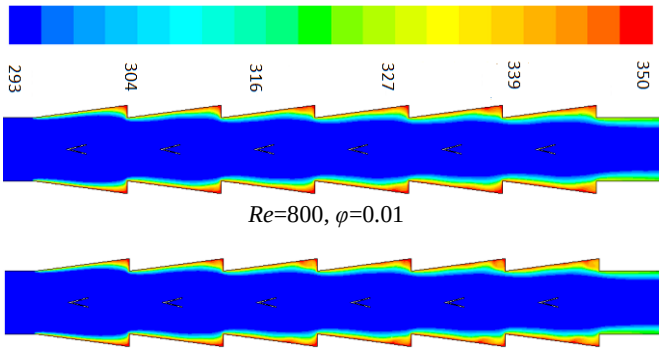

Re=800, φ=0.01

Re=800, φ=0.05

Figure 5: The temperature contours for different particle volume fractions (Re=800).

B. Nusselt Number and Thermo-hydraulic Performance

In this study, Nusselt number is defined by Equations (8-9) to calculate the local and average heat transfer in the channel.

$$Nu_x = \frac{q'' D_h}{k(T_{w,x} - T_{b,x})} \tag{8}$$

$$Nu = \frac{1}{L}\int_0^L Nu_x dx \tag{9}$$

where, k is the thermal conductivity coefficient of the nanofluid, D_h is the hydraulic diameter of the channel, L is the total channel length, the surface temperature of the T_w channel and the film temperature of the nanofluid calculated as $T_b = (T_{in} + T_{out}) / 2$. The heat transfer performance calculated based on the Nusselt number is defined as η and shown in Equation (10).

$$\eta = \frac{Nu_n}{Nu_s} \tag{10}$$

((8aaaa

where, Nu_n is the average Nusselt number calculated for the nanofluid, and Nu_s is the Nusselt number calculated for the base fluid.

On the other hand, depending on the particle volume fraction and fluid velocity, a significant pressure drop occurs in the wall and fluid. Due to the high viscosity of nanofluids compared to the base fluid, the pressure drop should also be evaluated in heat transfer improvement studies. In this study, the dimensionless friction factor $r = f_n / f_s$ is defined to determine the pressure drop of the nanofluid. Where, f_n shows the surface friction for the nanofluid flow and f_s is the surface friction for the base flow. Thermo hydraulic performance is achieved by the ratio of heat transfer performance to friction factorand is defined by Eqn.(11):

$$THP = \frac{(Nu_n / Nu_s)}{(f_n / f_s)^{1/3}} \tag{11}$$

The variations of the heat transfer performance with the Reynolds number for different particle volume fractions in Figure *5a*, the dimensionless friction factor in Figure *5b*, and the thermo-hydraulic performance in Figure *5c* are given. From the figures, it is seen that the heat transfer performance and friction factor increase with the increase of particle volume fraction and Reynolds number. The dashed line represents the base fluid for the same geometry. The frictions in the channel increase with the effect of the wings at zigzag channel and the increase in the particle volume fraction. The thermo-hydraulic performance values are obtained above the reference for all Reynolds numbers and particle volume fractions because the heat transfer improvement was greater than the friction in the channel, but remained unchanged for all parameters.

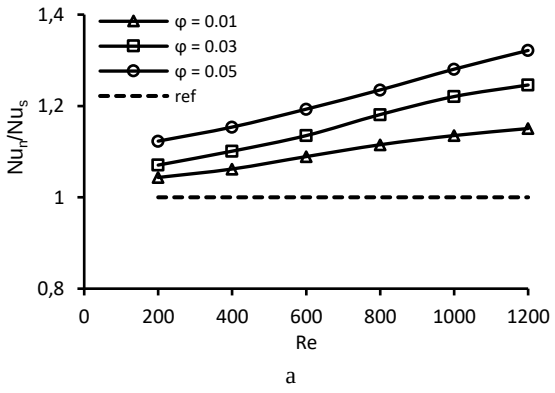

a

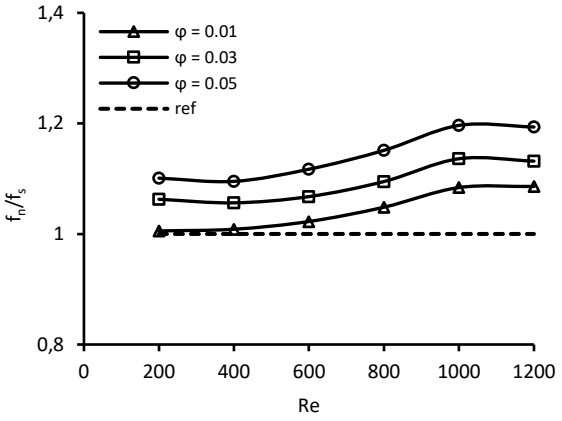

b

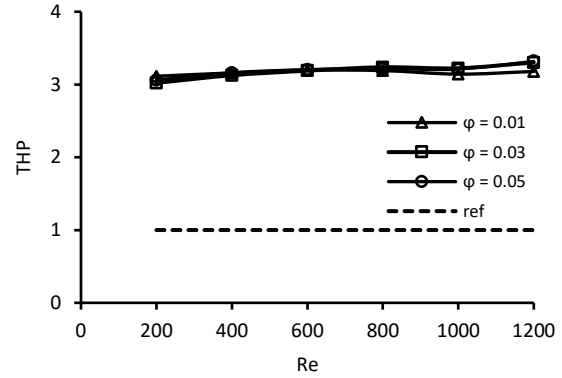

c

Figure 6: a- The heat transfer performance, b- The friction factor, c-The thermo-hydraulic performance with Reynolds number for different particle volume fractions.

IV. CONCLUSIONS

In this study, effects of Al_2O_3-water nanofluid in a zigzag channel with central wings on heat transfer and friction factor are investigated numerically for different Reynolds number and particle volume fraction. The results obtained in the study are listed below:

- The highest heat transfer performance was obtained as η=1.32 at Re = 1200 and φ = 0.05.
- The wings and nanofluids in the zigzag channel provided significant improvement in heat transfer, while an acceptable increase in friction factor was observed.
- The highest friction factor was found to be r=1.19 at Re = 1200 and φ = 0.05.
- Thermo-hydraulic performance values were obtained above the reference value for all Reynolds numbers and particle volume fractions.
- The thermo-hydraulic performance was obtained as approximately THP = 3.31 for all parameters.

REFERENCES

[1] Y.G. Lei,Y.L. He, R. Li, and Y.F. Gao, "Effects of baffle inclination angle on flow and heat transfer of a heat exchanger with helical baffles," *Chem. Eng. Process*, vol. 47(12), pp. 2336–2345, February 2008.

[2] Z. Li, andY. Gao, "Numerical study of turbulent flow and heat transfer in cross corrugated triangular ducts with delta-shaped baffles,"*Int. J. Heat Mass Transf.*, vol. 108, pp. 658–670, December 2017.

[3] P. Sriromreun, "Numerical study on heat transfer enhancement in a rectangular duct with incline shaped baffles,"*Chem. Eng. Trans.*, vol. 57, pp. 1243–1248, 2017.

[4] S. Rashidi, M. Eskandarian, O. Mahian, and S. Poncet, "Combination of nanofluid and inserts for heat transfer enhancement, Gaps and challenges,"*Journal of Thermal Analysis and Calorimetry*, vol. 135, pp. 437–460, February2019.

[5] D.E. Alnak, "Thermohydraulic performance study of different square baffle angles in cross-corrugated channel,"*Journal of Energy Storage*, vol. 28, pp. 101295, April 2020.

[6] S.W. Chang, and T.H. Cheng, "Thermal performance of channel flow with detached and attached pin-fins of hybrid shapes under inlet flow pulsation,"*International Journal of Heat and Mass Transfer*, vol. 164, pp. 120554, January 2021.

[7] P. Promvonge, S. Tamna, M. Pimsarn, and C. Thianpong, "Thermal characterization in a circular tube fitted with inclined horseshoe baffles,"*Appl. Therm. Eng.*, vol. 75, pp. 1147–1155, January 2015.

[8] R. Kumar, A. Kumar, R. Chauhan, and M. Sethi, "Heat transfer enhancement in solar air channel with broken multiple V-type baffle,"*Case Stud. Therm. Eng*.,vol. 8, 187–197, September 2016.

[9] D. Sahel, H. Ameur, R. Benzeguir, and Y. Kamla, "Enhancement of heat transfer in a rectangular channel with perforated baffles,"*Appl. Therm. Eng.*, vol. 101, pp. 156–164, May 2016.

[10] S. Akcay, andU. Akdag, 2018, "Parametric investigation of effect on heat transfer of pulsating flow of nanofluids in a tube using circular rings,"*Pamukkale University, Journal of Engineering Sciences*, vol. 24(4), pp. 597-604, 2018.

[11] H. Fazeli, S. Madani, and P.R. Mashaei, "Nanofluid forced convectionin entrance region of a baffled channel considering nanoparticle migration,"*Appl.Therm. Eng*., vol. 106, pp. 293–306, August 2016.

[12] S.H.H. Karouei,S.S.M. Ajarostaghi, M. GorjiBandpy,and S.R.H.Fard, "Laminar heat transfer and fuidfow of two various hybrid nanofuids in a helical double pipe heat exchanger equipped with an innovative curved conical turbulator,"*Journal of Thermal Analysis and Calorimetry*, vol. 143, pp. 1455–1466, February 2021.

[13] O. Manca, S. Nardini, and D. Ricci, "A numerical study of nanofluid forced convection in ribbed channels,"*Applied Thermal Engineering,*vol. 37, pp. 280-297, May 2012.

[14] A. Heshmati, H.A. Mohammed, and A.N. Darus, "Mixed convection heat transfer of nanofluids over backward facing step having a slotted baffle,"*Applied Mathematics and Computation*,vol. 240, pp. 368–386, August 2014.

[15] R.K. Ajeel,K. Sopian,and R. Zulkifli,"Thermal-hydraulic performance and design parameters in acurved-corrugated channel with L-shaped baffles and nanofluid,"*Journal of Energy Storage*, vol. 34, 101996, February 2021.

[16] Y. Menni, A.J. Chamkha, M. Ghazvini, M.H. Ahmadi, H. Ameur,A. Issakhov, and M. Inc, "Enhancement of the turbulent convective heat transfer in channels through the baffling technique and oil/multiwalled carbon nanotube nanofluids,"*Numerical Heat Transfer, Part A: Applications*,vol. 79(4), 311-351, December 2021.

[17] ANSYS Fluent user guide & theory guide- Release 15.0, Fluent AnsysInc, USA, 2015.

[18] S. Kakac, and A. Pramuanjaroenkij, "Review of convective heat transfer enhancement with nanofluids,"*Int. Jour. Heat and Mass Transfer*, vol. 52, pp. 3187–3196, June 2009.

[19] J.P. Meyer, and S.M. Abolarin, "Heat transfer and pressure drop in the transitional flow regime for a smooth circular tube with twisted tape inserts and a square-edged inlet,"*Int.Jour.Heat and Mass Transfer*, vol.117, 11-29, February 2018.

Electric Vehicle Mechanical Design, Manufacturing and Analysis Application

A.Engin ÖZÇELİK[1] , Hakan TERZİOĞLU[1], İrem Sena KÖK[1], Ömer Cem GÖKDOĞAN[1], Cüneyd YAVAŞOĞLU[1], Özgün KURT[1], Ayberk HALICI[1], Janset ALTAN[1], Muhammet KAYHAOĞLU[1] and Serhat ÇETİN[1]

[1] Selcuk University, Konya/Turkey, eozcelik@selcuk.edu.tr

[1] Selcuk University, Konya/Turkey, hterzioglu@selcuk.edu.tr

Abstract: **Today, energy is derived from a very large percentage of fossil-based sources, such as 80-85% worldwide. However, it is not sustainable that the use of fossil-based resources pollutes the environment, causes climate change, runs out of reserves and lacks price stability. The most important measure against climate change that poses a threat to the world is to reduce the share of fossil-based resources in energy supply.**

In this context, in order to encourage universities in our country to design and manufacture electric vehicles and equipment, TUBITAK organizes competitions for universities and high schools under the name electromobile every year. In this study, TUBITAK Electromobile Battery was designed and manufactured by designing a unique electric vehicle to compete in the Electric Powered Vehicle category. After the mechanical designs of this vehicle we produced were made, the chassis and shell production was carried out by analyzing.

Keywords **- Electric vehicle, mechanical design, chassis, analysis**

I. INTRODUCTION

Electric cars are called vehicles with technology that generates all or part of their driving power with an electric motor and rotates the wheels. It feeds the electric motor the energy stored in the vehicle's batteries and these batteries are charged in various ways [1]. The location of electric cars is very valuable today. The world began to use new technology and gradually abandon diesel and gasoline vehicles[2]. In order to be a part of this technology in our country, he has taken new steps and embarked on a new journey under the name of TOGG.

The process of producing cars begins to be designed by arisen from the needs. According to the researches obtained, the cars begin the journey with the start of the designers [3]. The automotive sector, which has a wide field of study and technique, covers many areas. The interior design of the vehicle is based on the science of ergonomics, figurine in the making of clay modeling in certain dimensions of the vehicle, mathematics and physics calculations of the vehicle include many sectors such as engineering, the battery systems of the vehicle, chemistry and electricity, etc. It is a very long process until the research of these issues, the decisions made and the latest production [4,5,6].

Therefore, in this process, which requires continuous development and follow-up, the vehicles should be designed and modeled and then the necessary analyses should be done in a computer environment [7,8]. According to the results of these tests, the production of the vehicle is started in the continuation [9,10]. After the parts such as the engines and batteries to be used in the vehicle, electrical components and chassis are designed and manufactured, the prototype vehicle is placed in the necessary places. As a result of successfully passing many tests such as necessary driving tests and accident tests on this vehicle, the vehicle will now be ready for mass production with the preparation of the necessary infrastructure preparations [11].

In this study, the chassis with light and good strength was designed and analyzed for the electric vehicle produced in the Automotive Technologies Laboratory of Selçuk University Faculty of Technology, and the chassis production was carried

II. CHASSIS DESIGN AND PRODUCTION

The chassis design can be considered as the skeleton of the vehicle, which should be light as a pain but also safe as strength. The manufacturing method to be used in the chassis should be considered as welding or bending, and principles such as material assignment profile geometry and thickness should be strictly taken into account [12].

Using the chassis design Solidworks program, the integrated points of the vehicle shell were also designed with the axle, distances in mind, "argon gas was attached to the under-gas welding and using ER 4043 aluminum welding wire, the 40x40x2 square 6063 T6 series profiles, which were cut in appropriate dimensions, were made from the inside out to avoid the dimmed punta, and after the process, the temperature distribution was made from the inside out so that there was no charge or pull on the profiles.

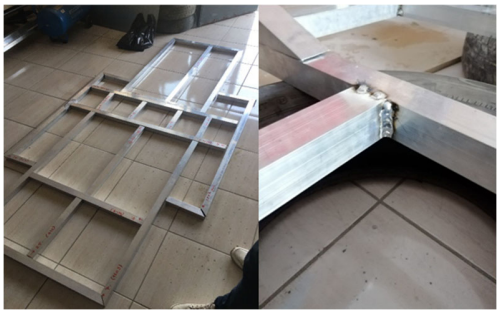

Figure 1: *Chassis miter and welding work*

Figure 2: *Front layout and installation of tires*

The roll bar and roll cage design, which is one of the main elements of the chassis, used a circular profile of 6082 T5 35x3 to be resistant and lightweight. The profile, which is cut with the appropriate bend diameters in mind, is bent in the pipe bending machine at appropriate diameters. The bent parts are first welded to the chassis, the support profiles are boiled with the under-gas welding to open the wolf's mouth and support the chassis and rollbar from four points.

Figure 3: *Rollbar and Rollcage locations on the vehicle*

Figure 4: *Rollbar ve Rollcage CAD*

III. CHASSIS and ROLL BAR ROLL CAGE ANALYSIS

Roll Bar Roll Cage Analysis Analizleri

R3 version of ANSYS 2019 program was used for analysis. Only the Rollbar and Rollcage parts of the vehicle were modeled and assembled, preparing for the relevant analysis and then continuing by meshing. In terms of accuracy of the analysis, the maximum Skewness value is intended to be below 0.7. Since the geometry is too large, this quality was deemed sufficient not to get a large number of nodes. Various errors were corrected by cleaning geometry using Spaceclaim. After reaching the Ansys mechanical interface, material was assigned to the geometries. 6082 Aluminum alloys were used as materials in Rollbar and Rollcage. The properties of this material used are seen in Figure 5.

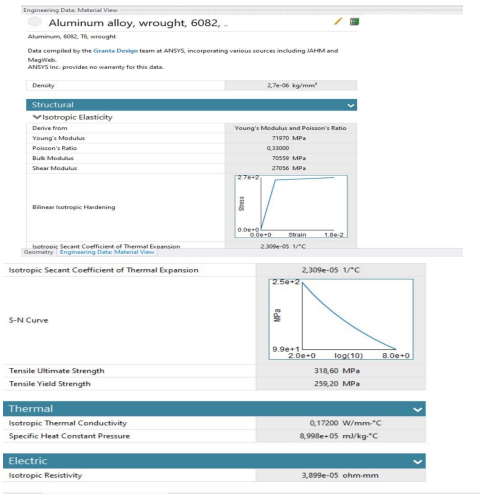

Figure 5: *6082 Mechanical properties of the material*

After the material assignment, the mesh throwing process was started. 0.63 Skewness Max using the Tetrahedron (Patch Independent) method after the settings are made. (Figure 6) and the analysis phase was started for the mesh structure, which was above the targeted quality.

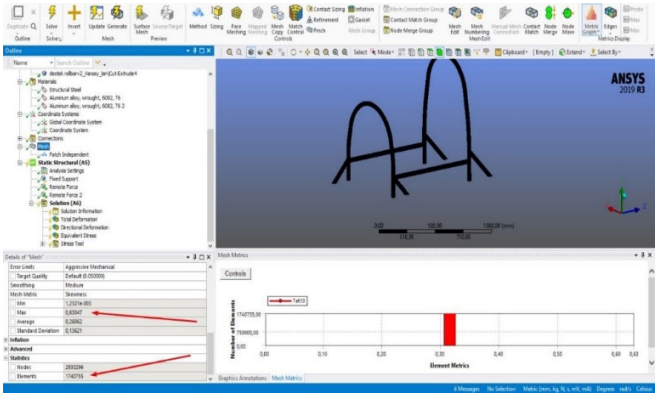

Figure 6: *Mesh quality*

As shown in Figure 7, rollbar and supports are boiled perpendicular to the chassis, so these surfaces are fixed.

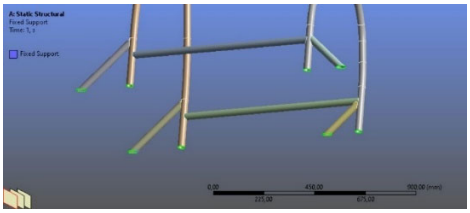

Figure 7: Fix points

After this process, nodal force was assigned to the top points as shown in Figure 8.

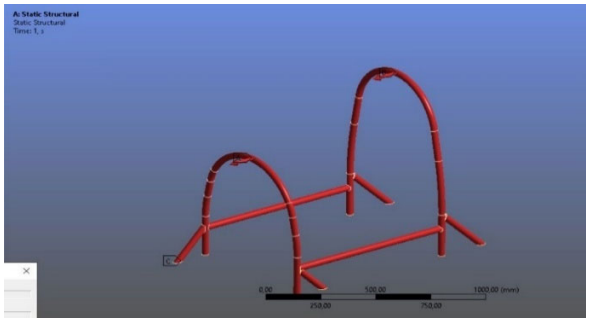

Figure 8: *Force points*

After this process, the Solution phase was started. The solution results are seen in Figure 9.

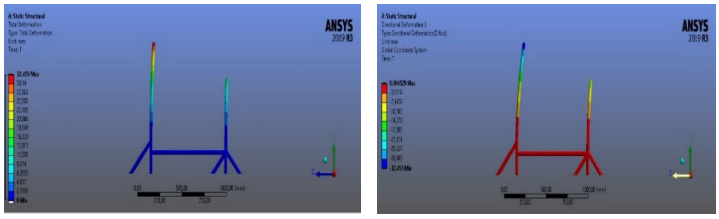

Figure 9: *Results as a result of the specified force*

Porya and Wheel Connection System and Analysis

AISI 1040 steel material was preferred in accordance with the rim measurements that have been changed due to the inefficiency of the aluminum porcelains received, taking into account factors such as high strength and easy access as well as easy to process. Steel-filled material was supplied and chip removal was performed with universal lathes of the same size. Figure 10 shows the Porya CAD model and chassis.

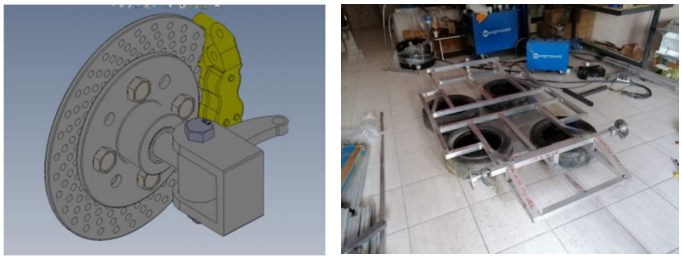

Figure 10: *Porya CAD model and chassis appearance*

Maximum stresses were determined by stress analysis of the direction of forces that can come on poryas. Maxumum stress analysis of porya is seen in Figure 11.

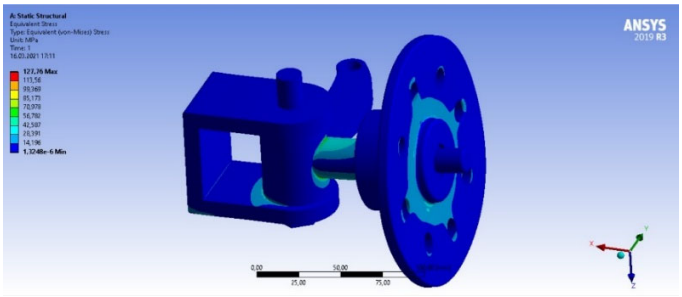

Figure 11: *Porya Maximum Stress Analysis*

Door Connection System and Analysis

After the installation of the chassis and shell, the chassis and door design were updated, taking into account the frame measuring 50x80 cm that must pass through the door. Our design was carried out in the dimensions that a frame with a size of 50x80 cm can enter. Piaggio Porter hinge was used in our door mechanism. The reason we chose this hinge was preferred because it made it easier to open the door outward. 3 profile connections placed inside the door have been added. The positions of the profiles are designed to minimize the strength of the vehicle door and the jolting during opening and closing. In Figure 12, the door gap is seen.

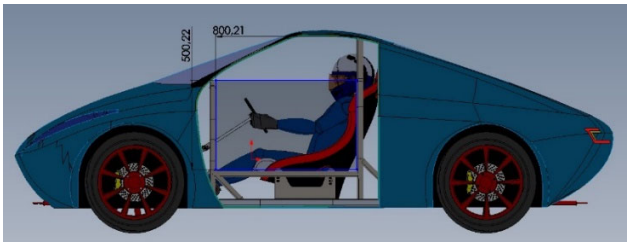

Figure 12: *Door cavity*

Door Consolidation Process

A rigid and non-moving door design had to be planned. Therefore, since the mold of the door will be prepared separately, the skeletal structure design was created by fixing it with aluminum profile (10x20) after production. The in-door skeletal system is seen in Figure 13.

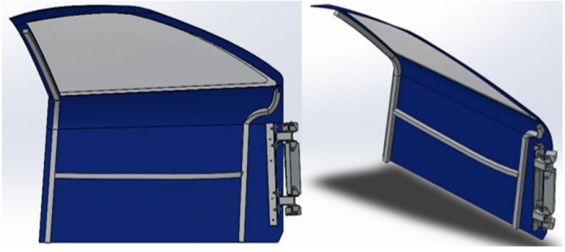

Figure 13: *In-door skeleton*

The foresground that might come from the top corner of the door is max. The 100 N force is transferred to the hinge edge with the moment calculation. The 91,617 N force coming to the edge of the hinge is shown in shapes. Our total deformation is 0.01 mm. The hinge design suitable for the door was determined to be as seen in Shape 14 in the analysis results.

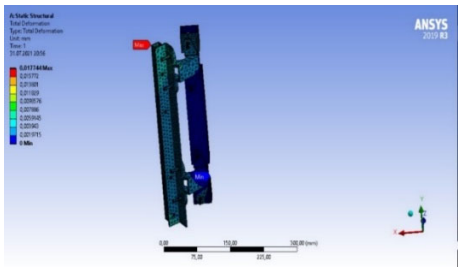

Figure 14:. *Hinge Total deformation analysis*

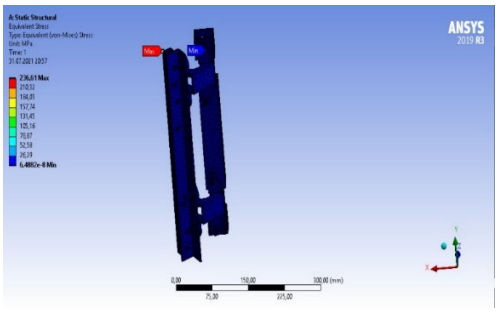

Figure 15. *Hinge stress analysis*

Araç CDF Analysis

By looking at the iteration chart, our Cd result is determined as 0.19. The pressure distribution on the vehicle is seen in Figure 16 and the cd coefficient that is the result of this test is given in Figure 17.

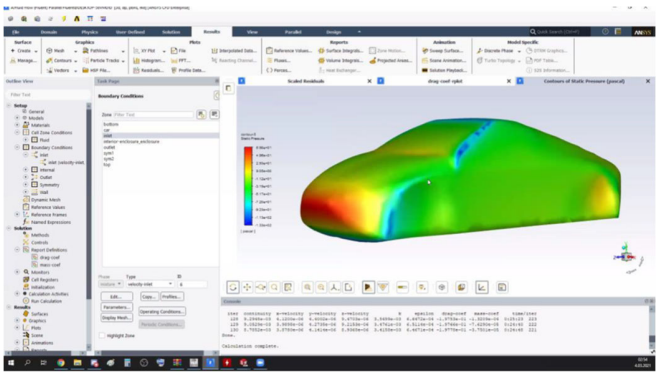

Figure 16:. *Vehicle CFD analysis*

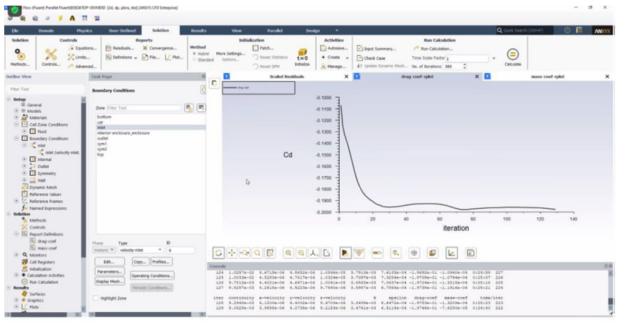

Figure 17: Itterization Chart

IV. RESULT

One of the most important problems of countries today is energy efficiency and energy cost. Countries that import nearly all of the oil it needs, such as our country, depend on oil exporting countries in terms of energy. Therefore, the issue of electric vehicles is of great importance for Turkey. The expansion of electric vehicles and the use of energy obtained from national power plants such as solar, wind, hydroelectric and thermal power plants to recharge the batteries of vehicles have the potential to reduce our country's oil needs. In addition, as a result of the use of electric vehicles, exhaust emissions that are highly harmful to the environment will be reduced by the use of fuels of petroleum origin. For these purposes, innovative studies on electric vehicles, which are popular today, will contribute to domestic and national production.

With this work, an electric vehicle with a unique design is designed and manufactured. In particular, the mechanical design, production and control of the electric vehicle's drivetrains with domestic software within the scope of the project constituted the original aspect of the project. In this vehicle we have carried out, the system circuits and software embedded in the control software and the management system and telemetry application are also industrial structure and have created a unique structure. truck. In this study, students were also greatly contributed to the development of domestic electric vehicles, which are the subject of innovation.

ACKNOWLEDGMENT

This study is from Selçuk University 21301003 with the numbered BAP project.

REFERENCES

[1] Abhijeet Chandratre, Himanshi Saini, Sai Hanuma Vemuri, M.B. Srinivas, 2011,''Battery management system for E-bike –A novel approach to measure crucial battery parameters for a VRLA battery'', India International Conference on Power Electronics,New Delhi, 28-30 January 2011,1-5.

[2] R. Hurlbrink, L. Wilson and R. Prins, Electric Vehicle Energy Usage Modeling Simulation and Testing for Range Estimation, James Madison University, November 2012.

[3] Ewgenij Starschich, Annette Muetze,2007, ''Comparison of the Performances of Different Geared Brushless-DC Motor Drives for Electric Bicycles'' IEEE International Electric Machines &Drives Conference, Antalya, 3-5 May 2007,140

[4] Chang Hua Lin,Hom Wei Liu, Chien-Ming Wang, 2010,''Design and implementation of a bi-directional power converter for electric bike with charging feature'',5th IEEE Conference on Industrial Electronics and Application, Taichung, 15-17 June 2010,538-543

[5] Chich-Chiang Hua, Shih-Jyun Kao ,2011,''Design and implementation of a regenerative braking system for electric bicycles based on DSP'', 6th IEEE Conference on Industrial Electronics and Applications, Beijing,21-23 June 2011,703-707.

[6] Eberhard, M. and Tarpenning, M. , "The 21st century electric car," Tesla Motors White Paper, 2006

[7] Devaneyan S. ,2010, '' Electronic control Unit for BLDC Motors in Electric Biccycles with 8- bit Microocontroller'' , International Conference on Communication and Computational Intelligence, Erode, 27-29 Dec. 2010 , 201-205.

[8] Manoj E. ,Dino Isa, Roselina Arelhi ,2010, '' Super Capacitor Battery Hybrid Powered Electic Bicycle Via A Smart Boost Converter'',World Electric Vehicle Journal Vol.4, 280-286

[9] Peide Liu, Xiujuan Zhang, 2011, ''The Design of Smart Battery Management Systems '', Journall Of Computers, Vol.6, No.11, 2484-2490.

[10] Chi-Ying Liang, Wai-Hon Lin, Bruce Chang, 2006, ''Applying Fuzzy Control To An Electric Bicycle'', First İnternational Conference on Innovative Computing, Information and Control, Beijing, 30 Aug. 2006+-1 Sept. 2006,513-516

[11] Lechner, G. and Naunheimer, H. , Automotive Transmissions—Fundamentals, Selection, Design and Application, Springer, Berlin, Germany, 1999.

[12] Shinn-Ming Sue, Yi-Shuo Huang, Jhih-Sian Syu, Chen-Yu Sun, 2010,'' A bi-directional power flow IPM-BLDC motor drive for electrical scooters'',5th IEEE Conference on Industrial Electronics and Applications, Taichung, 15-17 June 2010, 1330-1334.

Temporal Trends of Extreme Precipitation and Temperature Indices

C. KOYCEGIZ[1*] and M.BUYUKYILDIZ[1]

[1*]Konya Technical University, Konya/Turkey, ckoycegiz@ktun.edu.tr
[1]Konya Technical University, Konya/Turkey, mbuyukyildiz@ktun.edu.tr

***Abstract* – In this study, 45 years of daily total precipitation, daily minimum and maximum temperature data between 1975-2019 belonging to Niğde station (No: 17250) operated by the State Meteorology Office were used. A total of 8 precipitation and temperature indices were applied to these data. The changes of the determined index values were examined using Mann-Kendall and Mann-Kendall Rank Correlation tests. As a result of the application, a generally significant increase was observed in the indices of both low temperature data and high temperature data. There is a significant decrease in the number of consecutive wet days (CWD) in the analyzed precipitation indices, while there is an increase in the other precipitation indices, although there is no significant trend.**

***Keywords* – Mann-Kendall, precipitation, temperature, trend**

I. INTRODUCTION

CLIMATE is one of the most important components in our daily life. Knowing the climate of a region is very important in terms of managing the weather events that occur in that region in terms of benefits and harms. Average conditions, which have not changed for many years, are not sufficient to understand the climate. In addition, extreme values and related events should be known. In this way, it will be possible to reach more comprehensive information on how and how often the climate can oscillate [1].

It is observed that there are changes in temperature increases and precipitation regimes due to global warming, which affects the entire ecosystem. In our country, there are great differences in the amount of precipitation that varies according to the seasons throughout the year [2].

Precipitation and temperatures are the two main factors that make up the duality. For this reason, processing and monitoring of the recorded data as a result of intensive monitoring of precipitation and temperature data constitutes an important element [3]. Climate indices are the most important impact parameter of climate change studies, which are widely used in many disciplines and especially when extreme events are taken into account [4, 5].

Extreme precipitation and temperatures, precipitation and temperature indices, meteorological and climatological disasters such as heavy rains and floods and the effects of these disasters on human life and quality of life have been studied by many researchers [6, 7, 8, 9, 10, 11].

In this study, 8 climate indices were used among 27 indices prepared by The Expert Team on Climate Change Detection (ETCCDI). The climate indices were determined for the precipitation and temperature data of the Niğde meteorology station between 1975 and 2019, and the trend of the obtained indices in the observation period was examined.

II. DATA AND METHODOLOGY

A. Data

The Niğde meteorology station (No: 17250), whose data were used in the study, is located in the Konya Closed Basin. The Niğde station is located at 37°57' North latitude, 34°40' East longitude and its altitude is 1195 m. Within the scope of the study, daily total precipitation (P), daily minimum temperature (T_{min}) and maximum temperature (T_{max}) data for the period 1975-2019 measured in the Niğde station were used. Statistical properties of the data used are given in Table 1.

Table 1: Statistical characteristics of the data used

Parameter	minimum	maximum	mean	Standard Deviation
Daily total precipitation (mm)	0	54.5	3.03	4.78
Daily minimum temperature (^oC)	-24.2	25	5.45	7.83
Daily maximum temperature (^oC)	-10.9	38.5	17.77	9.94

B. Extreme Climate Indices and Trend Methods

In the analysis of climate indices of precipitation and temperature data, 8 of 27 extreme climate indices defined by The Expert Team on Climate Change Detection (ETCCD) [12] were used. These indices are annual or monthly statistics of modeled or observed climate data. Detailed information about indices is given by Zhang et al. [13]. Among these indices where the effects of climate change can be observed, the ones used in this study for daily temperatures and precipitation are given in Table 2.

Table 2: Temperature and precipitation indices used

Indice Code	Name	Definition
Precipitation		
Rx1day	Maximum 1-day precipitation	Annual maximum 1 day precipitation
Rx5day	Maximum 5-day precipitation	Annual maximum consecutive 5-day precipitation
CDD	Number of consecutive dry days	Maximum number of consecutive dry days with RR<1 mm
CWD	Number of consecutive wet days	Maximum number of consecutive wet days with RR≥1 mm
Temperature		
TXx	Warmest days	Maximum values of daily maximum temperature
TXn	Coldest days	Minimum values of daily maximum temperature
TNx	Warmest nights	Maximum values of daily minimum temperature
TNn	Coldest nights	Minimum values of daily minimum temperature

The Mann Kendall (MK) test [14] is a non-parametric test and is a special application of the test known as Kendall's Tau. The Mann-Kendall test is a test that does not require normal distribution of data and has low sensitivity to abrupt breaks due to inhomogeneous time series. This method is based on the rank of the data rather than its value [15]. If $|z| \leq Z_{critical}$ at the chosen α significance level, the Ho hypothesis is accepted, otherwise it is rejected. If the calculated z value is positive, there is an increasing trend, and if it is negative, there is a decreasing trend. This method is useful because it allows the existence of missing data and does not require the data to fit a certain distribution [14]. The Mann Kendal Rank Correlation (MKRC) Test, on the other hand, is a non-parametric test that is used to determine whether there is an increase or decrease over time in the examined series, the results of which are expressed graphically [16]. It can also determine the starting point of the trend. Positive values of the test statistic (u(t)) indicate an increasing trend over time, while negative values (u(t)<0) indicate a decreasing trend over time. When u(t) reaches critical values corresponding to the significance level, it indicates that the confidence level of the trend is significant. Graphically, u(t) and u′(t), which is calculated as a backward test statistic, converge at the point where the change starts, and then diverge from each other, showing their significance with the point where the trend started. If there is no trend in the series, u(t) and u′(t) oscillate closely by approaching each other many times. Detailed information and formulation of both methods are available in many studies in the literature [10, 15, 17, 18, 19].

III. Application and Result

A. Trend Results of Extreme Precipitation Indices

MK and MKRC tests were applied to the RX1day, RX5day, CWD and CDD precipitation indices calculated for the daily precipitation data of Niğde meteorology station for the period 1975-2019. In this study, ¸α=0.05 significance level was used. MK results are given in Table 3.

Table 3: Results of Mann Kendall for precipitation indices

Indice code	Mann-Kendall Statistic (S)	Test Statistic (Z)	p-value	Result
RX1day	7799	1.86	0.063	Insignificant positive trend
RX5day	6290	1.50	0.133	Insignificant positive trend
CWD	20	0.19	0.853	Insignificant positive trend
CDD	-320	-3.12*	0.002	Significant negative trend

**Statistically significant at 95% confidence level ($z_{critical}$=1.96 for 05)*

According to Table 3, since the Z values found for the RX1day, RX5day and CWD indices are lower than 1.96 (critical value at α=0.05 significance level) and at the same time positive, there is an insignificant positive trend in these indices. The MK statistical S value calculated for these indices was also positive. This indicates an increasing trend. In CDD index, both S value and z value are negative.

Therefore, there is a decreasing trend in the CDD index. Since z=|-3.12|>1.96, this increase is significant according to α=0.05 significance level.

According to the P values in Table 3, it can be evaluated that there is a trend in the CDD index because p<0.05, and there is no trend because p>0.05 in other indices.

The MKRC results for RX1day, RX5day, CWD and CDD precipitation indices are given in Figure 1. In the RX1day (Fig 1a) and RX5day (Fig 1b) indices, the u(t) curve shows an increasing trend from negative values to positive values, while there is a decrease from positive values to negative values in u′(t) curves. This situation reveals that there is an increasing trend. The intersection point of the u(t) and u′(t) curves in the RX1day and RX5day indices were determined as 2003 and 2004, respectively. In the CWD (Fig 1c) index, the two curves intersected in 2018 and showed a very small insignificant increase. In CDD index (Fig 1d), on the other hand, the u(t) curve shows a decreasing trend from positive values to negative values, while the u′(t) curve increases from negative values to positive values. This situation reveals that there is a downward trend. After both curves intersect in 2005, a decrease occurred and turned into a significant decrease. The results in Table 3 and Figure 1 support each other.

.

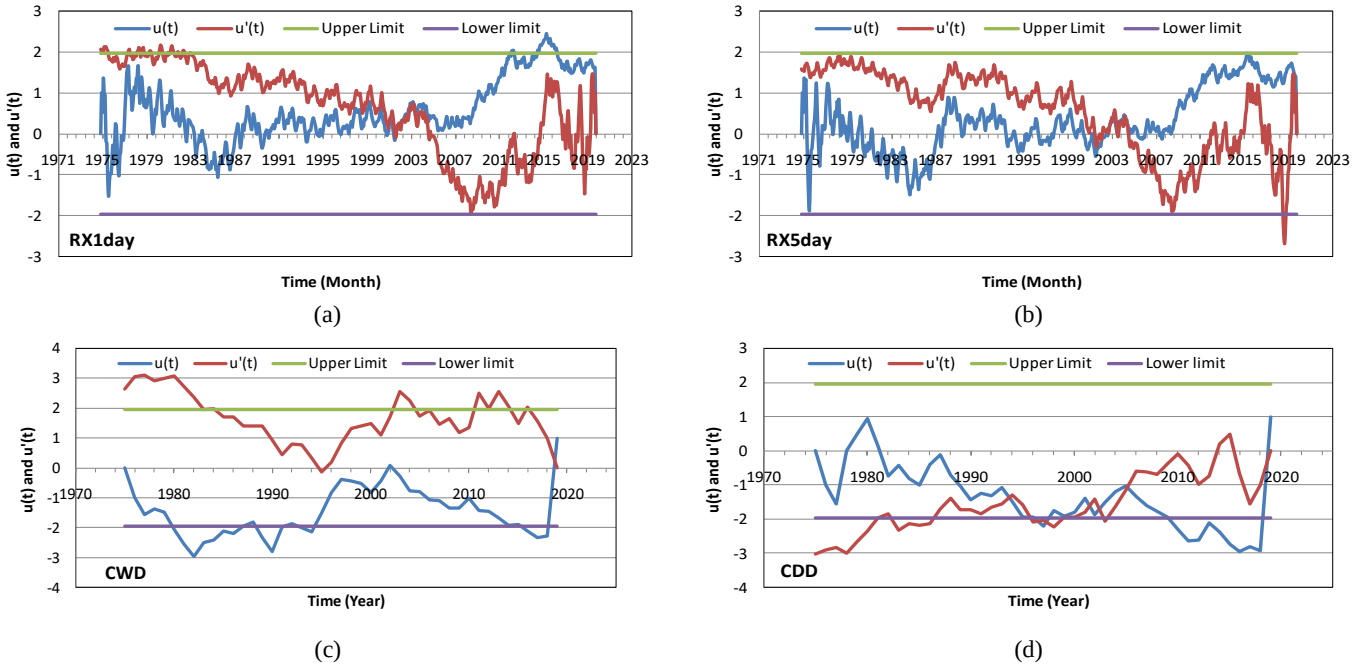

Figure 1: The graphics of Mann-Kendall Rank Correlation Test for extreme precipitation indices a) RX1day, b) RX5day, c) CWD, d) CDD

B. Trend Results of Extreme Temperature Indices

Among the temperature indices used in this study, TXx and TXn were calculated using daily maximum temperature data, and TNx and TNn indices were calculated using daily minimum temperature data. The MK test results applied to the obtained index values are given in Table 4. According to Table 4, since all S and Z values are positive, there is an increasing trend in temperature indices. However, since the TXn index is z=1.95<1.96 (p=0.051>0.05), there is an insignificant upward trend in this index. In other temperature indices, z values are >1.96 (p values <0.05) and there are significant increasing trends.

Table 4: Results of Mann Kendall for temperature extreme indices

Indice code	Mann-Kendall Statistic (S)	Test Statistic (Z)	p-value	Result
TXx	9707	2.32*	0.021	Significant positive trend
TXn	8160	1.95	0.051	Insignificant positive trend
TNx	8428	2.01*	0.044	Significant positive trend
TNn	8435	2.01*	0.044	Significant positive trend

**Statistically significant at 95% confidence level ($z_{critical}$=1.96 for α = 0.05)*

The MKRC results for the temperature indices are given in Figure 2. In all temperature indices, the u(t) curve shows an increasing trend from negative values to positive values, while the u′(t) curve shows a decrease from positive values to negative values. This indicates that there is an increasing trend.

According to the intersection points of the u(t) curves and u′(t) curves in Figure 2, the trend starting years for the TXx, TXn, TNx and TNn indices were determined as 2005, 2012, 1997 and 2007, respectively.

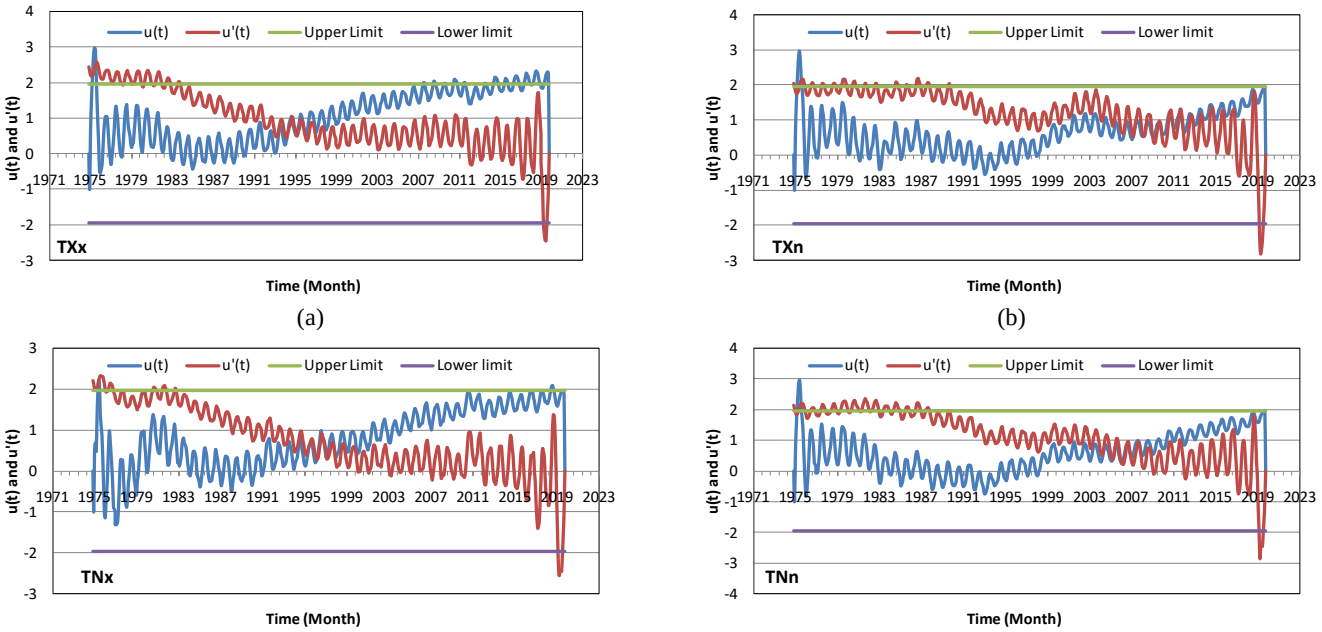

Figure 2: The graphics of Mann-Kendall Rank Correlation Test for extreme temperature indices a) TXx, b) TXn, c) TNx, d) TNn

IV. Conclusion

In this study, the temporal variation of precipitation and temperature indices of Niğde meteorological station for the period 1975-2019 was analyzed. For this purpose, 4 precipitation indices (RX1day, RX5day, CWD, CDD) and 4 temperature indices (TXx, TXn, TNx, TNn) were used.

Mann-Kendall and Mann-Kendall Rank Correlation tests were used for trend analysis of temperature and precipitation indices. As a result of trend analysis in precipitation indices, a statistically significant decrease trend was observed in the CDD index at the 95% confidence level. Non-significant increasing trends were determined in the RX1day, RX5day and CWD indices. An increasing trend has been determined in all temperature indices, and the increasing trend in the TXn index is insignificant, while the increasing trend in other temperature indices is significant.

In Turkey, especially in regions where agriculture is very important, analysis of precipitation and temperature data is important. By analyzing the precipitation and temperature data of the Central Anatolia Region, one of the first regions that come to mind when agriculture is mentioned, more effective results can be obtained in agriculture, so both the country's economy and the welfare of the people of the region will increase.

References

[1] F. Batıbeniz, "Yüksek çözünürlükteki bölgesel iklim modeli simülasyonu ile ekstrem iklim indekslerinin belirlenmesi" Yüksek Lisans Tezi, İstanbul Teknik Üniversitesi, Fen Bilimleri Enstitüsü, Meteoroloji Mühendisliği Anabilim Dalı, İstanbul, Türkiye, 2014.

[2] M.F. Emek, "Doğu Anadolu Bölgesi yıllık ve aylık toplam yağışların trend analizi" Yüksek Lisans Tezi, Atatürk Üniversitesi Fen Bilimleri Enstitüsü İnşaat Mühendisliği Anabilim Dalı, Erzurum, Türkiye, 2014.

[3] R. Acar, and S. Şenocak, S. (2008, April). "Detection of statistically significant trends in the short duration rainfalls (SDR) of Adana City," *EGU General Assembly* 2008: I522-H52.1 Session on Climate, Water and Health. Vienna

[4] L.V. Alexander, X. Zhang, T.C. Peterson, J. Caeser, B. Gleason,A.M.G. Klein Tank, M. Haylock, D. Collins, B. Trewin, F. Rahimzadeg, A. Tagipour, K. Rupa Kumar, J. Revadekar, G. Griffiths, L. Vincent, D.B. Stephenson, J. Burn, E. Aguilar, M. Brunet, M. Taylor, M. New, P. Zhai, M. Rusticucci, J.L. VazquezAguirre, "Global observed changes in daily climate extremes of temperature and precipitation", *Journal of Geophysical Research, 111*:D05109, 2006.

[5] E.M. Fischer, K.M., Oleson, D.M., Lawrence, "Contrasting urban and rural heat stress responses to climate change," *Geophysical Research Letters*, vol. 4, pp.1-8, 2013.

[6] Y. Tramblay, S. El Adlouni, S., and E. Servat, "Trends and variability in extreme precipitation indices over Maghreb countries," *Natural Hazards and Earth System. Sciences*, vol. 13 (2), pp. 3235–3248, 2013.

[7] I. de Lima, M.F.E. Santo Coelho, A.M. Ramos, and R.M. Trigo, "Trends and correlations in annual extreme precipitation indices for mainland Portugal, 1941 2007," *Theoretical and Applied Climatology*, vol, 119, pp. 55-75, 2015.

[8] R.C. Balling, M.S.K. Kiany, S.S. Roy, and J. Khoshhal, "Trends in extreme precipitation indices in Iran: 1951–2007," *Advances in Meteorology*, pp. 1–8, 2016.

[9] H. Tongal, "Spatiotemporal analysis of precipitation and extreme indices in the Antalya Basin, Turkey," *Theoretical and Applied Climatology*, vol. 138, pp. 1735–1754, 2019.
[10] A.S. Bhatti, G. Wang, W. Ullah, S. Ullah, D.F. Tawia Hagan, I.K. Nooni, . . . I. Ullah, "Trend in extreme precipitation indices based on long term In situ precipitation records over Pakistan," *Water*, vol. 12, pp. 1-19, 2020.
[11] A.A. Shawul and S. Chakma, "Trend of extreme precipitation indices and analysis of long-term climate variability in the Upper Awash basin, Ethiopia," *Theoretical and Applied Climatology*, vol. 140, pp. 635–652, 2020.
[12] https://www.wcrp-climate.org/data-etccdi
[13] X. Zhang, L. Alexander, G.C. Hegerl, P. Jones, A. K. Tank, T.C. Peterson, et al., "Indices for monitoring changes in extremes based on daily temperature and precipitation data," *WIREs Climate Change*, vol. 2, pp. 851–870, 2011.
[14] S. Yu, S. Zou, S. and D. Whittemore, D, "Non-parametric trend analysis of water quality data of rivers in Kansas," *Journal of Hydrology*, vol. 1, pp. 61-80, 1993.
[15] T. Partal and E. Kahya, "Trend analysis in Turkish precipitation data," *Hydrological Processes*, vol. 20, pp. 2011–2026, 2006.
[16] G. Ceribasi, E. Dogan, U, Akkaya, and U. Kocamaz, "Application of trend analysis and artificial neural networks methods: The case of Sakarya River," *Scientia Iranica*, vol. 24(3), pp. 993-999, 2017.
[17] J.M. Kampata, B.P. Parida, D.B. Moalafhi, "Trend analysis of rainfall in the headstreams of the Zambezi River Basin in Zambia," *Physics and Chemistry of the Earth, Parts A/B/C*, vol. 33 (8-13), pp. 621-625, 2008.
[18] Y. Wu, W. Wang, and G. Wang, "Detecting variation trends of temperature and precipitation for the Dadu River Basini Chine," *Advances in Meteorology*, Article ID 2564586, 2016.
[19] E. Kahya and S. Kalayci, "Trend analysis of streamflow in Turkey," Journal of Hydrology, vol. 289(1-4), pp.128-144, 2004..

Bézier and B-spline Curve Definition of Outer Boundary of an Object Template Using Sequential Edge Points

N. ARSLAN[1] and K. GÜRKAHRAMAN[2]

[1] Sivas University of Science and Technology, Sivas/Turkey, nihat58@hotmail.com
[2]Sivas Cumhuriyet University, Sivas/Turkey, kgurkahraman@cumhuriyet.edu.tr

Abstract **- Bézier and B-spline curves, which are defined parametrically, initially provided great convenience and precision in the design of automobile bodies. Today, these curves are also used in the fields of image processing and computer vision. Segmentation of an object in an image can be made using these parametric curves, including their different scales and orientations. For this, Bézier and B-spline curves can be generated using a cloud of points representing the outer boundary of a representative template of this object. The prerequisite for this process is that the points in the point cloud must be obtained sequentially. In this study, an algorithm has been developed that sequentially obtains the points constituting the outer boundary of the template belongs to the object to be searched in the image. This algorithm, unlike the other contour tracing algorithms in the literature, was implemented using a filter containing weights. It produces a unique numerical value that determines the next tracking direction thanks to the filter weights located at a certain position in the image whose edges are determined in binary format. After obtaining the ordered points, the control points determining the curve shape were obtained by reducing the number of ordered points. Thus, using these control points, the Bézier and B-spline curve equations, which define the outer boundary curve of the template, are obtained. It has been shown that by changing the positions of the control points, the template can be created in different translation, scaling and orientation, and also thanks to these curves, the missing part of the object can be completed. As a result, a template with outer boundary defined by Bézier and B-spline curves was created to be used in object recognition and segmentation processes especially in computer vision.**

Keywords **– Bézier curve, B-spline curve, Contour tracing algorithm, Template matching, Object recognition.**

I. INTRODUCTION

Calculation of geometric shapes is performed using computer aided geometric design. Curves are the basic shapes we use to describe and calculate geometric shapes. For example, curves can be used to describe, create and model alphanumeric characters, surfaces and volumes of objects [1]. Splines are very common curves and consist of several low-order polynomial curves that fit together. Like polynomials, splines play an important role in applied mathematics, numerical analysis, geometric modeling, and many other fields. At the same time, template shapes can be defined using these parametric curves. Template matching is one of the methods used to detect a certain object in an image in image processing and computer vision [2,3]. If the template of the object to be searched in the image exists, the curve equation defining the outer boundary of the object can be obtained. It is very difficult to develop scaling and rotation-invariant algorithms in object detection and recognition studies. An approach can be developed to overcome the scaling and rotation problems using the equation defining the outer boundary of the template. If the shape of the object template is obtained using the commonly used Bézier and B-spline parametric curves, any scale and orientation angle of the template can be achieved by changing the control points of the curves. The Bézier and B-spline curve equations can also fill the missing part of the object to be searched in the image due to reasons such as the shooting angle, the presence of a different object, or image defects. Because of these advantages they provide, in this study, expressing the template shape using these curves has been carried out.

In order to express the outer boundary of a template with curve equations, the points in the point cloud revealed by the edge detection algorithms must be sequenced. Square Tracing Algorithm, Moore-Neighbor Tracing, Radial Sweep, and Theo Pavlidis' Algorithm are the most widely used outer boundary tracing algorithms [4] in the literature to detects the boundary points sequentially. These algorithms have strengths and weaknesses. For example, most boundary tracing algorithms fail to find the boundaries of gaps in the pattern, and some algorithms perform unnecessary movements during boundary tracking. In this study, an algorithm has been developed that sequentially obtains the points constituting the outer boundary of the template of the object to be searched in the image. Unlike the methods in the literature, this algorithm uses a unique numerical value generating filter to determine the next tracing direction at a certain location in the binary image.

II. PARAMETRIC CURVES

Parametric curves can be defined as the movement of the point in a given time interval. A curve defined parametrically is a set of positions based on a continuous time variable. Parametric representations include Bézier curves, Bézier surfaces, B-spline curves, B-spline surfaces and Non-Uniform Rational B-Spline (NURBS) curves and surfaces. Parametric

curves and surfaces are compact representations and are easy to manipulate the shape of the surface. Bézier and B-spline curves were used in this study.

A. *Bézier Curves*

Bézier curves are parametric curves widely used especially in computer graphics [5, 6]. The curve is named by French engineer Pierre Bézier. He used Bézier curves in designing curves for the bodywork of cars. The equation of n^{th} degree Bézier curves with n+1 control points is expressed as in (1):

$$P(t) = \sum_{i=0}^{n} P_i \frac{n!}{i!(n-i)!} t^i (1-t)^{n-i} \quad (1)$$

where P_i are the control points and t is the time in [0, 1] interval. For example, a third-degree (n=3) Bézier curve is defined by 4 (n+1) control points (P_0, P_1, P_2 and P_3), and substituting n value in the above equation yields the following cubic curve equation in (2), which is commonly used, and samples of cubic curves are given in Figure 1 [7]:

$$P(t) = (1-t)^3 P_0 + 3(1-t)^2 t P_1 + 3(1-t) t^2 P_2 + t^3 P_3 \quad (2)$$

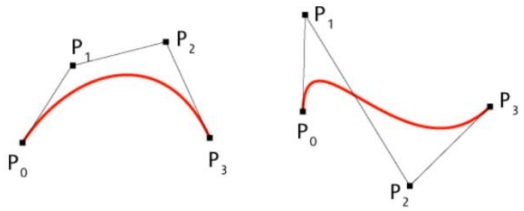

Figure 1: Samples of cubic Bézier curves with control points.

B. *B-spline Curves*

The B-spline curve was developed to overcome some of the disadvantages of the Bézier curve. B-spline curves are more general curves than Bézier curves and a Bézier curve is a special case of a B-spline curve. The biggest difference between B-spline and Bézier curves is smoothness. A B-spline curve consists of several smoothly joined curve segments as seen in Figure 2, while a Bézier curve is an entire curve. B-spline curves provide local control while Bézier curves provide only global control. Since the functions used by B-spline curves are equal to zero except for their segments, the shape of the curve depends only on its control points located in the related segment. In other words, when we change the position of any of the relevant control points in Bézier curves, the entire curve is affected, while only a certain segment of the curve is affected in B-spline curves.

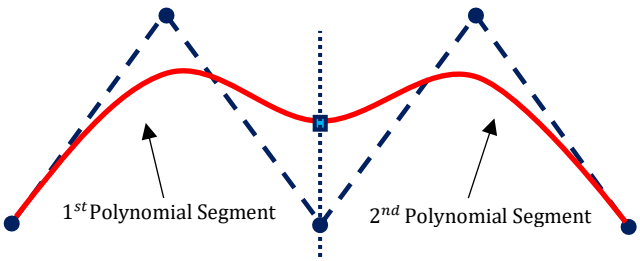

Figure 2: A B-spline curve with two segments.

In Bézier curves, the degree of the curve depends on the number of control points, while in B-spline curves it is independent of the number of control points, and the degree of the curve is one less than the order (k-1). The relationship between the number of control points and the order of the curve determines how many polynomial segments the curve will consist of. Hence, the order of the B-spline curve indicates the number of control points to be in each polynomial segment. Defining the B-spline curve with more control points than the number of orders leads to an increase in the number of segments in the curve. Each new control point will add an extra segment to the curve. We can increase the number of control points as much as we want by using lower order curves in B-splines. The mathematical representation of B-spline curves is very similar to the Bézier curves and the $P(u)$ curve defined by n+1 P_i control points is calculated by the Cox-de Boor algorithm, which runs recursively according to the node vector input.

$$P(u) = \sum_{i=0}^{n} P_i N_{i,k}(u) \quad (3)$$

where $u_{min} \leq u \leq u_{max}$ and order k is in the interval $2 \leq k \leq n+1$. P_i in the equation represents the control points and $N_{i,k}(u)$ are the basis functions of B-splines of k order. In a B-spline curve, each control point is associated with the basis function $N_{i,k}(u)$. Cox-deBoor recursive functions form the basis of B-spline curves, and the transition functions of B-spline curves are calculated using Cox-deBoor functions:

$$N_{i,k}(u) = \frac{u - t_i}{t_{i+k-1} - t_i} N_{i,k-1}(u) + \frac{t_{i+k} - u}{t_{i+k} - t_{i+1}} N_{i+1,k-1}(u) \quad (4)$$

The equation (5) is valid for all k=1 basis functions.

$$N_{i,1}(u) = \begin{cases} 1, & t_i \leq u < t_{i+1} \\ 0, & otherwise \end{cases} \quad (5)$$

For the calculation of k-order basis function $N_{i,k}(u)$ in equation (4), all basis functions less than k including the 1st order, can be calculated recursively.

III. Contour Tracing Algorithm

In computer vision, one of the methods for object recognition is using template of an object to be detected in an image. Cross correlation and sum of absolute differences are widely used methods for template matching [2]. The main difficulties in these methods are the gray level differences between the template and image, and deformed shape arising from different scaling and orientation. Using a method that changes scaling and orientation and does not use gray level values, we can overcome these problems. For this, Bézier or B-spline curves fitting the outer boundary points of the template may be a good solution for scaling and orientation. The points in the outer boundary point cloud must be put in order to create these curve equations. Although boundary detection algorithms such as Canny, Sobel, and Prewitt detect all edges in the image according to predefined threshold values, there is no option to

detect only the outer boundary points in a sequential manner. In this study, we develop a contour tracing algorithm to detect the outer boundary points in an order using binary image of the template. The algorithm, unlike the other contour tracing algorithms [4] in the literature, uses a filter containing weights. The filter was used to score a specific location in the binary image in order to determine the next tracing direction using the filter weights.

A. *Scoring Method*

In this algorithm, the image to be processed is a binary image in 8-bit format with object edges found, background black (0) and points belonging to the object or object boundaries white (255). The filtering at a specific location in the image g is given in equation (6). The filter weights and the image part being filtered is shown in Figure 3. T value of the filtering output is the unique numerical value that determines the next tracing direction.

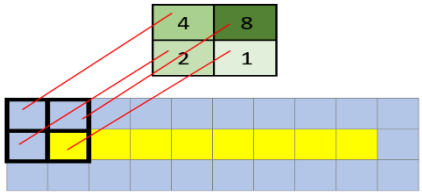

Figure 3: Filter weights and image region that the filter is located.

$$T = \sum_{i=0}^{1} \sum_{j=0}^{1} g(x+i, y+j) * f(i,j) \qquad (6)$$

Most contour tracing algorithms process already classified binary images. Cases to be considered are finding the starting pixel, possible neighborhood conditions of the contour pixel, determining the tracing direction, and stopping criteria. Problems in such algorithms are mostly related to neighborhood definition, unnecessary and repetitive movement, and stopping criteria. There are pixel types with 3 different colors in the image being processed. These are the black (0) pixel, the white pixel (255), and the gray (100) pixel labeled as the boundary point. Three different pixel values and four filter pixels arise 81 (3^4) different neighborhood cases. Some of these states are given in the Figure 4, and black and white are shown in different colors for clarity.

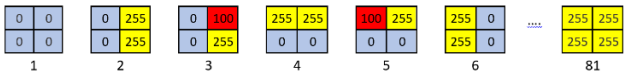

Figure 4: Neighborhood cases due to 3 pixel types at the filter location.

B. *Tracing Direction and Pixel Labeling*

Possible image pixel values and corresponding tracing directions at filter locations are shown in Figure 5. Experimentally, we noticed that most of the neighborhood cases at filter location did not occur, so only the ones that are likely to occur are shown in the figure.

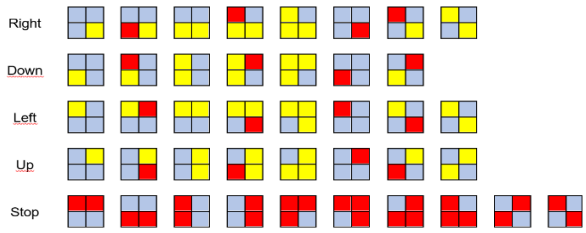

Figure 5: 2x2 image pixel values and corresponding next tracing direction.

In order to maximize the computational speed of the algorithm, instead of using conditional expressions such as switch-case and if-else for 81 cases, the array structure was used. Two arrays used in the algorithm and sample values are as follows.

ScoreAndIndex= [(0,0), (2295,4), (1055,0), (3060,5), (2440,0), (1530,2),…, (3825,0)]
LabelingAndDirection= [[0, 0, 0, 0], [1, 1, 0, 1], [1, 0, 1, 0], [0, 0, 0, -1], [0, 1, -1, 0], [0, 0, 0, 0]]

The length of ScoreAndIndex array is 81, and each element has two values. The first value is the score of filtering obtained at a specific filter location and the second value is the index of the element to be considered in the LabelingAndDirection array, which corresponds to the score value. Each element of LabelingAndDirection array has 4 values. The first two values are row and column values of the pixel that will be labeled as boundary point. The last two values indicate the tracing direction along row and column. For example if the LabelingAndDirection array element in the index obtained from ScoreAndIndex array has [1, 1, 0, 1] values, then the image pixel at (row+1, column+1) should be labeled as boundary point (image((row+1, column+1)=100), and the next tracing direction is one pixel to the right which also means no movement along the row.

In closed curves, the algorithm ends when the entire boundary of the curve is followed and the starting point is reached, while in open curves, the algorithm ends by following the curve from the starting point of the curve to the end. Therefore, the remaining of the curve before the starting point cannot be followed. For the solution of this problem, when the algorithm reaches the end of the curve with the forward (clockwise direction) tracing and is terminated, the algorithm is restarted at the starting point with reversing the moving direction (counter clockwise) in order to trace the remaining part. In Figure 6, an example of open counter curve and its tracing in both directions are given. So the definition of tracing direction has to made in clockwise and counter clockwise movements. Thus, in any open curve, whichever point of the curve is chosen as the starting point, boundary points can be obtained sequentially by following the boundary from the beginning to the end of the curve. Table 1 shows the pixel labeling with respect to tracing direction.

Figure 6: From left to right: open counter curve to be traced, the result of clockwise tracing and result of both clockwise and counter clockwise tracing.

Table 1: Pixel labeling with respect to tracing direction.

Direction	Index	Tracing step		Pixel to label			
				Clockwise		Counter clockwise	
		row	column	row	column	row	column
Right	1	0	1	1	1	0	1
Down	2	1	0	1	0	1	1
Left	3	0	-1	0	0	1	0
Up	4	-1	0	0	1	0	0

IV. Experimental Results

In this study, binary images taken from the tracing algorithm studies [8-10] were used. In binary images, the pixels of the object or edges were converted to 255 gray value in order to use our filter resulting unique value for determining the next tracing direction. Binary images were processed with the developed tracing algorithm. Figure 7 shows the binary images including template objects [8] and output images of tracing algorithm. The results show that the edge points detected by the tracing algorithm highly represent the outer boundaries of the templates.

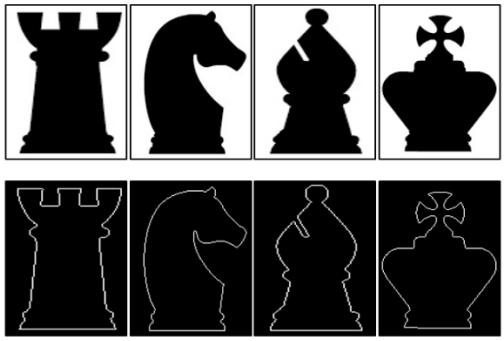

Figure 7: First row: Binary images, second row: Boundaries detected by contour tracing algorithm.

The object boundary can be reconstructed using parametric curve created with fewer edge points (dilution) than the points in the tracing algorithm output image. The number of edge points from output of tracing algorithm used as control points to create B-spline and Bézier curves can be seen in Table 2 for 6 samples given in this paper. As can be seen from the table, B-spline curves require much fewer control points for reconstruction compared to Bézier curves.

With the contour tracking algorithm developed, the boundary points of any object in the images are obtained sequentially, and instead of using all of these points, Bézier and B-spline curves were created using points selected at certain intervals as control points. The reconstructions of the samples using these parametric curves can be seen in Figure 8. From the results obtained, we conclude that local control of curves in segments in B-spline curves, achieves better reconstructions of samples than the ones obtained using Bézier curves. The reconstruction output images obtained using Bézier curve shows more deformations in boundaries.

Table 2: Point dilution with respect to output of tracing algorithm.

Sample	Number of edge points in tracing algorithm output	Number of edge points (control points) used to create curves	
		For B-Spline	For Bézier
	2106	212	703
	588	60	295
	672	69	337
	562	58	282
	766	78	384
	1442	146	722

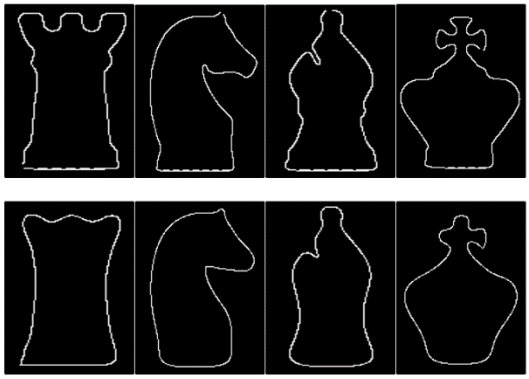

Figure 8: Reconstruction using B-Spline curves (first row) and Bézier curves.

The segmentation of the objects and their reconstructions including different scales and orientations can be performed using the parametric curves. In addition, reconstruction with fewer points (dilution) of the object used as control points can be achieved by using parametric curves to occupy less space. In Figure 9 shows reconstructions including scaling and orientation of a sample [9] using B-spline and Bézier curves by scaling and rotating the control points. The reconstruction output images of Bézier curve including scaling and orientation shows more deformations in boundaries as expected.

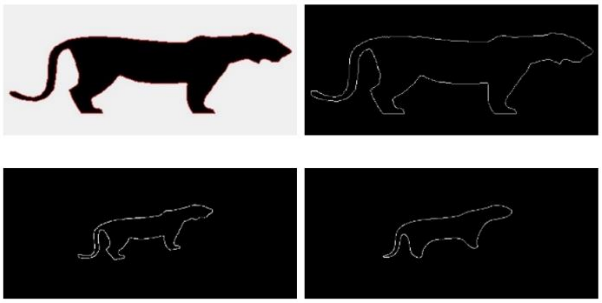

Figure 9: First row: Binary image and its contour tracing result, second row: B-spline curve and Bézier curve reconstructions including scaling and orientation.

The edge points of boundary were also translated by simply translating the control points of the curves. In Figure 10, the first and second rows shows the translation results of B-spline and Bézier curves, respectively.

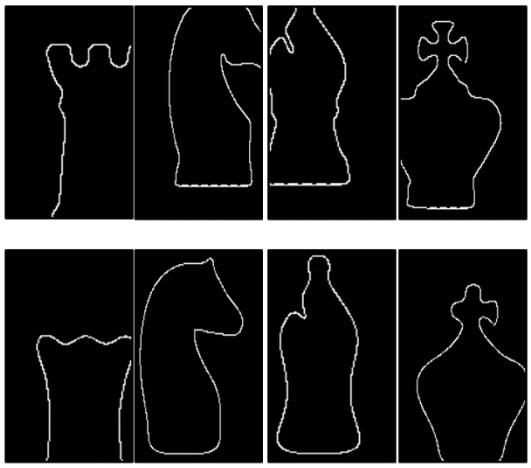

Figure 10: Translated contours using B-Spline (first row) and Bézier curves.

There may be missing part of an object in the image. By using the curve equations obtained using sufficient number of points that are well distributed along the object boundary, any missing parts of the boundary can be completed. In Figure 11, a binary input image [10] and a binary image with some points of the boundary deleted is given in first row. It can be seen in the second row of the figure, we completed the missing part using the B-spline and Bézier curves filling in these blanks with new points.

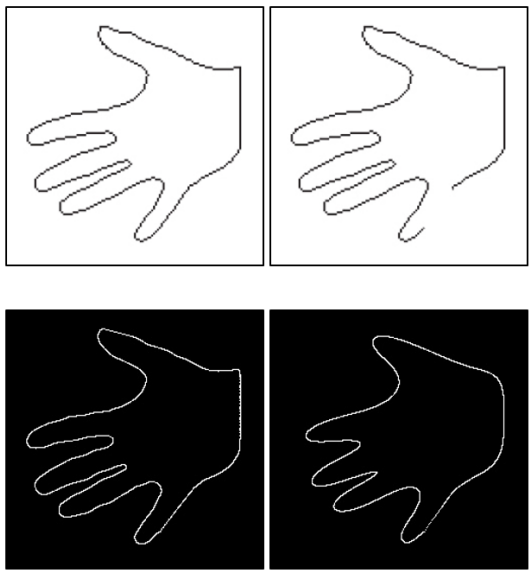

Figure 11: First row: Binary image and binary image with some points deleted, second row: reconstruction results of B-spline and Bézier curves.

V. Conclusion

In this study, a contour tracing algorithm was developed to obtained the outer boundary points of the templates in binary images. For this, a filter with weights was used to obtain a unique value determining the next tracing direction. According to the results, we can say that the tracing algorithm works well for simple template shapes. Then, the diluted points were used as control points to create the B-spline and Bézier curve equations in order to represent the template shapes. The results show that the B-spline curve representation of the template shape is better than Bézier curve due to its local segment control. The dilution of points results deformations in the reconstructed boundaries of the template using Bézier curve equations. This is because in Bézier curves, if any control point is deleted or its location is changed, the entire curve is affected. We have also reconstructed the shapes of the sample template objects in different translation, scaling and orientation angles by changing the control point locations used in the B-spline and Bézier curves.

In the next study, we will improve the tracing algorithm to obtain the outer boundaries of more complex template shapes including separate boundary parts in binary image. We will also use the curve equations for template matching considering scaling and rotation problems.

References

[1] M. Samuelčík, "Bézier and B-spline volumes," Project of Dissertation, Department of Algebra, Geometry and Didactics of Mathematics, Faculty of Mathemathics, Physics and Informatics, Comenius University, Bratislava, 2005.

[2] T. Mahalakshmi, P. Swaminathan, and R. Muthaiah, " An Overview of Template Matching Technique in Image Processing," *Research Journal of Applied Sciences, Engineering and Technology*, vol. 4, pp. 5469-5473, 2012.

[3] M. J. Atallah, "Faster image template matching in the sum of the absolute value of differences measure," *IEEE Transactions on Image Processing*, vol. 10, no. 4, pp. 659–663, 2001.

[4] J. Seo, S. Chae, J. Shim, D. Kim, C. Cheong, and T. Han, "Fast Contour-Tracing Algorithm Based on a Pixel-Following Method for Image Sensors," *Sensors*, vol. 16, pp. 353, 2016.

[5] E. Ülker, "Yapay Zeka Teknikleri Kullanılarak Yüzey Modelleme," Ph.D. dissertation, Selçuk University, Graduate School of Natural and Applied Sciences, Department of Electrical and Electronics Engineering, 2007.

[6] G. Farin, *Curves and surfaces for CAGD: A Practical Guide*, San Francisco, Fifth Edition, Morgan Kaufmann, 2002.

[7] Available: http://www.e-cartouche.ch/content_reg/cartouche/graphics/en/html/Curves_learningObject2.html.

[8] Y. Batko and V. Dyminskyi, *Fast Contour Tracing Algorithm Based on a Backward Contour Tracing Method*, Department of Computer Science, Ternopil National Economic University, Ukraine, 2018.

[9] J. Rao, J. Lin, S. Xu, and S. Lin, "A New Intelligent Contour Tracking Algorithm In Binary Image," *2012 Fourth International Conference on Digital Home*, 2012. Available: https://ieeexplore.ieee.org/document/6376377

[10] N. L. Narappanawar, B. M. Rao, T. Srikanth, and M. A. Joshi, "Vector Algebra Based Tracıng Of External And Internal Boundary Of An Object In Bınary Images," *Journal of Advances in Engineering Science*, Section C (4), pp. 57-70, January - June 2010.

The Effect of Specimen Size and Preparation Method on the Mechanical Properties of Ti-6Al-4V Sheets

Habip Gokay KORKMAZ [1,2], Serkan TOROS [1] and Mevlut TURKOZ [2]
[1] Nigde Omer Halisdemir University, Nigde/Turkey, hkorkmaz@ohu.edu.tr
[1] Nigde Omer Halisdemir University, Nigde/Turkey, serkantoros@ohu.edu.tr
[2] Konya Technical University, Konya/Turkey, mturkoz@ktun.edu.tr

Abstract **- In this study, a research is conducted to determine the effects of tensile test specimens prepared from 0.5 mm thick Ti-6Al-4V material, which is widely used in aviation industry, and the effects of preparation method on yield strength, ultimate tensile strength and fracture strain. In the experiments, tensile specimens of two different sizes in ASTM-E8 standard and cutting processes with laser, waterjet and Electrical Discharge Machining (EDM) are selected as preparation methods. When the results obtained from the tensile tests are evaluated, it is seen that the stress and strain values obtained as a result of repeated tests are more consistent in the samples cut with waterjet, while relatively inconsistent results are obtained from the samples of other cutting processes. It is also determined that the sample size affects the stress strain values at some extend.**

Keywords **- Ti-6Al-4V, Laser Cutting, Waterjet, Electrical Discharge Machining, Tensile Test**

I. INTRODUCTION

IN order to determine the mechanical properties of engineering materials, test setups such as uniaxial tensile test, biaxial tensile test and bulge test are generally used. The specimens used in these tests are prepared according to the dimensions specified in the standards. [1-3]. The specimens can be manufactured by laser, waterjet, cutting die, Electrical Discharge Machining (EDM) etc. These methods contain differences from each other in terms of application, and there are many studies on the working principles and details of these methods. [4-6]. The tensile test samples should have the same properties as the material removed from the plate material. Otherwise, the results may be misleading.

There are many factors that affect this situations, and the major ones are:

- Heat
- Surface roughness
- Specimen size
- Machining precision of the method

The factors mentioned above are the main factors affecting the mechanical properties of the test specimens. For example, Araújo et al. [7] carried out a study to determine the Heat Affected Zone (HAZ) of a CO2 laser-treated Al alloy and examined the laser cut part microstructurally. The team reported that laser cutting reduces the surface quality and this would affect the fatigue resistance. Zhou et al. [8] prepared tensile test specimens for DP980 material using cutting dies with different die cavities (%7t, %11t, %14t and %21t) and examined the effect of cutting surfaces on the specimen edges. They reported that the smoother and clearer the surface is, the better the results. Sergueeva et al. [9] investigated the effect of the sample size and gauge length measurement of the Ti-6Al-4V material used in this study on the Stress-Strain curve of the material and stated that the tensile test results depend not only on the material and test conditions (strain rate, temperature, etc.), but also on the sample size and geometry. In this case, the necessity of choosing the correct sample size also arises. The maximum allowable size difference and taper size in the active deformation zone are also given in the standards [1, 2]. Failure to provide this measurement accuracy may also cause an inaccurate Stress-Strain curve to be obtained.

Zhou et al. [8] used three different methods in the fabrication of the tensile test specimen: i.e. cutting die, laser and EDM. They stated that among the methods considered, EDM and laser provided a smoother and cleaner surface than the samples obtained via cutting die systems. In the study, it is also reported that in the hardness measurements performed from the areas close to the cutting edge, the samples cut with laser have higher hardness than the samples cut with EDM. As a result, it is concluded that laser cut samples could reach lower elongation values. Mäntyjärvi et al. [10] created fatigue specimens from ultra-high strength (UHS) steel using waterjet, milling, and two-laser cutting methods. It was reported that the fatigue strength of the laser cut samples was weaker than those of the other samples. Krahmer et al. [11] prepared samples using 5 mm thick Inconel 718 material in ASTM E 8 M-04 standard and AISI 1010 carbon steel material with 0.5 mm, 0.88 mm, 1.51 mm, 2.00 mm and 2.66 mm thicknesses in IRAM-IAS U500-214 standard using milling, waterjet, EDM, laser and punching methods. The authors stated that EDM and waterjet can be an alternative to milling and the laser method should be used carefully, although it is a relatively low cost and fast manufacturing method.

In this study, 0.5 mm thick Ti-6Al-4V material is prepared

in ASTM E8 subsize and standard tensile specimen sizes using laser, waterjet and EDM cutting methods and their effects on the stress strain curve and failure strains are investigated.

II. MATERIALS AND METHOD

Subsize and standard samples in ASTM E8 standard, whose technical drawings and dimensions are shown in Figure 1.a and Figure 1.b, are used to create tensile test specimens from 0.5 mm thick titanium material supplied as Grade 5.

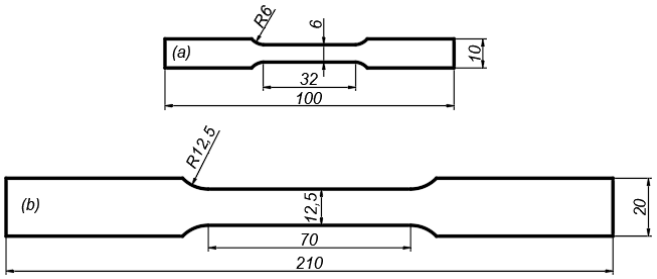

Figure 1. ASTM E8 sheet type tensile specimens
(a) Subsize specimen (b) Standard specimen

In this study, three methods, which are frequently used in practice, are preferred in sample preparation, namely laser, waterjet and EDM. In order to examine the effects of the sample size, both subsize sample and standard sample are prepared with waterjet. Samples prepared with laser are subsized, whereas samples prepared with EDM are produced in standard sizes. All experiments are performed in 5 repetitions.

Tensile tests are performed on a Shimadzu Autograph 100kN tensile device using a video extensometer. The gauge length is applied as 25 mm in subsize samples and 50 mm in standard samples as specified in the standard. Tensile tests are carried out at a strain rate of 0.001 s 1 for materials of all sizes.

III. RESULTS

The yield strength determined by 0.2% offset, tensile strength and fracture strain values from the tensile tests are given in Figure 3.a, Figure 3.b and Figure 3.c, respectively.

The yield strength, tensile strength and fracture strain values obtained by averaging the repeated test data are given in Table 1. In addition to these values, the standard deviation values given as plus and minus are obtained with 95% confidence level.

In the experiments, it is observed that considerable difference in the yield strength and UTS between the repetitions of the laser-cut subsized samples. As can be seen the standard deviations in the Table 1, between the repetitions of the laser-cut subsized samples there are differences not only in stresses but also in fracture strains. As can be seen from the table, the yield and ultimate tensile strengths are in good agreement in both subsize and standard samples cut with waterjet. Again, as in the laser cut samples, there are differences in the fracture strains in the samples cut with the waterjet. In the standard size samples cut with EDM, as in the laser cut samples, it is observed that there are differences in the yield point, plastic region and fracture strains.

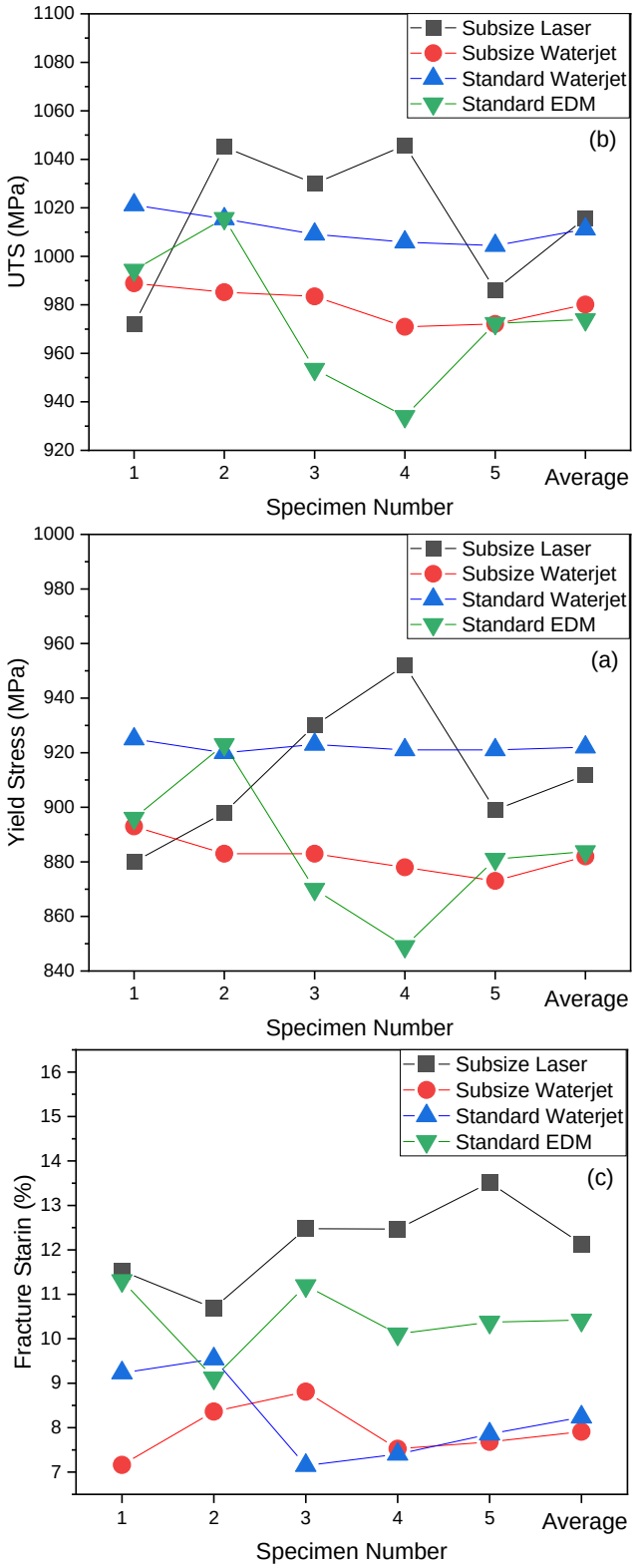

Figure 2. Average results from tensile tests (a) Yield strength (b) Ultimate tensile strength (c) Fracture strain

Table 1: Average and standard deviation values of yield stress, UTS and fracture strain obtained from different cutting methods and specimen sizes

	Yield Stress (MPa)	Ultimate Tensile Strength (MPa)	Fracture Strain (%)
Subsize Laser	911.8 ± 57.56	1015.8 ± 68.99	12.13 ± 2.14
Subsize Waterjet	882 ± 14.83	980.13 ± 16.19	7.90 ± 1.33
Standard Waterjet	922 ± 4	1011.21 ± 14	8.24 ± 2.17
Standard EDM	883.8 ± 55.63	973.97 ± 64.61	10.42 ± 1.78

IV. DISCUSSION

As can be seen in Figure 2, there are differences between the yield strengths and stresses of five repeated experiments on the samples prepared with laser. Likewise, there exist significant differences between yield strengths and stresses in samples prepared in EDM, which is another method of cutting by means of heat. However, the difference between the yield strengths and stresses of the tests performed with the samples prepared by the waterjet method, which is cut without the effect of heat, is less and at an acceptable level. One of the main reasons for this situation is too much Heat Affected Zones (HAZ) since the sample thickness is 0.5 mm and the temperature in this thin plate diffuses rapidly to the center of the sample. This causes changes in the internal structure of the material, and as a result, the mechanical properties of the material change. In the samples prepared with waterjet, it is observed that there are differences in the fracture strain values as in the samples prepared with laser and EDM. This can be based on two reasons. The first is due to the material itself. If there is any defect inside or on the surface of the sheets, it immediately breaks due to the weak hardening ability of the material as a result of local necking. The second is due to the cutting method. The occurrence of extra scratches formed by the particles of the waterjet on the cut surfaces of the material, which is already very unformable and which is significantly affected by the defects in it or on its surface, accelerates the onset of breakage.

When the test results of the subsize and standard tensile test samples prepared with waterjet are compared, it is seen that the yield and tensile strength of the subsize samples are slightly lower than those of the standard samples. Similar results are also concluded in a study conducted in the literature on the total elongation and tensile strength of the material at different gauge lengths for Ti-6Al-4V material [9]. It was reported that the relationship between gauge length and total elongation increases as the gauge length gets smaller, and the tensile strength remains almost the same (Figure 3).

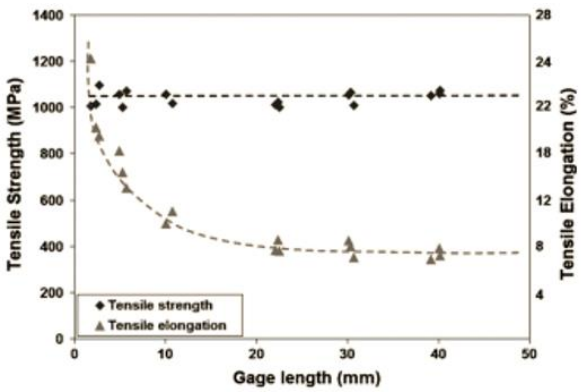

Figure 3. Relationship between the total elongation and tensile strength of the Ti-6Al-4V depending on the gauge length [9]

In Figure 4, the average yield stress, tensile stress and fracture strain values and min-max values for all cutting methods and obtained from all repetitions are given graphically. When the graph is examined, it is seen that the min-max values in laser and EDM methods, where the sample is in contact with heat, is at higher levels compared to the samples prepared with waterjet.

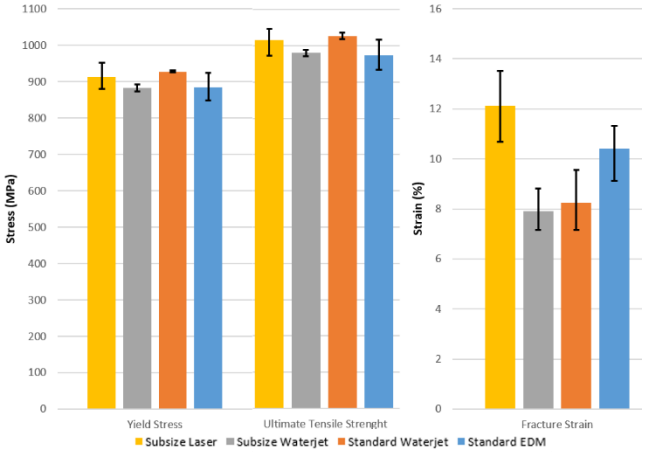

Fig. 4. Average values and error bars of yield stress, UTS and fracture strains obtained by different cutting methods

V. CONCLUSION

In this study, the effect of two different dimensions in ASTM-E8 standard tensile test specimens prepared, and cutting methods i.e laser, waterjet and EDM methods on the mechanical properties is investigated. It has been determined that the mechanical properties of the samples prepared by laser and EDM, in which the sample is in contact with heat, are affected by heat. When the results are examined in terms of refractive strains, it is seen that the standard deviations are high for all methods. It is concluded that the reason for this is due to the weak hardening ability of the material. The specimen size is also found to affect the yield and tensile strengths of the material. When preparing tensile test samples, it is recommended to use water jet and standard size sample among these three methods, since standard deviations are lower than those in other methods.

ACKNOWLEDGMENT

This study was supported by The Scientific and Technological Research Council of Turkey (TUBITAK) 1001 Project (Grant number: 219M489).

REFERENCES

[1] Standard Test Methods for Tension Testing of Metallic Materials, ASTM-E8/E8M, ASTM International, 1-27, 2009.

[2] Metallic Materials—Tensile Testing—Part 1: Method of Test at Room Temperature, ISO 6892-1, International Organization for Standardization: Geneva, Switzerland, 2019.

[3] Metallic materials-Sheet and strip-Biaxial tensile testing method using a cruciform test piece, ISO 16842, International Organization for Standardization: Geneva, Switzerland, 2014.

[4] K. Ho, S. Newman, State of the art electrical discharge machining (EDM), International Journal of Machine Tools and Manufacture, vol. 43, pp. 1287-1300, 2003.

[5] A. Lamikiz, L.L. de Lacalle, J. Sanchez, D. Del Pozo, J. Etayo, J. Lopez, "CO2 laser cutting of advanced high strength steels (AHSS)", Applied Surface Science, vol. 242, pp. 362 368, 2005.

[6] A.W. Momber, R. Kovacevic, "Principles of abrasive water jet machining", Springer Science & Business Media, 2012.

[7] D. Araujo, F. Carpio, D. Mendez, A. Garcıa, M. Villar, R. Garcıa, D. Jimenez, L. Rubio," Microstructural study of CO2 laser machined heat affected zone of 2024 aluminum alloy", Applied Surface Science, vol. 208, pp. 210-217, 2003.

[8] M. Zhou, Y. Li, Q. Hu, X. Li, J. Chen, "Investigations on edge quality and its effect on tensile property and fracture patterns of QP980", Journal of Manufacturing Processes, vol. 37, pp. 509-518, 2019.

[9] A. Sergueeva, J. Zhou, B. Meacham, D. Branagan, "Gage length and sample size effect on measured properties during tensile testing", Materials Science and Engineering: A, vol. 526, pp. 79-83, 2009.

[10] K. Mäntyjärvi, A. Väisänen, J. Karjalainen, "Cutting method influence on the fatigue resistance of ultra-high-strength steel", International Journal of Material Forming, vol. 2, pp. 547-550, 2009.

[11] D.M. Krahmer, R. Polvorosa, L.L. De Lacalle, U. Alonso-Pinillos, G. Abate, F. Riu, "Alternatives for specimen manufacturing in tensile testing of steel plates", Experimental Techniques, vol.40, pp. 1555-1565, 2016.

Biomedical Engineering

Computer Engineering

Electrical and Electronics Engineering

Mechanical Engineering

Mechatronic Engineering

Metallurgical and Materials Engineering

Civil Engineering

ICENTE'21

INTERNATIONAL CONFERENCE ON ENGINEERING TECHNOLOGIES

November 18-20, 2021

Konya/TURKEY

icente.selcuk.edu.tr